Study of Machinability of Metal Matrix Composites and its Effect on Surface Integrity

Nishita Anandan

A dissertation

submitted in partial fulfillment of the

requirements for the degree of

Doctor of Philosophy

University of Washington

2020

Reading Committee:

Ramulu Mamidala, Chair

Santosh Devasia

Ashis Banerjee

Program Authorized to Offer Degree:

Mechanical Engineering

© Copyright 2020

Nishita Anandan

University of Washington

Abstract

Study of Machinability of Metal Matrix Composites and its Effect on Surface Integrity

Nishita Anandan

Chair of the Supervisory Committee:
Professor Ramulu Mamidala
Mechanical Engineering

In recent years there has been growing interest in developing metal matrix composites, owing to their superior mechanical properties that can be tailored based on requirements. However, the reinforcement particles that strengthen the composite also lead to poor machinability. Often, these reinforcement particles are harder than the cutting tool material causing rapid tool wear which in turn, results in poor surface quality. Therefore, in order to avail the outstanding potential of metal matrix composites for structural components, it is imperative to study their machinability and fatigue performance.

Specifically, in this study, the machinability and surface integrity of functionally gradient SiCp/Al and SiCp/Mg were investigated through peripheral milling process. The functionally

gradient aluminum composites are typically used in disk brake applications that require gradient mechanical properties along the radius, while uniformly reinforced magnesium composites are finding applications in the aerospace and biomedical industries. The cutting forces, acoustic emissions, tool wear, and surface quality generated were analyzed as a function of feed rate and spindle speed. Statistical design of experiments approach was used, and the analysis of variance was performed to identify the significant parameters for these responses. Feed rate was observed to be the dominant parameter for both types of composites.

The surface integrity of the machined composite was evaluated through fatigue performance of milled coupons. The machining induced damage was found to have a significant effect on the fatigue life. In addition to the surface roughness parameters, the interaction between the reinforcement particles and the cutting edge were observed through SEM micrographs of the machined surface. Particle fracture, matrix cracking, voids due to particle debonding and particles pushed into the matrix were observed on the machined surface. The presence of voids and cracks resulted in poor surface finish and fatigue life.

Further, the events identified through SEM micrographs of the machined surface were used to develop a physics-based model to predict cutting forces in the peripheral milling of metal matrix composites. Three major events were considered, occurrence of particle fracture, plastic deformation of the metallic matrix and particles debonding due to mismatch in coefficient of thermal expansion. The probability of these events was calculated based on particle concentration and size in the matrix and was used to evaluate the contribution of each event to the total force experienced by the cutting edge. The predicted forces were in good agreement with the measured forces for lower feed rates from 0.1 to 0.765 mm/rev.

A major contribution of this study is to identify the effect of the presence of hard reinforcement particles dispersed in a ductile matrix in an intermittent cutting process like milling. Although, machinability of metal matrix composites has been studied for continuous cutting process like turning, the effect of repeated impact of cutting edge on the composite has not been reported extensively. In addition to the analysis of signals obtained during milling, a simple quantification technique was developed to measure the tool wear along the helical cutting edge using optical micrographs and adaptive thresholding technique. The cutting mechanism and machining induced surface defects were identified, and these observations were used to develop a physics-based model to predict the cutting forces generated based on the probability of each event.

Although secondary manufacturing processes like machining were found to have a significant effect on the fatigue life of composites, only the effects of primary manufacturing processes have been reported in the literature. In this study, the effect of machining induced surface damages were further investigated by evaluating the sub-surface damage and its effect on fatigue performance. Additionally, the fatigue crack initiation and propagation mechanism through the reinforcement particles, ductile matrix and particle-matrix interface has been investigated.

Table of Contents

Chapter 1 . Introduction 1

Chapter 2 . Literature Review 3

2.1 Metal matrix composites 3

2.2 Synthesis of Metal Matrix Composites 5

2.3 Strengthening mechanisms 7

2.4 Experimental work 11

2.4.1 Cutting forces 11

2.4.2 Tool wear 15

2.4.3 Surface finish 29

2.4.4 Chip morphology 37

2.5 Analytical Work 41

2.5.1 Prediction of cutting forces in machining metal matrix composites 41

2.5.2 Prediction of tool life 45

2.5.3 Mechanics of milling process 49

2.6 Mechanical properties and fatigue performance 53

2.6.1 Mechanical properties 54

2.6.1 Fatigue behavior 59

2.7 Summary 66

Chapter 3 . Research Goals and Objectives 70

3.1 Research scope 70

3.2 Research Goals 71

Chapter 4 . Material Characterization 74

4.1 Functionally gradient Al/SiCp 75

4.2 Tensile properties of functionally gradient Al/SiCp 82

4.3 Uniformly reinforced magnesium composite 86

5.4 Tensile properties of AZ91/SiCp/15% 88

Chapter 5 . Experimental Set up and Procedures 93

5.1 Cutting tool 93

5.2 Experiment set up 94

5.3 Initial tool alignment and cutting forces 96

5.3.1 Offset and Drift compensation 97

5.3.2 Forces in milling functionally gradient aluminum composite 105

5.3.3 Forces in milling of magnesium composite 107

5.4 Acoustic emission sensor 109

5.4.1 AE signal 109

5.5 Measurement of tool wear 110

5.6 Surface Topology 111

5.6.1 Surface Profiles 114

5.6.2 SEM micrographs 117

5.6.3 Chip Morphology 121

Chapter 6 . Machinability: Design of Experiments 125

6.1 Functionally gradient aluminum composite 125

6.2 Magnesium composite 127

Chapter 7 . Functionally gradient Al/SiCp 129

7.1 Cutting forces 129

7.2 Acoustic Emission 149

7.3 Investigation of tool wear 153

7.4 Surface topology 170

7.5 Chip morphology 181

7.6 Summary 195

Chapter 8 . AZ91/SiCp/15% 199

8.1 Cutting forces 199

8.2 Tool wear 205

8.3 Surface topology 216

8.4 Chip morphology 228

8.5 Summary 238

Chapter 9 . Analytical force model for end milling of magnesium composites. 240

9.1 Identification of events during milling 241

9.2 Development of force model 242

9.2.1 Determination of forces experienced by the element in contact with the matrix 244

9.2.2 Force experienced by the element when in contact with SiC particles 248

9.2.3 Determination of force experienced by the element when in contact with the particle and matrix 249

9.3 Comparison of predicted and experimental forces 252

9.4 Summary 255

Chapter 10 . Surface integrity of the machined composites 258

10.1 Aluminum Composite 260

10.1.1 Experiment setup and procedure 260

10.1.2 Machined surface topology 263

10.1.3 Fatigue performance 270

10.1.4 Summary 282

10.2 Magnesium Composites 283

10.2.1 Experimental set up and procedure 285

10.2.2 Surface topography of machined surface 288

10.2.3 Fatigue Performance 291

10.2.4 Summary 302

Chapter 11 . Conclusions and Future Research Recommendation 303

11.1 Conclusions 303

11.2 Future Research Recommendations 310

Reference 312

Appendix..... 327

List of Figures

Figure 2.1: SEM image at 2000X of the cutting edge after a cutting distance of 389 m[24].....19

Figure 2.2: Surface texture showing roughness, Waviness, Lay and Flaw.....30

Figure 2.3: Surface profile measured using a stylus probe. 31

Figure 2.4: SEM images of the machined surface at different feed rates on Al6061/SiCp in a turning operation[56]. 34

Figure 2.5: Subsurface generated in drilling ZC63/12%SiCp using cemented carbide-medium grain and PCD[34]. ...36

Figure 2.6: Chips formed during turning of ZK60A-T5 magnesium alloy reinforced with SiCp a) Free surface side of the chip indicating that ductile fracture is the main failure mechanism, b) free surface side of a chip showing extreme segmentation owing to the reduced ductility of the material[24].....39

Figure 2.7: a) Microcracking at tool-chip interface for Al6061/10/SiCp at a cutting speed of 16m/min and 0.3 mm depth of cut, b) shows the alignment of SiC particles with the flow lines in the shear zone[60].....40

Figure 2.8: Milling process , a) Up milling (conventional) , b) Down (climb) operation[70]. 50

Figure 2.9: Flute divided into elements along depth of cut, t_o.....51

Figure 2.10: UTS of aluminum composites as a function of volume fraction and size of the reinforcements. Data from [74,75,80–82]. 55

Figure 2.11: Ductility of aluminum composites as a function of volume fraction and size of the reinforcements. Data from [75–78,80].....56

Figure 2.12: SEM fractography of the fractured tensile specimen (the dog-bone-shaped, having a gage size of 6 mm in diameter and 40 mm in length,) showing dimples in the matrix, a) Al/SiCp/4.7 µm, showing particle decohesion, b) Al/SiCp/70.7µm, showing particle fragmentation[81] 57

Figure 2.13: UTS of magnesium composites as a function of volume fraction and size of the reinforcements. Data from [82,84,85].....58

Figure 2.14: SEM micrographs of AZ91/SiCp/0.2 µm(stir casted, extruded cylindrical coupons) a) 0.5% volume fraction, b) 5% volume fraction[83].....59

Figure 2.15: a) Cyclic behavior unreinforced aluminum matrix measured at different strain amplitudes, $\Delta\varepsilon p/2$, b) Cyclic behavior of Al/SiCp/20% measured at different strain amplitudes, $\Delta\varepsilon p/2$[91]. 61

Figure 2.16: Stress amplitude vs number of reversals for various Al/SiCp/20%[88].....62

Figure 2.17: Effect of volume fraction of reinforcement on the fatigue life of Al 2080/SiCp composite[71].....64

Figure 2.18: Crack propgatagation in fatigue of Al/SiCp[98].....65

.Figure 4.1: a) Centrifugally cast disk brake prior to machining, b) Section of the brake showing the increase in SiCp concentration.....75

Figure 4.2: Cross-section of the disk mounted in an epoxy mold. Optical micrographs were obtained from points 1 through 6. ..... *76*

Figure 4.3: a) Optical micrograph of functionally gradient Al/SiCp obtained from point 2, b) processed image with area of interest of 10000 μm^2 , c) Area of interest: 2.5 x 105 μm^2. ..... *77*

Figure 4.4: Reinforcement Percentage vs area of interest. *78*

Figure 4.5: Particle size distribution, X axis is the diameter of the particles in µm and Y axis is the count of the particles. *78*

Figure 4.6: Percentage reinforcement of SiC particles as a function of distance along the disk. *79*

Figure 4.7: SEM micrographs obtained from points along Al/SiCp *81*

Figure 4.8: a) Sketch of functionally gradient Al/SiCp disk before machining, b) a section of the disk is face milled to remove the dimples on the surface, c) Tensile specimen cut from faced section using waterjet, d) tensile specimen with dimensions in mm. *83*

Figure 4.9: : Stress-strain curve for functionally gradient Al/SiCp composite. *84*

Figure 4.10: Typical fractured Al/SiCp specimen in tensile testing *84*

Figure 4.11: SEM fractographs of functionally gradient Al/SiCp, a) at low magnification of 50 x, b) 500x, c and d) at 2000x. A: shows particle debonding from the matrix, B: fractured SiC particle, clearly visible cleavage lines, C: Matrix cracking, D: Matrix formin *85*

Figure 4.12: SEM image of AZ91/SiCp at a magnification of 1000x. *87*

Figure 4.13: Percentage reinforcement as a function of area of interest *87*

Figure 4.14: Particle size distribution in the matrix *88*

Figure 4.15: AZ91/SiCp/15% tensile specimen preparation, a) Extruded composite rod, b) disk face milled to a thickness of 3 mm, c) Tensile specimen machined from the face milled disk using abrasive waterjet, d) Tensile specimen with dimensions in mm. *89*

Figure 4.16: Stress strain curve for AZ91/SiCp/15%. *90*

Figure 4.17: SEM fractographs of specimen showing, A: SiC fractured along the plane with cleavage lines, B: Particle fracture perpendicular to the surface, C: dimples formed by the matrix *91*

Figure 5.1: Carbide cutting tool *93*

Figure 5.2: Experiment set up for peripheral milling of MMCs *95*

Figure 5.3: Kistler 9123 dynamometer showing the force measurement axis[108]. *96*

Figure 5.4: Schematic of a down milling process *99*

Figure 5.5: Preliminary data, Fx in peripheral milling of Al 6061-T6 at 635 mm/min and 6000 RPM. *100*

Figure 5.6: Offset compensated force data in peripheral milling of Al 6061-T6 at 635 mm/min and 6000 RPM. The red line represents the drift in the data. 102

Figure 5.7: Offset and drift compensated force data in peripheral milling of Al 6061-T6 at 635 mm/min and 6000 RPM. 102

Figure 5.8: Cutting forces experienced by the flutes aligned along y axis in 4 cutter rotations, a) Fy and Fr in climb milling, b) Fx and Ft in climb milling, c) Fy and Fr in conventional milling, d) Fx and Ft in conventional milling. 104

Figure 5.9: Cutting forces experienced by the flutes aligned along x axis in 4 cutter rotations, a) Fx and Fr in climb milling, b) Fy and Ft in climb milling, c) Fx and Fr in conventional milling, d) Fy and Ft in conventional milling. 105

Figure 5.10: Cutting forces, Fy, Fx and Fz measured at feed rate=0.05 mm/rev and S=1000 RPM. 107

Figure 5.11: Cutting forces, a) Fy, b) Fx and c) Fz generated in milling AZ91/SiCp/15% at a feed rate of 0.2 mm/rev and spindle speed of 1000 RPM. 108

Figure 5.12: Force and AE signal for Cast Al at 0.3 mm/rev and 1000 RPM. 110

Figure 5.13: Raw profile measured by the stylus probe. 111

Figure 5.14: Applying Gaussian filter to the raw data, a) Raw profile, shown in blue with the Gaussian profile mean line, b) Magnified view of the profile and the Gaussian mean line from 2 to 3 mm highlighted in a , c) Valleys below the mean line are removed 112

Figure 5.15: Surface roughness profile obtained after Gaussian filter. 113

Figure 5.16: Surface profiles of the milled Al/SiC surface 115

Figure 5.17: Surface Profiles of Mg/SiCp peripherally milled surface at a spindle speed of 1000, a) 0.254 mm/rev, b) 0.508 mm/rev, c) 0.762 mm/rev 116

Figure 5.18: SEM micrograph of machined surface at Zone A for 1000 RPM and 0.1 mm/rev. 117

Figure 5.19: SEM micrograph of machined surface at Zone A for 1000 RPM and 0.1 mm/rev. 118

Figure 5.20: SEM images of the machined surface at S=1000 rpm and F=0.1mm/rev. 118

Figure 5.21: SEM image of the workpiece machined at a feed rate of 0.254 mm/rev and 1000 RPM spindle speed 120

Figure 5.22: SEM image of the workpiece machined at a feed rate of 0.508 mm/rev and 1000 RPM spindle speed 120

Figure 5.23: SEM images of the chips formed at Zone C, machined at a feed rate of 0.1 mm/rev and 1000 RPM. ..122

Figure 5.24: SEM image of the chips at a feed rate of 0.254 mm/rev and 1000 rpm spindle speed 123

Figure 7.1: Geometry of the down-milling process, feed and speed in the same direction 130

Figure 7.2: Geometry of the up-milling process. 131

Figure 7.3: Cutting force for one cutter rotation. 133

Figure 7.4: Cutting forces, Fx, Fy and Fz measured at feed=0.05 mm/rev and spindle speed=1000 RPM. 135

Figure 7.5: Cutting forces, Fx, and Fy measured at feed=0.4 mm/rev and spindle speed=4000 RPM. 136

Figure 7.6: Feed force F_x in a) Zone A, b) B and c) C. 144

Figure 7.7: Radial forces, Fy in Zones a) A, b) B and c) C 146

Figure 7.8: Axial thrust forces in Zones a) A, b) B and c) C. 148

Figure 7.9: Feed force, Fx as a function of feed rate at 1000 RPM. 148

Figure 7.10: Root mean square of the acoustic emission(volts) vs material removal rate(function of speed and feed) 150

Figure 7.11: RMS as a function of feed, mm/rev for cast Al. 151

Figure 7.12: RMS value of AE as a function of feed rate and spindle speed for functionally gradient Al/SiCp. 152

Figure 7.13: Optical micrographs at 0.1 mm/rev and 1000 RPM of a,b) flutes of unused new tool c) BUE on flutes after a cutting distance of 96 mm (Zone A to C) , e,f) flutes after sonication 154

Figure 7.14: Optical micrographs at 0.1 mm/rev and 4000 RPM of a,b) flutes of unused new tool c) BUE on flutes after a cutting distance of 96 mm (Zone A to C), e,f) flutes after sonication 155

Figure 7.15: Optical micrographs at 0.4 mm/rev and 1000 RPM of a,b) flutes of unused new tool c) BUE on flutes after a cutting distance of 96 mm (Zone A to C), e,f) flutes after sonication 156

Figure 7.16: Optical micrographs at 0.4 mm/rev and 4000 RPM of a,b) flutes of unused new tool c) BUE on flutes after a cutting distance of 96 mm (Zone A to C), e,f) flutes after sonication 157

Figure 7.17: Tool wear measurement, a) Optical micrograph of the left flute after a cutting distance of 64 mm at 0.1 mm/rev and 3000 rpm, b) the boundary of the wear is identified, shown in A, c and d) the width of the wear is measured between the linear fit lines 160

Figure 7.18: Tool wear(µm) as a function of spindle speed(RPM) and feed rate(mm/rev). 162

Figure 7.19: Tool nose rounding at 0.4 mm/rev after 96 mm of milling after 15 seconds for 1000 RPM and 4 seconds for 5000 RPM 164

Figure 7.20: SEM micrographs of the cutting tool at 0.1 mm/rev and 1000 RPM. 165

Figure 7.21: SEM micrographs of the cutting tool at 0.3 mm/rev and 3000 RPM. 167

Figure 7.22: SEM micrographs of the cutting tool at 0.4 mm/rev and 4000 RPM. 169

Figure 7.23: Average surface roughness, R_a at Zones, a) A, b) B and c) C. 171

Figure 7.24: Surface topography in Zone A at 0.2 mm/rev and 2000 RPM. 175

Figure 7.25: Surface topography in Zone B at 0.2 mm/rev and 2000 RPM. 177

Figure 7.26: Surface topography in Zone C at 0.2 mm/rev and 2000 RPM. 178

Figure 7.27: Rz as a function of feed rate(mm/rev) and spindle speed(RPM) a) Zone A, b) Zone B and c) Zone C....180

Figure 7.28: Optical micrograph at 40x of chips at 0.1 mm/rev and 1000 RPM, red circle highlights tearing at the free surface. 183

Figure 7.29: Optical micrographs at 40X of chips a) 0.3 mm/rev 4000 RPM ,b) 0.4 mm/rev and 5000 RPM, red circle highlights tearing at the free surface. 184

Figure 7.30: SEM micrographs of chips at 0.1 mm/rev and 1000 RPM obtained from Zone C.....185

Figure 7.31: SEM micrographs of chips at 0.1 mm/rev and 1000 RPM obtained from Zone B.....186

Figure 7.32: SEM micrographs of chips at 0.1 mm/rev and 1000 RPM obtained from Zone A. 187

Figure 8.1: Cutting forces, Fy, Fx and Fz measured at feed=0.1 mm/rev and spindle speed=1000 RPM.....200

Figure 8.2: Cutting forces as a function of spindle speed and feed rate, a) Fx, b) Fy and Fz 201

Figure 8.3: Optical micrographs of (a, b) Left and right flutes, respectively, of square end carbide cutting tool as purchased, (c, d) Left and right flutes, respectively after a cutting distance of 64 mm at 0.5 mm/rev and 2000 RPM. 206

Figure 8.4: Tool wear measurement, a) Optical micrograph of the left flute after a cutting distance of 64 mm at 0.05 mm/rev and 3000 rpm, b) the tool wear is highlighted in white and the boundary of the wear is identified, c) the width of the wear is measured between the linear fit lines of the boundary at 120 µm from the tip multiplied by (0.1mm/30 pixels).....207

Figure 8.5: Tool wear(µm) as a function of feed rate(mm/rev) and spindle speed(RPM) 208

Figure 8.6: SEM image of a new cutting edge at 500x and 2000x magnification respectively.....211

Figure 8.7: SEM images of the cutting edge after machining 64 mm at 0.5 mm/rev and 4000 RPM. 213

Figure 8.8: SEM images of the cutting edge after machining 64 mm at 0.05 mm/rev and 1000 RPM 214

Figure 8.9: SEM images of cutting edge after machining 64 mm at 0.3 mm/rev and 1000 RPM 215

Figure 8.10: Surface profiles at 4000 RPM a) 0.05 mm/rev, b) 0.2 mm/rev and c) 0.5 mm/rev. 216

Figure 8.11: R_a plotted as a function of feed rate(mm/rev) and spindle speed(RPM).....217

Figure 8.12: R_q plotted as a function of feed rate(mm/rev) and spindle speed(RPM).....218

Figure 8.13: 3D primary surface profiles obtained at 1000 RPM, a) 0.254 mm/rev, b) 0.508, c) 1.27 mm/rev 220

Figure 8.14: Area height parameters, Sa, and Sz as a function of feed rate and spindle speed.....221

Figure 8.15: Average waviness, W_a vs feed rate, mm/rev. 223

Figure 8.16: Mg/SiCp machined surface at 0.254 mm/rev and 1000 RPM. 224

Figure 8.17: Mg/SiCp machined surface at 0.762 mm/rev and 1000 RPM, rectangle highlighting the SiCp along the grooves 225

Figure 8.18: Mg/SiCp machined surface at 1.27 mm/rev and 4000 RPM.....226

Figure 8.19: Optical micrographs of chips at 40x, a)0.762 mm/rev and 4000 RPM b) 0.762 mm/rev and 5000 RPM 230

Figure 8.20: SEM micrographs of chips generated at 0.05 mm/rev, 3000 RPM.....231

Figure 8.21: SEM micrographs of chips generated at 0.3 mm/rev at 3000 RPM 233

Figure 9.1: Elements along the cutting edge, in contact with only matrix, particle and a combination of particle and matrix, the forces exerted on an individual element. 243

Figure 9.2: (a)Optical micrograph of Mg/SiCp/15%, image processing is used to identify the size of the particles, b) counts and particle size distribution. The average particle size is 3 µm. 243

Figure 9.3: a) Feed force, Fx, b) radial thrust force, Fy and c) axial thrust force, Fz obtained in peripheral milling of AZ31 are shown as a function of feed and spindle speed.....247

Figure 9.4: Measurement of temperature at the cutting edge using Infrared camera. 250

Figure 9.5: Temperature at the cutting edge as a function of feed, mm/rev and speed, RPM. 250

Figure 9.6: Predicted and experimental force as a function of spindle rotation angle, a) feed: 0.2 mm/rev and spindle speed: 4000, b) feed 0.3 mm/rev and spindle speed: 3000 rpm.....253

Figure 9.7: Predicted and experimental forces as a function of feed and spindle speed, a) Fx, feed force, b) Fy, radial thrust force, c) Fz, axial thrust force 255

Figure 10.1: Schematic of specimen fabrication. All dimensions are in mm.....261

Figure 10.2: 3D view of the fatigue specimen showing the face milled surface (S1), peripherally milled surface(S2). 262

Figure 10.3: Typical surface roughness profiles of peripherally milled surface, S2 and face milled surface, S1.....266

Figure 10.4: SEM micrograph of Peripheral milled surface(S2) , a) 0.1 mm/rev, 1000 RPM, b) 0.1 mm/rev, 3000 RPM, c) 0.3 mm/rev, 1000 RPM, d) 0.3 mm/rev, 3000 RPM, e) Face milled surface at 0.3 mm/rev, 3000 RPM. 267

Figure 10.5: SEM micrographs of the peripherally milled surface showing matrix cracking, voids and SiC particles pushed into the surface. 268

Figure 10.6: Cross-section of the machined specimen showing the sub-surface plastic deformation, a) Peripherally milled at 0.1 mm/rev and 1000 RPM, b) Peripherally milled at 0.1 mm/rev and 3000 RPM, c) Face milled at 0.3 mm/rev and 3000 RPM 269

Figure 10.7: Microhardness measurements along the sub-surface, a) Optical micrograph of the sub surface showing Knoop indentation in step pattern, b) variation in average Knoop hardness as a function of distance from the machined surface.....270

Figure 10.8: Fatigue life of the machined coupons, the arrows indicate experiment run out, the specimen did not fail at five million cycles.....272

Figure 10.9: Optical micrographs of fractured surfaces, a) 1000 RPM, 0.1 mm/rev, 0.6S_{ut}, b) 1000 RPM, 0.1 mm/rev, 0.8, c) 3000 RPM, 0.1 mm/rev, 0.6S_{ut}, d) 3000 RPM, 0.1 mm/rev, 0.8S_{ut}, e) 1000 RPM, 0.3 mm/rev, 0.6S_{ut}, f) 1000 RPM, 0.3 mm/rev, 0.8S_{ut}, g) 3000 RPM, 0.3 mm/rev, $0.6Sut$, h) 3000 RPM, 0.3 mm/rev, $0.8Sut$. S2: Peripheral milled, S1: Face milled 275

Figure 10.10: SEM micrograph of fractured surface at 0.1 mm/rev and 3000 RPM at $0.6Sut$, a) 1000 x, showing the SiC particles and aluminum matrix, b) Magnified to 4000x, Region A: Fractured SiC showing cleavage line, B: matrix cracking, C: matrix forming dimples, c and d) EDS map showing aluminum and SiC respectively, e) 2000x, showing embedded SiC particle and matrix, f) Magnified to 4000x, region D: fractured SiC particles, E: Particle debonding from the matrix, g and h) EDS map showing aluminum and SiC respectively. 277

Figure 10.11: SEM micrograph of fractured surface at 0.3 mm/rev and 3000 RPM at $0.6Sut$, a) 1000 x, showing the SiC particles and aluminum matrix, region B: matrix cracking, D: fractured SiC particles, b) Magnified to 4000x, Region A: Fractured SiC showing cleavage line, C: matrix forming dimples, E: Particle debonding from the matrix, c and d) EDS map showing aluminum and SiC respectively, e) 2000x, showing embedded SiC particle and matrix, f) Magnified to 4000x, showing aluminum and SiC particles, g and h) EDS map showing aluminum and SiC respectively 279

Figure 10.12:SEM micrograph of fractured surface at 0.3 mm/rev and 1000 RPM at $0.6Sut$, a) 1000 x, showing the SiC particles and aluminum matrix, region A: Fractured SiC showing cleavage line, B: matrix cracking, C: matrix forming dimples, D: fractured SiC particles, and b and c) EDS map of (a) showing aluminum and SiC respectively, d) 1000x, showing embedded SiC particle and matrix, e and f) EDS map of (d) showing aluminum and SiC respectively 281

Figure 10.13: Schematic of steps involved in specimen fabrication. All dimensions are in mm. 286

Figure 10.14: Typical surface profiles of machined surfaces 289

Figure 10.15: SEM micrograph of surfaces peripherally milled edge (thickness) surface and face milled flat surface (width). 291

Figure 10.16: SEM micrographs of the machined surface showing voids(A), matrix cracking(B), particle agglomeration(C).....291

Figure 10.17: Maximum stress ratio vs Number of cycles to failure for machined magnesium composites, $Sut = 360\ MPa$ 292

Figure 10.18: Optical micrographs of fractured surfaces, a) 1000 RPM, 0.1 mm/rev, $0.6Sut$, b) 1000 RPM, 0.1 mm/rev, 0.8, c) 3000 RPM, 0.1 mm/rev, 0.6, d) 3000 RPM, 0.1 mm/rev, $0.8Sut$, e) 1000 RPM, 0.3 mm/rev, $0.6Sut$, f) 1000 RPM, 0.3 mm/rev, $0.8Sut$, g) 3000 RPM, 0.3 mm/rev, $0.6Sut$, h) 3000 RPM, 0.3 mm/rev, $0.8Sut$., arrow indicates crack initiation from peripherally milled surface.....294

Figure 10.19: SEM micrographs of crack initiation site, arrow indicates the crack origin.....295

Figure 10.20: SEM micrographs obtained at 0.1 mm/rev, 1000 RPM, $0.6Sut$, a) Fractured surface at 2000x, region E: ductile fracture of the matrix with smaller particles embedded, b) magnified view at 4000x, region A: cleavage lines typical for brittle fracture, B: particle fracture perpendicular to the fractured surface, C: voids due to particle pull out, c and d) EDS maps of (a) showing Si and Mg respectively, e) Fractured surface at 8000x, region D: matrix cracking, f and g) EDS maps of (e) showing Mg and Si respectively. 297

Figure 10.21: SEM micrographs obtained at 0.1 mm/rev, 3000 RPM, $0.6Sut$, a) Fractured surface at 2000x, showing particle-matrix debonding , b and c) EDS map of (a) showing Mg and Si respectively, d) Fractured surface at 2000x, showing particle fracture and ductile failure of the matrix , e and f) EDS map of (d) showing Mg and Si respectively 300

Figure 10.22: SEM micrographs obtained at 0.3 mm/rev, 1000 RPM, $0.6Sut$*, a) Fractured surface at 4000x, showing particular fracture, voids and matrix cracks , b and c) EDS map of (a) showing Mg and Si respectively, d) Fractured surface at 2000x, showing cleavage lines due to SiC fracture, e and f) EDS map of (d) showing Mg and Si respectively. 301*

List of Tables

Table 2.1: Metallic matrix properties *4*

Table 2.2: Reinforcement and cutting tool material hardness comparison *5*

Table 2.3: Tool wear investigations performed on magnesium matrix composites *21*

Table 2.4: Machining experiments performed on aluminum matrix composites *24*

Table 2.5: Surface Roughness parameters and equations *32*

Table 4.1: Chemical composition of aluminum matrix composite[65] *74*

Table 4.2: Chemical composition of magnesium matrix composite[103] *74*

Table 4.3: Zones with corresponding average particle concentration *81*

Table 5.1: End mill specifications *94*

Table 5.2: HAAS Tool Mill TM 1P specifications *94*

Table 5.3: Experimental conditions for peripheral milling of Al 6061-T6 ..... *98*

Table 6.1: Experiment conditions for aluminum matrix composite *125*

Table 6.2: Design of experiments for aluminum composite *126*

Table 6.3: Experiment conditions for magnesium matrix composite *127*

Table 6.4: Design of Experiments for magnesium composites *128*

Table 7.1: Zones with corresponding average particle reinforcement *134*

Table 7.2: : Response surface models for cutting forces in Al/SiCp *138*

Table 7.3: ANOVA results for Fx in Al/SiCp for Zone A *139*

Table 7.4: ANOVA results for Fy in Al/SiCp for Zone A *139*

Table 7.5: ANOVA results for Fz in Al/SiCp for Zone A *140*

Table 7.6: ANOVA results for Fx in Al/SiCp for Zone B *140*

Table 7.7: ANOVA results for Fy in Al/SiCp for Zone B *141*

Table 7.8: ANOVA results for Fz in Al/SiCp for Zone B *141*

Table 7.9: ANOVA results for Fx in Al/SiCp in Zone C *142*

Table 7.10: ANOVA results for Fy in Al/SiCp in Zone C *142*

Table 7.11: ANOVA results for Fz for Al/SiCp in Zone C *143*

Table 7.12: ANOVA table for tool wear model *163*

Table 7.13: Quadratic equation for R_a *173*

Table 7.14: ANOVA results for R_a in Zone A *173*

Table 7.15: ANOVA results for Ra in Zone B *174*

Table 7.16: ANOVA results for Ra in Zone C *174*

Table 7.17: Geometry of chips at different feed rates and spindle speeds. *182*

Table 8.1: Model for the cutting forces *203*

Table 8.2: Analysis of variance for Fx *203*

Table 8.3: Analysis of variance for Fy *204*

Table 8.4: Analysis of variance for Fz *204*

Table 8.5: Analysis of variance for tool wear *209*

Table 8.6: ANOVA results for Ra *219*

Table 8.7: Analysis of variance for S_a *222*

Table 8.8: Geometry of chips at different feed rates and spindle speeds. *229*

Table 9.1: Probability of an element encountering a particle of a given size. *244*

Table 9.2: Cutting conditions for AZ31 ..... *245*

Table 9.3: Cutting force coefficients and exponents for AZ31 magnesium alloy *247*

Table 10.1: Cutting tool and machining conditions *262*

Table 10.2: Average Surface Roughness parameters for face milled surface, S1 and peripherally milled surface, S2 ..... *265*

*Table 10.3: Fatigue life of the machined coupons, * indicates that the coupon has not failed* *271*

Table 10.4: Cutting tool and machining conditions *287*

***Table 10.5:** Average surface Roughness of face milled surface and peripherally milled surfaces* *289*

Acknowledgment

I would like to express my sincere gratitude to the Mechanical Engineering department, University of Washington for providing me the opportunity to use the Mechanical Testing Lab which enabled me to complete my PhD work. I am grateful to my adviser, Prof. Ramulu for his support and knowledge. Besides my advisor, I would also like to thank my PhD committee, Prof. Santhosh Devasia, Prof. Ashis Banerjee and Prof. Archis Ghate for their time and insightful comments. My sincere thanks to Mr. Bill Kuykendall and Eamon McQuaide for their time in training me use the ME research facilities.

Heartfelt thank you to my lab mates, Dr. Rishi Pahuja, Dr. Bryan Ferguson, Dr. Kapil Gangwar and current lab members for the stimulating discussions and reliable support. My extended thanks to Dr. Pahuja for training me and helping maintain numerous equipment in the lab. My acknowledgement will not be complete without expressing my sincere thanks to my husband, Dr. Rahul Warrier, for the constant encouragement and proofreading my papers and my parents, for their patience and support.

Dedication

Dedicated in memory of my grandfather, R.K. Ramachandran, who has always been a source of inspiration for me.

Chapter 1 . Introduction

Automotive and aerospace industries are moving towards developing technologies that offer enhanced performance with high fuel efficiency and reduced emissions. To achieve this, it is imperative to develop and study materials with high strength to weight ratio in addition to high wear and corrosion resistance leading to the development of wide range of composites[1–4]. Metal matrix composites(MMCs) are metallic matrices reinforced with hard reinforcement particles or fibers to significantly improve the properties of the monolithic metal alloys. The most common reinforcements are silicon carbide, boron carbide, aluminum oxide, aluminum nitride and graphene nanotubes. While, magnesium, aluminum, copper and titanium are typically used as the matrix material. [5–8]. The properties of MMCs can be tailored to suit a specific application by choosing the appropriate matrix alloy, the concentration and type of reinforcement and by engineering the matrix-reinforcement interface.

Specifically, there has been a lot of interest in development of metal matrix composites based on light weight structural metals like aluminum and magnesium. Aluminum alloy is the most preferred matrix alloy due to its high specific strength, stiffness, toughness, and impact resistance. The melting point of aluminum is high enough for most operating conditions while being sufficiently low for composite processing. In addition, MMCs with magnesium alloy matrix are also gaining preference due to its excellent properties , good castability, high damping capacity and electromagnetic shielding[4]. Among the reinforcements, silicon carbide particles are the most preferred due to their high modulus and strength, good corrosion and thermal resistance and compatibility with metal alloys. However, owing to the higher hardness and strength of the

reinforcements, machining of these composites becomes challenging due to rapid tool wear, leading to poor surface integrity of the machined components.

The focus of this research is to study the machinability and surface integrity of functionally gradient aluminum matrix composite, A359/SiC/12.8μm and magnesium matrix composite, AZ91/SiC/20p/3.5μm. The machinability of the composites is measured in terms of cutting forces and acoustic emission generated and amount of tool wear in a peripheral milling operation. Further, the mechanism of material removal and the interaction of the reinforcement particles with the cutting edge was identified through examination of scanning electron microscope images of the machined surface and the chips generated. The particles were either pushed into the workpiece or into the chip and eventually removed from the workpiece or were fractured by the sharp cutting edge. In addition, the surface integrity of the machined surface was evaluated through surface roughness and fatigue performance of milled compact specimen. Tensile tests were performed to identify the ultimate tensile strength of compact specimen and fatigue tests were performed to evaluate the effect of machining conditions on the fatigue life of the composites.

A physics-based model was developed to predict the cutting forces in milling of the magnesium composites. The forces exerted on the cutting tool during the interaction of reinforcement particles with the cutting edge are considered in this model.

Chapter 2 . Literature Review

2.1 Metal matrix composites

Metal matrix composites(MMCs) consists of light weight metallic matrix reinforced with ceramics of high strength and hardness. Typically, the reinforcement of metals results in increased specific strength and stiffness, improvement in creep resistance in comparison to conventional alloys, increased fatigue strength, thermal shock resistance, corrosion resistance and reduction in thermal elongation. Like other composites, the properties of metal matrix composites are highly tailorable depending on the type of metallic matrix and reinforcements used.

Commonly, aluminum, magnesium, titanium, copper and cobalt are used as the matrix material, properties listed in Table 2.1. The choice of matrix material used depends on the requirements of the specific applications. For example, Aluminum alloys exhibit excellent strength, toughness and corrosion resistance with a low density making it suitable for aerospace industries. Magnesium alloys have received great attention due to its very low density and natural availability. Casted magnesium alloys are particularly used in aircraft gearbox housings, chain saw housing and electronic equipment[9]. Titanium alloys have high specific strength and stiffness, good corrosion and oxidation resistance and retain these properties even at elevated temperatures. Owing to the high temperature resistance, titanium alloys are used in turbine and compressor blades in jet engines and fuselage parts. The properties of these alloys can be further enhanced by the addition of suitable reinforcements.

While, the reinforcements include silicon carbide(SiC), boron nitride(B_4C) and titanium carbide(TiC) particles[10–12]. Generally, reinforcements have low density, chemical and mechanical compatibility, high modulus, compression and tensile strength. Additionally, the

reinforcements can be in the form of particles, whiskers or fibers. Specifically, composites reinforced with particles tend to have higher hardness and improved stiffness and strength at a reasonable cost. For example, SiC and B_4C are inexpensive commercial abrasives that provide high wear resistance and improved specific stiffness, while, TiC offers high melting point and chemical inertness. While, the fiber reinforced MMCs show dramatic improvements in mechanical properties but manufacturing costs remain high.

Table 2.1: Metallic matrix properties

Matrix	Strength	Stiffness	Ductility	Melting Temperature
Aluminum	100-570 MPa	67-140 GPa	2.67 g/cc	554-662° C
Magnesium	165-275 MPa	44-80 GPa	1.8 g/cc	550-623° C
Titanium	870-1150 MPa	110-120 GPA	4.3-5.1 g/cc	1672° C

* Aluminum based on 6000 series[13]
* Magnesium based on AZ series[14]
* Titanium based on Ti_6Al_4V[15]

Several processing techniques are available to manufacture MMCs. Manufacturing methods for MMCs should produce good interfacial bond between the matrix and the reinforcements and not produce undesirable reactions at the interface weakening the bond. A few key manufacturing techniques are discussed in section 2.2. The improved strength of the MMCs produced with good interfacial bond can be attributed to five strengthening mechanisms, discussed in section 2.3 depending on the matrix material used.

Although the reinforcements serve to improve the properties of the metallic matrix, the abrasive nature of the reinforcement leads to accelerated tool wear. The hardness of the reinforcements is typically higher than the cutting tool materials, shown in Table 2.2 leading to rapid abrasive wear of the cutting edge. The rapid tool wear results in poor tool life, higher cutting forces and damages induced on the machined surface. This reduces the machinability of composites and is addressed in detail in section 2.4.

Table 2.2: Reinforcement and cutting tool material hardness comparison

Reinforcements	Hardness	Cutting tool material	Hardness
Al_2O_3 [16]	800-2400 HV	WC[17]	1600-1800 HV
SiC[18]	2400-3500 HV	TiC/TiCN[17]	3000-3100 HV
B_4C [19]	3000-3700 HV	PCD[17]	5000-8000 HV

In this study, functionally gradient aluminum composite reinforced with SiC particles and magnesium composites reinforced with SiC particles are investigated. The influence of SiC particles on the machinability of the composites are investigated in terms of cutting forces, acoustic emissions, tool wear and the machined surface topology. In addition, the surface integrity of the machined composites are studied through fatigue testing.

2.2 Synthesis of Metal Matrix Composites

Although MMCs show promising mechanical and thermal properties, their usage has been limited by expensive processing operations and the cost of the final product. The MMCs can be fabricated

using many techniques listed below.

Solid state processing

Solid state processing is employed when superior mechanical properties of MMCs are essential for a specific application. This processing technique minimizes the segregations effect and the precipitation of brittle byproducts, preserving the high strength of MMCs. In powder metallurgy, the metallic powder and reinforcements are blended to form a uniform mixture followed by the application of uniform pressure to form green compacts. These compacts are then forged or extruded into desired shapes.

Liquid state processing

Liquid state processing is the most commercially used technique to produce MMCs. Liquid state processing inherently has many advantages over solid state processing. Liquid metals are cheaper and easier to handle than metal powders. Existing processes like casting can be used to produce wide variety of shapes.

Infiltration technique

Porous body of reinforcement is formed within a mold and a molten alloy is infiltrated into the mold. The molten metal fills the pores to form a composite. The important parameters that decide the properties of the composites are, the initial composition, morphology, applied pressure, volume fraction and temperature of reinforcements and matrix material.

Dispersion process

Dispersion process is currently the most economical processing technique available for fabricating MMCs. In this process, the reinforcements are incorporated into the molten matrix. Mechanical force is applied when the reinforcements are added to the liquid metal to improve the wettability of the reinforcement. The mechanical force is generally applied in the form of stirring. The molten metal and reinforcements are vigorously stirred together for a prolonged time. However, the prolonged interaction between the molten matrix and the reinforcement promotes the formation of brittle byproducts. This limitation can be circumvented by the addition of appropriate agents to reduce the rate of reaction.

Spray process

Droplets of liquid molten metal is sprayed along with the reinforcements onto a substrate. The critical parameters that affect the properties of the composite are the initial temperature, size distribution and velocity of the droplets, temperature, and feed rate of the reinforcement particles.

2.3 Strengthening mechanisms

There are five major strengthening mechanisms attributed to the strengthening of the matrix alloy through the addition of hard reinforcement particle.

a) *Orowan strengthening mechanism*: Orowan strengthening occurs as a results of the resistance offered by the reinforcement particles to the movement of dislocation by work hardening around the reinforcements[20]. The contribution of Orowan strengthening is given by Orowan-Ashby equation

$$\sigma_{orowan} = \frac{0.13 * G * b}{\lambda} * ln\left(\frac{r}{b}\right) \quad (2.1)$$

where, G is the shear modulus of the matrix alloy, b is the Burgers vector, r is average radius of the particles and λ is the inter-particulate spacing and is given by the equation,

$$\lambda = d_p\left[\left(\frac{1}{2V_p}\right)^{\frac{1}{3}} - 1\right] \quad (2.2)$$

where, d_p is the average diameter and V_p is the volume fraction of the reinforcements.

b) *Hall-Petch effect*: Hall-petch strengthening refers to the strengthening of the material resulting from grain refinement[4]. Grain sizes are inversely proportional to strength of the material. Smaller grain sizes have higher grain boundaries that can impede the movement of dislocation resulting in materials exhibiting higher strength. The addition of reinforcement particles reduces the grain size of the matrix material thereby strengthening the MMC. The Hall-Petch equation is given by,

$$\sigma_{Hall-Petch} = KD^{-0.5} \quad (2.3)$$

where, K is the Hall-Petch coefficient, and D is the average grain diameter of the matrix alloy. The relationship between the grain size of the composite, average diameter of the particles and volume fraction of the reinforcements is given by[21],

$$d_m = \frac{4\alpha d_p}{3V_p} \quad (2.4)$$

where, α is the proportionality constant, d_p is the average diameter of the particles and V_p is the

volume fraction of the reinforcements.

c) *Forest strengthening*: This is a mechanism in which strengthening occurs due to the mismatch in the coefficient of thermal expansion (CTE) between the matrix and the reinforcement particle. The mismatch in CTE leads to the formation of several dislocations around the reinforcement particles. This increase in dislocation density impedes the movement of dislocations in the matrix. The equation describes the forest strengthening,

$$\sigma_{CTE} = A * M * G * b * \rho_{th}^{0.5} \tag{2.5}$$

$$\rho_{th} = \frac{12 * \sqrt[2]{2} * \Delta\alpha * \Delta T * f}{b.d.(1-f)} \tag{2.6}$$

where A is the characterizing constant that depends on the basal-basal interaction in the matrix alloy, ρ_{th} is the dislocation density, $\Delta\alpha$ is the difference in CTE between the reinforcement and the matrix material, ΔT is the temperature difference, G is the shear modulus, and M is the Taylor factor .

d) *Taylor strengthening*: In this mechanism, the strengthening occurs because of mismatch in the modulus of the reinforcement and the matrix material. This mismatch introduces necessary geometrical dislocations in the matrix under an external load. The high density of dislocations contributes towards strengthening the composite. The Taylor strengthening is expressed as,

$$\sigma_{EM} = \sqrt{3} * \alpha * G * b * \sqrt{\rho_{EM}} \tag{2.7}$$

$$\rho_{EM} = \frac{6V_p}{\pi * d^3} \tag{2.8}$$

where α is a constant, ρ_{EM} is the density of dislocation due to the modulus mismatch.

e) *Load transfer:* The MMCs get strengthened due to the load transfer from the matrix to the hard reinforcements. The strength can be expressed as,

$$\sigma_{LT} = 0.5 * V_p * \sigma_M \tag{2.9}$$

where, σ_M is tensile yield strength of the matrix.

In general, from the above equations it can be observed that the strength of MMCs depend on the size of the reinforcements and the strength increases as the particle size decreases. The volume fraction of the reinforcement plays a critical role in strengthening the MMC, higher the volume fraction greater is the improvement in the strength. Finally, the processing technique used in producing MMC also plays a major role, the uniform dispersion of the reinforcements in the matrix is the key to strengthening the matrix[4].

The dominant strengthening mechanism in Al/SiC composites was observed to be the Forest strengthening mechanism where increase in the density of dislocation and decrease in sub grain size results from the mismatch in coefficient of thermal expansion between SiC and Al matrix. Also, the strengthening of the composite due to load transfer was found to be the least contributing mechanism towards strengthening[22]. For Mg/SiC composites, Orowan strengthening mechanism was found to be the most dominant mechanism especially when the size of reinforcement particle is less than 1 μm and Hall-Petch strengthening mechanism becomes dominant when the particle size is greater than 1 μm. The contribution from Forest strengthening was found to be negligible for Mg/SiC composites. The Forest strengthening mechanism and load

transfer were only significant for high volume fraction of the reinforcement[23].

2.4 Experimental work

Machinability can be measured based on requirement, from cost point of view, machinability can be defined as the amount of material that can be machined before tool replacement or the time taken to finish a machining operation, from quality point of view, it can be quantified in terms of the quality of the surface and subsurface generated, or it can evaluated in terms of cutting forces generated during the machining process. Specifically, the challenges in machining aluminum and magnesium composites in terms of cutting forces, acoustic emissions, tool wear encountered, and surface topology generated are discussed in this section.

2.4.1 Cutting forces

Cutting forces indicate the mechanical stresses experienced by the cutting edge and the workpiece. These forces increase as the sharp cutting edge of the tool wears out and as the workpiece material adheres to the cutting edge forming a built up edge. Tool wear and formation of built up edge produces poor surface finish on the surface. Also, the cutting force is a function of temperature at the chip-tool and work-tool interface. Hence, the cutting and the thrust forces obtained during a machining process can be used to access the machinability of the material. While machining MMCs, the cutting forces are higher than machining conventional alloys. This is due to the presence of hard reinforcement particles that accelerate tool wear causing blunting of the cutting edge. Blunt cutting edge leads to higher cutting forces since the tool pushes rather than cutting the material leading to poor surface integrity. However, the cutting forces exerted during machining

of metal matrix composites are not extensively investigated. This section discusses the few studies that have reported the cutting forces generated while turning and drilling of aluminum and magnesium matrix composites[6,24–27]

The feed force, cutting force and the thrust force in facing of ZK60A-T5/20% SiCp was studied by Pedersen et al[24]. The cutting forces were observed to be constant throughout the run although the cutting speed decreased with the facing operation as the diameter of the workpiece decreased from 55.4 mm to 0. Similarly, side cutting angle did not show any significant influence on the cutting forces since small depth of cut and feed used in the study confined the tool engagement to the nose radius. Cutting force was found to increase significantly with the increasing feed rate and depth of cut. This can be attributed to the increase in material removal rate.

In a similar study performed by Manna and Bhatacharya, cutting forces in turning Al/SiCp/15% were reported[25]. The feed and the thrust forces were found to increase significantly with the increasing feed. However, these forces were observed to decrease with increasing cutting speed at a constant feed rate of 0.5 mm/rev and depth of cut of 0.5 mm. This observation was attributed to the decrease in the formation of the built-up edge with increasing cutting speed. However, Antonio et al[28] reported a rapid increase in cutting forces at higher cutting speed due to high flank wear of the tool in turning of A356/SiCp/20%-T6 with PCD tools. The increase in cutting force was observe to be more gradual at lower cutting speeds[28].

Additionally, the cutting forces were also influenced by the tool materials. The cutting tool materials with lower coefficient of friction and high hardness experienced a much lower frictional

force. This was studied by Tomac et al[29] by comparing the forces generated in turning of aluminum matrix composites with tungsten carbide tool and PCD tool. The cutting forces for PCD remained relatively constant over time in comparison to cemented carbide tools. The cutting force increased from 60 N to 370 N in 3.5 mins for cemented carbide tool, while for PCD the cutting force only increased marginally after 40 mins. As discussed earlier, the superior performance of PCD is due to its high thermal conductivity which prevents the raise of the cutting temperature, low coefficient of friction that reduces the frictional force at the tool-chip and tool-workpiece interface and lack of chemical affinity towards the workpiece material.

Similar observations were also made in a drilling operation, where the tool has multiple cutting edges, Weinert et al performed extensive studies on machinability of magnesium and its composites[26]. For carbide tools, the feed force increased rapidly from 450 to 1100 N in a short drilling distance of 75 mm, while for PCD tools the feed force only increased marginally for upto 400 mm of drilling distance. In addition, the authors also compared the feed force and drilling torque in machining QE22/Al_2O_3/20%, AZ91/A_2O_3/20% and ZC63/SiCp/12% composites. Reinforcements in the form of fiber or particles led to higher feed force. The feed force is reported to be highest for particle reinforced composites followed by the fiber reinforced composites[26]. Correspondingly, Ramulu et al performed drilling on 10% and 20% reinforced Al6061/Al_2O_3 composites using HSS, carbide and PCD tools[30] and reported that the drilling forces and torque were found to be dependent on the tool-material combinations. The cutting force experienced by HSS tools were the highest, owing to high tool wear experienced by the soft HSS tools[31]. Between carbide and PCD tools, PCD tools produced the lowest cutting force. The forces also drastically increased when the % reinforcement was doubled from 10 to 20% Al_2O_3.

Additionally, to mitigate the effects of reinforcements like SiC, Al_2O_3 and B_4C few studies have reinforced magnesium matrix with graphene to improve the machinability of the composite[32,33]. Graphene serves to reduce the friction between the cutting edge and the reinforcement particle, thereby reducing the tool wear and improving the machinability of composites [32]. The thrust force was measured as a function of feed, cutting speed and tool material in a drilling operation, listed in Table 2.3. In most cases, the thrust force was found to increase with increasing feed rate and decrease with increasing cutting speed. These results are consistent with the tool wear behavior reported by Weinert et al[26]. In PVD coated tools, the thrust force was almost constant at 60 N for lower feed and cutting speeds, 0.1-0.15 mm/rev and 30-40 m/min respectively. An increase in thrust force was observed when the feed increased to 0.2 mm/rev. the thrust force lowered by almost 20 N when the cutting speed increased to 50 m/min.

In conclusion, the cutting forces was found to be a dependent on the speed, feed, the cutting tool material and, also the type of reinforcement and the concentration used. Among the cutting conditions, feed rate was found to be the most dominant parameter, the cutting forces were found to increase with the feed rate. However, the effect of cutting speed remains inconclusive in the literature. This warrants for additional investigation to understand the effects of machining conditions. Additionally, in investigating the machinability of functionally gradient aluminum composite and magnesium composite, it is imperative to study the cutting forces generated since it reflects the effects of concentration and size of the SiC particles, the quality of surface generated and the extent of tool wear.

2.4.2 Tool wear

The machinability of metal matrix composites in terms of tool wear has been extensively studied since it directly reflects on the cost of the machining operation. The hardness of the reinforcement particles is often higher than the cutting tool material, tabulated in section 2.1, leading to rapid tool wear. In addition, high tool wear can also produce surface defects in the form of microcracks, pores, microstructural transformation, plastic deformation, residual stresses and changes in hardness[34]. Therefore, to make the composites economical, it is essential to study its machinability to minimize tool wear and improve the quality of the machined surface.

Tool wear is affected by the volume fraction, size and distribution of the reinforcement particles, the matrix properties for a given cutting tool material[35]. The tool wear occurred mostly due to abrasion caused by the impact of the hard reinforcement on the cutting edge and by the sliding motion of worn particles on the clearance and rake face leading to high mechanical stresses on the cutting edge[36]. In addition, high thermal stresses are also developed due to micro-contacts between the hard reinforcements and the cutting edge. Tool wear can occur through different mechanism depending on the relative hardness of the cutting tool and the reinforcements in the composite. Microploughing and microcutting are dominant mechanisms for ductile materials, while, microcracking is the dominant mechanism for brittle materials [9]. In microploughing, the reinforcement particles repeatedly impinge the cutting edge forming ridges and grooves through ploughing action. The repeated ploughing causes low cycle fatigue removing material from the cutting edge. Microcutting occurs when the grain size of the reinforcements is higher than the grain size of the tool. The reinforcement particles remove material in the form of chips resulting in the formation of grooves on the surface of the cutting edge. [37]. It is critical to identify the

mechanism of wear suffered by the tool in order to choose appropriate cutting tool material and to identify optimum machining conditions to manufacture components made from metal matrix composites [5].

Tool wear in drilling and reaming particle and fiber reinforced Mg composite was studied by Weinert and Lange[34]. The concentration and type of reinforcement, base alloy and cutting tool material used are listed in Table 2.3. The SEM images of the cutting edge were studied to identify the wear mechanism. While machining Al_2O_3 fiber reinforced Mg composite using cemented carbide tools, the dominant wear mechanisms were microcracking and fatigue. This can be attributed to the lower hardness of Al_2O_3 in comparison to cemented carbide. Since the hardness of the reinforcement particles are lower, it cannot remove cutting tool material through microcutting. Due to repeated contact with the reinforcement particles microcracks are developed and cutting tool material is removed by fatigue. The wear debri formed are about 1 to 3 μm in size and slide over the rake face and the flank face creating a polished surface. On the other hand, microcutting was found to be the dominant wear mechanism while machining SiC reinforced Mg composite with cemented carbide since the hardness of SiC is higher than cemented carbide. Microcutting causes extensive tool wear and form deep grooves on the cutting edge along the cutting direction. The authors also compared the performance of different tool material in drilling Mg composites. In case of drilling Al_2O_3, cemented carbide exhibited a flank wear of 0.1 mm at a drilling length of 400 mm. Flank wear for diamond coated tool was found to be higher than TiAlN coated tool. This was attributed to diamond coated tool exhibiting low resistance to tool wear when microcracking and fatigue is the dominant wear mechanism. The flank wear was observed to be much severe while drilling SiCp reinforced Mg composite with cemented carbide tool, about

0.36mm for a drilling length of 100 mm. TiAlN coated tool showed progressive tool wear owing to the higher hardness of SiC particles. While, diamond coated tool had a very low flank wear of about 0.01 mm after drilling 400 mm. Therefore, diamond coated tool was concluded to be the best option to drill SiC reinforced Mg to obtain high tool life.

In another study performed by Weinert[36], tool wear was measured as a function of time in turning particle and fiber reinforced Mg composite, listed in Table 2.3. In this study, the effect of cemented carbide grain size in turning aluminum magnesium alloy was analyzed. A vast difference in tool wear was reported in turning Mg composites with Al_2O_3, B_4C and SiC reinforcements. As discussed earlier, hardness of Al_2O_3 is lower than the hardness of cemented carbide, leading to the flank face looking polished due to the sliding action of wear debri generated by microcracking and fatigue. Fine grained cemented carbide showed better wear resistance in comparison to medium grain while machining Al_2O_3 reinforced Mg. The higher toughness of the fine grained cemented carbide improves wear resistance against microcracks and fatigue. For SiC and B_4C reinforcement particles, since microcutting was the dominant wear mechanism, coarser grains showed better wear resistance. The depth and the amount of grooves on the cutting edge was found decrease with increasing grain size. The larger grains can withstand the impact from the reinforcement particles, while the smaller grains can be easily dislodged from the binder. A flank wear of about 200 micron was observed for a grain size of 10 μm and the flank wear was more than double for a fine grain of 0.5-0.7 μm in 400 seconds. In addition, Weinert also studied the performance of PCD tools. The flank wear was observed to be significantly lower for the three reinforcement types. Consistent with the results observed in cemented carbide, medium and small

grains showed good wear resistance in tunring Al_2O_3 reinforced Mg, while coarser grains had higher wear resistance in turning SiC and B_4C reinforced Mg composite.

Further, the contact between hard reinforcement particles and cutting edge imparts high mechanical and thermal load on the cutting edge. The microcontact between cutting edge and the reinforcement particles leads to thermal load. Consequently, the tool wear also depends on the percentage reinforcement present in the matrix. Li and Lu[38] varied the concentration of SiC from 5 to 15% and the size from 15 to 38 μm to study the effects of variation of SiC particle size and concentration in a turning process. The flank wear was observed to increase with increasing particle size and concentration. The highest flank wear of 0.55 mm was observed for 38 micron size particle and 15% SiC reinforcement at cutting conditions listed in Table 2.3.

Facing of SiCp reinforced ZK60A-T5 magnesium composite was studied to identify the effects of variation of cutting speed, feed, tool side cutting edge angle and depth of cut[24]. The cutting conditions are listed are listed in Table 2.3. Flank wear was reported as a function of distance of cut and depth of cut. Abrasive wear was identified as the primary wear mechanism with greatest wear experienced by the flank face. The TiN coating on the cutting edge was completely worn out within a cutting distance of 20 m. The SEM images of the cutting edge revealed grooves of thickness comparable to the size of the reinforcement particles, about 3 to 4 μm. Since the thickness of the grooves match with the size of the reinforcement particles, the particles were not fractured by the cutting edge. Owing to the small size of these particles, they are either pushed into the matrix and removed in the chip. High magnification SEM image of the cutting edge after a cutting distance of 389 m is shown in Figure 2.1.

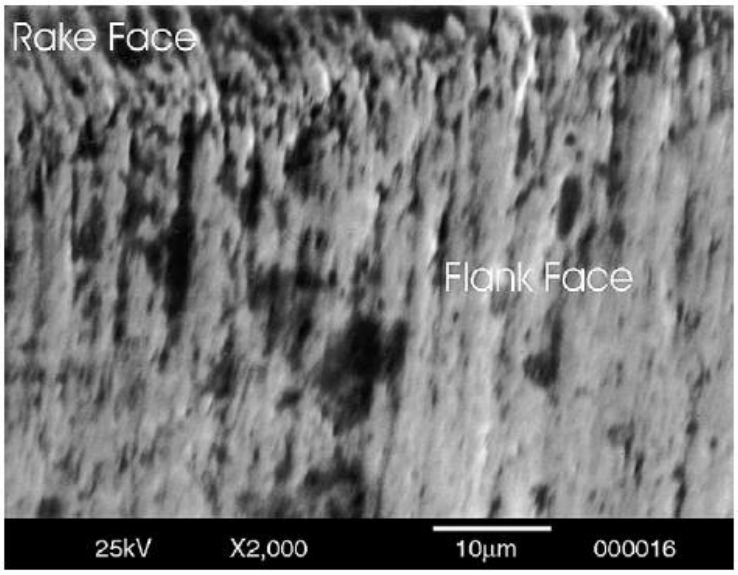

Figure 2.1: SEM image at 2000X of the cutting edge after a cutting distance of 389 m[24].

The flank wear is reported to be a function of number of tool-particle interactions. A steady increase in flank wear, 0.04 to 0.15 mm was observed when the cutting distance increased from 20 to 400 m. Also, larger depth of cut was found to have lower tool wear for a given volume of material removed. As the depth of cut increased, the number of tool-particle interaction decreased for a given volume of material removed leading to lower tool wear per volume of material removed. This agrees with the abrasive wear being the dominant wear mechanism and tool wear occurring primarily due to tool-particle interaction.

Weinert et al performed drilling tests on fiber reinforced magnesium alloy with TiAlN and diamond coated drill bits[26], listed in Table 2.3. The flank wear was measured between 25 to 45 mm. The tool wear increased with the increasing cutting speed for fine grit HW K10 tool. As reported earlier by Weinert, microcracking was found to be the dominant wear mechanism when

the hardness of the reinforcement was lower than the cutting tool material. The formation of microcracks and further fatigue leads to the formation of wear debri that creates a polished surface on the rake face and the flank face[26,36]. Microcracking increases as the cutting speed increases leading to higher tool wear. TiAlN and diamond coated tool were tested at high cutting speed of 300m/min. Reduced flank wear and reasonably smooth surface was observed while using TiAlN due to high hardness and good adhesion of the coating with the substrate. Significant flaking was observed while drilling with diamond coating resulting in higher tool wear. Flank wear was also studied as a function of feed rate. The tool wear was found to decrease with increasing feed rate. Although, increase in feed rate leads to increase in cutting force and stress on the cutting edge, it reduces the contact time between the cutting edge and the reinforcement particles leading to lower abrasive wear. The maximum width of the flank wear reduced from 0.16 to 0.04 mm when the feed rate increased from 0.16 to 0.04 mm/rev.

In conclusion, the tool wear mechanism depends on the relative hardness of the cutting tool with respect to the workpiece material. Microcutting and fatigue were found to be dominant wear mechanism while machining Al_2O_3 reinforced Mg composite with cemented carbides. While, microcutting was the dominant wear mechanism while machining SiC reinforced Mg with cemented carbide tools, owing to higher hardness of SiC. Fine grain cemented carbide showed good wear resistance while machining Al2O3f reinforced Mg, while coarse grain cemented carbide showed higher wear resistance while machining SiC reinforced Mg composites. PCD tools showed significantly lower tool wear for both particle and fiber reinforced Mg composites. Tool wear was significantly affected by the feed rate.

Table 2.3: Tool wear investigations performed on magnesium matrix composites

S. No	Authors	Workpiece material	Process	Tool material and geometry	Cutting conditions
1	Weinert and Lange [34]	ZC63, 12 Vol.% SiC	Drilling	Cemented carbide K10, Φ 6 mm	f:0.05 mm, v:75mm/min, drill length: 20 mm
2	Weinert K [36]	• AlSi12CuMgNi/20% Al_2O_3f • AlMgSi1Mn/20%SiC • AlMg3/10% B_4C	Turning	Cemented carbide: Fine(0.5-0.7 μm), medium(1.5-2 μm), coarse(10 μm	f: 0.01 mm/rev v: 100 m/min doc: 1 mm
3	Pederse n and Ramulu [24]	ZK60A-T5 20% SiC	Facing	PVD TiCN/TiN coated C2 carbide tool	f: 0.112-0.203 mm/rev v:93-122 m/min doc: 0.254-0.762 mm
4	Weinert et al [26]	AZ91/20% vol Al_2O_3f	Drilling	HW-FK K10 TiAlN coated Diamond coated Φ 6 mm	f: 0.1 mm/rev v: 25-300m/min drilling length: 20mm
5	Li, X.P and Lu, L [38]	MgAl/SiCp/5 to 15%/15 to 38 μm	Turning		f: 0.1 mm/rev v: 70 m/min doc: 0.4 mm
6	Tonshof f and Winkler [39]	AZ91 HP and MELRAM, 072TS	Turning	TiN coated, PCD α=7°	f: 0.2 to 0.4 mm/rev v: 100-2400 m/min
7	Tomac and Tonness en	AZ91	Turning	Carbide K10, α=7°	f: 0.1 mm/rev v: 400-850 m/min doc: 0.4 mm

	[40]				
8	Pu et al [41]	AZ31B	Turning	Carbide, clearance angle =7 º	f:0.1 mm/rev v: 100 m/min
9	Kurihara et al [42]	AZ31 and AZ80	Turning		f: 0.06-0.65 mm/rev v: 400-2200 m/min doc: 3-5 mm
10	Wang et al [43]	AZ91	Drilling	HSS, φ 5mm	f: 0.05 - 0.3 mm/rev v: 40-73 m/min drilling depth: 15 mm
11	Gariboli [44]	AM60B	drilling	TiN, CrN, and two different ZrN coatings using PVD, φ 10 mm	f: 0.27 - 0.7 mm/rev v: 63 m/min
12	Bhowmick and Alpas [45]	AM60	drilling	diamond coated HSS , φ 6.35 mm	f: 0.25 mm/rev v: 50 m/min
13	Bierman and Liu [46]	AZ31	drilling	Tungsten carbide, φ 5mm, 5.4 mm	f: 100, 200mm/min v: 80 m/min
14	Abdulgadir et al [32]	Mg/10% wt SiCp (40 μm)/0.25 wt% graphene nanoparticle (GNP)	drilling	Tungsten carbide, PVD coated Tungsten carbide, CVD coated Tungsten carbide Φ 5 mm	f: 0.1,0.15,0.2 mm/rev v: 30,40,50 m/min

Extensive research was performed on aluminum matrix composites to study the tool wear on a range of cutting tool materials. Brun et al studied the tool wear on PCD inserts of varying grain size, polycrystalline cubic BN, hot pressed titanium di-boride boron carbide, hot-pressed titanium diboride-titanium carbide and cemented carbide tools of varying grain size on Al6061/SiC composite/40p[17]. The flank wear was plotted as a function of Vicker hardness of the tool, shown in Figure 1. The authors report that the flank wear behaved differently when the tool tool is softer than the SiC particles, compared to the tools that are harder than SiC particles. For cutting tools harder than the reinforcements, the flank wear was reported to be inversely linearly proportional to the hardness of the tool material. Whereas, for softer tool material no simple trend was observed. The authors concluded that PCD tools maintain better tool life, surface finish in machining metal matrix composites in comparison to other tools like uncoated carbide, coated carbide tools, PCBN and diamond tools in machining MMCs[17]. In addition to the higher hardness, Andrewes et al have stated that due to the high thermal conductivity, any heat generated at the cutting edge is conducted away quickly and the chemical inertness of the tool minimizes the crater wear. Hence, the initial wear occurs due to abrasion of SiC particles on the flank face. After 53 minutes of cutting, a thin layer of aluminum matrix was found to be smeared flank face. This can be attributed to the high temperature and stress at the worn cutting edge due to intense rubbing of the reinforcement particles[18]. Similar results were observed in a comparison study between PCBN with varying grain and binder concentration and PCD tools, the authors conclude that PCD tools showed lowest flank wear and notch depth among all the other tools[47].

Although PCD tools exhibit longest tool life and good surface finish while machining aluminum matrix composites, the tool cost is very high[6,18,48]. This encourages researchers to explore other

cutting tools to make the process more economical.

Table 2.4: Machining experiments performed on aluminum matrix composites

S. No	Authors	Workpiece material	Process	Tool material and geometry	Cutting conditions
1	Brun et al	Al6061/40%SiCp	Turning	PCD, polycrystalline cubic boron nitride, Cemented carbide, Negative rake angle, nose radius: 0.79 mm	v: 152,305 m/min f: 0.254 mm/rev doc: 0.762 mm
2	Andrews et al	A380/20%SiCp/12.8 μm	Turning	PCD: KD100 CVD: KCD25 Cemented carbide: C2 TiN coated carbide $\alpha=5^o$	v: 190m/min, f: 0.1 mm/rev doc: 1mm
3	Chou et al	A359/20% SiCp	Turning	CVD: 30 μm, tungsten carbide substrate	v: 1 to 6 m/min f: 0.05 to 0.3 mm/rev doc: 1 to 2 mm
4	Monaghan et al	Al/25% SiCp	drilling	HSS, carbide, φ: 6 mm, β: 32°	v: 50,102 and 198 rev/min f: 0.1 to 0.3 mm/rev
5	Tomac et al	Al5083/14%SiCp/24	turning	carbide inserts with TiN. TiW , Al_2O_3 and TiN coatings	v: 20 to 80 m/min f: 0.1 to 0.6 mm/rev doc: 2 mm
6	Manna et al	Al/15% SiCp/23 μm	turning	Tungsten carbide, α: 5°	v:20-225 m/min, f: 0.1 to 1 mm/rev, doc: 0.25 to 1.5 mm

CVD tools are a recent addition to the diamond tooling family. They are produced by depositing a diamond film on a hard substrate usually tungsten carbide. This synthesis technique enables the production of diamond tools with complicated geometries. A film thickness of 10 to 30 µm is ideal for machining[2]. CVD tools of higher thickness have been developed recently and are more suitable to machine MMCs.

In a study performed by Chou et al, a 30 µm thick CVD diamond coated tool was used to perform turning operation on 20% reinforced A359/SiC[49]. The authors have reported that tool wear was affected by both feed rate and cutting speed and the feed rate was found to be the more dominant parameter. Initially, a slow steady progress in wear was observed in all conditions, followed by a drastic increase after a single turn. The tool wear mechanism for CVD tools was discussed by Andrews et al[18]. Unlike PCD tools, adhesive wear was found to be the more dominant wear mechanism in CVD diamond tool and can be attributed to the slightly honed cutting edges and the presence small crevices formed on the diamond coating due to the reinforcements promote the adhesion of the aluminum matrix, which is further compacted by high pressure at the secondary shear zone. The compaction leads to adhesion between diamond coating and the aluminum matrix and this adhesive bond may become stronger than the adhesive bond between the diamond coating and the substrate. The aluminum matrix is then chipped off with the diamond coating, rapidly increasing the tool wear.

The next class of cutting tools are coated, and uncoated carbide tools that have been used extensively to machine conventional metals over the last few decades due to the lower tool costs in comparison to diamond coated tools. However, the carbide tools experience high wear rate while

machining MMCs. Abrasive wear was observed to be the most dominant wear mechanism since the reinforcement particles are typically harder than the tool material and slide over the rake and flank surface of the tool forming sharp abrasive wear tracks. Adhesive wear and diffusion also contribute towards the tool wear. The high temperature at the tool chip interface promotes the material to stick to the rake and flank surface forming a built up edge(BUE) leading to a poor surface finish on the machined part. On the other hand, the built up edge protects the tool face from further abrasive wear.

The compatibility of drilling Al/SiC with carbide and high speed steel tools were studied by Monaghan et al[31]. The flank wear experienced by the HSS tools were found to be significantly different from the carbide tools especially at lower feed rates and the difference gradually decreased with increasing feed rate. For HSS tools, the flank wear decreased steeply with the increase in feed rate, while for carbide tools a small increase in the flank wear was found with the increase in feed rate. The decrease in flank wear for HSS can be explained by the reduction in cutting time as the feed rate increases. The reduction in cutting time reduces the interaction between the soft HSS tool and the hard SiC particles thereby reducing the tool wear. The rake face wear was found to increase substantially for HSS and carbide tools as the feed rate increased but is not significantly affected by the cutting speed. Since the hardness of HSS and WC tools are lower than SiC particles the wear in both the faces are much higher than wear in drilling conventional metals. The authors concluded that HSS tools were unsuitable to machine MMCs and carbide tools had a reasonable tool life before reaching the recommended ISO wear land of 0.3 mm making it suitable to machine MMCs.

Similar results were obtained by McGinty et al, the study reported that solid carbide tools were suitable to drill 50-55% Alumina fibers in aluminum[50]. The tool wear found to vary as a function of feed rate but remained unchanged with the spindle speed. The effectiveness of carbide tools in machining MMCs were also evaluated by Tomac et al on 14% reinforced Al/SiC composite[29]. Tomac et al have recommended that the carbide tools are suitable for rough turning operations and not finishing operation. The flank wear was observed to be 0.6 mm after only 6 mins of turning, which results in poor surface finish and dimensional tolerances making it unsuitable for finishing operations. The authors have also reported that using coated carbide tools only increased the tool life to 7.5 mins under similar machining conditions. This can be attributed to the coating material being chipped away due to abrasive action of the SiC particles owing to the lower hardness of the coating and binding material. Brun et al have reported that cemented carbide tools with lower binder content and higher grain size showed better tool life than carbide tools with higher binder content and smaller grains. The ductility of the binder agent seems to influence the durability of carbide tools while machining metal matrix composites[17].

Quigley et al tested the machinability of 25% reinforced Al/SiC with triple coated, combinations of TiN, TiCN and Al_2O_3 and uncoated carbide tools[51]. The flank wear was observed to increase with the cutting speed and the wear was higher than the recommended ISO value of 0.3 mm for all tool materials. A steep rise in the flank wear was found in uncoated carbide tools and the lowest rate of increase was observed in TiCN, Al_2O_3 and TiN coated tool. It was reported that TiC coating protect the tool from wear even when the coating has worn off exposing the WC substrate. When the TiC coating was 5 µm or greater, the coating is transported to the worn surface protecting it from further wear[52]. TiN coating reduces the frictional force at tool-chip interface, reducing the

rake and flank wear of the tool. The authors conclude that while triple coated carbide tools are suitable for machining MMCs, the uncoated carbide tools are unsuitable.

In a similar study by Manna et al, turning tests were performed on 15% reinforced Al/SiC with an average particle diameter of 23 μm[25]. The flank wear was observed to be below 0.3 mm at lower cutting speeds from 20 to 100 mm/min for all the feed rates from 0.14 to 1 mm/rev. However, as the cutting speed increased the flank wear rapidly rised above 0.3 mm for a small length of cut of 50 mm. The BUE is formed between the chip and the rake face causing the rake angle to increase. This leads to reduction in cutting forces. However, at lower cutting speeds the reinforced particles are not fractured but roll over the surface of tool and plough on the machined surface. This leads to larger BUE at lower cutting speeds.

In conclusion, the tool wear is affected by the volume fraction, size and distribution of the reinforcement particles, the matrix properties for a given cutting tool material. The tool wear was found to increase with feed rate and cutting speed. Formation of BUE was also reported while machining aluminum matrix composites with the increase in cutting speed. Owing to the higher hardness of the reinforcement particles in comparison with the cutting tool, abrasive wear was found to be the dominant wear mechanism. In addition, the size of the reinforcement was also found to have a significant effect on the tool wear. Reinforcement particles larger than grain size of the WC grains easily displace them on impact causing rapid tool wear. While, smaller reinforcements caused microcracking and fatigue due to repeated impact on the cutting edge. Therefore, since the life of the tool is significantly affected by the presence of the reinforcement

particles, it is important to evaluate the tool wear and understand the wear mechanism for economic production of MMCs of high surface quality.

The most critical parameter in the analysis of the machinability is the investigation of quality of surface produced. The quality of surface generated in a machining process directly affects the life of the component. Therefore, in addition to eliminating defects in the primary manufacturing process, it is critical to produce products with a good surface finish to ensure high performance. In MMCs, the high tool wear and the presence of reinforcement particles on the surface can produce defects on the surface. The quality of surfaces generated in machining MMCs are discussed in the following section.

2.4.3 Surface finish

Surface texture can be used as a measure of quality of the surfaces generated in a machining process. It can be defined as the deviations from the nominal surface. Surface texture can be categorized into three types, shown in Figure 2.2 a) Roughness, comprising of fluctuations of short wavelengths, it is characterized by peaks and valleys of varying spacing and amplitude, b) Waviness is often referred to as macro-roughness, it is the surface irregularities of larger wavelengths. Waviness usually occurs due to machine/workpiece deflection, chatter and vibrations during machining, c) Lay refers to the predominant direction on the surface depending on the manufacturing process used, d) flaws are unexpected defects that occur on the surface like cracks and dents that occur unintentionally.

The deviations from the nominal surface expected during a machining process can be categorized using statistical methods. The surface profile is obtained using a surface profilometer, shown in figure 3, where a stylus probe travels on the surface. The surface profile obtained includes both waviness and surface roughness on the surface. The surface roughness is obtained by applying Gaussian filter as per ISO 16610, and ISO 13565[53,54].

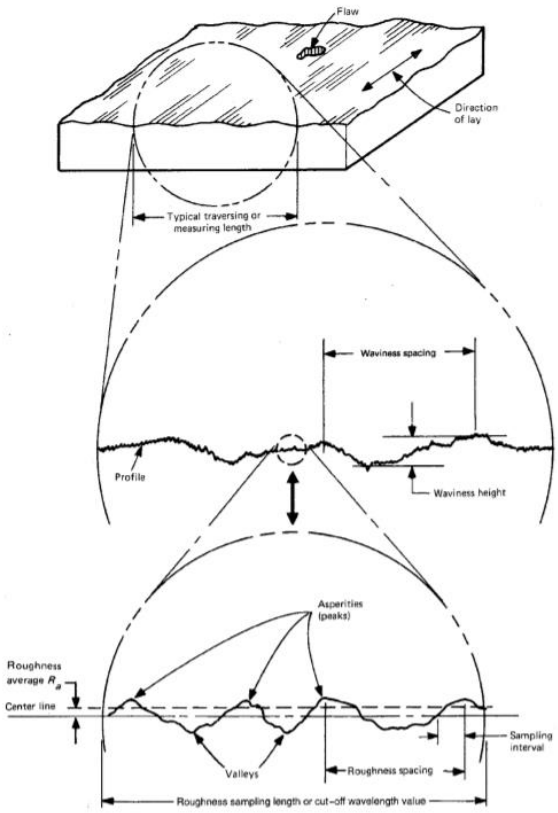

Figure 2.2: Surface texture showing roughness, Waviness, Lay and Flaw.

The maximum peak height, R_p measures the maximum peak height from the mean line, defined on the sampling length, gives information on the particles embedded on the surface. While,

maximum valley depth, R_v gives information on the voids and pits present on the surface. Similarly, other surface roughness parameters listed in table 2.5 are also analyzed. Additionally, area height measurements, S_a and S_v, were also performed

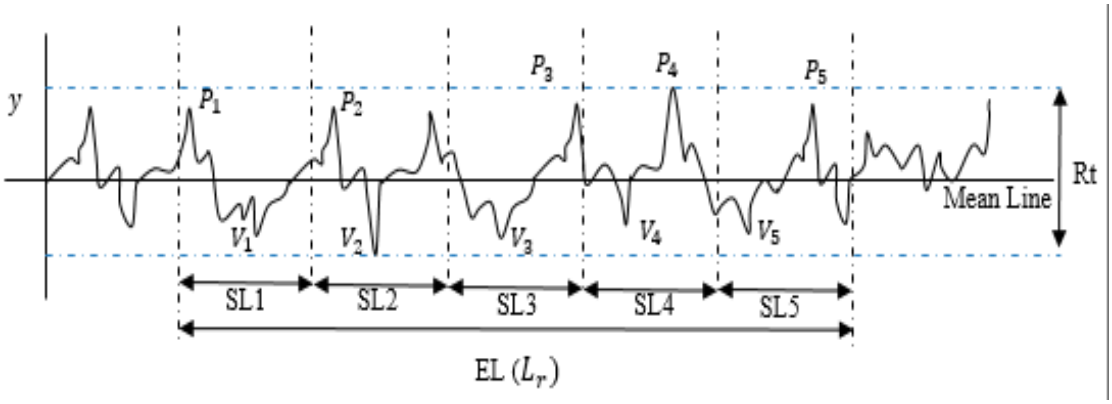

Figure 2.3: Surface profile measured using a stylus probe.

Where,

SL: Sampling length,

EL: evaluation length,

P_i : height of a peak,

V_i : depth of a valley.

Surface finish obtained in a machining process depends on the cutting conditions, tool and workpiece material. Damage to the surface caused by the machining process can significantly reduce the life of the component. The damage from machining can be in the form of pores, cracks, microstructural transformations, plastic deformation, residual stresses and changes in hardness. Therefore, it is critical to examine the surface and sub surface damage induced while machining.

There are two schools of thought on the influence of the operating conditions on the surface

Table 2.5: Surface Roughness parameters and equations

Surface Roughness Parameter	**Equations**
Average surface roughness, R_a (µm)	$R_a = \frac{1}{n} * \sum_{i=1}^{n} \lvert y_i \rvert = \frac{1}{Lr} * \int_0^{Lr} \lvert y \rvert \, dx$
RMS average value, R_q	$Rq = \sqrt{\frac{1}{n}\sum_{i=1}^{n} y_i^2} = \sqrt{\frac{1}{L_r}\int_0^{L_r} y^2 \, dx}$
Peak to valley height over EL, R_t	$\boldsymbol{R_t} = max(P_i, V_j)$ *over EL*
Peak to valley height over SL, R_z	$\boldsymbol{R_z} = \frac{1}{5} \sum_{i=j=1}^{5} \lvert P_i \rvert + \lvert V_i \rvert$
Skewness, R_{sk}	$Rsk = \frac{1}{Rq^3}\left[\frac{1}{Lr}\int_0^{Lr} y^3 dx\right]$
Kurtosis, R_{ku}	$Rku = \frac{1}{Rq^4}\left[\frac{1}{Lr}\int_0^{Lr} y^4 dx\right]$
maximum peak height, R_p	$\max(P_i)$
Maximum valley depth, R_v	$\max(\lvert V_i \rvert)$
Area height average, S_a	$S_a = \frac{1}{A} * (\iint \lvert Z(x,y) \rvert \, dxdy,$ Where, $Z(x, y)$ is the profile height as a fun of x and y
Area maximum height, S_z	$S_z = S_p + S_v$, S_p is the largest peak height, S_v is the deepest valley depth

roughness of the machined surface, the first one being that the surface roughness decreases with the increasing cutting speed until a critical value after which the surface roughness increases.

Second being that the surface roughness steadily decreases with the cutting speed. The following equations give the theoretical average roughness, R_a and maximum peak to valley distance, R_{max} of the machined surface,

$$R_a = \frac{0.0000321 * f^2}{r} \tag{2.10}$$

$$R_{max} = \frac{f^2}{8 * r} \tag{2.11}$$

where, R_a: average surface roughness in μm

R_{max}: maximum peak to valley in sampling length

f: feed in mm/rev

r: tool nose radius in mm

For MMCs, the theoretical relationship between the roughness parameters and feed rate holds good since the reinforcement percentages are low. The theoretical equation was found to be in agreement with the experimental results from many studies[29,55], while a few researchers obtained average roughness values marginally higher than the predicted value[6,51].

Generally, the surface roughness of the MMCs was found to be higher than the unreinforced matrix at lower feed rates. As the feed rate increased, the surface finish of the MMCs were reported to be better than the unreinforced matrix[48,49,50]. Pramanik et al performed turning tests on 20%

reinforced Al6061/SiCp composite to evaluate the trend in surface roughness[56]. The surface roughness was found to increase with increasing feed rates. At lower feed rates, the surface roughness of MMC was higher than unreinforced base alloy. However, at higher feed rates, the base alloy exhibited higher surface roughness than MMC. In addition, the authors also observed that the feed lines were not visible at lower feed rates and the surface was irregular owing to the particles embedded and pulled out from the machined surface, shown in Figure 2.4. While the feed marks were visible for all the feed rates in case of unreinforced alloys.

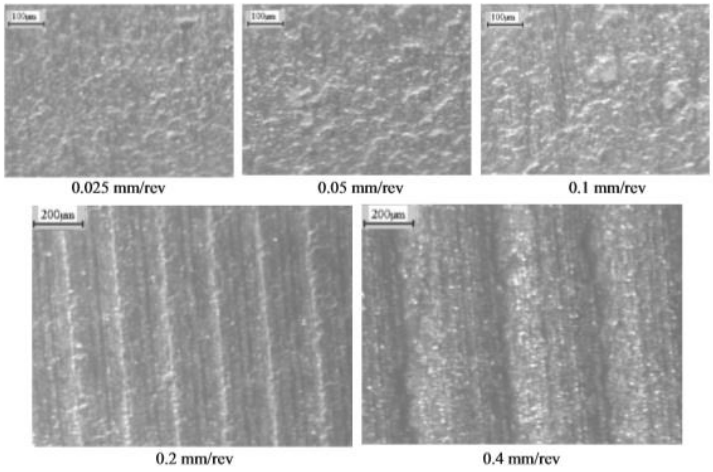

Figure 2.4: SEM images of the machined surface at different feed rates on Al6061/SiCp in a turning operation[56].

The surface finish of the machined surface is reported to improve as the tool is slightly worn out[55,57,58]. In a study by Kilickap et al, the surface finish produced by coated and uncoated carbide tools in turning 5% reinforced Al/SiCp were studied in addition to the influence of operating conditions[58]. Coated tools provided better surface finish in comparison to the uncoated carbide tools. In accordance with the results obtained by Pramanik et al, the surface roughness was

found to be highest at a lower cutting speed and the surface roughness decreased marginally with the increasing cutting speed and was observed to increase with increasing feed rate. Higher feed rates lead to higher cutting temperature that softens the matrix weakening the interfacial bond between the matrix and the particle. This causes the particles to fall out easily creating a void on the surface which can contribute to the increased surface roughness. The depth of cut was found to have the least influence on the surface finish.

For magnesium matrix composites, Pedersen et al reported that the surface finish in a facing operation was excellent[24]. The average surface roughness was about 2 μm at 0.2mm/rev and in agreement with the theoretical value. Surface smearing was observed at lower feed. While, depth of cut, cutting speed and side cutting angle did not have a significant influence on the surface roughness.

Another study by Abdulgadir et al[32], reported the surface roughness obtained in a drilling graphene and SiCp reinforced Mg composite. The measurements were performed parallel to the axis of the hole. The average surface roughness was in between 0.6 to 1 μm for all cutting conditions and tool materials. In most cases, a slight increase in Ra is observed with increasing feed rate. PVD coated tungsten carbide tool generally produced lower surface roughness and the lowest of 0.5 μm was reported at 30 m/min and 0.15 mm/rev. This can be attributed to the higher hardness of PVD tools in comparison to SiC particles.

The surface quality of a machined surface can also be deduced by inspecting the surface through SEM. Weinert et al evaluated the quality of the component produced through SEM imaging of the

machined surface and its cross-section[26,34]. Figure 2.5 shows the SEM image ZC63/12%SiCp machined at 0.1 mm/rev and 75 m/min using PCD and cemented carbide tools. While machining with cemented carbide, SiC particles up to 40 μm below the surface were damaged due to plastic deformation. On the other hand, for PCD almost no subsurface damage was observed due to the very sharp and hard cutting edge. Also, as the cutting speed reduced from 75 to 50 m/min, the sub surface damage reduced from 40 to 30 μm.

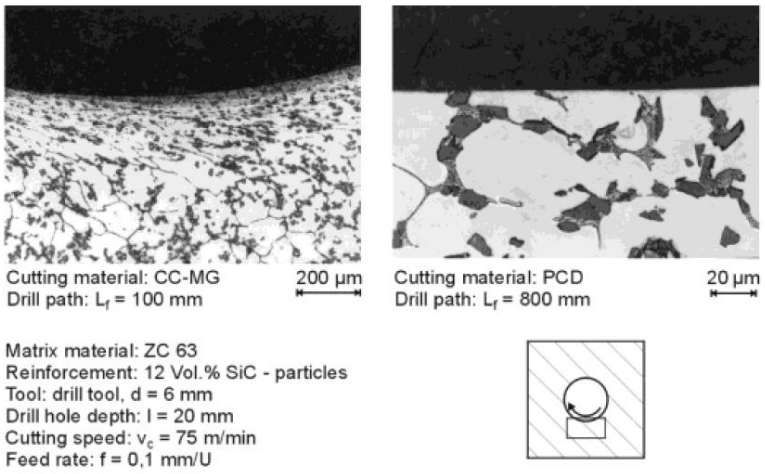

Figure 2.5: Subsurface generated in drilling ZC63/12%SiCp using cemented carbide-medium grain and PCD[34].

Abdulgadir et al[32] reported that high feed rates cause surface damage due to high contact pressure resulting in the formation of fine grooves and cracks due to strain hardening of Mg matrix. The authors compared the surfaces produced by uncoated, PVD and CVD tools. In case of uncoated and CVD tools, scratches and fine grooves were observed along the drilling direction.

Only a handful of studies have reported the surface quality of machined aluminum and magnesium composites. Feed rate was found to have a dominant effect on the surface finish generated. The surface roughness was found to increase with the feed rate. Additionally, fine grooves, voids, feed lines were also observed at high feed rates. However, the influence of cutting speed on average surface roughness has not been identified clearly. Therefore, the study of machinability cannot be complete without thorough investigation of surface finish and surface damage induced to MMCs while machining.

2.4.4 Chip morphology

The quality of surface generated is also reflected on the chip morphology. Generally, formation of continuous chips indicates a good surface finish on the work piece and discontinuous chips indicate rougher surface. The type of chip generated depends on the feed rate, spindle speed and the ductility of the workpiece material. In MMCs, the interaction between the reinforcement particles and the cutting edge can be deduced by studying the chip morphology. Therefore, studies reporting the chip morphologies are discussed in this section.

The chip morphology is generally studied using a quick stop device in the literature. This device shortens retraction time of the spindle to a few microseconds and leaves the chip attached to the work piece. This chip-workpiece is then removed and analyzed for the chip formation mechanism. The chip formation process depends on the ductility, thermal conductivity, and microstructure of the workpiece material. The instability in the cutting process is also reflected in the chip

morphology. The chip formation is a shearing process where plastic deformation occurs within the shear zone. In case of MMCs, the ductility of the workpiece is reduced significantly due to the presence of the reinforcement particles. The grain size of the base alloy is also altered due to Hall Petch effect. Therefore, analyzing the chip morphology aids in understanding the material flow in the presence of reinforced particles and the interaction of the of reinforcement particles with the cutting edge.

The chip morphology was studied through the finish machining of SiC particles reinforced Mg matrix by Pedersen et al through performing facing operation, listed in Table 2.3[24]. Different cutting speeds, feed, tool side cutting edge angle and depth of cut of low, center and high levels were tested. The chips were observed to be mostly highly segmented and semi-conitnuous. Upon inspection under SEM, the chips were found to have saw tooth edges with prominent shear band. Cyclic build up was caused by the 0 degree rake angle and the chips suffered from compression shear failure in periodic bands due to low ductility of the material experiencing severe strain, shown in Figure 2.6. The band spacing was found to be dependent on the cutting speed, with 40 μm spacing for 40 m/min and 100 μm spacing for 100 m/min. Also, the chips formed at the outer surface of the rod were continuous and the chips formed at the inner surface were mostly discontinuous. This can be attributed to higher cutting speeds at the surface generating more heat leading to matrix softening and increased ductility, while the cutting speed is lower at the inner surface leading to discontinuous chips sue to lower ductility of the matrix. In addition, the presence of hard reinforcement particles rapidly increases the tool wear as the tool proceeds from the outer to the inner surface. The tool wear could lead to change in tool geometry and ultimately different chip geometry.

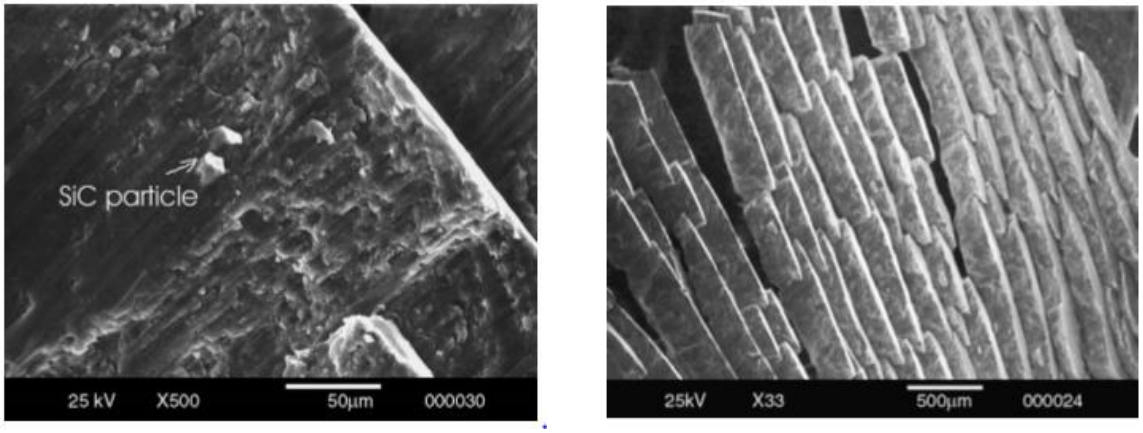

(a) (b)

Figure 2.6: Chips formed during turning of ZK60A-T5 magnesium alloy reinforced with SiCp a) Free surface side of the chip indicating that ductile fracture is the main failure mechanism, b) free surface side of a chip showing extreme segmentation owing to the reduced ductility of the material[24].

Similarly, Lin et al[59] studied the chip formation in 20% reinforced A359/SiCp composites using the quick stop device. The chips were categorized as 'saw toothed' chips. Severe plastic deformation occurs in the shear zone for monolithic metals. Saw toothed chips were formed owing to the reduced ductility of MMCs. This leads to initiation of the cracks at the shear zone forming segmented free surface on the chip. In addition, the SiC particles are often separated from the matrix material during the shearing, forming voids on the chip surface. These voids facilitate crack propagation when the voids coalesce along the shear plane causing the formation of segmented chips. The crack propagation is accelerated by upward and side curl action of the chip. The authors

concluded that the crack initiates from the free surface of the chip due to the high shear stress applied by the rake face and the crack is propagated particle to particle through ductile fracture of the matrix-particle decohesion[59].

In an extensive study performed by Hung et al[60], the chip formation in A359/SiCp/10% and Al6061/10/SiCp was compared with monolithic metals. The reduced ductility of the MMC causes stick-slip condition at the tool interface causing segmentation on the free surface. The interface of the segments could be identified with different flow line orientation and microcracks at the chip tool interface. Quick stop apparatus was used to obtain the chip-root attached to the workpiece. Upon inspection at the tool-chip interface, several microcracks were found to be initiating from the shear plane on the onset of the material flow lines, Figure 2.7 a. The long reinforcement particles were realigned along the material flow direction, shown in Figure 2.7 b.

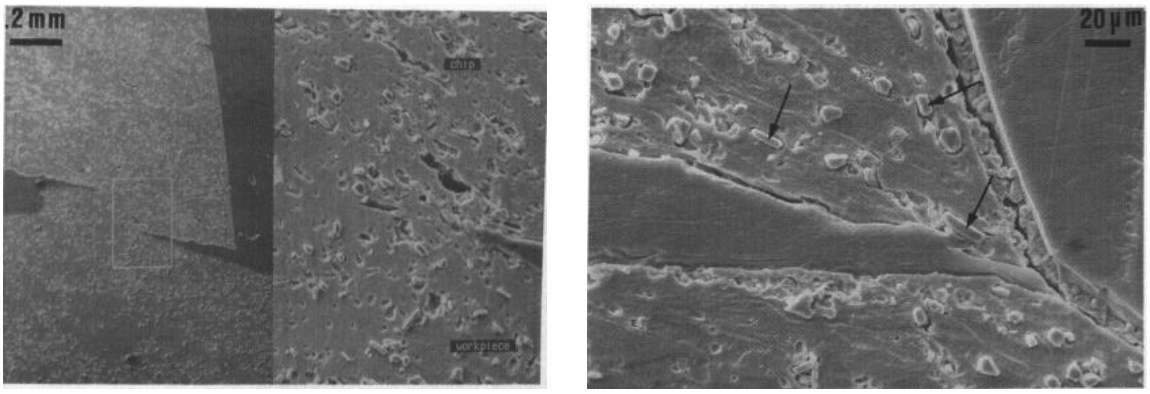

(a) (b)

Figure 2.7: a) Microcracking at tool-chip interface for Al6061/10/SiCp at a cutting speed of 16m/min and 0.3 mm depth of cut, b) shows the alignment of SiC particles with the flow lines in the shear zone[60].

Flow lines were also observed on the machined surface. Owing to the very high shear stress on the machined surface, the clustered SiC particles were broken and dragged along the feed direction over 100 µm.

2.5 Analytical Work

2.5.1 Prediction of cutting forces in machining metal matrix composites

In MMCs, metallic matrix is typically reinforced with rigid ceramic particles leading to increased strength, modulus and wear resistance. The reinforcement particles that enhance the mechanical properties of the composites generate higher cutting forces and cause rapid tool wear during machining in comparison to an unreinforced matrix.

The generated cutting forces are reflected on the integrity of the surfaces produced during a machining process. Therefore, it is imperative to develop a force model to predict the quality of the surfaces generated. But, only a few studies have reported a force model for metal matrix composites[61,62]. For example in [61], an energy-based predictive model was developed for orthogonal cutting of metal matrix composites. The authors considered the energy dissipated in the primary and secondary shear zones and the energy due to fracturing of particles from the matrix using Weibull distribution to estimate the probability of the event.

$$e = E_p + E_s + E_D \tag{2.12}$$

Where,

E_P: specific energy associated with the with the plastic deformation in primary shear zone,

E_s is the energy associated with the plastic deformation in the secondary shear zone

E_D is the energy per unit volume for particles debonding from the matrix.

E_p calculated using the basic orthogonal cutting model was given by,

$$E_p = \left(\frac{C}{n+1}\right) * \left[\left(\frac{1}{\sqrt{3}} * (\cos\gamma)/(\sin\varphi\cos(\varphi-\gamma)\right]^{n+1} \quad (2.13)$$

Where,

C is the strength coefficient

n is the strain hardening exponent

φ is the shear angle

γ is the rake angle of the cutting too.

The energy dissipated in the secondary shear zone, E_s was assumed to be one third of the energy dissipated in the primary shear zone. The energy dissipated during debonding was calculated using the Griffith theory for brittle fracture, where the energy change due to incremental crack growth, *da* is estimated. It was assumed that the cracking damage on the particle depends on the stress experienced by the particles. The crack extension force, G, the change in the strain energy dU due to the change in interfacial crack area, dA is given by,

$$G = \frac{dU}{dA} = \frac{\pi\sigma^2\, a\, w\,(1-\nu^2)}{Y} \quad (2.14)$$

σ: Fracture strength of the reinforcement particle

$a\ and\ w$: initial crack length and width respectively

Y: Youngs modulus

ν: Poisson's ratio

The predicted cutting forces were found to be in good agreement with the experimentally measured forces for 10% and 15% Al_2O_3 reinforced aluminum alloy.

However, the authors did not consider the ploughing of the matrix material under the rounded cutting edge. The contribution of ploughing action of the rounded tool was considered by Pramanik et al [62] and Sikder et al [63] for aluminum based SiC/Al_2O_3 particle reinforced composites. The authors considered the shearing of metal matrix to form chips, the ploughing force and the force due to particle fracture to develop an analytical force model.

Pramanik et al considered that the chip formation, ploughing of the matrix, particle fracture and displacement were considered to be the major events occurring during turning of MMCs. The forces $F_{cc}\ and\ F_{tc}$, in the cutting and the feed directions respectively, due to the chip formation were calculated using the orthogonal cutting model,

$$F_{cc} = \tau_s A_c * \left(\frac{\cos(\beta-\gamma)}{\sin\varphi\cos(\varphi+\beta-\gamma)}\right) \tag{2.15}$$

$$F_{tc} = \tau_s A_c * \left(\frac{\sin(\beta-\gamma)}{\sin\varphi\cos(\varphi+\beta-\gamma)}\right) \tag{2.16}$$

Where β is the friction angle.

When the cutting edge interacts with the particles, the particles get fractured or displaced and the matrix gets ploughed. The forces corresponding to these events were considered separately. The ploughing forces, $F_{cp}\ and\ F_{tp}$ in the cutting and thrust directions can be given as a function of

τ_{sm}, shear strength of the matrix material, active cutting edge length, l, nose radius, r_n and rake angle[64]

$$F_{cp} = \tau_{sm} l r_n \tan\left(\frac{\pi}{4} + \frac{\gamma}{2}\right) \quad (2.17)$$

$$F_{cp} = \tau_{sm} l r_n \left[1 + \frac{\pi}{2}\right] \tan\left(\frac{\pi}{4} + \frac{\gamma}{2}\right) \quad (2.18)$$

The cutting force associated with particle fracture, F_{cf} along a cutting distance, L was calculated by considering the average fracture energy per unit cutting edge length, μ_g. The authors estimated μ_g to be 0.01 J/mm for SiCp through interpolation of a range of data available in [65].

$$F_{cf} * L = E_{ft} = \mu_g l \quad (2.19)$$

$$F_{tf} = F_{cf} * \tan\delta \quad (2.20)$$

Where, δ is the angle between the resultant force and the cutting direction. The summation of the forces from chip formation, matrix ploughing, and particle fracture is the total forces in the cutting and the thrust forces.

Similar events were considered by Sikder et al to develop a force prediction model for a turning process [63].In addition, the authors considered the effect high temperature and strain rate at the cutting edge using Johnson-Cook model. The predicted forces were compared with 10 and 15% reinforced 7075 aluminum composite. Deviation of about 8% was reported.

These force models were developed based on the orthogonal cutting model suitable for a turning operation, which is a continuous cutting process. In contrast, an analytical cutting model for an *intermittent* cutting process, e.g., end milling of metal matrix composites has not been published yet. In this study, an analytical force model for end milling of SiC particles reinforced magnesium composites was developed based on Altintas model for milling of ductile materials[66].

2.5.2 Tool life

Development of comprehensive tool wear in turning of metal matrix composites were also investigated[67]. Taylor tool life equation is one of the first models to predict the life of a cutting tool as a function of cutting speed,

$$VT^n = C \tag{2.21}$$

Where,

V: the cutting speed, m/min

T: tool life, mins

C and n: intercept and slope, depends on the workpiece and tool material.

Since 1907, the Taylor tool life equation has been modified to accommodate the effects of feed rate and depth of cut in estimating the tool life,

$$T = CV^{-n_1} f^{-n_2} a^{-n_3} \tag{2.22}$$

Where,

f: feed rate, mm/rev

a: depth of cut

n_1, n_2, n_3: exponents for speed, feed and depth of cut respectively.

Several studies used the modified Taylor tool life equation as a basis to develop tool wear model for specific workpiece and cutting tool material combination[68–70]. Pederson et al[67], modified this to include the accelerated tool wear that occurs due to abrasion of reinforcement particles on the cutting edge in turning of aluminum matrix composites with diamond cutting tools. In this model, the percentage reinforcement was accounted for by considering that the particles are enclosed in a cube and calculating the distance between the centers of the particles, as the particle percentage increases, the distance decreases. The interactions of the particles were classified into four types, Type A: the cutting edge misses the particle completely, Type B: tool engages with the top of the particle, tending to rotate the particle out of the matrix and causing three body abrasion, type C: Center of the particle engages with the tool, the particle is pushed into the matrix resulting in two body abrasion and type D: the tool engages with the lower part of the particle, rotating it onto the rake face and being removed along with the chip. Probability of each event was calculated in terms of projected area of the particle and the cube,

$$P_A = 1 - \left(\frac{d_p}{l_c}\right) \tag{2.23}$$

$$P_B = \left(0.5 - \frac{P_A}{2}\right)\left(1 - \frac{r_{rotation}}{\frac{d_{particle}}{2}}\right) \tag{2.24}$$

$$P_C = 1 - P_A - P_B - P_C \tag{2.25}$$

$$P_D = \left(0.5 - \frac{P_A}{2}\right) \tag{2.26}$$

Where,

P_A, P_B, P_C, P_D: Probability of events A, B, C and D respectively

$r_{rotation}$: Particle rotation radius, assumed to be 75% of the particle radius

l_c: length of the cube enclosing the particle

d_p: diameter of the particle

The probability of each event was then used to determine the number and nature of interaction for a given cutting distance, $distance_{cut}$. The average cutting distance, $Event_C$ between C events was calculated using,

$$\frac{dist_{cut}}{Event_C} = \frac{l_c}{P_C} \tag{2.27}$$

The amount of wear due to events C and B were calculated by considering that the wear rate increased linearly on a log-log plot upto a certain particle size found in between the two bodies, after which it saturates as discussed by Rabinnowicz et al[71]. Following this, the wear due to two body and three body abrasion was given by,

$$V_b = K\left(\frac{x}{\frac{dist_{cut}}{Event_C}} + 0.1\frac{x}{\frac{dist_{cut}}{Event_B}}\right)^{m_1} d_a^{m_2} \tag{2.28}$$

Where,

V_b: Flank wear, mm

K: empirical constant

x: cutting distance

d_a: reinforcement size

m_1, m_2: Empirically derived constant

The higher hardness of the reinforcement particles in comparison to the cutting tool material leads to accelerated tool. When the tool hardness is 1.2 times higher than the reinforcement particles, then the flank wear is inversely proportional to the tool hardness[17]. In this case the hardness ratio was found to be 3. Therefore, the flank wear can be given by,

$$V_b \propto \left(\frac{P_a}{P_t}\right)^m \tag{2.29}$$

Additionally, the dependence of the tool wear on the grain size of the tool can be given by,

$V_b \propto d_t^m$

Where,

V_b: flank wear

P_a, P_t: hardness of composite and cutting tool respectively

d_t: grain size of the tool

m: empirical exponent

The final semi empirical wear equation adopted from the Taylor equation was given by,

$$V_b = K\left(\frac{x}{\frac{dist_{cut}}{Event_C}} + 0.1\frac{x}{\frac{dist_{cut}}{Event_B}}\right)^{m_1} V^{m_2} f^{m_3} a_p^{m_4} \left(\frac{P_a}{P_t}\right)^{m_5} \left(\frac{d_a}{d_t}\right)^{m_6} + error \quad (2.30)$$

Where,

V: cutting speed, m/min

F: feed, mm/rev

a_p: depth of cut

d_a: Abrasive particle size

d_t: tool grain size

$m's$: exponents from corresponding probabilities

Although the cutting forces and tool wear experienced while turning has been modelled in the literature, no attempt has been made to model the forces and wear in a milling process. In this study, the cutting force model in milling of uniformly distributed magnesium composite has been developed. Unlike the tuning process, milling is a discontinuous cutting process where the cutting edge engages and disengages gradually from the workpiece. The mechanics of milling process has been discussed in detail in the following section to understand the forces generated in this process.

2.5.3 Mechanics of milling process

In a milling operation, the milling cutter is attached to the rotating spindle and the workpiece is clamped on the stage. In a typical vertical CNC machine, the spindle can move linearly in the vertical direction and the stage can move linearly in a horizontal plane. A milling cutter has one or more radially spaced flutes or teeth. As the spindle rotates, the teeth engage and disengage repeated with the workpiece, making the milling process an intermittent cutting operation, where the tool is engaged with the workpiece for an immersion angle. The periodic loading and unloading of the teeth cause cyclic mechanical and thermal stresses leading to shorter life of the cutter. To mitigate the sharp variations in the load the helical flute geometries are used to enable gradually engagement and disengagement with the workpiece. Owing to these differences in the cutting tool geometry in comparison to a turning process, a simplified orthogonal cutting model cannot be used to understand the mechanics of the milling process. In this section, the mechanics of material removal and the forces exerted on the cutting tool are discussed.

The miller cutter can have a positive or a negative rake angle. Negative rake angle cutters are shock resistant and are used for heavy cutting operations. While, the positive rake angle is used for light and accurate cutting. The milling operation can be divided into three categories, face milling, up milling and down milling process. In a face milling processes, the entry and exit angles of the milling cutter is non-zero. Up and down milling processes are both peripheral milling operations. In an up-milling process, the entry angle is zero and the exit angle is non-zero and the chip load gradually increases, shown in Figure 2.8 a. The larger chip thickness at the disengagement leads to poor surface finish. The direction of the cutter rotation is opposite to the feed direction. The up milling was performed extensively before the advent of CNC machines since the backlash could not be compensated in manual machines. . This type of milling is used while machining heavy

metal removal rates to prevent sudden shock while machining. In a downmilling process, the exit angle is zero and the entry angle is non-zero. The chip load is highest at the beginning of the tooth engagement and gradually decreases with the immersion angle, shown in Figure 2.8 b. The down milling results in better surface finish owing to the smaller chip thickness at disengagement.

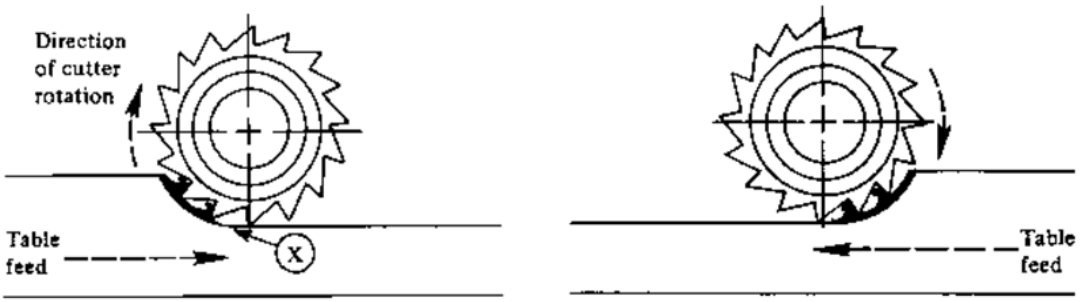

(a) (b)

Figure 2.8: Milling process , a) Up milling (conventional) , b) Down (climb) operation[70].

The experiments performed in this thesis are peripheral milling operations and the corresponding mechanics and the force equations are discussed.

The instantaneous chip thickness as a function of the immersion angle is given by,

$$h(\varphi_z) = f * \sin \varphi_z \tag{2.31}$$

where,

f is the mm/rev,tooth

φ_z is the instantaneous immersion angle at a distance z from the tool tip.

In addition, as the tool axially engages with the workpiece, it is imperative to consider the helical geometry of the flute along the axial depth of cut. As discussed earlier, the purpose of the helical geometry is to allow for gradual engagement and disengagement of the teeth. The lag angle along the helical flute is a function of helix angle (β), axial depth (z), shown in Figure 2.9 and the diameter of the cutting tool (D),

$$\psi = \frac{2z \tan \beta}{D} \tag{2.32}$$

The immersion angle, φ is maximum at the tip of the flute. A point that is z distance from the tip will have an immersion angle, $\varphi_z = \varphi - \psi$. As the cutter rotates, the cutting forces are estimated by summating the forces experienced by the points along the flute as they engage with the workpiece. This is achieved by dividing the cutting edge up to the final axial depth of cut, t_o into differential elements, shown in Figure 2.9.

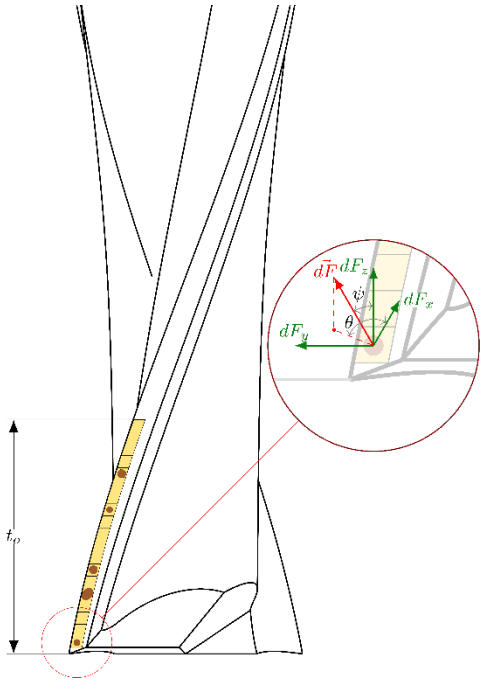

Figure 2.9: Flute divided into elements along depth of cut, t_o.

The tangential$\left(dF_t(\varphi)\right)$, radial$\left(dF_r(\varphi)\right)$ and axial$\left(dF_z(\varphi)\right)$ force experienced by each element can be given in terms of instantaneous chip area$\left(ah(\varphi)\right)$,

$$dF_t(\varphi_z) = K_{tc} ah(\varphi_z) + K_{te} a \tag{2.33}$$

$$dF_r(\varphi_z) = K_{rc} ah(\varphi_z) + K_{re} a \tag{2.34}$$

$$dF_z(\varphi) = K_{zc}ah(\varphi_z) + K_{ze}a \tag{2.35}$$

Where,

a: radial depth of cut

$K_{tc}, K_{rc} and\ K_{zc}$ are force coefficients in the tangential, radial and axial direction respectively. $K_{te}, K_{re}\ and\ K_{ze}$ are the edge constants.

These coefficients and constants are calculated using the oblique cutting model,

$$K_{tc} = \left(\frac{\tau_s}{\sin(\Phi_n)}\right) * \frac{\cos(\beta_n - \alpha_n) + \tan i\ \tan\eta \sin\beta_n}{\sqrt{\cos^2(\Phi_n + \beta_n - \alpha_n) + \tan^2\eta \sin^2\beta_n}} \tag{2.36}$$

$$K_{rc} = \left(\frac{\tau_s}{\sin(\Phi_n) * \cos i}\right) * \frac{\sin(\beta_n - \alpha_n)}{\sqrt{\cos^2(\Phi_n + \beta_n - \alpha_n) + \tan^2\eta \sin^2\beta_n}} \tag{2.37}$$

$$K_{zc} = \left(\frac{\tau_s}{\sin(\Phi_n)}\right) * \frac{\cos(\beta_n - \alpha_n)\tan i - \tan\eta \sin\beta_n}{\sqrt{\cos^2(\Phi_n + \beta_n - \alpha_n) + \tan^2\eta \sin^2\beta_n}} \tag{2.38}$$

Where,

α_n: rake angle

β_n: the friction angle

Φ_n: the flank angle

η: the chip flow angle

i: the oblique angle

τ_s: the shear stress of the work material

The coefficients can also be obtained experimentally using the force data from milling tests.

The cutting forces experienced by the cutting tool,

$$F_t(\varphi) = \sum_{z=0}^{t_o} K_{tc}ah(\varphi_z) + K_{xe} * a \tag{2.39}$$

$$F_r(\varphi) = \sum_{z=0}^{t_o} K_{rc}ah(\varphi_z) + K_{ye} * a \tag{2.40}$$

$$F_z(\varphi) = \sum_{z=0}^{t_o} K_{zc} a h(\varphi_z) + K_{ze} * a \quad (2.41)$$

Since milling in an intermittent cutting process, the forces are exerted on the cutting tool only when it is engaged with the workpiece material,

$F_t(\varphi), F_r(\varphi)\ and\ F_z(\varphi) > 0,\ when\ \varphi_{st} < \varphi < \varphi_{ex}$

$$F_t(\varphi), F_r(\varphi) and\ F_z(\varphi) = 0, \qquad when\ \varphi < \varphi_{st}\ and\ \varphi > \varphi_{ex}$$

Where, $\varphi_{st}\ and\ \varphi_{ex}$ are entry and exit angles respectively.

The radial spacing between the teeth is given by the tooth pitch angle,

$$\varphi_p = \frac{2\pi}{N} \quad (2.42)$$

Where

N: number of teeth in a cutter.

In some cases, more than one cutting tooth is engaged with the workpiece, when the pitch angle is smaller than the swept angle, $\varphi_{ex} - \varphi_{st}$. The total force in each direction will be a summation of forces exerted on all engaged teeth.

The resultant force exerted on the teeth is given by,

$$F = \sqrt{F_t^2 + F_r^2 + F_z^2} \quad (2.43)$$

Instantaneous cutting torque on the spindle is given by,

$$T = \frac{D}{2} * F_t \quad (2.44)$$

2.6 Mechanical properties and fatigue performance

2.6.1 Mechanical properties

The mechanical properties of the metal matrix composites depend on the type, size and volume fraction of the reinforcements used, the manufacturing process and the resulting refinement in matrix grain structure and porosity[72]. Several studies have investigated the effect of these parameters on strength and stiffness of the MMCs through tensile testing and hardness measurements as per ASTM standard E8/E8M[73–75]. Aluminum and magnesium alloys reinforced with SiC particles are the focus of this section.

Aluminum Composites

The manufacturing process was found to have a strong influence on the mechanical properties of the aluminum composites. The as cast aluminum composites were observed to have lower strength than the extruded composites for the same volume fraction and matrix alloy, can be observed in Figure 2.10. The extrusion process leads to reduction in porosity and more homogenous distribution of SiC particles in the matrix. This can be attributed to the higher strength exhibited by extruded composites under tensile load using cylindrical specimen of diameter 5 mm and gauge length 25 mm[76]. Consequently, the strength of the as cast aluminum composite was found to reduce after an optimal volume fraction of SiC particles. The initial increase in the strength can be attributed to the inherent high hardness of the SiC particles, increase in geometric constraint offered by the SiC particles to the movement of dislocations and the increase in density of dislocations in the matrix, grain refinement. However, beyond an optimal volume fraction, the interparticle distance becomes insufficient for relaxation leading to the early void formation due to accumulated dislocations at the interface, as [77].

The size of the SiC particles used was also found to have a significant effect on the mechanical properties. The tensile and yield strength was found to decrease with increase in particle size, also shown in Figure 2.10. One of the widely accepted reasons for this observation is that the smaller particles have higher matrix-particle interface area enabling more load transfer from the soft matrix to the reinforcement particles as reported by Yan et al in testing as extruded bars and by Singh et al as cylindrical specimens [78,79]. In addition, smaller sized particles also lead to finer grains in the matrix improving the strength of the composite. The ductility was found to be a function of interparticle distance, the ductility was found to decrease with decreasing particle size owing to the reduction of the interparticle space, shown in Figure 2.11. A large interparticle distance accommodates more dislocations during the deformation[80].

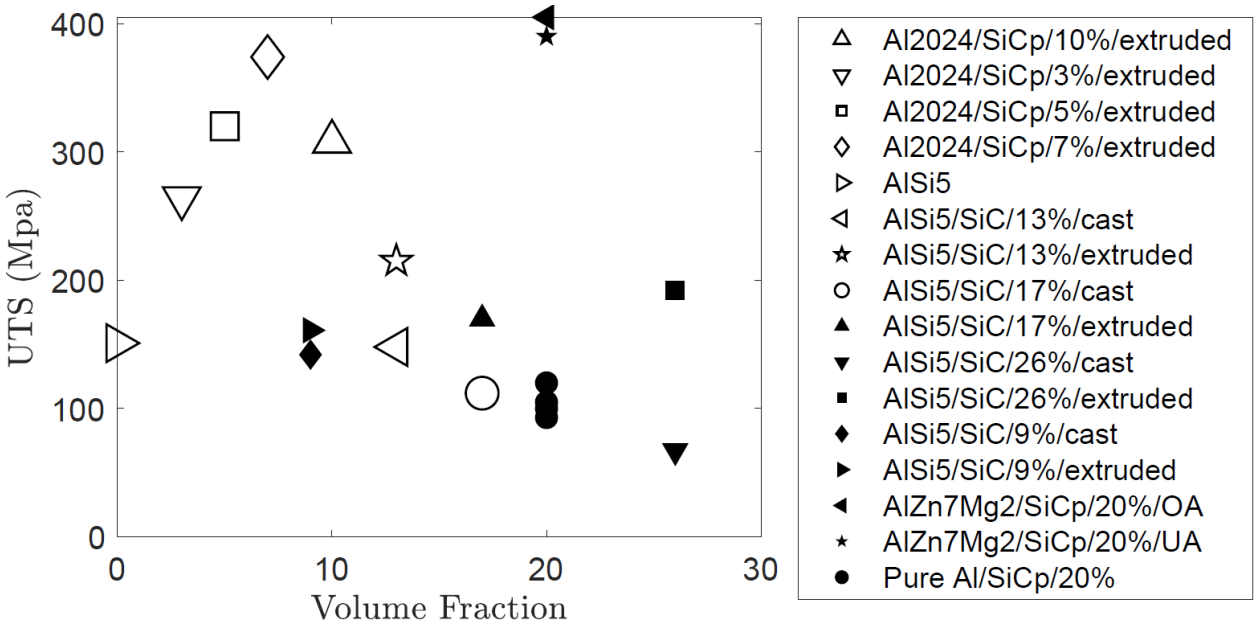

Figure 2.10: UTS of aluminum composites as a function of volume fraction and size of the reinforcements. Data from [74,75,80–82].

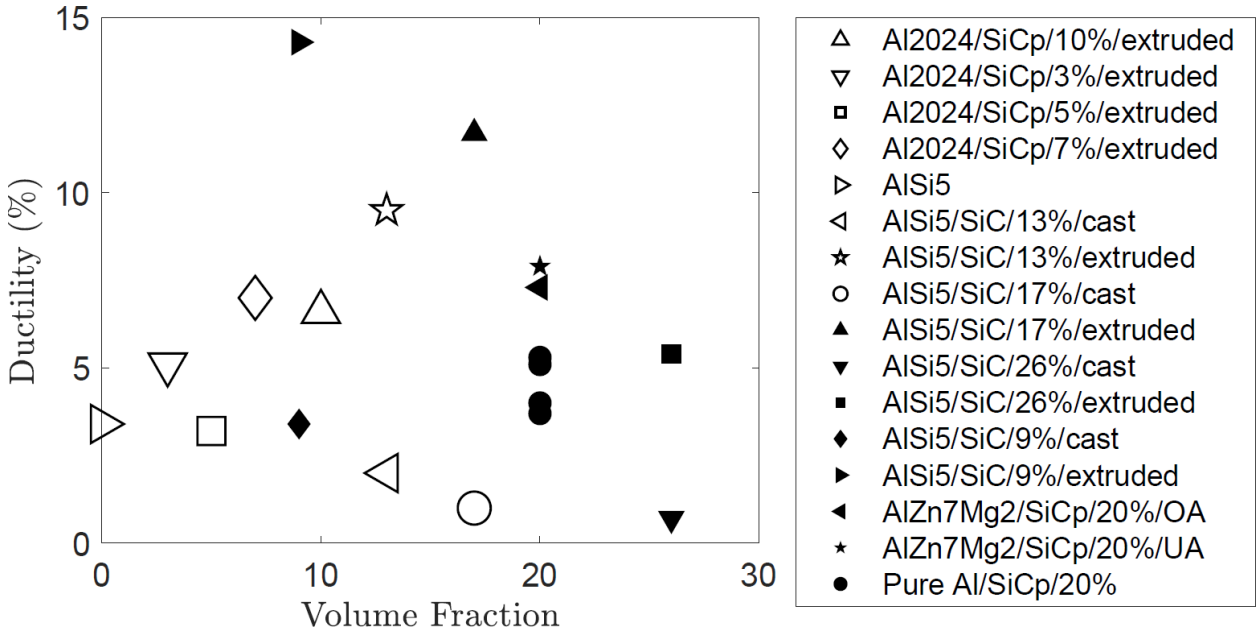

Figure 2.11: Ductility of aluminum composites as a function of volume fraction and size of the reinforcements. Data from [75–78,80]

The SEM fractography of the fractured surface showed a combination of ductile and brittle fracture features from the matrix and the reinforcement particles respectively. The matrix consisted numerous dimples as a result of void nucleation and coalition due to strong shear deformation and particle fragmentation and decohesion were also observed. The occurrence of particle fragmentation increased with the increasing particle size. While, particle decohesion was predominantly observed for smaller particles, shown in Figure 2.12.

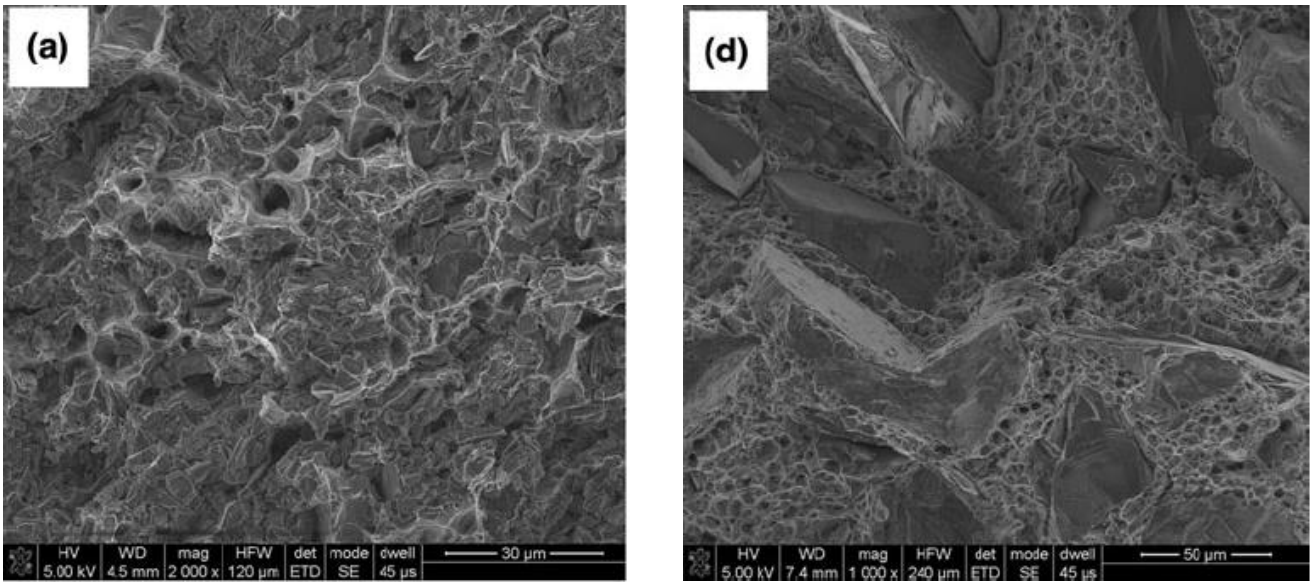

(a) (b)

Figure 2.12: SEM fractography of the fractured tensile specimen (the dog-bone-shaped, having a gage size of 6 mm in diameter and 40 mm in length,) showing dimples in the matrix, a) Al/SiCp/4.7 µm, showing particle decohesion, b) Al/SiCp/70.7µm, showing particle fragmentation[81]

Magnesium composites

Magnesium matrix composites are often reinforced with sub-micron and micron sized reinforcement particles[82]. The relative size of the particles with respect to the grain size of the matrix was found to play an important role since particles smaller than the matrix grains tend to be more uniformly distributed [82]. For the sub-micron particles, particle agglomeration and grain size of the matrix was found to be higher at higher volume fractions leading to weakening of the composites, shown in Figure 2.13, reported by Deng et al in testing extruded AZ91/SiCp,

cylindrical specimen[82]. Microcracks were found to emanate from the particle agglomerations, shown in Figure 2.14 causing premature failure and reduction in strength. For micron sized particles, the particles have a lower tendency to agglomerate and the grain size reduces in the matrix with increase in volume fraction[82] and also serve as a barrier for the dislocation motion leading to the increase in strength[83,84]. Additionally, the increase in Young's modulus can be attributed high modulus of the SiC particles and good interfacial bond between the matrix and the particles. A good bond results in significant increase in internal stresses between the reinforcements and the matrix leading to an increase in Young's modulus, reported by Lee et al in testing AZ91/SiCp produced through powder metallurgy and further extruded into bars[85]. The limited ductility of magnesium alloys were further reduced by the addition of SiC particles[84].

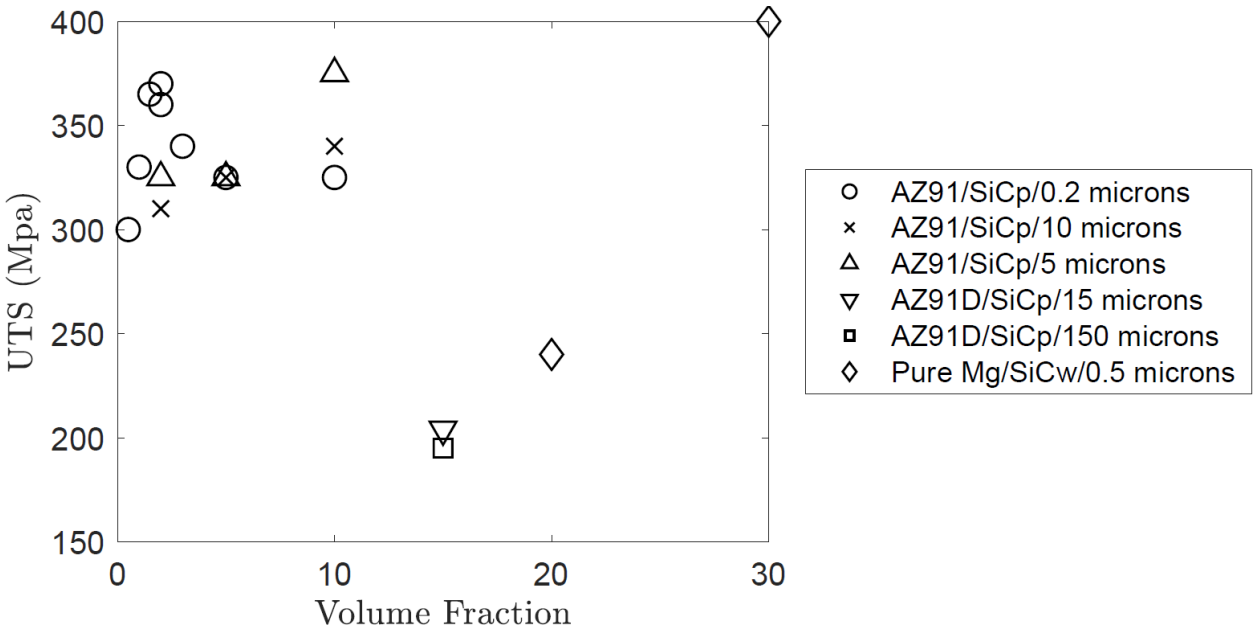

Figure 2.13: UTS of magnesium composites as a function of volume fraction and size of the reinforcements. Data from [82,84,85]

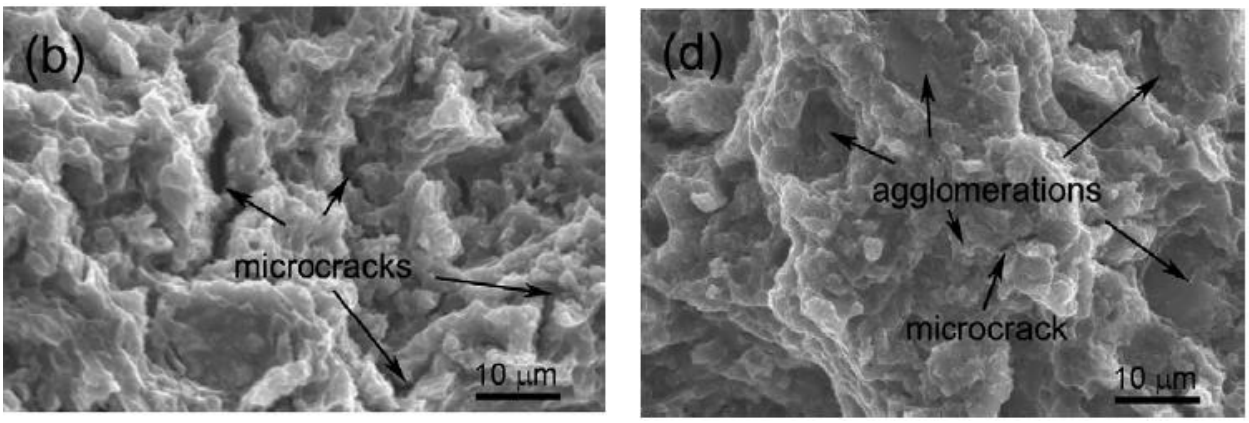

(a) (b)

Figure 2.14: SEM micrographs of AZ91/SiCp/0.2 μm(stir casted, extruded cylindrical coupons) a) 0.5% volume fraction, b) 5% volume fraction[83]

2.6.1 Fatigue behavior

In light of the outstanding potential of metal matrix composites for structural components in aerospace and automobile industries, it is imperative to study their behavior under cyclic loading. The addition of reinforcement particles to the metallic matrix may be beneficial or detrimental to the fatigue resistance of the material depending on processing method, size, type and volume fraction of reinforcement, heat treatment and the quality of interface between the particles and the matrix[86]. These factors affect the load transfer mechanisms and the associated stress concentrations, the residual stress from the heat treatment or the type of manufacturing process used, the microstructure of the metallic matrix. Owing to these variations the fatigue behavior of

the MMCs should be extensively studied. Fatigue behavior of a metal matrix composite can be quite complex due its dependence on the manufacturing technique used, reinforcement particles, metallic matrix and the interface between the particles and the matrix[87].

The metal matrix composites are usually produced through squeeze casting process, spray co-deposition of matrix and particles and powder metallurgy techniques. These primary manufacturing processes are conducted at high temperatures and the thermal expansion coefficient of the matrix is higher than the reinforcement particles, inducing thermal residual strain in the composite as it cools down to the room temperature. The large residual strain results in an increase in dislocation density in the matrix[88]. The dislocation density was measured for aluminum composites reinforced with whiskers and particles and unreinforced aluminum processed under the same conditions. The average dislocation density for composites were reported to be one order higher in magnitude than the unreinforced matrix[89,90]. This difference in dislocation density has a profound effect on the fatigue behavior of the composites. Han et al[91] performed constant strain amplitude and completely reversed cyclic experiments on commercially pure aluminum reinforced with 20% SiCp/10μm. The specimen used was of gauge length 14 mm and diameter 6 mm, machined and polished from the extruded composite rod. The stress amplitude, $\Delta\sigma/2$ was plotted as a function of number of cycles, shown in Figure 2.15. For the unreinforced aluminum, an increase in stress amplitude was observed for the first few cycles due to material hardening. After which the stress amplitude remained constant up to one tenth of the fatigue life and a slight material hardening was observed for the rest of the fatigue life, shown in Figure 2.15 a. While the composite also exhibited hardening for the first few cycles, material softening was observed for the rest of the fatigue life, shown in Figure 2.15 b.

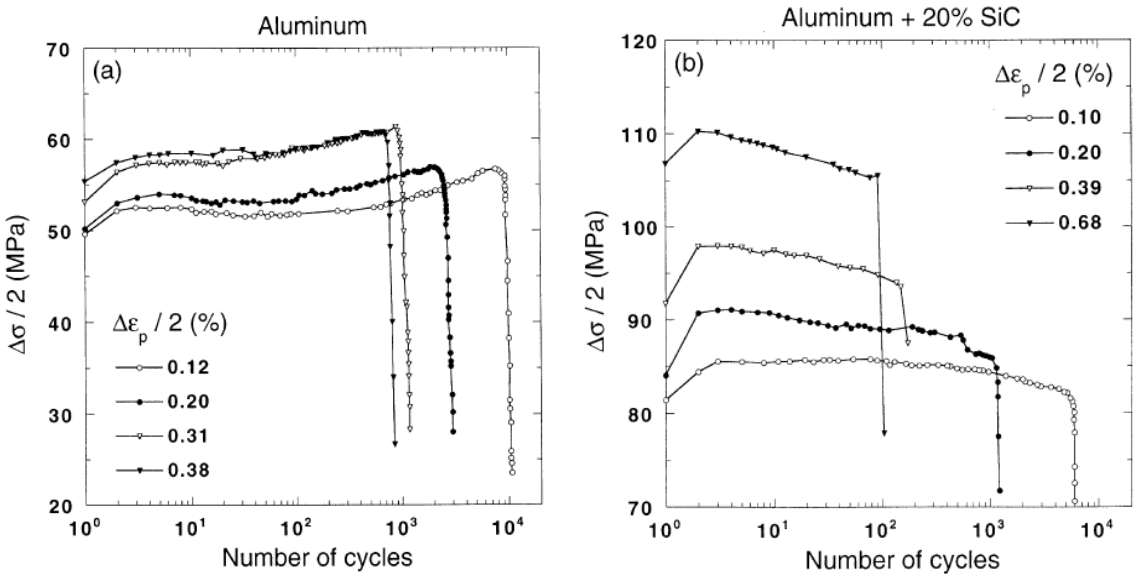

(a) (b)

Figure 2.15: a) Cyclic behavior unreinforced aluminum matrix measured at different strain amplitudes, Δεp/2, b) Cyclic behavior of Al/SiCp/20% measured at different strain amplitudes, Δεp/2[91].

The authors attributed the marked difference in behavior to the difference in dislocation densities. The moderate hardening shown by the unreinforced aluminum is a typical behavior for pure metal with a low dislocation density. On the other hand, the cyclic softening behavior of the composites was similar to the cold worked metal with high dislocation density. The initial hardening was due to the interaction between the dislocations and the cyclic softening was caused by the rearrangement of dislocation structure during the processing.

In addition to the dislocation densities, the pores and inclusions introduced in the composites during the manufacturing process also have a significant effect on its fatigue properties. Rohatgi et al studied the variations in the fatigue properties of T6 heat treated A359/SiCp/20% under strain controlled completely reversed cyclic tests[86]. The specimen was initially cast into a bar and heat treated at T6 condition, followed by machining into dimensionsof 12.5 mm in gauge length and

6.4 mm in diameter. The stress amplitudes were plotted as a function of number of reversals, shown in Figure 2.16. The T6 heat treated A359/SiCp/20% showed better life than A356/SiCp/20% but exhibited lower life than forged and extruded A2080/SiCp/20%. The authors attributed this to the cast composites containing porosity and inclusion in addition to the microstructural defects like particle clusters and non- uniform particle distribution. These defects can act as sites for fatigue crack initiation accelerating failure. This observation accedes with the report that secondary manufacturing processes life forging and rolling help in breaking up the reinforcement agglomeration, homogenizing the distribution, eliminating the porosity and improving the interfacial bonding[92].

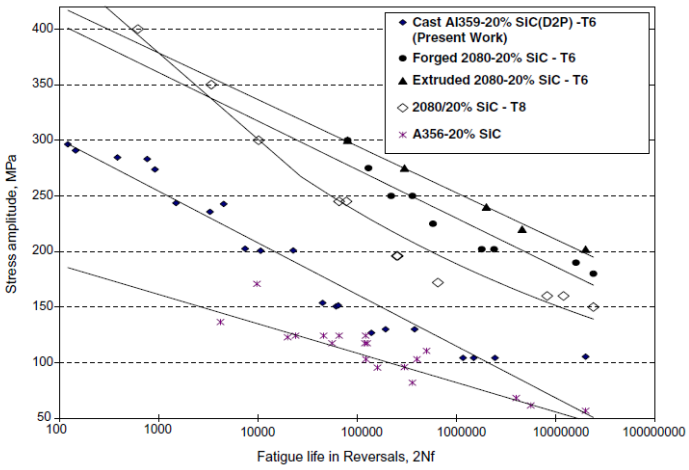

Figure 2.16: Stress amplitude vs number of reversals for various Al/SiCp/20%[88].

The effects of particle size, volume fraction and matrix strength on the fatigue behavior of Al/SiCp composites were studied by Hall et al[93]. The underaged, peak aged and over was developed using powder metallurgy technique with 10, 20 and 35% volume fraction of SiC particles into cylindrical specimen of diameter 5.5 mm and a gauge length of 18 mm . In order to study the effect of particle size, the 20% volume fraction composite was reinforced with particle sizes of 2,5,9 and 20 microns. Stress controlled completely reverse loaded fatigue tests showed that the fatigue life

increased with increase in volume fraction, decrease in particle size and increase in matrix strength. This increase in fatigue strength was found to consistent with increase in tensile strength observed in monotonic loading. Fatigue crack initiation sites were reported to be large intermetallic particles located near the surface and particle agglomerations that form during the manufacturing process. The reinforcement particles were found to be fractured at higher stress intensity, the number of fractured particles increased with the increase in particle size and volume fraction . Similar trend was observed for particle size by Shang et al and Bonen et al[94]. The influence of volume fraction on the particle fracture was also studied by Kumai et al on 15% and 30% SiCp reinforced 6061aluminum alloy[95]. The authors reported that the particles had a higher tendency to fracture as the volume fraction and matrix strength increased.

Chawla et al performed a similar study on wrought SiC reinforced 2080 aluminum alloy[72]. In accord with the previously discussed results, the authors reported reduction in ductility and increase in tensile strength with increasing volume fraction and decreasing particle size of SiC. The increase in strength with increasing volume fraction was attributed to higher load being transferred to the reinforcement particles. The reduced ductility is due to the early onset of void nucleation with higher amount of reinforcements in the matrix. Since the load is carried by particles with high modulus and strength the fatigue life was found to improve with increasing volume fraction of SiC particles. From Figure 2.17, it can be observed that this improvement in fatigue life is more at lower stresses and the fatigue life is closer to unreinforced matrix at higher stresses. This was attributed to limited ductility of composites at higher stresses. Increase in volume results smaller spacing between the particles in the matrix resulting in more barriers for reversible slip motion during fatigue.

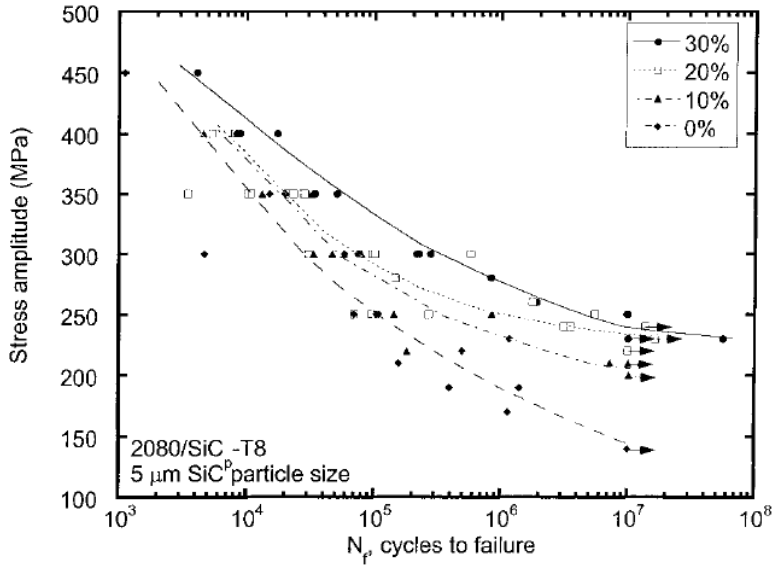

Figure 2.17: Effect of volume fraction of reinforcement on the fatigue life of Al 2080/SiCp composite[71].

High cycle fatigue performance of drilled and milled Al/SiCp/15% was investigated as a function of cutting speed, feed and reinforcement particle size[96]. The tool particle interaction resulted in particle fracture and pull out from the matrix on the machined surface. These defects were found to be more pronounced with increasing particle size. The authors found that the strain hardening from plastic deformation and heat generation during the milling process did not have a significant effect on the fatigue life. While, the size of reinforcement was found to have a significant effect on the fatigue life. In accordance with the results reported above, the fatigue life was reported to improve with decreasing particle size. In addition, the fatigue cracks were reported to be arrested or deviated by the large reinforcement particles present in the matrix, shown in Figure 2.18.

The effects of electrical discharge machining induced surface defects on fatigue life of Al/SiCp/15% was studied by Ramulu et al[97]. Surface and sub-surface damage caused by the

machining process is assessed using surface roughness measurements and SEM images of the machined surface. The average surface roughness of the coarse machining condition was reported to be about 3 times higher than the fine sparked condition. The SEM image analysis of the surface showed a significant difference between the

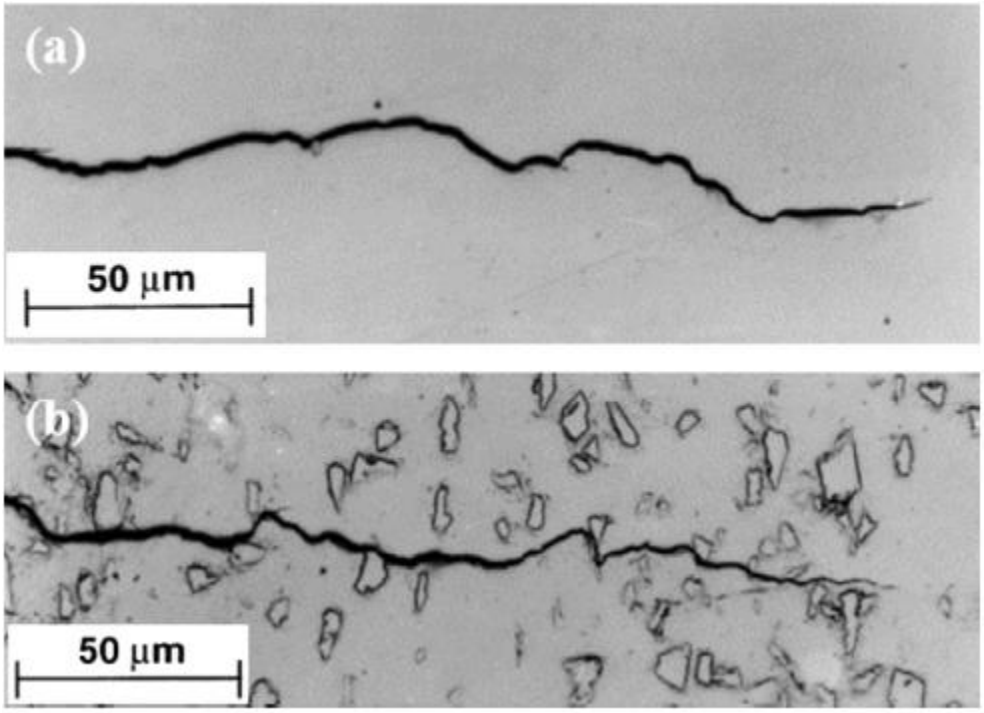

Figure 2.18: Crack propgatagation in fatigue of Al/SiCp[98].

two machining conditions. The fine sparked surface had more uniformly distributed crater and the damage zone was more evident. The microhardness tests showed that the EDM process resulted in surface softening. The fatigue life of the coarse machined composite was reported to be lower than the polished and the fine sparked specimen. The increase in surface roughness and surface softening was reported as the cause of the observed reduction in fatigue life. Fractographic examinations showed a short period of crack propagation with no classic striations. The authors

also reported that the fatigue crack initiations occurred on the surface possibly near particle clusters[99].

The fatigue failure that is initiated by nucleation of multiple cracks in the composite that propagate through the material during cyclic loading are also reported by a few other investigations. The fractured surface and the longitudinal sections along the loading directions. The fracture mechanism was found to be depend on the stress level during fatigue. Several microcracks nucleated throughout the specimen from broken or clustered particles during low cycle fatigue tests[100,101]. The microcracks grow and coalesce to form a dominant crack leading to complete fracture. Since the reinforcement particles and their interface with the matrix act as nucleation sites, the composites exhibit poor low cycle fatigue properties. A different mechanism of fatigue crack nucleation was reported in high cycle fatigue tests. The presence of imperfections like porosity, particle agglomeration formed during manufacturing processes[95,102]. The second contributor for the nucleation was found to be reinforcement particles. Several cracks were found to nucleate near the sharp corners of the particles, whiskers and fibers[95].

2.7 Summary

MMCs consists of light weight metallic matrix reinforced with ceramics of high strength and hardness. However, the reinforcement particles that increase the specific strength and stiffness of the matrix also results in difficulty while machining. This can be attributed to the hardness of the reinforcement particles being typically higher than the hardness of the cutting tool resulting in accelerated abrasive wear. The accelerated tool wear results in high machining costs and poor surface quality. The presence of defects on the surface significantly reduces the life of a component. Therefore, it is imperative to study the machining of MMCs for extensive adoption of these composites. Machinability can be studied in terms of cutting forces, tool wear and surface

finish generated in a machining process. Experiment and analytical work involving measurement of these parameters were discussed in this chapter.

The cutting forces reflect the mechanical stresses experienced by the cutting edge and the workpiece. In addition to the feed, speed and the cutting tool material, the cutting forces were also dependent on the type and concentration of reinforcement used. Among the cutting conditions, feed rate was found to be the most dominant parameter, the cutting forces were found to increase with the feed rate. However, the effect of cutting speed remains inconclusive in the literature. This warrants for additional investigation to understand the effects of machining conditions. Additionally, in investigating the machinability of functionally gradient aluminum composite and magnesium composite, it is imperative to study the cutting forces generated since it reflects the effects of concentration and size of the SiC particles, the quality of surface generated and the extent of tool wear.

The tool wear was affected by the volume fraction, size and distribution of the reinforcement particles, the matrix properties for a given cutting tool material and was found to increase with feed rate and cutting speed. Formation of BUE was also reported while machining aluminum matrix composites with the increase in cutting speed. Owing to the higher hardness of the reinforcement particles in comparison with the cutting tool, abrasive wear was found to be the dominant wear mechanism. In addition, the size of the reinforcement was also found to have a significant effect on the tool wear. Reinforcement particles larger than grain size of the WC grains easily displace them on impact causing rapid tool wear. While, smaller reinforcements caused microcracking and fatigue due to repeated impact on the cutting edge. Since the life of the tool is significantly affected by the presence of the reinforcement particles, it is important to evaluate the

tool wear and understand the wear mechanism for economic production of MMCs of high surface quality.

The most critical parameter in the analysis of the machinability is the investigation of quality of surface produced. The quality of surface generated in a machining process directly affects the life of the component. However, only a handful of studies have reported the surface quality of machined aluminum and magnesium composites. Feed rate was found to have a dominant effect on the surface finish generated. The surface roughness was found to increase with the feed rate. Additionally, fine grooves, voids, feed lines were also observed at high feed rates. However, the influence of cutting speed on average surface roughness has not been identified clearly. Therefore, the study of machinability cannot be complete without thorough investigation of surface finish and surface damage induced to MMCs while machining.

The quality of surface generated is also reflected on the chip morphology. Generally, a saw tooth profile was reported. The reduced ductility of the MMC causes stick-slip condition at the tool interface causing segmentation on the free surface. The chip morphology was also found to depend on the cutting edge geometry. Therefore, tool wear can be monitored by inspecting the chip morphology.

Finally, the fatigue performance of the composites was discussed to understand the crack initiation, propagation and failure mechanism in MMCs. The addition of reinforcement particles to the metallic matrix may be beneficial or detrimental to the fatigue resistance of the material depending on processing method, size, type and volume fraction of reinforcement, and the quality of interface

between the particles and the matrix[86]. In addition, the surface defects like voids formed due to particle pull out and microcracks generated during a machining process can act as stress concentration sites leading to poor fatigue life of the composite. Owing to these variations the fatigue performance of machined MMCs should also studied.

Most of the experimental and analytical work in the literature involved turning and drilling of MMCs. But, only a very few studies have investigated milling of aluminum and magnesium matrix composites. Unlike turning process, milling is a discontinuous process where the cutting edge impacts the workpiece in each tool rotation. The helical cutting edge gradually engages and disengages with the workpiece the helical cutting edge in a milling process gradually engages and disengages with the workpiece material. The repeated impact of the cutting tool on the reinforcement particle may have detrimental effect on the tool wear and surface quality generated. Therefore, it is essential to study milling and its effects on the fatigue behavior of MMCs.

Chapter 3 . Research Goals and Objectives

3.1 Research scope

The scope of this study is to investigate the machinability and structural integrity of metal matrix composites. The machinability is assessed through the analysis of cutting forces, surface roughness, tool wear and acoustic emission in peripheral milling of SiC particles reinforced aluminum and magnesium composites. The peripheral milling experiments were performed by varying the feed rate and spindle speed, while keeping the radial and axial depth of cut constant. The depth of cut was kept constant since it has the least influence on the surface finish of MMCs in comparison to feed and cutting speed [7]. The interaction between the cutting edge and reinforcement was studied through the analysis of machined surface and chip morphology. The reinforcement particles may be fractured, pushed into the matrix or fall out during the machining process. The influence of these events on the surface and sub-surface properties are reflected on the structural integrity of the parts. The impact of the machining induced surface defects on the fatigue life of the metal matrix composites were studied through cyclic loading of machined coupons.

Technovia research has reported that the global demand for metal matrix composites is projected to reach 10.8 kilotons by 2022 and aluminum based metal matrix composites accounts for 30% of this demand. However, despite the demand and successful production of the composites, the ins of this technology is limited by the concerns related to ease of manufacturing and inspection, scale-up, and cost[103]. The metal matrix composites are generally produced in near net shape using casting and powder metallurgy processes. However, secondary manufacturing processes like machining are required to obtain the final dimensional

tolerances and surface finish. This research aims to mitigate the concerns associated with milling of these composites by identifying the effects of cutting conditions on the quality of the surfaces generated and its influence on the surface integrity of the machined components.

3.2 Research Goals

Goal 1: Machinability of functionally gradient A359/SiCp and uniformly distributed AZ91/SiCp

- *Task 1: Measurement of cutting forces*

  Cutting forces indicate the mechanical stresses experienced by the cutting edge and is also a reflection of the resistance offered by the workpiece during machining. The cutting forces was measured as a function of varying reinforcement percentage, feed, spindle speed and constant depth of cut. The quality of the surfaces generated during a machining process can be assessed by monitoring the cutting forces during machining. This task aims to find the correlation between the cutting forces and the surface generated.

- *Task 2: Measurement of surface roughness*

  Surface profiles generated while machining MMCs were analyzed in terms of surface roughness parameters. The cutting edge interaction with MMC can lead to ploughing of the matrix material, particle fracture and particle displacement along the surface or pushed into the matrix or removed with the chip. These events are reflected in the surface profiles of the cut surface. The particles embedded on the surface can form peaks on the surface and the particles that fall out of the matrix or are pushed into the matrix form voids on the surface. Therefore, these events can be picked up from the surface profiles by choosing the

appropriate surface roughness parameters.

- *Task 3: Identify the tool particle interaction through SEM imaging*
    - The fate of the reinforcement particles that encounter the cutting edge can be assessed through SEM imaging of the work piece surface.
    - The chip morphology is studied to understand the material flow in the presence of reinforced particles and the effect of reinforcement particles on the tool wear. The chip formation processes depend on the ductility, thermal conductivity, and microstructure of the workpiece material. The chip morphology is studied through the analysis of SEM images of the chips at different operating conditions.
- *Task 5: Acoustic Emission analysis*
    - The generation of transient elastic waves within the material due to sudden and irreversible structural changes[104]. The dislocation motion and changes in microstructure have significant acoustic emission in alloys and metals[105].
    - Acoustic emission will be measured while machining MMCs and pure alloys. The acoustic emission will be characterized to identify the prominent damage mechanism in MMCs.

Goal 2: Development of cutting force model for end milling of functionally gradient and uniformly distributed MMCs.

- *Task 1: Prediction of cutting forces*

  Physics based model developed for milling conventional pure metals is extended to accommodate the presence of reinforcement particles in the matrix. The functionally gradient concentration of the reinforcement particles are considered by varying the

probability of the cutting edge interacting with a particle. The contribution of forces from the tool-particle and tool-matrix interaction are considered to predict the total forces acting on the cutting edge.

Goal 3: Evaluating the effect of machining on the mechanical Properties of functionally gradient A359/SiCp and AZ91/SiCp

- *Task 1: Identifying the optimum machining conditions*

  The optimum machining conditions are identified from goal 1.

- *Task 2: Tensile testing of machined composites*
  - Tensile tests were performed on machined specimen to identify the effect of machining on the tensile properties of the composites.
  - Fractographic analysis was performed to identify the effect of presence of reinforcement particles on the crack propagation.
- *Task 3: Measurement of fatigue properties*
  - The surface and sub-surface properties of the machined surface was evaluated
  - The effect of machining on the surface integrity was studied through fatigue testing
  - Fractographic analysis was performed to study the fatigue crack propagation through the specimen.

Chapter 4 . Material Characterization

Two categories of metal matrix composites are investigated in this study. Functionally gradient aluminum matrix composite reinforced with SiCp and magnesium composite reinforced with SiCp. The specific aluminum alloy used for the matrix was A359, chemical composition shown in Table 4.1 and magnesium alloy was AZ91, chemical composition shown in Table 4.2.

Table 4.1: Chemical composition of aluminum matrix composite[65]

	Si	Fe	Cu	Mg	Ti	Al
A359	8.50-9.50	0.20 max	0.20 max	0.45-0.65	0.20 max	net

Table 4.2: Chemical composition of magnesium matrix composite[103]

	Al	Zn	Cu	Mn	Mg
AZ91	8.3-9.7	0.35-1.0	0.03 max	0.15-0.5	net

This chapter discusses the material characterization and tensile properties of these MMCs. MMCs are characterized in terms of SiC particles percentage and size. The aluminum metal matrix composite in this study is a functionally gradient material. A varying material property is achieved across the material through controlled variation of microstructure. In this case, the difference in microstructure is achieved by reinforcing the matrix with gradient concentration of SiC particles. The mechanism by which the reinforcement particles affect the microstructure of the matrix was discussed in Chapter 2. This increase in SiCp concentration and through the matrix is quantified

in this chapter. Whereas, in magnesium MMC, the SiC particles were distributed uniformly throughout the matrix and the particle concentration and size were characterized.

Additionally, the tensile properties and the damage mechanism are also reported for the composites.

4.1 Functionally gradient Al/SiCp

A disk brake was produced in house by Pedersen et al through centrifugal casting to achieve the concentration gradient along the radius of the brake, details are given in reference [67], shown in Figure 4.1 . This production technique results in the concentration of the SiCp increasing towards the circumference of the disk. The average particle size of SiCp was found to 12.8 µm. The particle concentration and size distribution in the matrix was computed through image processing of micrographs and obtaining area based statistics using MATLAB.

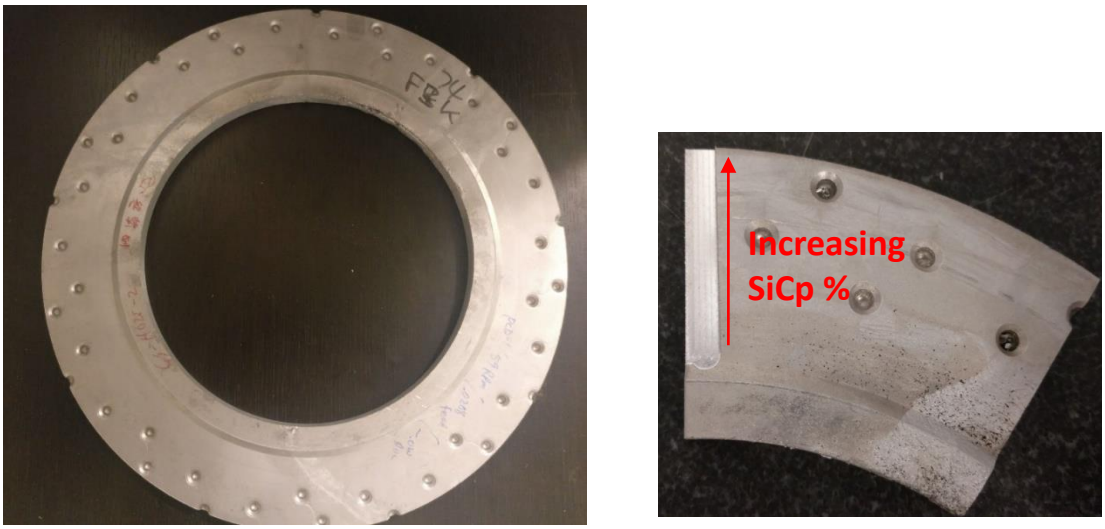

(a) (b)

.Figure 4.1: a) Centrifugally cast disk brake prior to machining, b) Section of the brake showing the increase in SiCp concentration.

Sample of the cross-section from disk were machined using waterjet and mounted in epoxy resin mold. The sample was polished down to 1 μm using diamond abrasives and optical micrographs were obtained at six locations along the cross-section of the disk, shown in Figure 4.2. At each position, optical micrographs were obtained from the center of the cross-section and points 2 mm above and below the center point. Optical micrographs were obtained at 10x, shown in Figure 4.3a.

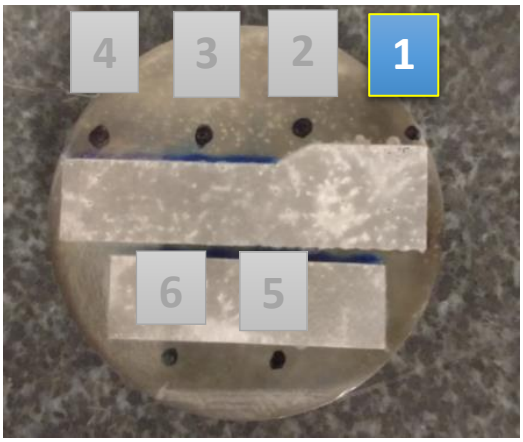

Figure 4.2: Cross-section of the disk mounted in an epoxy mold. Optical micrographs were obtained from points 1 through 6.

The optical micrograph obtained was converted to a binary image using a threshold intensity of 0.6, shown in Figure 4.3 b and c. In the binary images, the lighter reinforcement particles are given by 1 and the darker matrix material is given by 0. Therefore, the particle concentration can be calculated by,

$$Reinforcement\ \% = \frac{\sum pixel\ values}{total\ number\ of\ pixels} * 100 \quad (4.1)$$

The area of interest was increased from 5.66 x 10^4 µm^2 to 6.9 x 10^5 µm^2, shown in Figure 4.3. The percentage of reinforcement becomes constant at 15% with increasing area of interest, shown in Figure 4.4. This indicates that the percentage reinforcement does not vary significantly beyond an area of interest beyond, 5 x 10^6 µm^2. Therefore, the area measured through the optical micrographs at 10x is sufficient to obtain reliable percentage reinforcement.

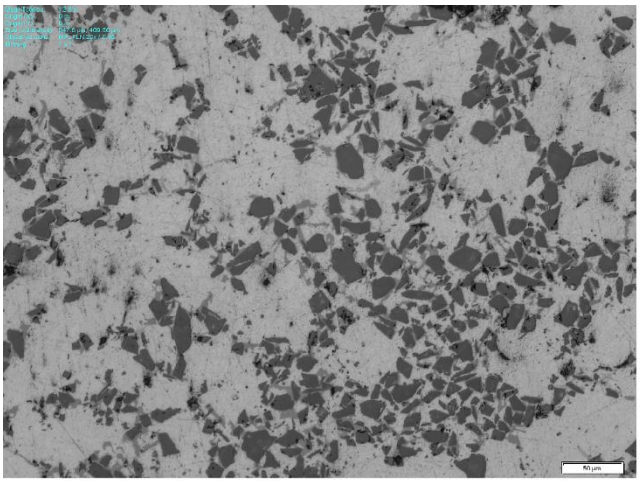

(a)

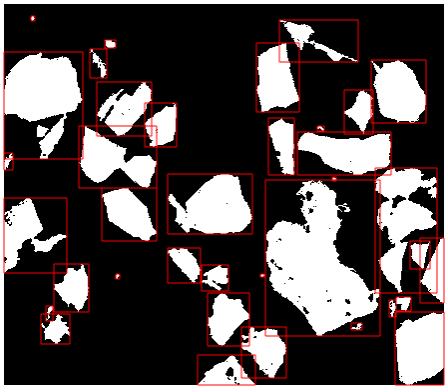

(b)

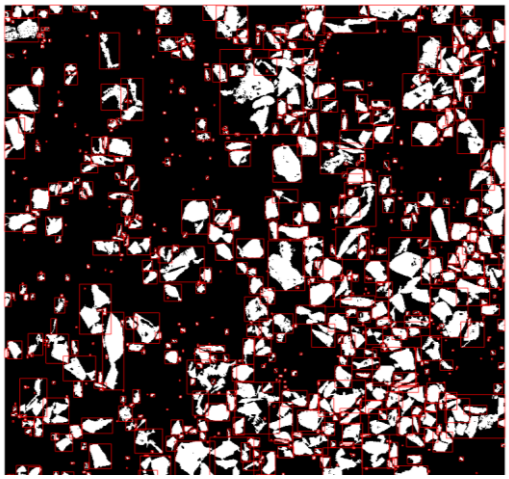

(c)

Figure 4.3: a) Optical micrograph of functionally gradient Al/SiCp obtained from point 2, b) processed image with area of interest of 10000 µm^2 , c) Area of interest: 2.5 x 105 µm^2.

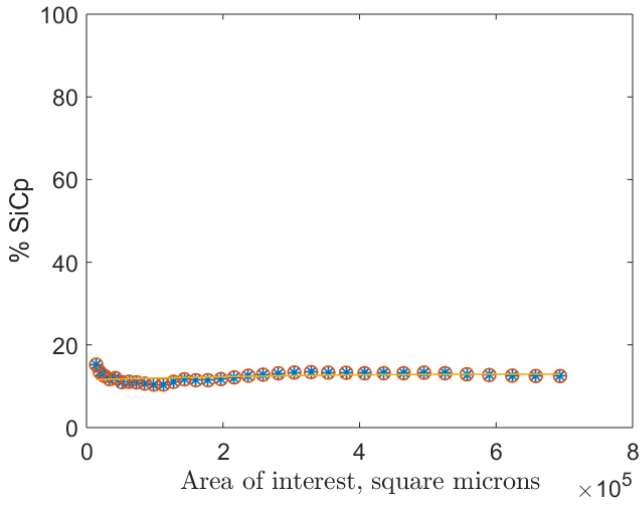

Figure 4.4: Reinforcement Percentage vs area of interest.

Additionally, the boundary and area of each particle was obtained to compute the equivalent diameter of the particles. The particle diameter distribution is shown in Figure 4.5. The average particle diameter was found to be 12.8 µm, with a standard deviation of 6.38 µm. The reinforcement % as a function of area of interest plots from all the points and MATLAB code are given in Appendix A.

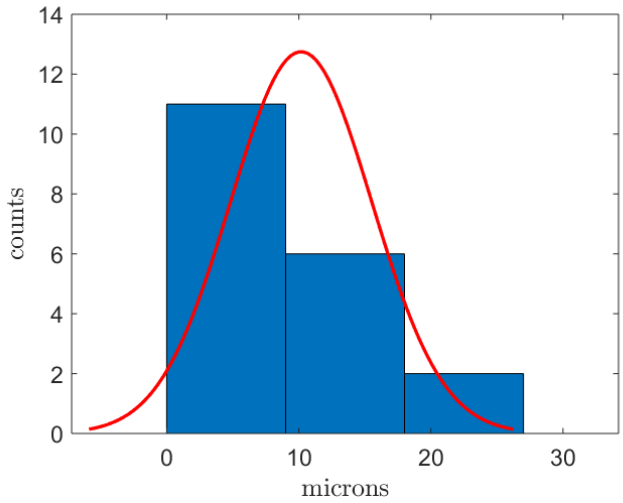

Figure 4.5: Particle size distribution, X axis is the diameter of the particles in µm and Y axis is the count of the particles.

Similar approach was followed for optical micrographs obtained from points along the cross-section of the disk. The percentage reinforcement at each point was plotted as function of distance from point 1, shown in Figure 4.6, data given in Appendix A and the corresponding SEM micrographs at points along the disk are shown in Figure 4.7.

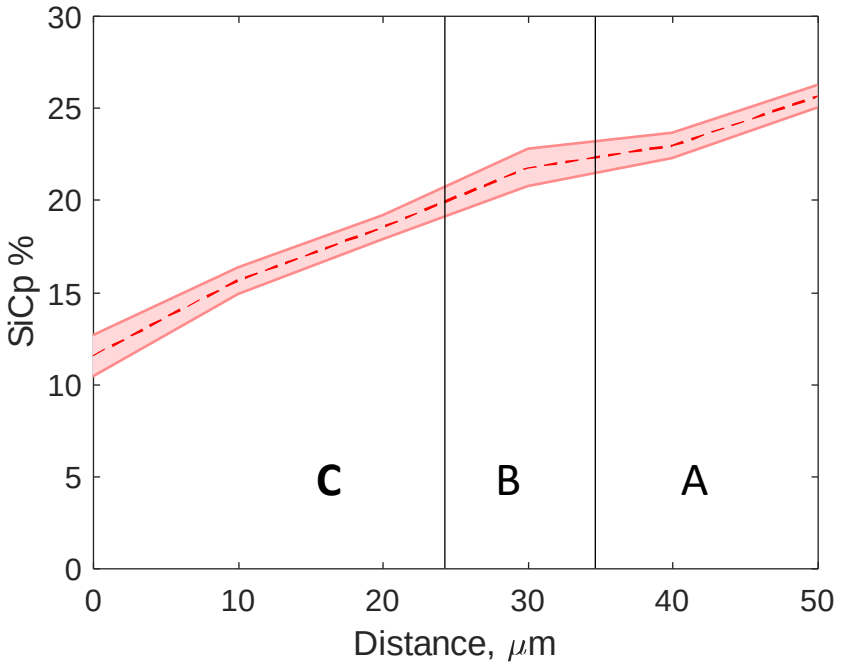

Figure 4.6: Percentage reinforcement of SiC particles as a function of distance along the disk.

A polynomial fit of the reinforcement percentage as a function of the distance was obtained,

$$P(x) = -0.0043x^2 + 0.522x + 10.5057 \quad (4.2)$$

Where,

$P(x)$: Reinforcement percentage, %

x: Distance from inner to outer radius of the disk

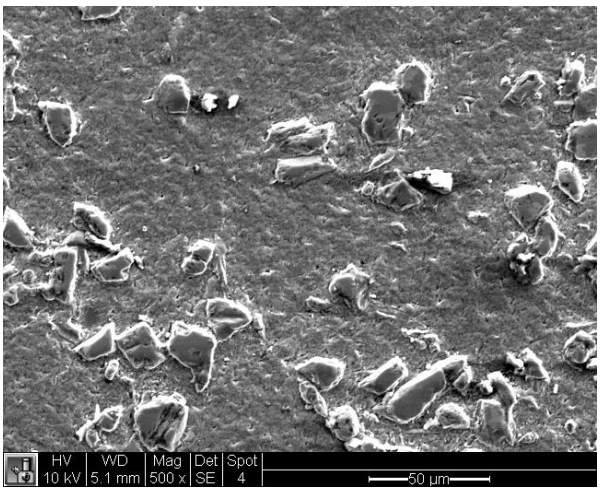

(a) Point 1

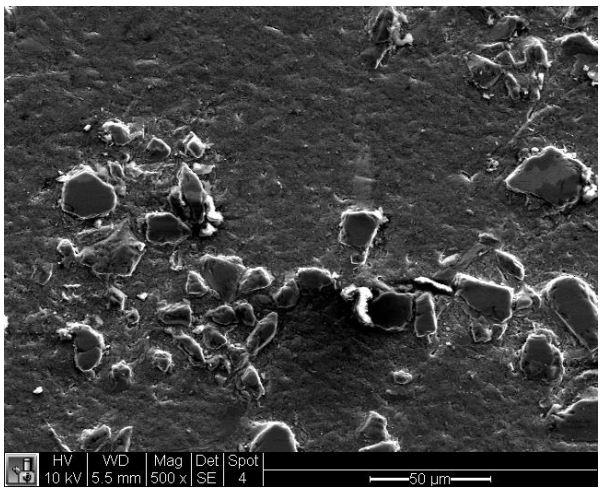

(b) Point 2

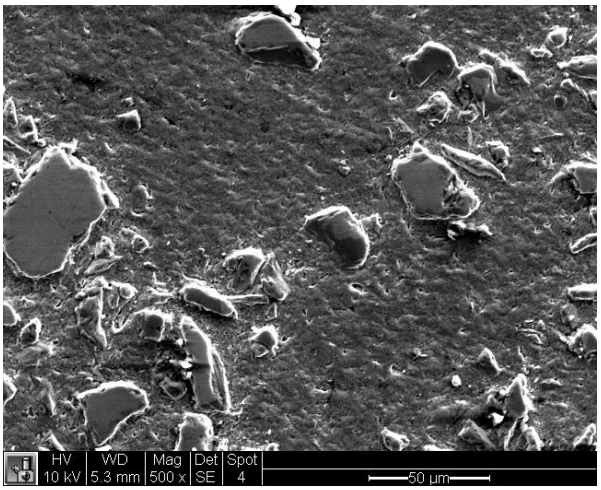

(c) Point 3

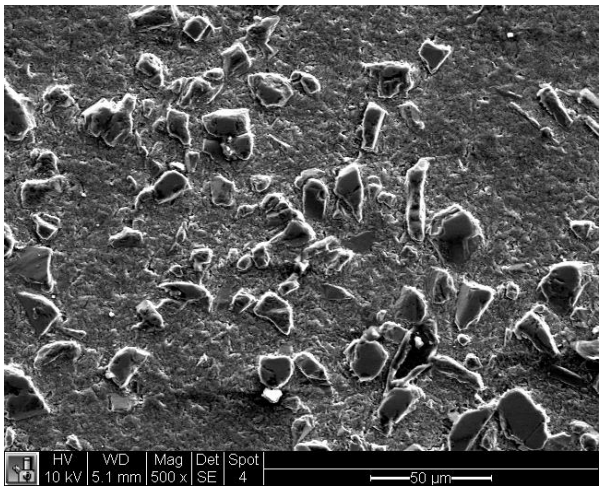

(d) Point 4

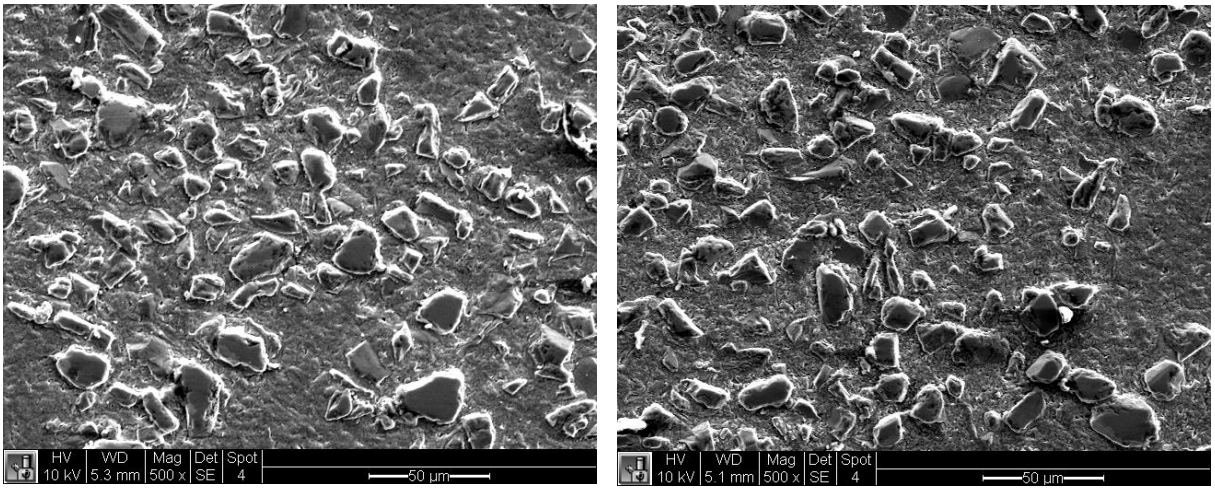

(e) Point 5 (f) Point 6

Figure 4.7: SEM micrographs obtained from points along Al/SiCp

For convenience, the functionally gradient material was discretized into three zones with decreasing average particle concentration, listed in Table 4.3. This enables analysis in terms of high, medium and low concentration zones of the functionally gradient composite.

Table 4.3: Zones with corresponding average particle concentration

Zones	Average Particle concentration
A(35<x<48)	23.4%
B (25<x<35)	20.2%
C(5<x<25)	17.5%

4.2 Tensile properties of functionally gradient Al/SiCp

Tensile properties of the functionally gradient aluminum composite were measured using the INSTRON 5585H electro-mechanical test frame. The tensile test was performed on compact specimens, preparation of these specimen is discussed in Figure 4.8. Crosshead speed was fixed at 1.27 mm/min. The stress-strain curve was obtained for three specimens. The differences in the tensile stress-strain curve can be attributed to the variations in the particle distribution in the matrix. The average ultimate tensile strength was found to be 160 MPa and the material exhibited limited ductility with average final strain of 0.0024. A typical stress strain curve in shown in Figure 4.9 and the fractured specimen is shown in Figure 4.10. The load displacement data is given in Appendix A. The fractured surface appeared extremely rough and were inspected through SEM fractography.

The SEM micrographs of the fractured specimen were studied to understand the mechanism of failure, shown in Figure 4.11. The fractured surface was observed to be rough at a low magnification of 50x, shown in Figure 4.11 a. The surface was observed at a higher magnification to understand the mechanism of failure. Particle debonding at the particle-matrix interface was observed on the fractured surface at point A, shown in Figures 4.11 b, c and d. The SiC particles act as barrier to the motion of the slip planes during plastic deformation. Void nucleation and separation at the particle-matrix interface was also observed by Lewandowski et al[106] in studying the effects of microstructure and reinforcement percentage on fracture of SiC reinforced aluminum matrix. Particle fracture was observed at point B, the fracture surface appeared relatively smooth, typical for crack propagation through cleavage. Similar observations were made by Roebuck in studying fractography of SiC reinforced aluminum matrix[107]. The author observed

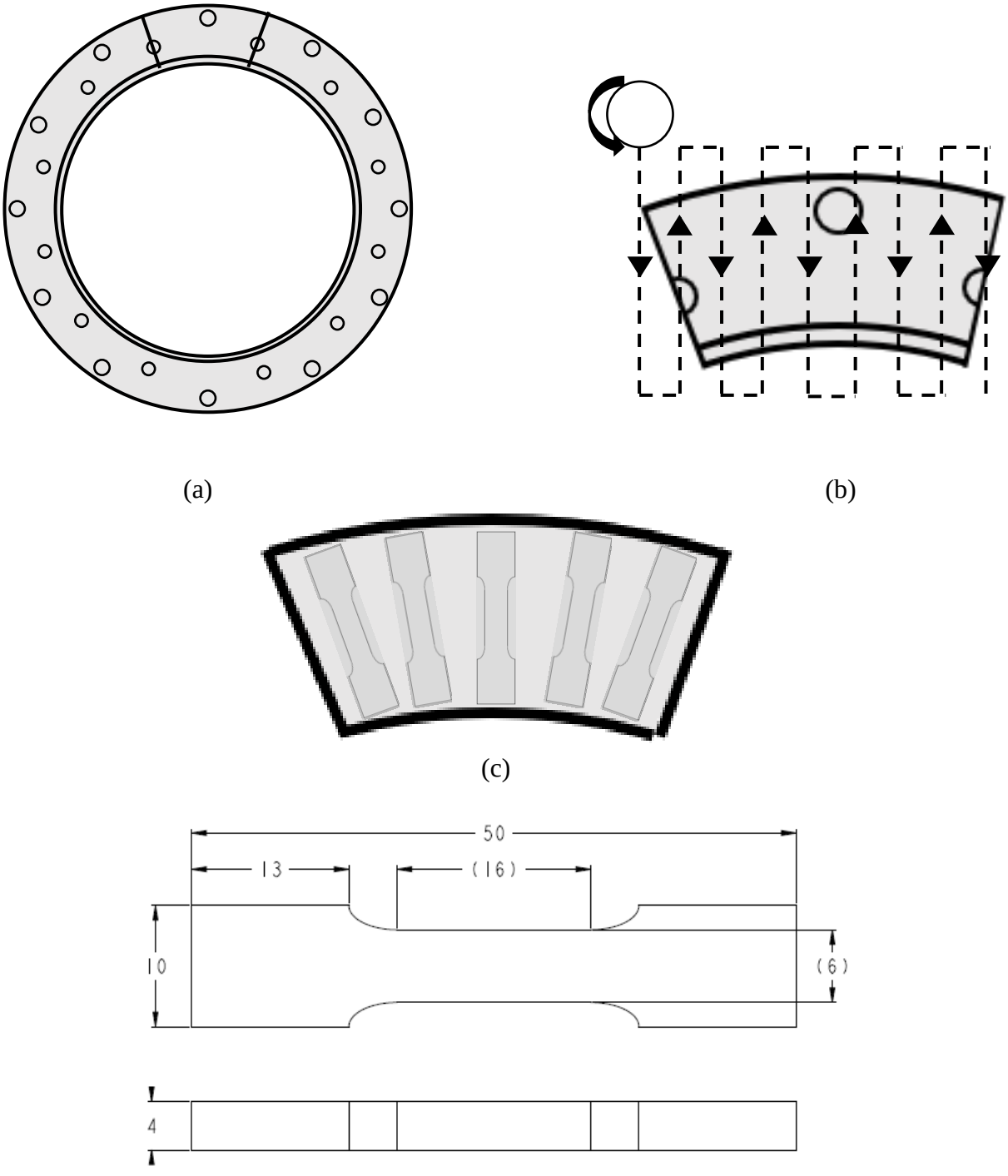

Figure 4.8: a) Sketch of functionally gradient Al/SiCp disk before machining, b) a section of the disk is face milled to remove the dimples on the surface, c) Tensile specimen cut from faced section using waterjet, d) tensile specimen with dimensions in mm.

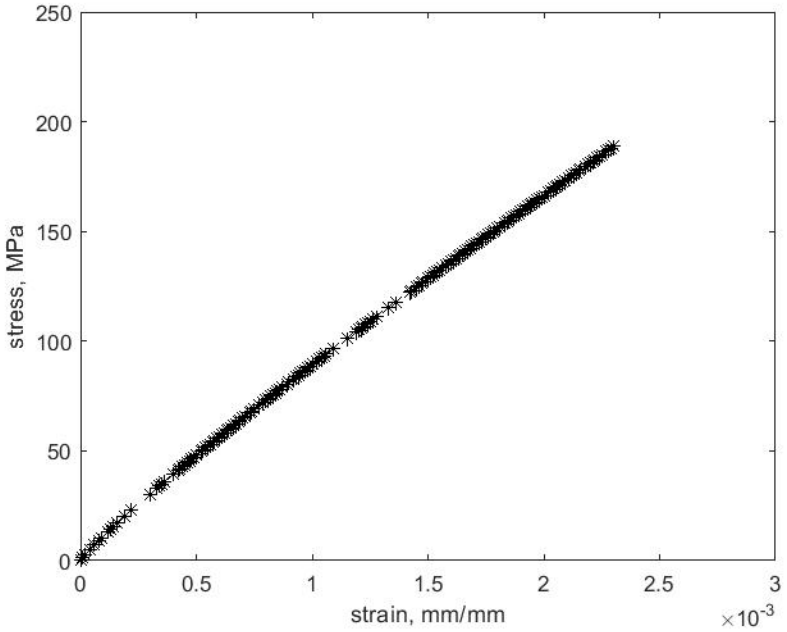

Figure 4.9: : Stress-strain curve for functionally gradient Al/SiCp composite.

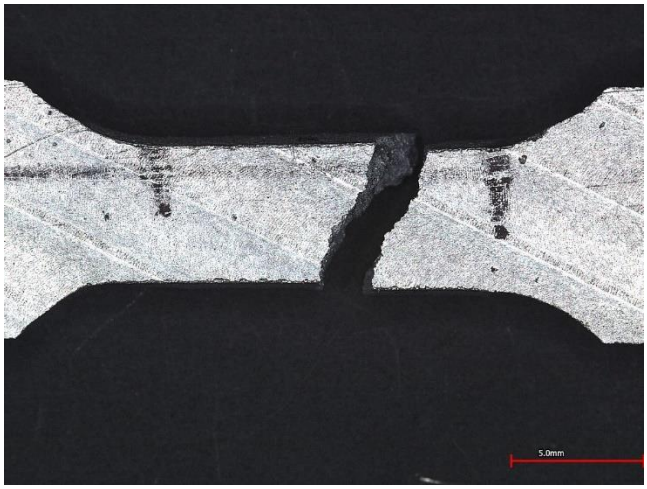

Figure 4.10: Typical fractured Al/SiCp specimen in tensile testing

both halves of the fractured tensile specimen and concluded that a considerable number of SiC particles have been traversed by crack through matching of the halves from the images.

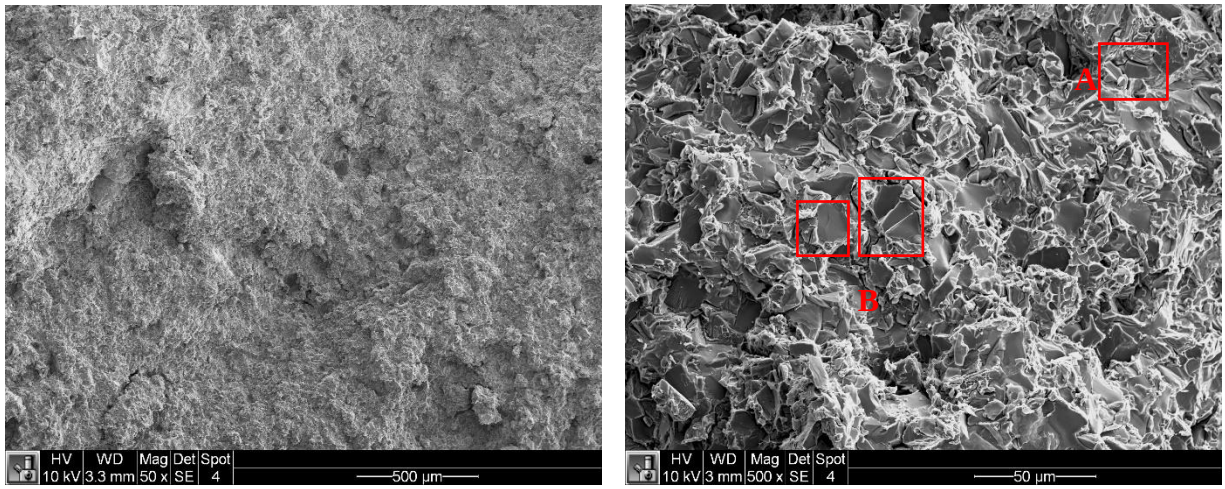

(a) (b)

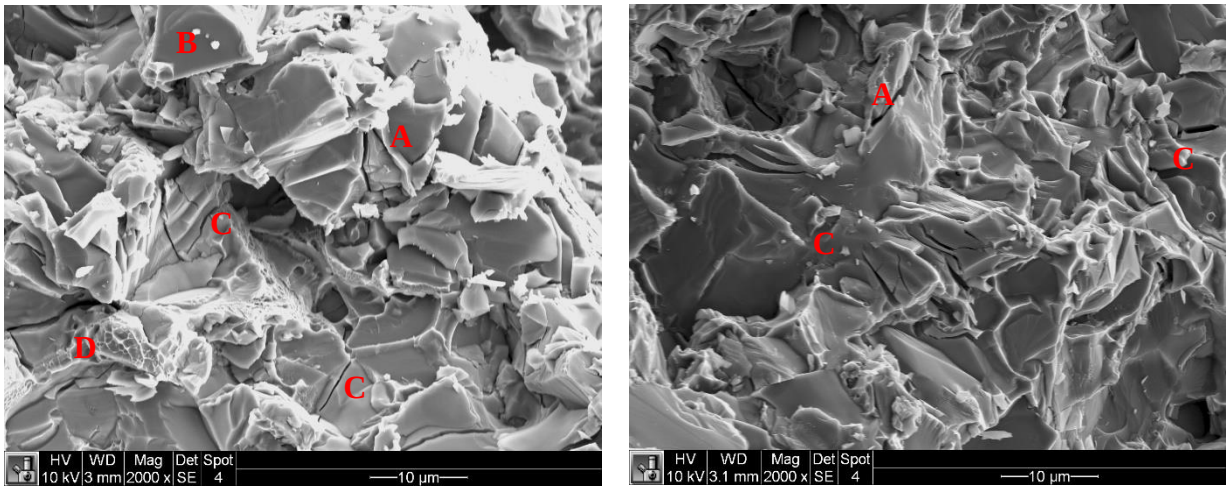

(c) (d)

Figure 4.11: SEM fractographs of functionally gradient Al/SiCp, a) at low magnification of 50 x, b) 500x, c and d) at 2000x. A: shows particle debonding from the matrix, B: fractured SiC particle, clearly visible cleavage lines, C: Matrix cracking, D: Matrix formin

Matrix cracking perpendicular to the fracture surface was also observed at point C in Figures 4.11 c and d. The ductile surface characterized by dimples were found at point D, in Figure 4.11 c. The matrix material bonded to the SiC particle along the path of crack propagation was found to fail by the formation of micro-voids creating shallow dimples on the surface. This observation is in agreement with the study performed by Doel and Bowen[108]. Tensile properties and fractography of 7075 aluminum alloy reinforced with SiCp of varying particle sizes were reported in this study. The important features were reported to be flat facets of the fractured particles, local matrix microvoid coalescence forming dimple failure surfaces.

4.3 Uniformly reinforced magnesium composite

The extruded rod was sectioned into disks using abrasive waterjet cutting machine. A cross-section of the disk was mounted in an epoxy mold and polished upto 1 μm using diamond abrasives. SEM images of the polished specimen were obtained at 1000x, owing to the smaller size of the SiC particles present in the magnesium composite, shown in Figure 4.12.

A similar approach as discussed in the previous section was followed to determine the reinforcement percentage. The area of interest was increased from 92 to 5.8 x 10^3 μm^2, until no significant change in the reinforcement percentage was observed, shown in Figure 4.13. The reinforcement percentage was found to be 15% by volume of SiC particles in AZ91 matrix. Unlike the aluminum composite discussed in this study, magnesium composite rod was manufactured to have a uniform distribution of SiC particles in the matrix. The average particle size was found to be 3.5 μm with a standard deviation of 0.99 μm, shown in Figure 4.14, data given in Appendix

A. SEM images were obtained from three locations on the rod to determine the reinforcement percentage and the particle size distribution.

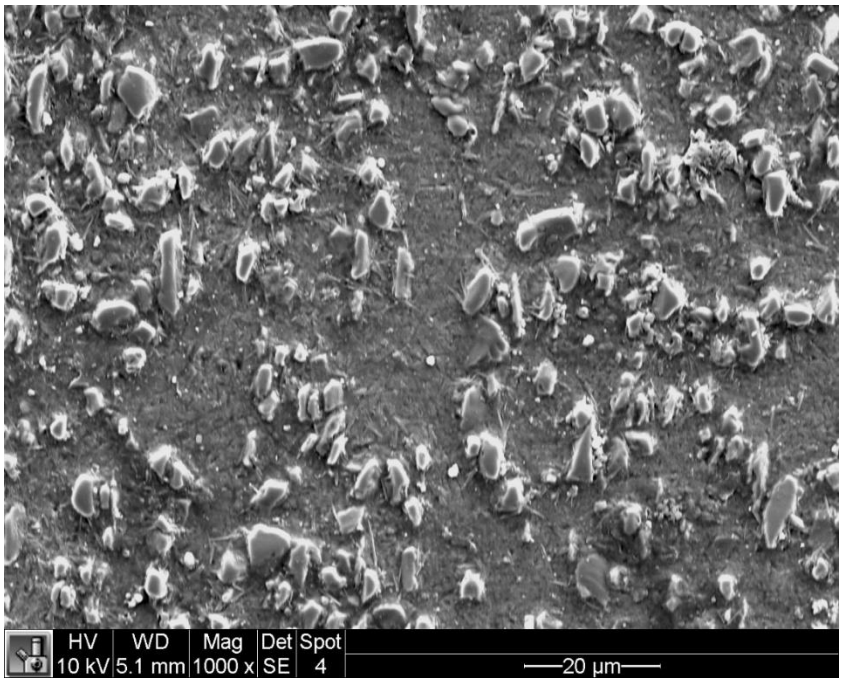

Figure 4.12: SEM image of AZ91/SiCp at a magnification of 1000x.

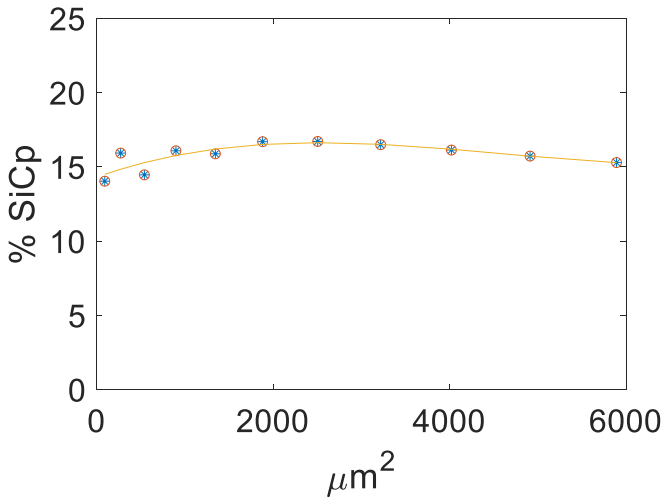

Figure 4.13: Percentage reinforcement as a function of area of interest

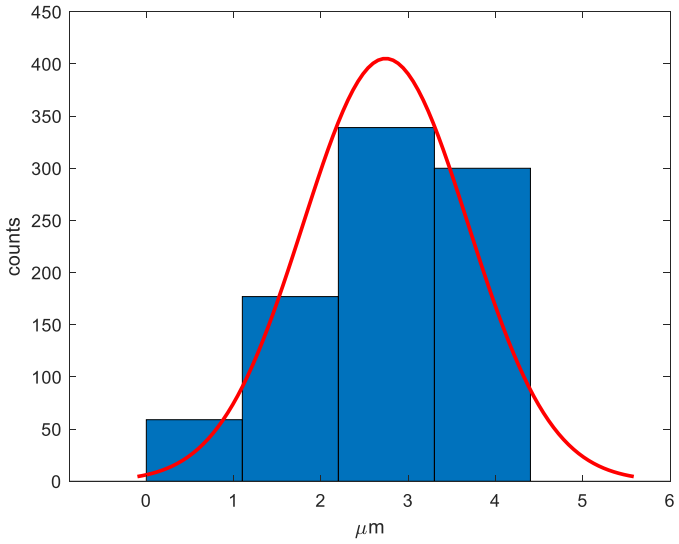

Figure 4.14: Particle size distribution in the matrix

5.4 Tensile properties of AZ91/SiCp/15%

Tensile properties of the magnesium composite were measured using the INSTRON 5585H electro-mechanical test frame. The tensile test was performed on compact specimens, preparation of these specimen is discussed in Figure 4.15. Crosshead speed was fixed at 1.27 mm/min. The typical stress strain data is shown in Figure 4.16. The ultimate tensile strength was found to be 360 MPa. The composite did not exhibit any necking before fracture, leading to limited ductility with average final strain of 0.0073. The test was performed on three specimens, raw data given in Appendix A

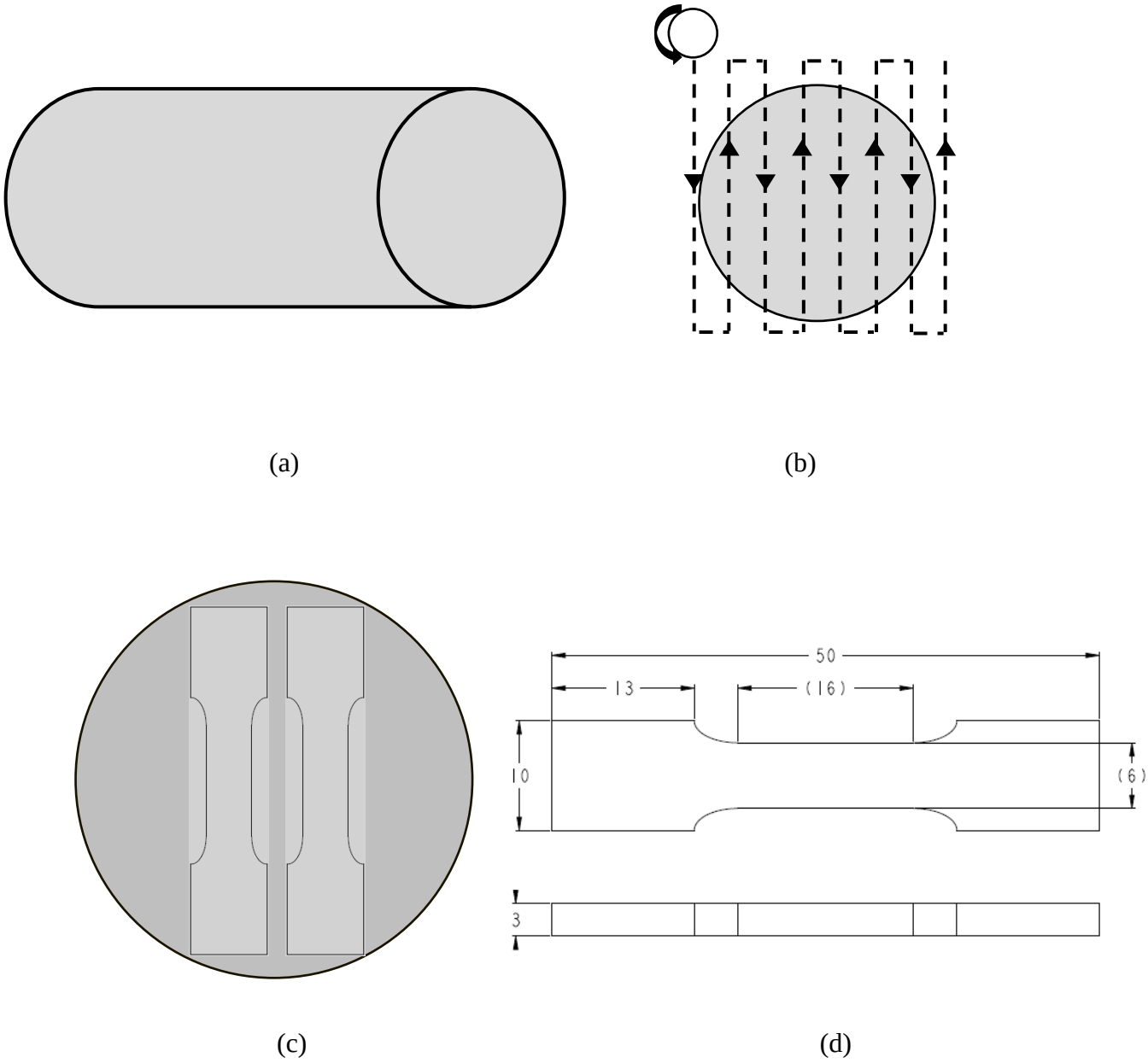

Figure 4.15: AZ91/SiCp/15% tensile specimen preparation, a) Extruded composite rod, b) disk face milled to a thickness of 3 mm, c) Tensile specimen machined from the face milled disk using abrasive waterjet, d) Tensile specimen with dimensions in mm.

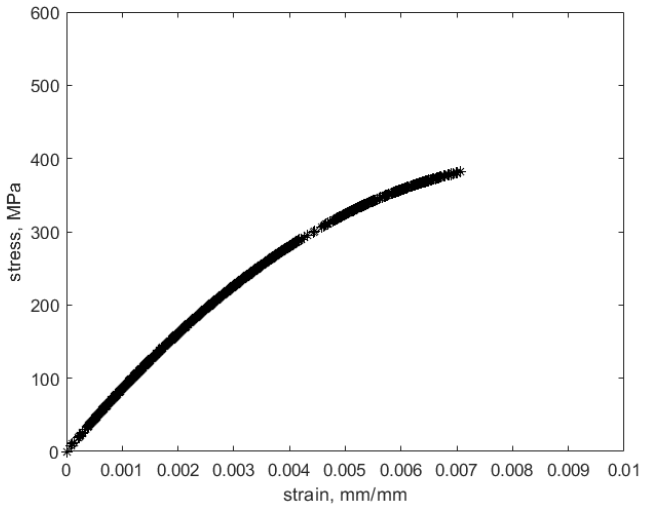

Figure 4.16: Stress strain curve for AZ91/SiCp/15%.

The limited ductility of the magnesium composite can be attributed to further reduction in ductility of the magnesium alloy due to the presence of SiC that hinder the motion of slip planes. Similar behavior was reported by Luo in studying the mechanical behavior of AZ91 matrix composites. The authors attributed the differences in ductility between the pure matrix and composite to the higher strain hardening rate observed in the composite. The crack propagation through the composite was studied through SEM fractography, shown in Figure 4.17.

Although aluminum alloys generally exhibit more ductility than magnesium alloys, the aluminum composite failed at a much lower strain in comparison to magnesium composite. This can be attributed to the increased hindrance to the plastic deformation due to higher concentration and particle size of SiC in the aluminum composite.

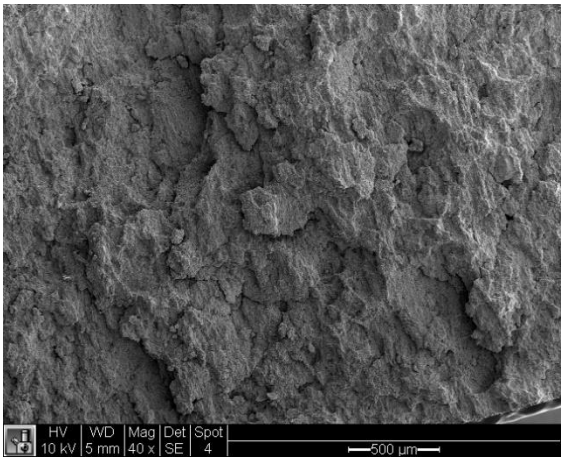

(a)

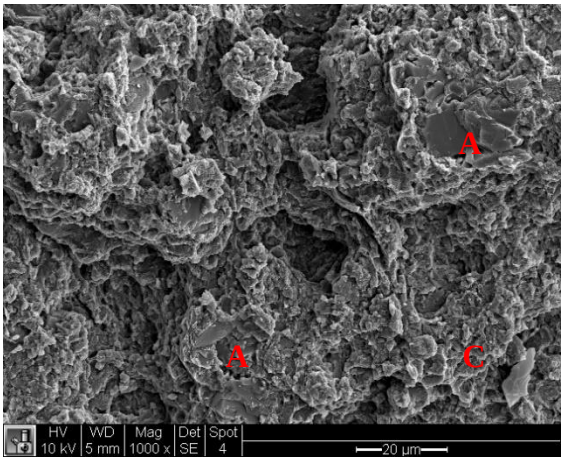

(b)

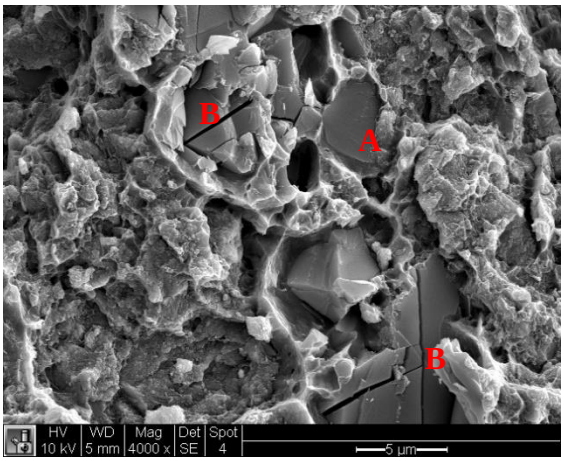

(c)

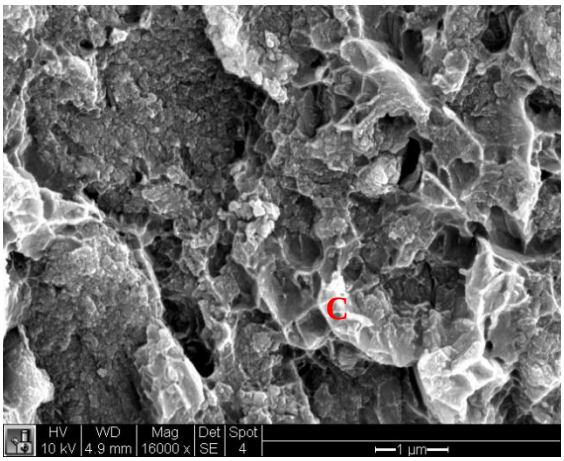

(d)

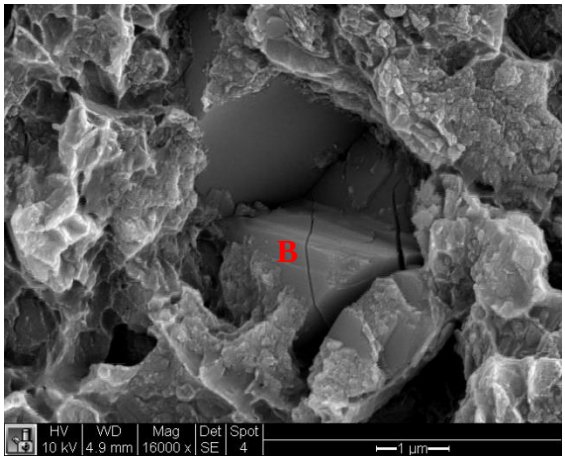

(e)

Figure 4.17: SEM fractographs of specimen showing, A: SiC fractured along the plane with cleavage lines, B: Particle fracture perpendicular to the surface, C: dimples formed by the matrix

The average particle size for the magnesium composite was lower than the aluminum composite. Particle debonding was not observed extensively in this case owing to the high wettability of magnesium matrix with SiCp[109]. The SiC particles exhibited a smooth fractured surface fracture at point A in Figures 4.17 b and c and were also observed to be cracked perpendicular to the fractured surface, shown at Point B on Figures 4.17 c and e. The matrix was found to form dimples typical of ductile fractures, shown in Figure 4.17 d. In conclusion, particle and matrix fracture was found to be the major damage mechanism for magnesium composite. Similar observations were made by Luo, in comparing the crack propagation in pure AZ91 and AZ91/SiCp composite[85]. The author concluded that particle debonding was not typically observed owing to good interfacial bond strength, and particle and matrix cracking were the major damage mechanisms.

Chapter 5 . Experimental Set up and Procedures

The cutting tool, experimental set up and analysis procedure used to measure the response of the composites during the machining process are discussed in this chapter. As discussed in the previous chapters, the cutting forces, acoustic emission, surface roughness and topography and tool wear are used as parameters for assessing the machinability of the composites.

5.1 Cutting tool

Square end carbide end mill of diameter of 6.35 mm was used in this study, shown in Figure 5.1. The tool specifications are listed in Table 5.1. The end mill was replaced after every cut to eliminate the effects of tool wear.

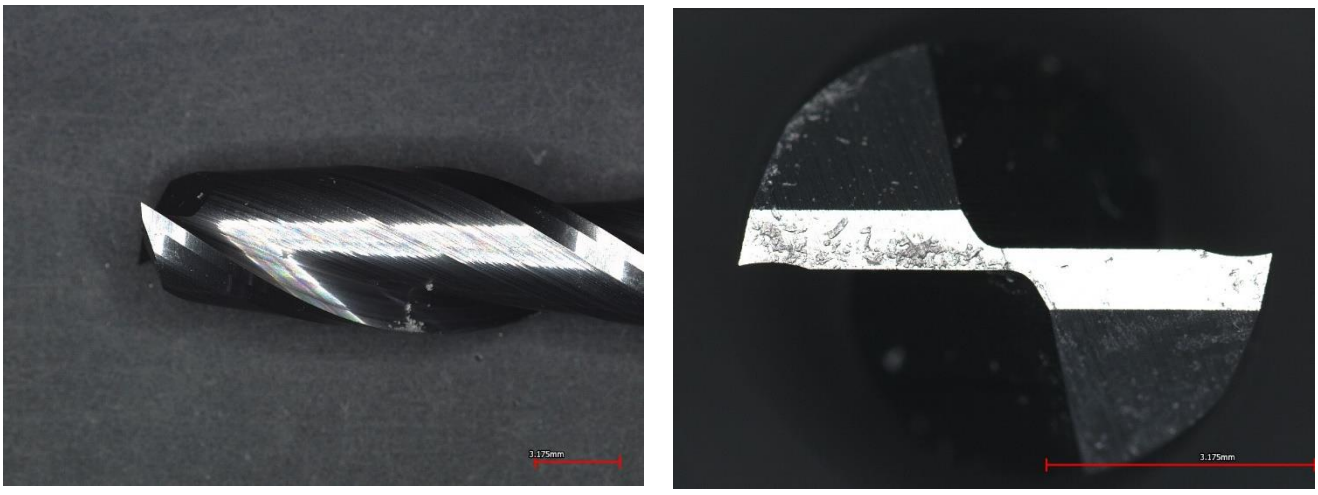

Figure 5.1: Carbide cutting tool

Table 5.1: End mill specifications

Diameter	6.35 mm
Grade	C2, average grain size: 1.2 μm
Nose radius	Square end, 40 μm
Helix angle	30°
Rake angle	4°
Overall length	63.5 mm

5.2 Experiment set up

The machinability of the aluminum and magnesium composites were evaluated through peripheral milling. The milling tests were performed on HAAS Tool Mill, Model TM 1P. The maximum spindle speed of this 3-axis numerically controlled machine is 6000 rpm. Maximum feed rate in X and Y directions is 10 m/min. Additional specifications are included in Table 5.2.

Table 5.2: HAAS Tool Mill TM 1P specifications

Maximum spindle speed	6000 RPM
Maximum torque	44.74 Nm at 1200 RPM
Accuracy	0.01 mm
Maximum thrust force	8900 N

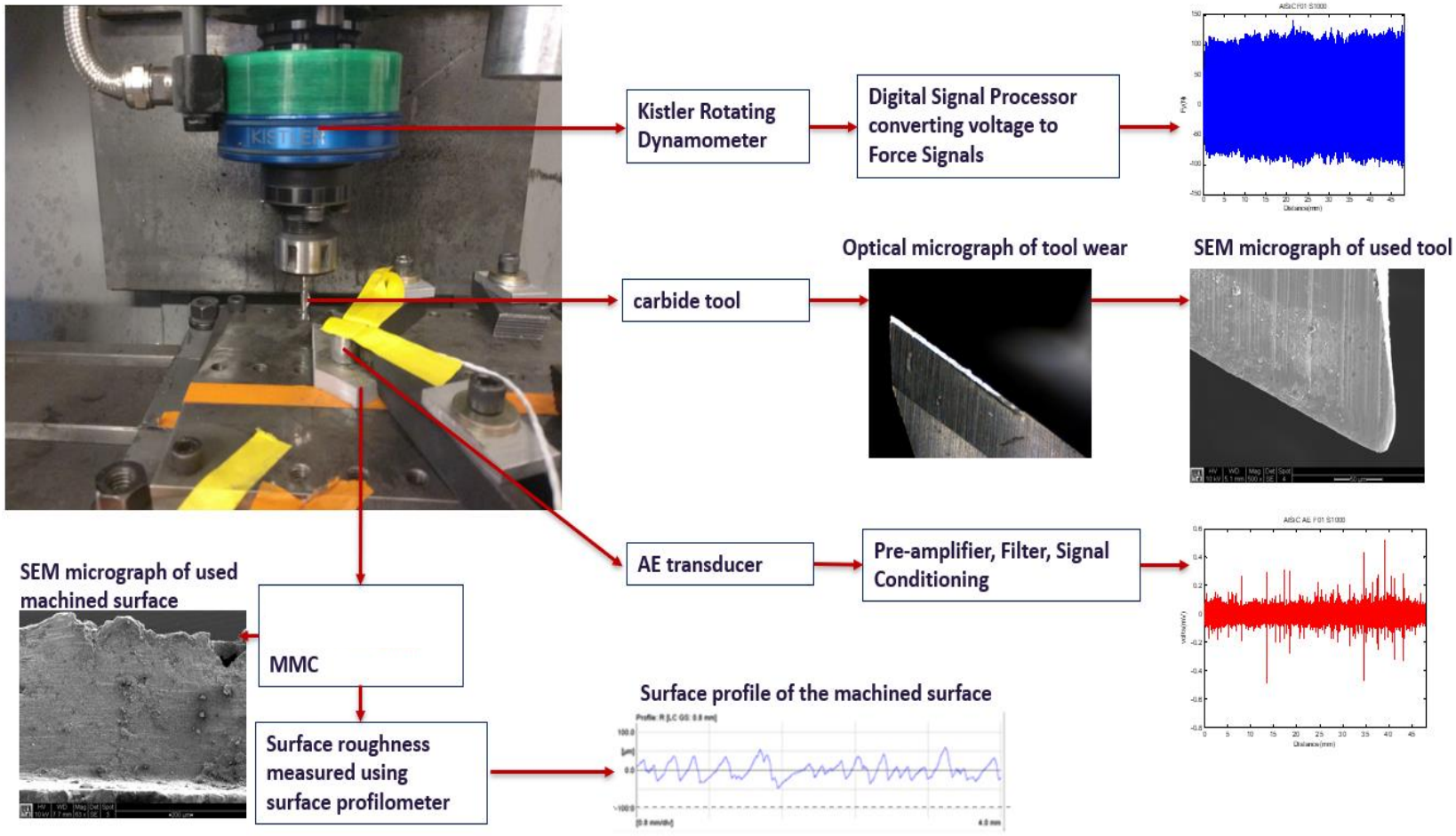

Figure 5.2: Experiment set up for peripheral milling of MMCs

5.3 Initial tool alignment and cutting forces

The cutting forces generated during the end milling process was measured using Kistler 9123 rotating dynamometer at a sampling frequency of 7999 Hz, shown in Figure 5.3. The Kistler dynamometer measures the cutting forces F_x, F_y and F_z along the x, y and z directions of the dynamometer respectively. In addition, the moment about the z axis, Mz is also measured, shown in Figure 5.3. The rotating dynamometer measures the moment and the forces at the cutting edge and is not influenced by the dynamics arising due to the variations in the mass of the workpiece.

The dynamometer is equipped with piezoelectric sensors aligned in the direction of force measurement. These piezoelectric sensors generate charge proportional to the effective load, which is then converted to proportional voltage by a signal amplifier. Each dynamometer has calibrated sensitivity values used to convert the voltage signals into force signals.



Figure 5.3: Kistler 9123 dynamometer showing the force measurement axis[108].

To ensure the correct measurement of forces, Kistler suggested aligning the cutting edges of the tool with the axis of the dynamometer. The two flute tools used in this study were always aligned with the y axis of the dynamometer. Therefore,

$F_x = F_t$

$|F_y| = F_r$

Where,

F_x and F_y : force along the x and y directions

F_t and F_r : force along the tangential and radial directions

In addition, the force signals were found to be offset and exhibit drift as the cutting progresses. Therefore, offset and drift compensation is necessary to analyze the force signals. The next section explains in detail about the drift and offset compensations.

5.3.1 Offset and Drift compensation

The correctness of the measurement and alignment were validated through preliminary peripheral milling performed on Al6061-T6 to measure the cutting forces using the rotating dynamometer. These experiments were performed to check the alignment of the dynamometer axis, to acquaint with obtaining the force signals and verify the results with [110].

The experimental conditions for the end milling and the alignment of the flutes with respect to the dynamometer coordinates are listed in Table 5.3. The obtained cutting force signals were compensated for offset and drift to obtain the average cutting force.

Table 5.3: Experimental conditions for peripheral milling of Al 6061-T6

Machining parameters	Values
Spindle speed	6000 RPM
Feed	635 mm/min
Depth of cut	6.35 mm
Radial depth of cut (along x axis of HAAS milling machine)	0.254 mm
Length of cut	89 mm
Tool geometry	12.7 mm, 2 flute
Alignment 1	Cutting edge aligned to the Y axis of the dynamometer
Alignment 2	Cutting edge aligned to X axis of the dynamometer

The peripheral milling was performed by achieving spindle rotation and feed rate in air before interaction with the work piece. The average value of the forces acting on the tool should be zero when the tool rotates in air. However, in an actual measurement, the average cutting force when rotating in air may not be zero. This could be due to the difference in the HAAZ equipment in comparison with the equipment used to calibrate the sensor. Also, the spindle rotating a certain RPM and moving at a certain feed could induce charge in the piezoelectric sensor. This force experienced by the sensor before actual material cutting should be compensated for while

obtaining the average cutting force for machining a material.

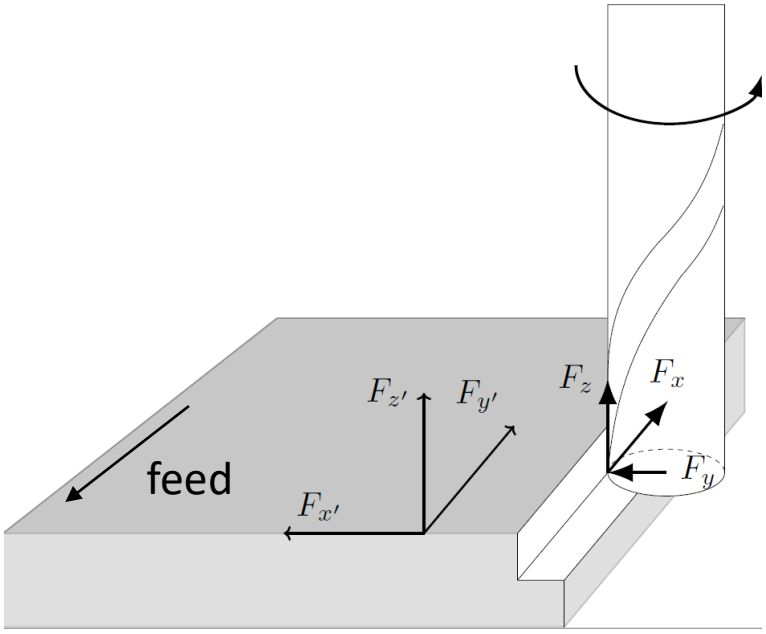

(a)

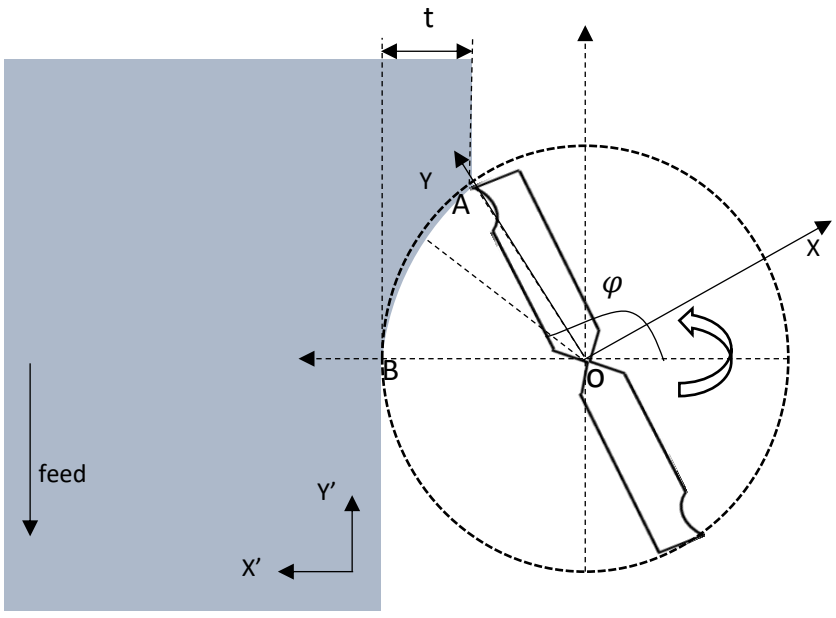

(b)

Figure 5.4: Schematic of a down milling process

The experimental data obtained from the dynoware while machining Al 6061 at 635 mm/min is shown in Figure 5.5. In Figure 5.5, the average cutting force between time=0 and line A is not zero. Therefore, the signal should be compensated to accommodate for this offset. The offset is compensated by finding the left average force, F_{lo} between time 0 and line A. The average force is then subtracted from the cutting force signal. This compensation was performed using MATLAB, the corrected data is shown in Figure 5.6.

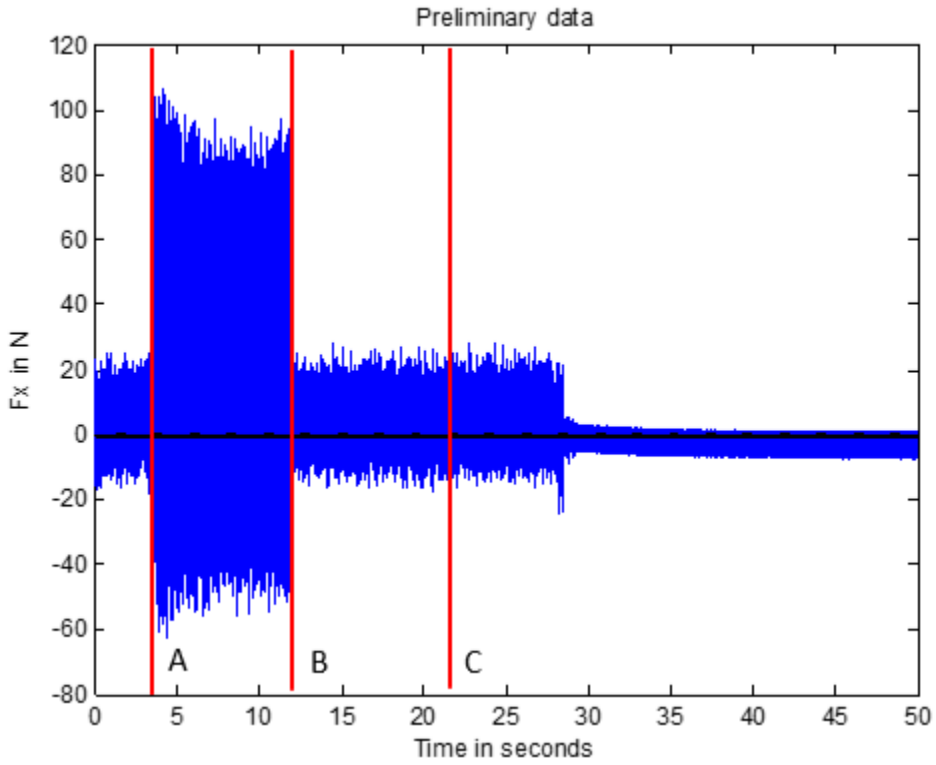

Figure 5.5: Preliminary data, Fx in peripheral milling of Al 6061-T6 at 635 mm/min and 6000 RPM.

After compensating for the left average force, the right average force between lines B and C may

not be zero. When the right average force is not zero, it indicates that there is a drift in the signal. The drift in the signal should also be compensated for before calculating the average cutting force. The drift can be defined as,

$$drift = slope * time + constant \tag{5.3}$$

$$slope = \frac{right\ avg.force - left\ avg.force}{t_l - t_0} \tag{5.4}$$

$$constant = 0,$$

$$since\ the\ drift\ line\ passes\ through\ the\ origin\ where\ force\ is\ zero\ at\ time = 0$$

Where,

t_o: time at start of spindle rotation

t_l : time at the end of spindle rotation.

However, in this case, the right average force was found to be 0.726 N which is negligible compared to the cutting force. The red line in Figure 5.5 shows the drift line. The slope is calculated to be 0.03N/s. The force data after offset and drift compensation is shown in Figure 5.7.

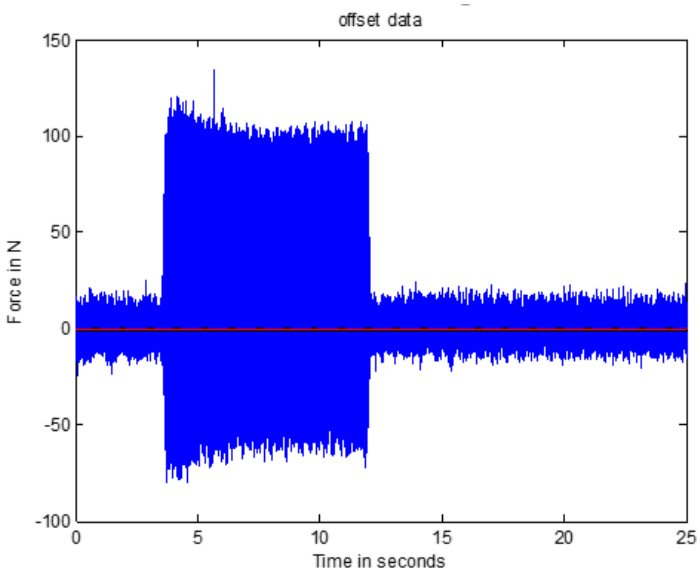

Figure 5.6: Offset compensated force data in peripheral milling of Al 6061-T6 at 635 mm/min and 6000 RPM. The red line represents the drift in the data.

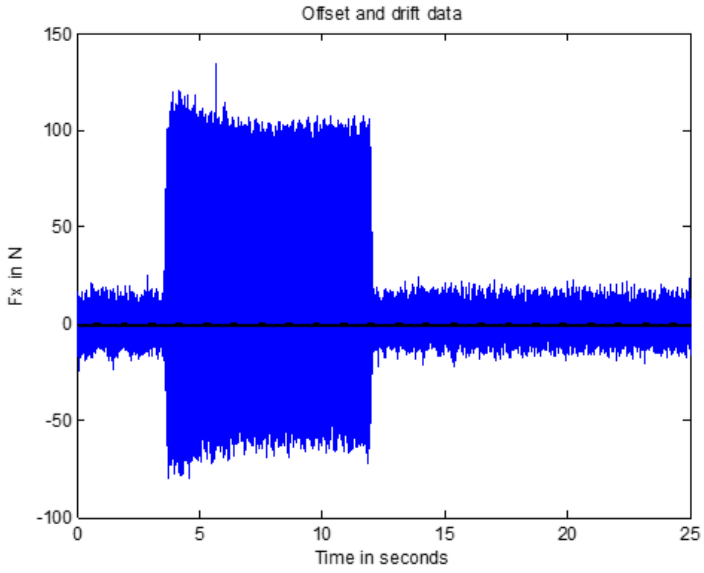

Figure 5.7: Offset and drift compensated force data in peripheral milling of Al 6061-T6 at 635 mm/min and 6000 RPM.

Upon developing an algorithm to compensate for the offset and drift in the data, the tool alignment

is checked for both, the flutes aligned to the y axis and the flutes aligned to the x axis.

When the flutes are aligned with the y axis,

$$F_x = F_t$$

$$|F_y| = F_r$$

The absolute value of the cutting force experienced by the tool in a few cutter rotations are plotted to check if the equations are satisfied. In Figure 5.8 a and b, the difference between F_y and F_r was found to be 17% and the difference between F_x and F_t was found to be about 2.5%. For conventional machining shown in Figure 5.8 c and d, the difference between F_r and F_y was found to be about 8% and about 2% between F_x and F_t. Similar difference in values between F_x and F_r, and F_y and F_t were obtained when the flutes were aligned with the x axis of the dynamometer, shown in Figure 5.8. Since the flutes are visually aligned to the dynamometer axis, the differences in the force values can arise due to small misalignment between the flutes and dynamometer axis.

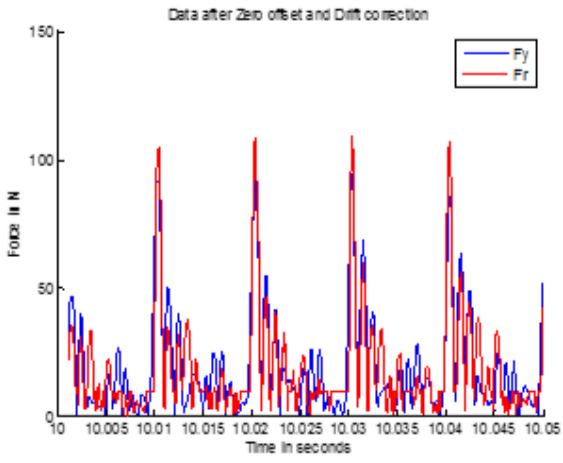

(a)

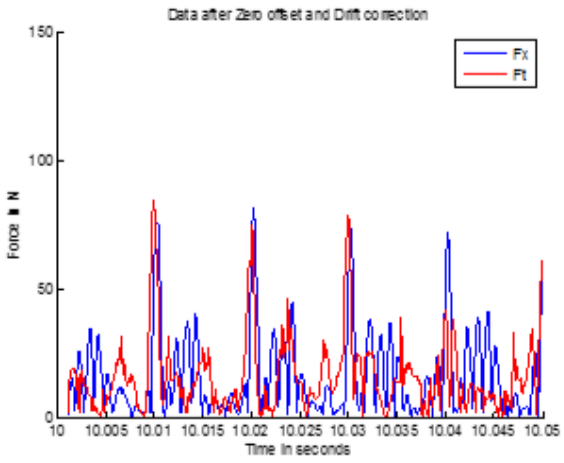

(b)

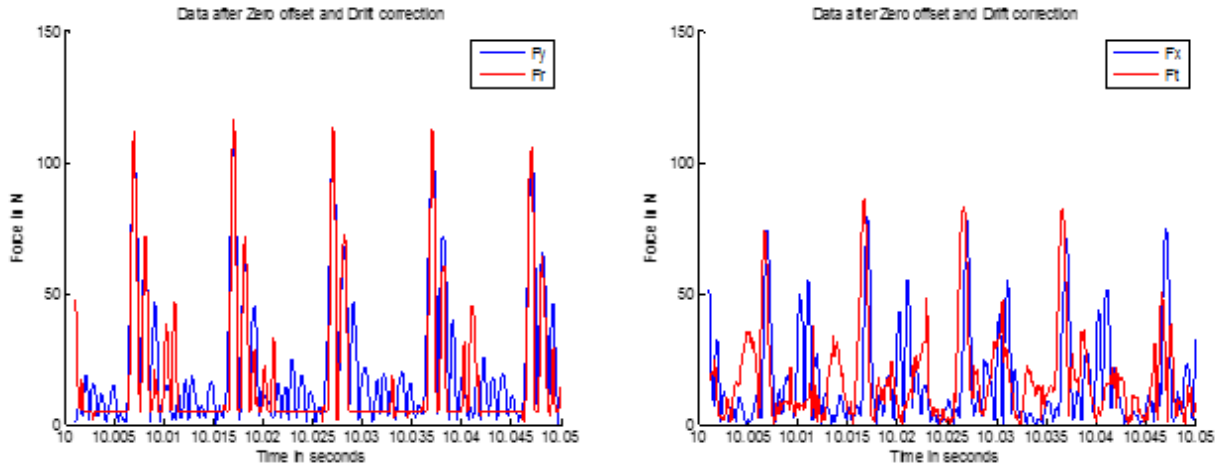

(c) (d)

Figure 5.8: Cutting forces experienced by the flutes aligned along y axis in 4 cutter rotations, a) Fy and Fr in climb milling, b) Fx and Ft in climb milling, c) Fy and Fr in conventional milling, d) Fx and Ft in conventional milling.

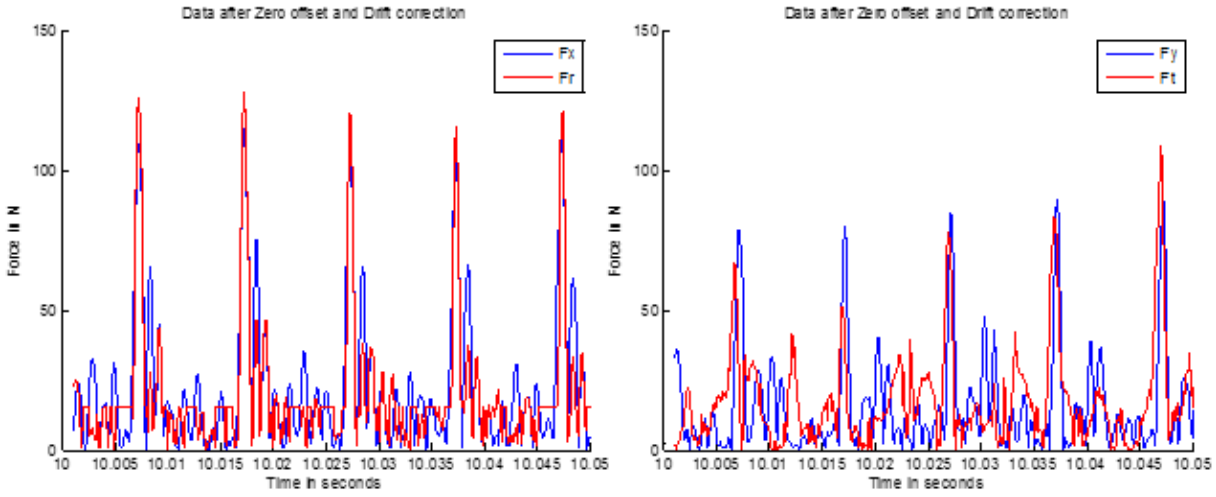

(a) (b)

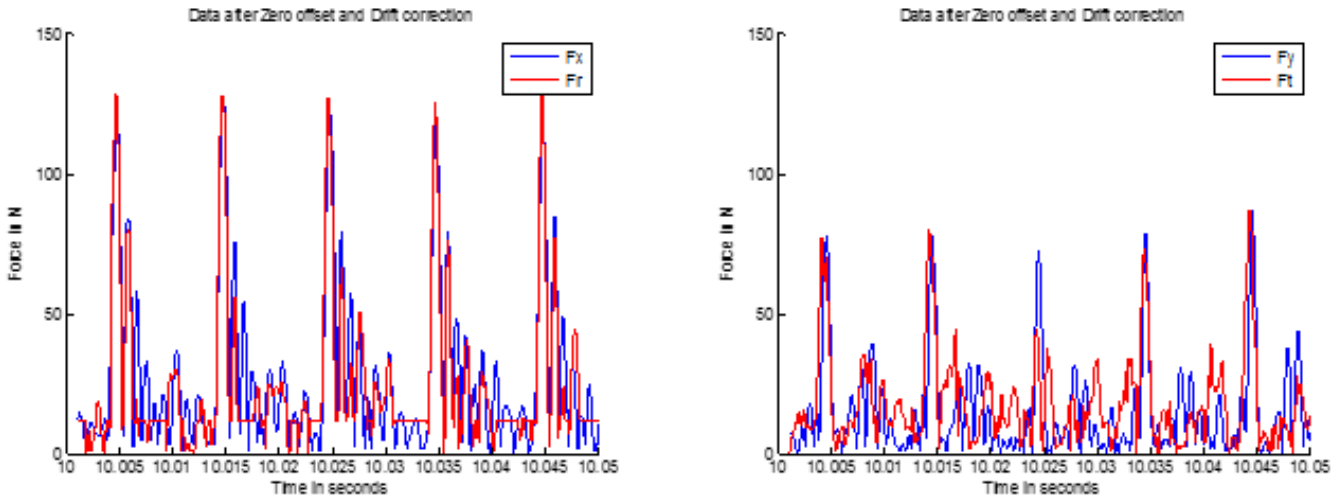

(c) (d)

Figure 5.9: Cutting forces experienced by the flutes aligned along x axis in 4 cutter rotations, a) Fx and Fr in climb milling, b) Fy and Ft in climb milling, c) Fx and Fr in conventional milling, d) Fy and Ft in conventional milling.

5.3.2 Forces in milling functionally gradient aluminum composite

Preliminary experiments were performed on the functionally gradient aluminum composites to measure the cutting forces. The composite was peripherally milled from the highest to the lowest SiC particle concentration to observe the variation in the cutting forces. The milling forces for machining MMCs are higher than machining conventional alloys due to the presence of hard reinforcement particles[111].

In Figure 5.10, measured forces Fy and Fx were found to gradually decrease with decreasing percentage of SiC particles at 0.05 mm/rev and 1000 RPM. Due to the alignment of the flutes with y axis of the dynamometer, |Fy| represents the radial force and |Fx| represents the tangential force and Fz is the reaction force along the tool axis. In addition to the high strength of the reinforcement particles, the hardness of the reinforcement particles is much higher than the tool material which rapidly increases tool wear generating higher cutting force while machining Al/SiCp[62]. When the cutting edge is in contact with a reinforcement particle, there is a higher probability of particles sliding over the cut surface resulting in the particle being pushed into the workpiece or removed along with the chips[25,112]. The tool experiences an increased friction force when the particles slide and pushed into the matrix. This can also be attributed to the observation of decrease in forces Fx and Fy as the SiC concentration decreases since the cutting edge will encounter fewer number of particles. The average cutting forces were obtained for the three zones, as classified in chapter 4 and data given in Appendix B. The forces were plotted as a function of feed rate and spindle speed to understand the effects of cutting conditions.

The relative motion of particles with respect to the tool and the workpiece can lead to two body rolling and three body abrasion which causes severe wear on the rake and flank surface of the tool. Abrasive wear is reported to be the most dominant type of tool wear since the hardness of the reinforcement particles is higher than WC[17]. In addition, the increase in friction force at the tool chip interface increases the temperature at the primary shear zone which results in the formation of built up edges(BUE) that produces poor surface finish and high cutting forces[113].

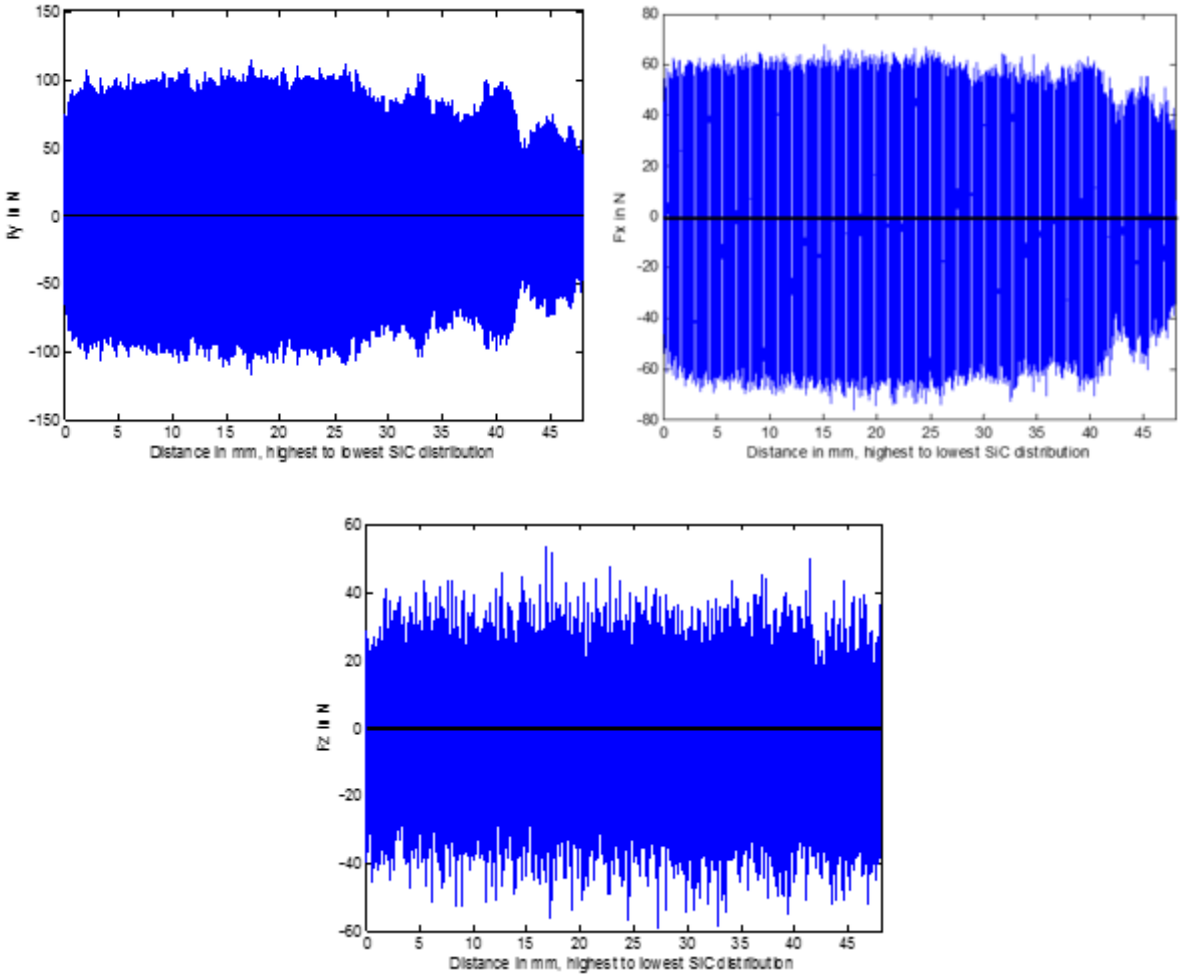

Figure 5.10: Cutting forces, Fy, Fx and Fz measured at feed rate=0.05 mm/rev and S=1000 RPM.

5.3.3 Forces in milling of magnesium composite

Similarly, the cutting forces measured during the peripheral milling tests are shown in Figure 5.11.

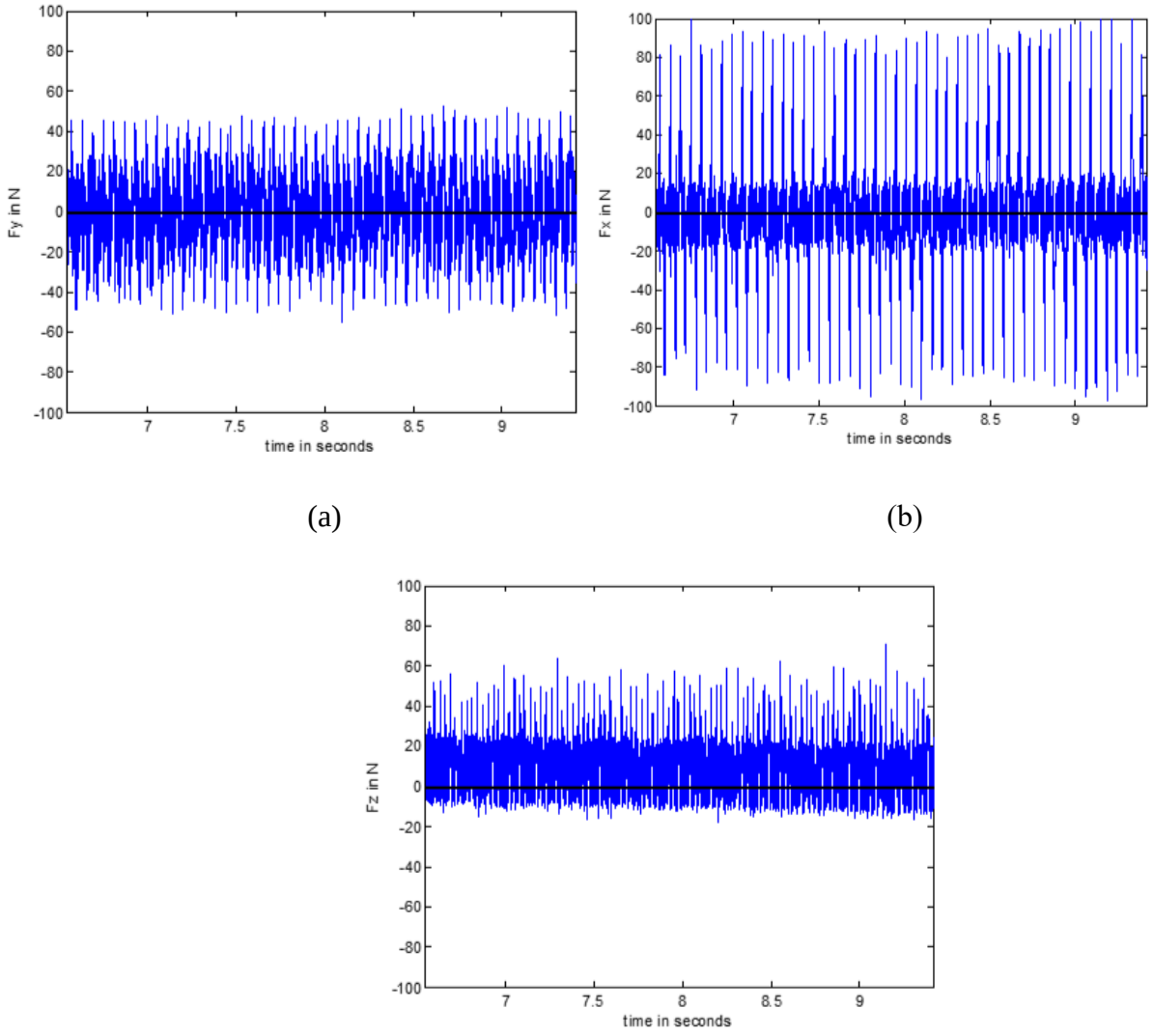

(a) (b)

(c)

Figure 5.11: Cutting forces, a) Fy, b) Fx and c) Fz generated in milling AZ91/SiCp/15% at a feed rate of 0.2 mm/rev and spindle speed of 1000 RPM.

Unlike the functionally gradient Al MMC, the average cutting force remains constant over the entire length for uniformly distributed Mg/SiCp. The feed force, radial and axial thrust forces were plotted as a function of feed rate and spindle speed to analyze the effect of machining conditions.

5.4 Acoustic emission sensor

The acoustic emission signal analysis is a powerful tool to examine the behavior of material undergoing plastic deformation. The rapid release of energy within the material due to plastic deformation while machining leads to the emission of transient elastic waves. These emissions were captured with PCI 2 based acoustic system using AE win PCI 2 software and WIN-POST post processing software

A piezoelectric transducer comprising of piezoelectric active material mounted in a metal cylinder for protection against electromagnetic interference is used in this study. The highly sensitive piezoelectric sensors should be attached to the workpiece material in a way that the acoustic signals from the shear zones passes into the transducer. This close contact is essential for transmittance of low-level acoustic signals. To exploit the high sensitivity of these transducers the intimate contact was achieved by using a Ultragel II couplant at the transducer-workpiece interface. In addition, the transducer was always placed at one centimeter from the cut, shown in Figure 5.2, to minimize variations in the experiments. A sampling frequency of 50 KHz with gain of 40 dB were used to obtain the signals in all the experiments conducted in this investigation.

5.4.1 AE signal

The acoustic emissions from the shear deformation zone due to plastic deformation of the ductile matrix and abrasion of SiC particles along the machined surface and the rake face of the tool are measured by placing piezoelectric transducer 1 cm from the cut.

The acoustic emissions were measured for cast Al workpiece to observe the emissions obtained from plastic deformation and no events associated with the presence of SiC particles. The data

collection from the dynamometer and from acoustic sensor began at the same time. Therefore, the duration of the signal from the acoustic sensor and the force sensor must coincide, shown in Figure 5.12. The transient elastic waves due to plastic deformation were picked up as soon as the cutting tool engaged with cast aluminum. The AE signals were captured to evaluate its potential for monitoring tool wear and identify events related to tool-particle interaction.

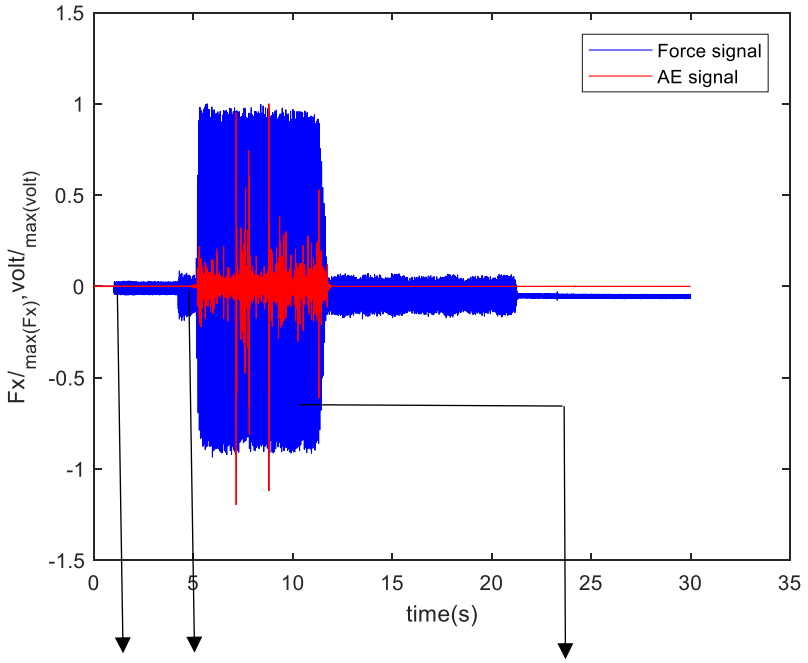

Spindle at rest Spindle rotation in air Active material cutting

Figure 5.12: Force and AE signal for Cast Al at 0.3 mm/rev and 1000 RPM.

5.5 Measurement of tool wear

The tool wear experienced by the carbide tools were measured after each cut. The carbide tool was replaced after each cut to obtain the tool wear as a function of feed rate and spindle speed. After

each cut, optical micrographs of the cutting tool were obtained using Micro-Vu Model Sol 16. The tool wear was identified as the bright white region in the optical micrograph. The width of the wear region was measured using image analysis technique discussed in chapter 7 and 8.

5.6 Surface Topology

The two-dimensional surface roughness profiles of the machined surfaces were measured using MAHR Marsurf Model GD 25. Stylus probe, 90° with a tip diameter of 2 μm was used to obtain the surface profiles with an evaluation length of 5.6 mm. A cut off length of 0.8 mm was chosen in obtaining the surface roughness profiles. The profile obtained includes waviness and surface roughness of the machined surface. Gaussian filter as per ISO 16610, and ISO 13565, was applied to obtain surface roughness profile eliminating the waviness from the surface [53,54].

The original typical raw surface profile is shown in Figure 5.13 and the Gaussian profile mean line is shown in Figure 5.13 a.

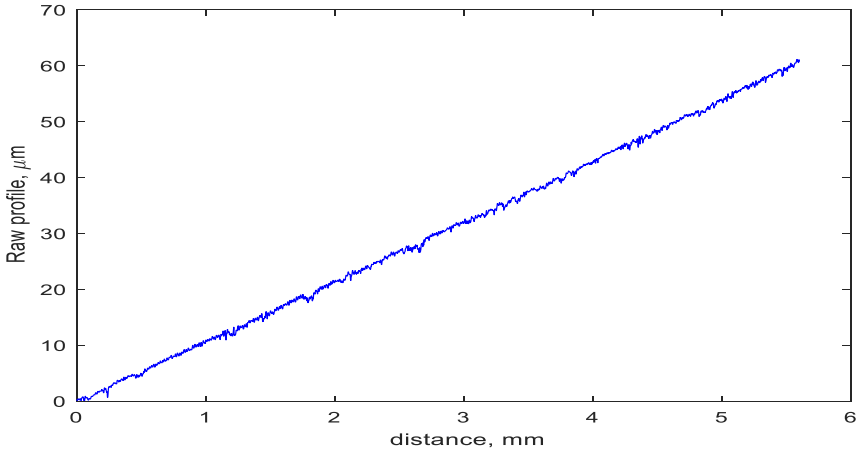

Figure 5.13: Raw profile measured by the stylus probe.

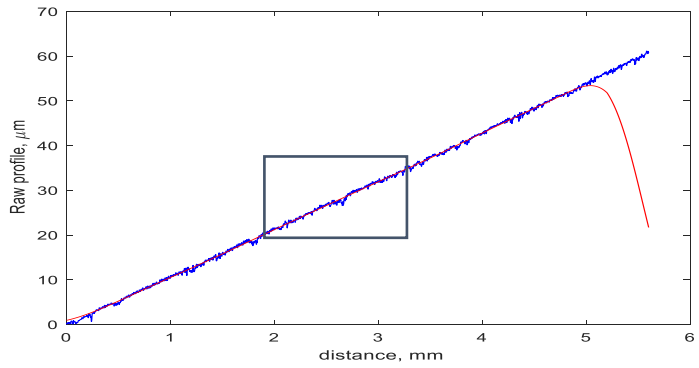

(a)

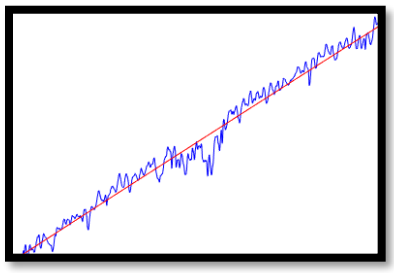

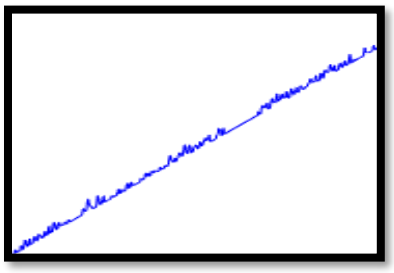

(b) (c)

Figure 5.14: Applying Gaussian filter to the raw data, a) Raw profile, shown in blue with the Gaussian profile mean line, b) Magnified view of the profile and the Gaussian mean line from 2 to 3 mm highlighted in a , c) Valleys below the mean line are removed

The Gaussian weighting function for an open profile is given by,

$$s(x) = \left(\frac{1}{\alpha\lambda_c}\right) * e^{\left[-\pi*\left(\frac{x}{\alpha\lambda_c}\right)^2\right]} \tag{5.5}$$

Where,

x: distance from the center of weighting function.

λ_c: cut-off wavelength, taken as 0.8 mm

$\alpha = \sqrt{\frac{\ln 2}{\pi}} = 0.4697$

All the valleys below the mean line are removed and replaced with the mean line, shown in Figure 4.4b. Same filter is then applied to the new profile to obtain the surface roughness profile, shown in Figure 5.15. A MATLAB code was developed to obtain the surface roughness profiles, given in Appendix C.

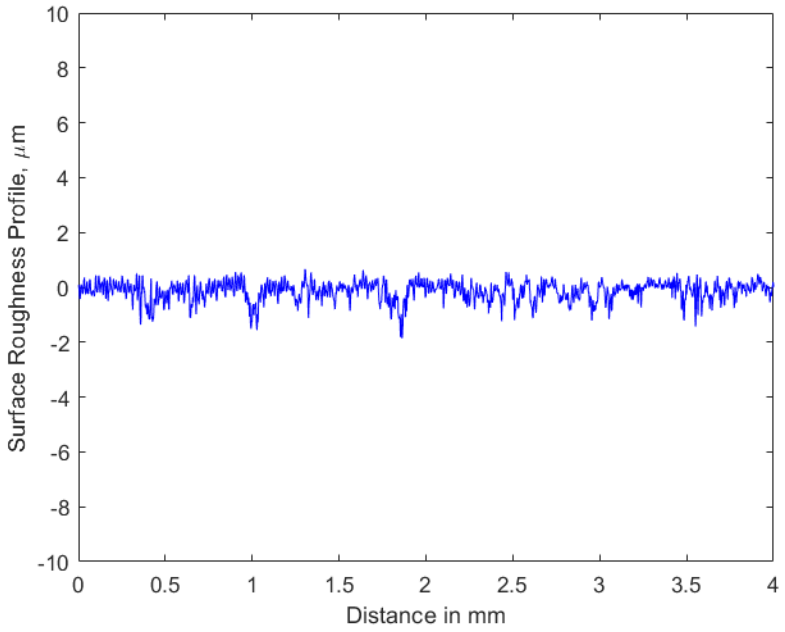

Figure 5.15: Surface roughness profile obtained after Gaussian filter.

To this profile, the statistical equations discussed in Chapter 2 are applied to obtain surface roughness parameters. These surface roughness parameters are used to quantity the machined surface.

Additionally, three-dimensional surface roughness and waviness profiles were also obtained using Keyence VR3100. The waviness or surface roughness profiles can be obtained by choosing the

appropriate filter. The S-filter eliminates small scale elements from the surface. Therefore, waviness profile can be obtained through this filter. Similarly, L filter eliminates large scale elements on the surface. Any surface undulations can be removed using this filter to extract only the roughness components. From these profiles, the area height parameters S_a and S_z were and average waviness, W_a were calculated.

The surface profiles were obtained at different feed rates and spindle speeds to evaluate the quality of the surface produced at each condition.

5.6.1 Surface Profiles

For functionally gradient Al/SiCp, the surface profile was found to depend on the concentration of the SiC particles although the machining condition is constant in all the three zones, shown in Figure 5.16.

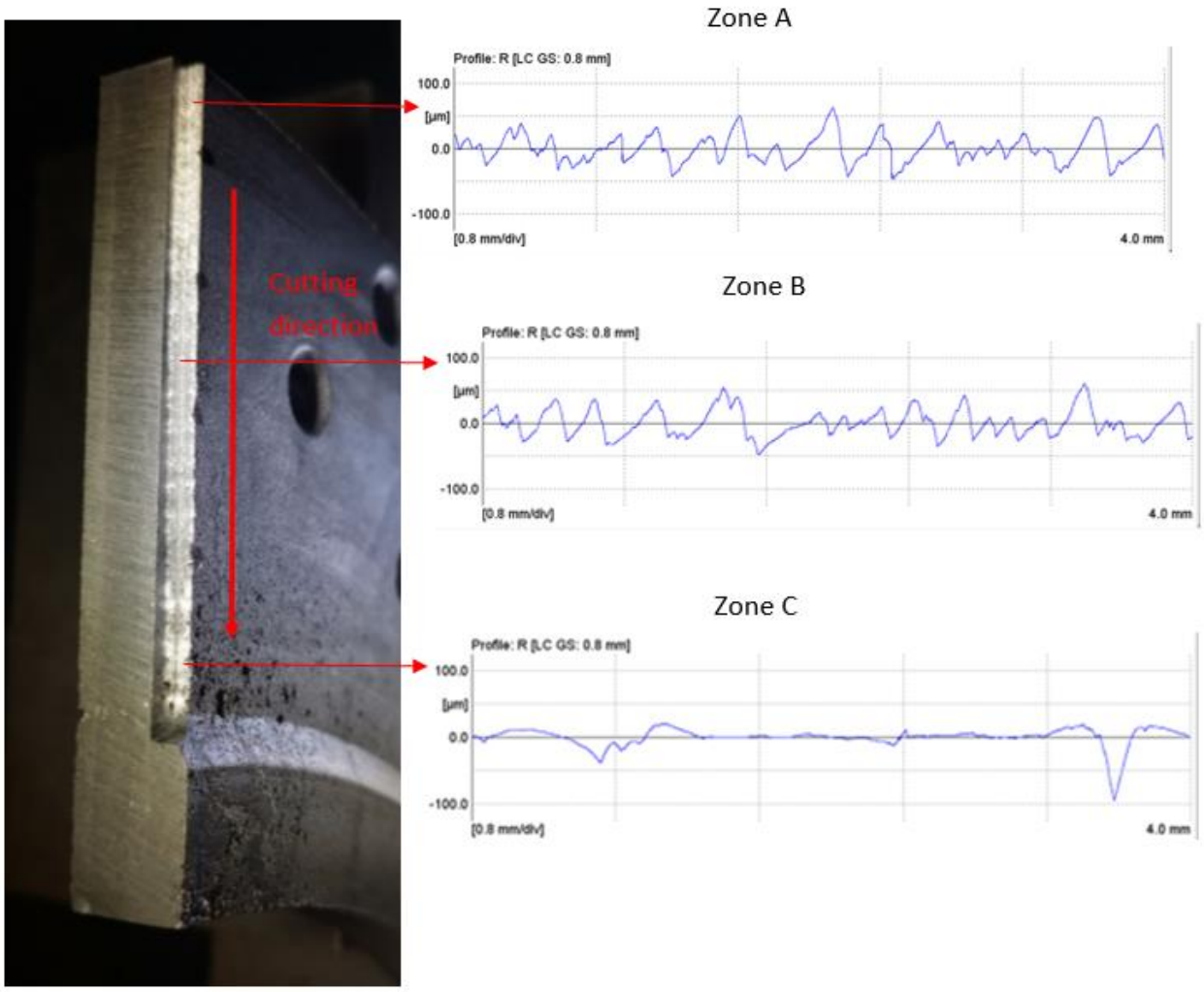

Figure 5.16: Surface profiles of the milled Al/SiC surface

Likewise, the surface profiles of the machined surface of Mg/SiCp at different cutting conditions are shown in Figure 5.17.

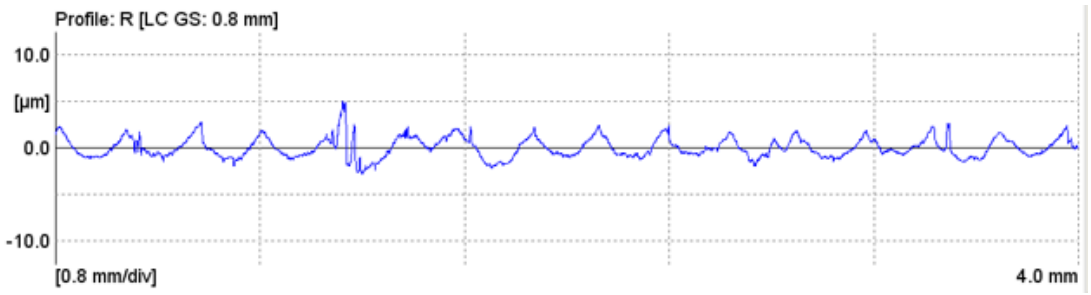

(a)



(b)



(c)

Figure 5.17: Surface Profiles of Mg/SiCp peripherally milled surface at a spindle speed of 1000, a) 0.254 mm/rev, b) 0.508 mm/rev, c) 0.762 mm/rev

The surface profiles were found to be depend on the particle concentration and the machining conditions.

5.6.2 SEM micrographs

Scanning electron microscope images of the cut surface and chips were taken to analyze the nature of interaction between the cutting edge and particles. The changes in surface topography for functionally gradient Al/SiCp with increasing particle concentration is shown in Figure 5.18, 5.19 and 5.20

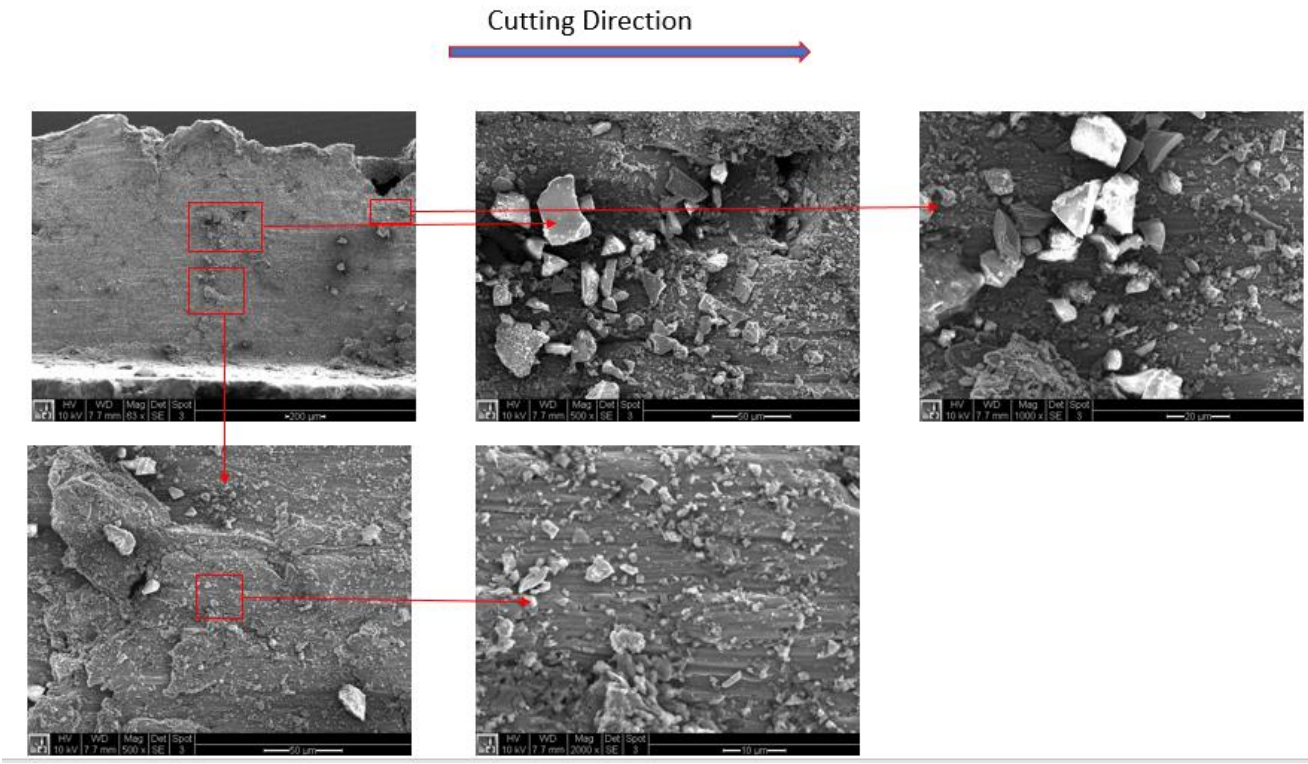

Figure 5.18: SEM micrograph of machined surface at Zone A for 1000 RPM and 0.1 mm/rev.

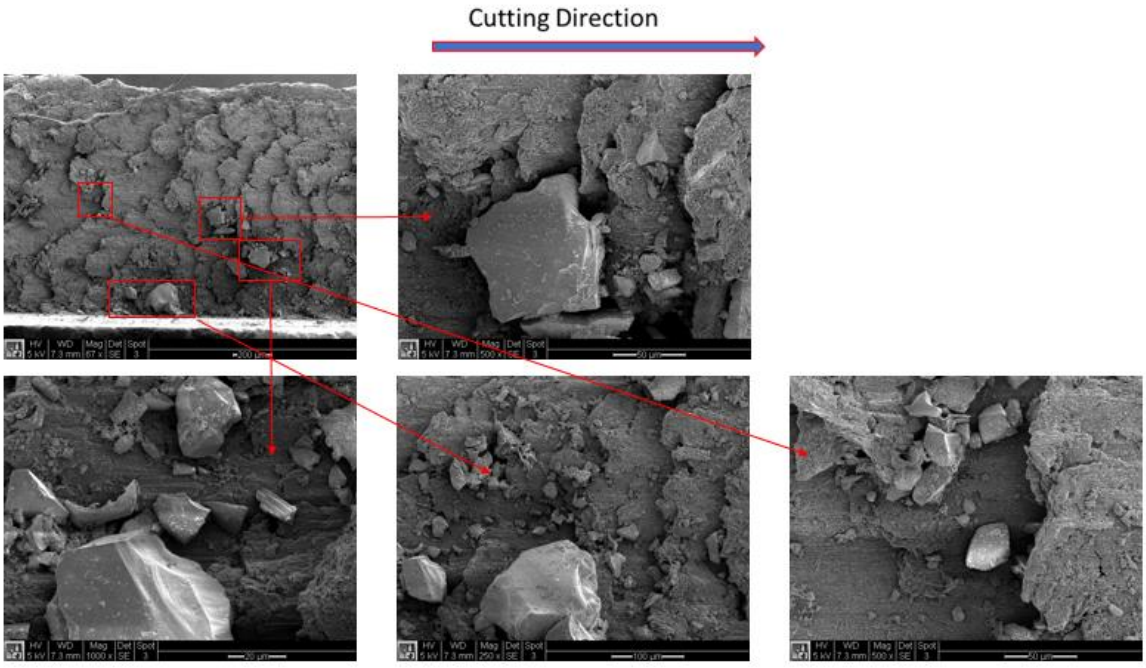

Figure 5.19: SEM micrograph of machined surface at Zone A for 1000 RPM and 0.1 mm/rev.

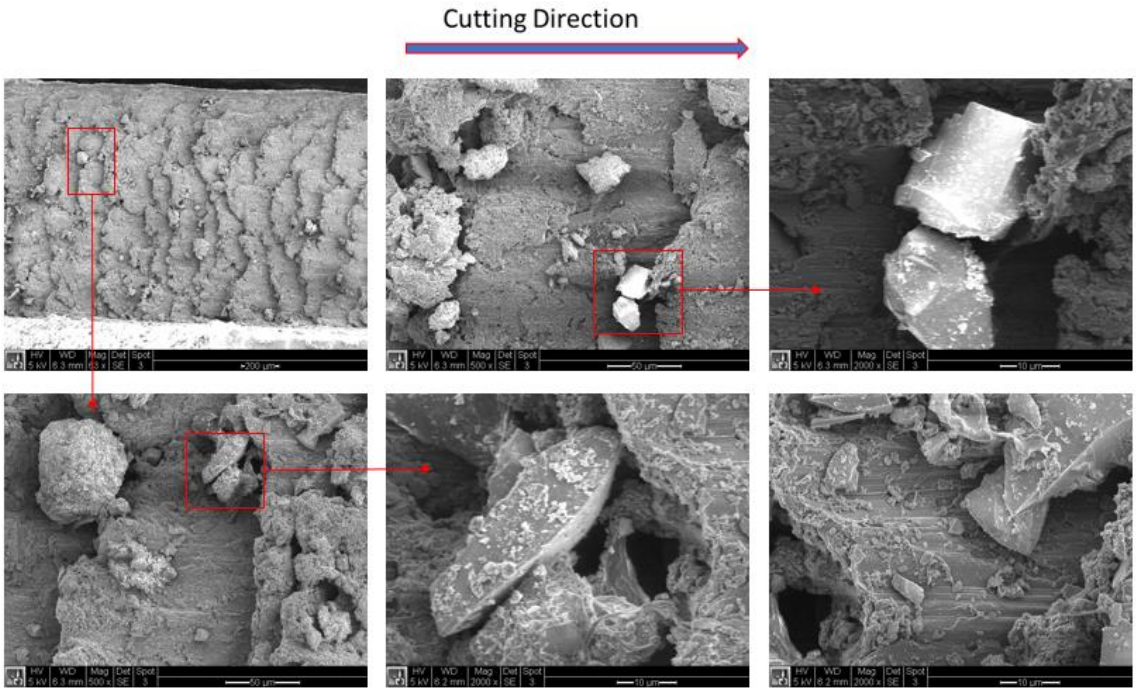

(c) Zone C, 1000 RPM, 0.1 mm/rev

Figure 5.20: SEM images of the machined surface at S=1000 rpm and F=0.1mm/rev.

The SEM images from this condition is studied to understand the possible damage mechanisms since the surface is more prone to damage from the cutting edge. The surface was observed to be smooth at Zone A, Figure 5.18. While, wave like projections were generated on the cut surface in Zones B and C, as seen in Figure 5.19 and 5.20. Zone C, Figure 5.20, shows that several loose or partially embedded SiC particles on the cut surface and a possible machining defect on the surface. Upon further magnification, it was observed that larger SiC particles were clustered near the defect, possibly pushed by the cutting edge along the surface. Magnification of the smoother region also showed SiC particles dispersed on the cut surface. Although Zone A had the highest particle concentration, it was observed to have a smoother surface in comparison to other two zones. In order to understand the differences in surface topography of Zones A, B, and C, factors like tool wear and chip formation mechanism need to be analyzed.

Correspondingly, the SEM images of the machined surfaces of Mg/SiCp were analyzed and a good surface finish was observed at both 0.254 m/rev and 0.508 mm/rev, shown in Figures 5.21 and 5.22. Unlike, functionally gradient Al/SiC composite previously discussed, the average particle size in this composite is only 3.5 μm. Therefore, the interaction of particles with the cutting edge may vary. A significant number of SiC particles were found to be scattered on the surface. These particles were mostly displaced or pushed into the matrix and extensive particle fracture could not be observed.

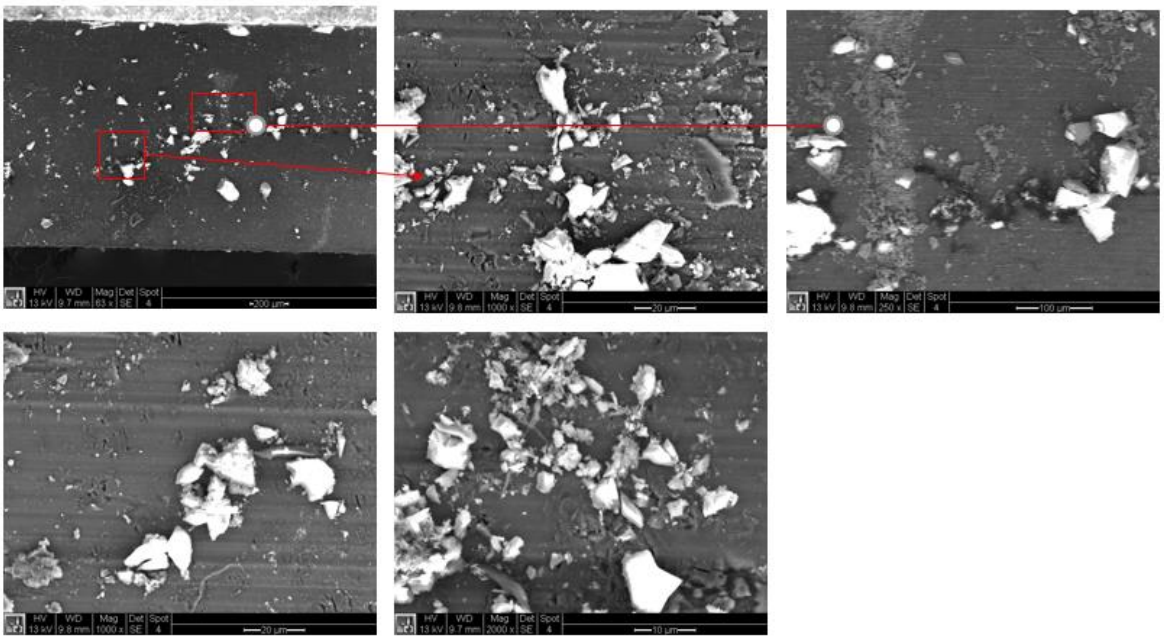

Figure 5.21: SEM image of the workpiece machined at a feed rate of 0.254 mm/rev and 1000 RPM spindle speed

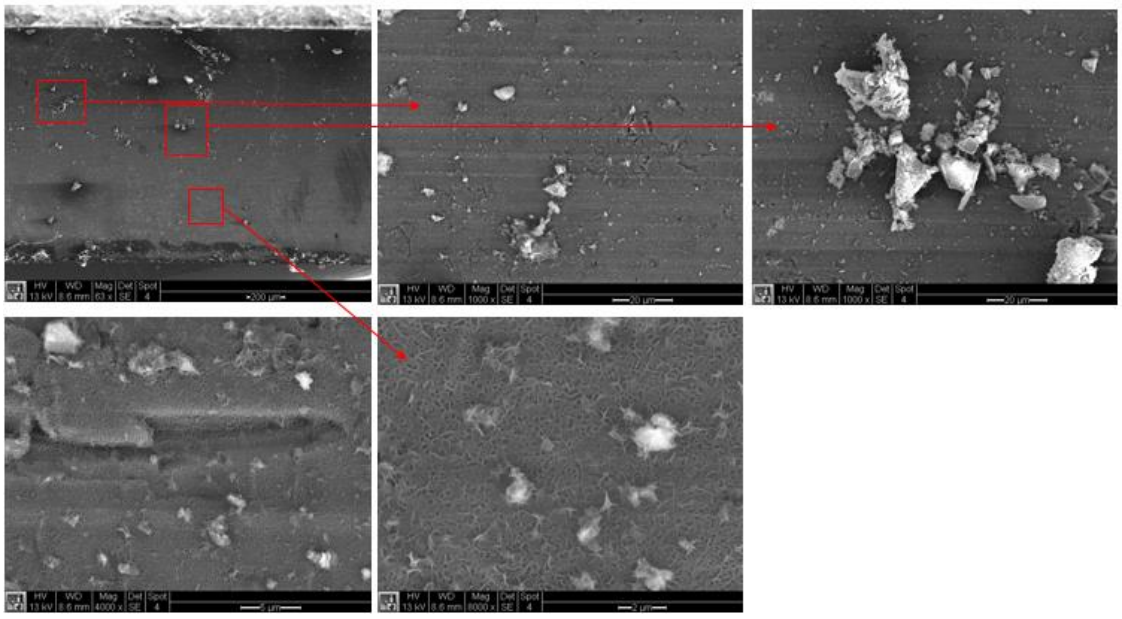

Figure 5.22: SEM image of the workpiece machined at a feed rate of 0.508 mm/rev and 1000 RPM spindle speed

5.6.3 Chip Morphology

The chip morphology was studied through SEM imaging to understand the flow of particles and matrix under severe plastic deformation during chip formation. The chips were collected by placing double sided tape along the length of cut.

The chips collected in milling of Al/SiCp at 0.1 mm/rev and 1000 RPM in Zone C are shown in Figure 5.23. Voids and cracks were observed on the surface owing to the plastic deformation of the aluminum matrix. Figure 5.23 B and C, L and M show the void formed on the surface due to particle fall out possibly due to mismatch in coefficient of thermal expansion. Figure 5.23 D shows the crack formed on the surface of the chip. This can be attributed to the compressive stress experienced by the chip on the surface and due to the reduced ductility of the matrix due to the addition of reinforcement particles. In a few cases, the cracks formed on the surface reveal the SiC particles embedded within the chip. These particles are embedded within the chip thickness and may not have interacted with the cutting edge, shown in figure 5.23 E, F, G and H. The particles on the surface of the chips were either fractured or displaced by the cutting edge. The SEM micrographs of Zones A and B, and at different cutting conditions are discussed in Chapter 7.

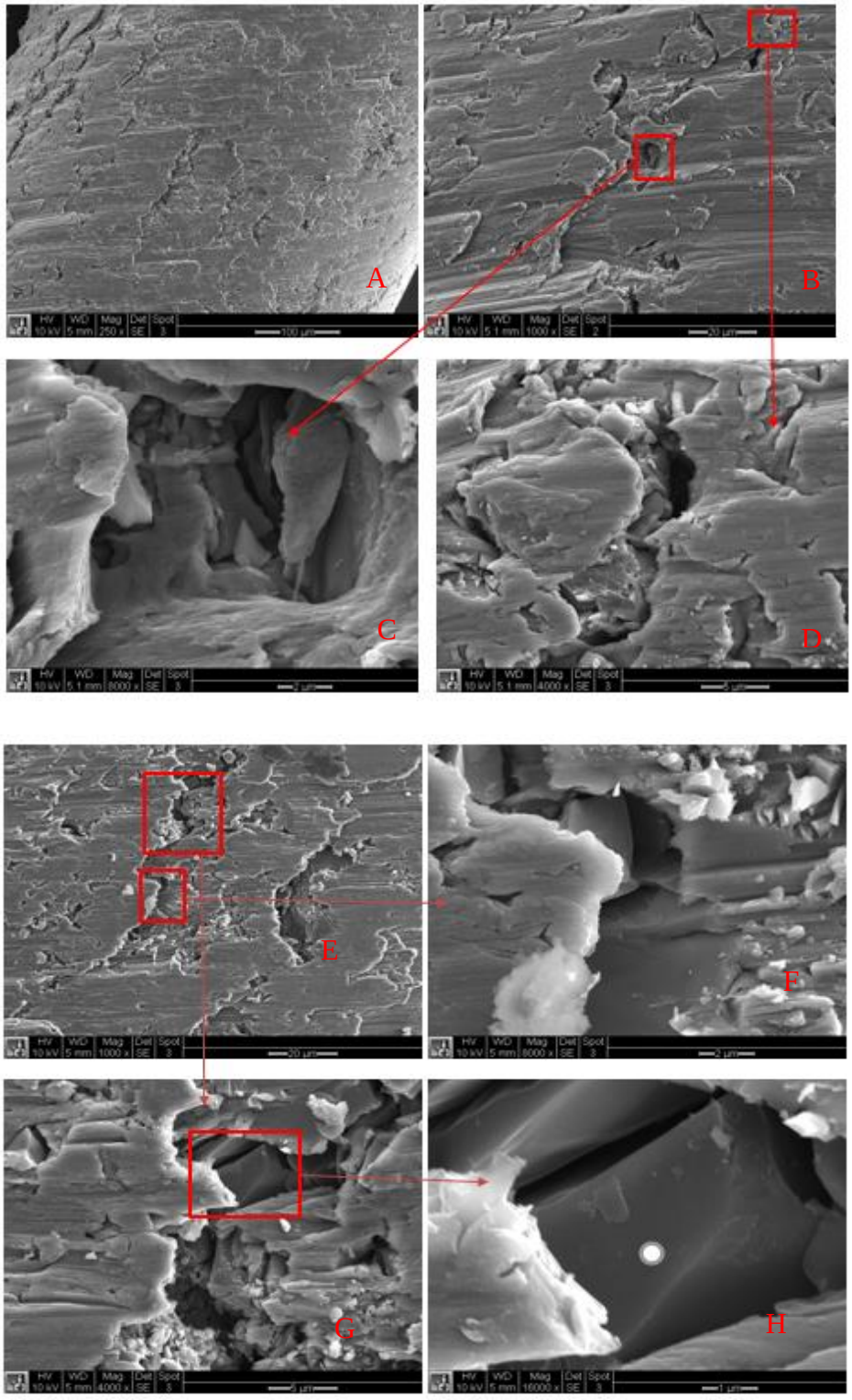

Figure 5.23: SEM images of the chips formed at Zone C, machined at a feed rate of 0.1 mm/rev and 1000 RPM.

The chips formed while machining Mg/SiC were found to be highly segmented, consistent with results found by Pedersen et al[24].The segmentation is formed as a result of stick-slip condition occurring at the tool-chip interface due to the reduced ductility of Mg/SiCp. Figure 5.21 shows low magnification of chip formed at 0.254 mm/rev and 1000 RPM. Agglomeration of SiC particles are found on the chip surface in Figures 5.22 a and b.

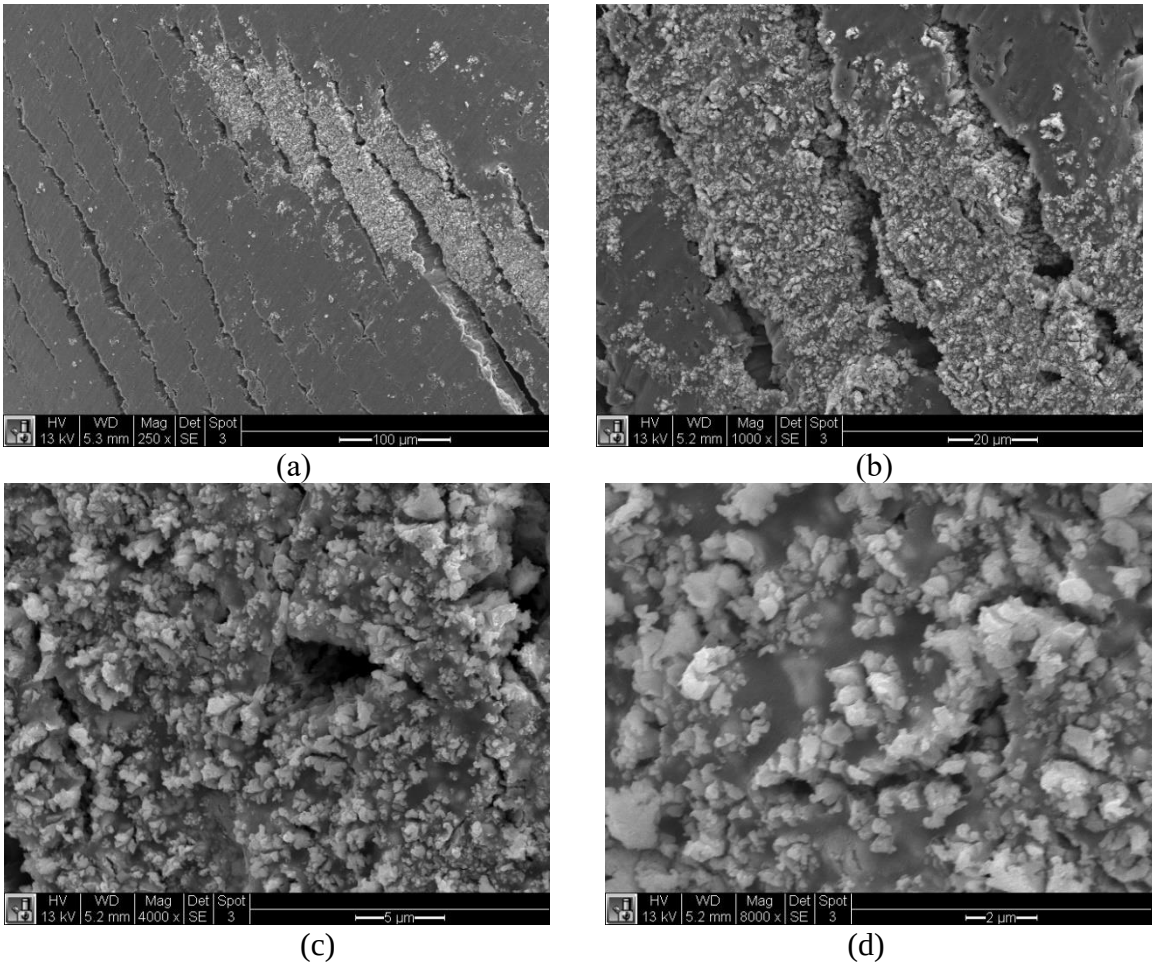

Figure 5.24: SEM image of the chips at a feed rate of 0.254 mm/rev and 1000 rpm spindle speed

The particles in the agglomeration were few hundred nanometers in size. The agglomerations were found both on the work piece and the chip surface indicating that agglomeration of the particles likely occurred during casting owing to the small diameter of the particles. In addition, voids corresponding to the size of the particles were observed on the surface of the chip owing to particle fall out, shown in Figures 5.22 c and d.

Chapter 6 . Machinability: Design of Experiments

6.1 Functionally gradient aluminum composite

The machining experiments were performed by varying the feed rate and the spindle speed, while maintaining constant axial and radial depth of cut. The feed rate and spindle speed were chosen in conformance with the published literature, listed in Table 2.4. The experiment conditions are listed in Table 6.1

Table 6.1: Experiment conditions for aluminum matrix composite

Parameters	**Values**
Cutting tool	¼ inch 2 flute square end mill, C2 square end carbide
Feed	0.1 to 0.5 mm/rev
Spindle speed	1000-5000
Axial depth of cut	1.27 mm
Radial depth of cut	1.27 mm
Length of cut/pass	48 mm
Direction of milling	High to low concentration of SiCp

The experiments were designed conducted using optimal design with replicates. I The depth-of-cut was kept constant since it has the least influence on the surface finish of MMCs in comparison to feed-rate and cutting speed [7]. The DoE table is shown in Table 6.2

Table 6.2: Design of experiments for aluminum composite

No	Feed rate, mm/rev	Spindle speed, RPM
1	0.5	5000
2	0.5	4000
3	0.5	3000
4	0.4	3000
5	0.3	4000
6	0.5	1000
7	0.3	5000
8	0.5	2000
9	0.1	5000
10	0.4	1000
11	0.4	5000
12	0.4	4000
13	0.4	2000
14	0.1	1000
15	0.2	5000
16	0.3	2000
17	0.2	4000
18	0.2	2000
19	0.1	4000
20	0.1	3000
21	0.2	1000
22	0.1	2000
23	0.3	1000
24	0.3	3000
25	0.2	3000

Response surface model was obtained, and analysis of variance was performed to identify the significant model terms. Model terms with p-value less than 0.05 were considered significant. The significant model terms help identify the dominant parameter for a particular response.

6.2 Magnesium composite

Similarly, the peripheral milling was performed for a range of feed rate and spindle speed to study the machinability of magnesium composites. The feed rate and spindle speed were chosen in conformance with the published literature, listed in Table 2.3. The chosen experiment conditions are listed in Table 6.3.

Table 6.3: Experiment conditions for magnesium matrix composite

Parameters	Values
Cutting tool	6.35 mm, 2 flute square end mill
Feed	0.2-1 mm/rev
Spindle speed	1000-4000
Axial depth of cut	1.27 mm
Radial depth of cut	1.27 mm
Length of cut/pass	32 mm

The experiments were designed conducted using optimal design with replicates. The depth-of-cut was kept constant since it has the least influence on the surface finish of MMCs in comparison to feed-rate and cutting speed [7]. The DoE table is shown in Table 6.4. Response surface model was

obtained, and analysis of variance was performed to identify the significant model terms. Model terms with p-value less than 0.05 were considered significant. The significant model terms help identify the dominant parameter for a particular response.

Table 6.4: Design of Experiments for magnesium composites

No	Feed rate, mm/rev	Speed, RPM
1	0.5	4000
2	0.2	4000
3	0.254	4000
4	0.508	4000
5	0.762	4000
6	1.016	4000
7	0.3	3000
8	0.254	3000
9	0.508	3000
10	0.762	3000
11	1.016	3000
12	0.5	2000
13	0.2	2000
14	0.254	2000
15	0.508	2000
16	0.762	2000
17	1.016	2000
18	0.3	1000
19	0.254	1000
20	0.508	1000
21	0.762	1000
22	1.016	1000

Chapter 7 . Functionally gradient Al/SiCp

Functionally gradient aluminum composite disk exhibits varying material property along the radius, and it is achieved through controlled variation of microstructure[67]. In this case, the difference in microstructure is achieved by reinforcing the matrix with gradient concentration of SiC particles. While machining the functionally gradient aluminum composite, the variation of SiC concentration through the material reflects in the cutting forces, acoustic emission, tool wear, the quality of the surface generated and the resulting chip morphology. In secondary processing, the presence of harder SiC particles result in accelerated tool wear, higher cutting forces and poor surface quality in comparison to the unreinforced matrix. The study of machining and machining induced surface defects are critical to expand the use of this composite. In this chapter, the effect of machining conditions and particle concentration on these parameters are investigated to find the optimum machining conditions. The DoE used in this study is given in section 6.1. In addition to these signals, the interaction of SiC particles with the cutting edge was also investigated through SEM micrographs of the cutting tool and the workpiece surface.

7.1 Cutting forces

The cutting forces were measured using a rotating dynamometer that allows direct measurement of forces at the cutting edge. The flutes were aligned along the y-axis of the dynamometer. Therefore, in this experiment, the radial force is given by the force in the Y-direction, F_Y and the tangential force is along the X-direction, F_x. The axial thrust force is given by F_z.

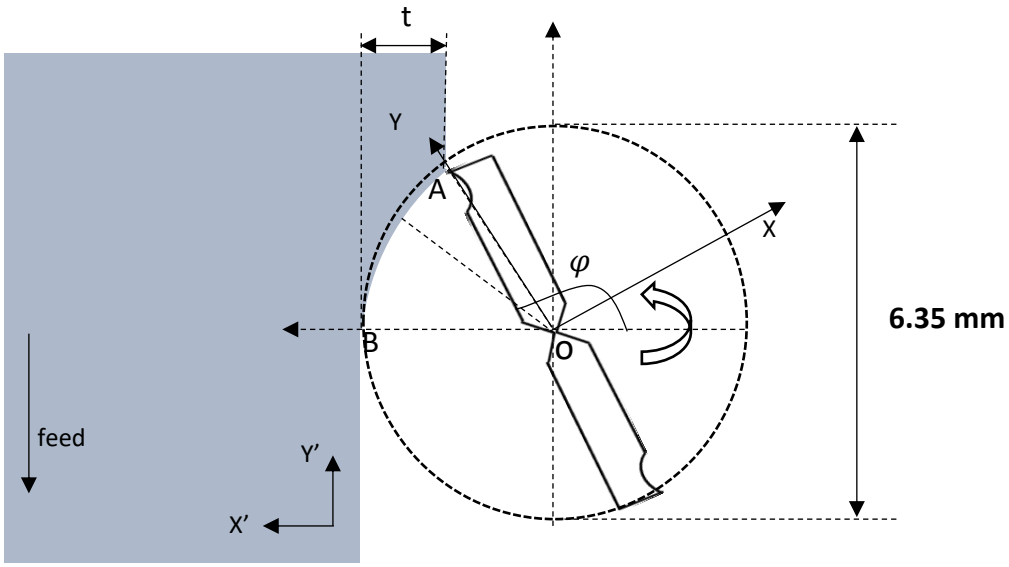

Figure 7.1: Geometry of the down-milling process, feed and speed in the same direction

The relationship between the feed, the normal direction and the coordinates of the dynamometer is discussed to understand the forces. Geometry of the down-milling process is shown in Figure 7.1. In down milling, the cutting tool and the workpiece move in the same direction at the point of contact. As a result, the chip thickness is highest at the tool entry and lowest at the exit. The coordinates of the dynamometer are represented by X-Y and the coordinates of the milling machine are represented by X'-Y'. The feed force is along the Y', while the radial thrust force is along the X'. The depth-of-cut is given by t, and φ is the instantaneous engagement angle of the tool with the workpiece. For a depth-of-cut of 1.27 mm and a tool diameter of 6.35 mm, the engagement angle varies from 126.86^{o} to 180°. The feed force, $F_{Y'}$, normal force $F_{X'}$ and thrust force, $F_{Z'}$ are given by,

$$F_{Y'} = F_Y \sin\varphi - F_X \cos\varphi \tag{7.1}$$

$$F_{X'} = -F_X \sin\varphi - F_Y \cos\varphi \tag{7.2}$$

$$F_{Z'} = F_Z \tag{7.3}$$

where, φ is the instantaneous tool engagement angle, shown in Figure 7.1, $126.86 \leq \varphi \leq 180$. At the tool exit, φ=180,

$$F_{x'} = F_y, F_{y'} = F_x, F_{z'} = F_z. \tag{7.4}$$

Similar analysis was also performed on an up-milling process to obtain the relationship between the feed force, thrust force on the workpiece and the measured forces. Figure 7.2 shown the up-milling process. In an up-milling process the cutting tool and the workpiece move in opposite direction at the point of contact. The chip thickness is lowest at the entry of the cutting tool and gradually increases until exit.

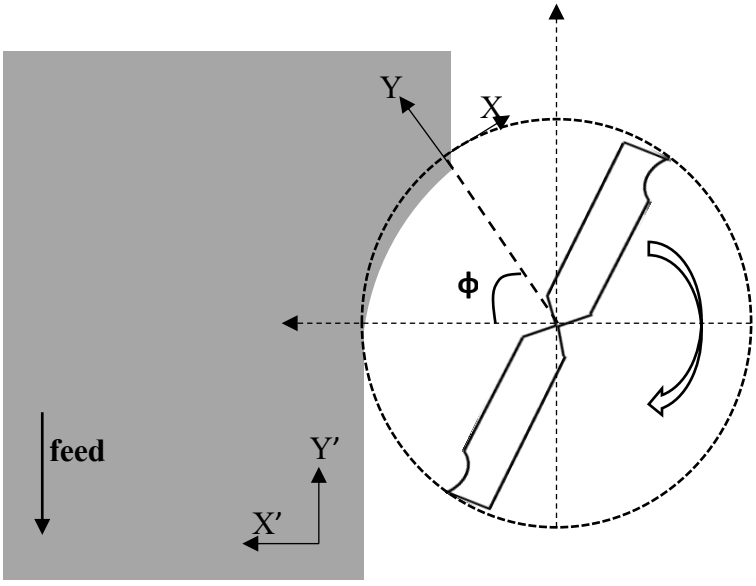

Figure 7.2: Geometry of the up-milling process.

The forces measured by the dynamometer are given by F_y, F_x and F_z and the forces experienced by the workpiece are $F_{x'}$ and $F_{y'}$ and $F_{z'}$. The relationship between these forces are given by,

$$F_{x'} = -F_x \sin\varphi + F_y \cos\varphi \tag{7.5}$$

$$F_{y'} = F_x \cos\varphi + F_y \sin\varphi \tag{7.6}$$

$$F_{z'} = F_z \tag{7.7}$$

Where the engagement angle, φ varies from 0 to 53.14^o as the cutting tool engages and disengages with the workpiece.

At the tool entry, φ=0,

$$F_{x'} = F_y, F_{y'} = F_x, F_{z'} = F_z. \tag{7.8}$$

Peripheral milling was performed on the functionally gradient aluminum using HAAS vertical milling machine. All the experiments were performed using two flute square end C2 carbide tools, specifications mentioned in section 5.1.

The cutting forces measured using the dynamometer for one cutter rotation is shown in Figure 7.3. The engagement of flute begins at 0 degrees and the peak force was attained at 53 degrees. Subsequently, the flute gradually disengages from the workpiece and the force decreases to zero until the second flute engages at 180 degrees.

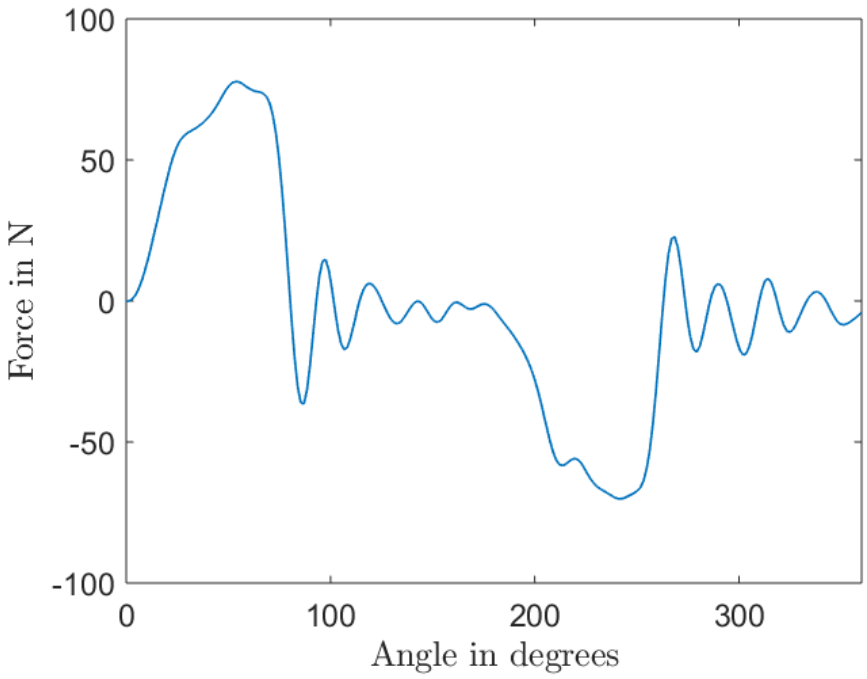

Figure 7.3: Cutting force for one cutter rotation.

The workpiece was milled from the highest to the lowest SiC particle concentration to observe the variation in the cutting forces with particle concentration. The cutting forces for machining MMCs are higher than machining conventional alloys due to the presence of hard reinforcement particles. The cutting forces obtained in a machining metal matrix composites depends on the particle concentration and distribution in the matrix[30]. The variation of forces F_x, F_y and F_z at 0.05 mm/rev and 1000 RPM with decreasing particle percentage is shown in Figure 7.4.

In Figure 7.4, forces F_y and F_x were found to decrease with decreasing percentage of SiC particles. Since the hardness of the reinforcement particles are much higher than the matrix material, higher cutting force is required to fracture the particles. More frequently, the particles slide over the cut surface resulting in the particle being pushed into the workpiece or removed along with the chips.

The tool experiences an increased friction force when the particles slide and pushed into the matrix. The decrease in forces F_x and F_y with the decrease in SiC concentration can be attributed to fewer number of particles encountered by the cutting edge as the concentration decreases. For convenience in studying the effect of particle concentration, the cutting distance was divided into zones based on particle concentration, discussed in chapter 4. The concentration in different zones are listed again in Table 7.1 for convenience.

Table 7.1: Zones with corresponding average particle reinforcement

Zone	Average Particle concentration
A	23.4%
B	20.2%
C	17.5%

However, as the feed rate increased to 0.4 mm/rev and spindle speed to 4000 RPM, the cutting forces were found to increase with decreasing particle concentration, shown in Figure 7.5. This can be attributed to the wear experienced by the carbide tool as it mills from high particle to low particle concentration. The tool wear experienced by the cutting tool was investigated to understand this response. The relative motion of particles with respect to the tool and the workpiece can lead to two body rolling and three body abrasion which causes severe wear on the rake and flank surface of the tool. Abrasive wear is reported to be the most dominant type of tool wear since the hardness of the reinforcement particles is higher than WC[17]. In addition, the increase in frictional force at the tool chip interface increases the temperature at the primary shear zone which results in the formation of built up edges(BUE) which produces poor surface finish and high

cutting forces[113]. The tool wear was found to increase with increasing feed rate, discussed in section 7.3. This results in higher cutting forces towards the end of the cutting distance, Zone C at higher feed rates. Although the particle concentration in this region is lower, the carbide tool has experienced significant wear from machining higher concentration zones A and B. This leads to increase in cutting forces at Zone C.

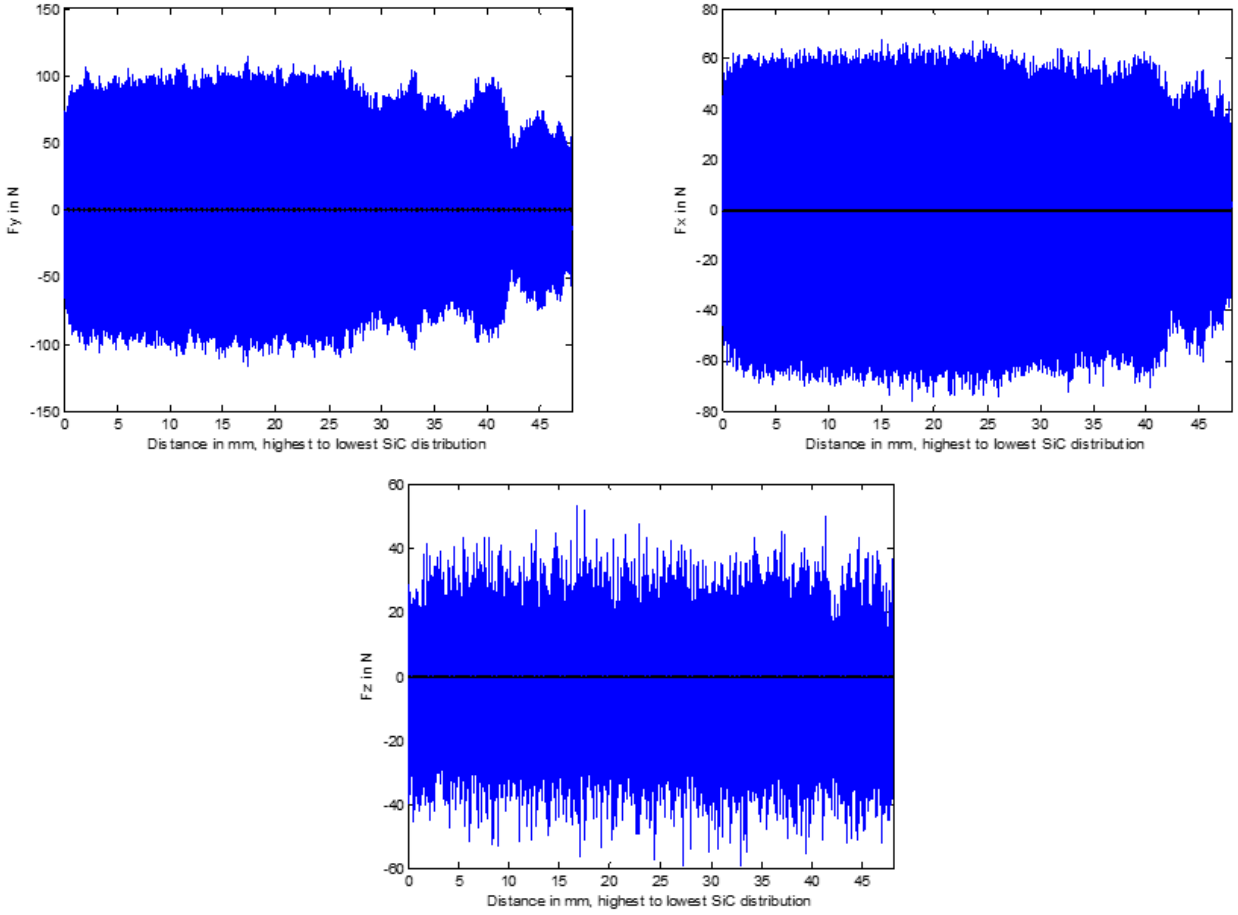

Figure 7.4: Cutting forces, Fx, Fy and Fz measured at feed=0.05 mm/rev and spindle speed=1000 RPM.

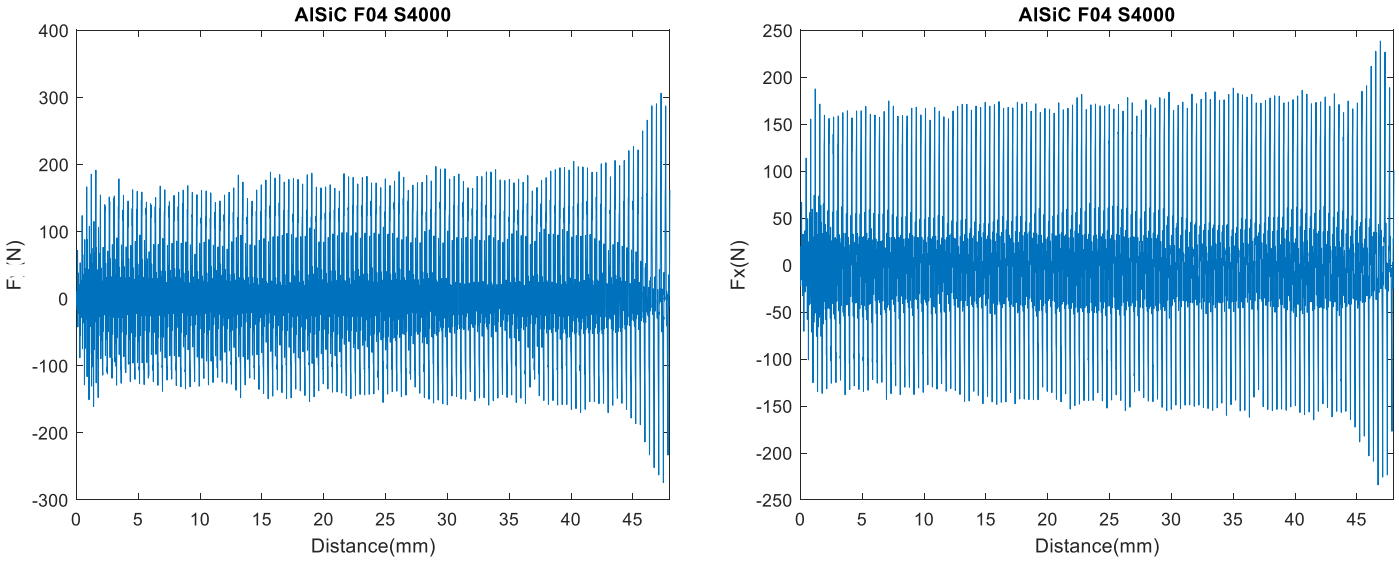

(a) (b)

Figure 7.5: Cutting forces, Fx, and Fy measured at feed=0.4 mm/rev and spindle speed=4000 RPM.

The average maximum cutting forces were obtained in each zone for a range of feed rates and spindle speeds, listed in chapter 6. The cutting forces F_x, F_y and F_z are plotted as a function of feed rate and spindle speed in the three zones, based on the force data given in Appendix D, shown in Figure 7.6,7.7 and 7.8.

To understand the significance of these parameters, response surface models relating the cutting forces with the machining conditions were developed for each zone, listed in Table 7.2. Based on the measured data, the response equations were developed using a multiple regression model. The response surface equations take the form,

$$r(x) = C_o + \sum_{i=1}^{2} C_i x_i + \sum_{i=1}^{2} C_{ii} x_i^2 + C_{12} x_1 x_2 \quad (7.9)$$

where r(x) is the response variable, x_i is the parameter, C_i is linear effect coefficient, C_{ii} is quadratic effect coefficient, C_{12} is the interaction effect coefficient. In this study, x_1 is the feed rate, x_2 is the spindle speed and the response variables are surface roughness parameters F_x, F_y and F_z for the three zones.

Analysis of variance was performed based on the design of experiments approach to identify the dominant parameter affecting the tool wear and surface quality. ANOVA results for the forces in the three zones are given in Tables 7.3 to 7.11. F value was used to identify the significance of the model and P-value to identify the significance of the model terms.

Table 7.2: : Response surface models for cutting forces in Al/SiCp

Zone	Force	Equation
A	F_y	$153.42 + -141.098 * Feed\ rate + -0.0481118 * Spindle\ speed + 0.013031 * Feed\ rate * Spindle\ speed + 773.471 * Feed\ rate^2 + 8.3027 * 10^{-6} * Spindle\ speed^2$
	F_x	$231.985 + -1118.33 * Feed\ rate + -0.0366874 * Spindle\ speed + 0.079421 * Feed\ rate * Spindle\ speed + 2415.9 * Feed\ rate^2 + 6.58214 * 10^{-6} * Spindle\ speed^2$
	F_z	$21.22 + -97.1714 * Feed\ rate + 0.00356857 * Spindle\ speed + -0.0206 * Feed\ rate * Spindle\ speed + 394.286 * Feed\ rate^2 + 1.02857 * 10^{-6} * Spindle\ speed^2$
B	F_y	$162.621 + -264.918 * Feed\ rate + -0.0460084 * Spindle\ speed + 0.00578925 * Feed\ rate * Spindle\ speed + 1036.84 * Feed\ rate^2 + 8.68626 * 10^{-6} * Spindle\ speed^2$
	F_x	$226.773 + -944.62 * Feed\ rate + -0.0444563 * Spindle\ speed + 0.080469 * Feed\ rate * Spindle\ speed + 2094.63 * Feed\ rate^2 + 8.61757 * 10^{-6} * Spindle\ speed^2$
	F_z	$28.445 + -149.419 * Feed\ rate + 0.001855 * Spindle\ speed + -0.01271 * Feed\ rate * Spindle\ speed + 427.714 * Feed\ rate^2 + 8.9 * 10^{-6} * Spindle\ speed^2$
C	F_y	$167.934 + -59.1145 * Feed\ rate + -0.0641673 * Spindle\ speed + -0.00437378 * Feed\ rate * Spindle\ speed + 744.298 * Feed\ rate^2 + 1.21282 * (10^{-5}) * Spindle\ speed^2$
	F_x	$244.731 + -816.391 * Feed\ rate + -0.079616 * Spindle\ speed + 0.019958 * Feed\ rate * Spindle\ speed + 2371.12 * Feed\ rate^2 + 1.70503 * 10^{-5} * Spindle\ speed^2$
	F_z	$35.02 + -173.923 * Feed\ rate + -0.00218 * Spindle\ speed + -0.00556 * Feed\ rate * Spindle\ speed + 419.571 * Feed\ rate^2 + 1.28 * 10^{-6} * Spindle\ speed^2$

Table 7.3: ANOVA results for F_x in Al/SiCp for Zone A

Source	Sum of Squares	df	Mean Square	F-value	p-value
Model	76309.04	5	15261.81	22.04	< 0.0001
A-Feed rate	65550.24	1	65550.24	94.65	< 0.0001
B-Spindle speed	1575.74	1	1575.74	2.28	0.1479
AB	169.81	1	169.81	0.2452	0.6262
A^2	4187.81	1	4187.81	6.05	0.0237
B^2	4825.45	1	4825.45	6.97	0.0162
Residual	13158.84	19	692.57		
Cor Total	89467.89	24			

Table 7.4: ANOVA results for F_y in Al/SiCp for Zone A

Source	Sum of Squares	df	Mean Square	F-value	p-value
Model	2.478E+05	5	49561.88	15.30	< 0.0001
A-Feed rate	1.622E+05	1	1.622E+05	50.04	< 0.0001
B-Spindle speed	35462.64	1	35462.64	10.94	0.0037
AB	6307.70	1	6307.70	1.95	0.1790
A^2	40856.01	1	40856.01	12.61	0.0021
B^2	3032.72	1	3032.72	0.9360	0.3455
Residual	61564.55	19	3240.24		
Cor Total	3.094E+05	24			

Table 7.5: ANOVA results for F_z in Al/SiCp for Zone A

Source	Sum of Squares	df	Mean Square	F-value	p-value
Model	5231.21	5	1046.24	9.85	< 0.0001
A-Feed rate	3010.88	1	3010.88	28.34	< 0.0001
B-Spindle speed	633.68	1	633.68	5.96	0.0245
AB	424.36	1	424.36	3.99	0.0602
A^2	1088.23	1	1088.23	10.24	0.0047
B^2	74.06	1	74.06	0.6970	0.4142
Residual	2018.63	19	106.24		
Cor Total	7249.84	24			

Table 7.6: ANOVA results for F_x in Al/SiCp for Zone B

Source	Sum of Squares	df	Mean Square	F-value	p-value
Model	86063.49	5	17212.70	30.75	< 0.0001
A-Feed rate	70145.19	1	70145.19	125.32	< 0.0001
B-Spindle speed	3077.95	1	3077.95	5.50	0.0300
AB	33.52	1	33.52	0.0599	0.8093
A^2	7525.26	1	7525.26	13.44	0.0016
B^2	5281.57	1	5281.57	9.44	0.0063
Residual	10634.60	19	559.72		
Cor Total	96698.09	24			

Table 7.7: ANOVA results for F_y in Al/SiCp for Zone B

Source	Sum of Squares	df	Mean Square	F-value	p-value
Model	2.449E+05	5	48973.69	11.82	< 0.0001
A-Feed rate	1.532E+05	1	1.532E+05	36.99	< 0.0001
B-Spindle speed	49265.98	1	49265.98	11.90	0.0027
AB	6475.26	1	6475.26	1.56	0.2263
A^2	30712.28	1	30712.28	7.42	0.0135
B^2	5198.38	1	5198.38	1.26	0.2765
Residual	78692.52	19	4141.71		
Cor Total	3.236E+05	24			

Table 7.8: ANOVA results for F_z in Al/SiCp for Zone B

Source	Sum of Squares	df	Mean Square	F-value	p-value
Model	4455.49	5	891.10	10.46	< 0.0001
A-Feed rate	2386.02	1	2386.02	28.00	< 0.0001
B-Spindle speed	571.90	1	571.90	6.71	0.0179
AB	161.54	1	161.54	1.90	0.1846
A^2	1280.58	1	1280.58	15.03	0.0010
B^2	55.45	1	55.45	0.6506	0.4299
Residual	1619.17	19	85.22		
Cor Total	6074.65	24			

Table 7.9: ANOVA results for F_x in Al/SiCp in Zone C

Source	Sum of Squares	df	Mean Square	F-value	p-value
Model	86916.79	5	17383.36	27.94	< 0.0001
A-Feed rate	70066.39	1	70066.39	112.63	< 0.0001
B-Spindle speed	2656.93	1	2656.93	4.27	0.0527
AB	19.13	1	19.13	0.0308	0.8627
A^2	3877.86	1	3877.86	6.23	0.0219
B^2	10296.48	1	10296.48	16.55	0.0007
Residual	11819.95	19	622.10		
Cor Total	98736.74	24			

Table 7.10: ANOVA results for F_y in Al/SiCp in Zone C

Source	Sum of Squares	df	Mean Square	F-value	p-value
Model	3.231E+05	5	64618.38	23.27	< 0.0001
A-Feed rate	2.219E+05	1	2.219E+05	79.90	< 0.0001
B-Spindle speed	41107.24	1	41107.24	14.80	0.0011
AB	398.32	1	398.32	0.1434	0.7091
A^2	39355.48	1	39355.48	14.17	0.0013
B^2	20349.85	1	20349.85	7.33	0.0140
Residual	52762.08	19	2776.95		
Cor Total	3.759E+05	24			

Table 7.11: ANOVA results for F_z for Al/SiCp in Zone C

Source	Sum of Squares	df	Mean Square	F-value	p-value
Model	3981.14	5	796.23	9.96	< 0.0001
A-Feed rate	1869.05	1	1869.05	23.38	0.0001
B-Spindle speed	734.21	1	734.21	9.19	0.0069
AB	30.91	1	30.91	0.3868	0.5414
A^2	1232.28	1	1232.28	15.42	0.0009
B^2	114.69	1	114.69	1.43	0.2457
Residual	1518.67	19	79.93		
Cor Total	5499.81	24			

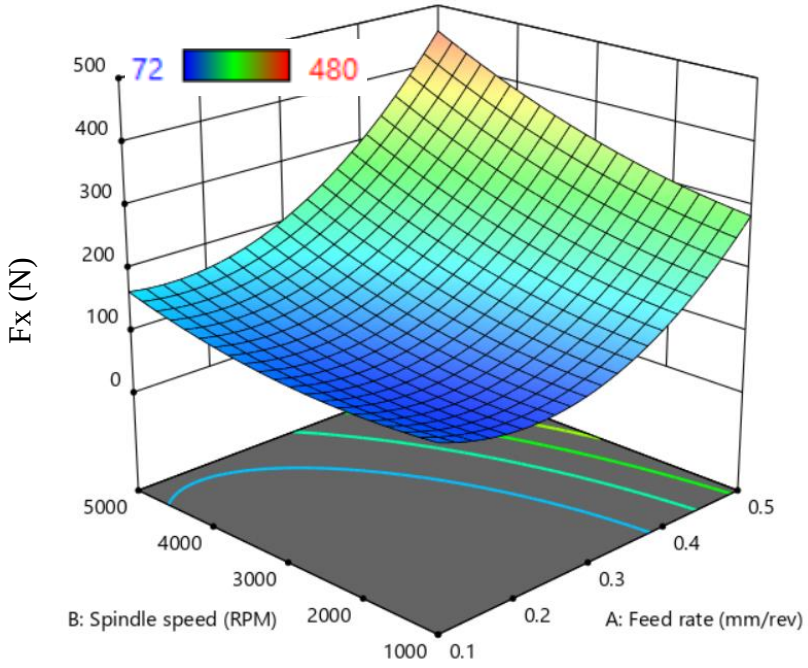

(a)

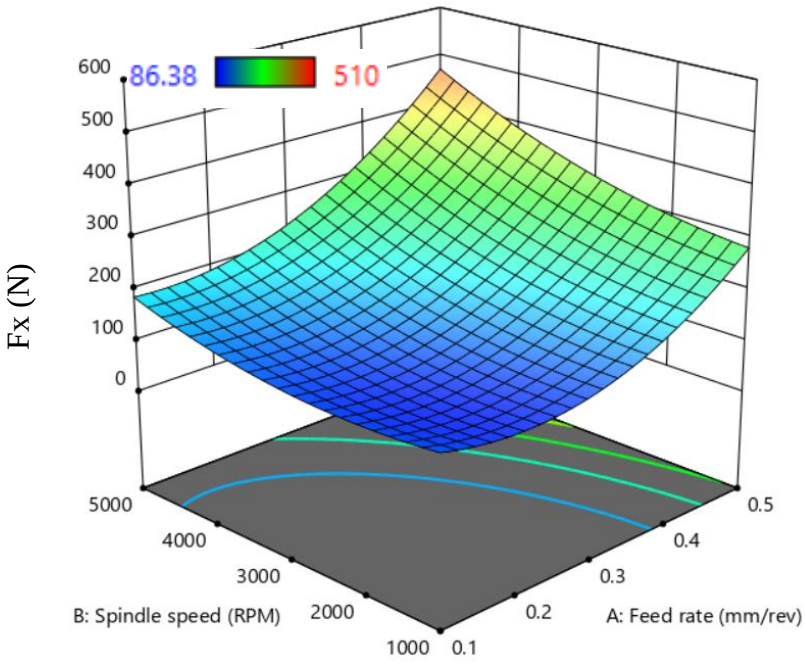

(b)

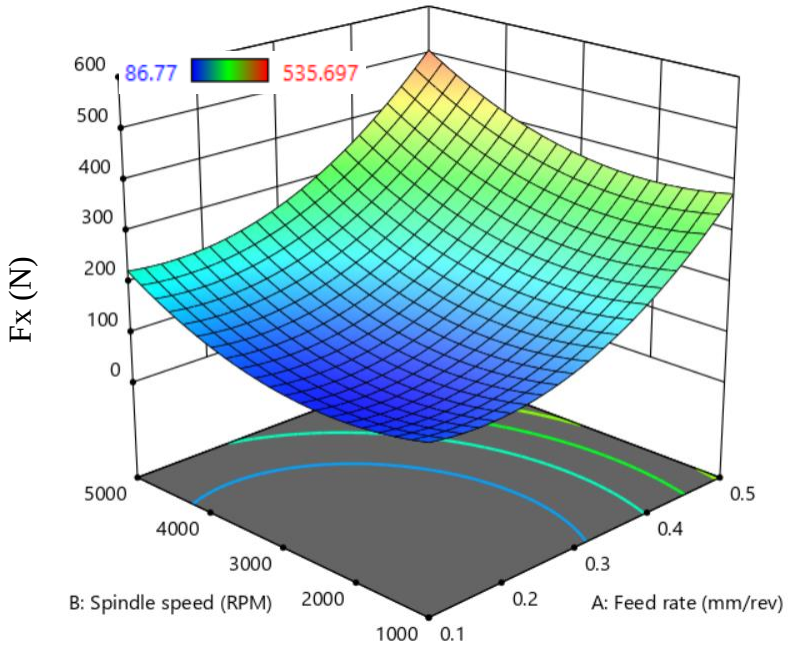

(c)

Figure 7.6: Feed force F_x in a) Zone A, b) B and c) C.

A significant increase in feed force, F_x with increase in feed rate was observed for all particle concentrations, shown in Figure 7.6. In zone A, F_x increased from 72 N to 480 N, from 86.3 to 510 N in Zone B and from 86.5 N to 535.69 N in Zone C. The increase in volume of material removed per revolution of the cutting tool leads to increase in cutting forces. Similar trends were observed in the radial and axial thrust forces, shown in Figures 7.7 and 7.8 . The radial force was found to increase from 84 N to 286 N in Zone A, 86.3 N to 296 N in Zone B and from 86.5 N to 313 N in Zone C. These results are consistent with observations made by Manna and Bhatacharya in turning Al/SiCp/15%[25], an increase in feed and thrust forces with increase in feed rate.

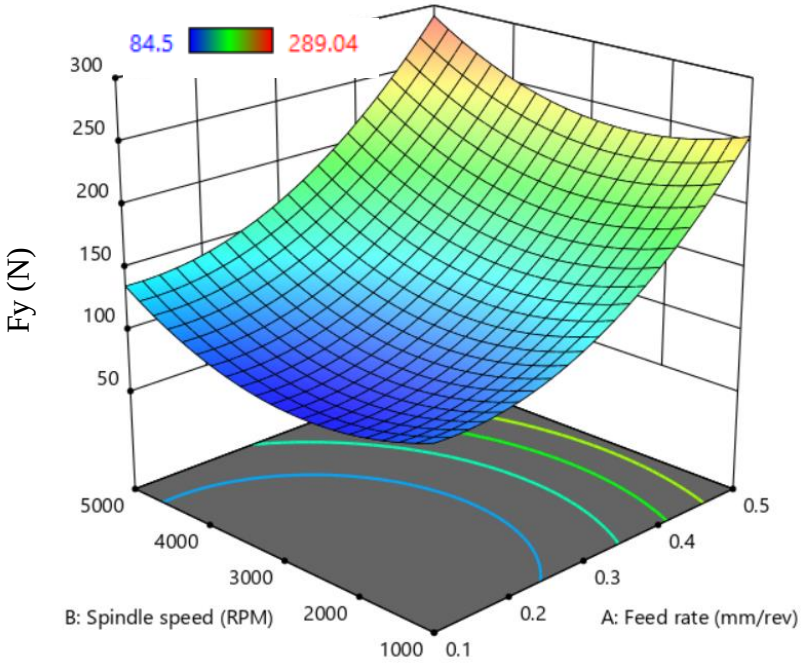

(a)

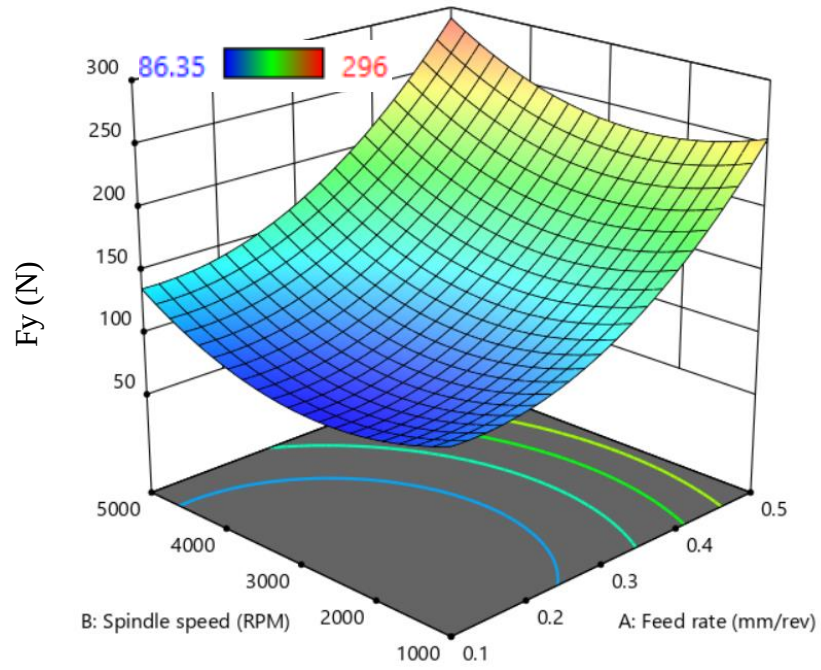

(b)

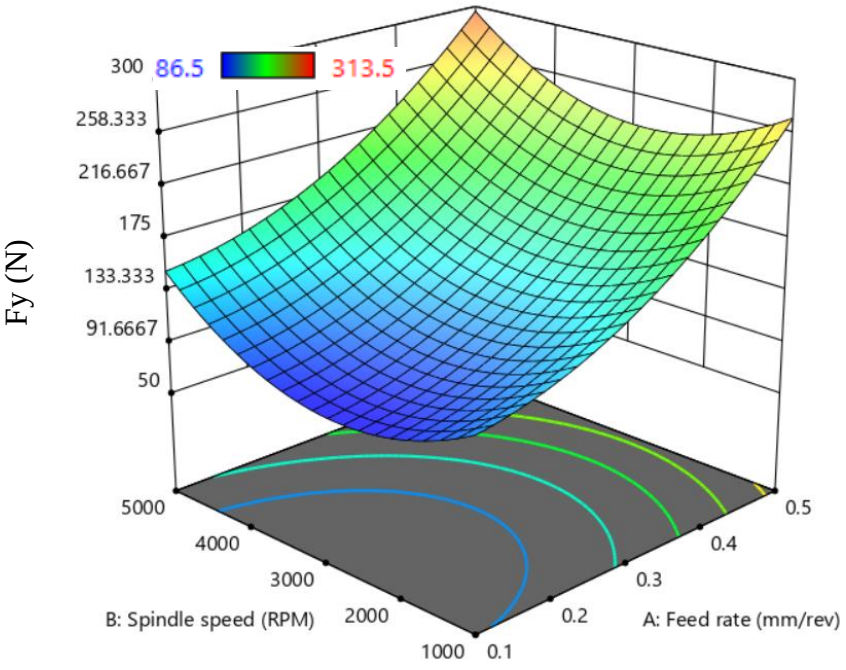

(c)

Figure 7.7: Radial forces, Fy in Zones a) A, b) B and c) C

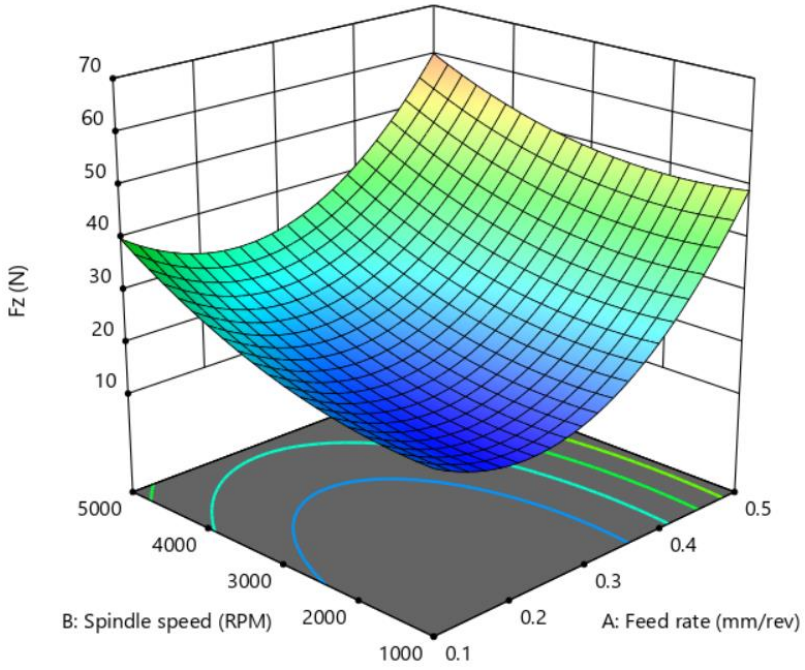
Fz (N)
70
60
50
40
30
20
10
5000
4000
3000
2000
1000
B: Spindle speed (RPM)
0.1
0.2
0.3
0.4
0.5
A: Feed rate (mm/rev)

(a)

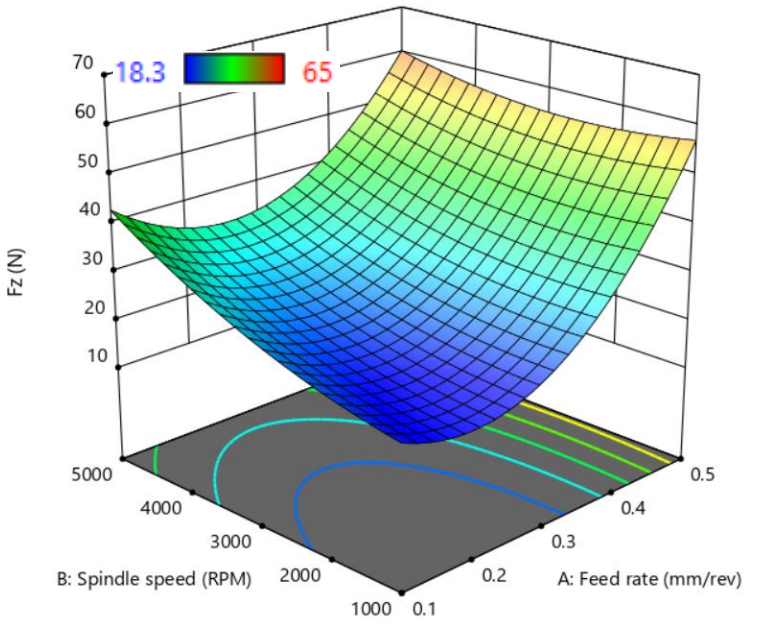
18.3
65
Fz (N)
70
60
50
40
30
20
10
5000
4000
3000
2000
1000
B: Spindle speed (RPM)
0.1
0.2
0.3
0.4
0.5
A: Feed rate (mm/rev)

(b)

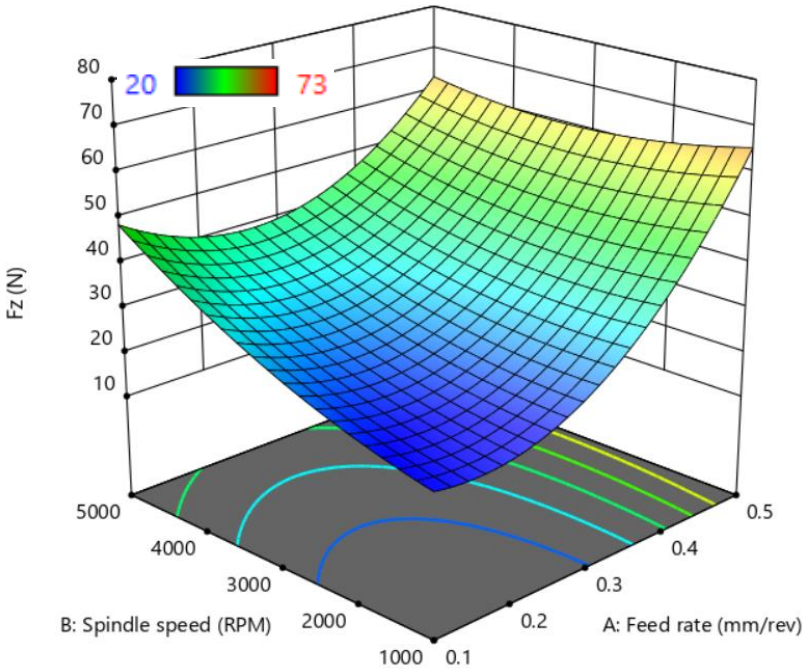

(c)

Figure 7.8: Axial thrust forces in Zones a) A, b) B and c) C

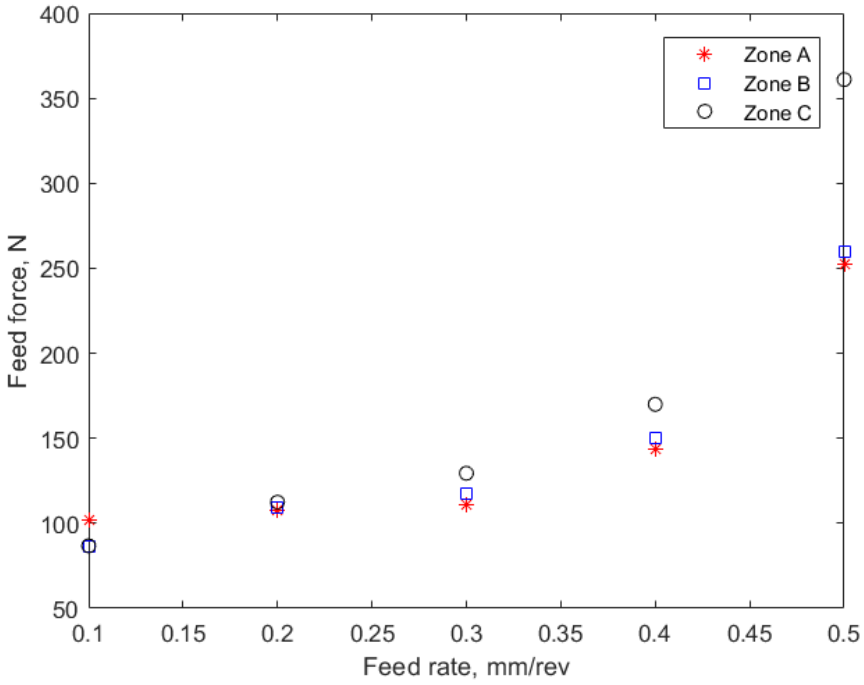

Figure 7.9: Feed force, Fx as a function of feed rate at 1000 RPM.

In addition, the difference between the cutting forces in Zones C and A increases with increasing feed, as shown in Figure 7.9. Although the average particle concentration in Zone C is lower than the concentration in Zone A, the cutting forces in Zone C were significantly higher than forces in Zone A, especially at higher feed rates. This behavior warrants for additional investigation of other factors that affect the cutting force in addition to the particle concentration.

7.2 Acoustic Emission

Transient elastic energy is dissipated from materials undergoing deformation or fracture. These transient elastic waves, also called acoustic emissions depend on the deformation mechanisms like dislocation motion, grain boundary sliding, twinning [114]. In a metal cutting process, the material undergoes plastic deformation at the shear zones leading to the emission of acoustic signals. These signals were captured using piezoelectric ceramic sensor for analysis. The energy contained in the acoustic emissions depend on the strain rate, the applied stress and the volume of material removed. Therefore, the milling process can be monitored through acoustic emissions if it can be related to one of these parameters mentioned above.

Two types of acoustic emissions have been identified in the literature, a) the high amplitude, low frequency signals that are erratic can be associated with surface events such as surface microcracks and fractures, while, b) low amplitude, high frequency continuous signals are associated with internal mechanisms during deformation. More specifically, in a metal cutting process the acoustic emissions can originate from five sources, a) the primary deformation zone, resulting in the

formation of chip, b) secondary deformation zone, where the chip slides along the rake face of the cutting tool, c) tertiary deformation zone, flank face rubs with the machined surface, d) Chip breaking and fracture, e) impact of broken chips on the tool and the workpiece[114].

The major source of AE in a metal cutting process is the primary and secondary shear deformation zones. The magnitude of emissions from other sources discussed above are insignificant in comparison. Acoustic emissions were captured during peripheral milling of cast aluminum alloy without reinforcements to analyze the signals emitted during plastic deformation without fracture of reinforcement particle. The root mean square value of the acoustic emissions as a function of volume removal rate is shown in Figure 7.10.

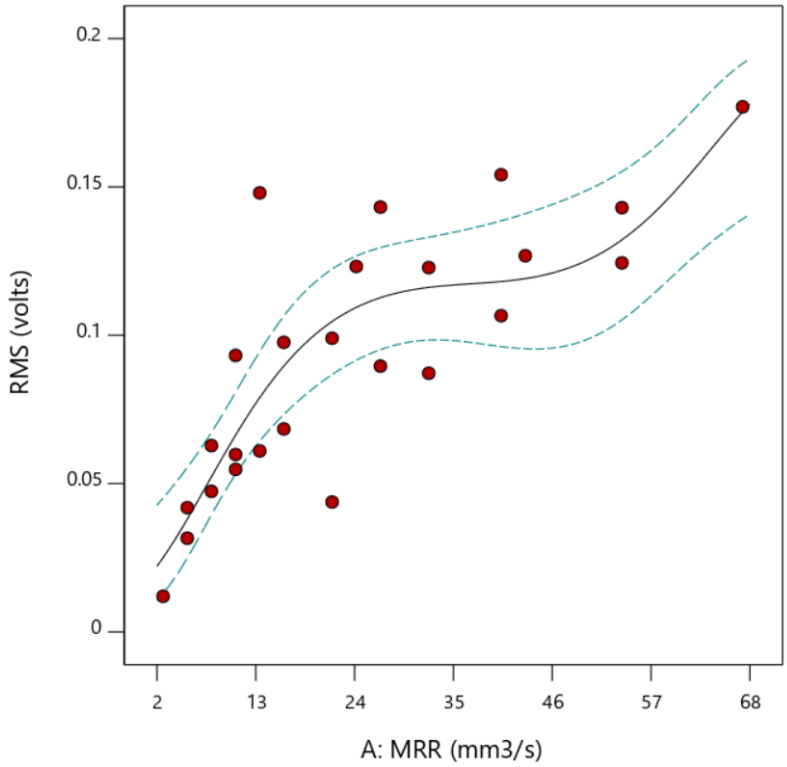

Figure 7.10: Root mean square of the acoustic emission(volts) vs material removal rate(function of speed and feed)

Rapid increase in the RMS value was observed during the initial increase in MRR. The rate of increase in MRR was observed to decrease from 24 to 50 mm^3/s, after which a drastic increase in MRR can be observed. Similar observation was reported by Dornfield et al in an orthogonal metal cutting process[114]. The authors observed an increase in RMS of the acoustic emissions with increasing strain rate as a function of dislocation density, magnitude of burgers vector and the average distance between the dislocations, cutting speed and feed rate. The RMS values were

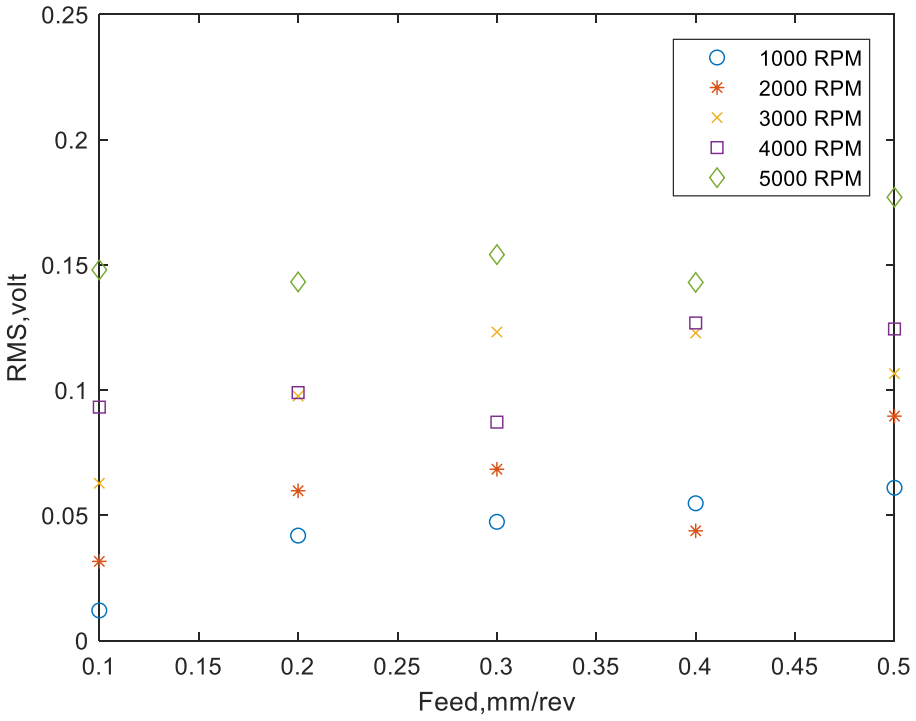

Figure 7.11: RMS as a function of feed, mm/rev for cast Al.

reported for three values of feed. The RMS was found to decrease first and then increase with increasing feed rate for lower cutting speeds. The initial decrease was expected since a decrease

in the feed rate typically resulted in increased strain rate. The later increase was attributed to formation of built up edge at lower cutting speeds[114]. In this study, the RMS was found to increase with feed rate and spindle speed especially at feed rates below 0.4 mm/rev owing to the increase in the rate of plastic deformation. . RMS values given in Appendix B.

Correspondingly, in metal matrix composites in addition to matrix shearing at the deformation zones, the particles are fractured, pushed into the matrix or debonds from the matrix. All these events lead to the emission of acoustic waves. Therefore, by characterizing the acoustic emissions in machining metal matrix composites, we can identify a correlation between the emitted signals and the events. Acoustic emission analysis from functionally gradient Al/SiCp is shown in Figure 7.12 and data given in Appendix B. Figure 7.12 shows the RMS of AE signal plotted as a function of feed rate. At feed rates below 0.3 mm/rev, the RMS value was found to increase with feed rate and spindle speed.

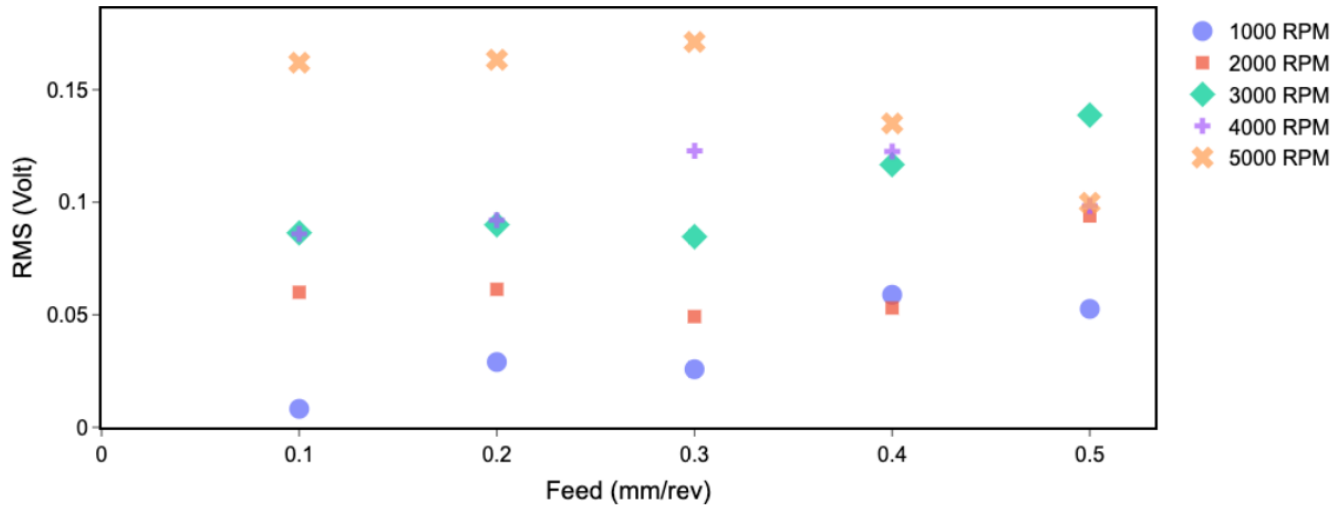

Figure 7.12: RMS value of AE as a function of feed rate and spindle speed for functionally gradient Al/SiCp.

7.3 Tool wear

Wear experienced by the carbide tools was quantified using optical micrographs and the wear mechanism identified through SEM micrographs of the cutting edge. Optical micrographs of the tools were obtained after each cut to measure the amount of tool wear for a constant cutting distance of 96 mm for a range machining conditions discussed in chapter 6. Comparison between the optical micrographs of as received and used tool is shown in Figures 7.13. Figures 7.13 a and b show the optical micrographs of left and right flutes of the tool before use. The micrographs were also obtained after use, shown in Figures 7.13 c and d. Formation of built up edge can be observed on the cutting edge. The SiC particles that are removed along with the chip rub on the rake face of the tool leading to higher cutting temperatures. The high temperature at the tool chip interface causes the aluminum matrix to soften and stick on the cutting tool leading to the formation of BUE, shown in Figure 7.13 b and c. Since the BUE forms over the sharp cutting edge, it alters the tool geometry, resulting in production of poor machined surface quality.

The amount of BUE on the cutting edge depended on the machining condition. This observation can be made from optical micrographs of cutting tools used at 0.1 mm/rev and 4000 RPM, 0.4 mm/rev and 1000 RPM and 0.4 mm/rev and 4000 RPM, shown in Figures 7.14, 7.15 and 7.16 respectively.

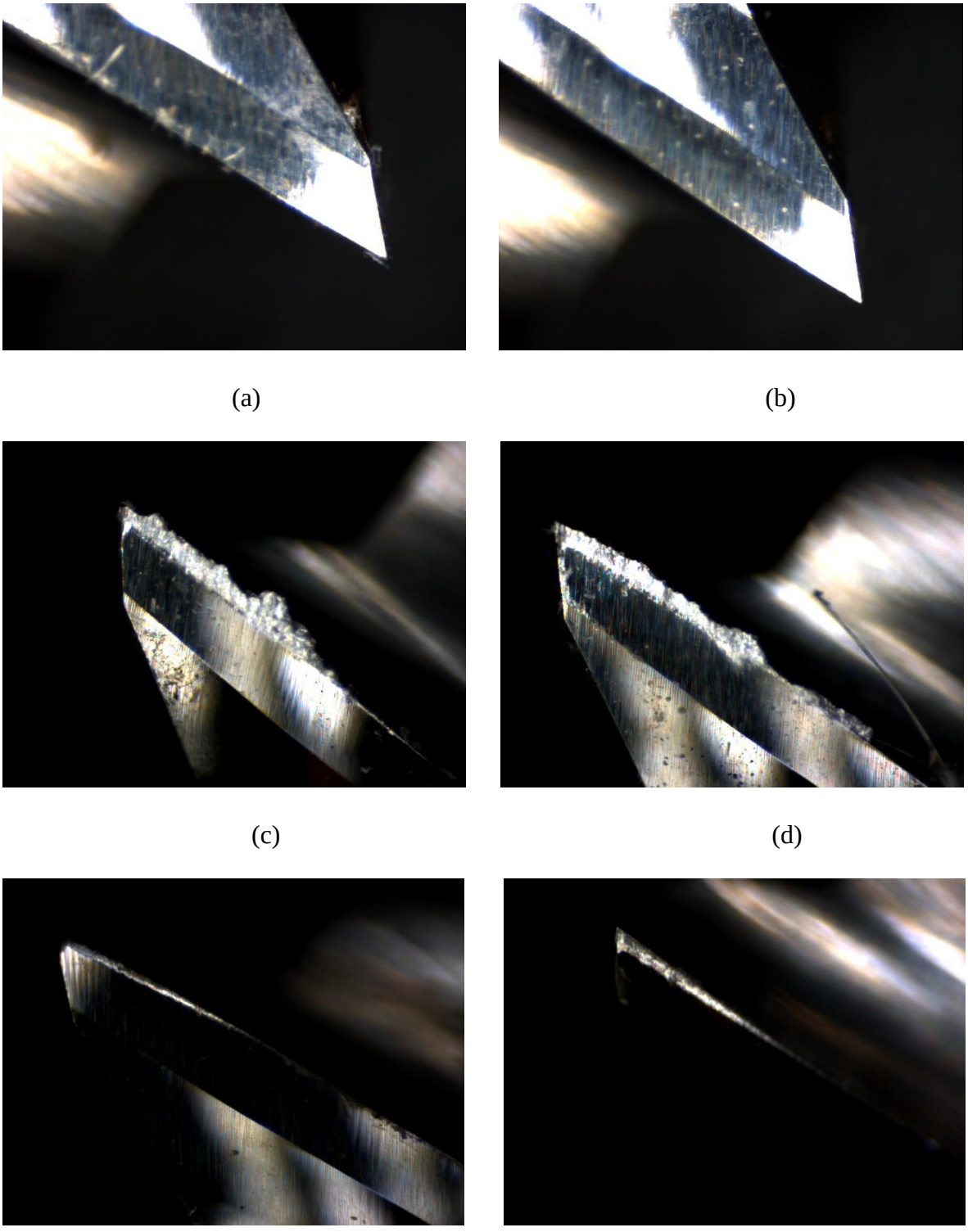

(a) (b)

(c) (d)

(e) (f)

Figure 7.13: Optical micrographs at 0.1 mm/rev and 1000 RPM of a,b) flutes of unused new tool c) BUE on flutes after a cutting distance of 96 mm (Zone A to C) , e,f) flutes after sonication

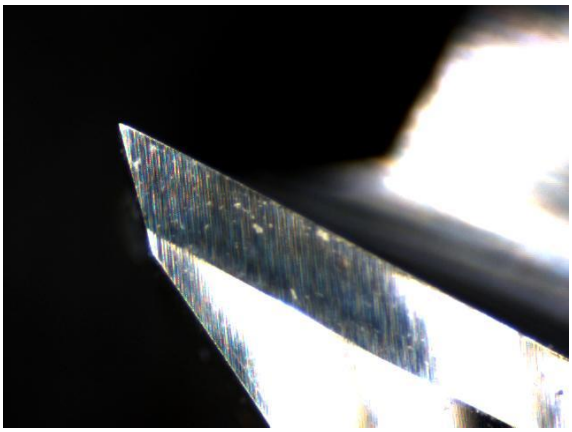

(a)

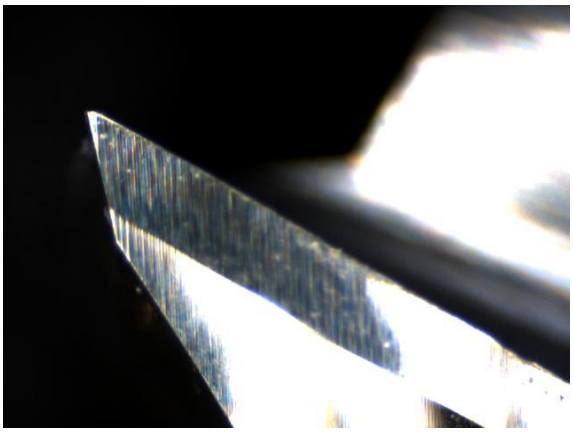

(b)

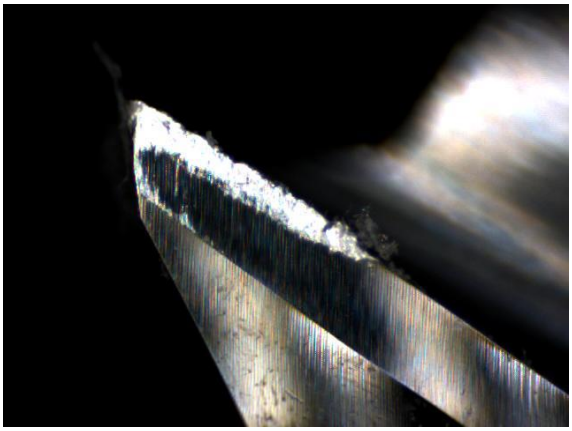

(c)

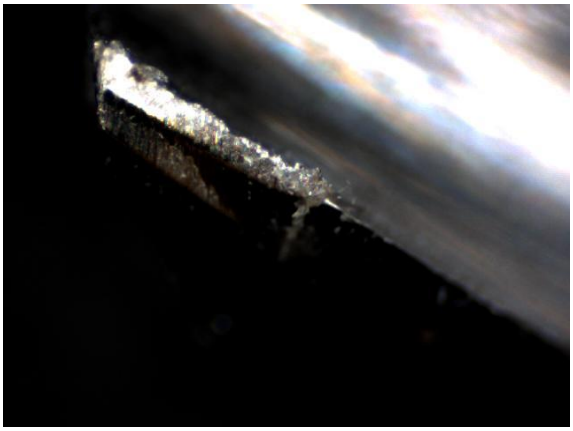

(d)



(e)

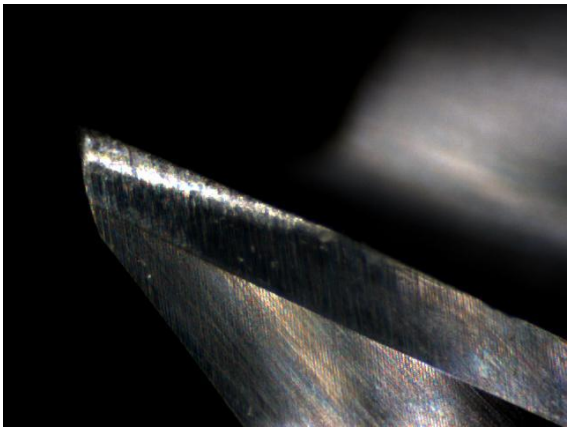

(f)

Figure 7.14: Optical micrographs at 0.1 mm/rev and 4000 RPM of a,b) flutes of unused new tool c) BUE on flutes after a cutting distance of 96 mm (Zone A to C), e,f) flutes after sonication

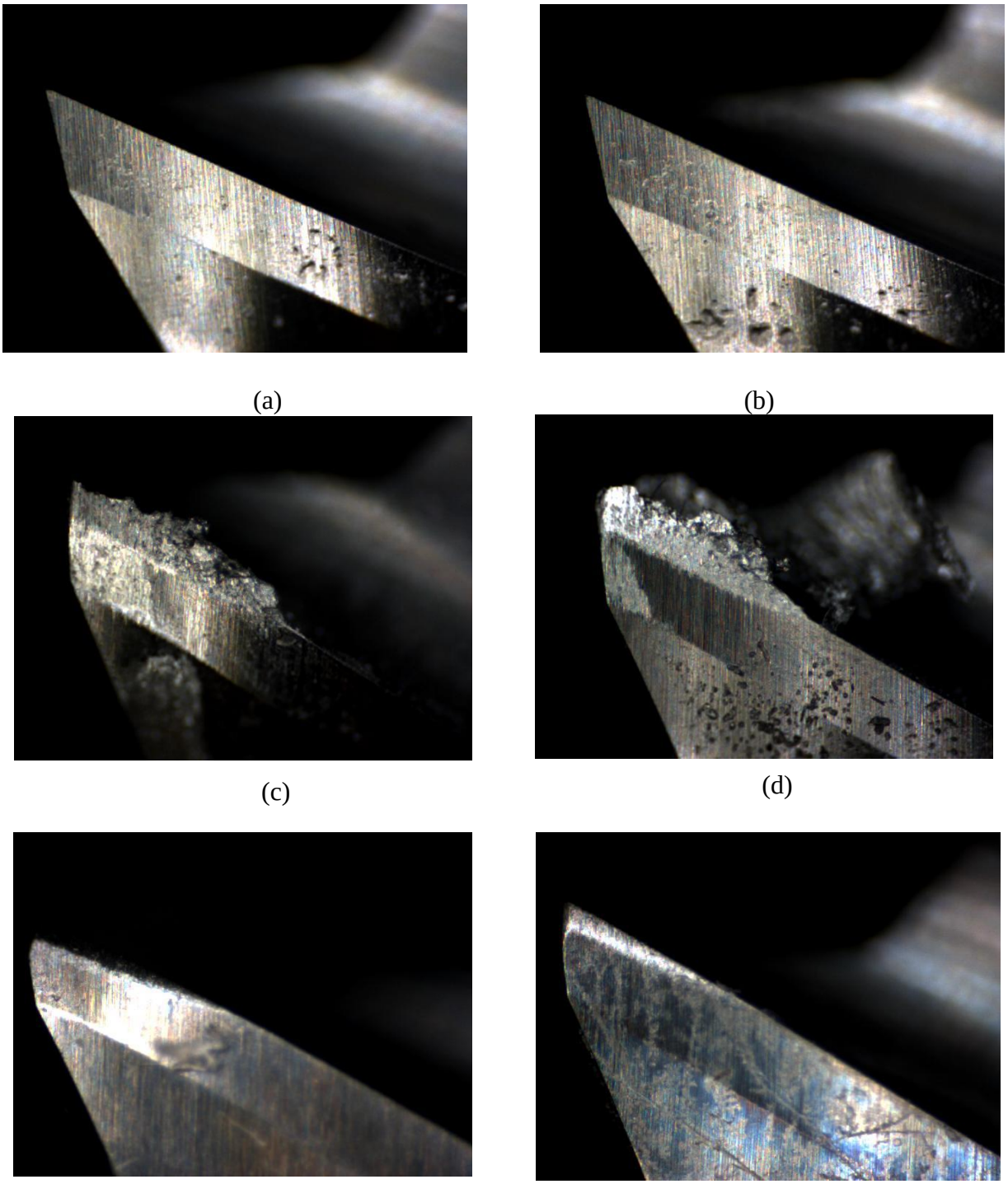

(a) (b)

(c) (d)

(e) (f)

Figure 7.15: Optical micrographs at 0.4 mm/rev and 1000 RPM of a,b) flutes of unused new tool c) BUE on flutes after a cutting distance of 96 mm (Zone A to C), e,f) flutes after sonication

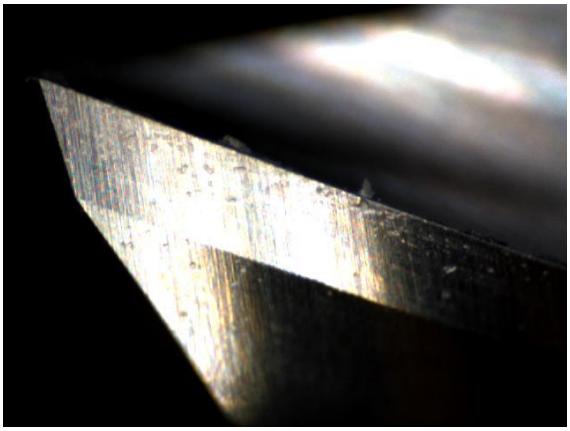

(a)



(b)

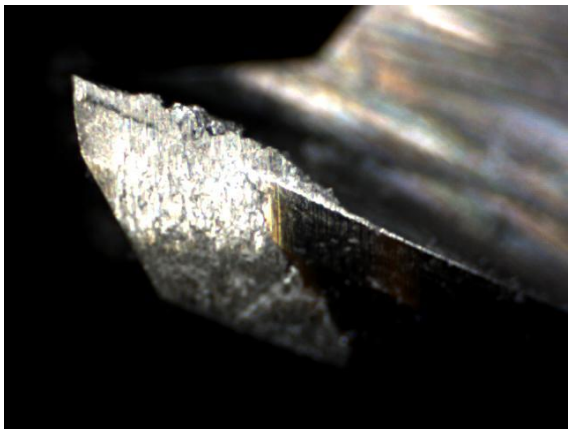

(c)

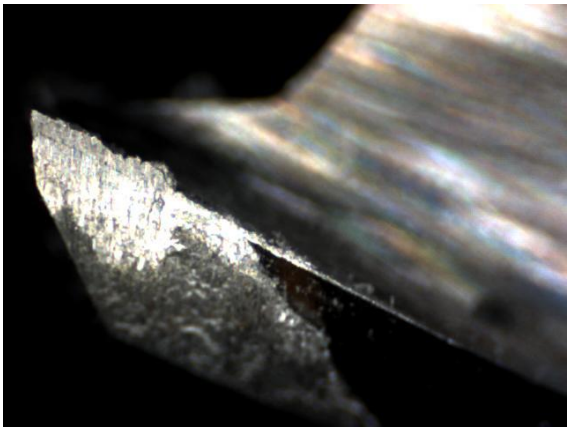

(d)

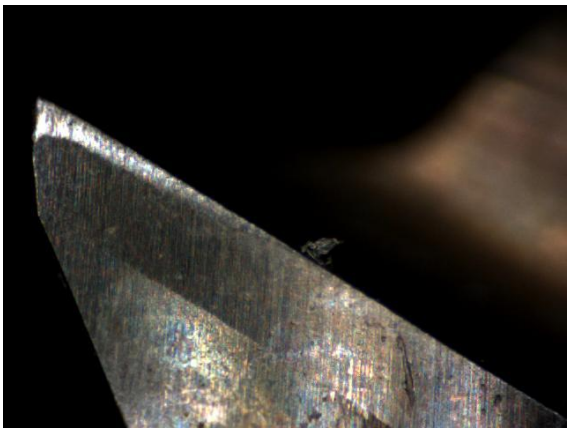

(e)



(f)

Figure 7.16: Optical micrographs at 0.4 mm/rev and 4000 RPM of a,b) flutes of unused new tool c) BUE on flutes after a cutting distance of 96 mm (Zone A to C), e,f) flutes after sonication

The formation of BUE was found to significantly increase with increasing feed rate. Figures 7.15 c and d show the BUE formed at a cutting condition of 0.4 mm/rev and 1000 RPM and Figures 7.13 c and d shows the BUE at 0.1 mm/rev and 1000 RPM. Similar observations were also made at higher spindle speed, the BUE formed at 0.4 mm/rev and 4000 RPM was considerably higher than BUE formed at 0.4 mm/rev and 1000 RPM, shown in Figures 7.16 c and d and 7.15 c and d. This can be attributed to higher temperature at the tool chip interface due to larger volume of material removed per revolution and increased abrasion of the reinforcement particles. Concurrent with the results obtained by Andrew et al, where smearing of aluminum matrix on the cutting edge of PCD tools were observed after 53 mins[18].

In order to measure the wear experienced by the tools, they were sonicated in KOH solution for 30 mins to remove the smeared aluminum matrix and to expose the worn region of the cutting region, shown in Figures 7.13, 7.14, 7.15 and 7.16 e and f. The tool wear was observed as the bright white region in the optical micrographs. The tool wear along the rake face of the tool appears to be tapered along the helix due to the lag experienced by the points on the cutting edge higher up along the helix in comparison to the tool tip. The helix provides a gradually increasing chip load along the helical flutes. The chip thickness varies in the axial direction. The tip of the flute is completely immersed into the cutting material. While, the points on the cutting edge along the axial direction lag by an angle ψ, given by,

$$\psi = \frac{2ztan\,\beta}{d} \tag{7.10}$$

Where,

β *is the hexlix angle,* z *is the distance from the tip and* d *is the diameter of the tool*

The chip thickness varies with the distance from the tip of the flute and the immersion angle,

$$chip\ thickness = feed\ per\ tooth * \sin(\varphi - \psi) \tag{7.11}$$

Due to the repeated abrasion of SiC particles and sliding of the matrix over the cutting edge, the worn region on the cutting edge is smoother than the rest of the area. Owing to the difference in surface roughness, the two regions scatter light differently. In a study performed by Bennet and Porteus[115], the total amount of light scattered by the surface is proportional to the surface roughness parameter, R_q of the surface. The relationship is given by,

$$TIS(R_q) = R_0\left[1 - e^{-\left(\frac{4\pi R_q \cos\Theta_i}{\lambda}\right)^2}\right] \tag{7.12}$$

Where,

TIS: is total amount of light scattered by the surface

R_0: Reflectance of the surface

λ: wavelength of the incident light

R_q: Root mean square roughness

Θ_i: angle of incidence

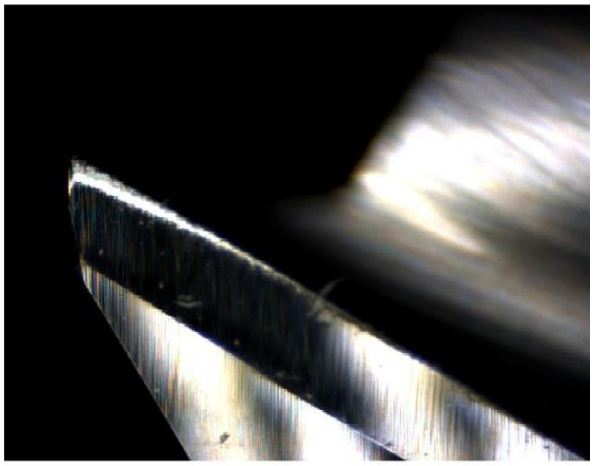

(a)

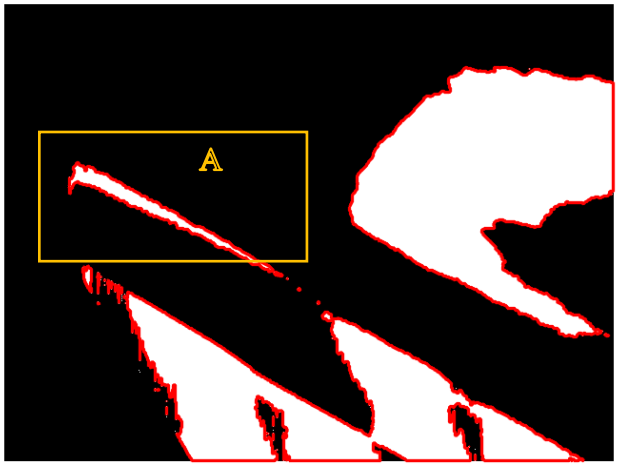

(b)

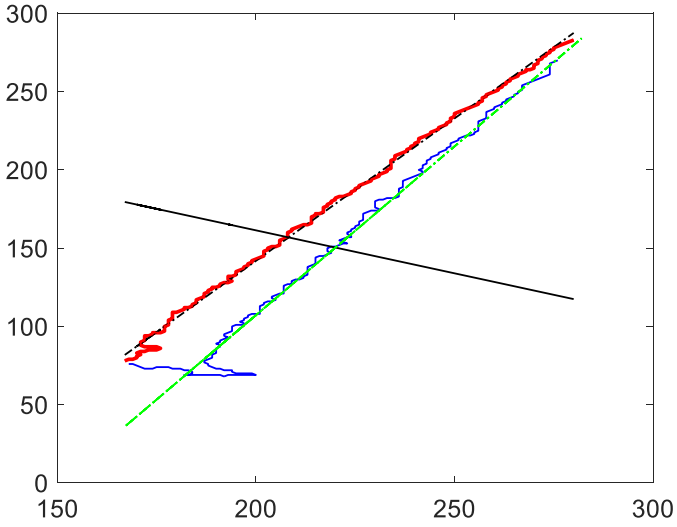

(c)

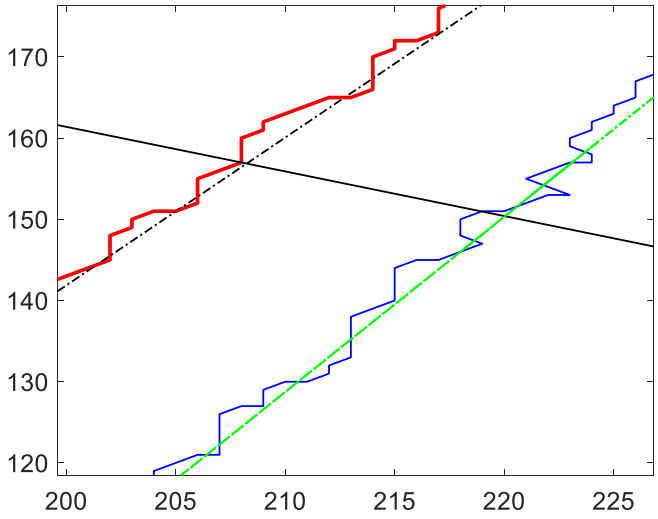

(d)

Figure 7.17: Tool wear measurement, a) Optical micrograph of the left flute after a cutting distance of 64 mm at 0.1 mm/rev and 3000 rpm, b) the boundary of the wear is identified, shown in A, c and d) the width of the wear is measured between the linear fit lines

Owing to the lower R_q of the worn region, it has a more specular reflection resulting in higher intensities in the captured micrographs. Therefore, the tool wear experienced by the cutting tool can be measured by analyzing the high intensity region on the cutting tool. The difference in pixel intensities between the worn area and rest of the tool was used to identify the wear boundary.

The optical micrographs of the cutting tools were binarized using adaptive thresholding. The boundaries of the regions in the image are identified, as shown in 7.17 b. The outer boundary of the cutting edge is identified in red and the inner boundary is identified in blue, as shown in Figure 7.17 c. A linear fit of the boundaries are obtained, shown as black and green lines in Figures 7.17 c and d. The tool wear measurement was taken as the perpendicular distance between the linear fits at a distance of 120 microns from the tool tip, shown in Figure 7.17 d. MATLAB code developed to identify the wear region is given in Appendix B.

Similar measurements were performed at all the machining conditions to compare the tool wear. The tool wear was plotted as a function of feed and spindle speed, shown in Figure 7.18 . The tool wear data and optical micrographs given in Appendix B and D. A response surface model was developed, and analysis of variance performed to identify the dominant factors, result shown in Table 7.12.

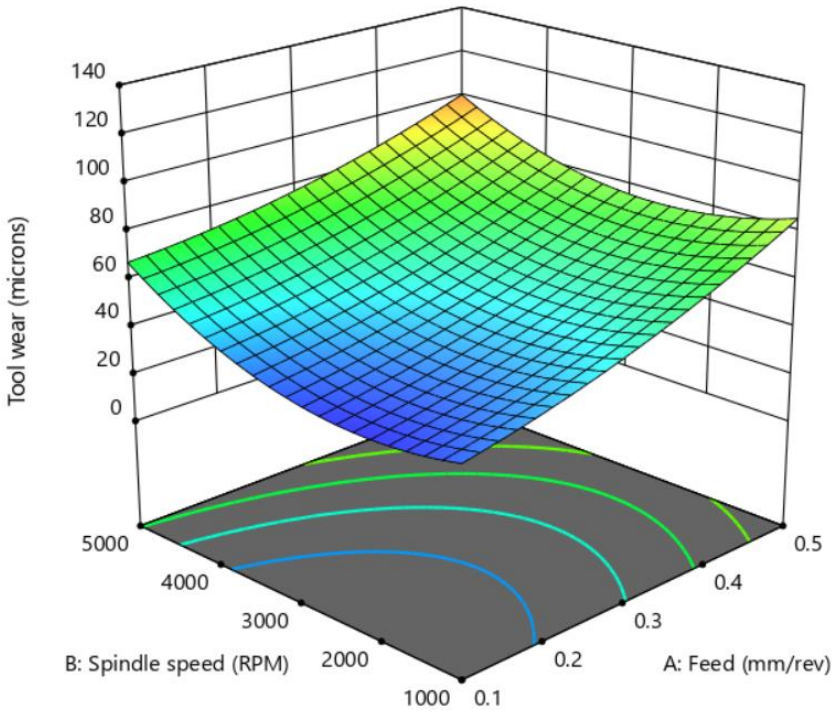

Figure 7.18: Tool wear(μm) as a function of spindle speed(RPM) and feed rate(mm/rev).

The tool wear was found to increase with both the feed rate and spindle speed. The response surface model is given by,

$$Tool\ wear, \mu m = 45.4249 + 48.2086 * Feed + -0.0162311 * Spindle\ speed + -0.0090664 * Feed * Spindle\ speed + 132.52 * Feed^2 + 4.0738 * 10^{-6} * Spindle\ speed^2 \quad (7.13)$$

Table 7.12: ANOVA table for tool wear model

Source	Sum of Squares	df	Mean Square	F-value	p-value
Model	7756.90	5	1551.38	6.85	0.0008
A-Feed	5255.31	1	5255.31	23.19	0.0001
B-Spindle speed	1296.31	1	1296.31	5.72	0.0273
AB	49.93	1	49.93	0.2203	0.6441
A^2	150.86	1	150.86	0.6657	0.4247
B^2	1004.47	1	1004.47	4.43	0.0488
Residual	4305.88	19	226.63		
Cor Total	12062.78	24			

In addition, the changes in tool nose geometry with the cutting conditions were also monitored. The tool nose of a new tool and tools used at 1000, 5000 RPM at 0.4 mm/rev after a constant milling distance of 96 mm is shown in Figure 7.19. At 0.4 mm/rev and 1000 RPM, the tool was used for 14 seconds, while at 5000 RPM for 4 seconds for a cutting distance of 96 mm. The nose rounding was found to increase marginally with the spindle speed. The MATLAB code is given in Appendix B.

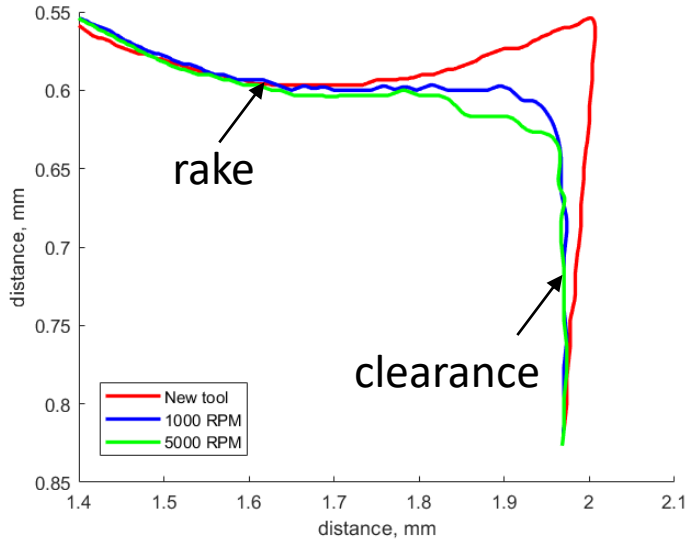

Figure 7.19: Tool nose rounding at 0.4 mm/rev after 96 mm of milling after 15 seconds for 1000 RPM and 4 seconds for 5000 RPM

The dominant wear mechanism is influenced by the cutting conditions, the relative particle size between the reinforcement particles present in the matrix and the grain size of the carbide tool, the cutting tool and the workpiece material. For PCD tools, the initial tool wear was observed to occur due to the abrasion of SiC particles on the flank face of the tool, after 53 mins of cutting, a thin layer of aluminum was smeared on the cutting edge due to continuous abrasion resulting in high temperature at the tool-chip interface[17].

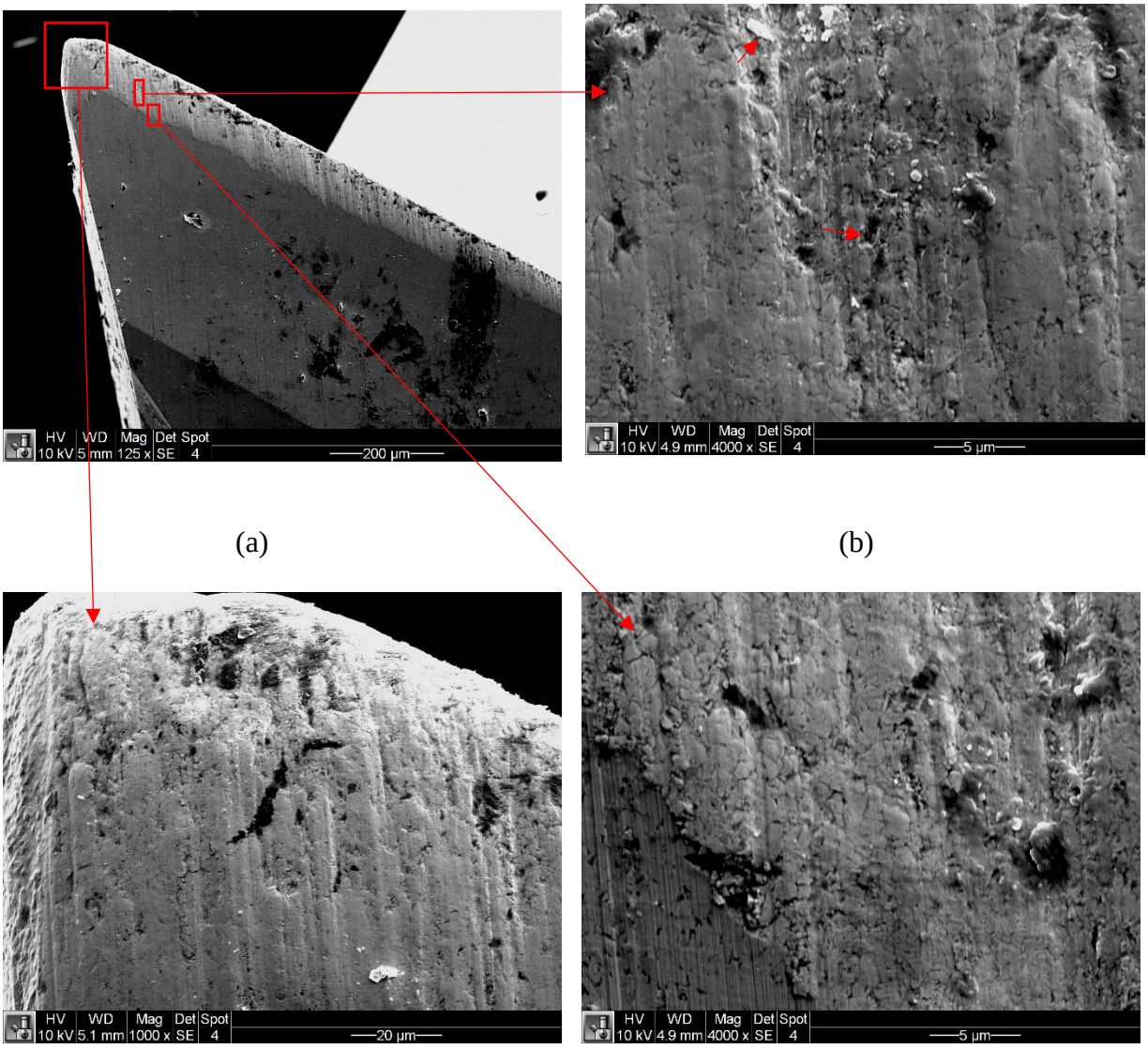

Figure 7.20: SEM micrographs of the cutting tool at 0.1 mm/rev and 1000 RPM.

The wear mechanism of the carbide tools in machining aluminum composites has not been thoroughly studied. The hardness of the SiC particle is higher than carbide cutting tool resulting in higher wear rate in comparison to the diamond cutting tools. SEM micrographs of the carbide tools

used in a range of feed rate and spindle speed were obtained to understand the wear mechanism, shown in Figure 7.20, 7.21 and 7.22. The SEM micrographs were obtained after sonicating the tool with KOH solution to remove the adhered aluminum layer and observe the wear. The tapered wear region can be observed at low magnification, shown in Figure 7.20 a. Upon further magnification, grooves and pits were found along the direction of the chip flow, shown in 7.20 b, c and d. This topography of the cutting edge indicated that the wear mostly occurred by abrasion. The SiC particles ploughed along the surface lead to the formation of grooves. Also, due to the high temperature, Al_2O_3 forms at the cutting edge and is sufficiently hard to form grooves on the surface[112]. The pits formed along the grooves, shown in Figure 7.20 b, were about 1 μm in size corroborating with the size of the grains in the C2 WC tool, indicating that the WC grains have been pulled out. This can be attributed to two factors, abrasion from the reinforcement particles or removal of grains with the BUE owing to the adhesive bond between the adhered layer and the grains being stronger.

Further, the SEM micrographs were obtained at 0.3 mm/rev and 3000 RPM. Increased tool wear can be observed in this condition from Figure 7.21. Owing to the high temperature and pressure at the cutting edge, aluminum matrix was smeared on the surface leading to the formation of BUE, shown in Figure 7.21 b. Due to repeated compaction at the cutting edge, the smeared aluminum form adhesive bond with the cutting edge and they may be chipped off due to the abrasion from SiC particles, shown in Figure 7.21 c, e and f. Figure 7.21 shows the smeared matrix abraded by

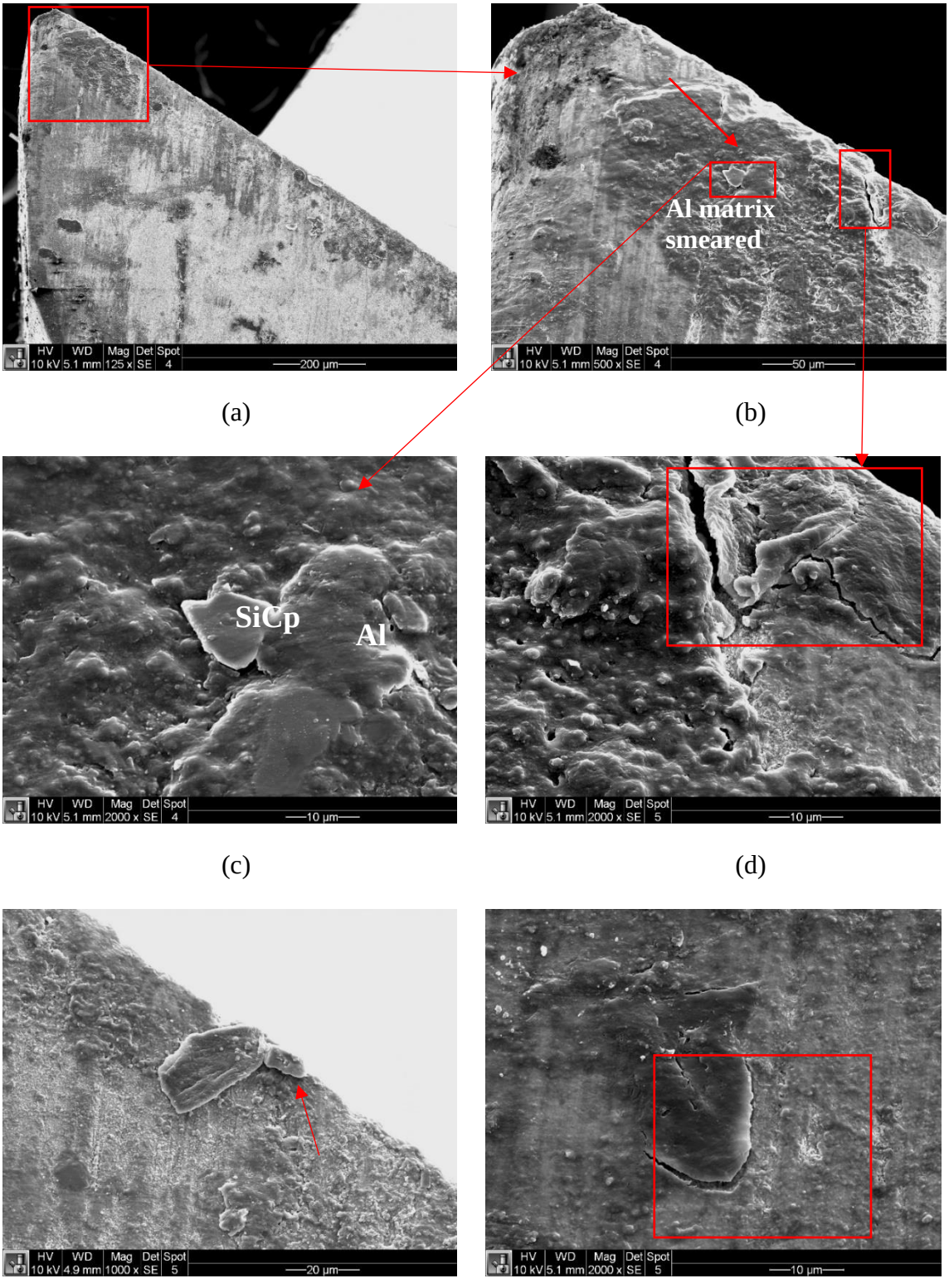

Figure 7.21: SEM micrographs of the cutting tool at 0.3 mm/rev and 3000 RPM.

the SiC particle. In addition, BUE form cracks due to low cycle fatigue caused by the repeated impact on the cutting edge, highlighted in Figures 7.21 c and f. Some WC grains are also removed when the BUE is chipped off the surface owing to the formation of strong adhesive bond, leading to accelerated tool wear.

The cutting edge at 0.4 mm/rev and 4000 RPM had aluminum matrix smeared on the surface and the presence of prominent grooves, shown in Figures 7.22 c and d. At this feed rate, the pressure and temperature at the cutting edge increase due to the higher amount of material undergoing plastic deformation in each flute engagement. Also, reflected in the increase in cutting forces with feed rate. The SiC particles under high pressure create prominent grooves on the surface of the tool, shown in Figures 7.22 a, b and c. The smeared aluminum layer protects the tool from further wear. Similar observations were also reported by Ubeyli et al[116] in milling of aluminum composite reinforced with B_4C reinforcement particles. The authors reported that the wear was proportional to the chip volume and the wear mechanism was a combination of both abrasive and adhesive wear.

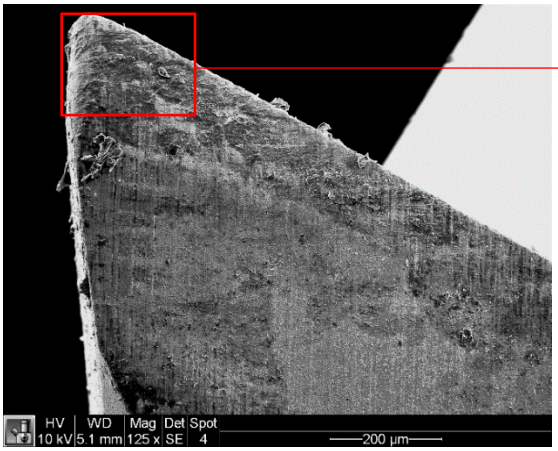

(a)

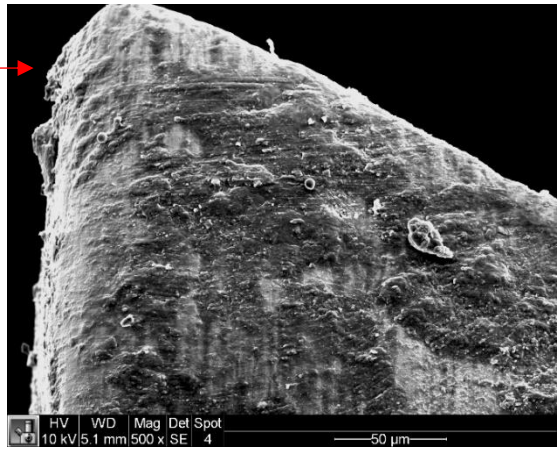

(b)

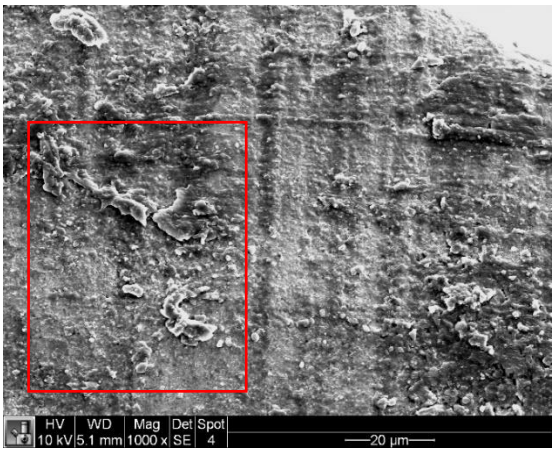

(c)

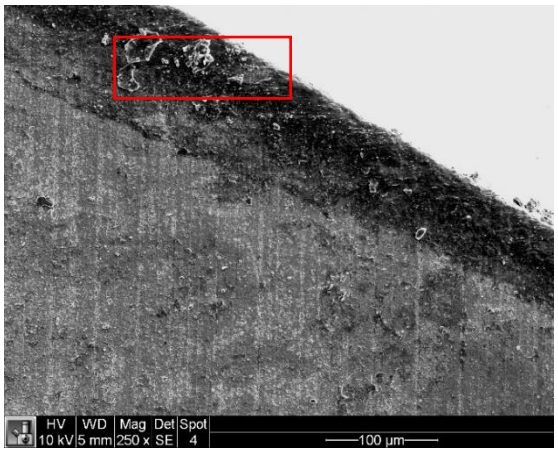

(d)

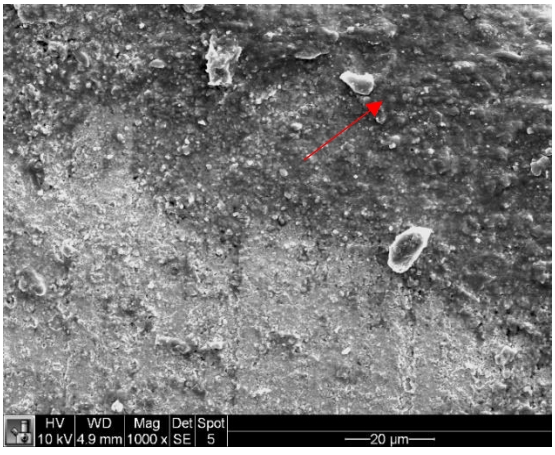

(e)

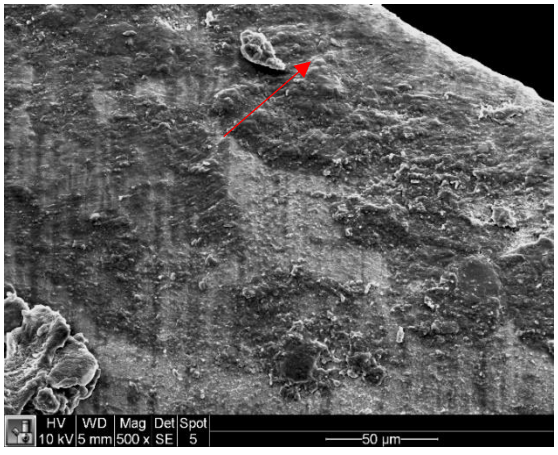

(f)

Figure 7.22: SEM micrographs of the cutting tool at 0.4 mm/rev and 4000 RPM.

7.4 Surface topology

In this section, the dependence of surface quality on the feed rate and spindle speed in a peripheral milling is studied. Unlike the turning process, milling is an intermittent cutting process where the tool engages and disengages repeatedly, impacting the workpiece in every cutter rotation. Therefore, the quality of the surface produced should studied to optimize the machining conditions. The average surface roughness as a function of feed rate and spindle speed is shown in Figure 7.23. The surface roughness profiles and data is given in Appendix C and D, respectively. The surface roughness profiles were measured in the three zones, A, B and C. R_a was found to increase significantly with the feed rate. In Zone A, Ra increased from 11.31 to 21.766 µm, from 13.896 to 30.28 µm in Zone B and 12.9 to 32 µm. Similar results were reported by Pramanik et al in turning of Al6061/SiCp/20%, the surface roughness was low at lower feed rate and increased with increasing feed rate[56].

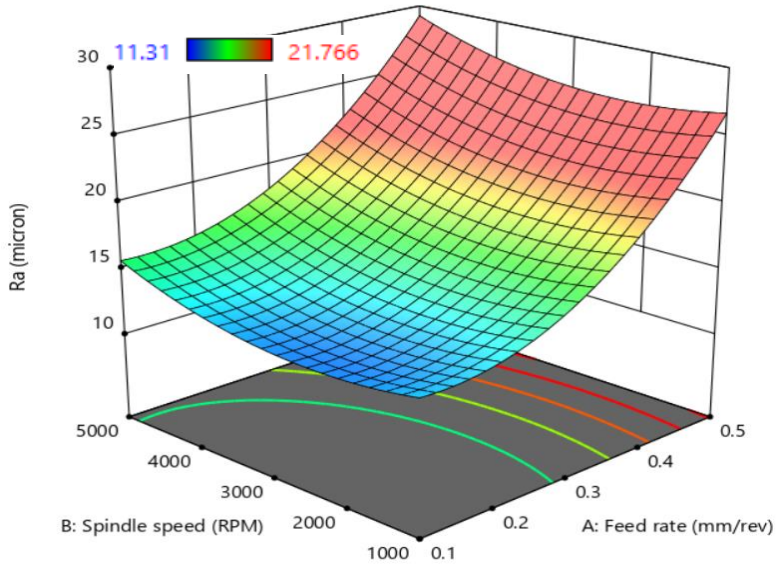

(a), Zone A

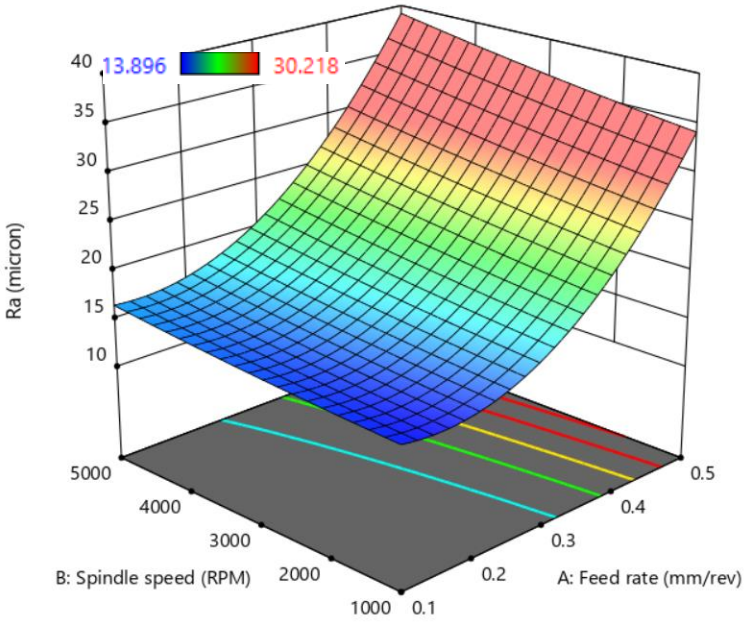

(b), Zone B

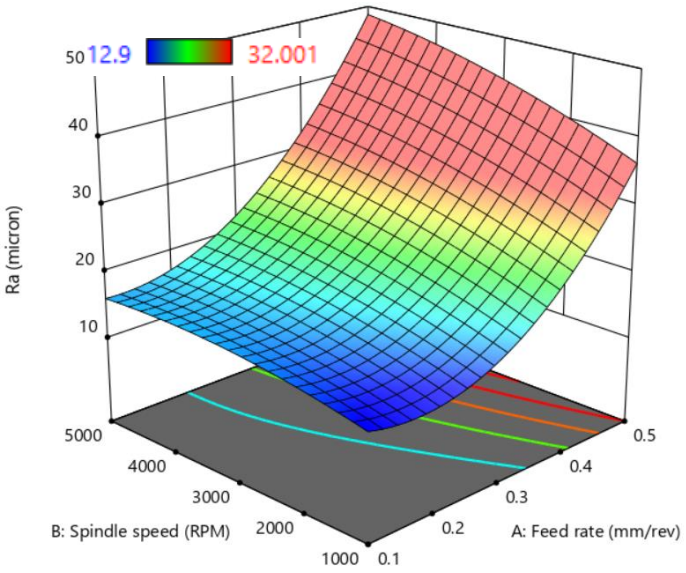

(c), Zone C

Figure 7.23: Average surface roughness, R_a at Zones, a) A, b) B and c) C.

In the current experiment, the functionally gradient aluminum composite is machined from high to low concentration of SiC particles. As discussed in the previous section, the carbide tool experiences wear along the cutting distance of 96 mm. The effect of tool wear is also reflected on the surface, resulting in higher surface roughness in Zone C in comparison to Zone A and B. Based on the measured data, the response equations were developed using a multiple linear regression models. The response surface equations take the form,

$$r(x) = C_o + \sum_{i=1}^{2} C_i x_i + \sum_{i=1}^{2} C_{ii} x_i^2 + C_{12} x_1 x_2 \quad (7.13)$$

where r(x) is the response variable, x_i is the parameter, C_i is linear effect coefficient, C_{ii} is quadratic effect coefficient, C_{12} is the interaction effect coefficient. In this study, x_1 is the feed rate, x_2 is the spindle speed and the response variables are surface roughness parameters R_a. The response surface models are given in Table 7.13 and the ANOVA results are presented in Table 7.14, 7.15 and 7.16 for zones A, B and C respectively.

Table 7.13: Quadratic equation for R_a

Zone A	$16.5202 + -24.604 * Feed\ rate + -0.00207194 * Spindle\ speed + 0.00014$ $Spindle\ speed + 96.203 * Feed\ rate\text{^}2 + 4.37829e-07 * Spindle\ speed\text{^}2$
Zone B	$17.6206 + -51.0646 * Feed\ rate + -3.39253e-05 * Spindle\ speed +$ $0.00177057 * Feed\ rate * Spindle\ speed + 164.795 * Feed\ rate^2 +$ $6.40713 * 10^{-8} * Spindle\ speed^2$
Zone C	$15.816 + -81.4097 * Feed\ rate + 0.0025929 * Spindle\ speed +$ $0.00568701 * Feed\ rate * Spindle\ speed + 224.664 * Feed\ rate^2 +$ $-3.894^{10^{-7}} * Spindle\ speed^2$

Table 7.14: ANOVA results for R_a in Zone A

Source	Sum of Squares	df	Mean Square	F-value	p-value
Model	105.65	5	21.13	3.98	0.0302
A-Feed rate	57.83	1	57.83	10.88	0.0080
B-Spindle speed	5.45	1	5.45	1.03	0.3349
AB	0.0053	1	0.0053	0.0010	0.9753
A^2	12.27	1	12.27	2.31	0.1596
B^2	8.16	1	8.16	1.54	0.2435
Residual	53.13	10	5.31		
Cor Total	158.79	15			

Table 7.15: ANOVA results for R_a in Zone B

Source	Sum of Squares	df	Mean Square	F-value	p-value
Model	234.62	5	46.92	6.46	0.0063
A-Feed rate	144.99	1	144.99	19.95	0.0012
B-Spindle speed	11.85	1	11.85	1.63	0.2306
AB	0.8094	1	0.8094	0.1113	0.7455
A^2	36.00	1	36.00	4.95	0.0502
B^2	0.1748	1	0.1748	0.0240	0.8799
Residual	72.69	10	7.27		

Table 7.16: ANOVA results for R_a in Zone C

Source	Sum of Squares	df	Mean Square	F-value	p-value
Model	413.08	5	82.62	12.71	0.0005
A-Feed rate	254.99	1	254.99	39.23	< 0.0001
B-Spindle speed	58.70	1	58.70	9.03	0.0132
AB	8.35	1	8.35	1.28	0.2835
A^2	66.91	1	66.91	10.29	0.0094
B^2	6.46	1	6.46	0.9933	0.3425
Residual	65.00	10	6.50		
Cor Total	478.08	15			

The surface topology is inspected through SEM micrographs of the three zones to identify the machining induced defects.

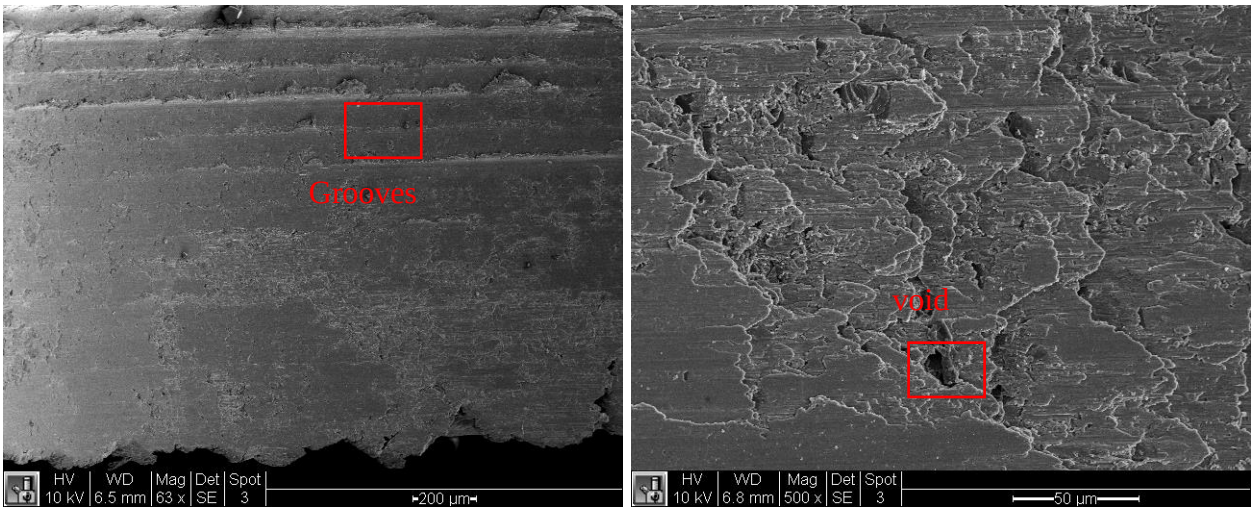

(a) (b)

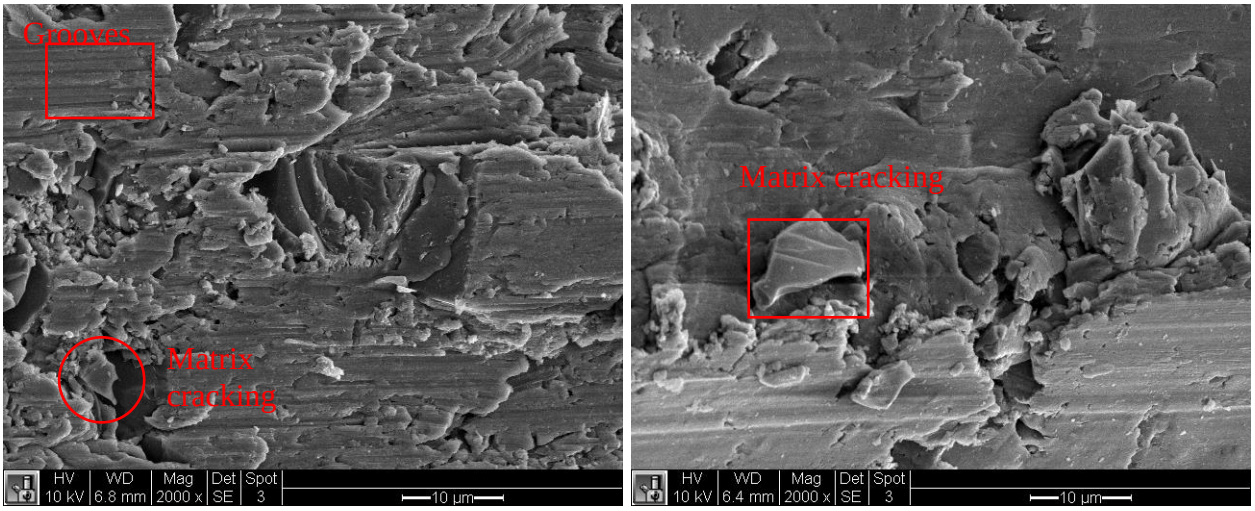

(c) (d)

Figure 7.24: Surface topography in Zone A at 0.2 mm/rev and 2000 RPM.

Typical surface topography of Zone A machined at 0.2 mm/rev and 2000 RPM is shown in Figure 7.24. Grooves, particle crushing, matrix cracking and voids could be observed on the surface. The presence of grooves can be observed in Figures 7.24 a, c and f, voids in Figures 7.24 b, c and matrix cracking in Figures 7.24 c and d.

Figure 7.25 shows the surface topography of Zone B at 0.2 mm/rev and 2000 RPM. The effects of tool wear can be observed clearly in comparing Figures 7.25 a and 7.24 a. The machined surface in Zone A appeared smoother in comparison to Zone B at 63x. The rapid tool wear experienced by the carbide tool lead to the formation of wave like features in Zone B. The tool wear leads to higher temperature rise on the machined surface leading to sticking of aluminum matrix on the cutting forming built up edge, as discussed in section 7.1. The BUE distorts the shape of the cutting edge leading to the formation of irregular features on the surface.

Figures 7.25 a and b shows the presence of the loose SiC particles on the surface. This can be attributed to the increased particle debonding on the surface owing to higher temperature on the machined surface. In addition, particle fracture was also observed in Figure 7.25 c. The surface of the SiC particles appeared smooth with cleavage lines typical of brittle fracture. Matrix cracking and particle debonding can also be observed in Zone B, Figure 7.25 d and e respectively.

Similar observations can be made for surface at Zone C. The tool wear results in the formation of rough wave like features on the machined surface. Debonded SiC particles were observed in Figures 7.26 b and d, the presence of void around the SiC particle can be observed in Figure 7.26 c.

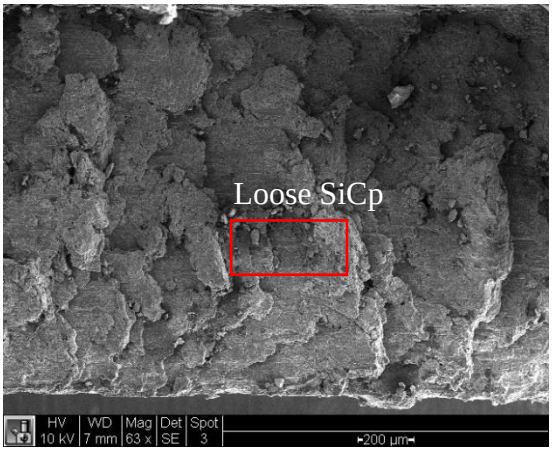

(a)



(b)

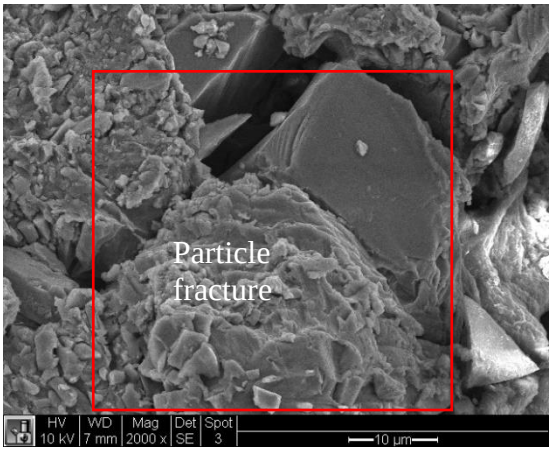

(c)

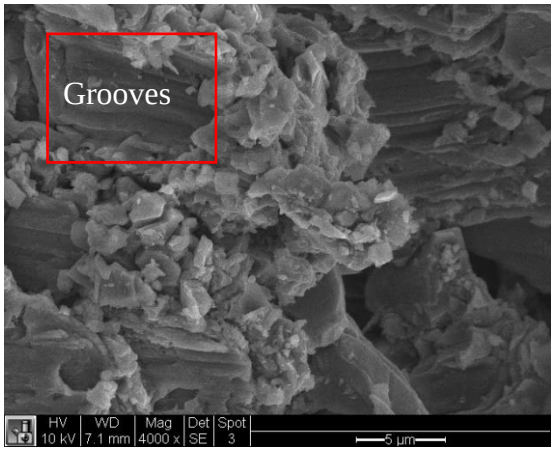

(d)

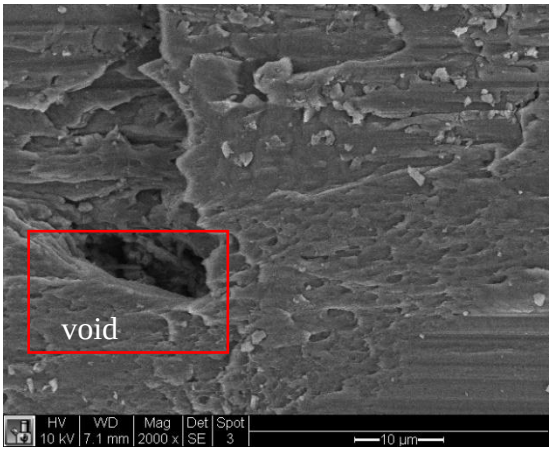

(e)

Figure 7.25: Surface topography in Zone B at 0.2 mm/rev and 2000 RPM.

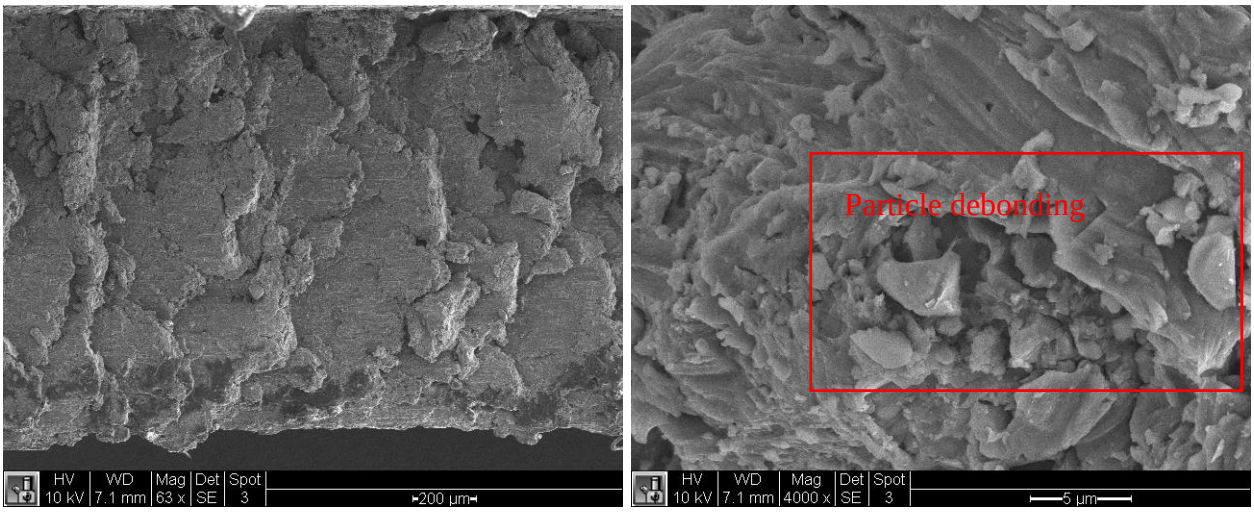

(a) (b)

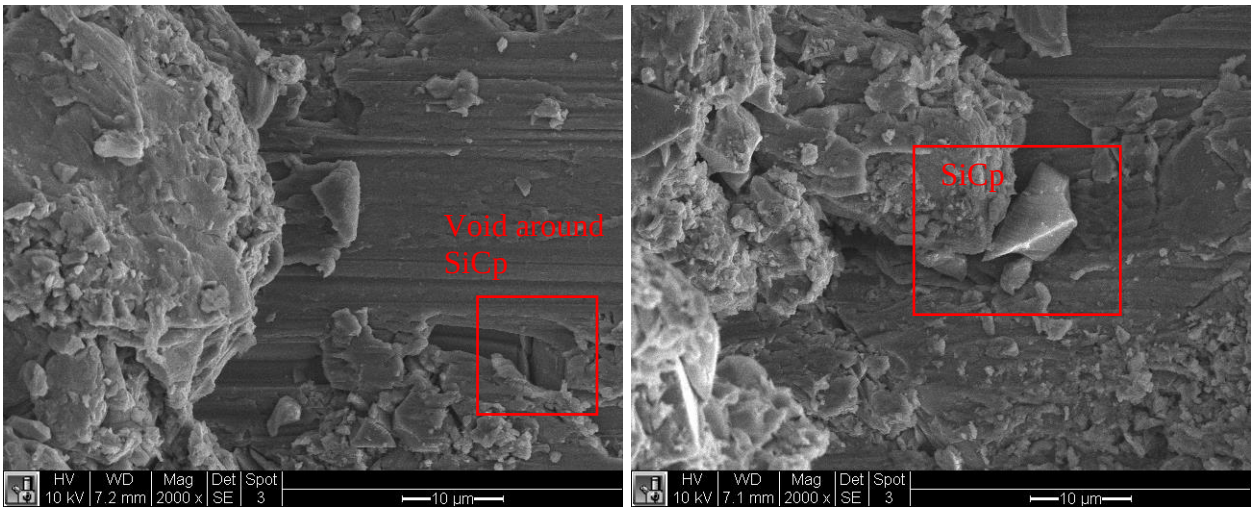

(c) (d)

Figure 7.26: Surface topography in Zone C at 0.2 mm/rev and 2000 RPM.

Owing to the particle pullout, debonding and matrix recasting, the ten point average roughness, Rz defined as the difference in height between the highest peaks and deepest valleys is used for comparison since it is more sensitive to surface damage. Rz as a function of feed and spindle speed is shown in Figure 7.27. Surface profiles and data given in Appendix C and D.

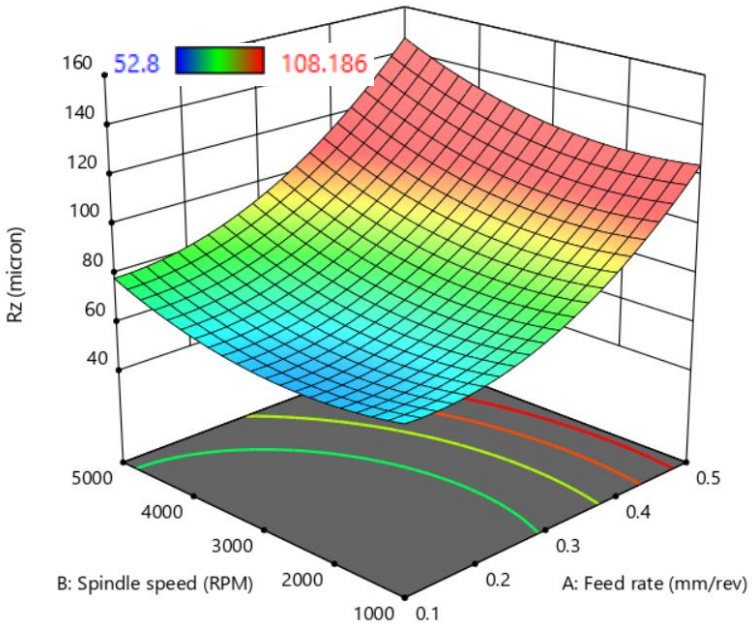
52.8
108.186
160
140
120
100
80
60
40
Rz (micron)
5000
4000
3000
2000
1000
B: Spindle speed (RPM)
0.1
0.2
0.3
0.4
0.5
A: Feed rate (mm/rev)

(a)

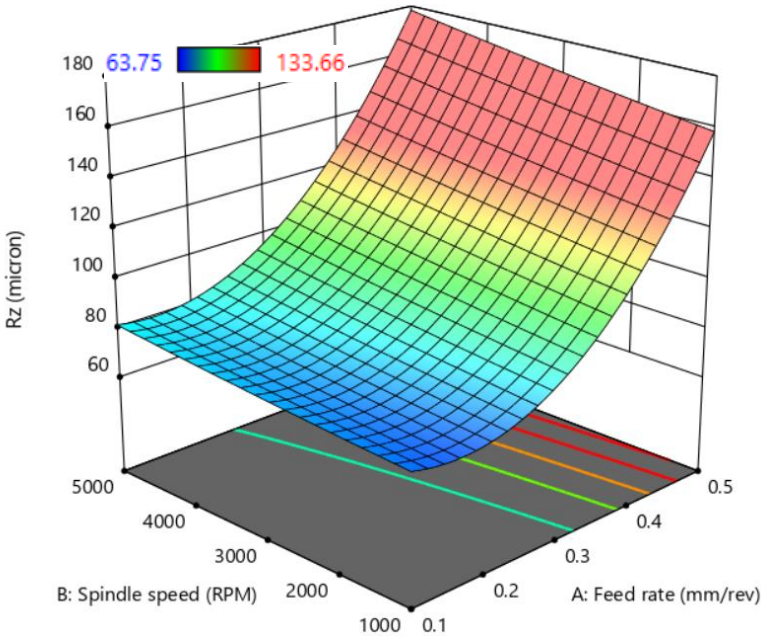
63.75
133.66
180
160
140
120
100
80
60
Rz (micron)
5000
4000
3000
2000
1000
B: Spindle speed (RPM)
0.1
0.2
0.3
0.4
0.5
A: Feed rate (mm/rev)

(b)

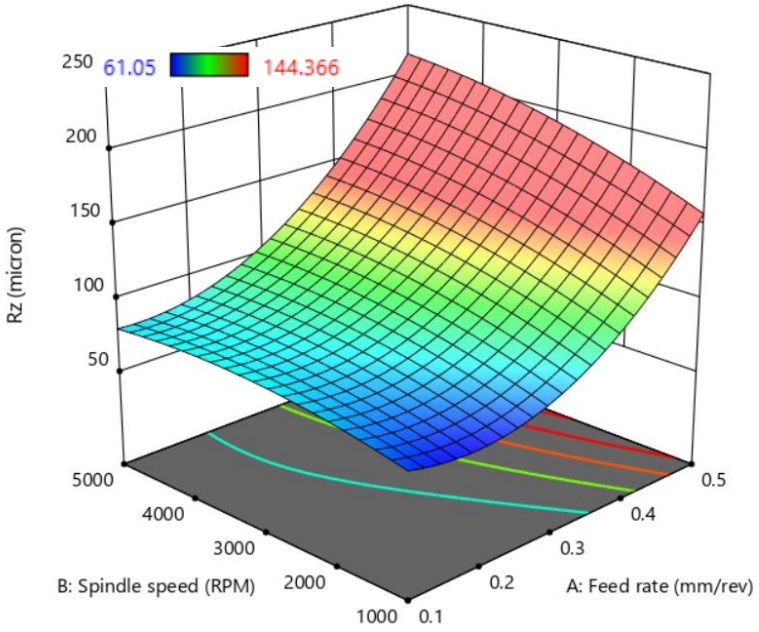

(c)

Figure 7.27: Rz as a function of feed rate(mm/rev) and spindle speed(RPM) a) Zone A, b) Zone B and c) Zone C

Predictably, Rz was found to be highest in Zone C, increasing from 61 to 144 µm and an increase of 63 to 133 µm for Zone B and from 52 to 108 µm in Zone A. The differences in surface topography between Zones A, B and C is reflected in Rz owing to the higher sensitivity. The presence of wave like features on the surface leads to higher surface roughness in Zones B and C.

7.5 Chip morphology

The types of chips formed in peripheral milling of aluminum composites are shown in Figure 8.8. The chips were observed to be semi-continuous and the shape and size of the chips formed was found to be a dependent on the spindle speed and feed rate of the process. At a low feed rate and spindle speed of 0.1 mm/rev and 1000 RPM, short segmented chips were observed. The chip segments were found to increase in length and form curls with the increase in feed rates and spindle speed, shown in Table 7.17.

The chips formed at 0.4 mm/rev and 5000 RPM appear long and curled in comparison to chips formed at 0.4 mm/rev and 1000 RPM. At high spindle speeds, the heat generated is accumulated at the tool-chip interface owing to the insufficient time for heat dissipation. The accumulated heat softens the matrix leading to increased ductility and sticking. Therefore, at a highest feed rate and spindle speed of 0.5 mm/rev and 5000 RPM, chips were observed to be the longest.

Table 7.17: Geometry of chips at different feed rates and spindle speeds.

	1000 RPM	3000 RPM	5000 RPM
0.1 mm/rev			
0.2			
0.3 mm/rev			
0.4 mm/rev			
0.5 mm/rev			

Upon inspection of these chips at a higher magnification of 40x, the chips were observed to have tearing occurring from the free surface. This separation of chip segments at the free edge is an indication of high strain experienced by the chips. The amount of tearing was observed to be dependent on the cutting conditions. The chips formed at 0.1 mm/rev and 1000 RPM, 0.3 mm/rev and 4000 RPM and 0.4 mm/rev and 5000 RPM are shown in Figures 7.28 and 7.29 respectively with red circle highlighting the tearing.



Figure 7.28: Optical micrograph at 40x of chips at 0.1 mm/rev and 1000 RPM, red circle highlights tearing at the free surface.

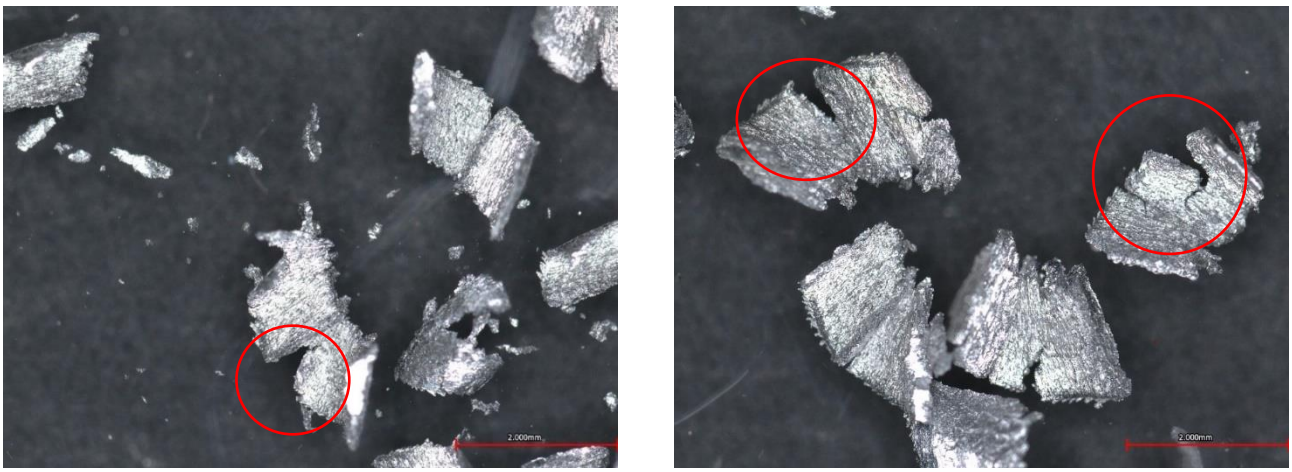

(a) (b)

Figure 7.29: Optical micrographs at 40X of chips a) 0.3 mm/rev 4000 RPM ,b) 0.4 mm/rev and 5000 RPM, red circle highlights tearing at the free surface.

Further, the SEM images of the chips were obtained to study the material flow and the SiCp as the surrounding matrix undergoes plastic deformation. Double sided adhesive tape was used to collect the chips from Zones A, B and C. Particle-matrix debonding, particle pull out, particle fracture was observed on the surface of the chip, shown in Figures 7.30, 7.31 and 7.32.

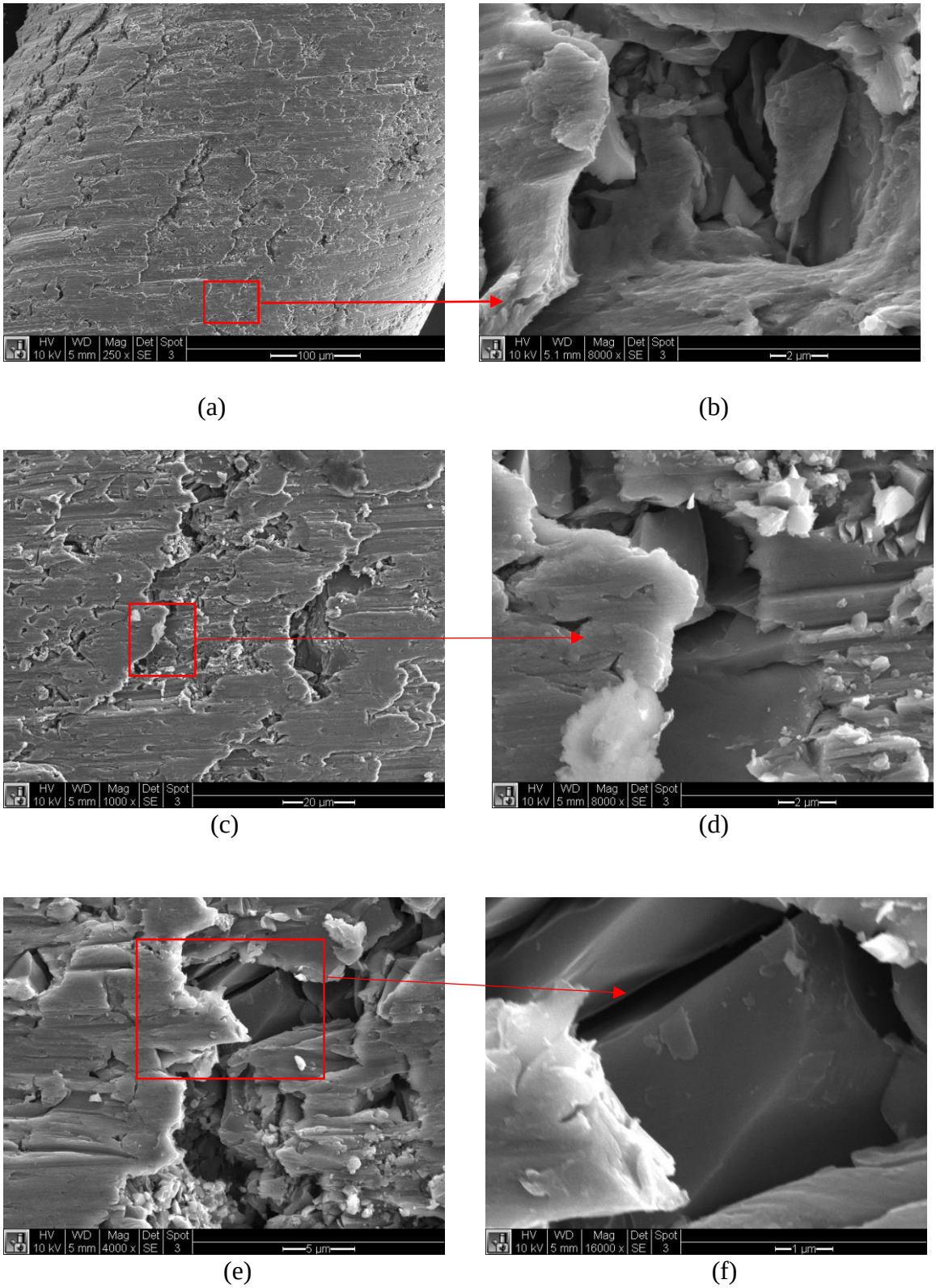

Figure 7.30: SEM micrographs of chips at 0.1 mm/rev and 1000 RPM obtained from Zone C.

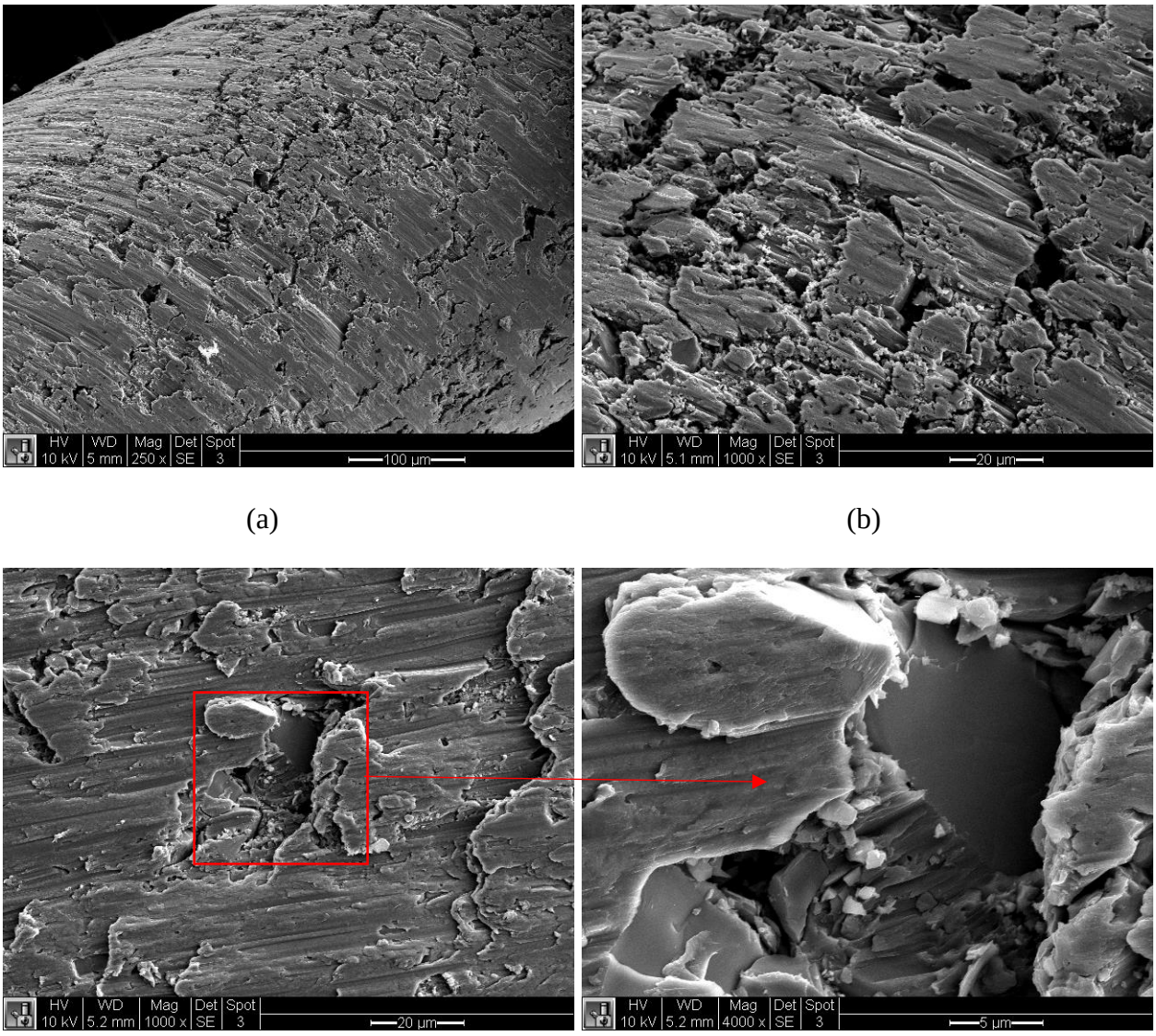

(a) (b)

(c) (d)

Figure 7.31: SEM micrographs of chips at 0.1 mm/rev and 1000 RPM obtained from Zone B.

The SEM images were obtained from curled side of the chip since it contacts the cutting edge. The curled surface at 250x showed grooves due to sliding on the cutting edge and cracks along the surface, shown in Figure 7.30 a. On further inspection, the matrix cracking was found to have voids from particle pull out and particle-matrix debonding as a consequence of stress

concentrations at the edge of the particles[59]. The void formed due to particle pull out can be seen in Figures 7.30 b. As discussed earlier, the cracks seem to propagate around the particles owing to weak particle-matrix interface, as observed in Figures 7.30 c, d and e. In addition, the SiC particles were found to be fractured by the cutting edge, circled in Figure 7.30 f.

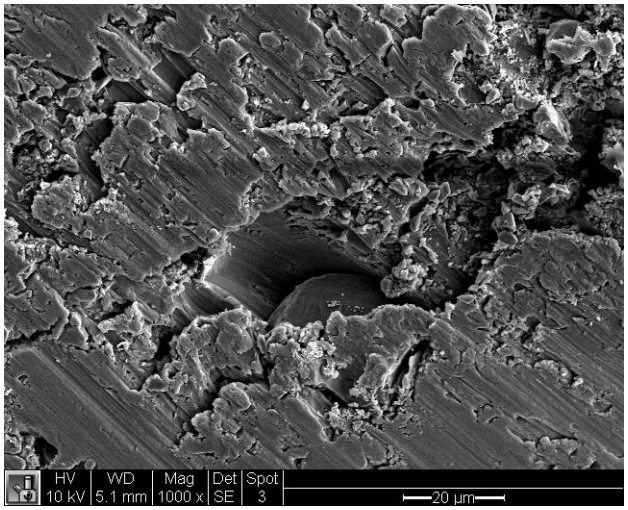

(a)

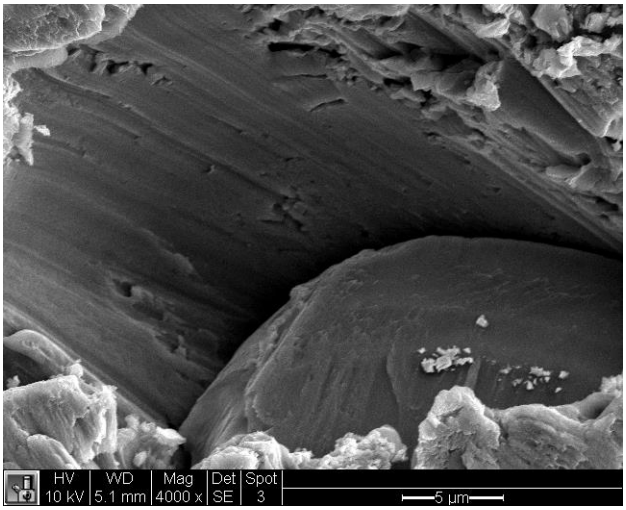

(b)

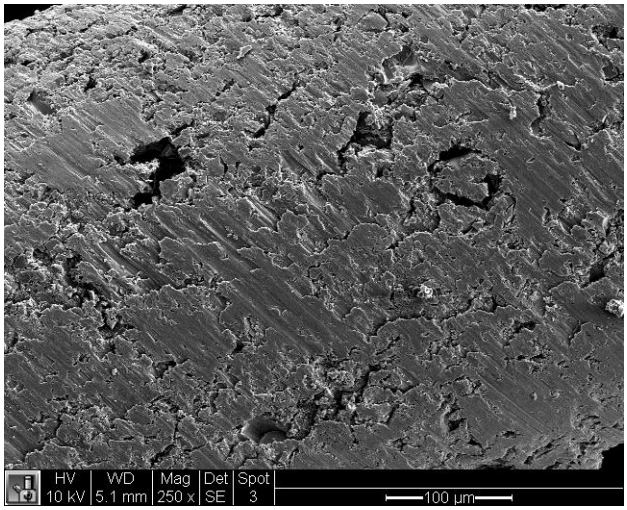

(c)

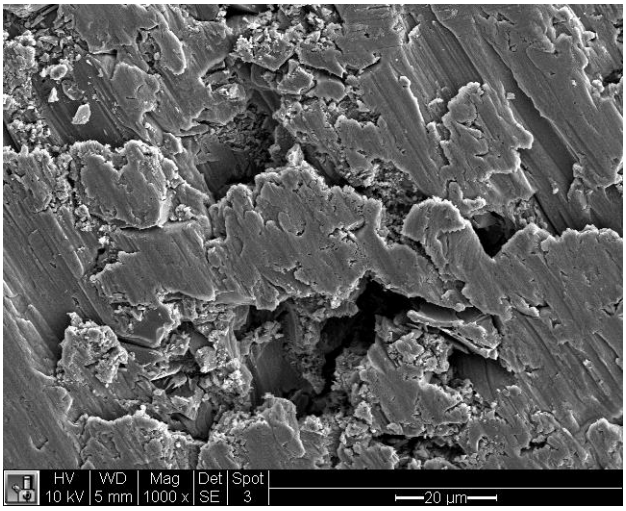

(d)

Figure 7.32: SEM micrographs of chips at 0.1 mm/rev and 1000 RPM obtained from Zone A.

Similar observations can be made for Zone B, higher number of cracks were observed on the surface of the chip in comparison to Zone C, shown in Figure 7.31 a and b, due to the higher particle percentage leading to higher discontinuities in the matrix that can promote crack growth. As in zone C, smooth matrix material was observed in between the cracks and voids formed on the surface

Presence of large voids and cracks were found on chips formed at zone A, shown in Figure 7.32 a and b. Void size of about 20 microns can be seen in Figure 7.32 b. This void may be generated due to particle fall out exposing the SiC particle embedded within the chip thickness. The particle being pushed into the matrix material by the cutting edge can be seen in Figure 7.32 c and d. The particle is seen to create a tunnel as it is displaced into the matrix material Figure 7.32 d.

7.6 Discussion

The machinability of functionally gradient Al/SiCp composite was investigated through the analysis of cutting forces, tool wear, surface topology and chip morphology. The cutting forces in a machining process are a reflection of the amount of mechanical stresses experienced by the cutting edge and the workpiece. Therefore, the presence of hard reinforcement particles had a significant effect on the magnitude of the forces in milling aluminum composite. At a feed rate of 0.05 mm/rev and 1000 RPM, Figure 7.4, the feed force and the thrust force were found to decrease with particle concentration. This observation is expected since the cutting edge encounters fewer number of hard SiC particles at lower concentration. Similar observation was made by Ramulu et in drilling of 10% and 20% Al_2O_3 reinoforced Al6061[30]. The feed force was found to increase

drastically as the particle concentration doubled. However, as the feed rate and spindle speed increases, the cutting forces were found to decrease with the increasing particle size, shown in Figure 7.5. This observation can be explained by considering the interaction between the SiC particles, aluminum matrix and the cutting edge. The SEM micrographs of the machined surfaces indicated the presence of SiC particles scattered along the surface, shown in Figures 7.24, 7.25 and 7.26, the relative motion of particles with respect to the tool and the workpiece can lead to two body rolling and three body abrasion which causes severe wear on the rake and flank surface of the tool. Since in this experimental set up, the milling operation is performed from high to low SiCp%, the tool was progressively worn out as it reaches the lower concentration of SiCp leading to higher cutting forces. Therefore, the cutting forces are also influenced by tool wear in addition to the SiCp%. Similar observation was made by Ramulu et in drilling of 10% and 20% Al_2O_3 reinoforced Al6061[30], where feed force was found to increase drastically as the particle concentration doubled.

The effect of cutting speed on the feed and thrust forces are not conclusive in the literature. Manna and Bhatacharya[25] observed a decrease in feed and thrust forces with an increase in cutting speed. The authors reported a decrease in feed force from 225 N to 130 N and the thrust force from 50 N to 30 N as the speed increased from 20 to 225m/min at a constant feed of 0.5 mm/rev. This was attributed to the decrease in formation of built up edge at higher cutting speeds. However, Antonio et al[28] observed an increase in the cutting forces as the cutting speed increased from 250 to 700 m/min at 0.1 mm/rev in turning of A356/SiCp/20%. The accelerated tool wear at high cutting speed was attributed to the increase in cutting forces. In this study, the cutting forces were observed to increase significantly with the increase in feed rate, shown in Figures 7.6, 7.7 and 7.8,

owing to the increase in material removal rates. Also, the forces were also observed to increase with the spindle speed expecially at higher feed rates.

Further, the effect of feed rate and spindle speed on the average cutting forces were analyzed through ANOVA results using the Design Expert 11 software. Tables 7.3 through 7.11 show the ANOVA results for the cutting forces in the three zones. The F-value in the ANOVA tables is used to compare the model variance with the residual error. The null hypothesis is supported or rejected based on the F-value. In this study, the factors, feed rate and spindle speed having no influence on the response is the null hypothesis. The greater the F-value, higher is the probability that the factor is significant, and P-value is the probability of obtaining the observed F-value if the null hypothesis is true. If the probability is high, then the null hypothesis may be true. The F-value is used in combination with the P-value to determine the significance of the model terms in a regression analysis. A high F value for the model and a P-value less than 0.05 for the model terms were considered significant. This value was obtained by considering the number of experiments to reduce the Type I error(false error). Considering the cutting force, F_x in three zones, with a model F value as high as 22.04, 30.75, 27.94 for zones A, B and C respectively, the quadratic model is significant. A P-value less than 0.05 was obtained for feed rate and feed rate^2 for all the zones, indicating that the cutting force is predominantly influenced by the feed rate. Similar observations were made for the axial and radial thrust forces, F_y and F_z, while both feed rate and spindle speed were found to have a significant effect.

A major limiting factor in machining of MMCs is the extensive tool wear. The high tool wear occurs when the abrasive reinforcement particles, which are typically harder than the cutting tool,

impacts the cutting edge. Consequently, the flank wear experienced by the tool was also found to increase with increasing reinforcement percentage and particle size [2, 6–8]. In this study, the tool wear along the helical cutting edge and rounding of the nose radius were quantified. The inspection of used tools under an optical microscope showed the formation of BUE, that increased with the spindle speed and feed rate. The BUE alters the geometry of the sharp cutting edge resulting in higher cutting forces and poor surface finish. A response surface model for tool wear along the helical cutting edge as a function of feed rate and spindle speed was developed and analysis of variance was performed to identify the significant model terms, given in Table 7.12. Feed rate and spindle speed were both found to be significant, while their interaction term was not significant.

From Figure 7.18, the tool wear was found to increase with both the spindle speed and the feed rate. The tool wear increased from 33.3 μm at 0.1 mm/rev and 1000 RPM to 105 μm at 0.5 mm/rev and 2000 RPM. These results are in agreement with the results reported by Chou et al in turning of A359/SiCp/20% with 30 μm thick CVD tools[49] and with the observations made by Monaghan et al[31] in drilling Al/SiCp/25% using carbide drill, the rake face was found to increase significantly with the feed rate and only a moderate increase was reported with increase in cutting speed. In CVD tools, adhesive wear was found to be the most dominant wear mechanism due to the slightly honed cutting edge and the presence of small crevices on the surface due to the abrasion of SiC particles in which the aluminum matrix are compacted due to high pressure at the tool-chip interface. Due to repeated compaction, the adhesion between the matrix and the tool may be stronger than the adhesive bond between the substrate and the diamond coating. This leads to the diamond coating chipping off with the aluminum matrix resulting rapid tool wear. However, in carbide tools, abrasive wear was identified as the dominant wear mechanism, with grooves and

pits found along the direction of chip flow on the cutting edge, shown in Figures 7.20, 7.21 and 7.22. The formation of grooves can be attributed to the harder SiCp particles ploughing along the cutting edge with the chip flow. Additionally, the pits formed on the cutting edge were about 1 μm, formed possibly due to the WC grains being pulled out by SiCp. Similar observations were reported by Weinert et al[26] when the reinforcement particle size is higher than the grain size of the WC.

The quality of surfaces produced during a milling process was studied through two-dimensional surface profile measurements. Surface roughness parameter, R_a was measured as a function of feed rate and spindle speed. A response surface model was developed, and analysis of variance performed, given in Table 7.14, 7.15 and 7.16. From the listed F and P values feed rate was found to be the significant factor for all the zones. Also, R_a was found to increase significantly with the feed rate. In Zone A, R_a increased from 11.31 to 21.766 μm, from 13.896 to 30.28 μm in Zone B and 12.9 to 32 μm. Similar results were reported by Pramanik et al in turning of Al6061/SiCp/20%, the surface roughness was low at lower feed rate and increased with increasing feed rate[56].

The SEM micrographs of the machined surface was inspected in Zones A, B and C to identify machining induced damages. Zone A showed the presence grooves, particle crushing, matrix cracking and voids on the surface. The formation of grooves can be attributed to the SiC particles being pulled out and dragged along the surface. The grooves can also be caused by hard oxidized aluminum[112]. The presence of voids can be observed in Figures 7.24 b, c. The voids are formed due to particles debonding from the surface, that can occur due to mismatch in coefficient of thermal expansion between the reinforcement particles and the matrix, leading to particles loosening and pulled out from the surface. In addition, matrix cracking can also be observed on

the surface in Figures 7.24 c and d. This can be attributed to the reduced ductility of the aluminum matrix leading to cracking under plastic deformation. In addition to these defects, the presence of loose SiC particles and decohesion between the SiCp and the matrix were also observed in Zones B and C. The increase in temperature at the machined surface leads to softening and recasting of aluminum matrix on the surface and debonding of the SiC particles. The formation of these voids can also be attributed to the strain hardening of the aluminum matrix due to pile up of dislocations around the SiC particles resulting in decohesion between the particles and the matrix[118]. The effect of these machining induced defects on the fatigue performance is discussed later in chapter 10.

The morphology of the chips generated during the milling process was also studied. Although, extensive research has been performed in understanding the chip formation mechanism in aluminum alloys, only a few studies have reported the chip formation mechanism for aluminum metal matrix composites[31,56,59,119]. The shearing of the workpiece material involving plastic deformation within the primary shear zone leads to the formation of chips. The chips are detached from the workpiece through fracture/rupture or crumbling process in the shear plane[31]. The segmentation of the chips was reported to be a function of the volume and size of the reinforcement particles, machining conditions and tool geometry. Joshi et al reported that an increase in volume fraction of SiC particles reduces the number of curls in the chip due to lower strain during orthogonal machining of 10%, 20% and 30% SiCp reinforced aluminum matrix[120]. In case of finer reinforcement composites, only the outer surface of the chip was found to be segmented, while, in coarser reinforcement composites, the chips were segmented through the thickness forming smaller chips[119].

The effect of cutting conditions on the chip morphology are not adequately understood for a peripheral milling process. Since the variations in the dimensional accuracy and surface finish of the machined surfaces are reflected on the types of chips generated during the machining process, the mechanism of chip formation should be studied adequately. The optical micrographs of chips formed at different feed rates and spindle speed is shown in Table 7.17. The chips were observed to be semi-continuous, similar to Lin et al's[59] observation in turning of Al/SiCp due to the reduced ductility of the matrix caused by the addition of SiCp. The shape and size of the chips formed was found to be a dependent on the spindle speed and feed rate of the process. At lower feed rates and spindle speeds, the chips were found not to experience high cutting temperatures and strain rates. Therefore, they tend to break in a brittle manner owing to the reduced ductility forming segmented chips. At higher feed rates, the amount of deformed material per flute engagement is higher leading to increased contact and temperature at the tool-chip interface. This results in chips changing from short segmented to curled C type due to softening and increased ductility at higher temperatures. The curl of the chips can be attributed to the non-uniform strain at the shear zone[121]. Similar observations were made at higher spindle speeds, the heat generated is accumulated at the tool-chip interface owing to the insufficient time for heat dissipation and softens the matrix leading to increased ductility and sticking. Further, tearing of the chips were observed to occur from the free surface. When the composite undergoes plastic deformation, cracks are initiated at the free surface of the chip owing to the reduced ductility of the matrix and small voids are formed due to the separation of matrix and the SiC particles. As the material shears further, these voids coalesce causing the cracks to grow further forming a saw tooth profile. The amount of tearing was found to be dependent on the cutting conditions. The segmented chips

occurring at 0.1 mm/rev and 1000 RPM show small tearing from the edge, circled in Figure 7.28. At higher feed rates and spindle speeds, as the chip length increases(before segmentation), the crack was found to traverse most of the chip thickness, shown in Figure 7.29. Similar observations were made by Lin et al, the authors commented that the crack propagation seemed to follow the SiC particle boundaries owing to the SiC-aluminum interface being weak[59].

Through the analysis of cutting forces and surface topology, the feed rate was identified as the most dominant parameter. The lowest cutting forces and best surface finish was obtained at 0.1 mm/rev. The cutting force, F_x varied between 100 to 132 N and average surface roughness varied between 12 to 16 μm at 0.1 mm/rev for all spindle speeds. However, both feed rate and spindle speed were identified as significant factors for tool wear. The tool wear increased from 33 to 50 μm as the spindle speed increased from 1000 to 5000 RPM at 0.1 mm/rev. Therefore, the optimum machining condition considering the three responses, cutting force, tool wear and surface topology is 0.1 mm/rev and 1000 RPM.

7.7 Summary

This chapter experimentally investigated the peripheral milling of functionally gradient aluminum composite. The machinability of these composites was studied in terms of cutting forces, acoustic emission, tool wear, surface topology and chip morphology. The interaction between the SiC particles and the cutting edge is reflected in these parameters. Owing to the high strength of the SiC particles, higher stresses are generated while machining which is measured through cutting

forces. When the particle encounters the cutting edge, three major events were observed to occur, the particle debonding owing to the mismatch in coefficient of thermal expansion, or the particles can be pushed into the matrix, or particles may be fractured. Therefore, in addition to the plastic deformation of the matrix, these events also generate acoustic emissions which can be studied to understand the interaction. Additionally, the debonded particles may lead to two body and three body abrasion on the cutting edge leading to rapid tool wear. The rapid tool wear leads to poor surface quality. Therefore, machinability of functionally gradient aluminum composite can be assessed by analyzing these parameters. The milling was performed from high to low concentration of SiC particles and the effects of concentration gradient was investigated.

At lower feed rate, the cutting forces were found to decrease with decreasing particle concentration. This behavior is expected since the cutting edge encounters fewer number of particles at lower concentration leading to lower cutting forces. However, as the feed rate increases the cutting forces were found to increase as the workpiece was milled from high to low concentration of SiCp. This distinctive behavior was further analyzed by studying other factors like the tool wear that also affect cutting forces . The cutting tools were examined before and after each cut. Formation of BUE was observed through optical micrographs at higher feed rates and spindle speeds. The formation of BUE distorts the geometry of the cutting edge there by generating higher forces while machining and produced poor surface finish.

To measure the actual tool wear and examine the wear mechanism, the BUE was removed by sonicating the tools in KOH solution. The tool wear was found to increase significantly with increase in feed rate and spindle speed. The increase in tool wear and formation of built up edge

can be attributed to the higher cutting forces in lower particle concentration zone. Since the milling was performed from high to low SiCp concentration. The tool experiences significant abrasion in the higher concentration before finally reaching the lower concentration region. This results in tool wear and formation of BUE leading to higher cutting forces. Consequently, the difference in cutting forces between the high and low concentration zones was found to increase with increasing feed rate due to rapid tool wear at higher feed rates.

Furthermore, investigation SEM micrographs of the cutting edge showed grooves and pits along the direction of the chip flow. The topography of the cutting edge indicated that the wear mostly occurred by abrasion and can be attributed to the higher hardness of SiC particles in comparison to the WC tool. The SiC particles dragged along the surface lead to the formation of grooves. The pits formed along the grooves, were about 1 μm in size corroborating with the size of the grains in the C2 WC tool, indicating that the WC grains have been pulled out. This can be attributed to two factors, abrasion from the reinforcement particles or removal of grains with the BUE owing to the adhesive bond between the adhered layer and the grains being stronger.

The influence of this behavior on surface topology was studied through surface roughness parameters and machined surface SEM micrography. The surface roughness parameters, R_a and R_q were both found to increase with increasing feed rate and spindle speed. As expected, Zone C was found to have higher surface roughness than Zones A and B. The trends in tool wear and cutting forces were also observed in surface roughness parameters. Upon inspection, grooves, particle crushing, particle fracture, matrix cracking and voids could be observed on machined surface. The formation of grooves can be attributed to the SiC particles being pulled out and

dragged along the surface. Owing to the mismatch in coefficient of thermal expansion between the SiC particles and the aluminum matrix, particle debonding occurs leading to the formation of voids on the surface. The matrix cracking can be attributed to the reduced ductility of the aluminum matrix leading to cracking under plastic deformation. In general, the surface appeared smoother at zone A, and rougher at zone C with wavelike projections on the surface.

Since the quality of surface is reflected by type of chips generated, the chip morphology was also studied. At high spindle speed, the chips appeared long and curled in comparison to chips formed at lower spindle speed for a constant feed rate. At high spindle speeds, the heat generated is accumulated at the tool-chip interface owing to the insufficient time for heat dissipation. The accumulated heat softens the matrix leading to increased long curled chips. Therefore, at a highest feed rate and spindle speed of 0.5 mm/rev and 5000 RPM, chips were observed to be the longest. Upon further magnification, the chips appeared highly segmented with tearing occurring from the free surface. When the composite undergoes plastic deformation, cracks are initiated at the free surface of the chip owing to the reduced ductility of the matrix and small voids are formed due to the separation of matrix and the SiC particles. As the material shears further, these voids coalesce causing the cracks to grow further forming a saw tooth profile. The SEM micrographs of the chips collected from different concentration zones showed similar defects as the machined surface, particle-matrix debonding, voids due particle pull out, particle fracture and matrix cracking. From these observations machining at a low feed rate and spindle speed of 0.1 mm/rev and 1000 RPM resulted in good surface finish and the cutting tool was observed to experience low tool wear.

Chapter 8 . AZ91/SiCp/15%

8.1 Cutting forces

Peripheral milling was performed on uniformly distributed AZ91/15%/SiCp with using HAAS vertical milling machine. Unlike the aluminum composite discussed in the previous chapter, the magnesium is reinforced with smaller SiCp with an average particle size of 3.5 μm and standard deviation of 1 μm. All the experiments were performed using square end C2 carbide tools. The cutting forces and tool wear were measured for a range of spindle speed and feed rate, presented in chapter 6, maintaining a constant axial and radial depth of cut of 1.27 mm and a length of cut of 32 mm. Cutting forces were measured using Kistler 9123C dynamometer. The detailed experiment set up and measurement procedure is discussed in Chapter 5.

The cutting forces were measured using a rotating dynamometer that allows direct measurement of forces at the cutting edge. The flutes were aligned along the y-axis of the dynamometer. Therefore, in this experiment, the radial force is given by the force in the Y-direction, F_Y and the tangential force is along the X-direction, F_x. The axial thrust force is given by F_z. The forces measured in X, Y and Z direction of the dynamometer are compensated for zero offset and drift, discussed in section 5.1. The cutting forces in milling AZ91/SiCp/15% at 0.1 mm/rev and 1000 RPM obtained after compensation is shown in Figure 8.1.

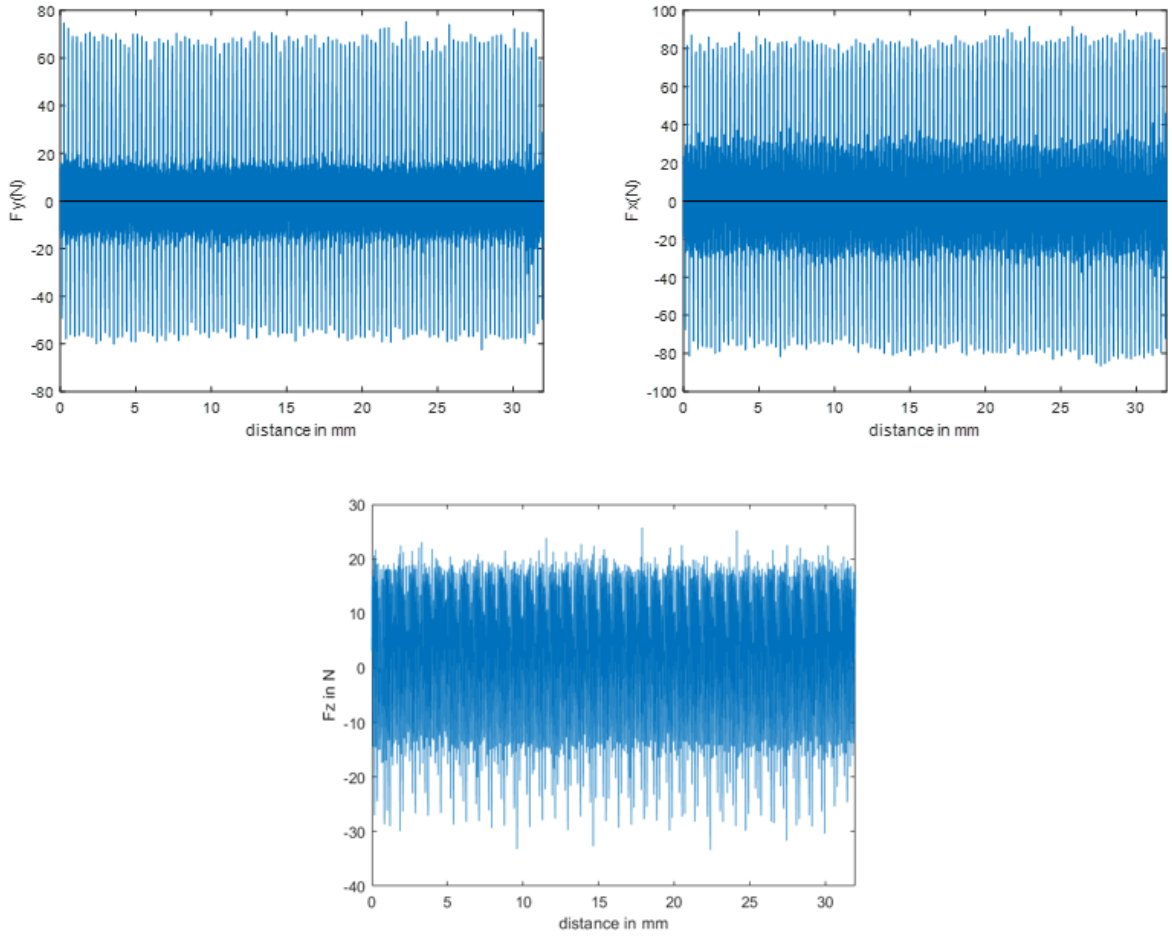

Figure 8.1: Cutting forces, Fy, Fx and Fz measured at feed=0.1 mm/rev and spindle speed=1000 RPM.

The cutting forces were observed to attain the equal maximum value throughout the entire length of cut owing to the uniform distribution of SiC particles in the matrix. The force signals between 10 to 25 mm cutting distance were considered to find the average cutting forces.

The average forces for a range of feed rate and spindle speed were calculated by finding the average of peak cutting forces in this window. The cutting forces Fx, Fy and Fz as a function of feed rate

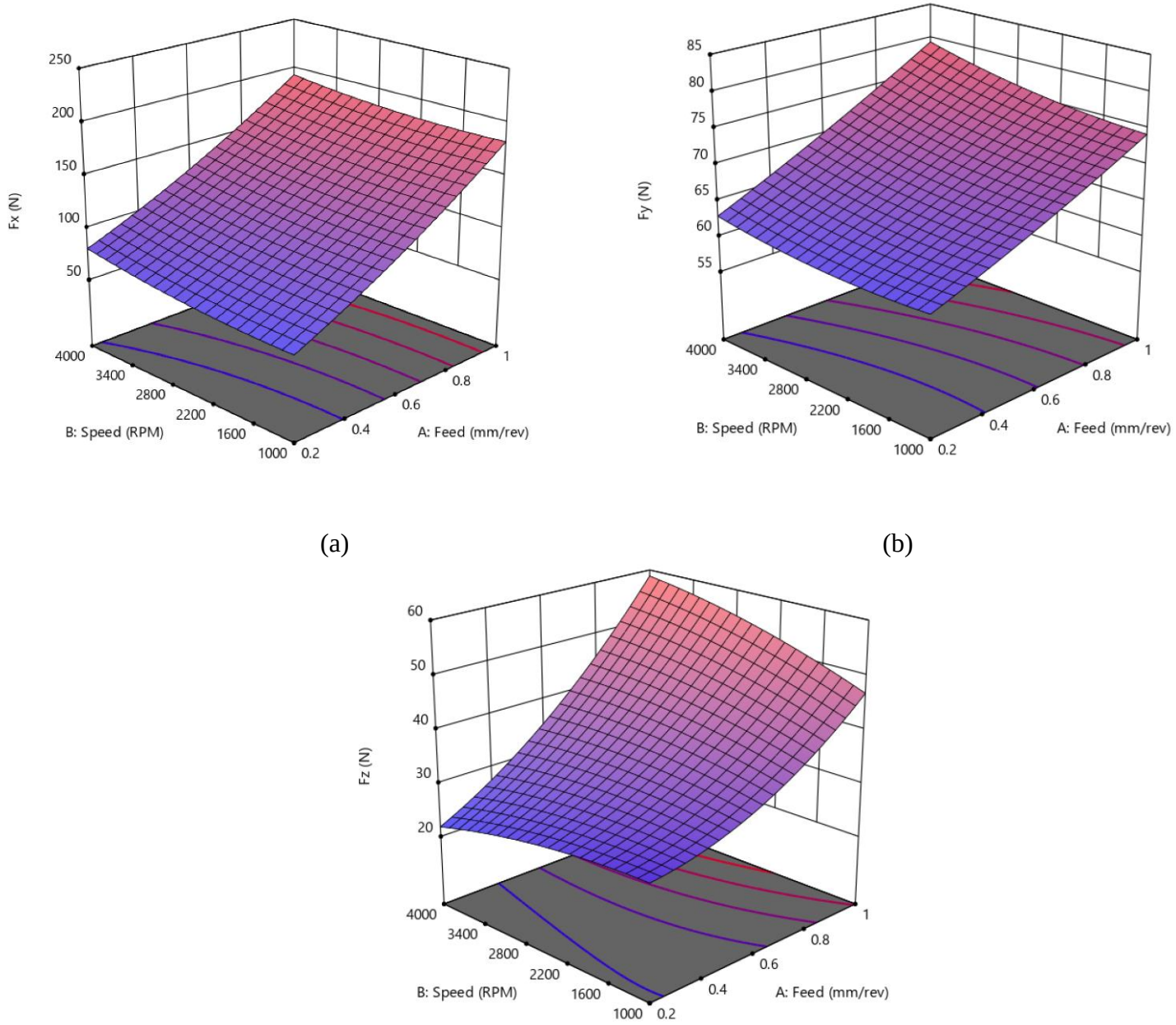

Figure 8.2: Cutting forces as a function of spindle speed and feed rate, a) Fx, b) Fy and Fz

and spindle speed are shown in Figure 8.2. To eliminate the effect of tool wear, the cutting distance was kept constant at 32 mm and a new tool was used for every condition. Figure 8.2a shows a significant increase in the feed force was observed with increasing feed for all spindle speeds. The feed force increased from 70N at 0.2 mm/rev, 1000 RPM to 188N at 1 mm/rev and 4000 RPM. This observation is attributed to the increase in material removed per revolution as the feed increases. The radial and axial thrust forces, F_Y and F_Z were also found to increase with feed, shown in Figure 8.2 b and 8.2 c. A slight increase of 17N was observed in the radial thrust force as the feed increased from 0.2 to 1 mm/rev. Force plots and average data given in Appendix B and D.

Response surface model was developed, and analysis of variance was performed to identify the significant model terms. Based on the measured data, the response equations were developed using a multiple linear regression model. The response surface equations generally take the form,

$$r(x) = C_o + \sum_{i=1}^{2} C_i x_i + \sum_{i=1}^{2} C_{ii} x_i^2 + C_{12} x_1 x_2 \quad (8.1)$$

where r(x) is the response variable, x_i is the parameter, C_i is linear effect coefficient, C_{ii} is quadratic effect coefficient, C_{12} is the interaction effect coefficient. In this study, x_1 is the feed rate, x_2 is the spindle speed and the response variables are surface roughness parameters F_x, F_y and F_z.

Table 8.1: Model for the cutting forces

Force	Equation
F_x	$42.2746 + 103.667 * feed\ rate + -0.00342175 * spindle\ speed + -0.00295911 * feed\ rate * spindle\ speed + 41.087 * feed\ rate^2 + 2.00132 * 10^{-6} * spindle\ speed^2$
F_y	$55.0305 + 18.5107 * feed\ rate + 0.00108034 * spindle\ speed$
F_z	$28.7396 + -12.6562 * feed\ rate + -0.000296647 * spindle\ speed + 0.00742039 * feed\ rate * spindle\ speed + 24.3179 * feed\ rate^2 + -6.29688 * 10^{-7} * spindle\ speed^2$

Table 8.2: Analysis of variance for F_x

Source	Sum of Squares	df	Mean Square	F-value	p-value
Model	38913.41	5	7782.68	54.17	< 0.0001
A-feed rate	37994.97	1	37994.97	264.45	< 0.0001
B-spindle speed	602.84	1	602.84	4.20	0.0573
AB	19.38	1	19.38	0.1349	0.7183
A^2	159.49	1	159.49	1.11	0.3077
B^2	87.36	1	87.36	0.6080	0.4469
Residual	2298.85	16	143.68		
Cor Total	41212.25	21			

Table 8.3: Analysis of variance for F_y

Source	Sum of Squares	df	Mean Square	F-value	p-value
Model	636.11	2	318.05	11.76	0.0005
A-feed rate	609.88	1	609.88	22.55	0.0001
B-spindle speed	32.03	1	32.03	1.18	0.2901
Residual	513.86	19	27.05		
Cor Total	1149.97	21			

Table 8.4: Analysis of variance for F_z

Source	Sum of Squares	df	Mean Square	F-value	p-value
Model	2475.82	5	495.16	76.23	< 0.0001
A-feed rate	2167.75	1	2167.75	333.73	< 0.0001
B-spindle speed	26.95	1	26.95	4.15	0.0585
AB	121.84	1	121.84	18.76	0.0005
A^2	55.87	1	55.87	8.60	0.0098
B^2	8.65	1	8.65	1.33	0.2655
Residual	103.93	16	6.50		
Cor Total	2579.75	21			

From the analysis of variance, given in Table 8.2, 8.3 and 8.4, only feed rate was found to be significant for all the cutting forces. The spindle speed and the interaction between the spindle speed and feed rate were not found to be significant.

8.2 Tool wear

Peripheral milling of magnesium composite AZ91 magnesium matrix with 15 vol.% SiC particles was performed to study the tool wear experienced by carbide helical cutting tools. The tool wear was measured along the helical cutting edge, as discussed in the previous section and the wear mechanism was studied through SEM images of the cutting edge. In this case, a C2 carbide cutting tool with 10% Co binder is used. The SiC particles exhibit higher hardness than the cutting tool material. In addition, the average grain size of C2 cutting tool is about 1.2 microns, while the average reinforcement particle size is about 3 microns. This can lead to rapid abrasive tool wear depending on the cutting conditions. Figure 8.3 shows the cutting tool before and after the cutting at 0.5 mm/rev and 2000 rpm.

The tool wear can be observed as the bright white region in the optical micrographs, Figures 8.3 c and d. The tool wear along the rake face of the tool appears to be tapered along the helix. This can be attributed to the lag experienced by the points on the cutting edge higher up along the helix in comparison to the tool tip. The helix provides a gradually increasing chip load along the helical flutes. The chip thickness varies in the axial direction. The tip of the flute is completely immersed into the cutting material. While, the points on the cutting edge along the axial direction lag by an

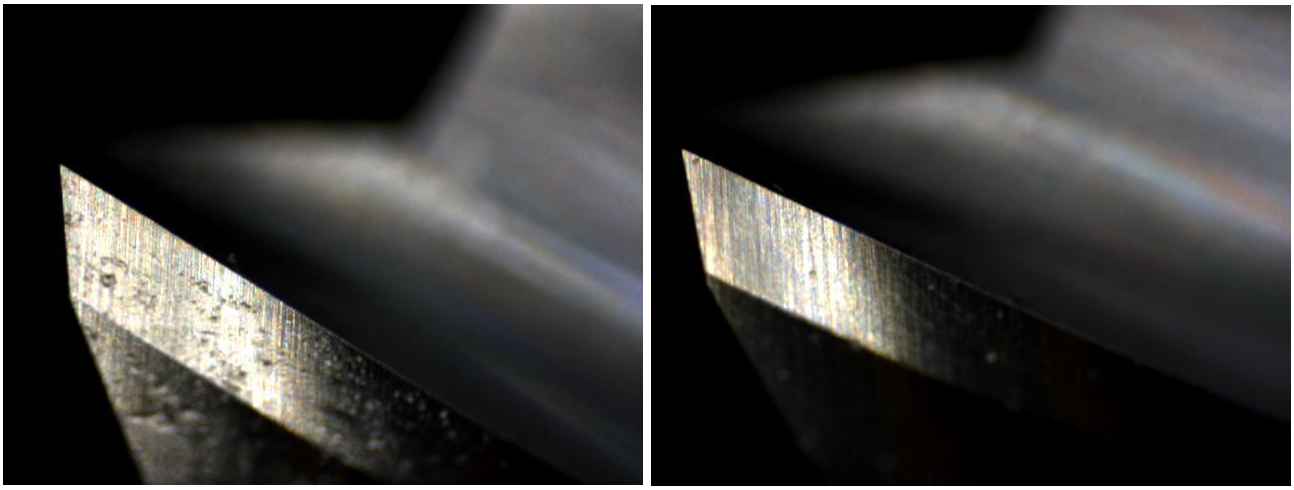

(a) (b)

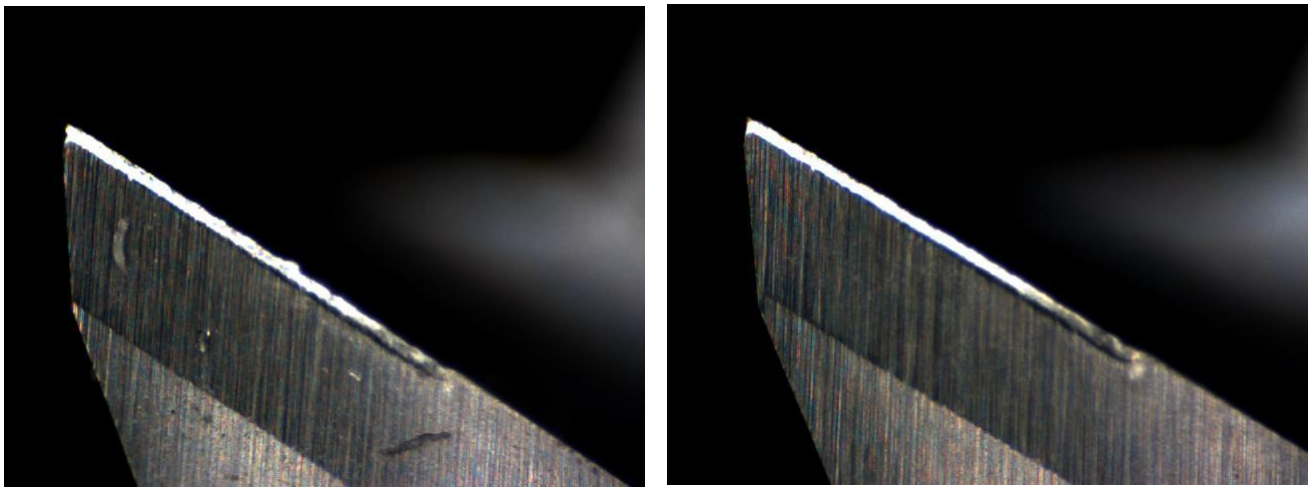

(c) (d)

Figure 8.3: Optical micrographs of (a, b) Left and right flutes, respectively, of square end carbide cutting tool as purchased, (c, d) Left and right flutes, respectively after a cutting distance of 64 mm at 0.5 mm/rev and 2000 RPM.

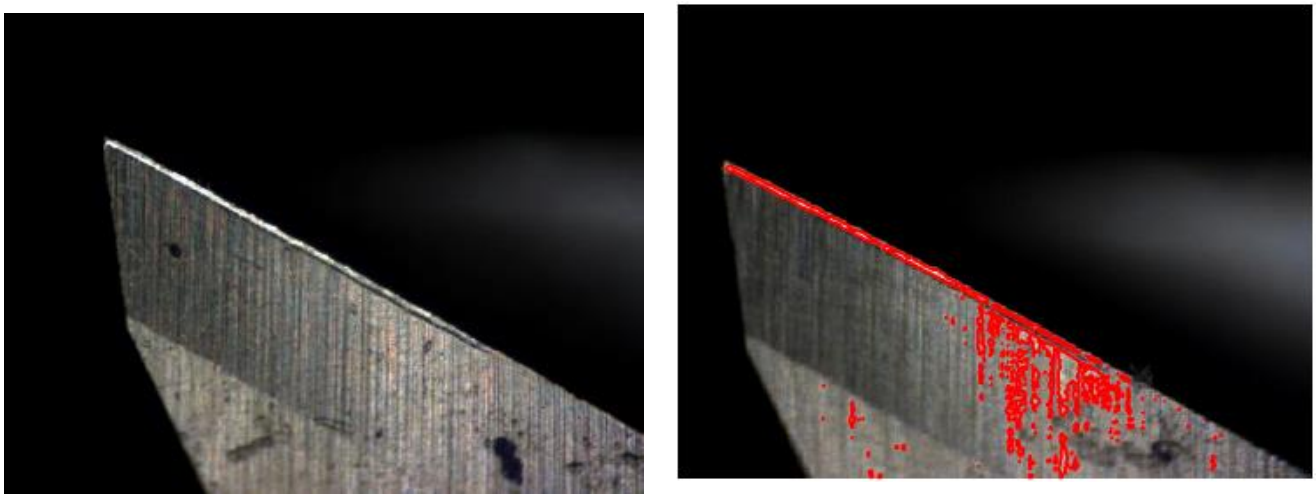

(a) (b)

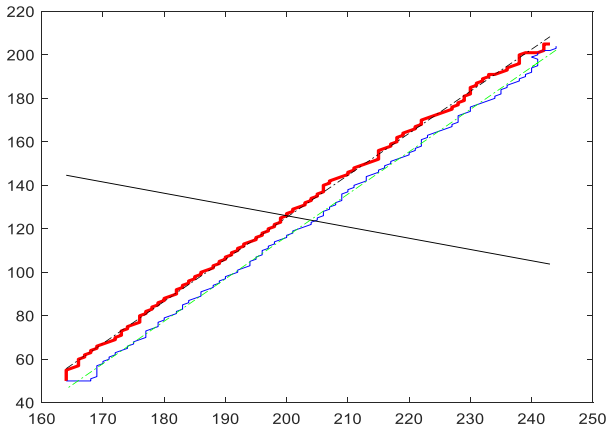

(c)

Figure 8.4: Tool wear measurement, a) Optical micrograph of the left flute after a cutting distance of 64 mm at 0.05 mm/rev and 3000 rpm, b) the tool wear is highlighted in white and the boundary of the wear is identified, c) the width of the wear is measured between the linear fit lines of the boundary at 120 μm from the tip multiplied by (0.1mm/30 pixels).

angle ψ. To quantify the tool wear at different cutting conditions, it is required to measure the width of the tapered wear region, method described in Figure 8.4. The width was measured at three times the tool tip radius from the tool tip, 120 μm.

The tool wear measurement obtained through this method is plotted as a function of feed rate and spindle speed. Feed rate was found to have dominant effect on the tool wear in comparison to the cutting speed. Figure 8.5 shows the tool wear as a function of feed and speed. The optical micrographs used to measure the tool wear and the wear data are given in Appendix B and D. At lower feed rate of 0.05 mm/rev, the tool wear was between 40 to 45 microns. When the feed rate increased by ten times, the wear was about 20 microns. This increased wear rate at lower feed rates can be attributed to the higher number of impacts of the cutting tool on the work piece at a lower cutting feed for a given cutting distance of 32 mm. The higher number of impacts leads to a higher encounter of reinforcement particles accelerating the abrasive wear on the cutting edge.

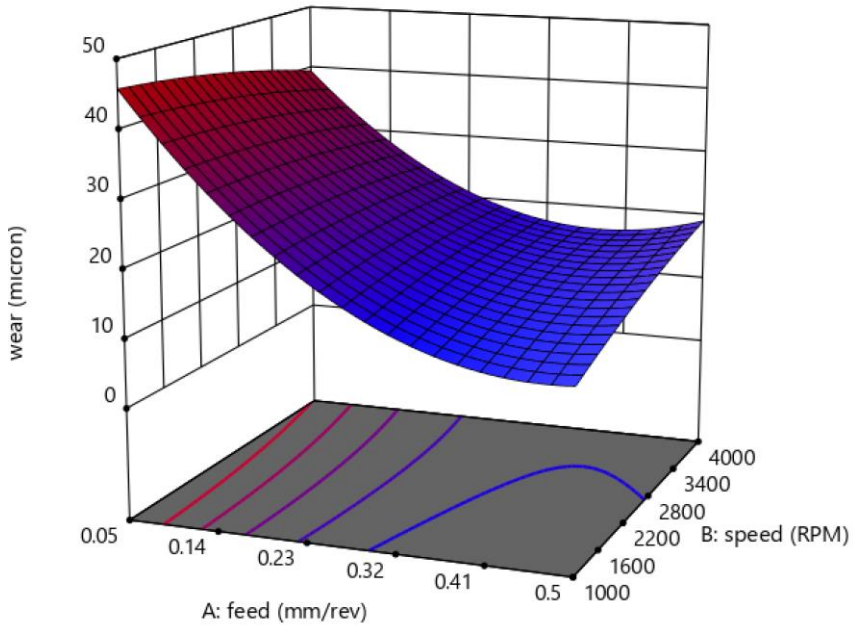

Figure 8.5: Tool wear(μm) as a function of feed rate(mm/rev) and spindle speed(RPM)

The response surface model is,

$$tool\ wear = 49.04 - 202.05feed + 0.00291speed + 0.01324feed * speed + 217055 * feed^2 - 1.14 * 10^{-6}speed^2 \quad (8.1)$$

ANOVA results indicated that the feed rate was the significant factor influencing tool wear.

Table 8.5: Analysis of variance for tool wear

Source	**Sum of Squares**	**df**	**Mean Square**	**F-value**	**p-value**
Model	1486.54	5	297.31	16.65	0.0003
A-feed	941.01	1	941.01	52.71	< 0.0001
B-speed	11.39	1	11.39	0.6382	0.4449
AB	91.15	1	91.15	5.11	0.0502
A^2	396.55	1	396.55	22.21	0.0011
B^2	12.35	1	12.35	0.6917	0.4271
Residual	160.68	9	17.85		
Lack of Fit	111.70	4	27.93	2.85	0.1405
Pure Error	48.98	5	9.80		
Cor Total	2050.35	15			

The SEM images of the tool tip were studied to understand the wear mechanism at the cutting edge.

Cutting edge topography

High tool wear is caused when the reinforcement particles, harder than the cutting tool material impacts the cutting edge removing material through abrasion. Depending on the hardness of the reinforcement particles and the cutting tool different wear mechanisms can occur, microploughing, microcutting, microfatigue and microcracking[122]. In microploughing the reinforcement particles impinge on the cutting edge but do not detach particles from the cutting edge. The material is ploughed repeatedly forming ridges adjacent to the groove produced. Due to repeated ploughing action material may be removed due to low cycle fatigue. In microcutting, the material removed in the form of chips from the cutting edge is equal to the volume of the groove produced on the cutting edge. Microcutting often occurs when the grain size of the reinforcement particles is larger than the grain size of tool. Microcutting and microploughing are dominant wear mechanism for ductile materials. When highly concentrated stress is induced by the reinforcement particles microcracking occurs on the surface of the cutting edge. The microcracking mechanism is dominant in brittle materials and due to the crack formation and propagation large wear debris are removed from the cutting edge[123]. For this purpose, SEM micrographs of the new and the used tools are shown in Figures 8.6, 8.7, 8.8 and 8.9 respectively.

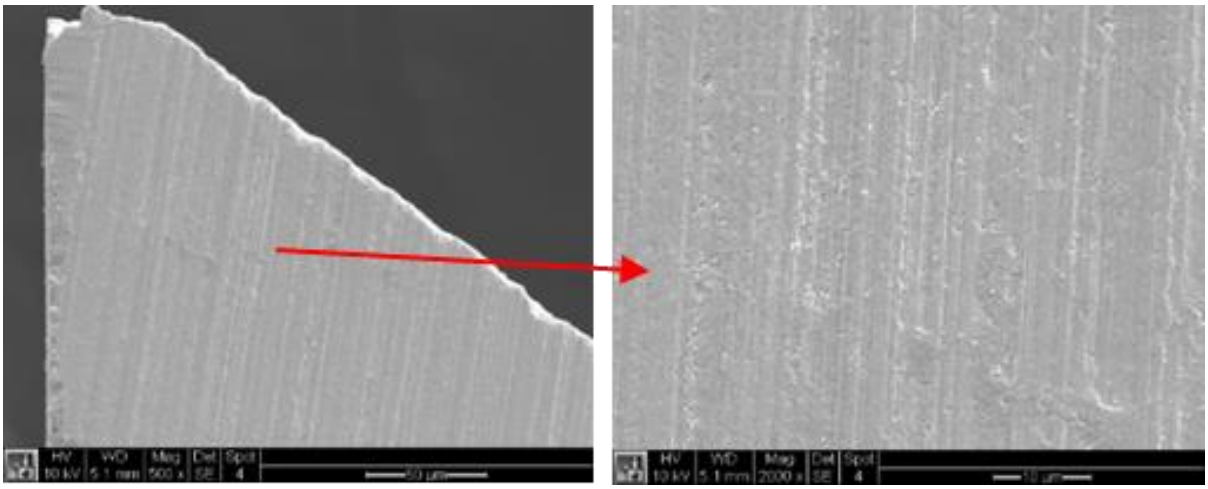

Figure 8.6: SEM image of a new cutting edge at 500x and 2000x magnification respectively.

The SiC particles are harder than fine grain carbide tools. The SEM image of a tool after 64 mm cutting distance at 0.5 mm/rev and 4000 rpm is shown in Figure 8.7. Tool tip magnified at 500x is shown in Figure 8.7 a, grooves, ridges, pits and built up edges can be seen at the tool tip. These features are further magnified for observation in Figures 8.7 b, c, d and e. The presence of grooves and ridges can be observed in Figure 8.7 e, the width of the grooves varies between 2 to 3 microns, consistent with the SiC particle size range. Ridges are found adjacent these grooves indicating that the particles have ploughed into the cutting edge. Repeated ploughing action can lead to low cycle fatigue. Since the SiC particle sizes are small of average particle size 3 μm, the probability of particle fracture is low. The SiC particles are either pushed into the matrix or carried away by the chip.

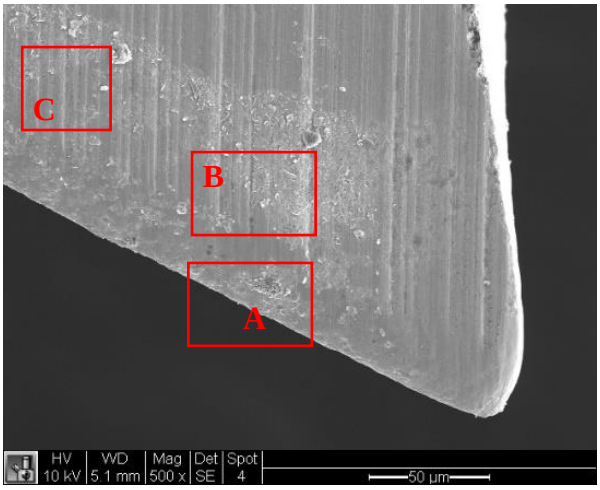
C
B
A
HV
10 kV
WD
5.1 mm
Mag
500 x
Det
SE
Spot
4
50 µm

(a)

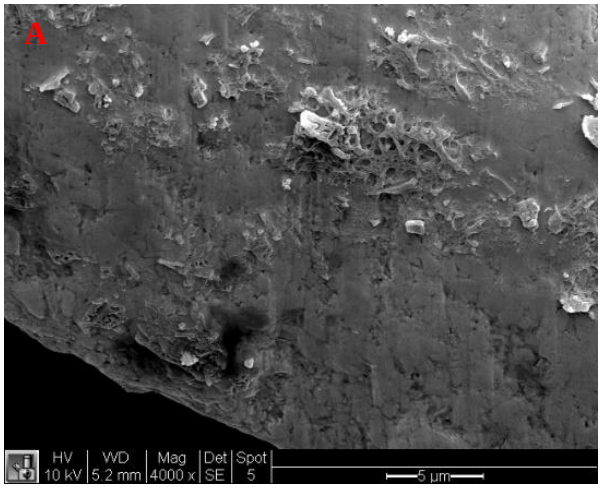
A
HV
10 kV
WD
5.2 mm
Mag
4000 x
Det
SE
Spot
5
5 µm

(b)

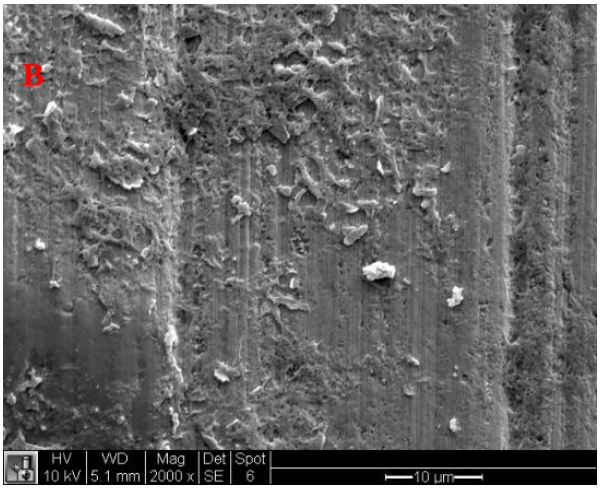
B
HV
10 kV
WD
5.1 mm
Mag
2000 x
Det
SE
Spot
6
10 µm

(c)

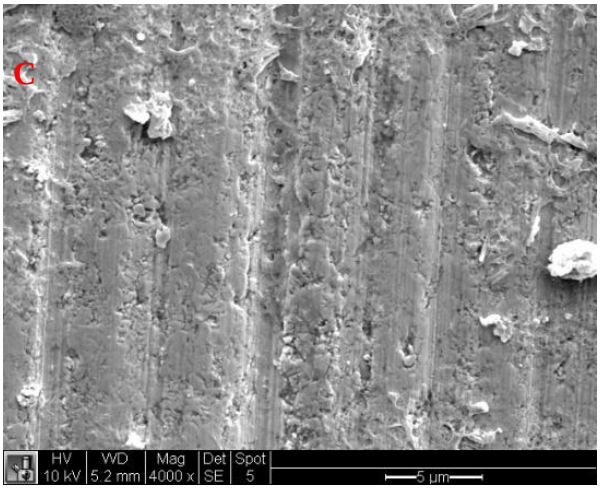
C
HV
10 kV
WD
5.2 mm
Mag
4000 x
Det
SE
Spot
5
5 µm

(d)

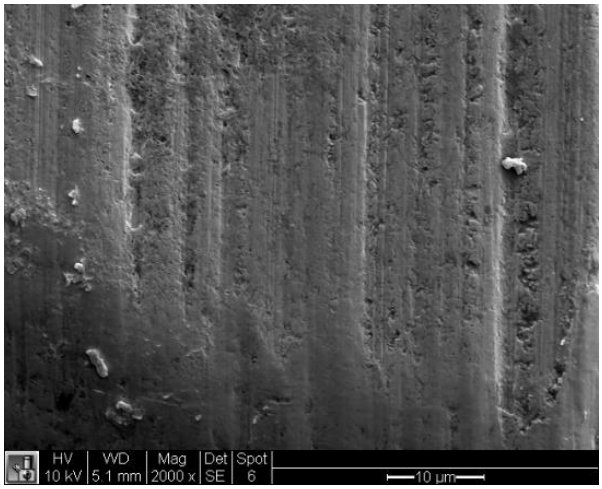

(e)

Figure 8.7: SEM images of the cutting edge after machining 64 mm at 0.5 mm/rev and 4000 RPM.

In addition to the grooves, pits are also observed in Figures 8.7 b, d and e. The average size of these pits is about 1 micron corresponding to the grain size of the WC carbides in C2 grade. The formation of the pits can be attributed to the abrasive wear since the hardness and the average particle size of SiC particles is higher than the hardness and grain size of C2 carbide tool. These debonded grains form wear debris which further abrade the cutting edge. Figure 8.7 c shows the matrix along with the wear debris smeared on the tool.

Cutting edge after a cutting distance of 64 mm at 0.05 mm/rev and 1000 rpm is shown in Figure 8.8. Grooves and ridges can be observed at the tool tip, shown in Figure 8.8 b. The number of contacts between the cutting edge and the workpiece is highest for fixed cutting distance at the lowest speed and feed. This leads to higher tool wear, shown in Figure 8.8, due to increased

interaction with the SiC particles. The worn surface has a smooth appearance at this cutting speed. The repeated abrasion with smaller SiC particles can lead to a smooth surface. Higher tool wear leads to higher cutting temperatures leading to matrix smearing on the cutting edge and formation of built up edge, shown in Figure 8.8 b and c.

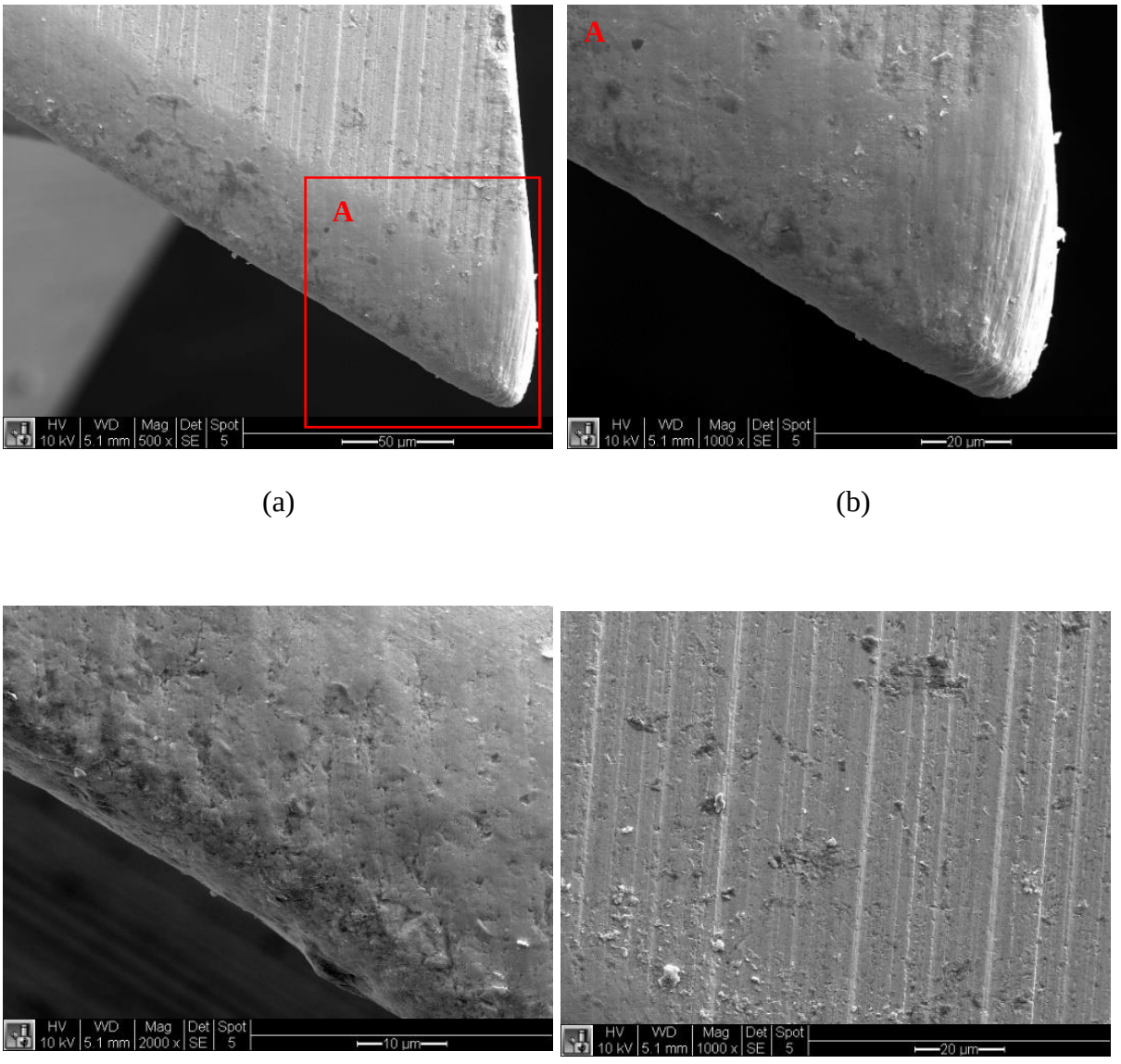

(a) (b)

(c) (d)

Figure 8.8: SEM images of the cutting edge after machining 64 mm at 0.05 mm/rev and 1000 RPM

Figure 8.9 shows the cutting edge after machining 64 mm at 0.3 mm and 1000 rpm. The cutting edge was observed to be smooth while, some micropitting and ploughing could also be observed on the surface, shown in Figures 8.9 a and c. A prominent groove with SiC particle is shown in Figure 8.9 c. A 4 µm wide groove, consistent with the SiC particle can be observed on the surface. In addition, WC grains were removed forming micropits. The dislodged WC grains form wear debri. The tool tip at 2000x is shown in Figure 8.8 b, where microploughing and scratches can be observed.

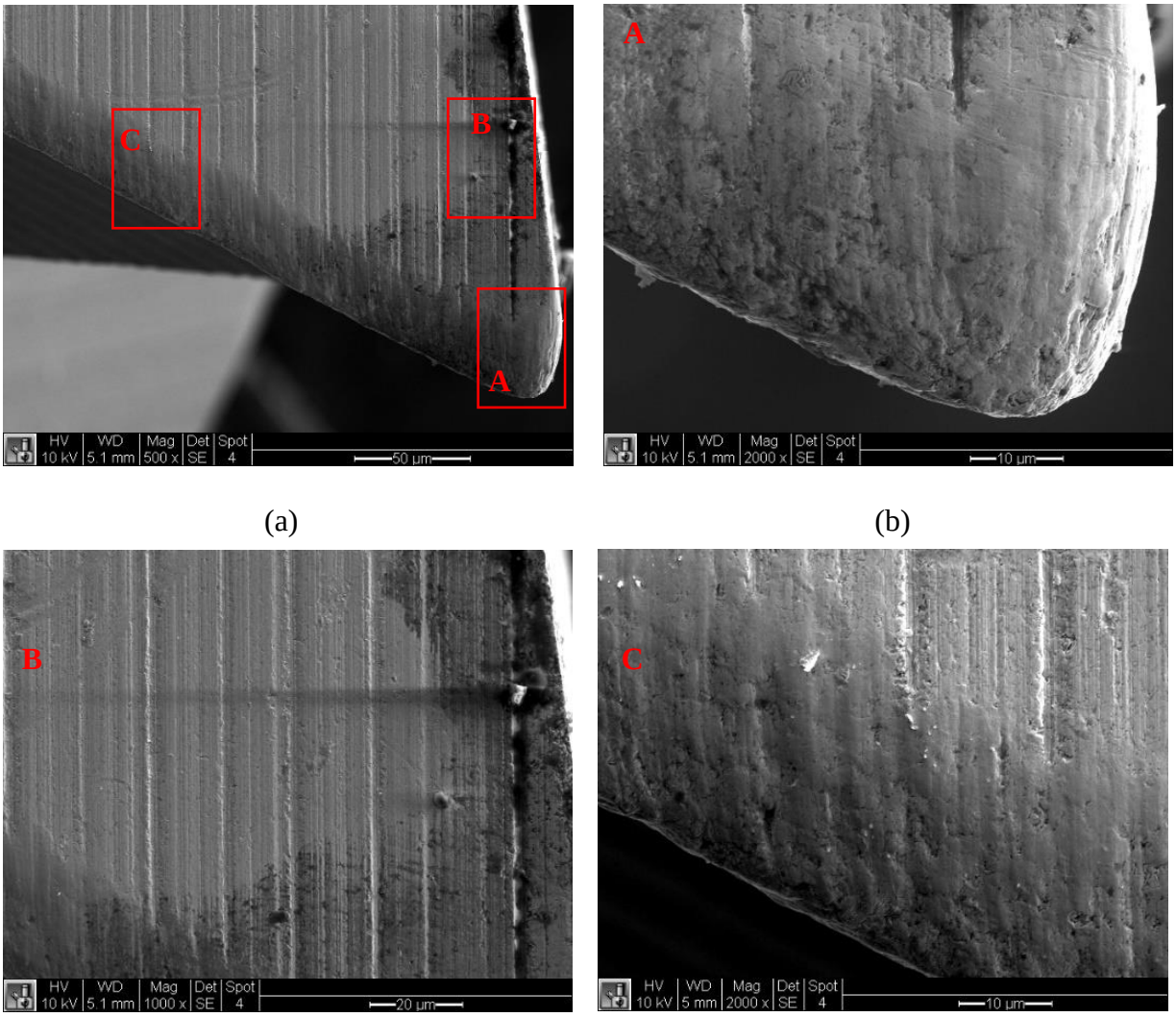

(a) (b)

(c) (d)

Figure 8.9: SEM images of cutting edge after machining 64 mm at 0.3 mm/rev and 1000 RPM

8.3 Surface topology

Surface finish obtained in a machining process depends on the operating conditions, tool and workpiece material and can be quantified in the form of surface roughness parameters. The damage can be in the form of pores, cracks, microstructural transformations, plastic deformation, residual stresses and changes in hardness leading to significant reduction in life of the part produced. Therefore, it is critical to examine the surface and sub surface damage induced while machining.

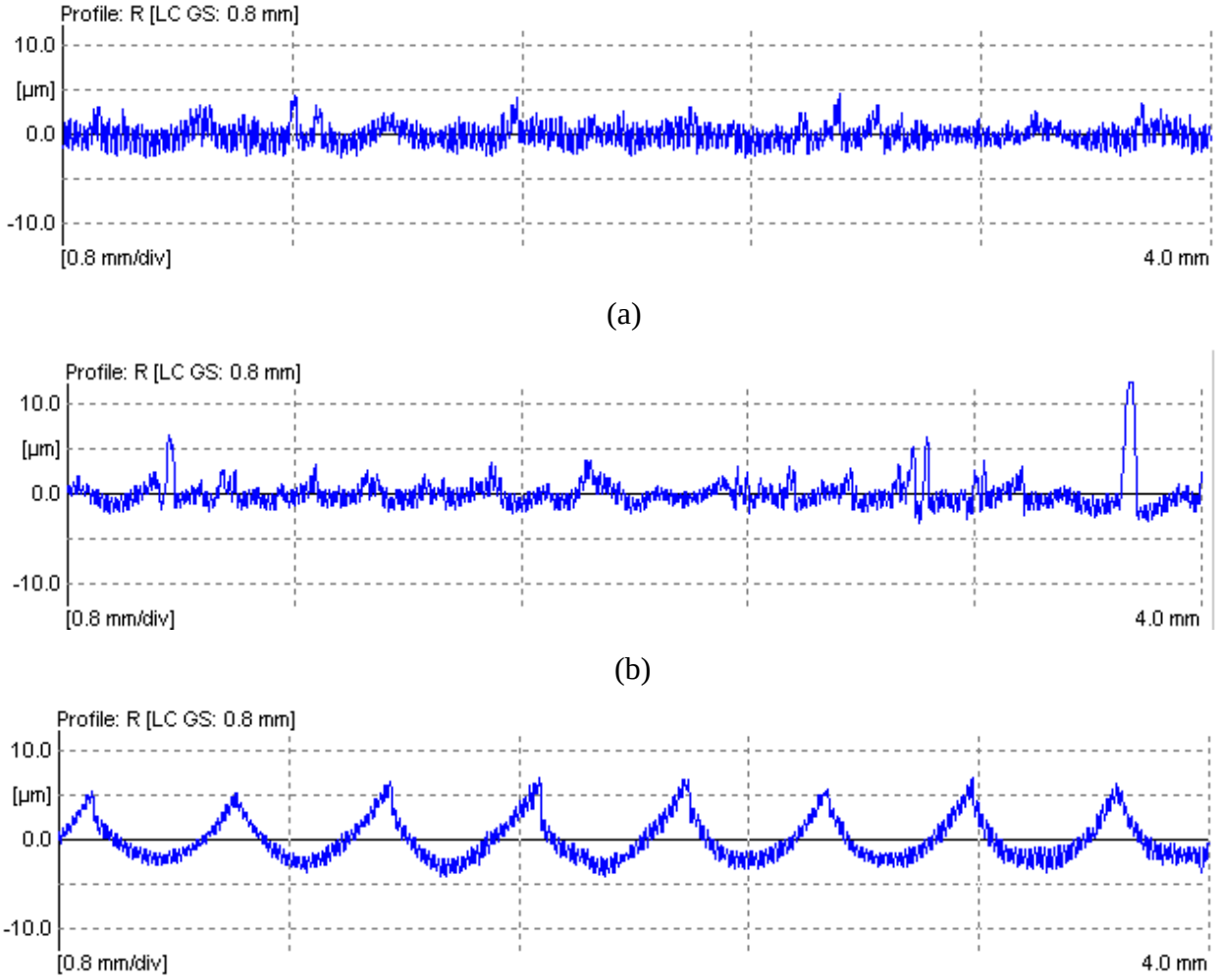

Figure 8.10: Surface profiles at 4000 RPM a) 0.05 mm/rev, b) 0.2 mm/rev and c) 0.5 mm/rev.

In this study, the surface topology was studied through the analysis of two and three dimensional surface roughness and waviness profiles. Figure 8.10 shows the two-dimensional surface profiles obtained at 4000 RPM and 0.05, 0.2, and 0.5 mm/rev. Surface profiles showed feed marks at higher feed rates. Surface profiles at 0.2 mm/rev and 0.5 mm/rev showed periodic peaks at an interval of 0.2 mm and 0.5 mm respectively, shown in Figures 8.9 b and c. The average surface roughness, R_a and ten point average, R_z. as plotted as a function of feed rate and spindle speed, in Figures 8.10 and 8.11, respectively. The surface profiles and parameters are given in Appendix C and D.

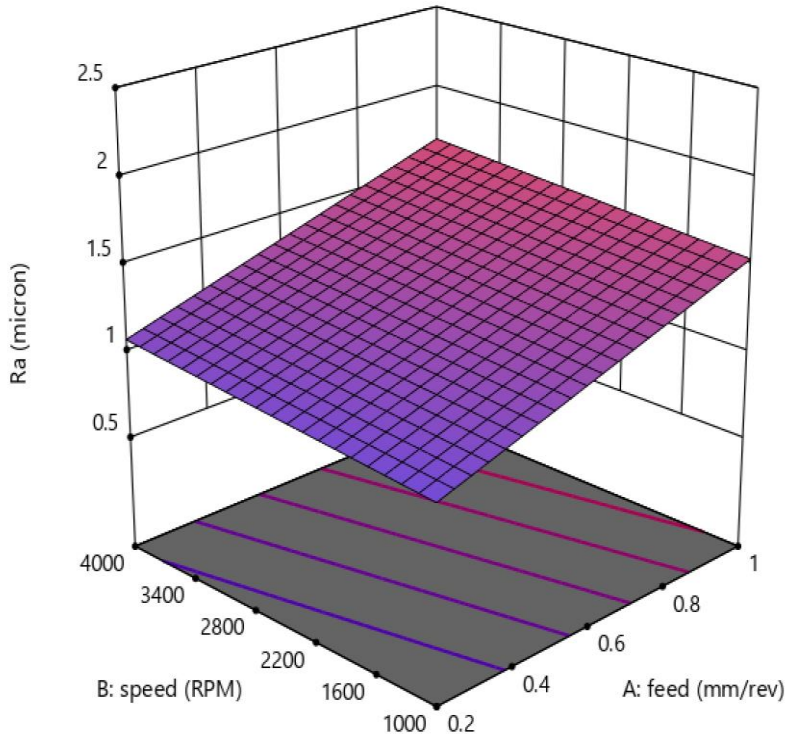

Figure 8.11: R_a plotted as a function of feed rate(mm/rev) and spindle speed(RPM)

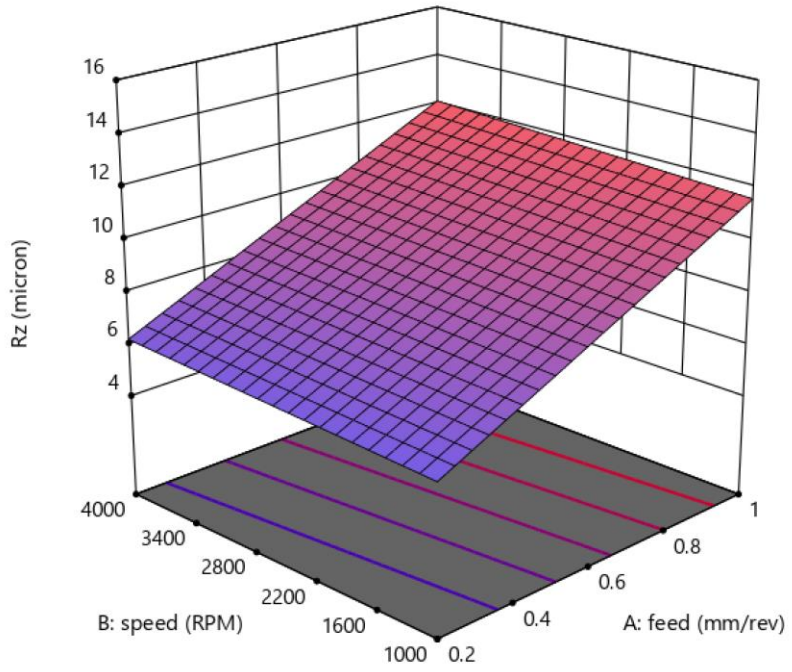

Figure 8.12: R_q plotted as a function of feed rate(mm/rev) and spindle speed(RPM)

The R_a value was found to be between 1 to 2 μm with the increase in feed rate. R_z defined as the difference in height between the highest peaks and deepest valleys is used since it more sensitive to the presence of these defects on the surface. The R_z was found to increase from 6 to 12 μm. The ANOVA results indicated that the feed rate was the only significant factor.

The surface response equation for R_a is given by,

$$R_a = 0.54 * feed\ rate + 0.037 * spindle\ speed + 1.48$$

Table 8.6: ANOVA results for R_a

Source	Sum of Squares	df	Mean Square	F-value	p-value
Model	1.48	2	0.7405	5.89	0.0103
A-Feed rate	1.45	1	1.45	11.55	0.0030
B-Spindle speed	0.0173	1	0.0173	0.1373	0.7150
Residual	2.39	19	0.1258		
Lack of Fit	1.92	14	0.1368	1.44	0.3639
Pure Error	0.4752	5	0.0950		
Cor Total	3.87	21			

However, the parameters defined from a single 2D trace may not satisfactorily define a machined surface since the surfaces interact three-dimensionally with the cutting edge. Hence, three-dimensional surface profiles were obtained to study the surface texture, shown in Figure 8.12. The machined surfaces were observed to be a combination of small scale and large scale features, indicating that it is imperative to study both the surface roughness and waviness parameters. The three-dimensional surface roughness profiles were obtained using an L-filter of 200 microns to eliminate the undulations. The area height parameters, S_a, and S_z, defined in chapter 2 were calculated as a function of feed and cutting speed.

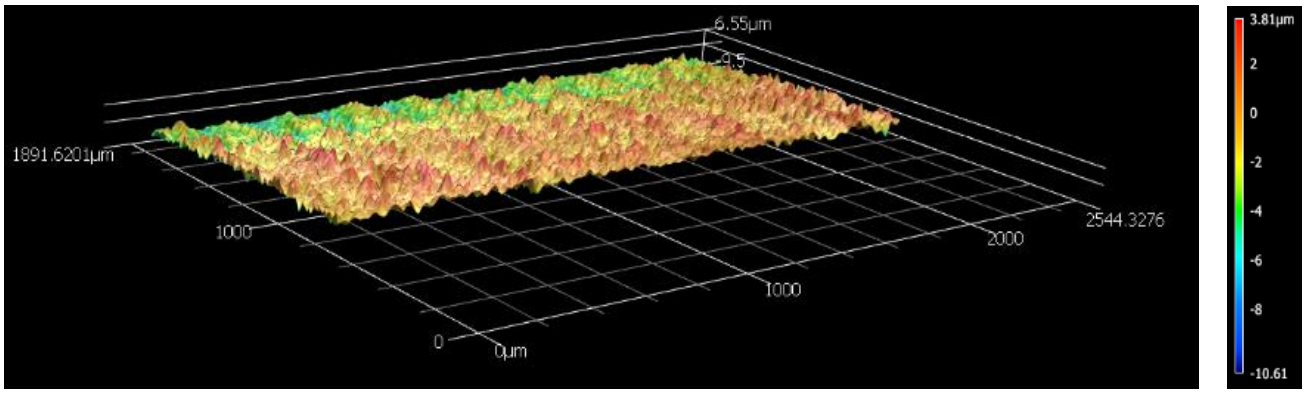

(a)

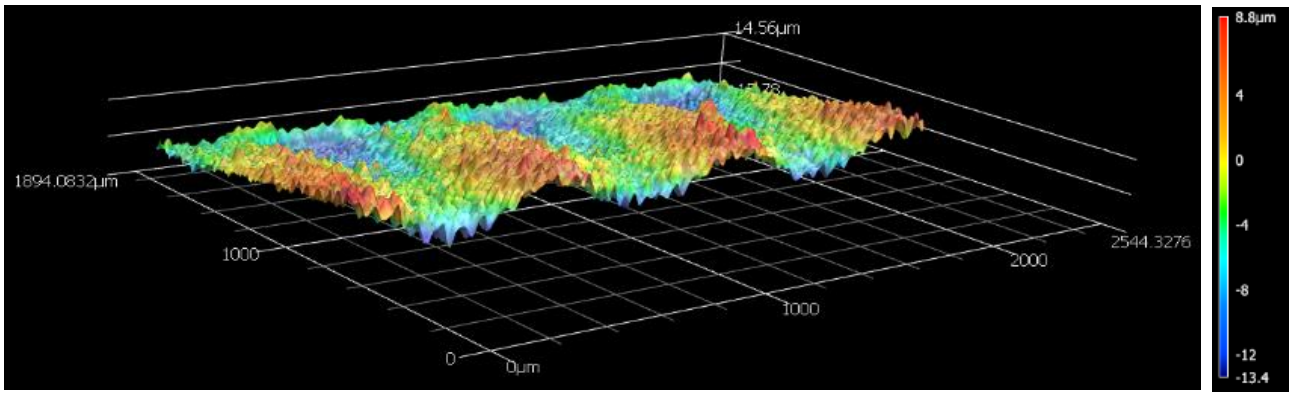

(b)

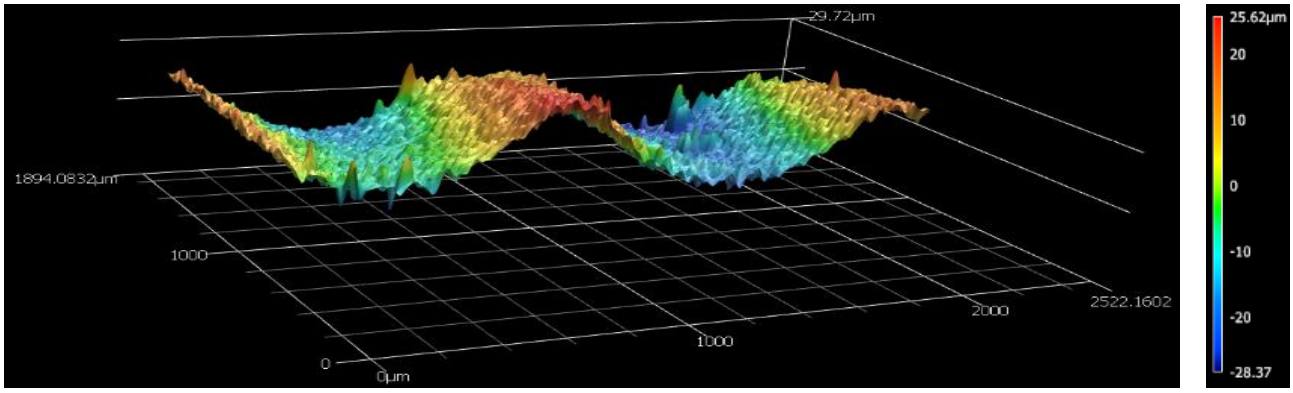

(c)

Figure 8.13: 3D surface profiles obtained at 1000 RPM, a) 0.254 mm/rev, b) 0.508, c) 1.27 mm/rev

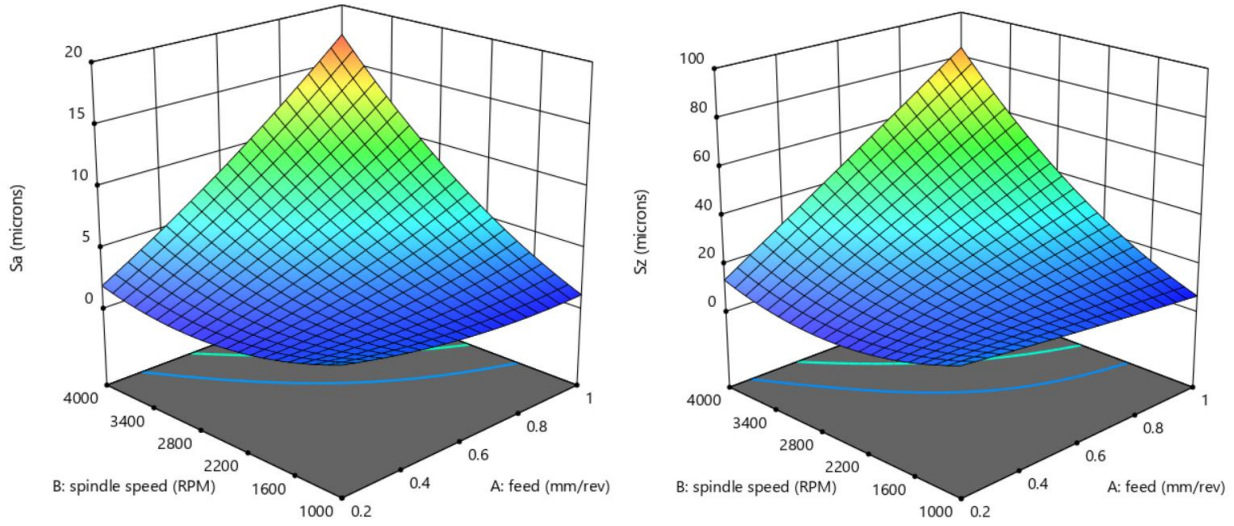

(a) (b)

Figure 8.14: Area height parameters, Sa, and Sz as a function of feed rate and spindle speed.

The response surface model for the area height parameter as a function of feed rate and spindle speed are plotted in Figures 8.13 a and b. The S_a and S_z were found to increase from 1.08 to 17.9 μm and 6.87 to 94.99 μm respectively as the feed and spindle speed increased from 0.2 mm/rev and 1000 RPM to 1.0 mm/rev and 4000 RPM. From the analysis of variance shown in Table 8.7, the area height parameters were found to be impacted by the interaction effect between the feed rate and the spindle speed.

Based on the measured data, the response equations were developed using a multiple linear regression models. The response surface equations take the form,

$$r(x) = C_o + \sum_{i=1}^{2} C_i x_i + \sum_{i=1}^{2} C_{ii} x_i^2 + C_{12} x_1 x_2 \qquad (7.13)$$

where r(x) is the response variable, x_i is the parameter, C_i is linear effect coefficient, C_{ii} is quadratic effect coefficient, C_{12} is the interaction effect coefficient. In this study, x_1 is the feed rate, x_2 is the spindle speed and the response variables are surface roughness parameters R_a.

Regression models for S_a and S_z,

$$S_a = 10.3798 + -16.2655 * feed + -0.00601285 * spindle\ speed + 0.00749205 * feed * spindle\ speed + 4.76233 * feed^2 + 7.89583e-07 * spindle\ speed^2$$

$$S_z = 47.8911 + -51.9109 * feed + -0.0301604 * spindle\ speed + 0.0346072 * feed * spindle\ speed + 1.8765 * feed^2 + 4.29914e-06 * spindle\ speed^2$$

Table 8.7: Analysis of variance for S_a

Source	**Sum of Squares**	**Degrees of freedom**	**Mean Square**	**F-value**	**p-value**
A-feed	4.48	1	4.48	0.5336	0.4791
B-spindle speed	0.4690	1	0.4690	0.0558	0.8172
AB	116.08	1	116.08	13.81	0.0029
A^2	1.61	1	1.61	0.1917	0.6693
B^2	11.09	1	11.09	1.32	0.2730
Residual	100.84	12	8.40		
Cor Total	456.72	17			

The waviness of the primary surface was obtained using S-filter of 80 μm to remove the small-scale elements from the surface. The average waviness, W_a was found to increase with feed rate, shown in Figure 8.14.

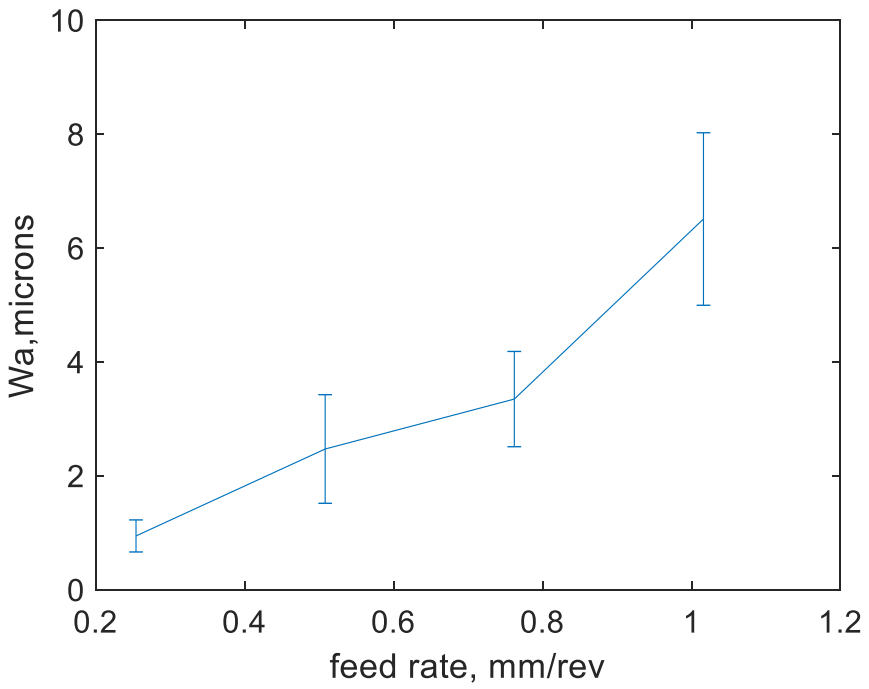

Figure 8.15: Average waviness, W_a vs feed rate, mm/rev.

The SEM micrographs of the machined surfaces were studied to understand the interaction between the cutting edge and SiC particles. Figure 8.15 shows the SEM micrographs of machined surface at 0.1 mm/rev and 1000 RPM. The presence of fine grooves and matrix cracking can be observed, shown in Figure 8.15 b. This can be attributed to the strain hardening of the matrix. Pulled out SiC particles were found to be dragged on surface. In addition, the particles were found to be crushed into the matrix, shown in Figure 8.15 e.

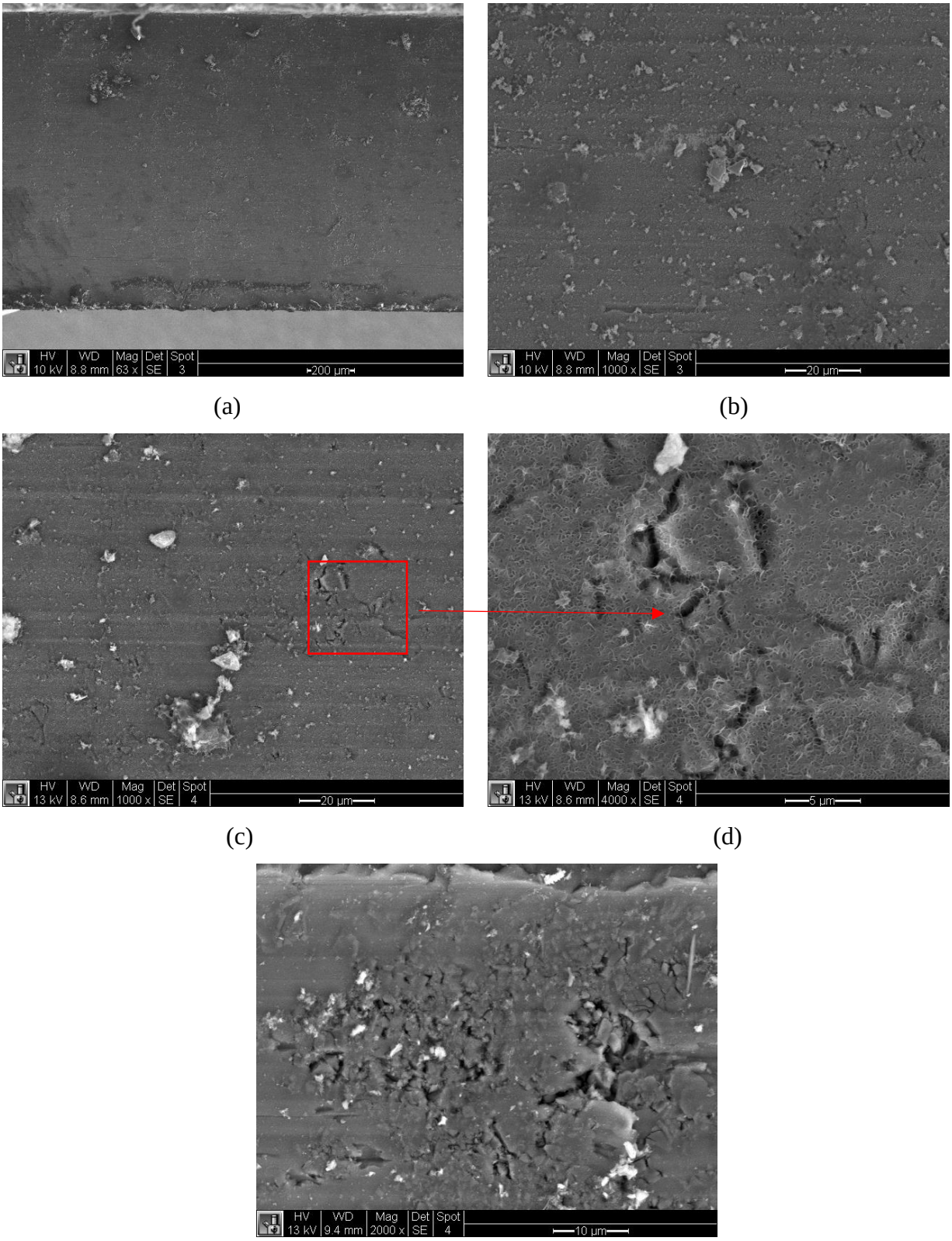

Figure 8.16: Mg/SiCp machined surface at 0.254 mm/rev and 1000 RPM.

The SEM micrographs were also obtained at 0.762 mm/rev and 1000 RPM, shown in Figure 8.16. The machined surface appeared to be rougher with higher number of particles found on the surface. Prominent grooves and ridges were found on the surface, shown in Figure 8.16 a.

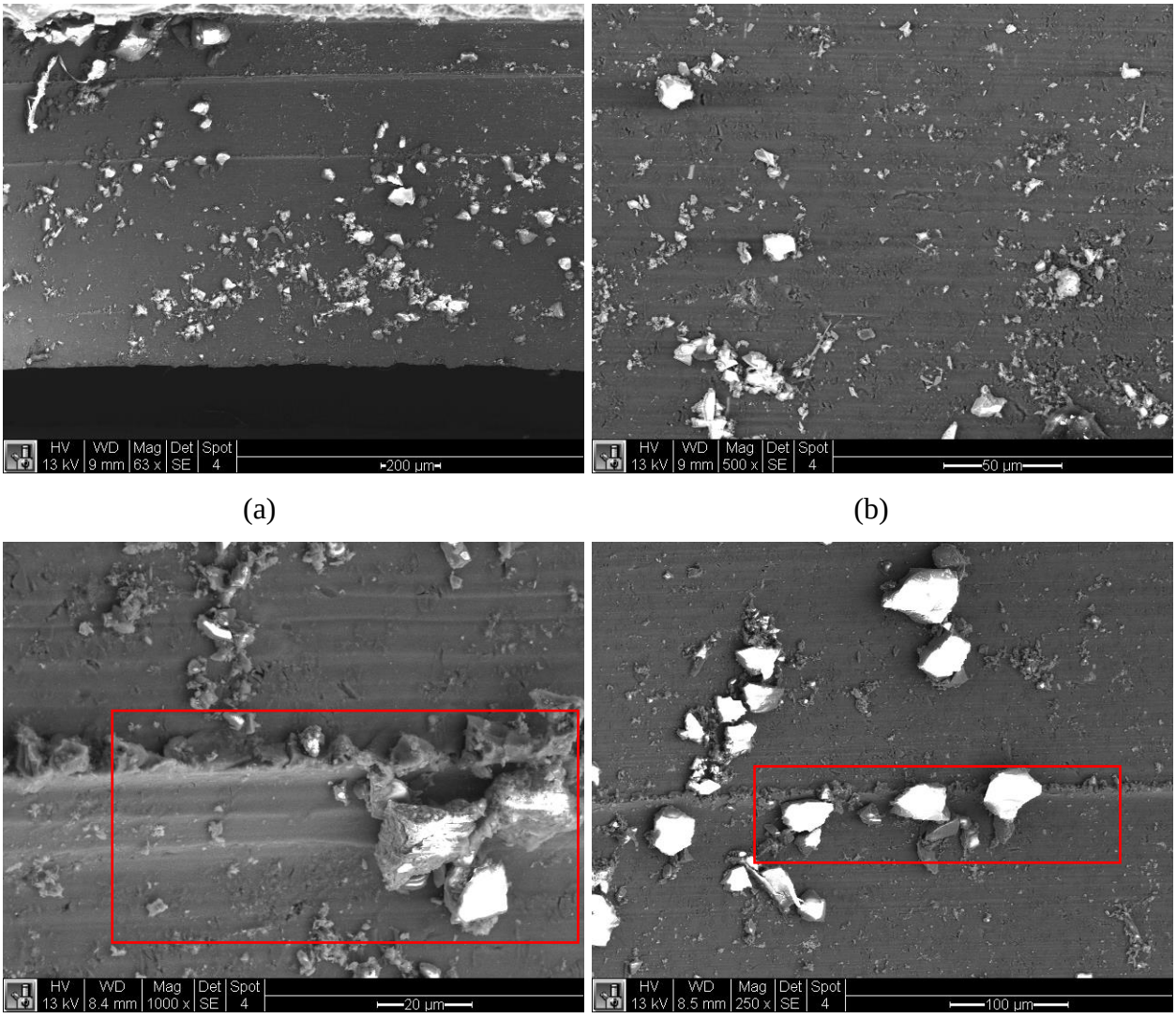

(a) (b)

(c) (d)

Figure 8.17: Mg/SiCp machined surface at 0.762 mm/rev and 1000 RPM, rectangle highlighting the SiCp along the grooves

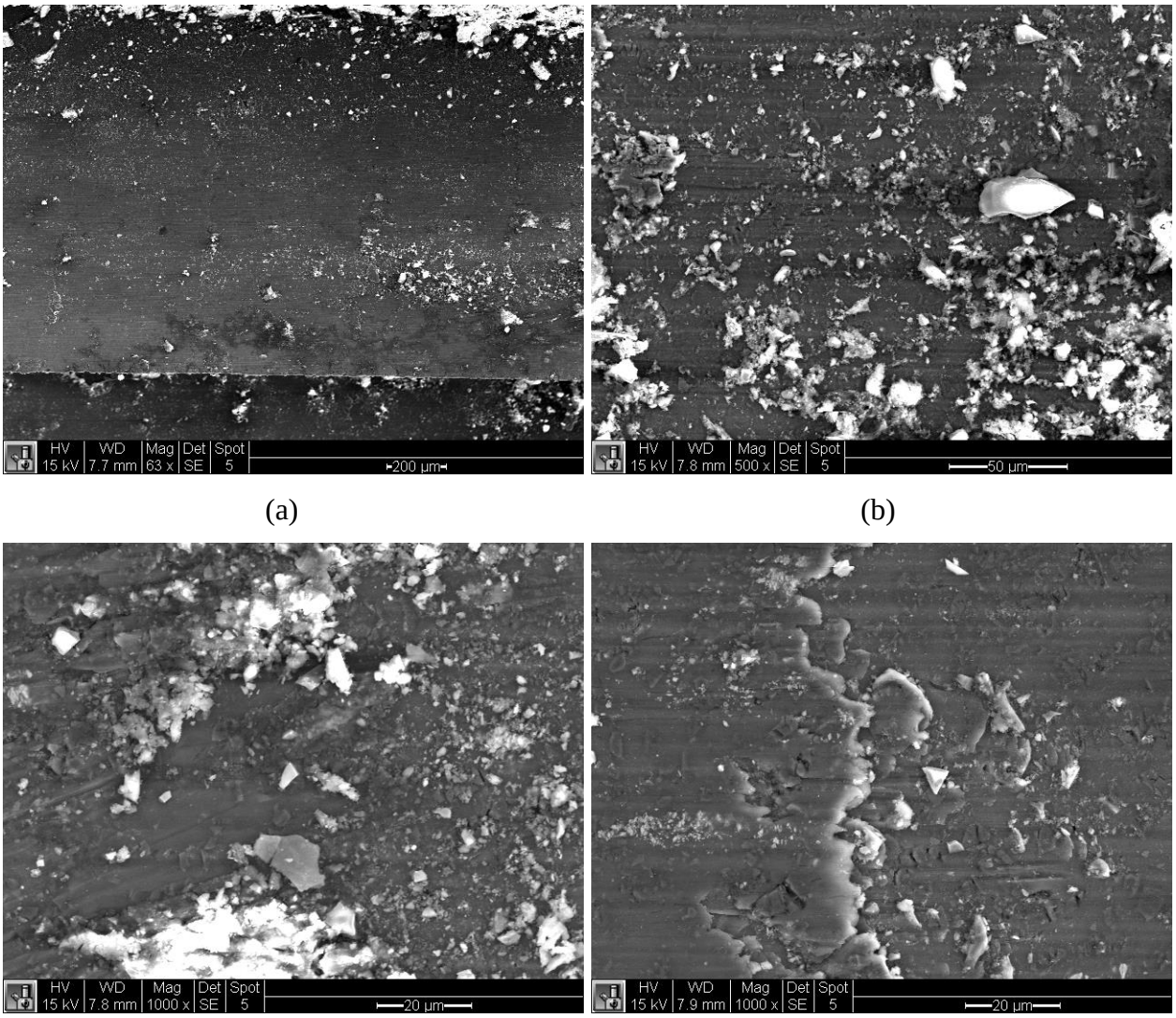

Figure 8.18: Mg/SiCp machined surface at 1.27 mm/rev and 4000 RPM.

The prominent ridges are formed by the dragging of SiC particles along the surface. This can be deduced from the SiC particles aligned along the ridges, shown in Figures 8.16 c and d. In addition, matrix cracking, particles crushing can also be observed in this condition, shown in Figure 8.17 b. The feed rate and spindle speed were further increased to 1.27 mm/rev and 4000 RPM. The

machined surface appeared to be damaged with regions of matrix cracking and SiC particles embedded on the surface, shown in Figure 8.17.

At this feed rate, the matrix appears to be smeared on the surface due to high temperatures induced while machining, observed in Figures 8.17 c and d. The presence of higher number of number of SiC particles dragged along the surface can be attributed to the higher plastic deformation occurring at this feed rate and the mismatch in coefficient of thermal expansion between the matrix and the SiC particles causing particle debonding from the matrix. Particle fracture was not observed owing to smaller size of the SiC particles. Similar observations were reported by Abdulgadir et al, at high feed rates the surface damage was caused due to high contact pressure resulting in the formation of fine grooves and cracks due to strain hardening of magnesium matrix. The authors compared the surfaces produced by uncoated, PVD and CVD tools. In case of uncoated and CVD tools, scratches and fine grooves were observed along the drilling direction, while PCD tools resulted in smoother surfaces.

8.4 Chip morphology

The chips formed during the peripheral milling of the magnesium composite are shown in Table 8.8. The chips were found to be highly segmented with a saw tooth profile. The segmentation of chips can be attributed to the limited ductility of magnesium alloy further reduced by the addition of SiC particles. The chips experience high strains in the primary deformation zone, the chips form periodic shear bands and fail from compressive shear owing to the reduced ductility of the composites. The chips were fragile and the broken upon collection, especially at higher feed rates. The curling of chips caused the cracks to traverse through the chip thickness, shown in Figure 8.18. This results in fragmentation of the chips.

Table 8.8: Geometry of chips at different feed rates and spindle speeds.

Cutting conditions	1000 RPM	2000 RPM	4000 RPM
0.254 mm/rev			
0.504 mm/rev			
0.762 mm/rev	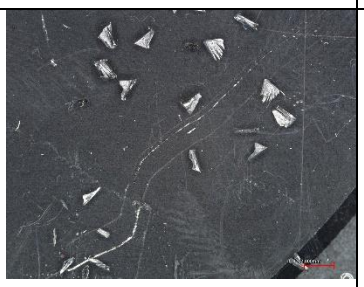	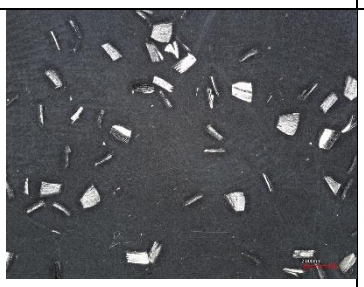	
1.01 mm/rev		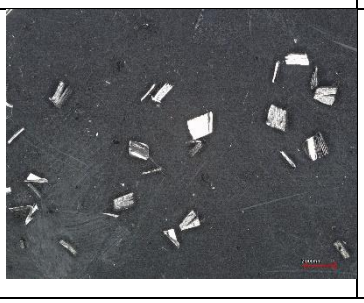	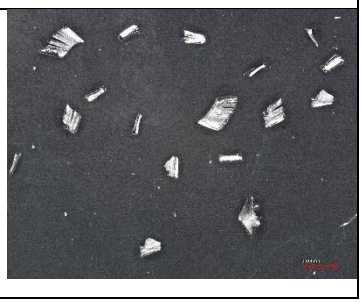



(a)

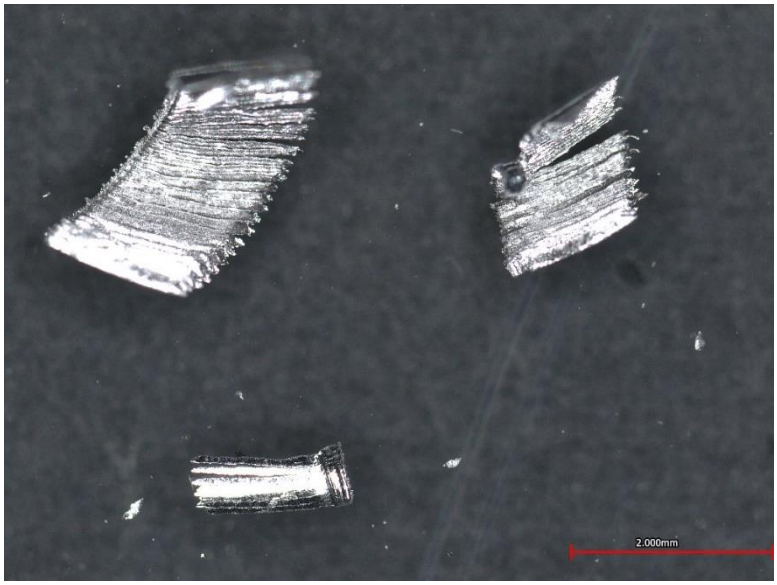

(b)

Figure 8.19: Optical micrographs of chips at 40x, a)0.762 mm/rev and 4000 RPM b) 0.762 mm/rev and 5000 RPM

The chips were further investigated through SEM to understand the interaction between the SiC particles and the cutting edge. Both the free surface and the surface in contact with the cutting edge were examined, shown in Figures 8.20 and 8.21.

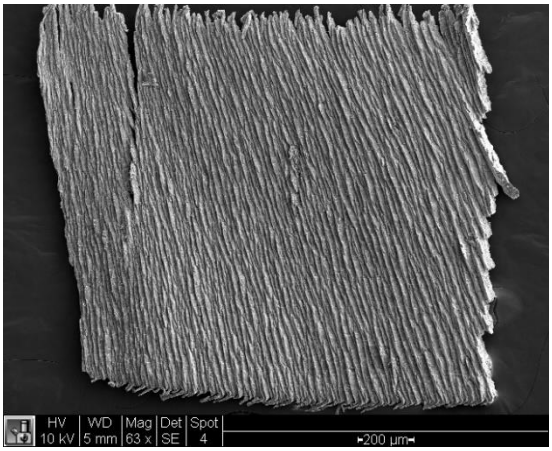

(a)

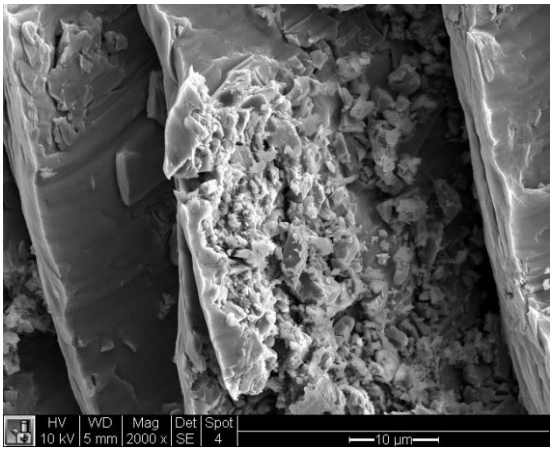

(b)

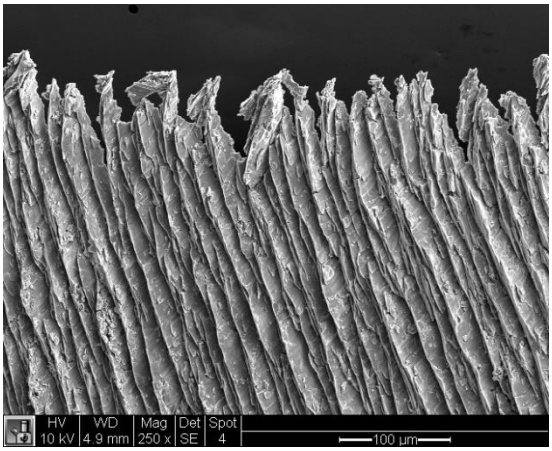

(c)

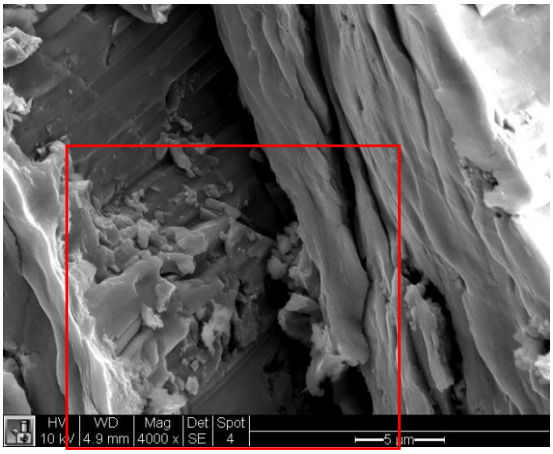

(d)

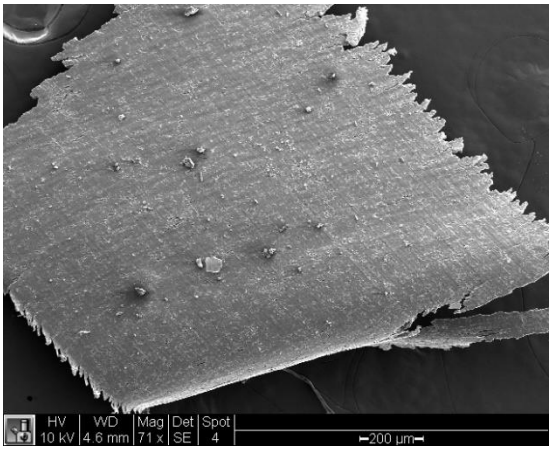

(e)

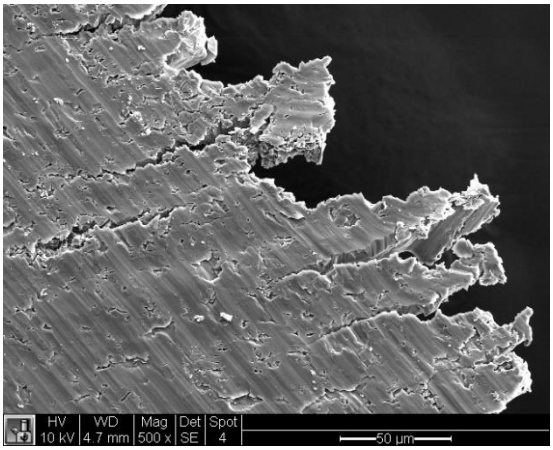

(f)

Figure 8.20: SEM micrographs of chips generated at 0.05 mm/rev, 3000 RPM

Figure 8.20 a, b, c and d shows the SEM micrographs of the free surface of the chip. The high segmentation of the chips can be observed, the free surface showed the formation of periodic bands that failed due compressive shear. The periodic shear band was found to be about 16 microns thick at this shear rate. Owing to the small size, the particles were found to accumulate with in the shear band, shown in Figures 8.20 b and d. The sawtooth profile of the chips can be seen in Figure 8.20 c. However, the crack does not traverse through the thickness of the chip at this feed rate. Also, due to high shear in the deformation zones, the material was found to extrude at the free edge of the chip. Figures 8.20 e and f shows the tool side of the chip. Matrix cracking and voids can be found on the surface. Matrix cracking can be attributed to high strain and limited ductility of the material. The presence of the voids can be due to particle pull out from the matrix. This can be attributed to the particle- matrix interface weakening due to the mismatch in coefficient of thermal expansion at elevated temperatures.

Since higher amount of material was deformed at 0.3 mm/rev is higher, the shear bands were observed to be thicker about 100 microns, shown in Figure 8.21. The presence of intact SiC particles can be observed within these shear bands, shown in Figure 8.21 d. Extensive SEM imaging of chips did not show any particle fracture owing to the small size of the SiC particles. Similar observations were reported by Pedersen et al in facing of magnesium composite[24]. At this feed rate, the cracks from the free edge of the chips were found to traverse through the thickness of the cracks, circled in Figures 8.21 a and b. Workpiece extrusion at the free edge is shown in Figure 8.21 c.

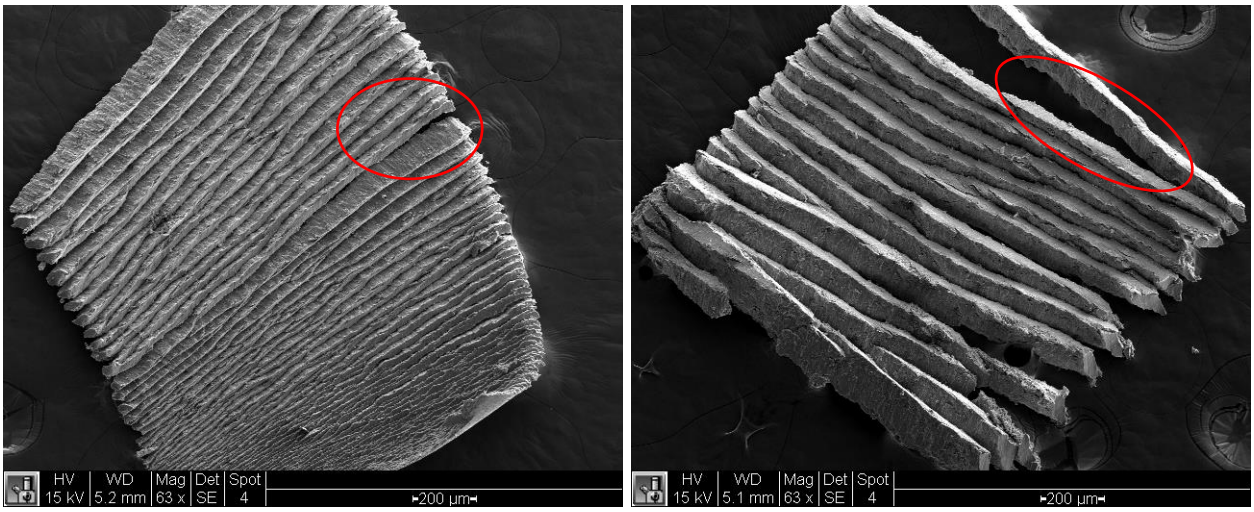

(a) (b)

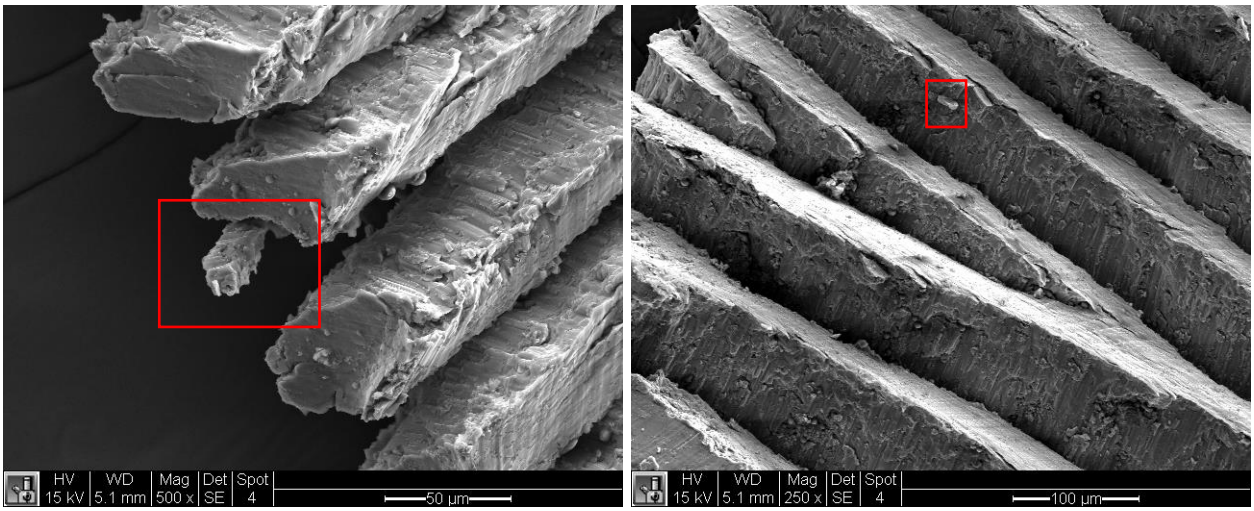

(c) (d)

Figure 8.21: SEM micrographs of chips generated at 0.3 mm/rev at 3000 RPM

8.5 Discussion

Machinability of magnesium composite, AZ91/SiCp/15% was studied through the analysis of cutting forces, tool wear, surface topology and chip morphology. The cutting forces indicate the mechanical stresses experienced by the cutting edge, the temperature at the tool-chip and work-tool interface. Hence, the cutting and the thrust forces obtained during a machining process can be used to access the machinability of the material. While machining MMCs, the cutting forces are higher than machining conventional alloys. This is due to the presence of hard reinforcement particles that accelerate tool wear causing blunting of the cutting edge. Blunt cutting edge pushes rather than cutting the material leading to poor surface integrity and higher cutting forces. However, only a few studies have reported cutting forces generated in machining magnesium matrix composites. In this study, the average cutting forces were obtained for a range of feed rates and spindle speeds and response surface was plotted to observe the trend. From The cutting forces were found to increase significantly with the feed rate and remained almost constant with varying spindle speed, Figure 8.2. Statistical significance of the observation was obtained through ANOVA, the response surface model had a high F-value of 54, 12 and 76 for the feed, radial and axial thrust forces, and feed rate was the only significant factor with a P-value less than 0.05. Similar results were reported by Pedersen et al[24] in facing of ZK60A-T5/SiCp/20% magnesium composite. The authors reported that the cutting forces increased significantly with feed rate and depth of cut, concurring with the observations made in the current study. In another study performed by Abdulgadir et al, the feed and the thrust forces were found to increase with the increasing feed in drilling of graphene nanoparticles reinforced Mg/SiCp[32].

The tool wear experienced by the carbide tool was measured using optical micrographs discussed in section 8.2. From the response surface model, Figure 8.5, at lower feed rate of 0.05 mm/rev, the tool wear was 44.17 microns and when the feed rate increased by ten times, the wear was about 20 microns. The higher number of impacts of the cutting tool on the workpiece causes an increase in the wear at a lower cutting feed rate for a given cutting distance of 32 mm. The higher number of impacts leads to an increase in encounters with the reinforcement particles accelerating the abrasive wear on the cutting edge. However, in this study, the highest tool wear experienced by was much lower than the recommended flank wear limit of 300 μm for carbide tools. The ANOVA results, Table 8.5 indicated that the model is significant, with an F value of 16.62. The results indicate that $feed$ and $feed^2$ are significant model terms with a p-value less than 0.05, while the spindle speed did not have a significant influence on the tool wear.

The surface finish obtained in a machining process depends on the cutting conditions and the tool material. In MMCs, the interaction between the cutting edge and SiC can cause damage in the form of voids, cracks, plastic deformations, and induce residual stresses[124]. Yet, only a limited number of studies have reported the machining induced surface and sub surface damage in magnesium metal matrix composites. Pedersen et al reported that the surface finish of the magnesium composite in a facing operation was excellent[24]. The average surface roughness was about 2 μm at 0.2mm/rev and in agreement with the theoretical value. The surface roughness obtained in a drilling graphene and SiCp reinforced magnesium composite was reported by Abdulgadir et al[32]. The average surface roughness was reported to be below 1 μm for all cutting conditions and tool materials. In most cases, an increase in R_a is observed with increasing feed rate. The effect of tool material was studied by Weinert et al[26], Mg/SiCp showed a subsurface

damage of 40 μm due to plastic deformation induced with cemented carbide drill while, PCD drills showed no sub surface damage.

The machined surface topology was investigated through the analysis of two- and three-dimensional surface roughness. The R_a value was found to be between 1 to 2 μm and increased with increasing feed rate, concurrent with the results reported in the literature[24,26,32]. However, R_z defined as the difference in height between the highest peaks and deepest valleys is used since it more sensitive to the presence of the defects on the surface and was found to increase from 6 to 12 μm with the increase in feed rate. The ANOVA results indicated that the feed rate was the only significant factor, Table 8.6. Further, the three-dimensional inspection of the surface profiles, shown in Figure 8.12, showed the presence of both roughness and waviness elements. The ANOVA results for the area height parameters, S_a and S_z indicated that the interaction effect between the feed rate and the spindle speed to be the most significant. While, the feed rate was found to be the dominant parameter for waviness observed along the surface.

Additionally, the morphology of the chips generated during the machining process reflects the behavior of the matrix and particles under severe plastic deformation. While, continuous chips are typically produced while machining metals, in MMCs, semi-continuous are generated due to the reduction in ductility of the matrix caused by the addition of reinforcement particles. In industries, semi continuous chips are preferred for safety reasons and the continuous chips are broken using chip breakers. In this study, the chips were collected and observed under the optical microscope, given in Table 8.8. The chips were fragile and highly segmented with a saw tooth profile, owing to the limited ductility of the magnesium alloy further reduced by the addition of SiCp. Similar observations were made by Pedersen et al [24], during the facing of ZK60A-T5/SiCp/20%. At

higher feed rates, the amount of deformed material per flute engagement is higher leading to increased contact and temperature at the tool-chip interface. This resulted in curled chips due to softening and increased ductility at higher temperatures. The curl of the chips can be attributed to the non-uniform strain at the shear zone[121]. However, the curling of chips caused the cracks to traverse through the chip thickness, circled in optical micrographs shown in Figure 8.18. This results in fragmentation of the chips.

To further investigate the chip segmentation mechanism, SEM micrographs were investigated. The free surface of the chips generated at 0.05 mm/rev and 3000 RPM is shown in Figure 8.20, the periodic bands formed due to segmentation can be observed. At this machining condition, the width of the shear band was observed to be about 16 microns. As the feed rate increased six times to 0.3 mm/rev, the width was found to increase to 100 μm, shown in Figure 8.21 a, which is about six times the width observed at 0.05 mm/rev. Additionally, the behavior of SiC particles were further investigated at higher magnifications. Owing to the small particle size, the particles were found to agglomerate within the shear band, Figure 8.20 b and d and Figure 8.21 d. Extensive SEM imaging of chips did not show any particle fracture.

The crack initiation and propagation mechanism was investigated by observing the free edge of the chip, shown in Figure 8.20 c, Figure 8.21 a and b. At a lower feed rate, a few cracks were observed to develop from the free surface. However, these crack does not traverse through the thickness of the chip plausibly due to the smaller and closely placed shear bands. With the increase in feed rate and shear band width, the cracks were found to traverse through the chip

causing segmentation, Figure 8.21 b. The material extruded at the free edge of the chip because of high shear in the deformation zones can be observed in Figure 8.21 c.

Through the analysis of cutting forces and surface topology, the feed rate was identified as the most dominant parameter and spindle speed did not have any significant influence. The lowest cutting forces and best surface finish was obtained at 0.1 mm/rev and all spindle speeds. Although tool wear was higher at lower feed rates, the tool wear at 0.1 mm/rev was about 30 μm, which is significantly lower than the recommended wear limit for carbide tools. Therefore, a feed rate of 0.1 mm/rev and spindle speed ranging from 1000 to 4000 RPM are optimum for milling magnesium composite.

8.6 Summary

This study investigated the peripheral milling of AZ91/SiCp/15% by analyzing the cutting forces, tool wear, machined surface topology and chip morphology. The variation of these parameters with the machining conditions were studied to find the optimum machining condition.

The cutting forces were found to increase with increasing feed rate, due to the higher volume of material removed per revolution. The analysis of variance of the regression model terms indicated that the feed rate was the only significant term affecting the cutting forces. Further, the tool wear was investigated by observing the cutting tool before and after use. Unlike, milling Al/SiCp, no significant BUE formation was observed for the magnesium composite. The width of the wear along the rake face was found to depend on only the feed rate. The primary wear mechanism was abrasive wear. The cutting edge showed the presence of micro-plowing and micro-pitting. The cutting edges appeared to be smooth due to repeated rubbing against SiC particles and wear debris.

Further, the surface finish was generally found to be excellent for the magnesium composites. The area height profile parameters, S_a, and S_z were significantly affected by the interaction between the feed rate and spindle speed. While, the average waviness, W_a was observed to be dependent on the feed rate. Upon, investigation of the machined surfaces, the presence of fine grooves and matrix cracking due to strain hardening of the matrix were found. The SiC particles were dragged, causing ridges on the machined surface. SEM micrographs did not reveal any particle fracture due to the small particle size.

The chips generated were found to be fragile with saw tooth edges. The limited ductility of the magnesium composites caused the chips to fail in compressive shear forming periodic bands. Additionally, this study showed a dependence between the thickness of the shear bands and the feed rate, with the particles observed to be accumulating within these bands.

From this investigation, the cutting forces and surface roughness were found to be minimum at 0.1 mm/rev. The cutting forces and two-dimensional surface roughness parameters identify feed rate as the only significant factor. While, for the area height parameters the interaction between the feed rate and the spindle speed was identified to be significant. Therefore, a low feed of 0.1 mm/rev and spindle speeds of 1000 to 4000 RPM should be ideal for machining this composite.

Chapter 9 . Analytical force model for end milling of magnesium composites.

Metal matrix composites are being increasingly used in the automotive industry due to their excellent mechanical and physical properties. Specifically, aluminum and magnesium composites are receiving more attention due to higher specific strength and modulus. Metallic matrix is typically reinforced with rigid ceramic particles leading to increased strength, modulus and wear resistance. The reinforcement particles that enhance the mechanical properties of the composites generate higher cutting forces and cause rapid tool wear during machining in comparison to an unreinforced matrix.

The generated cutting forces are reflected on the integrity of the surfaces produced during a machining process. Therefore, it is imperative to develop a force model to predict the quality of the surfaces generated. But, only a few studies have reported a force model for metal matrix composites[61,62]. For example in [61], an energy-based predictive model was developed for orthogonal cutting of metal matrix composites. The authors considered the energy dissipated in the primary and secondary shear zones and the energy due to fracturing of particles from the matrix using Weibull distribution to estimate the probability of the event. The energy dissipated in the secondary shear zone was assumed to be one third of the energy dissipated in the primary shear zone. Also, the authors did not consider the ploughing of the matrix material under the rounded cutting edge. The contribution of ploughing action of the rounded tool was considered by Pramanik et al [62] and Sikder et al [63] for aluminum based SiC/Al_2O_3 particle reinforced composites. The authors considered the shearing of metal matrix to form chips, the ploughing force and the force due to particle fracture to develop an analytical force model. The force models were developed

based on the orthogonal cutting model for a turning operation, which is a continuous cutting process. In contrast, an analytical cutting model for an *intermittent* cutting process, e.g., end milling of metal matrix composites has not been published yet. In this chapter an analytical force model for end milling of SiC particles reinforced magnesium composites was developed based on Altintas model for milling of ductile materials[66].

9.1 Identification of events during milling

This study considered end milling of magnesium matrix reinforced with 15% by volume SiC particles with an average particle size of 3 μm using a square end carbide cutting tool. When the cutting edge engages with the composite, it encounters the SiC particles and the magnesium matrix leading to matrix shearing, particle debonding and particle fracture[26,61,122]. In this case, matrix ploughing is not significant due to the use of a square-end cutting edge with a radius of 40 μm which is much smaller than the nose-radius of turning tools.

Fracture of reinforcement particles and particle debonding have been observed through SEM images of machined surfaces in the current study and in other reports [112,113,125,126]. For example, Gallab et al [112] studied the surface integrity of Al/SiCp/20% in a turning process; SEM images showed the presence of voids in the matrix, debonded SiC particles, and fractured SiC particles. The formation of voids and particle debonding occurs due to decohesion of particles and the matrix[112]. This can be attributed to the difference in thermal expansion coefficients between the reinforcement particles and the matrix leading to particle loosening due to mismatch in thermal strains[127]. Similar results have been reported by Kannan et al[113]; particle debonding and fracture was reported in both dry and wet turning operation. On further inspection of chip morphology, it was concluded that uneven heat distribution in the composite led to crack

propagation at the particle matrix interface leading to particle debonding[113]. Simulations studies of metal matrix composites to identify the tool particle interaction have also reported similar observations[126,128]. Pramanik et al studied the tool particle interaction through finite element analysis, debonding of particles were observed when the particles along the were along and above the cutting edge due to uneven stress distribution and particle fracture occurred when the stresses were sufficiently high. When the particles are located immediately below the cutting path, severe plastic deformation of the matrix material was observed[128].

From these studies and observation of machined surface morphology through SEM micrographs in chapter 8, it can be concluded that matrix shearing, particle debonding and particle fracture are the major events that occur when a cutting edge engages with the composite. Therefore, these events were considered while developing the predictive force model.

9.2 Development of force model

In accordance with the Altintas force modeling for milling[129], the helical cutting edge was segmented into several square elements of length equal to average diameter of the particles, 3 µm. This implies that each of these elements may encounter a particle, combination of matrix and particle or purely matrix material, shown in Figure 9.1. The forces, $dF_x, dF_y and\ dF_z$ experienced by the elements along the feed, radial and axial thrust directions and the resultant force, dF on the element are shown in Figure 9.1. The probability of these encounters is calculated using particle size distribution and volume percentage of SiC particles in magnesium matrix shown in Figure 9.2.

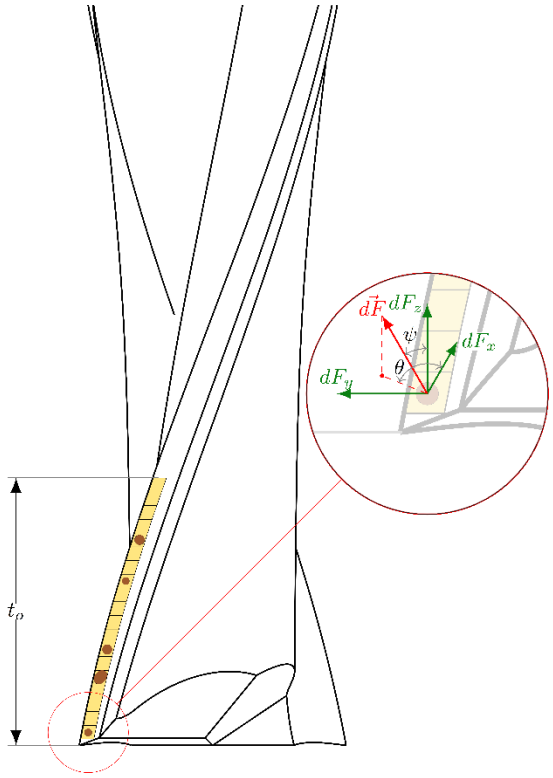

Figure 9.1: Elements along the cutting edge, in contact with only matrix, particle and a combination of particle and matrix, the forces exerted on an individual element.

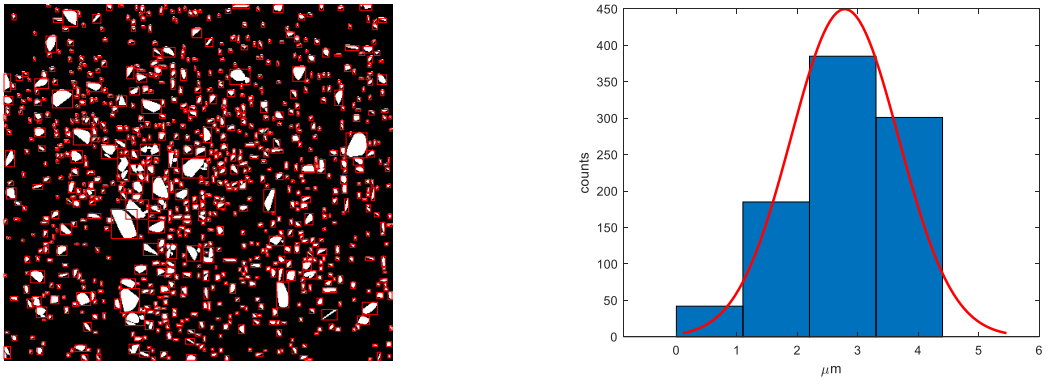

(a) (b)

Figure 9.2: (a)Optical micrograph of Mg/SiCp/15%, image processing is used to identify the size of the particles, b) counts and particle size distribution. The average particle size is 3 µm.

The total number of elements, $n_{tot} = \frac{1260}{3} = 423$. Since the volume fraction of particles is 15%, it is assumed that 15% of 423 elements encounter the particles, $n_p = 64$. The probability of occurrence of a given particle size, shown in Table 9.1 is used to assign the particle size encountered by these elements. The force experienced by the cutting edge is the cumulative of forces experienced by the elements.

Table 9.1: Probability of an element encountering a particle of a given size.

Particle size(microns)	**No of particles present**	**Probability of occurrence**
0.5	19	0.0218
1	44	0.0505
1.5	73	0.0837
2	83	0.0952
2.5	115	0.1319
3	150	0.1720
3.5	188	0.2156
4	200	0.2294

9.2.1 Determination of forces experienced by the element in contact with the matrix

The cutting edge causes the ductile matrix to undergo plastic deformation. The force experienced by the elements due to plastic deformation of the matrix is calculated based on the Altintas model [66]. Since milling is an intermittent cutting process, the instantaneous chip thickness, *h* is given by,

$$h = f * \sin\varphi \tag{9.1}$$

The cutting forces can be written as a function of speed and instantaneous chip thickness,

$$\left.\begin{aligned} F_{x,m} &= K_{xc} * s^{m_x} * (f * \sin\varphi)^{n_x} \\ F_{y,m} &= K_{yc} * s^{m_y} * (f * \sin\varphi)^{n_y} \\ F_{z,m} &= K_{zc} * s^{m_z} * (f * \sin\varphi)^{n_z} \end{aligned}\right\} \quad (9.2)$$

Where, K_{xc}, K_{yc}, K_{zc} are the cutting force coefficients in the *x*, *y* and *z* directions, s is speed in RPM, f is the feed in mm/rev-tooth, φ is the engagement angle and $m_x, n_x, m_y, n_y, m_z, n_z$ are exponents. The cutting force coefficients and the exponents were obtained from experiments.

Peripheral milling of AZ31 magnesium alloy was performed to obtain the cutting forces. The experiment conditions are listed in Table 9.2.

Table 9.2: Cutting conditions for AZ31

Conditions	
Speed	1000-4000 RPM
feed	0.2 to 1 mm/rev
Radial and axial depth of cut	1.27 mm
Cutting tool	6.35 mm, square end, carbide tool
Material	AZ31

The feed force Fx, was found to increase with feed and not a significant trend was observed with respect to the spindle speed, shown in Figure 9.3. The cutting force coefficients and exponents calculated from the cutting forces for Altintas model for milling of ductile metals are shown in Table 9.3.

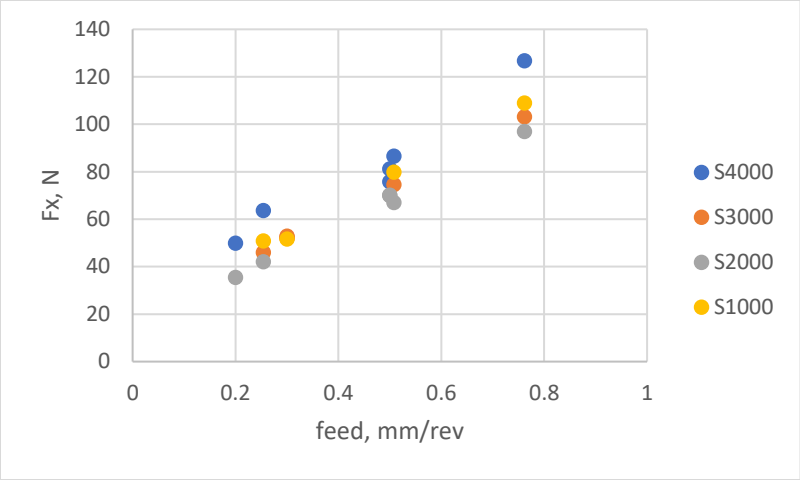
140
120
100
80
60
40
20
0
Fx, N
0
0.2
0.4
0.6
0.8
1
feed, mm/rev
S4000
S3000
S2000
S1000

(a)

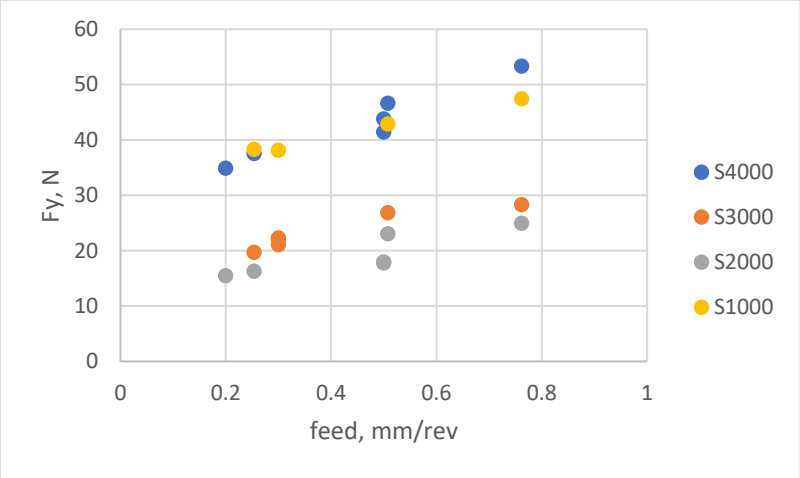
60
50
40
30
20
10
0
Fy, N
0
0.2
0.4
0.6
0.8
1
feed, mm/rev
S4000
S3000
S2000
S1000

(b)

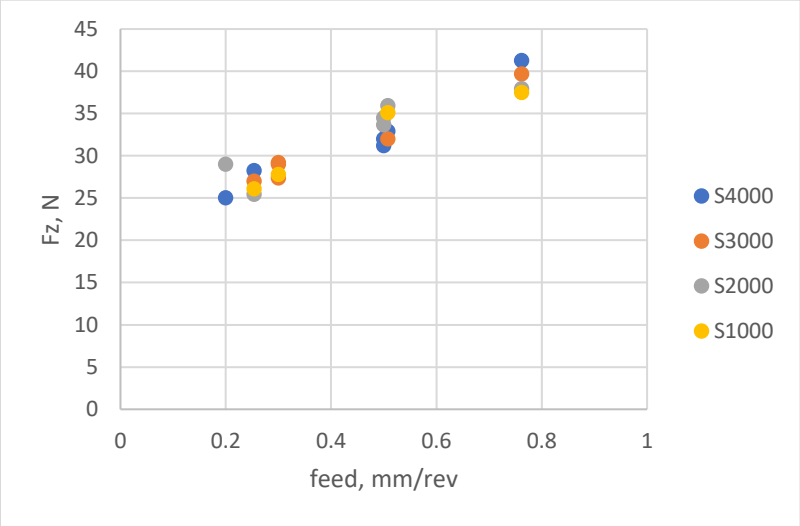
45
40
35
30
25
20
15
10
5
0
Fz, N
0
0.2
0.4
0.6
0.8
1
feed, mm/rev
S4000
S3000
S2000
S1000

(c)

Figure 9.3: a) Feed force, Fx, b) radial thrust force, Fy and c) axial thrust force, Fz obtained in peripheral milling of AZ31 are shown as a function of feed and spindle speed.

Table 9.3: Cutting force coefficients and exponents for AZ31 magnesium alloy

Force	Force coefficient	m	n
F_x	102.05	0.045	0.67
F_y	42.5	0.029	0.1338
F_z	45	-0.002	0.31

The force prediction equation for AZ31 can be given by,

$$\left.\begin{aligned} F_{x,m} &= 102.053 * speed^{0.045} * (f * \sin\varphi)^{0.67} \\ F_{y,m} &= 42.5 * speed^{0.029} * (f * sin\,\varphi)^{0.1338} \\ F_{z,m} &= 45 * speed^{-0.002} * (f * sin\,\varphi)^{0.31} \end{aligned}\right\} \quad (9.3)$$

Where, $F_{x,m}, F_{y,m}, F_{z,m}$ are taken as the cutting forces along feed, radial and axial thrust directions in end milling of AZ31.

These equations give the average force exerted on the cutting edge at a given feed and spindle speed. The force exerted on each element due to matrix shearing can be obtained by dividing these forces by the number of elements along the cutting edge,

$$F_{x,me} = \frac{F_{x,m}}{n_{tot}}, F_{y,me} = \frac{F_{y,m}}{n_{tot}}, F_{z,me} = \frac{F_{z,m}}{n_{tot}} \quad (9.4)$$

9.2.2 Force experienced by the element when in contact with SiC particles

When the elements encounter the SiC particles, the maximum force experienced by the elements is the force required to fracture the particles. The stress required to fracture the particles can be given by,

$$\sigma_f = \left[\frac{2 * E * \gamma_s}{\pi * d}\right]^{0.5} \quad (9.5)$$

Where, E, γ_s and d are Young's modulus, surface energy and diameter of the SiC particles.

The resultant fracture force, F_{pf} is given by,

$$F_{pf} = \left[\frac{2 * E * \gamma_s}{(\pi * d)}\right]^{0.5} * \frac{\pi * d^2}{4} \quad (9.6)$$

Where the independent components along the x, y and z directions are given by,

$$\left.\begin{aligned} F_{x,pf} &= F_{pf} * \sin\Psi * \cos\theta \\ F_{y,pf} &= F_{pf} * \sin\Psi * \sin\theta \\ F_{z,pf} &= F_{pf} * \cos\Psi \end{aligned}\right\} \quad (9.7)$$

Where, Ψ is the angle between the resultant force and z axis , Θ is the angle made by the projection of the resultant force on the xy plane with the x axis. The angles are shown in Figure 9.1.

9.2.3 Determination of force experienced by the element when in contact with the particle and matrix

When the cutting edge comes in contact with the particles and the matrix, the temperature at the cutting-edge increases. Due to mismatch in thermal expansion coefficients, the thermal strain experienced by the matrix is much higher than the thermal strain experienced by the particles. This leads to particles debonding from the matrix. The mean stress experienced by the matrix as the particle debonds can be calculated using the Eshelby's model for non-dilute systems,

$$\sigma_m = f_p * E * (\varepsilon^m - \varepsilon^P) = f_p * E * (\alpha_m - \alpha_P)\Delta T \quad (9.8)$$

Where, f_p is the volume fraction of the particle reinforcement, $\varepsilon^m \; and \; \varepsilon^P$ are the thermal strains experienced by the matrix and the particle, respectively, ΔT is the temperature rise at the cutting edge, E is the Youngs modulus.

The temperature at the cutting edge was measured using the infrared camera**,** shown in Figure 9.4. A maximum temperature of only 60°C was observed at the cutting edge, even at an aggressive machining condition of 0.4 mm/rev and 4000 rpm. The maximum temperatures at the cutting edge as a function of cutting conditions are shown in Figure 9.5.

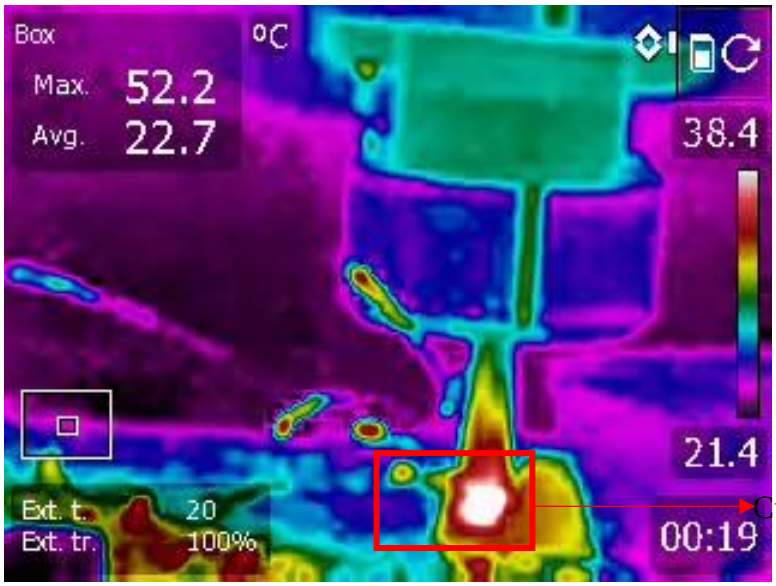

Figure 9.4: Measurement of temperature at the cutting edge using Infrared camera.

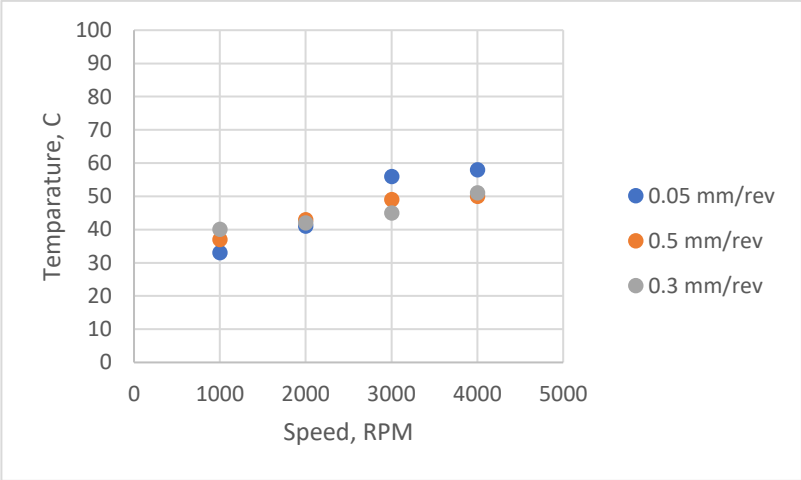

Figure 9.5: Temperature at the cutting edge as a function of feed, mm/rev and speed, RPM.

Therefore, resultant force exerted on the element is given by,

$$F_{pm} = \sigma_m * \left(9 - \frac{\pi * d^2}{4}\right) \tag{9.9}$$

Forces in the x, y and z directions are given by,

$$\left.\begin{aligned} F_{x,pm} &= F_{pm} * \sin\Psi * \cos\theta \\ F_{y,pm} &= F_{pm} * \sin\Psi * \sin\theta \\ F_{z,pm} &= F_{pm} * \cos\Psi \end{aligned}\right\} \tag{9.10}$$

Since the rise in temperature at the cutting edge is only about 60°C, about one tenth of the melting point of the matrix, the thermal strain experienced by the matrix will be small, resulting in lower stress induced in the matrix due to particle debonding.

The force exerted on the cutting edge, $F_{x_{pr}}, F_{y_{pr}}\ and\ F_{z_{pr}}$ are given by the sum of the forces experienced by all the element,

$$\left.\begin{aligned} F_{x_{pr}} &= \sum_{i=1}^{n_{tot}} E_{pf} * F_{x,pf} + E_m * F_{x,me} + E_{pm} * F_{x,pm} \\ F_{y_{pr}} &= \sum_{i=1}^{n_{tot}} E_{pf} * F_{y,pf} + E_m * F_{y,me} + E_{pm} * F_{y,pm} \end{aligned}\right\} \tag{9.11}$$

$$F_{z_{pr}} = \sum_{i=1}^{n_{tot}} E_{pf} * F_{z,pf} + E_m * F_{z,me} + E_{pm} * F_{z,pm}$$

Where, $E_{pf}, E_m and\ E_{pm}$ are 1 or 0 depending on the occurrence of the event.

9.3 Comparison of predicted and experimental forces

The predictive force equations for 15% SiCp reinforced magnesium matrix is given by,

$$\begin{aligned}
&\boldsymbol{F_{x_{pr}}} \\
&= \sum_{i=1}^{n_{tot}} \boldsymbol{C_x} * \left\{ \begin{array}{c} \boldsymbol{E_{pf}} * \left[\dfrac{\boldsymbol{2} * \boldsymbol{E} * \boldsymbol{\gamma_s}}{(\boldsymbol{\pi} * \boldsymbol{d})}\right]^{\boldsymbol{0.5}} * \dfrac{\boldsymbol{\pi} * \boldsymbol{d^2}}{\boldsymbol{4}} + \boldsymbol{E_m} * \dfrac{\boldsymbol{102.053}}{\boldsymbol{n_{tot}}} * \boldsymbol{speed}^{\boldsymbol{0.045}} * (\boldsymbol{f} * \boldsymbol{\sin\varphi})^{\boldsymbol{0.67}} \\ \boldsymbol{+ E_{pm} * 0.15 * E * (\alpha_m - \alpha_P)\Delta T * \dfrac{\pi * d^2}{4}} \end{array} \right\} \\
&\boldsymbol{F_{ypr}} \\
&= \sum_{i=1}^{n_{tot}} \boldsymbol{C_y} * \left\{ \begin{array}{c} \boldsymbol{E_{pf}} * \left[\dfrac{\boldsymbol{2} * \boldsymbol{E} * \boldsymbol{\gamma_s}}{(\boldsymbol{\pi} * \boldsymbol{d})}\right]^{\boldsymbol{0.5}} * \dfrac{\boldsymbol{\pi} * \boldsymbol{d^2}}{\boldsymbol{4}} + \boldsymbol{E_m} * \dfrac{\boldsymbol{42.5}}{\boldsymbol{n_{tot}}} * \boldsymbol{speed}^{\boldsymbol{0.029}} * (\boldsymbol{f} * \boldsymbol{\sin\varphi})^{\boldsymbol{0.1338}} + \\ \boldsymbol{E_{pm} * 0.15 * E * (\alpha_m - \alpha_P)\Delta T * \dfrac{\pi * d^2}{4}} \end{array} \right\} \\
&\boldsymbol{F_{z_{pr}}} \\
&= \sum_{i=1}^{n_{tot}} \boldsymbol{C_z} * \left\{ \begin{array}{c} \boldsymbol{E_{pf}} * \left[\dfrac{\boldsymbol{2} * \boldsymbol{E} * \boldsymbol{\gamma_s}}{(\boldsymbol{\pi} * \boldsymbol{d})}\right]^{\boldsymbol{0.5}} * \dfrac{\boldsymbol{\pi} * \boldsymbol{d^2}}{\boldsymbol{4}} + \boldsymbol{E_m} * \dfrac{\boldsymbol{45}}{\boldsymbol{n_{tot}}} * \boldsymbol{speed}^{\boldsymbol{-0.002}} * (\boldsymbol{f} * \boldsymbol{\sin\varphi})^{\boldsymbol{0.31}} + \\ \boldsymbol{E_{pm} * 0.15 * E * (\alpha_m - \alpha_P)\Delta T * \dfrac{\pi * d^2}{4}} \end{array} \right\}
\end{aligned} \quad (9.12)$$

Where, C_x, C_y *and* C_z are empirical constants, equal to 1.69,1.5 and 1 respectively. The feed force as a function of spindle rotation angle is shown in Figure 9.6 and the code is given in Appendix E.

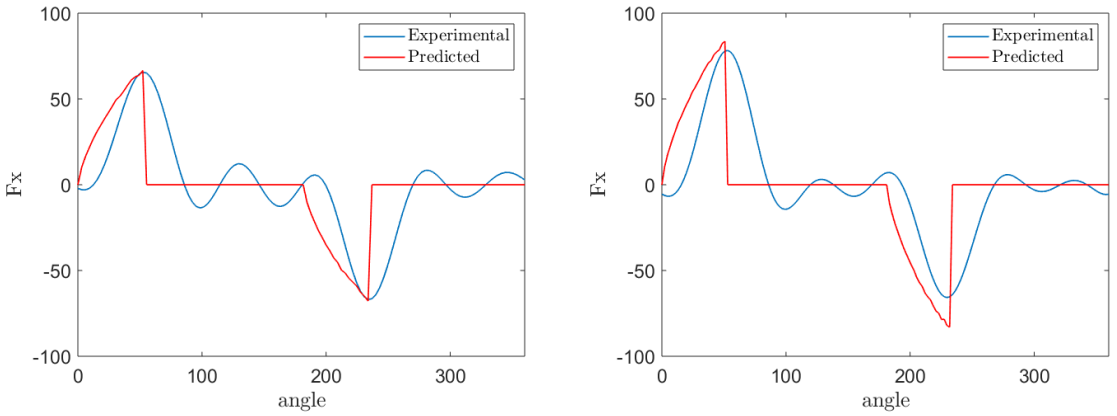

(a) (b)

Figure 9.6: Predicted and experimental force as a function of spindle rotation angle, a) feed: 0.2 mm/rev and spindle speed: 4000, b) feed 0.3 mm/rev and spindle speed: 3000 rpm

Comparison of predictive force model with the measured forces as function of cutting conditions is shown in Figure 9.7. The predicted and experimental feed forces are in good agreement for all the cutting conditions. However, the predicted values for radial and axial thrust forces were observed to deviate from experimental forces at high spindle speed and feed. The significant increase in the thrust forces at 1 mm/rev was not captured by the model.

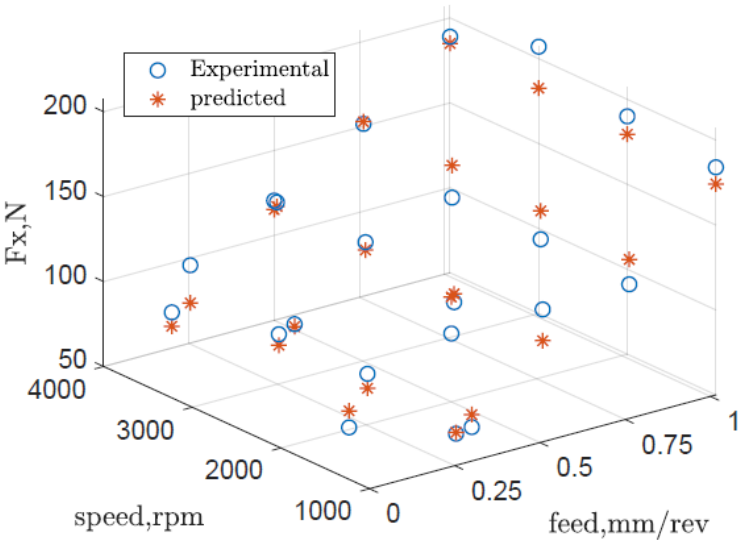
Experimental
predicted
Fx,N
200
150
100
50
4000
3000
2000
1000
speed,rpm
0
0.25
0.5
0.75
1
feed,mm/rev

(a)

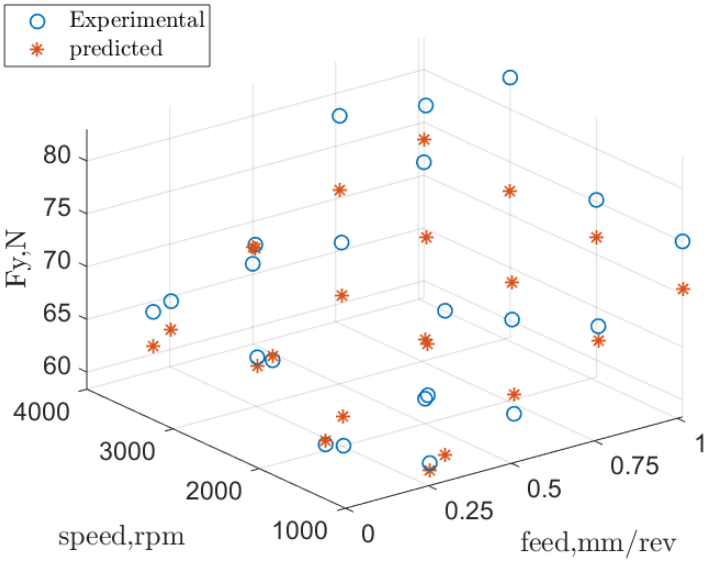
Experimental
predicted
Fy,N
80
75
70
65
60
4000
3000
2000
1000
speed,rpm
0
0.25
0.5
0.75
1
feed,mm/rev

(b)

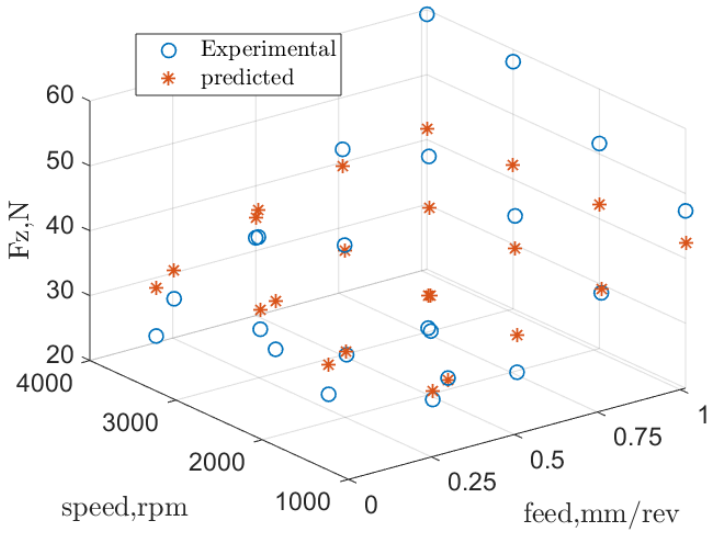

(c)

Figure 9.7: Predicted and experimental forces as a function of feed and spindle speed, a) Fx, feed force, b) Fy, radial thrust force, c) Fz, axial thrust force

9.4 Discussion

The predicted feed force as a function of feed rate and spindle speed was in good agreement with the experimental forces, shown in Figure 9.7 a. ANOVA performed on the cutting forces indicated that feed is the only significant factor, from chapter 8. The predicted feed force also exhibited a similar trend, from Eq.9.12, with exponent of feed rate, 0.67 significantly higher than the spindle speed, 0.045. Along the axial and radial directions, the predicted thrust forces were in good agreement with the measured forces at lower feed rates, while significant deviation was observed at high feed rate of 1 mm/rev. For the thrust forces, the exponents of feed rate and spindle speed

were found to be 0.029 and 0.1338, and -0.002 and 0.31 along the radial and axial directions respectively, indicating that feed rate was the dominant parameter.

The underestimation of thrust forces at higher feed could be addressed by considering the interactions between the SiCp and the cutting edge that are more pronounced at higher feed rate. Through SEM micrographs, the number of loose SiC particles along the machined surface was observed to increase significantly with the feed rate, Figures 8.16, 8.17 and 8.18. The sliding of SiCp resulted in the formation formation of grooves along the surface. The contribution of this event was not captured by the model. Therefore, by assuming that only particle fracture, debonding and matrix plastic deformation occurred to estimate the cutting forces resulted in poor prediction at higher feed rates, where the formation of grooves due to sliding of SiCp along the surface was also prominent.

9.5 Summary

The forces generated in the peripheral milling of metal matrix composites can be modelled by identifying the events when the cutting edge interacts with the composite. Three major events were identified in this study, when an element of the cutting edge encounters just the particles, it may fracture the particle, when the element encounters pure matrix, the matrix undergoes plastic deformation and when the elements are in contact with both the particle and matrix, particle debonding occurs due to mismatch in coefficient of thermal expansion.

The stresses and forces experienced by the elements when these events occur were calculated. The probability of these events was estimated based on particle concentration and distribution in the matrix. For the first event, the maximum force experienced by the element is force required to fracture the particle, calculated using Griffth's theory. The forces involved in plastic deformation of matrix can be determined using Altintas model for milling of alloys. The forces due to particle debonding can be estimated using Esheby's model.

Feed was observed to be the dominant parameter for all the cutting forces, in agreement with the ANOVA results of the measured forces. The predicted forces were found to be in good agreement with the measured forces for feed rates of 0.1mm/rev to 0.765 mm/rev . However, the predictive thrust forces were found to diverge at higher feed of 1 mm/rev. This was attributed to the assumptions of the model that only particle fracture, debonding and matrix deformation occurred, while loose SiCp sliding along the surface resulting in the formation of grooves were also found to be significant at higher feed rates.

Chapter 10 . Surface integrity of the machined composites

Surface integrity in a machining context is a measure of effect that a material removal process has on the surface of a component. The three major aspects studied when analyzing the surface integrity are, the surface topography viz. roughness and waviness and its effect on the fatigue performance, the surface metallurgy namely, the surface and sub surface changes in the microstructure and the alterations in mechanical properties on the surface like hardness and residual stress.

Fatigue and fracture behavior of a metal matrix composite can be quite complex due its dependence on the manufacturing technique used, reinforcement particles, metallic matrix and the interface between the particles and the matrix[87,102,130]. Several studies reported improvement in fatigue life with the addition of reinforcement particles owing to the improved tensile strength of the composites. Consequently, the fatigue strength further increased with increase in volume fraction and decrease in particle size[93,131,132].

Furthermore, the influence of primary manufacturing processes on the fatigue performance of aluminum composites has also been extensively reported in the literature[98]. The primary manufacturing processes for metal matrix composites include squeeze casting process, spray co-deposition of matrix and particles and powder metallurgy techniques. These processes are typically conducted at high temperatures and the thermal expansion coefficient of the matrix is higher than

the reinforcement particles, inducing thermal residual strain in the composite as it cools down to the room temperature. The large residual strain results in an increase in dislocation density in the matrix[88]. The dislocation density was measured for aluminum composites reinforced with whiskers and particles and unreinforced aluminum processed under the same conditions. The average dislocation density for composites were reported to be one order higher in magnitude than the unreinforced matrix[89,90]. This difference in dislocation density has a profound effect on the fatigue behavior of the composites as reported by Han et al [91].

In addition, surface damage induced by secondary manufacturing processes like machining also leads to reduction in fatigue life of components. The small scale elements from the surface topography can act as stress concentrations leading to a drastic reduction in fatigue strength[133]. This is of critical concern in metal matrix composites owing to the presence of reinforcement particles affecting the machined surface topology. When the reinforcement particles encounter the cutting edge, owing to the high temperature the particles may debond and fall from the matrix due to the mismatch in thermal coefficients[113], the particles may be pushed into the matrix or be fractured by the cutting edge[134]. These events result in cracks and voids on the machined surface that act as stress concentrators causing premature failure[97]. These defects were found to be more pronounced with increasing particle size and volume fraction[96]. Therefore, the effects of machining induced surface damage on fatigue life of metal matrix composites should be carefully studied. Yet, only a few studies have reported this effect.

In this chapter, the effect of end milling process induced surface topography damage on fatigue behavior of functionally gradient A359/SiCp composite and AZ91/SiCp are investigated. The

surface topology of the milled specimens were first investigated through 2D and 3D surface profiles and SEM micrographs. Stress life approach was used to determine the fatigue life at varying stress levels. Fractographic examination was made to understand the fracture mechanism using optical and SEM micrographs were obtained to study the fracture behavior of the machined composite.

10.1 Aluminum Composite

10.1.1 Experiment setup and procedure

Specimen fabrication

Compact rectangular specimens were machined from functionally gradient A359/SiCp disk, method, steps shown in Figure 10.1a. The functionally gradient aluminum disk was sectioned using waterjet and then face milled to remove the dimples and reduce the thickness to 4 mm, shown in Figure 10.1b. Figures 10.1 c and d show the rectangular specimen with 9.04 mm wide gauge section machined using waterjet. Peripheral milling was used to reduce the width of the gauge section to 6 mm by removing 1.52 mm on either side. The geometry of the rectangular compact specimen with dimensions is shown in Figure 10.1 e. The radius of curvature of the fillet results to a stress concentration factor, K_t of 1.4 in the specimen[135]. The SiCp concentration was found to vary from 18 to 23% within the gauge section. The effect of machining conditions on the fatigue life was studied by varying the machining conditions for the face milling and peripheral milling process, listed in Table 10.1.

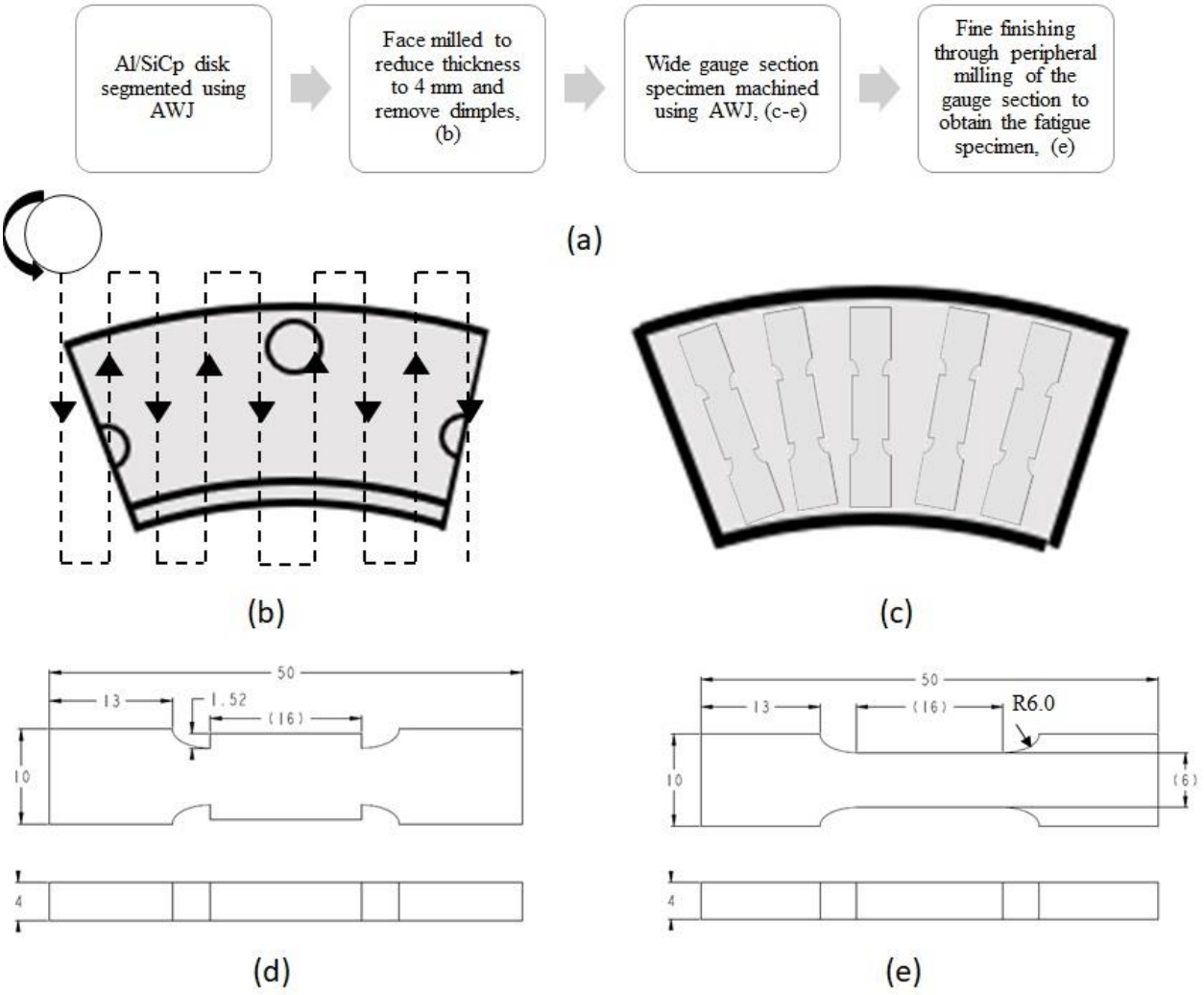

Figure 10.1: Schematic of specimen fabrication. All dimensions are in mm

Three-dimensional view of the specimen is shown in Figure 10.2. The face milled gauge section is highlighted in blue, considered as surface S1 and the peripherally milled edges are highlighted

in yellow, considered as surface S2. From now, face milled and edge milled surfaces will be referred to as S1 and S2 respectively.

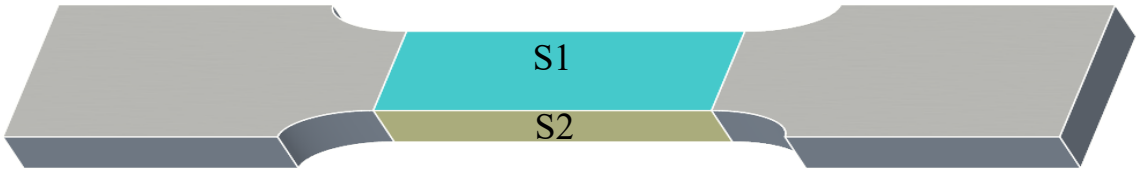

Figure 10.2: 3D view of the fatigue specimen showing the face milled surface (S1), peripherally milled surface(S2).

Table 10.1: Cutting tool and machining conditions

Parameters	Face milled surface	Peripheral milled surface
S2, Cutting tool	PCD tool, 6.35 mm, helix: 0°	Square end Carbide tool, 6.35 mm, C2 grade, helix: 30°, rake angle: 4°
Feed rate	0.3 mm/rev	0.1, 0.3 mm/rev
Spindle speed	3000 RPM	1000, 3000 RPM
Axial depth of cut	0.254 mm	4 mm
Radial depth of cut	3.175 mm	0.506 mm

Peripheral milling of the gauge section wad performed using carbide tools, while the face milling process was performed with PCD tools. The feed rate and spindle speed used for peripheral milling process were chosen from the machinability studies, discussed in chapter 7, the best surface finish was obtained at 0.1 mm/rev and 1000 RPM, while a reasonable surface finish was obtained at 0.3 mm/rev. Higher feed rates were not considered owing to excessive surface damage observed. A small axial depth of cut was used for the face milling process to ensure minimum damage on the surface, discussed in section 3.2. A total of 35 specimen were fabricated in this experimental study.

The dimensions and surface roughness of each specimen were examined and measured. The surface roughness of the peripheral and face milled surfaces were quantified through 2D surface roughness profiles using Mahr surface profilometer and quantified in terms of average surface roughness, R_a, root mean square roughness, R_q, peak to valley height roughness, R_y, and ten point average roughness, R_z. Further, the machined surfaces were inspected using FEI XL30 SEM to identify the defects induced due to machining and the damage induced to the sub-surface was inspected through optical micrographs and Knoop microhardness measurements. The indents were made on the subsurface in a step pattern with a gap of 25 μm between each step.

Fatigue testing

The axial fatigue tests were performed using Instron 8511 20 kN servo-hydraulic test frame at 10 Hz. Constant stress amplitude tension-tension tests were performed with stress ratio, R = 0.1 at four stress levels, $0.8S_{ut}, 0.6S_{ut}, 0.4S_{ut}$ and $0.25\ S_{ut}$, where S_{ut} is the ultimate tensile strength of the material to obtain the number of cycles to failure. The S_{ut} was measured to be 160 MPa, discussed in chapter 4. The fatigue tests were run up to five million cycles. If the fracture had not occurred by then, the test was stopped, and infinite life was assumed for the specimen. The fatigue crack origin and fracture behavior were analyzed through optical and SEM micrographs obtained from Stereo-microscope and FEI XL30 SEM respectively.

10.1.2 Machined surface topology

The machining induced defects on the surface and the changes in sub-surface properties may have a detrimental effect on fatigue life. Particularly, in machining MMCs, poor surfaces may be generated due to the much higher hardness of the reinforcements causing accelerated tool

wear[29]. Therefore, it is imperative to study the surface integrity of the machined specimen and its effect on the fatigue performance. In this study, the surface integrity was evaluated in two steps, 1) the surface morphology was quantified by obtaining the surface roughness profiles and the machined surfaces were inspected for defects through SEM micrographs, 2) the sub surface damage was evaluated by measuring the changes in microhardness and examining the cross-section of the machined surface.

The two-dimensional surface roughness profiles were obtained for all the specimens, given in Appendix F. Typical roughness profiles of the peripheral and face milled surfaces are shown in Figure 10.3. As expected, the face milled surfaces were observed to have a much better surface finish, . Since, a lower depth of cut of 0.254 mm and PCD tool were chosen to minimize the damage on the surface due to face milling. The higher hardness and thermal conductivity of the PCD tools produce good quality surface.

While, peripheral milling was performed using carbide tool, discussed in Chapter 5. At lower feed rate, the surface profiles had randomly spaced high peaks and valleys, Figure 10.3. Extensive softening and solidifying of aluminum matrix on the machined surface at lower feed rate can be attributed to the irregular peaks on the surface. At 0.1 mm/rev, the cutting tool experiences higher number of engagements with the composite, resulting in higher abrasion from the SiC particles, leading to the generation of high frictional heat. The frictional heat was found to increase as the spindle speed increased to 3000 RPM possibly due to insufficient time for heat removal. Owing to the small size of the coupons, the heat generated at the cutting edge remained localized having a significant effect on the surface topology. Further, the machined surface topology was further

studied through SEM micrographs. Typical machined surfaces at 0.1 mm/rev are shown in Figure 10.4 a and b. The surface appeared rough with irregularly spaced peaks and valleys, typical of softened and re-solidified surface

At 0.3 mm/rev, the surface profiles appeared smoother with smaller deviations from the nominal surface. Extensive recast aluminum on the machined surface was not observed at this feed rate, Figure 10.4 c and d, resulting in lower surface roughness, given in Figure 10.3. At this feed rate, the material removal rate is higher, and the heat generated does not transfer to the machined surface due to insufficient time resulting in a smoother surface due to the minimal matrix softening and re-solidification.

Table 10.2: Average Surface Roughness parameters for face milled surface, S1 and peripherally milled surface, S2

Milling	Feed (mm/rev)	Speed (RPM)	R_a (μm)	R_q (μm)	R_z (μm)	R_y (μm)
Face	0.3	3000	0.55 ± 0.05	0.704 ± 0.04	3.84 ± 0.6	4.89 ± 0.95
Peripheral	0.1	1000	9.88 ± 1.8	12.44 ± 1.9	42.3 ± 3.9	71.7 ± 13.2
Peripheral	0.1	3000	15.42 ± 3.2	19.20 ± 5.6	72.7 ± 8.1	99.3 ± 10.2
Peripheral	0.3	1000	5.4 ± 0.9	6.82 ± 1.6	12.8 ± 1.9	42.3 ± 5.2
Peripheral	0.3	3000	2.63 ± 1.5	3.66 ± 1.2	15.7 ± 2.1	24.7 ± 3.5

The surface roughness parameters were measured for all the specimens, the average with standard deviations for the face and peripherally milled surfaces are given in Table 10.2. The surface profiles are given in Appendix F.

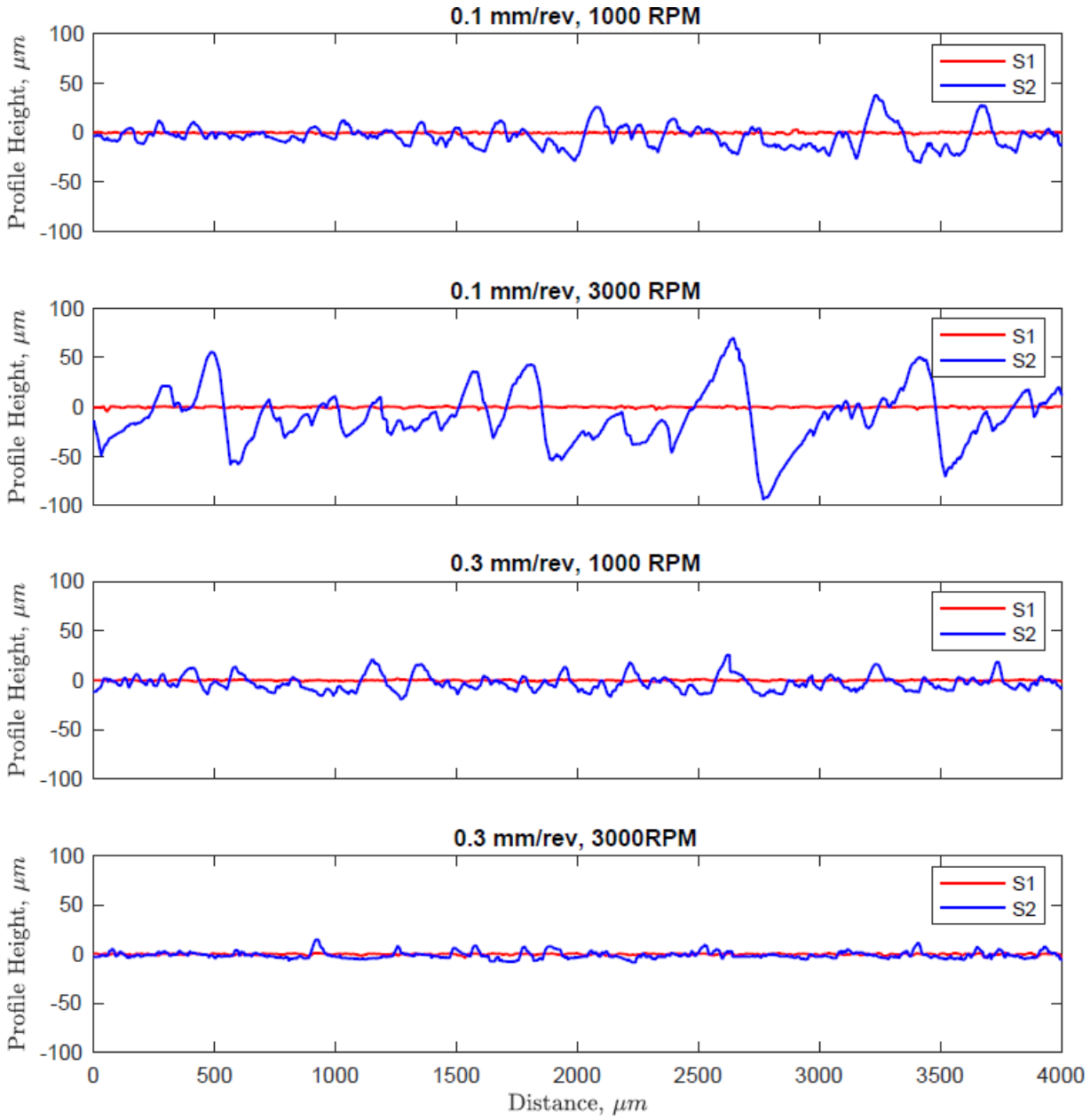

Figure 10.3: Typical surface roughness profiles of peripherally milled surface, S2 and face milled surface, S1.

Upon further magnification, the SEM micrographs obtained at 1000x, Figure 10.5, showed voids formed from particle pull out or debonding, the matrix cracking and SiCp pushed into the matrix.

Each of these defects have the potential to act as stress concentrators that cause early onset of fatigue crack initiation and propagation.

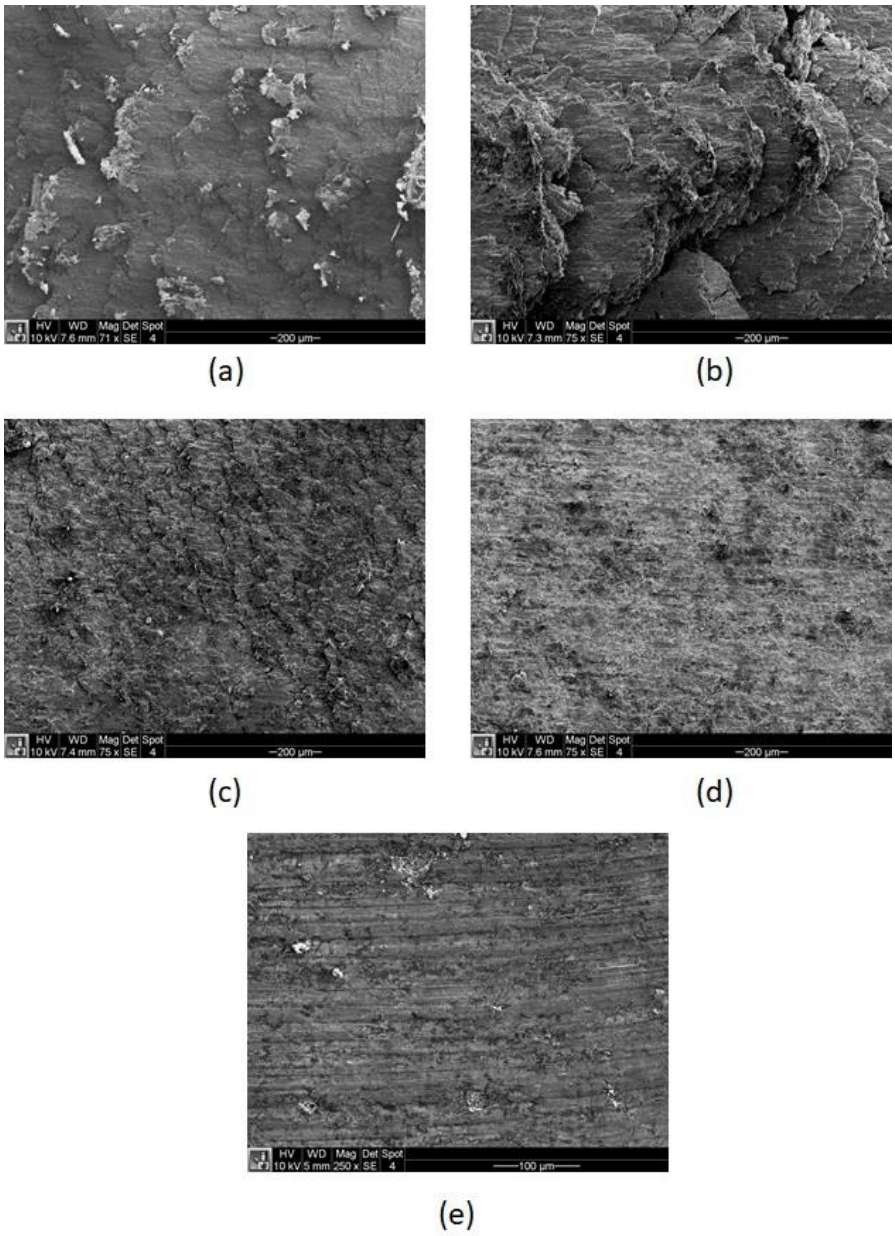

Figure 10.4: SEM micrograph of Peripheral milled surface(S2) , a) 0.1 mm/rev, 1000 RPM, b) 0.1 mm/rev, 3000 RPM, c) 0.3 mm/rev, 1000 RPM, d) 0.3 mm/rev, 3000 RPM, e) Face milled surface at 0.3 mm/rev, 3000 RPM.

Further, the machining induced changes to the sub-surface was inspected through changes in hardness and optical micrographs beneath the surface. A cross-section of the machined gage specimen is shown in Figure 10.6. The average plastic deformation in the sub surface was found to be 80 μm at 0.1 mm/rev and 1000 RPM and the deformation was about 60 μm at 0.1 mm/rev and 3000 RPM, shown in Figure 10.6 a and b. However, a significant sub-surface damage was not observed for face milled surfaces, shown in Figure 10.6 c. Microhardness measurements along the sub surface showed a slight increase in hardness in the deformed region, shown in Figure 10.7, consistent with the results reported by Gallab et al[112] and Dabade et al[136]. This observation can be attributed to the increase in dislocation density due to plastic deformation.

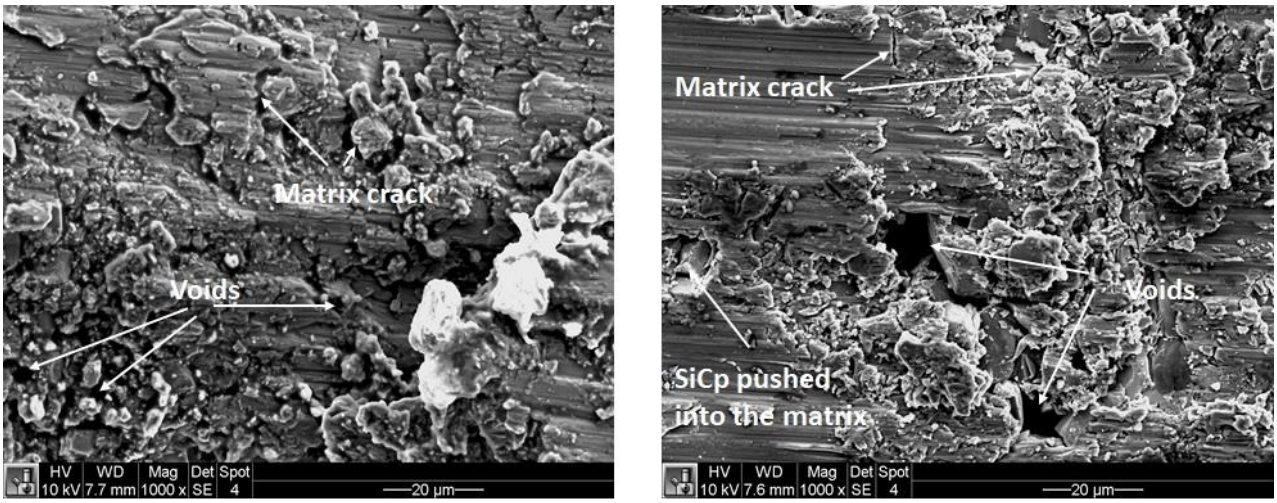

(a) (b)

Figure 10.5: SEM micrographs of the peripherally milled surface showing matrix cracking, voids and SiC particles pushed into the surface.

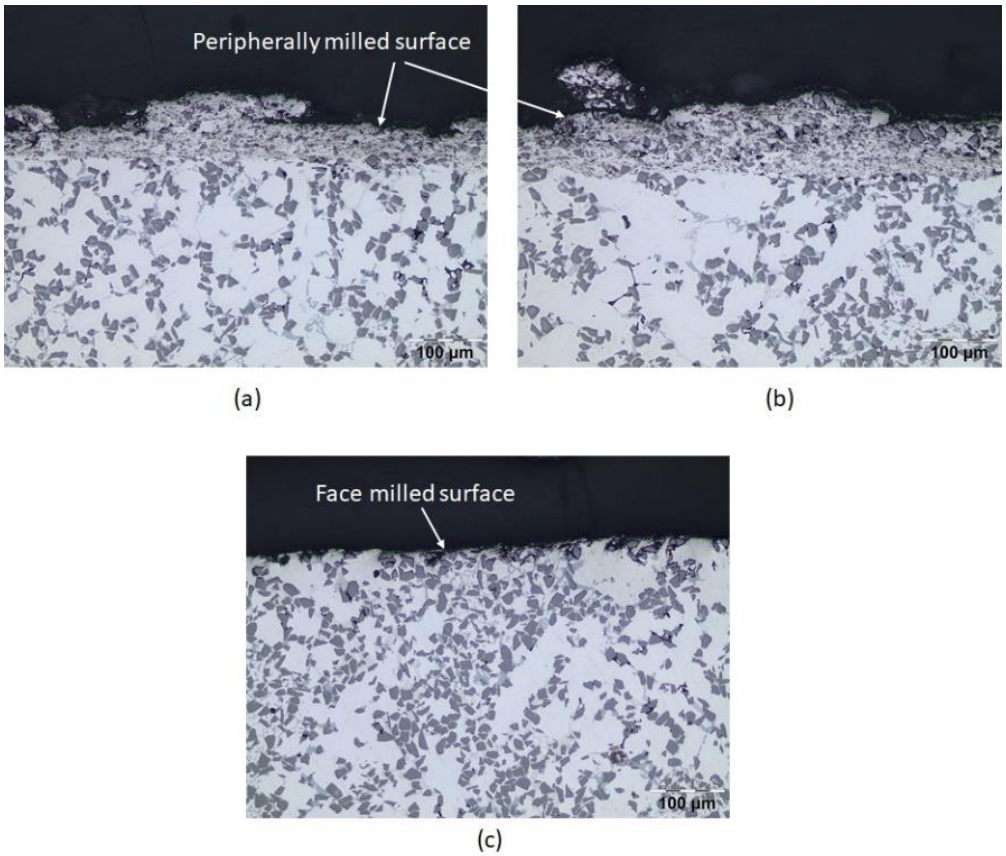

Figure 10.6: Cross-section of the machined specimen showing the sub-surface plastic deformation, a) Peripherally milled at 0.1 mm/rev and 1000 RPM, b) Peripherally milled at 0.1 mm/rev and 3000 RPM, c) Face milled at 0.3 mm/rev and 3000 RPM

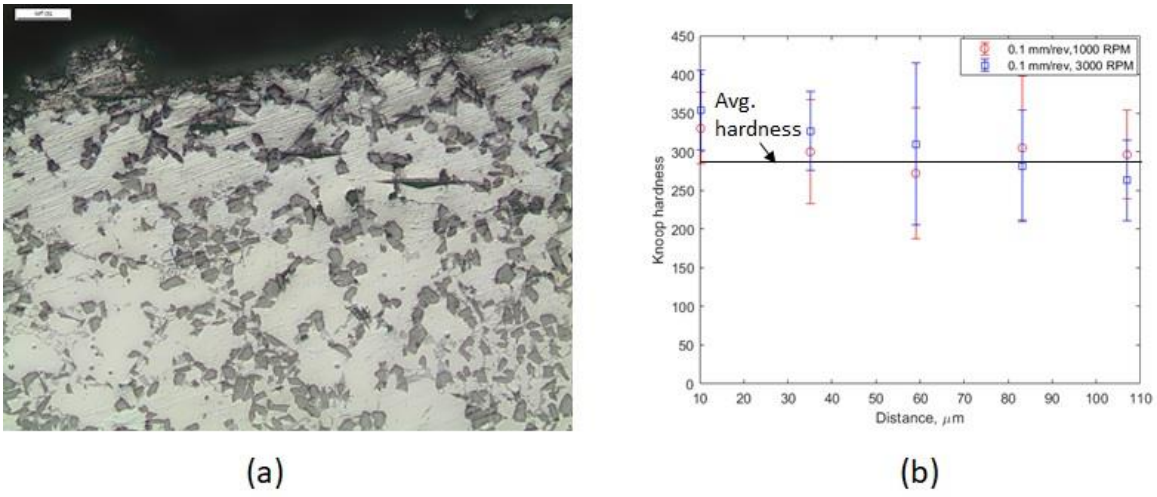

Figure 10.7: Microhardness measurements along the sub-surface, a) Optical micrograph of the sub surface showing Knoop indentation in step pattern, b) variation in average Knoop hardness as a function of distance from the machined surface.

10.1.3 Fatigue performance

The effect of machining induced damage was evaluated by performing axial fatigue tests with constant stress amplitude loading to obtain the number of cycles to failure. Tension-tension fatigue tests were performed at four stress levels up to five million cycles. If the coupon had not fractured, the test was stopped, and the specimen was considered to have infinite life. The fatigue life of the machined coupons at different load ratios is shown in Table 10.4 and plotted in Figure 10.5. The specimen has functionally gradient concentration of SiC particles. The % SiCp varies from 18 to 23 % in the gauge section. The concentration of SiCp at which the failure occurred is also tabulated in Table 10.4. Most of the failure was observed to occur between 19 to 21% SiCp.

Table 10.3: Fatigue life of the machined coupons, * indicates that the coupon has not failed

No	$R_a, \mu m$	$R_z, \mu m$	S/S_{ut}	Speed, RPM	Feed, mm/rev	No of cycles, N	%SiCp at failure
NA-2	7.83	39.52	0.25	1000	0.1	5502571*	-
NA-5	9.87	59.7	0.4	1000	0.1	5903542*	-
NA-6	8.94	53.89	0.6	1000	0.1	208610	20.7%
NA-3	13.02	67.5	0.8	1000	0.1	527	18.9%
NA-10	9.4	53.7	0.6	1000	0.1	230435	19.2%
NA-13	7.84	38.55	0.8	1000	0.1	323	20.7%
NA-18	18.2	90.37	0.6	3000	0.1	32933	19.08%
NA-19	16.91	82.8	0.8	3000	0.1	1272	21.63%
NA-30	17.4	88.25	0.25	3000	0.1	5925324*	-
NA-21	12.91	64.8	0.4	3000	0.1	79039	20.49%
NA-17	10.25	48.5	0.6	3000	0.1	14853	19.7%
NA-20	11.75	56.98	0.8	3000	0.1	1473	20.49%
NA-16	5.2	9.212	0.25	3000	0.3	5894238*	-
NA-14	2.8	14.42	0.4	3000	0.3	1542159	19.7
NA-8	1.78	12.07	0.6	3000	0.3	2481519	19.8%
NA-11	2.8	14.7	0.8	3000	0.3	2289	21.5%
NA-15	5.3	13.45	0.4	3000	0.3	5625766*	-
NA-9	2.5	15.9	0.6	3000	0.3	489699	18.5%

NA-12	1.8	14.76	0.8	3000	0.3	9552	20.77%
NA-27	6.4	34.7	0.4	1000	0.3	6895196*	-
NA-24	4.511	24.6	0.6	1000	0.3	276695	19.7%
NA-28	3.7	21.45	0.8	1000	0.3	4810	18.6%
NA-31	4.7	24.8	0.25	1000	0.3	5599742*	-
NA-26	5.8	26.6	0.6	1000	0.3	1846754	20.8%
NA-25	5.3	26.1	0.4	1000	0.3	5967842*	-
NA-29	4.5	22.5	0.8	1000	0.3	472	22.4%

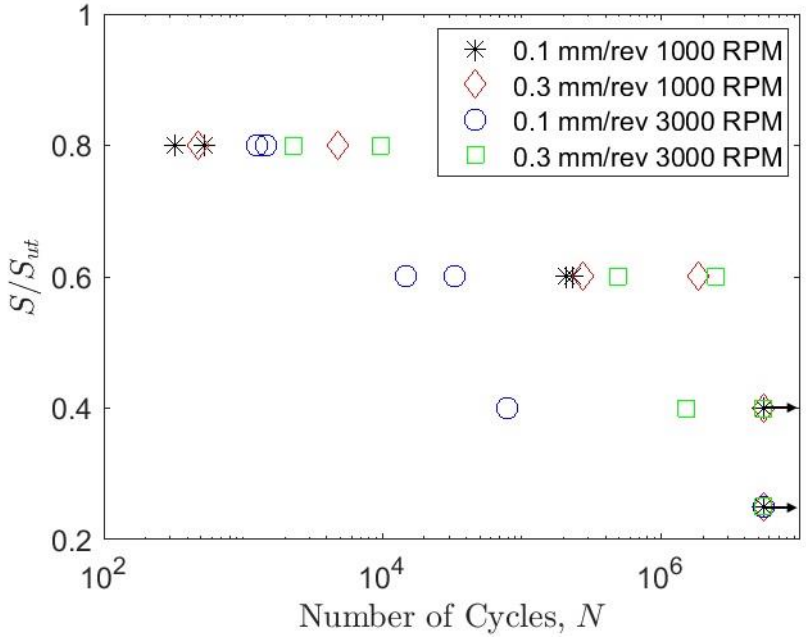

Figure 10.8: Fatigue life of the machined coupons, the arrows indicate experiment run out, the specimen did not fail at five million cycles.

From Figure 10.8, the coupons machined at 0.3 mm/rev and 3000 RPM were found to exhibit best fatigue life in comparison to other cutting conditions. This was closely followed by the coupons machined at 0.3 mm/rev and 1000 RPM. While, the fatigue life was reduced by about 75% for coupons machined at 0.1 mm/rev and 3000 RPM. This can be attributed to the presence of stress concentrators on the surface due to the irregular surface topology at this cutting condition. Although, the microhardness tests indicated an increase in hardness near the machined surface, the severe plastic deformation and frictional heat may deteriorate the interfacial bond strength between the SiCp and aluminum matrix promoting crack propagation.

Fractography

Fatigue crack initiation sites were identified through optical micrographs, shown in Figure 10.8. Multiple cracks were found to initiate from the defects on the machined surface. The arrows in Figure 10.10 indicate the crack initiation sites. Cracks were observed to initiate from the peripherally milled surface and going inward into the specimen can be observed. In addition to surface defects, particle clusters also act as stress concentrators. The fractured surface appeared rough. At lower loads, a short region of ductile fatigue crack propagation can be observed before overloading occurred, shown in Figures 10.10 a, c, e and g. However, at higher loads, the fractured surface appeared brittle. Owing to the reduced ductility of the specimen, the specimen did not exhibit significant plastic deformation at all loading conditions.

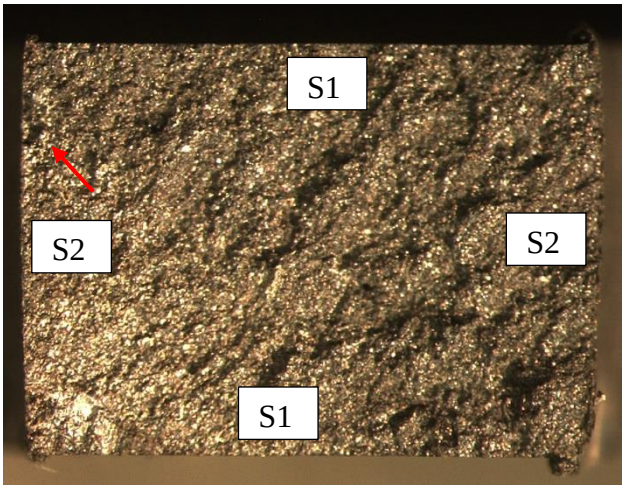

(a)

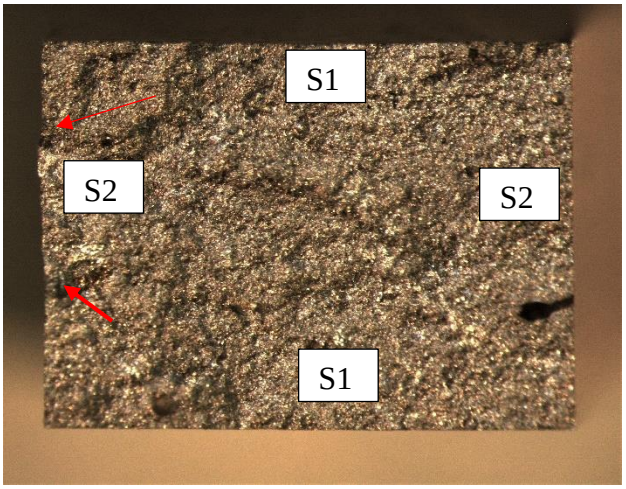

(b)

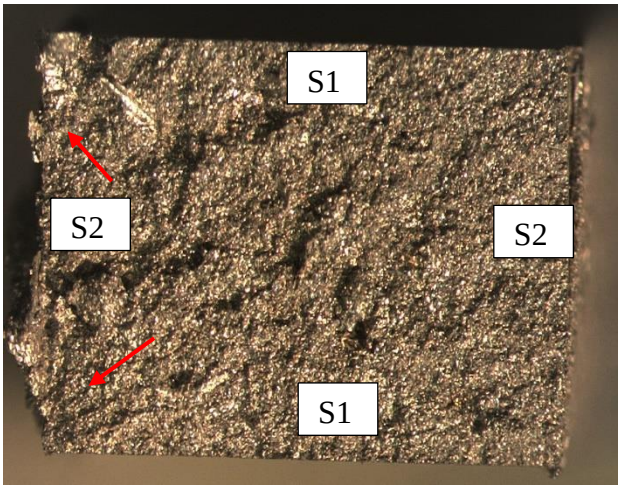

(c)

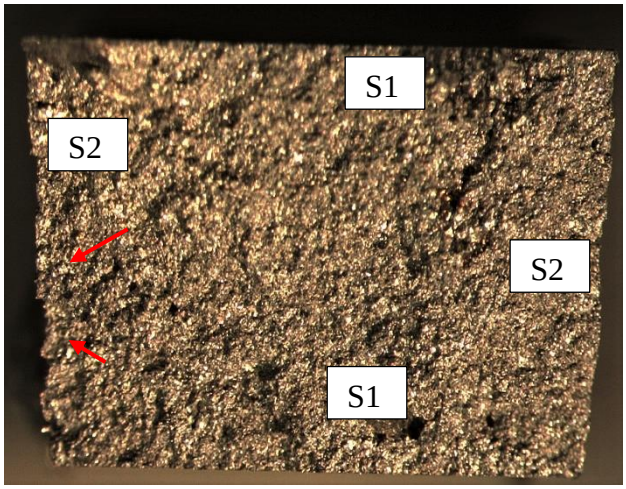

(d)

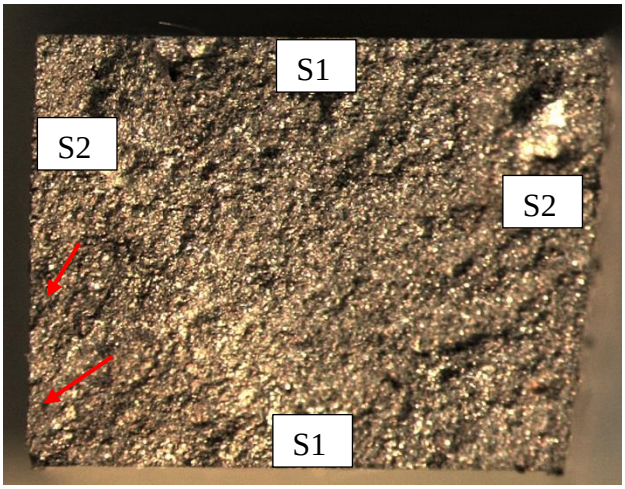

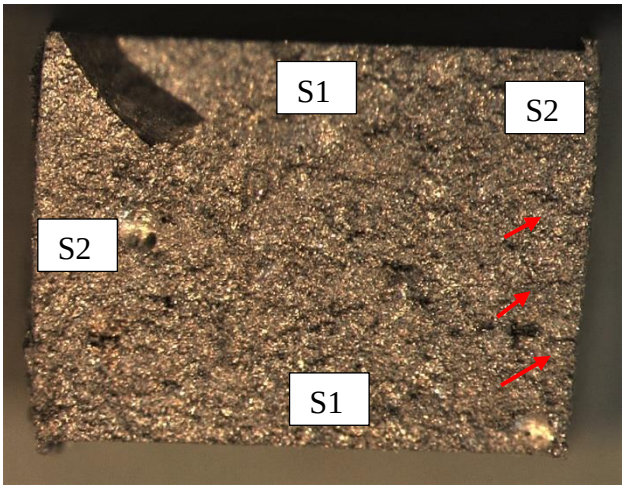

(e) (f)

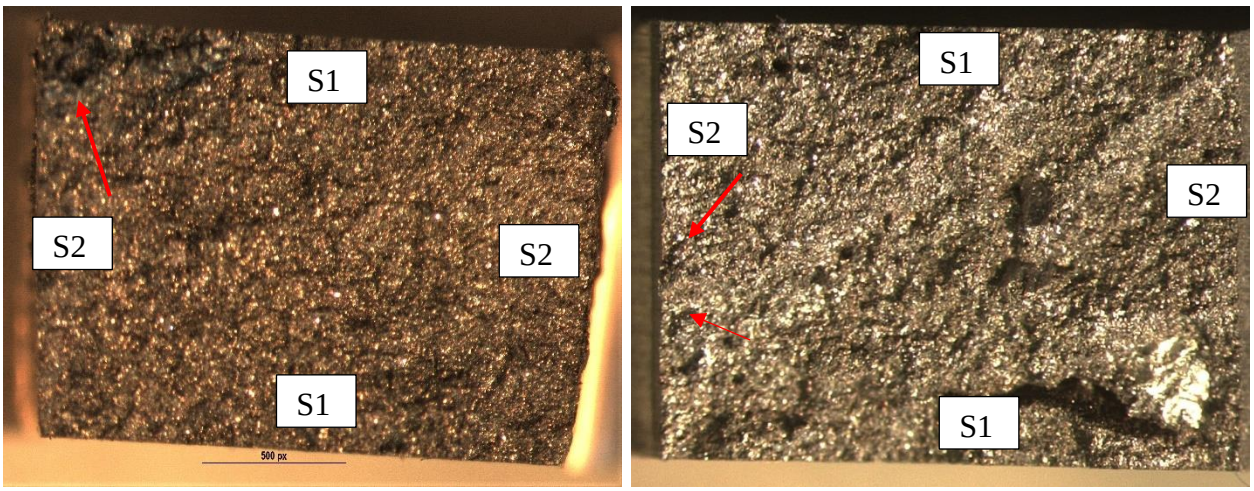

(g) (h)

Figure 10.9: Optical micrographs of fractured surfaces, a) 1000 RPM, 0.1 mm/rev, $0.6S_{ut}$, b) 1000 RPM, 0.1 mm/rev, 0.8, c) 3000 RPM, 0.1 mm/rev, $0.6S_{ut}$, d) 3000 RPM, 0.1 mm/rev, $0.8S_{ut}$, e) 1000 RPM, 0.3 mm/rev, $0.6S_{ut}$, f) 1000 RPM, 0.3 mm/rev, $0.8S_{ut}$, g) 3000 RPM, 0.3 mm/rev, $0.6S_{ut}$, h) 3000 RPM, 0.3 mm/rev, $0.8S_{ut}$. S2: Peripheral milled, S1: Face milled

The crack propagation mechanism was further investigated using SEM micrographs, shown in Figures 10.11, 10.12, 10.13. Four types of damage mechanism was identified by inspecting the fractured surface. They are particle fracture, particle-matrix debonding, matrix fracture, dimples formed by the matrix, highlighted in region (A,D), E, B, C respectively in Figures 10.11, 10.12 and 10.13, concurring with observations made by Li et al [137]. The damage mechanisms remained the same in all the machining and loading conditions. EDS mapping of the images were obtained to determine the aluminum and SiC present in the composite.

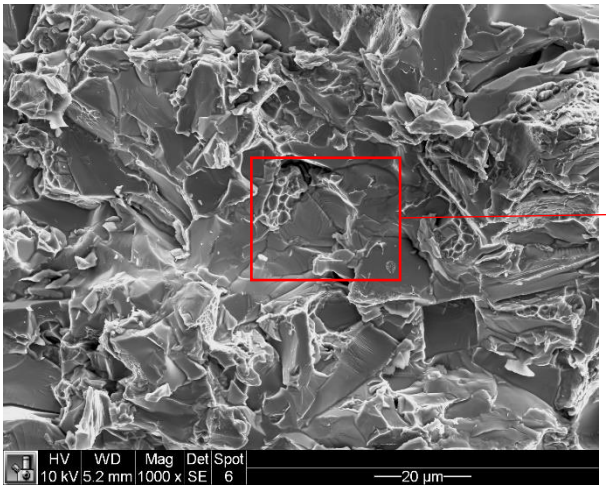
HV
10 kV
WD
5.2 mm
Mag
1000 x
Det
SE
Spot
6
20 µm

(a)

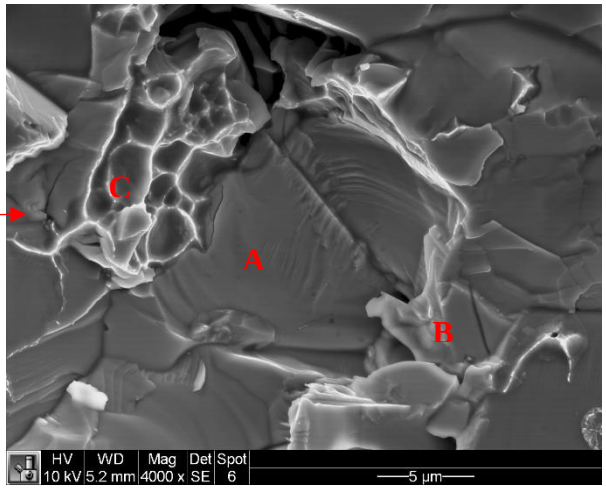
C
A
B
HV
10 kV
WD
5.2 mm
Mag
4000 x
Det
SE
Spot
6
5 µm

(b)

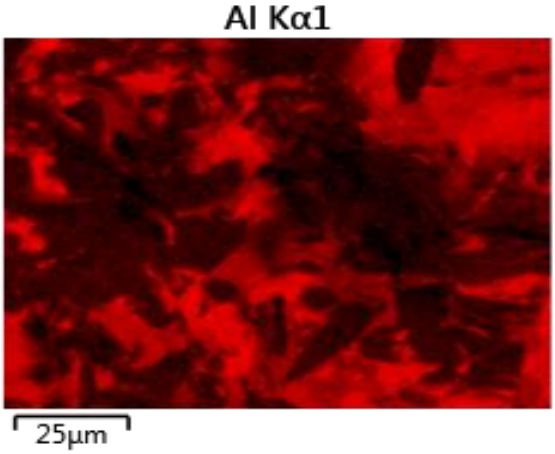
Al Kα1
25µm

(c)

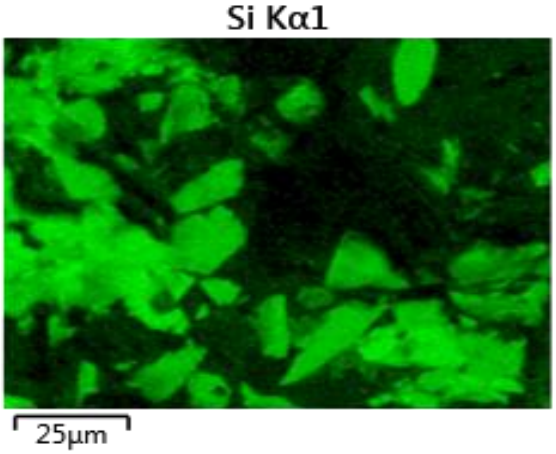
Si Kα1
25µm

(d)

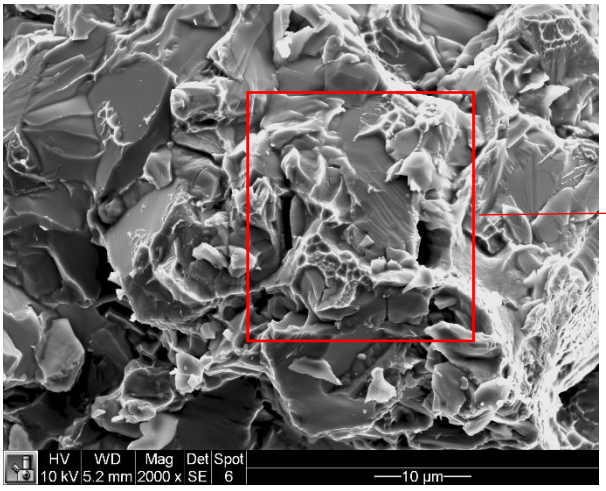
HV
10 kV
WD
5.2 mm
Mag
2000 x
Det
SE
Spot
6
10 µm

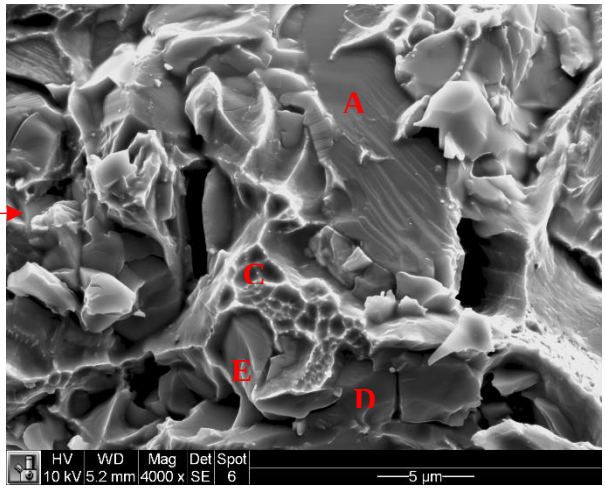
A
C
E
D
HV
10 kV
WD
5.2 mm
Mag
4000 x
Det
SE
Spot
6
5 µm

(e) (f)

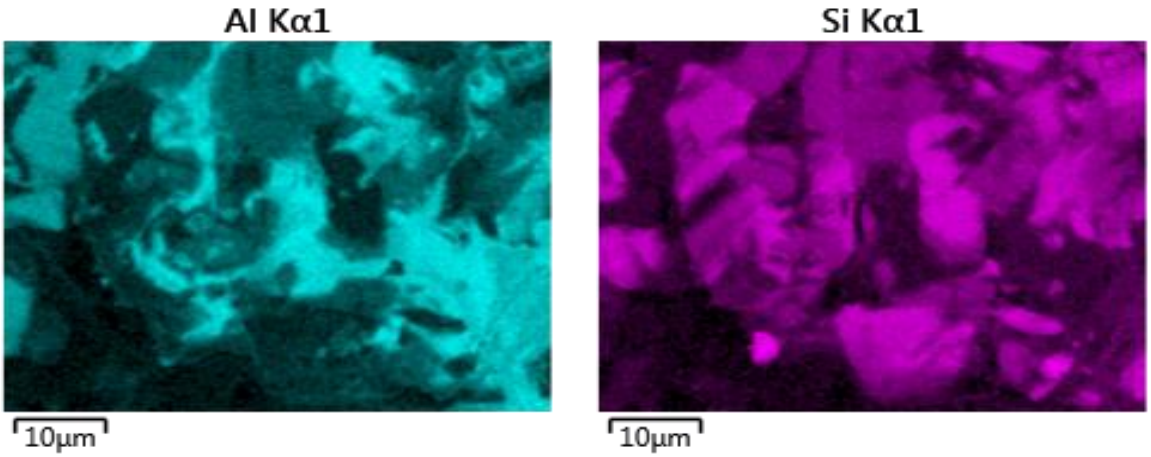

(g) (h)

Figure 10.10: SEM micrograph of fractured surface at 0.1 mm/rev and 3000 RPM at $0.6S_{ut}$, a) 1000 x, showing the SiC particles and aluminum matrix, b) Magnified to 4000x, Region A: Fractured SiC showing cleavage line, B: matrix cracking, C: matrix forming dimples, c and d) EDS map showing aluminum and SiC respectively, e) 2000x, showing embedded SiC particle and matrix, f) Magnified to 4000x, region D: fractured SiC particles, E: Particle debonding from the matrix, g and h) EDS map showing aluminum and SiC respectively.

Particle fracture was typically observed in particles that were larger than 10 μm. Two types of particle fractures were identified on the fractured surface. Cleavage lines were observed on large SiC particles with aspect ratio close to 1, indicating that these particles have fractured along the fractured surface, highlighted as region A. Additionally, particles with large aspect ratio, with larger axis oriented along the crack path were found to experience fracture perpendicular to the

fractured surface, region D. Owing to the high strength of SiC particles, the occurrence of particle fracture was low.

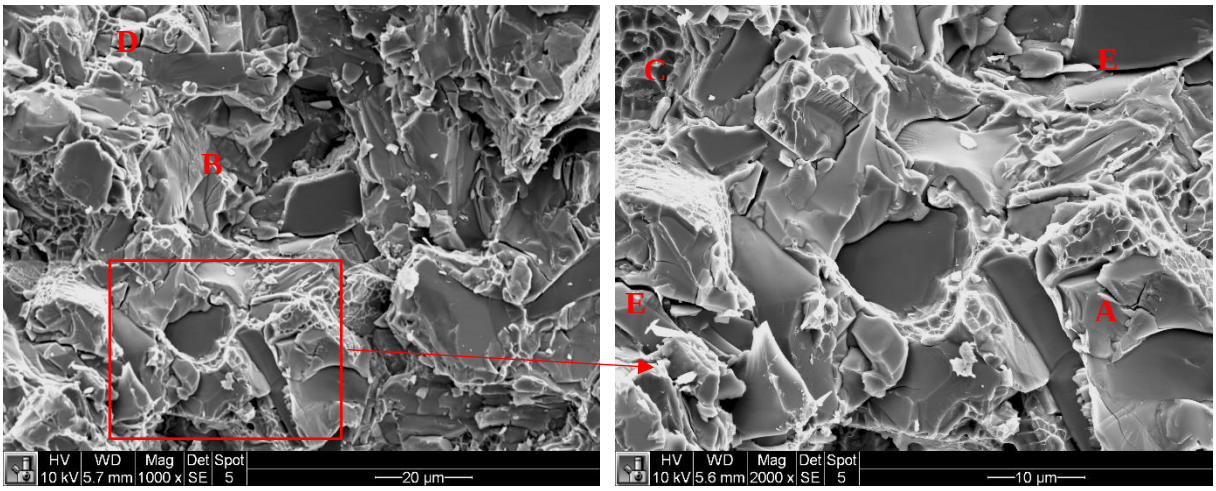

(a) (b)

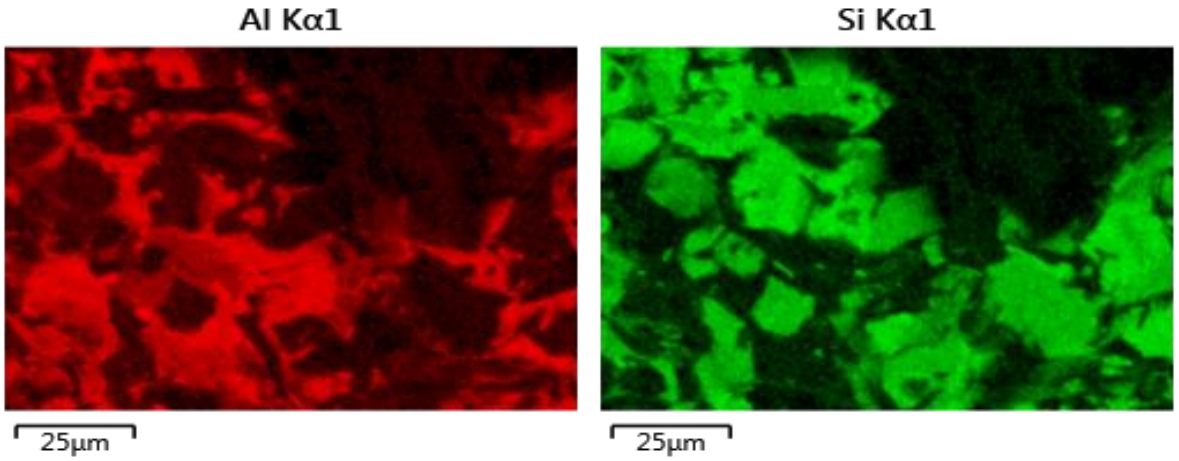

(c) (d)

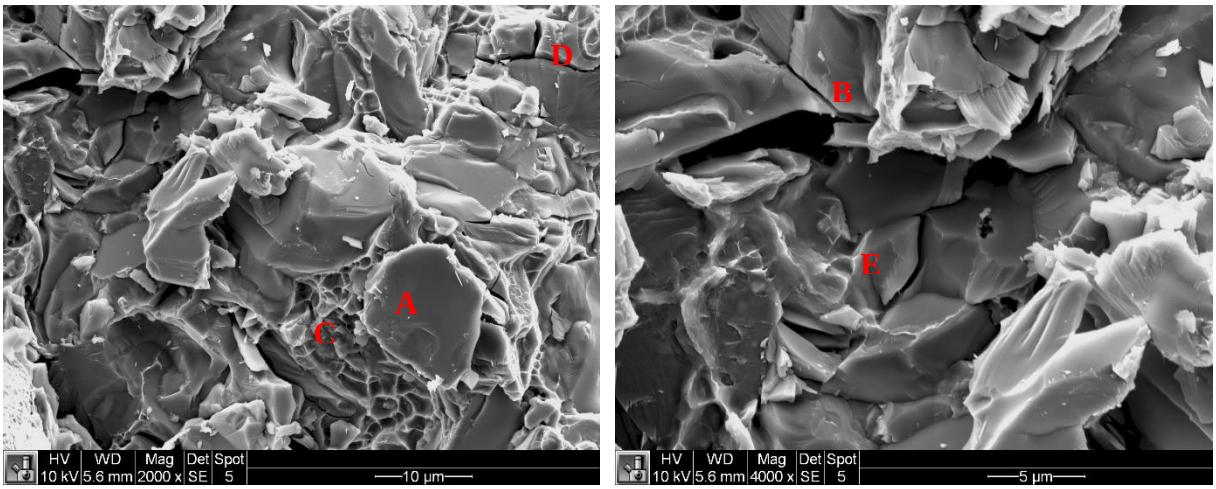

(e) (f)

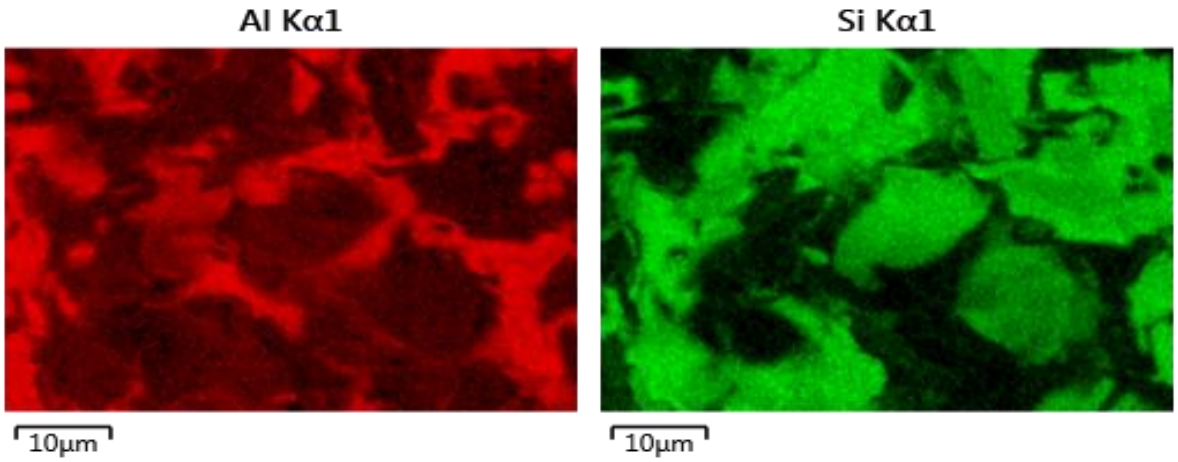

(g) (h)

Figure 10.11: SEM micrograph of fractured surface at 0.3 mm/rev and 3000 RPM at $0.6S_{ut}$, a) 1000 x, showing the SiC particles and aluminum matrix, region B: matrix cracking, D: fractured SiC particles, b) Magnified to 4000x, Region A: Fractured SiC showing cleavage line, C: matrix forming dimples, E: Particle debonding from the matrix, c and d) EDS map showing aluminum and SiC respectively, e) 2000x, showing embedded SiC particle and matrix, f) Magnified to 4000x, showing aluminum and SiC particles, g and h) EDS map showing aluminum and SiC respectively

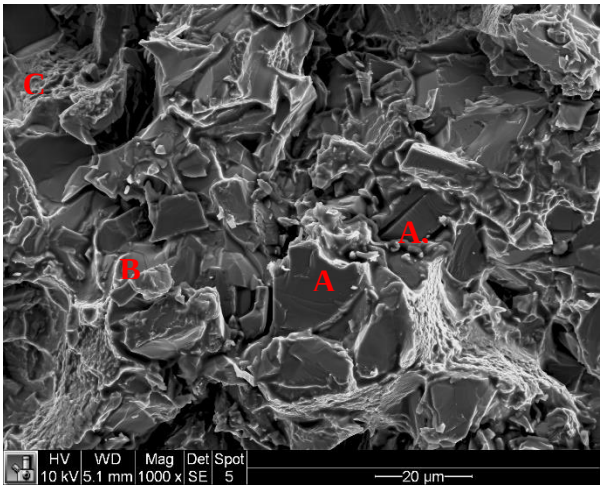
C
A
B
A
HV
10 kV
WD
5.1 mm
Mag
1000 x
Det
SE
Spot
5
20 µm

(a)

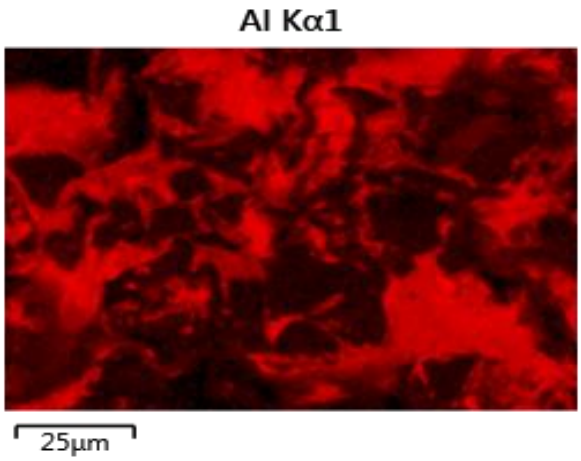
Al Kα1
25µm

(b)

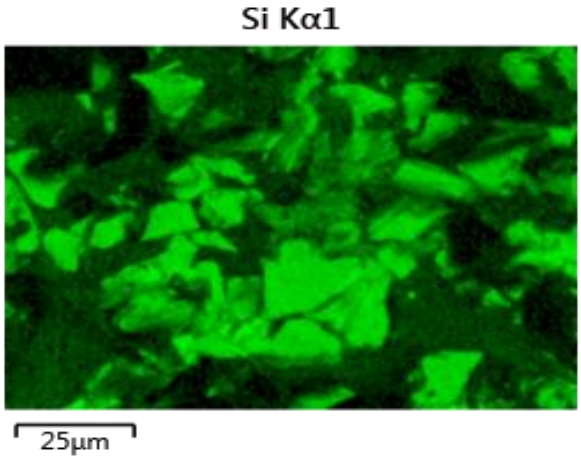
Si Kα1
25µm

(c)

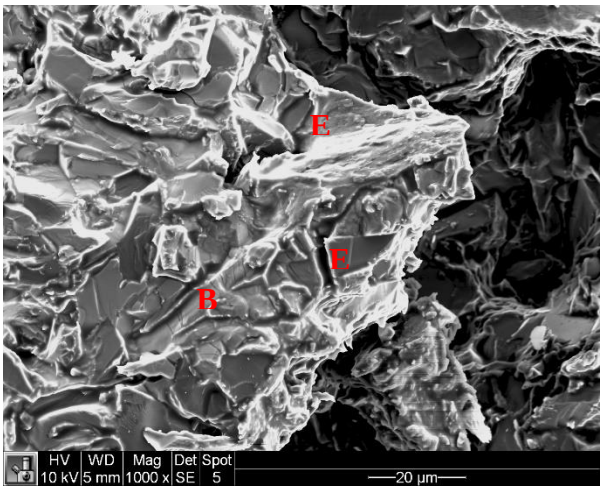
E
E
B
HV
10 kV
WD
5 mm
Mag
1000 x
Det
SE
Spot
5
20 µm

(d)

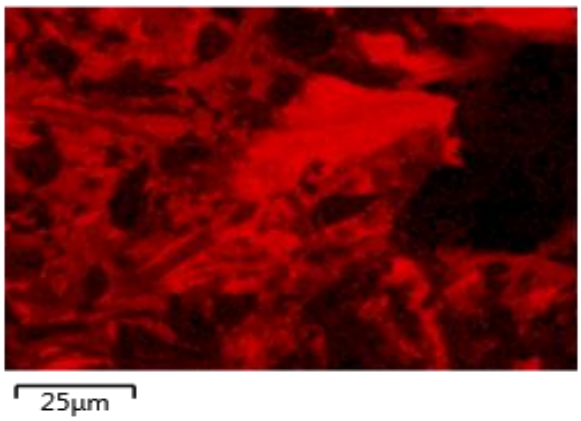
Al Kα1
25µm

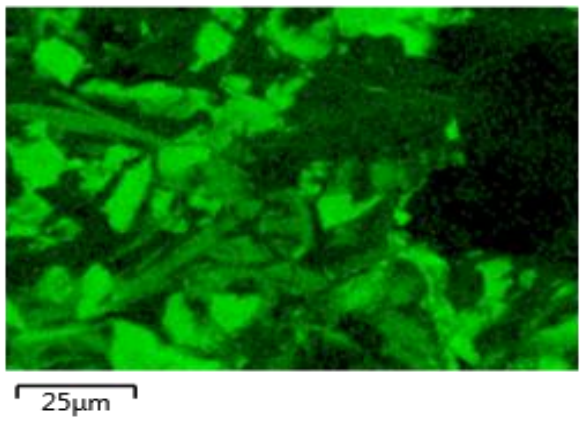
Si Kα1
25µm

(e) (f)

Figure 10.12:SEM micrograph of fractured surface at 0.3 mm/rev and 1000 RPM at $0.6S_{ut}$, a) 1000 x, showing the SiC particles and aluminum matrix, region A: Fractured SiC showing cleavage line, B: matrix cracking, C: matrix forming dimples, D: fractured SiC particles, and b and c) EDS map of (a) showing aluminum and SiC respectively, d) 1000x, showing embedded SiC particle and matrix, e and f) EDS map of (d) showing aluminum and SiC respectively

Particle debonding from the matrix was found to occur more often, highlighted in region E and voids present on the surface. As the crack propagates through the surface, the debonding may occur due to localized high stresses around the crack tip. The high stresses results in the failure of the weaker interfacial bond between the particles and the matrix. Debonding was found to occur in both small and large particles.

Two types of matrix failure were observed on the surface, matrix cracking and dimples highlighted in regions B and C respectively, in Figures 10.11, 10.12 and 10.13. Matrix cracking was found to typically occur in the vicinity of particle debonding and fracture. This results in rapid overloading of the neighboring matrix, causing it to exhibit brittle failure. Matrix strongly adhered to the SiC particles were found to form dimples on the surface, shown in region C. As the crack propagates, voids begin to form in the matrix at the matrix-particle interface due to its lower strength . These voids grow and coalesce causing failure. The formation and coalition of voids in the matrix form the dimple features.

Therefore, it can be concluded that the damage mechanism depends on the particle size and aspect ratio and the interfacial bond strength. The crack initiation sites were influence by the machining defects on the surface, however, the crack propagation and damage mechanisms remained the same for all the machining conditions.

10.1.4 Summary

Surface integrity of the milled functionally gradient composites were evaluated through roughness measurements and inspection of machined and sub-surface micrographs and variation in microhardness and its subsequent effect on their fatigue behavior.

- Specimens machined at 0.1 mm/rev exhibited rough surface with randomly spaced high peaks and valleys, typical of softened and re-solidified surface.
- Owing to the extensive plastic deformation, sub-surface damage extending upto 60 μm and 80 μm were observed for 0.1 mm/rev, 1000 RPM and 0.1 mm/rev, 3000 RPM respectively and the microhardness was found to increase near the machined surface.
- Coupons machined at 0.1mm/rev and 3000 RPM exhibited lowest fatigue life owing to the high surface roughness due to the presence of surface defects and sub-surface damages induced while machining.
- The fatigue cracks were found to initiate from the peripherally milled surface and the fracture was typically found occur between 19 to 21% SiCp along the gauge length

- SEM fractography indicated the presence of four distinct fracture mechanisms, 1) particle fracture along the fractured surface, perpendicular to the fractured surface 2) particle-matrix debonding 3) matrix fracture 4) dimples formed by the matrix.

10.2 Magnesium Composites

Metal matrix composites(MMCs) consists of light weight metallic matrix incorporating various reinforcing phases. Reinforcing aluminum and magnesium alloys with ceramics such as SiC, B_4C and Al_2O_3 resulted in MMCs with increased specific strength and stiffness, improved creep resistance, thermal shock resistance, corrosion resistance and reduction in thermal elongation[3,7]. However, owing to the high hardness of these reinforcements surface damage is induced while machining. When the cutting edge interacts with the reinforcement particles, they may be pulled out or pushed into the matrix forming a void on the surface, are dragged along the surface producing ridges, or the particles may fracture and matrix cracking occurs owing to the limited ductility[138]. The damages on the machined surface act as stress concentrators and have a detrimental effect on fatigue life. Therefore, in order to avail the outstanding potential of metal matrix composites for structural components, it is imperative to study their behavior under cyclic loading. The fatigue performance of aluminum composites is reported by several studies[92,98], while only very few studies were performed on magnesium composites[139,140]. Magnesium composites are very promising in aerospace and biomedical industries owing to the matrix being the lightest metal with a density of 1.74 g/cm^3 and having highly tailorable mechanical properties through the addition of ceramics [9,141]. In addition, magnesium alloys possess high dimensional stability, excellent damping capacity and recyclability[142].

Fatigue behavior of MMCs are quite complex due its dependence on the manufacturing processes used, reinforcement particles, metallic matrix and the interface between the particles and the matrix[87]. The composites are usually produced through squeeze casting process, spray co-deposition of matrix and particles and powder metallurgy techniques, that are conducted at high temperatures and mismatch in coefficient of thermal expansion between the matrix and the reinforcements induces thermal residual strain in the composite as it cools down to the room temperature. The large residual strain results in an increase in dislocation density in the matrix[88–90]. As a result, cyclic softening behavior was exhibited by composites similar to the cold worked metal with high dislocation density[91].

In addition to the dislocation densities, the pores and inclusions introduced in the composites during the manufacturing process also have a significant effect[86]. Cast composites were observed to have lower fatigue life due to the presence of porosity and inclusion in addition to the microstructural defects like particle clusters and non- uniform particle distribution in comparison to forged and extruded composites. Secondary manufacturing processes like forging and rolling help in breaking up the agglomeration, homogenizing the distribution, eliminating the porosity and improving the interfacial bonding[92].

Only limited studies have reported the effect of machining induced damage on fatigue life of composites[96,97]. The machining induced surface damage were studied as a function of particle size and machining conditions. The damage in the form of particle fracture and pull out were reported to be increase with the particle size[96]. Consequently, the fatigue life improved with decreasing particle size. The fatigue life was found to depend significantly on the surface and sub-

surface quality generated, with coarser surface finish exhibiting a significantly lower life. In addition, the deformation in a machining resulted in surface softening reducing the fatigue life[97]. Therefore, it is imperative to study the surface and sub surface damage induced while machining on the fatigue life to produce reliable components.

The purpose of this study is to experimentally investigate the machined surface topography and the effect of milling induced surface defects on the fatigue behavior of extruded AZ91/SiCp/15%. The surface topology was studied in terms of surface roughness parameters and inspection of machined surface through SEM micrographs. SEM fractography was performed to identify the crack initiation and fracture mechanism of the matrix and the SiC reinforcement particles.

10.2.1 Experimental set up and procedure

Material

The material used in this investigation was supplied by Pacific Northwest Laboratory in the rod form. Material was vacuum cast into 203 mm diameter billets and then extruded into rods of final diameter 55 mm, followed by heat treatment at T5 condition. The composite consists of AZ91-T5 magnesium matrix reinforced with 15 vol.% SiC particles.

Specimen geometry and fabrication

The sequence of steps involved in the fabrication of the specimen are shown in Figure 10.14. The extruded composite was sectioned into 5 mm thick disks using waterjet. The disk was then face milled to reduce the thickness to 3mm, shown in 10.14 a. Figures 10.14 c and d show the rectangular specimen with 9.04 mm wide gauge section machined using waterjet. Peripheral

milling was used to reduce the width of the gauge section to 6 mm by removing 1.52 mm on either side. The machining conditions used for face milling and peripheral milling operations are given in Table 10.4. The geometry of the rectangular miniature specimen with dimensions is shown in Figure 10.14 e. The radius of curvature in the specimen resulted in a stress concentration factor of 1.4[135].

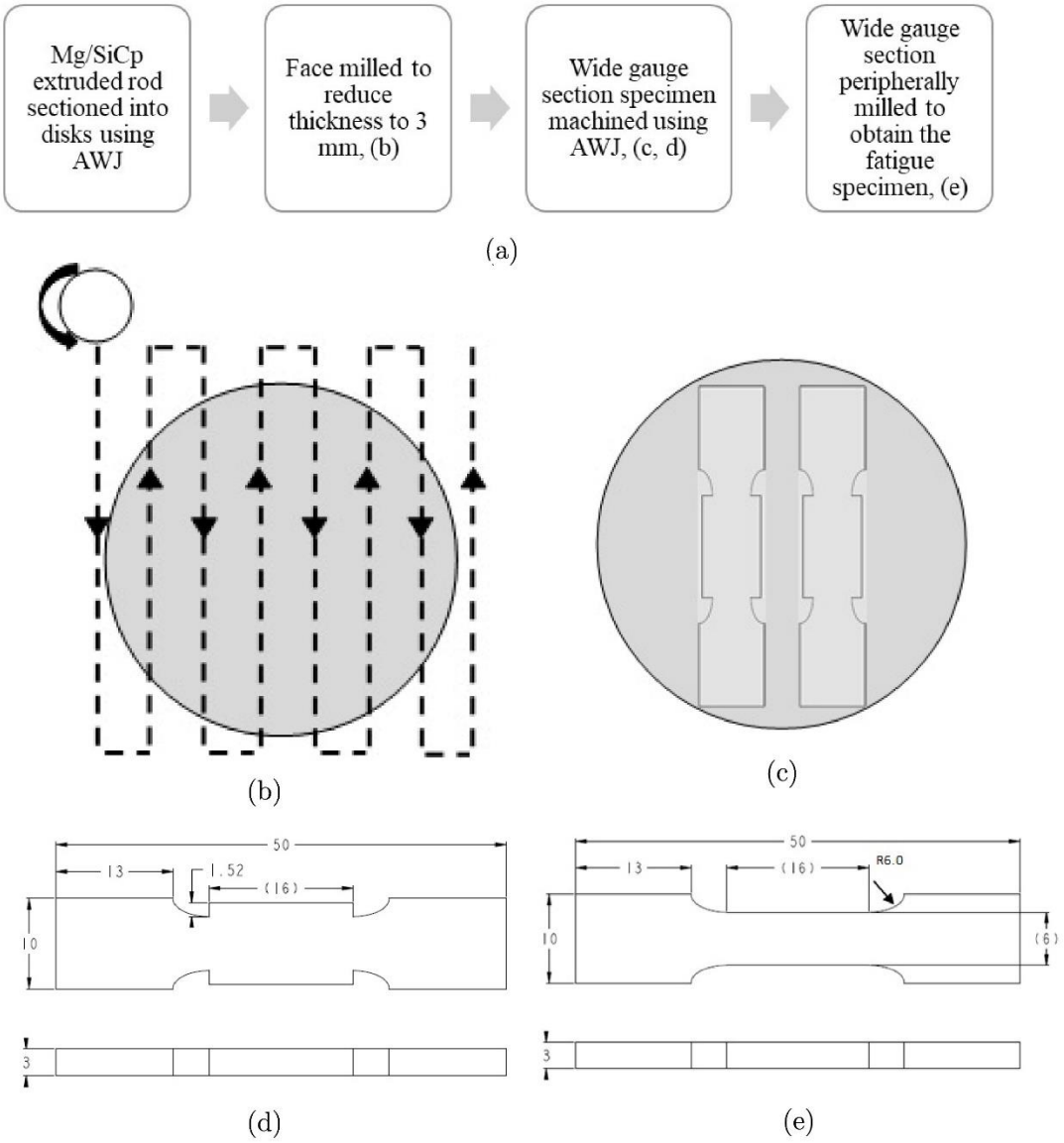

Figure 10.13: Schematic of steps involved in specimen fabrication. All dimensions are in mm.

The face milled surface and the peripherally milled surfaces are referred to S1 and S2 respectively. PCD with small axial depth of cut was used for the face milling process to ensure minimum surface damage on S1. Owing to the limitation of the composite rod dimension, miniature specimens were developed and tested in this study. A total of 35 specimen were fabricated in this experimental study using the machining conditions presented in Table 10.6. All the dimensions of the machined specimen after face milling of width and peripheral milling of specimen edges and their surface roughness were examined and quantified. Peripherally milled and face milled surfaces were analyzed through the measurement of 2D surface roughness profiles using Mahr surface profilometer. The surface roughness was quantified in terms of average surface roughness, R_a, root mean square roughness, R_q, peak to valley height roughness, R_y, and ten point average roughness, R_z.

Table 10.4: Cutting tool and machining conditions

Parameters	Face milled: S1	Peripherally milled: S2
S2, Cutting tool	PCD tool, 6.35 mm, helix: 0°	Square end Carbide tool, 6.35 mm, C2 grade, helix: 30°, rake angle: 4°
Feed rate	0.3 mm/rev	0.1, 0.3 mm/rev
Spindle speed	3000 RPM	1000, 3000 RPM
Axial depth of cut	0.254 mm	3 mm
Radial depth of cut	3.175 mm	0.506 mm

Fatigue testing

The axial fatigue tests were performed using INSTRON 8511 20 kN servo-hydraulic test frame at 10 Hz. Constant stress amplitude tension-tension tests were performed with stress ratio, R = 0.1 at four stress levels, $0.8S_{ut}, 0.6S_{ut}, 0.4S_{ut}$ and $0.25\ S_{ut}$, where S_{ut} is the ultimate tensile strength of

the material to obtain the number of cycles to failure. The cycles to failure were measured and recorded through LABVIEW interface. The fatigue tests were run up to five million cycles. If the fracture had not occurred by then, the test was stopped, and infinite life was assumed for the specimen.

Further, the optical and SEM micrographs were also utilized to examine the fractured surface to identify mechanisms of fracture. EDS was employed to distinguish the matrix and particle fracture on the surface.

10.2.2 Surface topography of machined surface

The surface quality of the machined surface was studied through two-dimensional surface roughness profile measurements along the gauge section through contact profilometry. Machining induced damages on the surface are detrimental to the life of a component. The roughness profiles of the machined surface show the deviations from the nominal surface that can act as stress concentration sites. Typical roughness profiles of the peripheral and face milled surfaces are shown in Figure 10.15. Good surface finish was obtained for all the machining conditions, observed in Figure 10.15 and through SEM micrographs in Figure 10.16. Surface profiles of all the specimens were obtained and the average surface roughness parameters with standard deviations for face milled and peripheral milled surfaces are given in Table 10.5. Surface profiles are given in Appendix F.

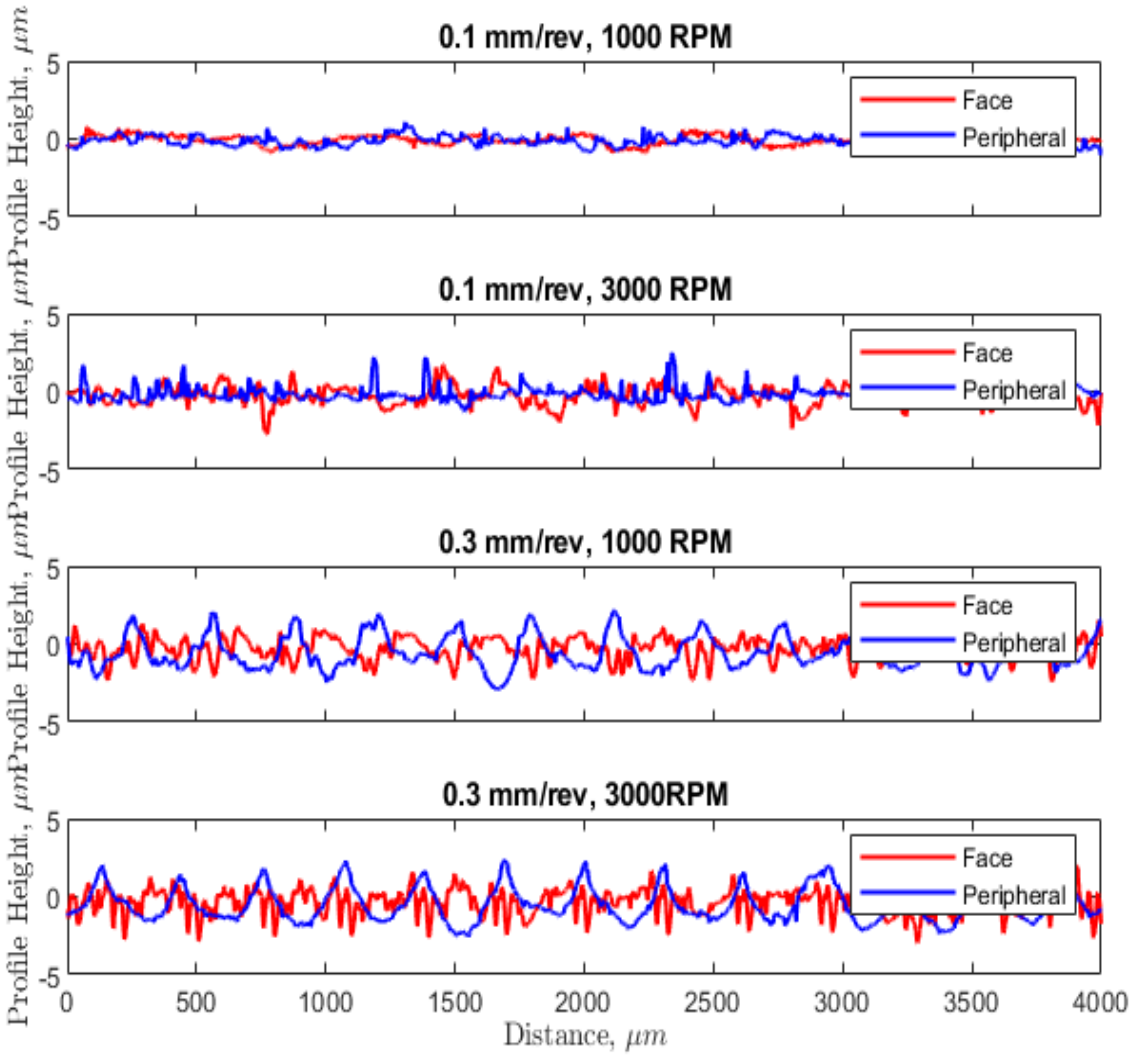

Figure 10.14: Typical surface profiles of machined surfaces

Table 10.5: Average surface Roughness of face milled surface and peripherally milled surfaces

Milling	Feed (mm/rev)	Speed (RPM)	R_a (µm)	R_q (µm)	R_y (µm)	R_z (µm)
Face	0.3	3000	0.53 ± 0.13	0.67 ± 0.18	3.42 ± 0.72	4.25 ± 0.79
Peripheral	0.1	1000	0.29 ± 0.07	0.39 ± 0.11	2.97 ± 0.85	2.22 ± 0.63
Peripheral	0.1	3000	0.37 ± 0.04	0.57 ± 0.08	4.63 ± 0.58	3.15 ± 0.36
Peripheral	0.3	1000	1.00 ± 0.02	1.14 ± 0.05	5.60 ± 0.24	4.51 ± 0.28
Peripheral	0.3	3000	0.97 ± 0.01	1.13 ± 0.02	4.80 ± 0.18	4.18 ± 0.12

The SEM micrographs of specimen machined at 0.1 mm/rev did not show any feed marks on the surface at 67x, observed in Figure 10.16 a and b. The SiC particles were found to be scattered on the surface. At 0.3 mm/rev, prominent feed marks were observed on the surface. Although, extensive scattering of SiC particles were not observed at this condition, the feed marks contribute to the increased surface roughness, shown in Figure 10.16 c and d. The feed marks were clearly visible on the face milled surface, shown in Figure 10.16 e.

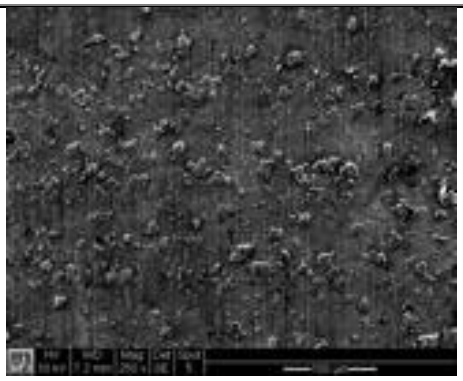

(a) 0.1 mm/rev, 1000 RPM

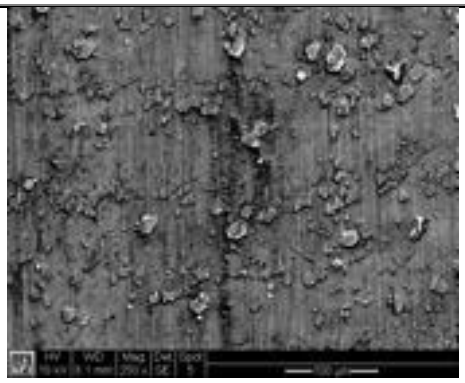

(b) 0.1 mm/rev, 3000 RPM

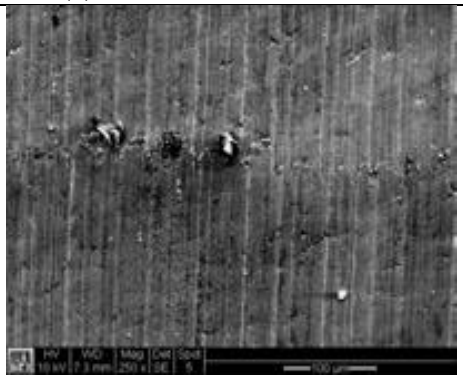

(c) 0.3 mm/rev, 1000 RPM

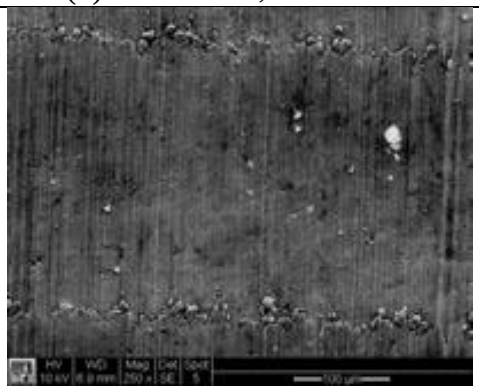

(d) 0.3 mm/rev, 3000 RPM,

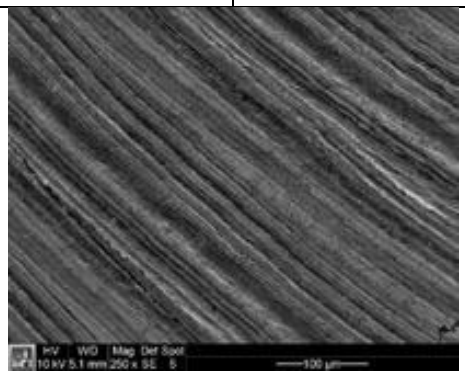

(e) Face milled surface: 0.3 mm/rev, 3000 RPM

Figure 10.15: SEM micrograph of surfaces peripherally milled edge (thickness) surface and face milled flat surface (width).

Upon further magnification, surface defects such as voids due to particle pull out, matrix cracking and particle agglomeration were observed on the surface, shown in Figure 10.17. The matrix cracking can be attributed to the lower ductility of the matrix, and due to hard reinforcement particles dragged along the surface. These defects on the surface act as stress concentrators resulting in early onset of crack initiation and propagation.

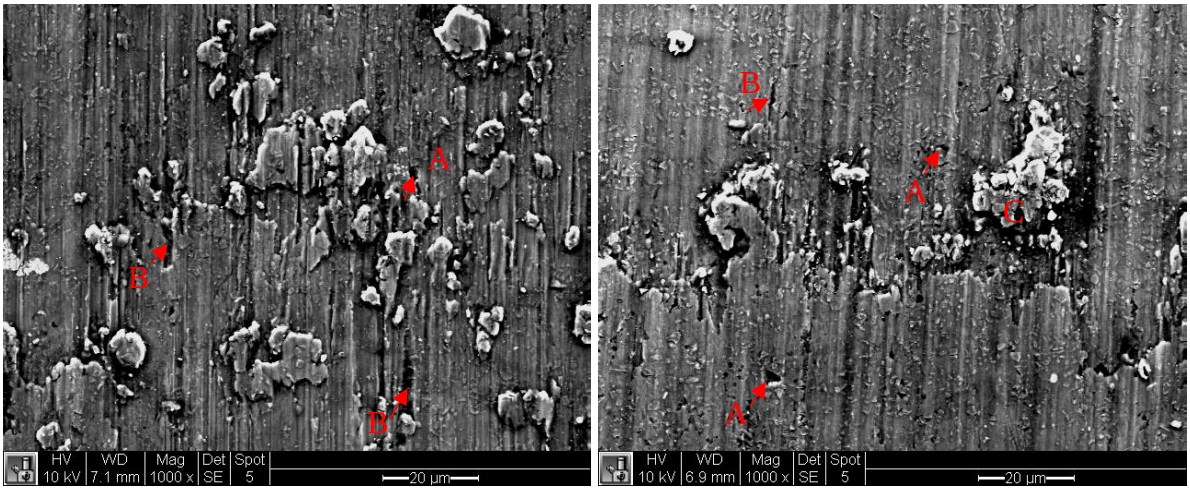

(a) (b)

Figure 10.16: SEM micrographs of the machined surface showing voids(A), matrix cracking(B), particle agglomeration(C)

10.2.3 Fatigue Performance

Fatigue performance of the machined coupons were evaluated by conducting tension-tension fatigue tests to develop the S-N curve. The test was stopped at five million cycles, if the specimen

had not failed by then, it was considered to have infinite life. The maximum stress ratio and number of cycles to failure for all the machining conditions is plotted in Figure 10.18.

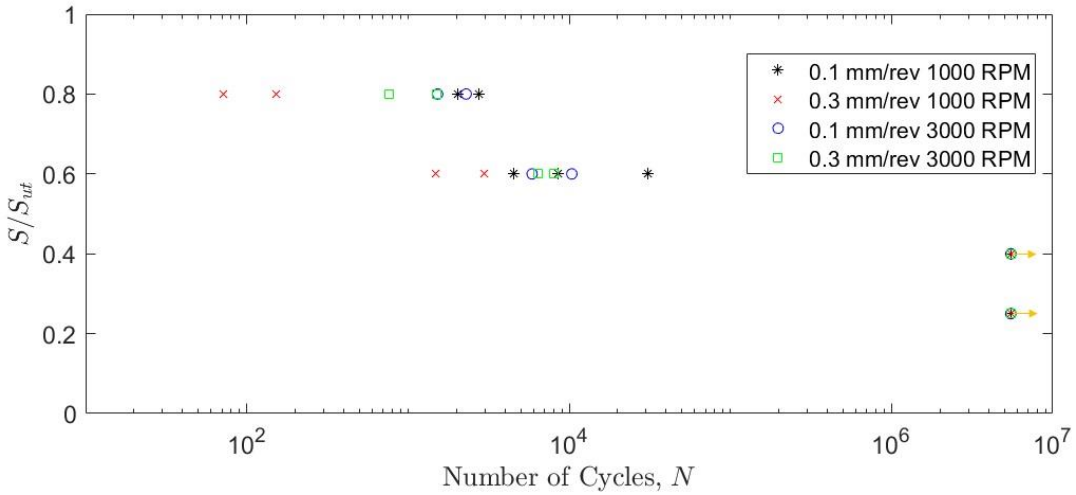

Figure 10.17: Maximum stress ratio vs Number of cycles to failure for machined magnesium composites, $S_{ut} = 360\ MPa$

The fatigue life of the machined specimen machined 0.1 mm/rev was found to be similar irrespective of the spindle speed. This can be attributed to the smoother surface finish with average roughness of 0.3 μm at this feed rate. At 0.3 mm/rev, the roughness increased to about 1 μm. This increase in surface roughness was reflected in the reduction of fatigue life of specimen machined at this feed rate. Although, at 0.3 mm/rev, the surface roughness parameters are about the same for the both the spindle speeds, the specimens machined at 1000 RPM was found to have much lower fatigue life than specimens machined at 3000 RPM.

Fractography

Additionally, the fractured surfaces of specimen under fatigue loading was also investigated. Optical micrographs of the fractured surface were observed to identify the crack initiation sites on

the surface. The cracks were clearly found to initiate from the defects on the peripheral milled surface. Figure 10.18 shows the optical micrograph of fractured surface of specimen with the arrows indicate the crack initiation site. The crack initiation was typically found to occur on the peripheral milled surface(S2). At a load of $0.6S_{ut}$, three distinct regions can be identified from the micrographs, the crack initiation site indicated by arrows, followed by smooth region corresponding to crack propagation and the rough region corresponding to fracture from overloading. However, at a high load of $0.8S_{ut}$, fractured surface did not show a significant crack propagation region. The crack initiation site was further investigated through SEM micrographs, shown in Figure 10.20.

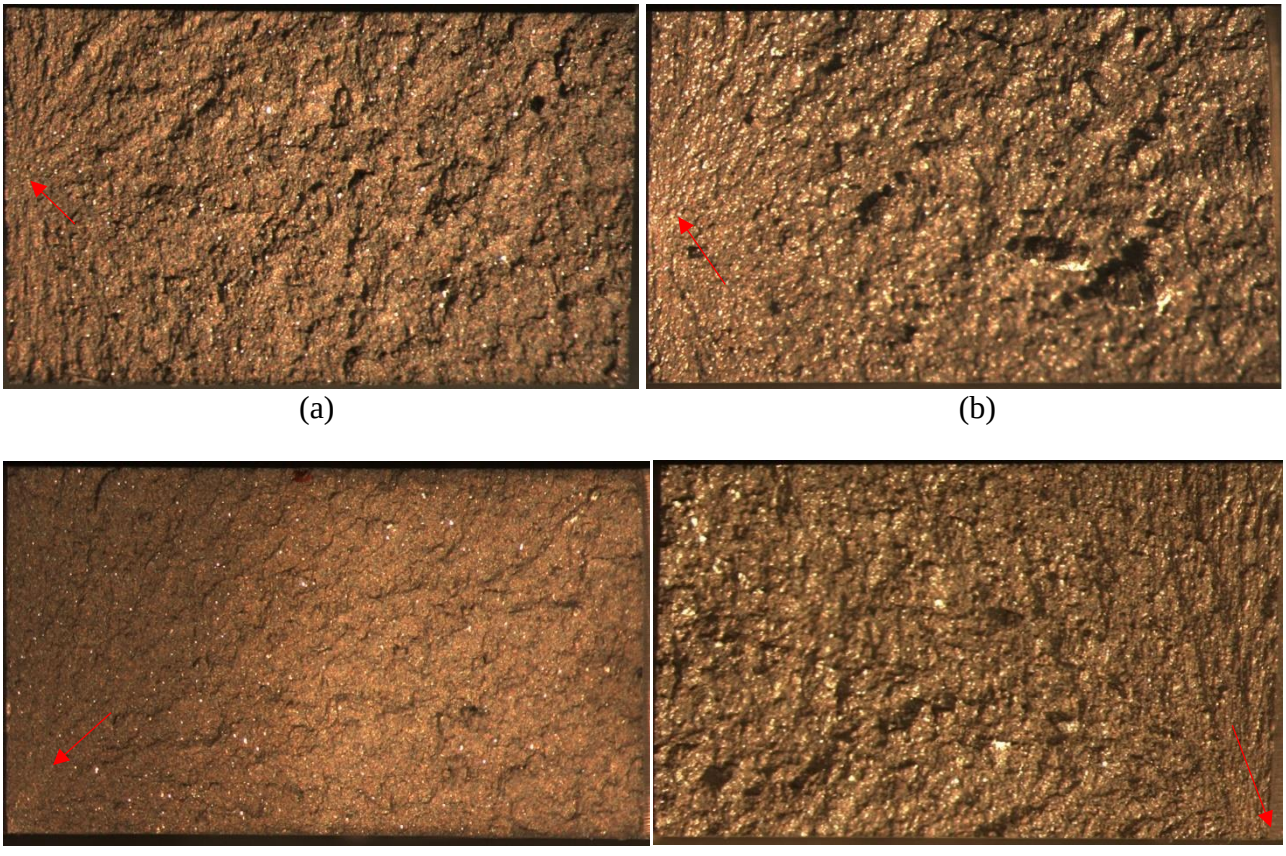

(a) (b)

(c) (d)

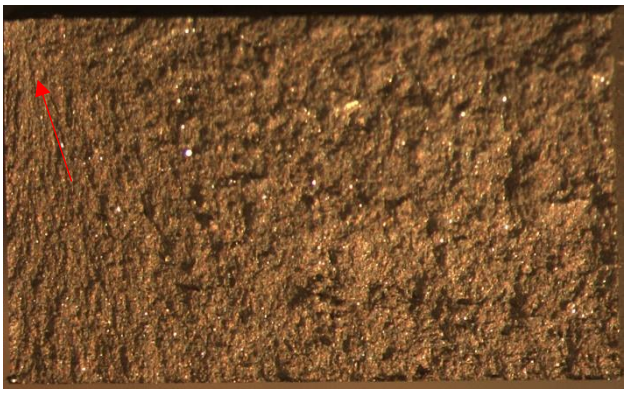

(e)



(f)



(g)



(h)

Figure 10.18: Optical micrographs of fractured surfaces, a) 1000 RPM, 0.1 mm/rev, $0.6S_{ut}$, b) 1000 RPM, 0.1 mm/rev, 0.8, c) 3000 RPM, 0.1 mm/rev, 0.6, d) 3000 RPM, 0.1 mm/rev, $0.8S_{ut}$, e) 1000 RPM, 0.3 mm/rev, $0.6S_{ut}$, f) 1000 RPM, 0.3 mm/rev, $0.8S_{ut}$, g) 3000 RPM, 0.3 mm/rev, $0.6S_{ut}$, h) 3000 RPM, 0.3 mm/rev, $0.8S_{ut}$., arrow indicates crack initiation from peripherally milled surface

Characteristic inward lines were found to be emanating from the crack initiation site, shown in Figure 10.18. Upon further magnification, a crack was found to originate from the surface. The

presence of machining induced defects such as sharp valleys and the presence of particle agglomerations, shown in Figure 10.16, act as stress concentrators initiating cracks.

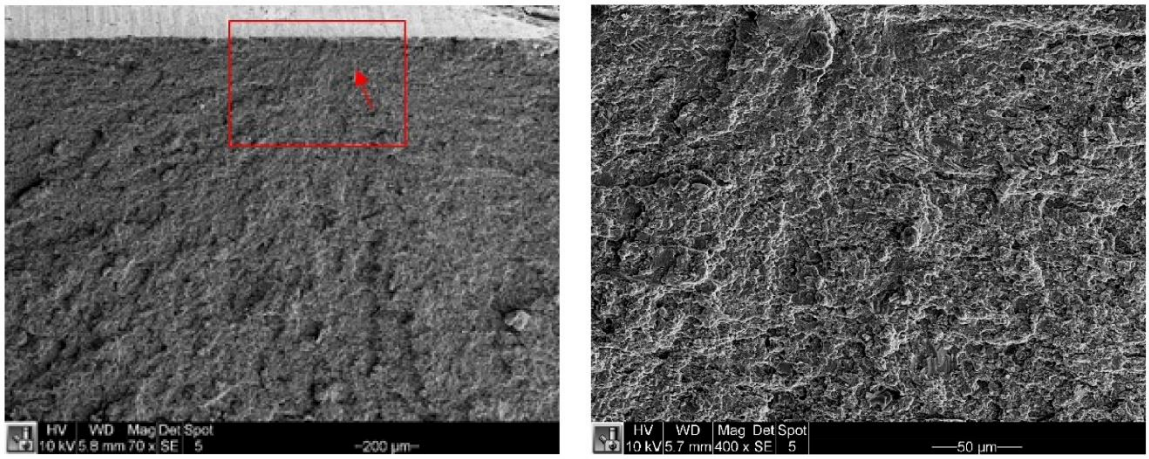

Figure 10.19: SEM micrographs of crack initiation site, arrow indicates the crack origin

Three distinct regions can be identified from the micrographs, the crack initiation site indicated by arrows, followed by smooth region corresponding to crack propagation and the rough region corresponding to fracture from overloading. The interaction of the crack with the reinforcement particles and the matrix was further investigated using SEM micrographs. The SEM micrographs of the fractured surface at $0.6S_{ut}$ is shown in Figures 10.21,10.22 and 10.23 for all the machining conditions.

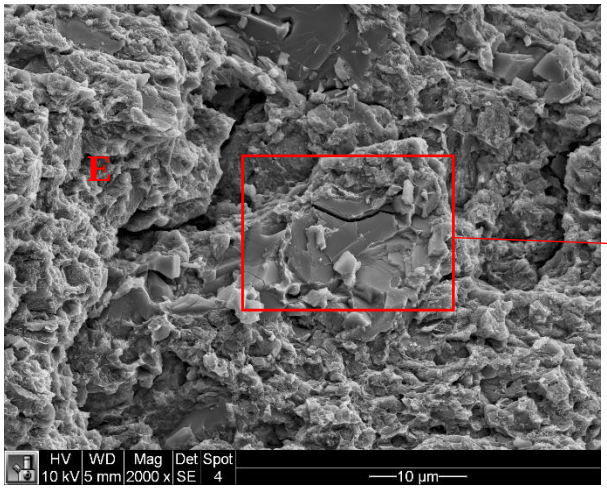
E
HV 10 kV
WD 5 mm
Mag 2000 x
Det SE
Spot 4
10 µm

(a)

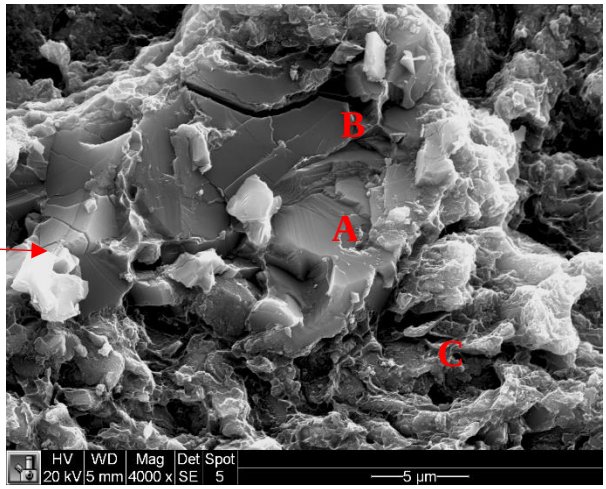
B
A
C
HV 20 kV
WD 5 mm
Mag 4000 x
Det SE
Spot 5
5 µm

(b)

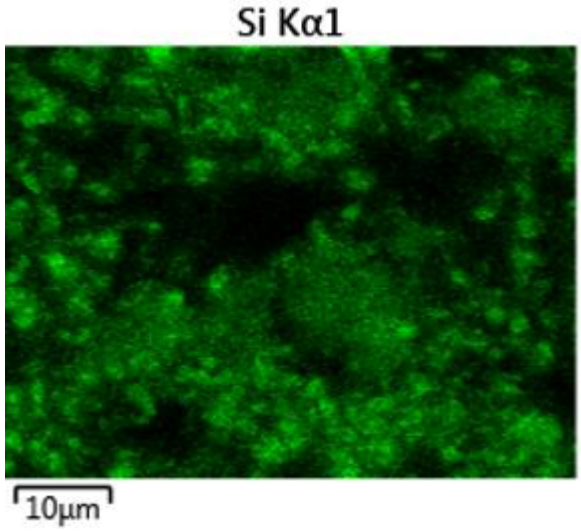
Si Kα1
10µm

(c)

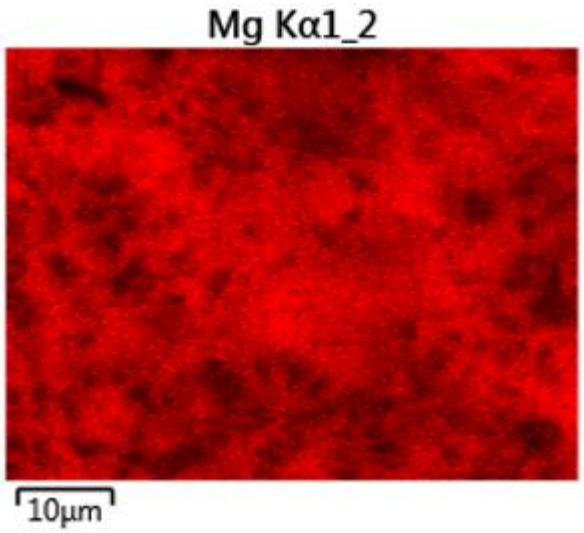
Mg Kα1_2
10µm

(d)

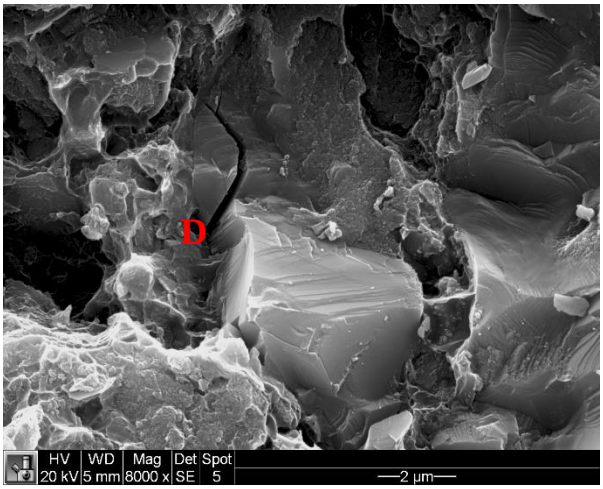

(e)

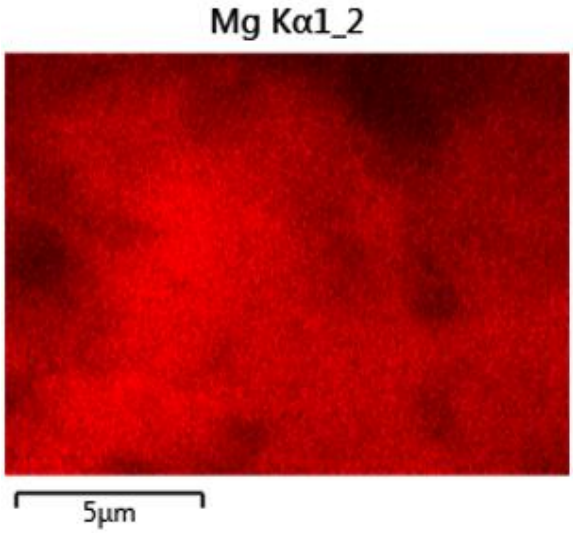

(f)

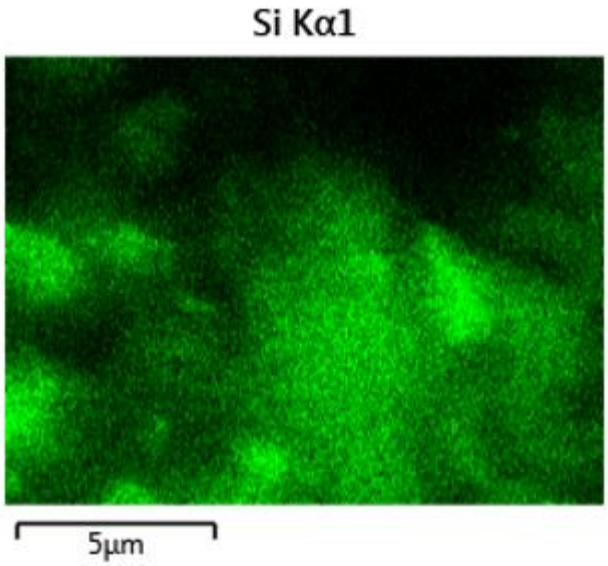

(g)

Figure 10.20: SEM micrographs obtained at 0.1 mm/rev, 1000 RPM, $0.6S_{ut}$, a) Fractured surface at 2000x, region E: ductile fracture of the matrix with smaller particles embedded, b) magnified view at 4000x, region A: cleavage lines typical for brittle fracture, B: particle fracture perpendicular to the fractured surface, C: voids due to particle pull out, c and d) EDS maps of (a)

showing Si and Mg respectively, e) Fractured surface at 8000x, region D: matrix cracking, f and g) EDS maps of (e) showing Mg and Si respectively.

Five distinct regions could be identified for the magnesium composites, (1) Particle fracture along the surface, showing cleavage lines typical for brittle fracture, highlighted as region A, (2) Particle fracture perpendicular to the surface, shown in region B, (3) voids due to debonding and particle pull out, region C (4) Matrix cracking, region D, can be attributed to overloading(5) ductile failure of matrix with embedded SiC particles, region E. Most of the SiC particles were found to be embedded in the matrix and voids represent the particles pulled out from the matrix as in regions C and E. Particle fracture was not extensively observed in this composite due to the smaller SiC particle size in comparison to the aluminum composite. The fractured particles were observed to be 10 μm or larger.

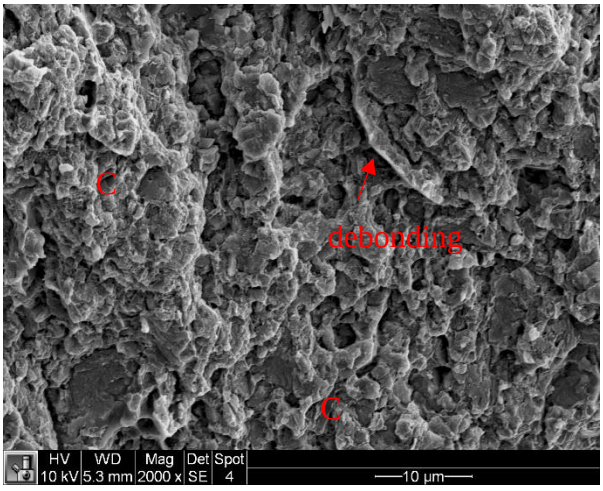
C
debonding
C
HV
10 kV
WD
5.3 mm
Mag
2000 x
Det
SE
Spot
4
10 µm

(a)

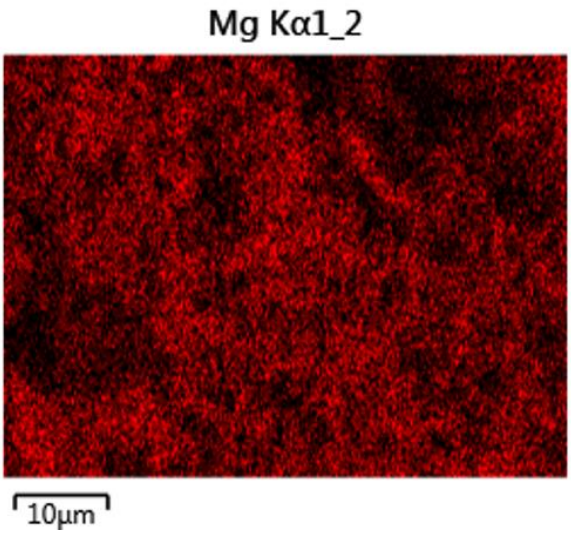
Mg Kα1_2
10µm

(b)

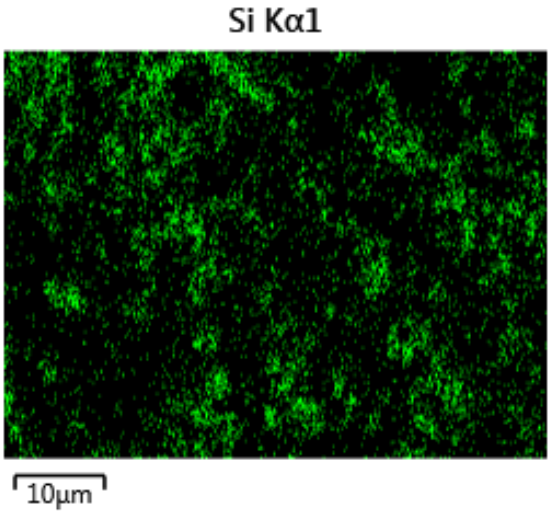
Si Kα1
10µm

(c)

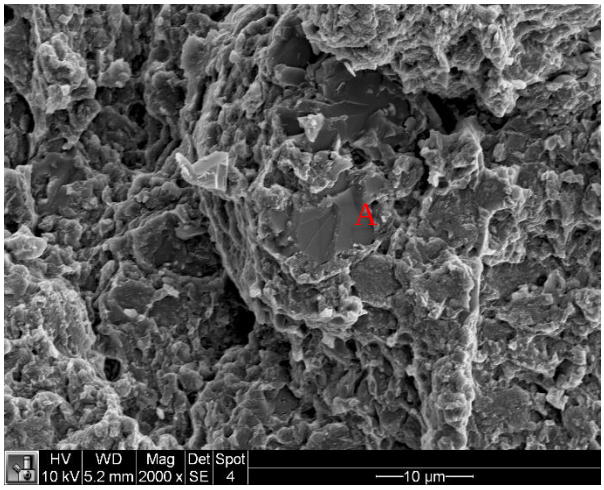
A
HV
10 kV
WD
5.2 mm
Mag
2000 x
Det
SE
Spot
4
10 µm

(d)

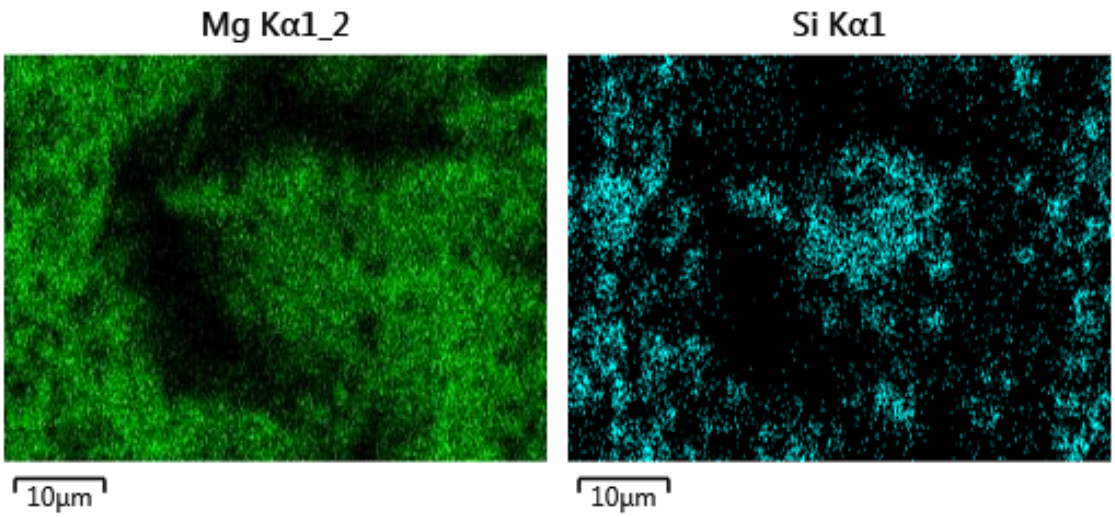

(e) (f)

Figure 10.21: SEM micrographs obtained at 0.1 mm/rev, 3000 RPM, $0.6S_{ut}$, a) Fractured surface at 2000x, showing particle-matrix debonding , b and c) EDS map of (a) showing Mg and Si respectively, d) Fractured surface at 2000x, showing particle fracture and ductile failure of the matrix , e and f) EDS map of (d) showing Mg and Si respectively

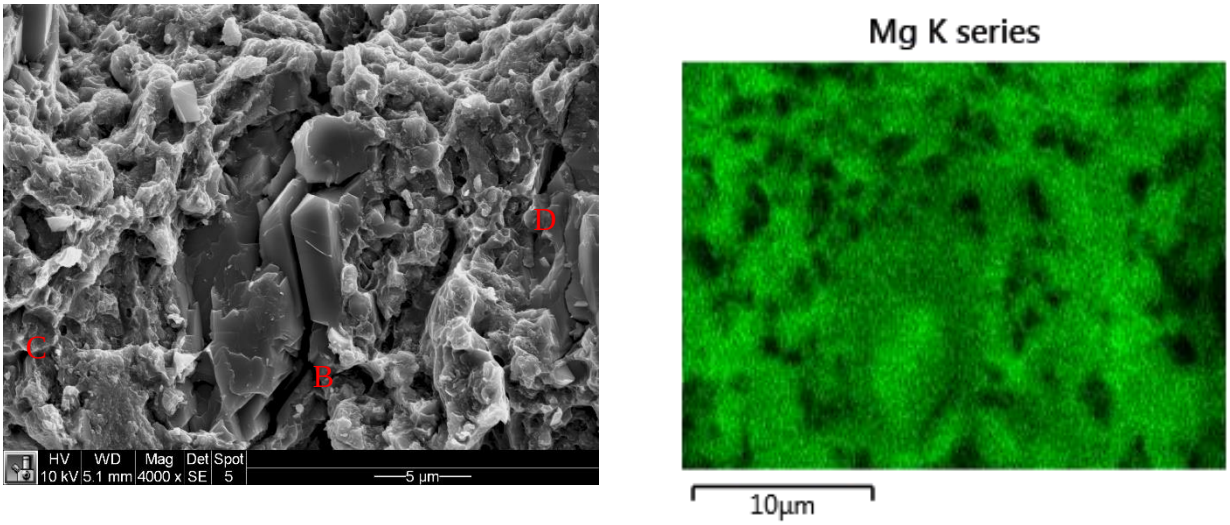

(a) (b)

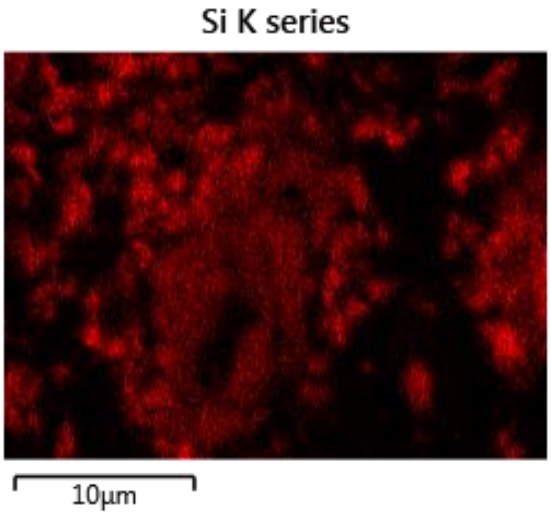

(c)

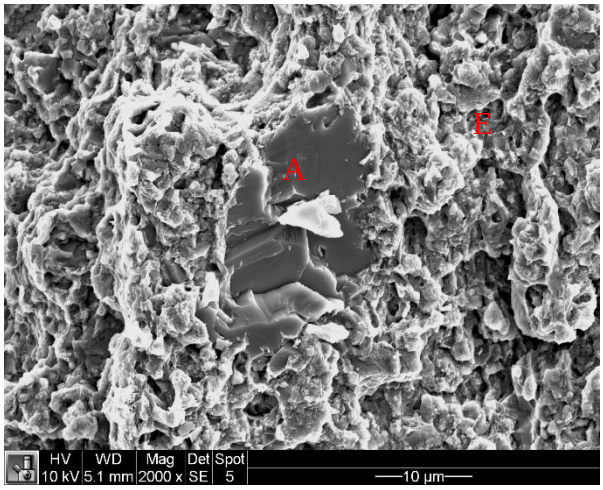

(d)

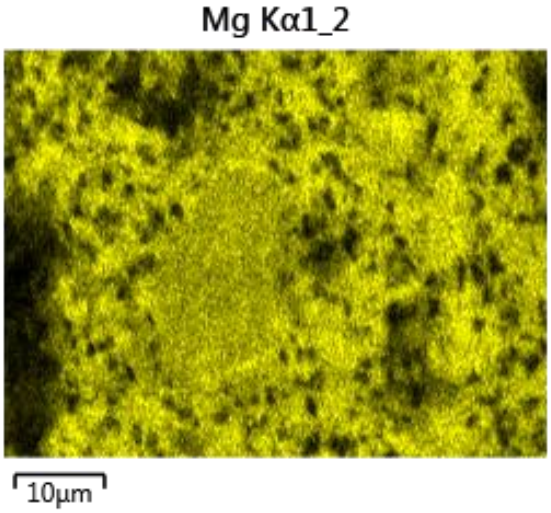

(e)

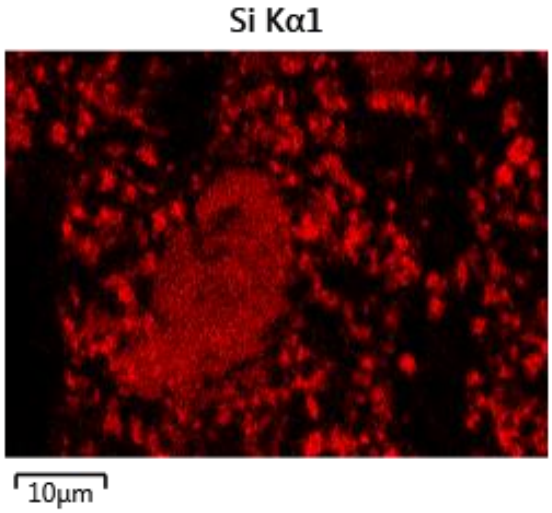

(f)

Figure 10.22: SEM micrographs obtained at 0.3 mm/rev, 1000 RPM, $0.6S_{ut}$, a) Fractured surface at 4000x, showing particular fracture, voids and matrix cracks , b and c) EDS map of (a) showing Mg and Si respectively, d) Fractured surface at 2000x, showing cleavage lines due to SiC fracture, e and f) EDS map of (d) showing Mg and Si respectively.

10.2.4 Summary

Surface quality of the milled magnesium composites were evaluated through roughness measurements and inspection of machined surface SEM micrographs and its subsequent effect on their fatigue behavior was evaluated.

- Specimens machined at 0.1 mm/rev exhibited a good surface finish, with $R_a = 0.29\ and\ 0.37\ \mu m$ at 1000 and 3000 RPM. At a higher feed rate, R_a was close to 1 μm. SEM micrographs indicated the presence of feed marks at higher feed rate, resulting in higher surface roughness. Surface defects such as voids and matrix cracking were observed on the surface.
- Consequently, specimen machined at 0.1 mm/rev exhibited the highest fatigue life.
- Crack initiation site, propagation and final fracture region could be identified through optical micrographs. The crack was found to initiate from the peripherally milled surface. The extent of these regions was found to depend on the loading condition.
- Additionally, the crack propagation mechanism was identified by investigating the SEM micrographs of the fractured surface. Particle fracture, matrix cracking, voids due to particle debonding, ductile failure of the matrix were observed. Owing to the smaller size of the reinforcement particles, particle fracture was not observed extensively. The smaller particles were embedded within the matrix or pulled out from the matrix as the crack propagated.

Chapter 11 . Conclusions and Future Research Recommendation

11.1 Conclusions

The machinability and surface integrity of functionally gradient aluminum matrix composite, A359/SiCp/12.8μm and magnesium matrix composite, AZ91/SiCp/15%/3.5μm were investigated in this study. A major contribution was identifying the effect of the presence of hard reinforcement particles dispersed in a ductile matrix in an intermittent cutting process like milling and studying its effects on the fatigue performance. The cutting forces, acoustic emission generated, tool wear and surface topology generated in a peripheral milling operation were used to evaluate the machinability. Further investigation was carried out through the examination of scanning electron microscope images of the machined surface, cutting tool and the chips generated to identify the surface damage. Having identified the optimum conditions based on these responses, the effect of machining induced surface damage was investigated through fatigue testing.

Functionally gradient aluminum composite.

Material Characterization

- The aluminum matrix composite was reinforced with a functionally gradient concentration of SiC particles with an average particle size of 12.8 μm and a standard deviation of 6.38 μm. The concentration was found to vary from 12 to 25% along the radial direction.

- The average ultimate tensile strength was found to be 160 MPa and the material exhibited limited ductility with average final strain of 0.0024

Machinability

Experimentally investigated through peripheral milling of functionally gradient Al/SiCp along a linear path from high to low concentration of SiCp.

- At lower feed rate, the cutting forces behaved as expected and were found to decrease with decreasing particle concentration, due to the cutting edge encounters fewer number of particles at lower concentration leading to lower cutting forces. However, as the feed rate increases the cutting forces were found to increase as the workpiece was milled from high to low concentration of SiCp. This unforeseen behavior was attributed to the formation of BUE at higher feed rates and spindle speeds, that altered the cutting edge. Further, ANOVA results showed that the cutting forces are predominantly influenced by the feed rate.
- The tool wear measured along the helical cutting edge was found to increase significantly with increase in feed rate and spindle speed. Abrasive wear was identified dominant wear mechanism, inferred through the investigation of SEM micrographs of the cutting edge showing the presence of grooves and pits, due to SiCp ploughing along the surface and displacing WC grains.
- The effect of formation of BUE and tool wear were also reflected on the surface finish. the machined surface at lower SiCp concentration was observed to have rougher surface finish than the region with higher SiCp%, trend similar to the cutting forces. Consistent with the

cutting forces, the ANOVA results indicated that the feed rate was the only dominant parameter.

- The SEM micrographs of the machined surface and the chips generated showed the presence of grooves, voids due to particle debonding, particle fracture, matrix cracking and particles being pushed into the matrix. These surface defects act as stress concentrators.
- Through the analysis of cutting forces, surface topology and tool wear the optimum machining condition was identified to be 0.1 mm/rev and 1000 RPM.

Fatigue Performance

- Surface integrity of the milled functionally gradient composites were evaluated through roughness measurements and inspection of machined and sub-surface micrographs and variation in microhardness and its subsequent effect on their fatigue behavior. Feed rates of 0.1 mm/rev and 0.3 mm/rev and spindle speeds of 1000 RPM and 3000 RPM were chosen based on the machinability results. Higher feed rates and spindle speeds were avoided to eliminate vibration related errors owing to the compact size of the coupons.
- Specimens machined at 0.1 mm/rev exhibited high surface roughness with randomly spaced high peaks and valleys, typical of softened and re-solidified surface. Inspection of sub surface damage through optical micrographs showed extensive plastic deformation with damage extending upto 60 μm and 80 μm beneath the surface at 1000 RPM and 3000 RPM respectively and the microhardness was found to increase near the machined surface. Consequently, coupons machined at 0.1mm/rev and 3000 RPM exhibited lowest fatigue life

- Although the machinability results indicated that 0.1 mm/rev is an optimum machining condition, the lowest fatigue life was observed at 0.1 mm/rev and 3000 RPM. This can be attributed to the extensive surface damage owing to the higher depth of cut and localization of frictional heat generated while machining due to the compact size of the specimen.
- The fatigue cracks were found to initiate from the peripherally milled surface and the fracture was typically found occur between 19 to 21% SiCp, lower end of the SiCp% along the gauge length.
- Four distinct fracture mechanisms were identified through SEM fractography, 1) particle fracture along the fractured surface, perpendicular to the fractured surface 2) particle-matrix debonding 3) matrix fracture 4) dimples formed by the matrix

AZ91/SiCp/15%

Material Characterization

- The AZ91 magnesium alloy was reinforced with SiCp with an average particle size of 3.5 μm and standard deviation of 0.99 μm.
- The ultimate tensile strength was measured to be 360 MPa. The composite did not exhibit any necking before fracture, leading to limited ductility with average final strain of 0.0073.

Machinability

Peripheral milling experiments were performed to study the machinability of the uniformly reinforced magnesium composite.

- The cutting forces were found to increase with increasing feed rate, due to the higher volume of material removed per revolution. The analysis of variance of the regression model terms indicated that the feed rate was the only significant term affecting the cutting forces.
- Unlike the aluminum composite, the inspection of used tool did not show any BUE on the cutting edge. The width of the wear along the helical cutting edge was found to depend on only the feed rate. The cutting edges appeared to be smooth due to repeated rubbing against SiC particles and wear debris. The primary wear mechanism was abrasive wear. The cutting edge showed the presence of micro-plowing and micro-pitting, although much less severe than Al/SiCp owing to the smaller particle size.
- The surface finish was generally found to be excellent for the magnesium composites. The area height profile parameters, S_a, and S_z were significantly affected by the interaction between the feed rate and spindle speed. While, the average waviness, W_a was observed to be dependent on the feed rate.
- The investigation of the machined surfaces showed the presence of fine grooves and matrix cracking due to strain hardening of the matrix were found. The SiC particles were dragged, causing ridges on the machined surface. However, no particle fracture was observed, possibly due to small particle size.
- From this investigation, the cutting forces and surface roughness were found to be minimum at 0.1 mm/rev. The cutting forces and two-dimensional surface roughness parameters identify feed rate as the only significant factor. While, for the area height parameters the interaction between the feed rate and the spindle speed was identified to be

significant. Therefore, a low feed of 0.1 mm/rev and spindle speeds of 1000 to 4000 RPM is be ideal for machining this composite.

Fatigue Performance

Surface quality of the milled magnesium composites were evaluated through roughness measurements and inspection of machined surface SEM micrographs and its subsequent effect on their fatigue behavior. Feed rates of 0.1 mm/rev and 0.3 mm/rev and spindle speeds of 1000 RPM and 3000 RPM were chosen based on the machinability results. Higher feed rates and spindle speeds were avoided to eliminate vibration related errors owing to the compact size of the coupons.

- Specimens machined at 0.1 mm/rev exhibited a good surface finish, while the roughness increased at a higher feed rate. SEM micrographs indicated the presence of feed marks at higher feed rate, resulting in higher surface roughness. Surface defects such as voids and matrix cracking were observed on the surface. Owing to the excellent surface finish, the sub surface damage was not investigated. Consequently, specimen machined at 0.1 mm/rev exhibited the highest fatigue life.
- Crack initiation site, propagation and final fracture region could be identified through optical micrographs. The crack was found to initiate from the peripherally milled surface. The extent of these regions was found to depend on the loading condition. Additionally, the crack propagation mechanism was identified by investigating the SEM micrographs of the fractured surface. Particle fracture, matrix cracking, voids due to particle debonding, ductile failure of the matrix were observed. Owing to the smaller size of the reinforcement particles, particle fracture was not observed extensively. The smaller particles were embedded within the matrix or pulled out from the matrix as the crack propagated.

Physics based model for cutting forces

The forces generated in the peripheral milling of metal matrix composites can be modelled by identifying the events when the cutting edge interacts with the composite. Three major events were identified in this study,

1) When an element of the cutting edge encounters only particles, it may fracture the particle, estimated through Griffith's theory.
2) When the element encounters pure matrix, the matrix undergoes plastic deformation, calculated using Altintas model for milling of alloys.
3) When the elements are in contact with both the particle and matrix, particle debonding occurs due to mismatch in coefficient of thermal expansion, determined using Eshelby's model.

The stresses and forces experienced by the elements when these events occur were calculated and the probability of these events estimated based on particle concentration and distribution in the matrix. The predicted feed force was found to be in good agreement with the measured feed force for all the cutting conditions, while the predictive thrust forces were found to diverge at higher feed of 1 mm/rev.

11.2 Future Research Recommendations

This research focused on machinability and surface integrity of functionally gradient aluminum composite and uniformly reinforced magnesium composite. The cutting forces, tool wear, surface finish and surface topology were investigated, and the surface integrity of the machined specimen was studied through the fatigue performance of milled composites.

In addition to these responses, the following analysis will further extend our understanding of MMCs,

Acoustic emission analysis

In this study, the spikes in the acoustic signal could be traced back to the damage induced on the surface during machining. Therefore, by characterizing the spikes, the AE signals can be used to identify the type of damage on the surface. Extensive statistical analysis is required for a strong correlation between the AE signals and the events occurring on the surface.

Sub-surface damage and Residual stresses measurements

In machining aluminum composites, extensive formation of BUE edge on the cutting tool and wavelike like projections on the machined surface were observed at high feed rates. These features on the cutting tool and the machined surface indicate high temperatures at the cutting edge. The changes in grain structure and the resulting alterations in hardness and induction of residual stresses could also be characterized for a more reliable production of components.

Strain field in functionally gradient aluminum composite

In this study, the tensile properties of the functionally gradient aluminum composite were measured globally. However, by using digital image correlation technique, the entire strain field can be obtained to analyze the deformation as a function of the reinforcement percentage.

Cutting force model

The cutting forces in peripheral milling of aluminum composite showed that in addition to the feed rate, spindle speed and particle concentration, the formation of BUE and the associated tool wear also had a significant effect. Therefore, in developing cutting force model, a factor accounting for the formation of BUE and resulting reduction in sharpness of the cutting edge should be included for an accurate prediction.

Reference

[1] Kainer KU. Metal matrix composites : custom-made materials for automotive and aerospace engineering. Wiley-VCH; 2006.

[2] Gururaja S, Ramulu M, Pedersen W. MACHINING OF MMCs: A REVIEW. Mach Sci Technol 2013;17:41–73.

[3] Abdulgadir MM, Emİr BD. Magnesium Matrix Composites Machining Aspects : A Review. Int Res J Eng Technol 2017;4:2297–307.

[4] Meenashisundaram GK, Gupta M. Emerging Environment Friendly, Magnesium-Based Composite Technology for Present and Future Generations. JOM 2016;68:1890–901.

[5] Sahin Y, Sur G. The effect of Al2O3, TiN and Ti (C,N) based CVD coatings on tool wear in machining metal matrix composites. Surf Coatings Technol 2004;179:349–55.

[6] Davim JP, Conceição António C. Optimal drilling of particulate metal matrix composites based on experimental and numerical procedures. Int J Mach Tools Manuf 2001;41:21–31.

[7] Nicholls CJ, Boswell B, Davies IJ, Islam MN. Review of machining metal matrix composites. Int J Adv Manuf Technol 2016;90:1–13.

[8] Rashad M, Pan F, Tang A, Asif M, She J, Gou J, et al. Development of magnesium-graphene nanoplatelets composite. J Compos Mater 2015;49:285–93.

[9] Rohatgi PK. Metal-matrix composites. Def Sci J 1993;43:323–49.

[10] El-Gallab M, Sklad M. Machining of Al/SiC particulate metal-matrix composites Part I: Tool performance. J Mater Process Technol 1998;83:151–8.

[11] Babu TSM, Sugin MSA, Muthukrishnan N. Investigation on the Characteristics of Surface Quality on Machining of Hybrid Metal Matrix Composite (Al-SiC-B4C). Procedia Eng

2012;38:2617–24.

[12] Man HC, Zhang S, Cheng FT, Yue TM. In situ synthesis of TiC reinforced surface MMC on Al6061 by laser surface alloying. Scr Mater 2002;46:229–34.

[13] Davis JR. ASM Specialty Handbook: Al and Al alloys. ASM International; 1993.

[14] Avedesian MM, Baker H, ASM International. Handbook Committee. Magnesium and magnesium alloys. ASM International; 1999.

[15] Boyer R, Welsch G, Collings EW. Materials properties handbook : titanium alloys. ASM International; 1994.

[16] Mubaraki B, Bandyopadhyay S, Fowle R, Mathew P, Heath PJ. Drilling studies of an Al2O3-Al metal matrix composite - Part I Drill wear characteristics. J Mater Sci 1995;30:6273–80.

[17] Brun MK, Lee M, Gorsler F. Wear characteristics of various hard materials for machining sic-reinforced aluminum alloy. Wear 1985;104:21–9.

[18] Andrewes CJ. E, Feng H, Lau W. M. Machining of an aluminum / SiC composite using diamond inserts. J Mater Process Technol 2000;102:25–9.

[19] Patidar D, Rana RS. Effect of B4C particle reinforcement on the various properties of aluminium matrix composites: A survey paper. Mater. Today Proc., 2017, p. 2981–8.

[20] Smithells CJ (Colin J, Gale WF (William F, Totemeier TC (Terry C. Smithells metals reference book. Elsevier Butterworth-Heinemann; 2004.

[21] Goh CS, Wei J, Lee LC, Gupta M. Properties and deformation behaviour of Mg–Y 2 O 3 nanocomposites. Acta Mater 2007;55:5115–21.

[22] Sendeckyj G, Wang S, Steven Johnson W, Stinchcomb W, Pagano N, Arsenault R. Relationship Between Strengthening Mechanisms and Fracture Toughness of

Discontinuous SiC/Al Composites. J Compos Technol Res 1988;10:140.

[23] Chawla N, Habel U, Shen Y-L, Andres C, Jones JW, Allison JE. The effect of matrix microstructure on the tensile and fatigue behavior of SiC particle-reinforced 2080 Al matrix composites. Metall Mater Trans A 2000;31:531–40.

[24] Pedersen W, Ramulu M. Facing SiCp/Mg metal matrix composites with carbide tools. J Mater Process Technol 2006;172:417–23.

[25] Manna A, Bhattacharayya B. Influence of machining parameters on the machinability of particulate reinforced Al/SiC–MMC. Int J Adv Manuf Technol 2005;25:850–6.

[26] Weinert K, Liedschulte M, Opalla D, Schroer M. High-Tech Machining of Magnesium and Magnesium Composites. Magnesium– Alloy. Technol., Weinheim, FRG: Wiley-VCH Verlag GmbH & Co. KGaA; 2004, p. 130–51.

[27] Ramulu M, Rao P., Kao H. Drilling of (Al2O3)p/6061 metal matrix composites. J Mater Process Technol 2002;124:244–54.

[28] Conceição António CA, Paulo Davim J. Optimal cutting conditions in turning of particulate metal matrix composites based on experiment and a genetic search model. Compos Part A Appl Sci Manuf 2002;33:213–9.

[29] Tomac N, Tannessen K, Rasch FOO. Machinability of Particulate Aluminium Matrix Composites. CIRP Ann - Manuf Technol 1992;41:55–8.

[30] Ramulu M, Rao P, Kao H. Drilling of Al2O3p/6061 metal matrix composites. J Mater Process Technol 2002:244–54.

[31] Monaghan J, O ’reilly P. The drilling of an A1/SiC metal-matrix composite. J Mater Process Technol 1992;33:469–80.

[32] Abdulgadir MM, Demir B, Turan ME. Hybrid reinforced magnesium matrix composites

(Mg/Sic/GNPs): Drilling investigation. Metals (Basel) 2018;8:1–14.

[33] Saravanakumar M, Natarajan N, Krishnaraj V. Study of cutting forces in machining of magnesium composite by response surface methodology. Carbon-Science Technol 2015;7:36–58.

[34] Weinert BK, Lange M, Weinert K, Lange M, Weinert BK, Lange M. Machining of Magnesium Matrix Composites. Magnesium– Alloy Technol 2001;3:975–9.

[35] Ramrattan S, Sitkins F, Nallakatala M. Optimization of the casting and machining processes for a metal-matrix composite. Proc Can Soc 1996.

[36] Weinert K, König W. A Consideration of Tool Wear Mechanism when Machining Metal Matrix Composites (MMC). CIRP Ann - Manuf Technol 1993;42:95–8.

[37] Zum Gahr K-H. Microstructure and wear of materials. Elsevier; 1987.

[38] XP L, L L. Study of the reinforcement percentage of Mg-Al-SiC MMC in relation to the mechanical properties and machinability. Mater Sci Forum 2003;437–4:185–8.

[39] Tönshoff HK, Winkler J. The influence of tool coatings in machining of magnesium. Surf Coatings Technol 1997;94–95:610–6.

[40] Tomac N, Tonnessen K, Rasch FO. Formation of Flank Build-up in Cutting Magnesium Alloys. CIRP Ann 1991;40:79–82.

[41] Pu Z, Outeiro JC, Batista AC, Dillon OW, Puleo DA, Jawahir IS. Enhanced surface integrity of AZ31B Mg alloy by cryogenic machining towards improved functional performance of machined components. Int J Mach Tools Manuf 2012;56:17–27.

[42] KURIHARA K, TOZAWA T, KATO H. Cutting temperature of magnesium alloys at extremely high machining speeds. J Japan Inst Light Met 1981;31:255–60.

[43] Wang J, Liu YB, An J, Wang LM. Wear mechanism map of uncoated HSS tools during

drilling die-cast magnesium alloy. Wear 2008;265:685–91.

[44] Gariboldi E. Drilling a magnesium alloy using PVD coated twist drills. J Mater Process Technol 2003;134:287–95.

[45] Bhowmick S, Lukitsch MJ, Alpas AT. Dry and minimum quantity lubrication drilling of cast magnesium alloy (AM60). Int J Mach Tools Manuf 2010;50:444–57.

[46] Biermann D, Liu Y. Innovative flow drilling on magnesium wrought alloy AZ31. Procedia CIRP 2014;18:209–14.

[47] Ding X, Liew WYH, Liu XD. Evaluation of machining performance of MMC with PCBN and PCD tools. Wear 2005;259:1225–34.

[48] Durante S, Rutelli G, Rabezzana F. Aluminum-based MMC machining with diamond-coated cutting tools. Surf Coatings Technol 1997;94–95:632–40.

[49] Chou YK, Liu J. CVD diamond tool performance in metal matrix composite machining. Surf Coatings Technol 2005;200:1872–8.

[50] McGinty M, Preuss C. Machining Ceramic Fibre Metal Matrix Composites. Int Conf High Product Mach Mater 1985:231–43.

[51] Quigley O, Monaghan J, O'Reilly P. Factors affecting the machinability of an Al/SiC metal-matrix composite. J Mater Process Technol 1994;43:21–36.

[52] Hale T, Graham D. The influence of coating thickness and composition upon metal-cutting performance. Cut Tool Mater 1980:175–91.

[53] ISO 13565-1:1996 - Geometrical Product Specifications (GPS) -- Surface texture: Profile method; Surfaces having stratified functional properties -- Part 1 1996.

[54] ISO 16610-21:2011 - Geometrical product specifications (GPS) -- Filtration -- Part 21 n.d.

[55] Lin JT, Bhattacharyya D, Lane C. Case Study Machinability of a silicon carbide

reinforced matrix composite aluminium metal. Wear 1995;183:883–8.

[56] Pramanik A, Zhang LCC, Arsecularatne JAA. Machining of metal matrix composites: Effect of ceramic particles on residual stress, surface roughness and chip formation. Int J Mach Tools Manuf 2008;48:1613–25.

[57] Pedersen WE, Ramulu M. A study of drilling of varying reinforcement SiCp/Al with solid carbide and carbide tipped drills. Trans. North Am. Manuf. Res. Inst. SME North, 2003, p. 279–86.

[58] Kılıçkap E, Çakır O, Aksoy M, İnan A. Study of tool wear and surface roughness in machining of homogenised SiC-p reinforced aluminium metal matrix composite. J Mater Process Technol 2005;164:862–7.

[59] Lin JT, Bhattacharyya D, Ferguson WG. Chip formation in the machining of SiC-particle-reinforced aluminium-matrix composites. Compos Sci Technol 1998;58:285–91.

[60] Hung NP, Yeo SH, Lee KK, Ng KJ. Chip Formation in Machining Particle-Reinforced Metal Matrix Composites. Mater Manuf Process 1998;13:85–100.

[61] Kishawy H a., Kannan S, Balazinski M. An Energy Based Analytical Force Model for Orthogonal Cutting of Metal Matrix Composites. CIRP Ann - Manuf Technol 2004;53:91–4.

[62] Pramanik A, Zhang LCC, Arsecularatne JAA. Prediction of cutting forces in machining of metal matrix composites. Int J Mach Tools Manuf 2006;46:1795–803.

[63] Sikder S, Kishawy HA. Analytical model for force prediction when machining metal matrix composite. Int J Mech Sci 2012;59:95–103.

[64] Waldorf DJ. A Simplified Model for Ploughing Forces in Turning. J Manuf Process 2006;8:76–82.

[65] Yan C, Zhang L. Single-point scratching of 6061 Al alloy reinforced by different ceramic particles. Appl Compos Mater 1995;1:431–47.

[66] Altintas Y. Manufacturing Automation. Cambridge: Cambridge University Press; 2011.

[67] Pedersen W. Machinability of a functionally gradient Al/SiCp metal matrix composite. University of Washington, 2003.

[68] Masounave J, Litwin J, Hamelin D. Prediction of tool life in turning aluminium matrix composites. Mater Des 1994.

[69] Hung NP, Boey FYC, Khor KA, Oh CA, Lee HF. Machinability of cast and powder-formed aluminum alloys reinforced with SiC particles. J Mater Process Tech 1995;48:291–7.

[70] Lin JT, Bhattacharyya D, Lane C. Machinability of a silicon carbide reinforced aluminium metal matrix composite. Wear 1995;181–183:883–8.

[71] Rabinowicz E. Friction and wear of materials. Wiley; 1995.

[72] Chawla N, Shen Y-L. Mechanical Behavior of Particle Reinforced Metal Matrix Composites. Adv Eng Mater 2001;3:357–70.

[73] Poovazhagan L, Kalaichelvan K, Rajadurai A, Senthilvelan V. Characterization of hybrid silicon carbide and boron carbide nanoparticles-reinforced aluminum alloy composites. Procedia Eng., 2013, p. 681–9.

[74] Kala H, Mer KKS, Kumar S. A Review on Mechanical and Tribological Behaviors of Stir Cast Aluminum Matrix Composites. Procedia Mater Sci 2014;6:1951–60.

[75] Sirahbizu Yigezu B, Mohan Mahapatra M, Kumar Jha P. Influence of Reinforcement Type on Microstructure, Hardness, and Tensile Properties of an Aluminum Alloy Metal Matrix Composite. J Miner Mater Charact Eng 2013:124–30.

[76] Cöcen Ü, Önel K. Ductility and strength of extruded SiCp/aluminium-alloy composites. Compos Sci Technol 2002;62:275–82.

[77] Davies CHJ, Raghunathan N, Sheppard T. Structure–property relationships of SiC reinforced advanced Al–Zn–Mg–Cu alloy. Mater Sci Technol 2014;8:977–84.

[78] Singh PM, Lewandowski JJ. Effects of heat treatment and reinforcement size. Metall Trans A 1993;24:2531–43.

[79] Yan YW, Geng L, Li AB. Experimental and numerical studies of the effect of particle size on the deformation behavior of the metal matrix composites. Mater Sci Eng A 2007;448:315–25.

[80] Song M, Xiao D. Modeling the fracture toughness and tensile ductility of SiCp/Al metal matrix composites. Mater Sci Eng A 2008;474:371–5.

[81] Sun C, Song M, Wang Z, He Y. Effect of particle size on the microstructures and mechanical properties of SiC-reinforced pure aluminum composites. J Mater Eng Perform 2011.

[82] Deng KK, Wang XJ, Wu YW, Hu XS, Wu K, Gan WM. Effect of particle size on microstructure and mechanical properties of SiCp/AZ91 magnesium matrix composite. Mater Sci Eng A 2012;543:158–63.

[83] Zheng M. Effect of submicron size SiC particulates on microstructure and mechanical properties of AZ91 magnesium matrix ... J Alloys Compd 2010;504:542–7.

[84] Chang SY, Jun Cho S, Hong SK, Hyuk Shin D. Microstructure and tensile properties of bi-materials with macro-interface between unreinforced magnesium and composite. J Alloys Compd 2001;316:275–9.

[85] Luo A. Processing, microstructure, and mechanical behavior of cast magnesium metal

matrix composites. Metall Mater Trans A 1995;26:2445–55.

[86] Rohatgi PK, Alaraj S, Thakkar RB, Daoud A. Variation in fatigue properties of cast A359-SiC composites under total strain controlled conditions: Effects of porosity and inclusions. Compos Part A Appl Sci Manuf 2007;38:1829–41.

[87] Johnson W. Fatigue Testing and Damage Development in Continuous Fiber Reinforced Metal Matrix Composites. Met. Matrix Compos. Testing, Anal. Fail. Modes, 2008, p. 194-194–28.

[88] Povirk GL, Stout MG, Bourke M, Goldstone JA, Lawson AC, Lovato M, et al. Thermally and mechanically induced residual strains in Al-SiC composites. Acta Metall Mater 1992;40:2391–412.

[89] Christman T, Suresh S. Microstructural development in an aluminum alloy-SiC whisker composite. Acta Metall 1988;36:1691–704.

[90] Suresh S, Christman T, Sugimura Y. Accelerated aging in cast Al alloy-SiC particulate composites. Scr Metall 1989;23:1599–602.

[91] Han NL, Wang ZG, Sun L. Effect of reinforcement size on low cycle fatigue behavior of SiC particle reinforced aluminum matrix composites. Scr Metall Mater 1995;33:781–7.

[92] Lloyd DJ. Particle reinforced aluminium and magnesium matrix composites. Int Mater Rev 1994;39:1–23.

[93] Hall JN, Wayne Jones J, Sachdev AK. Particle size, volume fraction and matrix strength effects on fatigue behavior and particle fracture in 2124 aluminum-SiCp composites. Mater Sci Eng A 1994;183:69–80.

[94] Jian Ku Shang, Yu W, Ritchie RO. Role of silicon carbide particles in fatigue crack growth in SiC-particulate-reinforced aluminum alloy composites. Mater Sci Eng A

1988;102:181–92.

[95] Kumai S, King JE, Knott JF. Fatigue in SiC-particulate-reinforced aluminium alloy composites. Mater Sci Eng A 1991;146:317–26.

[96] Pramanik A, Islam MN, Davies IJ, Boswell B, Dong Y, Basak AK, et al. Contribution of machining to the fatigue behaviour of metal matrix composites (MMCs) of varying reinforcement size. Int J Fatigue 2017;102:9–17.

[97] Ramulu M, Paul G, Patel J. EDM surface effects on the fatigue strength of a 15 vol% SiCp/Al metal matrix composite material. Compos Struct 2001;54:79–86.

[98] Llorca J, Ruiz J, Healy JC, Elices M, Beevers CJ. Fatigue crack propagation in salt water, air and high vacuum in a spray-formed particulate-reinforced metal matrix composite. Mater Sci Eng A 1994;185:1–15.

[99] Karayaka M, Sehitoglu H. Thermomechanical fatigue of particulate-reinforced aluminum 2xxx-T4. Metall Trans A 1991;22:697.

[100] Chen EY, Lawson L, Meshii M. The effect of fatigue microcracks on rapid catastrophic failure in Al/SiC composites. Mater Sci Eng A 1995;200:192–206.

[101] Sasaki M, Lawson L, Meshii M. Low-Cycle fatigue properties of a SiC Whisker-reinforced 2124 aluminum alloy. Metall Mater Trans A 1994;25:2265–74.

[102] Masuda C, Tanaka Y. Fatigue properties and fatigue fracture mechanisms of SiC whiskers or SiC particulate-reinforced aluminium composites. J Mater Sci 1992;27:413–22.

[103] Rawal SP. Metal-matrix composites for space applications. JOM 2001;53:14–7.

[104] Chmelík F, Moll F, Kiehn J, Mathis K, Lukác P, Kainer K-U, et al. Acoustic Emission from magnesium based alloys and metal matrix composites. J Acoust Emiss 2002;20:108–20.

[105] Heiple. CR, Carpenter SH. Acoustic emission produced by deformation of metals and alloys - A review. J Acoust Emiss 1982;6:215–37.

[106] Lewandowski JJ, Liu C, Hunt WH. Effects of matrix microstructure and particle distribution on fracture of an aluminum metal matrix composite. Mater Sci Eng A 1989;107:241–55.

[107] Roebuck B. Fractography of a SiC particulate reinforced aluminium metal matrix composite. J Mater Sci Lett 1987;6:1138–40.

[108] Doel TJA, Bowen P. Tensile properties of particulate-reinforced metal matrix composites. Compos Part A Appl Sci Manuf 1996;27:655–65.

[109] Mordike BL, Lukáč P. Interfaces in magnesium-based composites. Surf Interface Anal 2001;31:682–91.

[110] Miller JL. Investigation of Machinability and Dust Emissions in Edge Trimming of Laminated Carbon Fiber Composites 2014.

[111] Ekici E, Gülesin M. The machinability of Al/B4C composites produced by hot pressing based on reinforcing the element ratio. Sci Eng Compos Mater 2016;23:743–50.

[112] El-Gallab M, Sklad M. Machining of Al/SiC particulate metal matrix composites Part II: Workpiece surface integrity. J Mater Process Technol 1998;83:277–85.

[113] Kannan S, Kishawy HA. Tribological aspects of machining aluminium metal matrix composites. J Mater Process Technol 2008;198:399–406.

[114] Dornfeld DA, Kannatey-Asibu E. ACOUSTIC EMISSION DURING ORTHOGONAL METAL CUTTING. Int I Mech Sci 1980;22:285–96.

[115] Bennett HE, Porteus JO. Relation Between Surface Roughness and Specular Reflectance at Normal Incidence. J Opt Soc Am 1961;51:123.

[116] Übeyli M, Karakaş MS, Acır A, Ögel B. Study on performance of uncoated and coated tools in milling of Al–4%Cu/B $_4$ C metal matrix composites. Mater Sci Technol 2007;23:945–50.

[117] Li XP, Lu L. Study of the Reinforcement Percentage of Mg-Al-SiC MMC in Relation to the Mechanical Properties and Machinability. Mater Sci Forum 2003;437–438:185–8.

[118] Zhao Z, Yingkun X, Wenduo W, Zhuangqi H. Effect of matrix microstructure on mechanical properties of 2124 aluminium alloy-SiC particle composite. Mater Sci Technol (United Kingdom) 1991;7:592–5.

[119] Dabade UA, Dapkekar D, Joshi SS. Modeling of chip-tool interface friction to predict cutting forces in machining of Al/SiCp composites. Int J Mach Tools Manuf 2009;49:690–700.

[120] Joshi S., Ramakrishnan N, Ramakrishnan P. Analysis of chip breaking during orthogonal machining of Al/SiCp composites. J Mater Process Technol 1999;88:90–6.

[121] Oxley P. Shear angle solutions in orthogonal machining. Int J Mach Tool Des Res 1962;2:219–29.

[122] Weinert K, Biermann D. Turning of fiber and particle reinforced aluminium. Proc. Int. Conf. Mach. Adv. Mater., 1993, p. 437–53.

[123] Karabulut Ş, Gökmen U, Çinici H. Study on the mechanical and drilling properties of AA7039 composites reinforced with Al2O3/B4C/SiC particles. Compos Part B Eng 2016;93:43–55.

[124] Boswell B, Islam MN, Davies IJ, Pramanik A. Effect of machining parameters on the surface finish of a metal matrix composite under dry cutting conditions. Proc Inst Mech Eng Part B J Eng Manuf 2015;2:1–11.

[125] Fathipour M, Zoghipour P, Tarighi J, Yousefi R. Investigation of reinforced sic particles percentage on machining force of metal matrix composite. Mod Appl Sci 2012;6:9–20.

[126] Dandekar CR, Shin YC. Multi-step 3-D finite element modeling of subsurface damage in machining particulate reinforced metal matrix composites. Compos Part A Appl Sci Manuf 2009;40:1231–9.

[127] Eshelby JD. The determination of the elastic field of an ellipsoidal inclusion, and related problems. Collect Work J D Eshelby 2007:209–29.

[128] Pramanik A, Zhang LC, Arsecularatne JA. An FEM investigation into the behavior of metal matrix composites: Tool–particle interaction during orthogonal cutting. Int J Mach Tools Manuf 2007;47:1497–506.

[129] Altintas Y. Manufacturing automation : metal cutting mechanics, machine tool vibrations, and CNC design. Cambridge University Press; 2012.

[130] Bonnen JJ, Allison JE, Jones JW. Fatigue behavior of a 2XXX series aluminum alloy reinforced with 15 vol. % SiCp. Metall Trans A 1991;22:1009–17.

[131] Chawla N, Andres C, Jones JW, Allison JE. Effect of SiC volume fraction and particle size on the fatigue resistance of a 2080 Al/SiCp composite. Metall Mater Trans A Phys Metall Mater Sci 1998;29:2843–2854.

[132] Crowe CR, Hasson DF. Corrosion Fatigue of SiC/Al Metal Matrix Composites in Salt Ladened Moist Air. Strength Met. Alloy. (ICSMA 6), 2013, p. 859–65.

[133] Thomas WN. The effect of scratches and of various workshop finishes upon the fatigue strength of steel. University of Oxford, 1923.

[134] Cheung CF, Chan KC, To S, Lee WB. Effect of reinforcement in ultra-precision machining of Al6061/SiC metal matrix composites. Scr Mater 2002;47:77–82.

[135] Nisbett JK, Budynas RG. Shigley's Mechanical Engineering Design. vol. New York,. 2002.

[136] Dabade UA, Jadhav MR. Experimental Study of Surface Integrity of Al/SiC Particulate Metal-matrix Composites in Hot Machining. Procedia CIRP, vol. 41, Elsevier B.V.; 2016, p. 914–9.

[137] Li C, Ellyin F. Fatigue damage and its localization in particulate metal matrix composites. Mater Sci Eng A 1996;214:115–21.

[138] Anandan N, Ramulu M. Experimental investigation of peripheral milling of functionally gradient Al-SiC metal matrix composite. ASME Int. Mech. Eng. Congr. Expo. Proc., vol. 14, ASME; 2017, p. V014T11A008.

[139] Riehemann W, Trojanová Z, Mielczarek A. Fatigue in magnesium alloy AZ91-γAlumina fiber composite studied by internal friction measurements. Procedia Eng., vol. 2, 2010, p. 2151–60.

[140] Qi L, Ju L, Zhou J, Li S, Zhang T, Tian W. Tensile and fatigue behavior of carbon fiber reinforced magnesium composite fabricated by liquid-solid extrusion following vacuum pressure infiltration. J Alloys Compd 2017;721:55–63.

[141] Bommala VK, Krishna MG, Rao CT. Magnesium matrix composites for biomedical applications: A review. J Magnes Alloy 2019;7:72–9.

[142] Al-maamari AEA, Iqbal AA, Nuruzzaman DM. Wear and mechanical characterization of Mg–Gr self-lubricating composite fabricated by mechanical alloying. J Magnes Alloy 2019;7:283–90.

Appendix A

MATERIAL CHARACTERIZATION

A.1 SiC_p *distribution in A59 matrix*

A.1.1 Optical micrographs

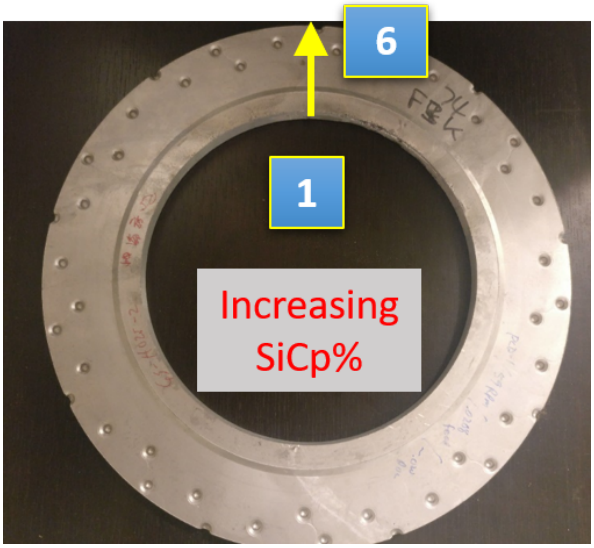

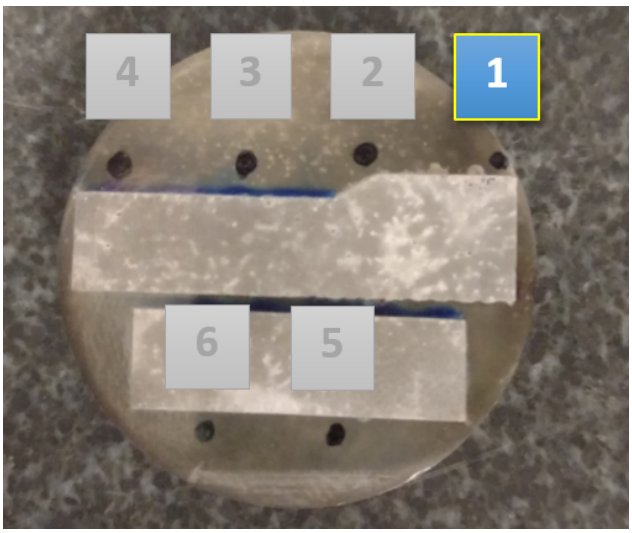

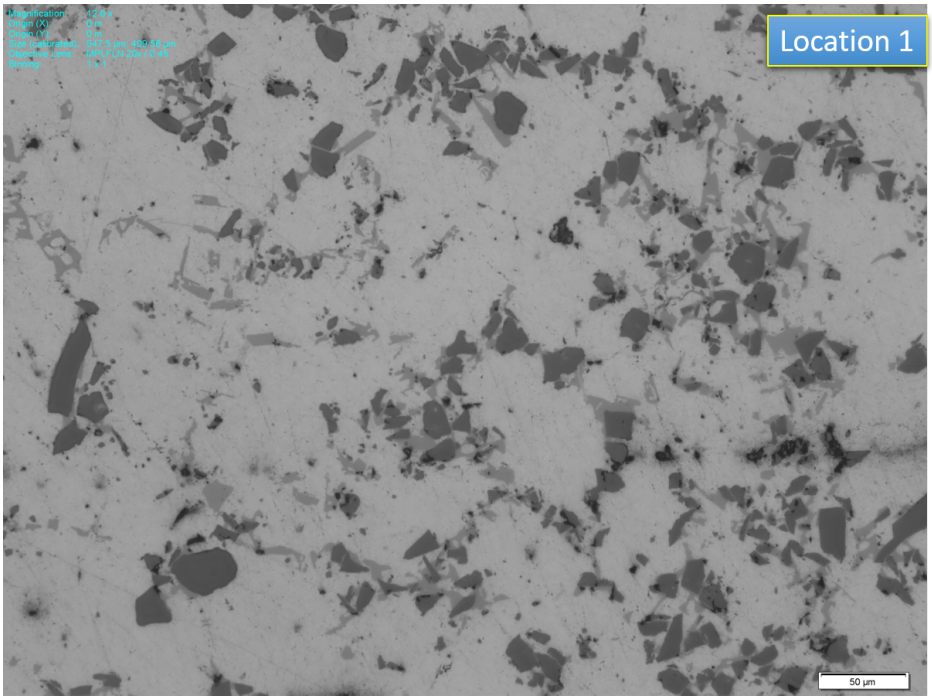
Location 1
50 µm

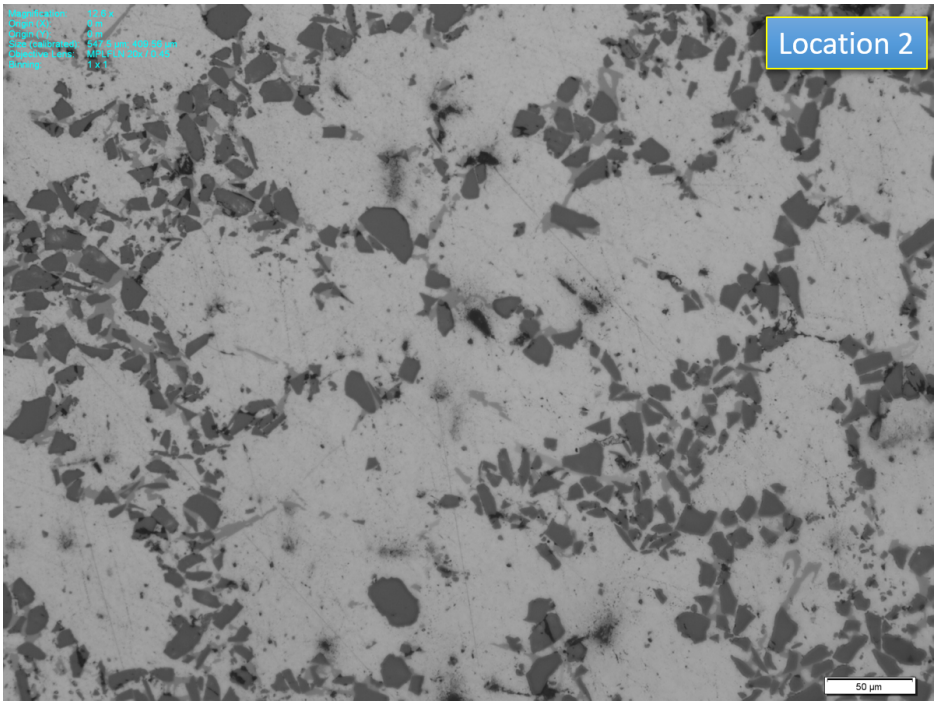
Location 2
50 µm

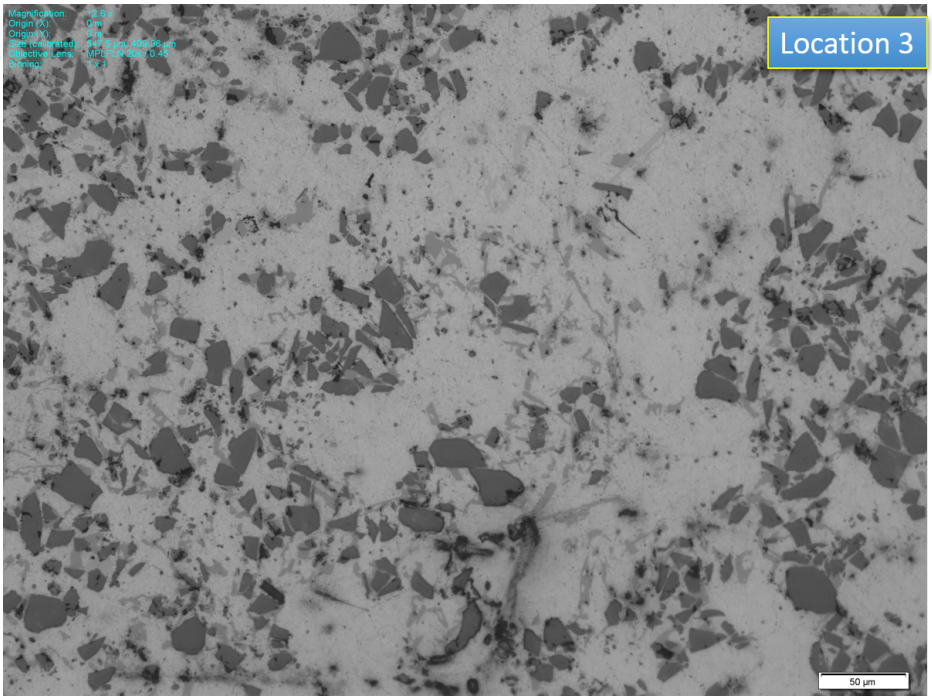
Location 3
50 µm

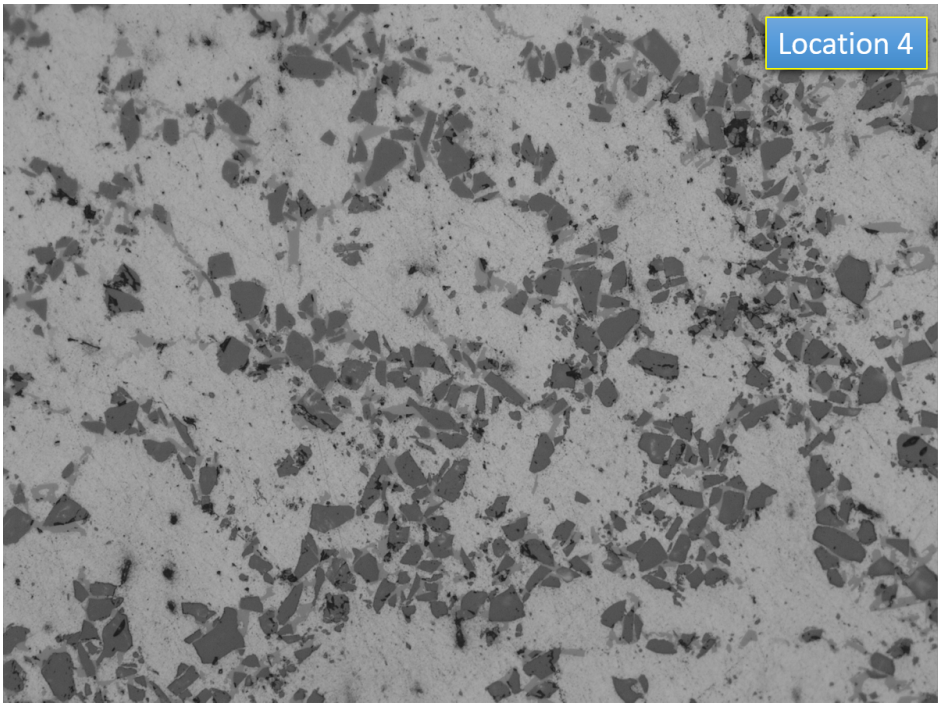
Location 4

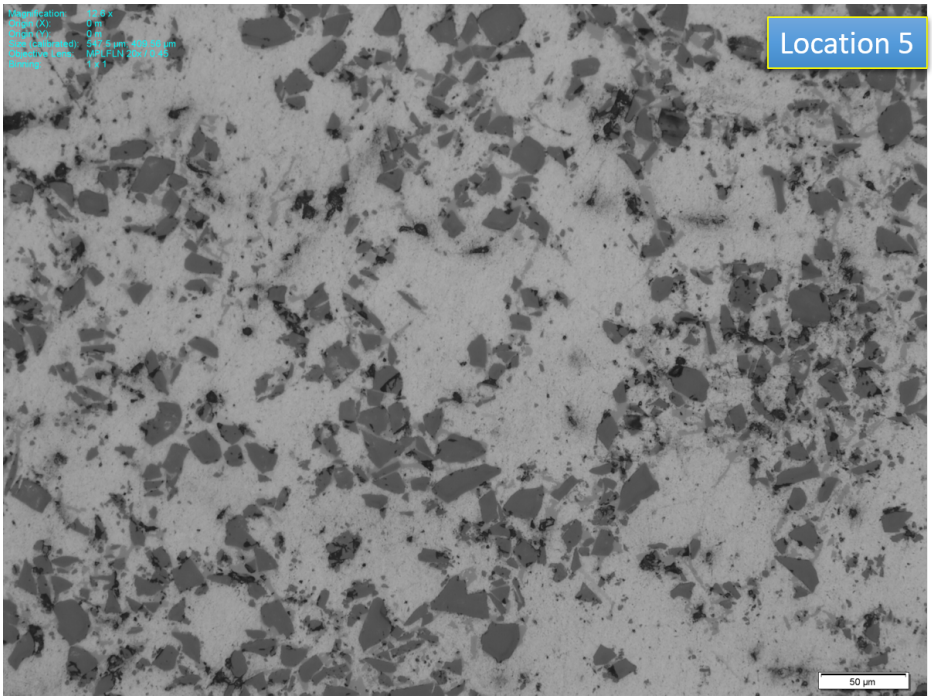
Location 5
50 µm

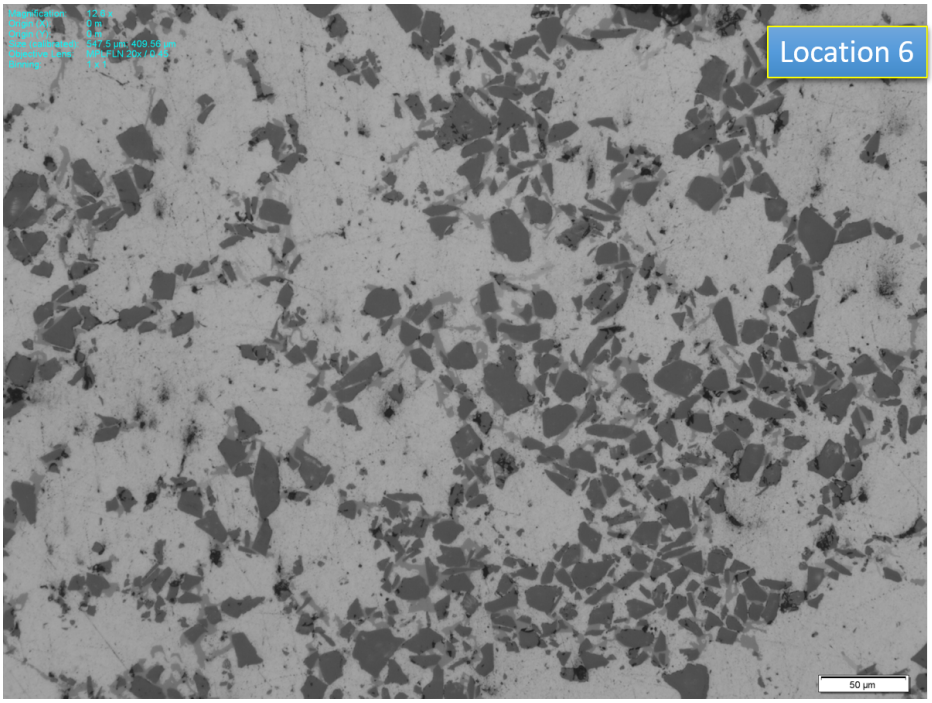
Location 6
50 µm

A.1.2 Matlab code for particle concentration and distribution

```
close all
clear all
clc
addpath('U:\MgSiC_percentage')
I1=imread('1a.TIF');
%16
%subplot(121)
figure();
imshow(I1)

I1=localcontrast(I1);
I1=imsharpen(I1);

%I1=imreducehaze(I1);
%subplot(122)
figure();
imshow(I1)
%imtool(I1)
r1=50/172;
%I2=im2bw(I1(1:470,:),.2);
s=size(I1);
In1=floor(s(1,1)/2);
In2=floor(s(1,2)/2);
%imshow(I2)
%imtool(I2)
t=110;
area_o=numel(I1);
for p=1:1:33
    % 50 microns = 182 pixels
    I2=im2bw(I1(In1-t:In1+t,In2-(t+30):In2+(t+30)),.31);
```

```
31      I2=imcomplement(I2);
32      I2=bwareaopen(I2,9);
33      I2=bwconvhull(I2,'objects');
34      figure();
35      imshow(I2)
36      measurements=regionprops(I2,'FilledArea','EquivDiameter',...
37          'Boundingbox','centroid');
38      data1=struct2cell(measurements);
39      data1=cell2mat(data1');
40      for p1=1:1:numel(measurements)
41          rectangle('Position',[measurements(p1).BoundingBox(1,1),...
42              measurements(p1).BoundingBox(1,2),...
43              measurements(p1).BoundingBox(1,3),...
44              measurements(p1).BoundingBox(1,4)],'EdgeColor','r')
45      end
46
47      A1(p1,1)=measurements.FilledArea;
48      D1(p1,1)=measurements.EquivDiameter;
49      A2=sort(A1,'descend');
50      D2=sort(D1,'descend');
51      [¬,p2]=max(D1);
52
53      Diameter=D2*(50)/172;
54
55      % Average Particle size determination
56      Diameter=D2*r1;
57      j=1;
58      s1=length(Diameter);
59      for i=1:1:s1
60          if Diameter(i,1)>5
61              Diameter1(j,1)=Diameter(i,1);
62              Area1(j,1)=A2(i,1);
63              j=j+1;
```

```
64          end
65      end
66
67      total_area1(p,1)=sum(double(I2(:)));
68      total_area(p,1)=numel(I2);
69      Percentage(p,1)=total_area1(p,1)/total_area(p,1) * 100;
70      t=20+t;
71      area_covered=total_area1(p,1)/area_o;
72  end
73  figure();
74  total_area=total_area.*(r1)^2;
75  plot(total_area,Percentage,'*')
76  hold on
77  f = polyfit(total_area,Percentage,4);
78  plot(total_area,Percentage,'o',total_area,polyval(f,total_area),'-')
79  ylim([0 30])
80  ylabel('% SiCp')
81  xlabel('\mum^2','interpret','Tex')
82
83  %imtool(I2)
84  figure();
85  imshow(I2)
86  figure();
87  imshow(I2) % figure
88  for p1=1:1:numel(measurements)
89      rectangle('Position',[measurements(p1).BoundingBox(1,1),...
90          measurements(p1).BoundingBox(1,2),...
91          measurements(p1).BoundingBox(1,3),...
92          measurements(p1).BoundingBox(1,4)],'EdgeColor','r')
93  end
94  %Area1=sort(Area1(:,1),'descend');
95  A_avg=mean(A1(1:15,1));
96  D=sqrt(A_avg*4/pi);
```

```
Da=D*r1;
D_all=sqrt(Area1.*(4/pi));
D_alla=D_all.*(r1);
figure();
histfit(D_alla,4)
xlabel('\mum','Interpret','Tex')
ylabel('counts')

figure();
histfit(Diameter1,3)
xlabel('\mum','Interpret','Tex')
ylabel('counts')
%span=(20*645/120)*(20*522/120);
```

A.1.3 SiCp percentage for points 1 through 6

Point 1

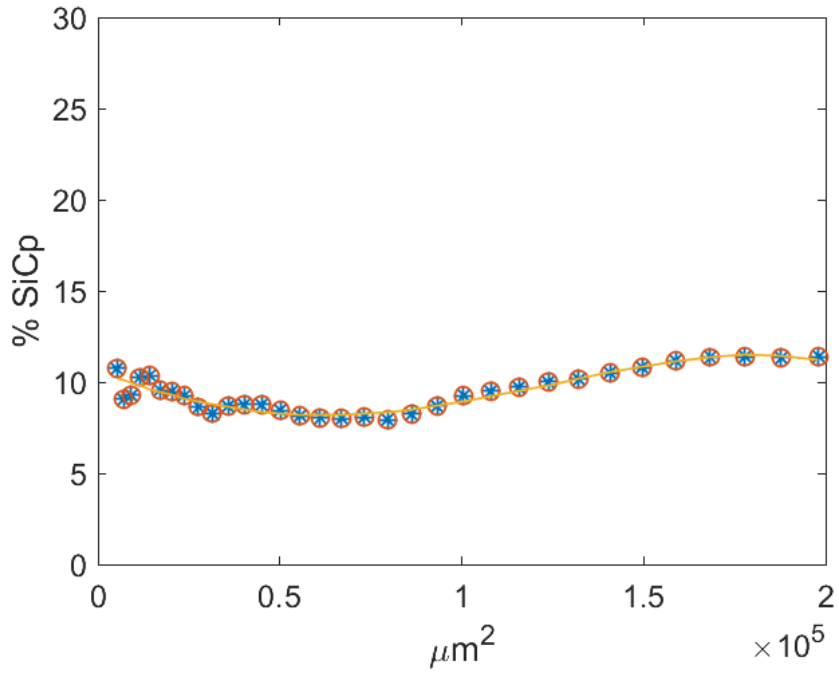

Point 2

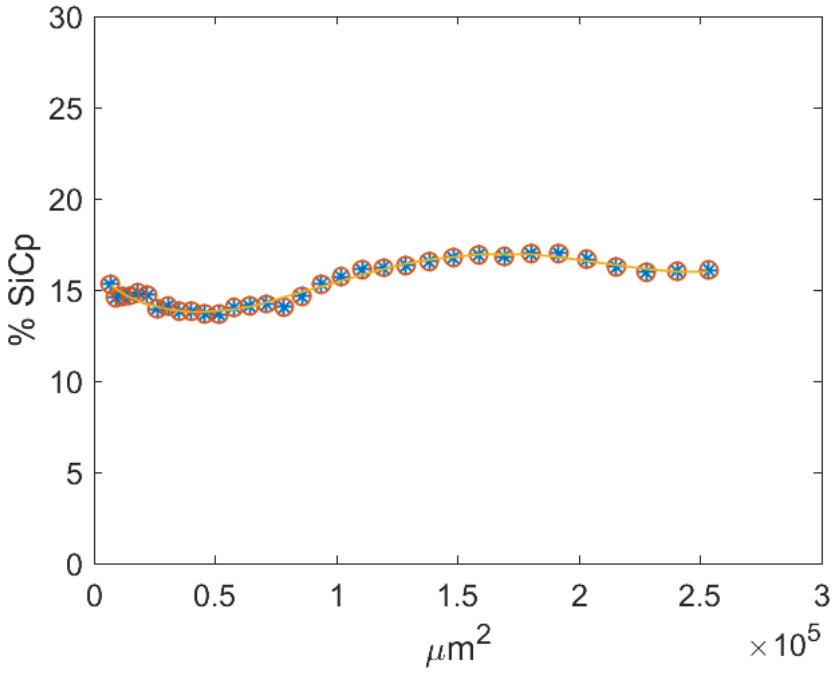

Point 3

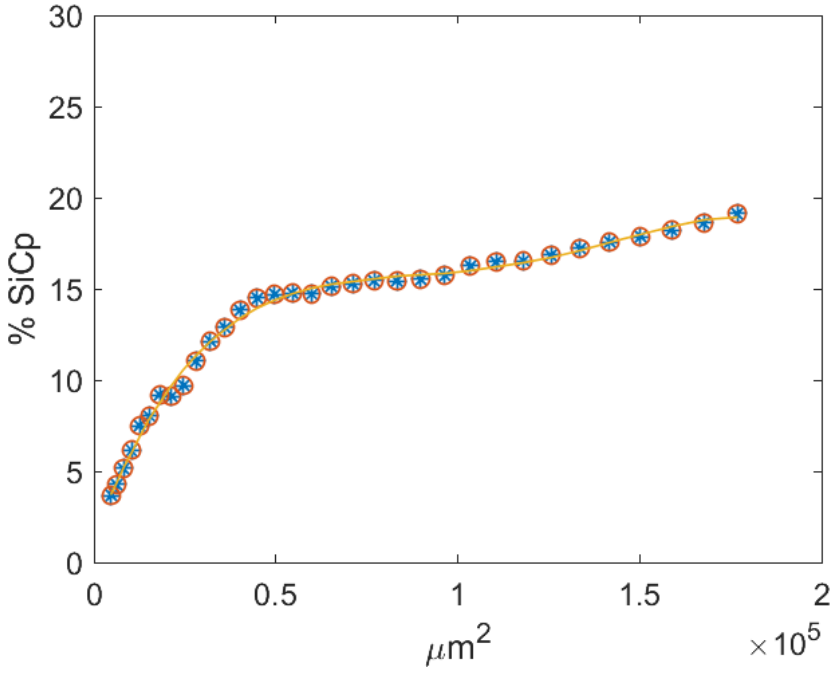

Point 4

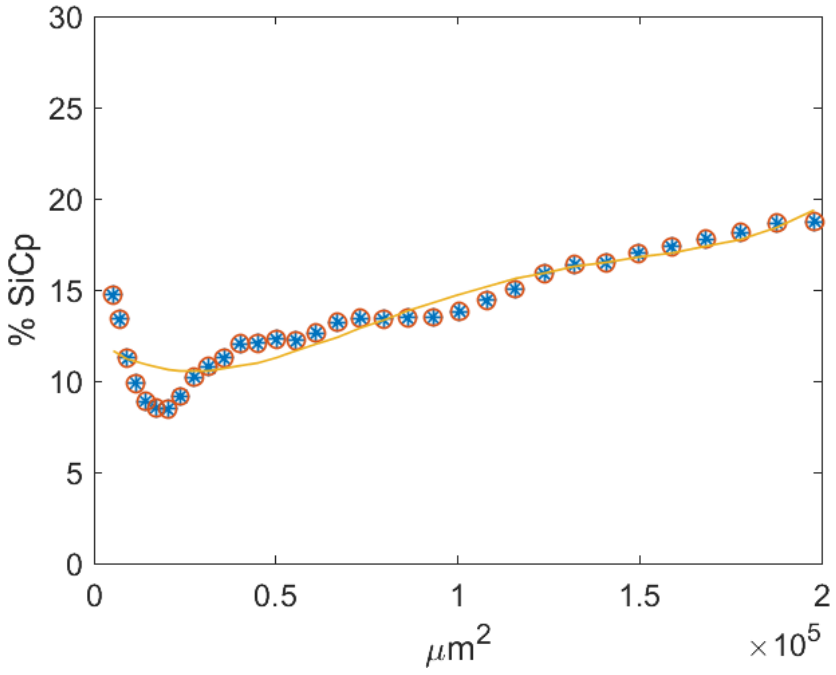

Point 5

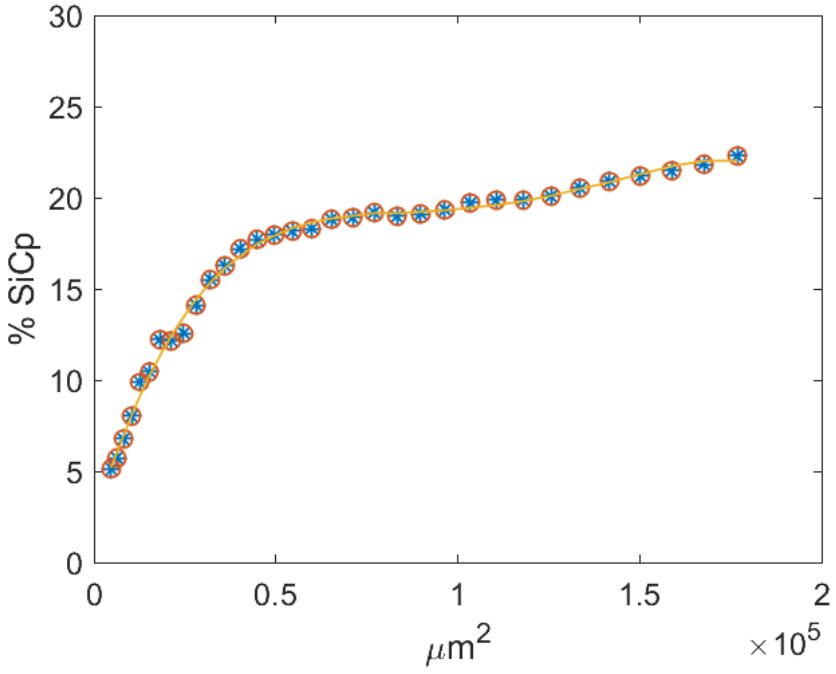

Point 6

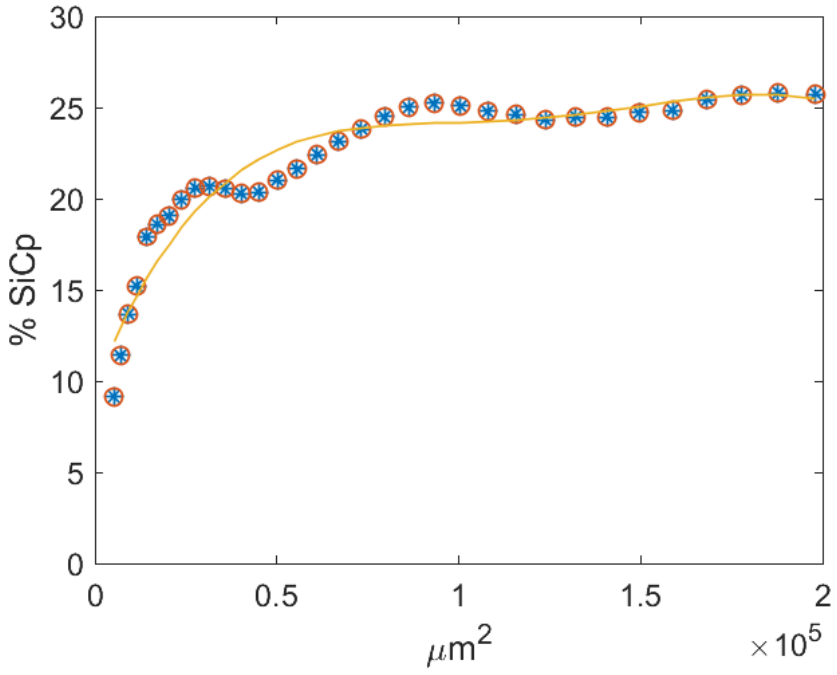

A.1.4 Particle concentration distribution

Point	Set1,SiCp%	Set2,SiCp%	Set3,SiCp%
1	11.16	10.13	12.46
2	13.7	15.8	17.45
3	18.3	19.4	18.58
4	19.9	22.56	22.57
5	23	23.42	22.97
6	25.2	26.49	25.35

A.1.5 Particle size distribution

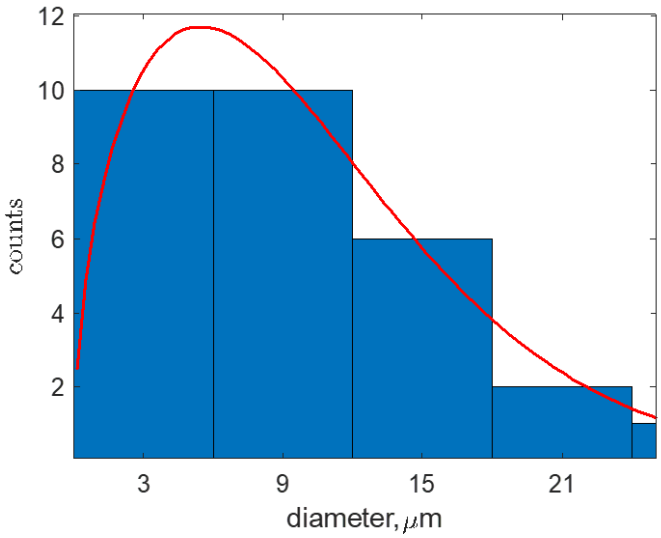

A.2 Tensile Properties of Functionally gradient A359/SiC_p

A.2.1 Tensile test

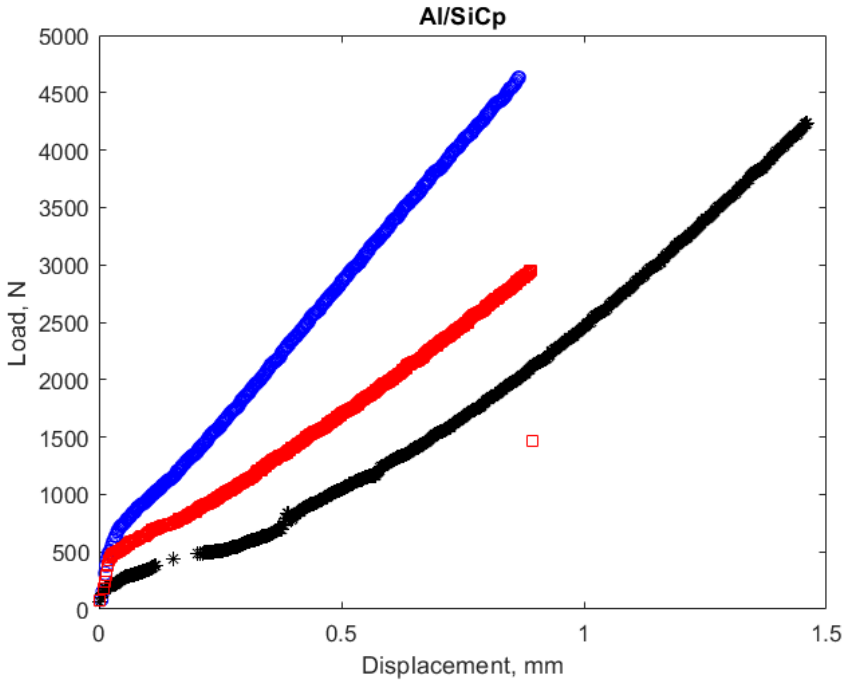

A.2.2 Tensile specimen fractography

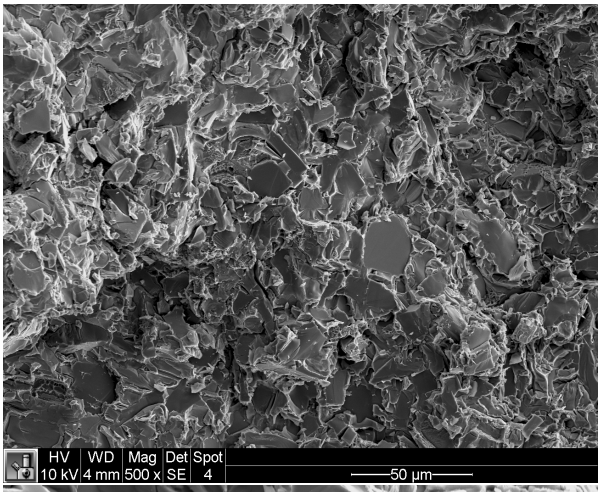

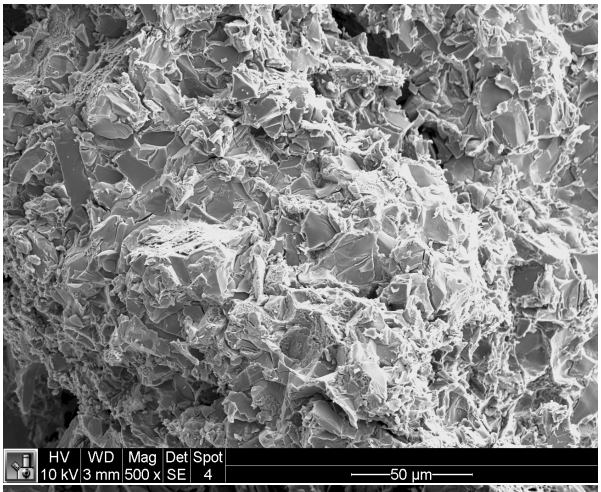

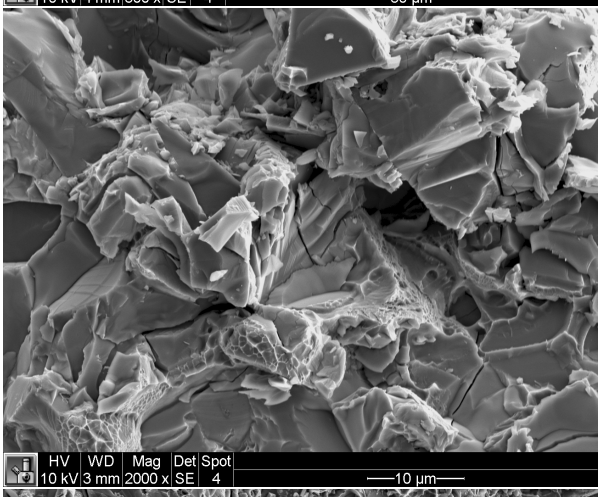

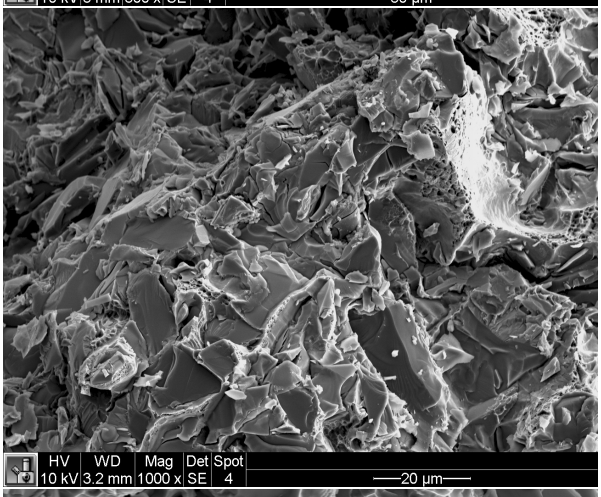

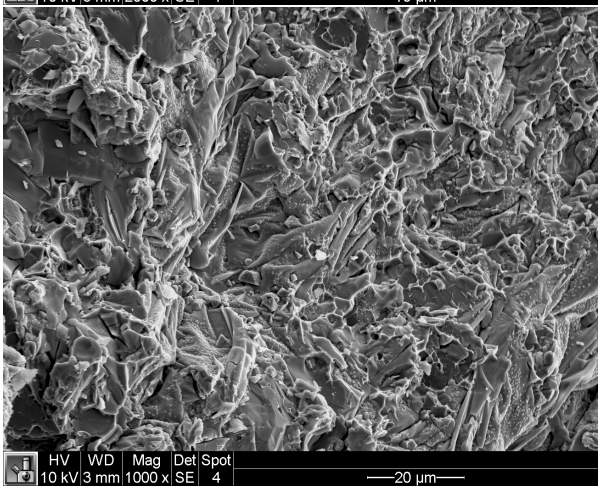

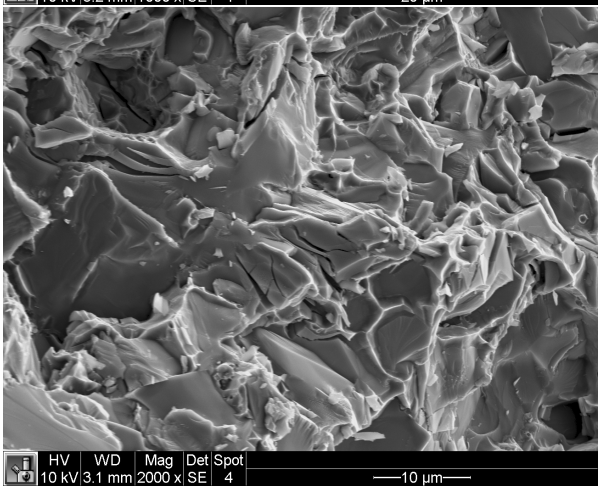

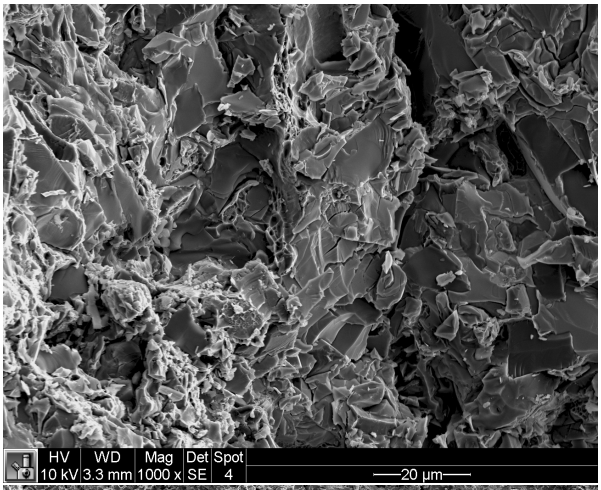
HV
10 kV
WD
3.3 mm
Mag
1000 x
Det
SE
Spot
4
20 µm

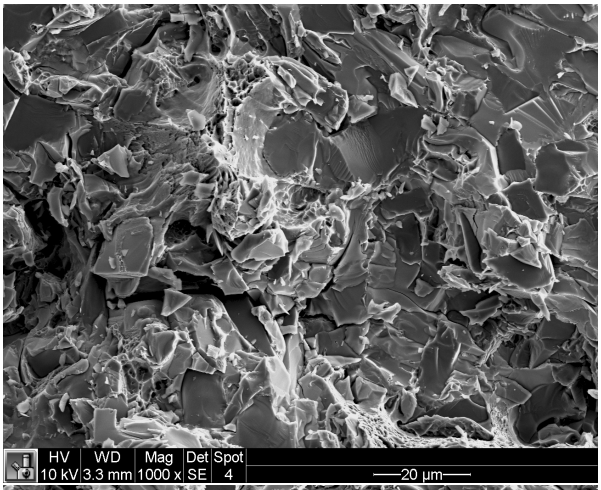
HV
10 kV
WD
3.3 mm
Mag
1000 x
Det
SE
Spot
4
20 µm

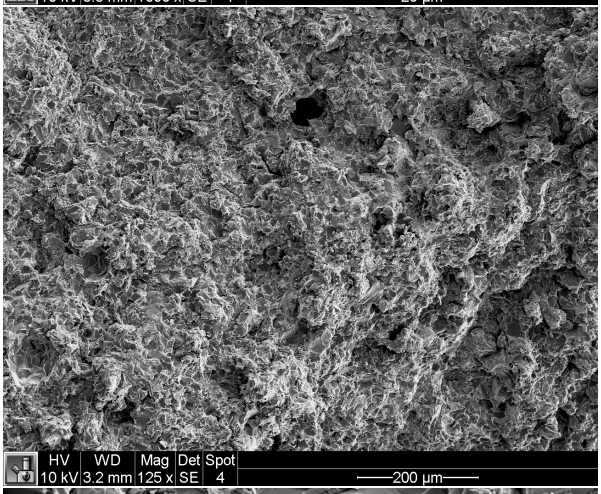
HV
10 kV
WD
3.2 mm
Mag
125 x
Det
SE
Spot
4
200 µm

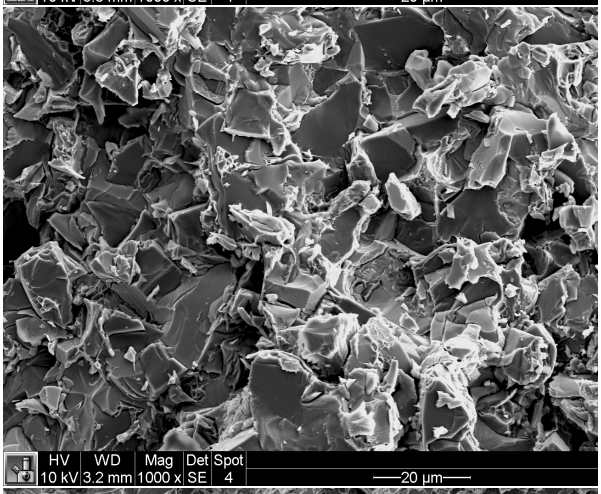
HV
10 kV
WD
3.2 mm
Mag
1000 x
Det
SE
Spot
4
20 µm

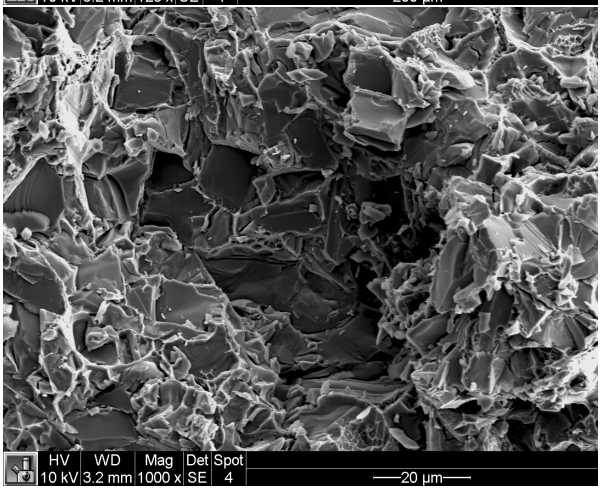
HV
10 kV
WD
3.2 mm
Mag
1000 x
Det
SE
Spot
4
20 µm

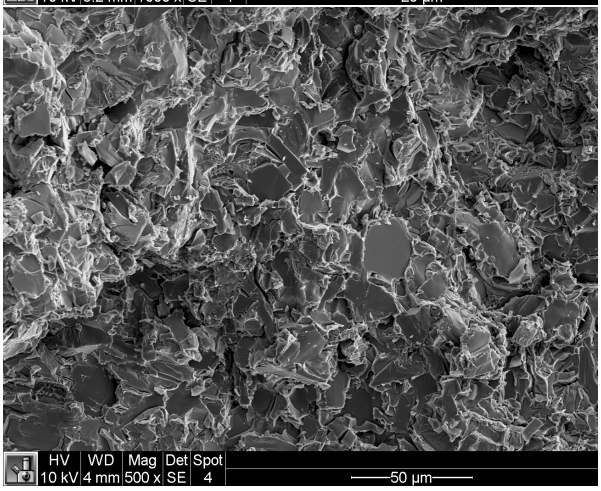
HV
10 kV
WD
4 mm
Mag
500 x
Det
SE
Spot
4
50 µm

A.3 SiC_p **distribution in AZ91**

A.3.1 Optical Micrograph

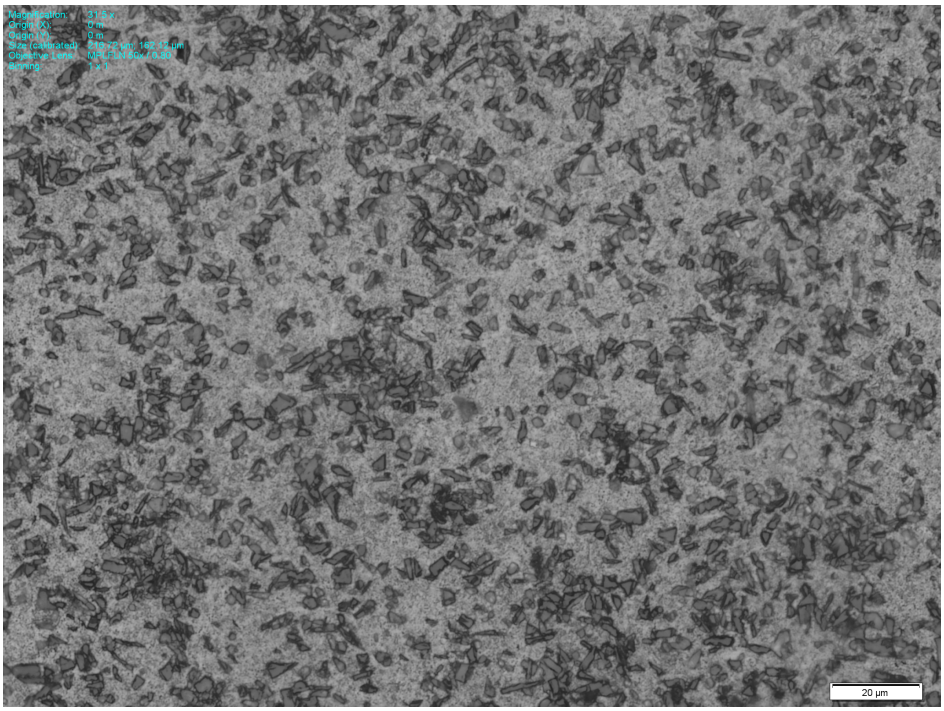

A.3.2 Matlab code for particle concentration and distribution

```
\subsection{Matlab code for particle concentration and distribution}
\begin{lstlisting}
close all
clear all
clc
%addpath('U:\MgSiC_percentage')
I1=imread('mgsic.TIF');
%16
%subplot(121)
figure();
imshow(I1)
% I1=im2bw(I1,0.4);
% I1=imcomplement(I1)
```

```
% figure();
% imshow(I1)
%imcontrast(I1);
%
I1=localcontrast(I1);
I1=imsharpen(I1);

%I1=imreducehaze(I1);
%subplot(122)
figure();
imshow(I1)
%imtool(I1)
r1=20/182;
%I2=im2bw(I1(1:470,:),.2);
s=size(I1);
In1=floor(s(1,1)/2);
In2=floor(s(1,2)/2);
%imshow(I2)
%imtool(I2)
t=110;
area_o=numel(I1);
for p=1:1:33
% 50 microns = 182 pixels
I2=im2bw(I1(In1-t:In1+t,In2-(t+30):In2+(t+30)),.22);
I2=imcomplement(I2);
I2=bwareaopen(I2,9);
I2=bwconvhull(I2,'objects');
figure();
imshow(I2)
measurements=regionprops(I2,'FilledArea','EquivDiameter','Boundingbox',...
                         'centroid');
data1=struct2cell(measurements);
data1=cell2mat(data1');
```

```
for p1=1:1:numel(measurements)
rectangle('Position', [measurements(p1).BoundingBox(1,1),...
                       measurements(p1).BoundingBox(1,2),...
                       measurements(p1).BoundingBox(1,3),...
                       measurements(p1).BoundingBox(1,4)],...
          'EdgeColor', 'r')
end

A1(p1,1)=measurements.FilledArea;
D1(p1,1)=measurements.EquivDiameter;
A2=sort(A1,'descend');
D2=sort(D1,'descend');
[¬,p2]=max(D1);

% Particle size determination
Diameter=D2*(50)/182;

% Average Particle size determination
Diameter=D2*r1;
j=1;
s1=length(Diameter);
for i=1:1:s1
    if Diameter(i,1)>5
        Diameter1(j,1)=Diameter(i,1);
        Area1(j,1)=A2(i,1);
        j=j+1;
    end
end

total_area1(p,1)=sum(double(I2(:)));
total_area(p,1)=numel(I2);
Percentage(p,1)=total_area1(p,1)/total_area(p,1) * 100;
t=20+t;
```

```
area_covered=total_area1(p,1)/area_o;
end
figure();
total_area=total_area.*(r1)^2;
plot(total_area,Percentage,'*')
hold on
  f = polyfit(total_area,Percentage,4);
        plot(total_area,Percentage,'o',total_area,polyval(f,total_area),'-')
        ylim([0 30])
        ylabel('% SiCp')
        xlabel('\mum^2','interpret','Tex')

figure();
imshow(I2)
figure();
imshow(I2) % figure
for p1=1:1:numel(measurements)
rectangle('Position', [measurements(p1).BoundingBox(1,1),...
                       measurements(p1).BoundingBox(1,2),...
                       measurements(p1).BoundingBox(1,3),...
                       measurements(p1).BoundingBox(1,4)],...
          'EdgeColor','r')
end

A1=sort(A1,'descend');
A_avg=mean(A1(1:15,1));
D=sqrt(A_avg*4/pi);
Da=D*r1;
D_all=sqrt(Area1.*(4/pi));
D_alla=D_all.*(r1);
figure();
histfit(D_alla,4)
xlabel('\mum','Interpret','Tex')
```

```
113 ylabel('counts')
114
115 figure();
116 histfit(Diameter1,3)
117 xlabel('\mum','Interpret','Tex')
118 ylabel('counts')
```

A.3.3 SiC_p percentage

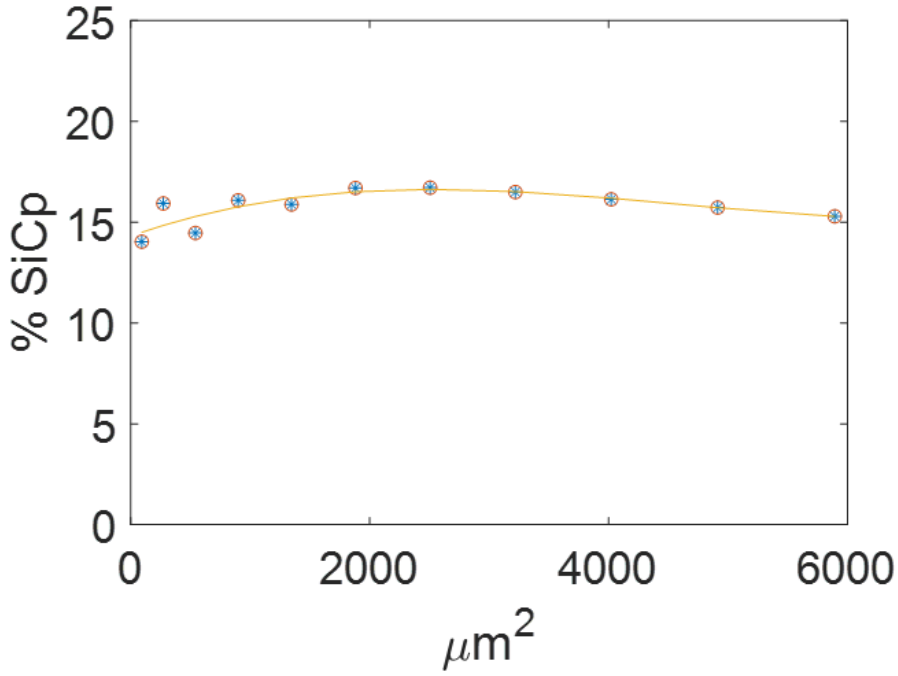

A.3.4 SiC_p size distribution

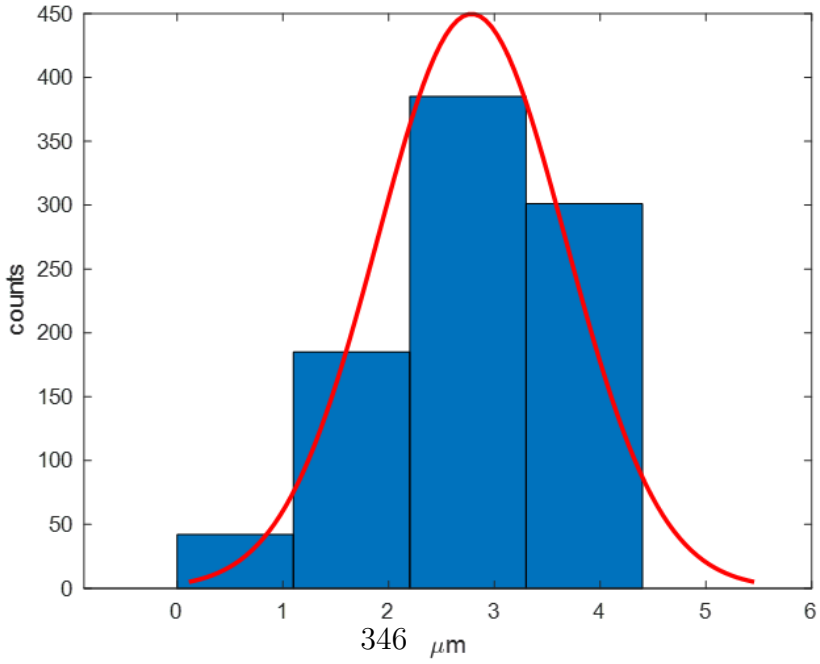

A.3.5 SiC_p percentage

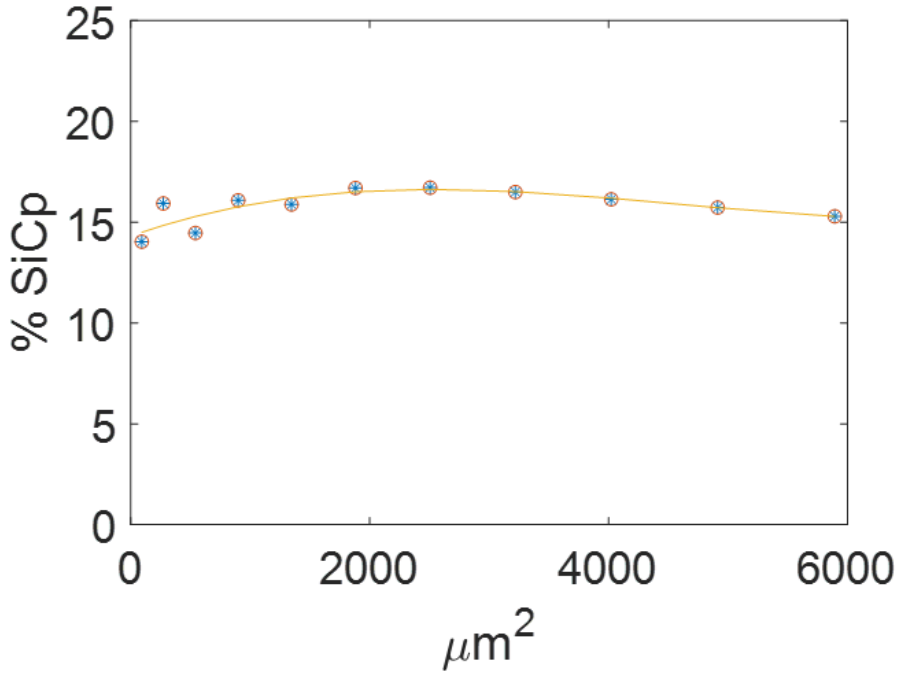

A.3.6 SiC_p size distribution

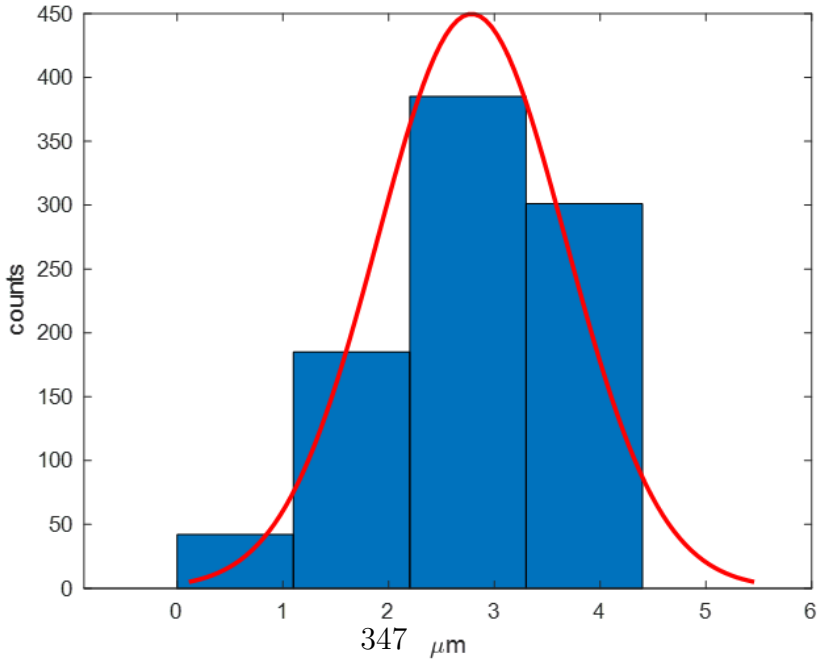

A.3.7 Tensile test

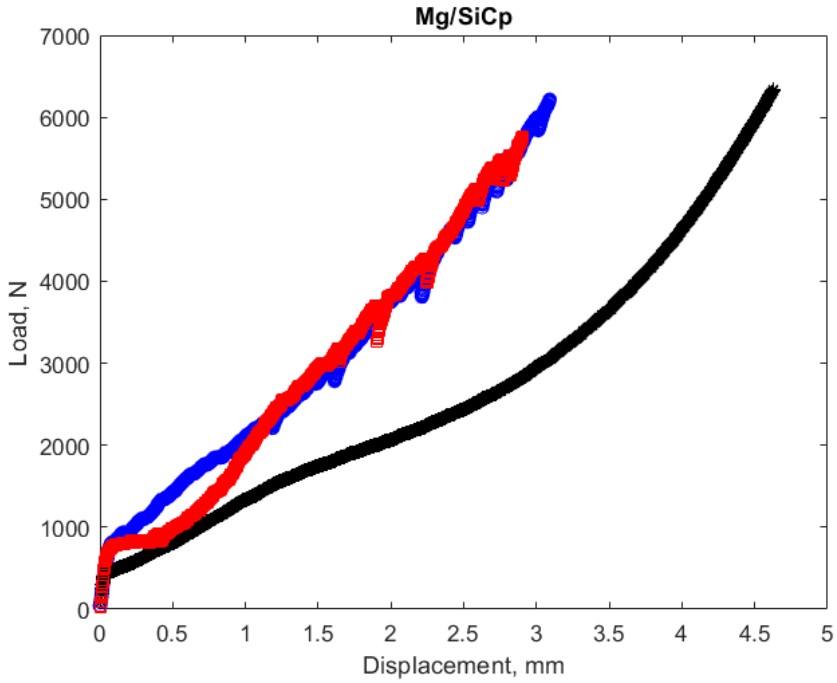

A.3.8 Tensile specimen fractography

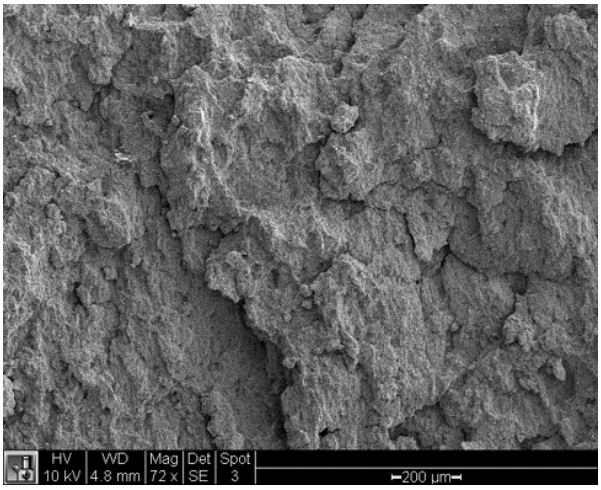

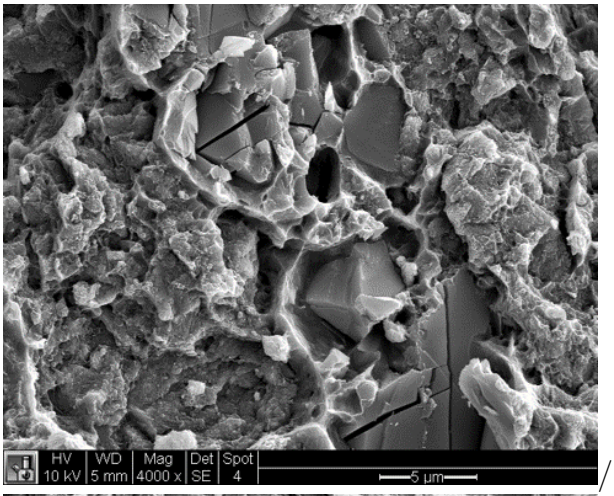

//

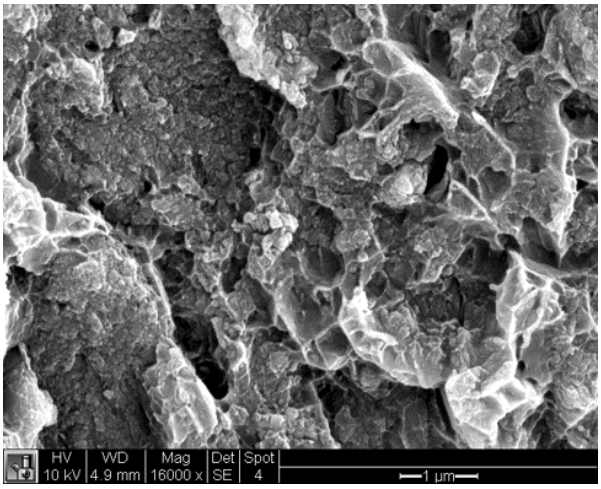

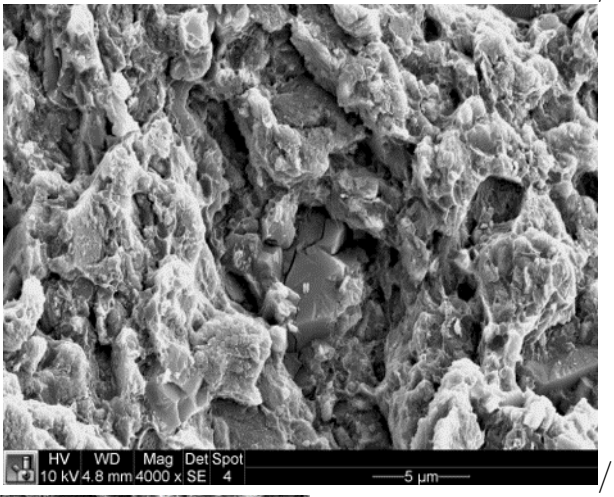

//

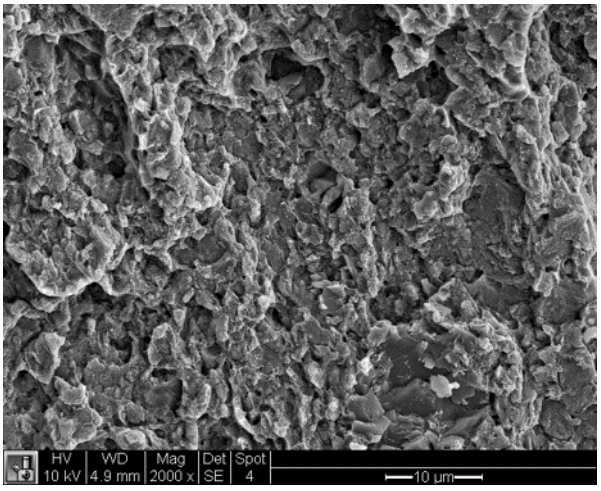

Appendix B

CUTTING FORCES, ACOUSTIC EMISSIONS AND TOOL WEAR

B.1 Functionally gradient A359/SiCp

B.1.1 Cutting forces

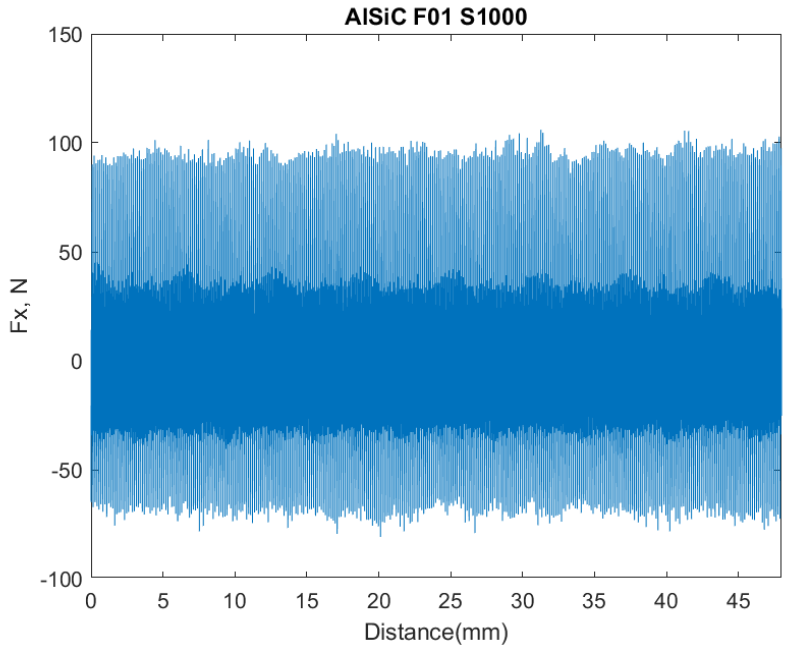

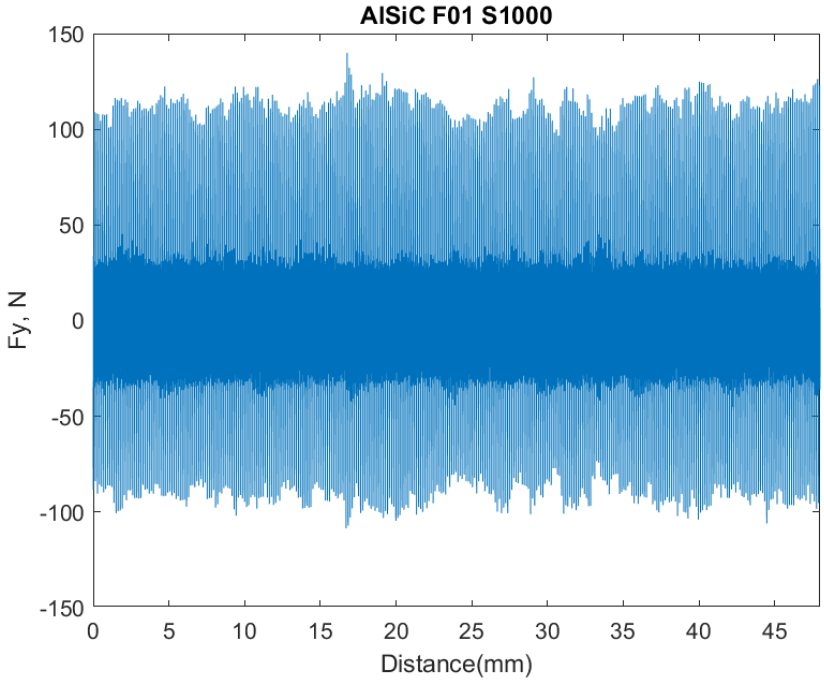
AlSiC F01 S1000
Fy, N
Distance(mm)
150
100
50
0
-50
-100
-150
0
5
10
15
20
25
30
35
40
45

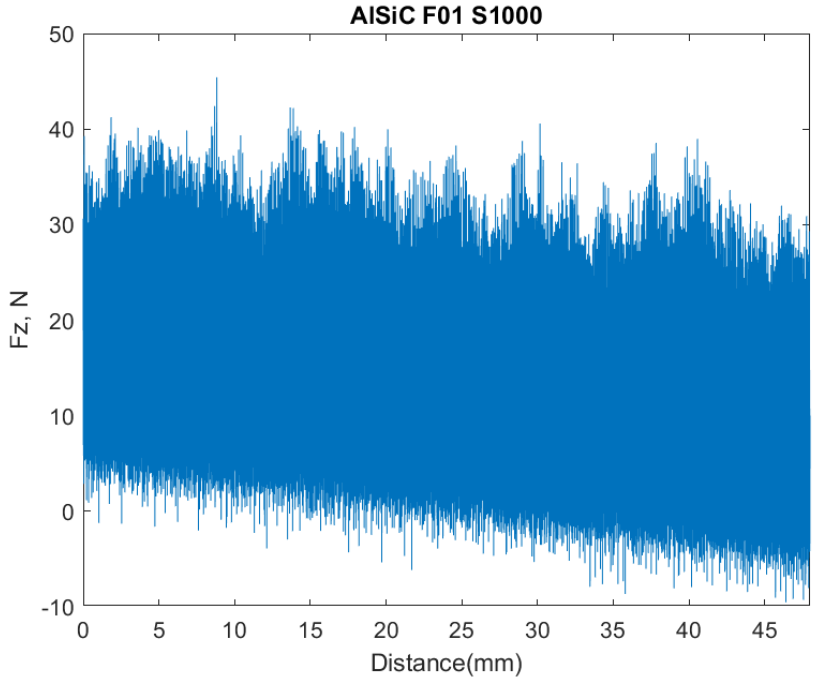
AlSiC F01 S1000
Fz, N
Distance(mm)
50
40
30
20
10
0
-10
0
5
10
15
20
25
30
35
40
45

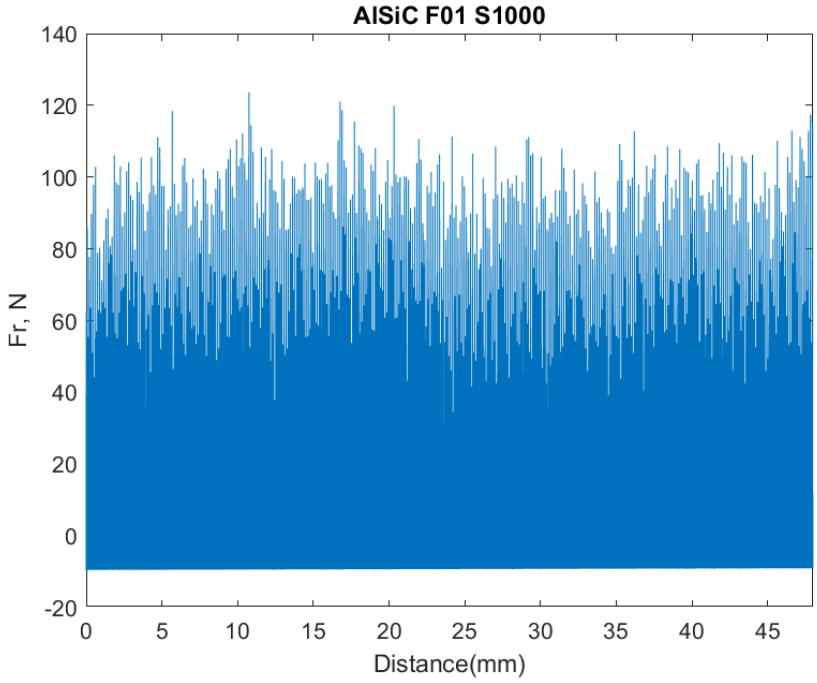
AlSiC F01 S1000
Fr, N
Distance(mm)
140
120
100
80
60
40
20
0
-20
0
5
10
15
20
25
30
35
40
45

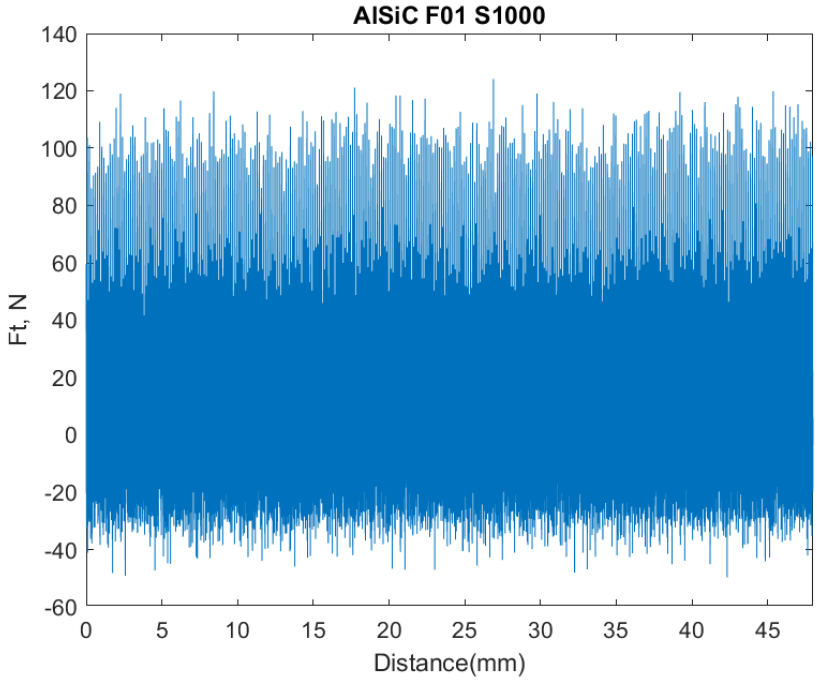
AlSiC F01 S1000
Ft, N
Distance(mm)
140
120
100
80
60
40
20
0
-20
-40
-60
0
5
10
15
20
25
30
35
40
45

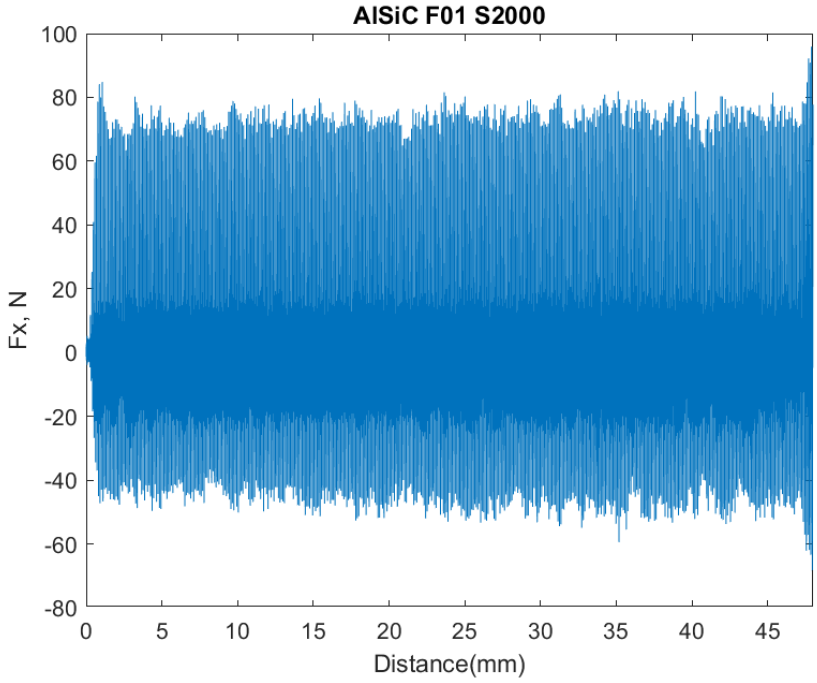
AlSiC F01 S2000
Fx, N
Distance(mm)
100
80
60
40
20
0
-20
-40
-60
-80
0
5
10
15
20
25
30
35
40
45

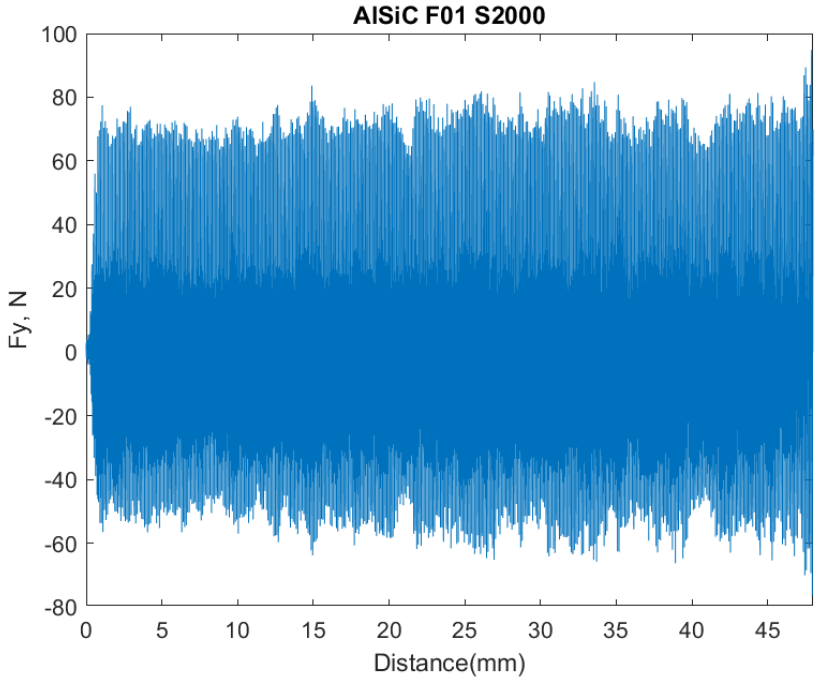
AlSiC F01 S2000
Fy, N
Distance(mm)
100
80
60
40
20
0
-20
-40
-60
-80
0
5
10
15
20
25
30
35
40
45

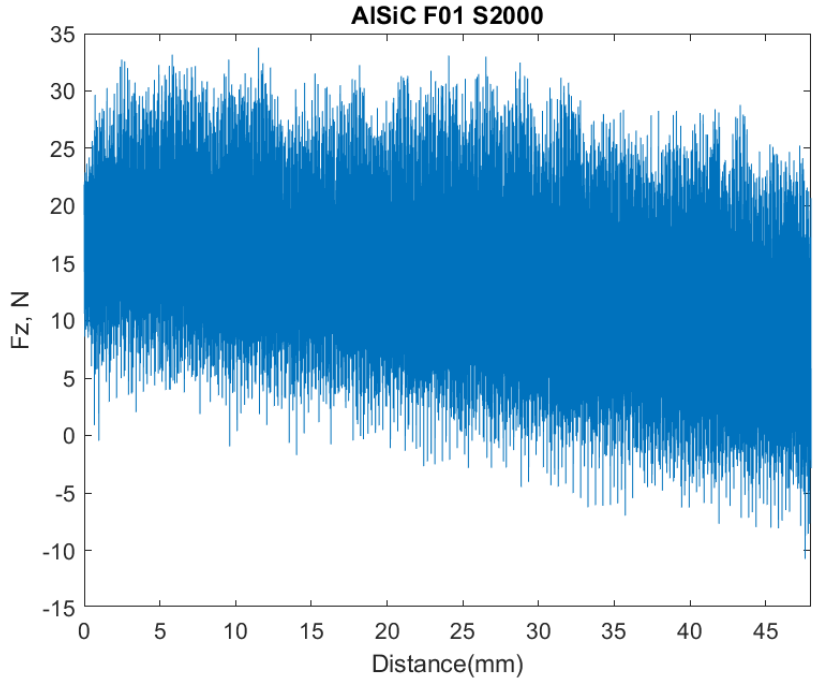
AlSiC F01 S2000
Fz, N
Distance(mm)
35
30
25
20
15
10
5
0
-5
-10
-15
0
5
10
15
20
25
30
35
40
45

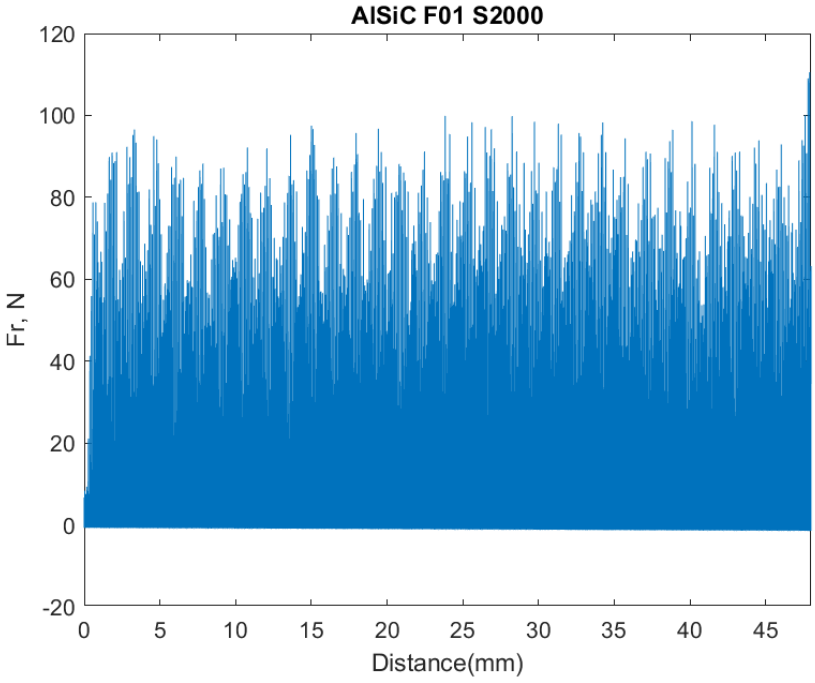
AlSiC F01 S2000
Fr, N
Distance(mm)
120
100
80
60
40
20
0
-20
0
5
10
15
20
25
30
35
40
45

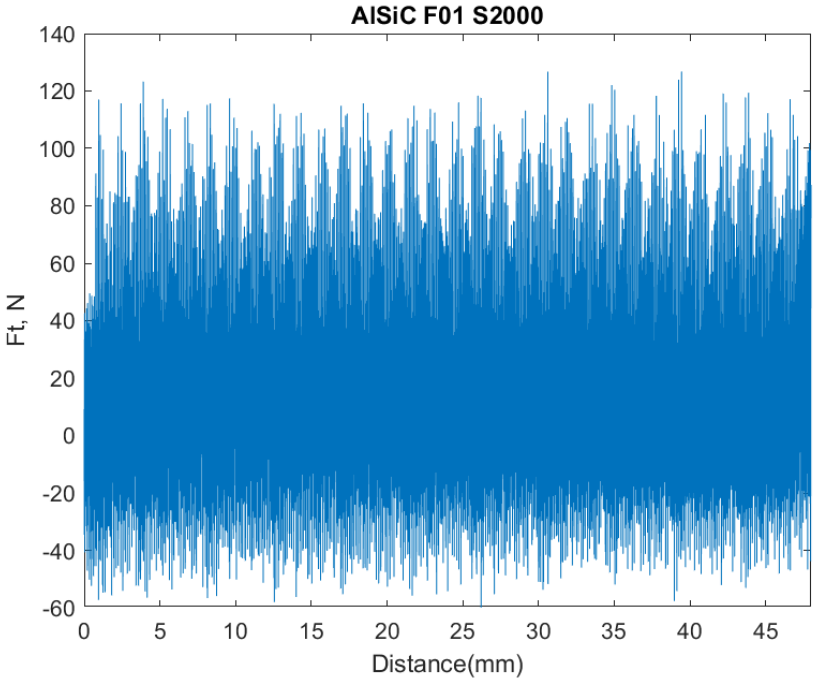
AlSiC F01 S2000
Ft, N
Distance(mm)
140
120
100
80
60
40
20
0
-20
-40
-60
0
5
10
15
20
25
30
35
40
45

0.9em

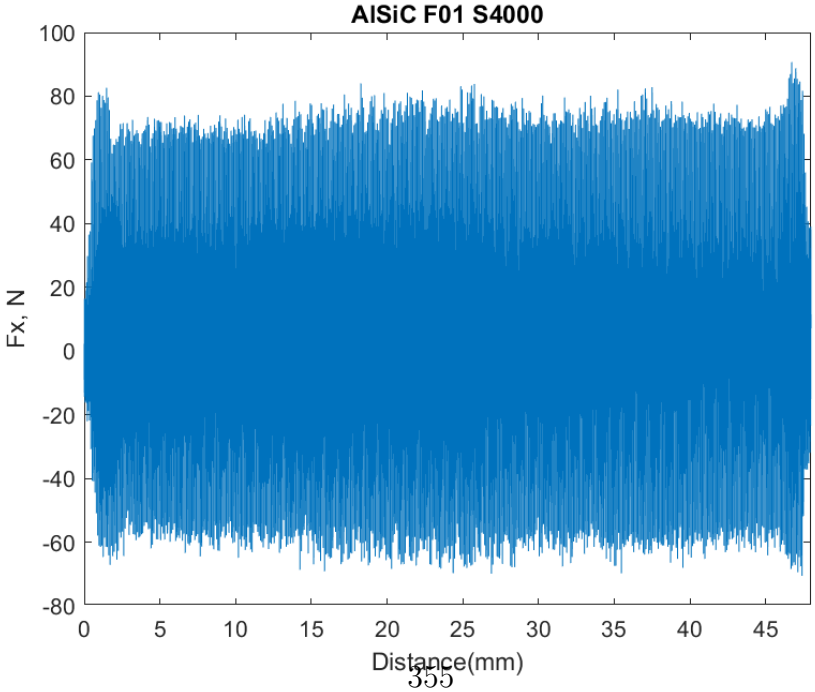
AlSiC F01 S4000
Fx, N
Distance(mm)
100
80
60
40
20
0
-20
-40
-60
-80
0
5
10
15
20
25
30
35
40
45

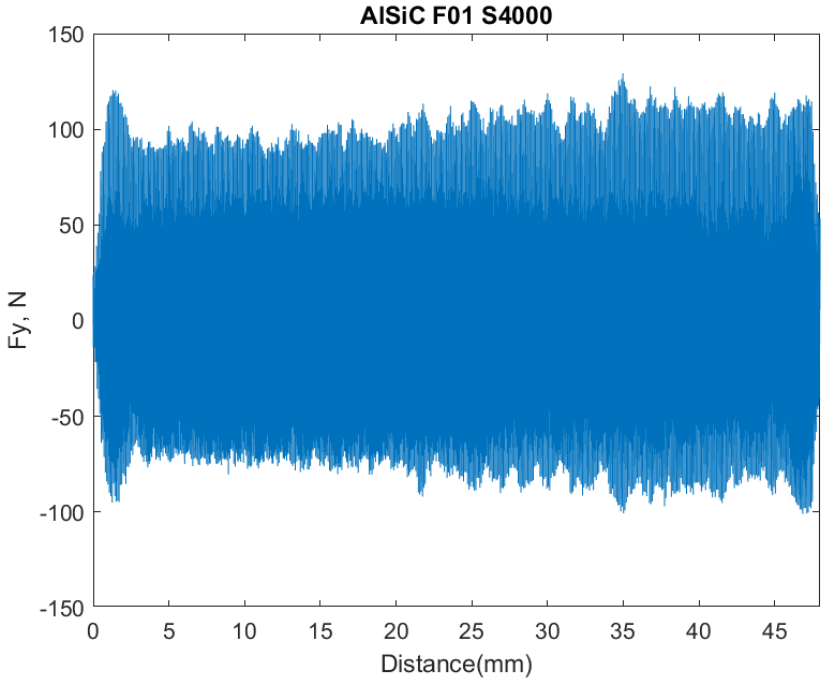
AlSiC F01 S4000
Fy, N
Distance(mm)
150
100
50
0
-50
-100
-150
0
5
10
15
20
25
30
35
40
45

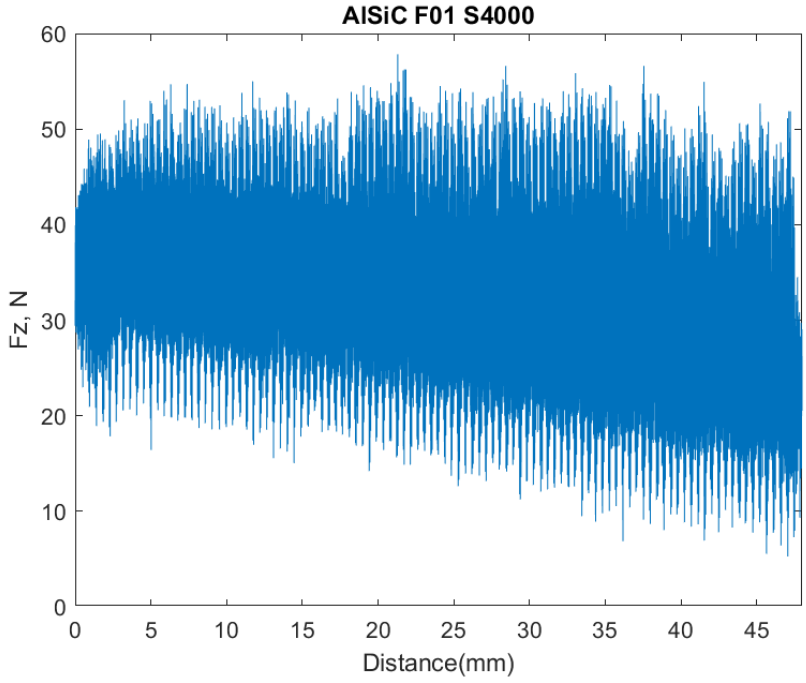
AlSiC F01 S4000
Fz, N
Distance(mm)
60
50
40
30
20
10
0
0
5
10
15
20
25
30
35
40
45

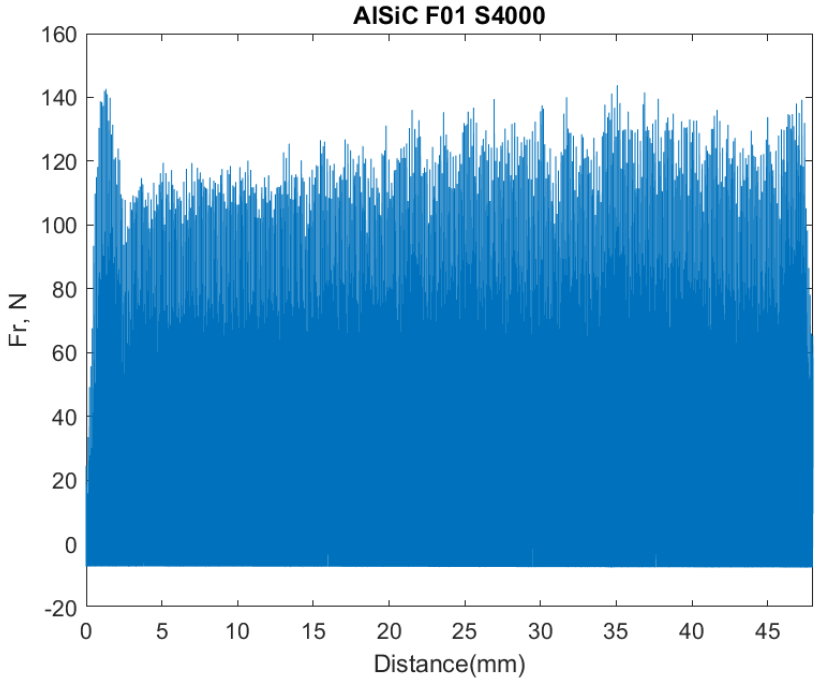
AlSiC F01 S4000
Fr, N
Distance(mm)
160
140
120
100
80
60
40
20
0
-20
0
5
10
15
20
25
30
35
40
45

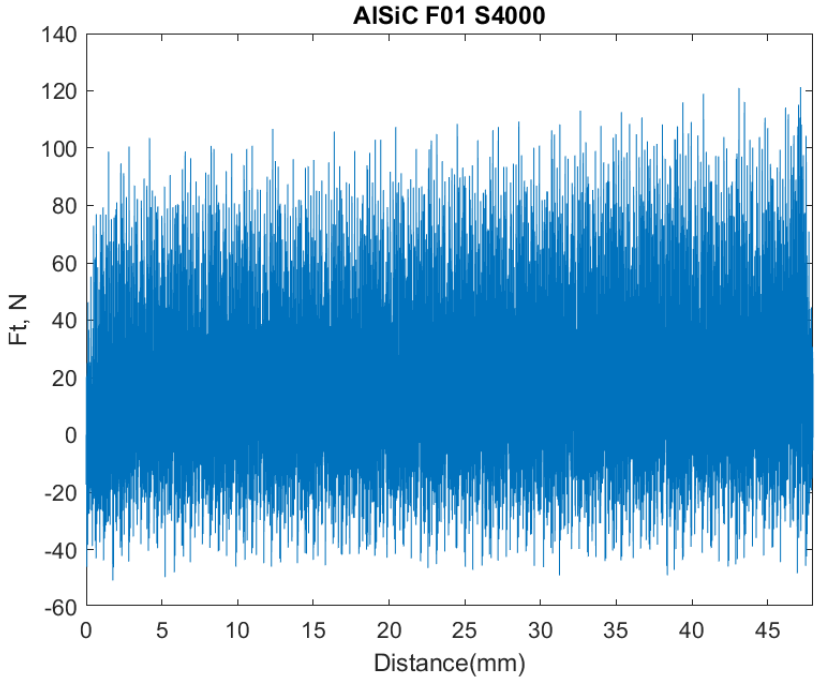
AlSiC F01 S4000
Ft, N
Distance(mm)
140
120
100
80
60
40
20
0
-20
-40
-60
0
5
10
15
20
25
30
35
40
45

0.9em

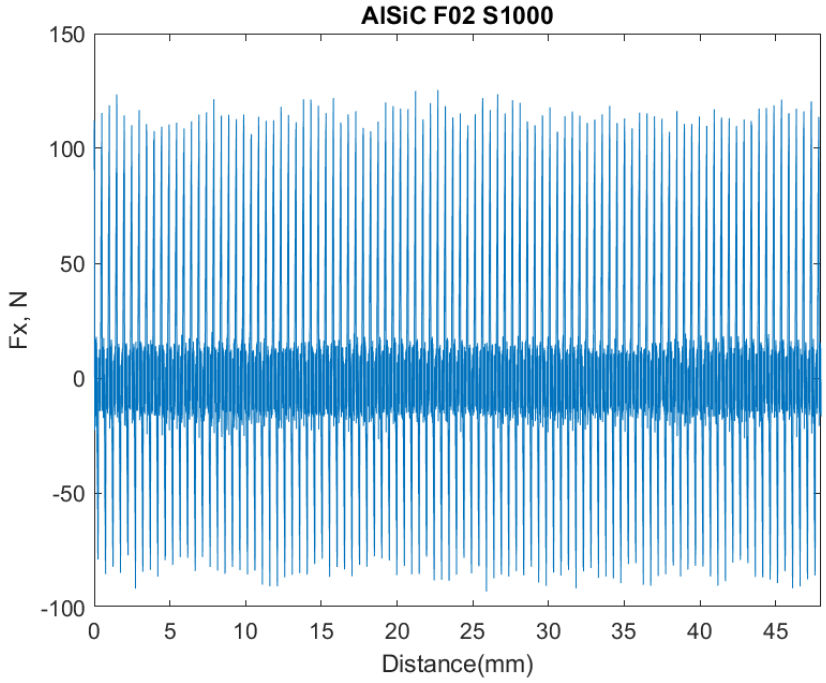
AlSiC F02 S1000
Fx, N
Distance(mm)
150
100
50
0
-50
-100
0
5
10
15
20
25
30
35
40
45

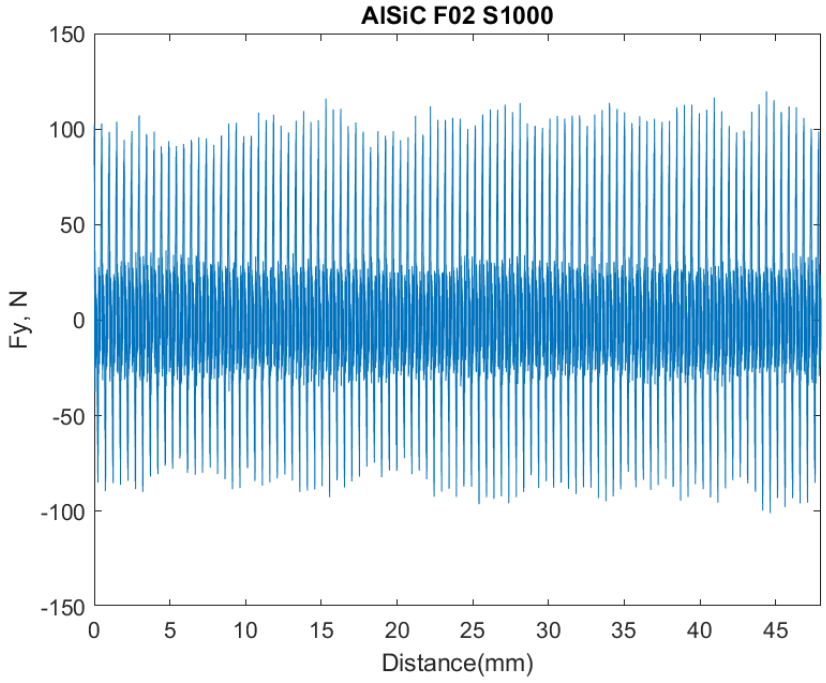
AlSiC F02 S1000
Fy, N
Distance(mm)
150
100
50
0
-50
-100
-150
0
5
10
15
20
25
30
35
40
45

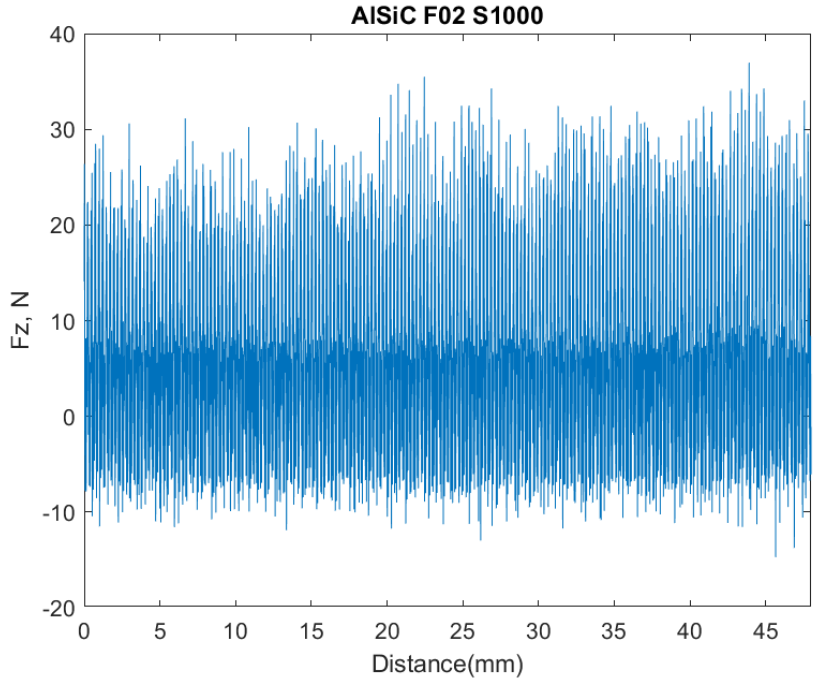
AlSiC F02 S1000
Fz, N
Distance(mm)
40
30
20
10
0
-10
-20
0
5
10
15
20
25
30
35
40
45

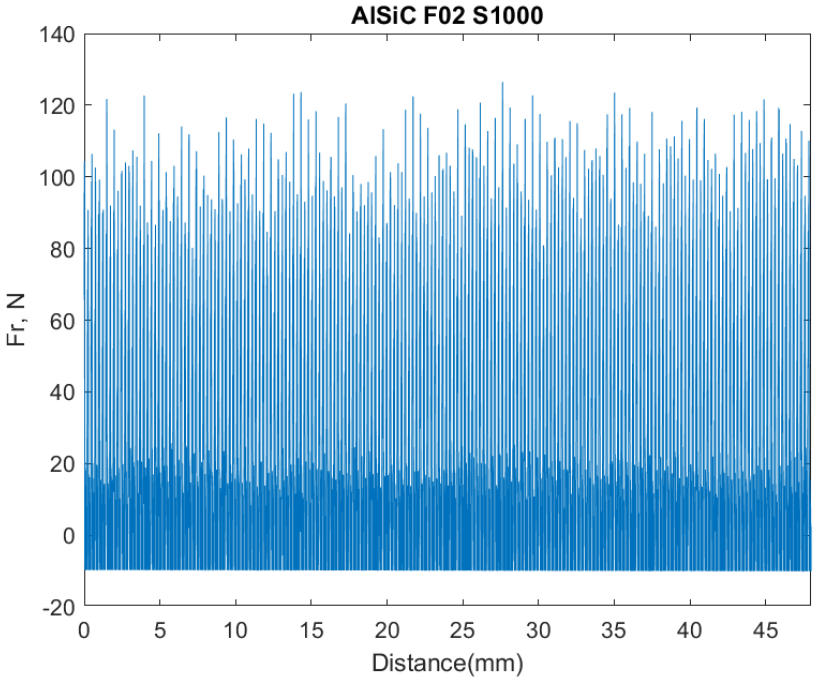
AlSiC F02 S1000
Fr, N
Distance(mm)
140
120
100
80
60
40
20
0
-20
0
5
10
15
20
25
30
35
40
45

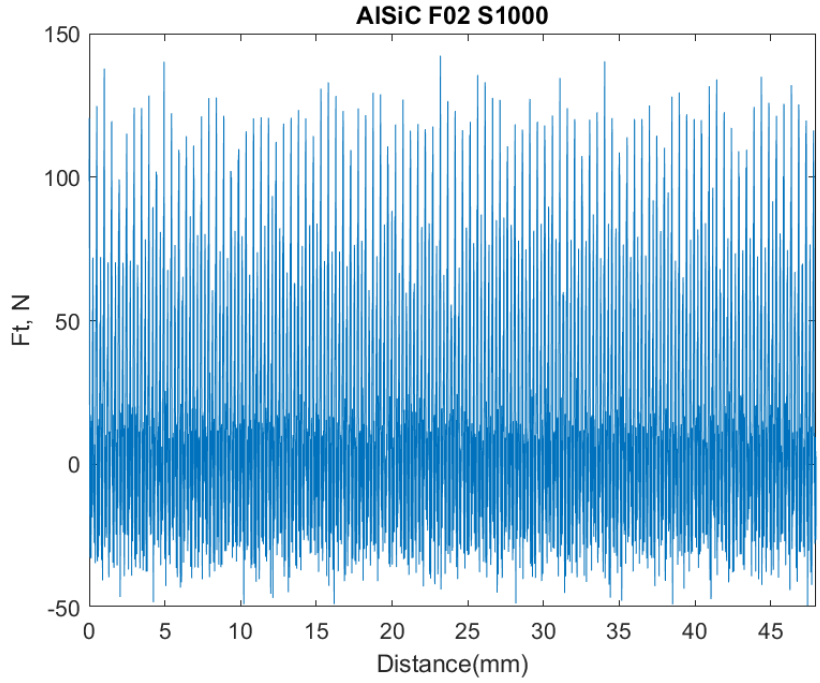
AlSiC F02 S1000
Ft, N
150
100
50
0
-50
0
5
10
15
20
25
30
35
40
45
Distance(mm)

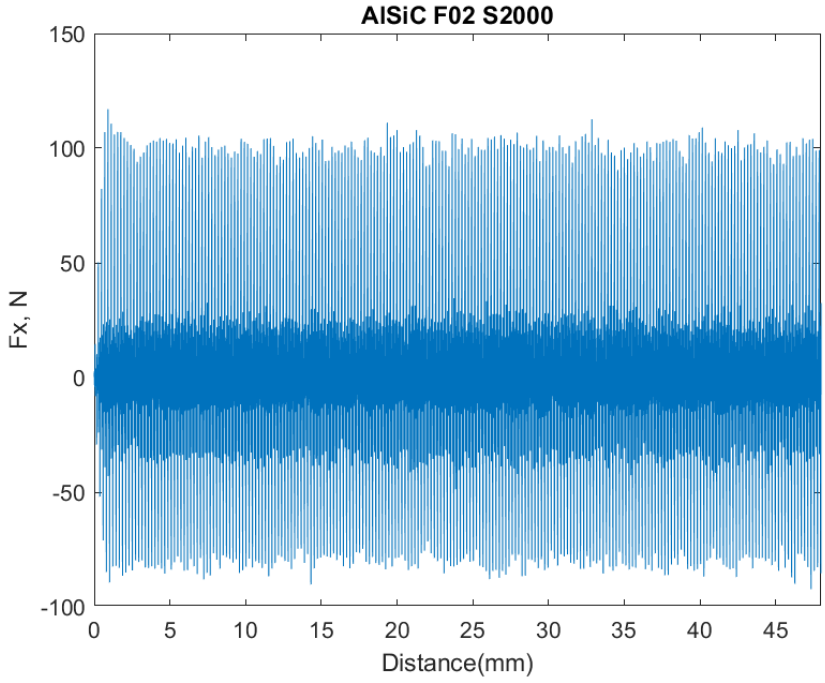
AlSiC F02 S2000
Fx, N
150
100
50
0
-50
-100
0
5
10
15
20
25
30
35
40
45
Distance(mm)

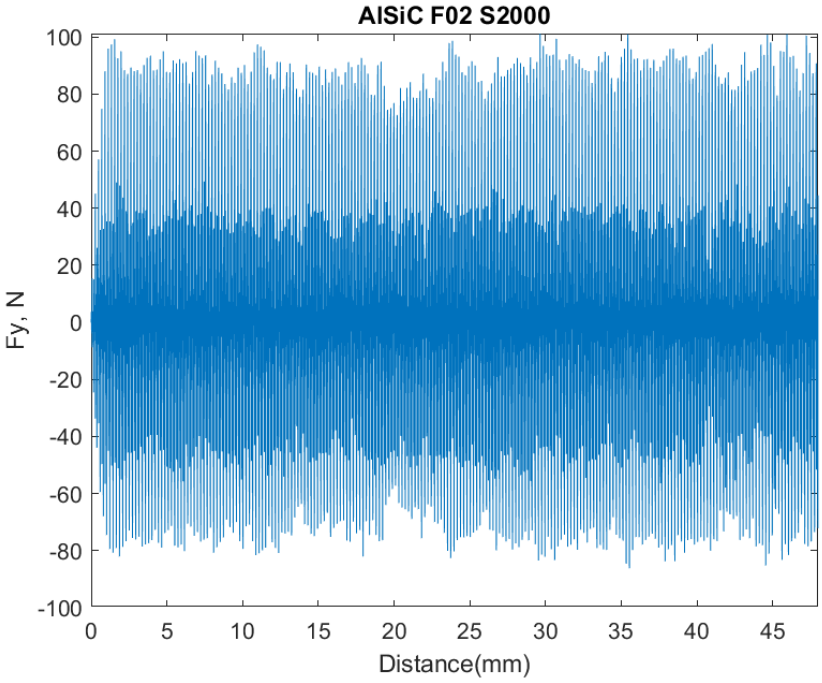
AlSiC F02 S2000
Fy, N
Distance(mm)
100
80
60
40
20
0
-20
-40
-60
-80
-100
0
5
10
15
20
25
30
35
40
45

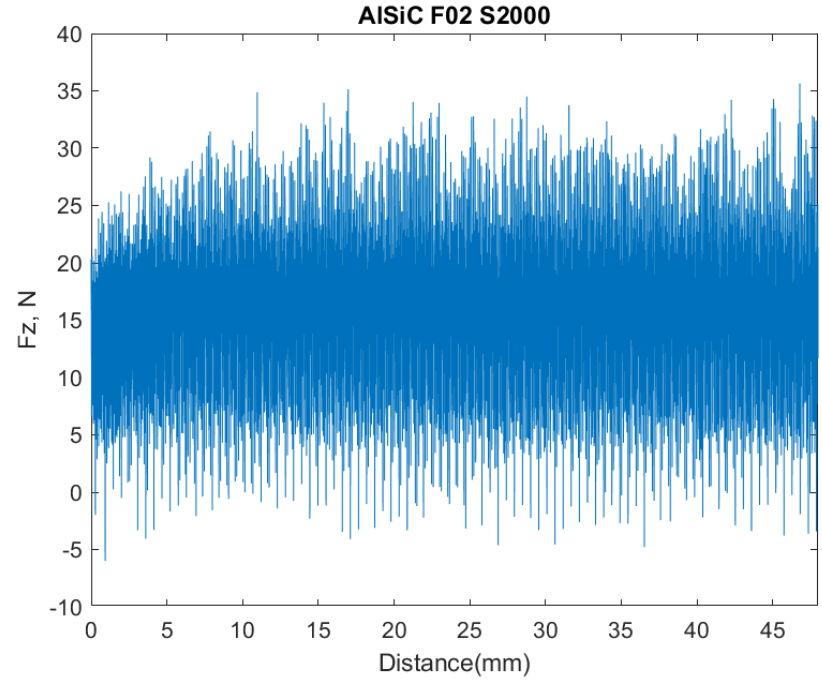
AlSiC F02 S2000
Fz, N
Distance(mm)
40
35
30
25
20
15
10
5
0
-5
-10
0
5
10
15
20
25
30
35
40
45

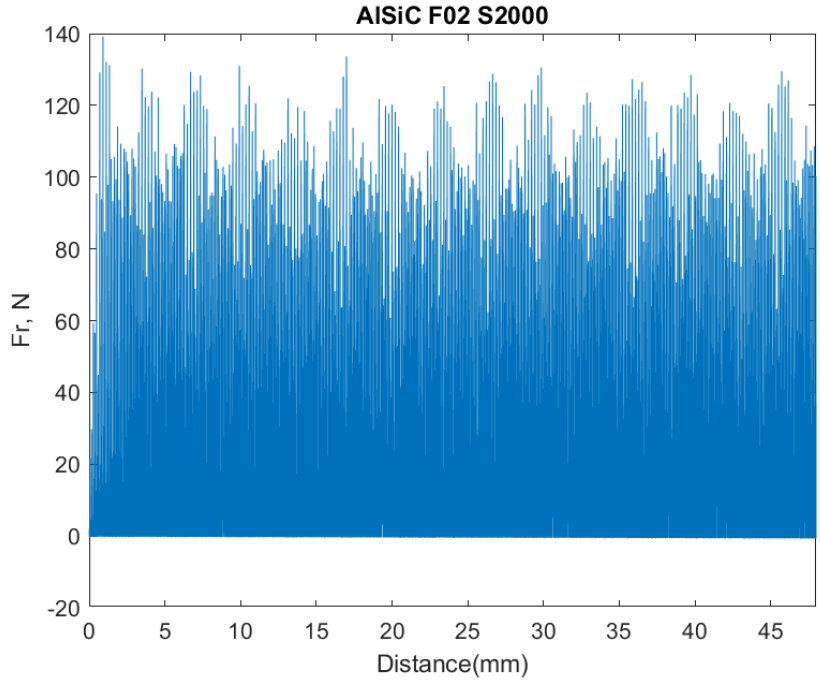
AlSiC F02 S2000
Fr, N
Distance(mm)
140
120
100
80
60
40
20
0
-20
0
5
10
15
20
25
30
35
40
45

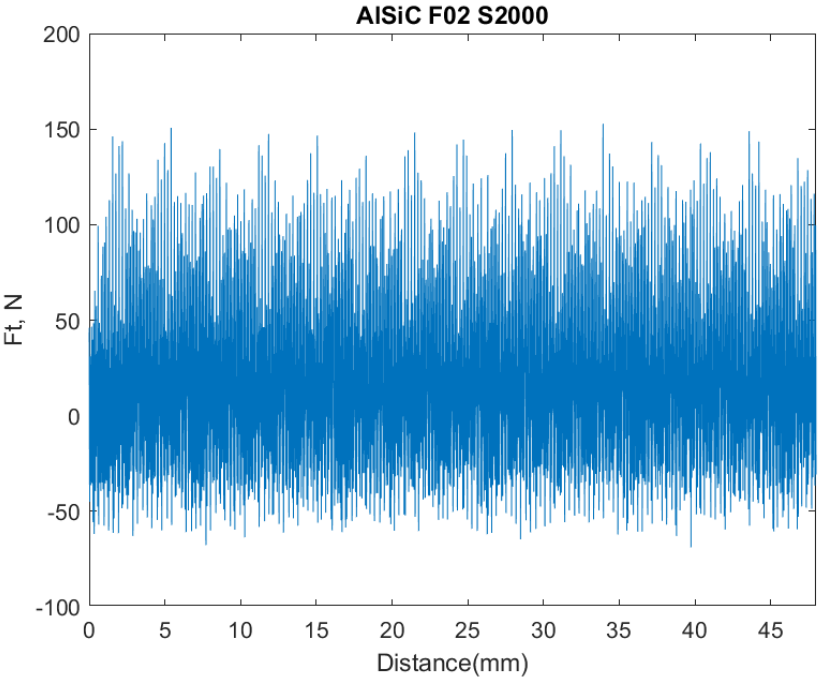
AlSiC F02 S2000
Ft, N
Distance(mm)
200
150
100
50
0
-50
-100
0
5
10
15
20
25
30
35
40
45

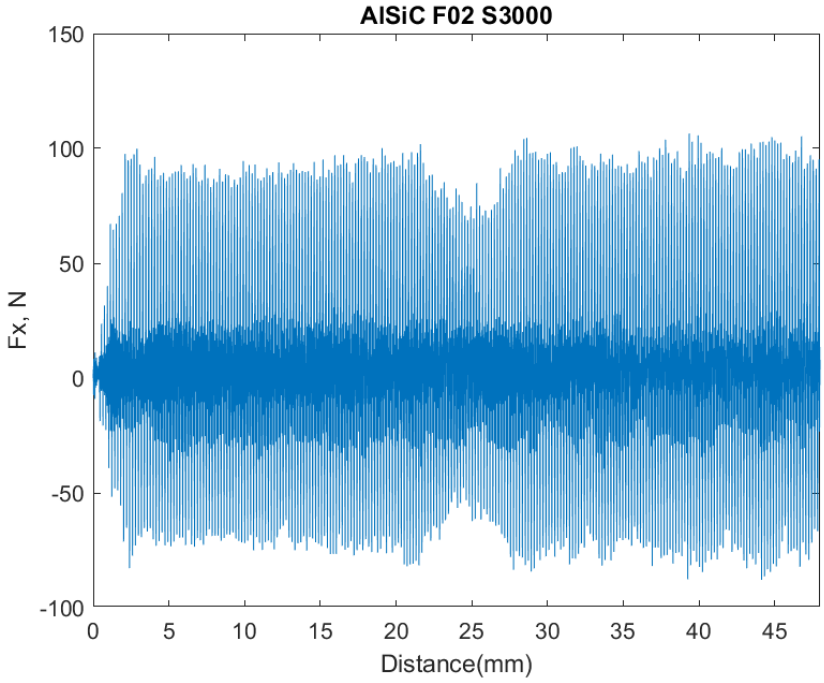
AlSiC F02 S3000
Fx, N
Distance(mm)
150
100
50
0
-50
-100
0
5
10
15
20
25
30
35
40
45

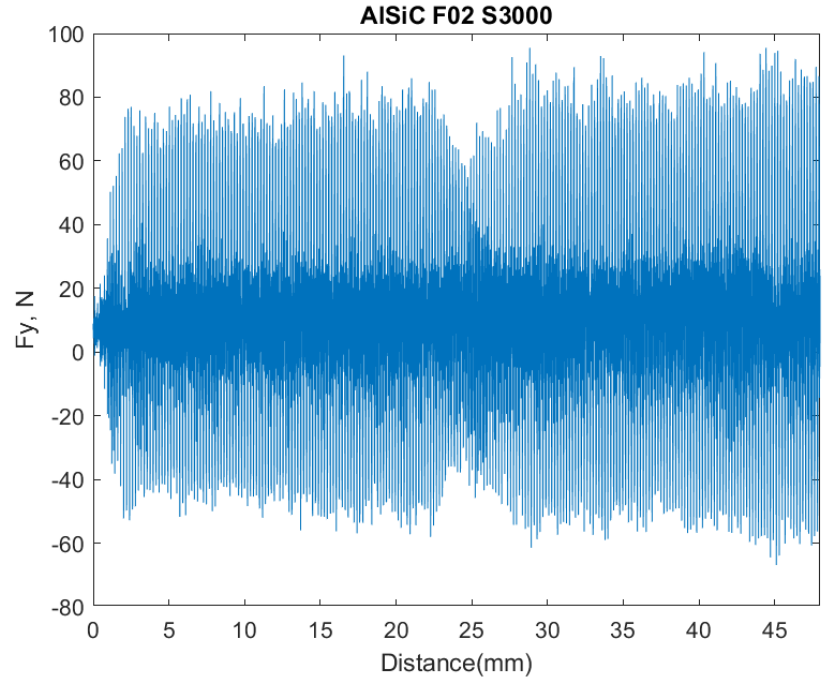
AlSiC F02 S3000
Fy, N
Distance(mm)
100
80
60
40
20
0
-20
-40
-60
-80
0
5
10
15
20
25
30
35
40
45

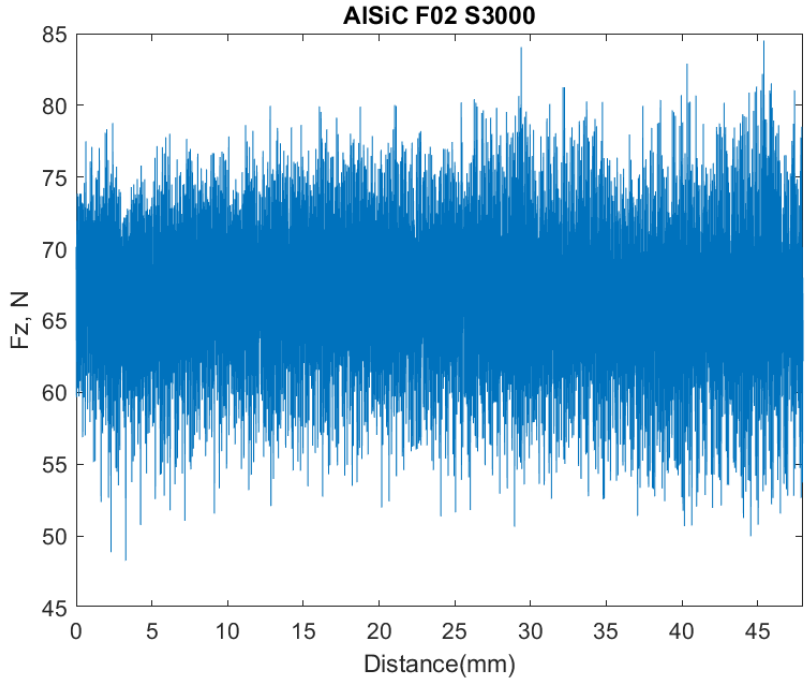
AlSiC F02 S3000
Fz, N
Distance(mm)
85
80
75
70
65
60
55
50
45
0
5
10
15
20
25
30
35
40
45

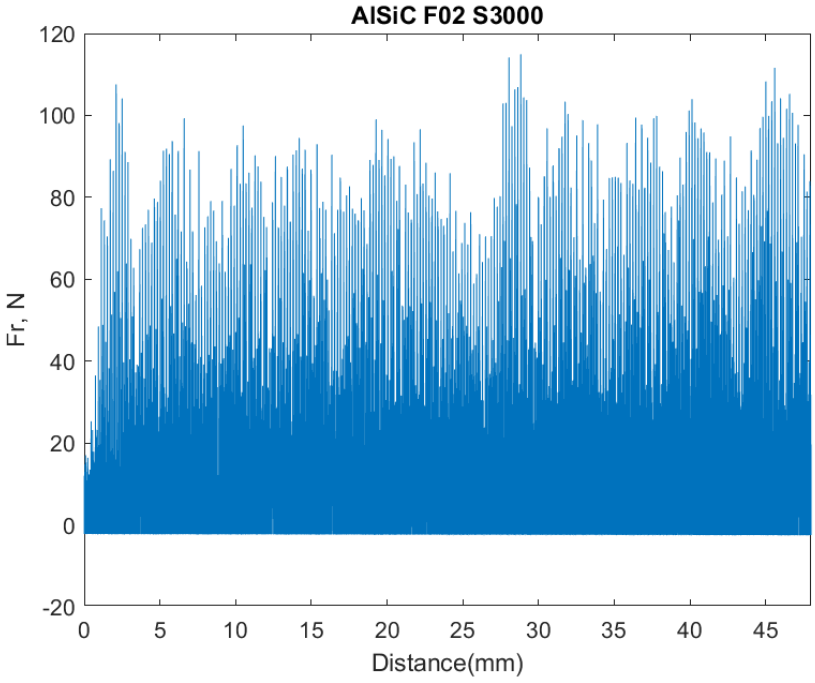
AlSiC F02 S3000
Fr, N
Distance(mm)
120
100
80
60
40
20
0
-20
0
5
10
15
20
25
30
35
40
45

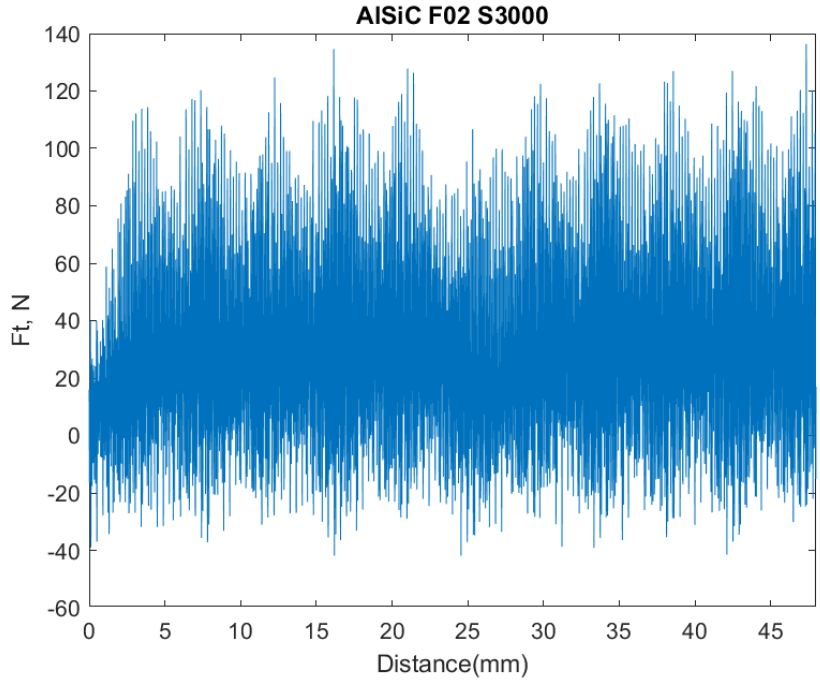
AlSiC F02 S3000
Ft, N
Distance(mm)
140
120
100
80
60
40
20
0
-20
-40
-60
0
5
10
15
20
25
30
35
40
45

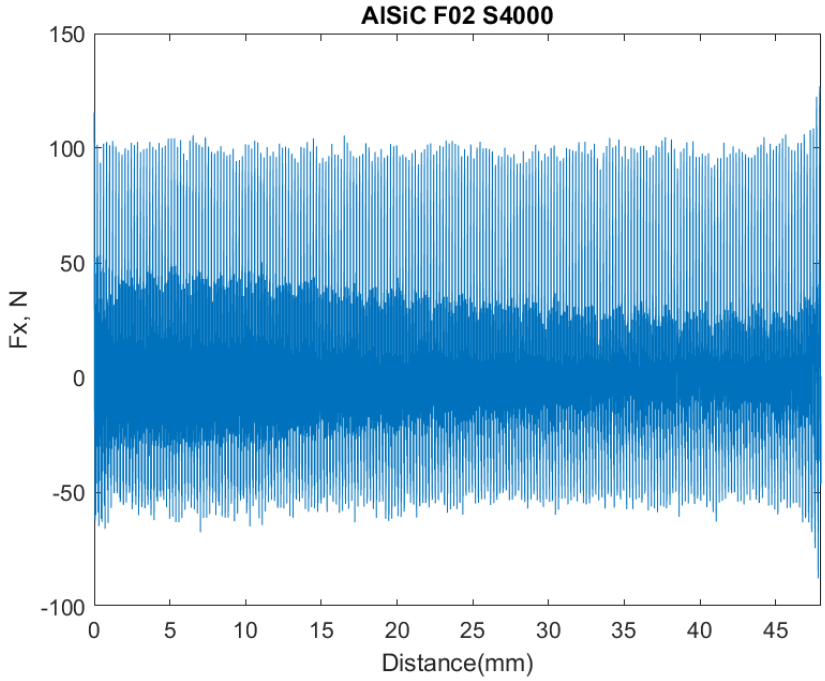
AlSiC F02 S4000
Fx, N
Distance(mm)
150
100
50
0
-50
-100
0
5
10
15
20
25
30
35
40
45

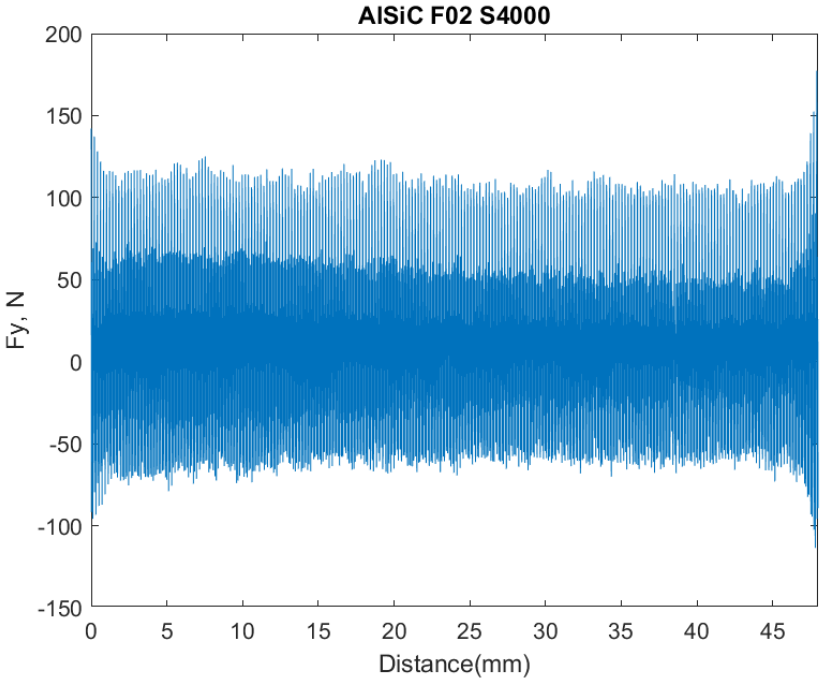
AlSiC F02 S4000
Fy, N
Distance(mm)
200
150
100
50
0
-50
-100
-150
0
5
10
15
20
25
30
35
40
45

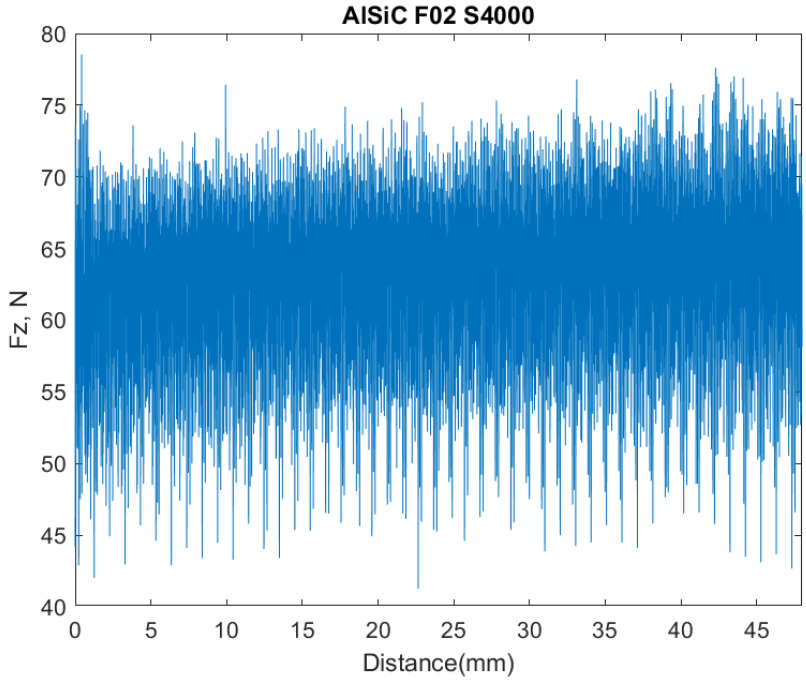
AlSiC F02 S4000
Fz, N
Distance(mm)
80
75
70
65
60
55
50
45
40
0
5
10
15
20
25
30
35
40
45

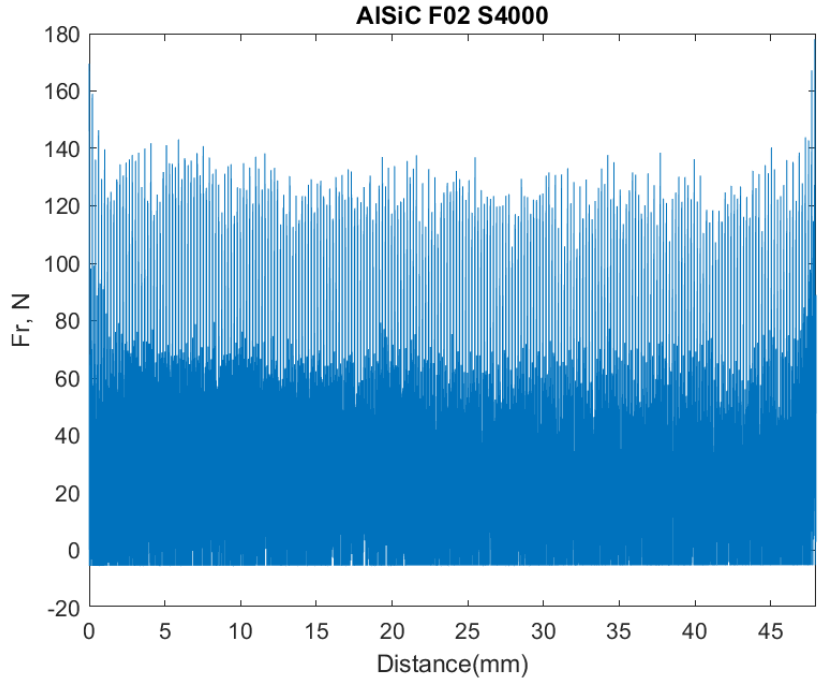
AlSiC F02 S4000
Fr, N
Distance(mm)
180
160
140
120
100
80
60
40
20
0
-20
0
5
10
15
20
25
30
35
40
45

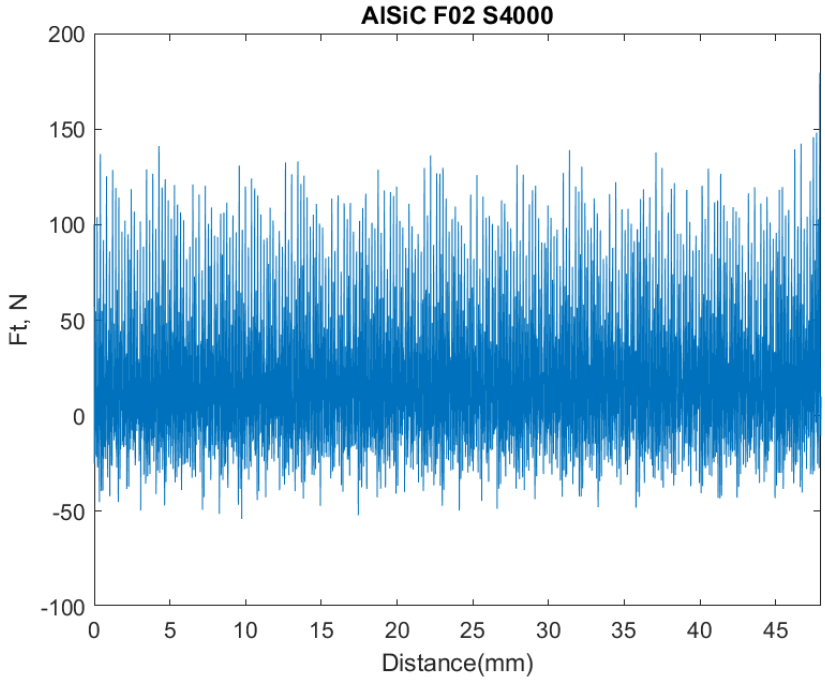
AlSiC F02 S4000
Ft, N
Distance(mm)
200
150
100
50
0
-50
-100
0
5
10
15
20
25
30
35
40
45

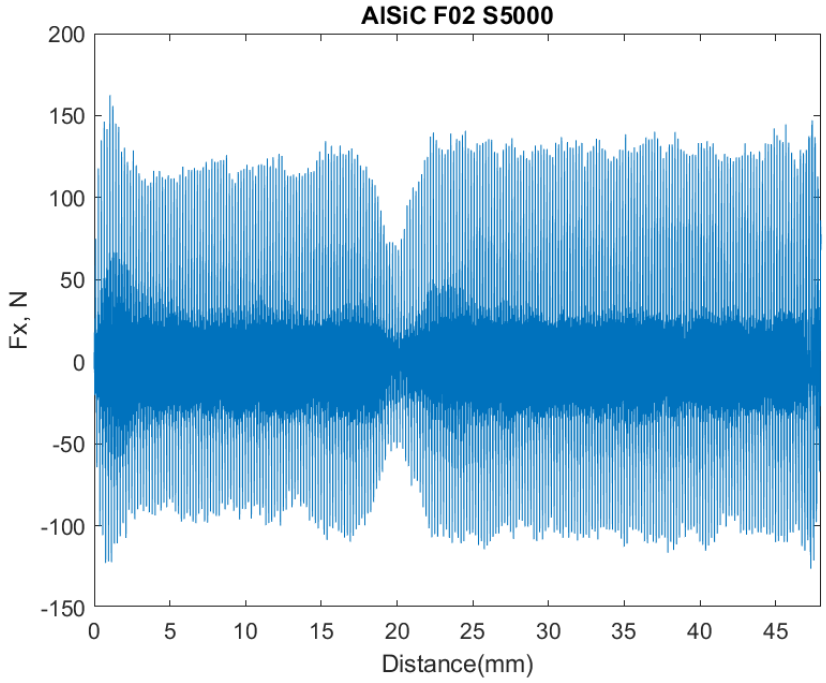
AlSiC F02 S5000
Fx, N
Distance(mm)
200
150
100
50
0
-50
-100
-150
0
5
10
15
20
25
30
35
40
45

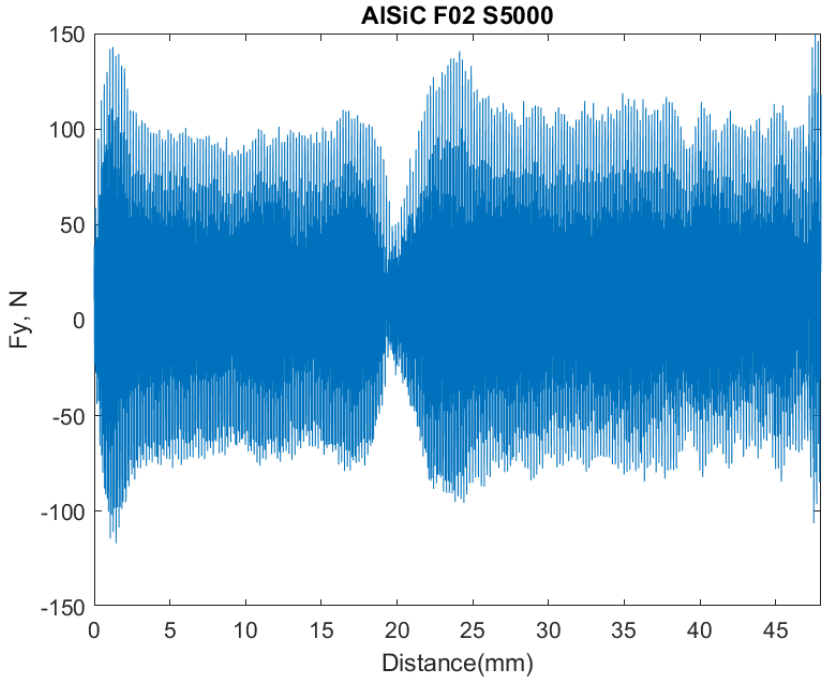
AlSiC F02 S5000
Fy, N
Distance(mm)
150
100
50
0
-50
-100
-150
0
5
10
15
20
25
30
35
40
45

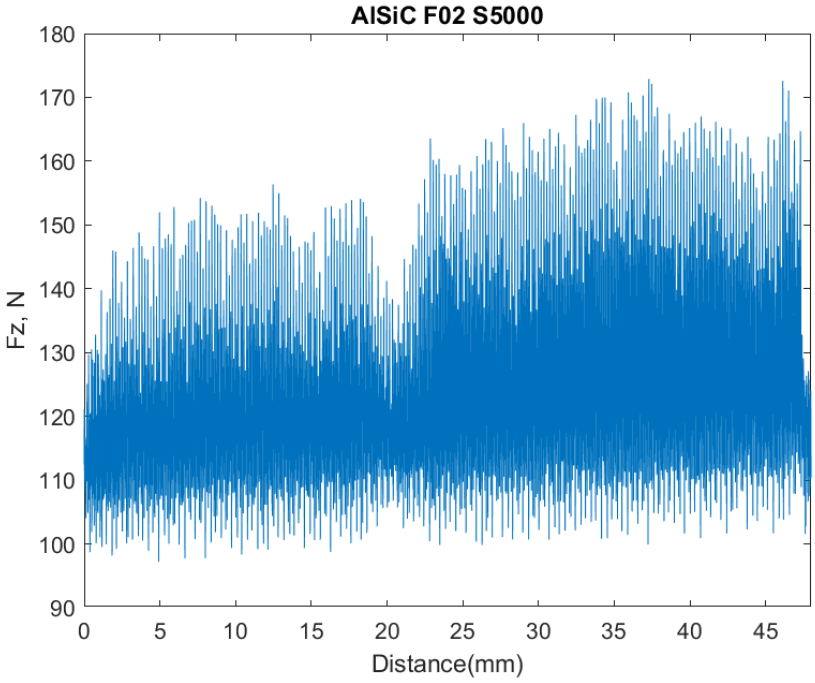
AlSiC F02 S5000
Fz, N
Distance(mm)
180
170
160
150
140
130
120
110
100
90
0
5
10
15
20
25
30
35
40
45

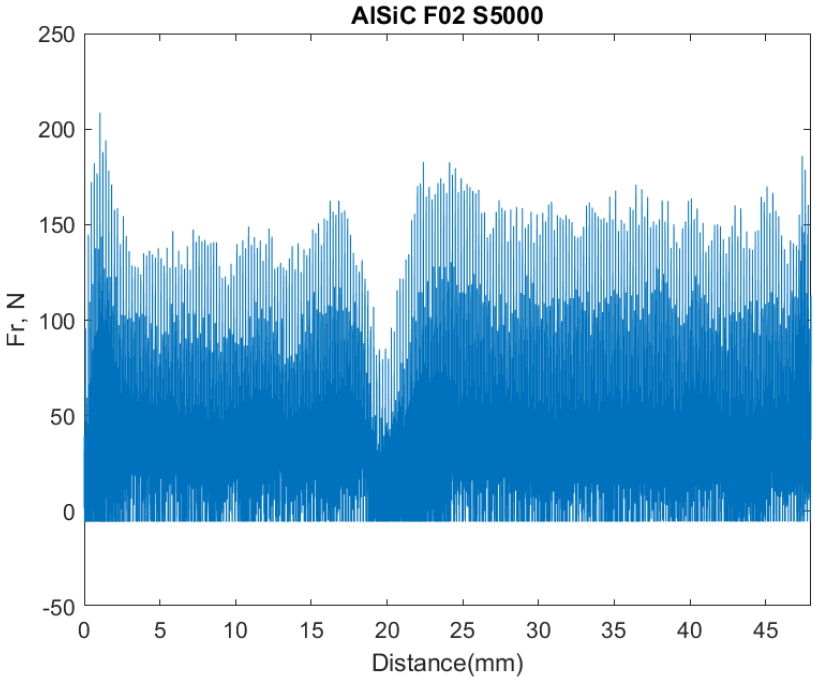
AlSiC F02 S5000
Fr, N
Distance(mm)
250
200
150
100
50
0
-50
0
5
10
15
20
25
30
35
40
45

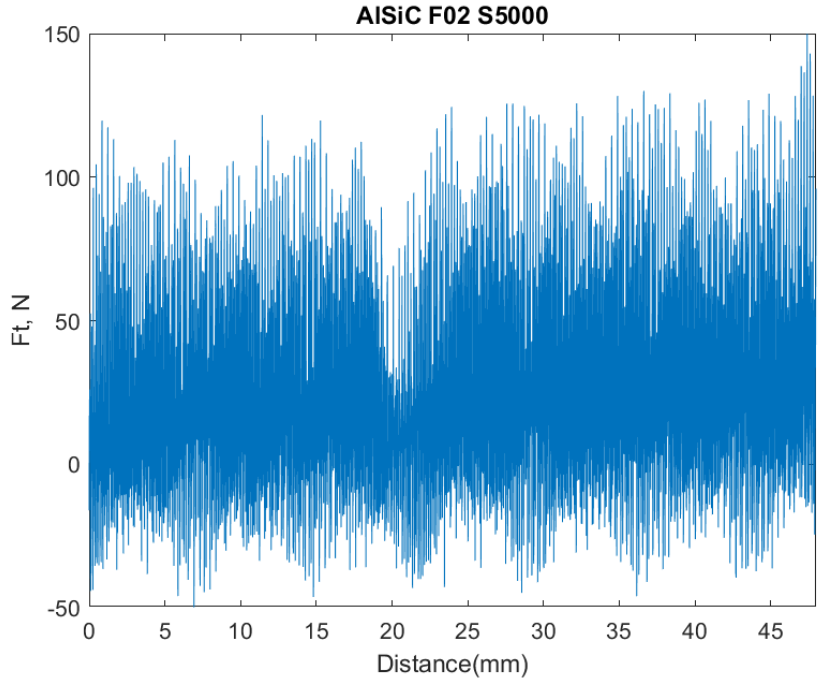
AlSiC F02 S5000
Ft, N
Distance(mm)
150
100
50
0
-50
0
5
10
15
20
25
30
35
40
45

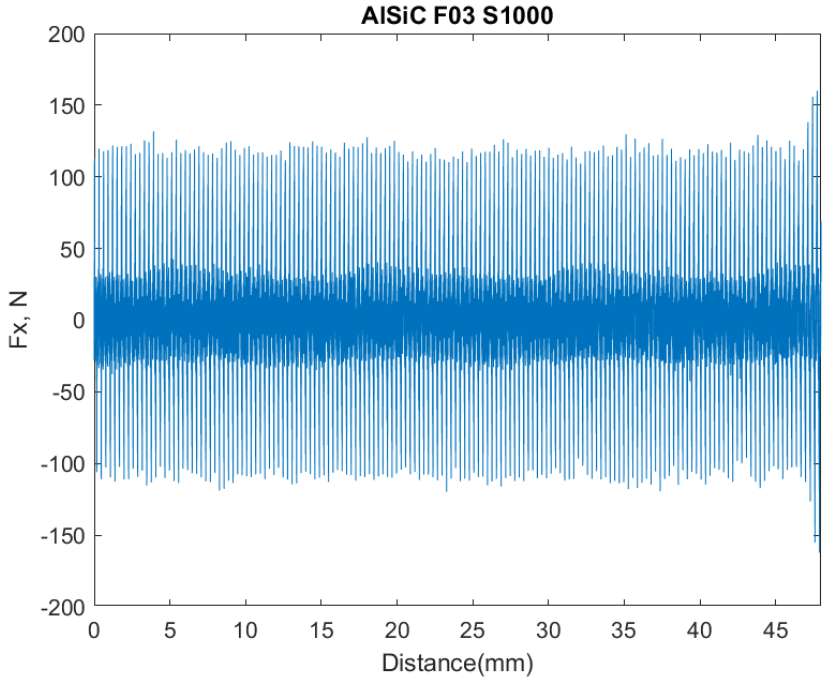
AlSiC F03 S1000
Fx, N
Distance(mm)
200
150
100
50
0
-50
-100
-150
-200
0
5
10
15
20
25
30
35
40
45

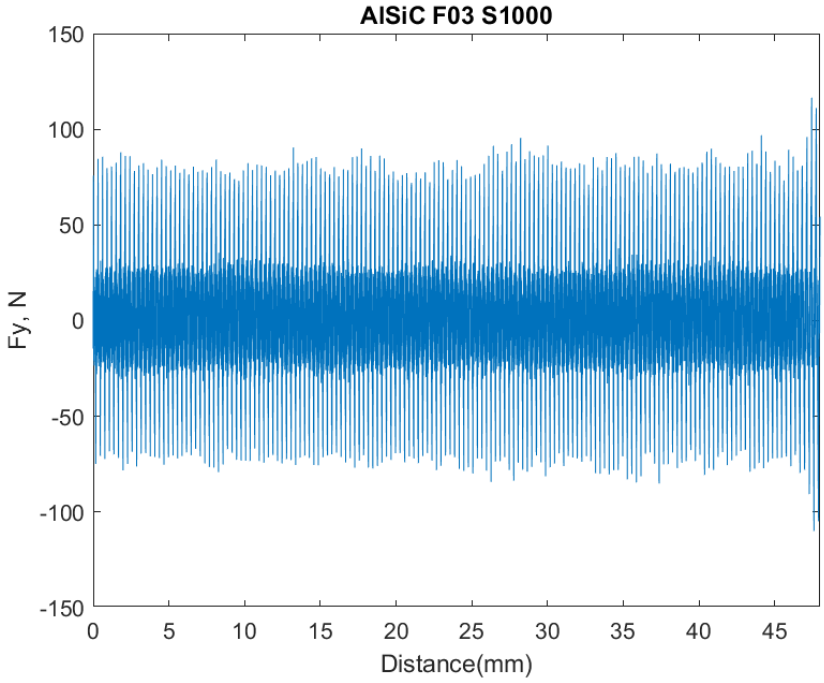
AlSiC F03 S1000
150
100
50
0
-50
-100
-150
Fy, N
0
5
10
15
20
25
30
35
40
45
Distance(mm)

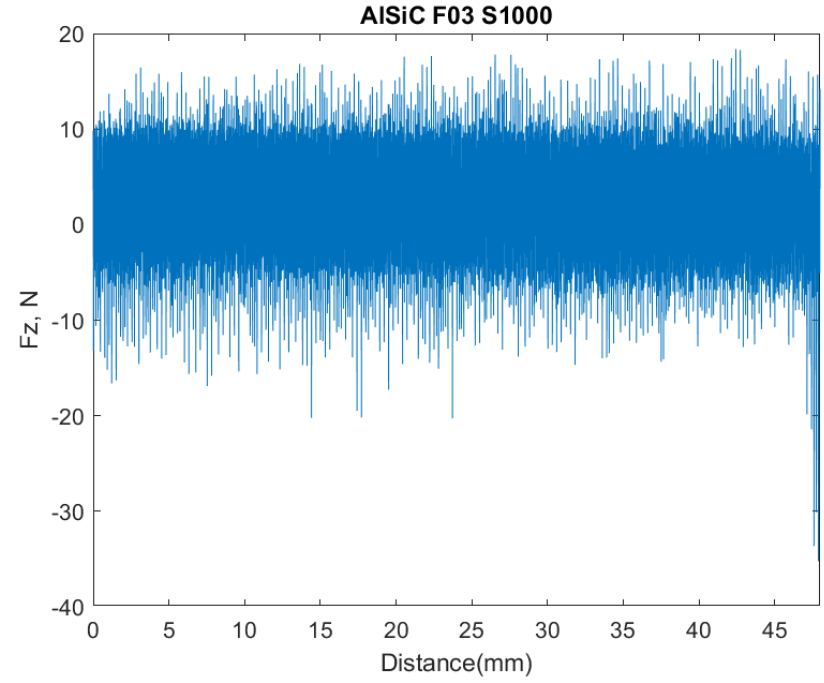
AlSiC F03 S1000
20
10
0
-10
-20
-30
-40
Fz, N
0
5
10
15
20
25
30
35
40
45
Distance(mm)

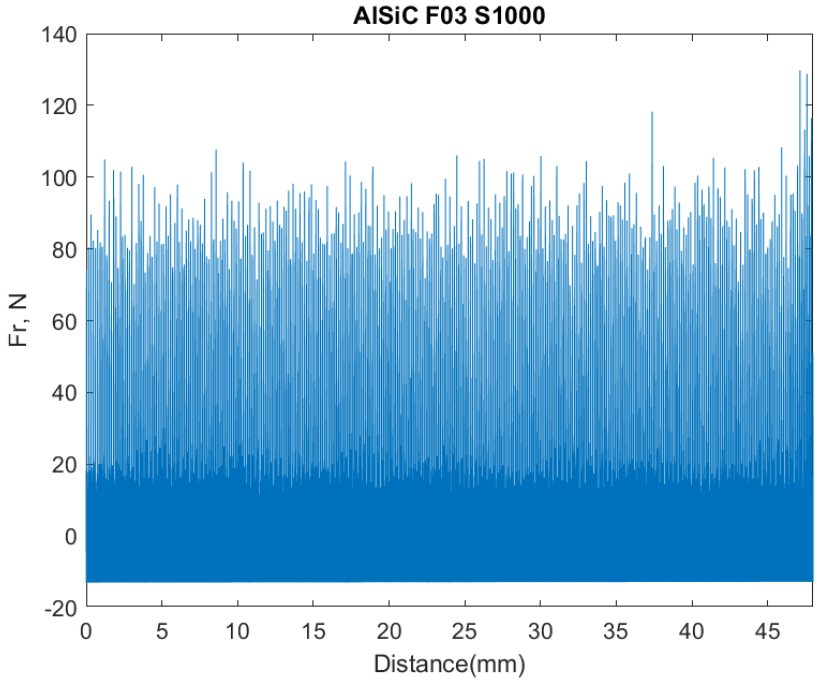
AlSiC F03 S1000
Fr, N
Distance(mm)
140
120
100
80
60
40
20
0
-20
0
5
10
15
20
25
30
35
40
45

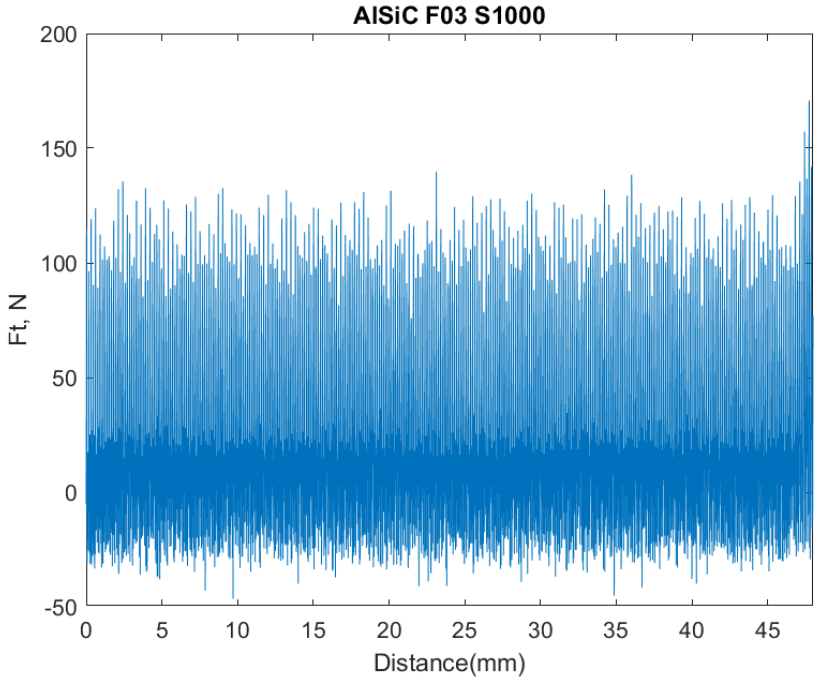
AlSiC F03 S1000
Ft, N
Distance(mm)
200
150
100
50
0
-50
0
5
10
15
20
25
30
35
40
45

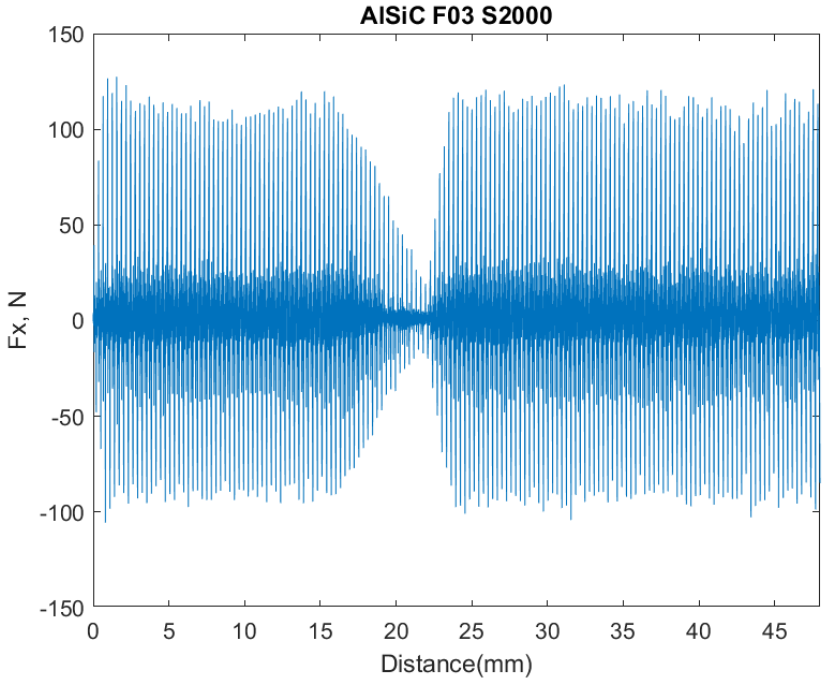
AlSiC F03 S2000
150
100
50
0
-50
-100
-150
Fx, N
0
5
10
15
20
25
30
35
40
45
Distance(mm)

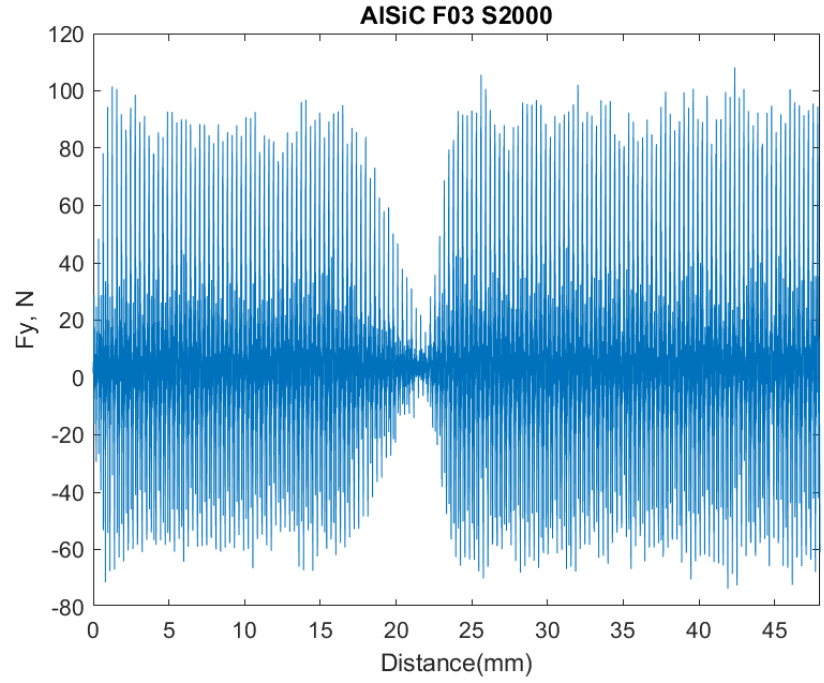
AlSiC F03 S2000
120
100
80
60
40
20
0
-20
-40
-60
-80
Fy, N
0
5
10
15
20
25
30
35
40
45
Distance(mm)

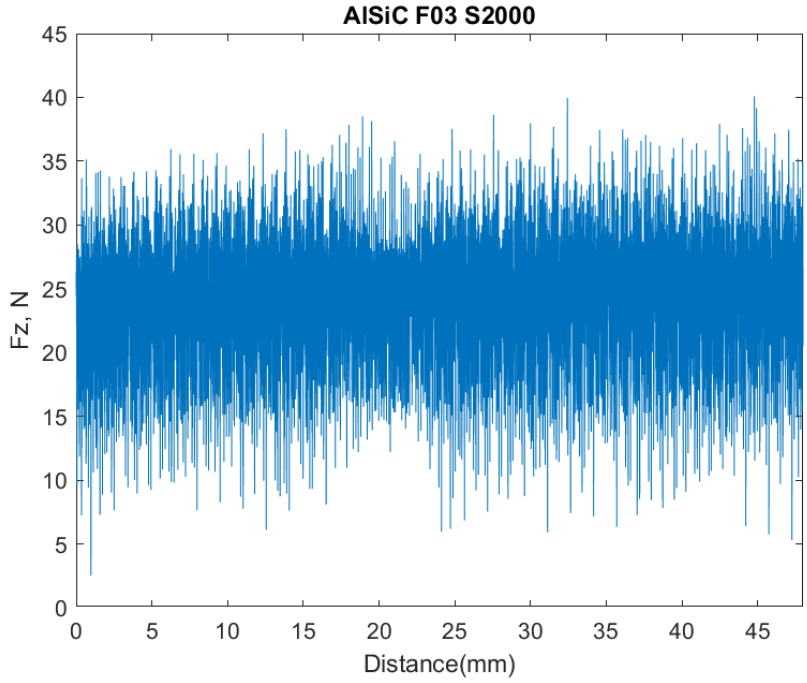
AlSiC F03 S2000
Fz, N
Distance(mm)
0
5
10
15
20
25
30
35
40
45

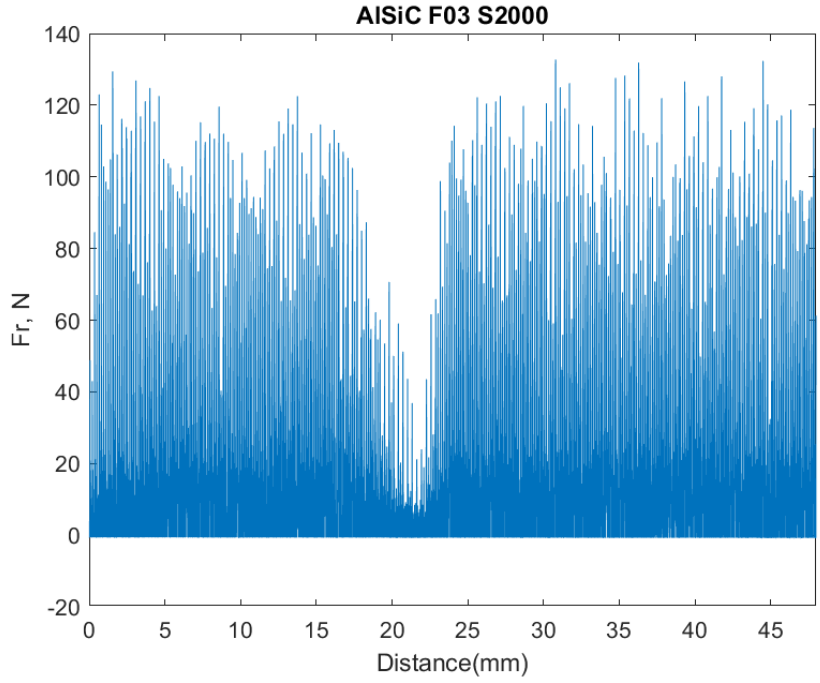
AlSiC F03 S2000
Fr, N
Distance(mm)
-20
0
20
40
60
80
100
120
140
0
5
10
15
20
25
30
35
40
45

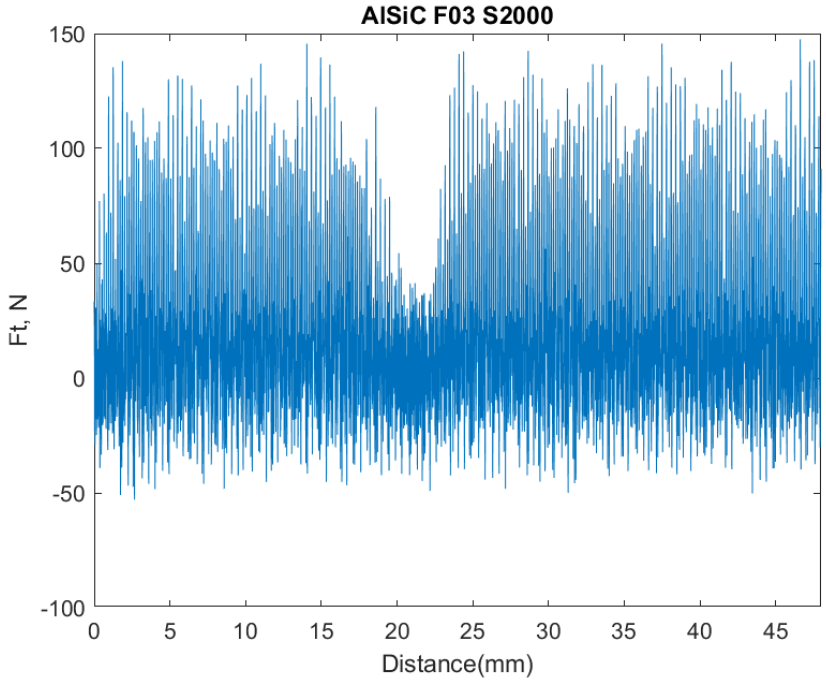
AlSiC F03 S2000
Ft, N
150
100
50
0
-50
-100
0
5
10
15
20
25
30
35
40
45
Distance(mm)

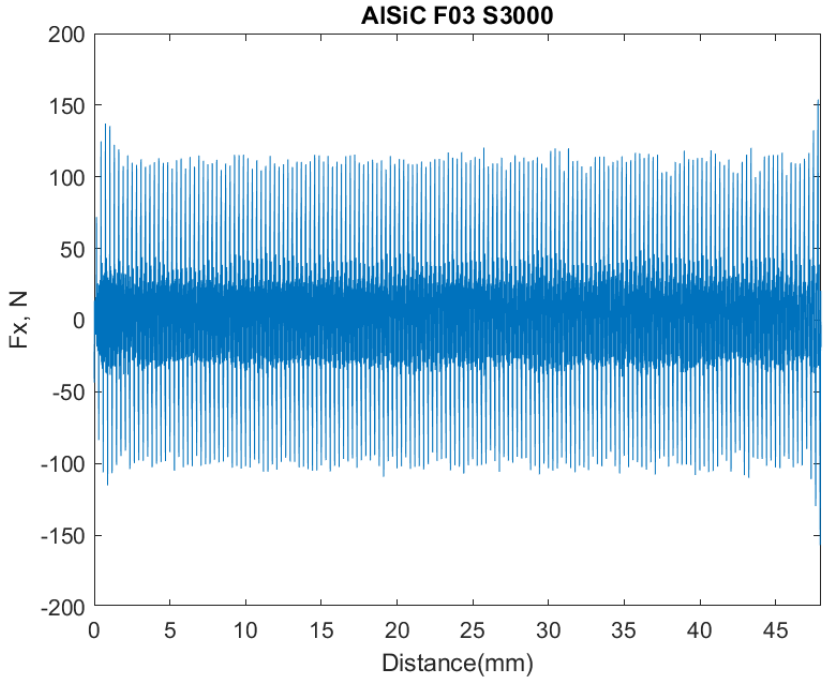
AlSiC F03 S3000
Fx, N
200
150
100
50
0
-50
-100
-150
-200
0
5
10
15
20
25
30
35
40
45
Distance(mm)

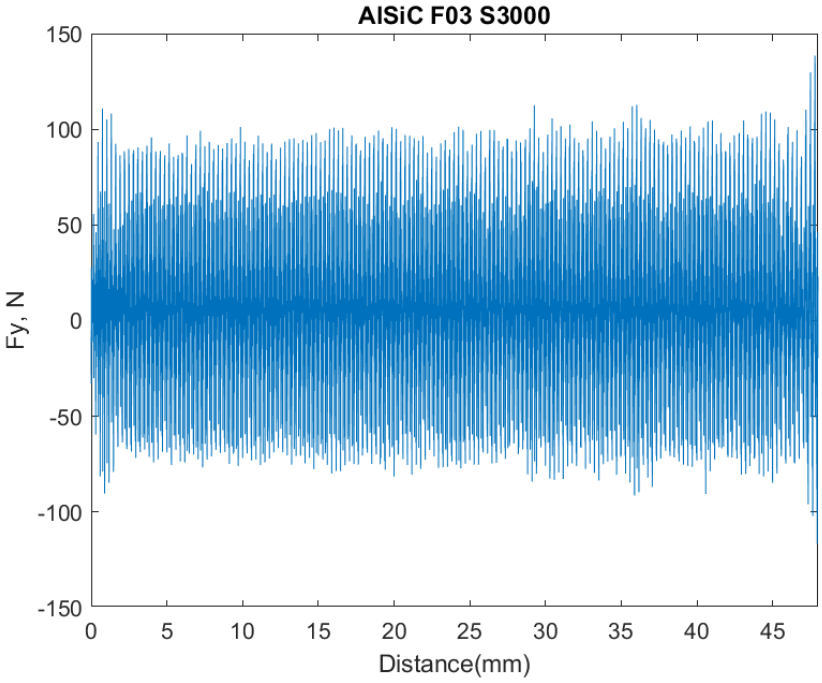
AlSiC F03 S3000
150
100
50
0
-50
-100
-150
Fy, N
0
5
10
15
20
25
30
35
40
45
Distance(mm)

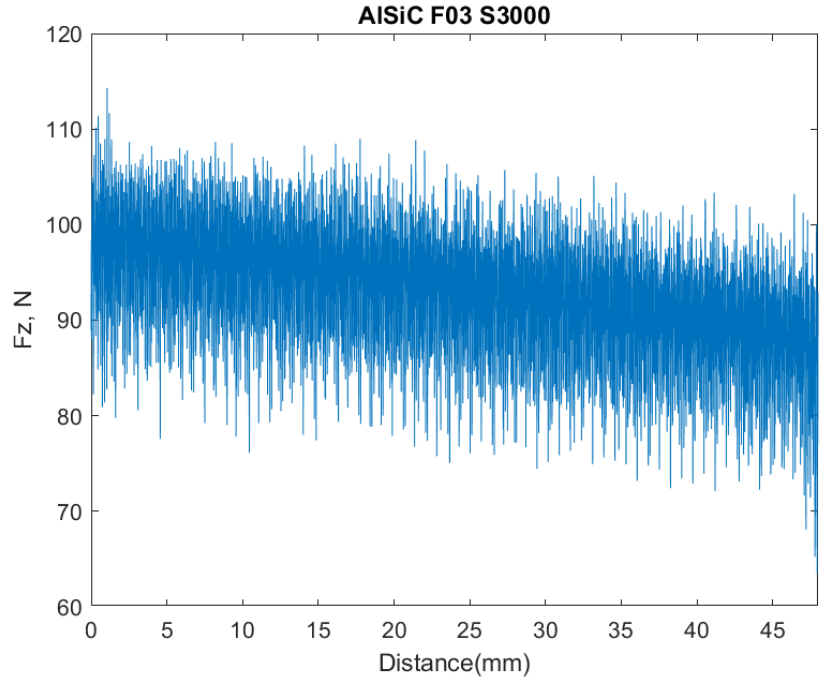
AlSiC F03 S3000
120
110
100
90
80
70
60
Fz, N
0
5
10
15
20
25
30
35
40
45
Distance(mm)

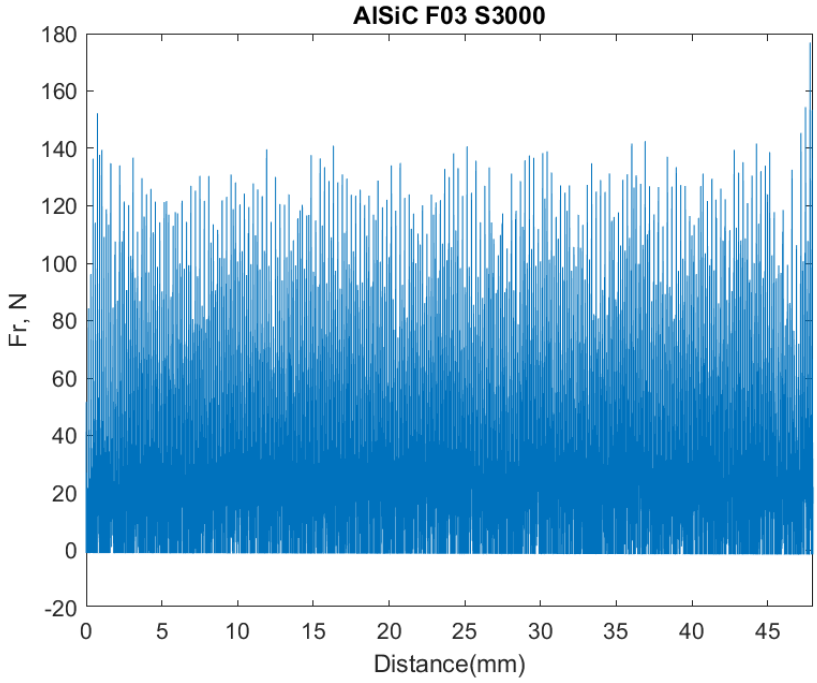
AlSiC F03 S3000
Fr, N
Distance(mm)
180
160
140
120
100
80
60
40
20
0
-20
0
5
10
15
20
25
30
35
40
45

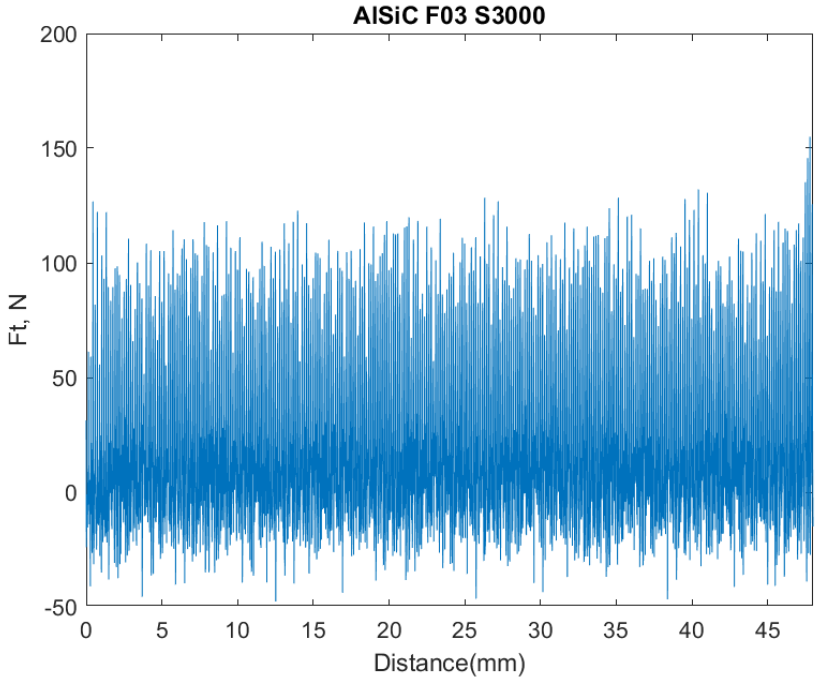
AlSiC F03 S3000
Ft, N
Distance(mm)
200
150
100
50
0
-50
0
5
10
15
20
25
30
35
40
45

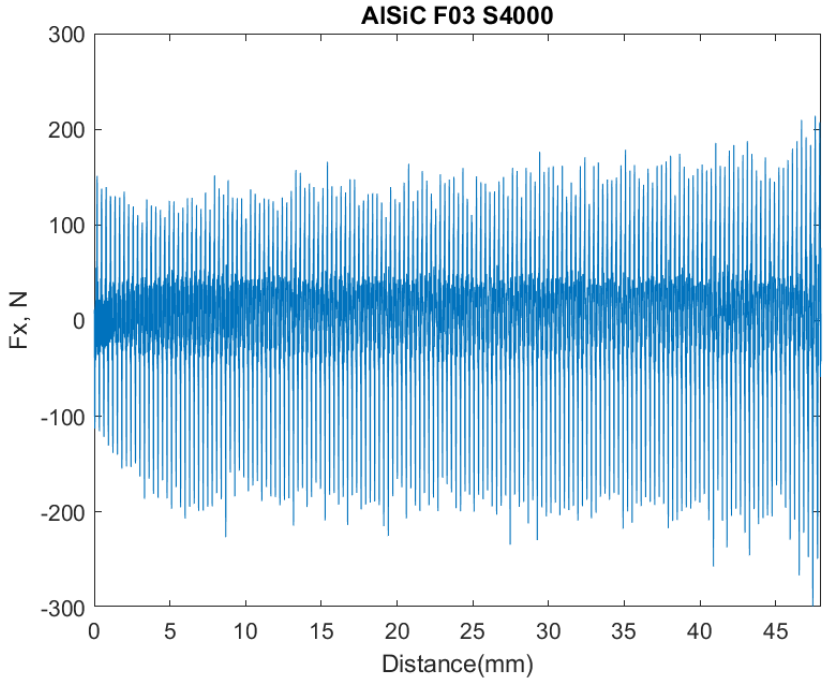
AlSiC F03 S4000
Fx, N
Distance(mm)
300
200
100
0
-100
-200
-300
0
5
10
15
20
25
30
35
40
45

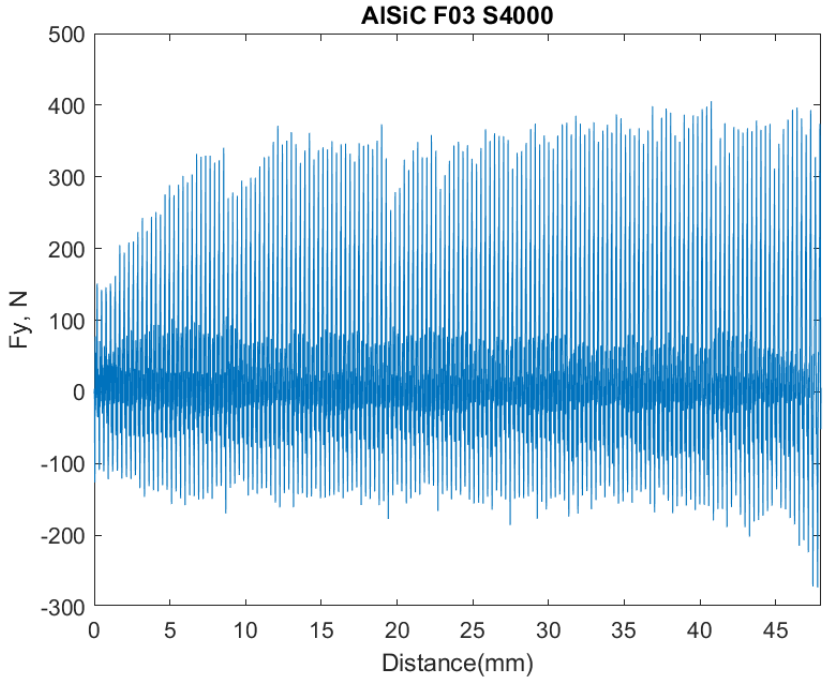
AlSiC F03 S4000
Fy, N
Distance(mm)
500
400
300
200
100
0
-100
-200
-300
0
5
10
15
20
25
30
35
40
45

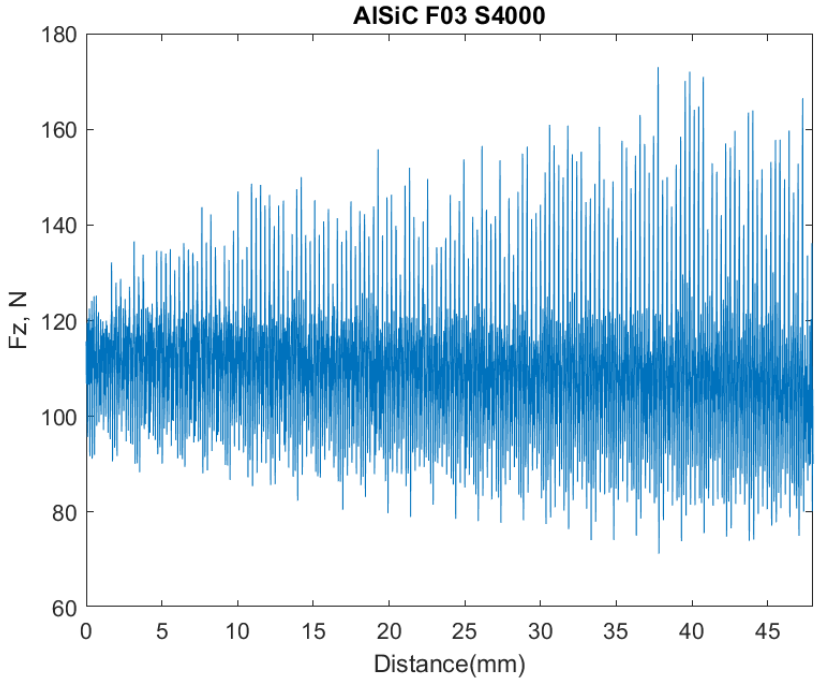
AlSiC F03 S4000
Fz, N
Distance(mm)
180
160
140
120
100
80
60
0
5
10
15
20
25
30
35
40
45

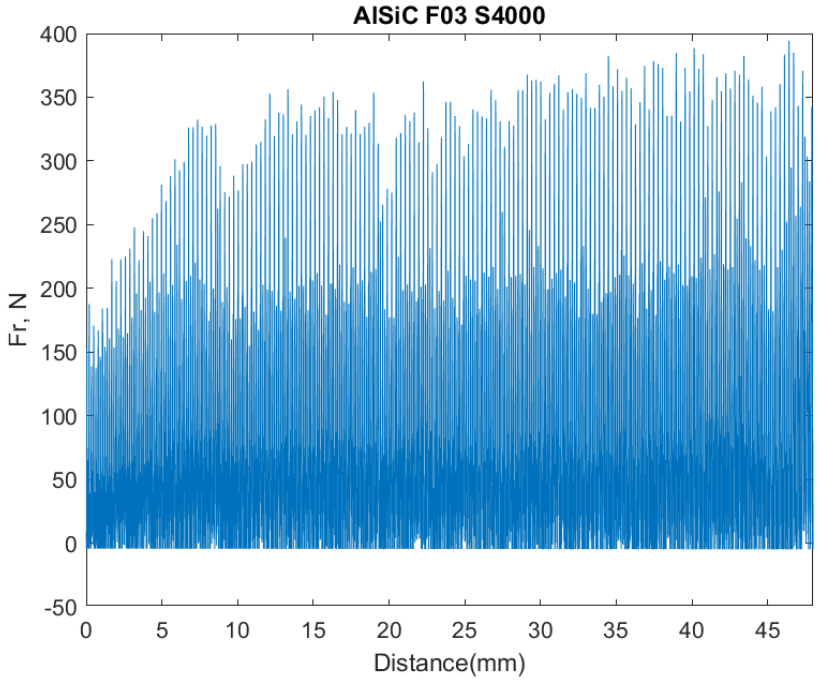
AlSiC F03 S4000
Fr, N
Distance(mm)
400
350
300
250
200
150
100
50
0
-50
0
5
10
15
20
25
30
35
40
45

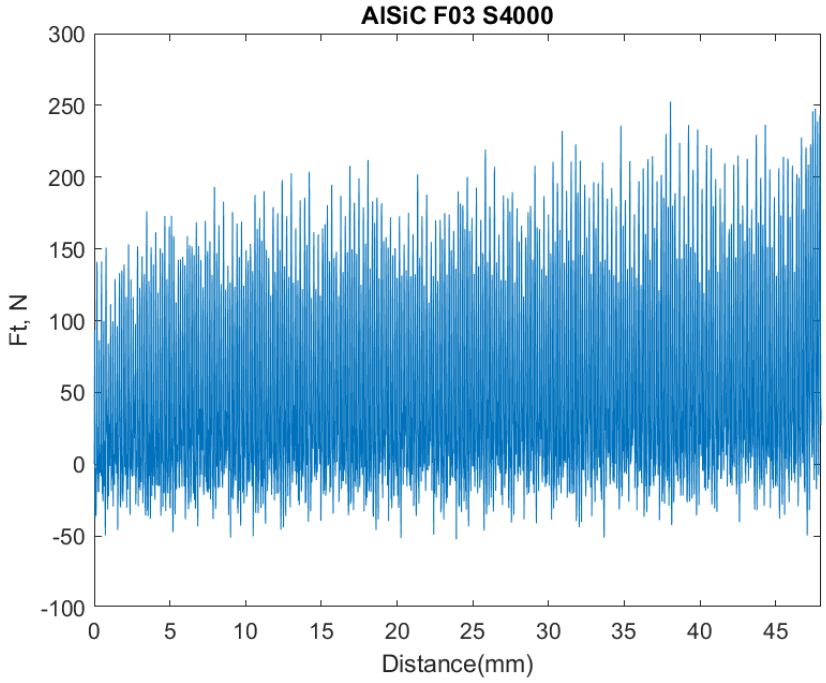
AlSiC F03 S4000
Ft, N
Distance(mm)
300
250
200
150
100
50
0
-50
-100
0
5
10
15
20
25
30
35
40
45

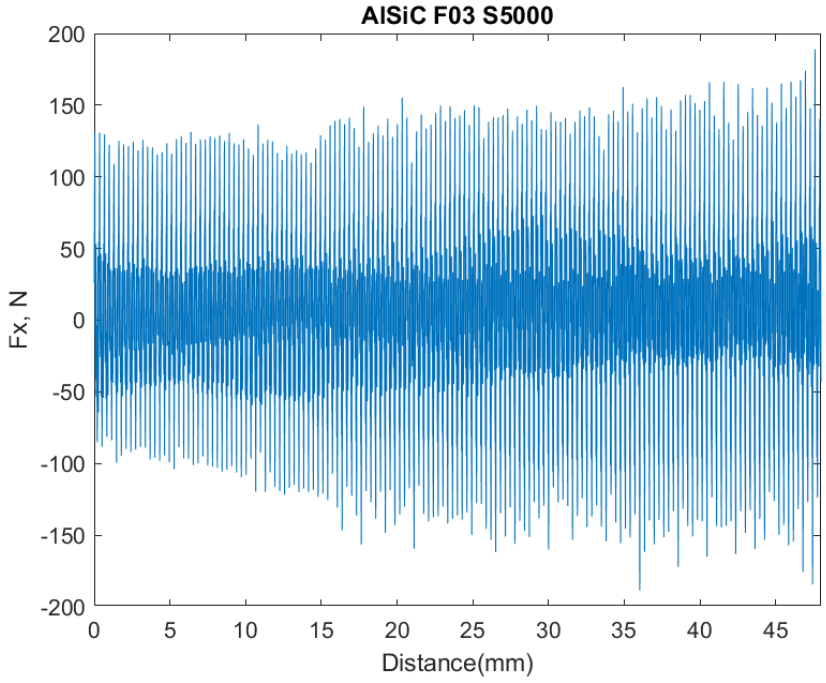
AlSiC F03 S5000
Fx, N
Distance(mm)
200
150
100
50
0
-50
-100
-150
-200
0
5
10
15
20
25
30
35
40
45

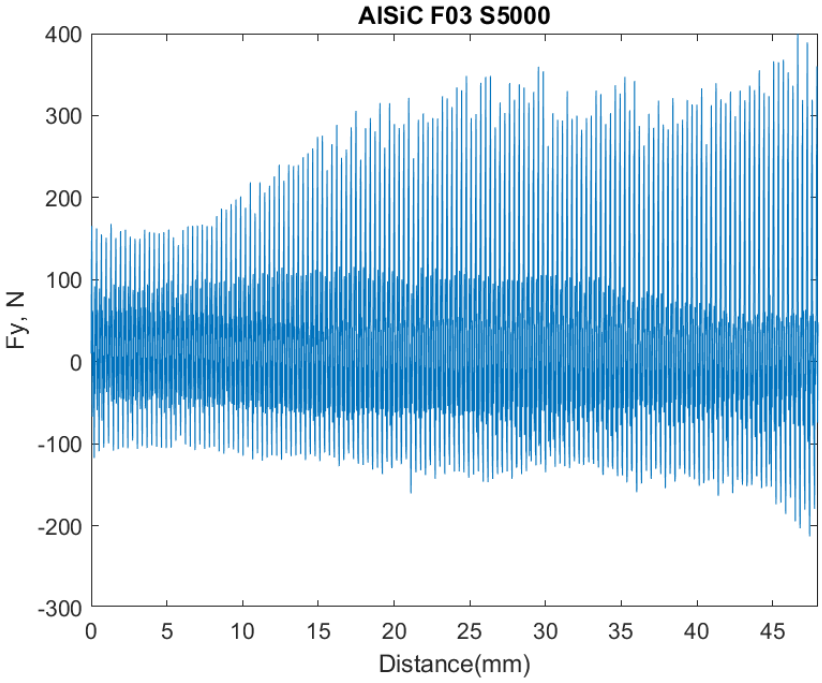
AlSiC F03 S5000
Fy, N
Distance(mm)
400
300
200
100
0
-100
-200
-300
0
5
10
15
20
25
30
35
40
45

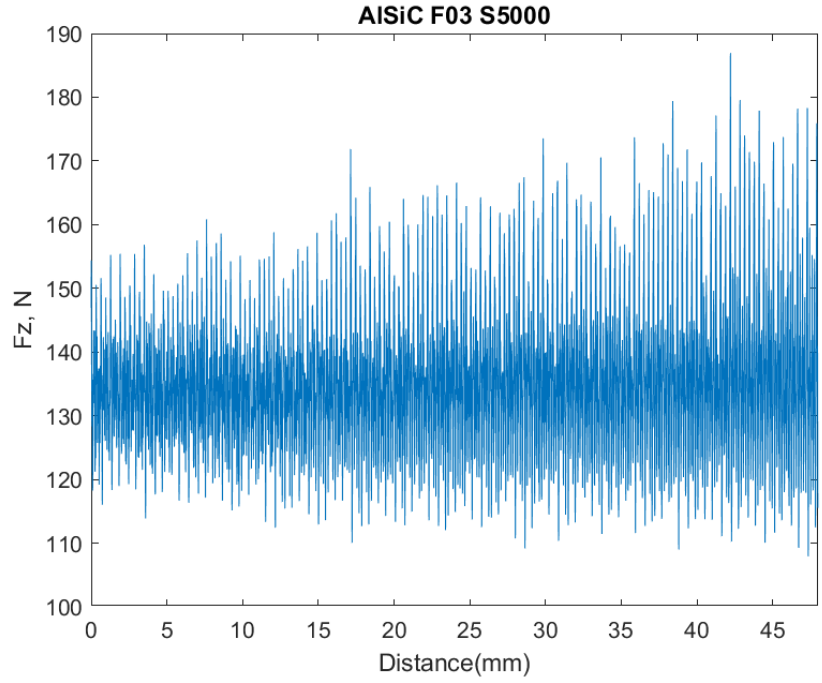
AlSiC F03 S5000
Fz, N
Distance(mm)
190
180
170
160
150
140
130
120
110
100
0
5
10
15
20
25
30
35
40
45

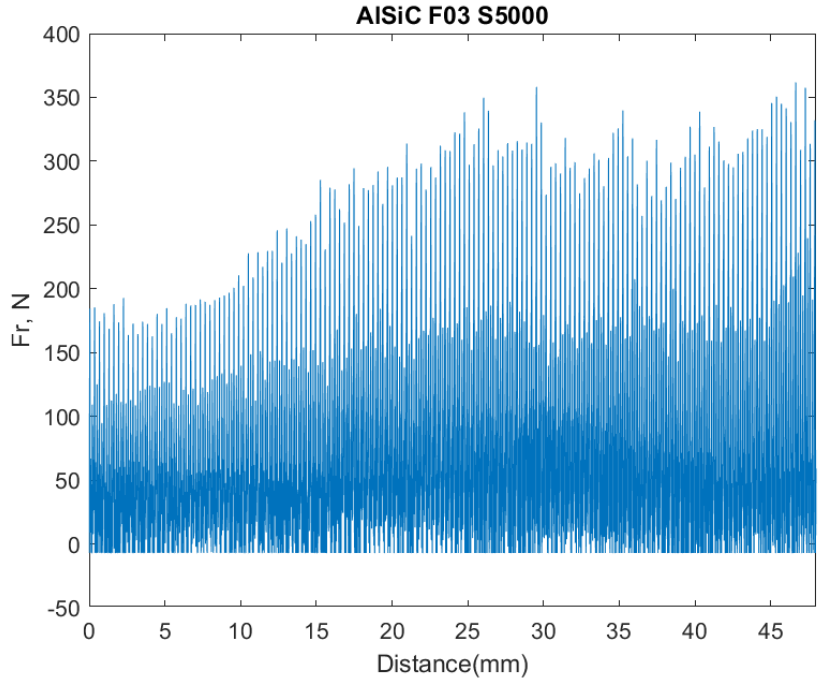
AlSiC F03 S5000
Fr, N
Distance(mm)
400
350
300
250
200
150
100
50
0
-50
0
5
10
15
20
25
30
35
40
45

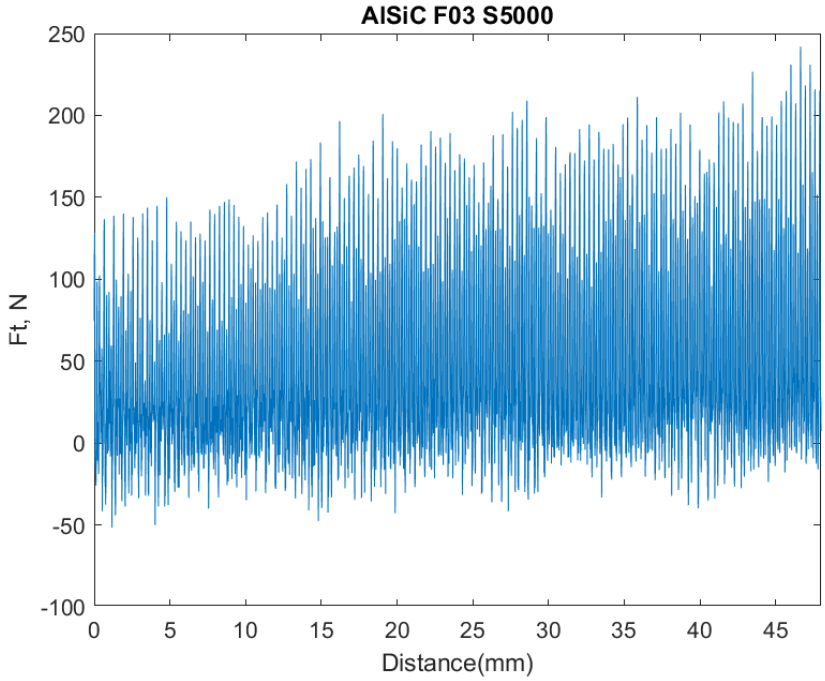
AlSiC F03 S5000
Ft, N
Distance(mm)
250
200
150
100
50
0
-50
-100
0
5
10
15
20
25
30
35
40
45

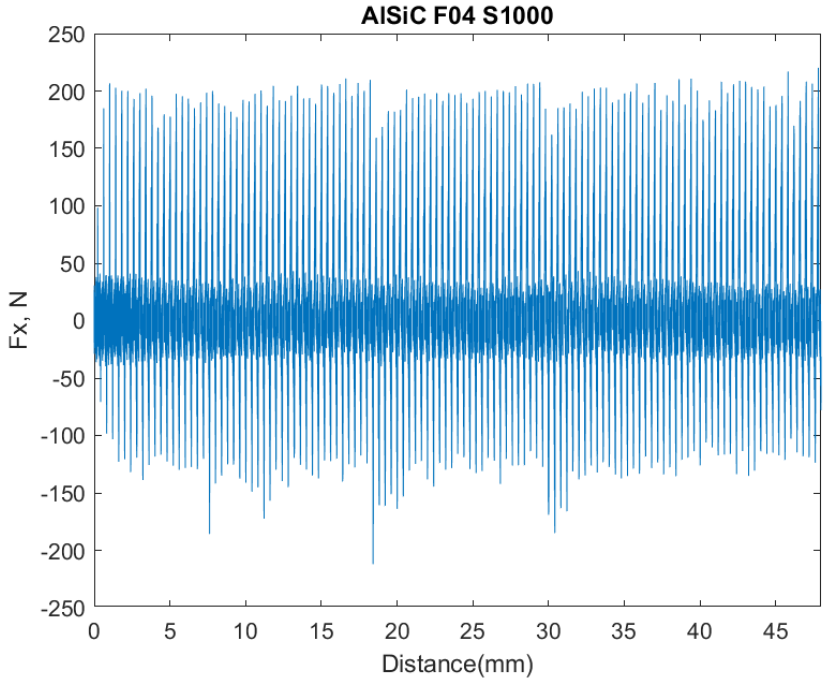
AlSiC F04 S1000
Fx, N
Distance(mm)
250
200
150
100
50
0
-50
-100
-150
-200
-250
0
5
10
15
20
25
30
35
40
45

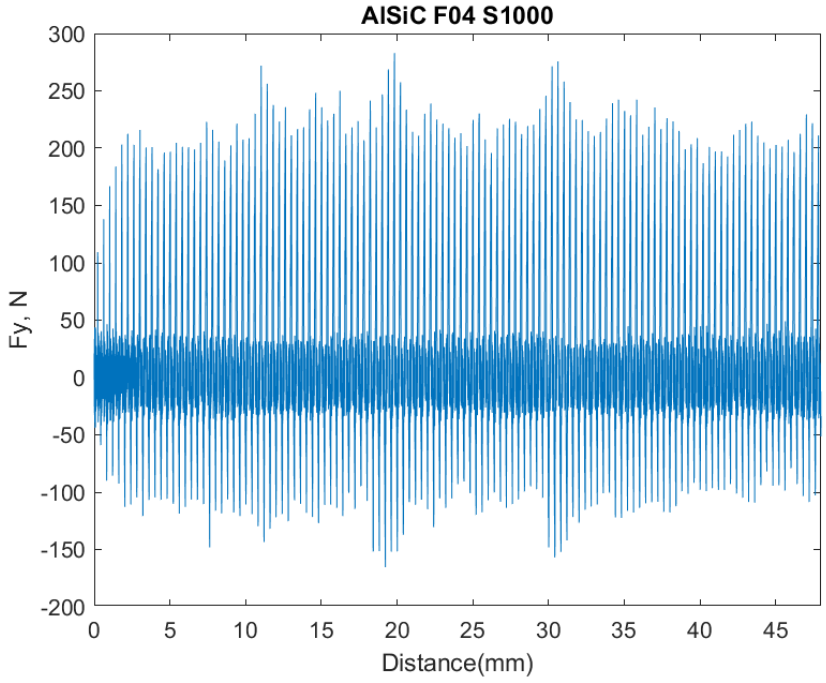
AlSiC F04 S1000
Fy, N
Distance(mm)
300
250
200
150
100
50
0
-50
-100
-150
-200
0
5
10
15
20
25
30
35
40
45

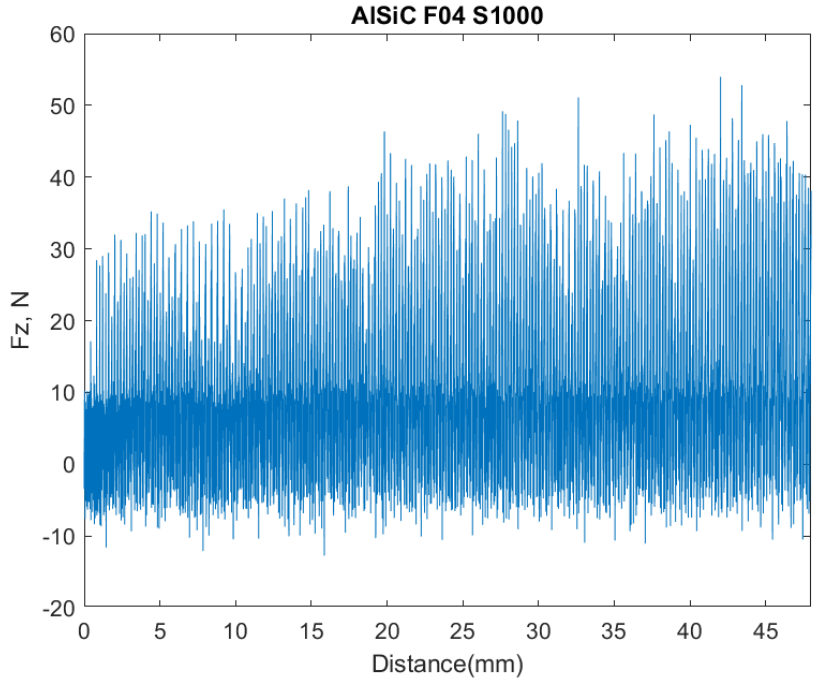
AlSiC F04 S1000
Fz, N
Distance(mm)
60
50
40
30
20
10
0
-10
-20
0
5
10
15
20
25
30
35
40
45

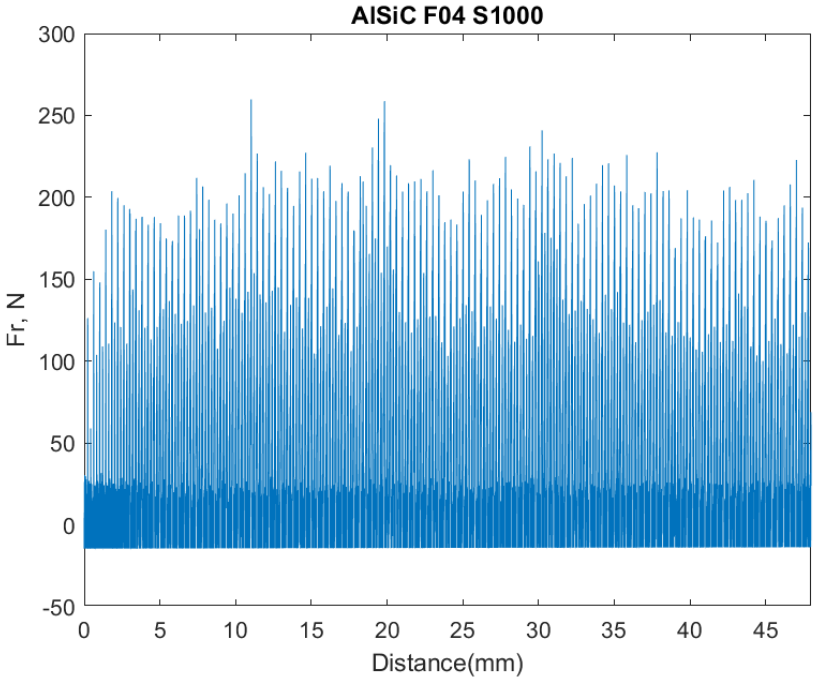
AlSiC F04 S1000
Fr, N
Distance(mm)
300
250
200
150
100
50
0
-50
0
5
10
15
20
25
30
35
40
45

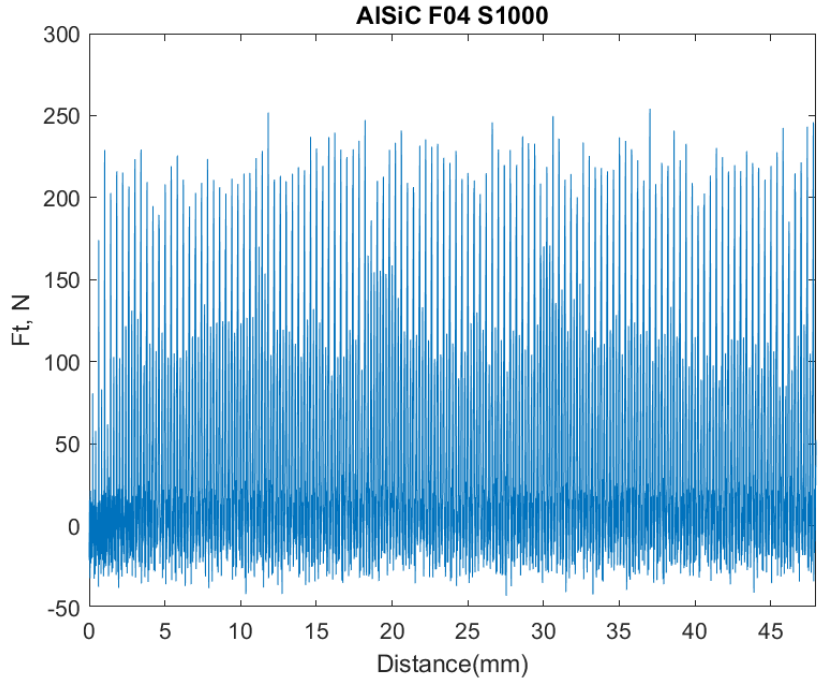
AlSiC F04 S1000
Ft, N
Distance(mm)
300
250
200
150
100
50
0
-50
0
5
10
15
20
25
30
35
40
45

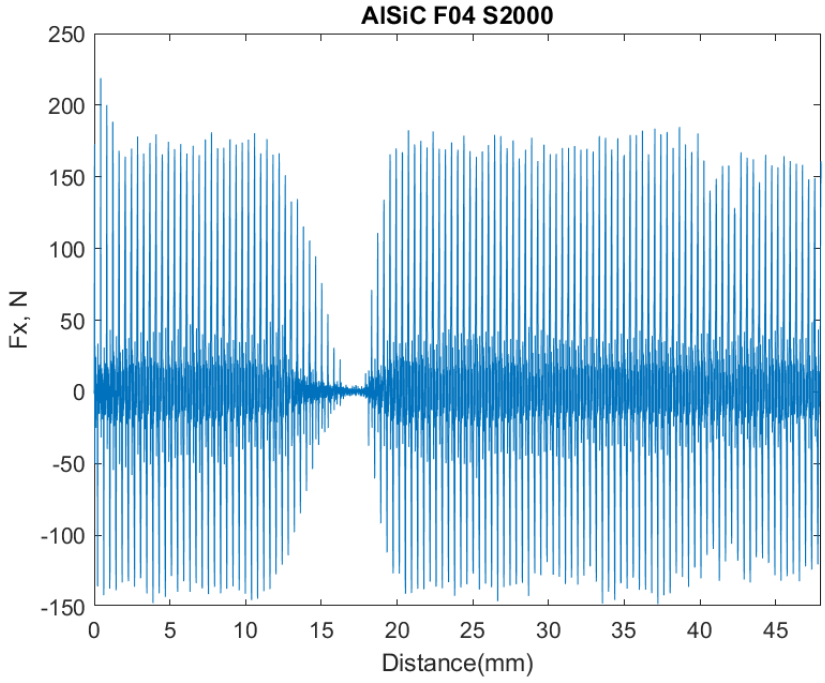
AlSiC F04 S2000
Fx, N
Distance(mm)
250
200
150
100
50
0
-50
-100
-150
0
5
10
15
20
25
30
35
40
45

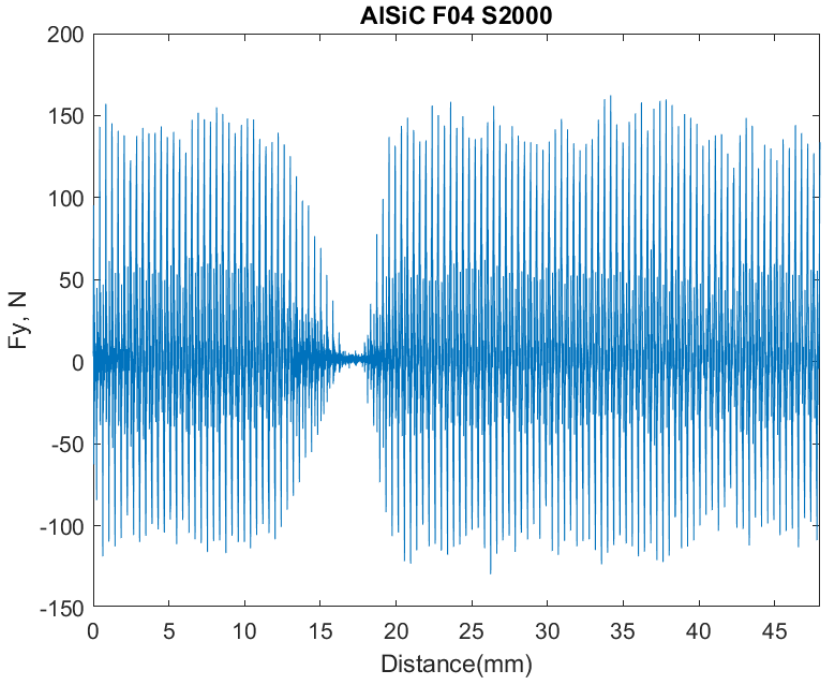
AlSiC F04 S2000
Fy, N
Distance(mm)
200
150
100
50
0
-50
-100
-150
0
5
10
15
20
25
30
35
40
45

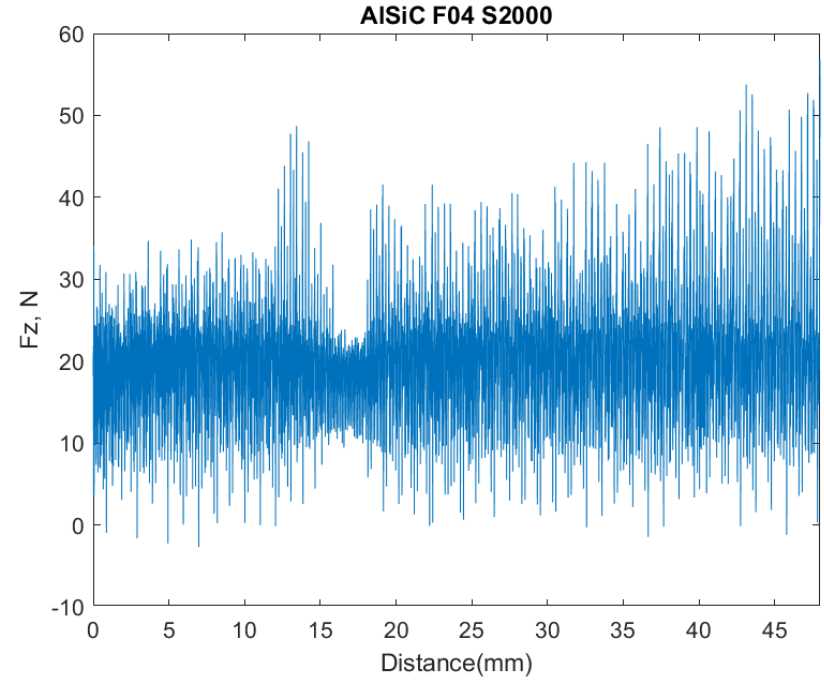
AlSiC F04 S2000
Fz, N
Distance(mm)
60
50
40
30
20
10
0
-10
0
5
10
15
20
25
30
35
40
45

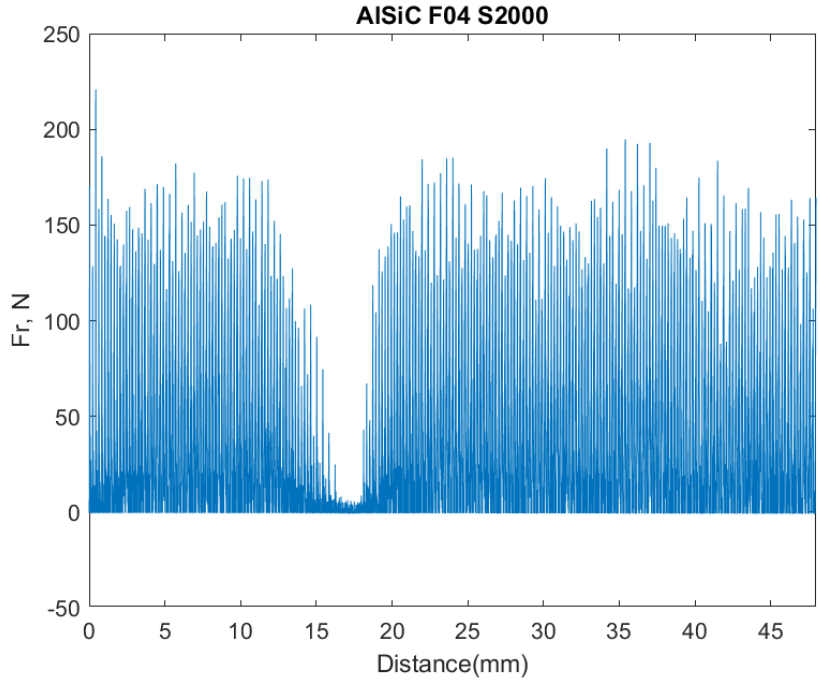
AlSiC F04 S2000
Fr, N
Distance(mm)
250
200
150
100
50
0
-50
0
5
10
15
20
25
30
35
40
45

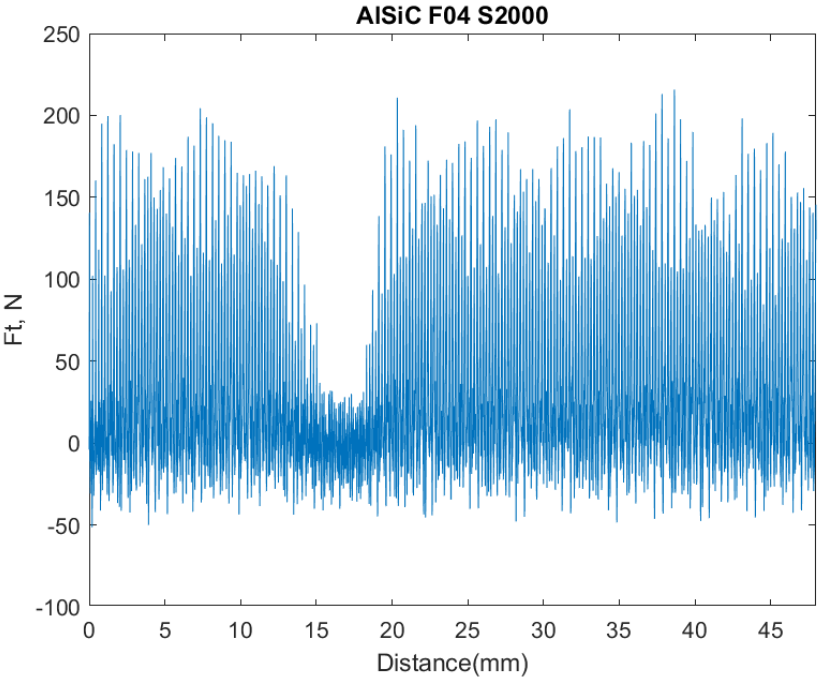
AlSiC F04 S2000
Ft, N
Distance(mm)
250
200
150
100
50
0
-50
-100
0
5
10
15
20
25
30
35
40
45

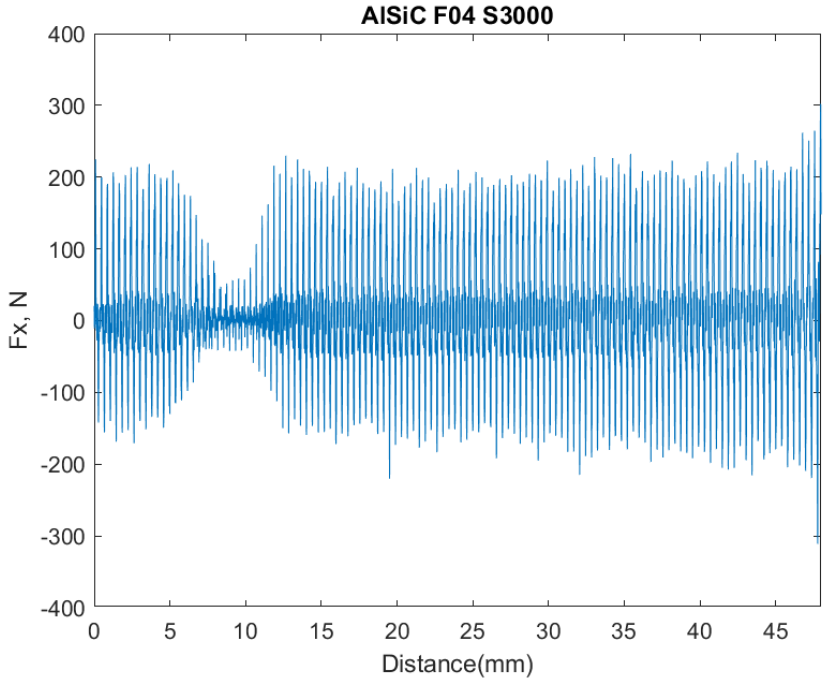
AlSiC F04 S3000
Fx, N
Distance(mm)
400
300
200
100
0
-100
-200
-300
-400
0
5
10
15
20
25
30
35
40
45

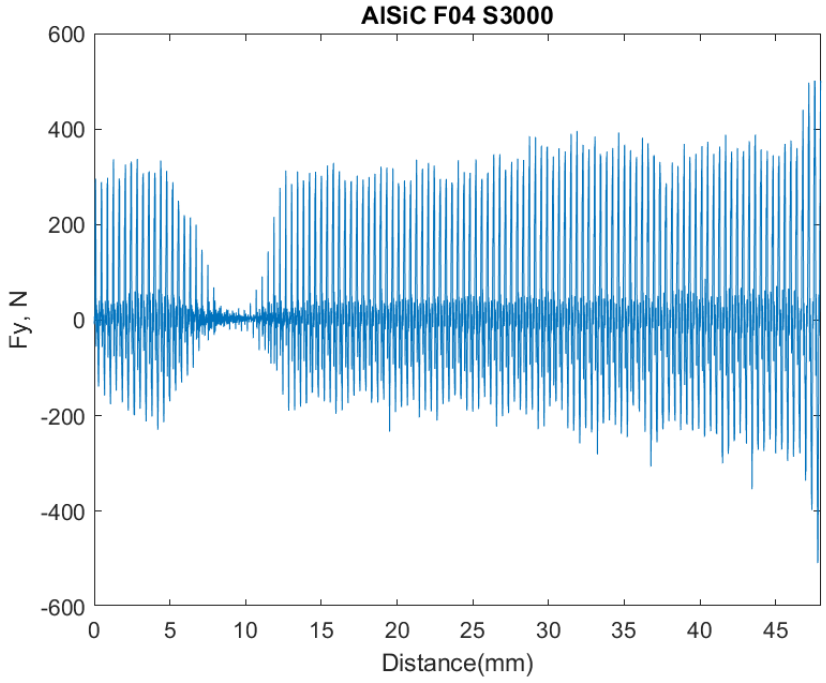
AlSiC F04 S3000
Fy, N
Distance(mm)
600
400
200
0
-200
-400
-600
0
5
10
15
20
25
30
35
40
45

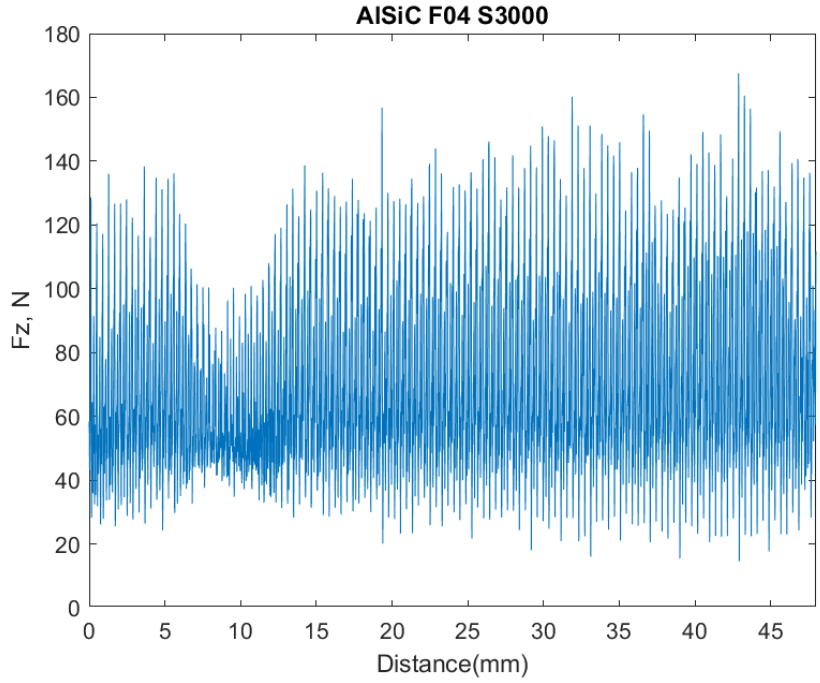
AlSiC F04 S3000
Fz, N
Distance(mm)
0
20
40
60
80
100
120
140
160
180
0
5
10
15
20
25
30
35
40
45

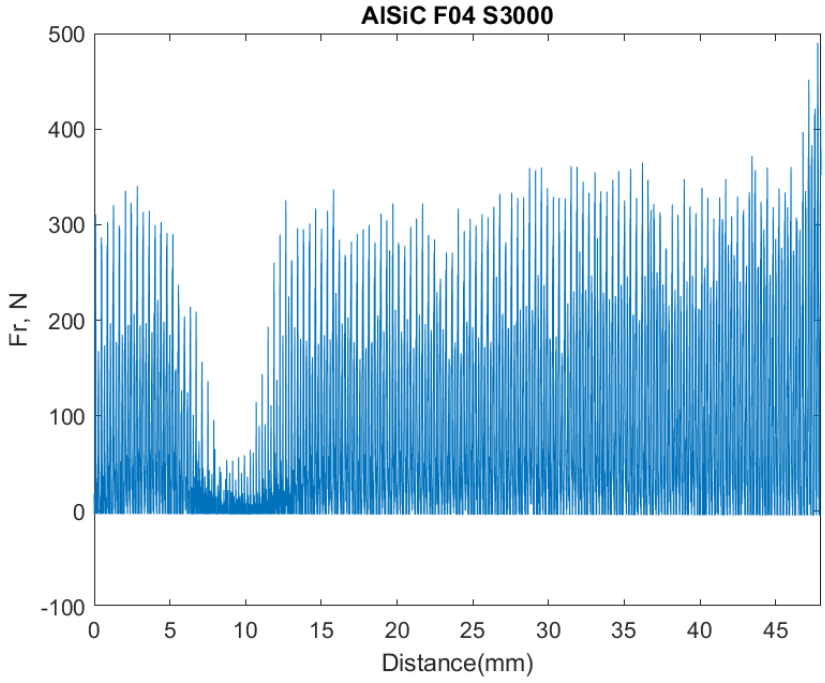
AlSiC F04 S3000
Fr, N
Distance(mm)
-100
0
100
200
300
400
500
0
5
10
15
20
25
30
35
40
45

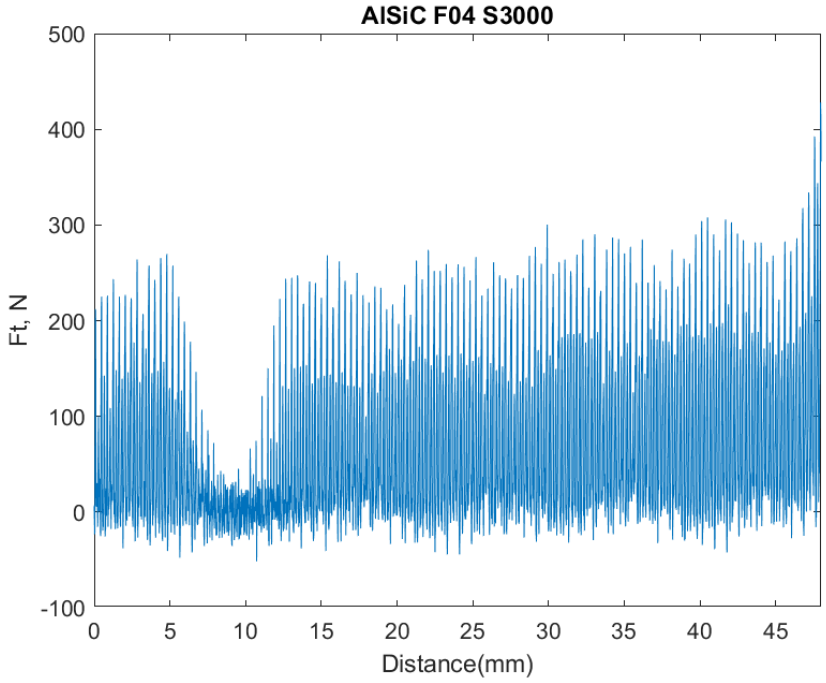
AlSiC F04 S3000
Ft, N
Distance(mm)
500
400
300
200
100
0
-100
0
5
10
15
20
25
30
35
40
45

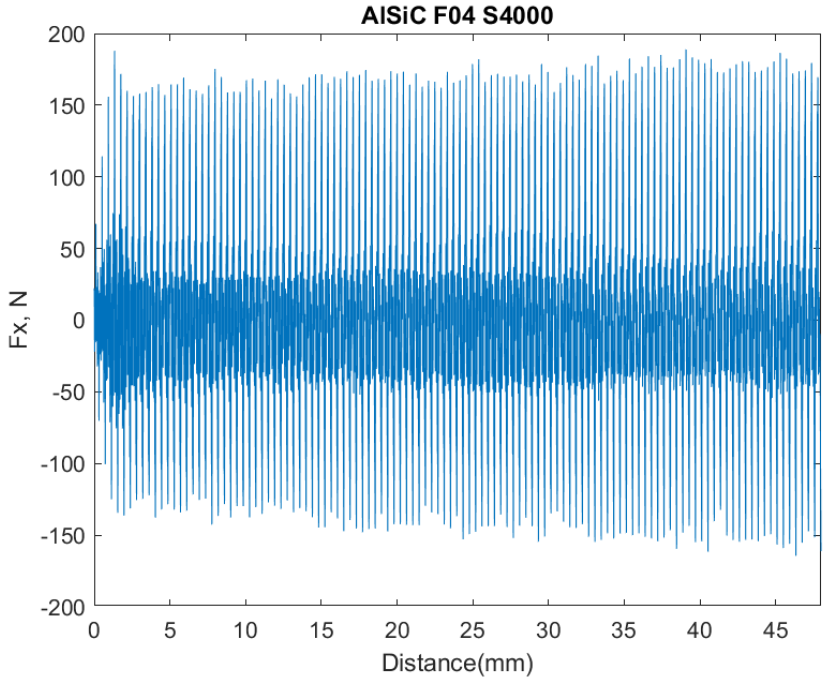
AlSiC F04 S4000
Fx, N
Distance(mm)
200
150
100
50
0
-50
-100
-150
-200
0
5
10
15
20
25
30
35
40
45

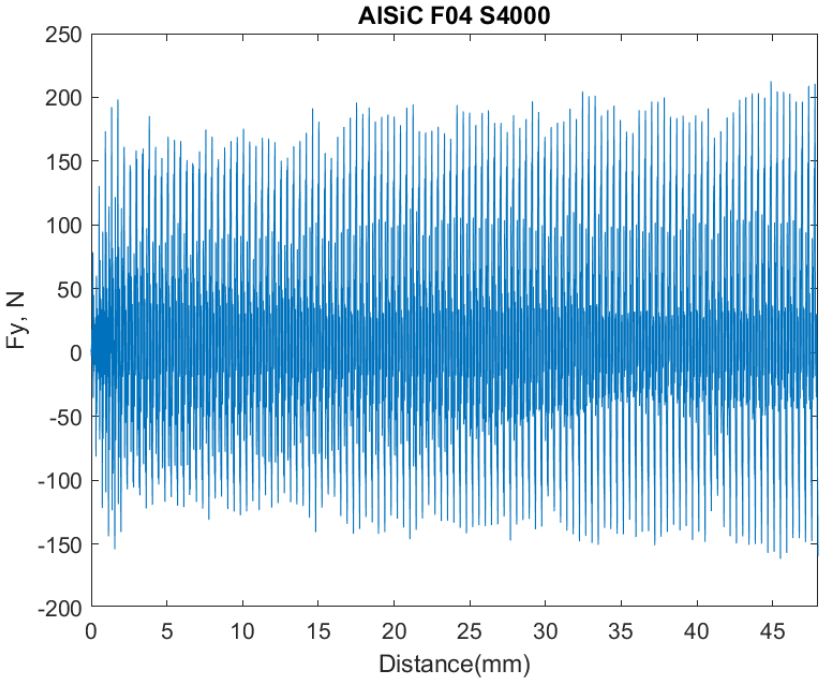
AlSiC F04 S4000
Fy, N
Distance(mm)
250
200
150
100
50
0
-50
-100
-150
-200
0
5
10
15
20
25
30
35
40
45

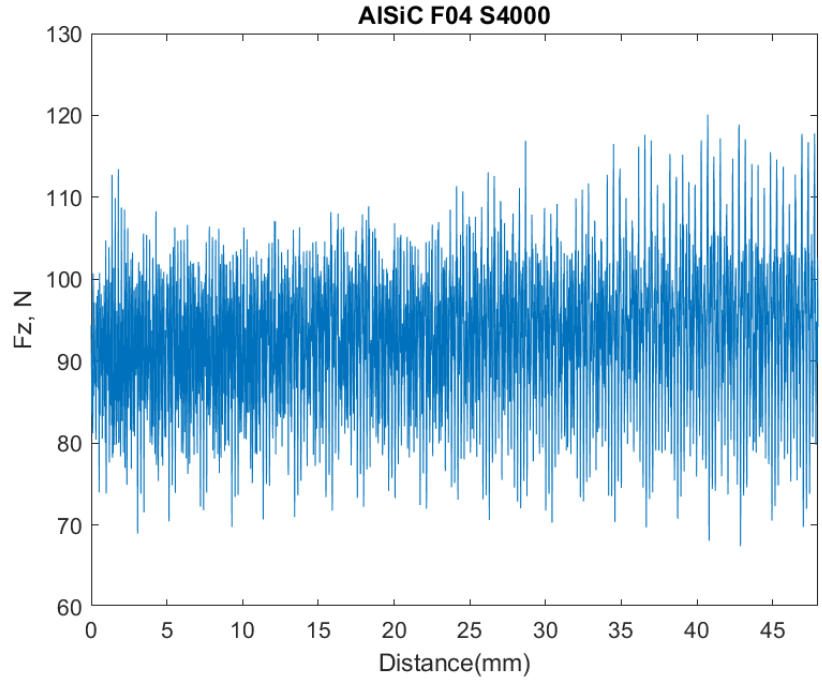
AlSiC F04 S4000
Fz, N
Distance(mm)
130
120
110
100
90
80
70
60
0
5
10
15
20
25
30
35
40
45

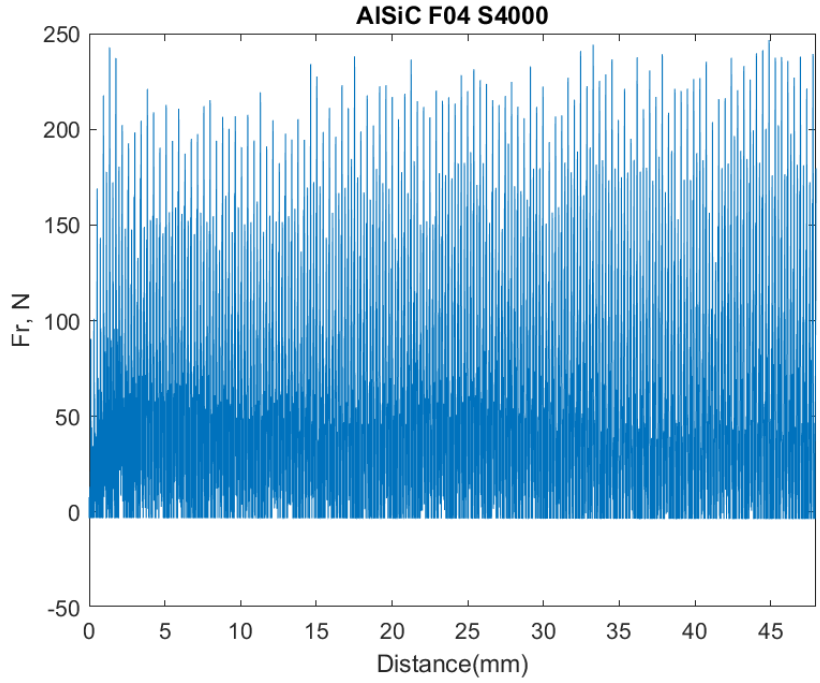
AlSiC F04 S4000
Fr, N
Distance(mm)
250
200
150
100
50
0
-50
0
5
10
15
20
25
30
35
40
45

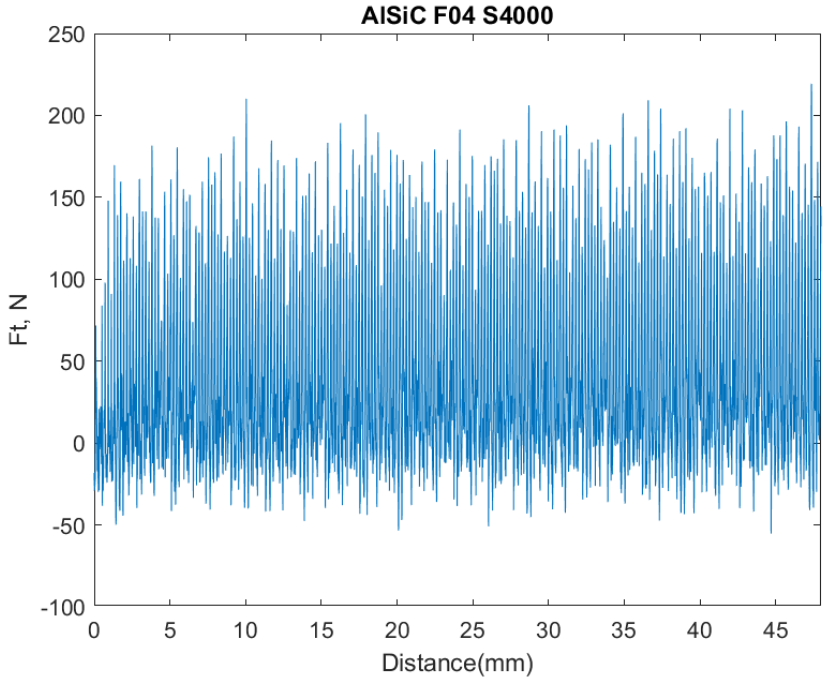
AlSiC F04 S4000
Ft, N
Distance(mm)
250
200
150
100
50
0
-50
-100
0
5
10
15
20
25
30
35
40
45

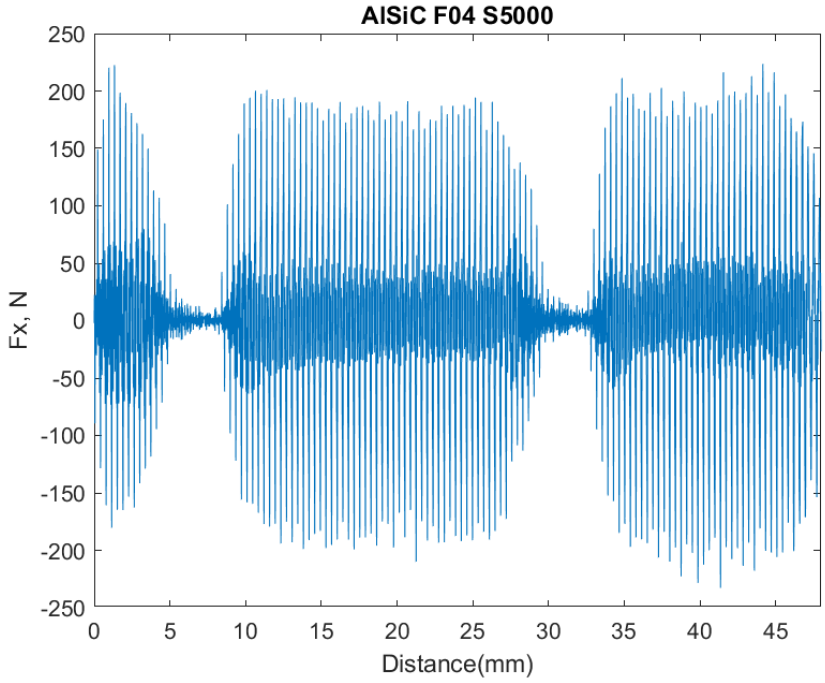
AlSiC F04 S5000
Fx, N
Distance(mm)
250
200
150
100
50
0
-50
-100
-150
-200
-250
0
5
10
15
20
25
30
35
40
45

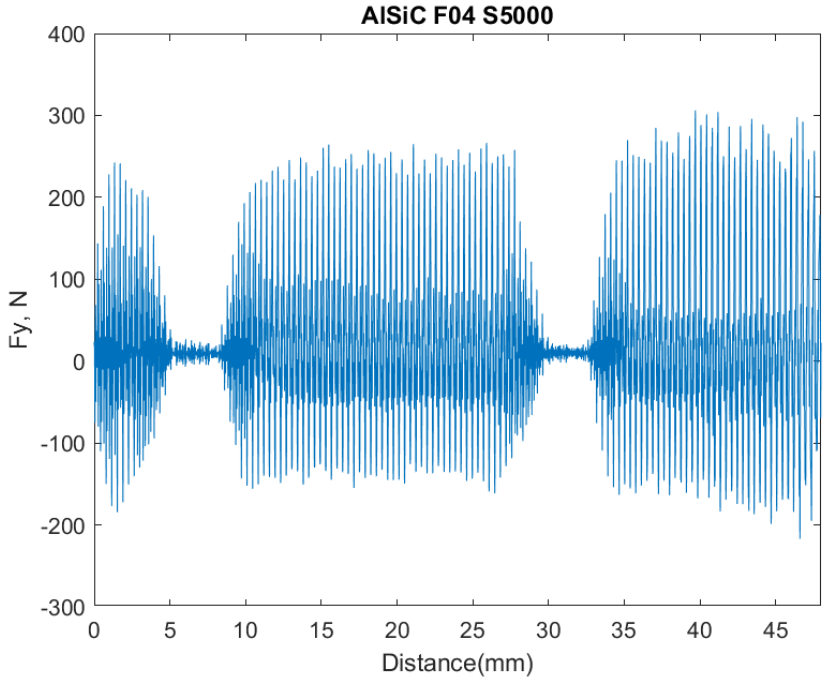
AlSiC F04 S5000
Fy, N
Distance(mm)
400
300
200
100
0
-100
-200
-300
0
5
10
15
20
25
30
35
40
45

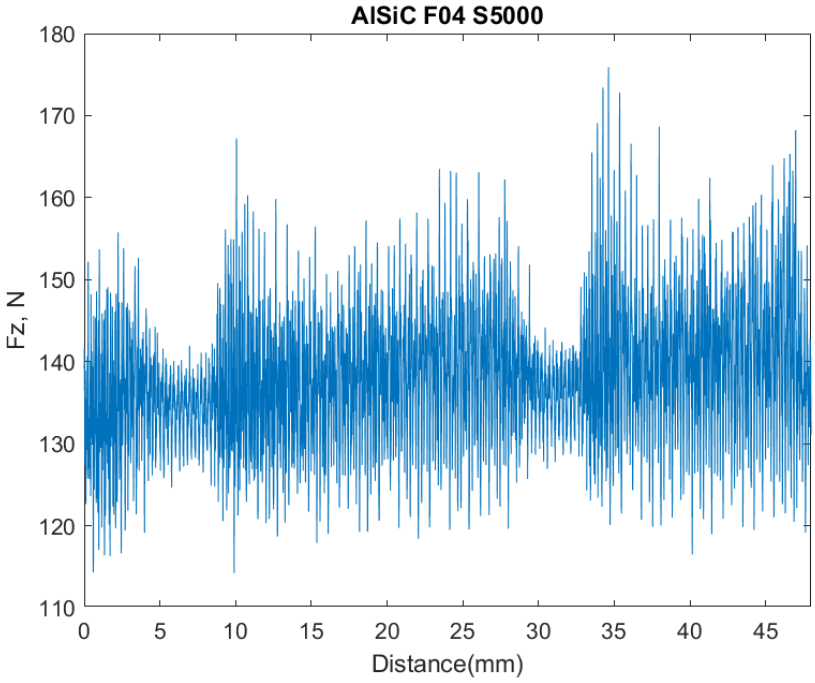
AlSiC F04 S5000
Fz, N
Distance(mm)
180
170
160
150
140
130
120
110
0
5
10
15
20
25
30
35
40
45

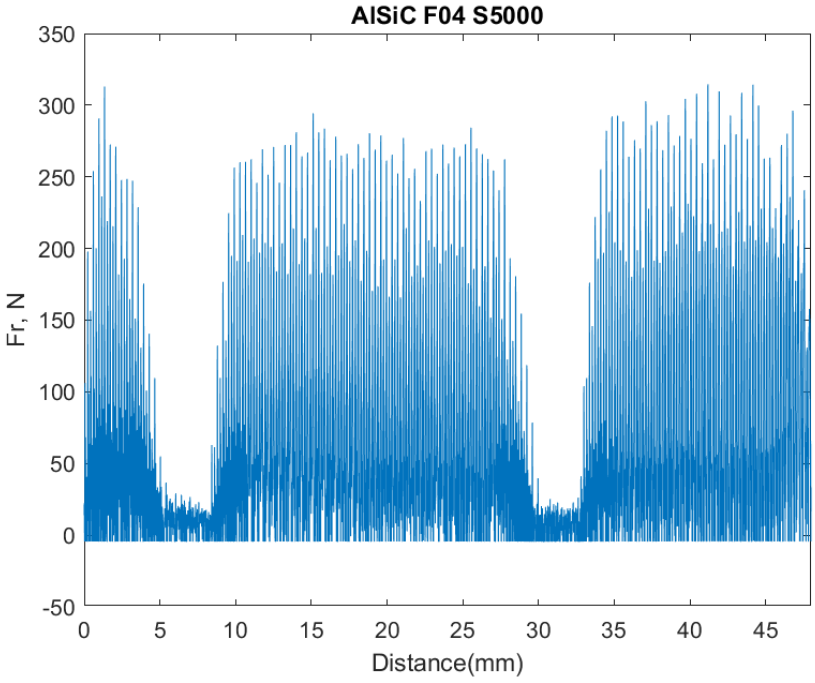
AlSiC F04 S5000
Fr, N
Distance(mm)
350
300
250
200
150
100
50
0
-50
0
5
10
15
20
25
30
35
40
45

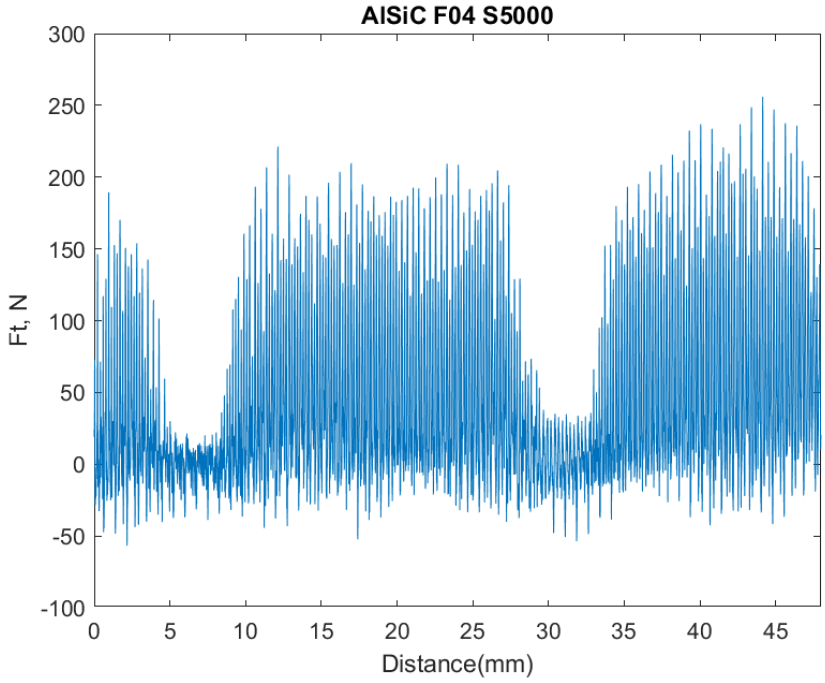
AlSiC F04 S5000
Ft, N
300
250
200
150
100
50
0
-50
-100
0
5
10
15
20
25
30
35
40
45
Distance(mm)

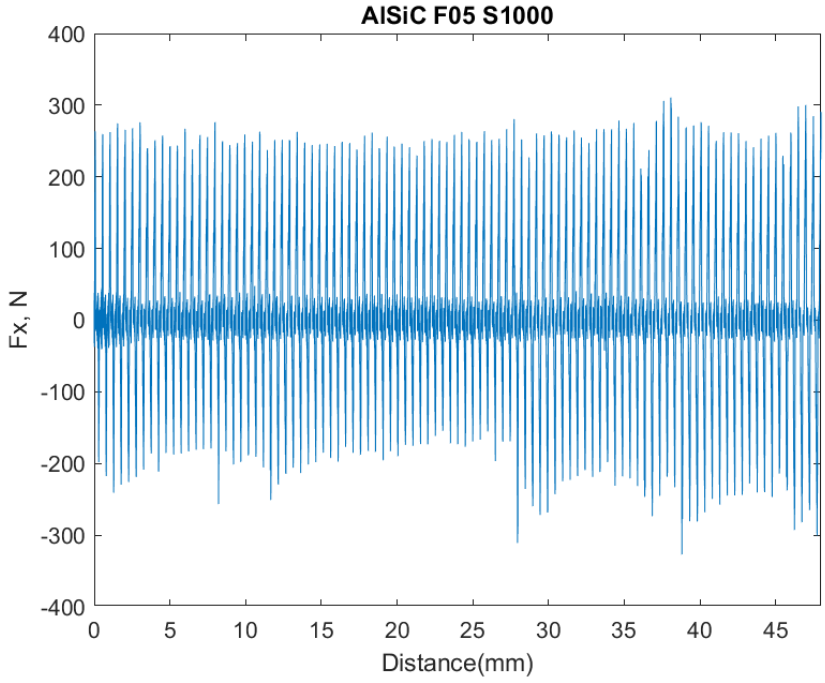
AlSiC F05 S1000
Fx, N
400
300
200
100
0
-100
-200
-300
-400
0
5
10
15
20
25
30
35
40
45
Distance(mm)

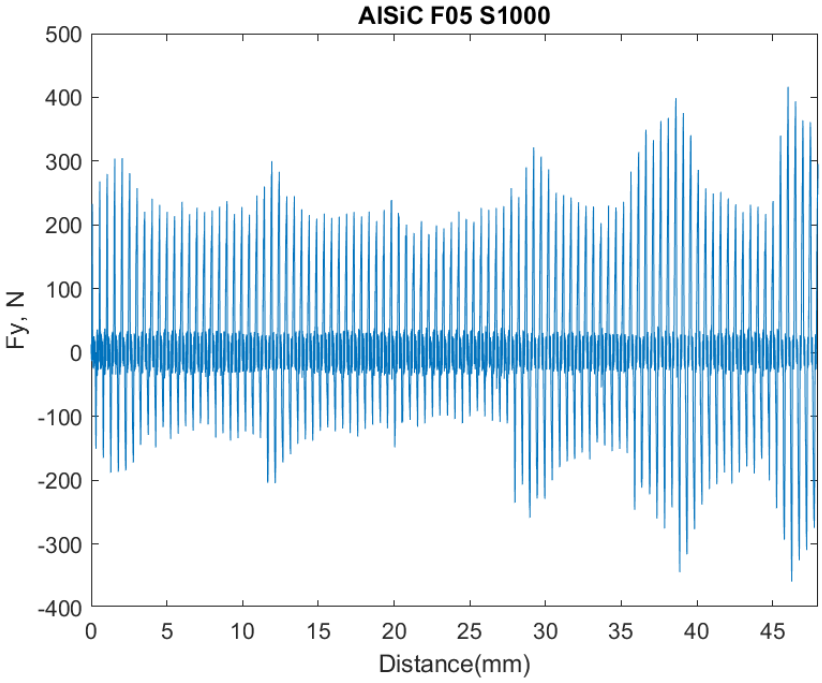
AlSiC F05 S1000
Fy, N
Distance(mm)
500
400
300
200
100
0
-100
-200
-300
-400
0
5
10
15
20
25
30
35
40
45

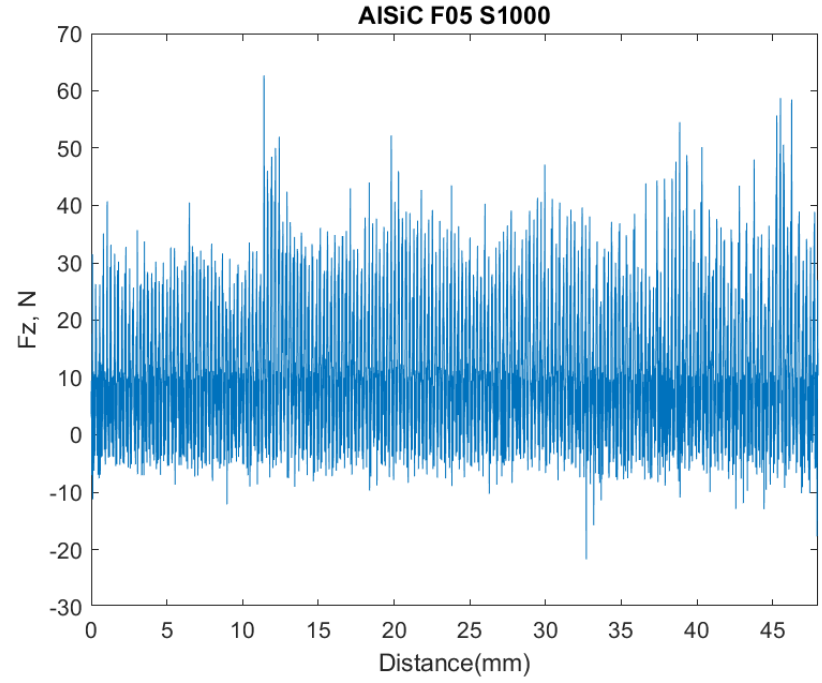
AlSiC F05 S1000
Fz, N
Distance(mm)
70
60
50
40
30
20
10
0
-10
-20
-30
0
5
10
15
20
25
30
35
40
45

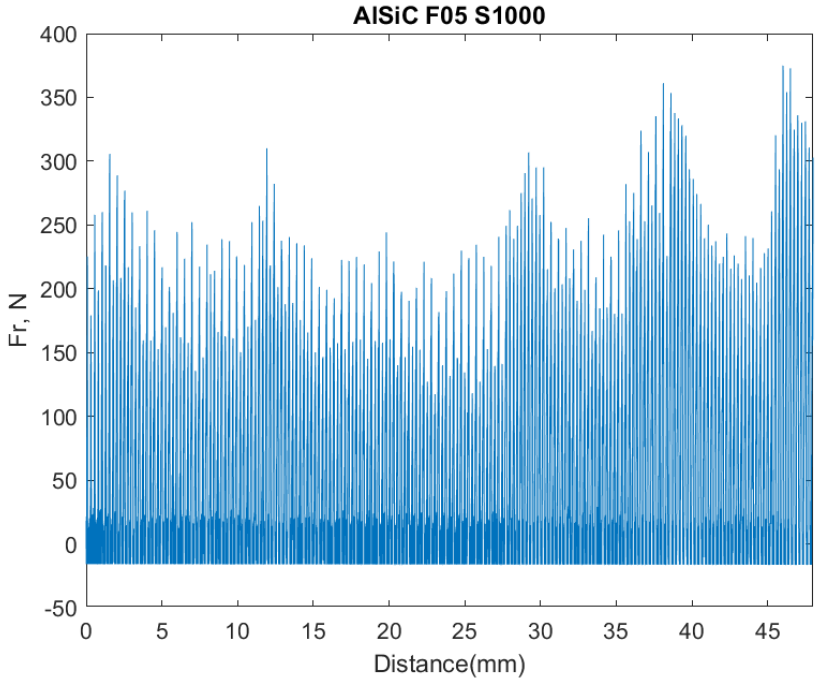
AlSiC F05 S1000
Fr, N
Distance(mm)
400
350
300
250
200
150
100
50
0
-50
0
5
10
15
20
25
30
35
40
45

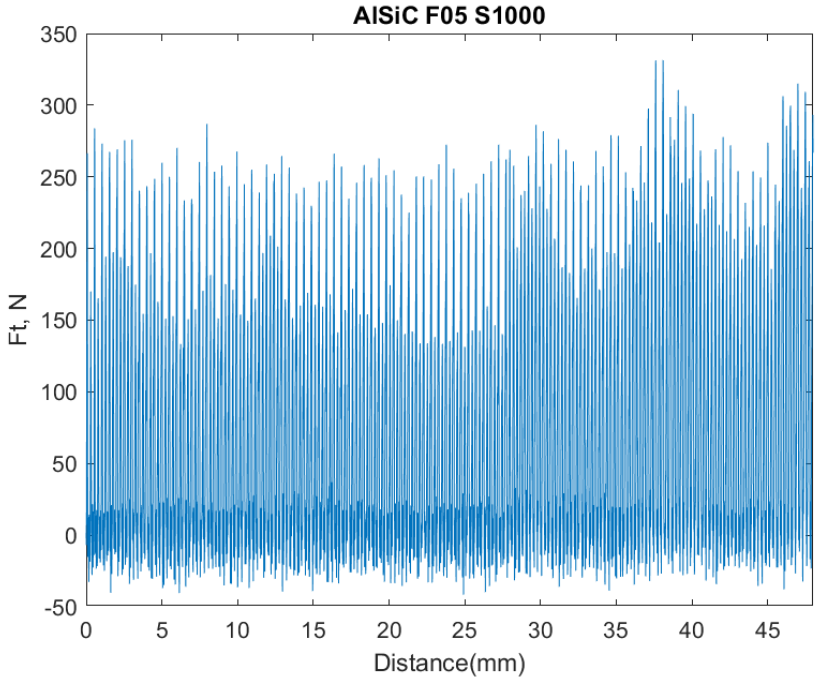
AlSiC F05 S1000
Ft, N
Distance(mm)
350
300
250
200
150
100
50
0
-50
0
5
10
15
20
25
30
35
40
45

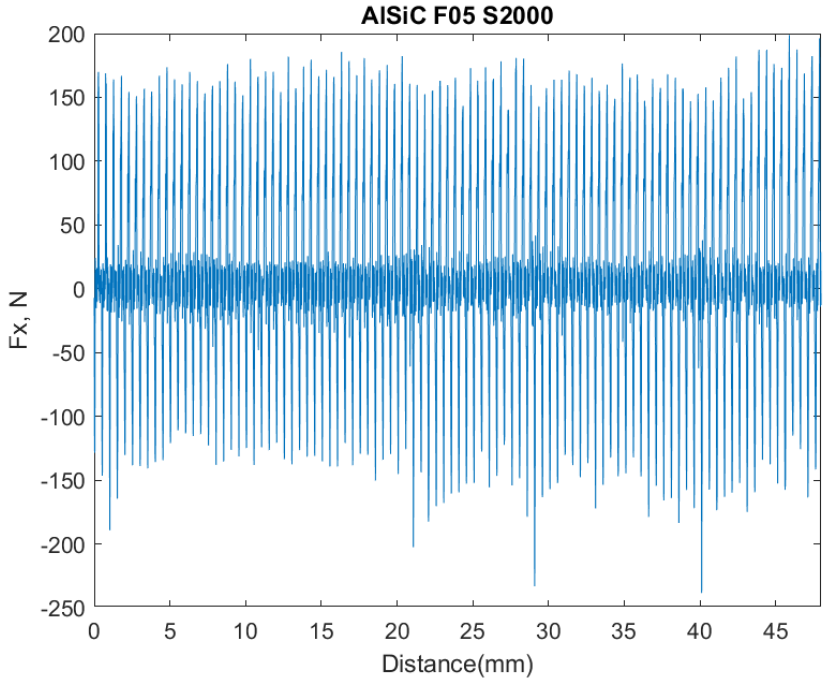
AlSiC F05 S2000
Fx, N
Distance(mm)
200
150
100
50
0
-50
-100
-150
-200
-250
0
5
10
15
20
25
30
35
40
45

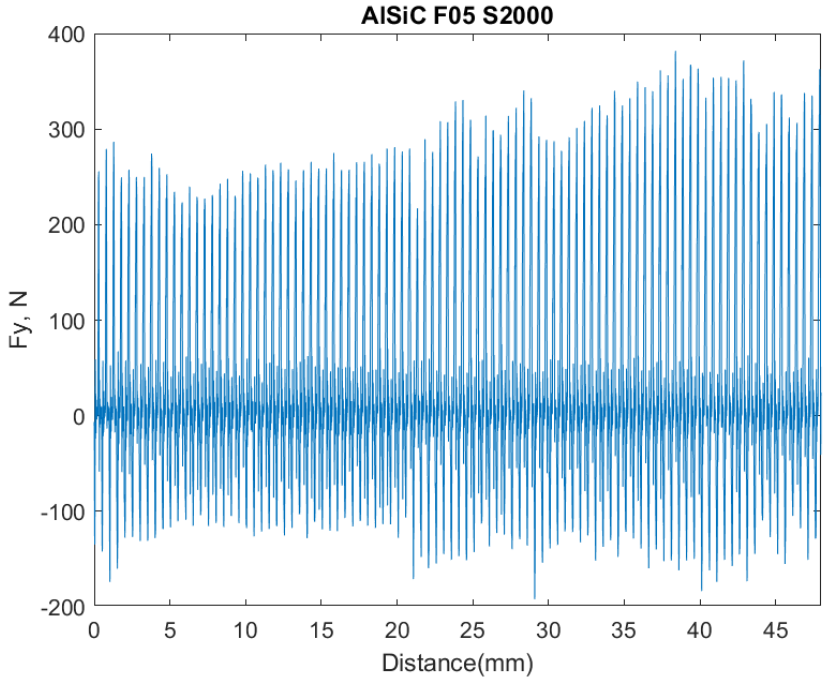
AlSiC F05 S2000
Fy, N
Distance(mm)
400
300
200
100
0
-100
-200
0
5
10
15
20
25
30
35
40
45

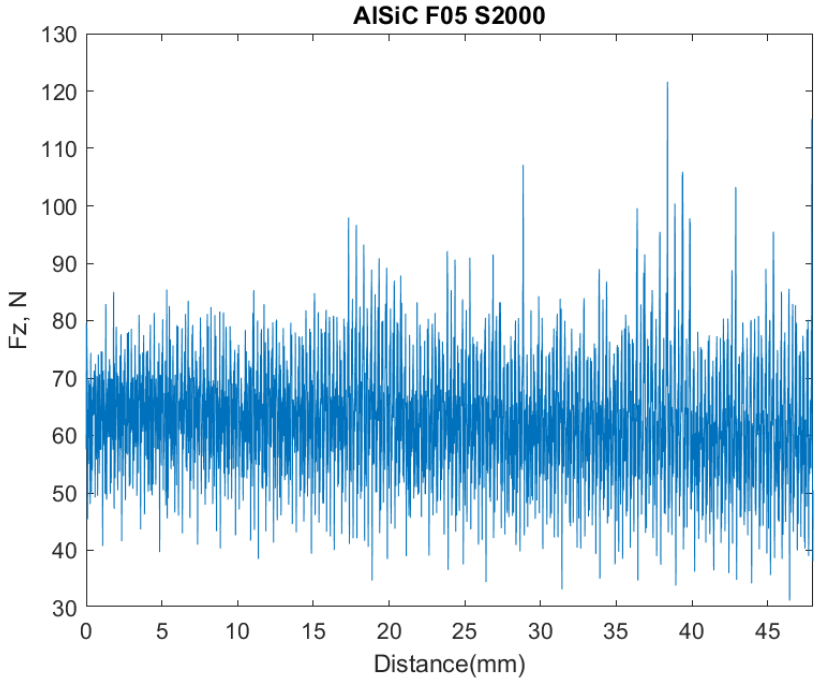
AlSiC F05 S2000
Fz, N
Distance(mm)
130
120
110
100
90
80
70
60
50
40
30
0
5
10
15
20
25
30
35
40
45

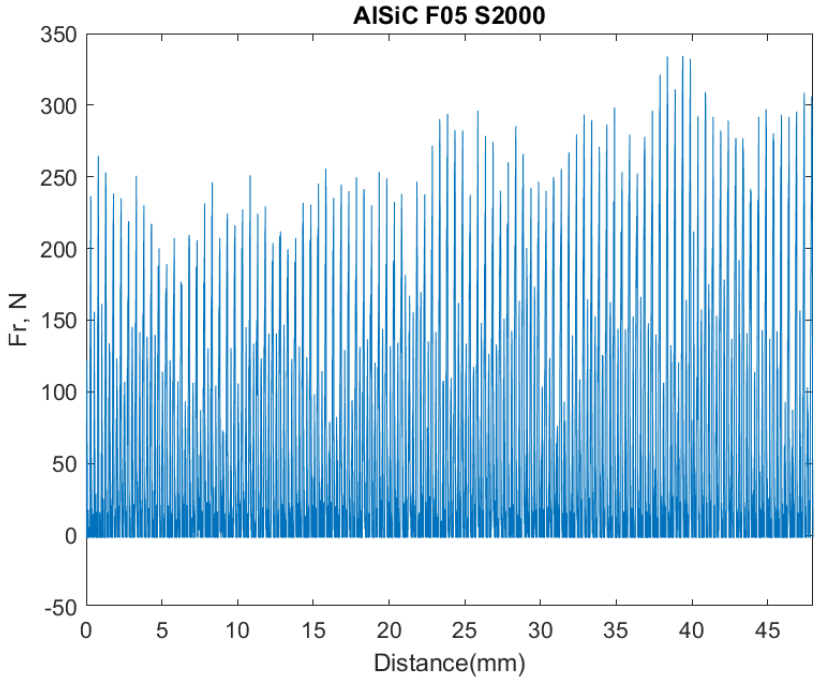
AlSiC F05 S2000
Fr, N
Distance(mm)
350
300
250
200
150
100
50
0
-50
0
5
10
15
20
25
30
35
40
45

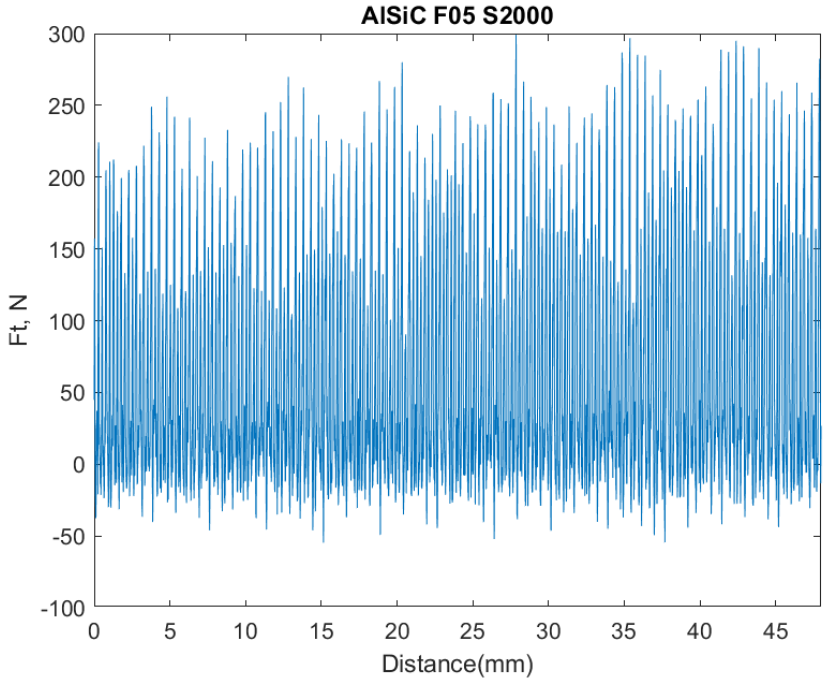
AlSiC F05 S2000
Ft, N
Distance(mm)
300
250
200
150
100
50
0
-50
-100
0
5
10
15
20
25
30
35
40
45

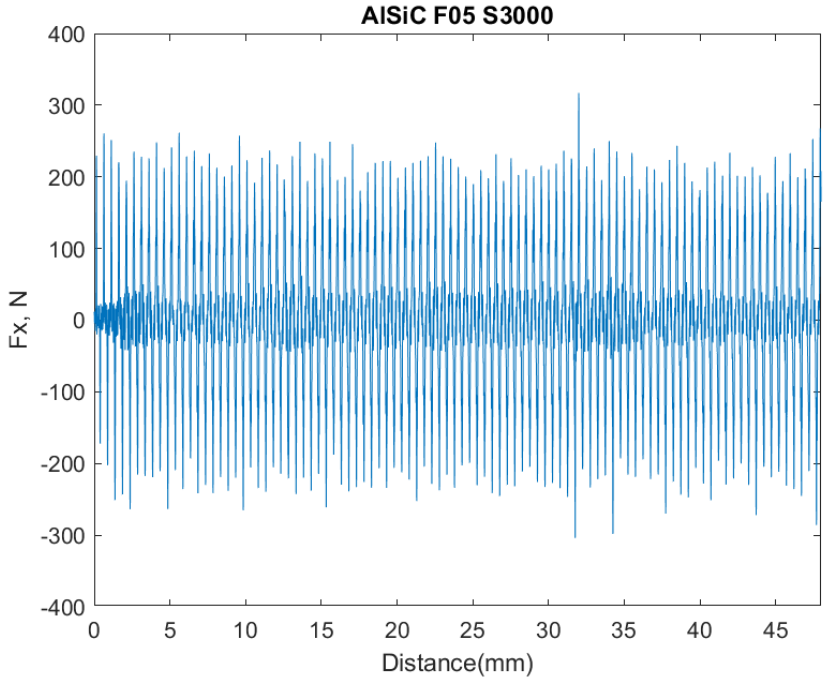
AlSiC F05 S3000
Fx, N
Distance(mm)
400
300
200
100
0
-100
-200
-300
-400
0
5
10
15
20
25
30
35
40
45

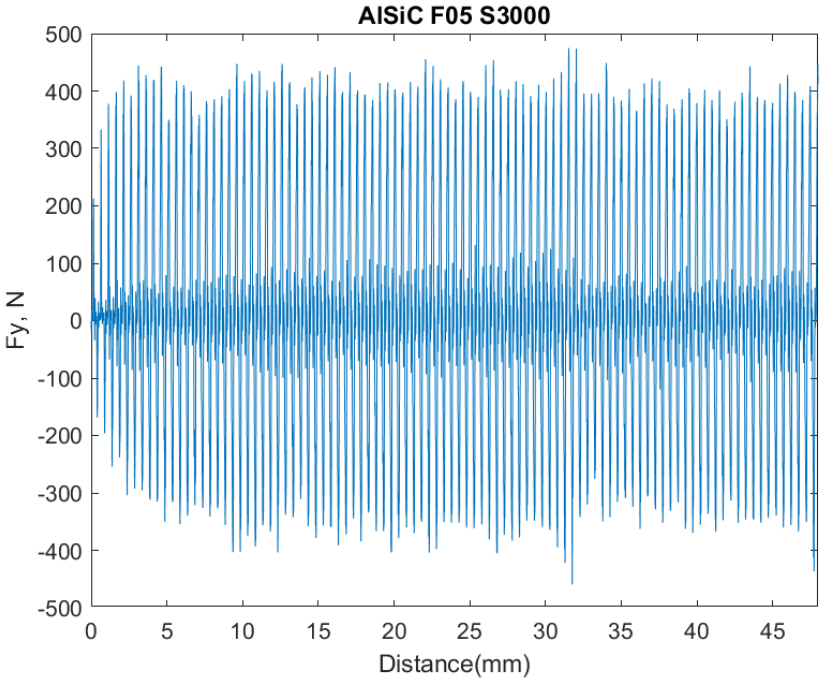
AlSiC F05 S3000
Fy, N
Distance(mm)
500
400
300
200
100
0
-100
-200
-300
-400
-500
0
5
10
15
20
25
30
35
40
45

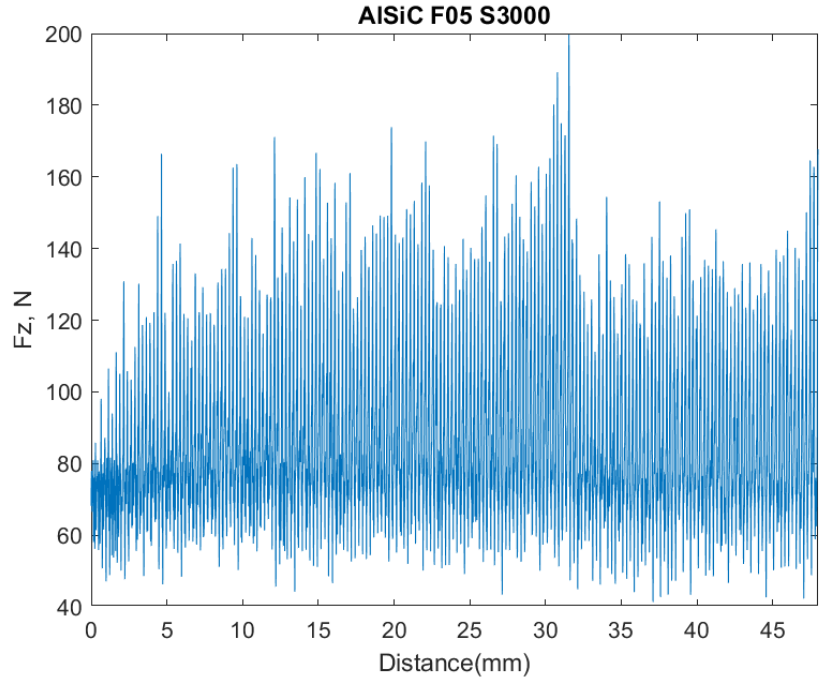
AlSiC F05 S3000
Fz, N
Distance(mm)
200
180
160
140
120
100
80
60
40
0
5
10
15
20
25
30
35
40
45

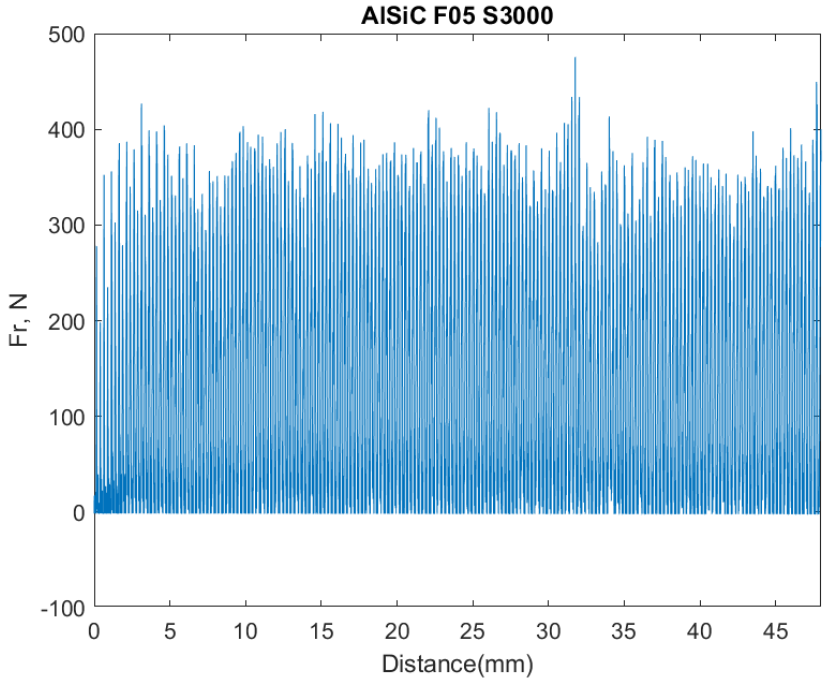
AlSiC F05 S3000
Fr, N
Distance(mm)
500
400
300
200
100
0
-100
0
5
10
15
20
25
30
35
40
45

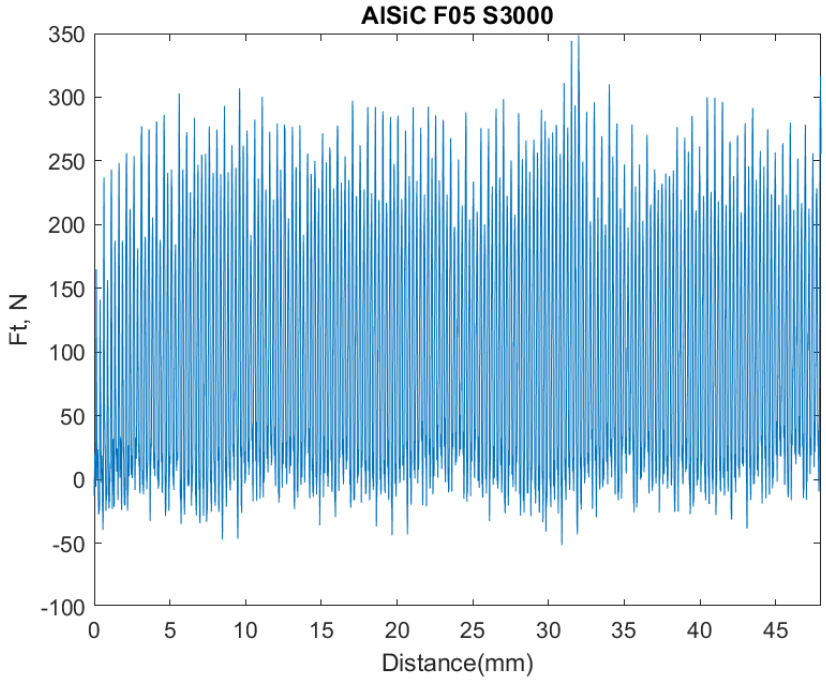
AlSiC F05 S3000
Ft, N
Distance(mm)
350
300
250
200
150
100
50
0
-50
-100
0
5
10
15
20
25
30
35
40
45

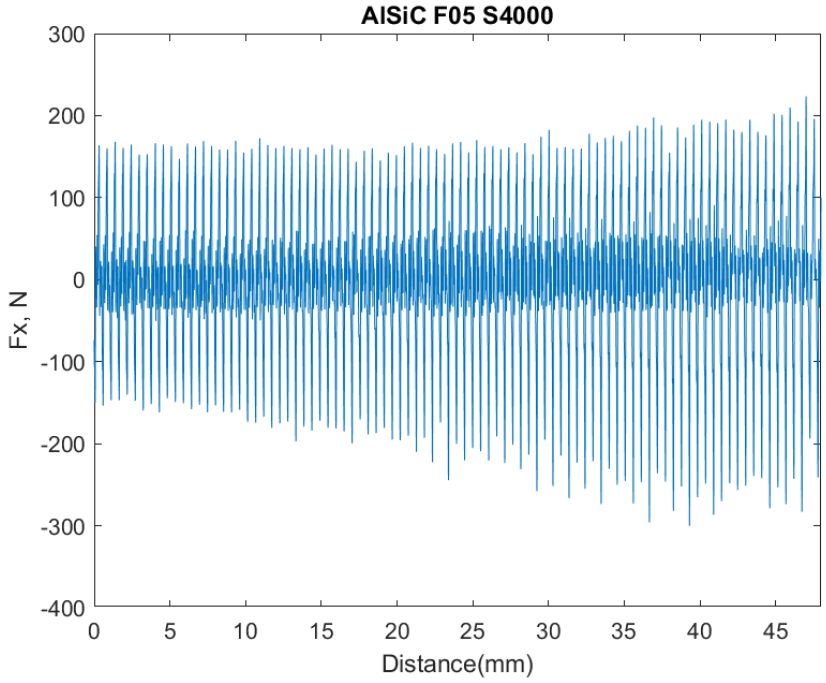
AlSiC F05 S4000
Fx, N
Distance(mm)
300
200
100
0
-100
-200
-300
-400
0
5
10
15
20
25
30
35
40
45

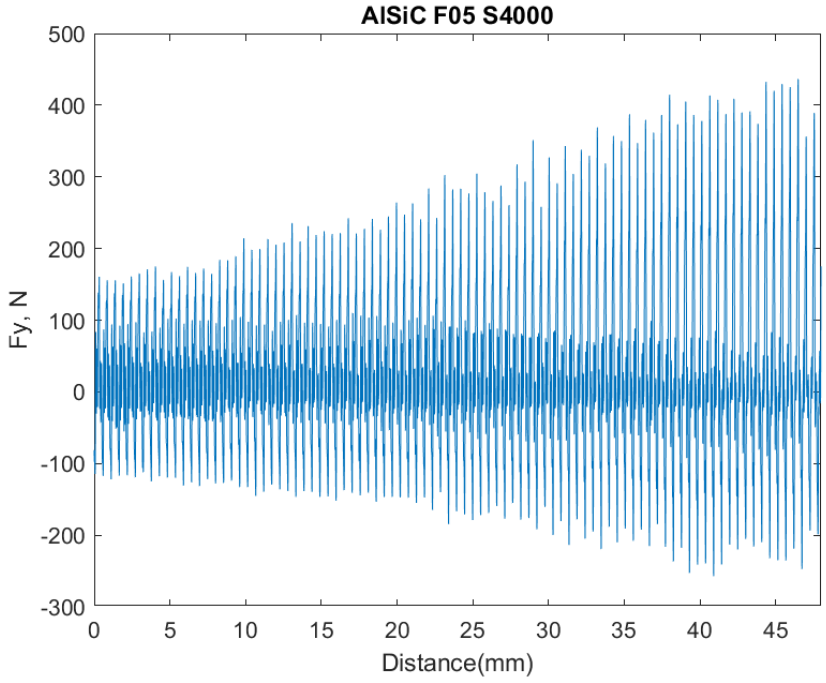
AlSiC F05 S4000
Fy, N
Distance(mm)
500
400
300
200
100
0
-100
-200
-300
0
5
10
15
20
25
30
35
40
45

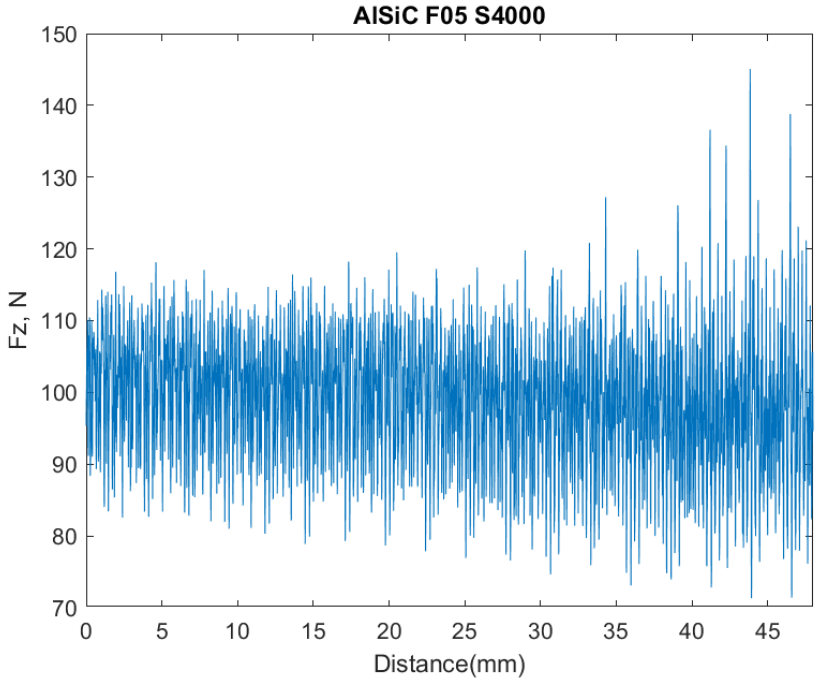
AlSiC F05 S4000
Fz, N
Distance(mm)
150
140
130
120
110
100
90
80
70
0
5
10
15
20
25
30
35
40
45

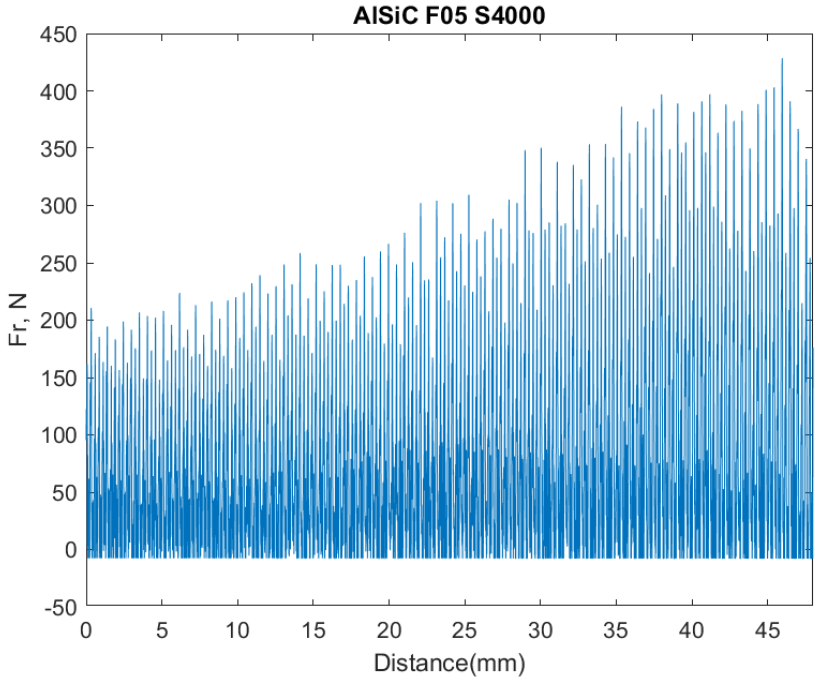
AlSiC F05 S4000
Fr, N
Distance(mm)
450
400
350
300
250
200
150
100
50
0
-50
0
5
10
15
20
25
30
35
40
45

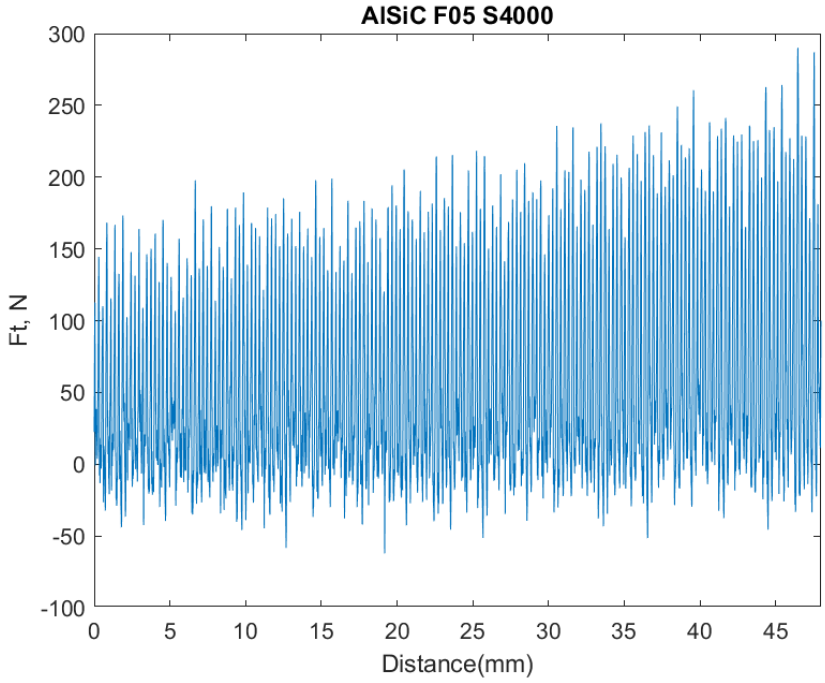
AlSiC F05 S4000
Ft, N
Distance(mm)
300
250
200
150
100
50
0
-50
-100
0
5
10
15
20
25
30
35
40
45

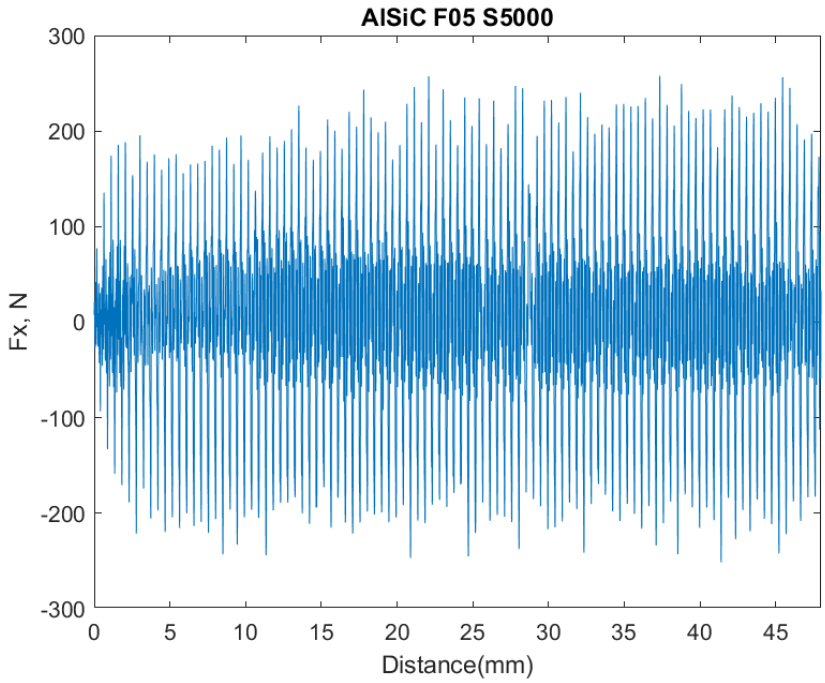
AlSiC F05 S5000
Fx, N
Distance(mm)
300
200
100
0
-100
-200
-300
0
5
10
15
20
25
30
35
40
45

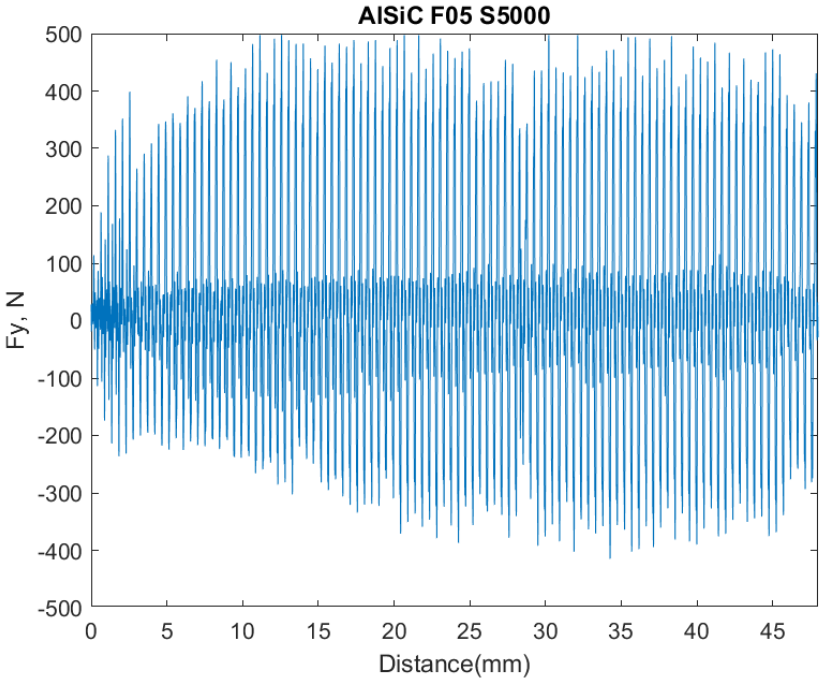
AlSiC F05 S5000
Fy, N
Distance(mm)
500
400
300
200
100
0
-100
-200
-300
-400
-500
0
5
10
15
20
25
30
35
40
45

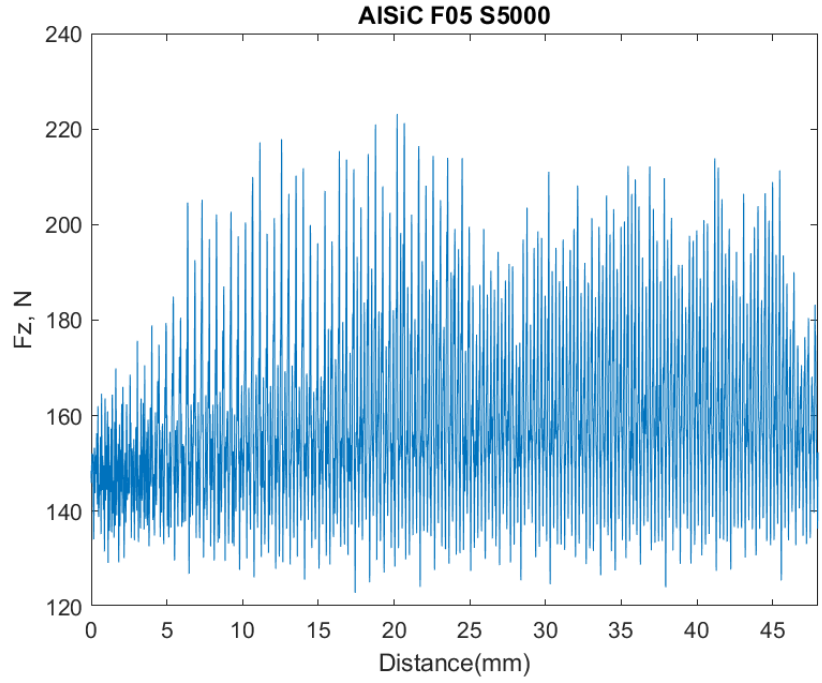
AlSiC F05 S5000
Fz, N
Distance(mm)
240
220
200
180
160
140
120
0
5
10
15
20
25
30
35
40
45

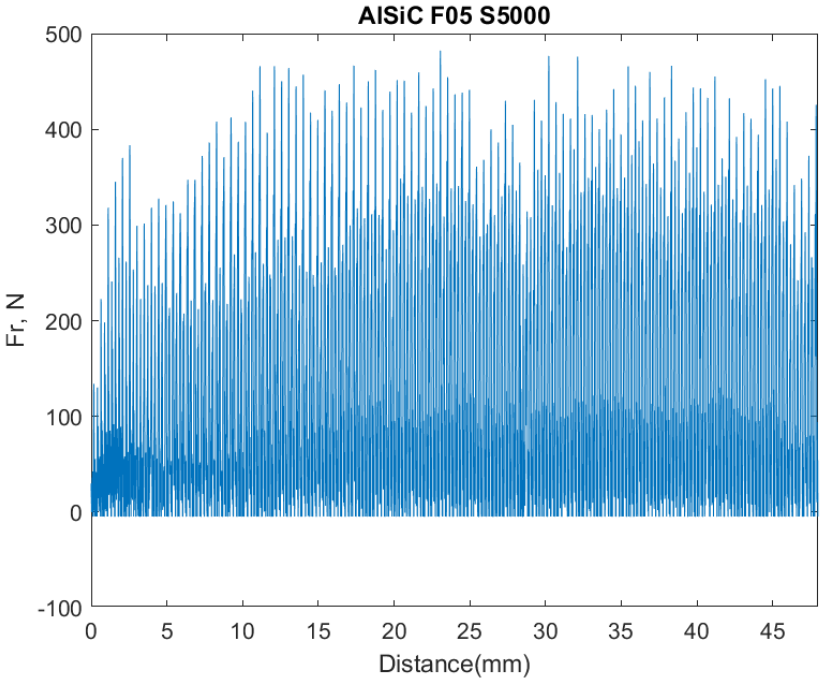

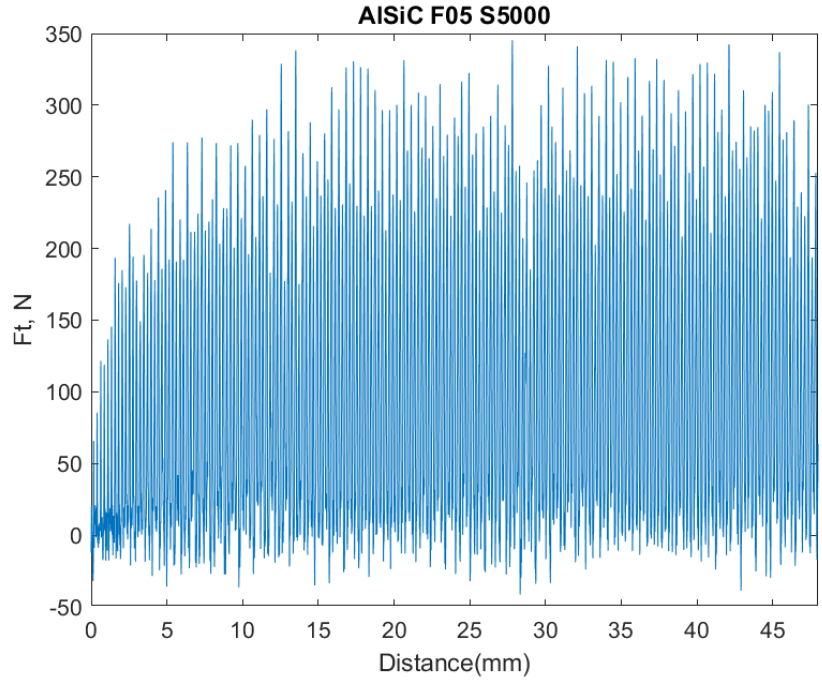

0.9em

B.1.2 Offset and drift compensation MATLAB code

```
close all
clear all
clc
load('AlSiC_AE_F01_S2000_1.mat');
F={Fx
    Fy
    Fz
    Fr
    Ft};
Fl={'Fx, N','Fy, N','Fz, N','Fr, N','Ft, N'}
  ff=6;
for dd=1:1:5
   Fy=F{dd};

plot(time,Fy)
to=7.05;
tl=21.8;
res=1/8000;
t0i=to/res;
tli=tl/res;
xl=48;
step_x=xl/(tli-t0i);
x=0:step_x:48;
x=x';
size2=size(Fy,1);
m1=1;
for q=1:1:size2
    if(time(q,1)<to)
        left_Fy(m1,1)=Fy(q,1);
        m1=m1+1;
    end
end
left_avg=mean(left_Fy);
```

```
q=1;
m1=1;
for q=1:1:size2
    offset_Fy(q,1)=Fy(q,1)-left_avg;
end

for q=1:1:size2
    if(time(q,1)<to)
        oleft_Fy(m1,1)=offset_Fy(q,1);
        m1=m1+1;
    end
end
oleft_avg=mean(oleft_Fy);
m1=1;
for q=1:1:size2
    if(time(q,1)>tl)
        right_Fy(m1,1)=offset_Fy(q,1);
        m1=m1+1;
    end
    if(time(q,1)==tl)
        right_pos=q;
    end
end
right_avg=mean(right_Fy);
slope=(right_avg-oleft_avg)/(time(size2)-to);

%last=drift(q,1);

for q=1:1:size2
    const=-slope*to; % varies with feed
    drift(q,1)=slope.*time(q,1)+const;
    drift_Fy(q,1)=offset_Fy(q,1)-drift(q,1);
end
```

```
x1(:,1)=0:xl/size2:xl-xl/size2;
plot(x,drift_Fy(t0i:tli,1))
xlim([0 48])
xlabel('Distance(mm)')

ylabel(Fl{dd})
title('AlSiC F01 S1000')
saveas(gcf,sprintf('fig%d',ff),'png')
ff=ff+1;
end
```

B.1.3 Acoustic Emission

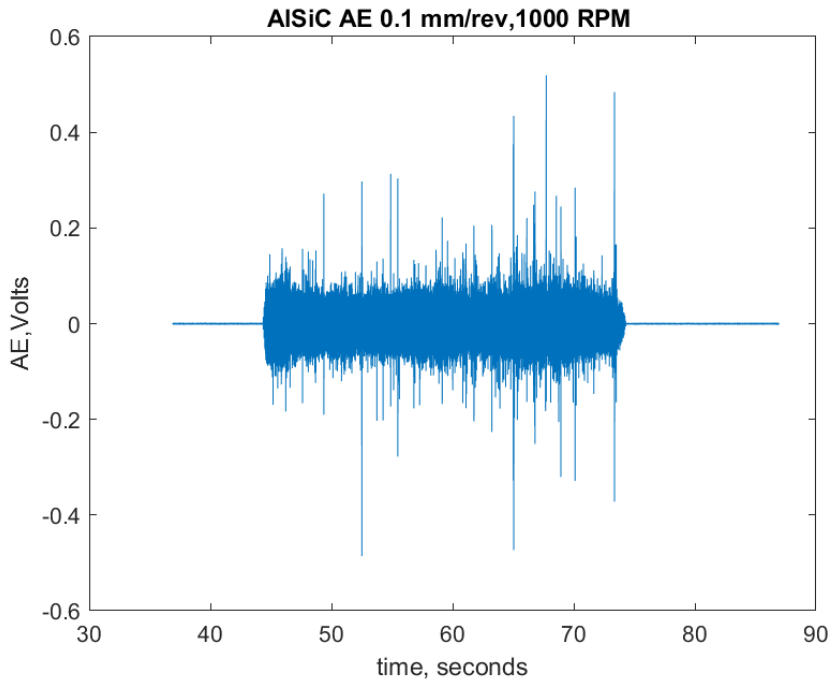

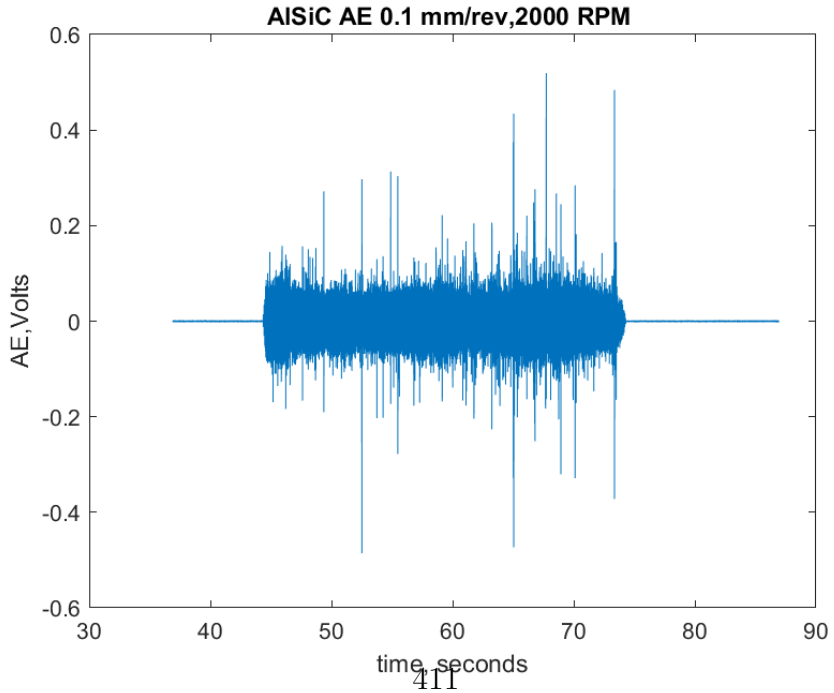

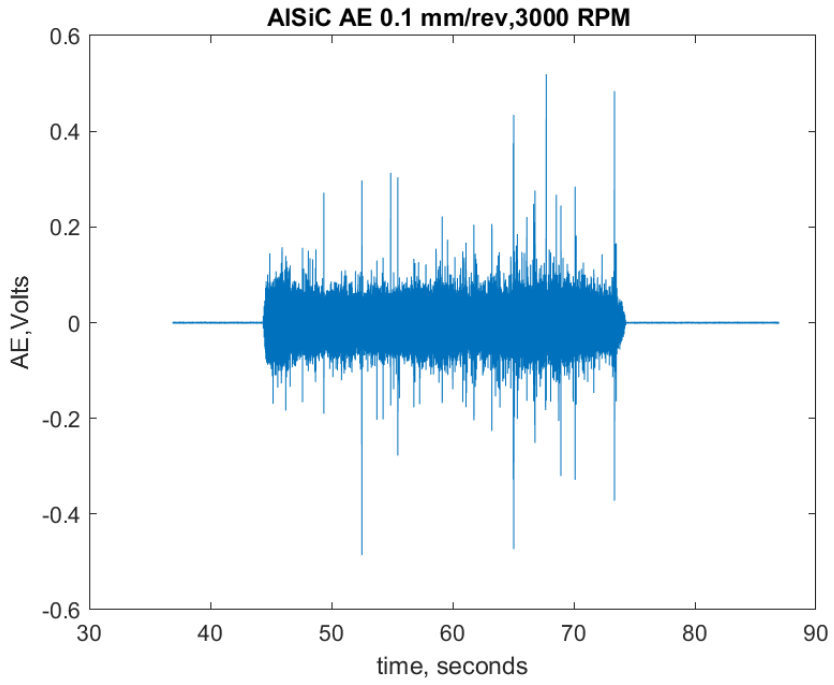
AlSiC AE 0.1 mm/rev,3000 RPM
AE,Volts
time, seconds
0.6
0.4
0.2
0
-0.2
-0.4
-0.6
30
40
50
60
70
80
90

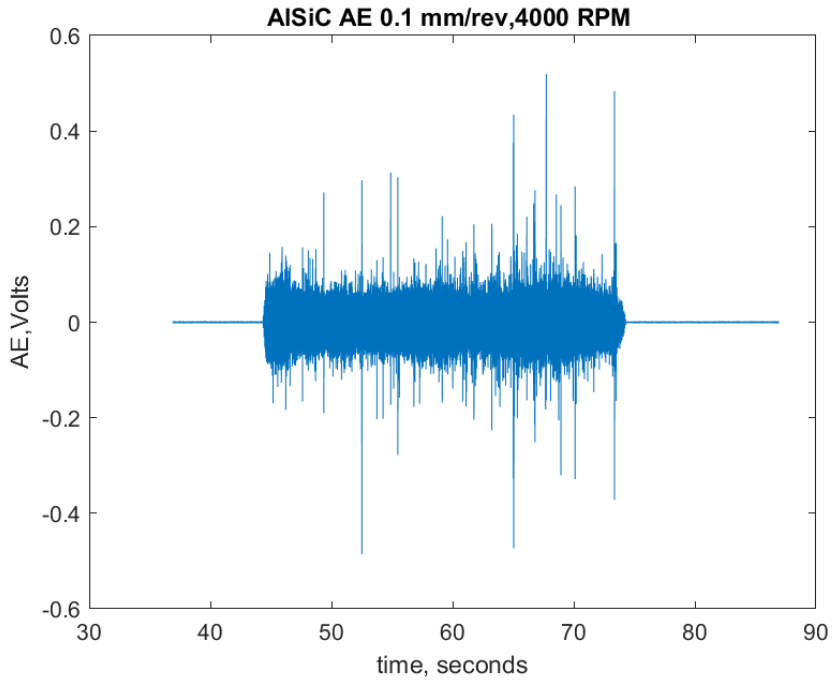
AlSiC AE 0.1 mm/rev,4000 RPM
AE,Volts
time, seconds
0.6
0.4
0.2
0
-0.2
-0.4
-0.6
30
40
50
60
70
80
90

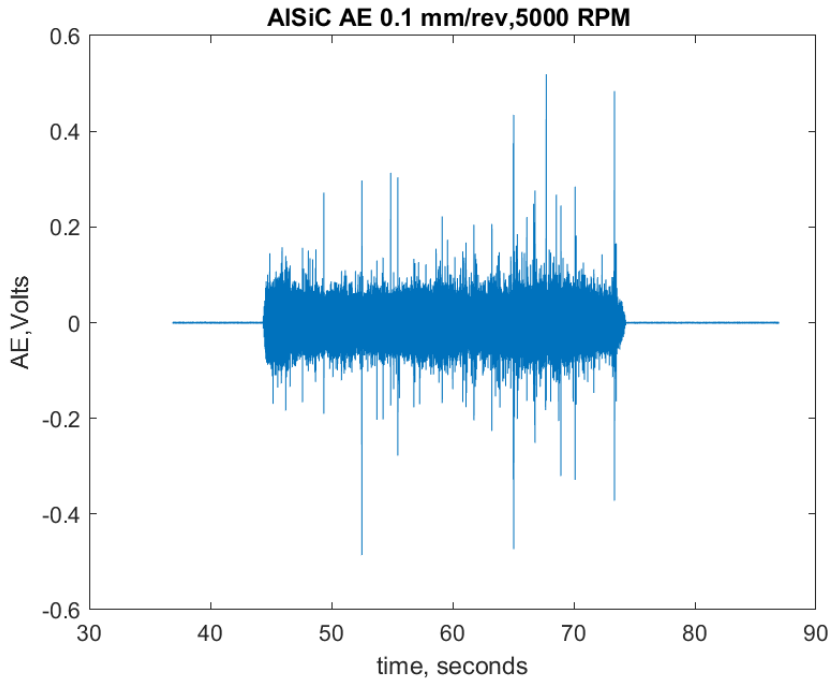
AlSiC AE 0.1 mm/rev,5000 RPM
AE,Volts
time, seconds
0.6
0.4
0.2
0
-0.2
-0.4
-0.6
30
40
50
60
70
80
90

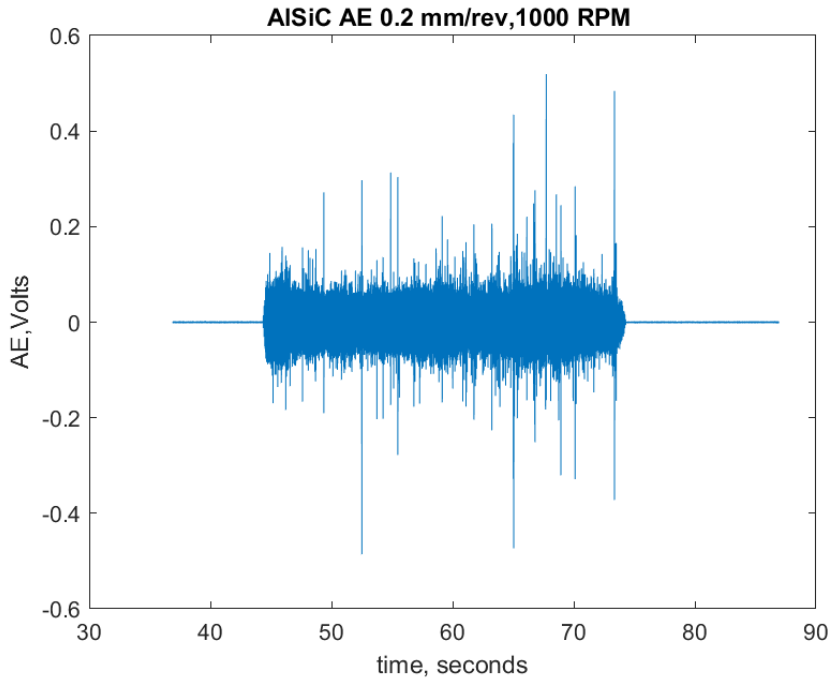
AlSiC AE 0.2 mm/rev,1000 RPM
AE,Volts
time, seconds
0.6
0.4
0.2
0
-0.2
-0.4
-0.6
30
40
50
60
70
80
90

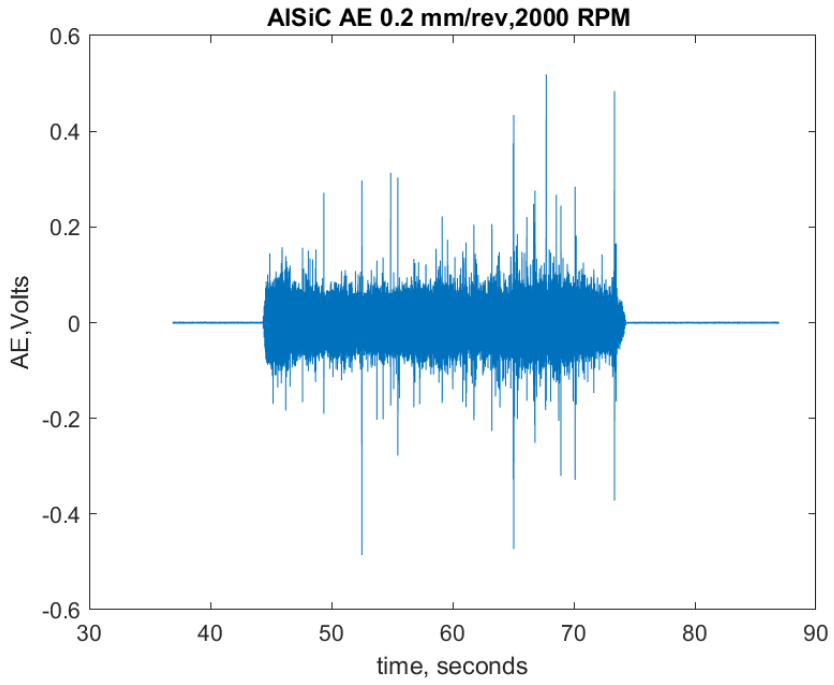
AlSiC AE 0.2 mm/rev,2000 RPM
AE,Volts
time, seconds
0.6
0.4
0.2
0
-0.2
-0.4
-0.6
30
40
50
60
70
80
90

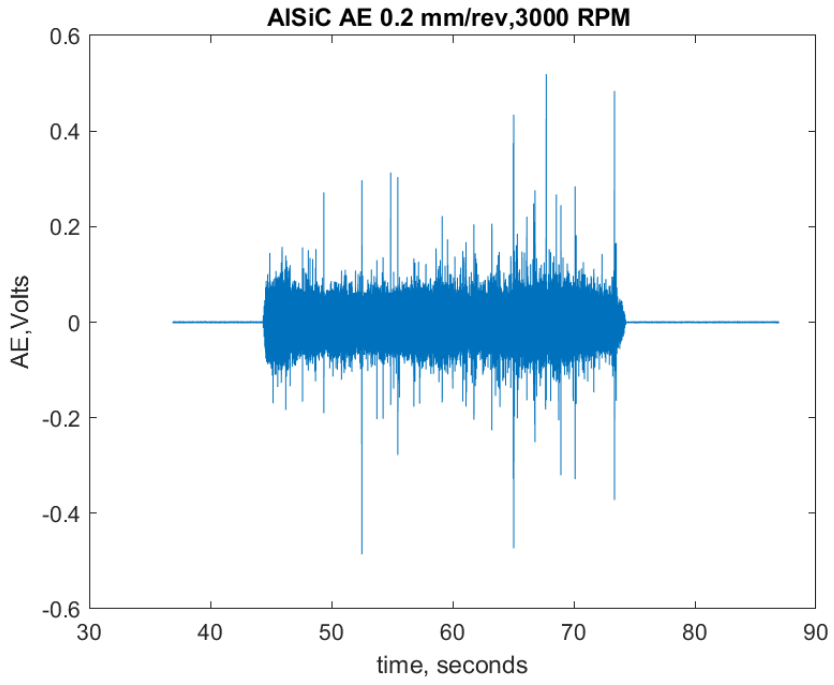
AlSiC AE 0.2 mm/rev,3000 RPM
AE,Volts
time, seconds
0.6
0.4
0.2
0
-0.2
-0.4
-0.6
30
40
50
60
70
80
90

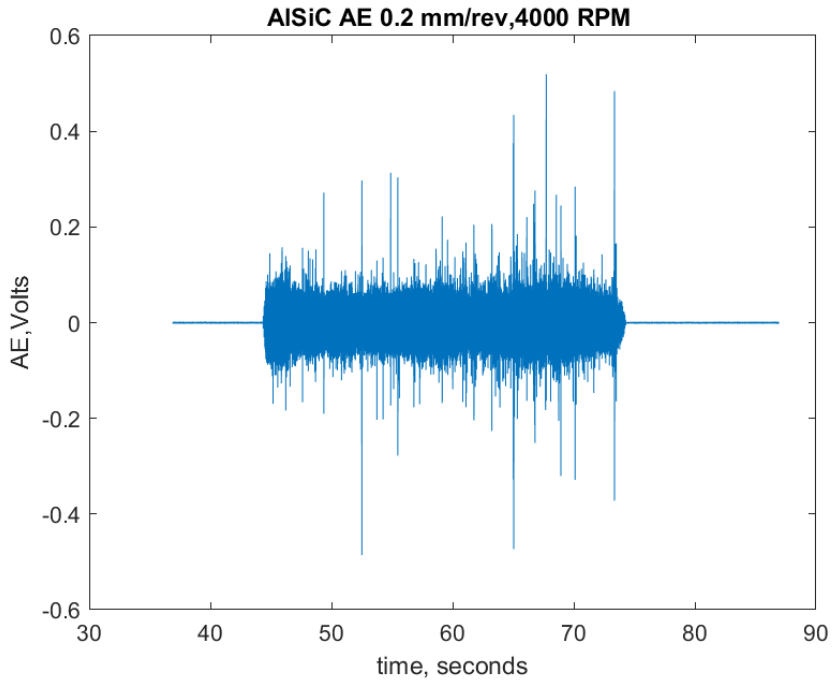
AlSiC AE 0.2 mm/rev,4000 RPM
AE,Volts
time, seconds
0.6
0.4
0.2
0
-0.2
-0.4
-0.6
30
40
50
60
70
80
90

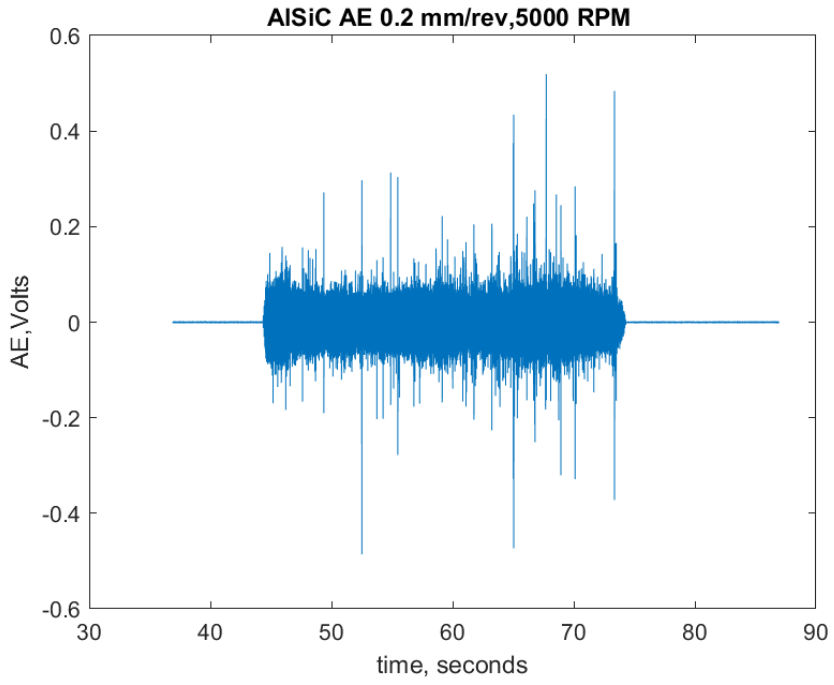
AlSiC AE 0.2 mm/rev,5000 RPM
AE,Volts
time, seconds
0.6
0.4
0.2
0
-0.2
-0.4
-0.6
30
40
50
60
70
80
90

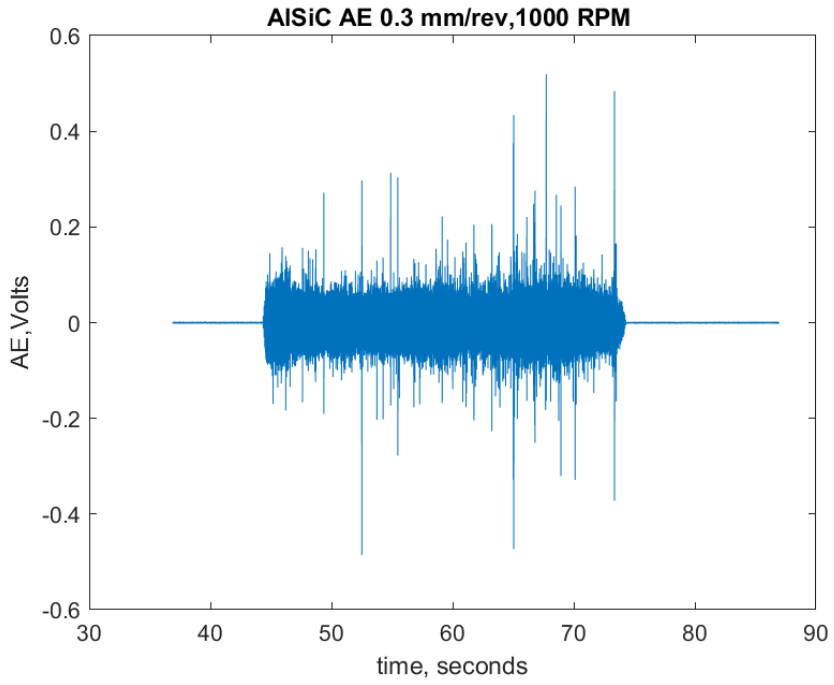
AlSiC AE 0.3 mm/rev,1000 RPM
AE, Volts
time, seconds
0.6
0.4
0.2
0
-0.2
-0.4
-0.6
30
40
50
60
70
80
90

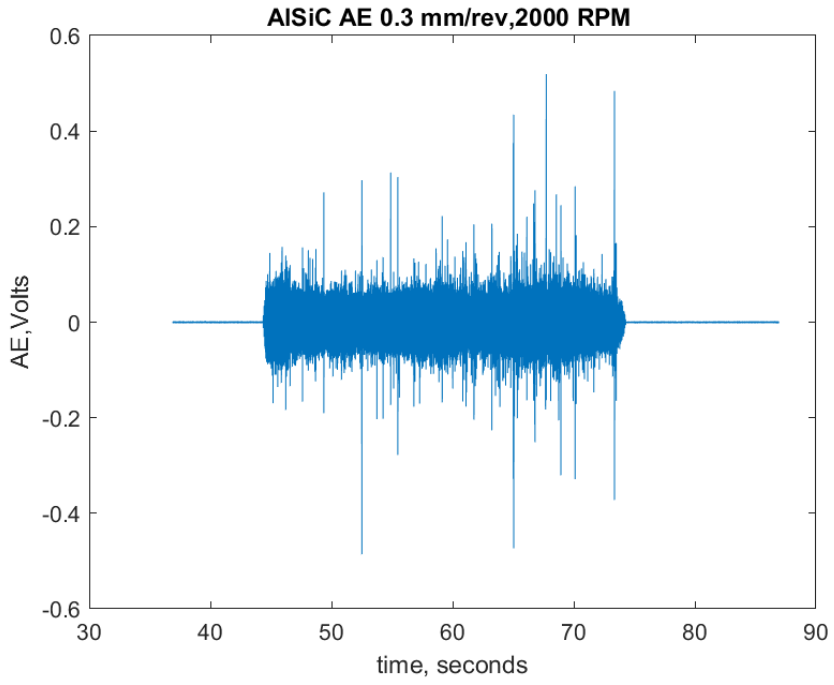
AlSiC AE 0.3 mm/rev,2000 RPM
AE, Volts
time, seconds
0.6
0.4
0.2
0
-0.2
-0.4
-0.6
30
40
50
60
70
80
90

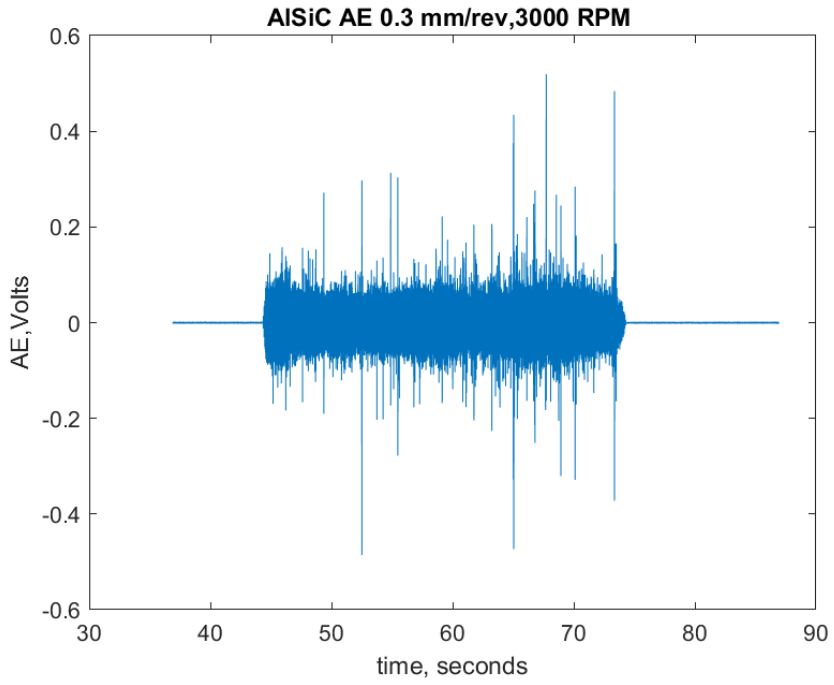
AlSiC AE 0.3 mm/rev,3000 RPM
AE,Volts
time, seconds
0.6
0.4
0.2
0
-0.2
-0.4
-0.6
30
40
50
60
70
80
90

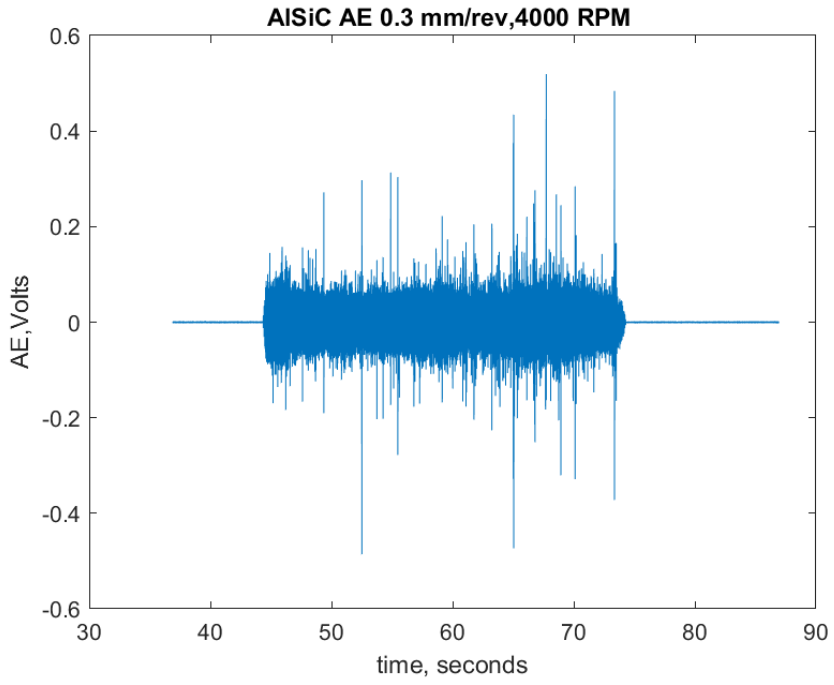
AlSiC AE 0.3 mm/rev,4000 RPM
AE,Volts
time, seconds
0.6
0.4
0.2
0
-0.2
-0.4
-0.6
30
40
50
60
70
80
90

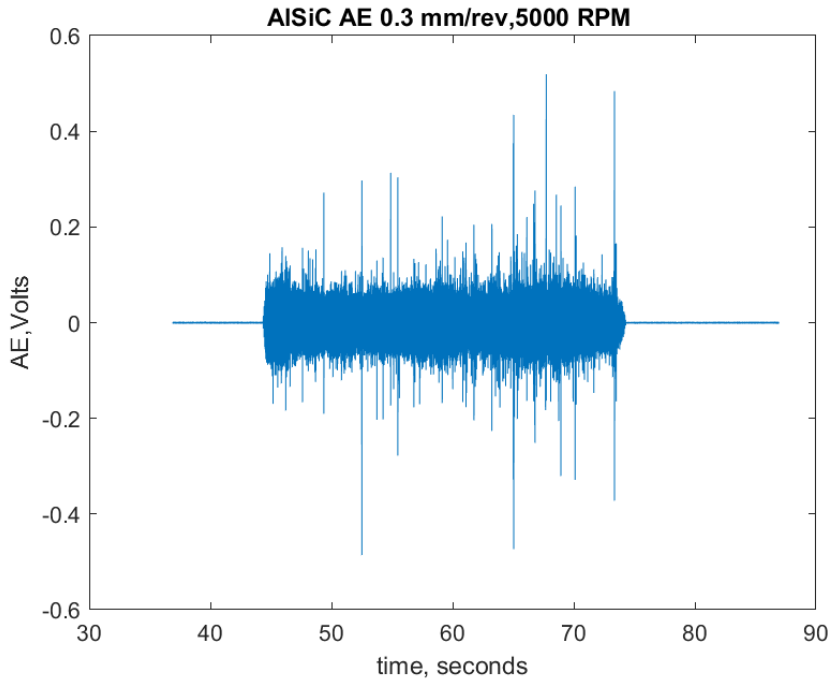
AlSiC AE 0.3 mm/rev,5000 RPM
AE, Volts
time, seconds
0.6
0.4
0.2
0
-0.2
-0.4
-0.6
30
40
50
60
70
80
90

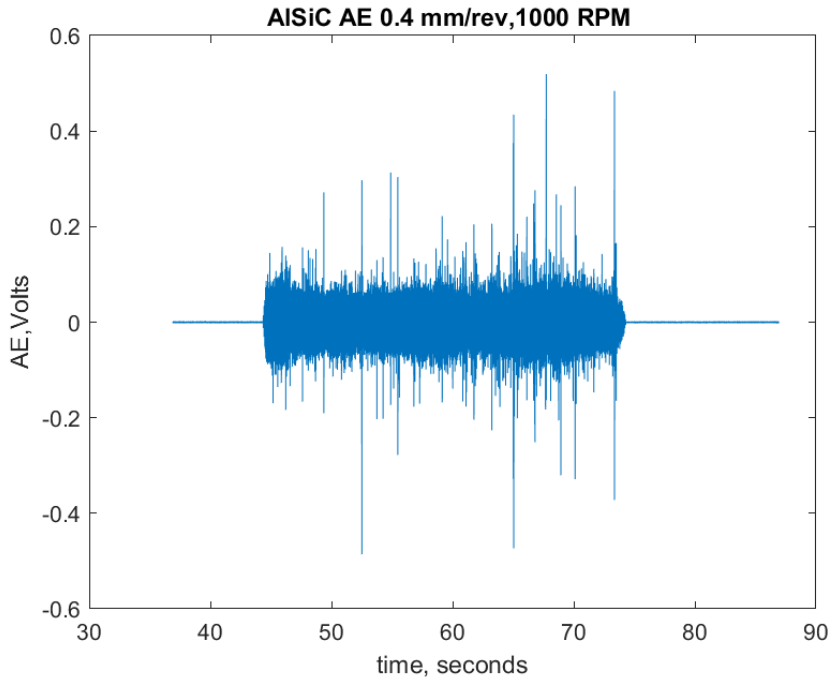
AlSiC AE 0.4 mm/rev,1000 RPM
AE, Volts
time, seconds
0.6
0.4
0.2
0
-0.2
-0.4
-0.6
30
40
50
60
70
80
90

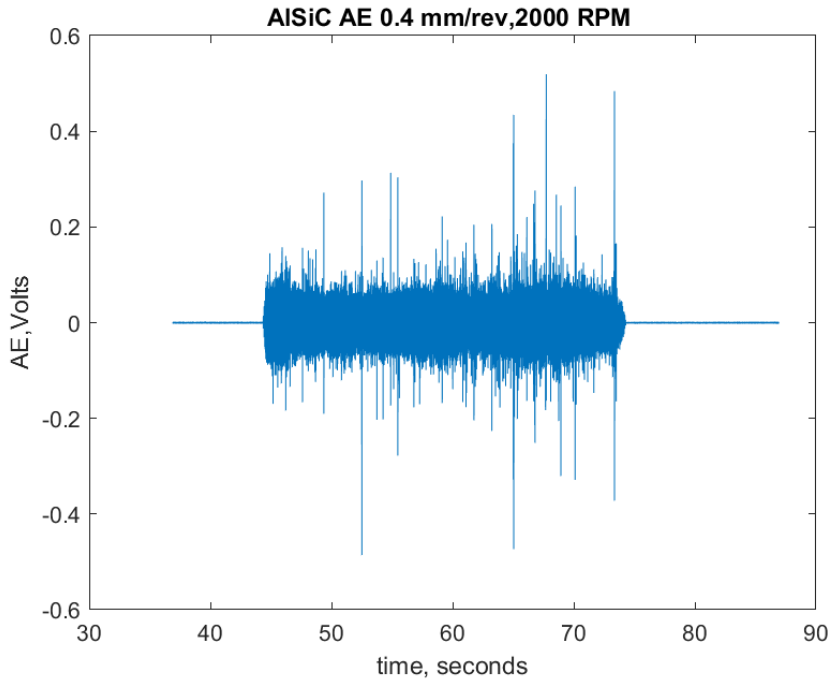
AlSiC AE 0.4 mm/rev,2000 RPM
AE,Volts
time, seconds
0.6
0.4
0.2
0
-0.2
-0.4
-0.6
30
40
50
60
70
80
90

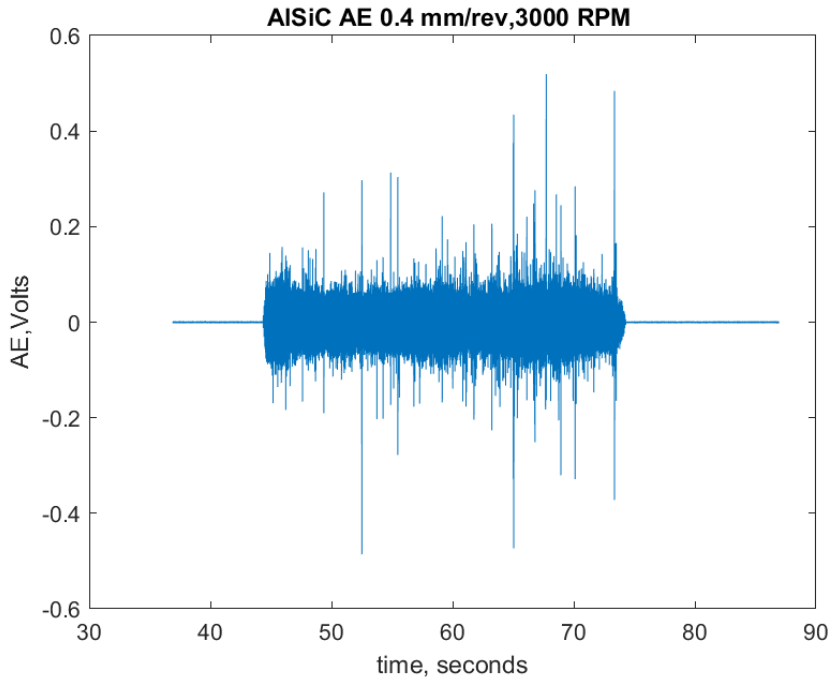
AlSiC AE 0.4 mm/rev,3000 RPM
AE,Volts
time, seconds
0.6
0.4
0.2
0
-0.2
-0.4
-0.6
30
40
50
60
70
80
90

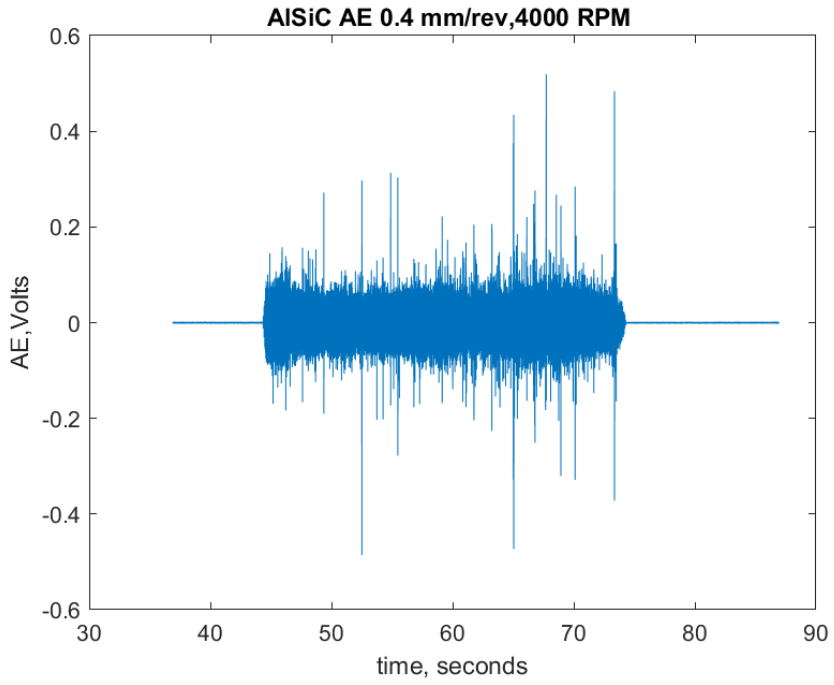
AlSiC AE 0.4 mm/rev,4000 RPM
AE,Volts
time, seconds
0.6
0.4
0.2
0
-0.2
-0.4
-0.6
30
40
50
60
70
80
90

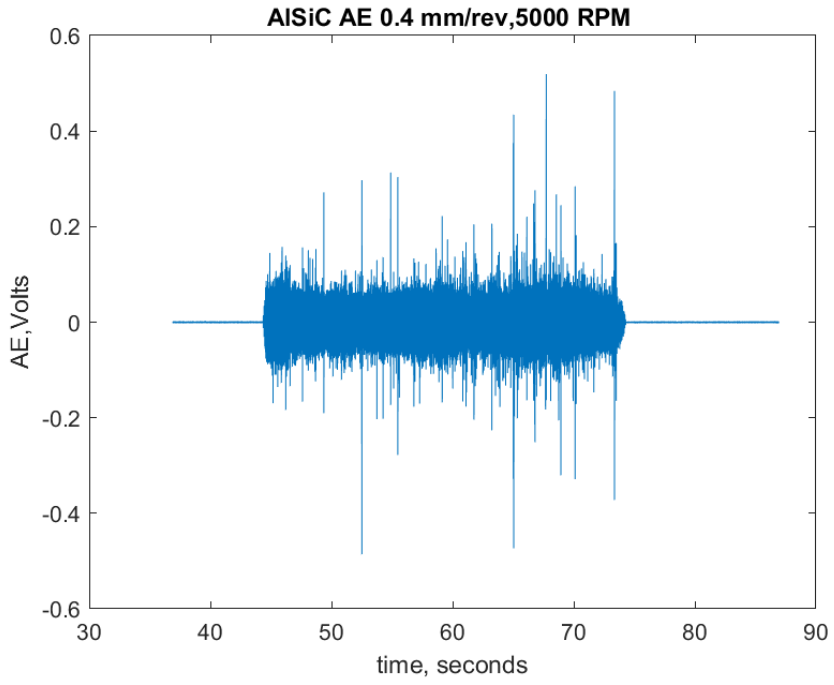
AlSiC AE 0.4 mm/rev,5000 RPM
AE,Volts
time, seconds
0.6
0.4
0.2
0
-0.2
-0.4
-0.6
30
40
50
60
70
80
90

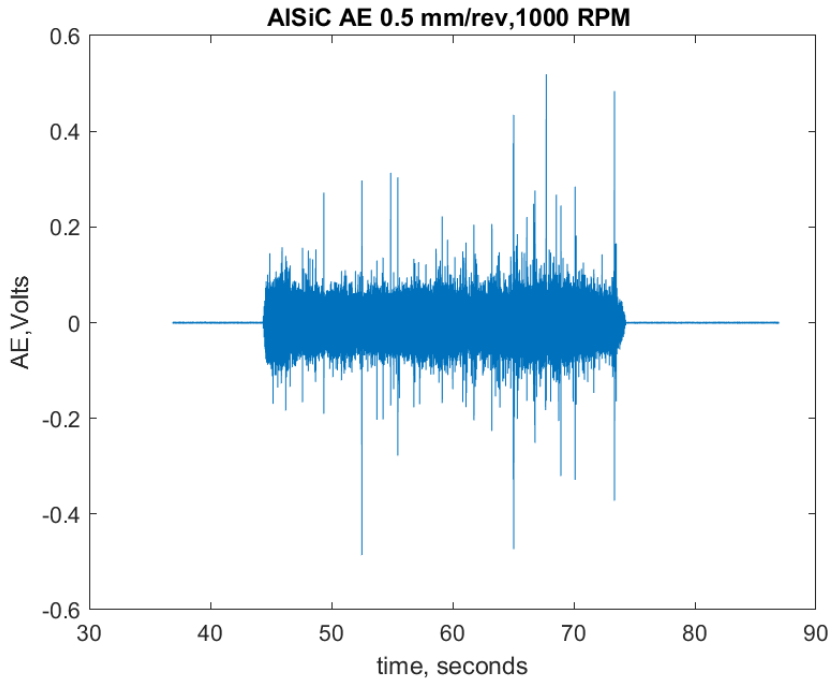
AlSiC AE 0.5 mm/rev,1000 RPM
AE,Volts
time, seconds
0.6
0.4
0.2
0
-0.2
-0.4
-0.6
30
40
50
60
70
80
90

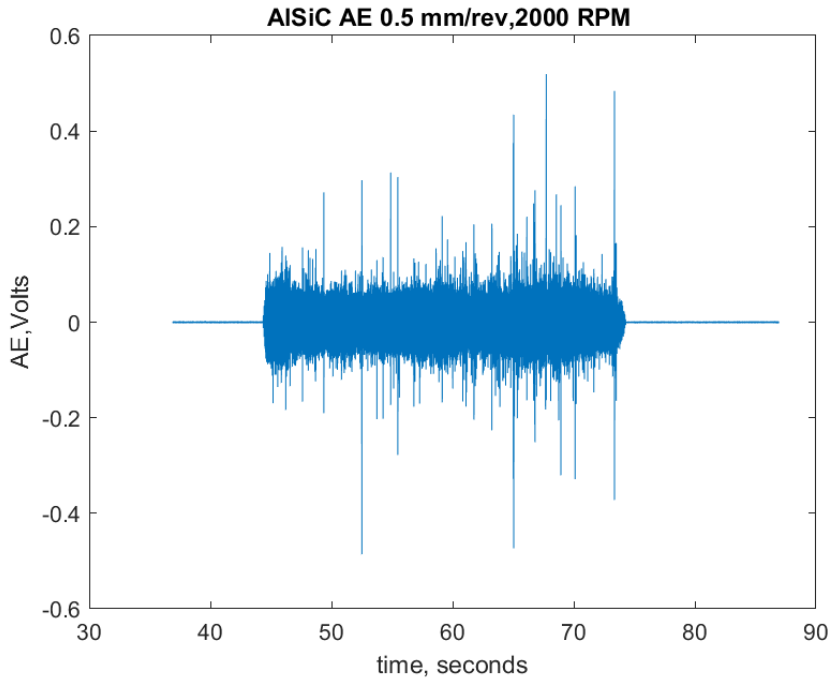
AlSiC AE 0.5 mm/rev,2000 RPM
AE,Volts
time, seconds
0.6
0.4
0.2
0
-0.2
-0.4
-0.6
30
40
50
60
70
80
90

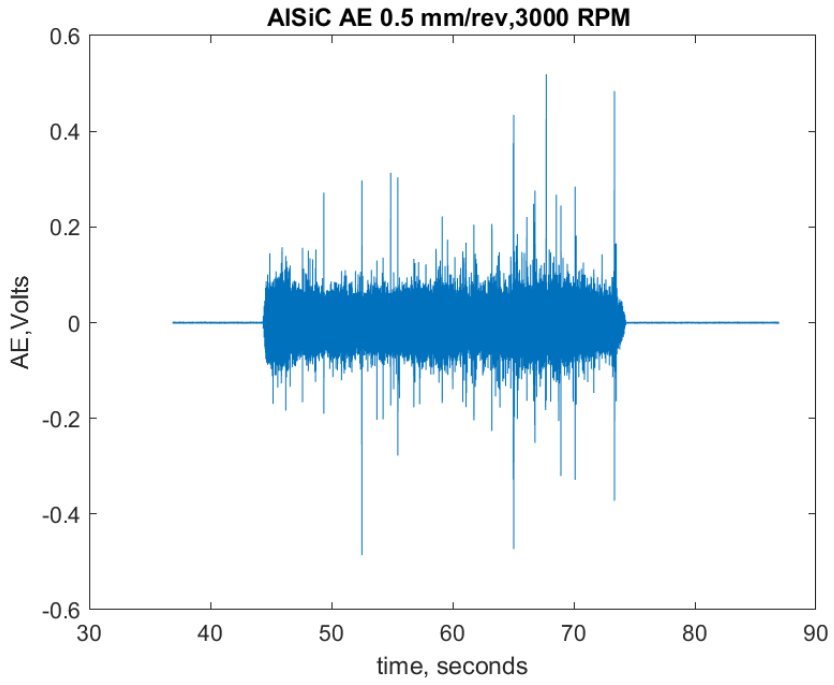
AlSiC AE 0.5 mm/rev,3000 RPM
AE,Volts
time, seconds
0.6
0.4
0.2
0
-0.2
-0.4
-0.6
30
40
50
60
70
80
90

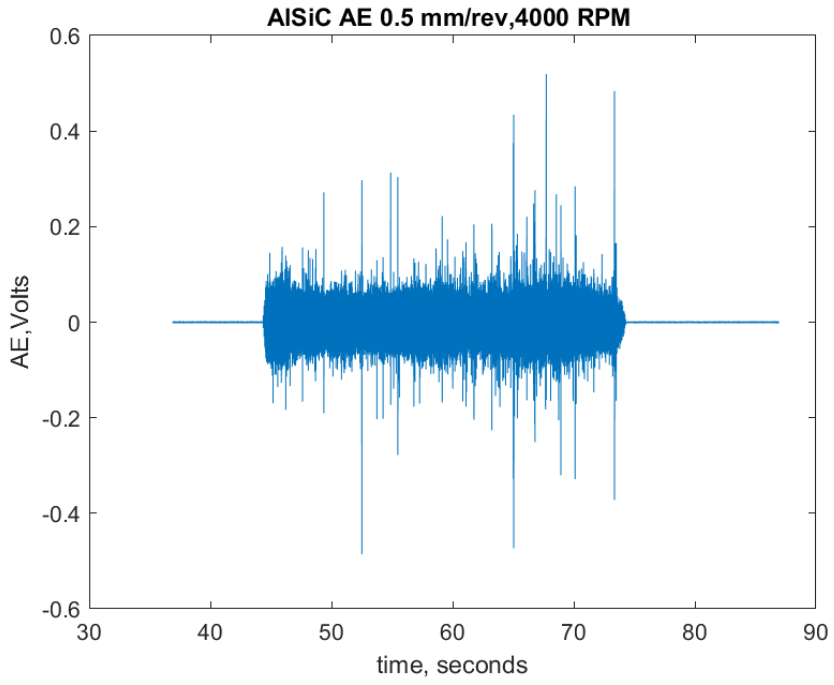
AlSiC AE 0.5 mm/rev,4000 RPM
AE,Volts
time, seconds
0.6
0.4
0.2
0
-0.2
-0.4
-0.6
30
40
50
60
70
80
90

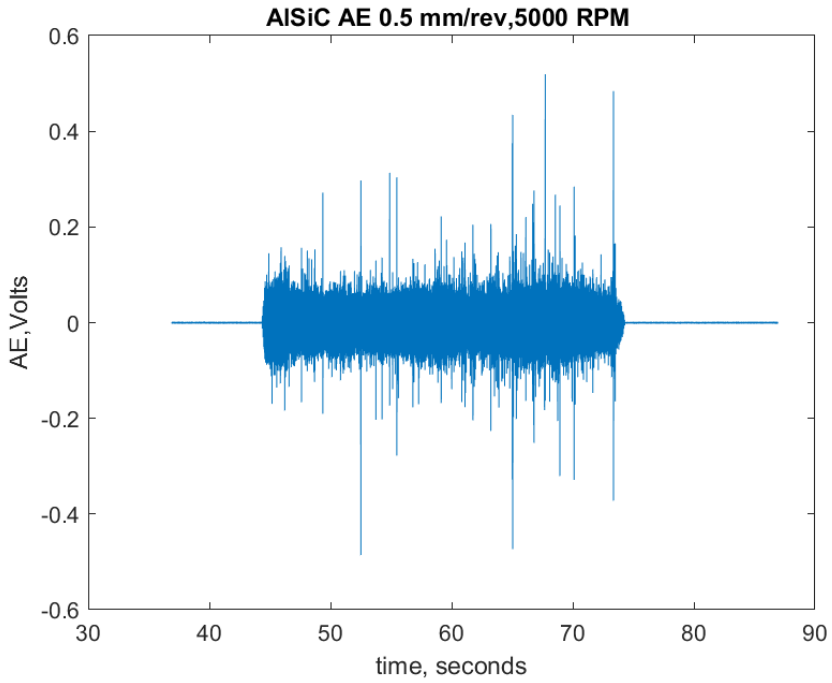
AlSiC AE 0.5 mm/rev,5000 RPM
AE,Volts
time, seconds
0.6
0.4
0.2
0
-0.2
-0.4
-0.6
30
40
50
60
70
80
90
0.9em

B.1.4 RMS of AE signals from cast Al

Feed	Speed	Volt(rms)
0.1	1000	0.0012
0.1	2000	0.0316
0.1	3000	0.0628
0.1	4000	0.0932
0.1	5000	0.148
0.2	1000	0.0419
0.2	2000	0.0598
0.2	3000	0.0976
0.2	4000	0.099
0.2	5000	0.1432
0.3	1000	0.0374
0.3	2000	0.0684
0.3	3000	0.1232
0.3	4000	0.0872
0.3	5000	0.1541
0.4	1000	0.0548
0.4	2000	0.0438
0.4	3000	0.1228
0.4	4000	0.1268
0.4	5000	0.143
0.5	1000	0.0539
0.5	2000	0.0896
0.5	3000	0.1066
0.5	4000	0.1244
0.5	5000	0.177

B.1.5 Tool wear

0.1 mm/rev, 1000 RPM

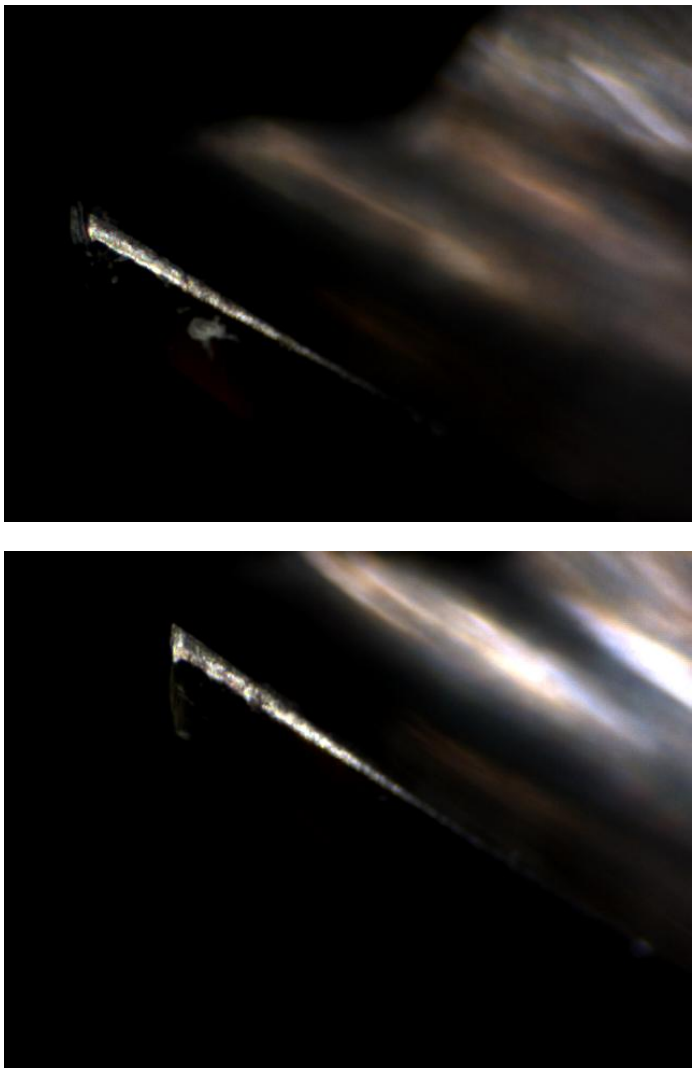

0.1 mm/rev, 2000 RPM

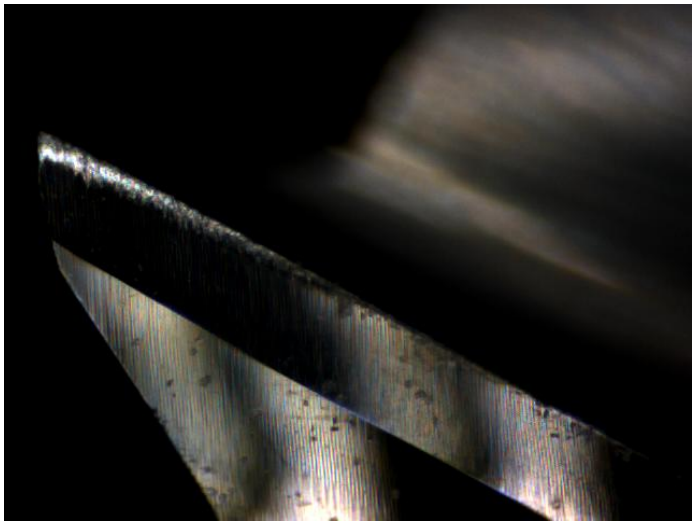



0.1 mm/rev, 3000 RPM



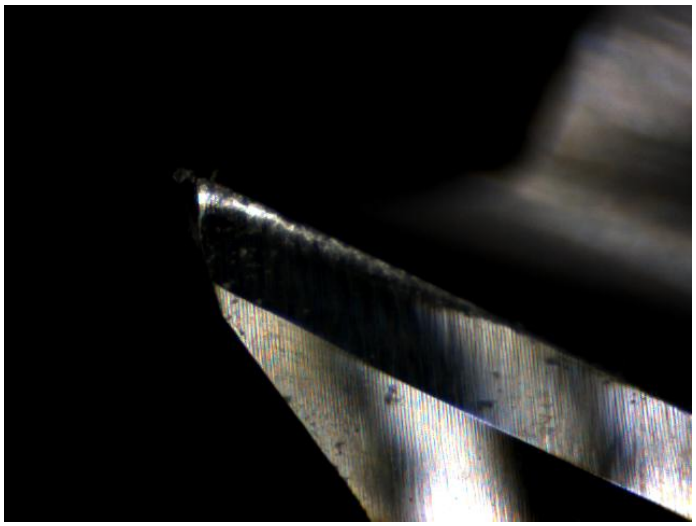

0.1 mm/rev, 4000 RPM

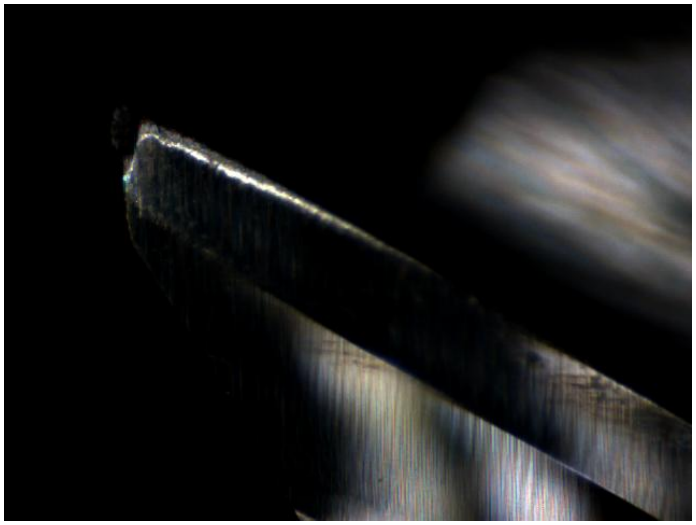

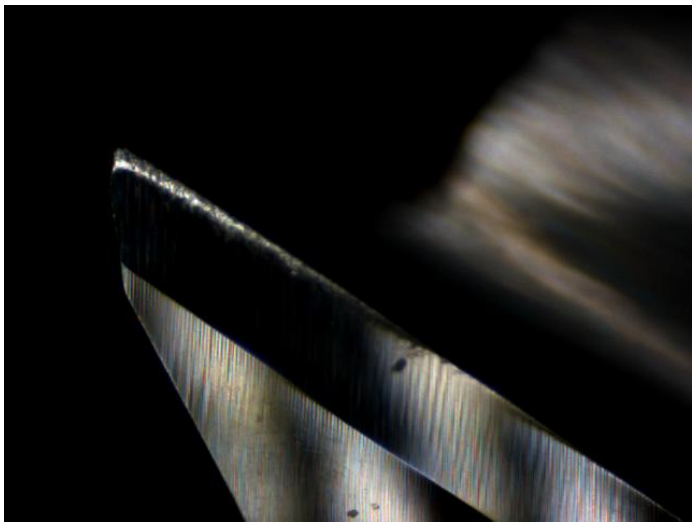

0.1 mm/rev, 5000 RPM

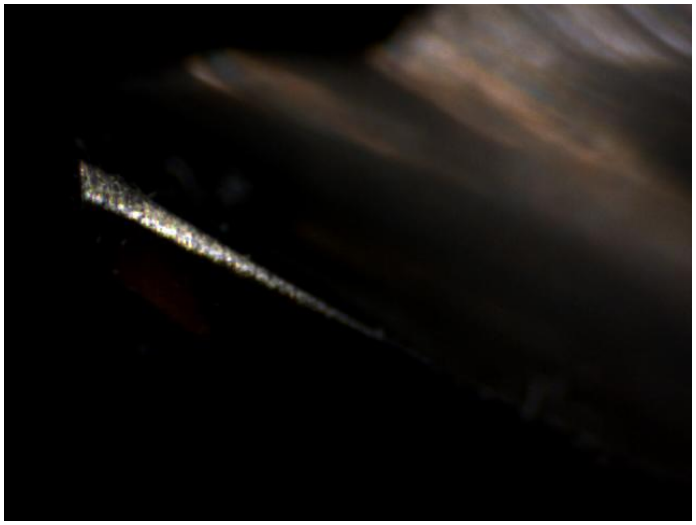

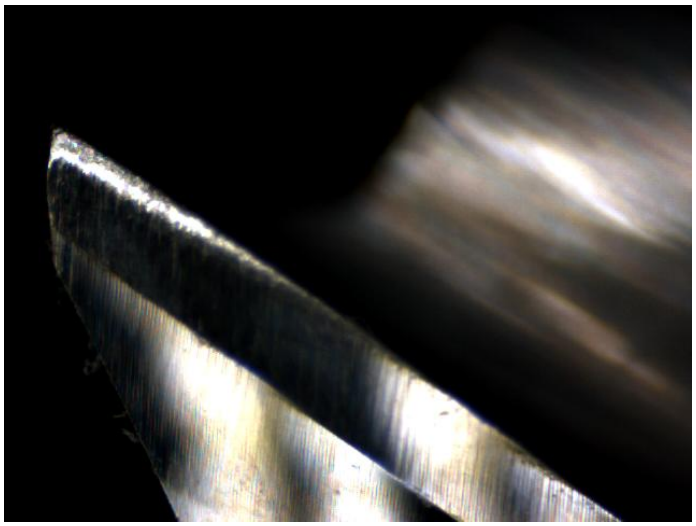

0.2 mm/rev, 1000 RPM



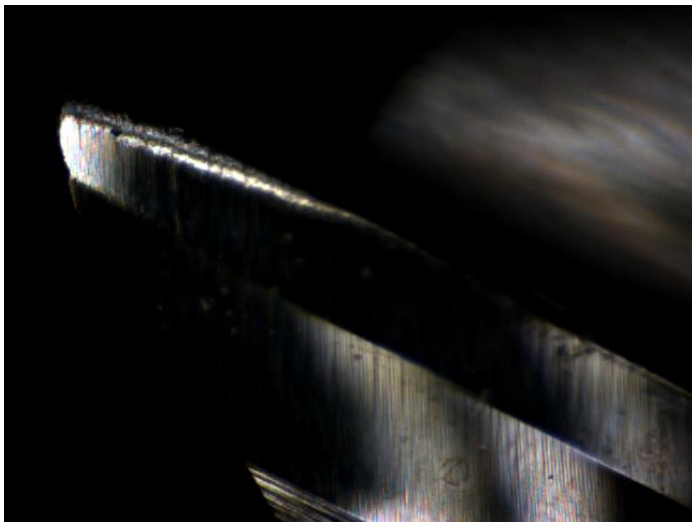

0.2 mm/rev, 2000 RPM

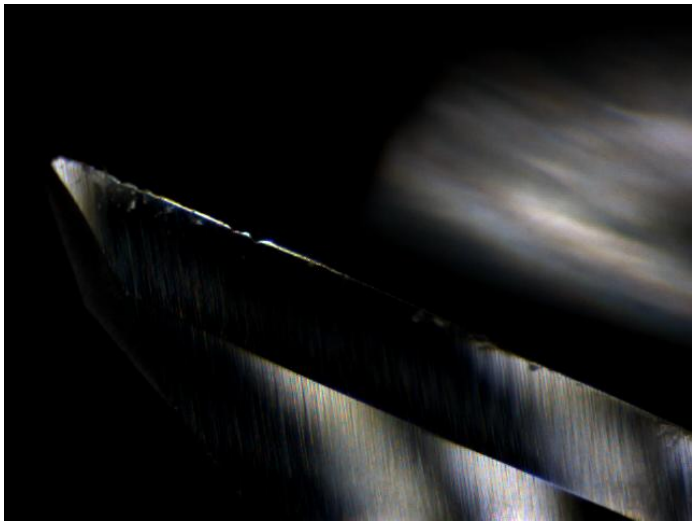



0.2 mm/rev, 3000 RPM

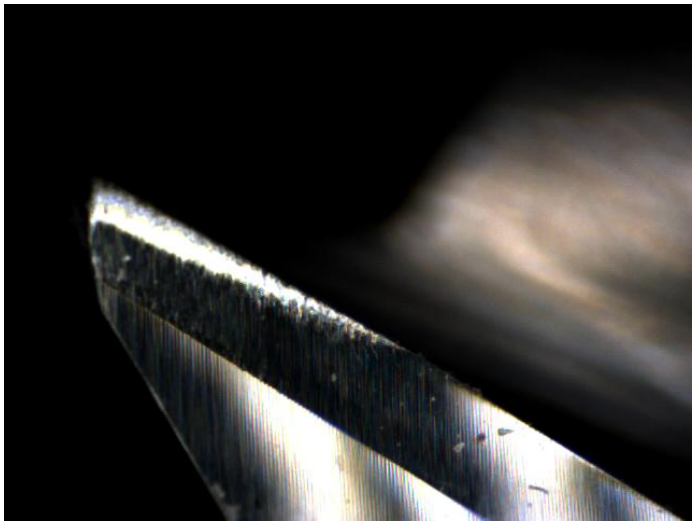

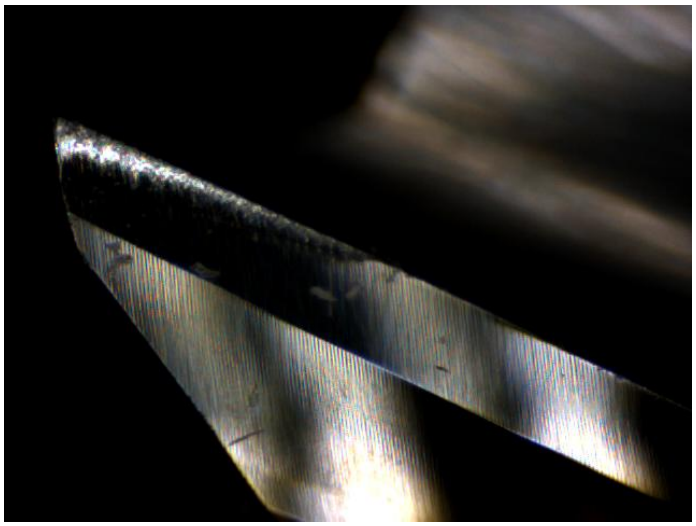

0.2 mm/rev, 4000 RPM

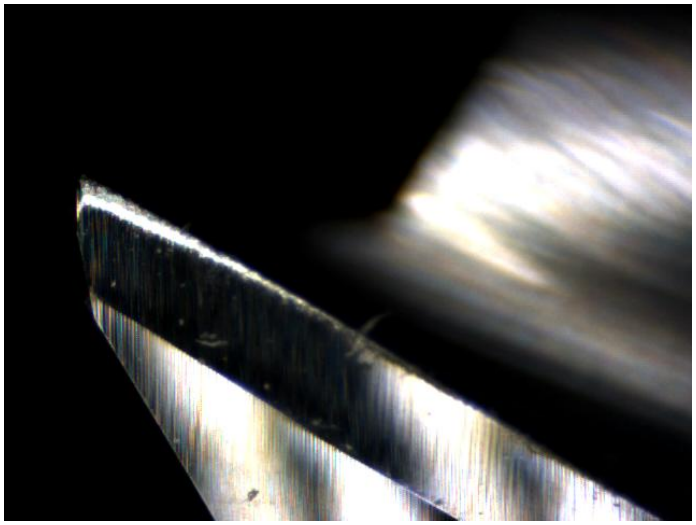

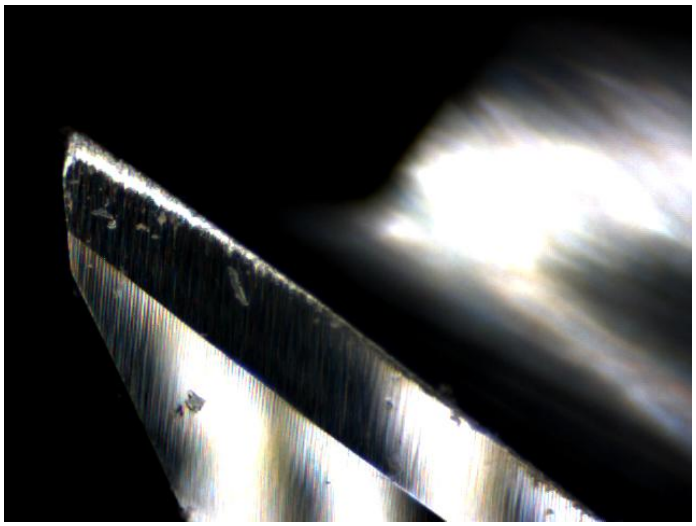

0.2 mm/rev, 5000 RPM

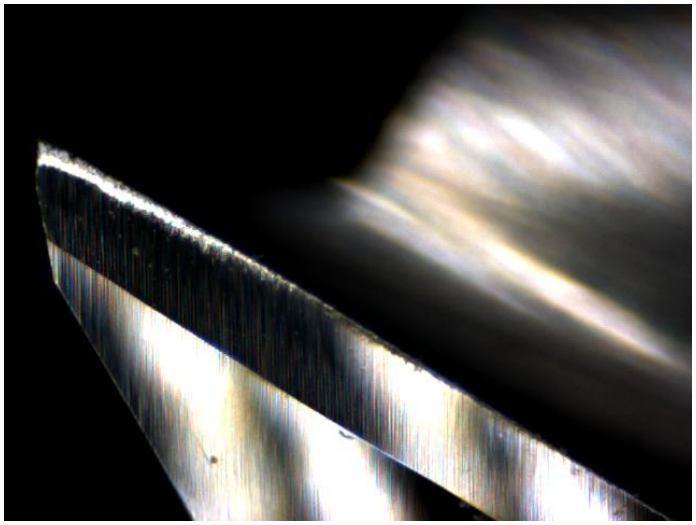

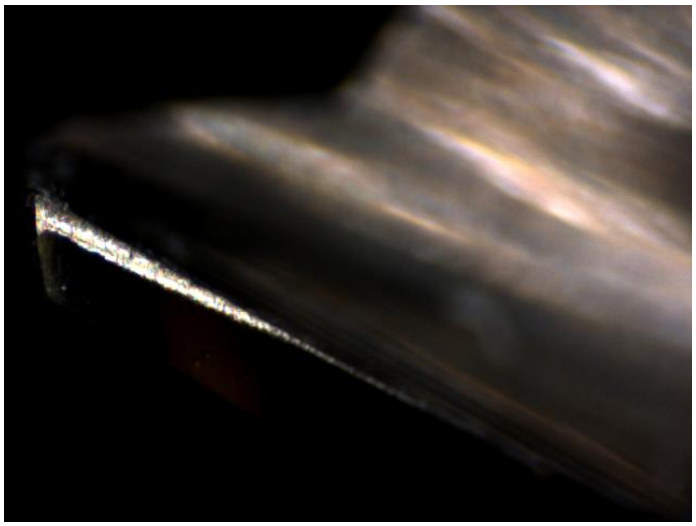

0.3 mm/rev, 1000 RPM



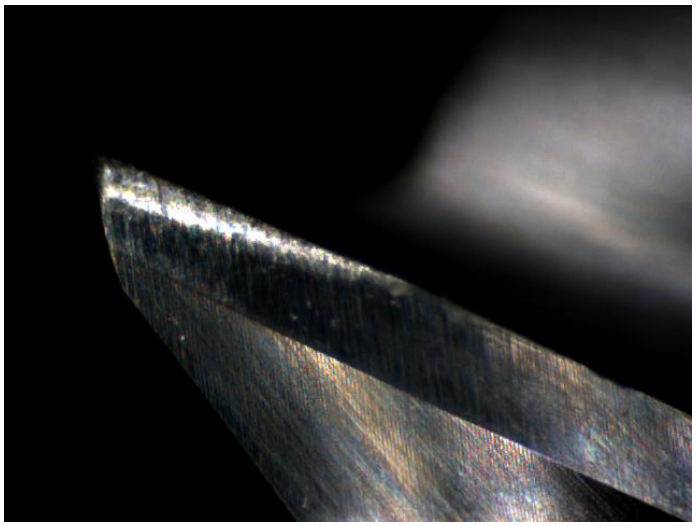

0.3 mm/rev, 2000 RPM

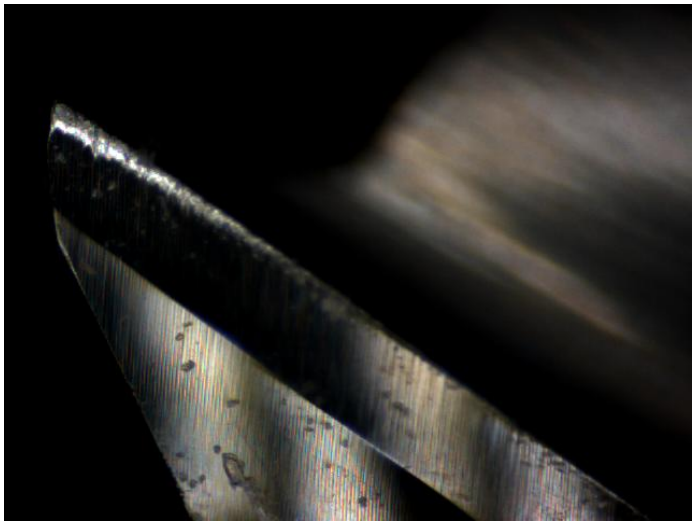

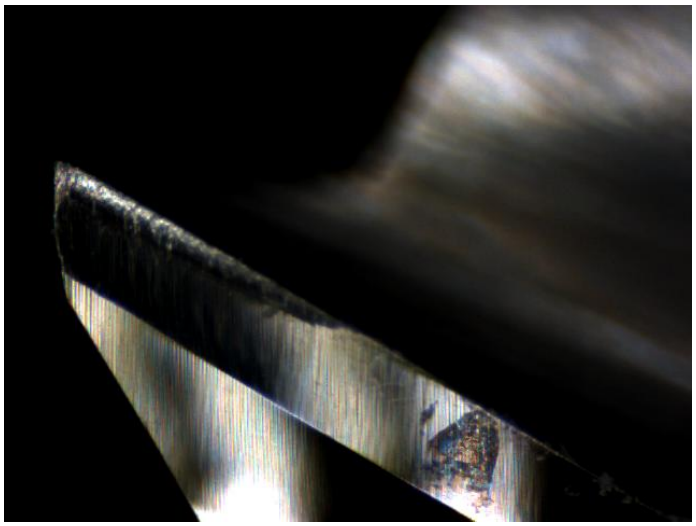

0.3 mm/rev, 3000 RPM

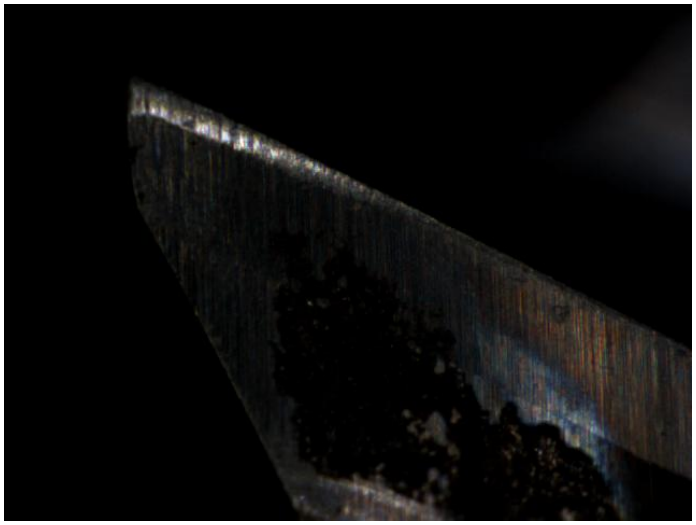

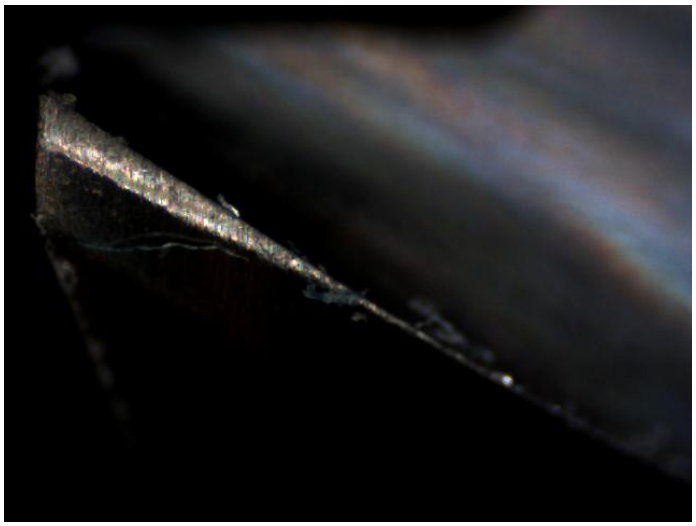

0.3 mm/rev, 4000 RPM

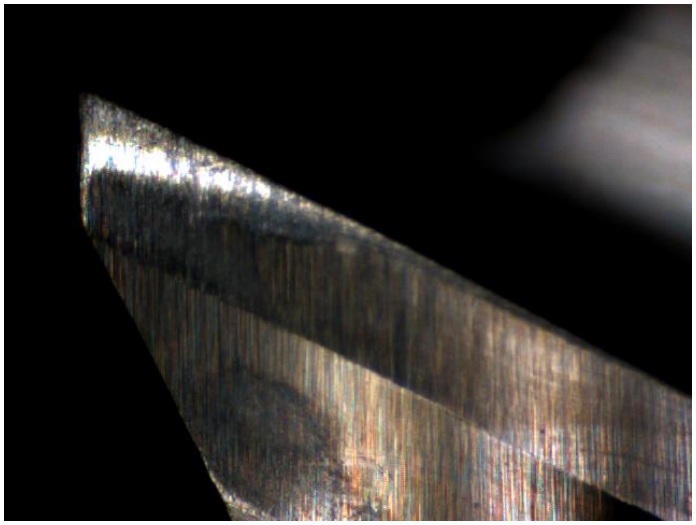



0.3 mm/rev, 5000 RPM

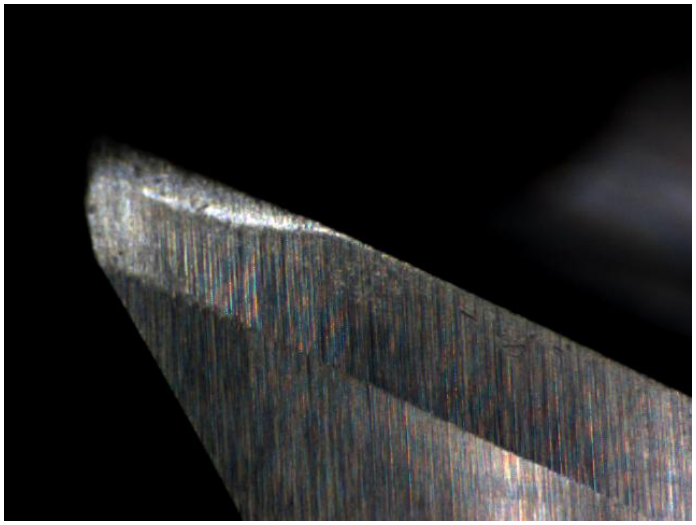

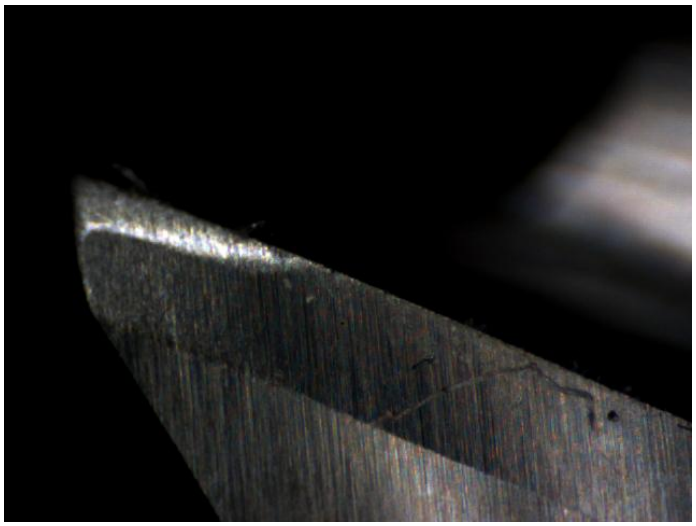

0.4 mm/rev, 1000 RPM



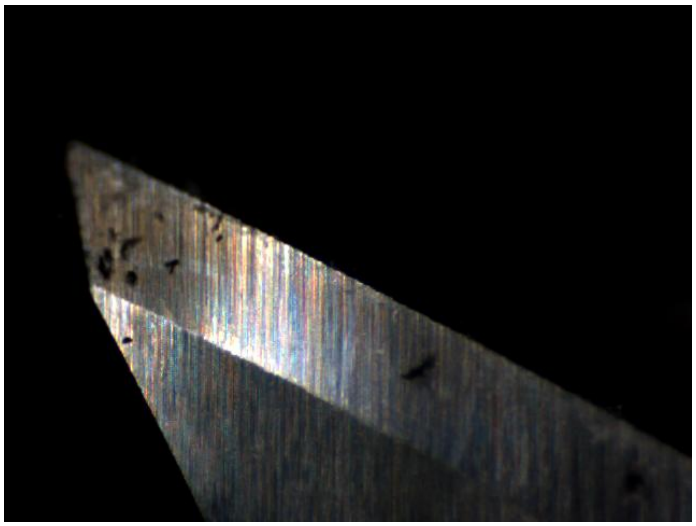

0.4 mm/rev, 2000 RPM

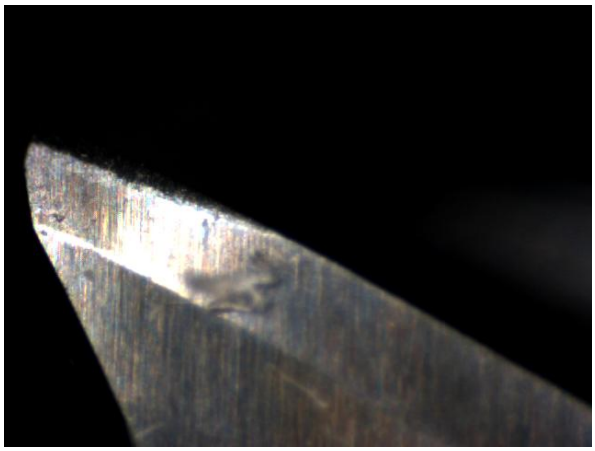
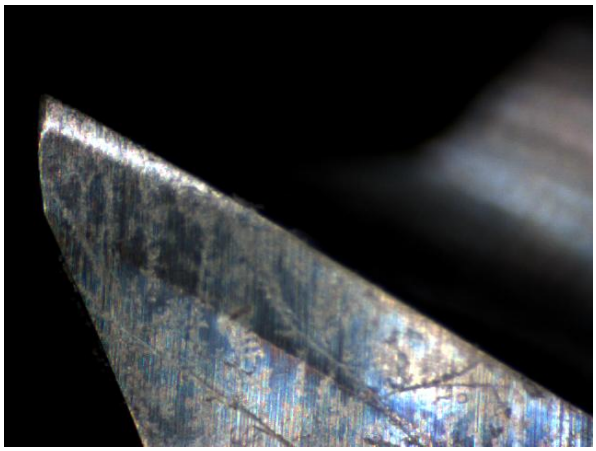
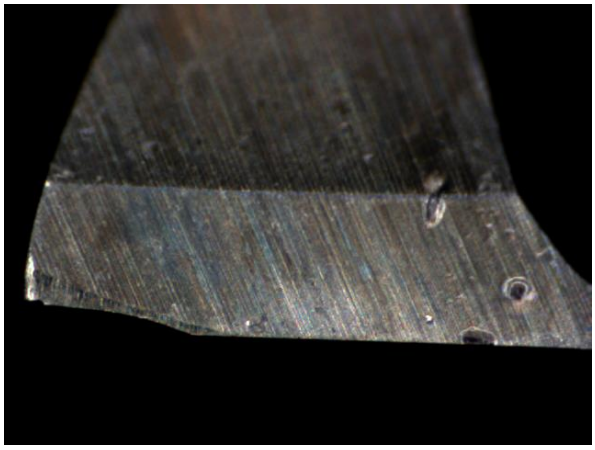
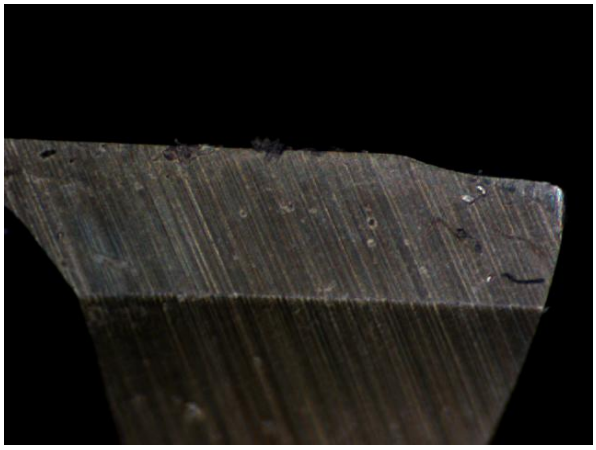

0.4 mm/rev, 3000 RPM

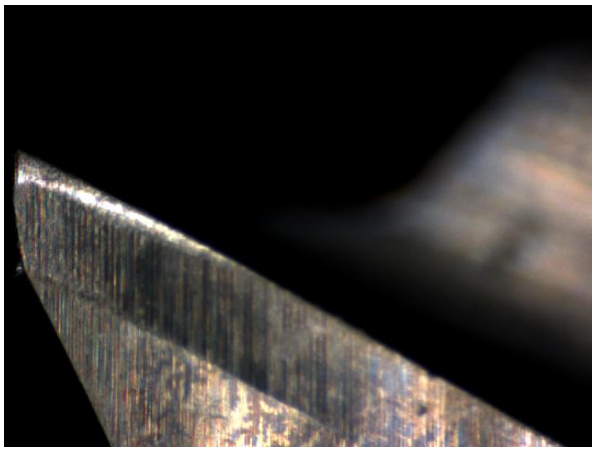
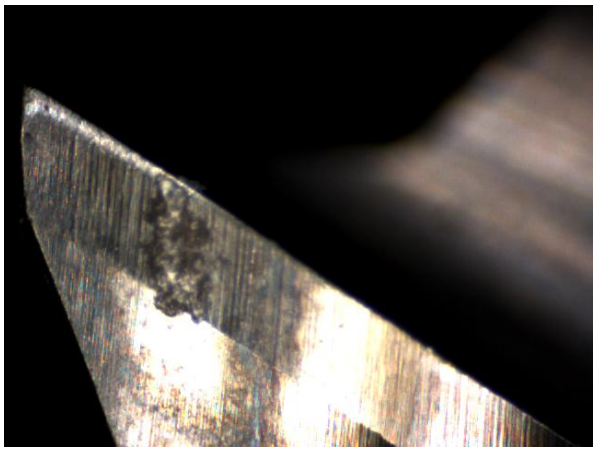
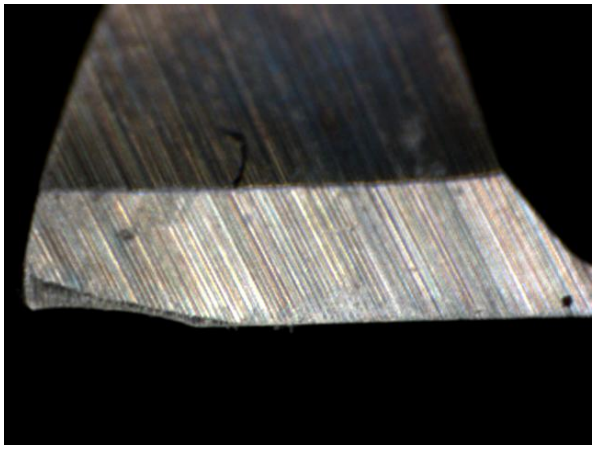
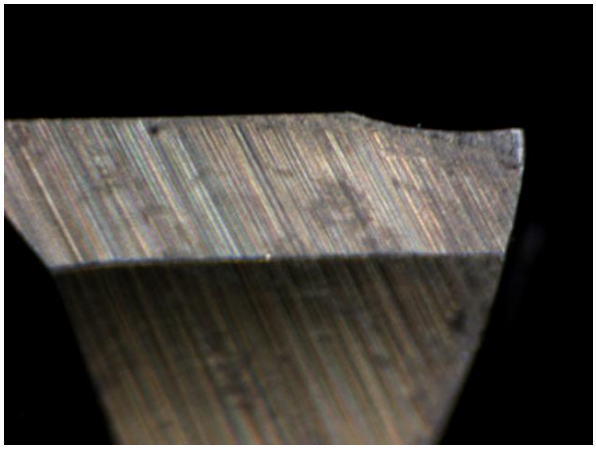

0.4 mm/rev, 4000 RPM

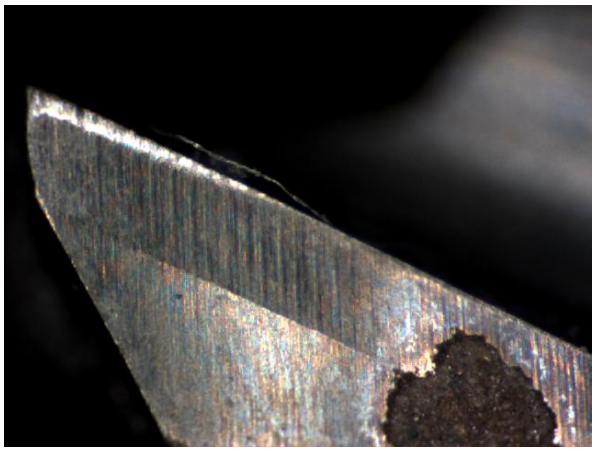

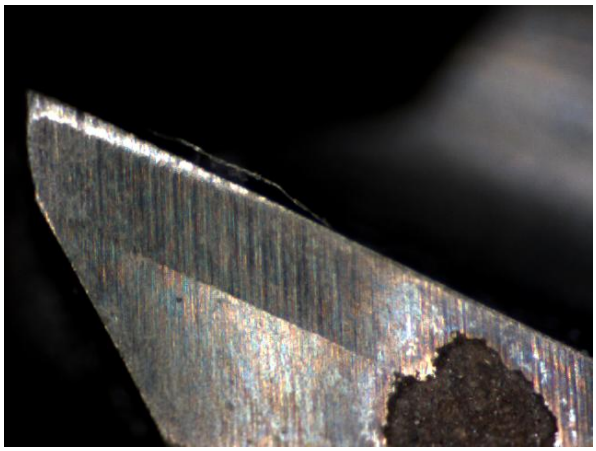

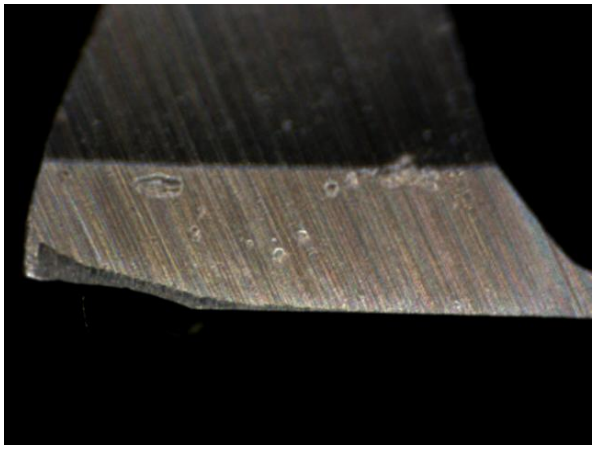

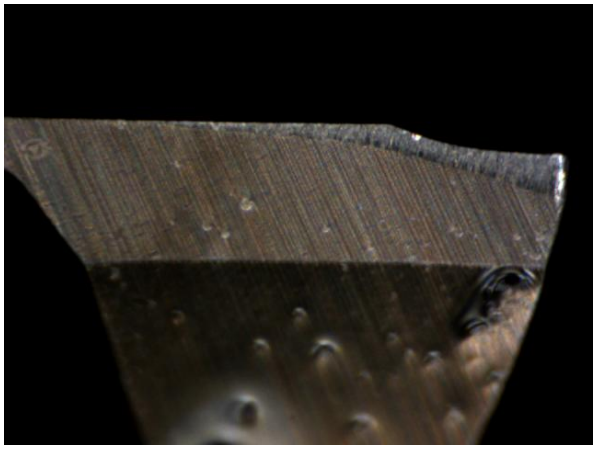

0.4 mm/rev, 5000 RPM


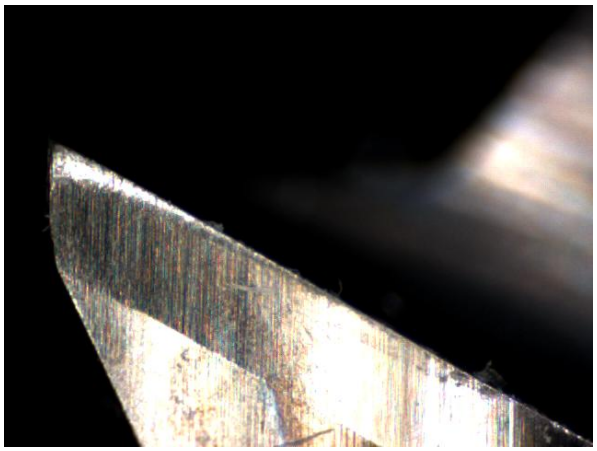
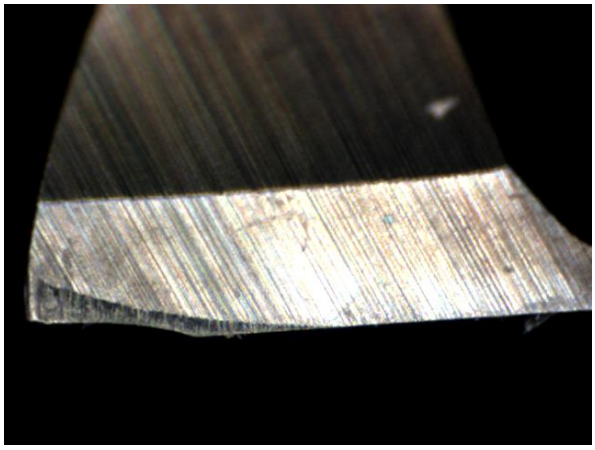
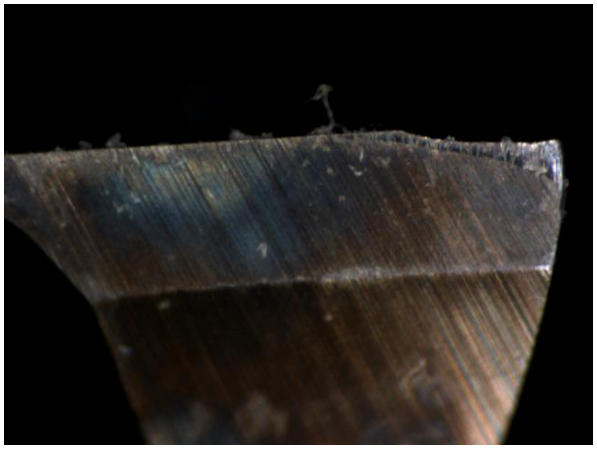

0.5 mm/rev, 1000 RPM


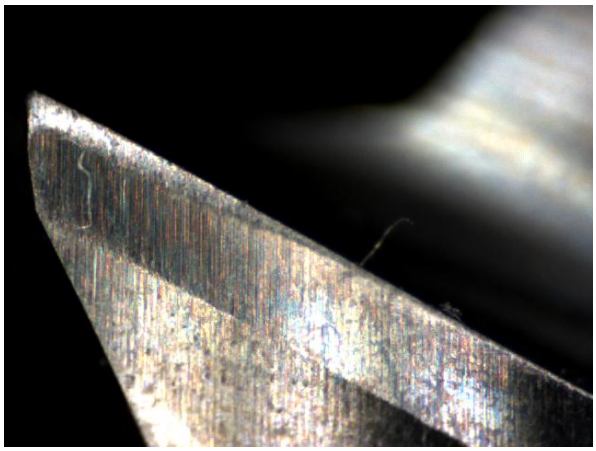
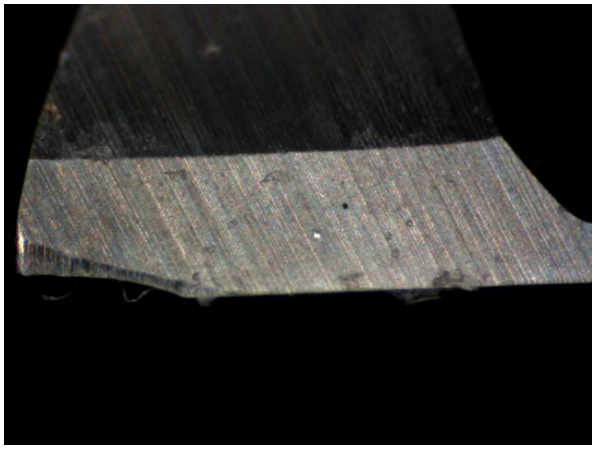
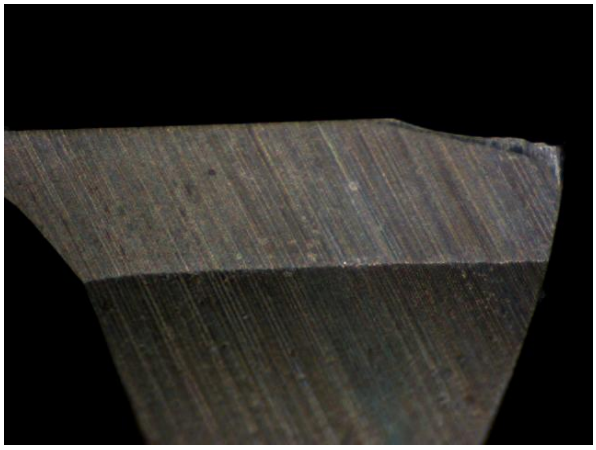

0.5 mm/rev, 2000 RPM

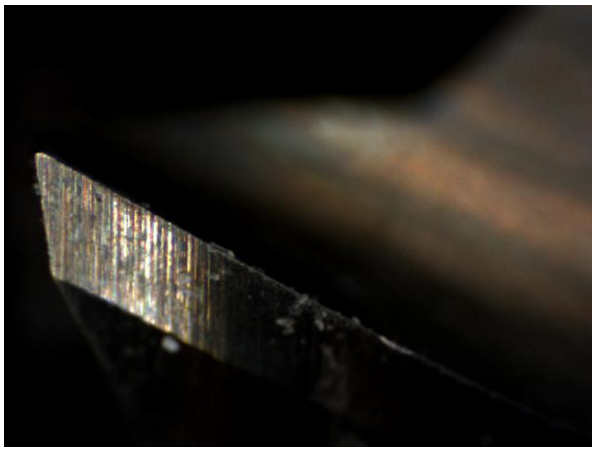
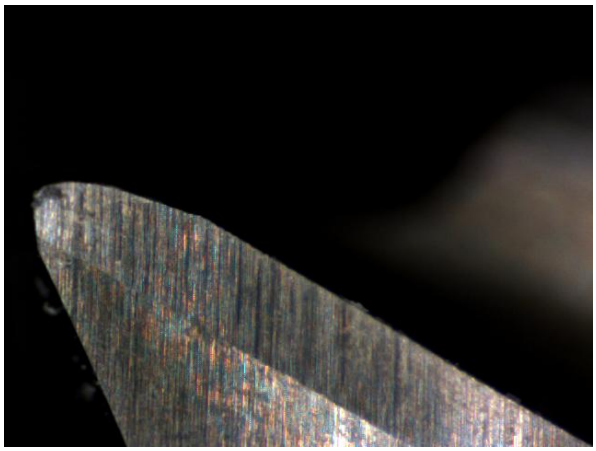
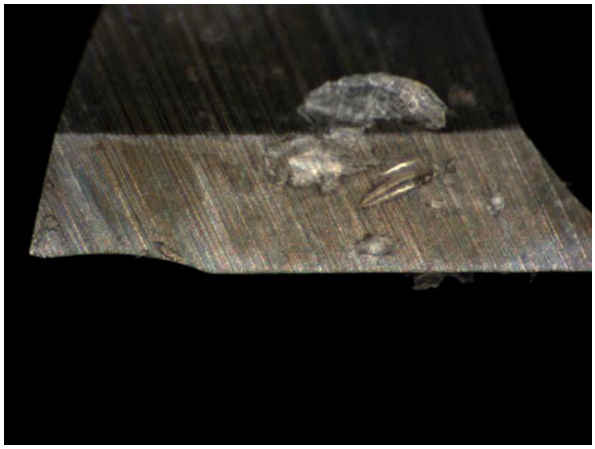
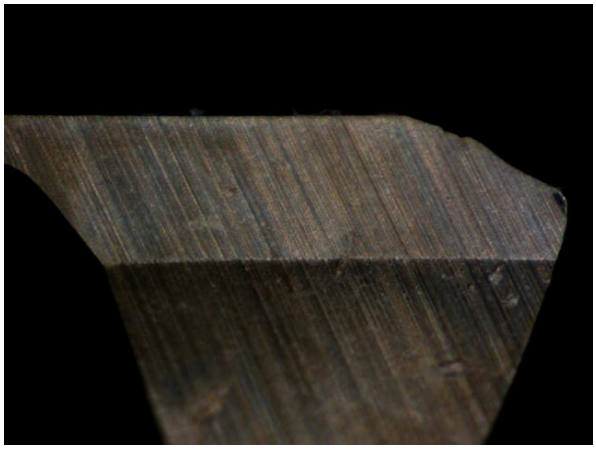

0.5 mm/rev, 3000 RPM

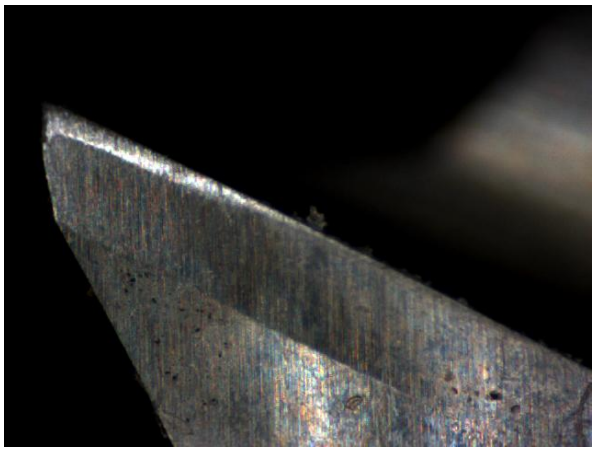

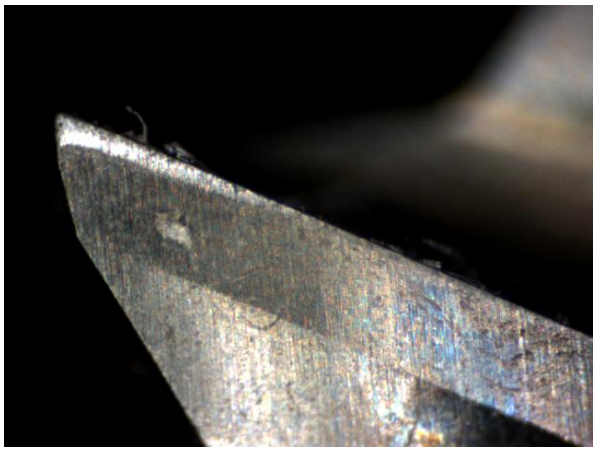

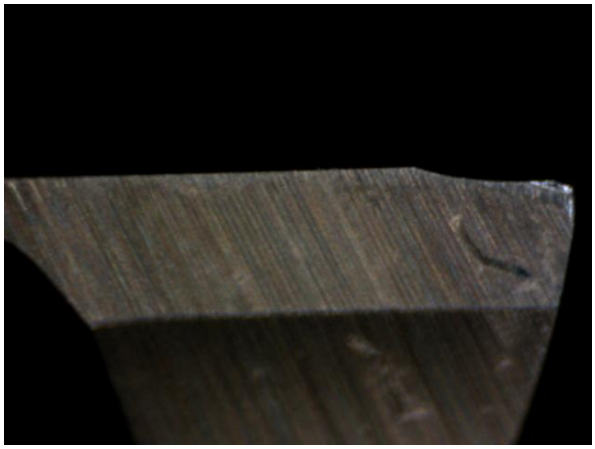

0.5 mm/rev, 4000 RPM



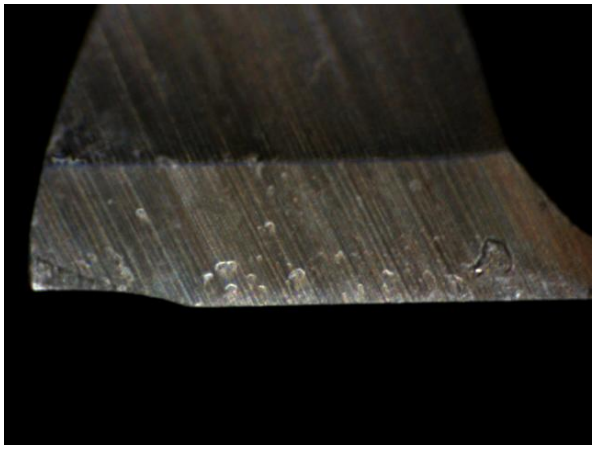
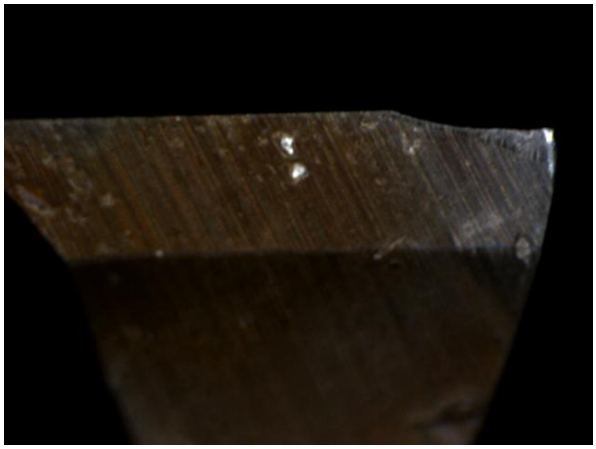

0.5 mm/rev, 5000 RPM

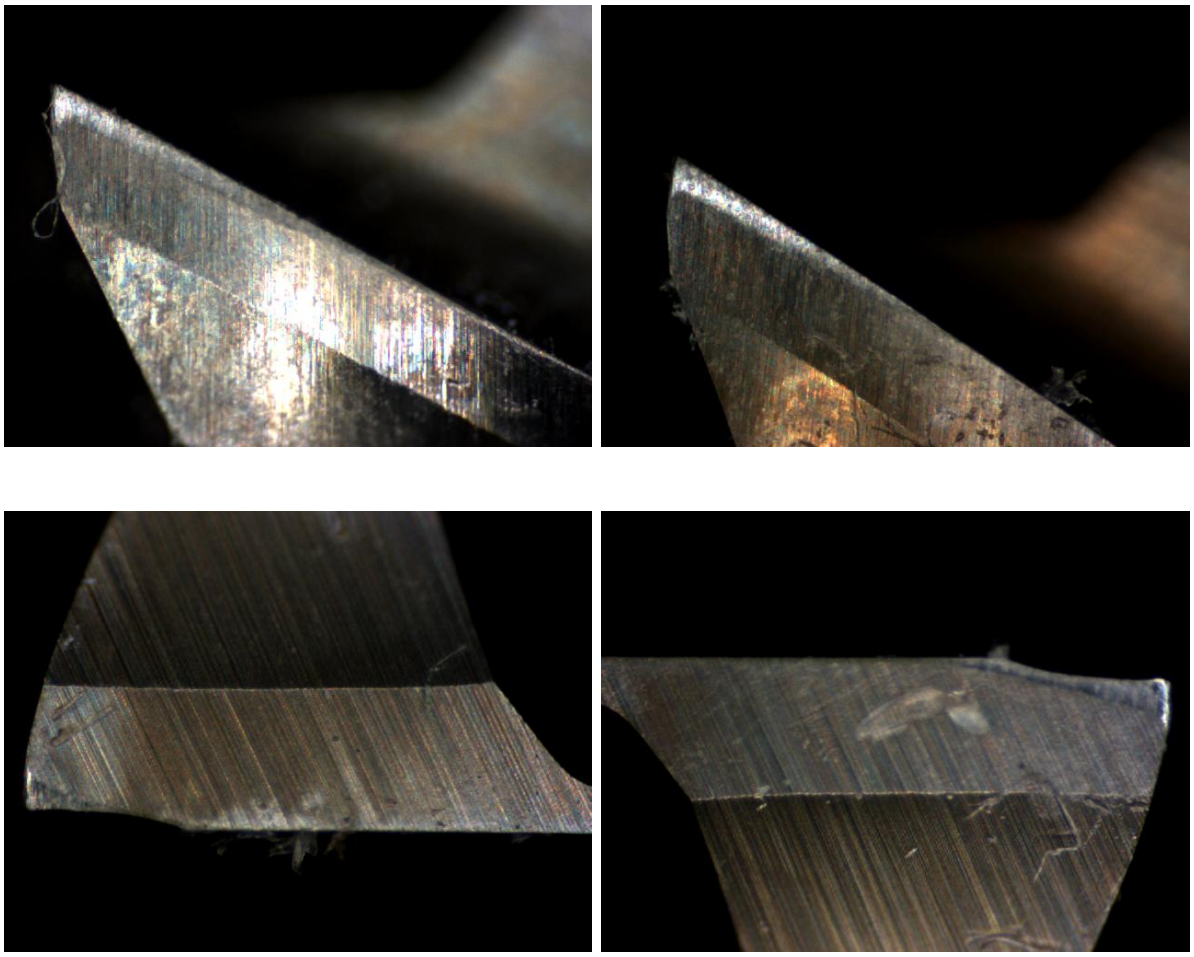

B.1.6 Tool wear measurement MATLAB code

```
close all
clear all
clc
I=imread('tool23_side_right.jpg');
I1=rgb2gray(I);
I2=im2bw(I1,0.6);
I3=imfill(I2,'holes');
imshow(I);
% 0.1 mm = 30 pixels
figure
imshow(I3)
%stats=regionprops(I3,'area','perimeter','BoundingBox');
hold on
[B,L,N] = bwboundaries(I3,'noholes');
for k = 1:(length(B))
   boundary = B{k};

   plot(boundary(:,2), boundary(:,1), 'r', 'LineWidth', 2)
end
o=B{1,1};
% wear area we are interested in
% m=(o(100,2)-o(1,2))/(o(100,1)-o(1,1));
% m1=1/m; % slope of the perpendicular line


    [xlow,L1]=min(o(:,1));
    ymax=max(o(:,2));

    for i=1:1:size(o)
        if o(i,1)==xlow
```

```
            e=i;
        end
        if(o(i,2)==ymax)
            e1=i;
        end
    end
    red = o(e:e1,:);
    blue = [o(1:e-1,:);o(e1+1:end,:)];
    % Find linear fit of the profile
    figure();
    plot(o(e:e1,1),o(e:e1,2), 'r', 'LineWidth', 2)
   hold on
    P = polyfit(o(e:e1,1),o(e:e1,2),1);
    yfit = P(1)*o(e:e1,1)+P(2);
    %hold on;
%   plot(o(e:e1),yfit,'k-.')

   % figure();
    plot(blue(:,1),blue(:,2),'b');%plot(o(:,1),o(:,2),'b')
    hold on
     plot(o(e:e1),yfit,'k-.')
     hold on
    plot(red(:,1),red(:,2),'r')%plot(o(e:e1,1),o(e:e1,2),'r')
    hold on
    % Finding a perpendicular line
    x1=xlow+35; % 35 units from low point
    for j=e:1:e1
      if o(j,1)>x1
          l1=j;
          break
      end
    end
    % required line
```

```
    c=o(l1,2)-(-1/P(1))*o(l1,1);
    y_new=(-1/(P(1)))*o(e:e1,1)+c;
    plot(o(e:e1,1),y_new,'k')
    p1=1;
    black = [o(e:e1,1) y_new(:)];
    %[c,ia]=min(abs((y_new(:,1)-o(e:e1,2))));
    min=1e6;
    %C=intersect(y_new,o(:,2))
    for p1=1:size(black,1)
        for p2=1:size(blue,1)
            if min>norm(black(p1,:)-blue(p2,:))
                min=norm(black(p1,:)-blue(p2,:));
                l2=p1;
                l3=p2;
            end
        end
    end
    min=1e6;
     for p1=1:size(black,1)
        for p2=1:size(red,1)
            if min>norm(black(p1,:)-red(p2,:))
                min=norm(black(p1,:)-red(p2,:));
                l4=p1;
                l5=p2;
            end
        end
    end
    l2;
    l3;
    blue(l3,:)
    %Distance between the intercepts
wear=sqrt((o(l1,2)-blue(l3,2))^2+((o(l1,1)-blue(l3,1))^2));
wear_1=(wear*0.1/30)*1000 % 35 units
```

```
 % finding fit on the side
  P1 = polyfit(blue(:,1),blue(:,2),1);
    yfit1 = P1(1)*blue(:,1)+P1(2);
    plot(blue(:,1),yfit1,'g-.')

    % intercept between two lines
line1=[o((e:e1),1) yfit];
line2=[o((e:e1),1) y_new];
line3=[blue(:,1) yfit1];
min=1e6;
% intersection

for p1=1:size(yfit,1)
        for p2=1:size(y_new,1)
            if min>norm(line1(p1,:)-line2(p2,:))
                min=norm(line1(p1,:)-line2(p2,:));
                l6=p1; % intersection of black
                l7=p2; % intersection of line2
            end
        end
        %l7=p2;
end
  min=1e6;
for p1=1:size(yfit1)
        for p2=1:size(y_new)
            if min>norm(line3(p1,:)-line2(p2,:))
                min=norm(line3(p1,:)-line2(p2,:));
                l8=p1;
                l9=p2;
            end
        end
end
```

```
 wear1=sqrt((line2(l9,2)-line2(l7,2))^2+((line2(l9,1)-line2(l7,1))^2));
 wear_2=(wear1*0.1/30)*1000


% Finding a perpendicular line
    x1=xlow+40;
    for j=e:1:e1
      if o(j,1)>x1
          l1=j;
          break
      end
    end
    % required line
    c=o(l1,2)-(-1/P(1))*o(l1,1);
    y_new=(-1/(P(1)))*o(e:e1,1)+c;
    plot(o(e:e1,1),y_new,'k')
    p1=1;
    black = [o(e:e1,1) y_new(:)];
    %[c,ia]=min(abs((y_new(:,1)-o(e:e1,2))));
    min=1e6;
    %C=intersect(y_new,o(:,2))
    for p1=1:size(black,1)
        for p2=1:size(blue,1)
            if min>norm(black(p1,:)-blue(p2,:))
                min=norm(black(p1,:)-blue(p2,:));
                l2=p1;
                l3=p2;
            end
        end
    end
    min=1e6;
     for p1=1:size(black,1)
```

```
        for p2=1:size(red,1)
            if min>norm(black(p1,:)-red(p2,:))
                min=norm(black(p1,:)-red(p2,:));
                l4=p1;
                l5=p2;
            end
        end
    end
    l2;
    l3;
    blue(l3,:)
    %Distance between the intercepts
 wear=sqrt((o(l1,2)-blue(l3,2))^2+((o(l1,1)-blue(l3,1))^2));
 wear_1=(wear*0.1/30)*1000

 % finding fit on the side
  P1 = polyfit(blue(:,1),blue(:,2),1);
    yfit1 = P1(1)*blue(:,1)+P1(2);
    plot(blue(:,1),yfit1,'g-.')

    % intercept between two lines
line1=[o((e:e1),1) yfit];
line2=[o((e:e1),1) y_new];
line3=[blue(:,1) yfit1];
min=1e6;
% intersection

for p1=1:size(yfit,1)
        for p2=1:size(y_new,1)
            if min>norm(line1(p1,:)-line2(p2,:))
                min=norm(line1(p1,:)-line2(p2,:));
                l6=p1; % intersection of black
                l7=p2; % intersection of line2
```

```
            end
        end
        %l7=p2;
end
  min=1e6;
for p1=1:size(yfit1)
        for p2=1:size(y_new)
            if min>norm(line3(p1,:)-line2(p2,:))
                min=norm(line3(p1,:)-line2(p2,:));
                l8=p1;
                l9=p2;
            end
        end
end


 wear2=sqrt((line2(l9,2)-line2(l7,2))^2+((line2(l9,1)-line2(l7,1))^2));
 wear_3=(wear2*0.1/30)*1000 % 40 units
```

```
% Tool Profiler

filenames = {'tool22_top_right.jpg'
 'tool21_top_right.jpg',
'tool25_top_right.jpg',};

% Read raw images
raw = {}; binary_=[];
boundary = {};

for i=1:numel(filenames)
    raw{i} = imread(filenames{i});
end

% unit_test_boundary(raw);

% Align images to the reference image
boundary_={};
fixed = raw{1}(:,:,2);
binary_ = imbinarize(fixed);
[B,L] = bwboundaries(binary_, 'noholes');
boundary_{1} = B{1};

for i=1:numel(raw)
    moving = raw{i}(:,:,2);
    moving_aligned = alignimages(fixed,moving);
    binary_ = imbinarize(moving_aligned);
    [B,L] = bwboundaries(binary_, 'noholes');
    boundary_{i} = B{1};
end

% Plot the boundaries
linspec = {'r','b','g','y','k','m'};
```

```
figure(1); clf;
hold all
% Now smooth with a Savitzky–Golay sliding polynomial filter
for i=1:numel(boundary_)
    v = boundary_{i};
    x = v(:,2);
    y = v(:,1);
    keep = x > 200 & y < 250;
    x = x(keep); y = y(keep);
    plot(movmean(x,5)/300,movmean(y,5)/300, linspec{i}, 'LineWidth', 2);
    xlabel('distance, mm')
    ylabel('distance, mm')
    xlim([1.4 2.1])
    legend('New tool','1000 RPM','5000 RPM')
end
set ( gca, 'ydir', 'reverse' )



function unit_test_boundary(raw)
    fixed = rgb2gray(raw{1});
    moving = rgb2gray(raw{2});

    fixed =  raw{1}(:,:,2);
    moving = raw{2}(:,:,2);

    moving_aligned = alignimages(fixed,moving);

    % misaligned images
    figure(1); clf;
    subplot(1,2,1)
    imshowpair(fixed,moving,'Scaling','joint');
    subplot(1,2,2)
```

```
    imshowpair(fixed,moving_aligned,'Scaling','joint');
    hold all
    binary_{1} = imbinarize(fixed);
    binary_{2} = imbinarize(moving_aligned);
    [B,L] = bwboundaries(binary_{1}, 'noholes');
    boundary = B{1};
    plot(boundary(:,2), boundary(:,1), 'b', 'LineWidth', 2)
    [B,L] = bwboundaries(binary_{2}, 'noholes');
    boundary = B{1};
    plot(boundary(:,2), boundary(:,1), 'r', 'LineWidth', 2)
end

function movingAligned = alignimages(fixed,moving)
    % Get a configuration suitable for registering images from different
    % sensors.
    [optimizer, metric] = imregconfig('multimodal');

    % Tune the properties of the optimizer to get the problem to converge
    % on a global maxima and to allow for more iterations.
    optimizer.InitialRadius = 0.005;
    optimizer.Epsilon = 1.5e-4;
    optimizer.GrowthFactor = 1.05;
    optimizer.MaximumIterations = 100;

    % Align the moving image with the fixed image
    movingAligned = imregister(moving, fixed, 'similarity', optimizer, metric);
end
```

B.2 AZ91/SiCp

B.2.1 Cutting forces

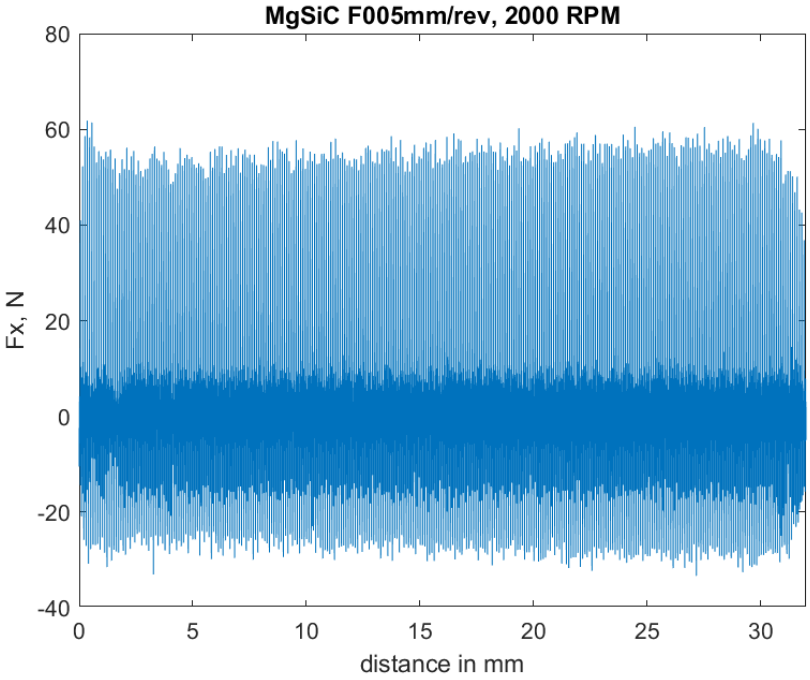

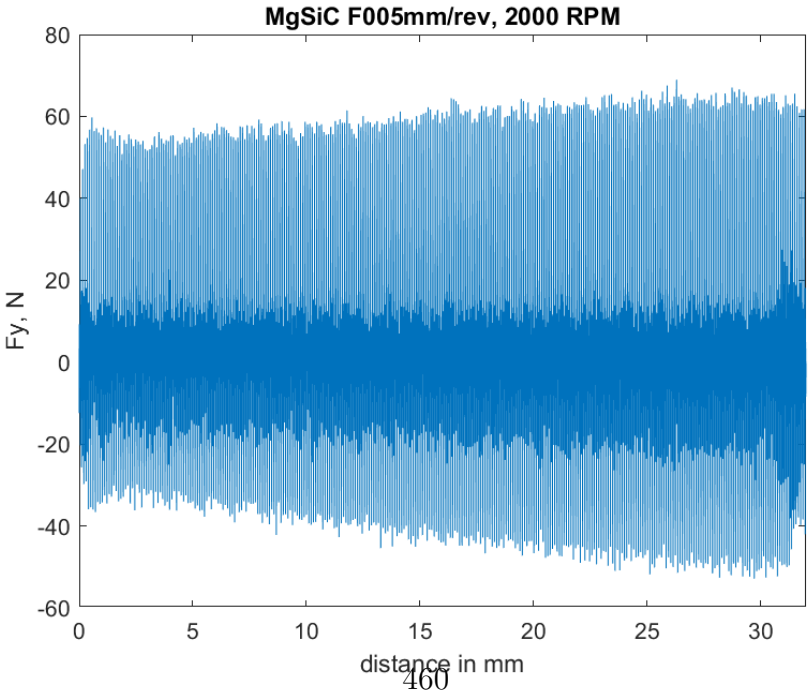

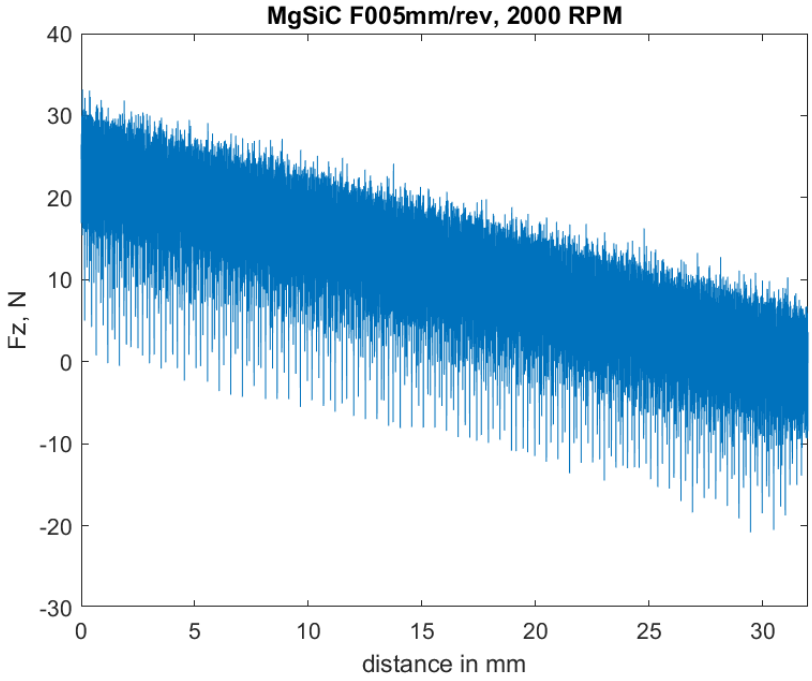
MgSiC F005mm/rev, 2000 RPM
Fz, N
distance in mm
40
30
20
10
0
-10
-20
-30
0
5
10
15
20
25
30

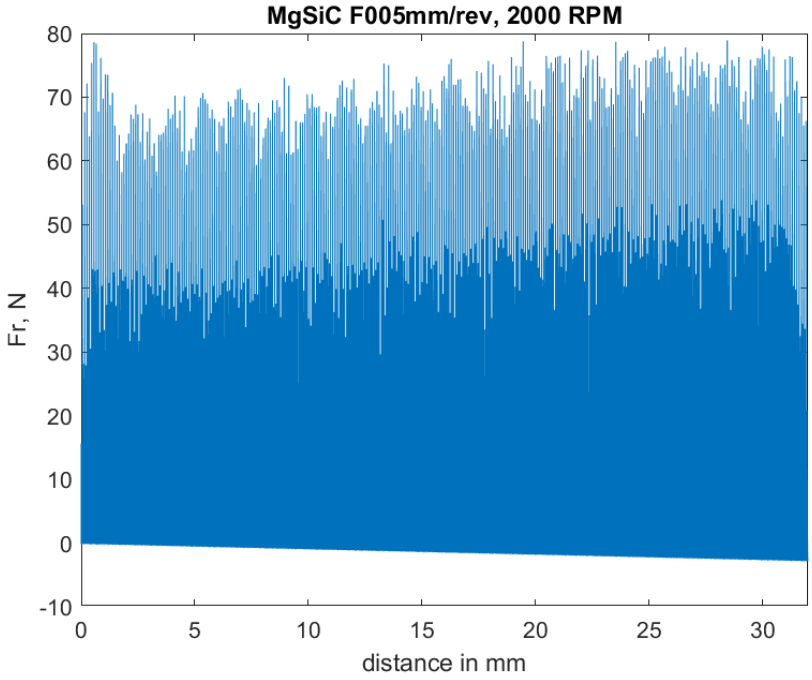
MgSiC F005mm/rev, 2000 RPM
Fr, N
distance in mm
80
70
60
50
40
30
20
10
0
-10
0
5
10
15
20
25
30

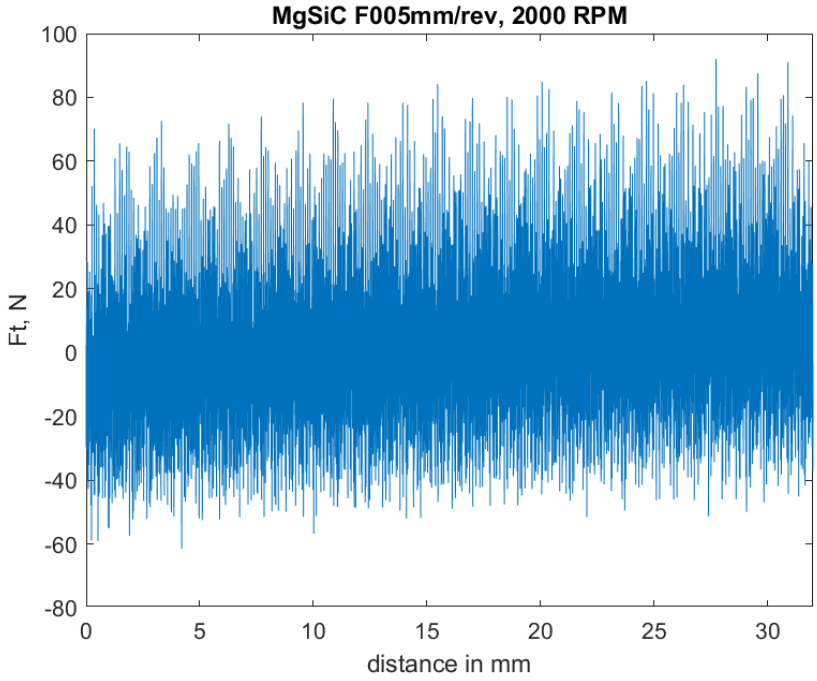
MgSiC F005mm/rev, 2000 RPM
Ft, N
distance in mm
100
80
60
40
20
0
-20
-40
-60
-80
0
5
10
15
20
25
30

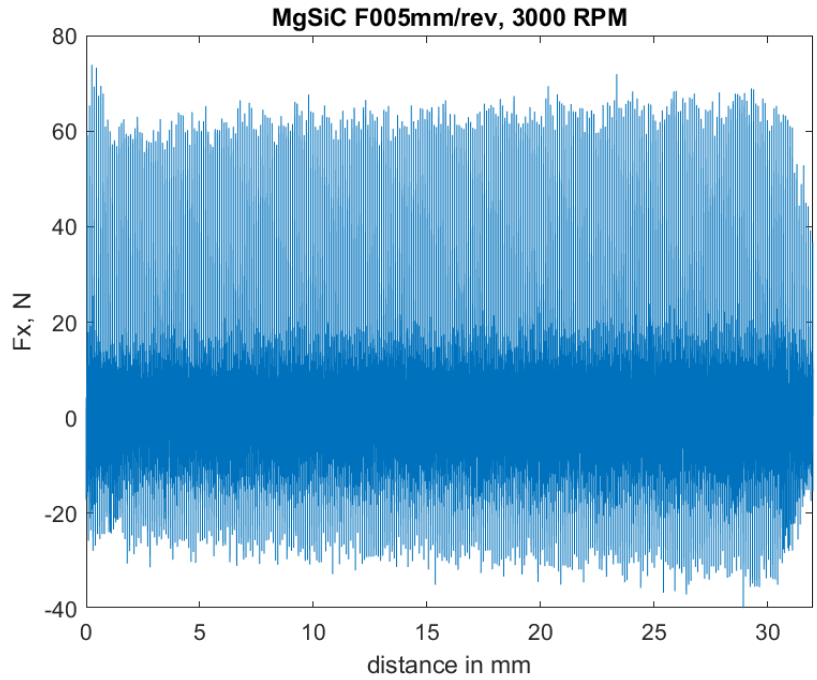
MgSiC F005mm/rev, 3000 RPM
Fx, N
distance in mm
80
60
40
20
0
-20
-40
0
5
10
15
20
25
30

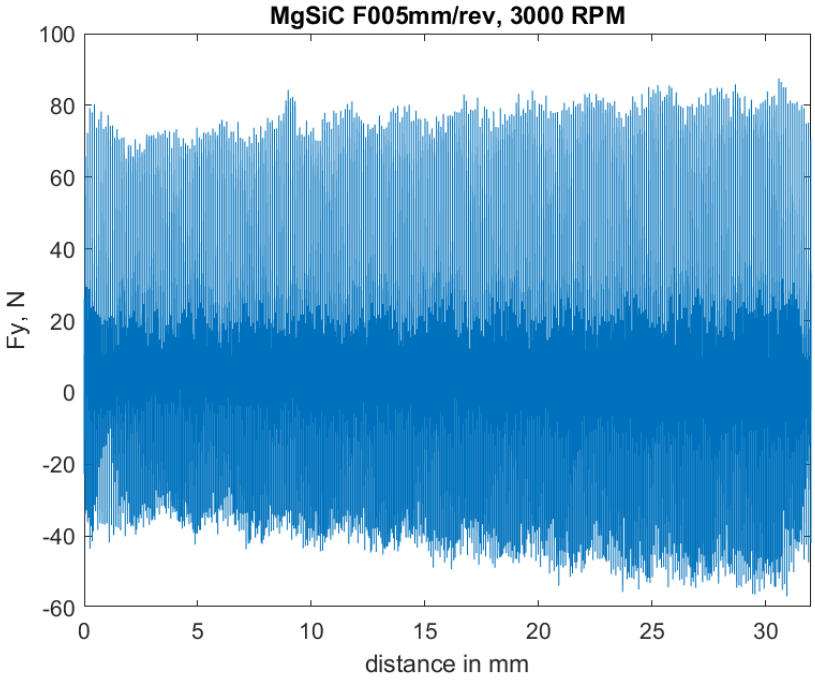
MgSiC F005mm/rev, 3000 RPM
Fy, N
distance in mm
100
80
60
40
20
0
-20
-40
-60
0
5
10
15
20
25
30

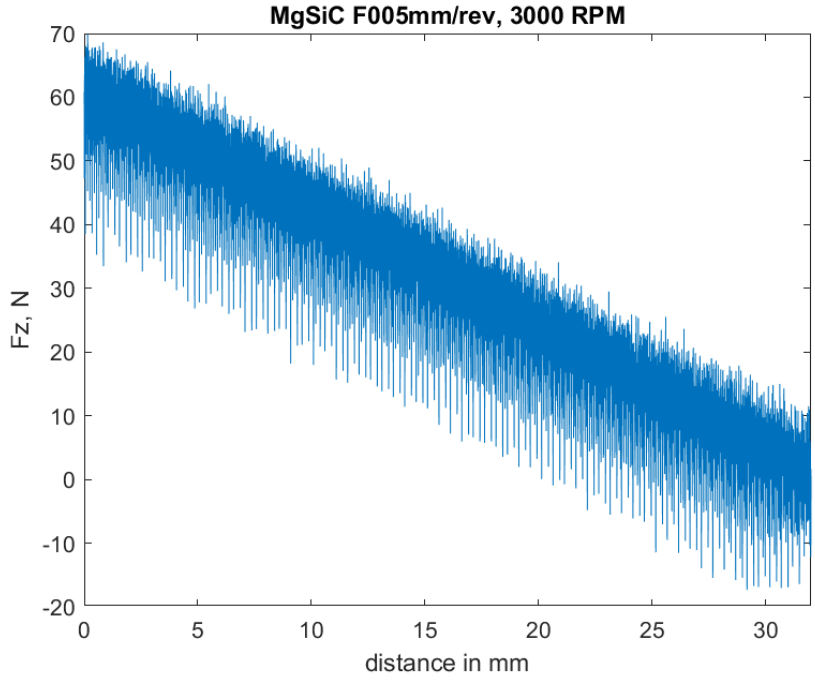
MgSiC F005mm/rev, 3000 RPM
Fz, N
distance in mm
70
60
50
40
30
20
10
0
-10
-20
0
5
10
15
20
25
30

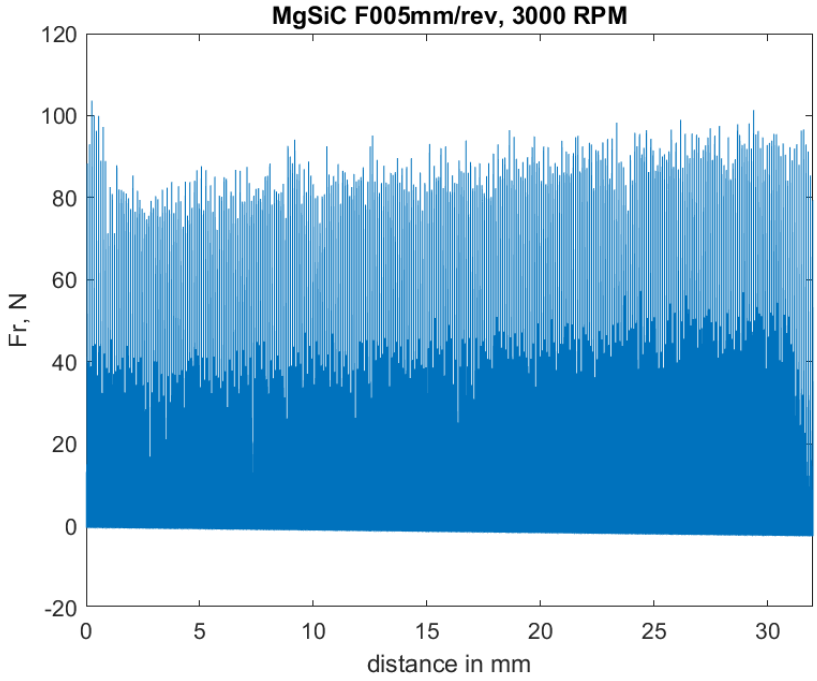
MgSiC F005mm/rev, 3000 RPM
Fr, N
distance in mm
120
100
80
60
40
20
0
-20
0
5
10
15
20
25
30

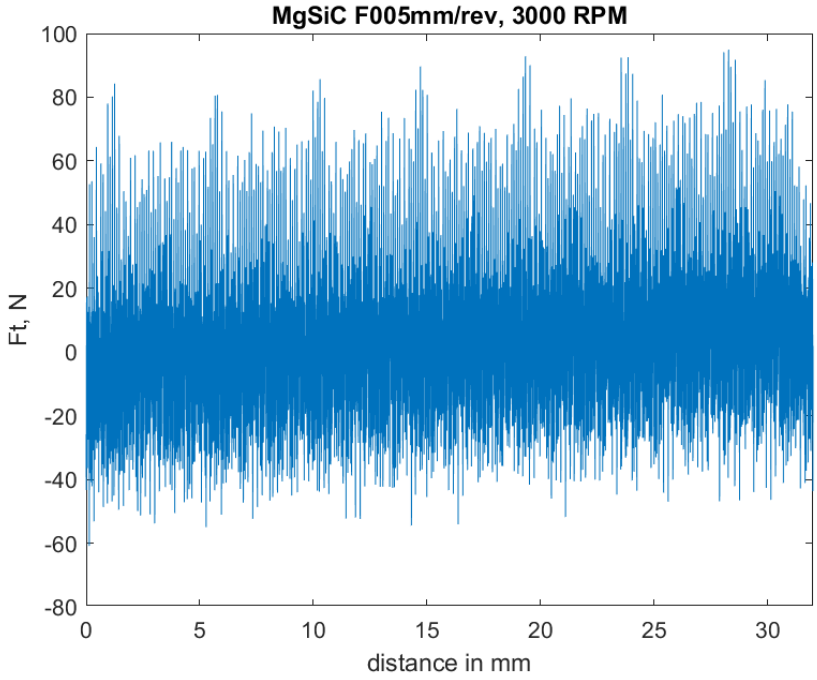
MgSiC F005mm/rev, 3000 RPM
Ft, N
distance in mm
100
80
60
40
20
0
-20
-40
-60
-80
0
5
10
15
20
25
30

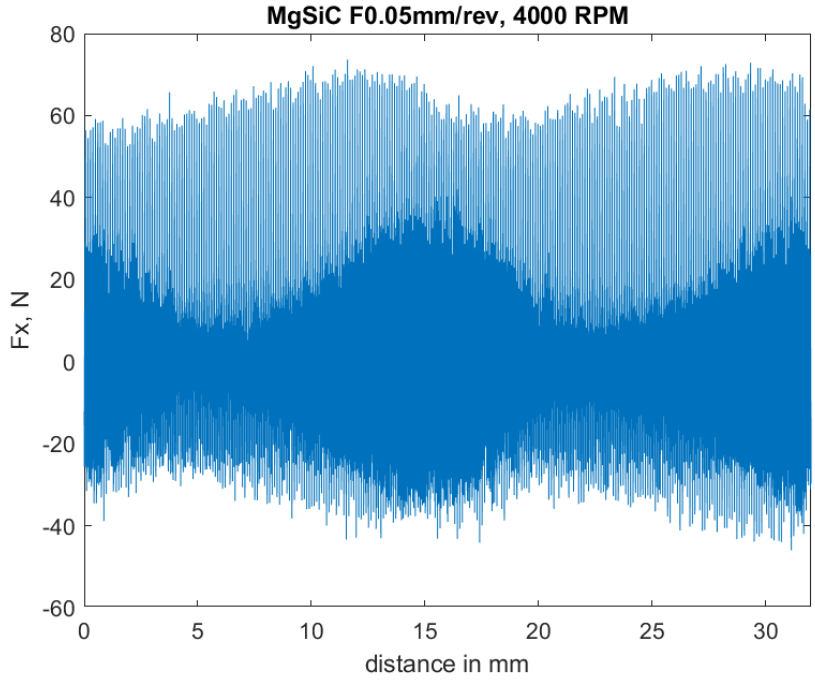
MgSiC F0.05mm/rev, 4000 RPM
Fx, N
distance in mm
80
60
40
20
0
-20
-40
-60
0
5
10
15
20
25
30

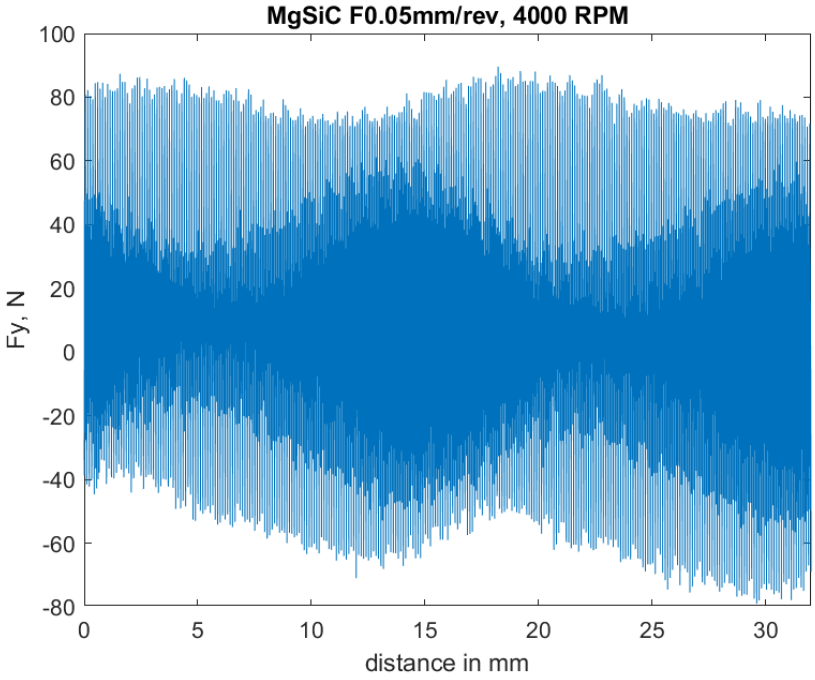
MgSiC F0.05mm/rev, 4000 RPM
Fy, N
distance in mm
100
80
60
40
20
0
-20
-40
-60
-80
0
5
10
15
20
25
30

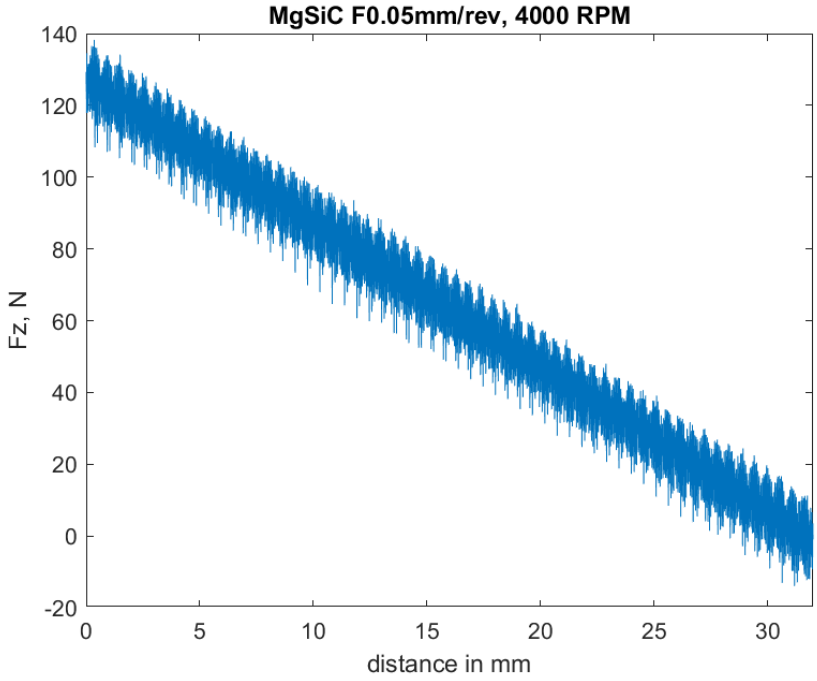
MgSiC F0.05mm/rev, 4000 RPM
Fz, N
distance in mm
140
120
100
80
60
40
20
0
-20
0
5
10
15
20
25
30

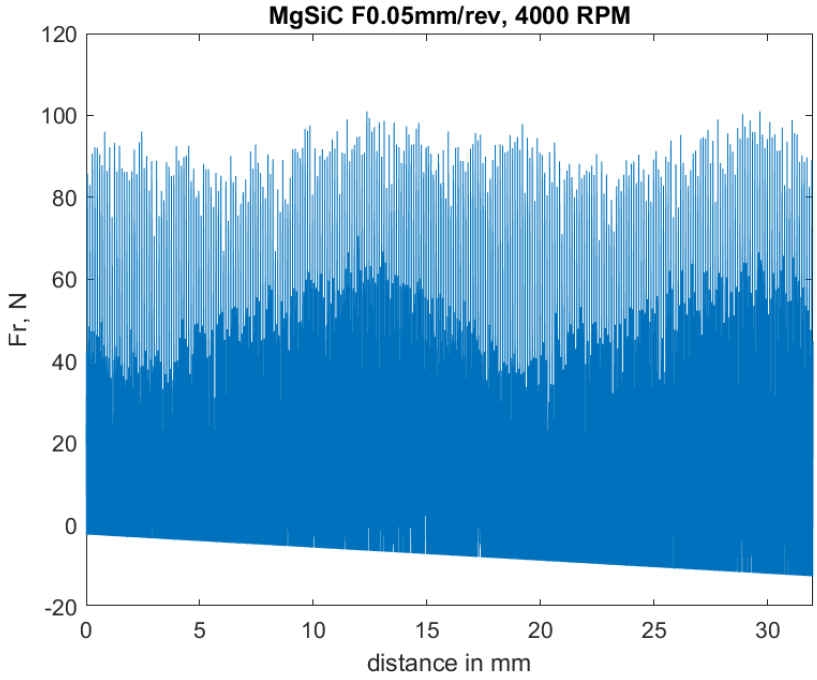
MgSiC F0.05mm/rev, 4000 RPM
Fr, N
distance in mm
120
100
80
60
40
20
0
-20
0
5
10
15
20
25
30

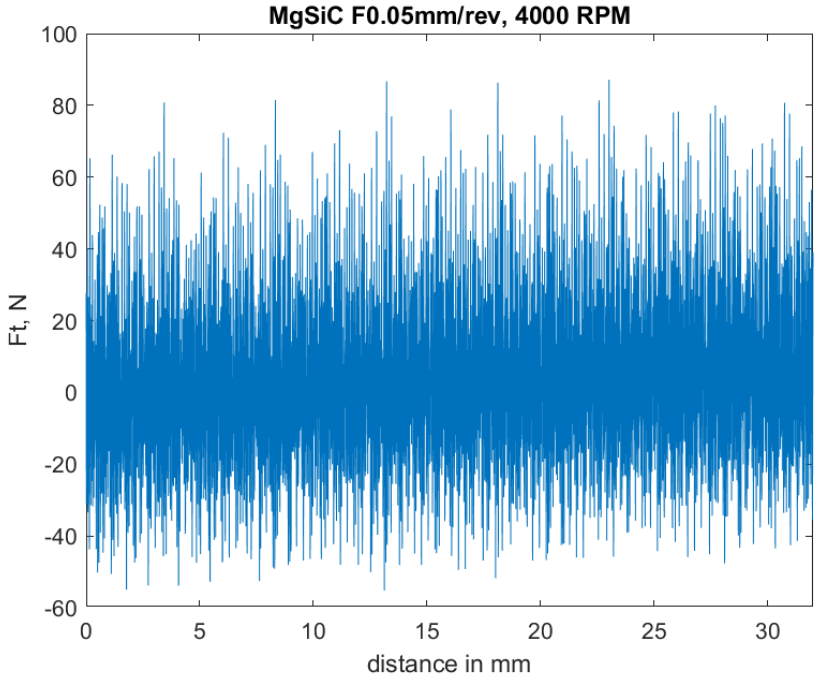
MgSiC F0.05mm/rev, 4000 RPM
Ft, N
distance in mm
100
80
60
40
20
0
-20
-40
-60
0
5
10
15
20
25
30

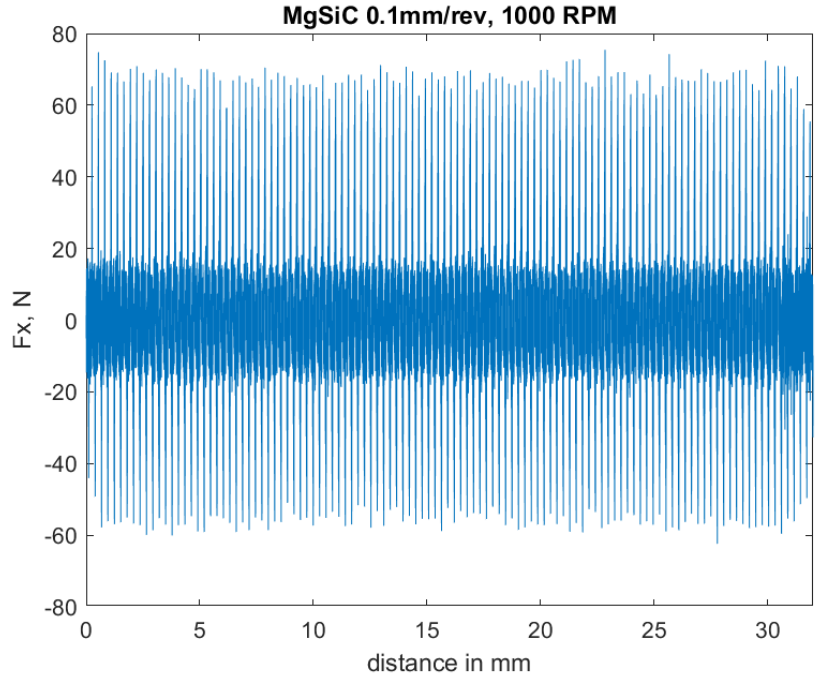
MgSiC 0.1mm/rev, 1000 RPM
Fx, N
distance in mm
80
60
40
20
0
-20
-40
-60
-80
0
5
10
15
20
25
30

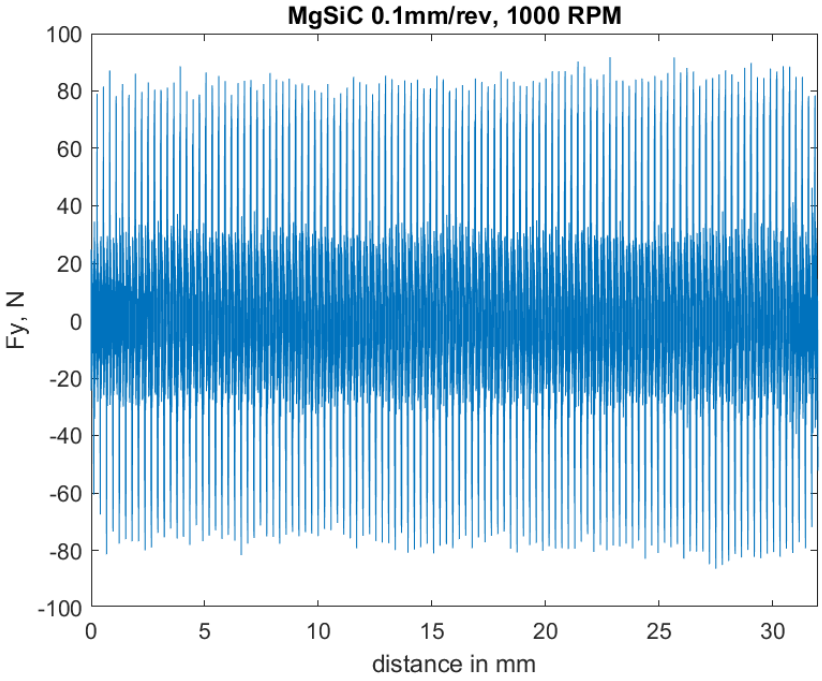
MgSiC 0.1mm/rev, 1000 RPM
Fy, N
distance in mm
100
80
60
40
20
0
-20
-40
-60
-80
-100
0
5
10
15
20
25
30

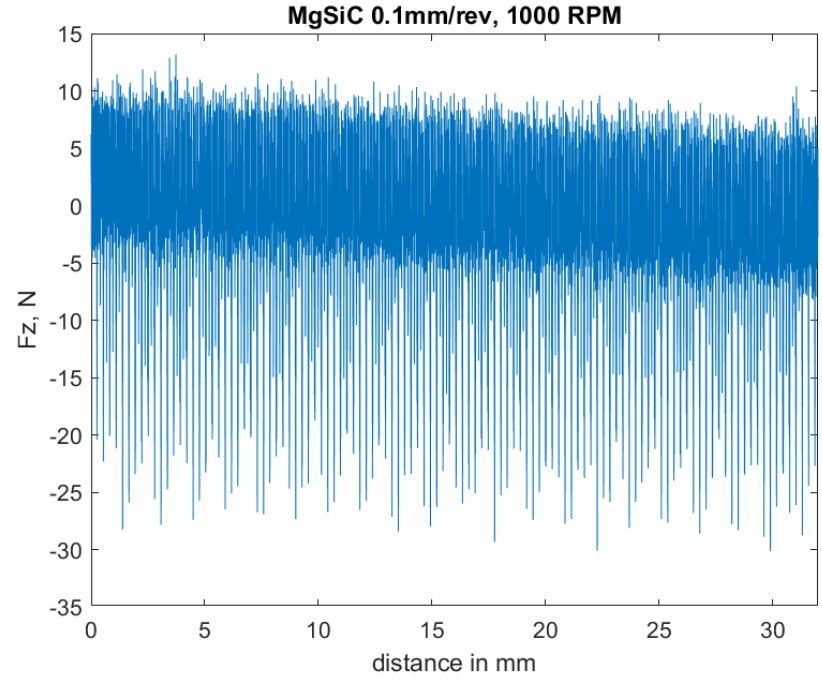
MgSiC 0.1mm/rev, 1000 RPM
Fz, N
distance in mm
15
10
5
0
-5
-10
-15
-20
-25
-30
-35
0
5
10
15
20
25
30

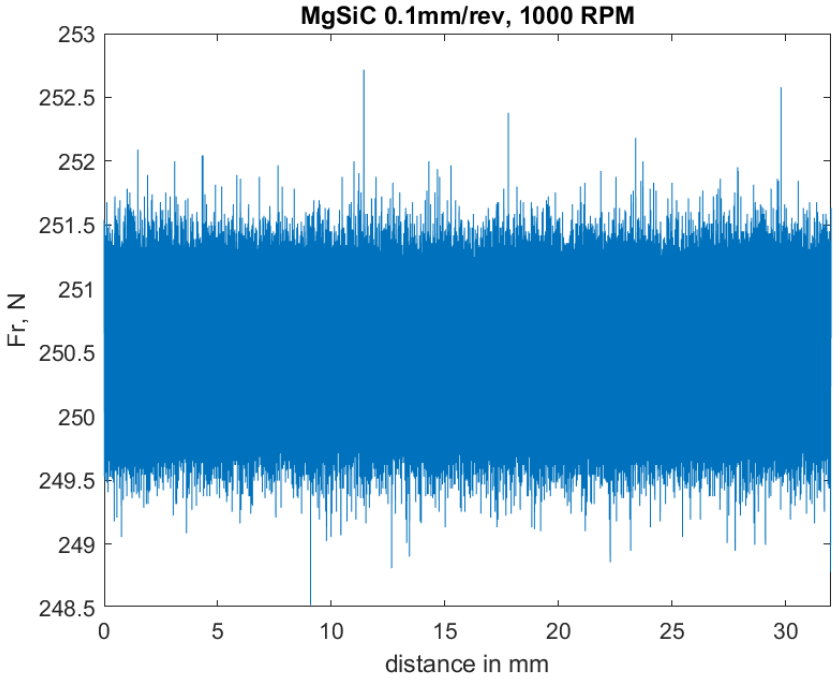
MgSiC 0.1mm/rev, 1000 RPM
Fr, N
253
252.5
252
251.5
251
250.5
250
249.5
249
248.5
0
5
10
15
20
25
30
distance in mm

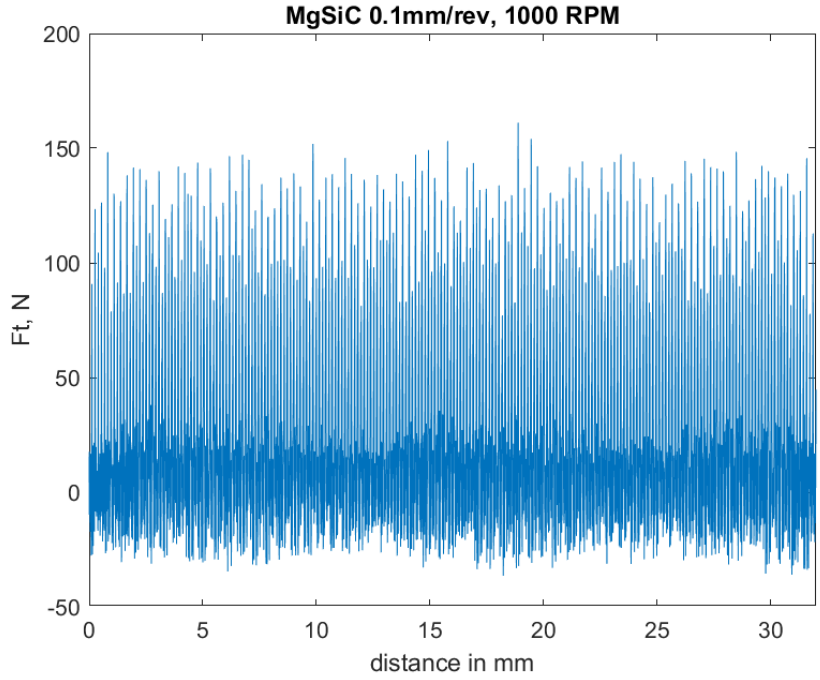
MgSiC 0.1mm/rev, 1000 RPM
Ft, N
200
150
100
50
0
-50
0
5
10
15
20
25
30
distance in mm

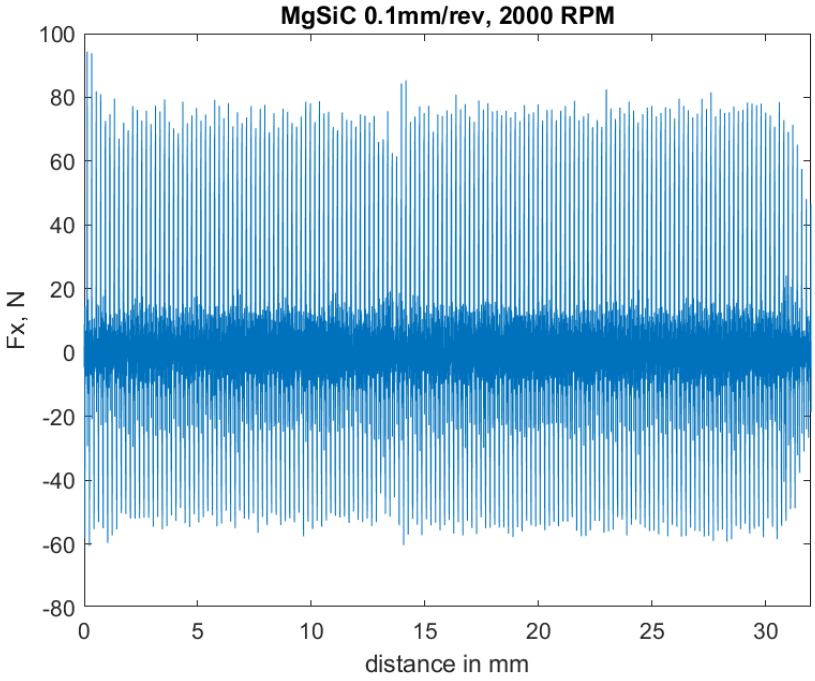
MgSiC 0.1mm/rev, 2000 RPM
Fx, N
distance in mm
100
80
60
40
20
0
-20
-40
-60
-80
0
5
10
15
20
25
30

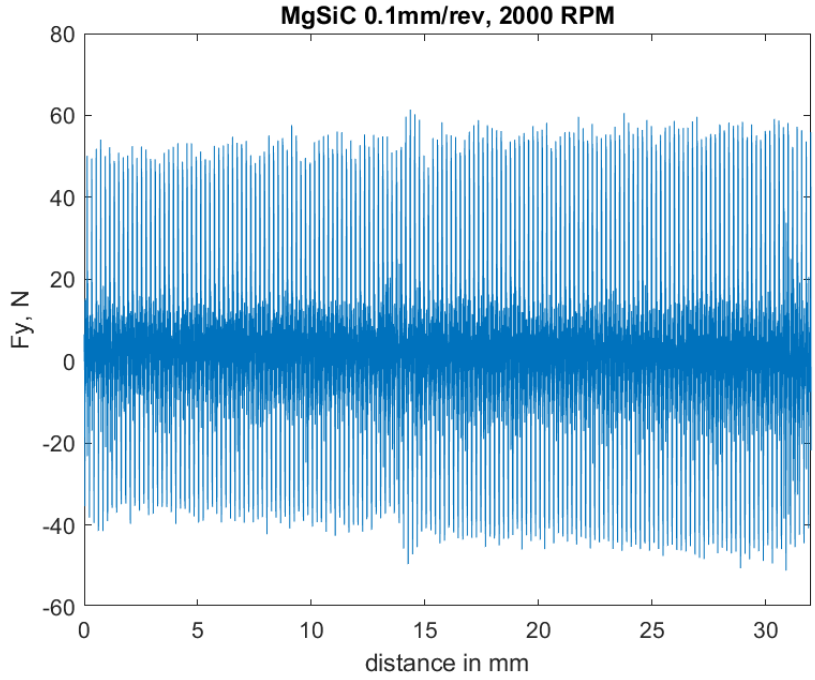
MgSiC 0.1mm/rev, 2000 RPM
Fy, N
distance in mm
80
60
40
20
0
-20
-40
-60
0
5
10
15
20
25
30

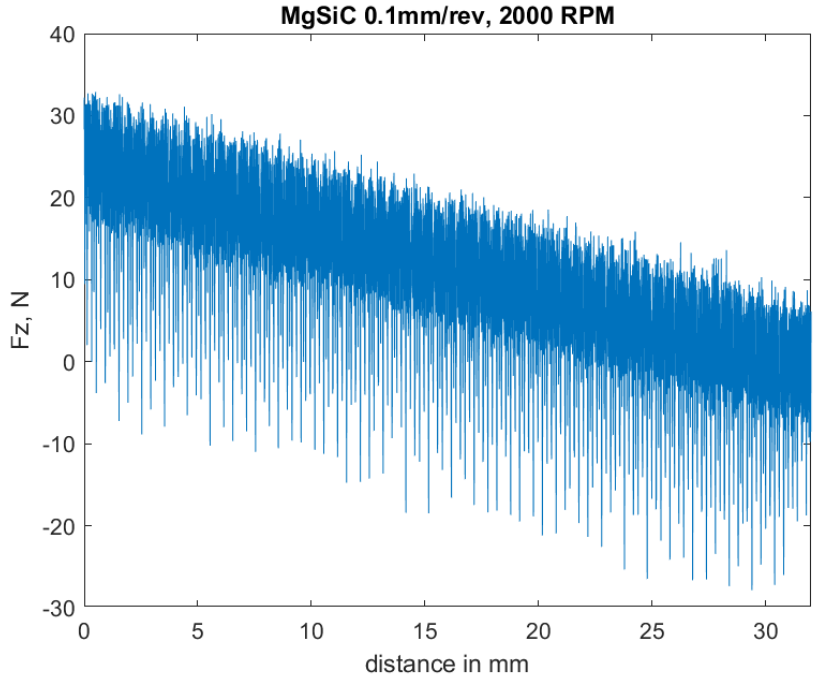
MgSiC 0.1mm/rev, 2000 RPM
Fz, N
distance in mm
40
30
20
10
0
-10
-20
-30
0
5
10
15
20
25
30

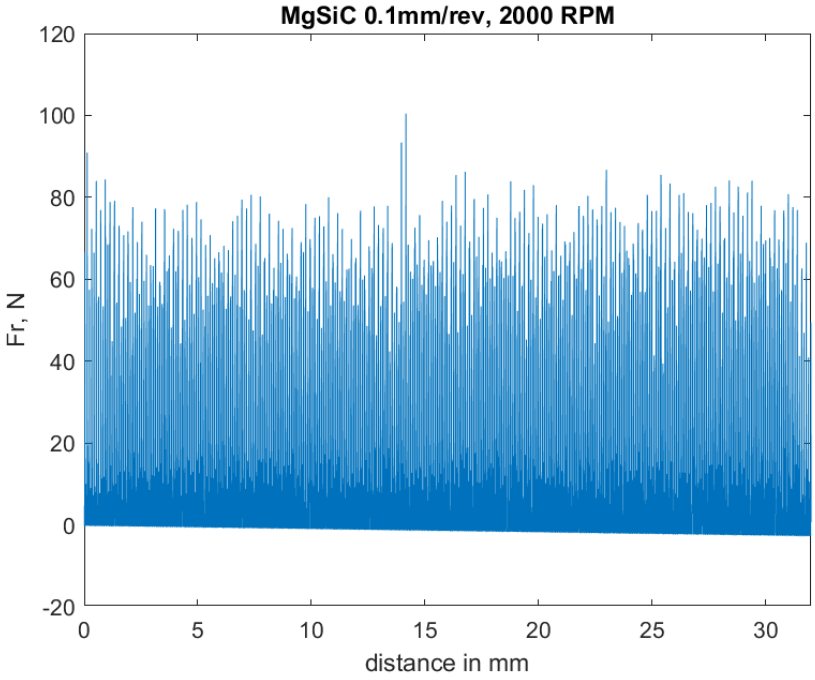
MgSiC 0.1mm/rev, 2000 RPM
Fr, N
distance in mm
120
100
80
60
40
20
0
-20
0
5
10
15
20
25
30

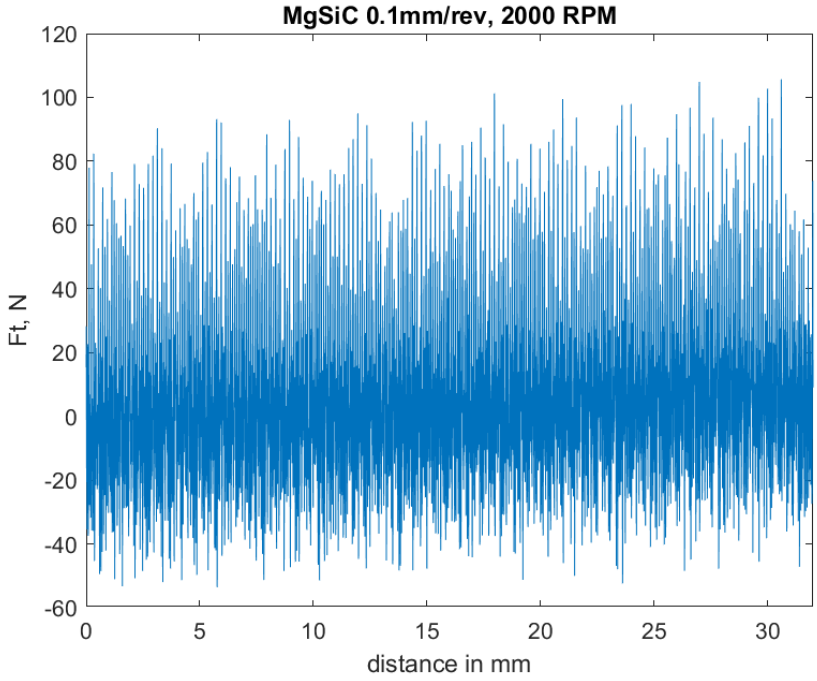
MgSiC 0.1mm/rev, 2000 RPM
Ft, N
distance in mm
120
100
80
60
40
20
0
-20
-40
-60
0
5
10
15
20
25
30

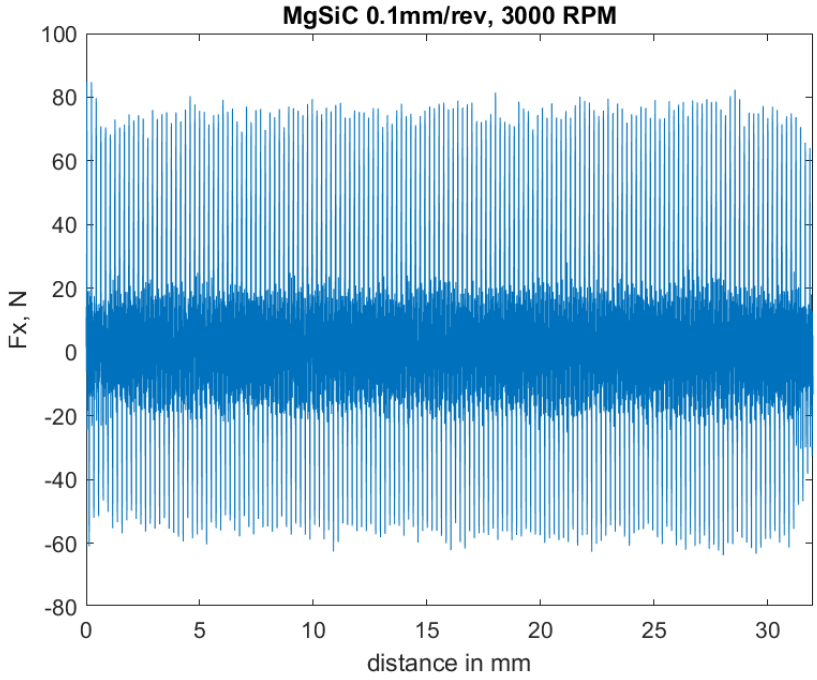
MgSiC 0.1mm/rev, 3000 RPM
Fx, N
distance in mm
100
80
60
40
20
0
-20
-40
-60
-80
0
5
10
15
20
25
30

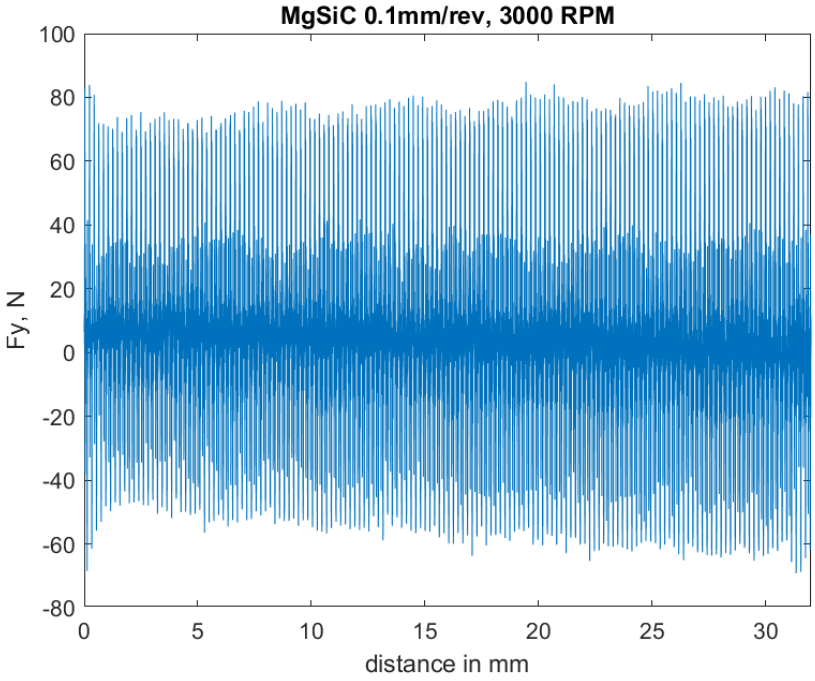
MgSiC 0.1mm/rev, 3000 RPM
Fy, N
distance in mm
100
80
60
40
20
0
-20
-40
-60
-80
0
5
10
15
20
25
30

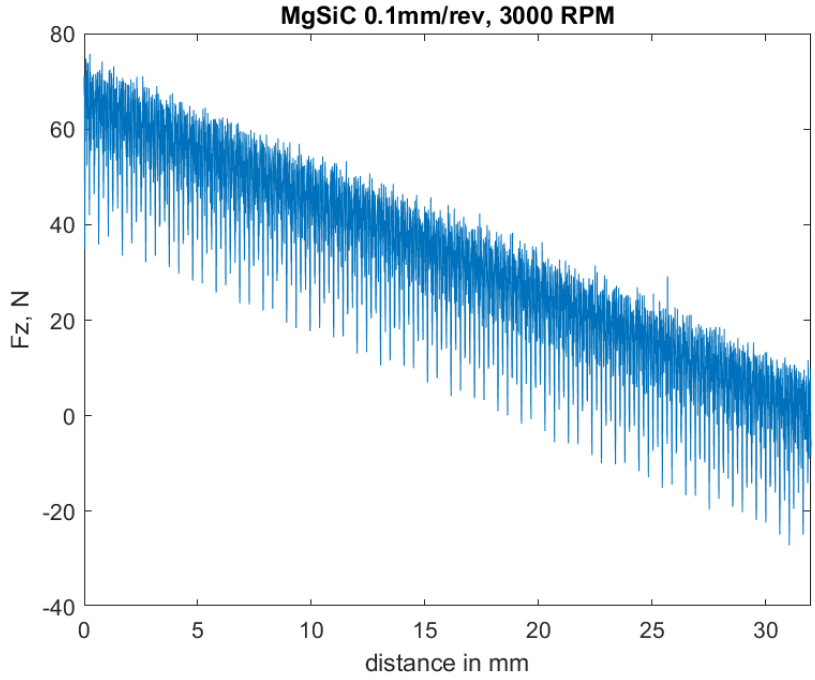
MgSiC 0.1mm/rev, 3000 RPM
Fz, N
distance in mm
80
60
40
20
0
-20
-40
0
5
10
15
20
25
30

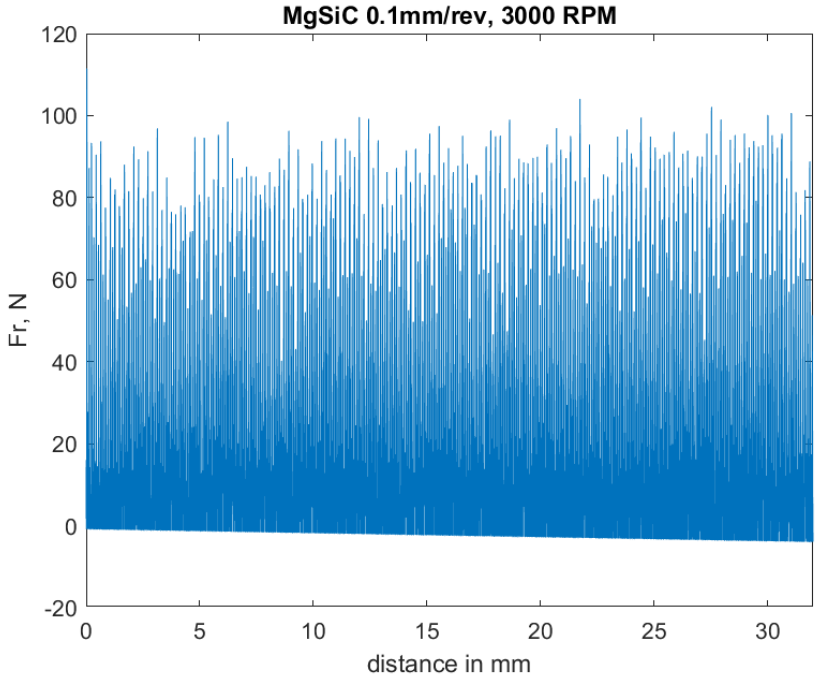
MgSiC 0.1mm/rev, 3000 RPM
Fr, N
distance in mm
120
100
80
60
40
20
0
-20
0
5
10
15
20
25
30

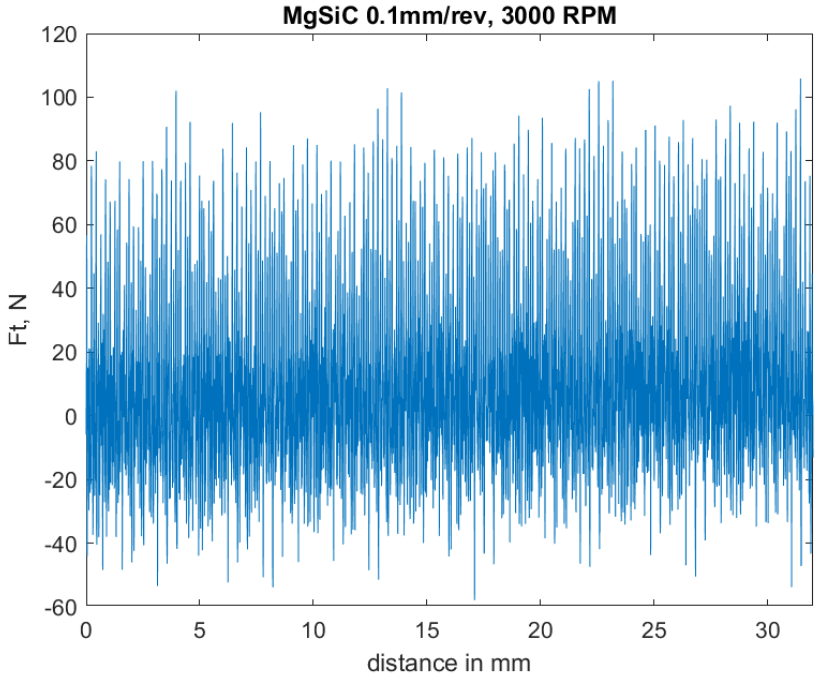
MgSiC 0.1mm/rev, 3000 RPM
Ft, N
distance in mm
120
100
80
60
40
20
0
-20
-40
-60
0
5
10
15
20
25
30

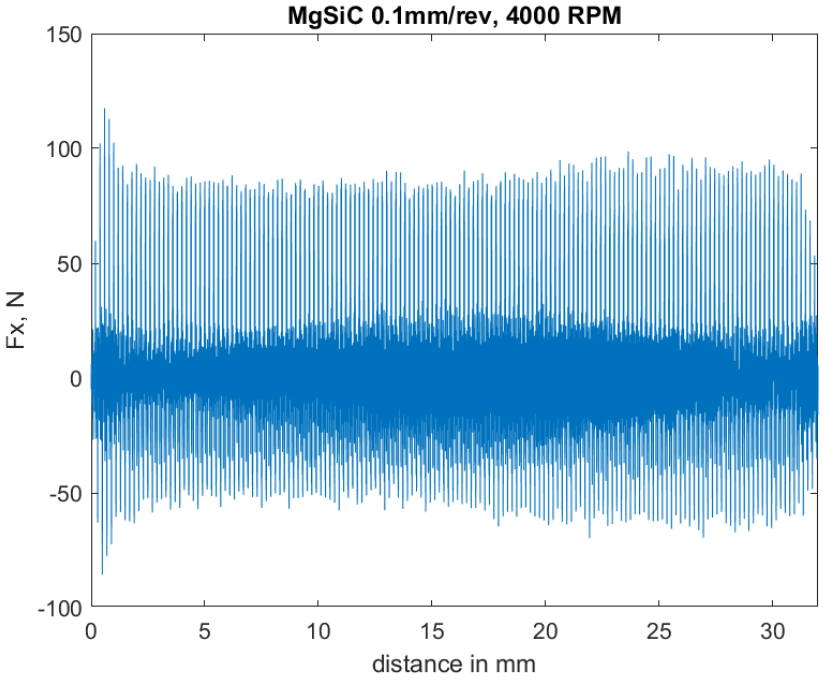
MgSiC 0.1mm/rev, 4000 RPM
Fx, N
distance in mm
150
100
50
0
-50
-100
0
5
10
15
20
25
30

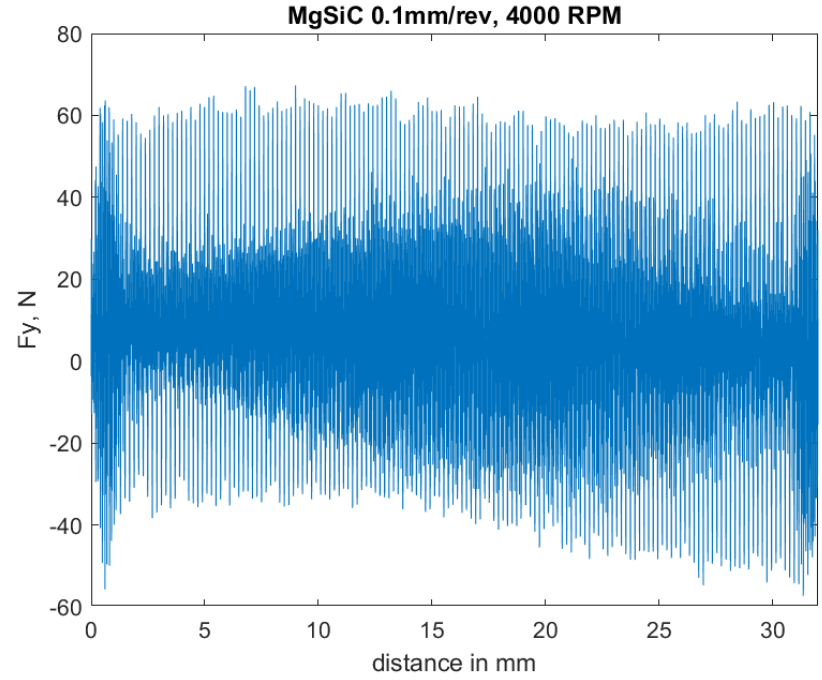
MgSiC 0.1mm/rev, 4000 RPM
Fy, N
distance in mm
80
60
40
20
0
-20
-40
-60
0
5
10
15
20
25
30

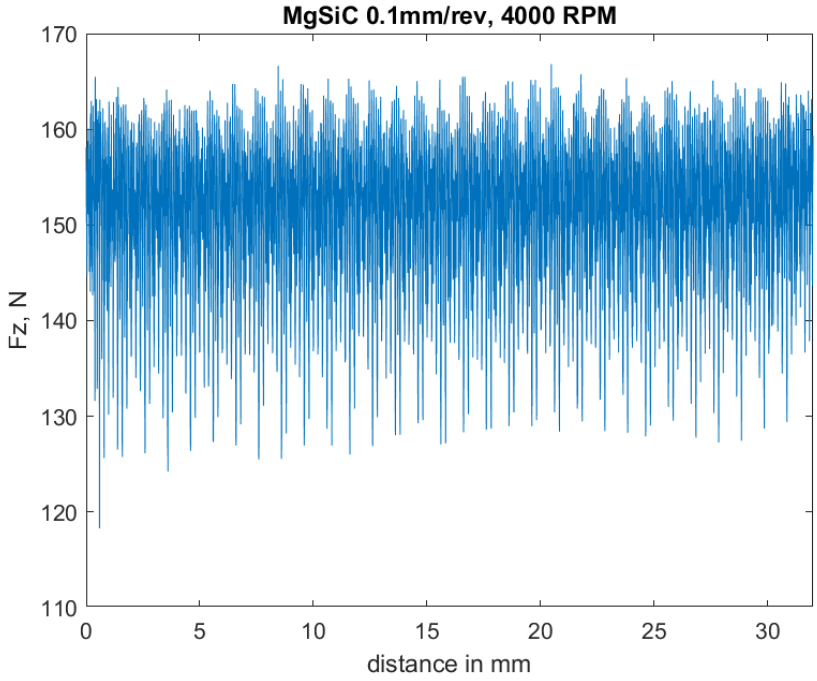
MgSiC 0.1mm/rev, 4000 RPM
Fz, N
distance in mm
170
160
150
140
130
120
110
0
5
10
15
20
25
30

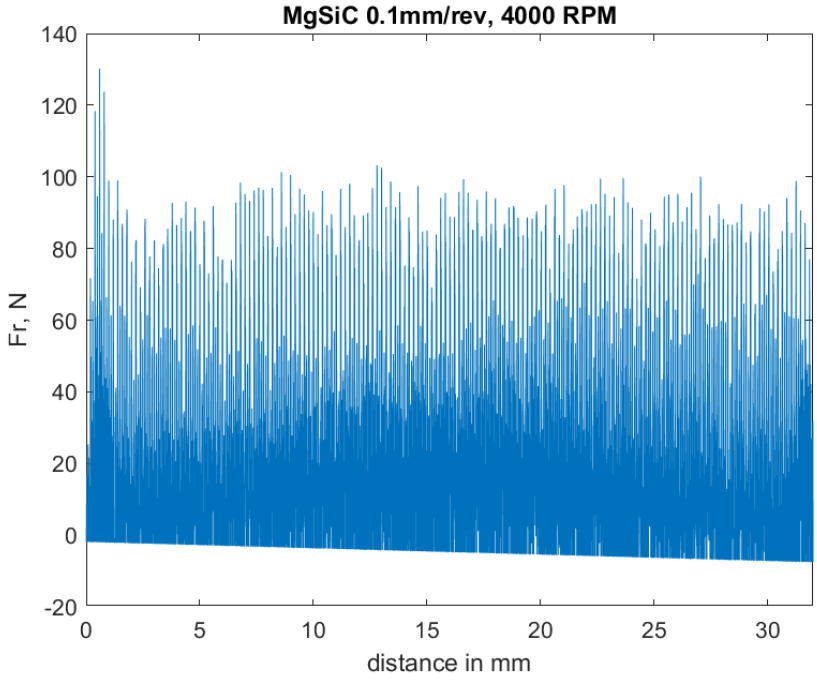
MgSiC 0.1mm/rev, 4000 RPM
Fr, N
distance in mm
140
120
100
80
60
40
20
0
-20
0
5
10
15
20
25
30

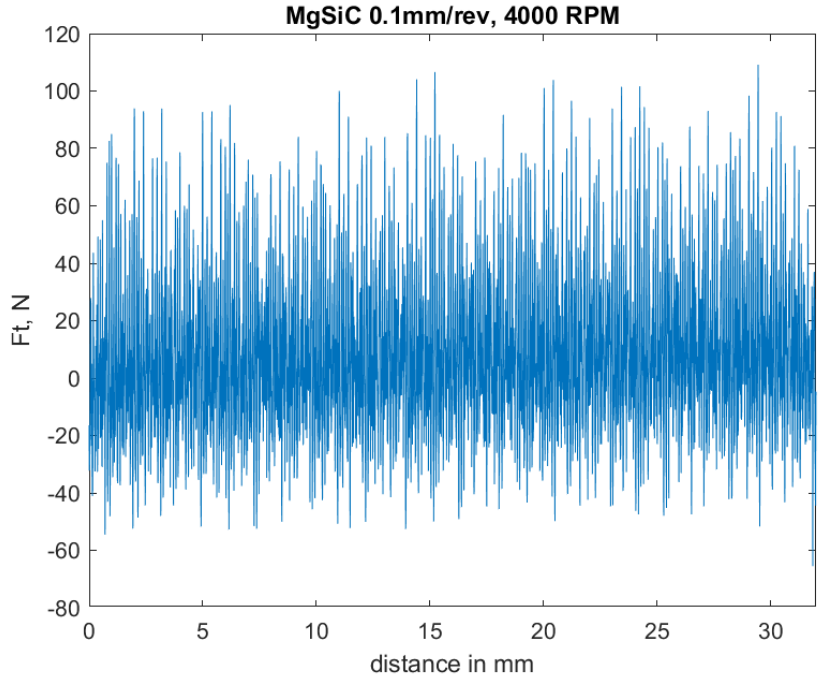
MgSiC 0.1mm/rev, 4000 RPM
Ft, N
distance in mm
120
100
80
60
40
20
0
-20
-40
-60
-80
0
5
10
15
20
25
30

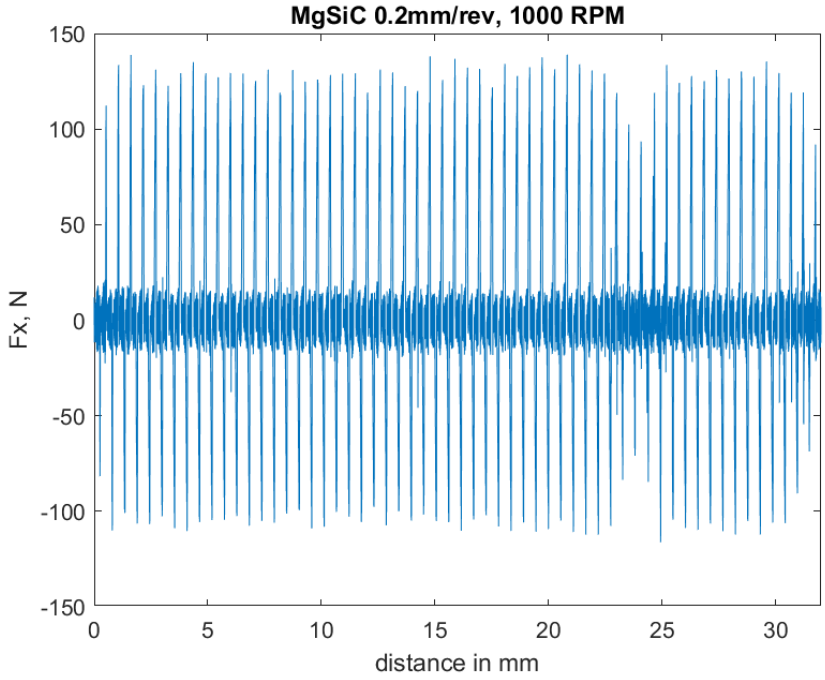
MgSiC 0.2mm/rev, 1000 RPM
Fx, N
distance in mm
150
100
50
0
-50
-100
-150
0
5
10
15
20
25
30

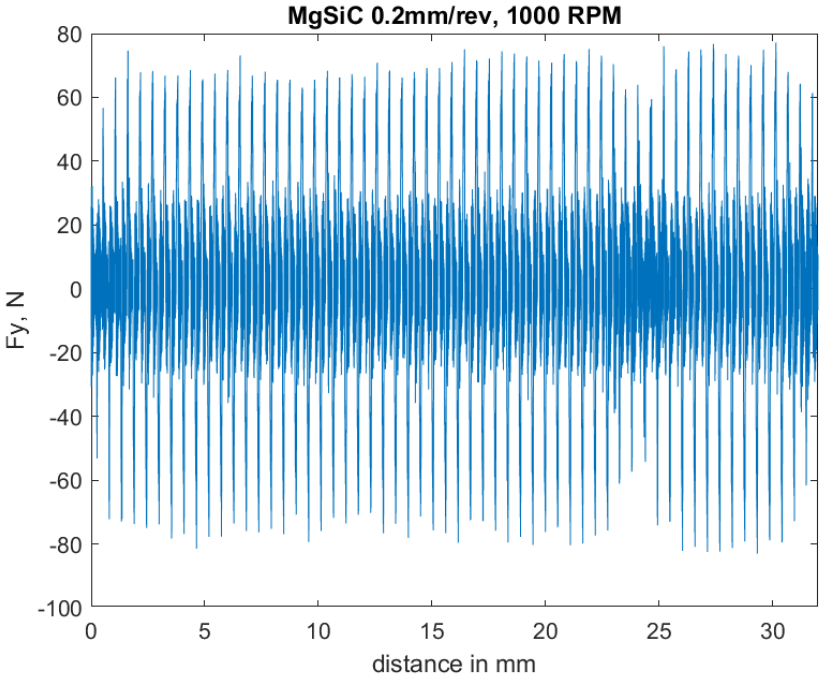
MgSiC 0.2mm/rev, 1000 RPM
Fy, N
distance in mm
80
60
40
20
0
-20
-40
-60
-80
-100
0
5
10
15
20
25
30

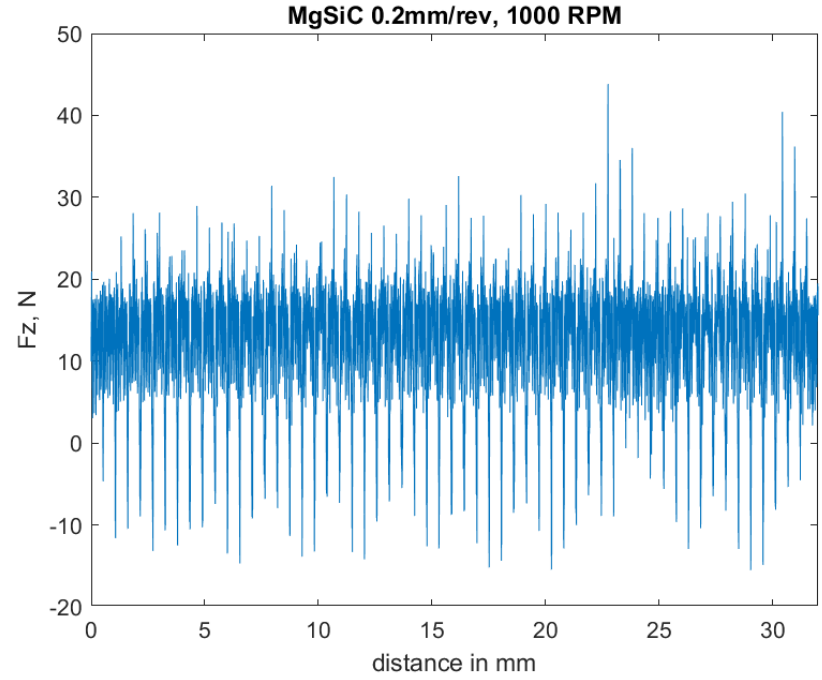
MgSiC 0.2mm/rev, 1000 RPM
Fz, N
distance in mm
50
40
30
20
10
0
-10
-20
0
5
10
15
20
25
30

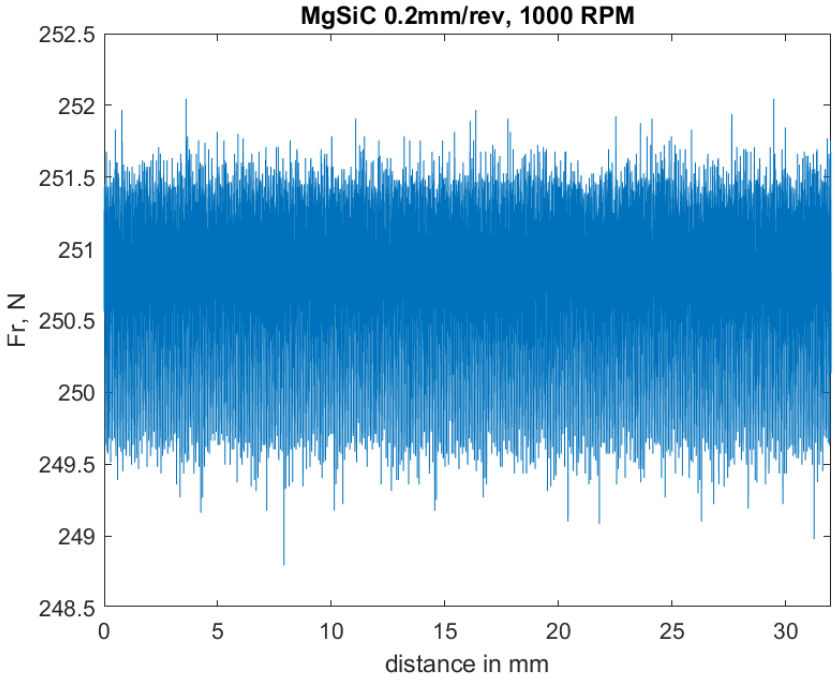
MgSiC 0.2mm/rev, 1000 RPM
Fr, N
252.5
252
251.5
251
250.5
250
249.5
249
248.5
0
5
10
15
20
25
30
distance in mm

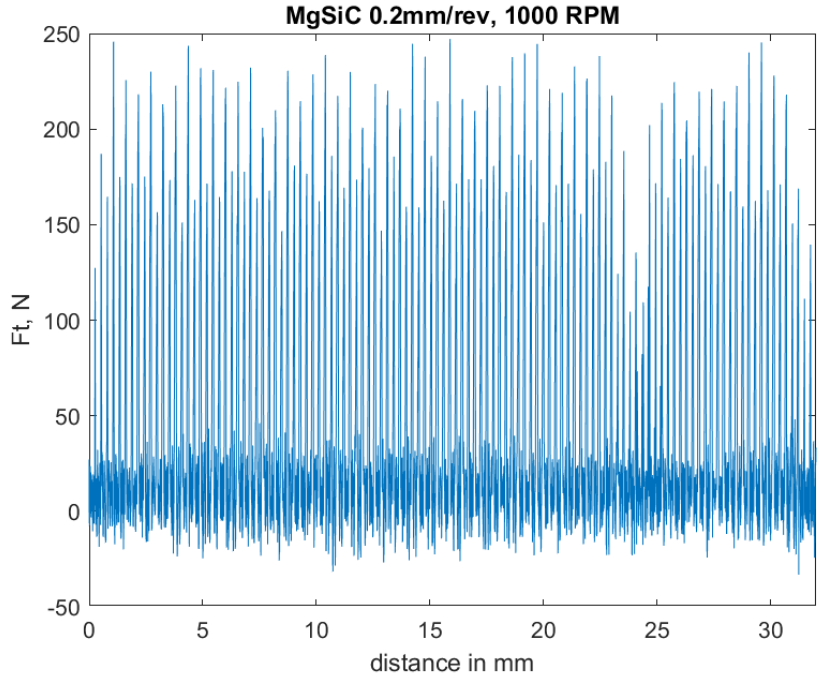
MgSiC 0.2mm/rev, 1000 RPM
Ft, N
250
200
150
100
50
0
-50
0
5
10
15
20
25
30
distance in mm

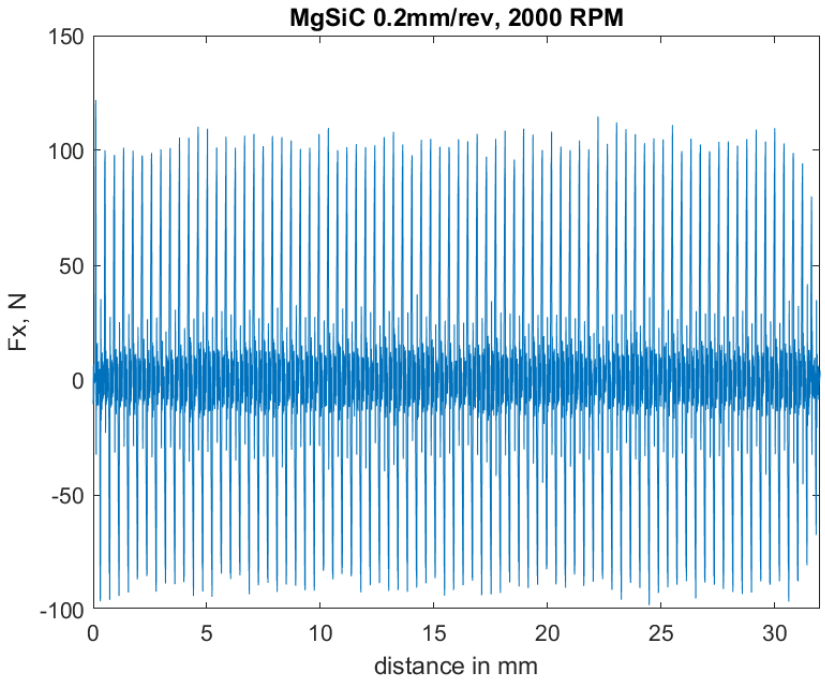
MgSiC 0.2mm/rev, 2000 RPM
Fx, N
distance in mm
150
100
50
0
-50
-100
0
5
10
15
20
25
30

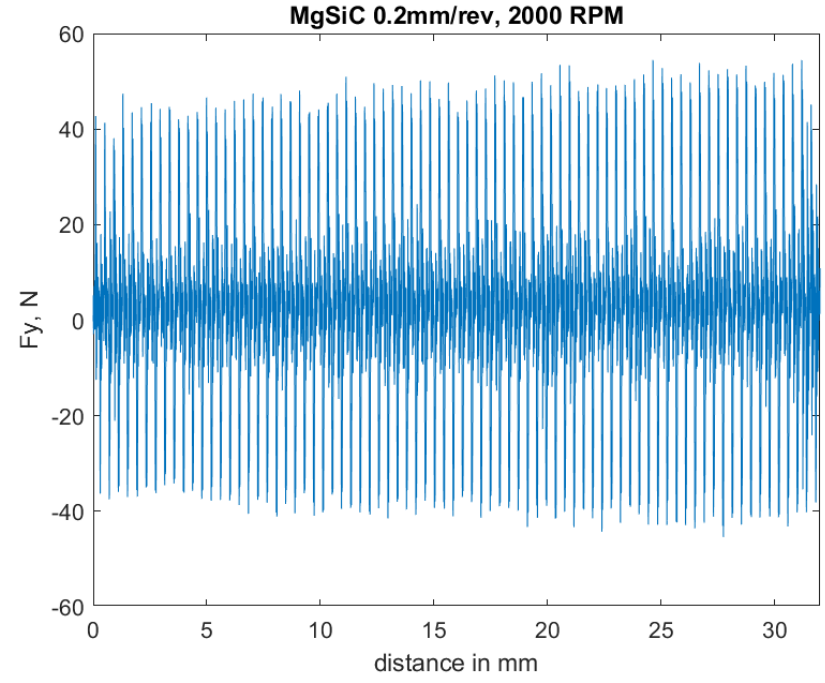
MgSiC 0.2mm/rev, 2000 RPM
Fy, N
distance in mm
60
40
20
0
-20
-40
-60
0
5
10
15
20
25
30

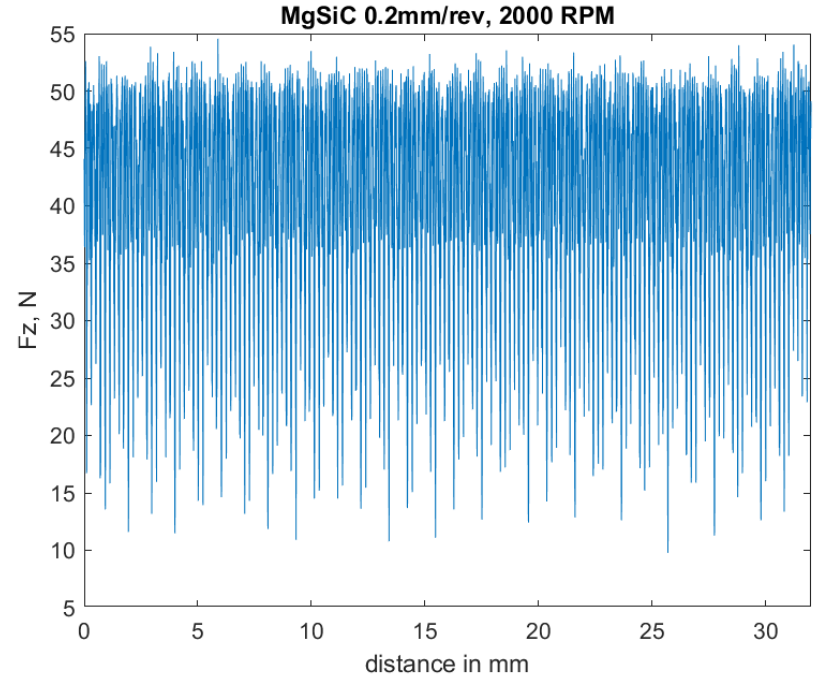
MgSiC 0.2mm/rev, 2000 RPM
Fz, N
distance in mm
55
50
45
40
35
30
25
20
15
10
5
0
5
10
15
20
25
30

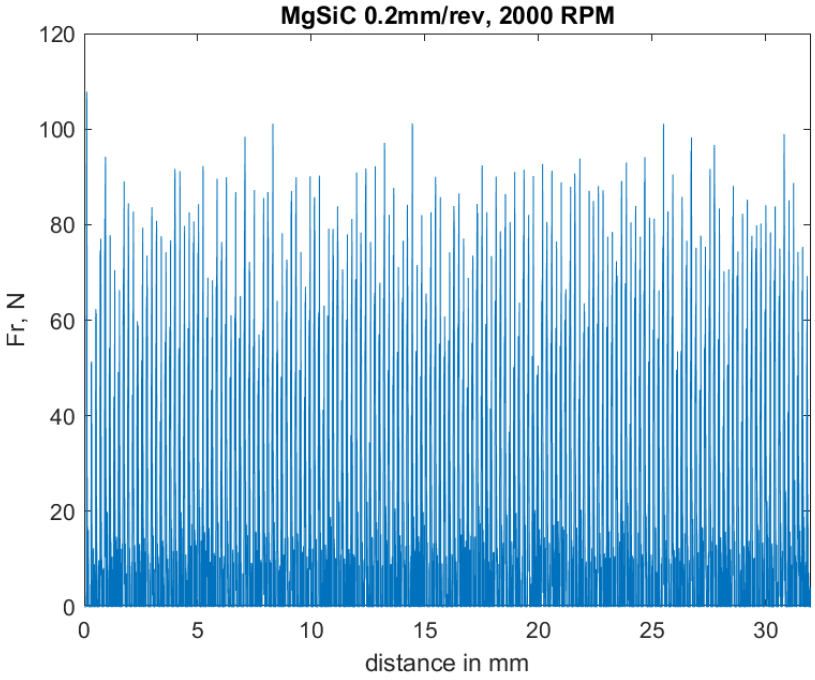
MgSiC 0.2mm/rev, 2000 RPM
Fr, N
distance in mm
120
100
80
60
40
20
0
0
5
10
15
20
25
30

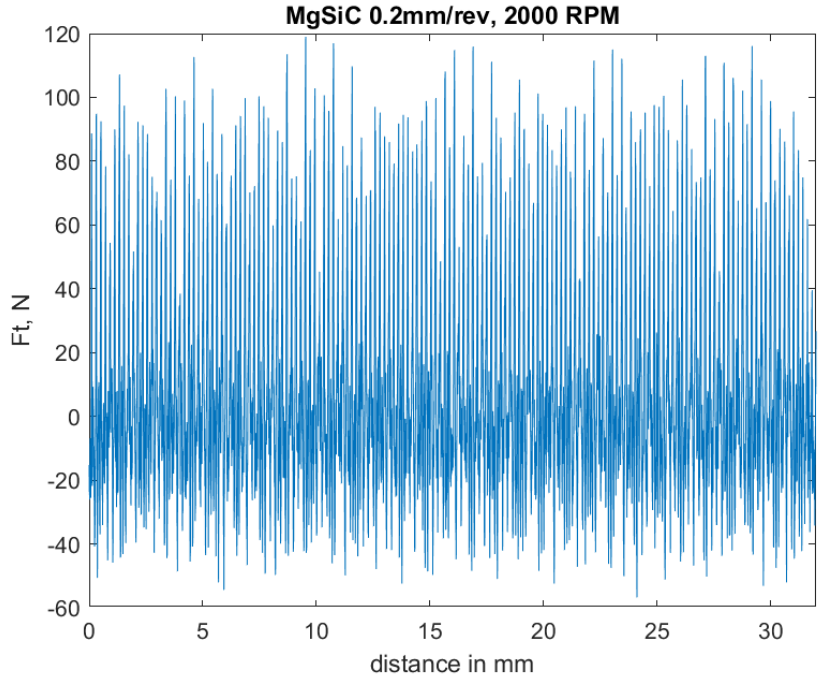
MgSiC 0.2mm/rev, 2000 RPM
Ft, N
distance in mm
120
100
80
60
40
20
0
-20
-40
-60
0
5
10
15
20
25
30

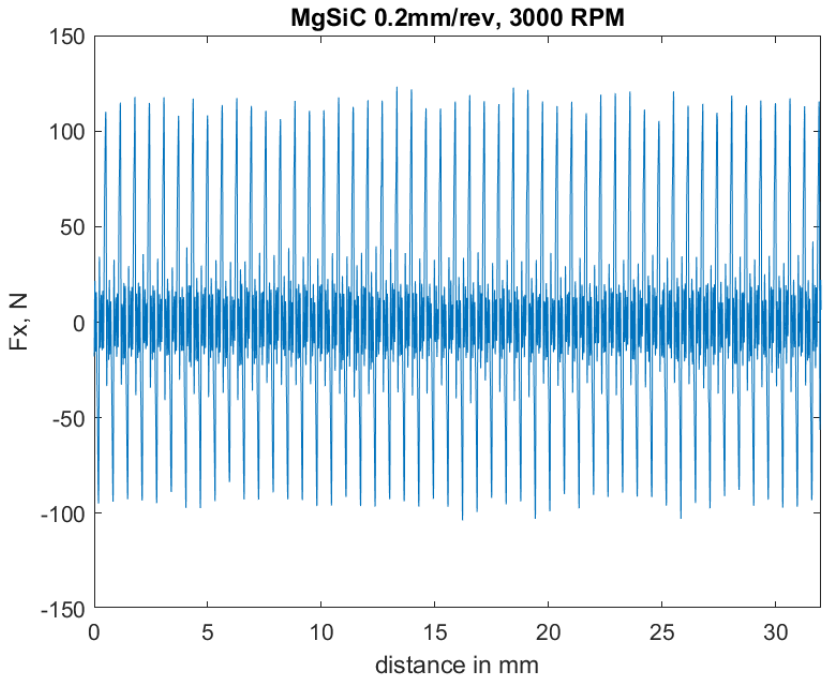
MgSiC 0.2mm/rev, 3000 RPM
Fx, N
distance in mm
150
100
50
0
-50
-100
-150
0
5
10
15
20
25
30

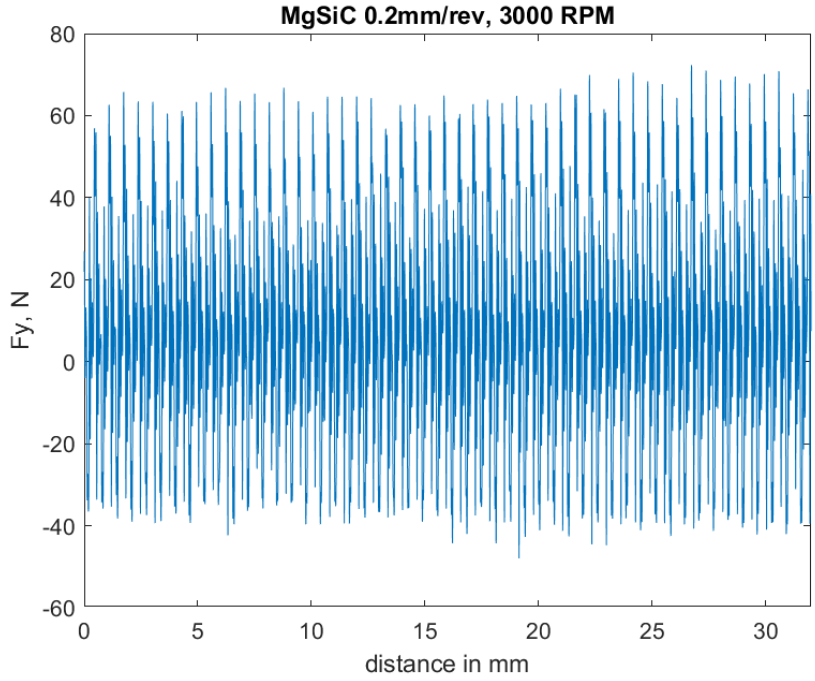
MgSiC 0.2mm/rev, 3000 RPM
Fy, N
distance in mm
80
60
40
20
0
-20
-40
-60
0
5
10
15
20
25
30

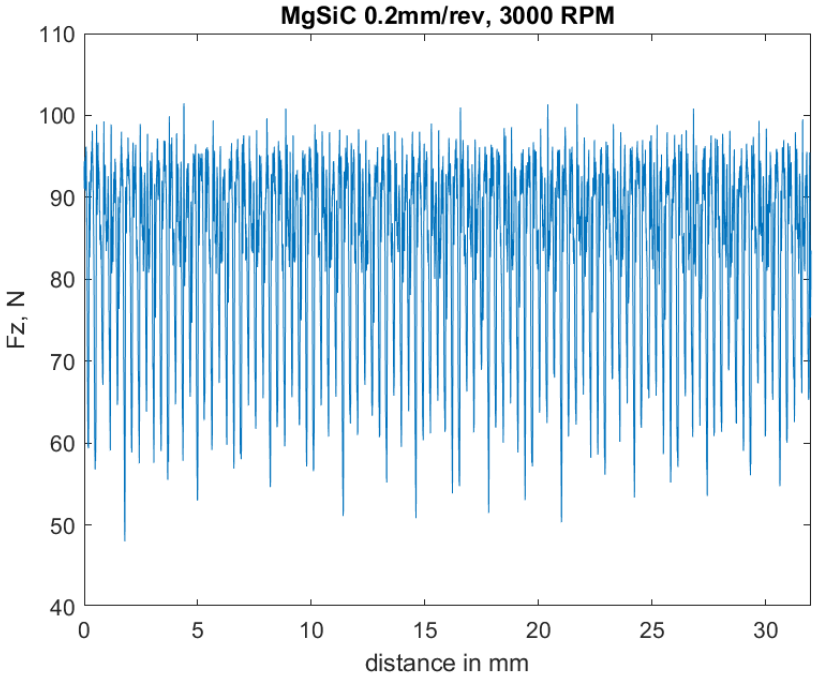
MgSiC 0.2mm/rev, 3000 RPM
Fz, N
distance in mm
110
100
90
80
70
60
50
40
0
5
10
15
20
25
30

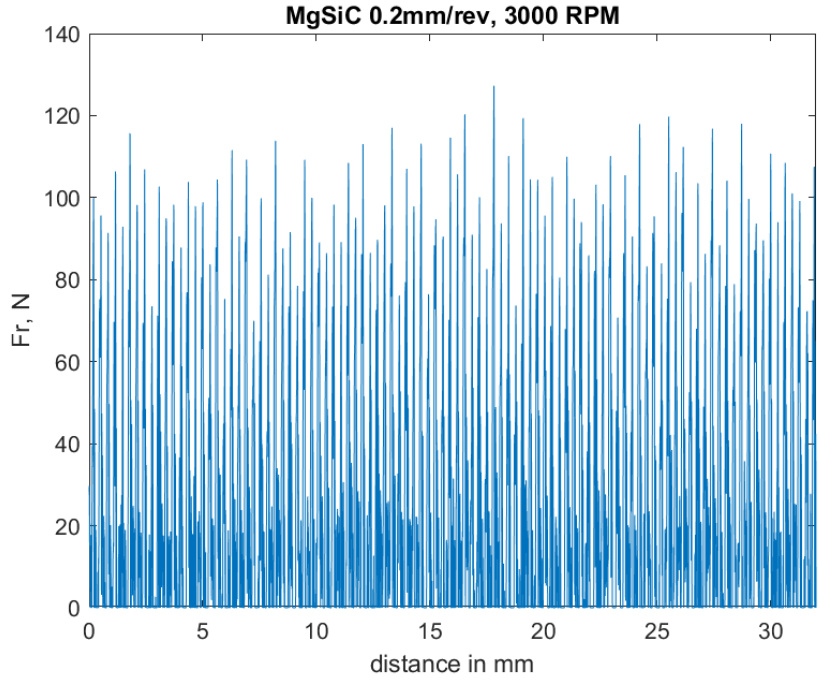
MgSiC 0.2mm/rev, 3000 RPM
Fr, N
distance in mm
0
20
40
60
80
100
120
140
0
5
10
15
20
25
30

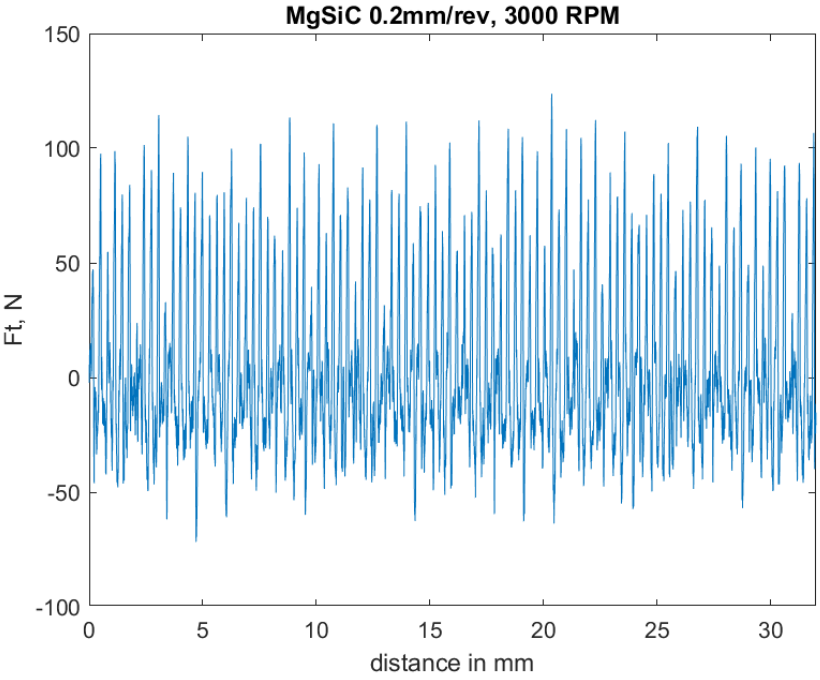
MgSiC 0.2mm/rev, 3000 RPM
Ft, N
distance in mm
-100
-50
0
50
100
150
0
5
10
15
20
25
30

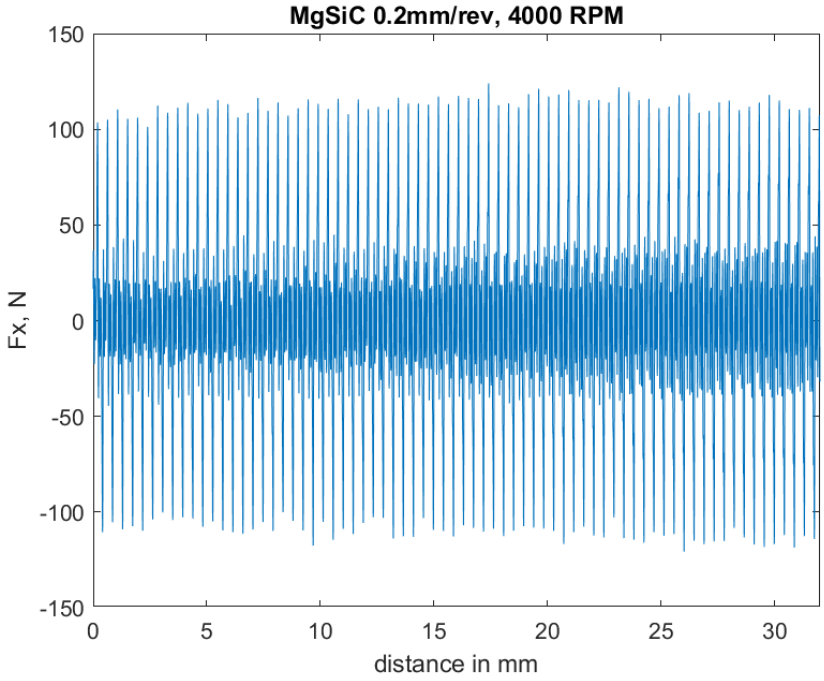
MgSiC 0.2mm/rev, 4000 RPM
Fx, N
distance in mm
150
100
50
0
-50
-100
-150
0
5
10
15
20
25
30

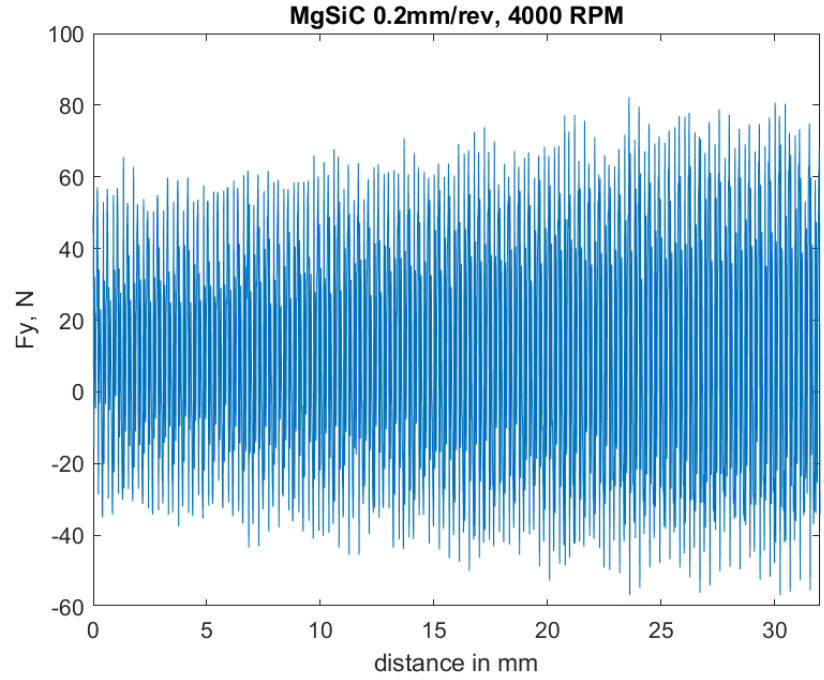
MgSiC 0.2mm/rev, 4000 RPM
Fy, N
distance in mm
100
80
60
40
20
0
-20
-40
-60
0
5
10
15
20
25
30

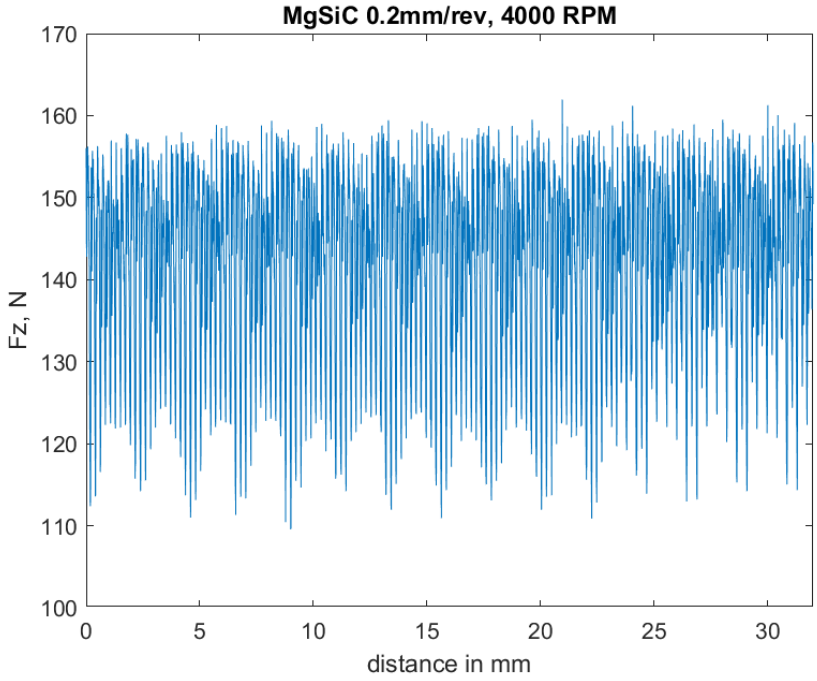
MgSiC 0.2mm/rev, 4000 RPM
Fz, N
distance in mm
170
160
150
140
130
120
110
100
0
5
10
15
20
25
30

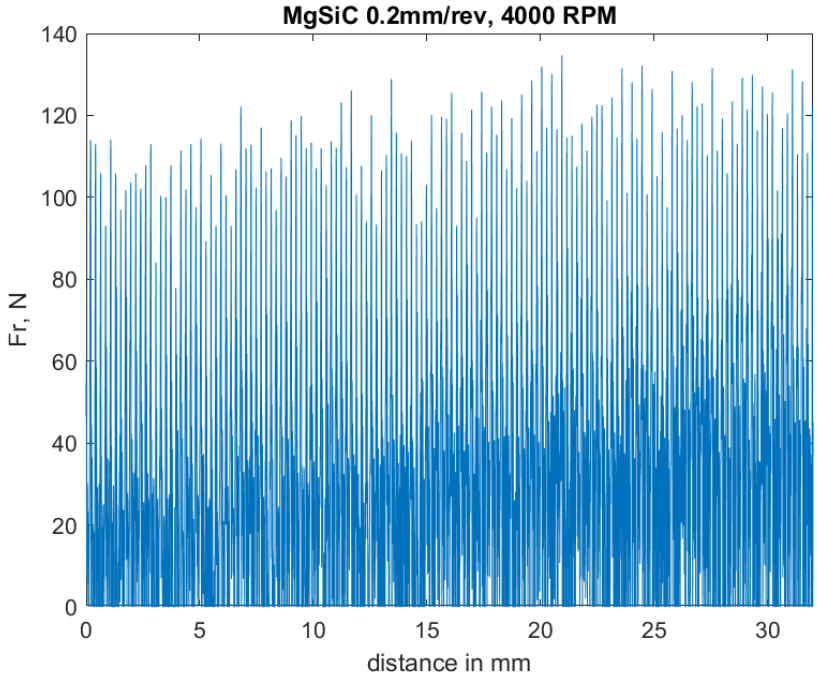
MgSiC 0.2mm/rev, 4000 RPM
Fr, N
distance in mm
140
120
100
80
60
40
20
0
0
5
10
15
20
25
30

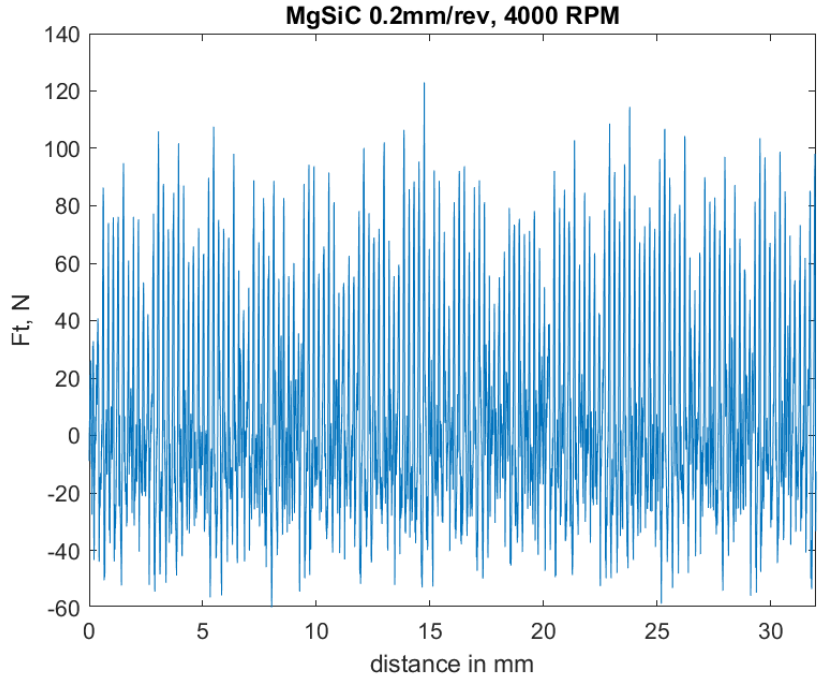
MgSiC 0.2mm/rev, 4000 RPM
Ft, N
distance in mm

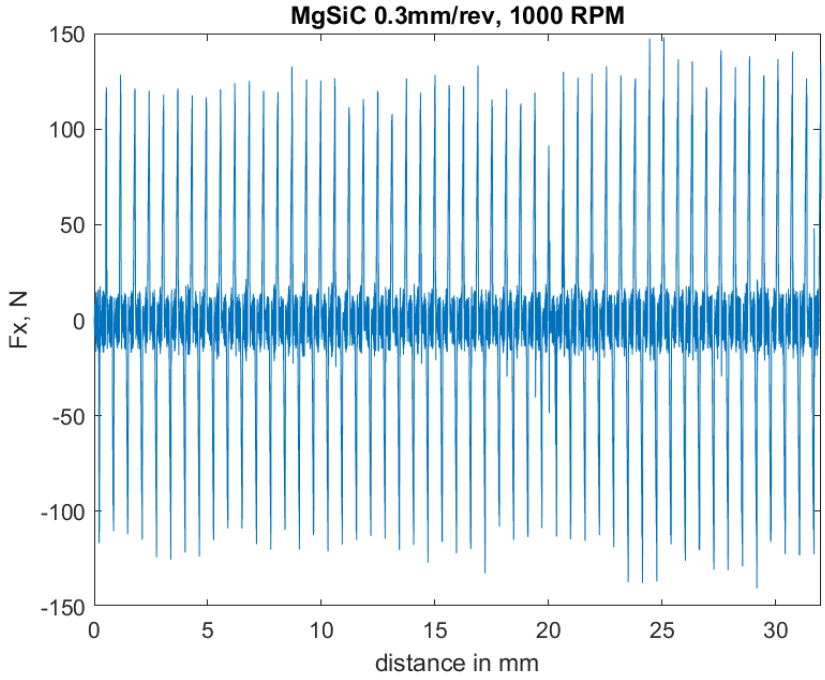
MgSiC 0.3mm/rev, 1000 RPM
Fx, N
distance in mm

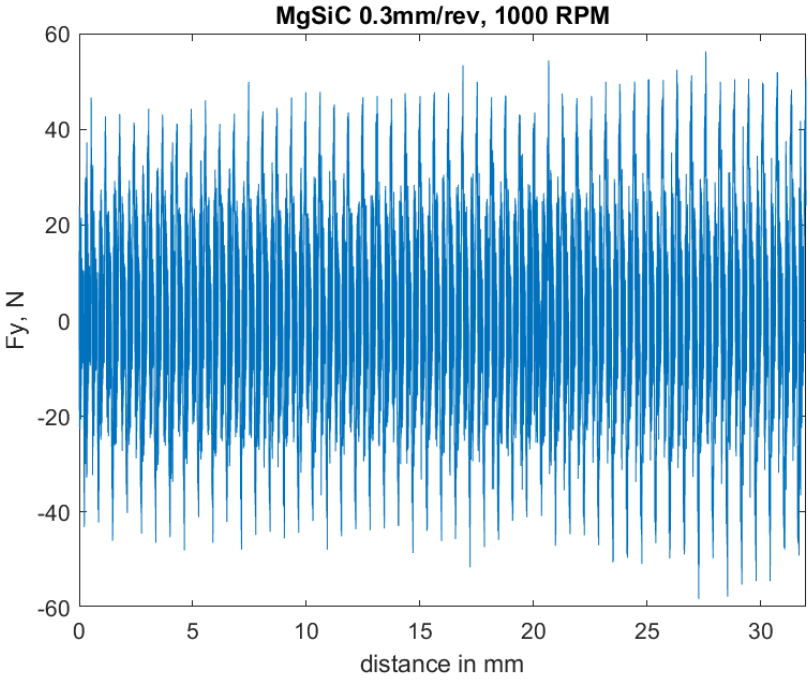
MgSiC 0.3mm/rev, 1000 RPM
Fy, N
distance in mm
60
40
20
0
-20
-40
-60
0
5
10
15
20
25
30

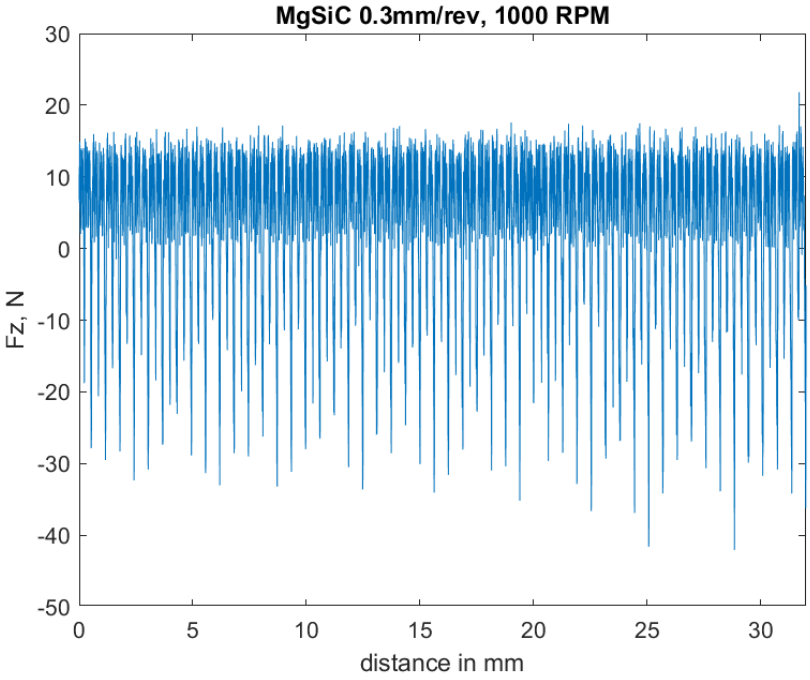
MgSiC 0.3mm/rev, 1000 RPM
Fz, N
distance in mm
30
20
10
0
-10
-20
-30
-40
-50
0
5
10
15
20
25
30

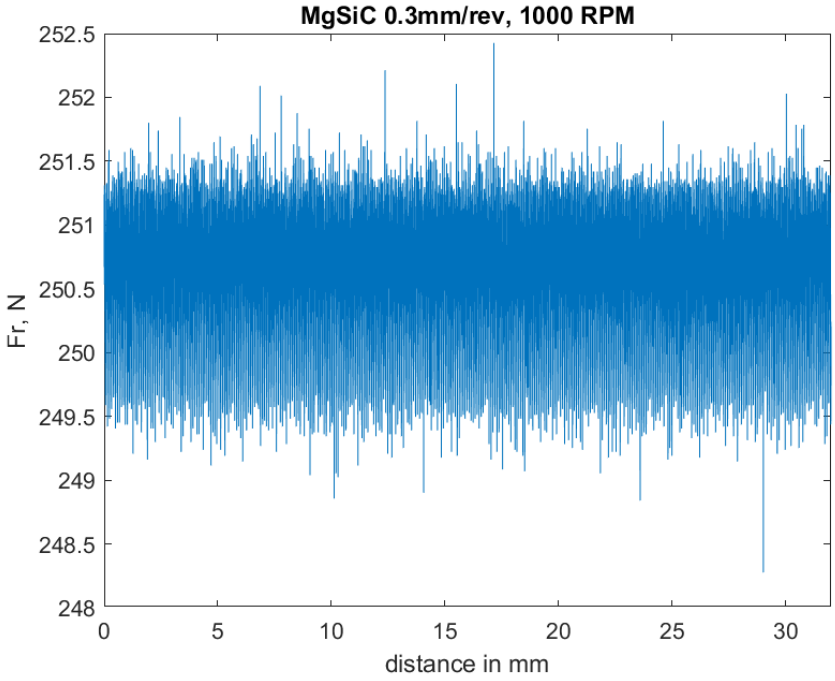
MgSiC 0.3mm/rev, 1000 RPM
Fr, N
252.5
252
251.5
251
250.5
250
249.5
249
248.5
248
0
5
10
15
20
25
30
distance in mm

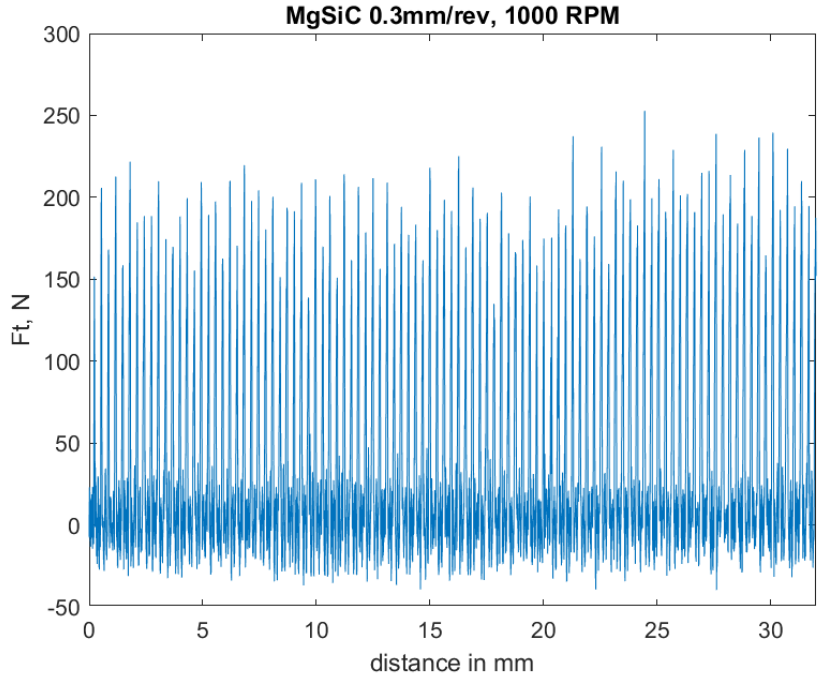
MgSiC 0.3mm/rev, 1000 RPM
Ft, N
300
250
200
150
100
50
0
-50
0
5
10
15
20
25
30
distance in mm

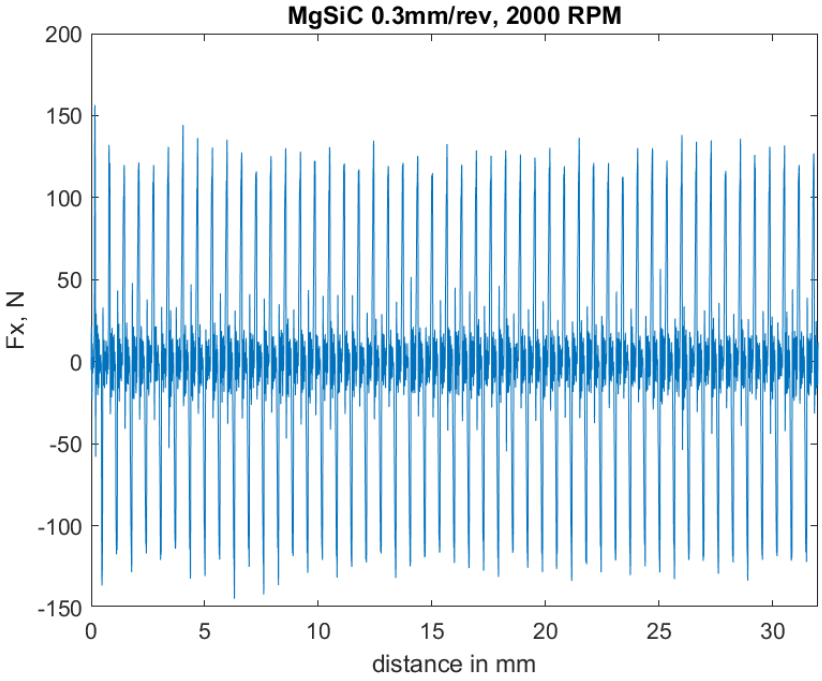
MgSiC 0.3mm/rev, 2000 RPM
Fx, N
distance in mm
200
150
100
50
0
-50
-100
-150
0
5
10
15
20
25
30

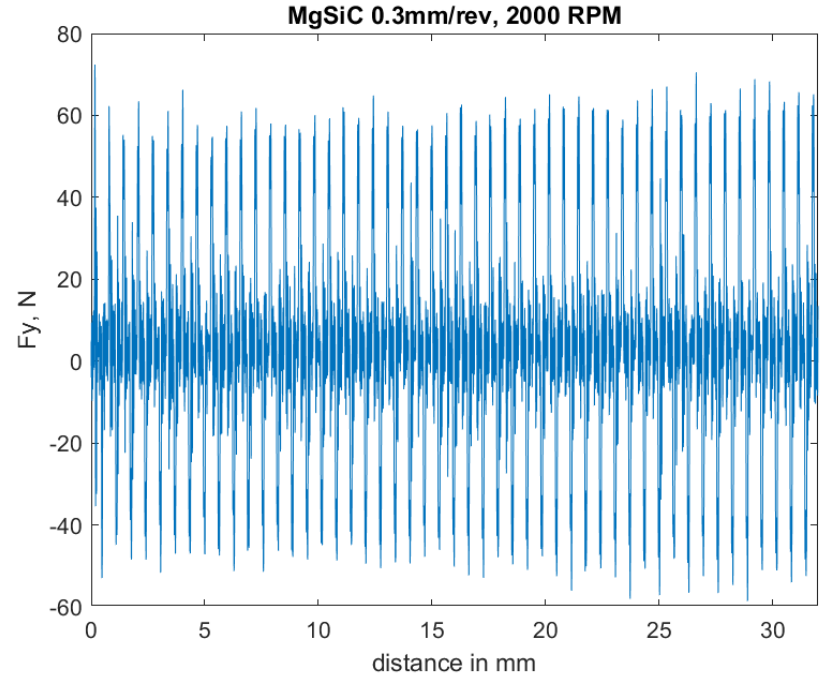
MgSiC 0.3mm/rev, 2000 RPM
Fy, N
distance in mm
80
60
40
20
0
-20
-40
-60
0
5
10
15
20
25
30

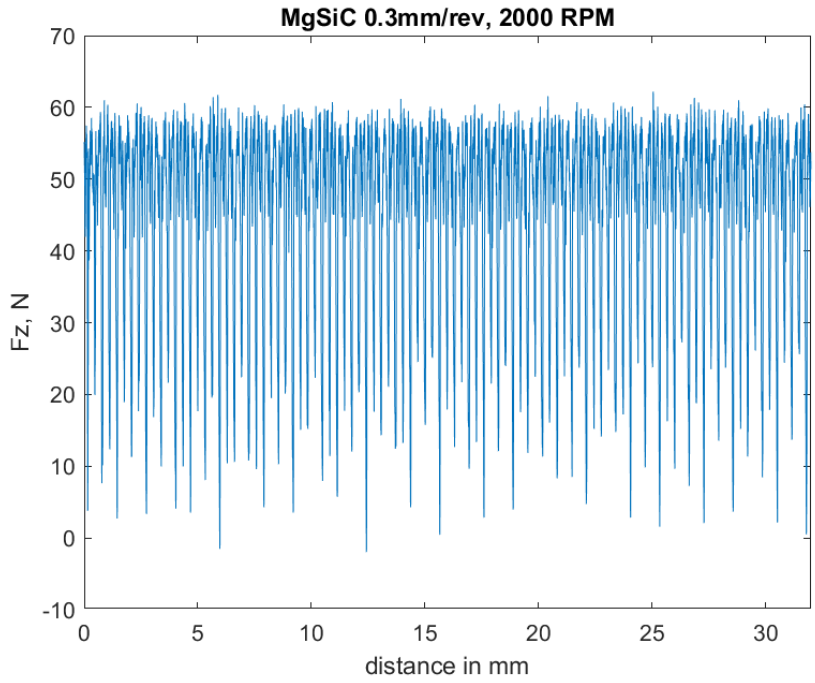
MgSiC 0.3mm/rev, 2000 RPM
Fz, N
distance in mm
70
60
50
40
30
20
10
0
-10
0
5
10
15
20
25
30

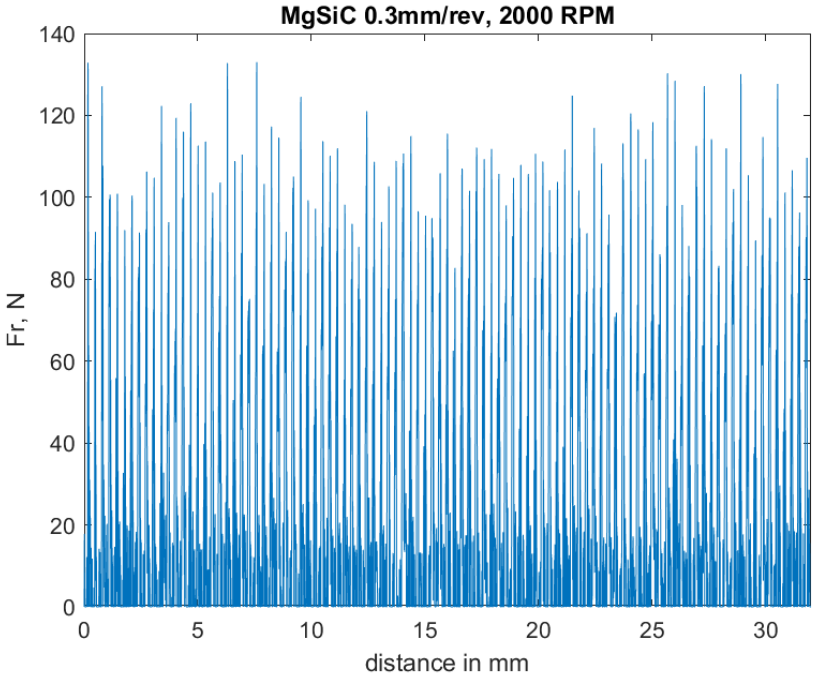
MgSiC 0.3mm/rev, 2000 RPM
Fr, N
distance in mm
140
120
100
80
60
40
20
0
0
5
10
15
20
25
30

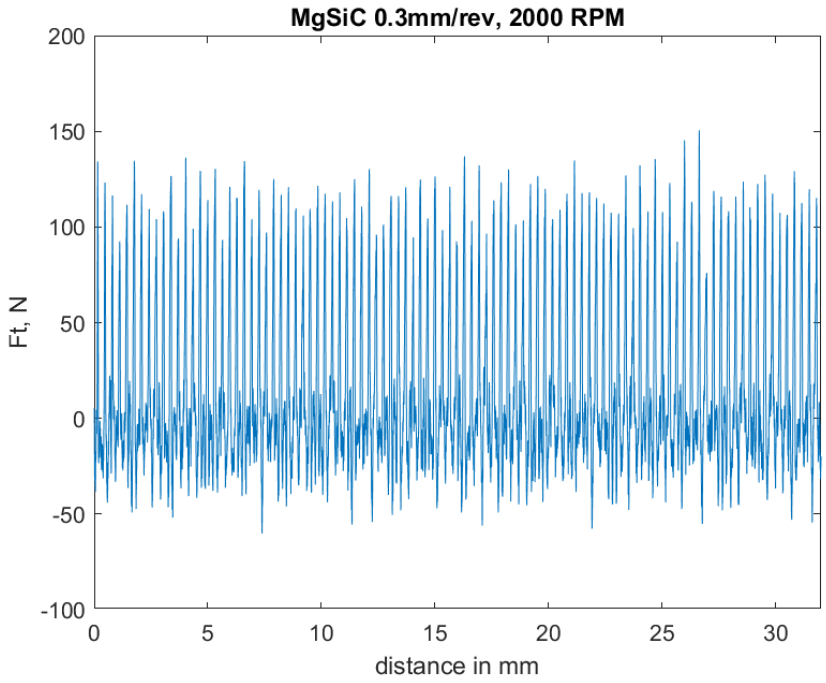
MgSiC 0.3mm/rev, 2000 RPM
Ft, N
distance in mm
200
150
100
50
0
-50
-100
0
5
10
15
20
25
30

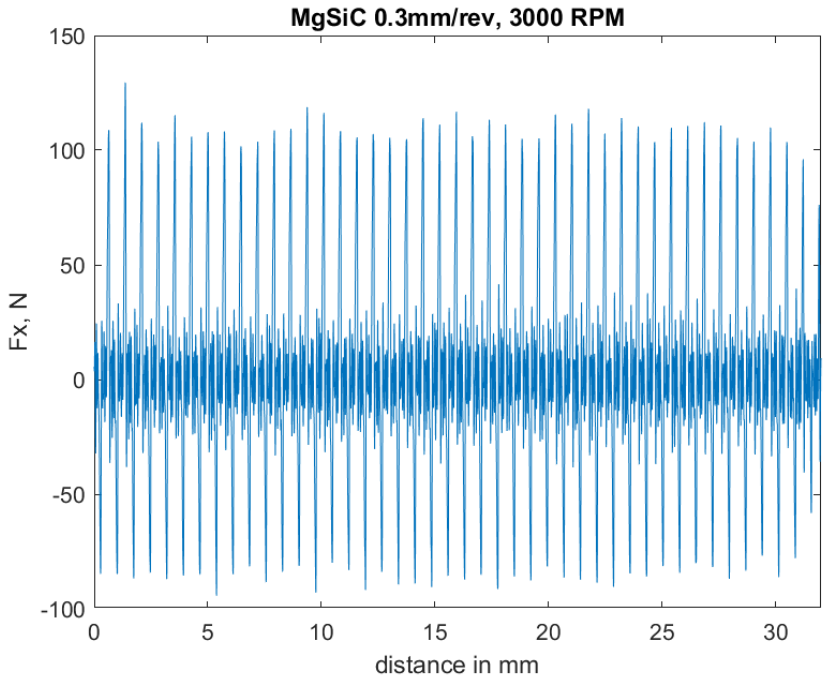
MgSiC 0.3mm/rev, 3000 RPM
Fx, N
distance in mm
150
100
50
0
-50
-100
0
5
10
15
20
25
30

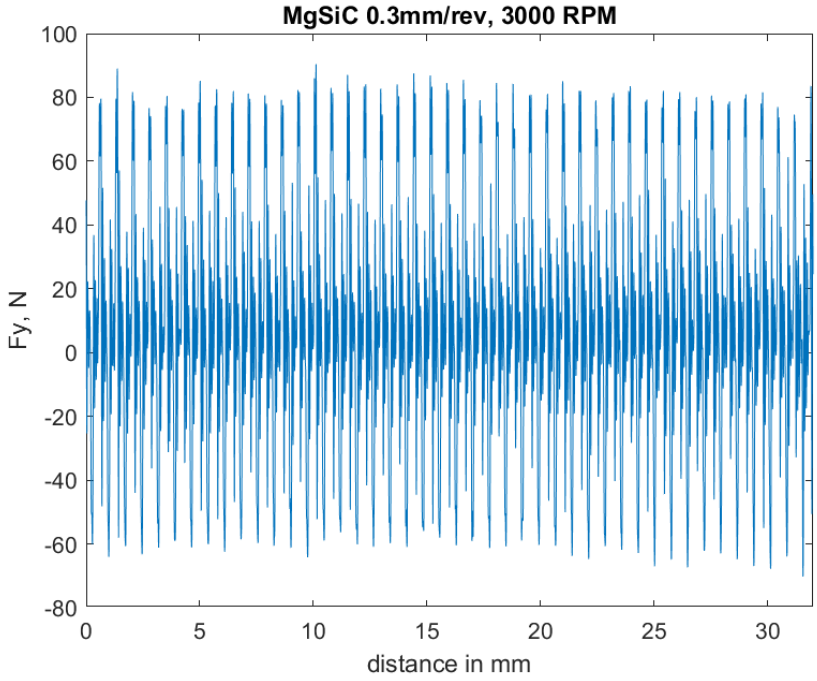
MgSiC 0.3mm/rev, 3000 RPM
Fy, N
distance in mm
100
80
60
40
20
0
-20
-40
-60
-80
0
5
10
15
20
25
30

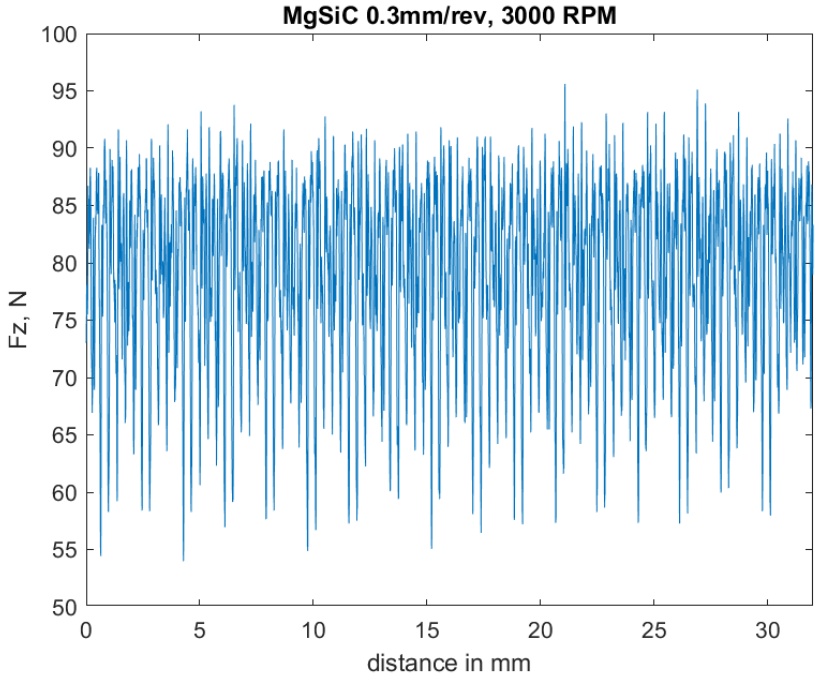
MgSiC 0.3mm/rev, 3000 RPM
Fz, N
distance in mm
100
95
90
85
80
75
70
65
60
55
50
0
5
10
15
20
25
30

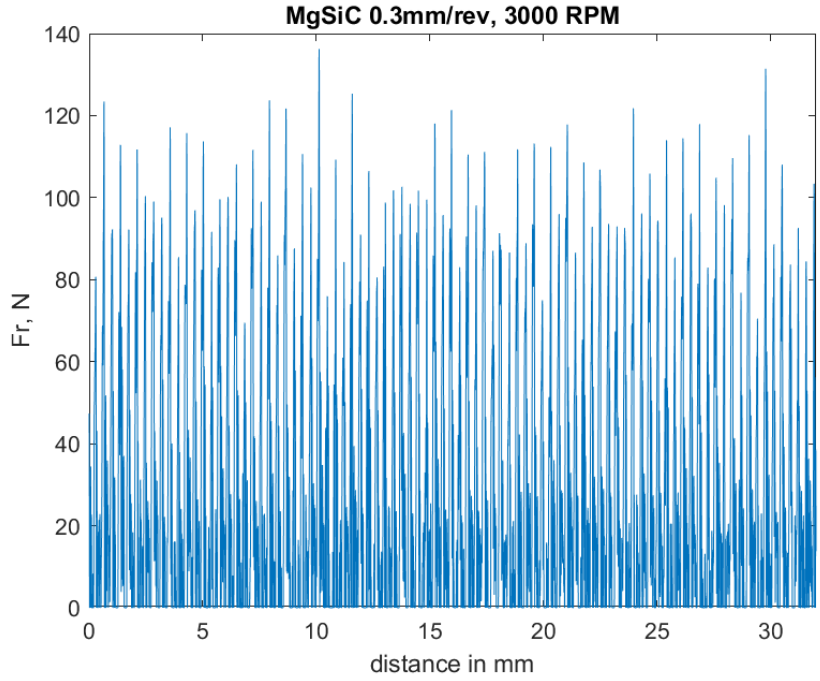
MgSiC 0.3mm/rev, 3000 RPM
Fr, N
distance in mm
0
20
40
60
80
100
120
140
0
5
10
15
20
25
30

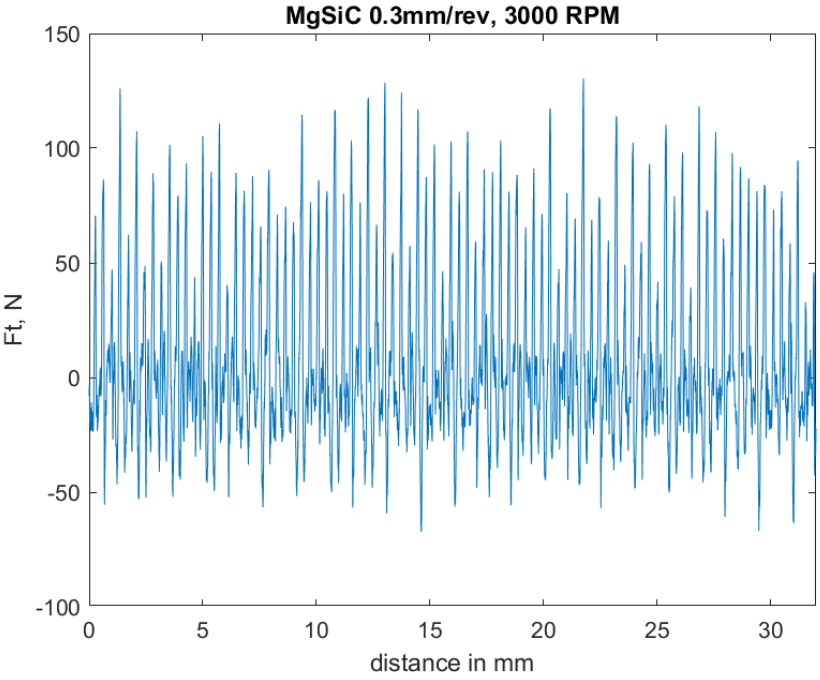
MgSiC 0.3mm/rev, 3000 RPM
Ft, N
distance in mm
-100
-50
0
50
100
150
0
5
10
15
20
25
30

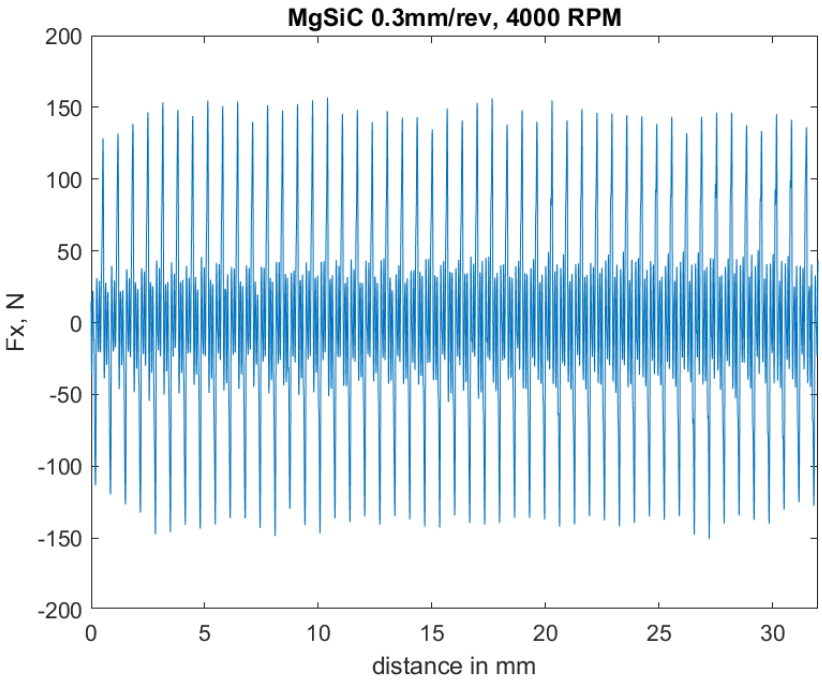
MgSiC 0.3mm/rev, 4000 RPM
Fx, N
distance in mm
200
150
100
50
0
-50
-100
-150
-200
0
5
10
15
20
25
30

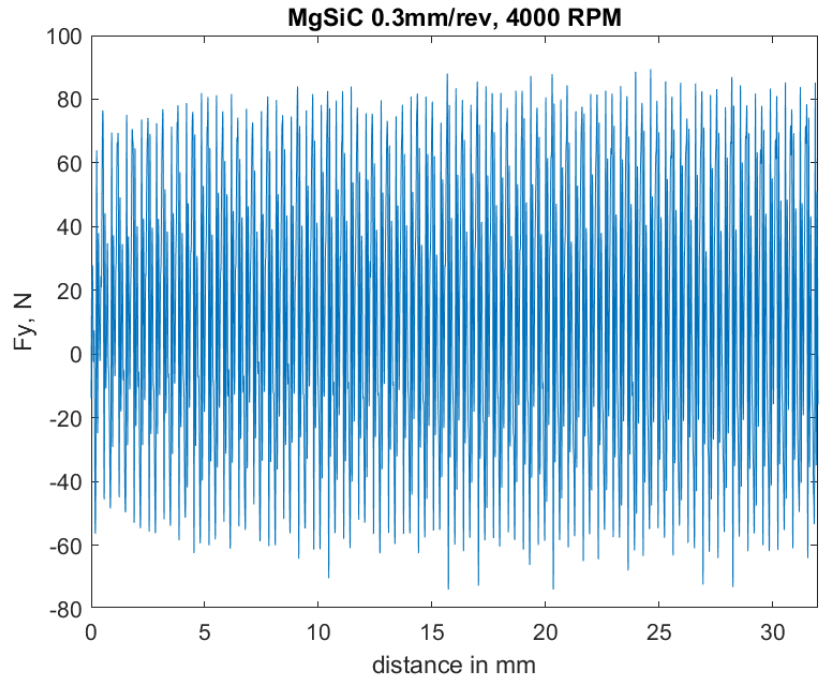
MgSiC 0.3mm/rev, 4000 RPM
Fy, N
distance in mm
100
80
60
40
20
0
-20
-40
-60
-80
0
5
10
15
20
25
30

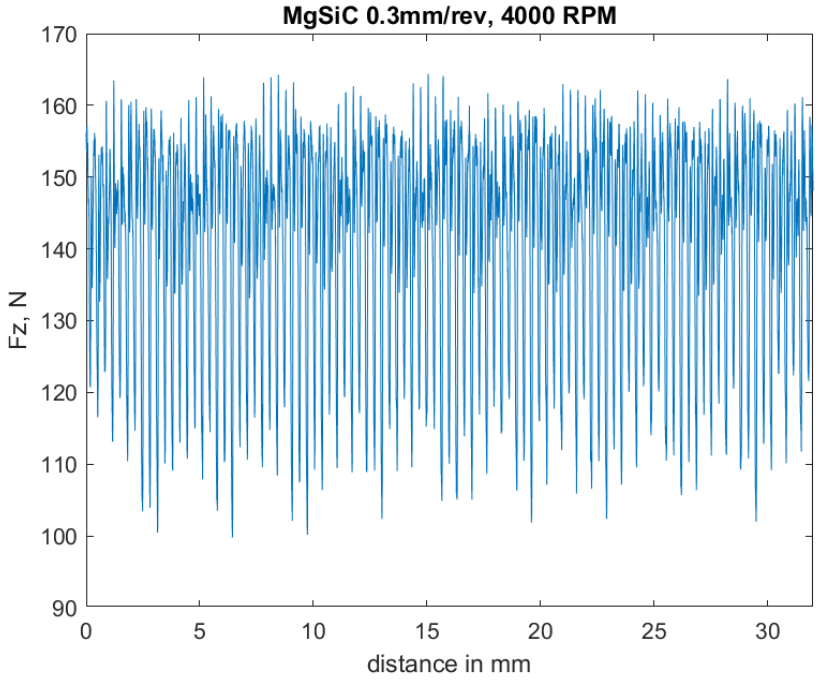
MgSiC 0.3mm/rev, 4000 RPM
Fz, N
distance in mm
170
160
150
140
130
120
110
100
90
0
5
10
15
20
25
30

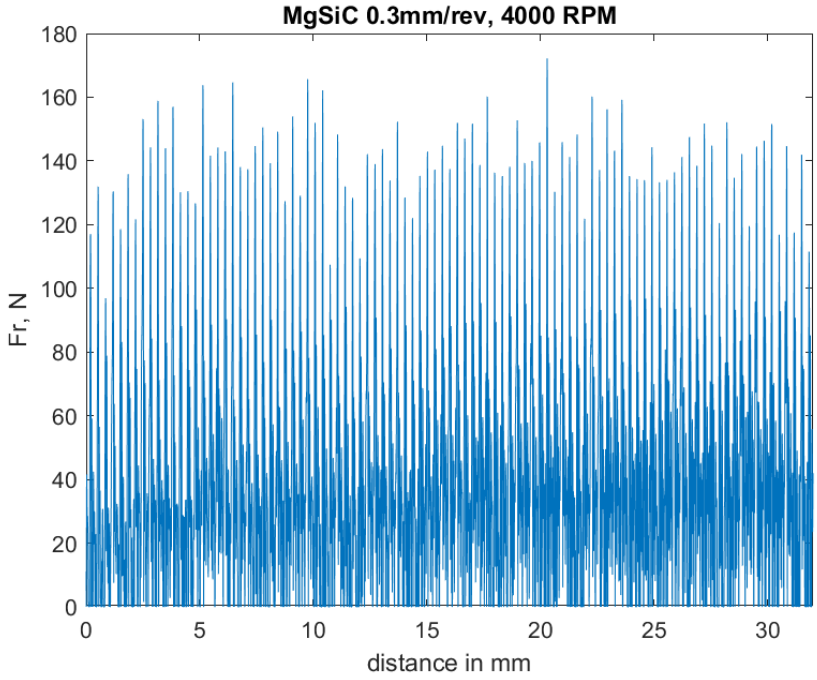
MgSiC 0.3mm/rev, 4000 RPM
Fr, N
distance in mm
180
160
140
120
100
80
60
40
20
0
0
5
10
15
20
25
30

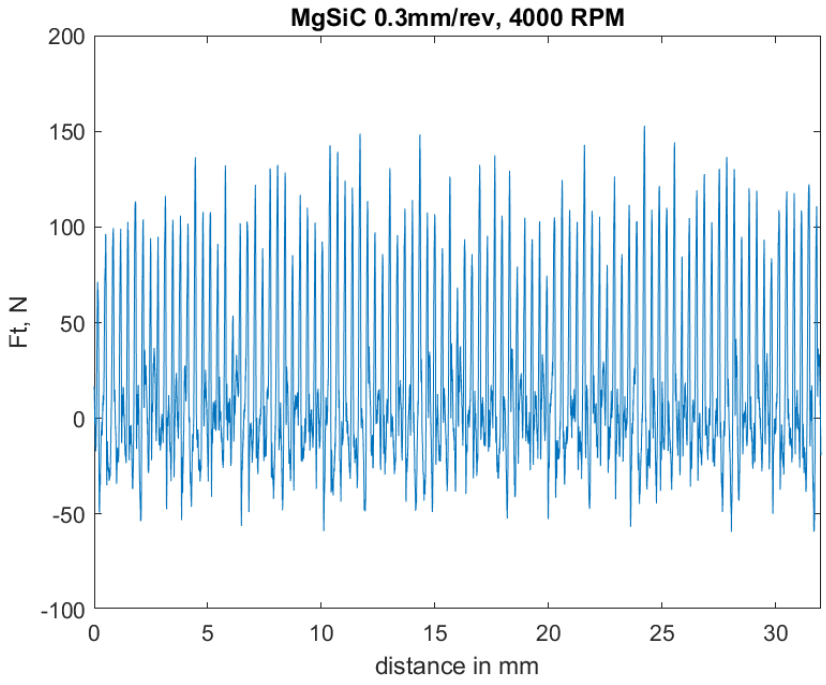
MgSiC 0.3mm/rev, 4000 RPM
Ft, N
distance in mm
200
150
100
50
0
-50
-100
0
5
10
15
20
25
30

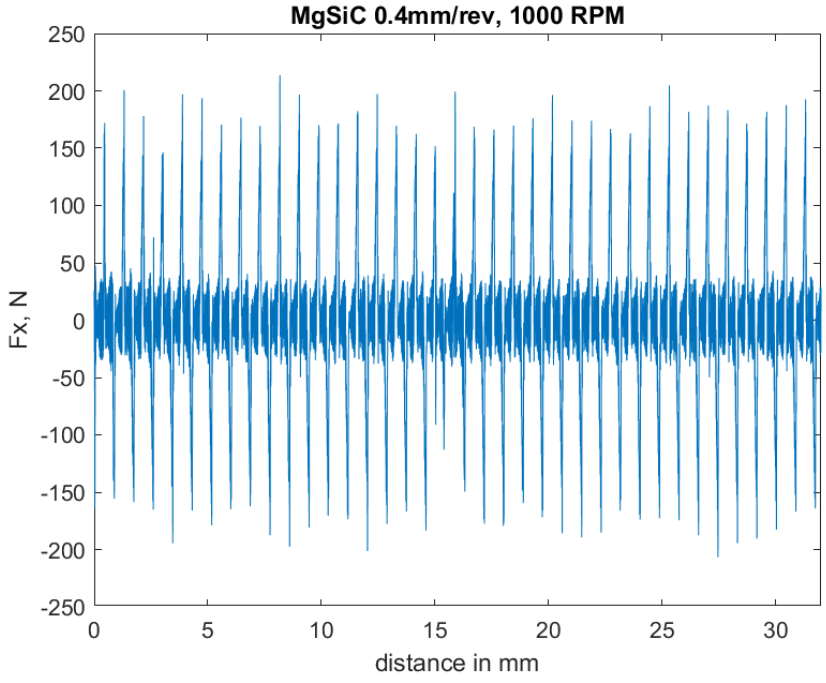
MgSiC 0.4mm/rev, 1000 RPM
Fx, N
distance in mm
250
200
150
100
50
0
-50
-100
-150
-200
-250
0
5
10
15
20
25
30

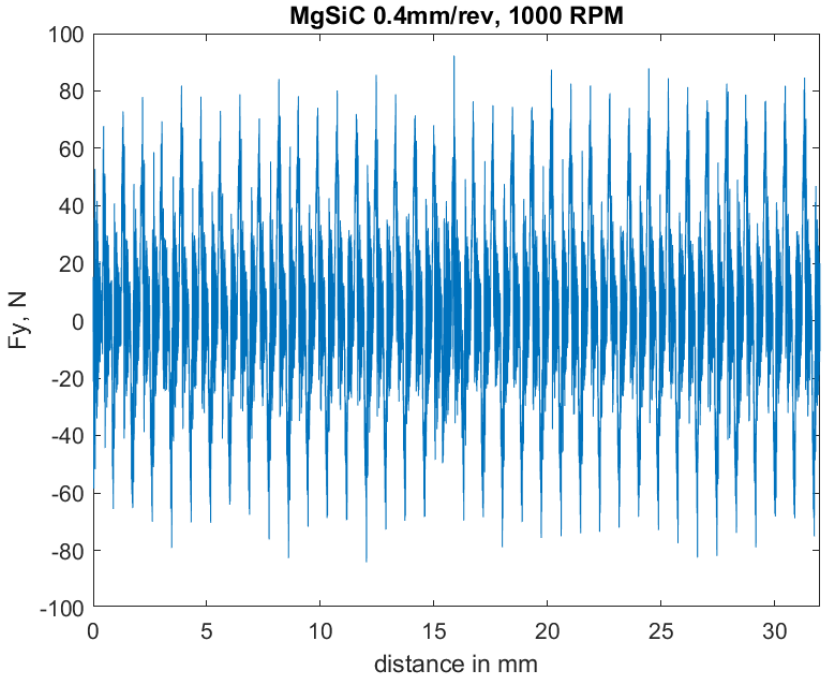
MgSiC 0.4mm/rev, 1000 RPM
Fy, N
distance in mm
100
80
60
40
20
0
-20
-40
-60
-80
-100
0
5
10
15
20
25
30

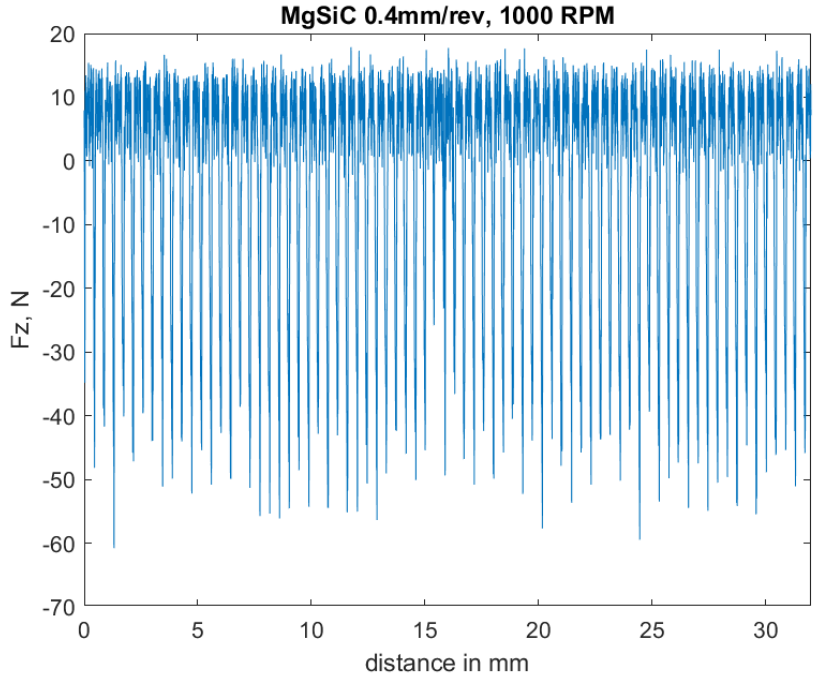
MgSiC 0.4mm/rev, 1000 RPM
Fz, N
distance in mm
20
10
0
-10
-20
-30
-40
-50
-60
-70
0
5
10
15
20
25
30

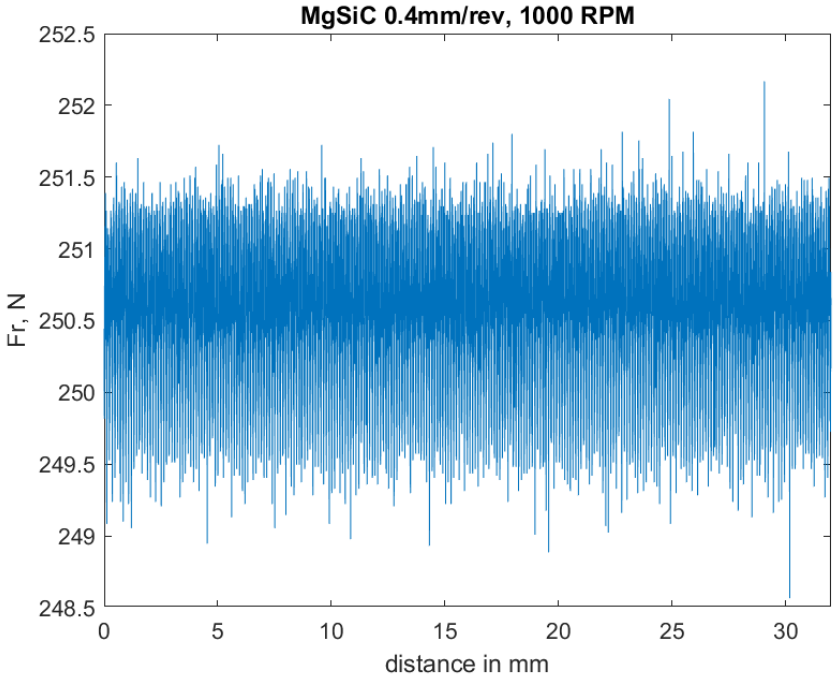
MgSiC 0.4mm/rev, 1000 RPM
Fr, N
252.5
252
251.5
251
250.5
250
249.5
249
248.5
0
5
10
15
20
25
30
distance in mm

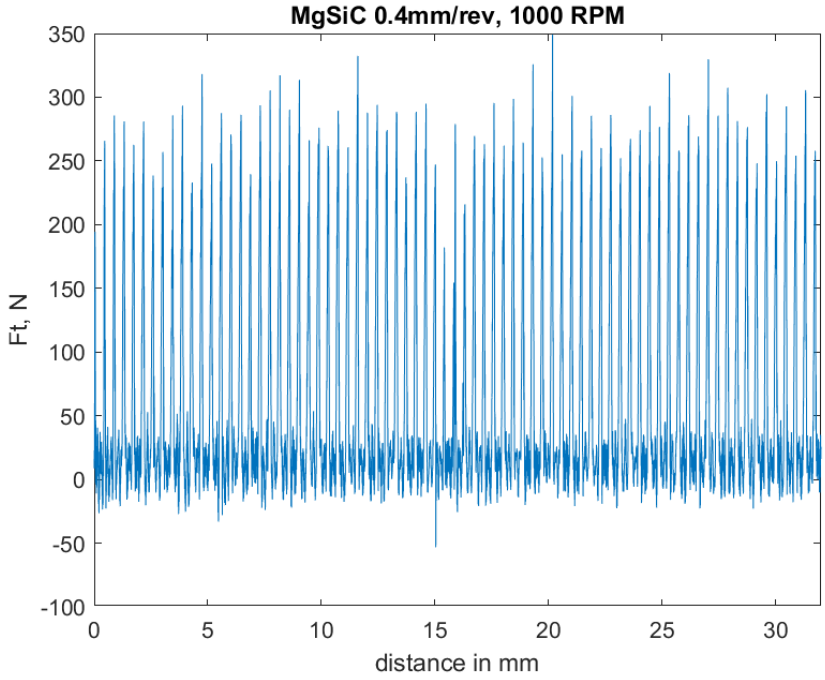
MgSiC 0.4mm/rev, 1000 RPM
Ft, N
350
300
250
200
150
100
50
0
-50
-100
0
5
10
15
20
25
30
distance in mm

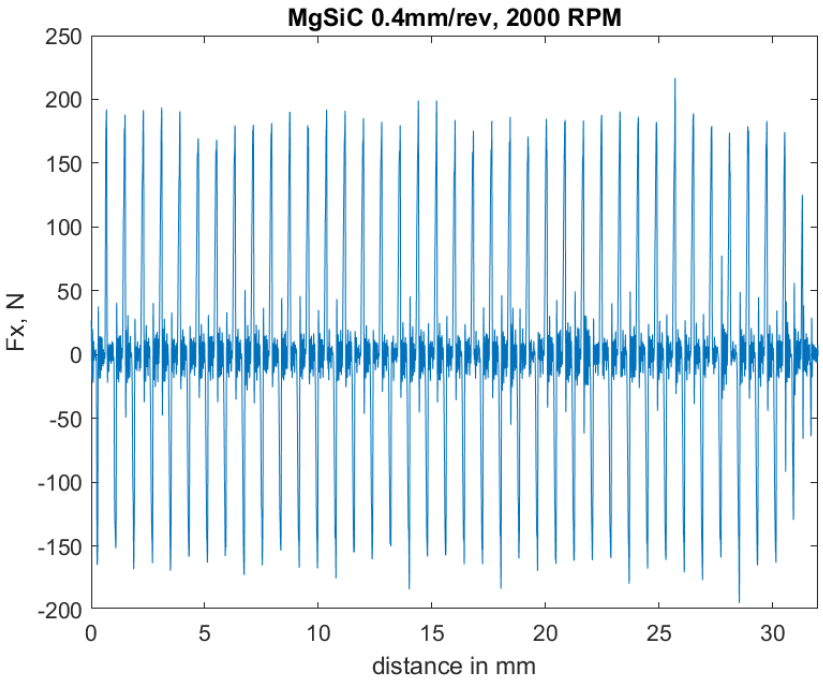
MgSiC 0.4mm/rev, 2000 RPM
Fx, N
250
200
150
100
50
0
-50
-100
-150
-200
0
5
10
15
20
25
30
distance in mm

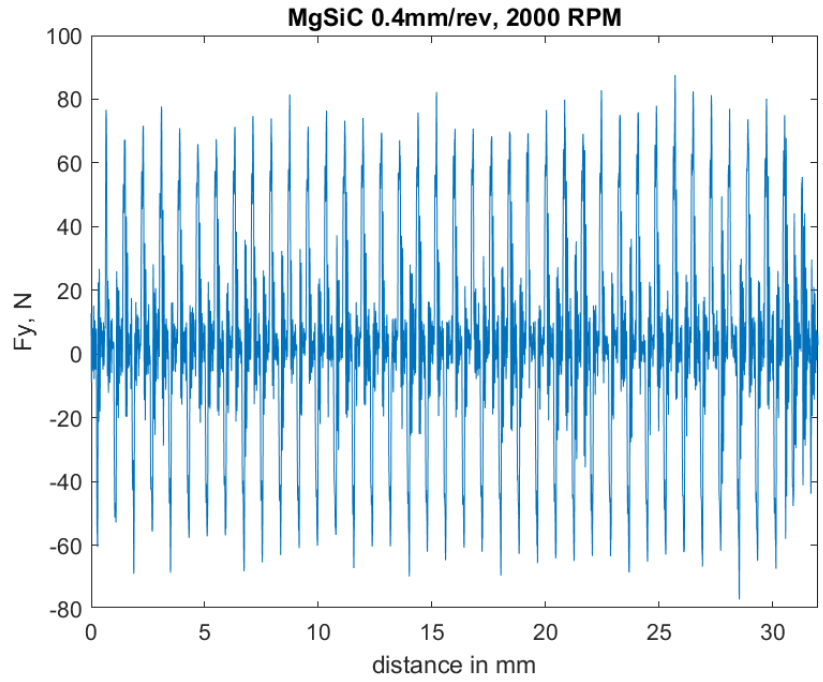
MgSiC 0.4mm/rev, 2000 RPM
Fy, N
100
80
60
40
20
0
-20
-40
-60
-80
0
5
10
15
20
25
30
distance in mm

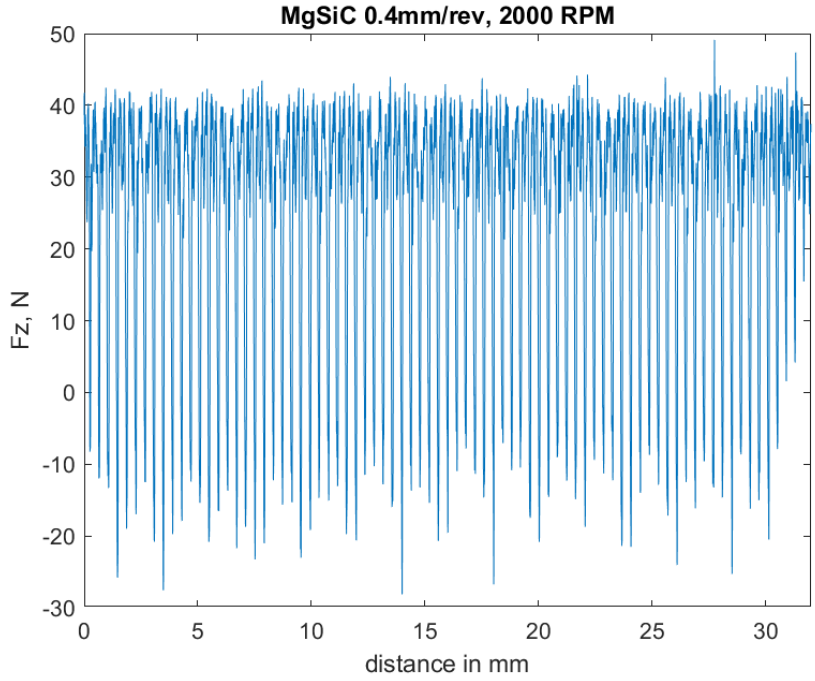
MgSiC 0.4mm/rev, 2000 RPM
Fz, N
distance in mm
50
40
30
20
10
0
-10
-20
-30
0
5
10
15
20
25
30

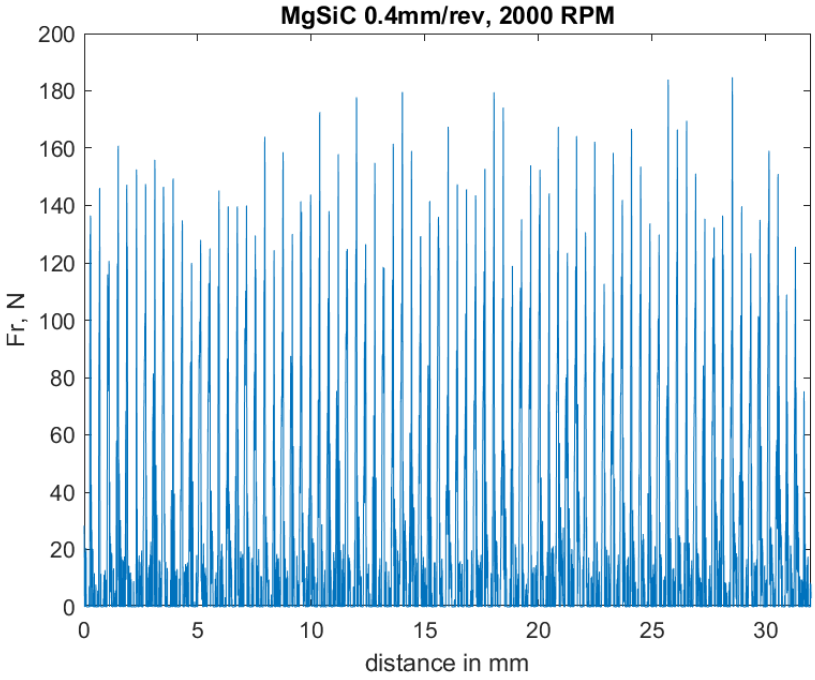
MgSiC 0.4mm/rev, 2000 RPM
Fr, N
distance in mm
200
180
160
140
120
100
80
60
40
20
0
0
5
10
15
20
25
30

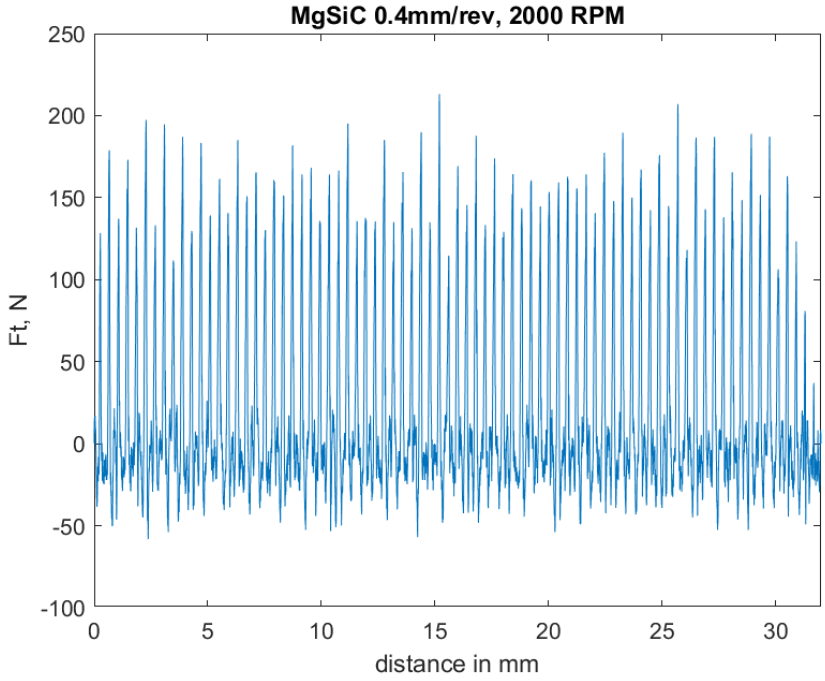
MgSiC 0.4mm/rev, 2000 RPM
Ft, N
250
200
150
100
50
0
-50
-100
0
5
10
15
20
25
30
distance in mm

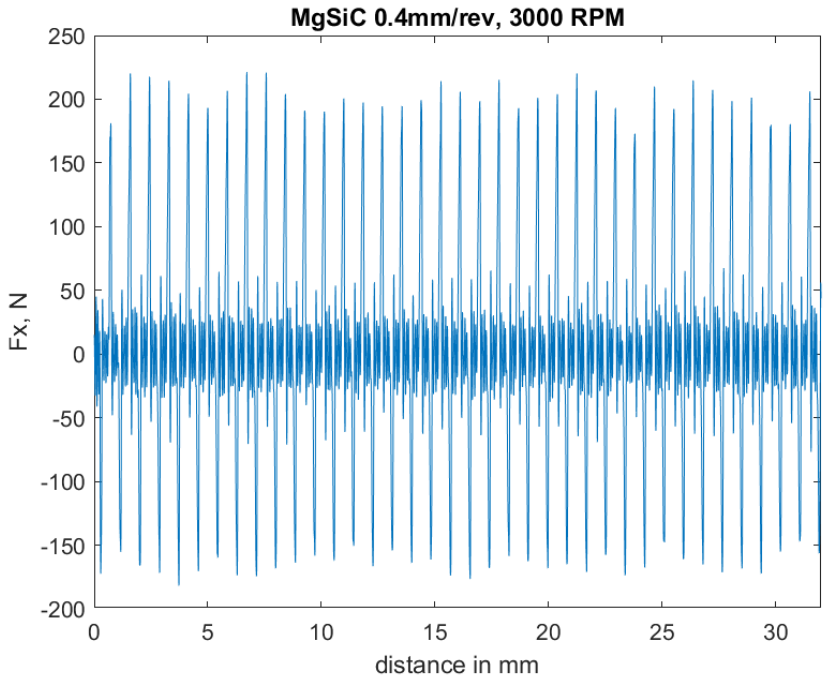
MgSiC 0.4mm/rev, 3000 RPM
Fx, N
250
200
150
100
50
0
-50
-100
-150
-200
0
5
10
15
20
25
30
distance in mm

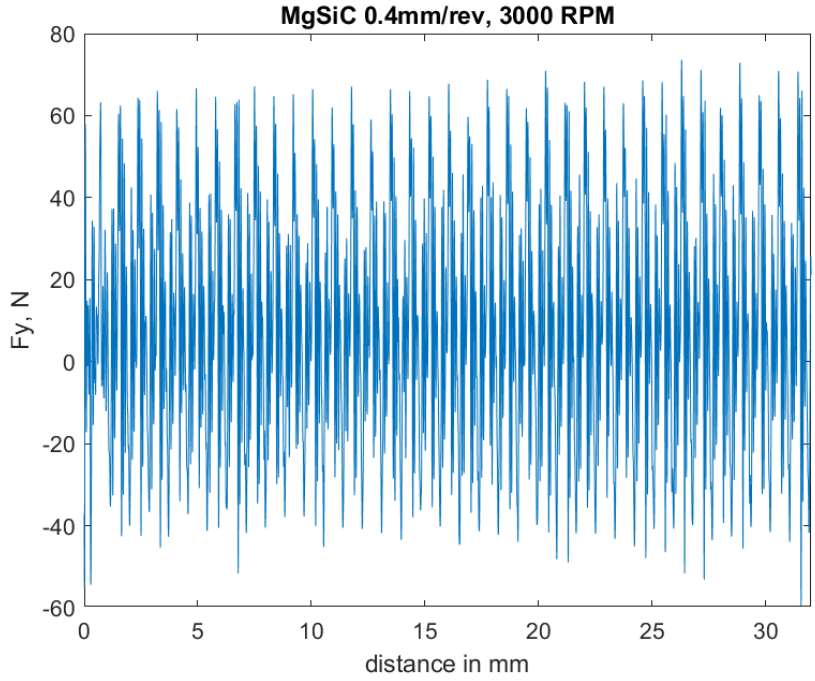
MgSiC 0.4mm/rev, 3000 RPM
Fy, N
distance in mm
80
60
40
20
0
-20
-40
-60
0
5
10
15
20
25
30

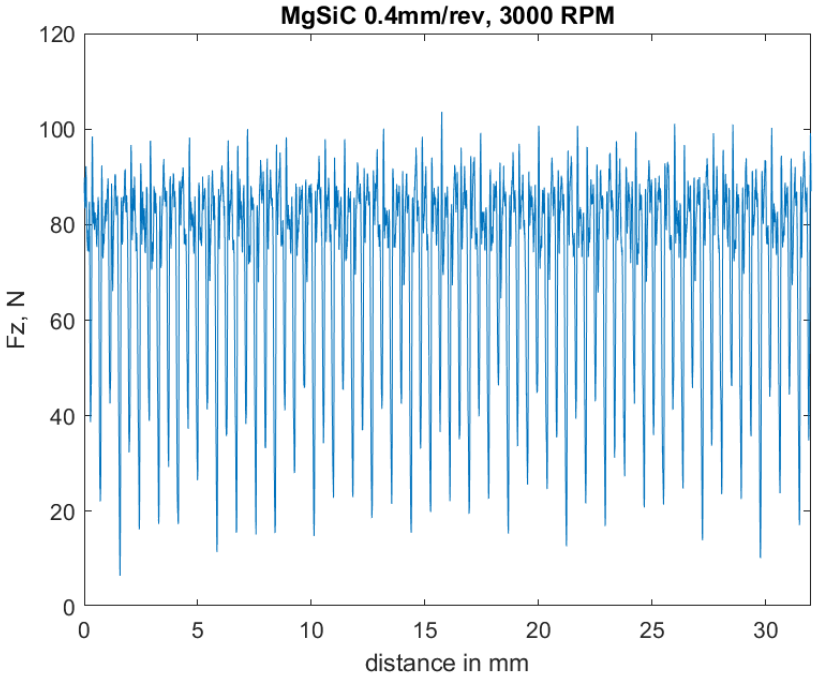
MgSiC 0.4mm/rev, 3000 RPM
Fz, N
distance in mm
120
100
80
60
40
20
0
0
5
10
15
20
25
30

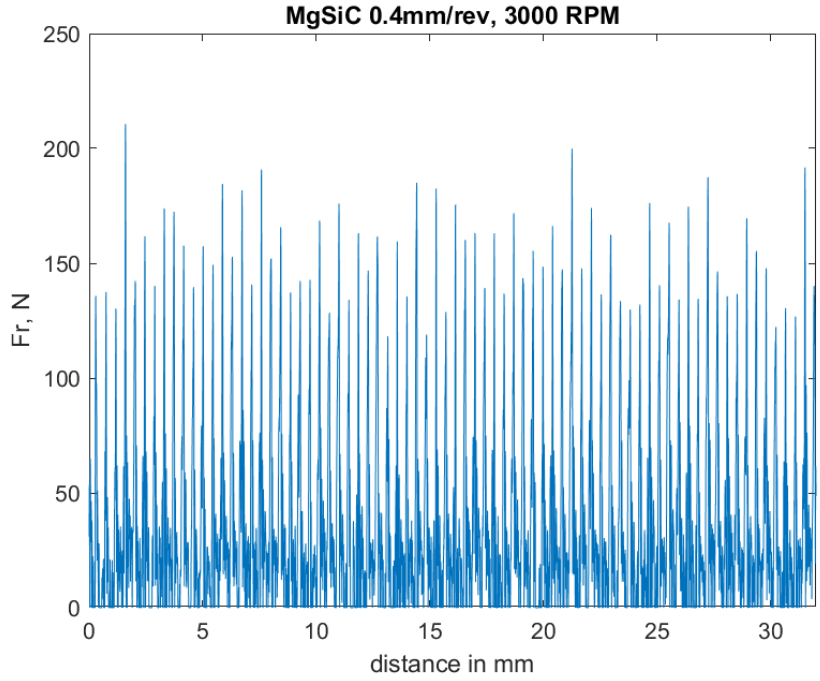
MgSiC 0.4mm/rev, 3000 RPM
Fr, N
250
200
150
100
50
0
0
5
10
15
20
25
30
distance in mm

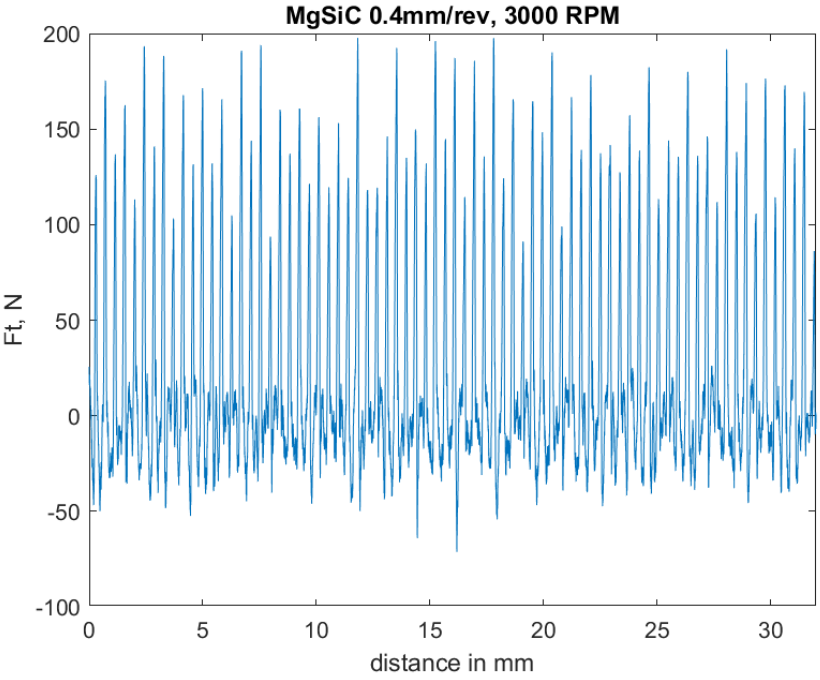
MgSiC 0.4mm/rev, 3000 RPM
Ft, N
200
150
100
50
0
-50
-100
0
5
10
15
20
25
30
distance in mm

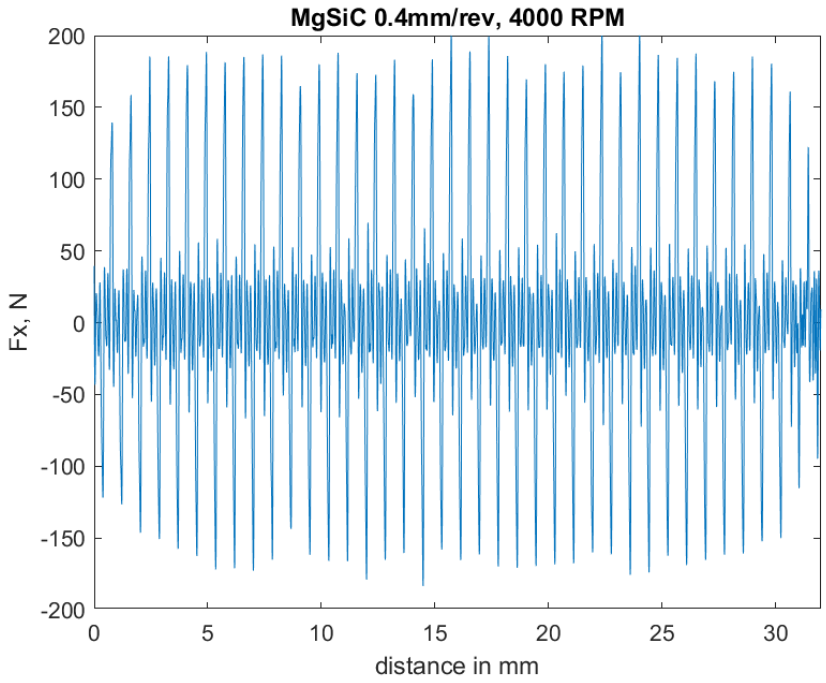
MgSiC 0.4mm/rev, 4000 RPM
Fx, N
distance in mm
200
150
100
50
0
-50
-100
-150
-200
0
5
10
15
20
25
30

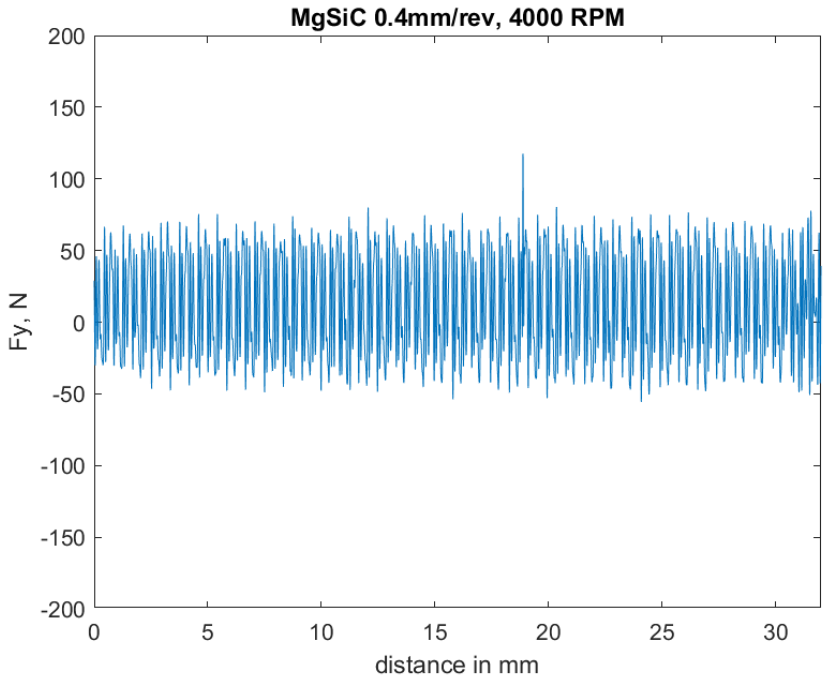
MgSiC 0.4mm/rev, 4000 RPM
Fy, N
distance in mm
200
150
100
50
0
-50
-100
-150
-200
0
5
10
15
20
25
30

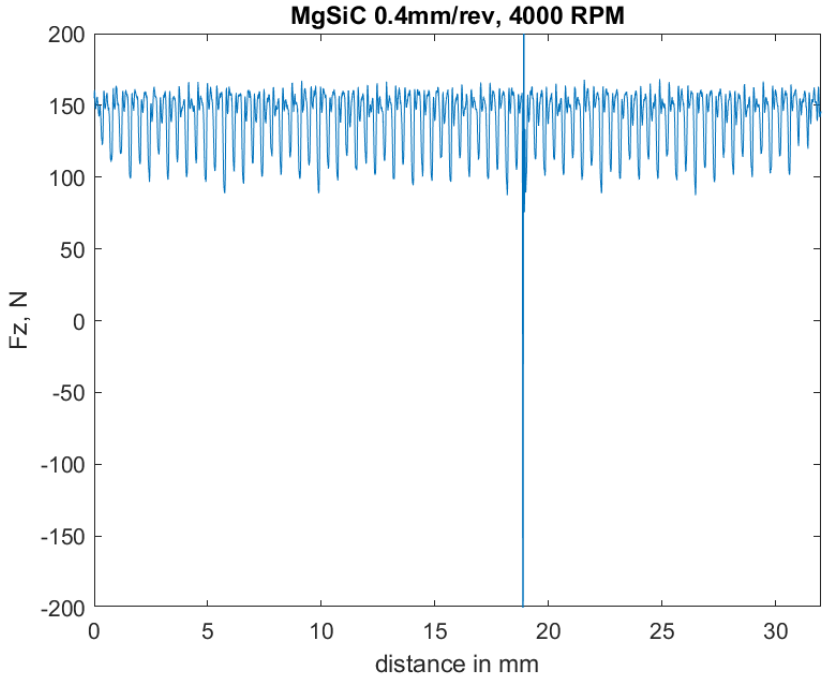
MgSiC 0.4mm/rev, 4000 RPM
Fz, N
distance in mm
200
150
100
50
0
-50
-100
-150
-200
0
5
10
15
20
25
30

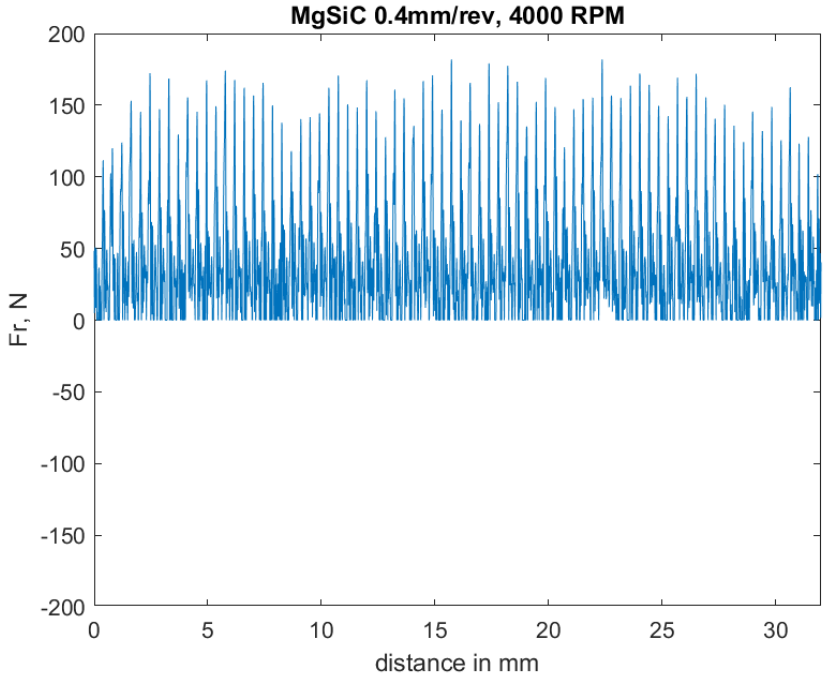
MgSiC 0.4mm/rev, 4000 RPM
Fr, N
distance in mm
200
150
100
50
0
-50
-100
-150
-200
0
5
10
15
20
25
30

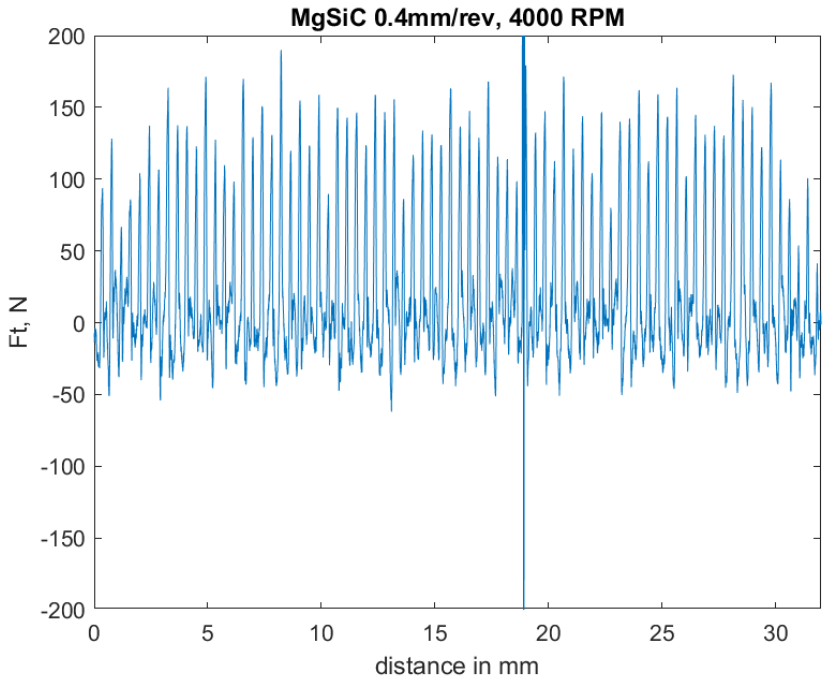
MgSiC 0.4mm/rev, 4000 RPM
Ft, N
distance in mm
200
150
100
50
0
-50
-100
-150
-200
0
5
10
15
20
25
30
0.9em

B.2.2 Acoustic emission

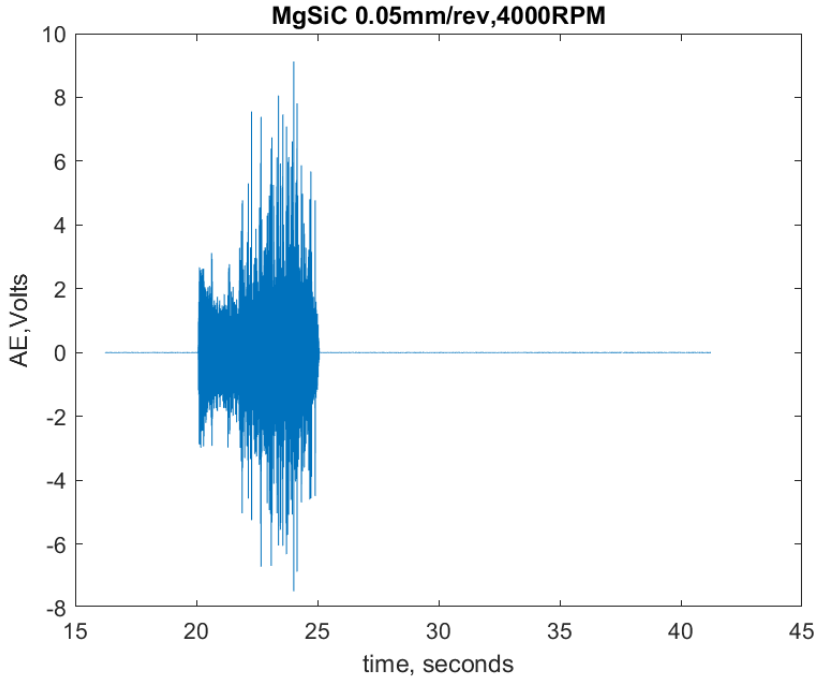

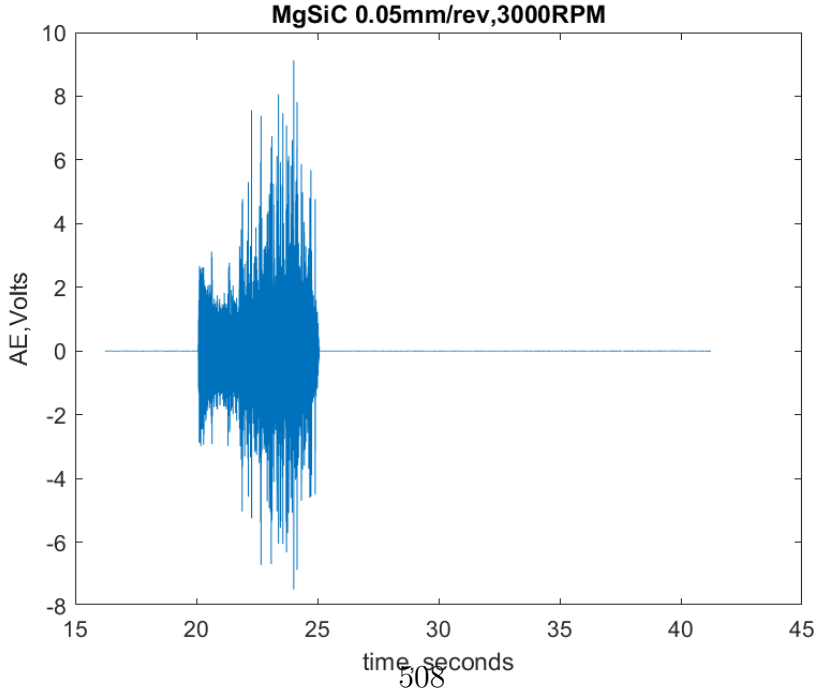

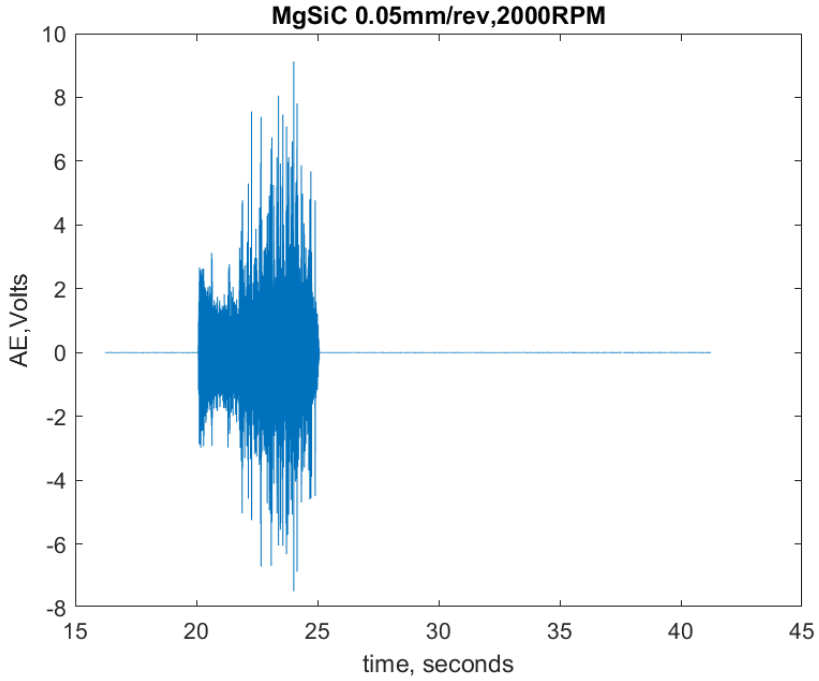
MgSiC 0.05mm/rev,2000RPM
AE,Volts
time, seconds
10
8
6
4
2
0
-2
-4
-6
-8
15
20
25
30
35
40
45

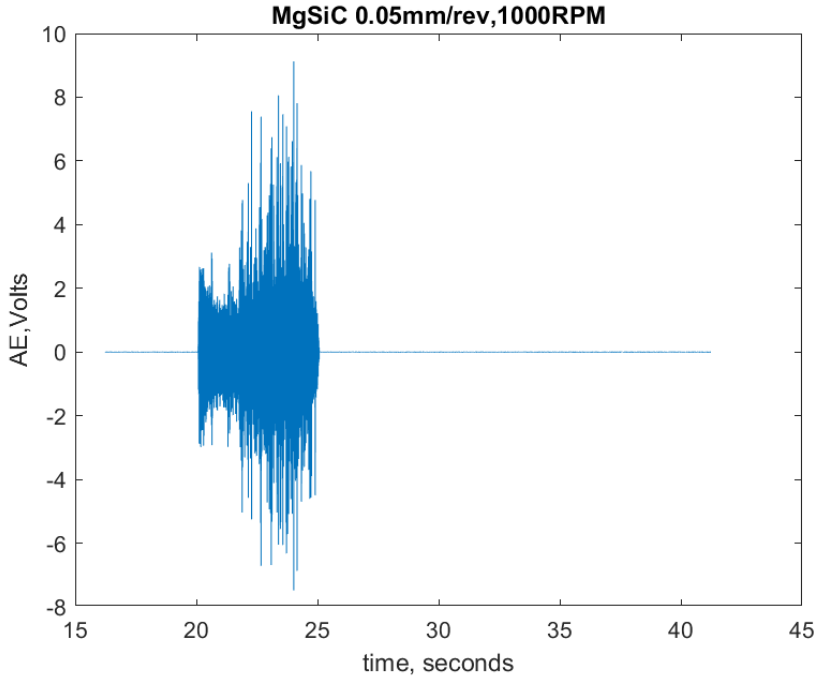
MgSiC 0.05mm/rev,1000RPM
AE,Volts
time, seconds
10
8
6
4
2
0
-2
-4
-6
-8
15
20
25
30
35
40
45

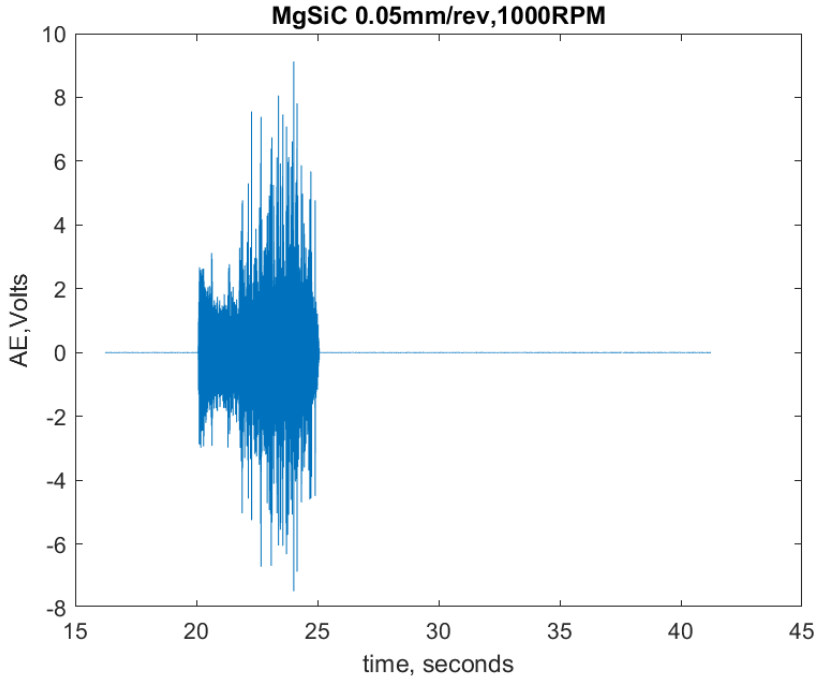
MgSiC 0.05mm/rev,1000RPM
AE,Volts
time, seconds
10
8
6
4
2
0
-2
-4
-6
-8
15
20
25
30
35
40
45

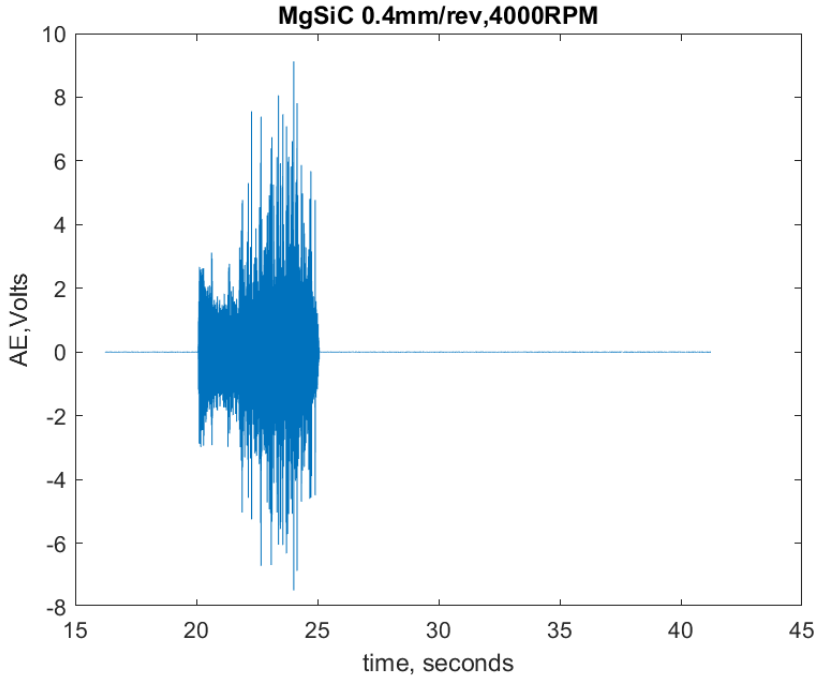
MgSiC 0.4mm/rev,4000RPM
AE,Volts
time, seconds
10
8
6
4
2
0
-2
-4
-6
-8
15
20
25
30
35
40
45

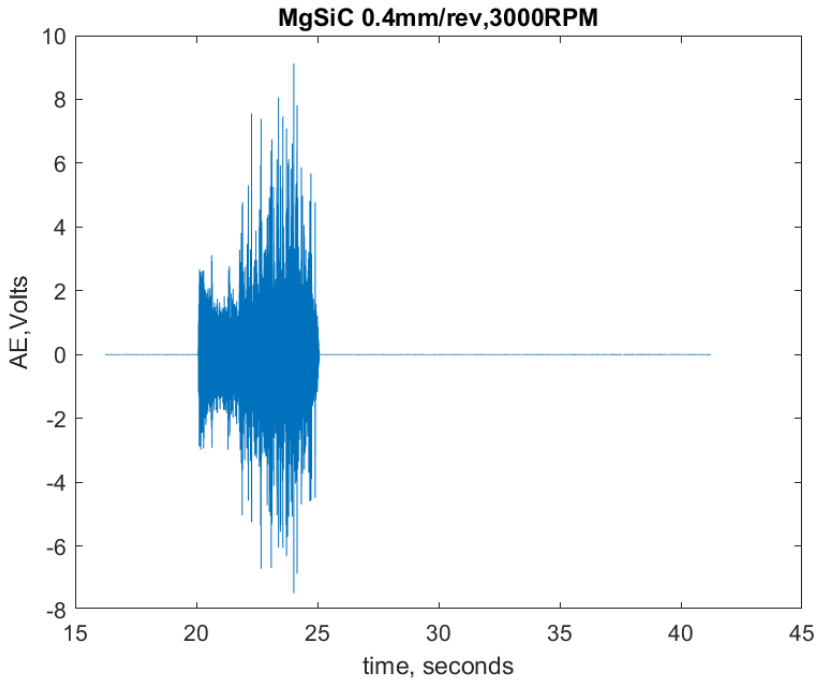
MgSiC 0.4mm/rev,3000RPM
AE,Volts
time, seconds
10
8
6
4
2
0
-2
-4
-6
-8
15
20
25
30
35
40
45

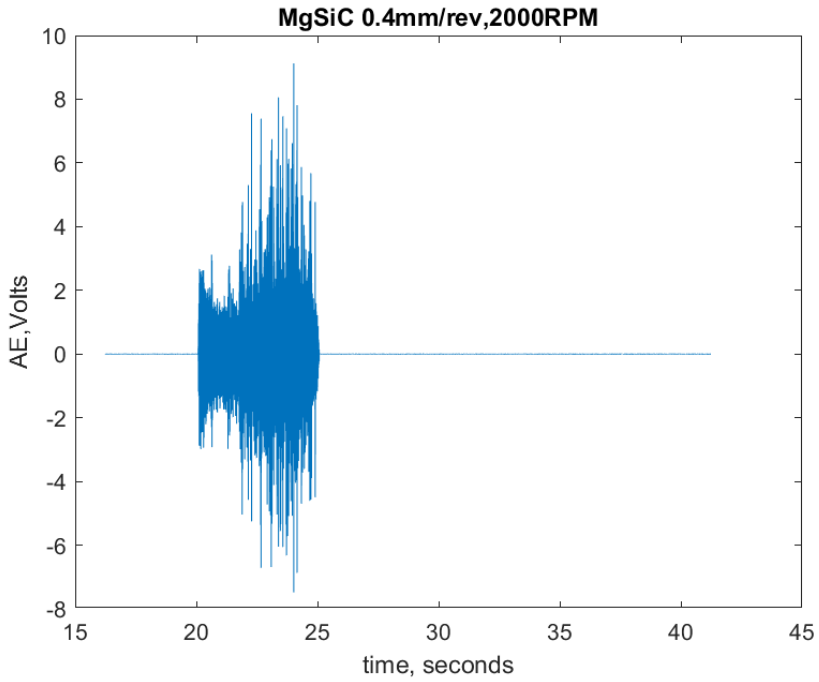
MgSiC 0.4mm/rev,2000RPM
AE,Volts
time, seconds
10
8
6
4
2
0
-2
-4
-6
-8
15
20
25
30
35
40
45

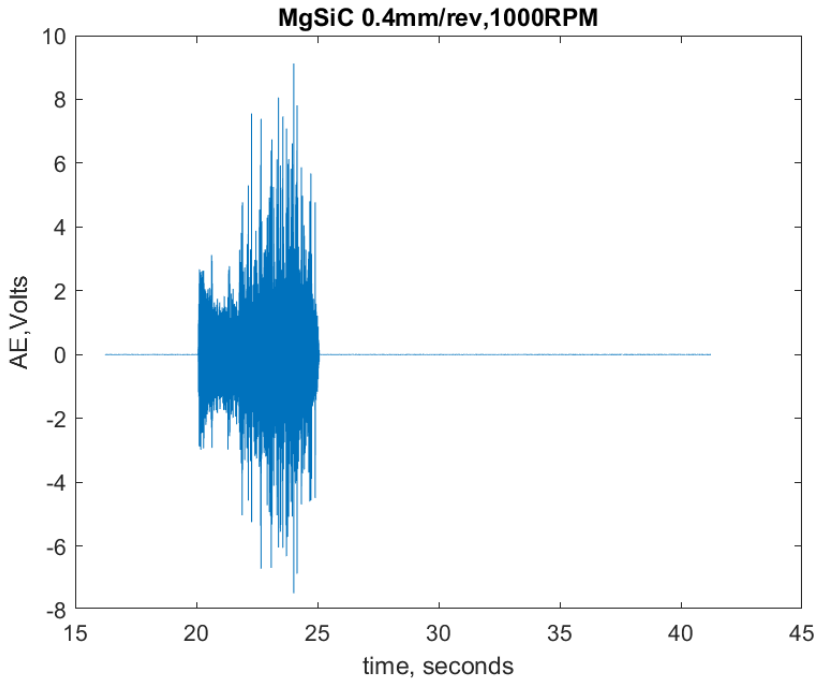
MgSiC 0.4mm/rev,1000RPM
AE,Volts
time, seconds
10
8
6
4
2
0
-2
-4
-6
-8
15
20
25
30
35
40
45

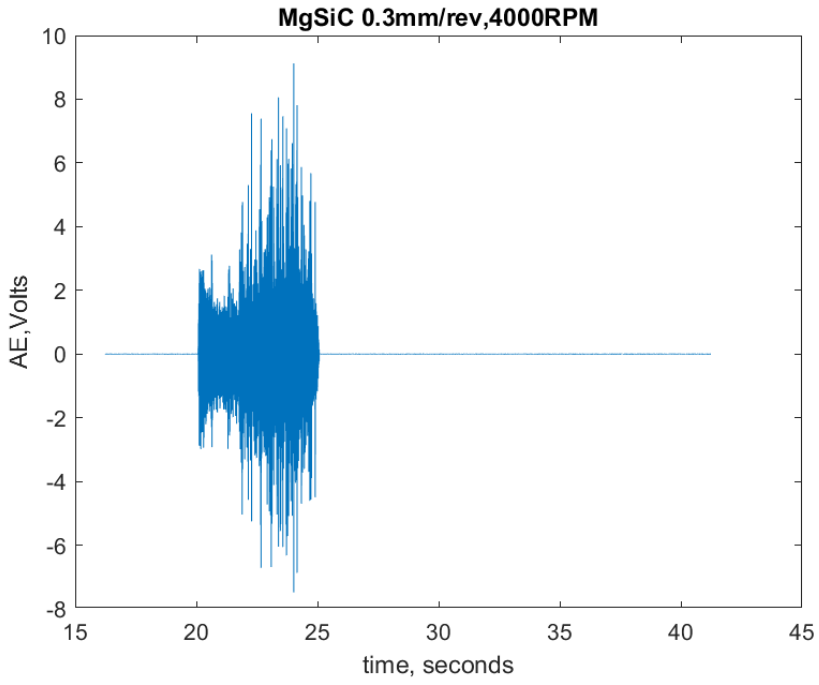
MgSiC 0.3mm/rev,4000RPM
AE,Volts
time, seconds
10
8
6
4
2
0
-2
-4
-6
-8
15
20
25
30
35
40
45

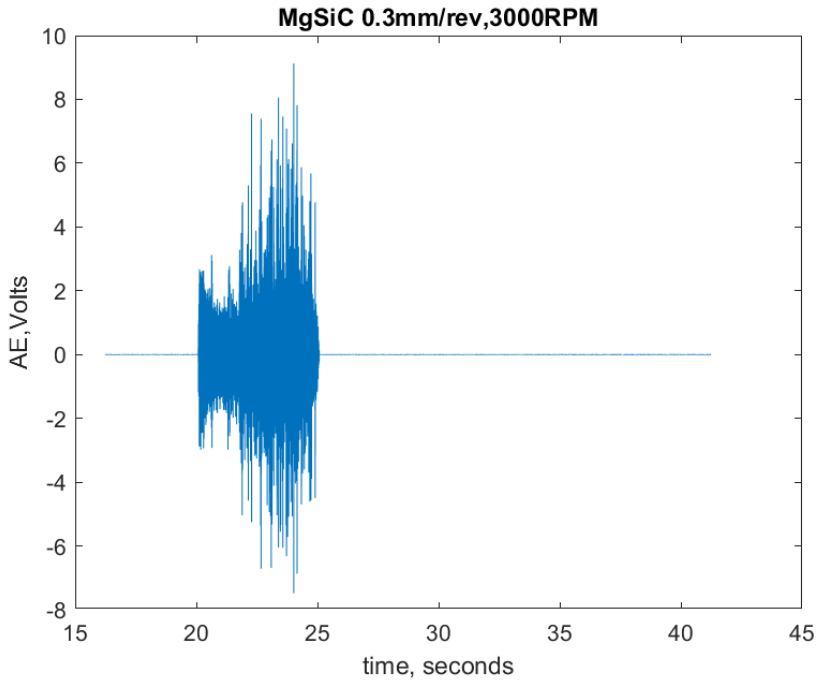
MgSiC 0.3mm/rev,3000RPM
AE,Volts
time, seconds
10
8
6
4
2
0
-2
-4
-6
-8
15
20
25
30
35
40
45

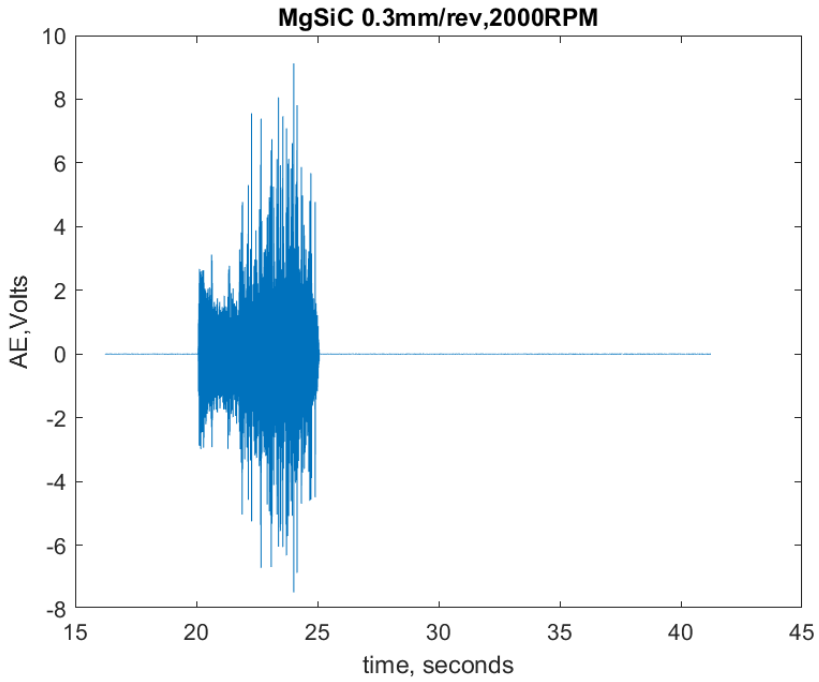
MgSiC 0.3mm/rev,2000RPM
AE,Volts
time, seconds
10
8
6
4
2
0
-2
-4
-6
-8
15
20
25
30
35
40
45

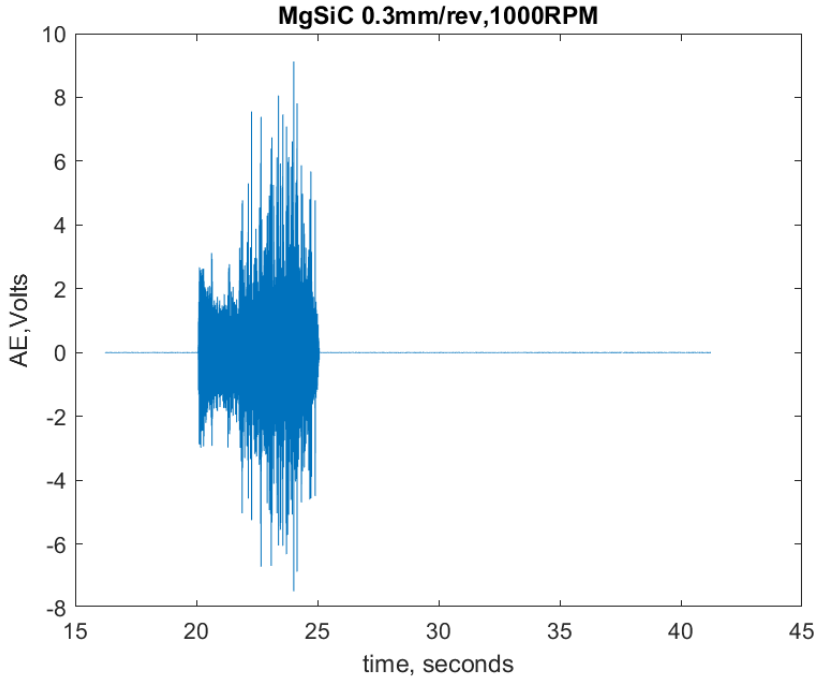
MgSiC 0.3mm/rev,1000RPM
AE,Volts
time, seconds
10
8
6
4
2
0
-2
-4
-6
-8
15
20
25
30
35
40
45

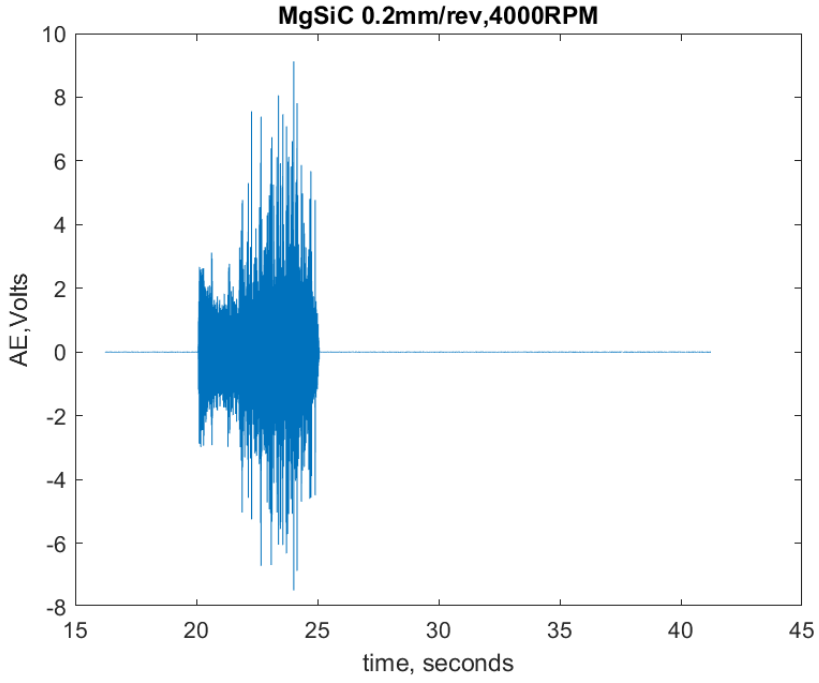
MgSiC 0.2mm/rev,4000RPM
AE,Volts
time, seconds
10
8
6
4
2
0
-2
-4
-6
-8
15
20
25
30
35
40
45

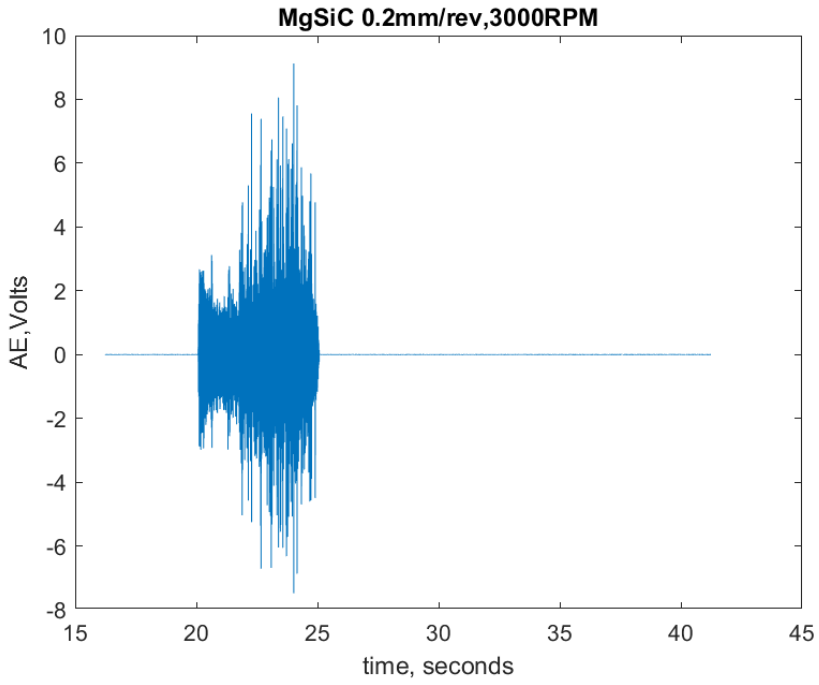
MgSiC 0.2mm/rev,3000RPM
AE,Volts
time, seconds
10
8
6
4
2
0
-2
-4
-6
-8
15
20
25
30
35
40
45

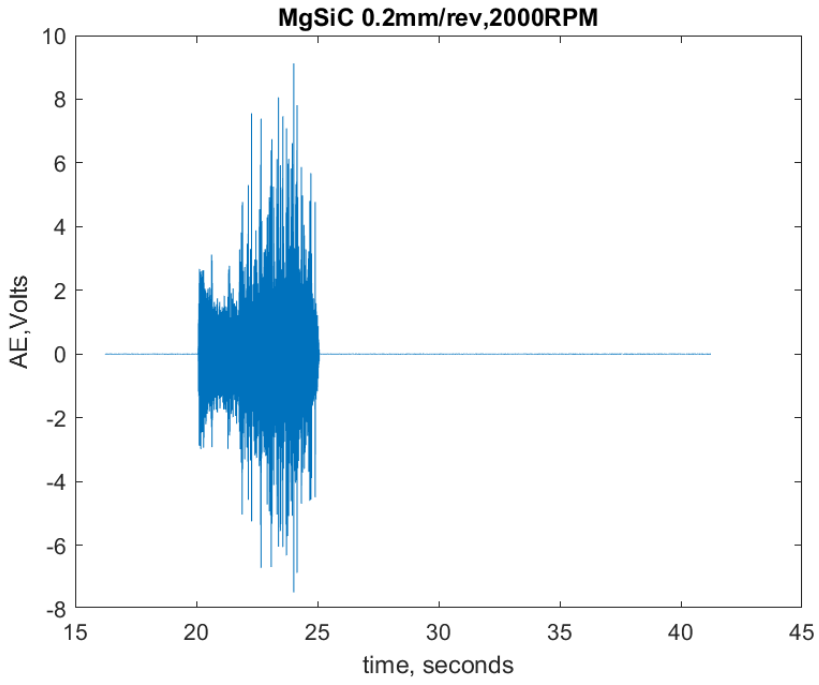
MgSiC 0.2mm/rev,2000RPM
AE,Volts
time, seconds
10
8
6
4
2
0
-2
-4
-6
-8
15
20
25
30
35
40
45

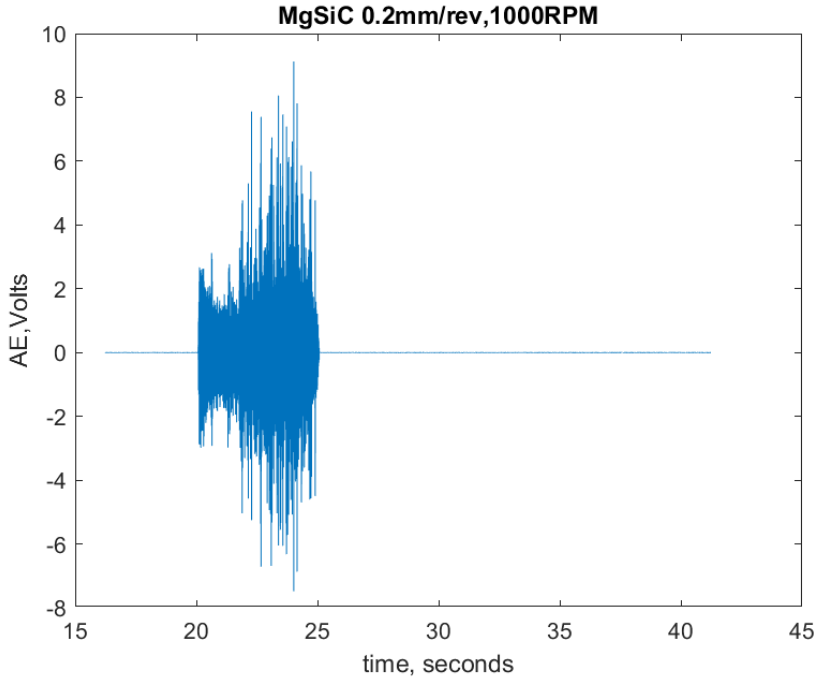
MgSiC 0.2mm/rev,1000RPM
AE,Volts
time, seconds
10
8
6
4
2
0
-2
-4
-6
-8
15
20
25
30
35
40
45

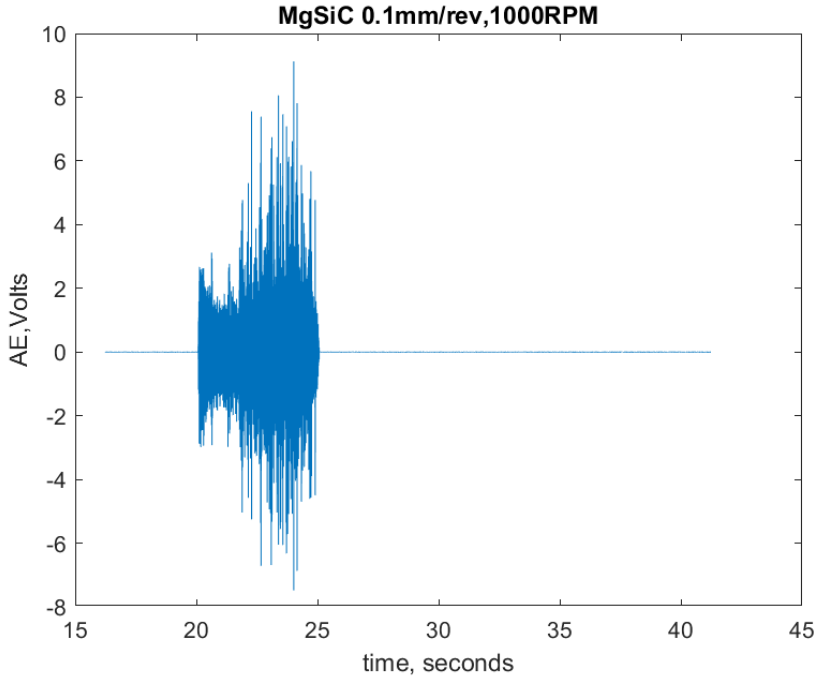
MgSiC 0.1mm/rev,1000RPM
AE,Volts
time, seconds
10
8
6
4
2
0
-2
-4
-6
-8
15
20
25
30
35
40
45

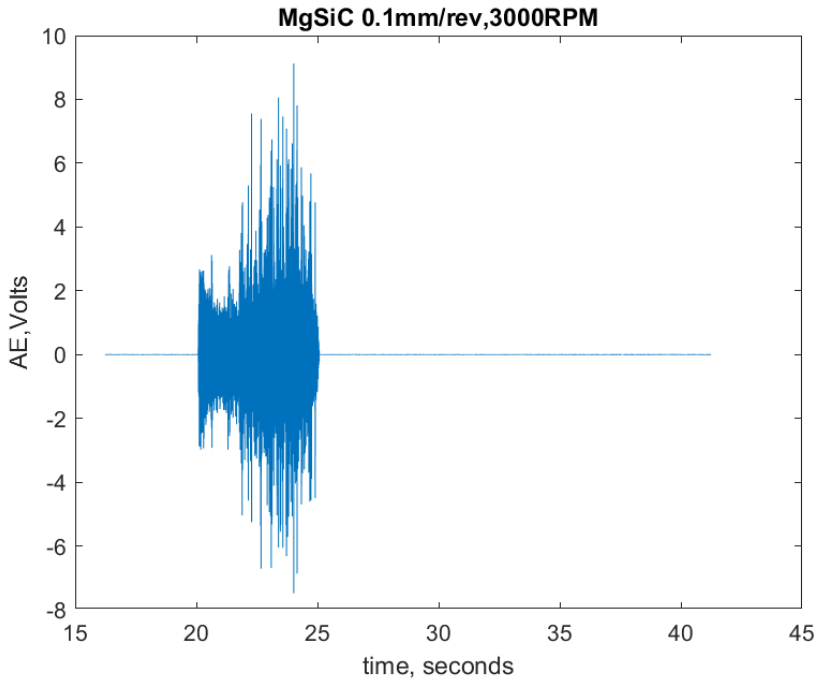
MgSiC 0.1mm/rev,3000RPM
AE,Volts
time, seconds
10
8
6
4
2
0
-2
-4
-6
-8
15
20
25
30
35
40
45
1.5em

B.2.3 Tool Wear

0.5 mm/rev, 4000 RPM

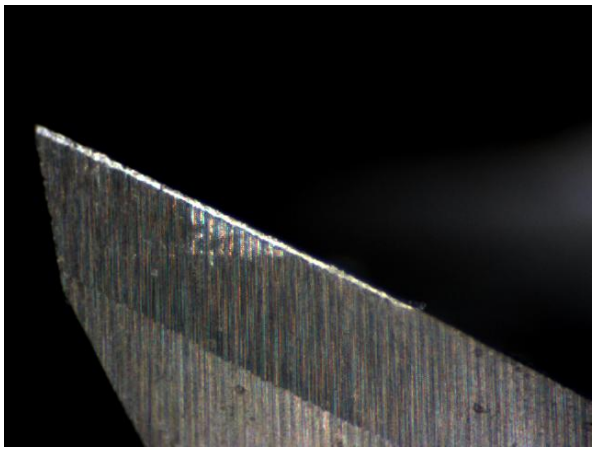



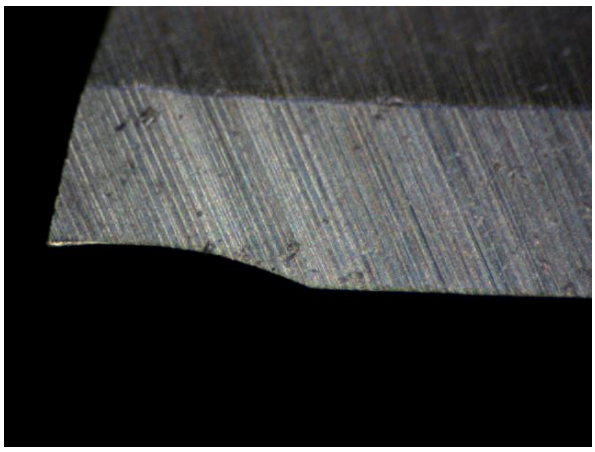

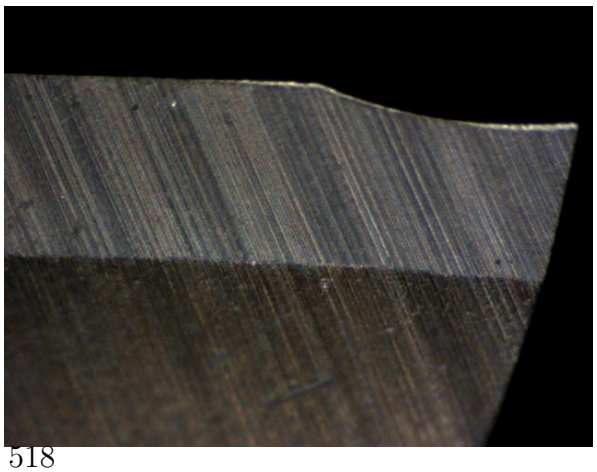

0.5 mm/rev, 4000 RPM

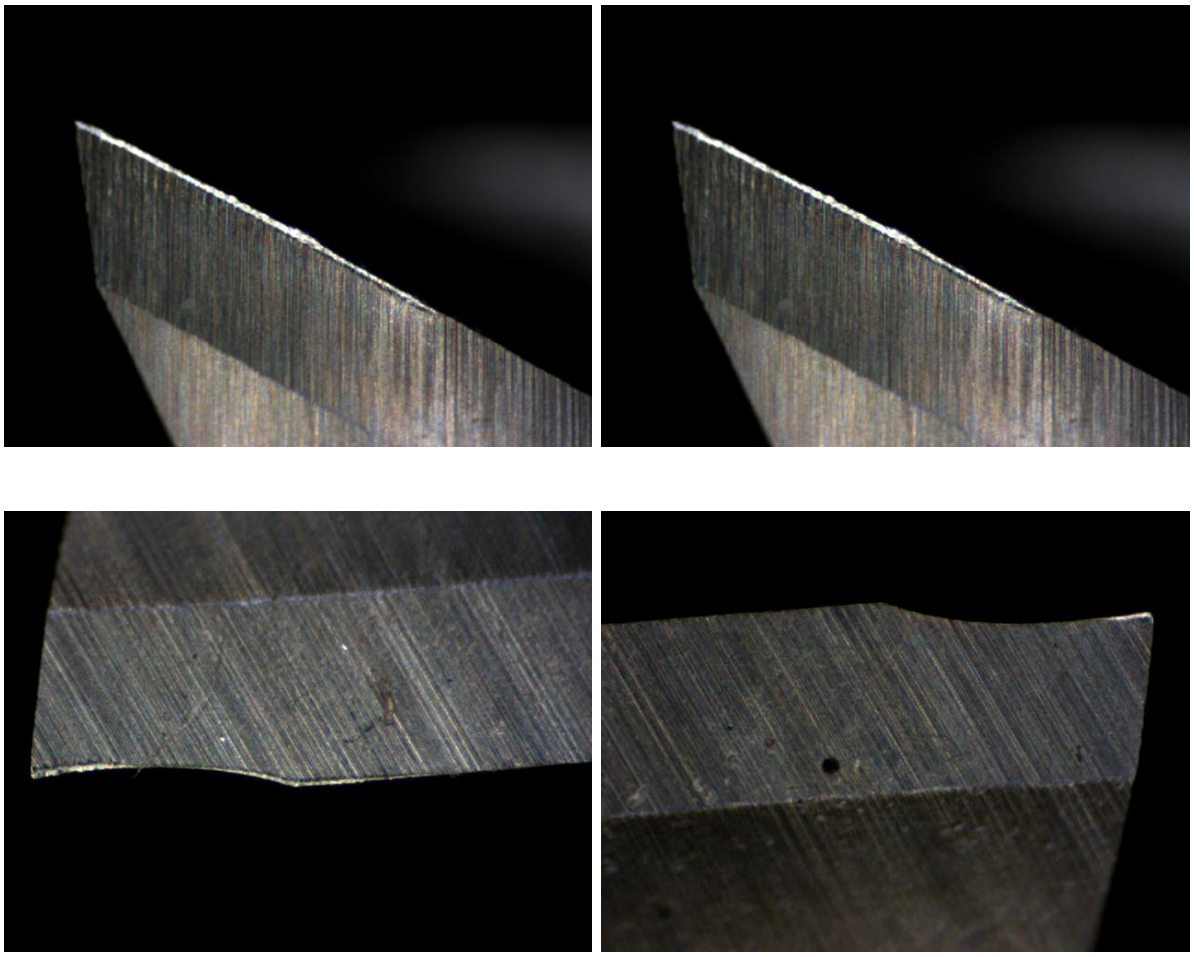

0.3 mm/rev, 1000 RPM

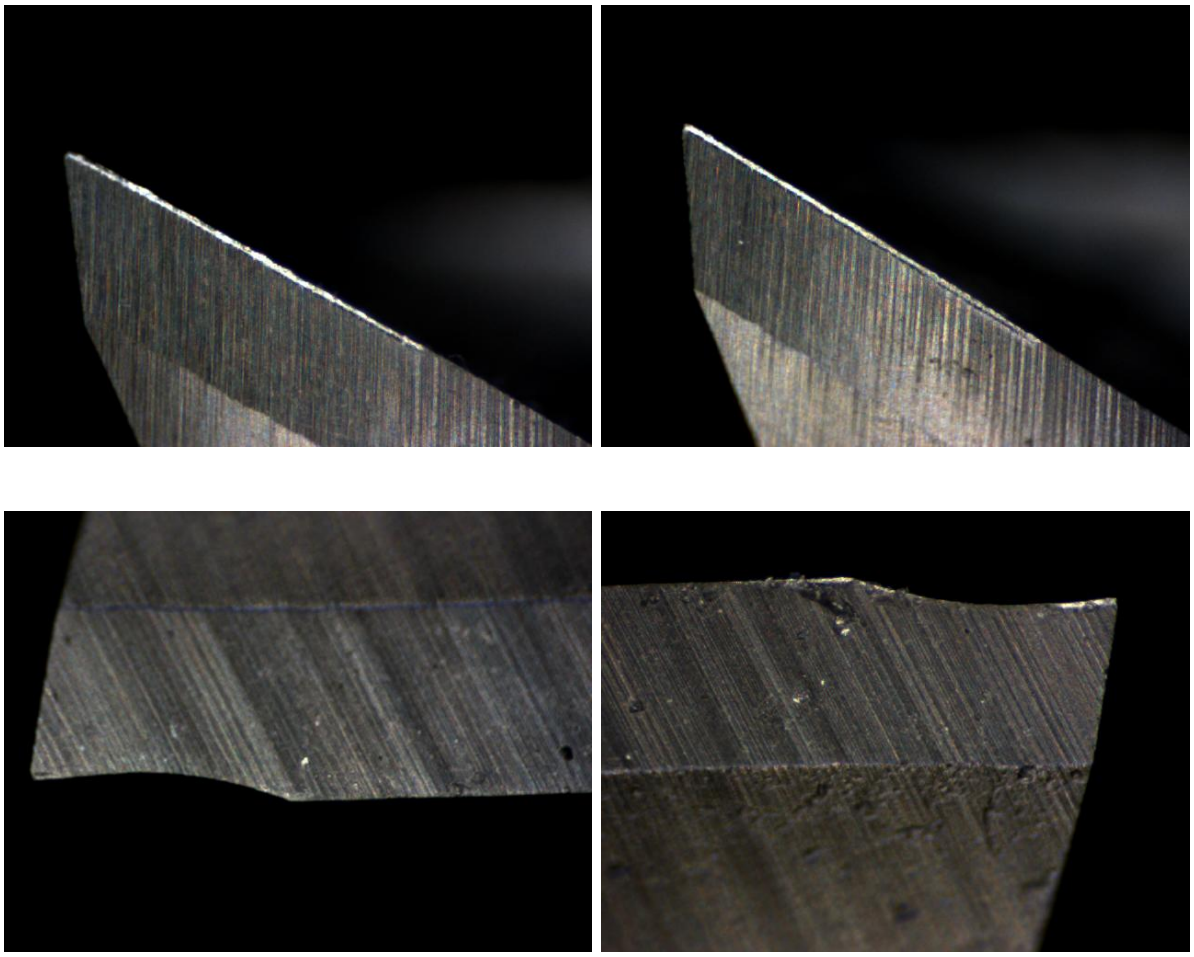

0.05 mm/rev, 1000 RPM

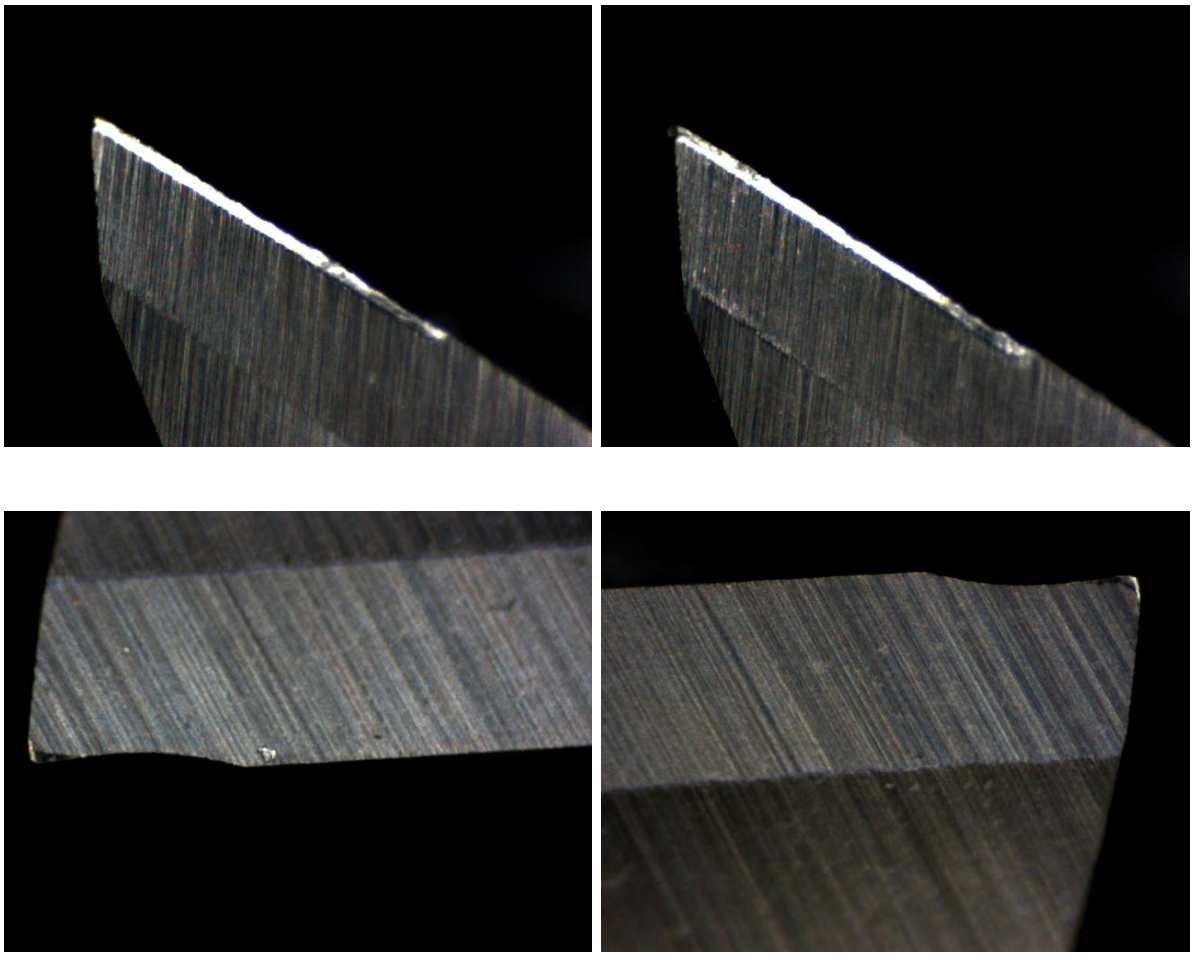

0.05 mm/rev, 4000 RPM

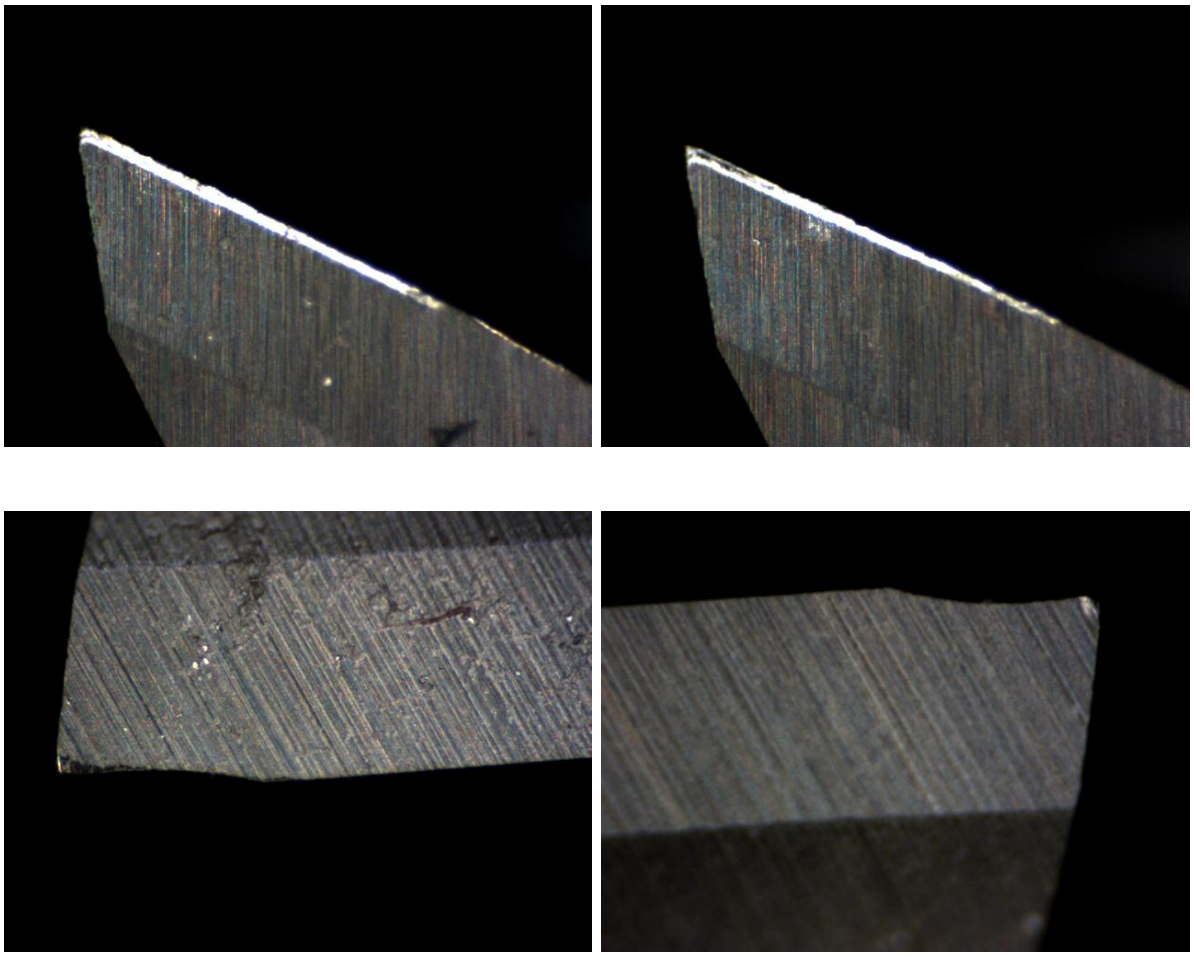

0.05 mm/rev, 4000 RPM

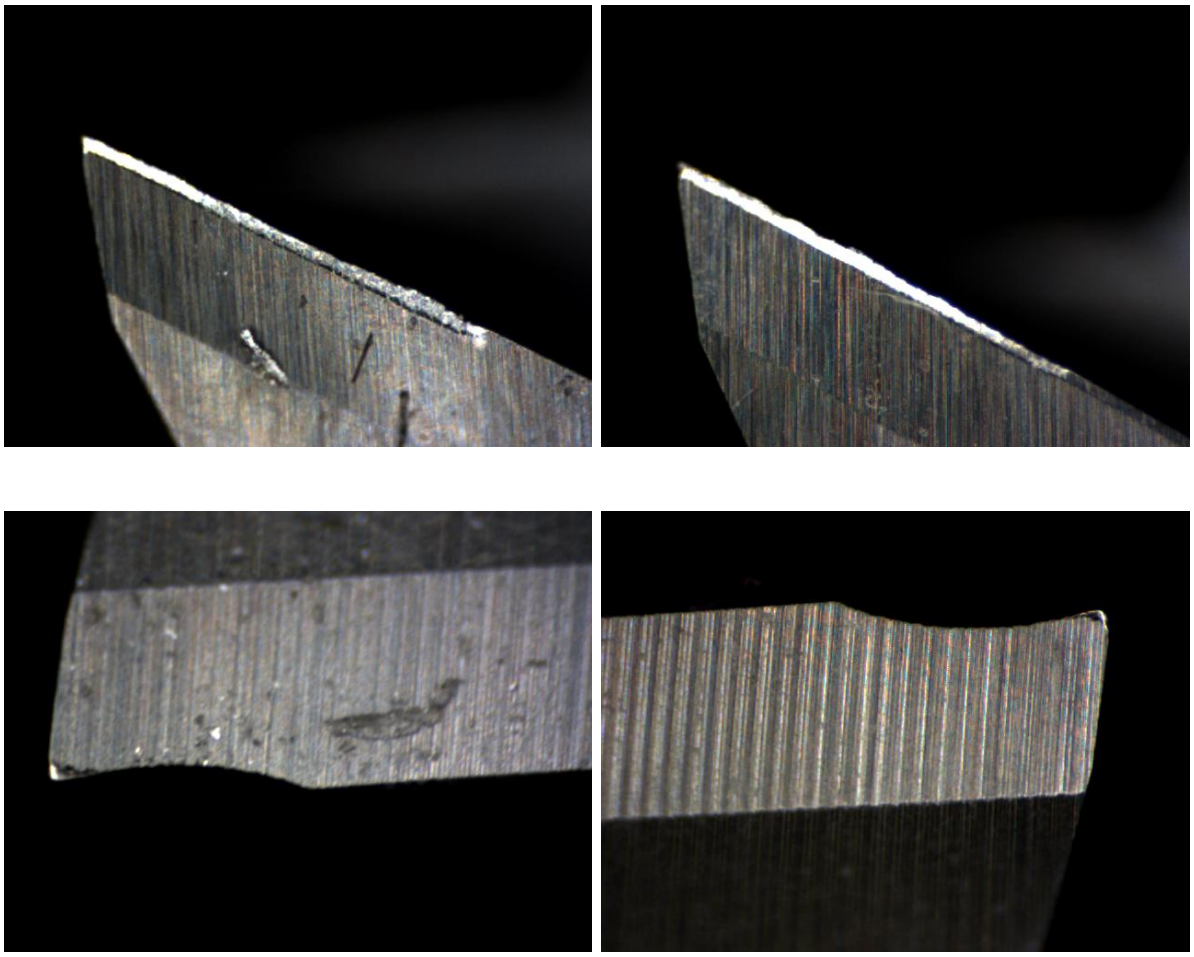

0.5 mm/rev, 4000 RPM




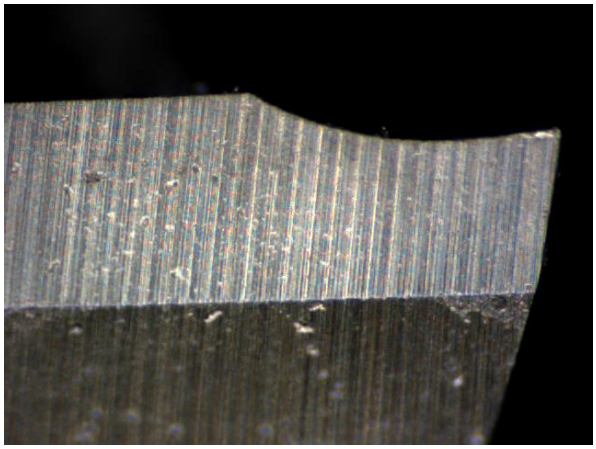

0.3 mm/rev, 1000 RPM

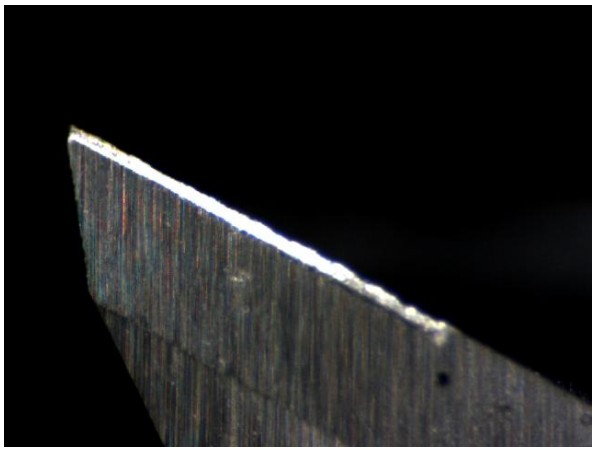
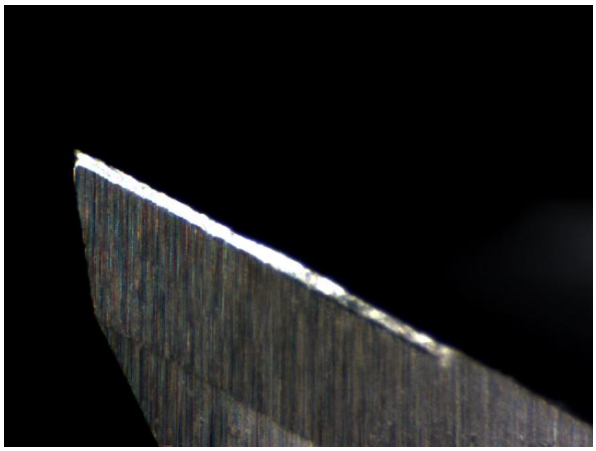
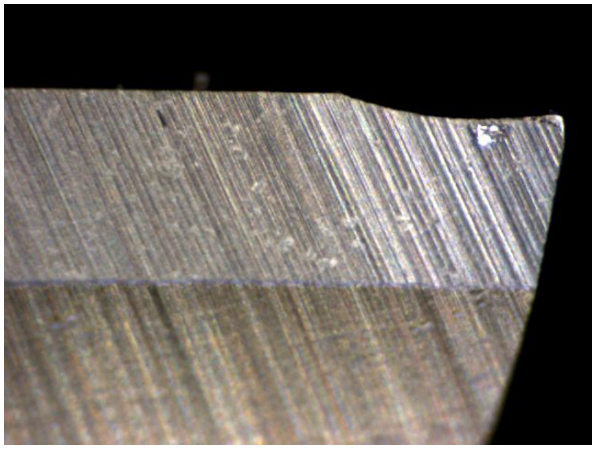
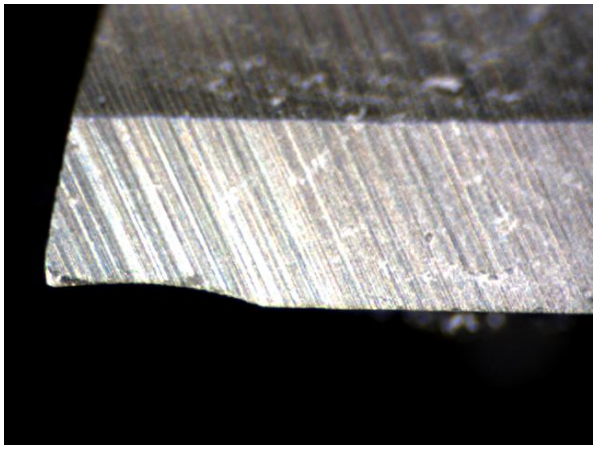

0.05 mm/rev, 3000 RPM

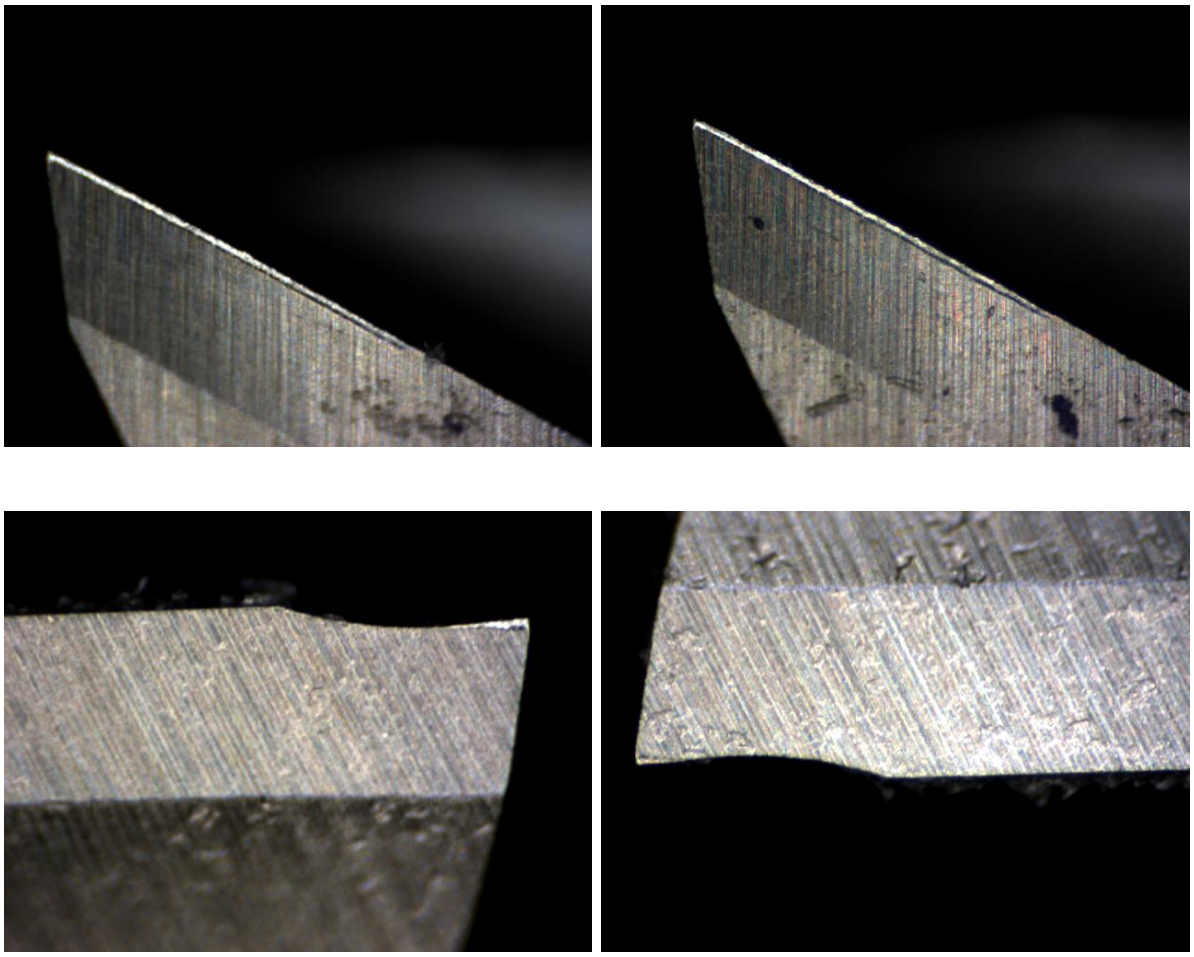

0.3 mm/rev, 3000 RPM

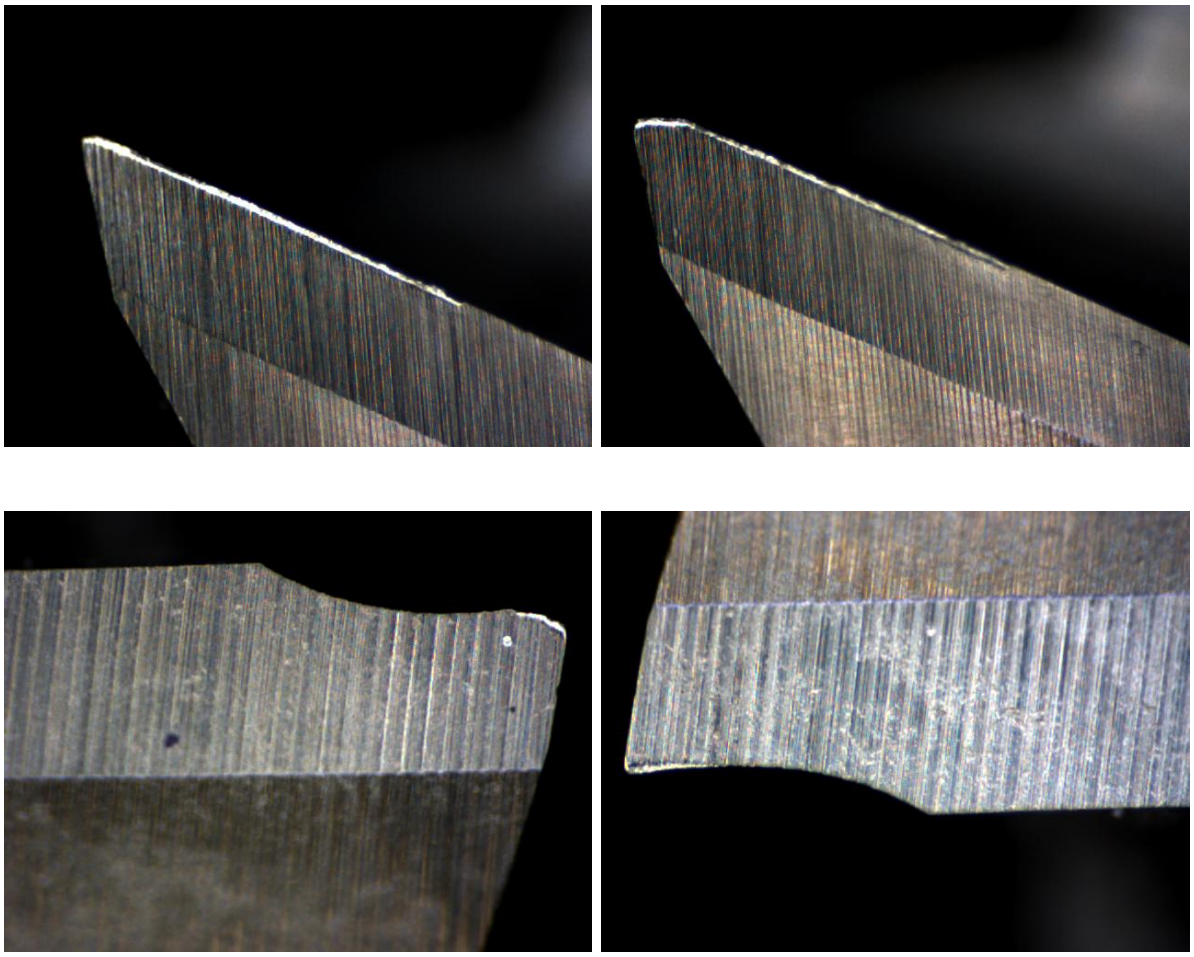

0.5 mm/rev, 2000 RPM

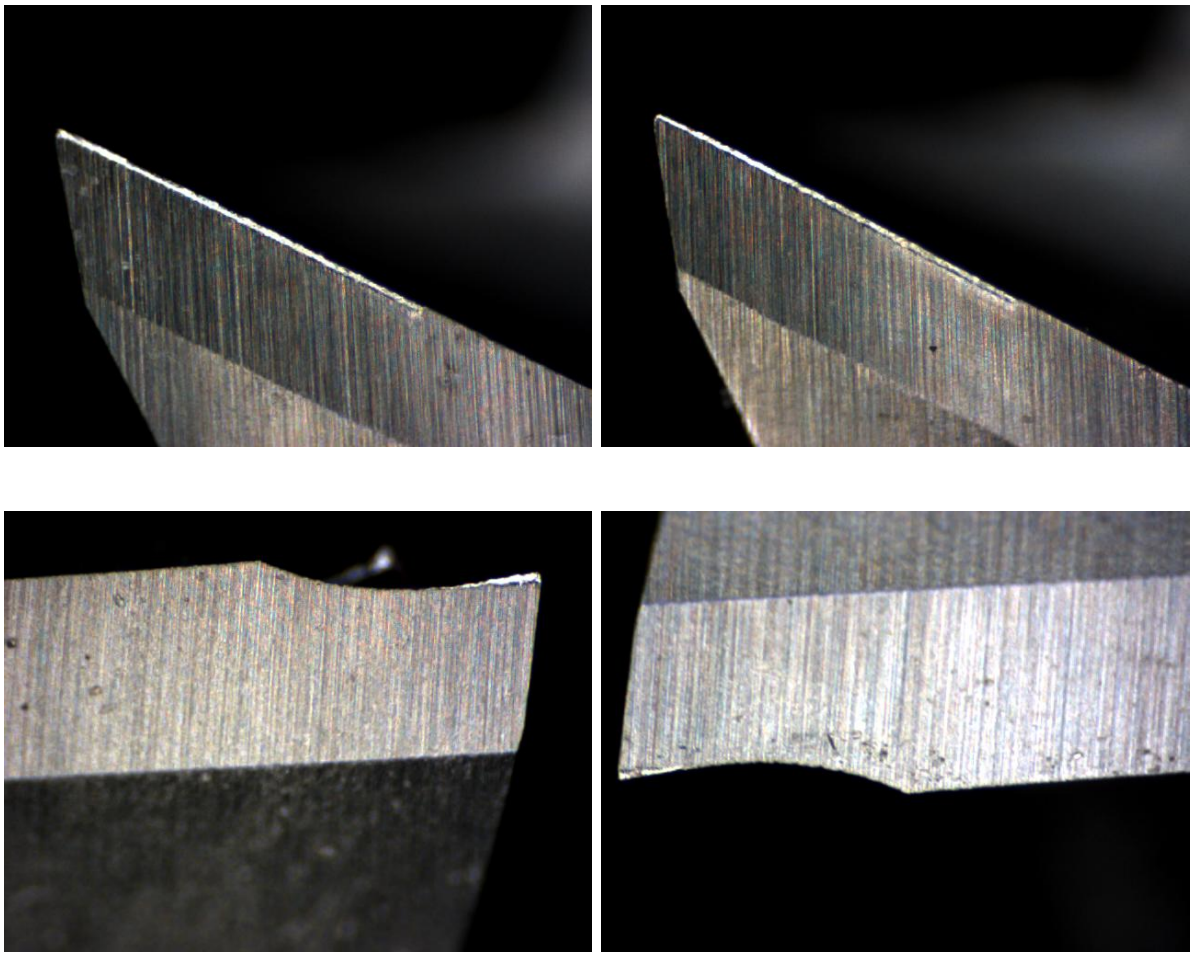

0.5 mm/rev, 2000 RPM

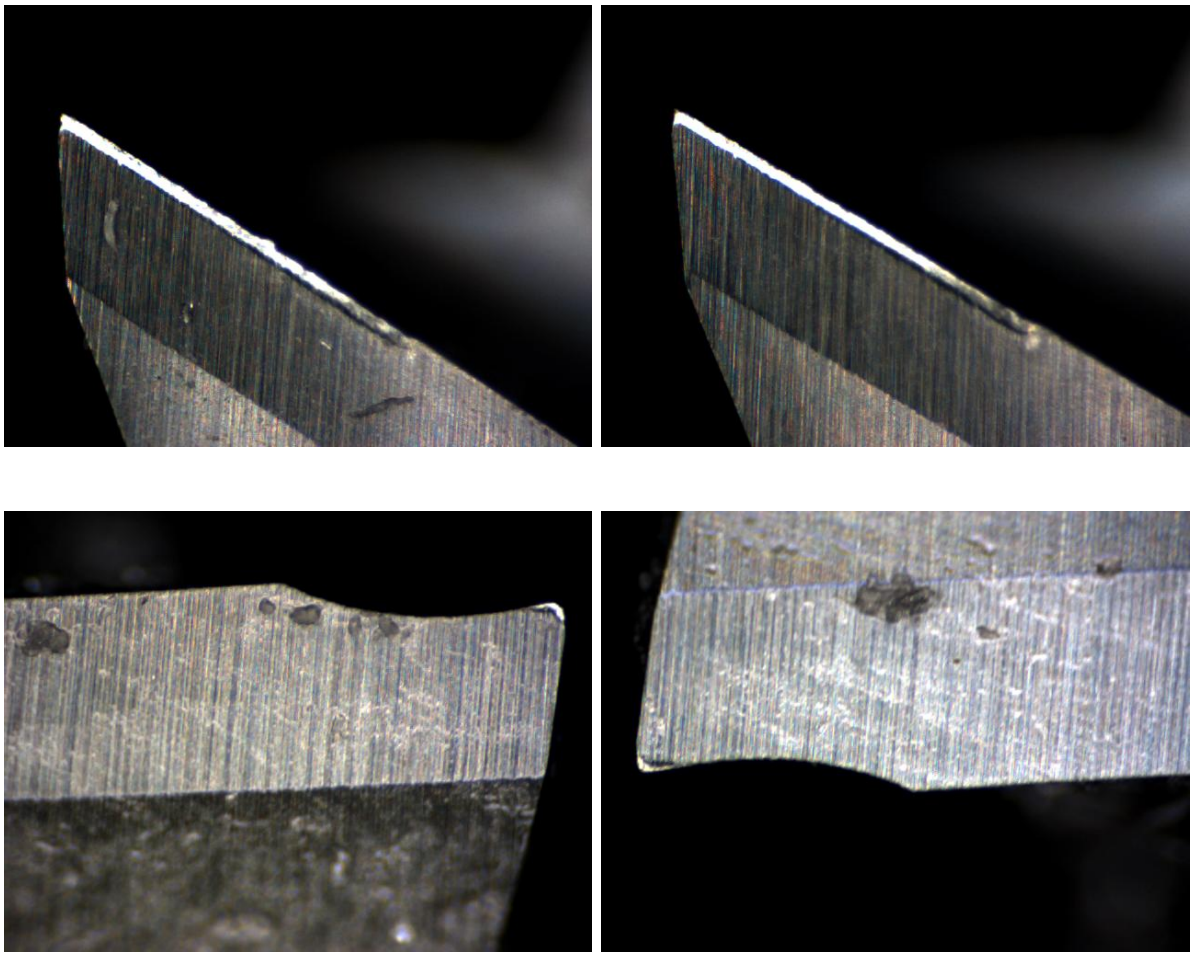

0.05 mm/rev, 2000 RPM

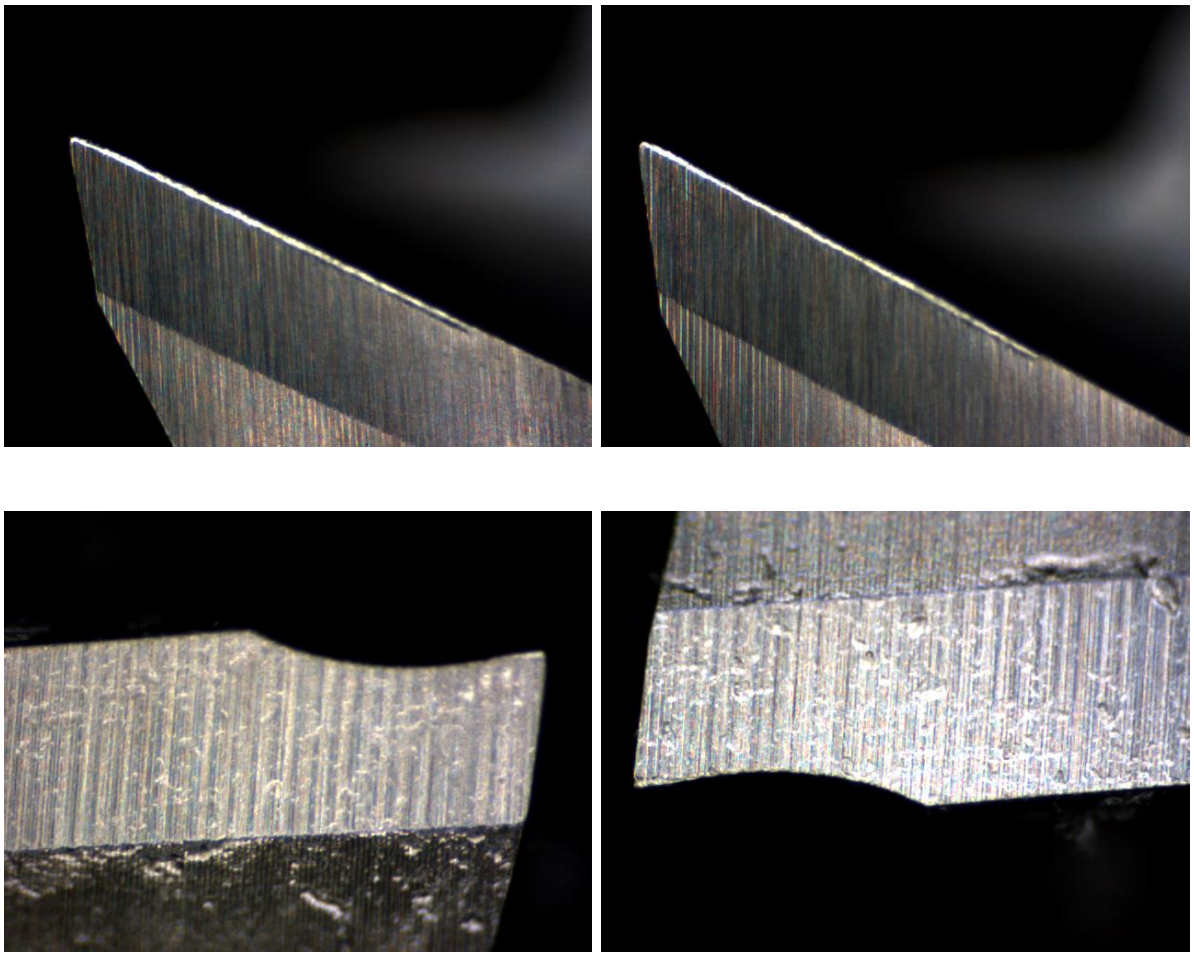

0.3 mm/rev, 3000 RPM

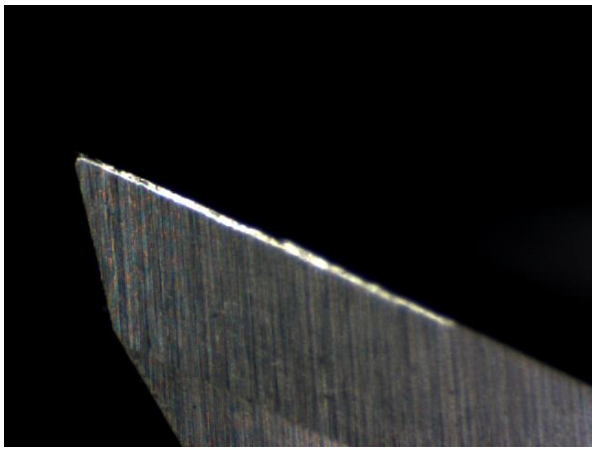
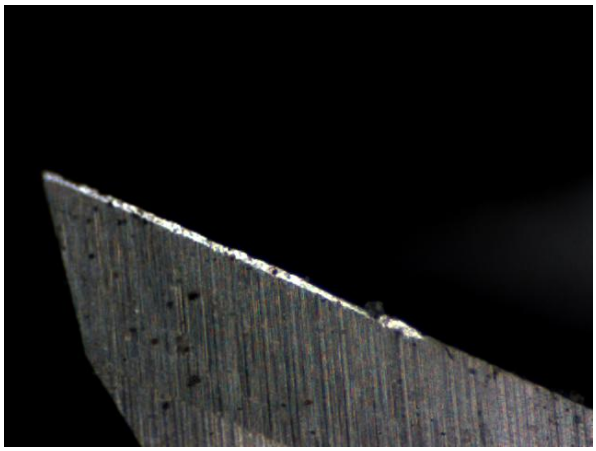
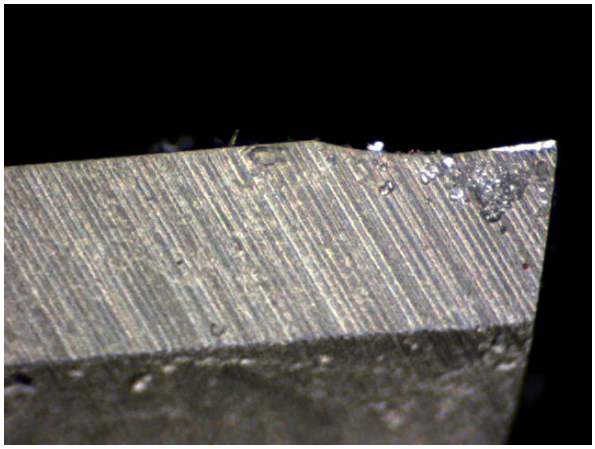
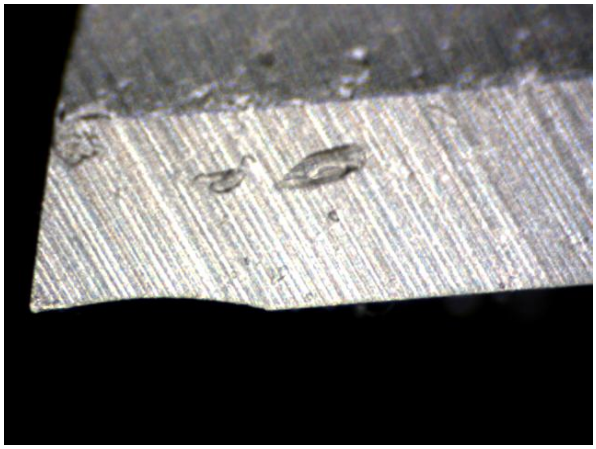

0.3 mm/rev, 3000 RPM

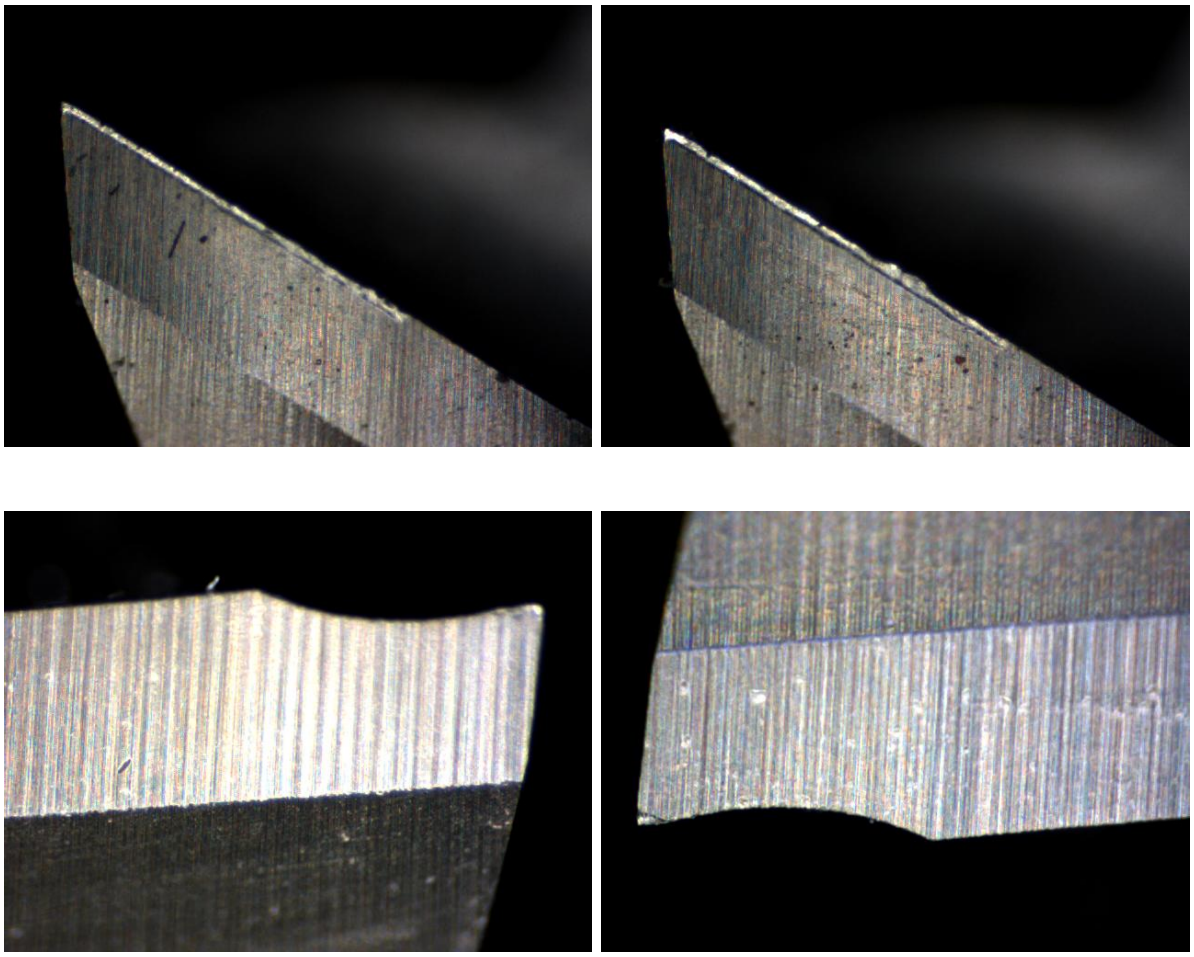

0.2 mm/rev, 4000 RPM

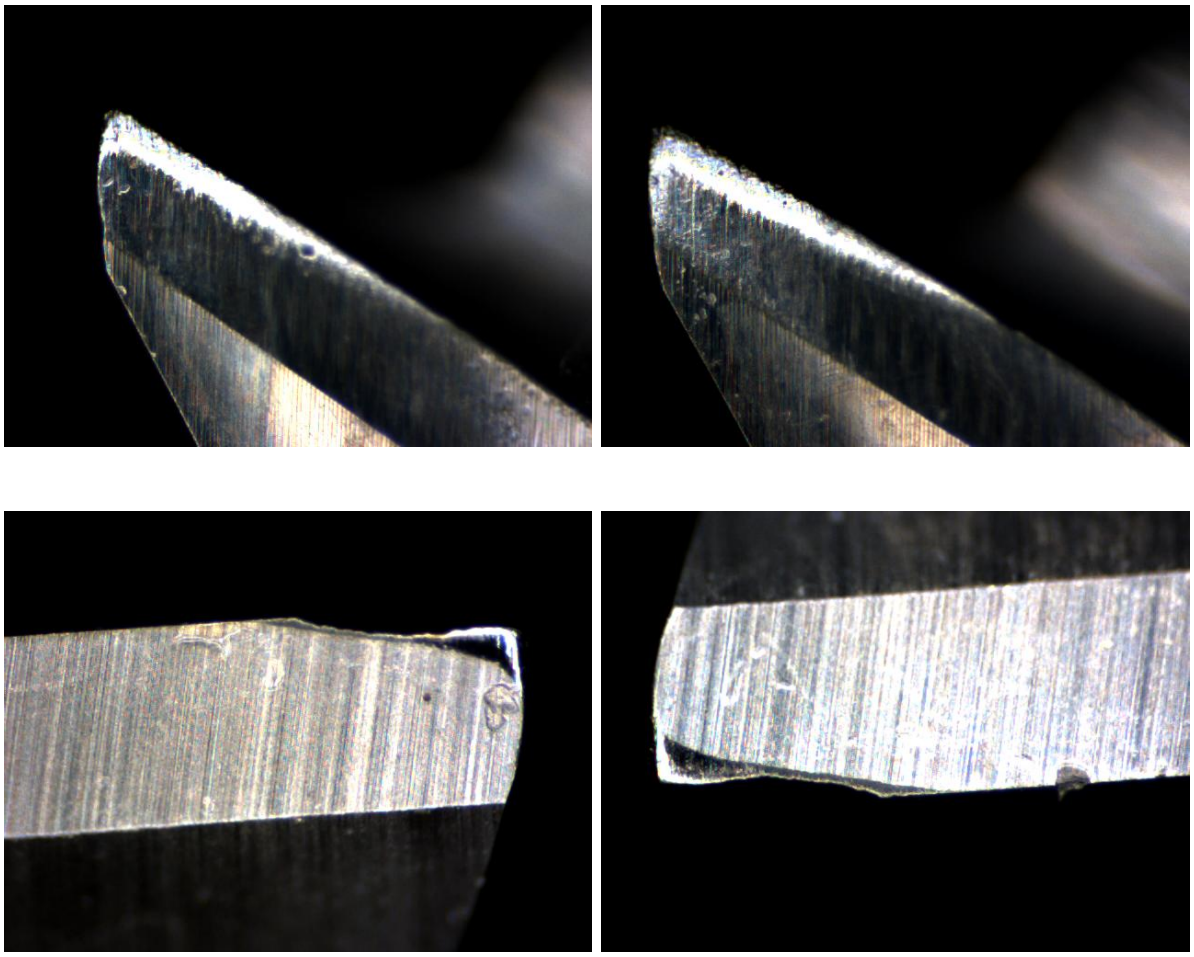

B.3 Measurement of temperature during machining

The temperature at the cutting edge while machining was measured using TESTO 845 Infrared (IR) gun and FLIR T640 IR camera. The emissivity of the composites was fixed by matching the readings of contact probe with the readings of the IR gun. Emissivity is the measure of radiation emitted by a body in comparison to amount of radiation emitted by a perfect black body. The emissivity of the objects generally range from 0.1 to 0.95. A mirror finished surface has an emissivity around 0.1, while an oxidized surface has a higher emissivity.

The camera receives radiation not only from the object but also from the surroundings reflected from the object itself. In addition to this, the radiations get attenuated by the atmosphere. These occurrences are accounted for while developing an equation for measurement of object temperature [114],

$$U_{obj} = \left(\frac{1}{\epsilon\tau}\right) \times U_{tot} - \frac{1-\epsilon}{\epsilon} \times U_{refl} - \frac{1-\tau}{\epsilon\tau} \times U_{atm}, \tag{B.1}$$

where,

- U_{obj}: calculated camera voltage for a blackbody at a temperature, T_{obj}
- U_{tot}: Measured camera output for the actual case.
- U_{refl}: Theoretical camera output voltage for a blackbody at temperature, T_{refl}, taken as 20°C
- U_{atm}: Theoretical camera output voltage for a blackbody at T_{atm}, taken as 20°C
- ϵ: emissivity of the object
- τ: transmittance of the atmosphere, usually taken as 0.88 [114]

The emissivity of the aluminum and magnesium matrix composites were measured by matching the temperatures obtained from contact probe and IR gun. The emissivity of the object was varied until the temperature measurements were equal. The emissivity of Al/SiCp and Mg/SiCp shown in Tables B.1 and B.2, respectively. A emissivity of 0.92 and 0.83 were chosen for Al/SiCp and Mg/SiCp respectively to measure the temperature at the cutting edge.

Table B.1: Emissivity measurement for Al/SiCp

Emissivity, ϵ	Probe Temperature (°C)	IR gun temperature (°C)
0.5	26.9	33.4
0.7	26.9	30
0.8	26.8	29.4
0.9	26.9	27.5
0.92	26.9	26.8

Table B.2: Emissivity measurement for Mg/SiCp

Emissivity, ϵ	Probe Temperature (°C)	IR gun temperature (°C)
0.94	24.6	26.2
0.92	24.5	26.0
0.90	24.6	26.0
0.85	24.5	25.3
0.83	24.6	24.7

Appendix C

SURFACE PROFILES AND SEM MICROGRAPHS

C.1 Surface Roughness Profile code as per ISO 16610 and 13565

```
clear all;
close all;
clc;
addpath('C:\Users\rahul\Desktop\Nishita_research\fatigue_SR')
p=1;
p1=1;
sum1=0;
% angle=[0 10 20 30]
file_n={'S1_e1.txt','S1_e2.txt','S3_e1.txt','S3_e2.txt'};
result=cell(length(file_n),1);
for jj=1:length(file_n)
   result{jj}.sample=file_n{jj};
    %clear data data1 a Lc lambda_c Nfft x1 x s data_filt data_filt2 ...
        step2_value x3 profile

data=importfile(file_n{jj});
data1=table2array(data);

% data1=xlsread('10_0_xcel.xlsx','A1:A11200');
a=sqrt(log(2)/pi);
Lc=0.5;
lambda_c=0.8;
Nfft = numel(data1);
```

```
x1=linspace(0,5.6,numel(data1));
x = linspace(-Nfft/2,Nfft/2,Nfft)*5.6/Nfft;
s = 1/(a*lambda_c)*exp(-pi*(x/(a*lambda_c)).^2);
s(abs(x)>Lc*lambda_c)=0;
data_filt = conv(s/sum(s),data1,'same');
%data_filt= conv(s/sum(s),flipud(data_filt),'same');

%plot(x1,data1,'b',x1,data_filt,'r');
%figure
%plot(x1,data1,'b')
%%step 2: cropped profile
for i=1:11200
    if data1(i)<data_filt(i)
        step2_value(i,1)=data_filt(i);
    else
        step2_value(i,1)=data1(i);
    end
end
% step 3: finding mean line
data_filt2 = conv(s/sum(s),step2_value,'same');
%data_filt2= conv(s/sum(s),flipud(data_filt2),'same');
%figure;
%plot(x1,step2_value,'b',x1,data_filt2,'r');
x3=linspace(0,4,8000);
data_filt3=data_filt2(1601:9600);
data2=data1(1601:9600);
profile=data2(:)-data_filt3(:);
figure();
eval(sprintf('profile%d=profile',jj));
eval(sprintf('x3_%d=x3',jj));
%plot(eval(sprintf('x3_%d',jj)),eval(sprintf('profile%d',jj)));
figure();
plot(x3*1000,profile)
```

```
hold on
% plot(x3,0,'k')
%drawaxis(gca, 'x', 0, 'movelabel', 1)

ylim([-80 80])
xlabel('Distance, \mum','interpreter','Tex')
ylabel('Profile height, \mum','interpreter','Tex')
grid on

 saveas(gcf,sprintf('fig%d.png', jj),'jpg')

end
```

C.2 Functionally gradient aluminum composite

C.2.1 Surface Profiles

0.1 mm/rev, 1000 RPM

Zone C

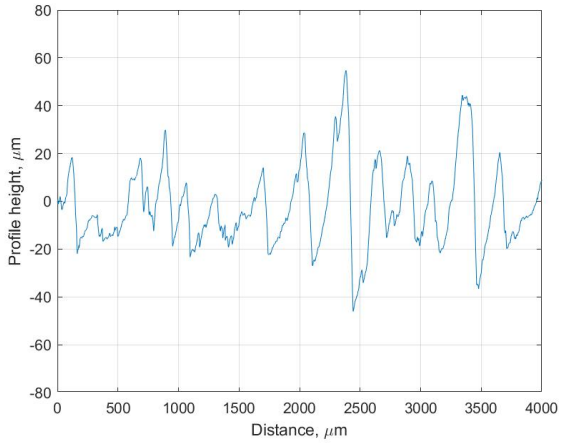

Zone B

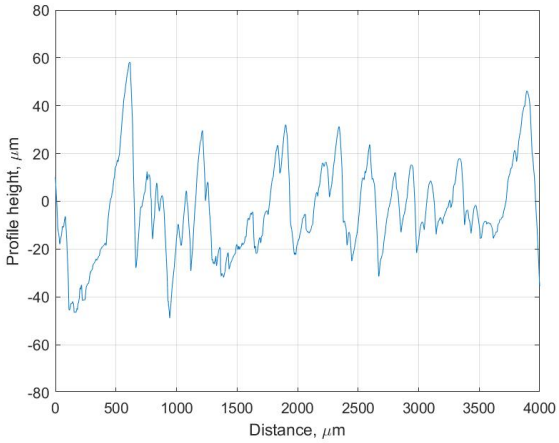

Zone A

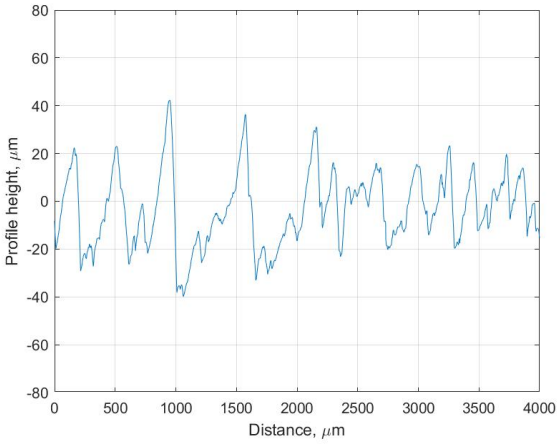
80
60
40
20
0
-20
-40
-60
-80
Profile height, μm
0
500
1000
1500
2000
2500
3000
3500
4000
Distance, μm

0.1 mm/rev, 2000 RPM

Zone C

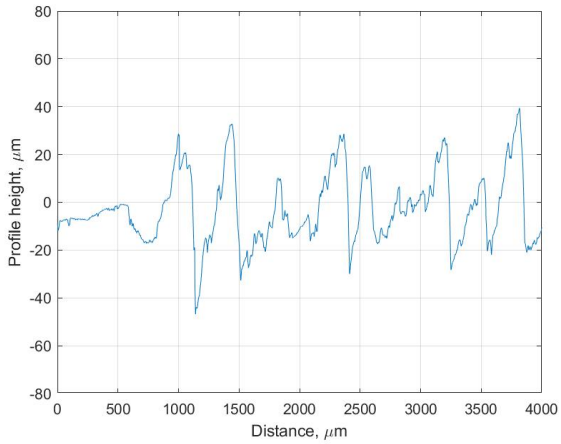

Zone B

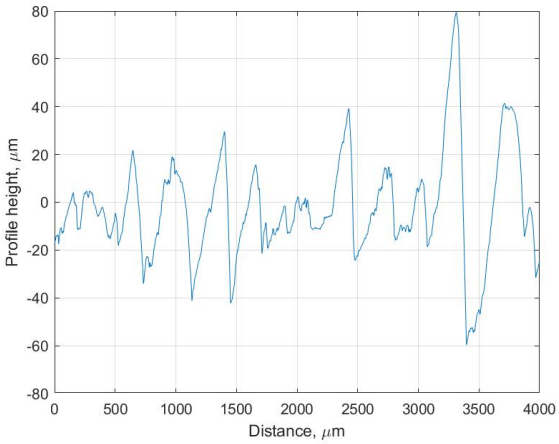

Zone A

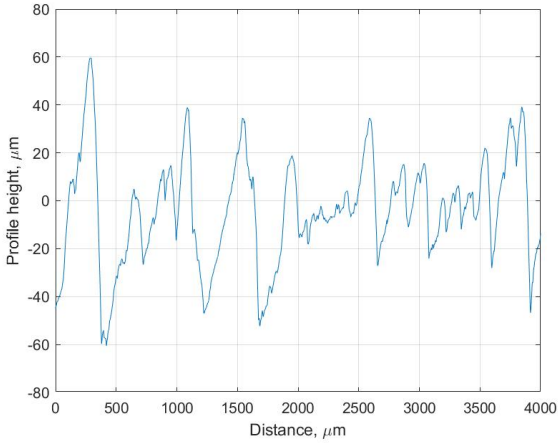

0.1 mm/rev, 3000 RPM

Zone C

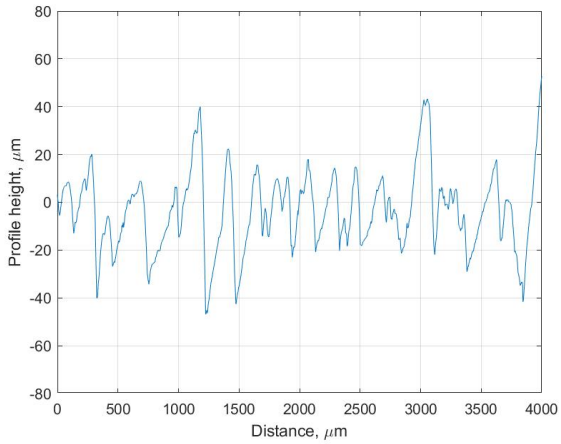

Zone B

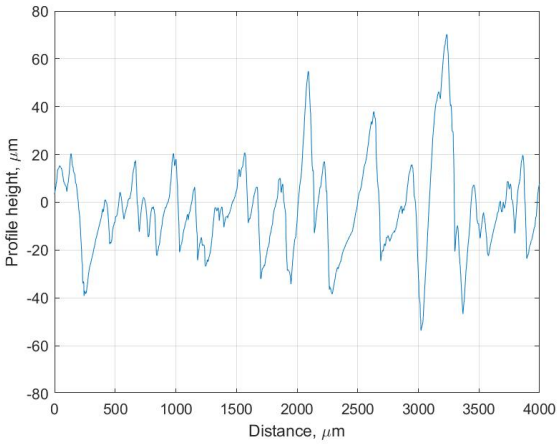

Zone A

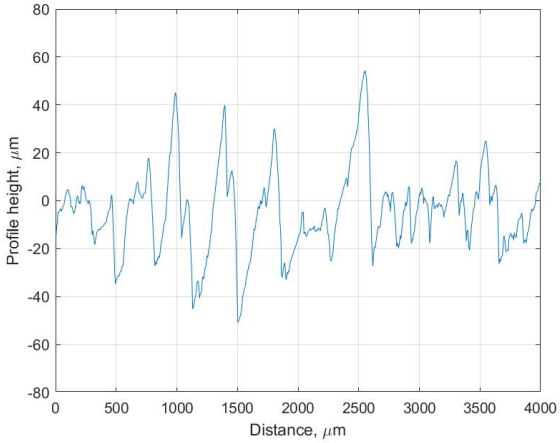

0.1 mm/rev, 4000 RPM

Zone C

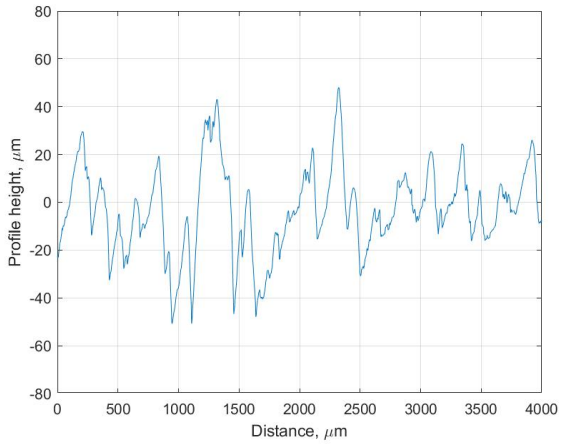

Zone B

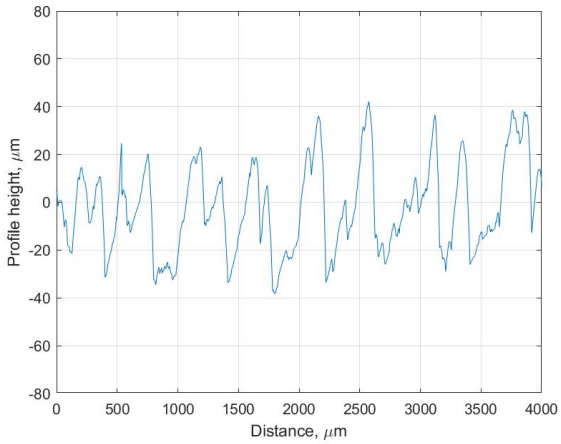

Zone A

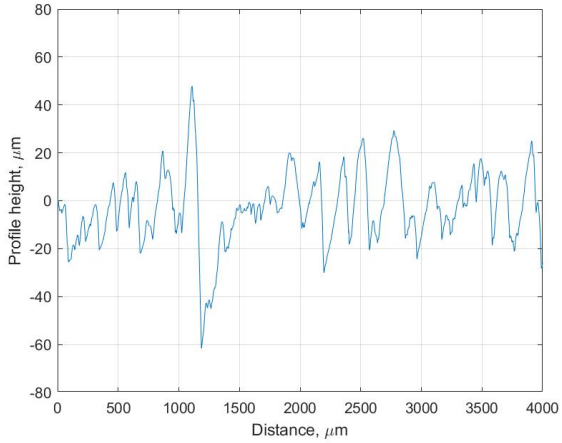

0.1 mm/rev, 5000 RPM

Zone C

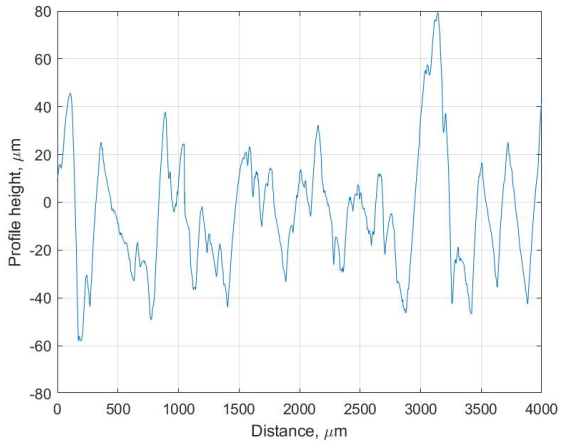

Zone B

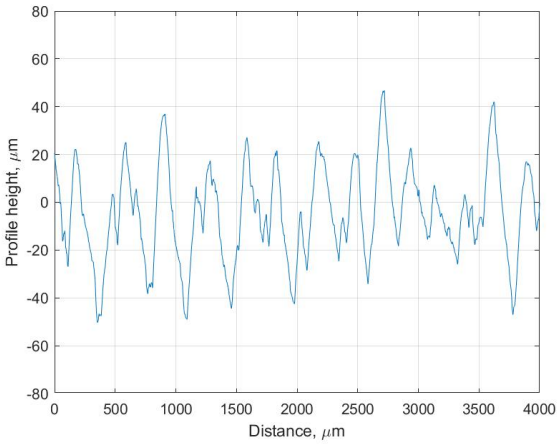

Zone A

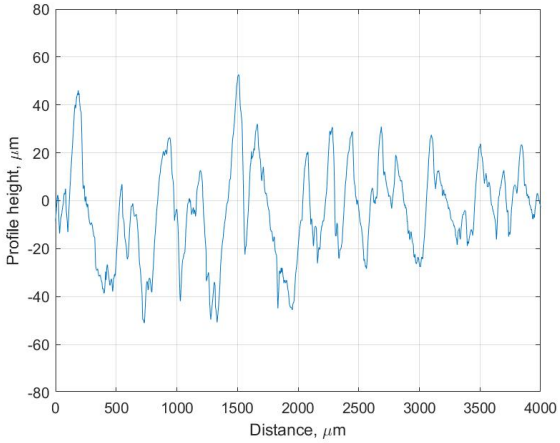

0.2 mm/rev, 1000 RPM

Zone C

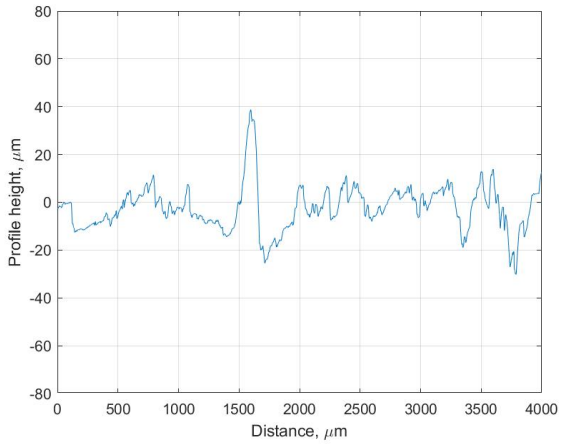

Zone B

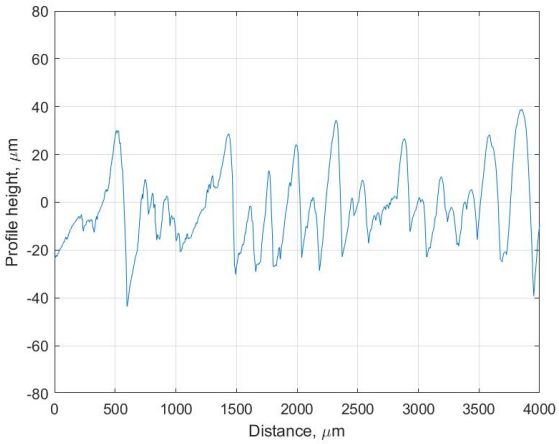

Zone A

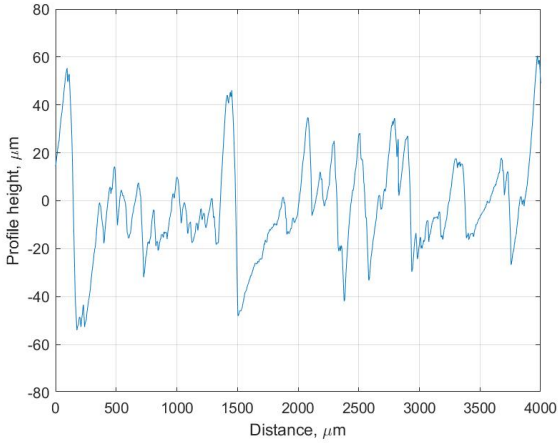

0.2 mm/rev, 2000 RPM

Zone C

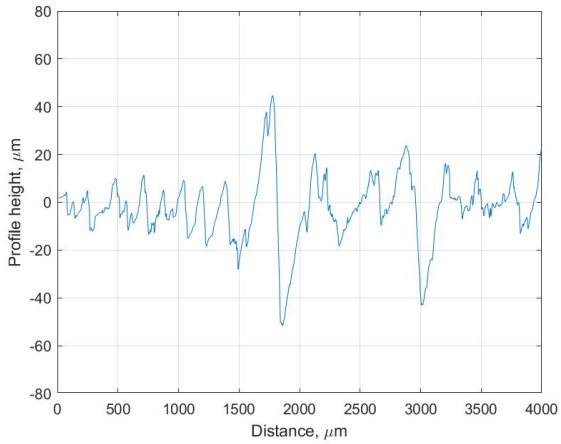

Zone B

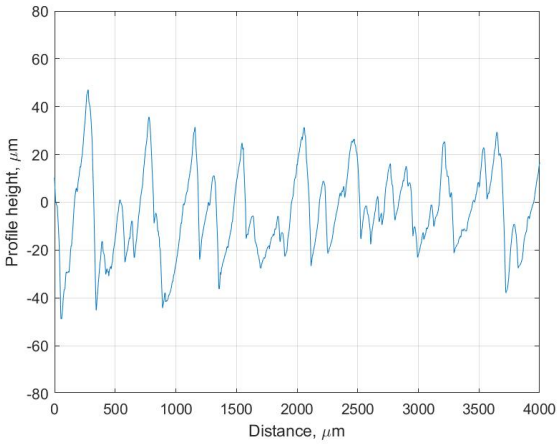

Zone A

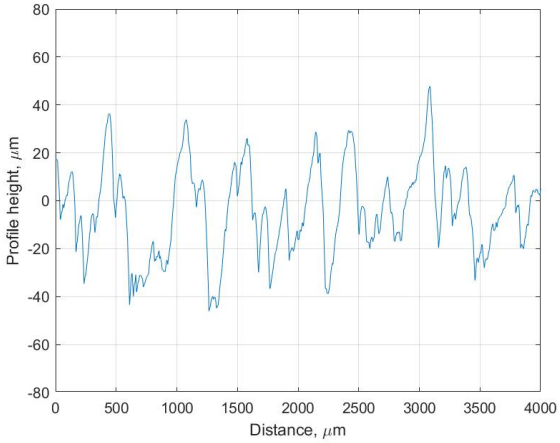

0.2 mm/rev, 3000 RPM

Zone C

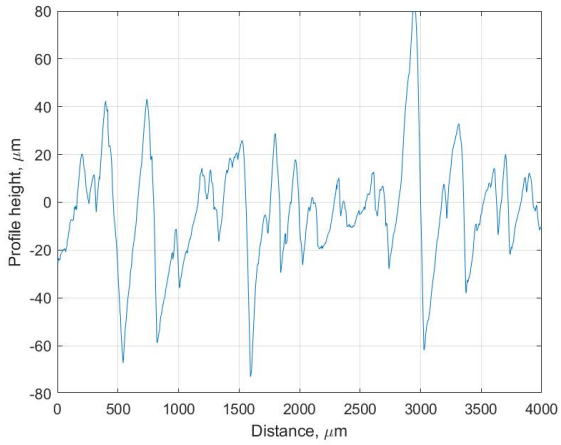

Zone B

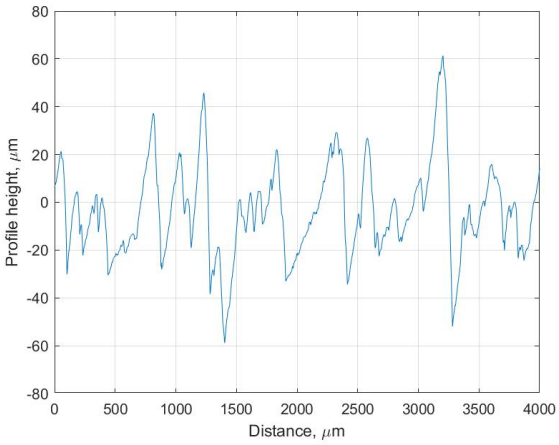

Zone A

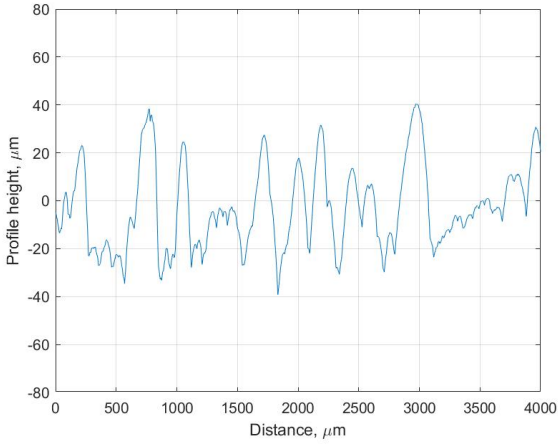

0.2 mm/rev, 4000 RPM

Zone C

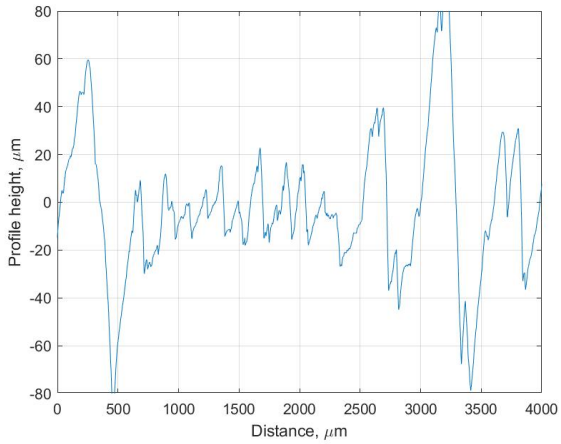

Zone B

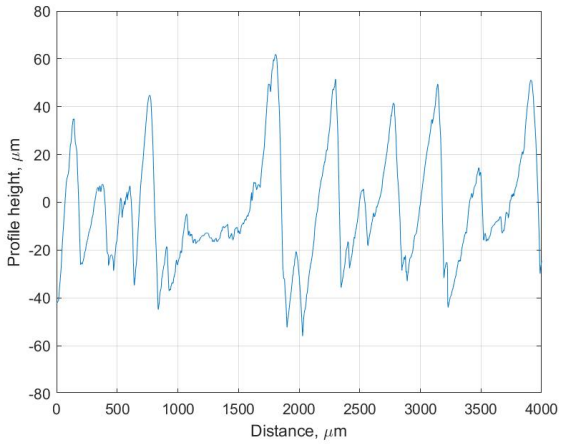

Zone A

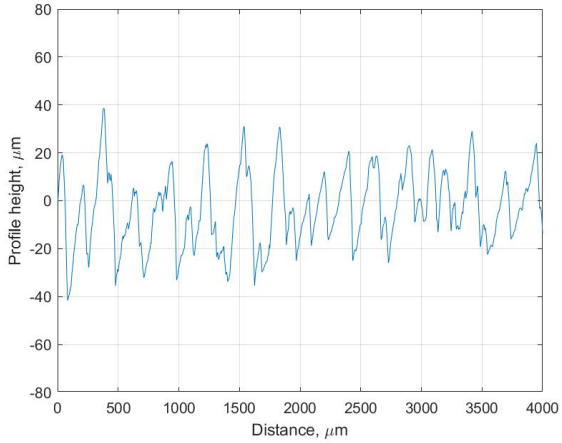

0.3 mm/rev, 1000 RPM

Zone C

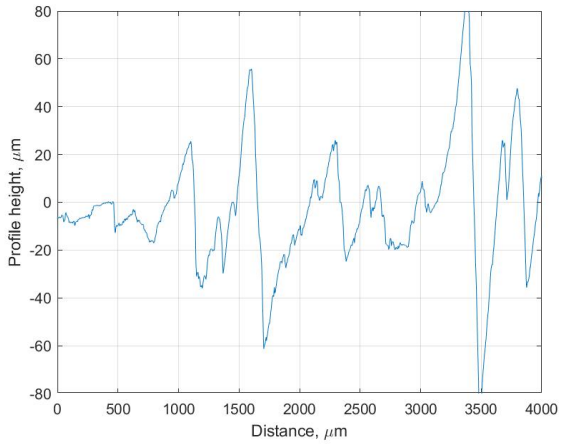

Zone B

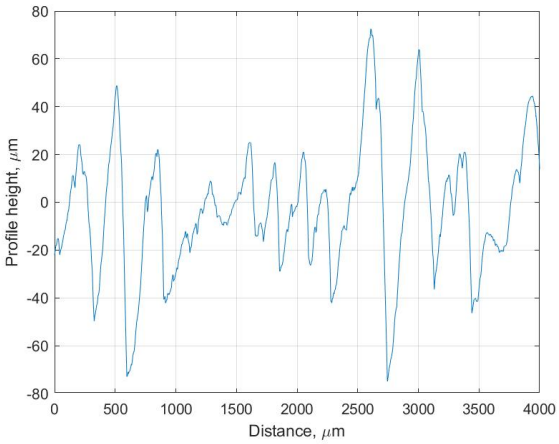

Zone A

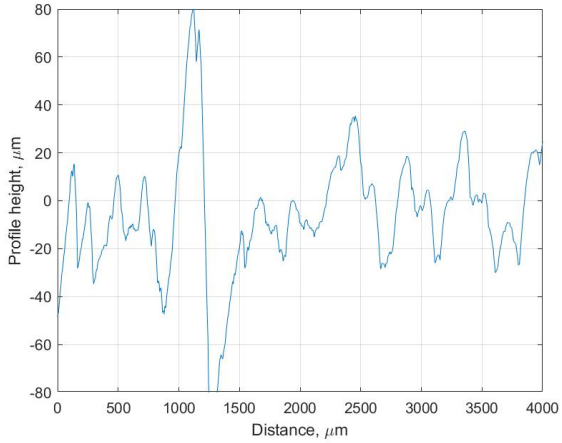

0.3 mm/rev, 2000 RPM

Zone C

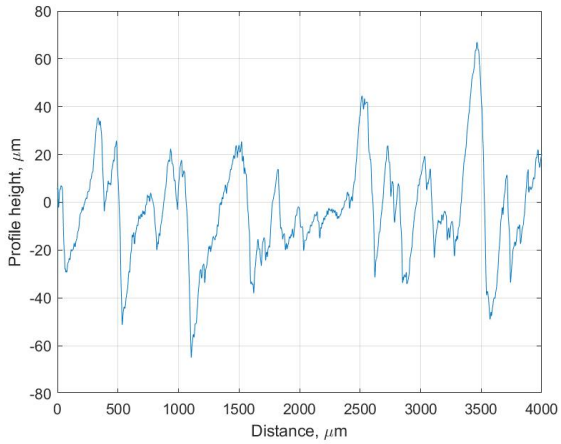

Zone B

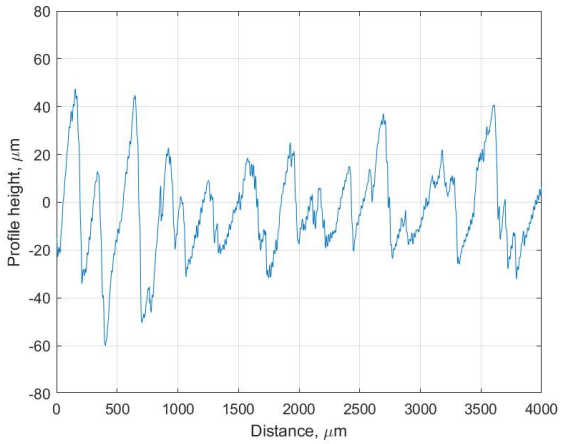

Zone A

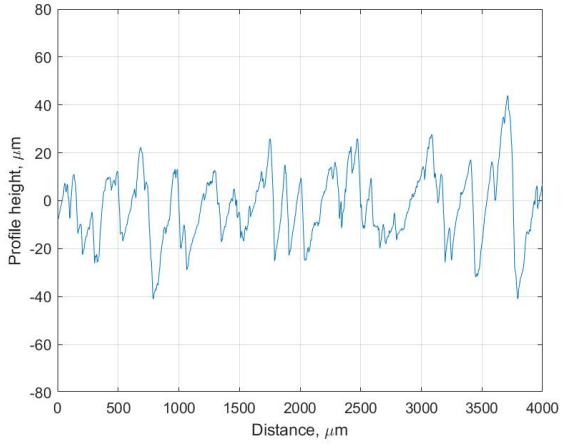

0.3 mm/rev, 3000 RPM

Zone C

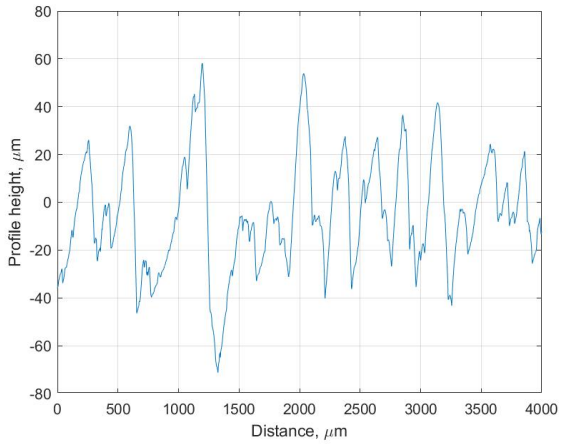

Zone B

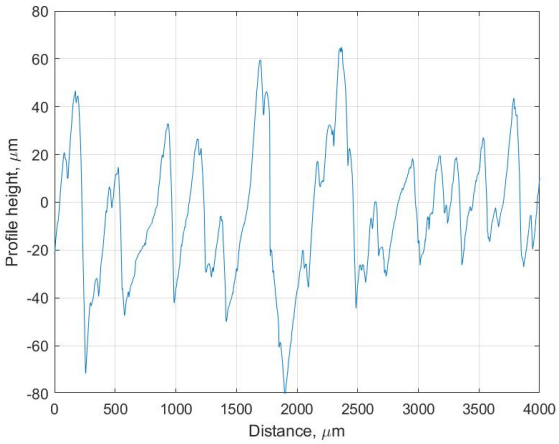

Zone A

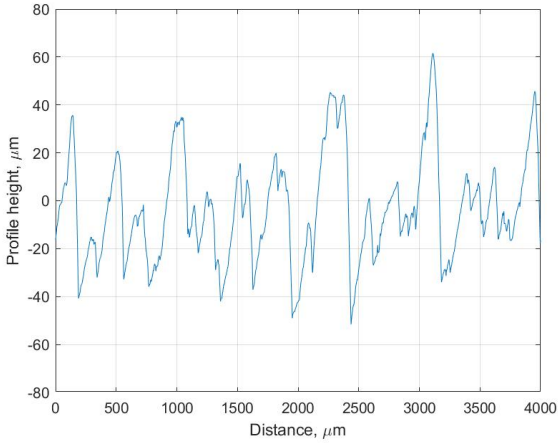

C.2.2 SEM Micrographs of machined surface

0.2 mm/rev, 4000RPM, Zone A

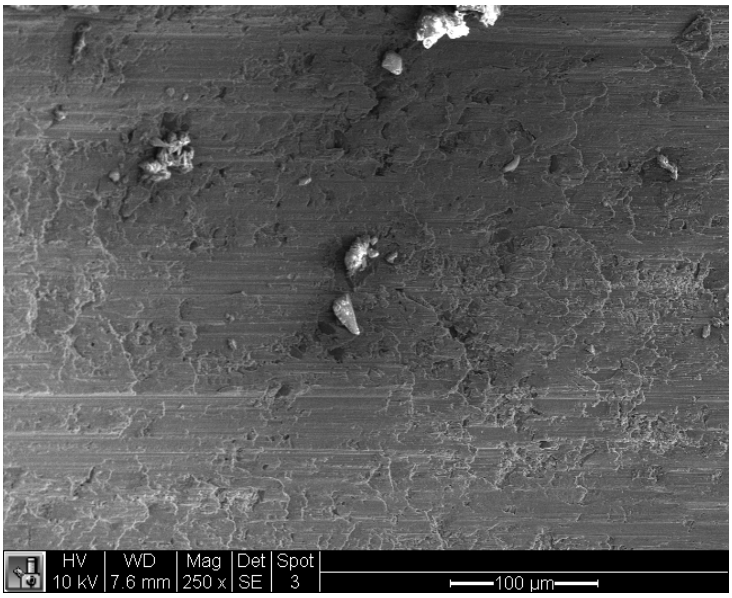

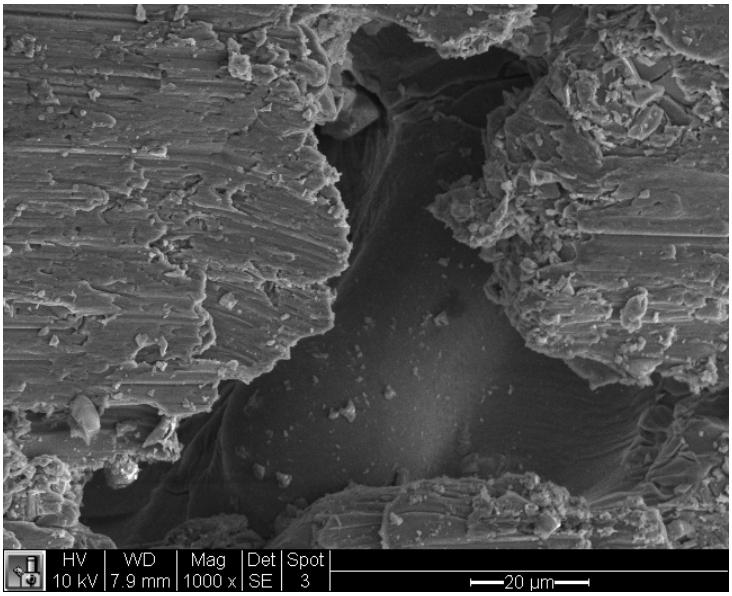
HV
10 kV
WD
7.9 mm
Mag
1000 x
Det
SE
Spot
3
20 µm

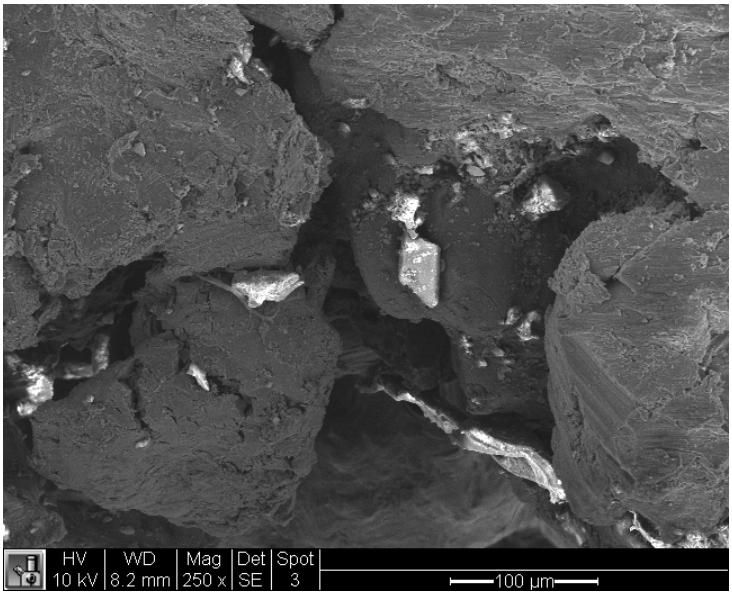
HV
10 kV
WD
8.2 mm
Mag
250 x
Det
SE
Spot
3
100 µm

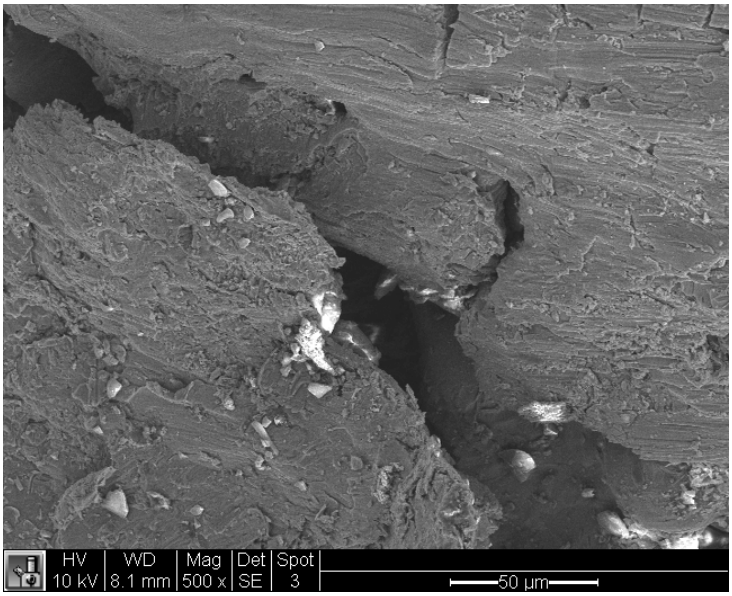
HV
10 kV
WD
8.1 mm
Mag
500 x
Det
SE
Spot
3
50 µm

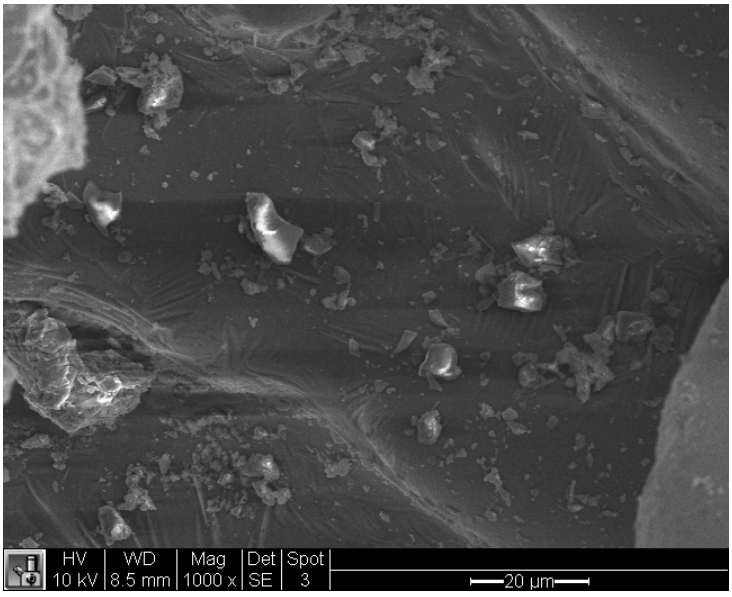
HV
10 kV
WD
8.5 mm
Mag
1000 x
Det
SE
Spot
3
20 µm

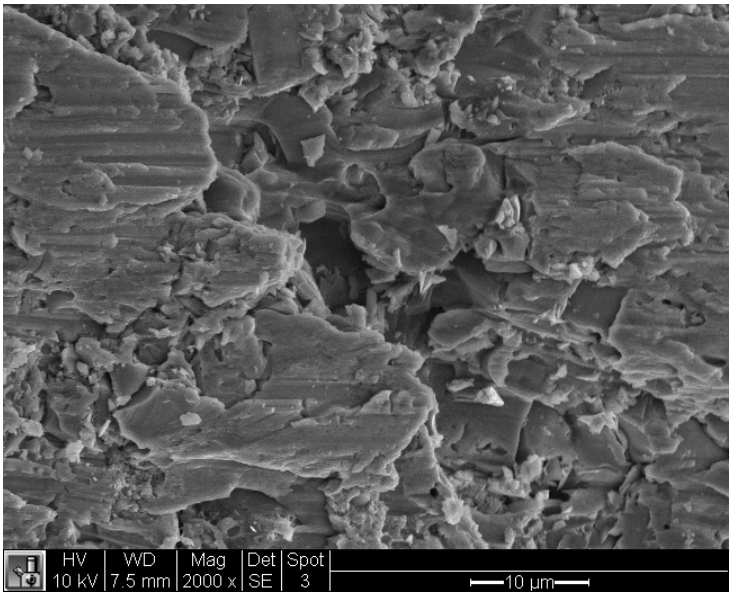
HV
10 kV
WD
7.5 mm
Mag
2000 x
Det
SE
Spot
3
10 µm

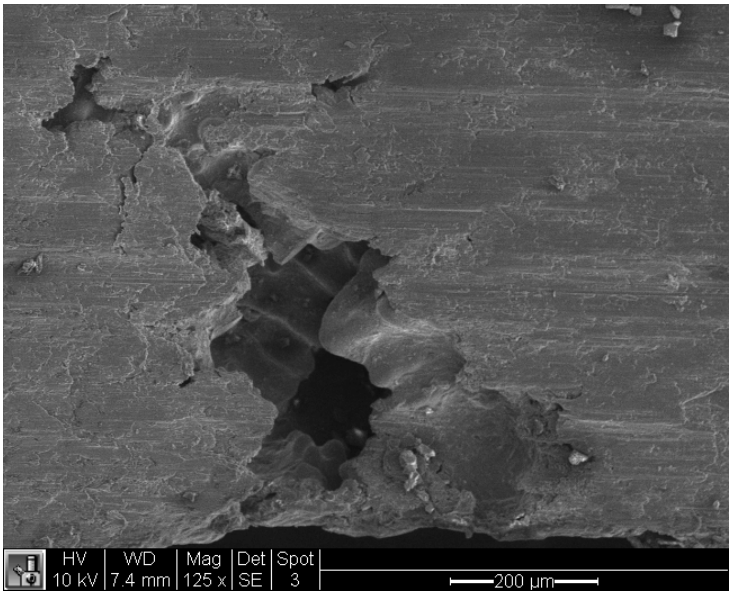
HV
10 kV
WD
7.4 mm
Mag
125 x
Det
SE
Spot
3
200 µm

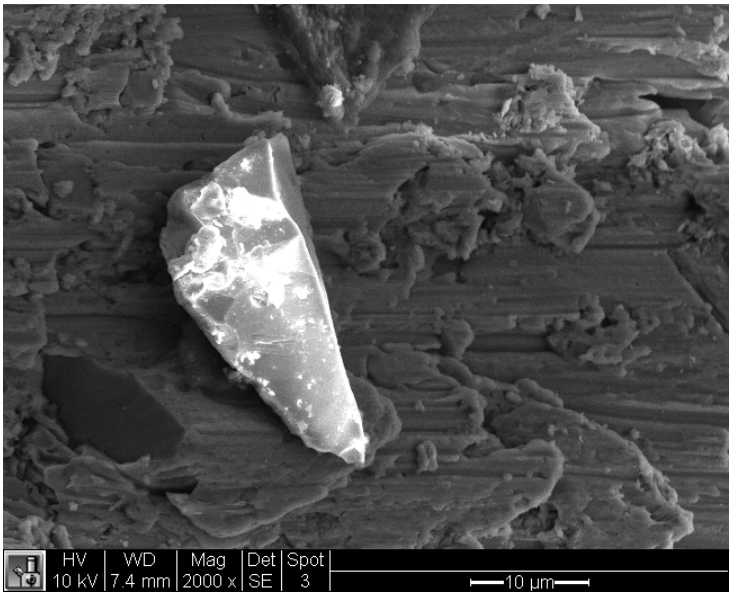
HV
10 kV
WD
7.4 mm
Mag
2000 x
Det
SE
Spot
3
10 µm

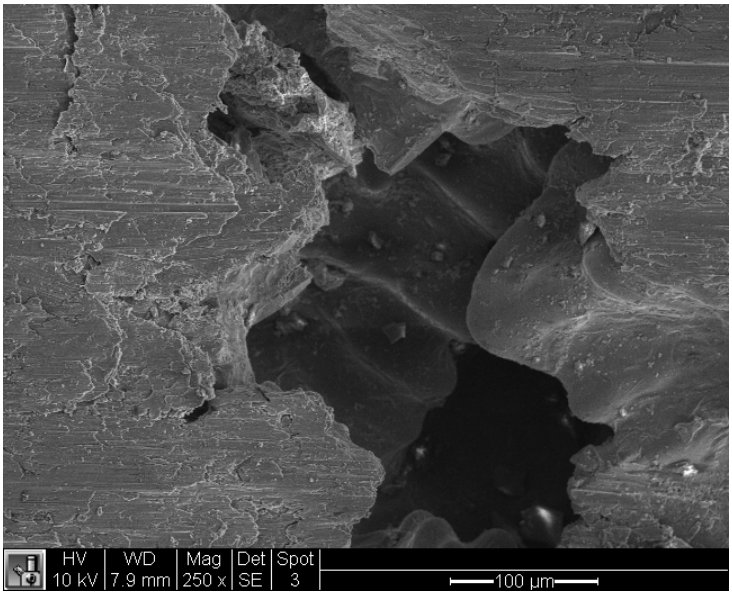
HV
10 kV
WD
7.9 mm
Mag
250 x
Det
SE
Spot
3
100 µm

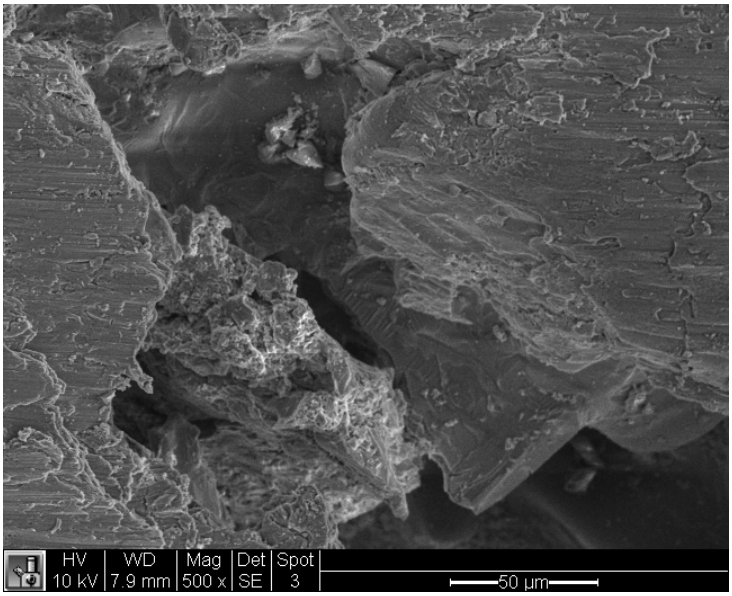

0.2 mm/rev, 4000RPM, Zone B

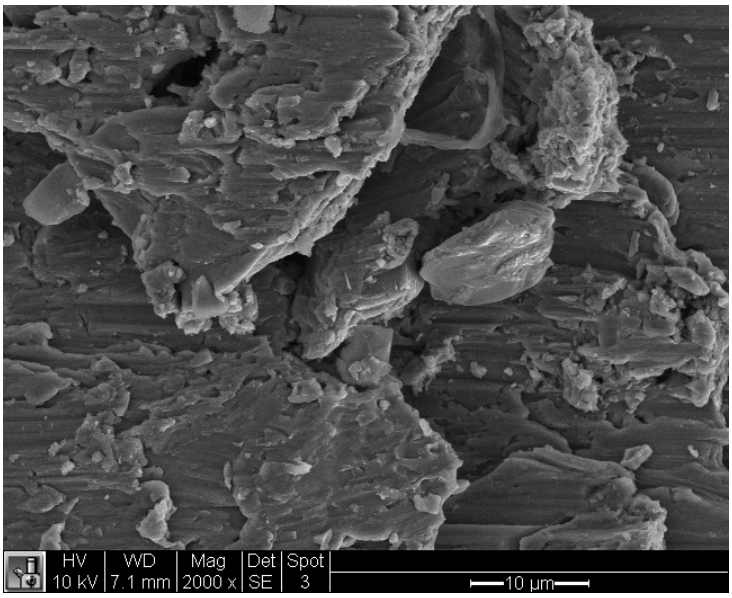

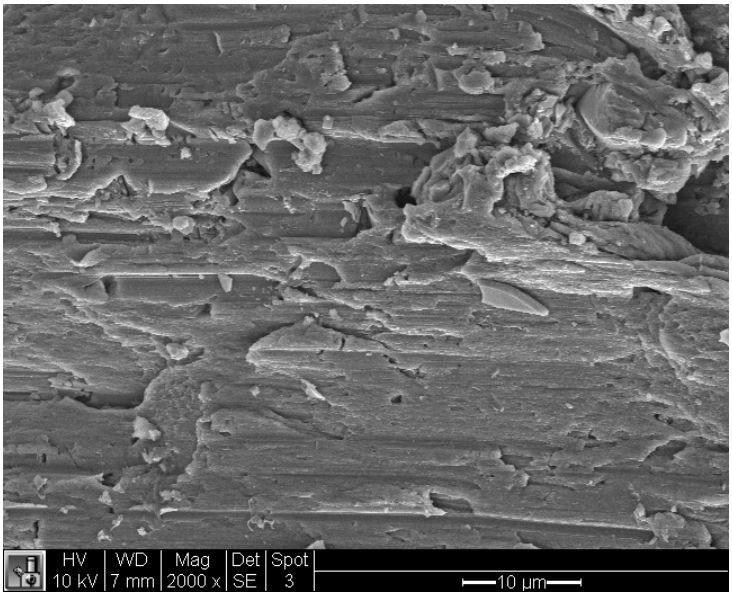
HV
10 kV
WD
7 mm
Mag
2000 x
Det
SE
Spot
3
10 µm

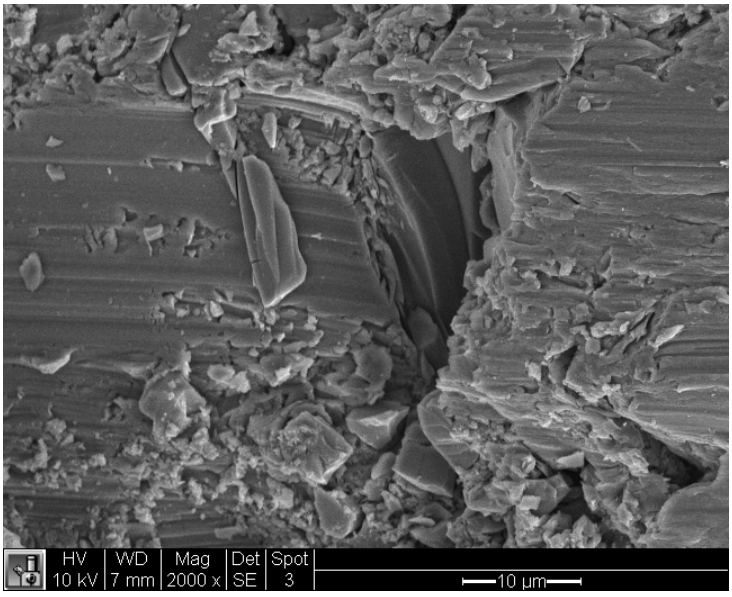
HV
10 kV
WD
7 mm
Mag
2000 x
Det
SE
Spot
3
10 µm

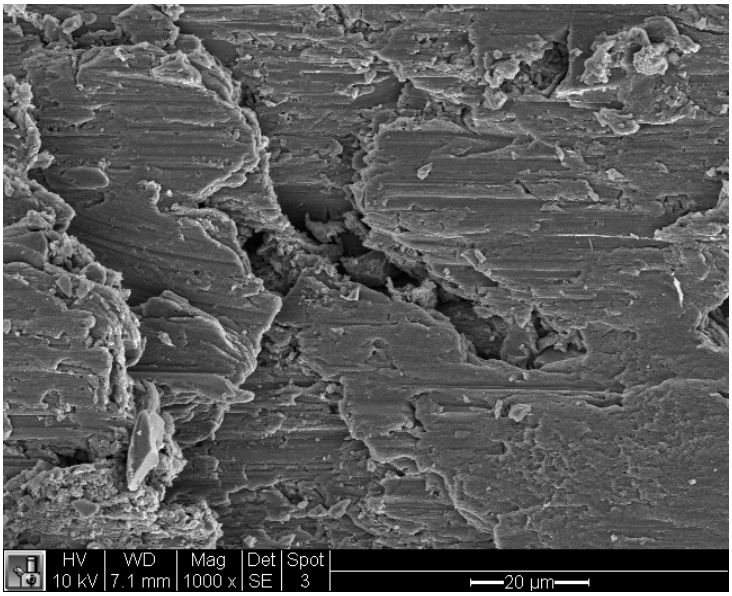
HV
10 kV
WD
7.1 mm
Mag
1000 x
Det
SE
Spot
3
20 µm

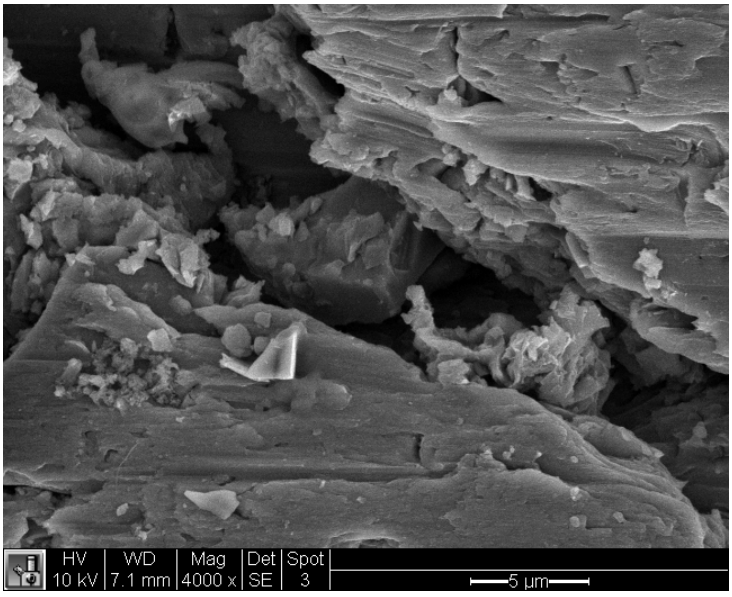
HV
10 kV
WD
7.1 mm
Mag
4000 x
Det
SE
Spot
3
5 µm

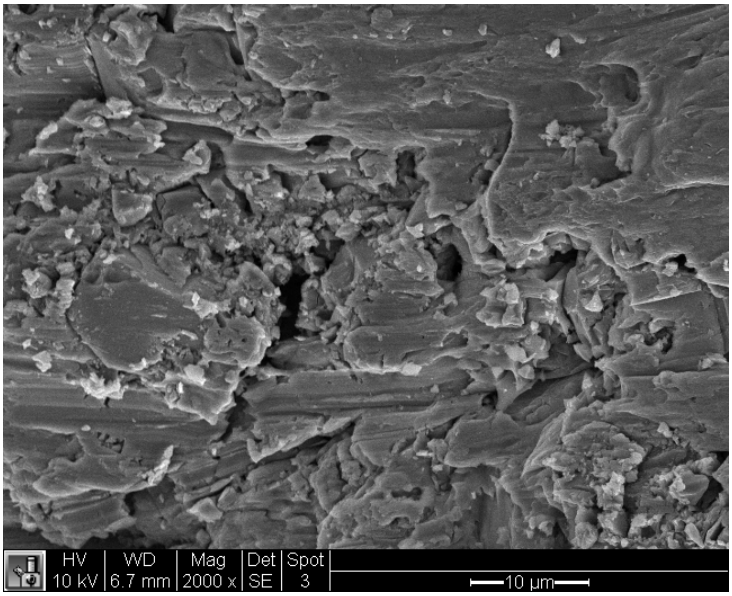
HV
10 kV
WD
6.7 mm
Mag
2000 x
Det
SE
Spot
3
10 µm

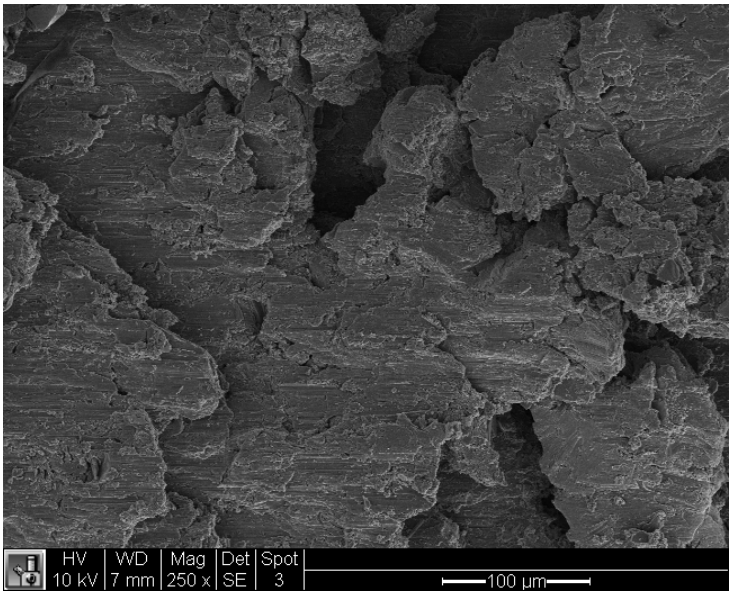
HV
10 kV
WD
7 mm
Mag
250 x
Det
SE
Spot
3
100 µm

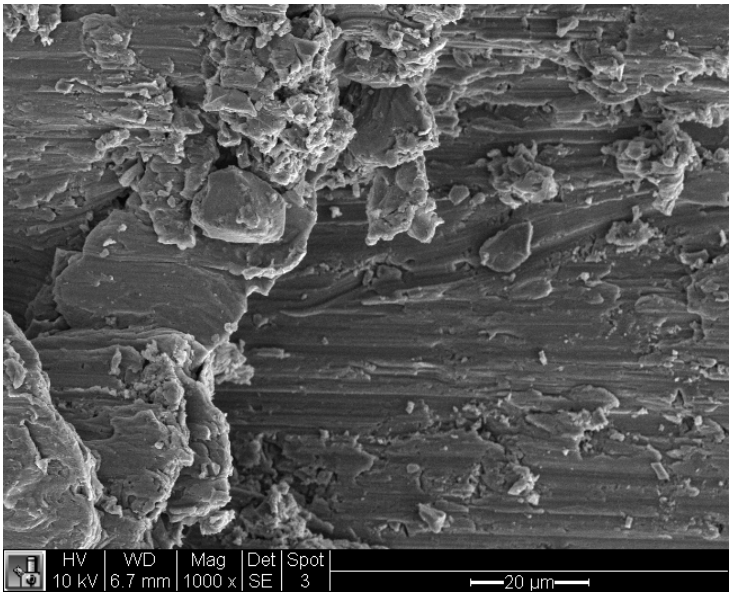
HV
10 kV
WD
6.7 mm
Mag
1000 x
Det
SE
Spot
3
20 µm

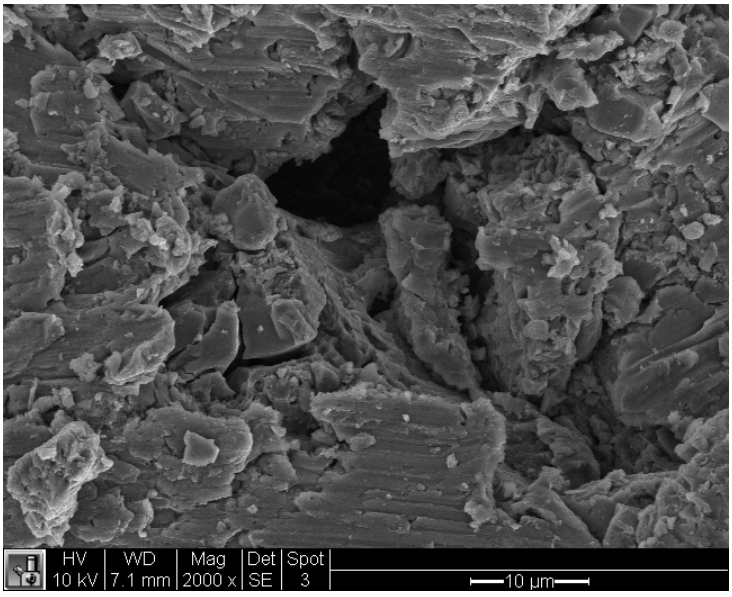
HV
10 kV
WD
7.1 mm
Mag
2000 x
Det
SE
Spot
3
10 µm

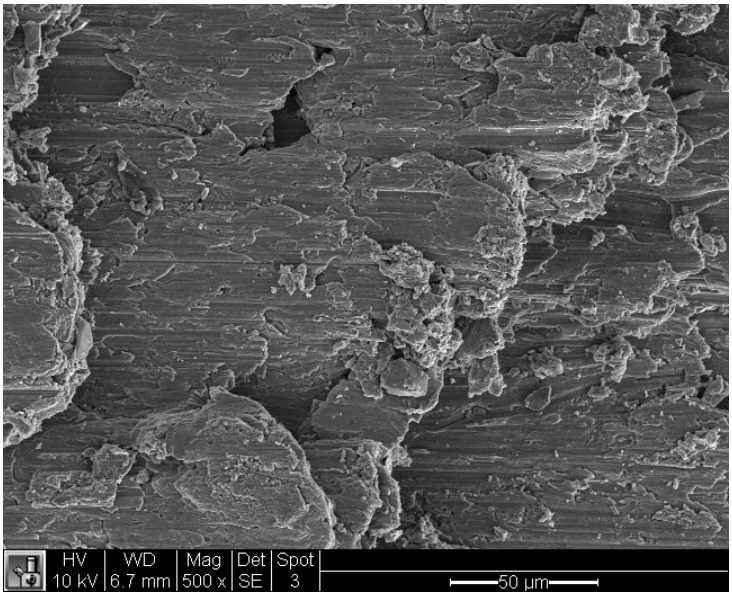

0.2 mm/rev, 4000RPM, Zone C

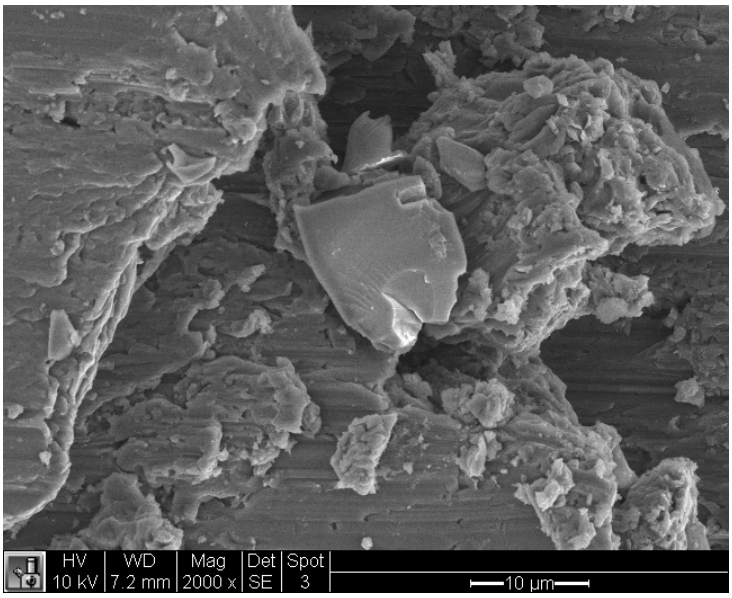

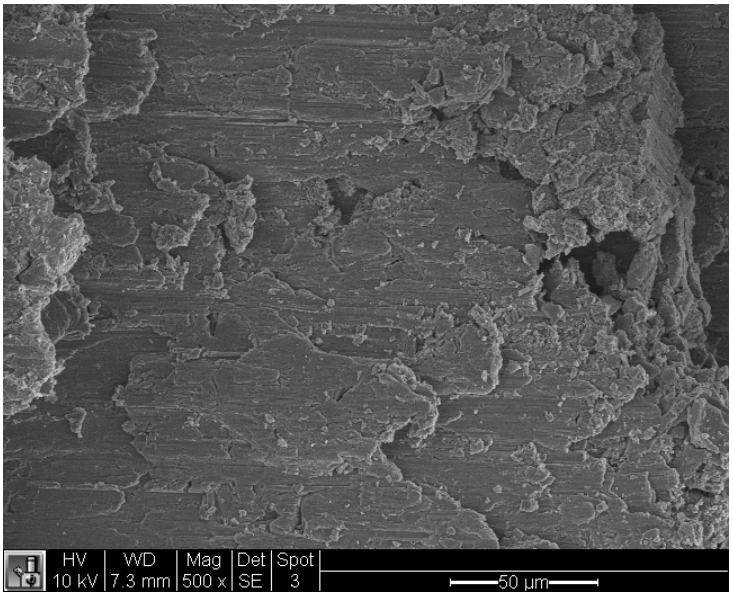
HV
10 kV
WD
7.3 mm
Mag
500 x
Det
SE
Spot
3
50 µm

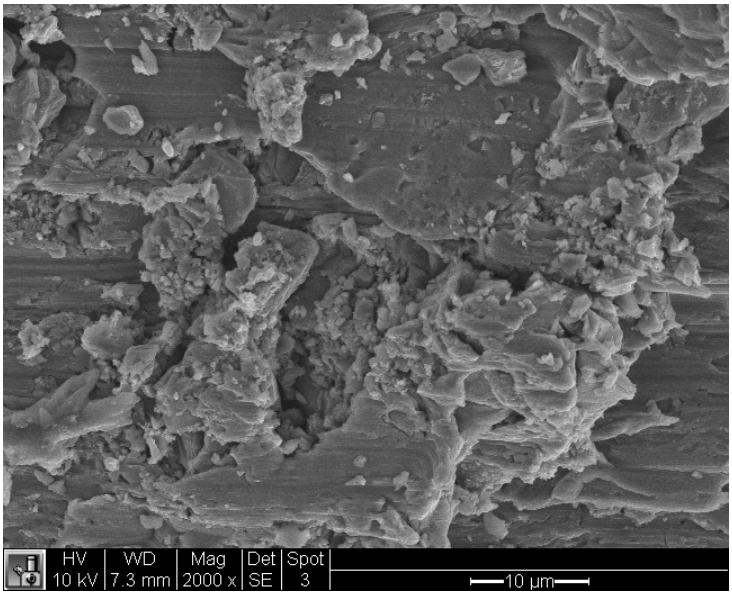
HV
10 kV
WD
7.3 mm
Mag
2000 x
Det
SE
Spot
3
10 µm

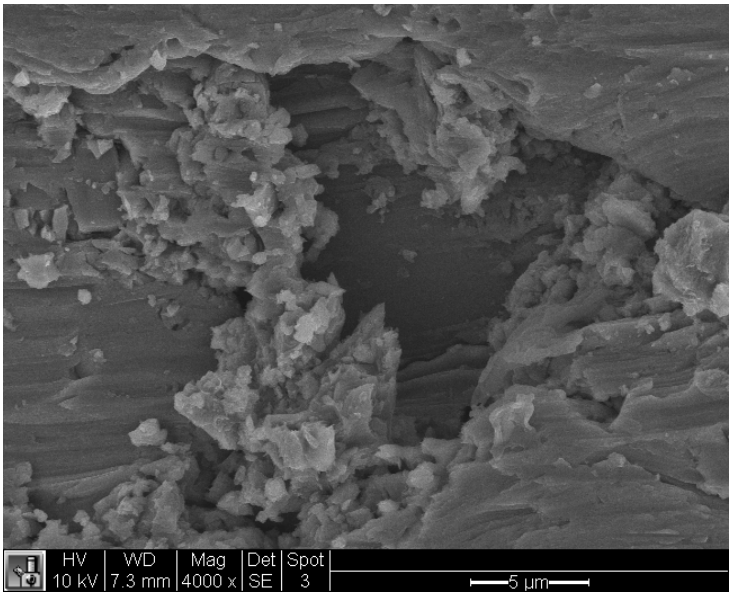
HV
10 kV
WD
7.3 mm
Mag
4000 x
Det
SE
Spot
3
5 µm

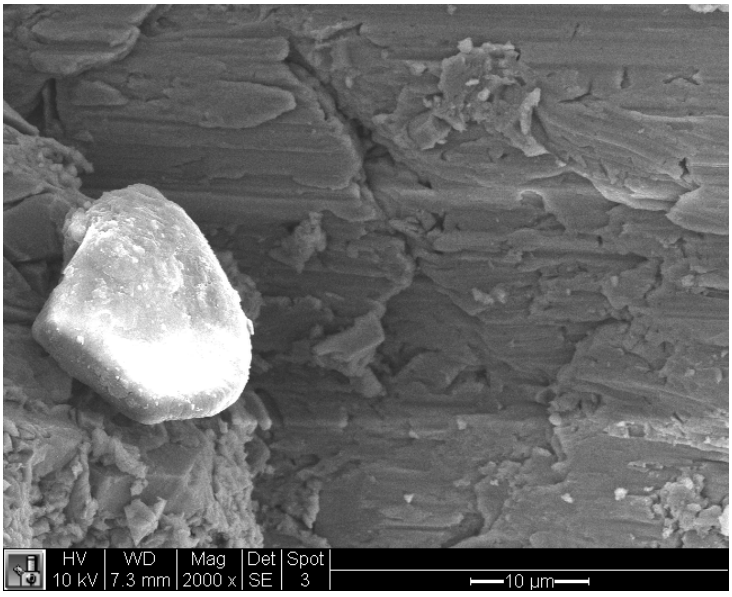
HV
10 kV
WD
7.3 mm
Mag
2000 x
Det
SE
Spot
3
10 µm

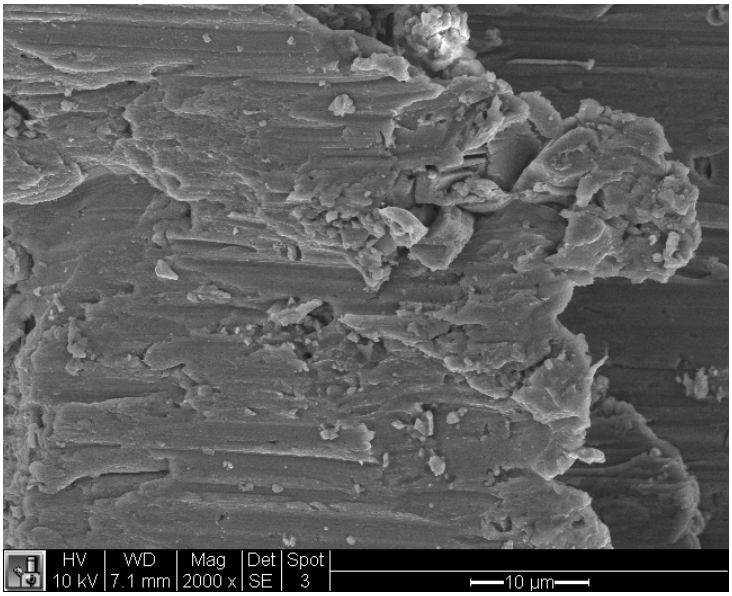
HV
10 kV
WD
7.1 mm
Mag
2000 x
Det
SE
Spot
3
10 µm

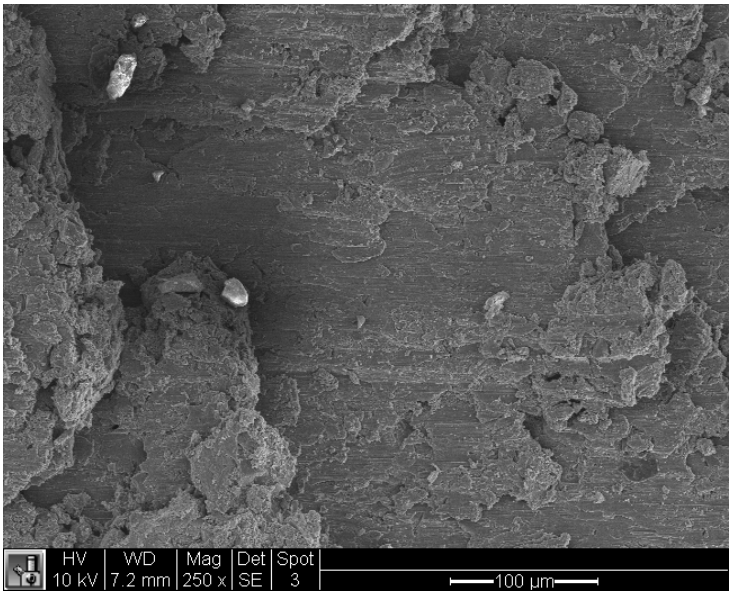
HV
10 kV
WD
7.2 mm
Mag
250 x
Det
SE
Spot
3
100 µm

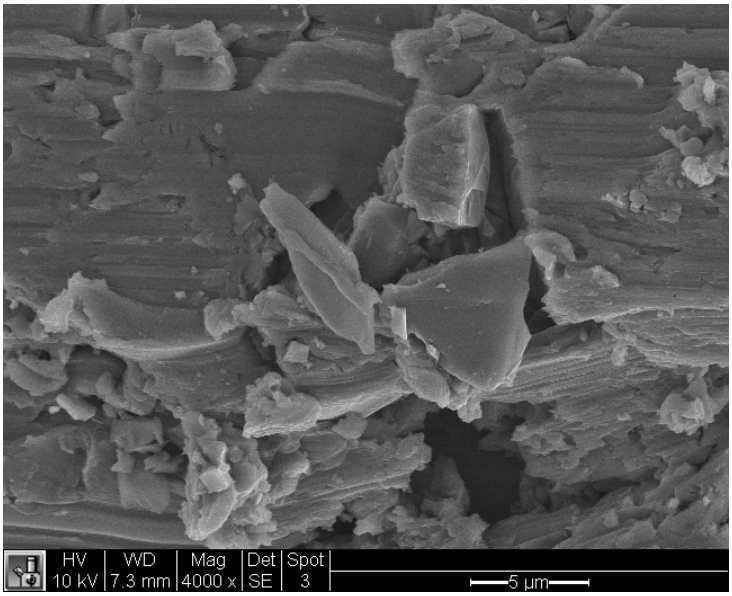
HV
10 kV
WD
7.3 mm
Mag
4000 x
Det
SE
Spot
3
5 µm

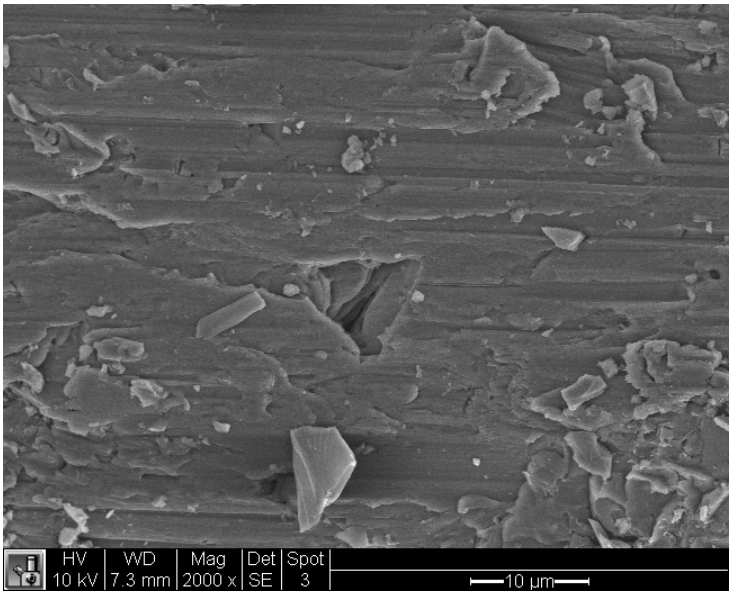
HV
10 kV
WD
7.3 mm
Mag
2000 x
Det
SE
Spot
3
10 µm

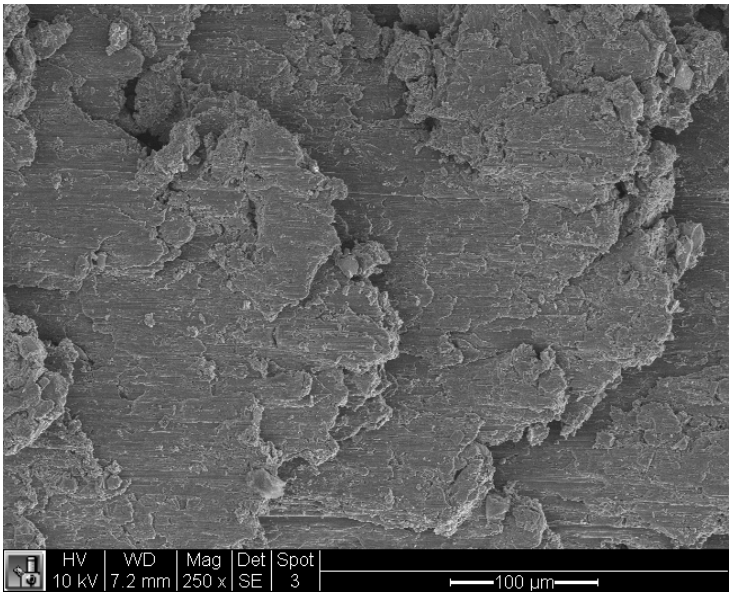
HV
10 kV
WD
7.2 mm
Mag
250 x
Det
SE
Spot
3
100 µm

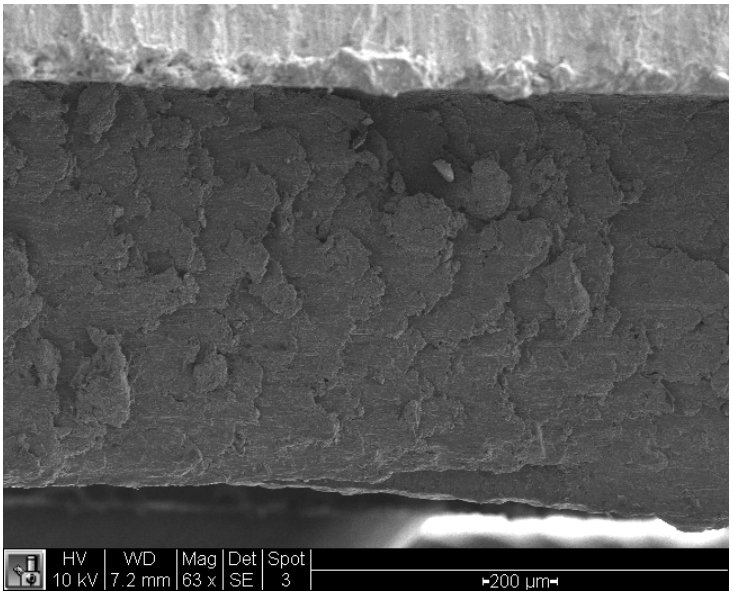
HV
10 kV
WD
7.2 mm
Mag
63 x
Det
SE
Spot
3
200 µm

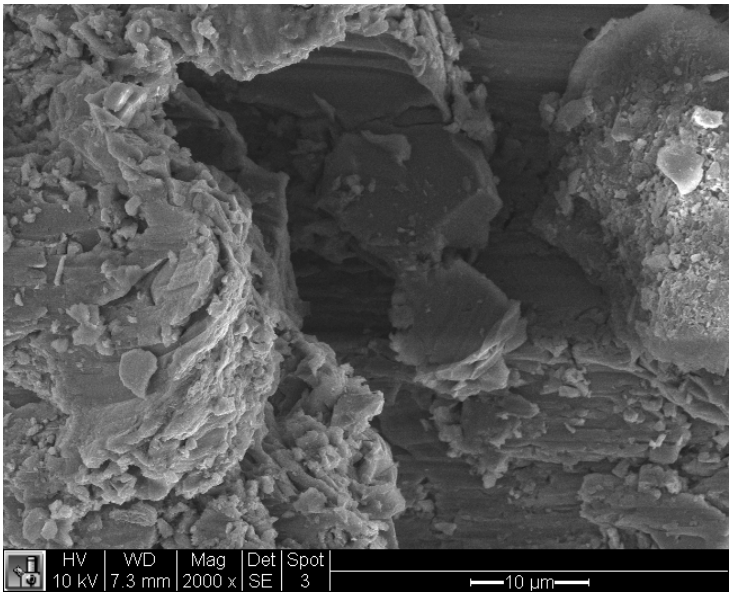

C.3 Magnesium composite

0.2 mm/rev, 2000 RPM

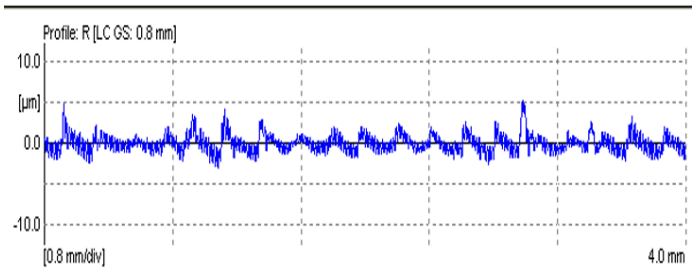

0.2 mm/rev, 4000 RPM

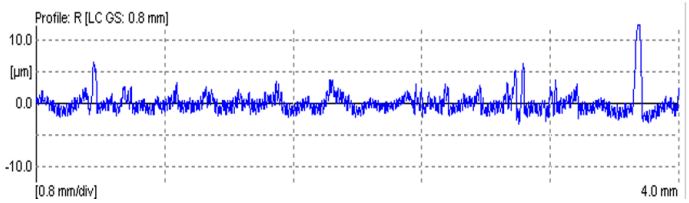

0.3 mm/rev, 1000 RPM

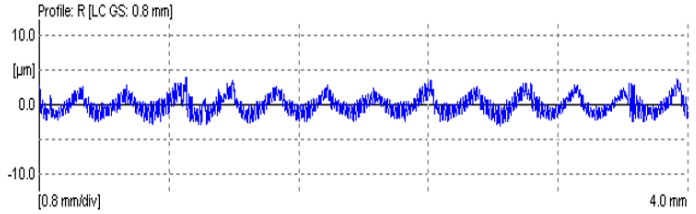

0.3 mm/rev, 1000 RPM

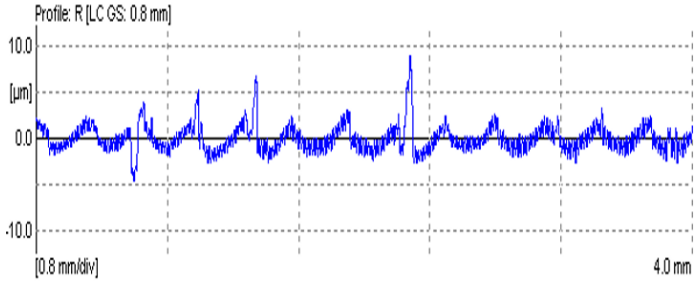

0.3 mm/rev, 3000 RPM

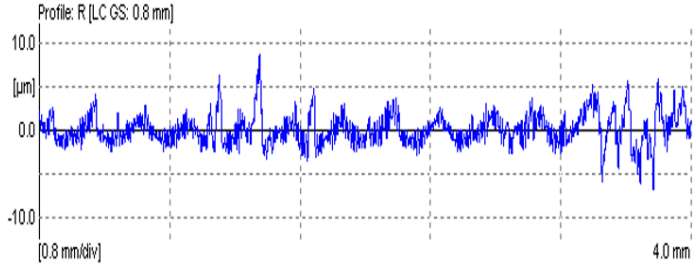

0.3 mm/rev, 3000 RPM

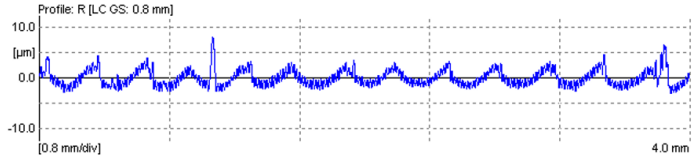

0.3 mm/rev, 3000 RPM

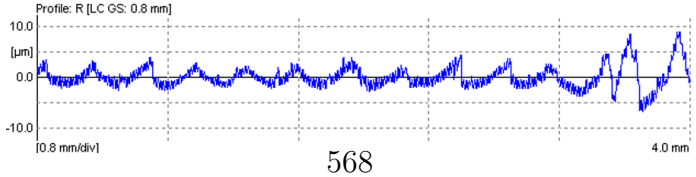

0.05 mm/rev, 1000 RPM

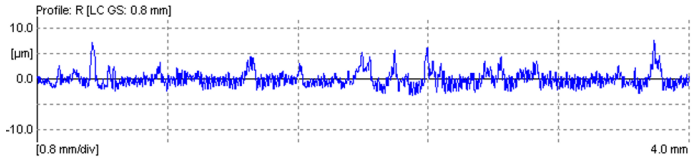

0.05 mm/rev, 2000 RPM

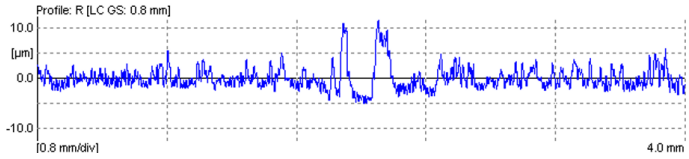

0.5 mm/rev, 2000 RPM

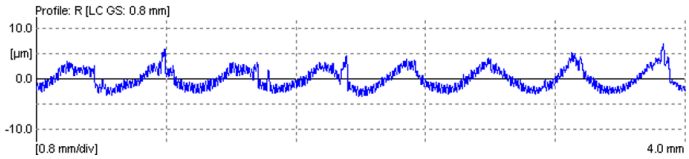

0.5 mm/rev, 2000 RPM

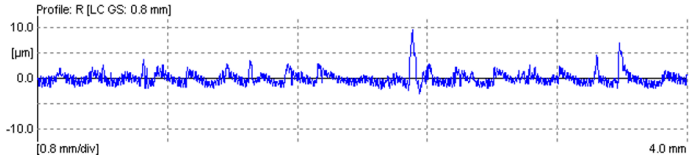

0.05 mm/rev, 3000 RPM

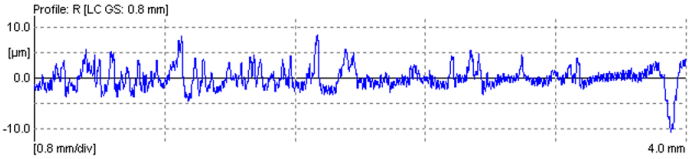

0.5 mm/rev, 4000 RPM

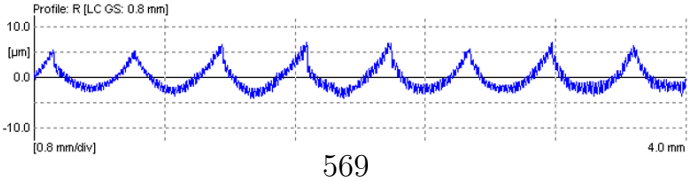

0.05 mm/rev, 4000 RPM



0.005 mm/rev, 4000 RPM

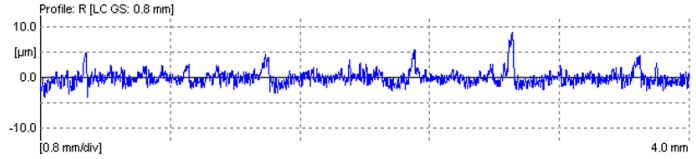

C.3.1 SEM micrographs of the machined surface

0.3 mm/rev, 3000 RPM

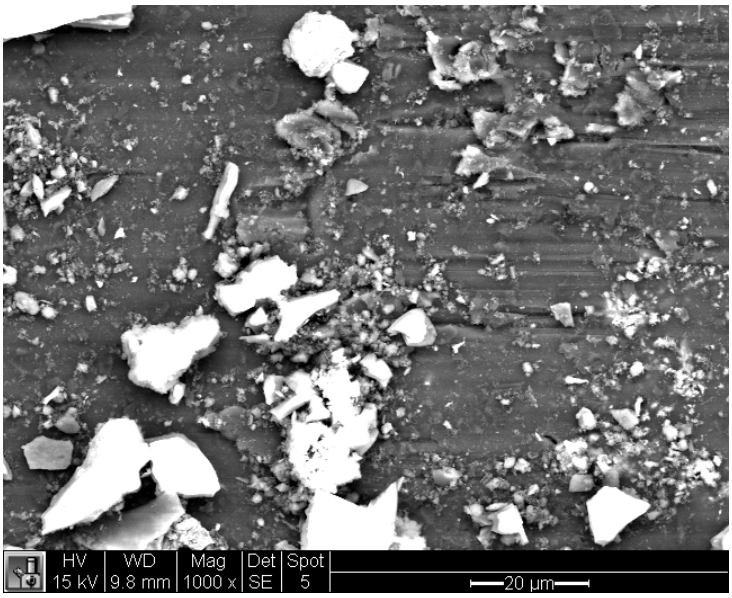

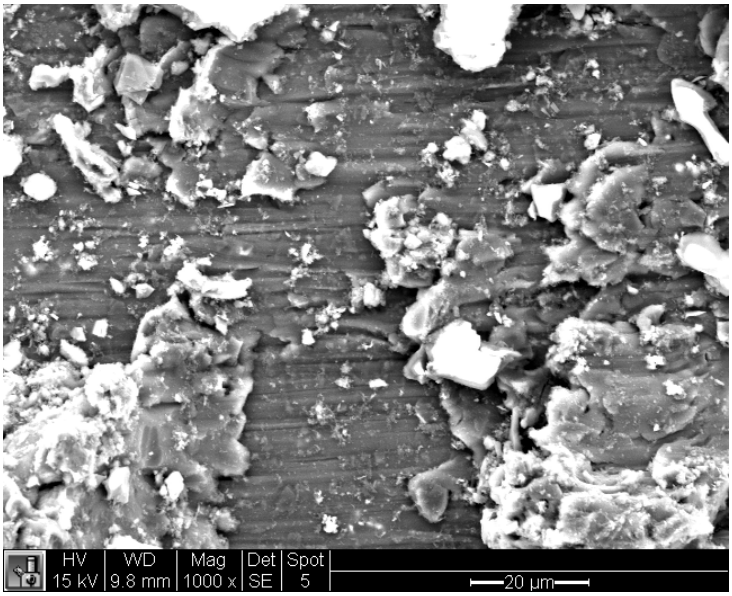
HV
15 kV
WD
9.8 mm
Mag
1000 x
Det
SE
Spot
5
20 µm

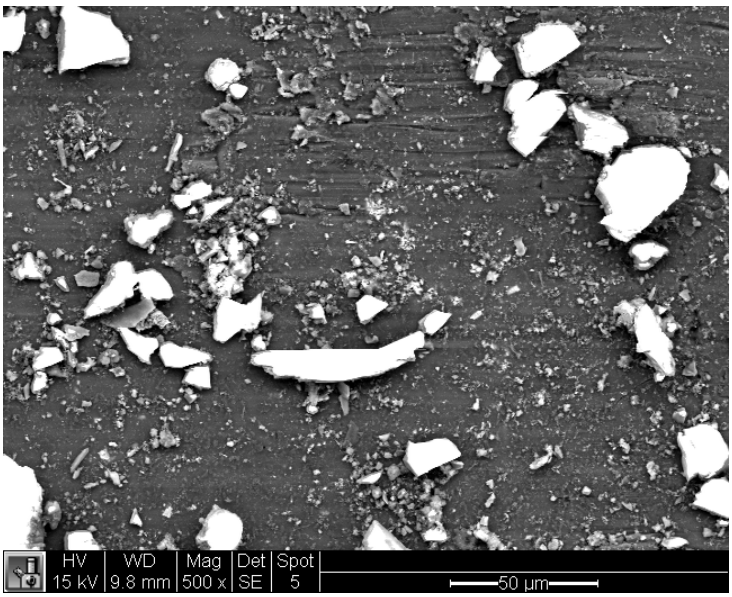
HV
15 kV
WD
9.8 mm
Mag
500 x
Det
SE
Spot
5
50 µm

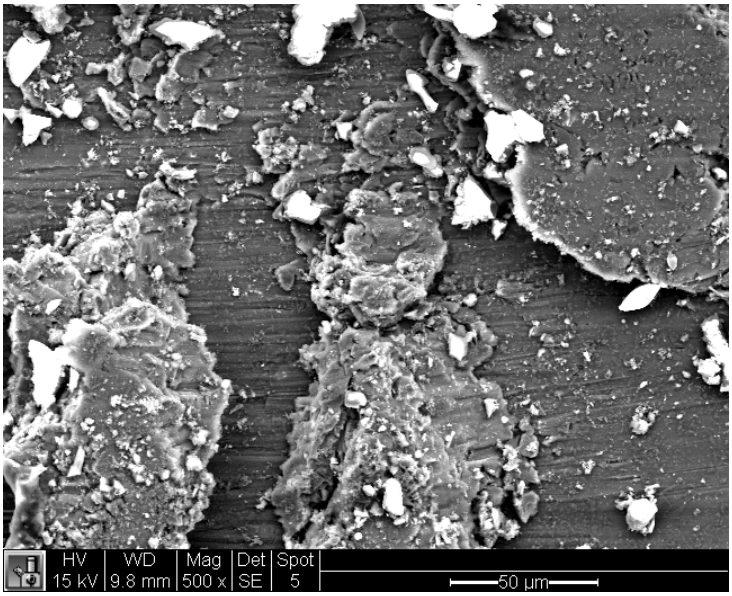
HV
15 kV
WD
9.8 mm
Mag
500 x
Det
SE
Spot
5
50 µm

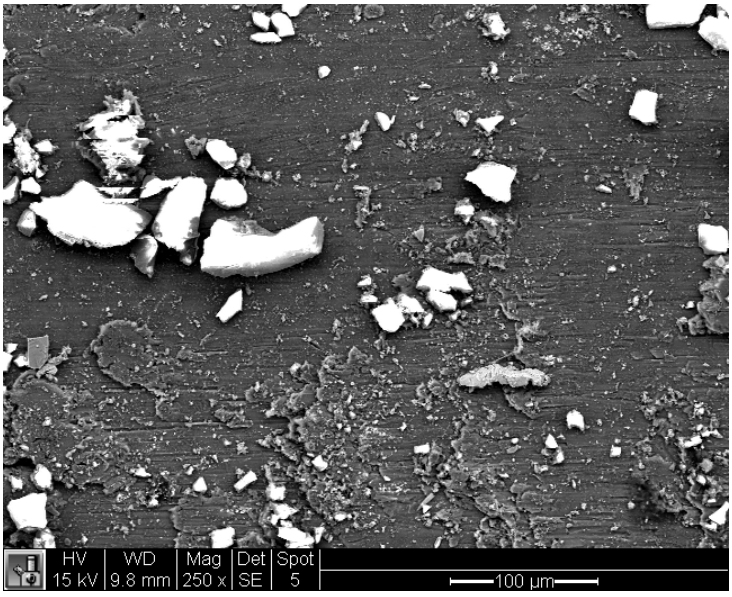
HV
15 kV
WD
9.8 mm
Mag
250 x
Det
SE
Spot
5
100 µm

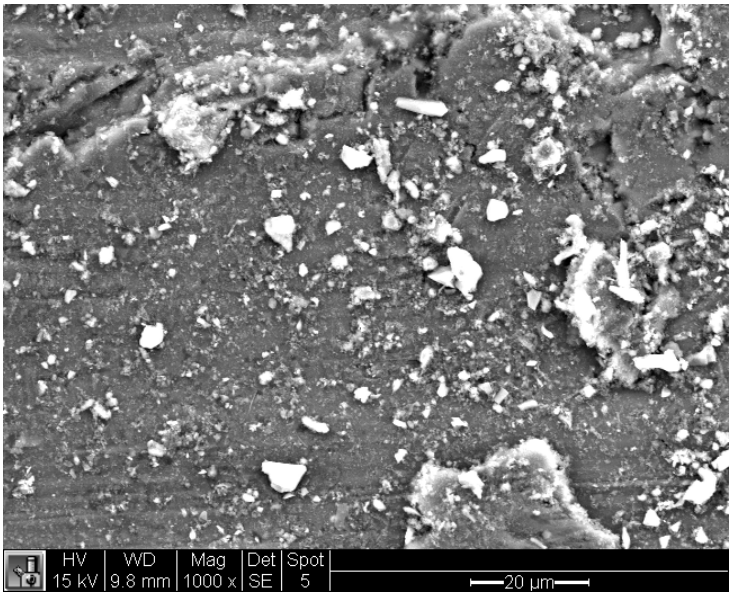
HV
15 kV
WD
9.8 mm
Mag
1000 x
Det
SE
Spot
5
20 µm

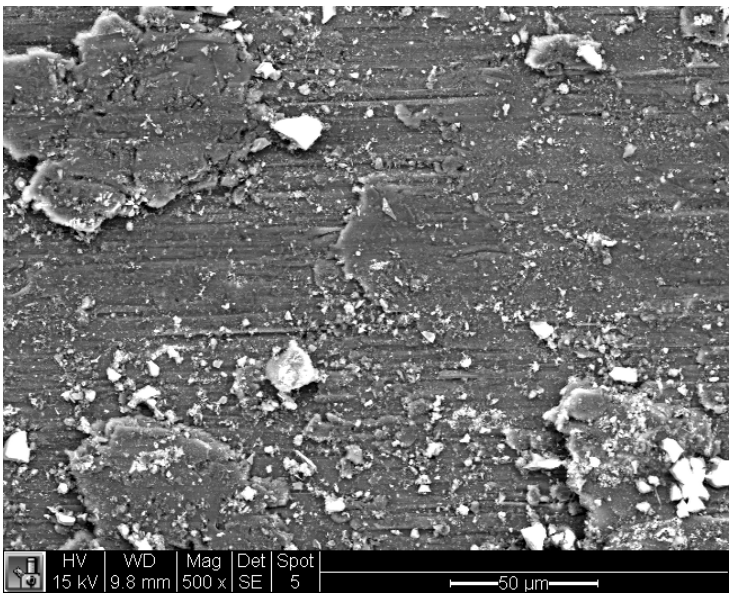
HV
15 kV
WD
9.8 mm
Mag
500 x
Det
SE
Spot
5
50 µm

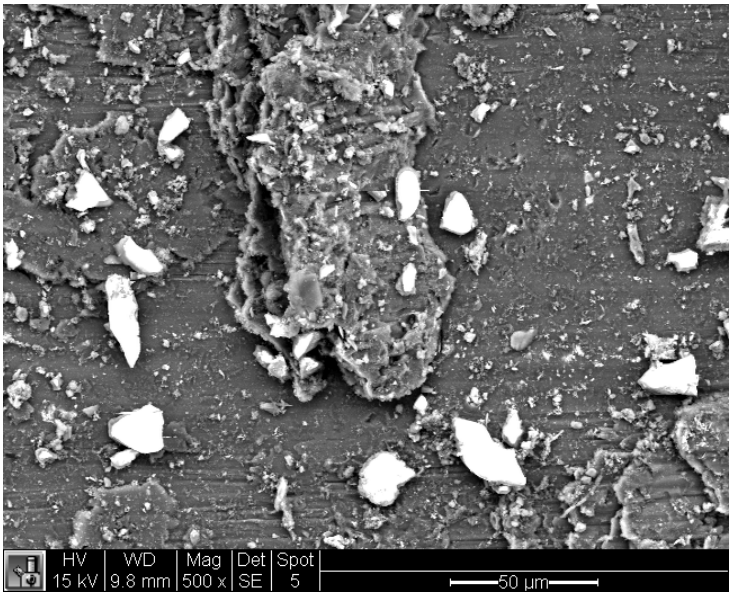

0.5 mm/rev, 4000 RPM

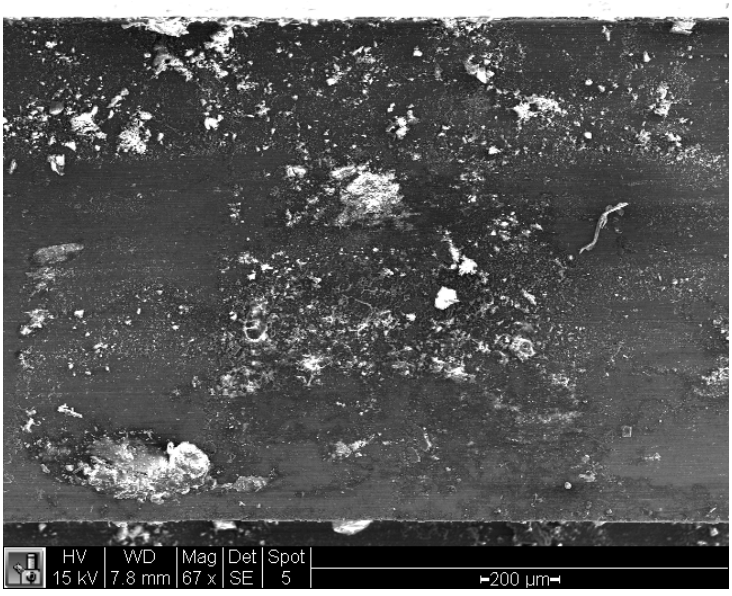

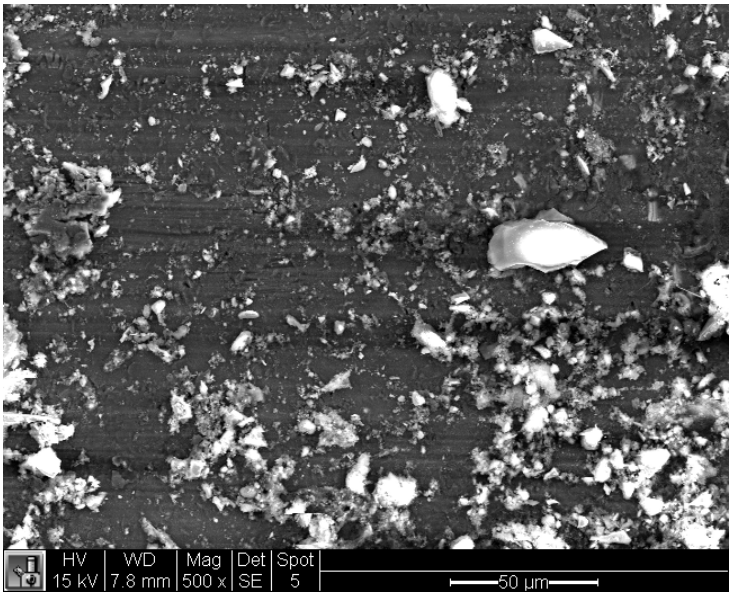
HV
15 kV
WD
7.8 mm
Mag
500 x
Det
SE
Spot
5
50 µm

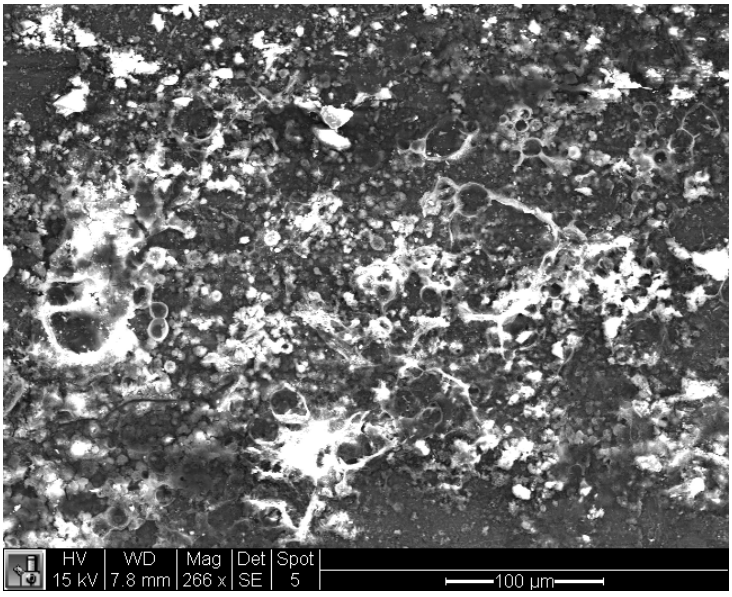
HV
15 kV
WD
7.8 mm
Mag
266 x
Det
SE
Spot
5
100 µm

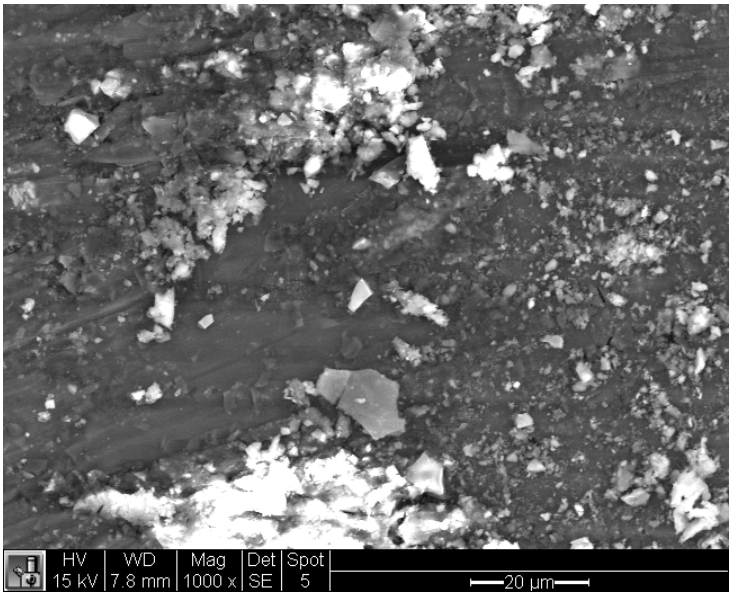
HV
15 kV
WD
7.8 mm
Mag
1000 x
Det
SE
Spot
5
20 µm

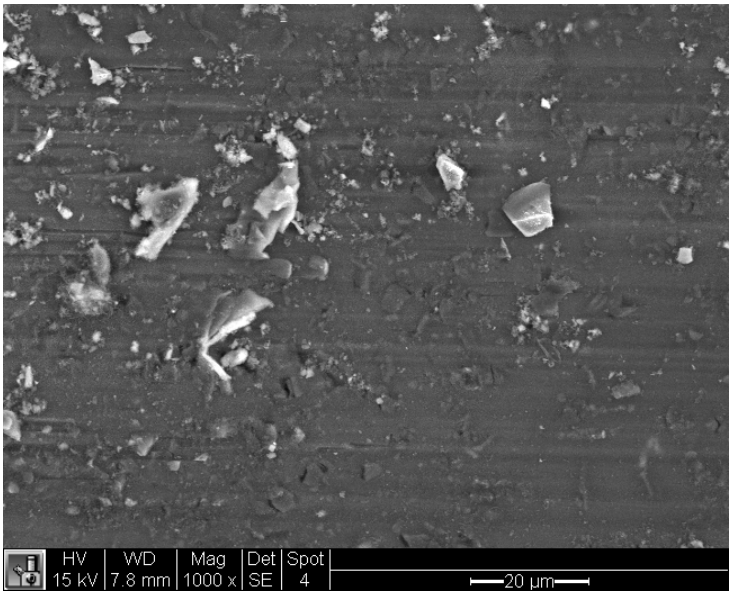
HV
15 kV
WD
7.8 mm
Mag
1000 x
Det
SE
Spot
4
20 µm

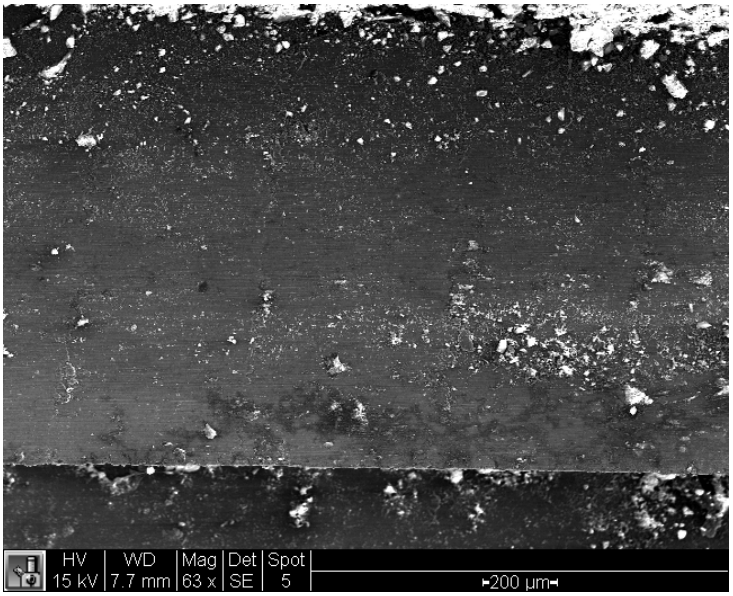
HV
15 kV
WD
7.7 mm
Mag
63 x
Det
SE
Spot
5
200 µm

Appendix D

D.1 Average Cutting forces for Functionally gradient Al/SiCp

Feed, mm/rev	Speed, RPM	Fx, A, N	Fy, A, N	Fz, A, N	Fx, B, N	Fy,B, N	Fz, B, N	Fx, C, N	Fy, C, N	Fz, C, N
0.1	1000	132	111	20	137	114.3	21	141	123	20
0.2	1000	104.39	119.9	20	116.6	112.3	20	119.6	121	20
0.3	1000	100.2	125	23	103.5	122	21	117.05	137	20
0.4	1000	203	191	27	263.3	187	24	298.2	243	20
0.5	1000	281.2	286	59	238.2	296	53	377	300	52
0.1	2000	102.3	84.5	31	86.38	86.35	25.3	86.77	86.5	24
0.2	2000	107.36	105.2	21	109.54	109.0889	18.3	112.43	109.63	15
0.3	2000	111.2	125.7	25	117.2	127	21	129.45	130	18
0.4	2000	143.51	167	26	150.5	166	22	170	166	20
0.5	2000	252.2	152	44	260.1	170.5	40	361	186	34.3
0.1	3000	104.5	90.7	20	109.5	87.23	21	114.15	90.79	20
0.2	3000	72	87	23	89.26	101.52	23	90.5	103.3	20
0.3	3000	93.3	111	27	105	116	24	137	164	23
0.4	3000	304.52	206	47	340	203	38	212.788	140.5134	37
0.5	3000	387	219	50	363	238	41	361	253	39

0.1	4000	105.9	91.2	38	140.36	92.4	24	99.7267	95.44	20
0.2	4000	111.13	100.41	42	113.71	98.53	38	150.25	118.25	30
0.3	4000	293.12	152	55	325.2	165.2	47	338	178	38
0.4	4000	178.53	169.2	25	180.3	170	20	285.5	222	20
0.5	4000	427	289.04	27	434	283.45	25	436.8521	240.4611	23
0.1	5000	212.18	116.56	60	247.53	145.24	53	278.1	157.35	48
0.2	5000	130.35	143.96	60	143.56	144.6	55	143.54	146.38	43
0.3	5000	262.5	153	73	270	168.9	65	310	182	59
0.4	5000	202	222.5	63	237.33	199.43	60	277	219	60
0.5	5000	315	253.5	67	510	294.2584	65	335.6973	313.5	65

D.2 Average surface roughness parameters for Functionally gradient Al/SiCp

Feed mm/rev	Speed RPM	Ra, A (µm)	Rz, A (µm)	Ra, B (µm)	Rz, B (µm)	Ra, C (µm)	Rz, C (µm)
0.1	1000	12.82	68.286	14.016	73.154	13.2265	67.276
0.1	2000	11.31	52.8	15.84	75.69	15.84	80.4
0.1	3000	11.61	56.94	14.478	86.65	12.9	69.549
0.1	4000	14.842	72.099	15.003	63.75	15.381	74.72
0.1	5000	16.63	86.381	15.581	78.7	15.58	78.79
0.2	1000	16.83	79.905	14.739	64.376	13.172	67.31
0.2	2000	14.599	67.63	13.896	69.346	14.36	85.868
0.2	3000	14.6	69.5	14.2	75.9	15.6	93.5
0.2	4000	12.31	61.215	18.404	88.58	21.009	107.52
0.2	5000	17.017	87.56	20.438	97.747	20.455	95.262
0.3	1000	16.843	88.637	20.341	99.545	14.496	68.067
0.3	2000	11.747	61.05	14.794	70.263	15.764	61.05
0.3	3000	17.084	85.961	18.988	91.59	20.596	99.002
0.3	4000	16.5	87	19.7	95.4	20.7	103.5
0.3	5000	16.93	84.871	17.687	85.209	19.634	93.896
0.4	1000	18.015	77.842	23.899	112.593	23.427	108.46
0.4	2000	21.59	108.186	23.075	111.617	28.61	134.092
0.4	3000	21.766	106.521	30.218	133.66	32.001	144.366
0.4	4000	23.8	110.5	33.5	145.9	33.8	147.8
0.5	1000	23.5	111.8	24.8	114.5	30.8	115.8
0.5	2000	27.8	121.75	30.6	137	33.5	138
0.5	3000	29.8	138	32.3	142	31.5	132

D. 3 Average 3D surface roughness parameters for Functionally gradient Al/SiCp

Feed	Speed	Sa, A	Sz, B	Sa, B	Sz, B	Sa, C	Sa, C
0.1	1000	16.51	144.42	21.89	121.97	18.2	119.35
0.1	2000	16.2	148.6	20.5	124.78	19.75	125.69
0.1	3000	15.48	142.9	19.06	144.9	20.60	175.83
0.1	4000	50.240	311.3	38.702	247.21	36.965	247.21
0.1	5000	52.49	342.6	46.28	323.19	88.077	481.62
0.2	1000	20.23	152.31	13.367	129.66	18.102	123.95
0.2	2000	15.22	120.79	20.915	136.13	36.724	253.551
0.2	3000	20.997	138.86	44.13	256.30	67.914	532.39
0.2	4000	9.81107	74.5742	31.347	197.12	31.533	299.118
0.2	5000	44.71	238.86	57.208	279.763	75.012	416.46
0.3	1000	20.795	105.65	30.101	145.53	44.6234	307.386
0.3	2000	41.489	198.35	41.185	233.78	50.603	241.00
0.3	3000	34.99	193.95	43.27	255.21	56.696	342.080
0.3	4000	92.966	376.04	50.2591	285.702	91.915	633.382
0.3	5000	76.21	389.53	62.641	364.55	116.31	677.12
0.4	1000	28.862	174.00	35.3179	242.06	50.167	336.62
0.4	2000	63.6189	357.01	52.095	368.68	77.379	417.08
0.4	3000	28.935	176.248	64.736	368.53	126.705	747.918
0.4	4000	48.78	189.457	62.78	345	98.5	455.258
0.4	5000	52.417	329.494	66.6539	384.696	84.0354	454.243
0.5	1000	35.5169	217.397	52.4636	419.606	50.9984	294.626
0.5	3000	63.3638	312.403	79.2232	358.212	65.3766	353.428
0.5	4000	38.6046	257.812	79.4566	711.412	54.0928	361.04
0.5	5000	73.7376	551.9579	84.25899	703.8596	86.52508	682.686

D.4 Average Tool wear for A/SiCp

Feed, mm/rev	Speed, RPM	Tool Wear, µm
0.1	1000	33.15
0.2	1000	36.45
0.3	1000	49.81
0.4	1000	79
0.5	1000	81
0.1	2000	35.43
0.2	2000	51.4498
0.3	2000	55
0.4	2000	58
0.5	2000	102.7626
0.1	3000	60.39
0.2	3000	41.77
0.3	3000	38
0.4	3000	68
0.5	3000	59.32
0.1	4000	53
0.2	4000	35
0.3	4000	65
0.4	4000	54.0514
0.5	4000	79
0.1	5000	50
0.2	5000	60
0.3	5000	70
0.4	5000	69
0.5	5000	60

D.4 Average data for Mg/Sicp

Feed, mm/rev	Speed, RPM	Tool wear, µm	Fy, N	Fx, N	Fz, N	Ra, µm	Rq, µm	Rz, µm
0.5	4000	29.8142	82.5	120.5	30	1.416	2.56	10.73
0.5	4000	22.3607	73.5	106	40	2.017	2.4	10.03
0.3	1000	17.9505	65.93	70.1	7	1.087	1.32	6.1
0.05	1000	43.4613	94.14	46.96	11	1.097	1.497	8.7
0.05	4000	37.2678	98	46.5	9	0.98	1.38	8.62
0.05	4000	40.2768	94.7612	50.1	11	0.952	1.183	6.35
0.3	1000	14.9071	74.53	70	10	1.073	1.459	8.057
0.05	3000	44.174	101.5	32.5	8	1.577	2.163	11.52
0.3	3000	17.9505	70.7	74	8.2	1.33	1.76	9.2
0.5	2000	12.18	66.74	93.78	7	1.635	1.9	8.6
0.5	2000	14.9071	64.3647	90.1931	7	0.904	1.274	7.54
0.05	2000	36.0555	83.8	46.2989	9	1.604	2.28	9.71
0.3	3000	12.0185	71.7478	82.5893	8	1.282	1.606	7.83
0.3	3000	16.1	61	75.1456	6.7	1.504	2.072	8.2
0.2	4000	16.6667	64	71	8	1.061	1.712	9.55
0.2	2000	29.8142	58.96	51.2275	14	0.821	1.081	6.4

Appendix E

FORCE MODELING

E.1 Force modeling MATLAB code

```
% considering particle size
close all
clear all
clc
tic
% addpath('U:\Force data_MgSiC_new\MgSiC_new1')
% load('Mgsic_F02_S4000_1.mat');
%Fx=Fy;
%plot(Fx)
%fft(Fx);
sum2=0;
sum1=0;
num=xlsread('MgSiC_force_analysis_new.xlsx',10,'A2:E23');
f=num(:,4); % mm/rev
speed=num(:,5);

s1=length(f);

v=speed.*f/1000; % m/min
fpm=(f.*speed)/25.4;
p2=1;
n_interactions= (32./f ).* 2;
N=[19;44;73;83;115;150;188;200]; % particle size count
```

```
total=sum(N);
l1=1;
l2=1;
l3=1;
p3=1;
ch=1;
element_size=3;
w=N/total;
p1=1;
phi=53.5;
p=1;
n=[0.5;1;1.5;2;2.5;3;3.5;4];
n_elements=1270/3; % size of the element is 3 microns
n_elements_p=floor(0.15*n_elements);
n_elements=floor(n_elements);
sign=1;
for t8=1:1:length(f)
    force_plot=[];
    sum1=[];
    sum2=[];
    %phi=[];
for j=1:1:n_interactions(t8,1)
    sign=sign+1;
% for each engagement
total_force_per_angle =[];
p3=1;
t=1;
%clear force_interaction force_plot
for phi=0:1:180
     % for every 180
  if phi > 0 & phi ≤54
for i =1:1:n_elements
Area_ratio=[];
```

```
fr_stress_p=[];
y=randsample(n,n_elements_p,true,w);
Area_p=pi/4 * y.^2;
Area_matrix= 9-Area_p;
Area_ratio(:,1)= Area_matrix./9; % matrix/element
Area_ratio(64:n_elements,1)=1;
avg=3;
surface_energy=5.95/2; % J/m2
a=y; % diameter of the particles
E=110; % Gpa = 10*9 N/m2
   psi=tand(2*3*i*tand(30)/(6.35*1000));
    eng_angle=phi-psi;
    ch_eng=53-psi; % check if engaged or not

if eng_angle<ch_eng

if Area_ratio(i,1)<0 % particles bigger than the elements are fractured ...
    completely.
frac_stress(:,1)=3.3*10^6/(pi*y(i,1)*10^-6)^0.5;
%frac_stress=((2*E*10^9*surface_energy)./(pi*3*10^-6)).^0.5;
fr_force_p=frac_stress*((pi/4)*y(i,1)^2).* (10^-12); % normal loading ...
    condition
sum2=fr_force_p+sum2;
element_force=fr_force_p*sind(eng_angle);
l1=l1+1;
end
s=0;
t=1;
if Area_ratio(i,1)==1 % only matrix is present in the element, no particle
%fr_stress_p(n_elements,1)=0;+
%fr_actual = fr_stress_p(randperm(size(fr_stress_p, 1)), 1);
%f1=0.75*1200*v^(-0.529)*(f)^(0.85)*Area_ratio(i,1);
f1=1.69.*102.053*(speed(t8,1)).^(0.0449).*(f(t8,1) * ...
```

```
      sind(phi-psi)).^0.6777;
element_force=f1*(1/n_elements);
    %element_force(i,1)=(f1(i,1)+fr_actual(t,1))*sind(eng_angle);
    t=t+1;

    l2=l2+1;
end
if Area_ratio(i,1)<1 && Area_ratio(i,1)>0
    %Area_ratio(i,1)>(pi/4) % Particle debonding occurs, using ...
        Eshelby's criteria
        matrix_force=Area_matrix(i,1)*10^-12*(45*10^9*(25.2-4)*10^-6*(50-25))*(1270/3);
        sum1=sum1+matrix_force;
        %particle_force=
         element_force= matrix_force*sind(phi-psi);
         l3=l3+1;
end

else
         element_force=0; % takes care of the disengagement
         ch=ch+1;
end
if eng_angle<=0 % takes care of the engagement
    element_force=0;
end
force_interaction(p1,1)=element_force;


p1=p1+1;
end
total_force_per_angle(p2,1)=sum(force_interaction);
force_plot(p2,1)=(-1)^sign * total_force_per_angle(p2,1);
p2=p2+1;
p1=1;
```

```
119
120    else
121        force_plot(p2,1)=0;
122        p2=p2+1;
123    end
124
125 end
126 if j==2
127     sim_force=force_plot;
128 end
129 % total_force_interaction= sum(total_force_per_angle);
130 % force_plot(j,1)=(-1)^2 * total_force_interaction;
131  p3=p3+1;
132 end
133 C(t8,1)=max(force_plot(:,1));
134 end
135 toc
```

Appendix F

FUNCTIONALLY GRADIENT A359/SICP COMPOSITE FATIGUE

F.1 Surface Profiles

F.1.1 Feed: 0.1 mm/rev, Spindle speed: 1000 RPM

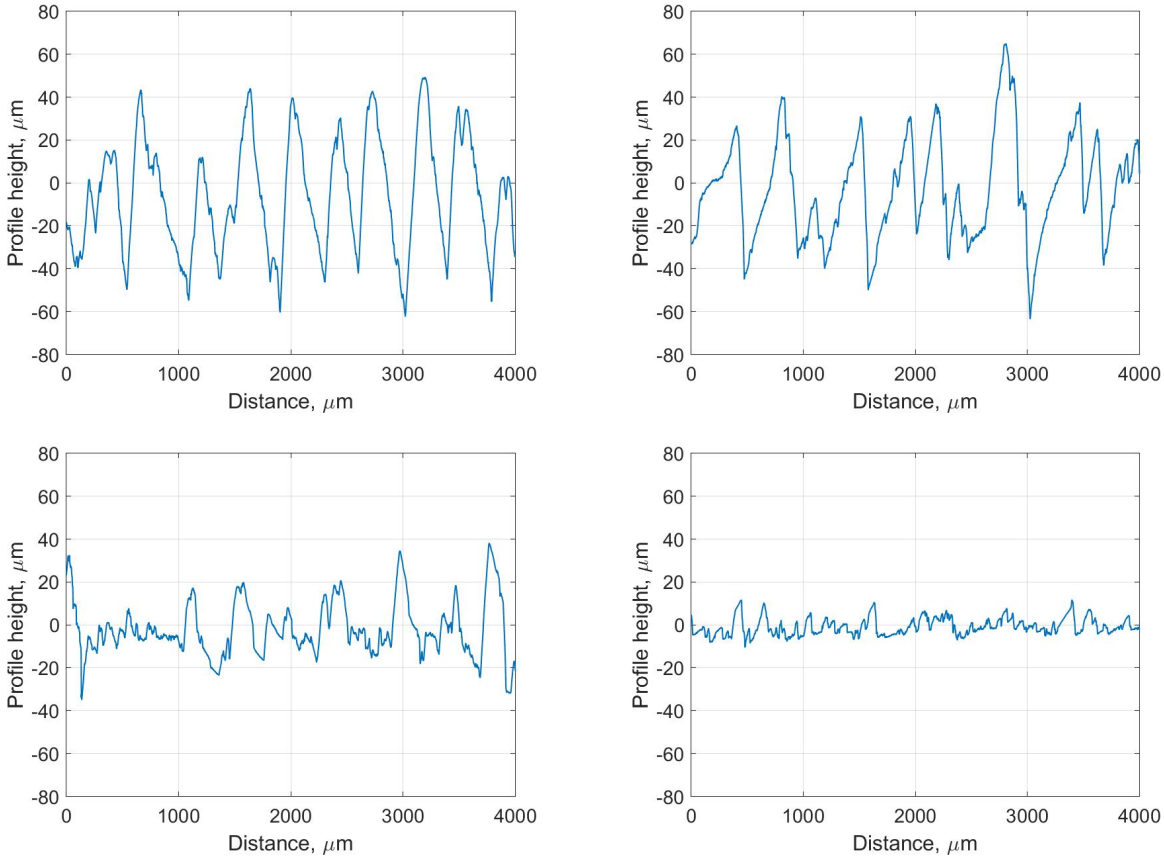

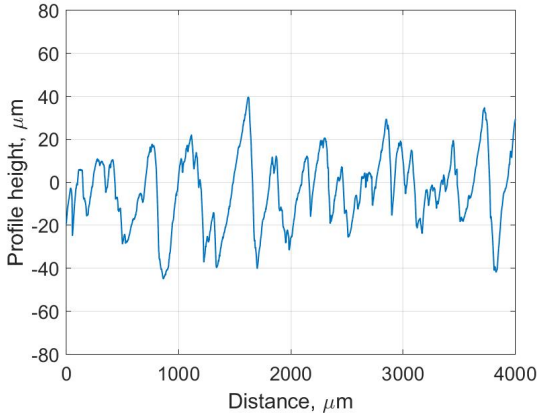
Profile height, μm
Distance, μm
80
60
40
20
0
-20
-40
-60
-80
0
1000
2000
3000
4000

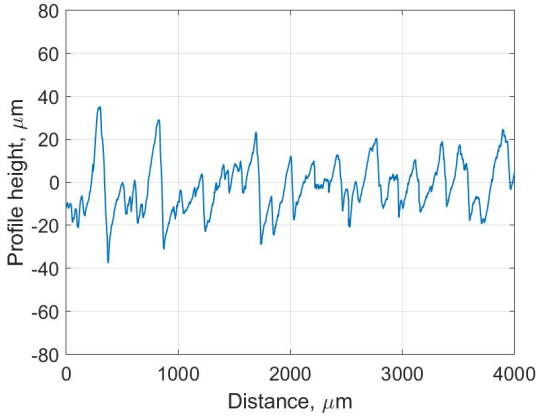
Profile height, μm
Distance, μm
80
60
40
20
0
-20
-40
-60
-80
0
1000
2000
3000
4000

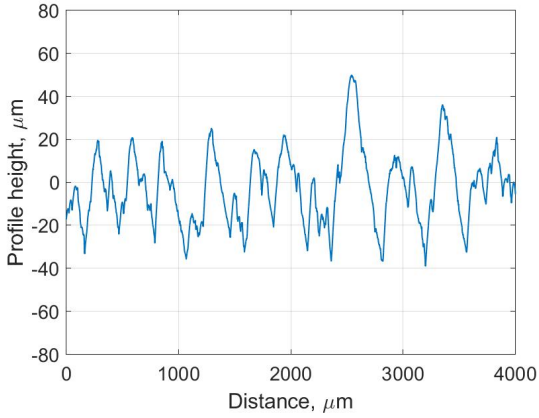
Profile height, μm
Distance, μm
80
60
40
20
0
-20
-40
-60
-80
0
1000
2000
3000
4000

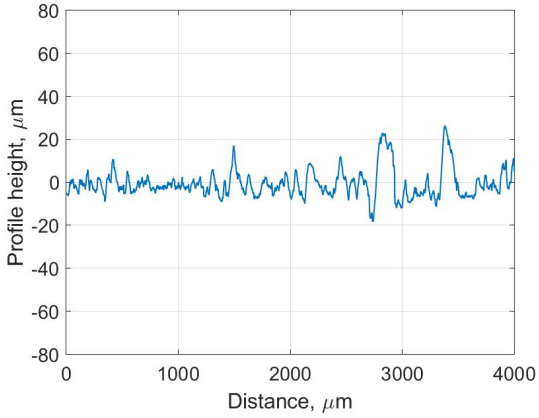
Profile height, μm
Distance, μm
80
60
40
20
0
-20
-40
-60
-80
0
1000
2000
3000
4000

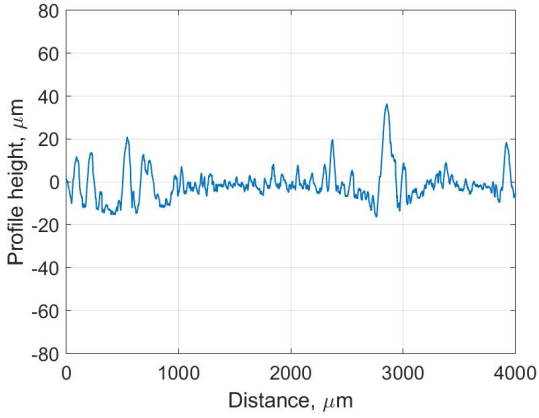
Profile height, μm
Distance, μm
80
60
40
20
0
-20
-40
-60
-80
0
1000
2000
3000
4000

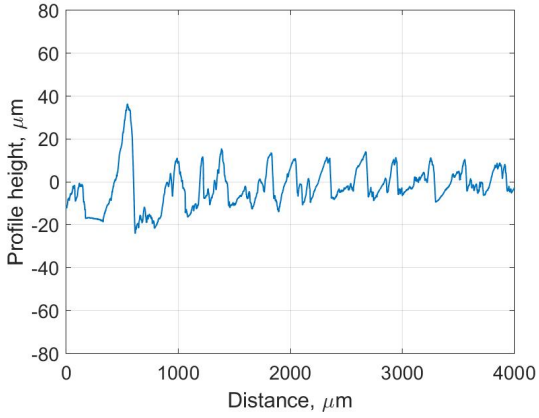
Profile height, μm
Distance, μm
80
60
40
20
0
-20
-40
-60
-80
0
1000
2000
3000
4000

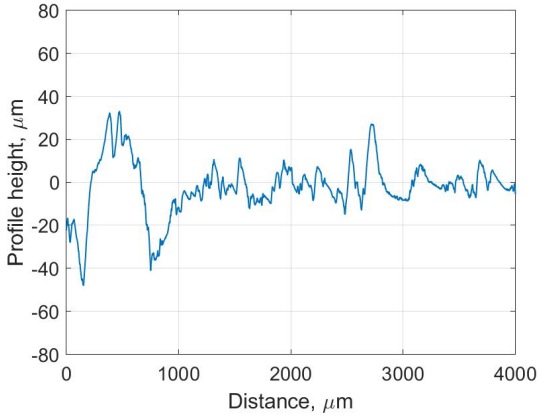
Profile height, μm
Distance, μm
80
60
40
20
0
-20
-40
-60
-80
0
1000
2000
3000
4000

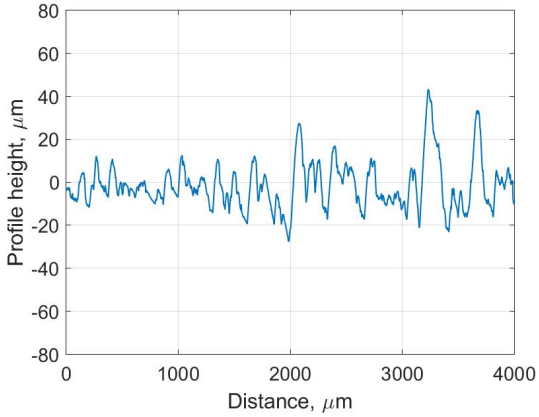
Profile height, μm
Distance, μm
80
60
40
20
0
-20
-40
-60
-80
0
1000
2000
3000
4000

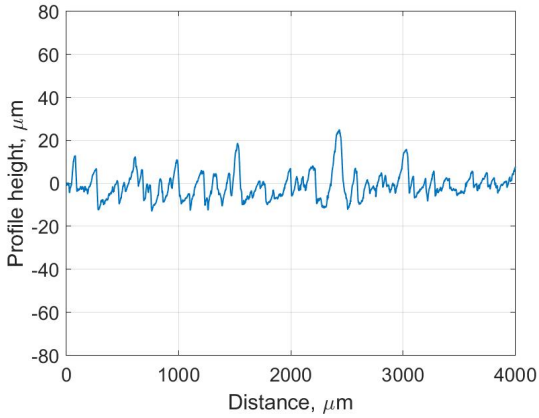
Profile height, μm
Distance, μm
80
60
40
20
0
-20
-40
-60
-80
0
1000
2000
3000
4000

F.1.2 Feed: 0.1 mm/rev, Spindle speed: 3000 RPM

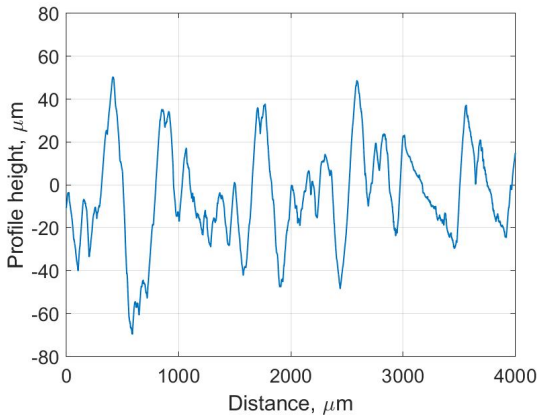

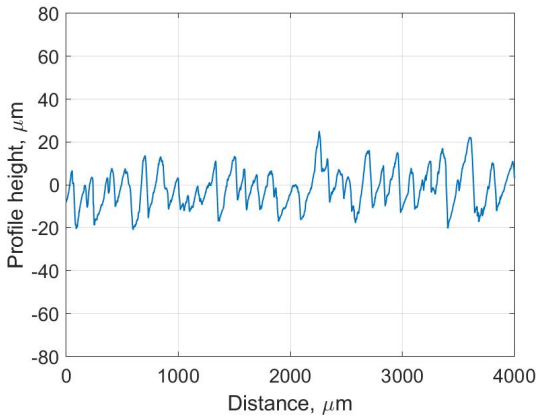

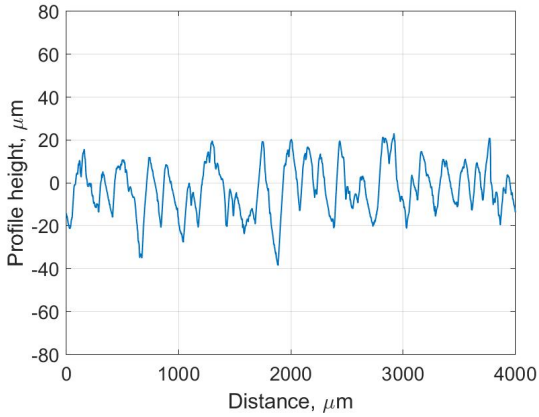

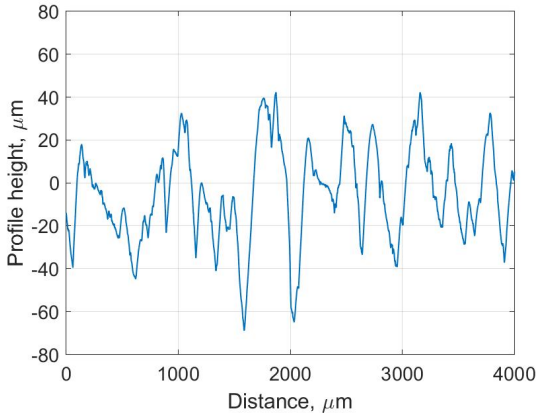

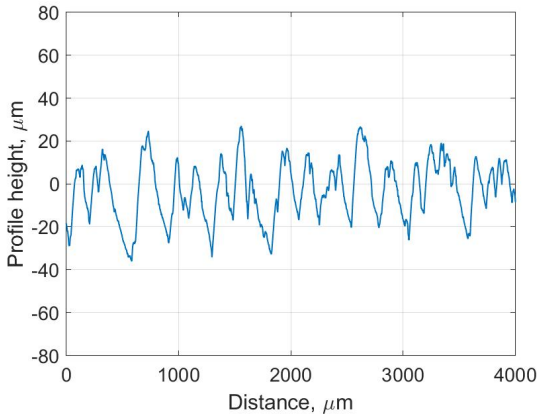

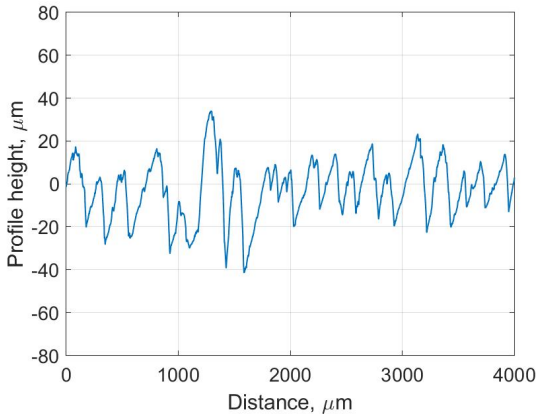

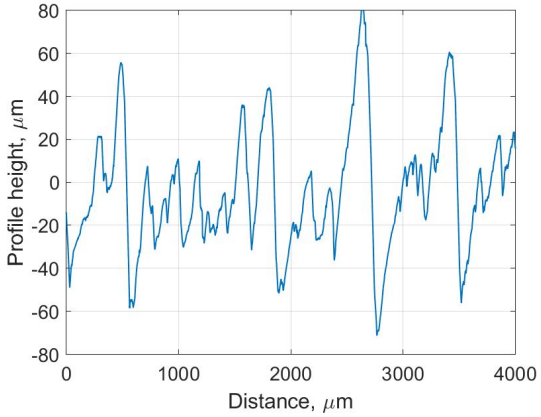
80
60
40
20
0
-20
-40
-60
-80
Profile height, μm
0
1000
2000
3000
4000
Distance, μm

F.1.3 Feed: 0.3 mm/rev, Spindle speed: 1000 RPM

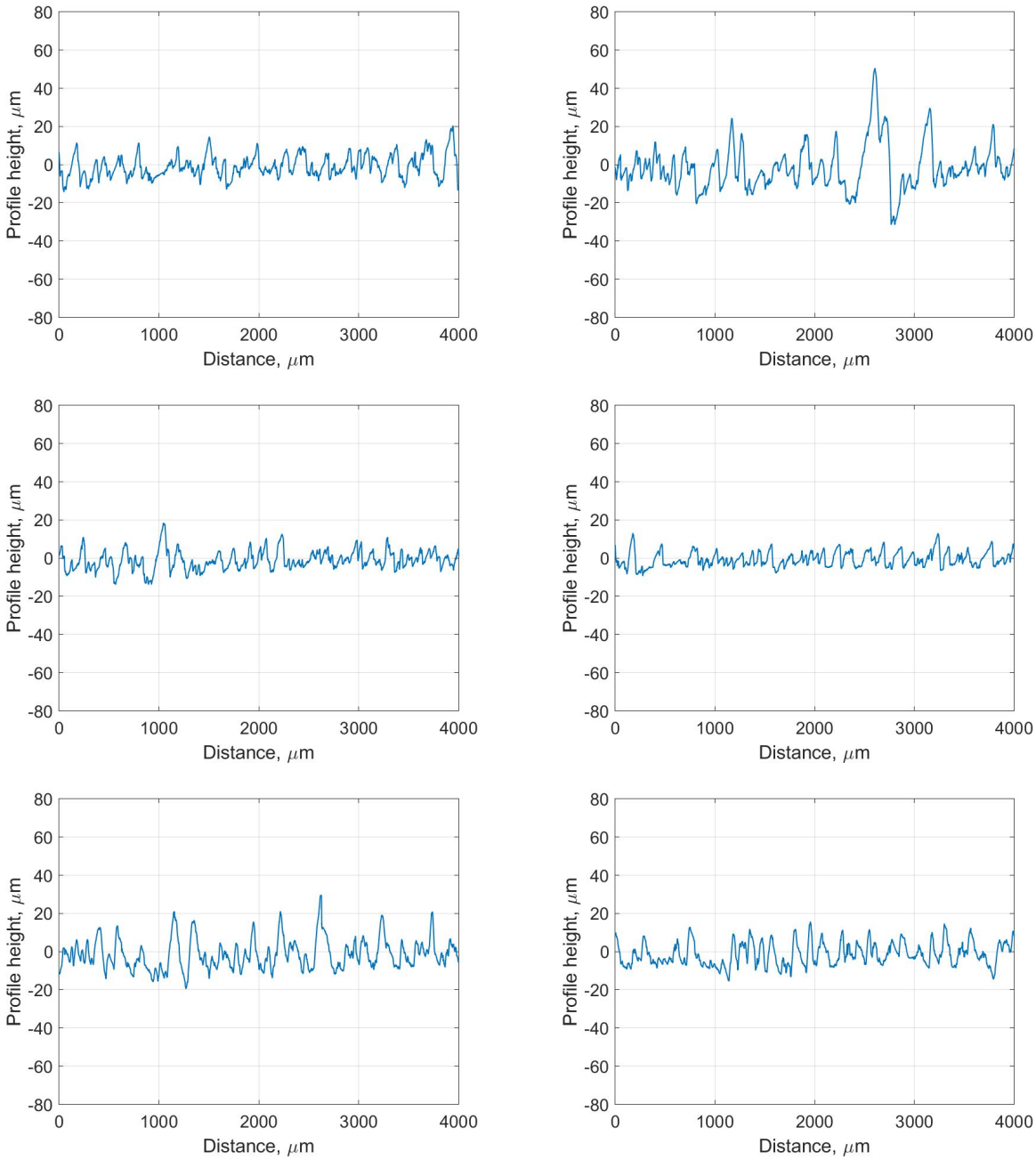

F.1.4 Feed: 0.3 mm/rev, Spindle speed: 3000 RPM

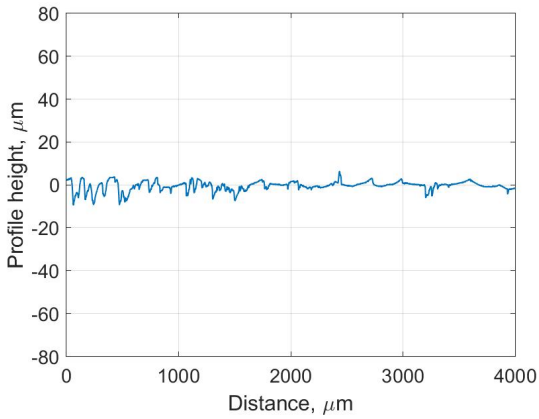

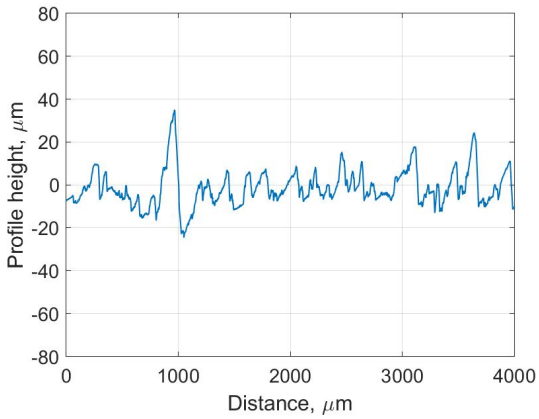

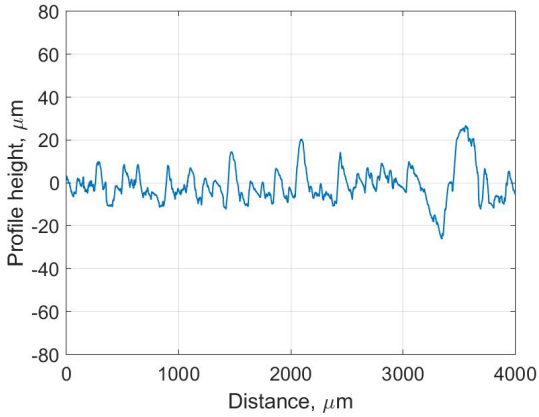

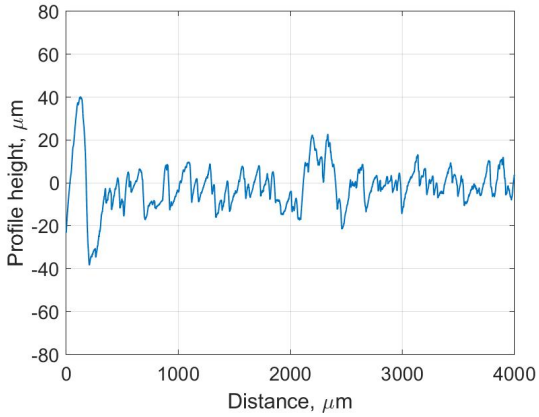

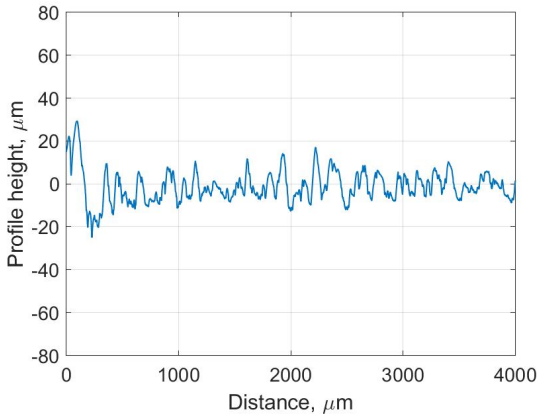

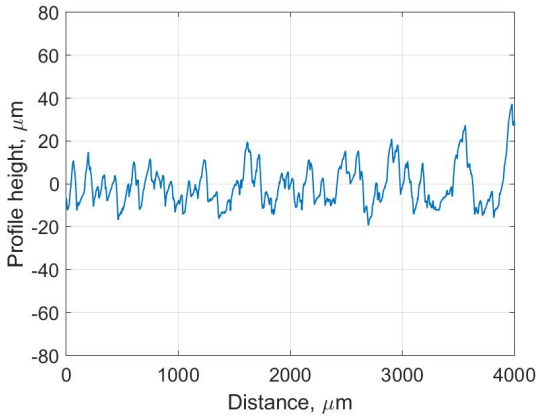

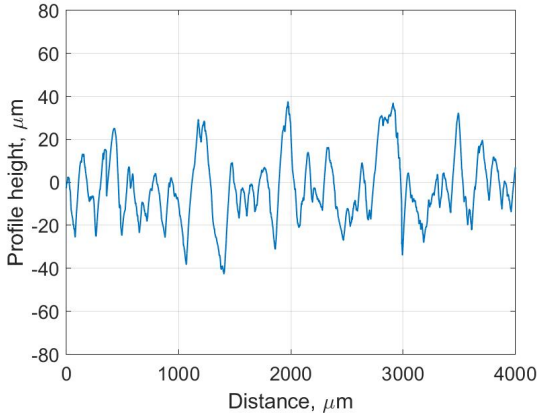
80
60
40
20
0
-20
-40
-60
-80
Profile height, μm
0
1000
2000
3000
4000
Distance, μm

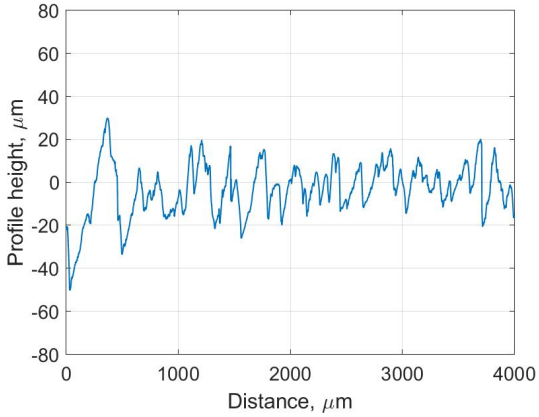
80
60
40
20
0
-20
-40
-60
-80
Profile height, μm
0
1000
2000
3000
4000
Distance, μm

F.2 Fatigue Performance

Sample	$\frac{S}{S_{ut}}$	Feed mm/rev	Speed RPM	No of cycles, N
NA-2	0.25	1000	0.1	5502571
NA-5	0.4	1000	0.1	5903542
NA-6	0.6	1000	0.1	208610
NA-3	0.8	1000	0.1	527
NA-10	0.6	1000	0.1	230435
NA-13	0.8	1000	0.1	323
NA-18	0.6	3000	0.1	32933
NA-19	0.8	3000	0.1	1272
NA-30	0.25	3000	0.1	5925324
NA-21	0.4	3000	0.1	79039
NA-17	0.6	3000	0.1	14853
NA-20	0.8	3000	0.1	1473
NA-16	0.25	3000	0.3	5894238
NA-14	0.4	3000	0.3	1542159
NA-8	0.6	3000	0.3	2481519

NA-11	0.8	3000	0.3	2289
NA-15	0.4	3000	0.3	5625766
NA-9	0.6	3000	0.3	489699
NA-12	0.8	3000	0.3	9552
NA-27	0.4	1000	0.3	6895196
NA-24	0.6	1000	0.3	276695
NA-28	0.8	1000	0.3	4810
NA-31	0.25	1000	0.3	5599742
NA-26	0.6	1000	0.3	1846754
NA-25	0.4	1000	0.3	5967842
NA-29	0.8	1000	0.3	472

F.3 SEM micrographs of the machined surface

F.3.1 Peripherally milled, Feed: 0.1 mm/rev, Spindle speed: 1000 RPM

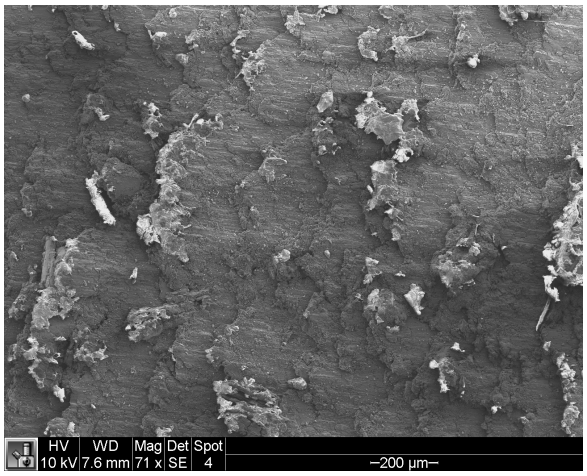

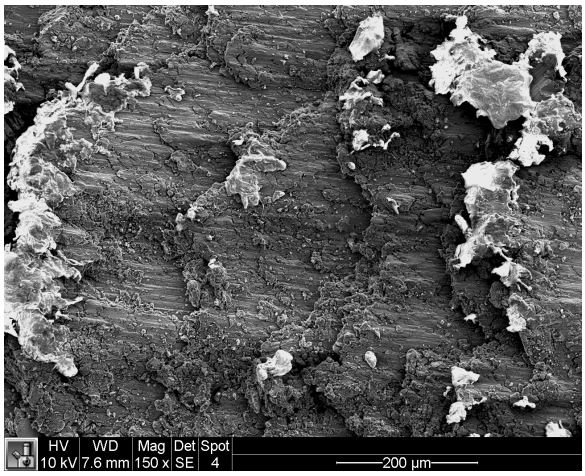

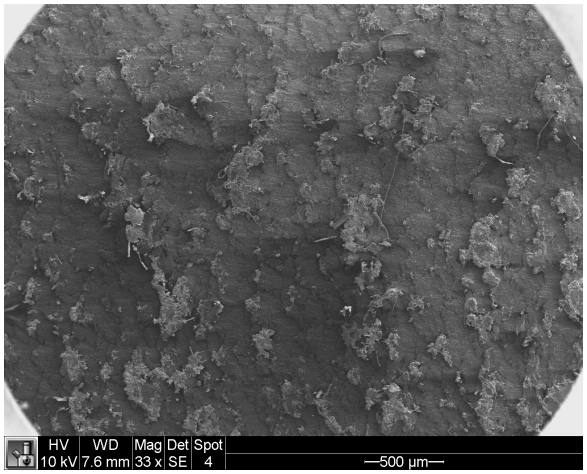

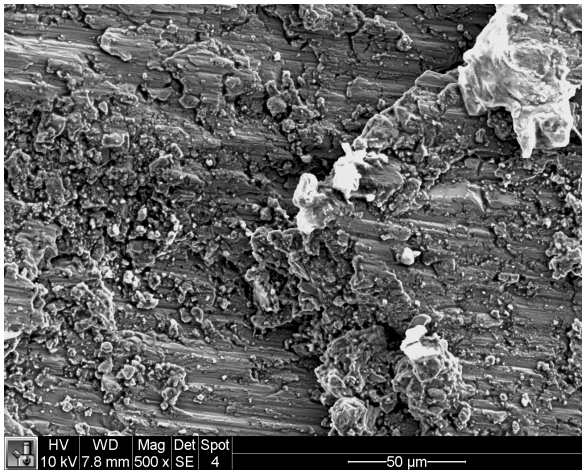

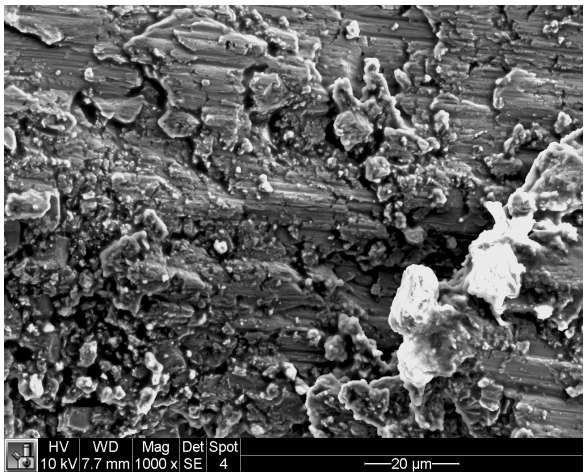

F.3.2 Peripherally milled, Feed: 0.1 mm/rev, Spindle speed: 3000 RPM

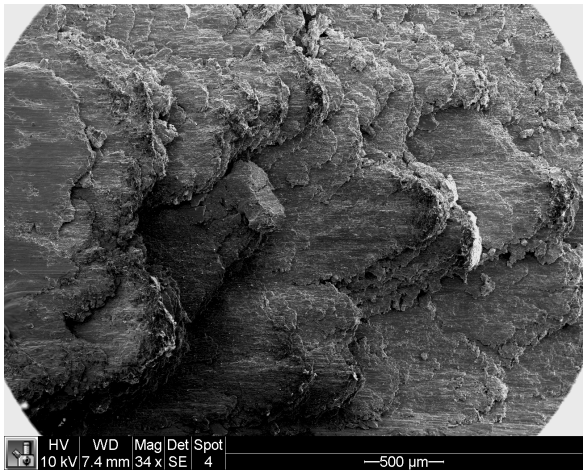

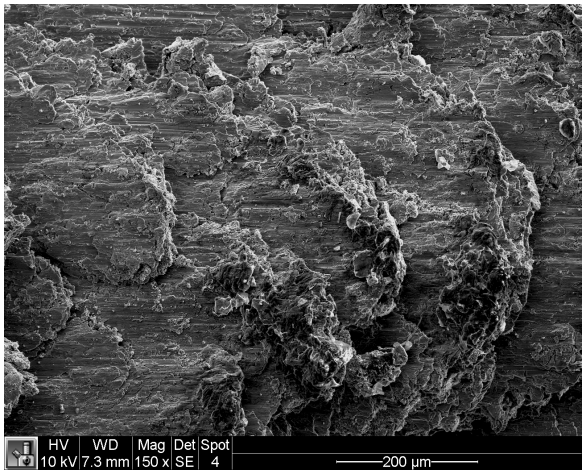

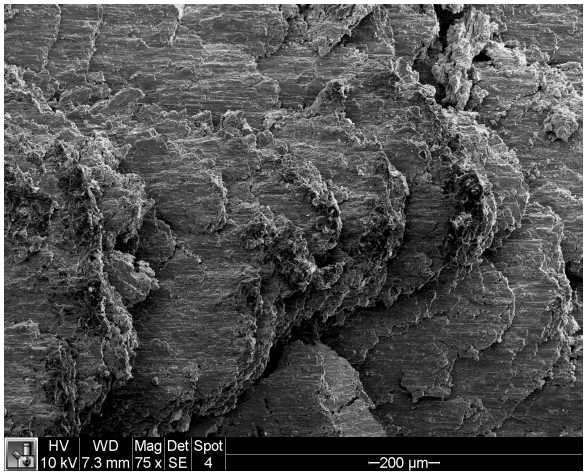

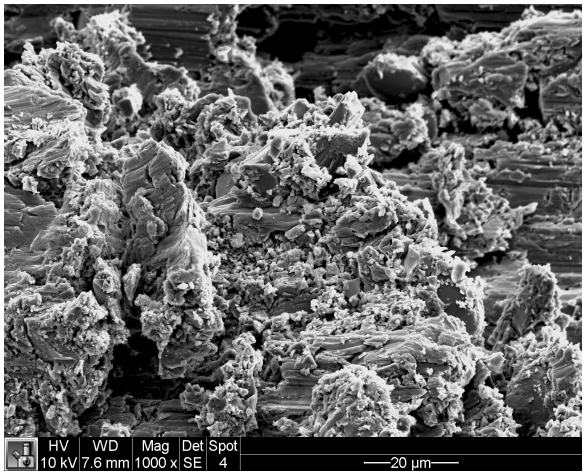

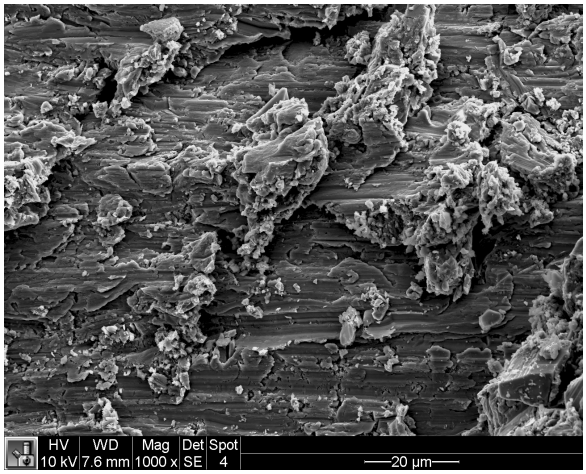

F.3.3 Peripherally milled, Feed: 0.3 mm/rev, Spindle speed: 1000 RPM

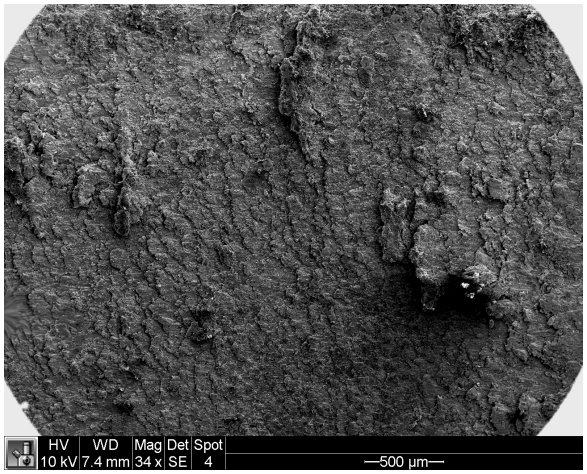

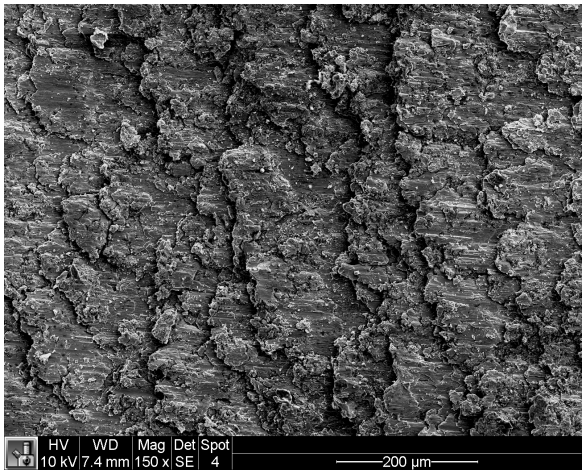

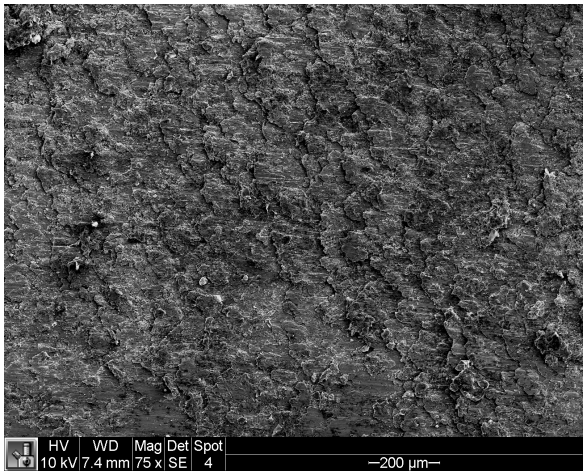

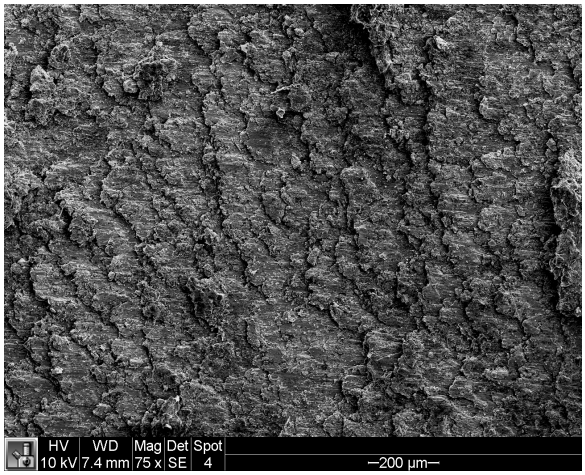

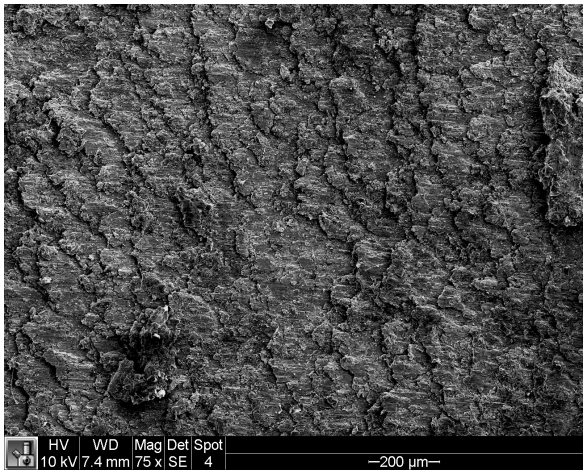

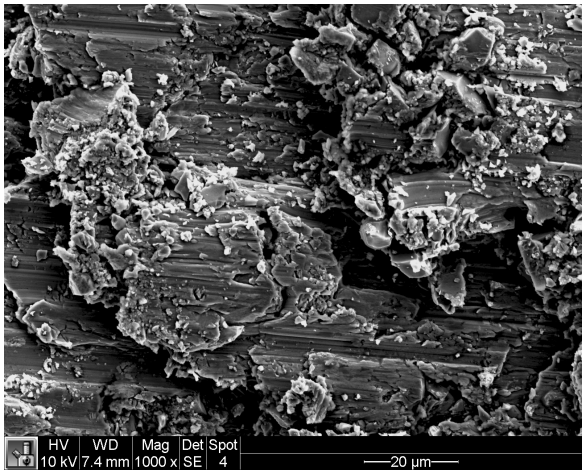

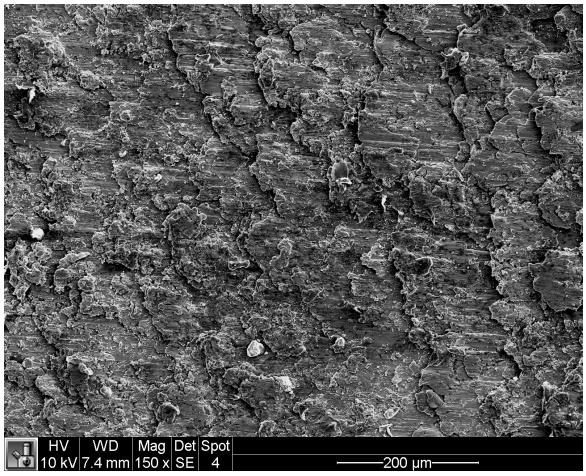

F.3.4 Peripherally milled, Feed: 0.3 mm/rev, Spindle speed: 3000 RPM

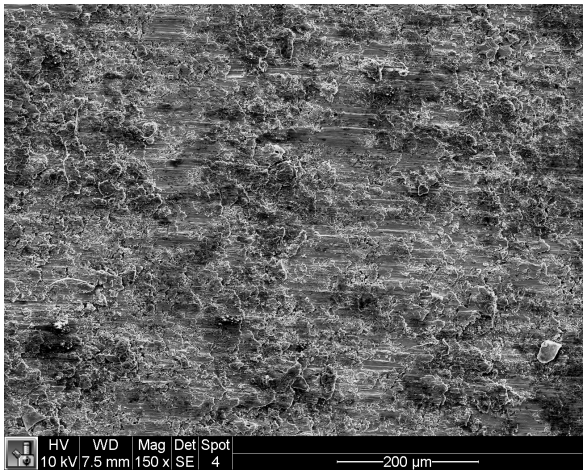

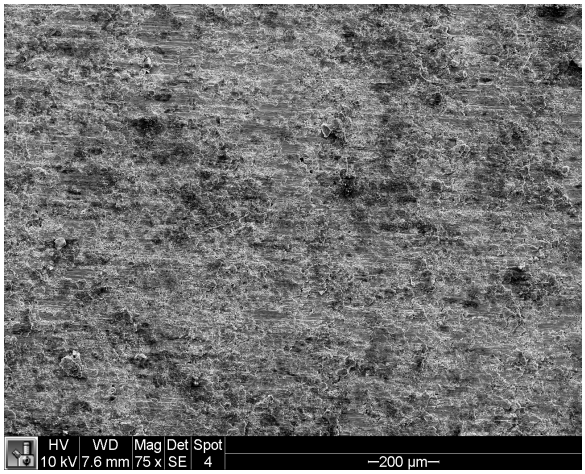

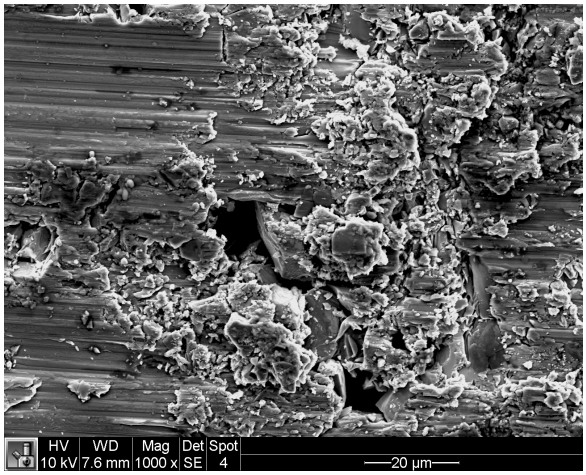

F.3.5 Face milled surface,Feed: 0.3 mm/rev, Spindle speed: 3000 RPM

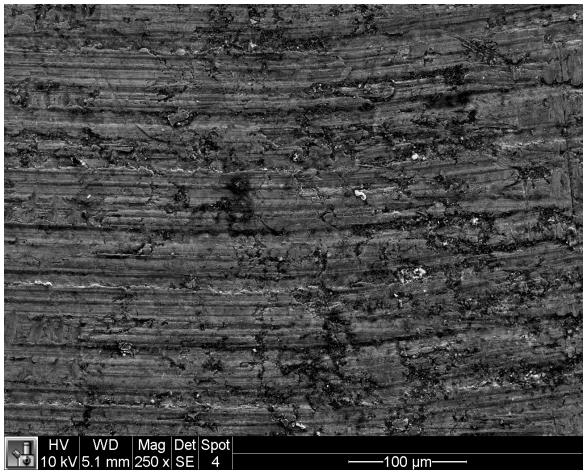

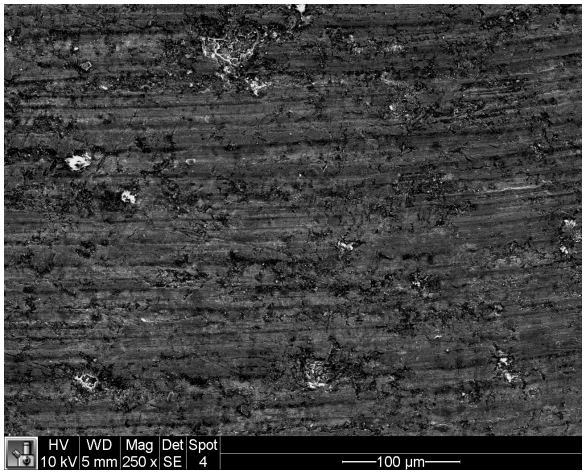

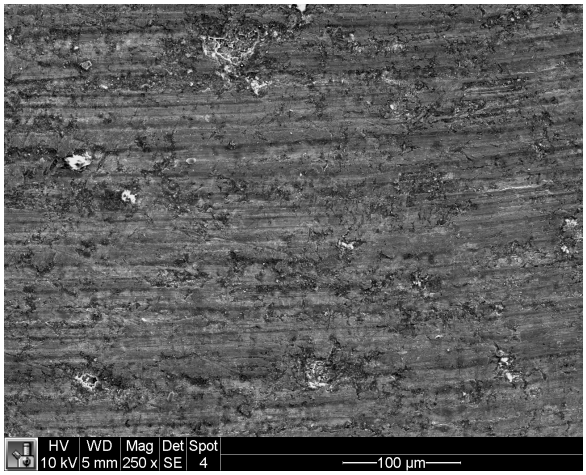

F.4 Fractography

F.4.1 $0.8S/S_{ut}$*, 0.1 mm/rev, 1000 RPM*

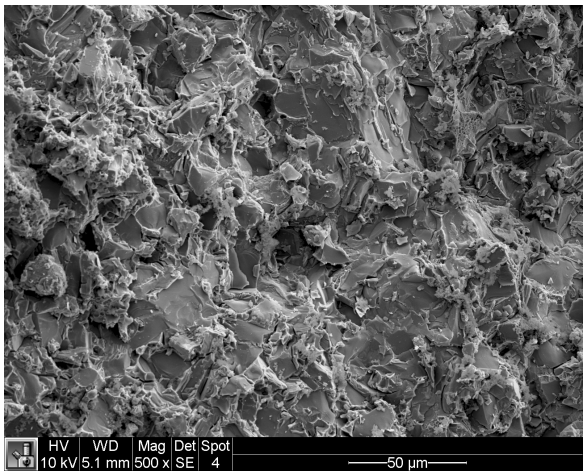

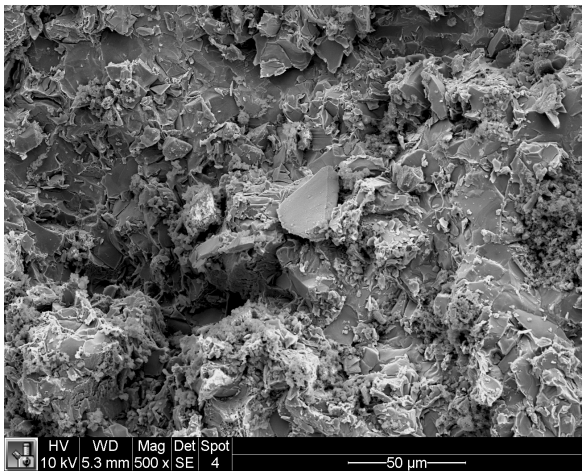

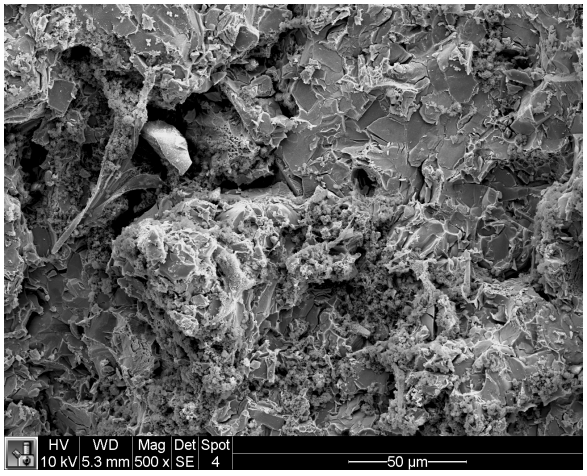

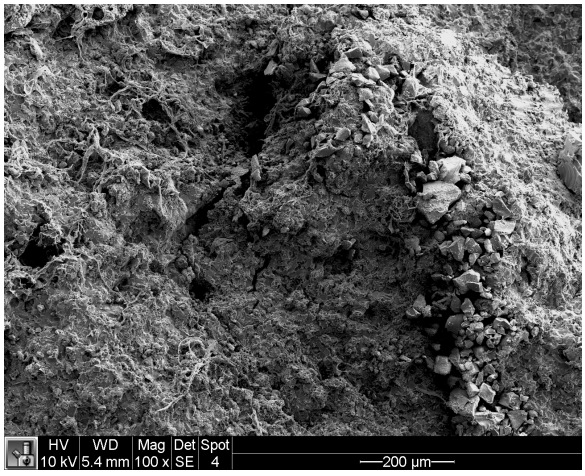

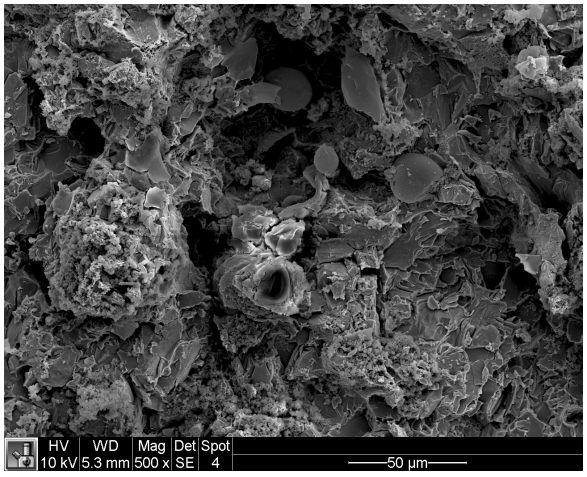

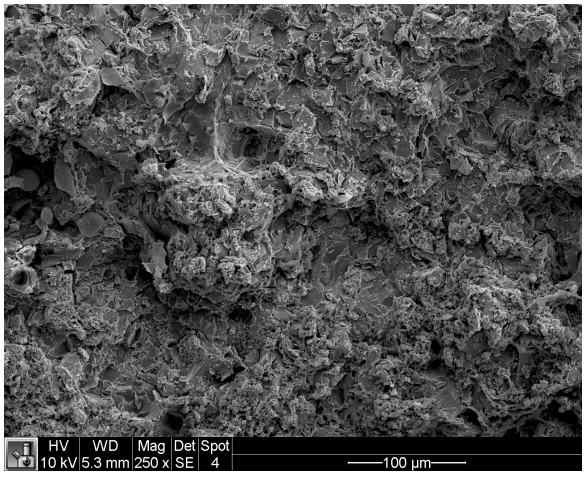

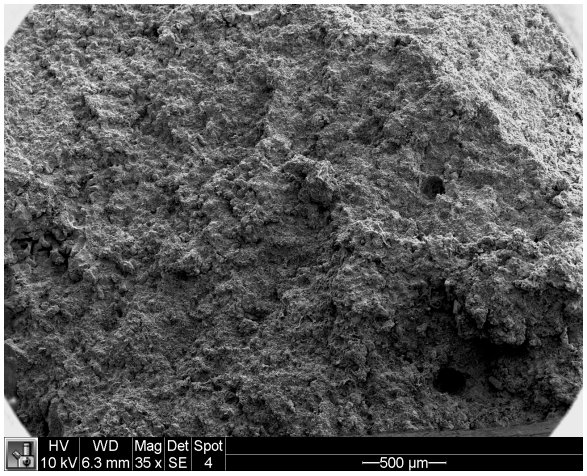
HV
10 kV
WD
6.3 mm
Mag
35 x
Det
SE
Spot
4
—500 µm—

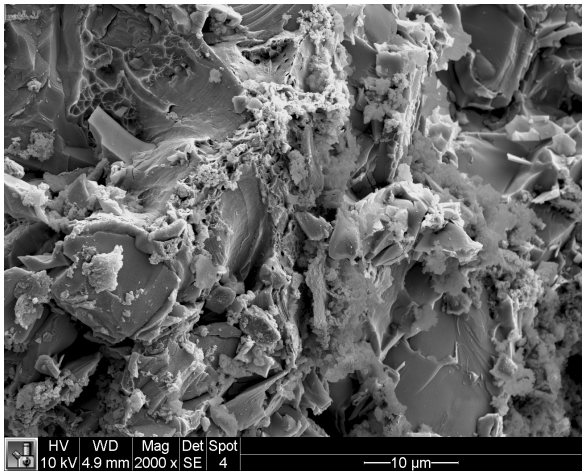
HV
10 kV
WD
4.9 mm
Mag
2000 x
Det
SE
Spot
4
—10 µm—

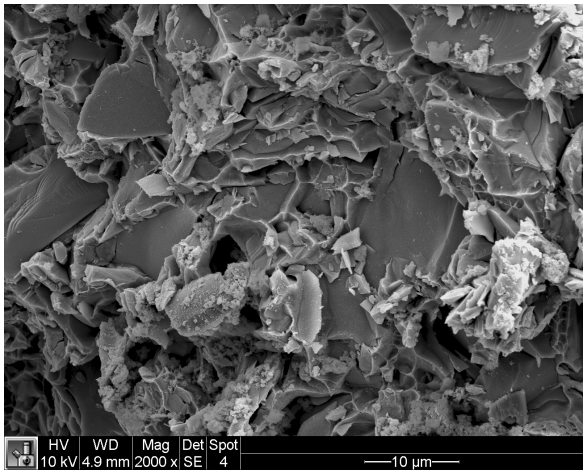
HV
10 kV
WD
4.9 mm
Mag
2000 x
Det
SE
Spot
4
—10 µm—

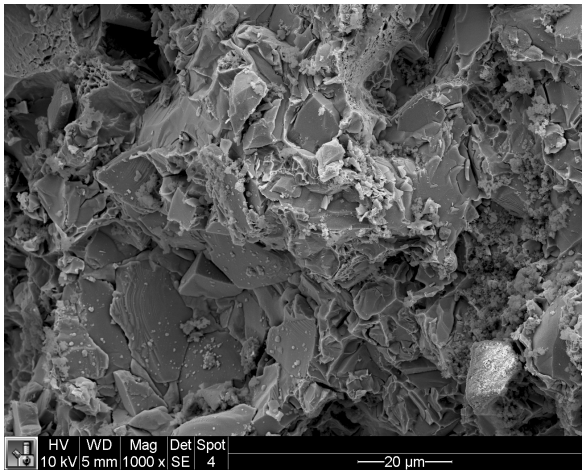
HV
10 kV
WD
5 mm
Mag
1000 x
Det
SE
Spot
4
—20 µm—

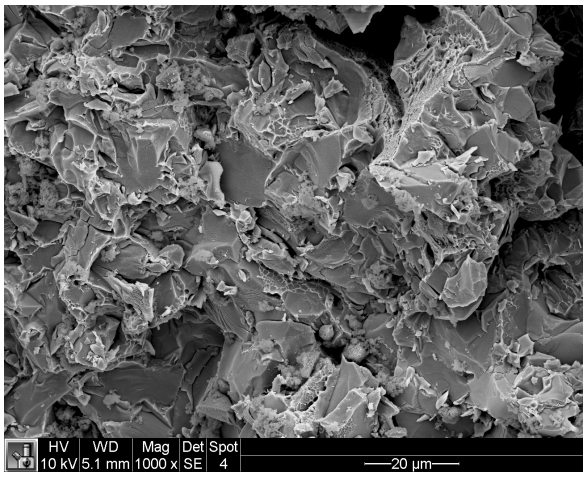
HV
10 kV
WD
5.1 mm
Mag
1000 x
Det
SE
Spot
4
—20 µm—

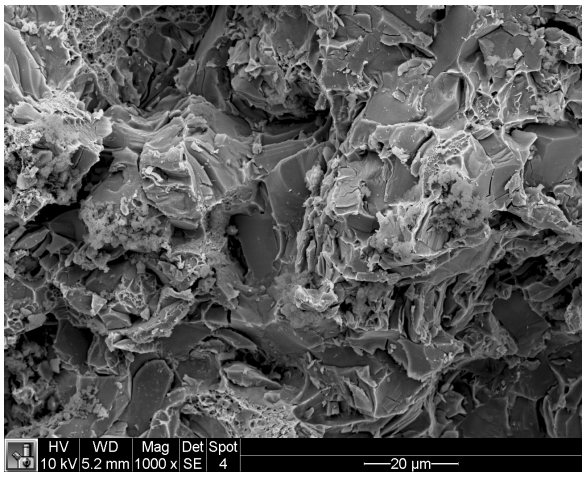
HV
10 kV
WD
5.2 mm
Mag
1000 x
Det
SE
Spot
4
—20 µm—

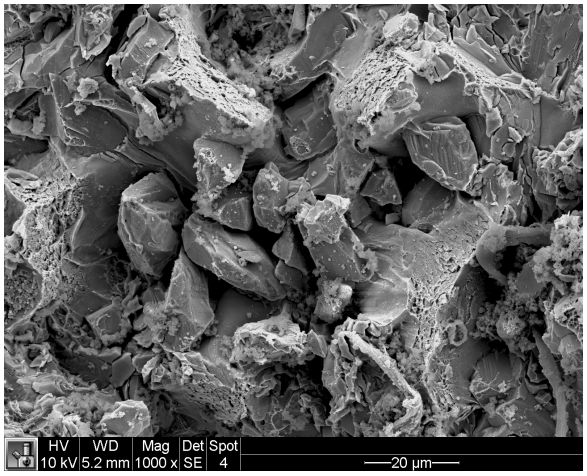
HV
10 kV
WD
5.2 mm
Mag
1000 x
Det
SE
Spot
4
20 µm

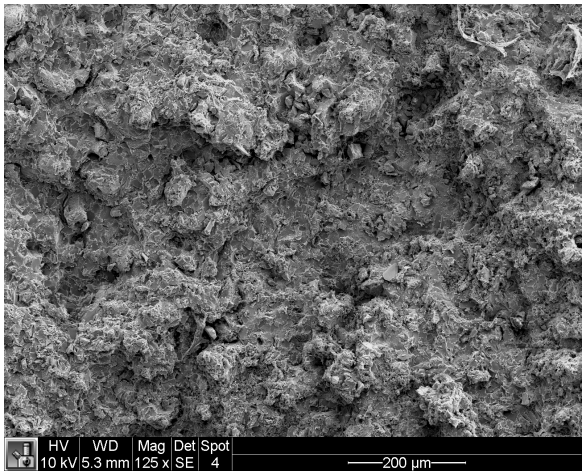
HV
10 kV
WD
5.3 mm
Mag
125 x
Det
SE
Spot
4
200 µm

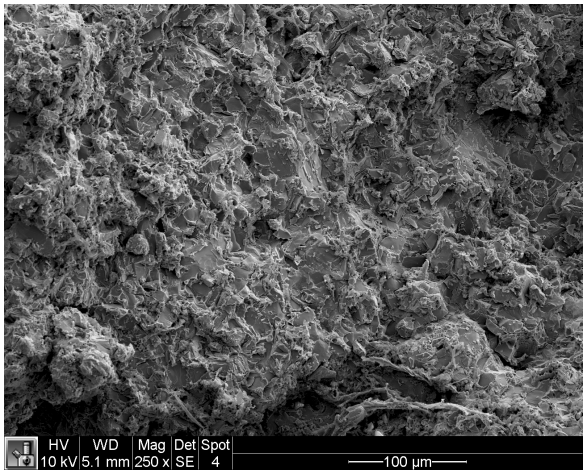
HV
10 kV
WD
5.1 mm
Mag
250 x
Det
SE
Spot
4
100 µm

F.4.2 $0.6S/S_{ut}$*, 0.1 mm/rev, 1000 RPM*

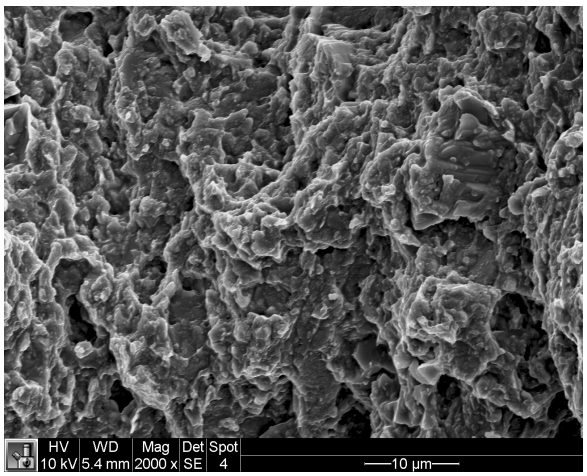

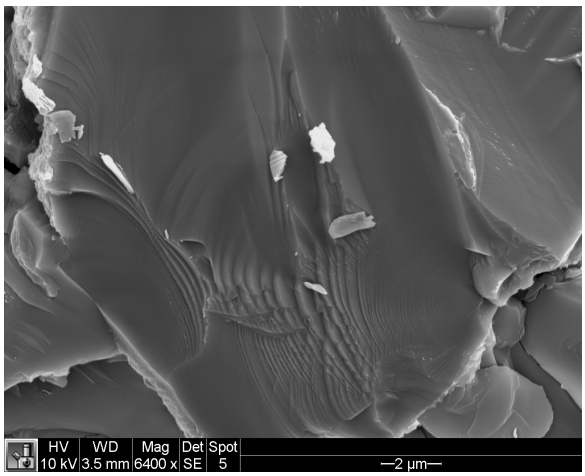

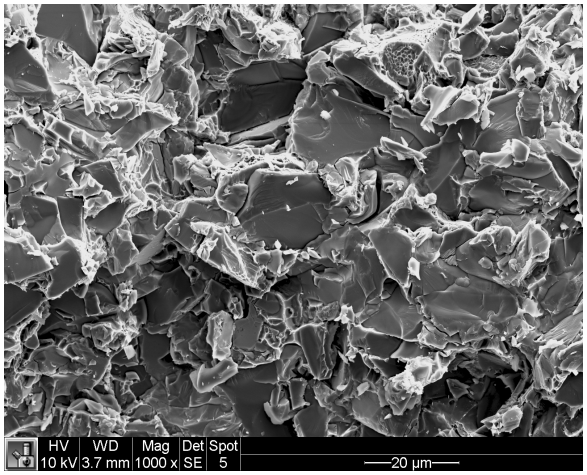

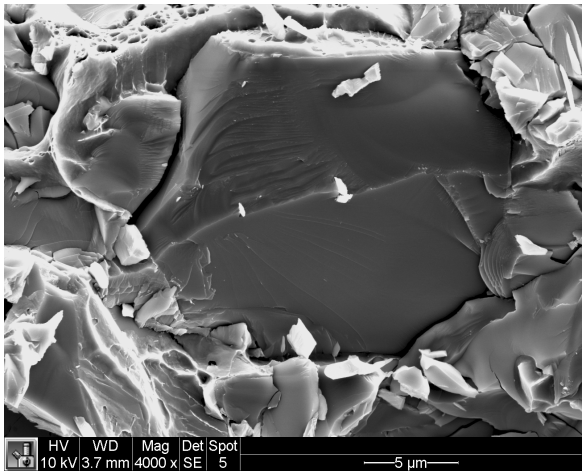

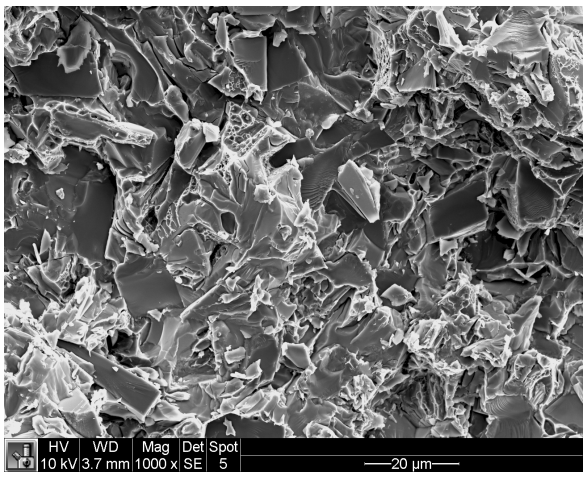



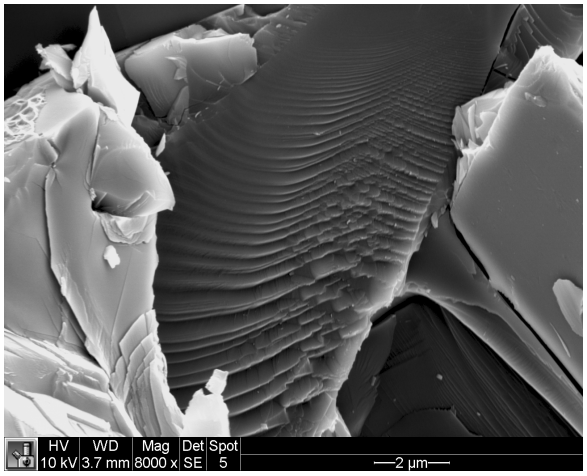
HV
10 kV
WD
3.7 mm
Mag
8000 x
Det
SE
Spot
5
2 µm

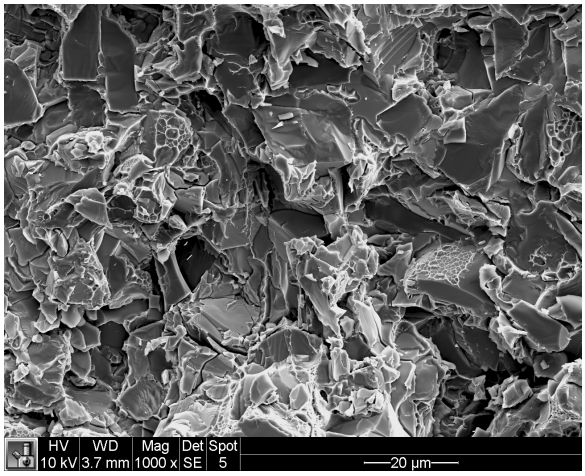
HV
10 kV
WD
3.7 mm
Mag
1000 x
Det
SE
Spot
5
20 µm

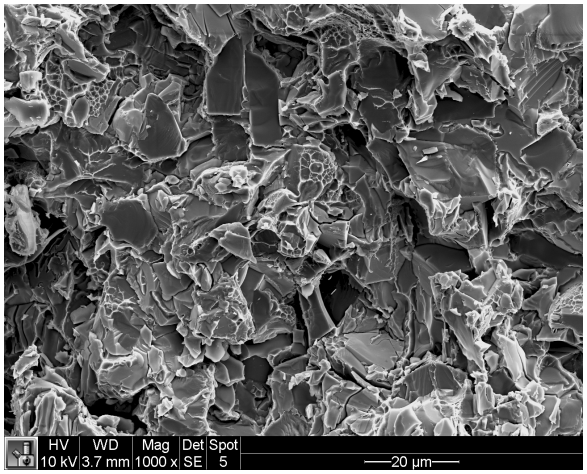
HV
10 kV
WD
3.7 mm
Mag
1000 x
Det
SE
Spot
5
20 µm

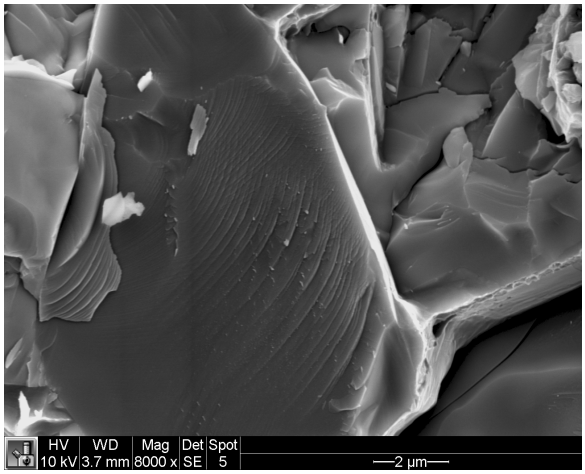
HV
10 kV
WD
3.7 mm
Mag
8000 x
Det
SE
Spot
5
2 µm

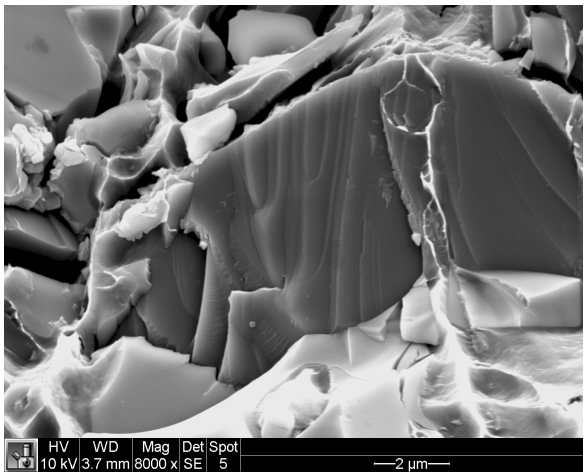
HV
10 kV
WD
3.7 mm
Mag
8000 x
Det
SE
Spot
5
2 µm

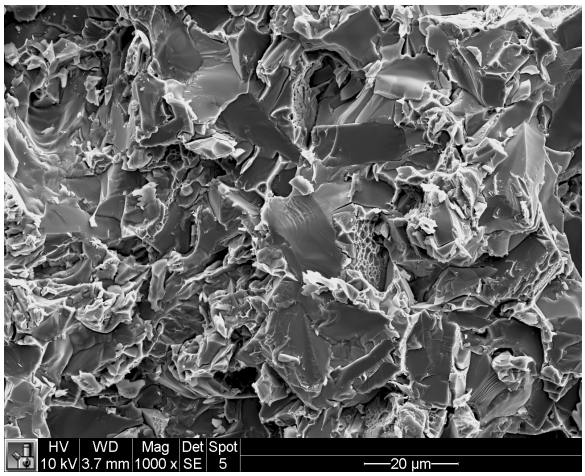
HV
10 kV
WD
3.7 mm
Mag
1000 x
Det
SE
Spot
5
20 µm

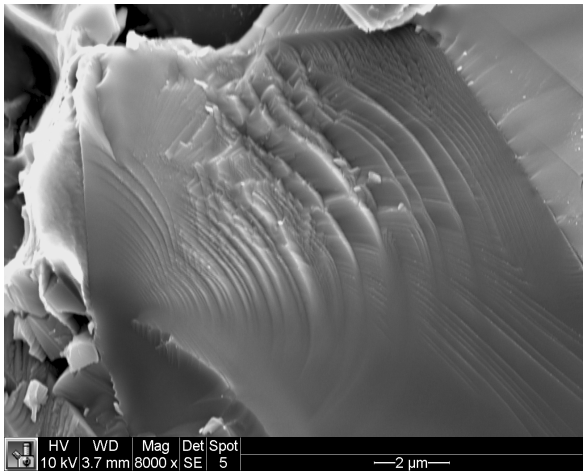
HV
10 kV
WD
3.7 mm
Mag
8000 x
Det
SE
Spot
5
2 µm

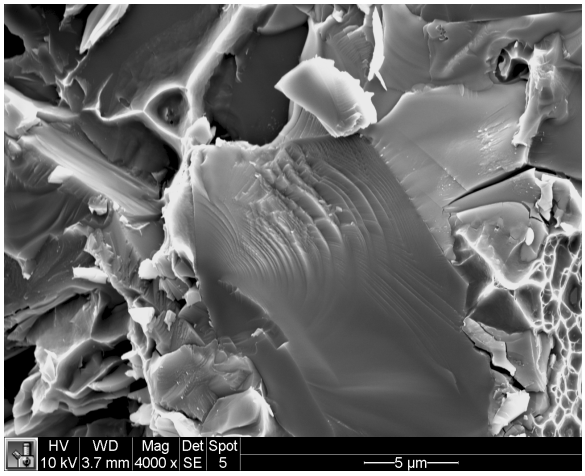
HV
10 kV
WD
3.7 mm
Mag
4000 x
Det
SE
Spot
5
5 µm

F.4.3 Fracture mechanism, $0.6S/S_{ut}$, 0.1 mm/rev, 3000 RPM

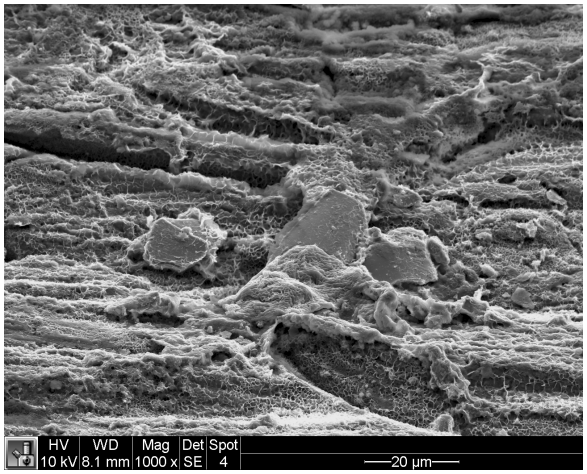

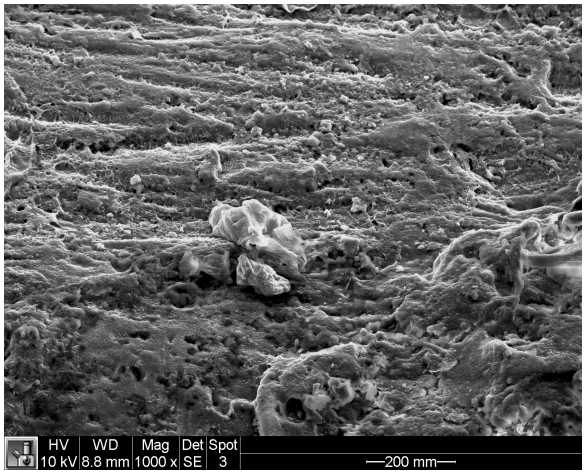

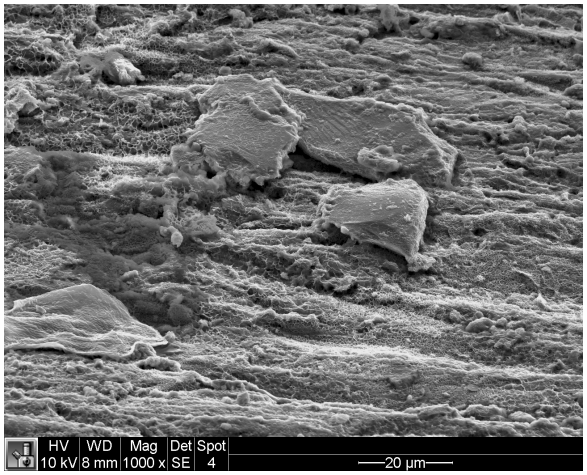

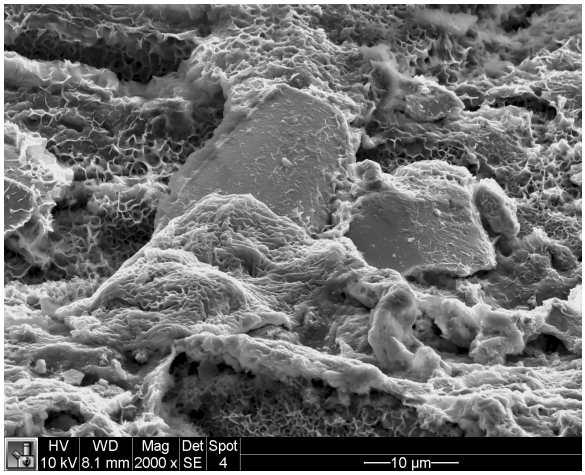

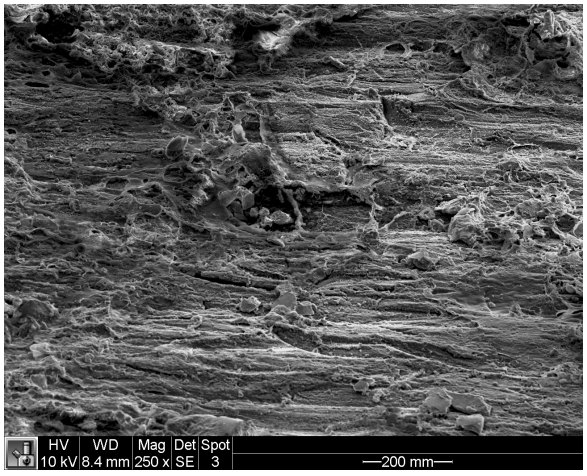

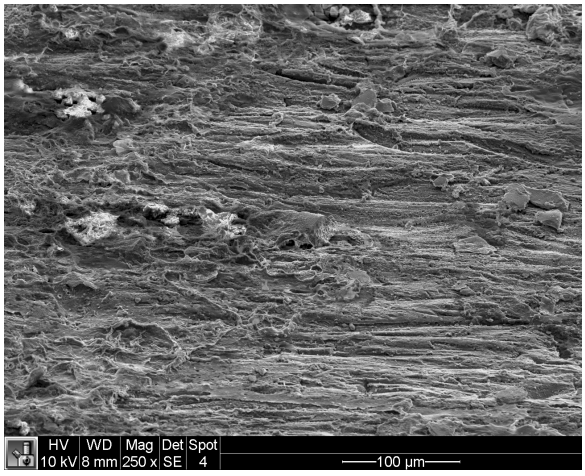

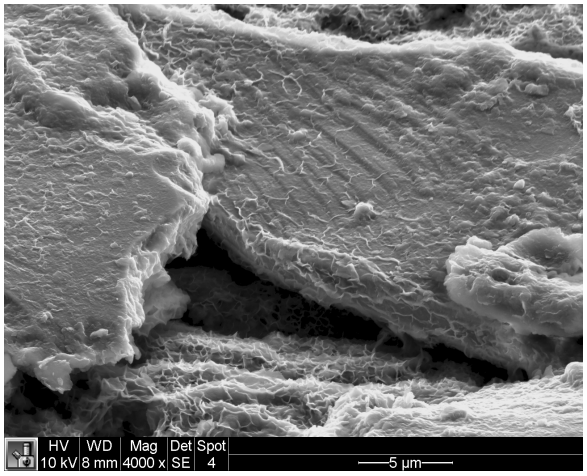
HV
10 kV
WD
8 mm
Mag
4000 x
Det
SE
Spot
4
5 µm

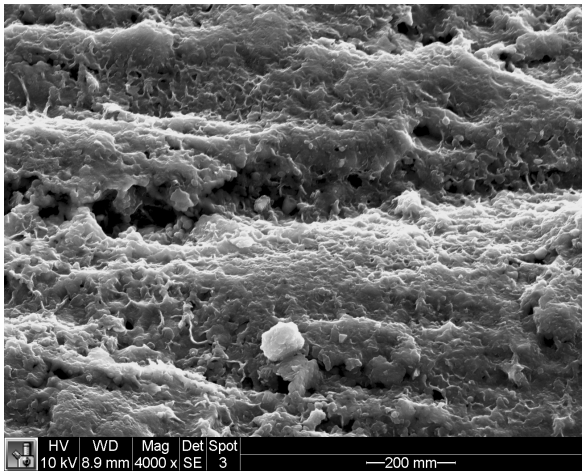
HV
10 kV
WD
8.9 mm
Mag
4000 x
Det
SE
Spot
3
200 mm

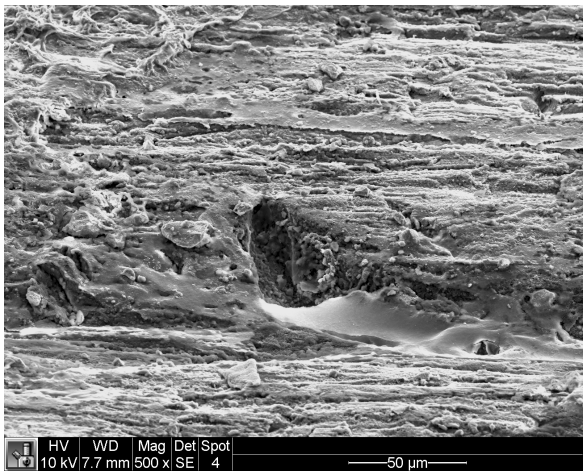
HV
10 kV
WD
7.7 mm
Mag
500 x
Det
SE
Spot
4
50 µm

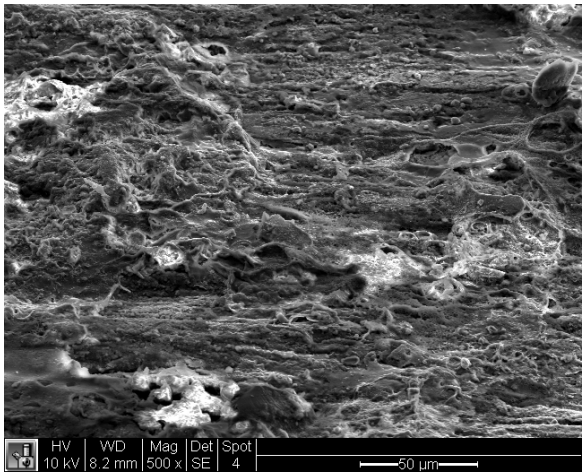
HV
10 kV
WD
8.2 mm
Mag
500 x
Det
SE
Spot
4
50 µm

F.5 Fractured specimen, some used for further analysis

F.5.1 NA-3



F.5.2 NA-7

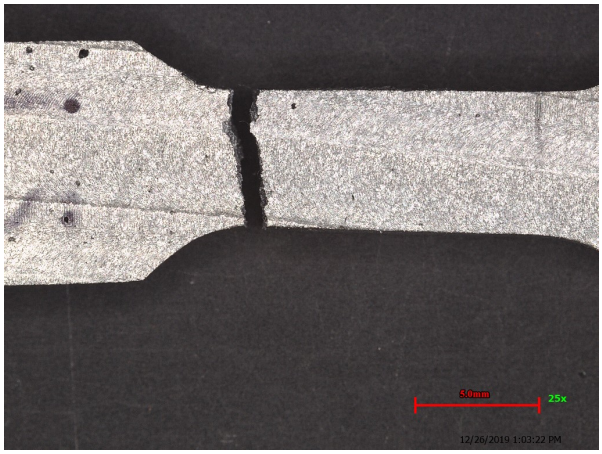

F.5.3 NA-8

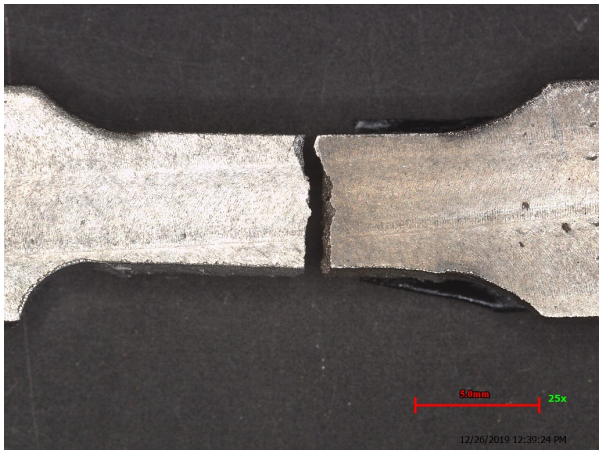

F.5.4 NA-9

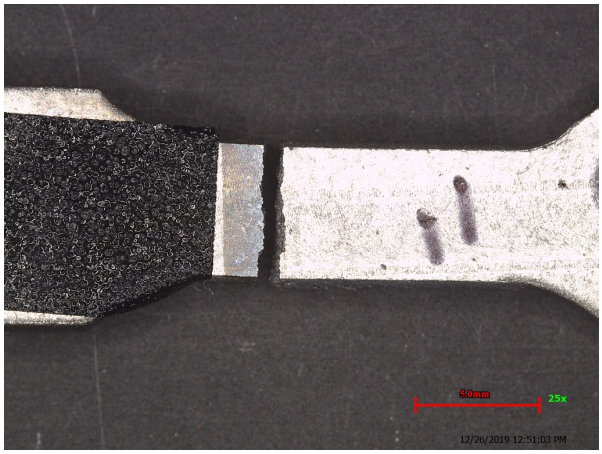

F.5.5 NA-10

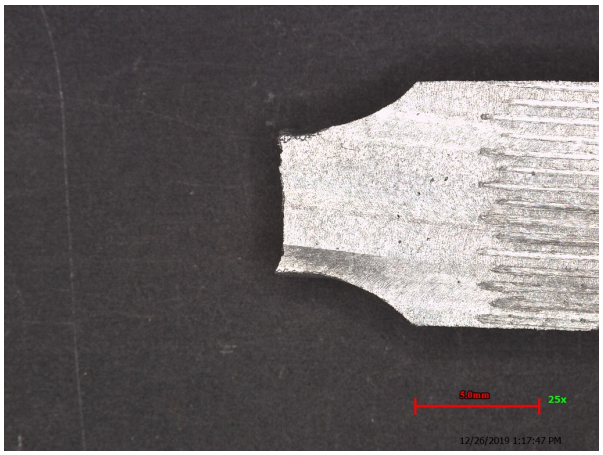

F.5.6 NA-11

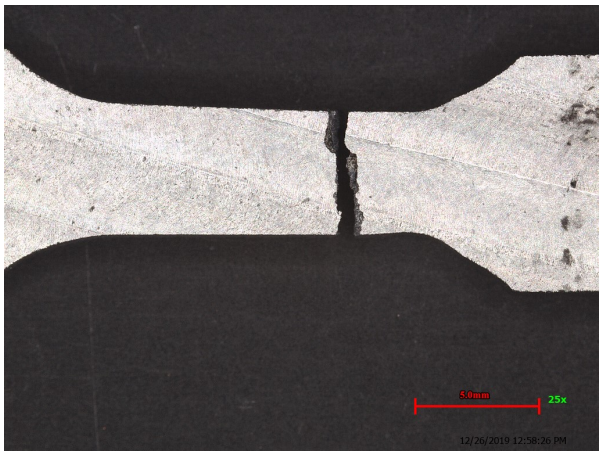

F.5.7 NA-13

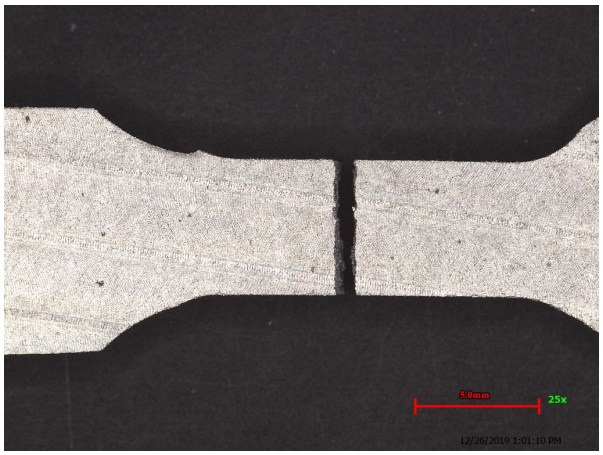

F.5.8 NA-14

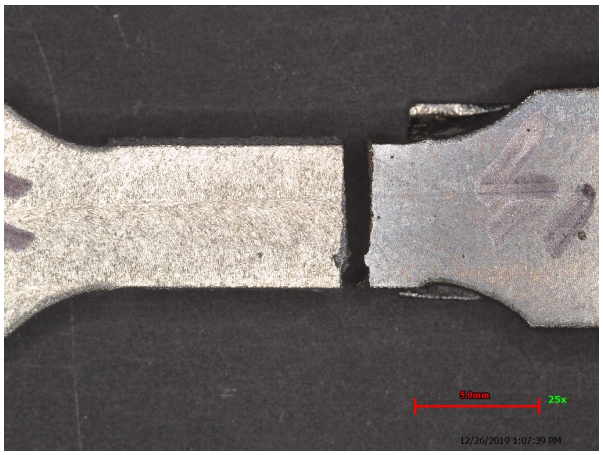

F.5.9 NA-12

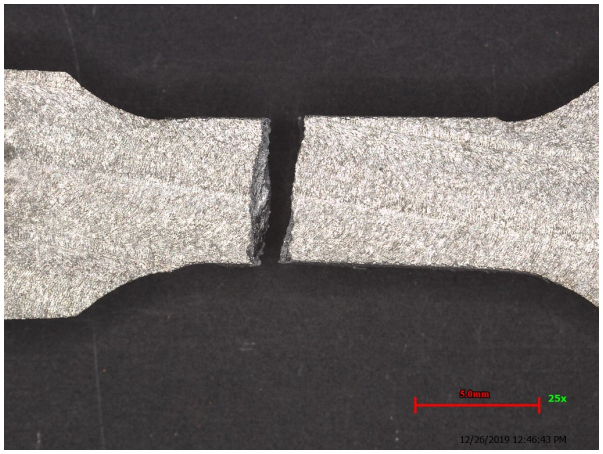

F.5.10 NA-17

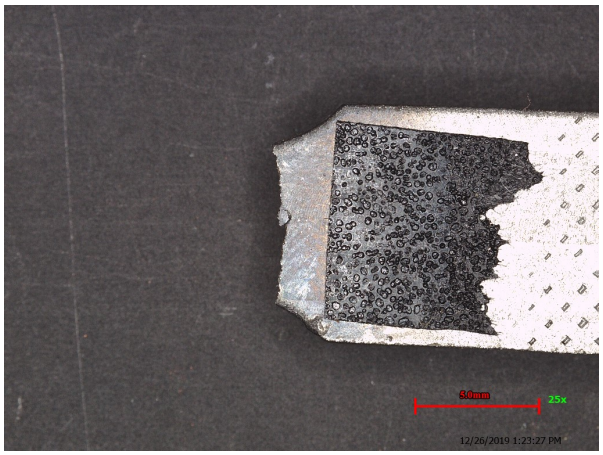

F.5.11 NA-19



F.5.12 NA-20

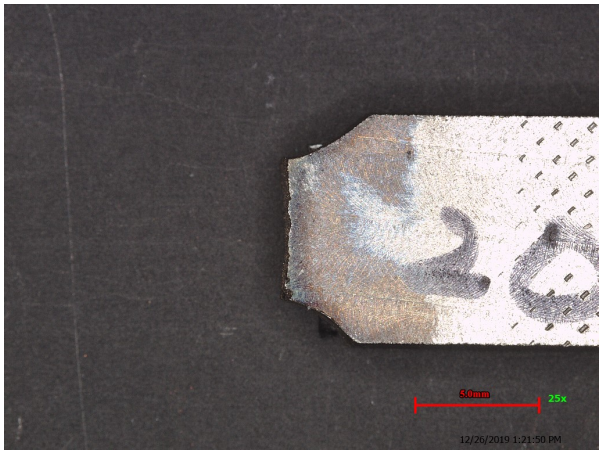

F.5.13 NA-21

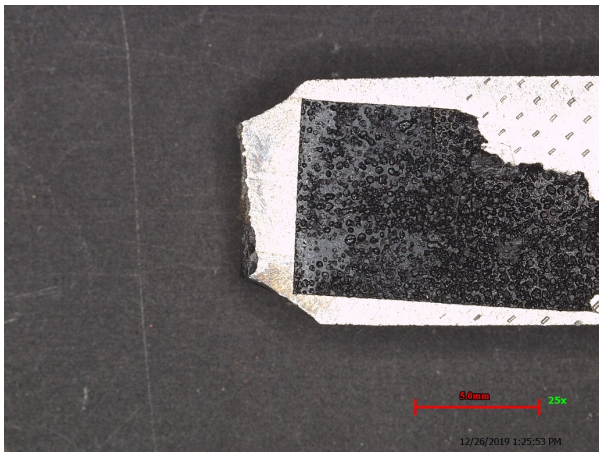

F.5.14 NA-24

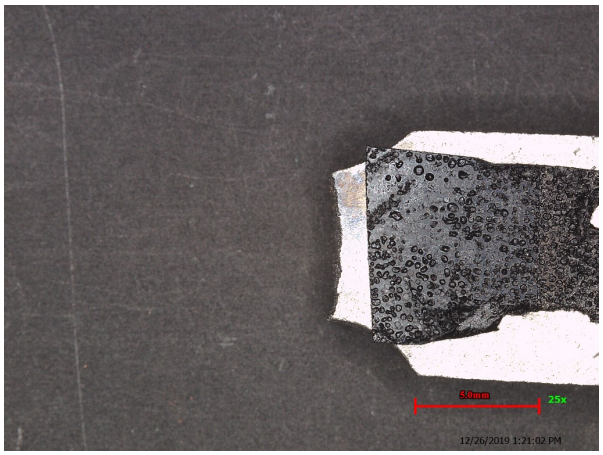

F.5.15 NA-26

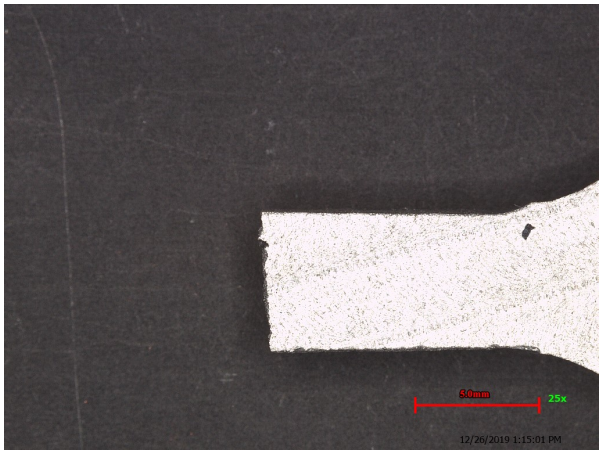

F.5.16 NA-29

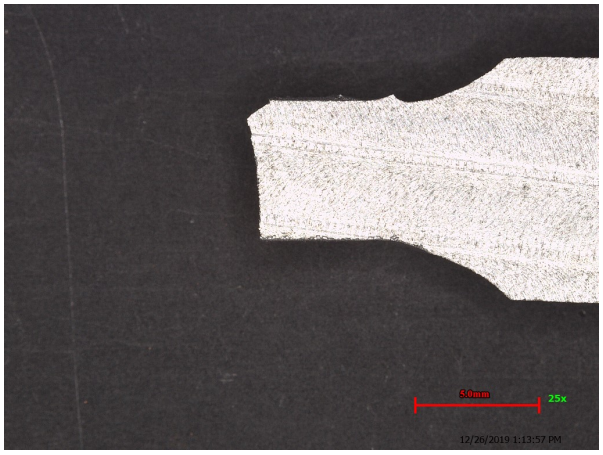

F.6 Fractography, EDS results

F.6.1 NA-3

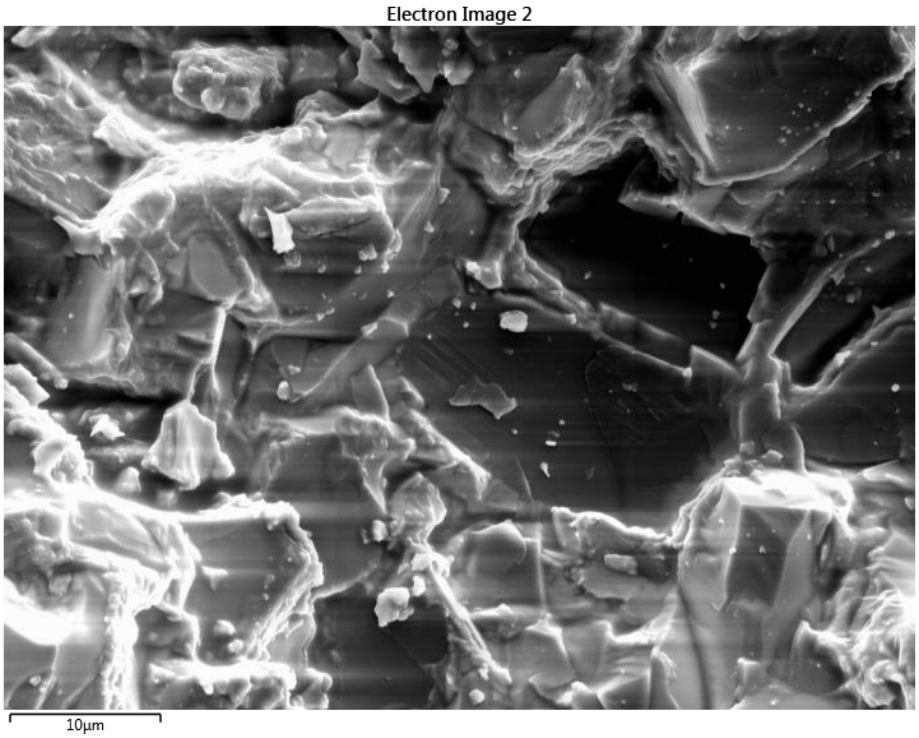

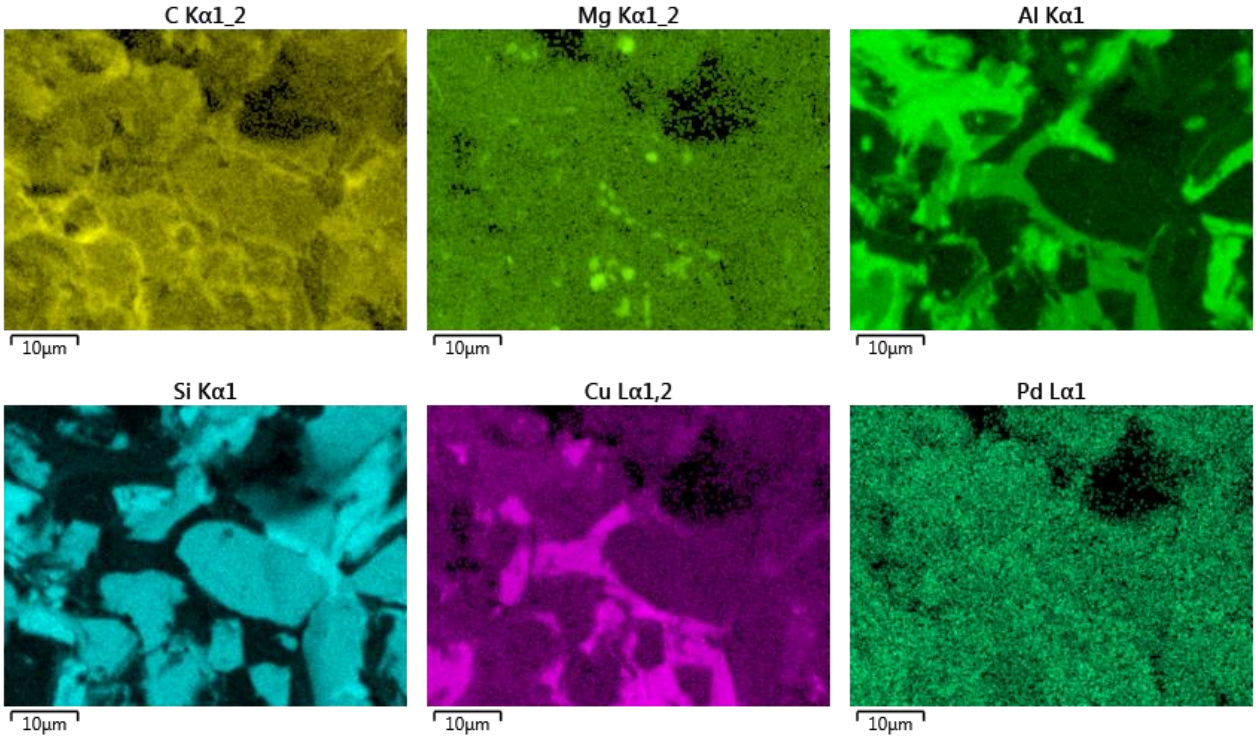
C Kα1_2
10μm
Mg Kα1_2
10μm
Al Kα1
10μm
Si Kα1
10μm
Cu Lα1,2
10μm
Pd Lα1
10μm

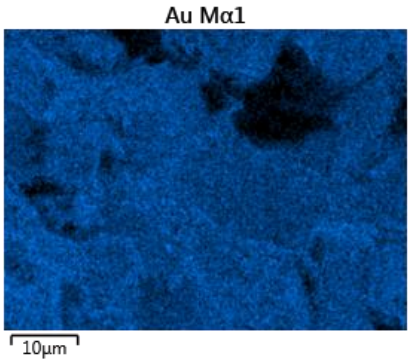
Au Mα1
10μm

Electron Image 3

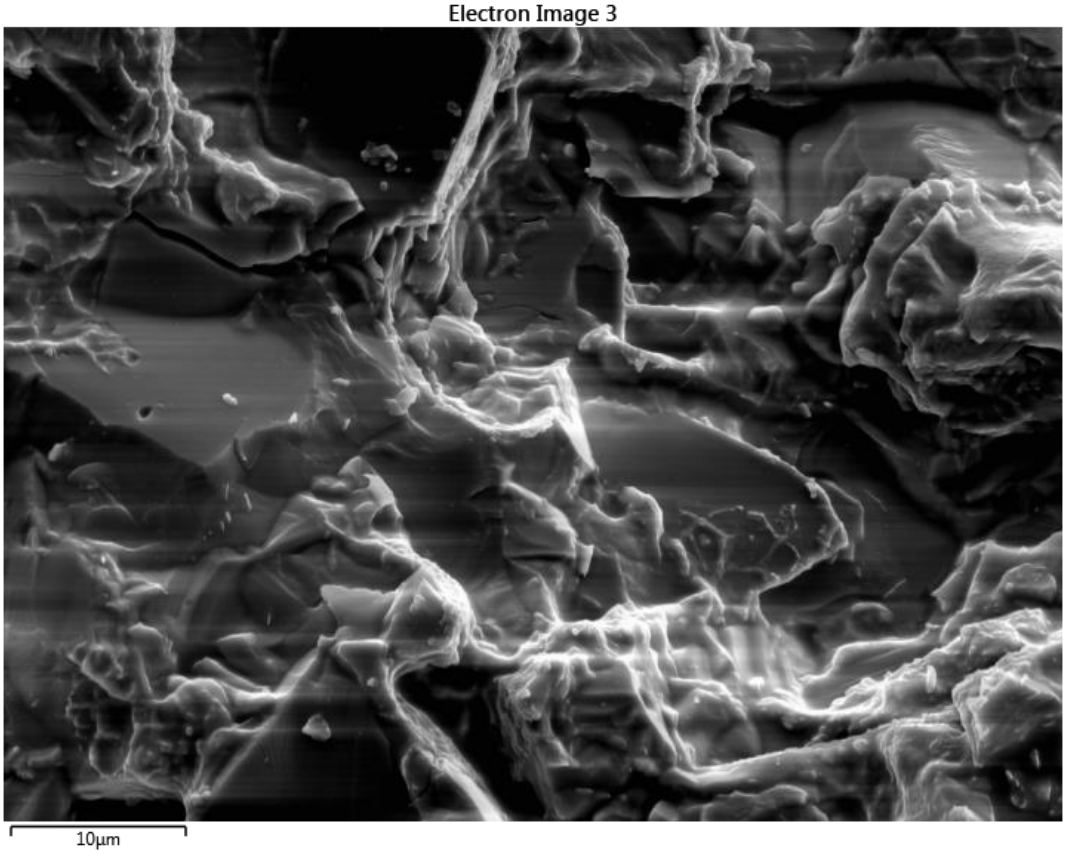

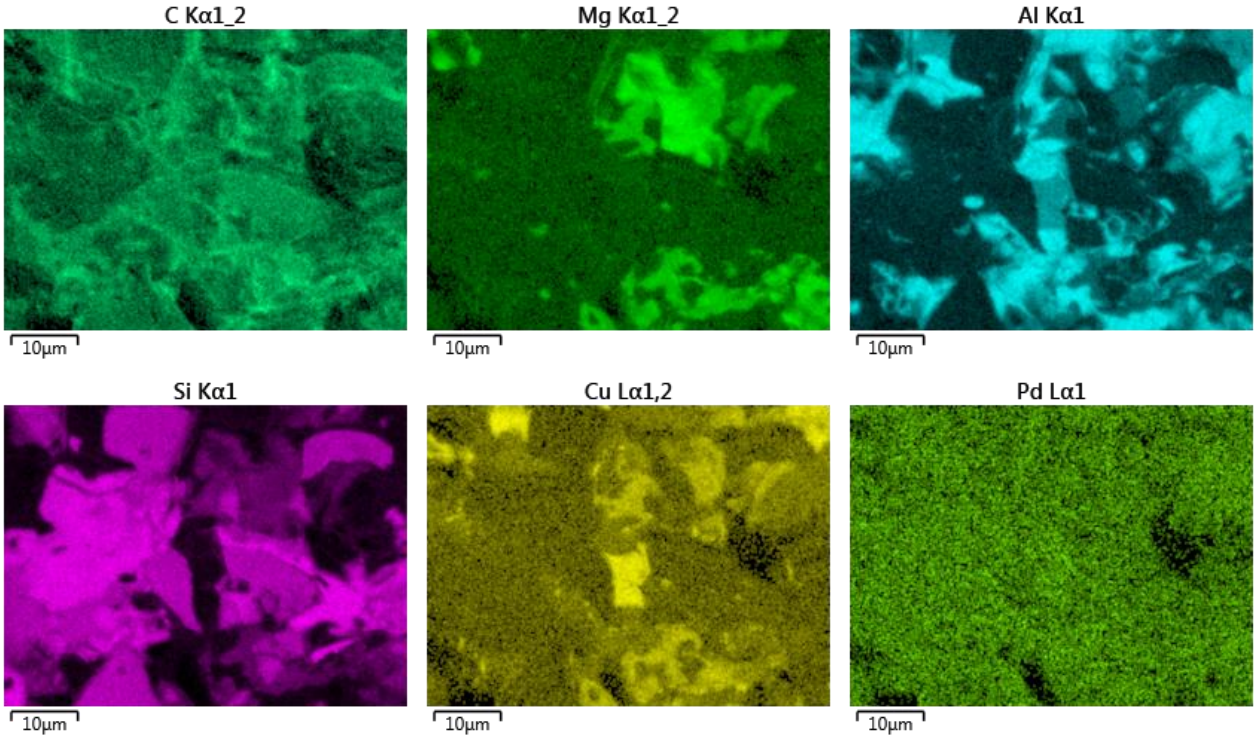
C Kα1_2
Mg Kα1_2
Al Kα1
10µm
10µm
10µm
Si Kα1
Cu Lα1,2
Pd Lα1
10µm
10µm
10µm

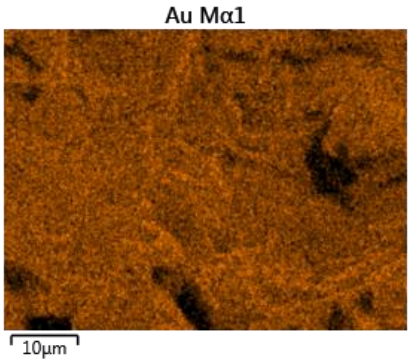
Au Mα1
10µm

Electron Image 4

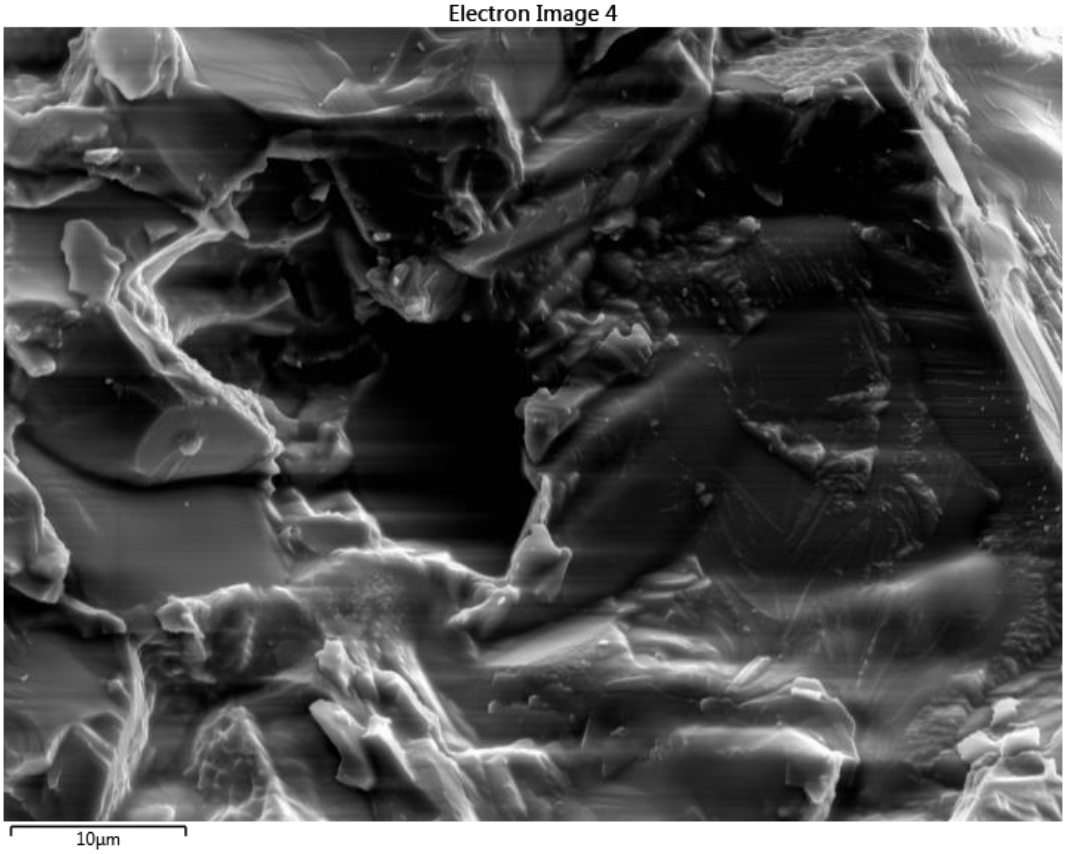

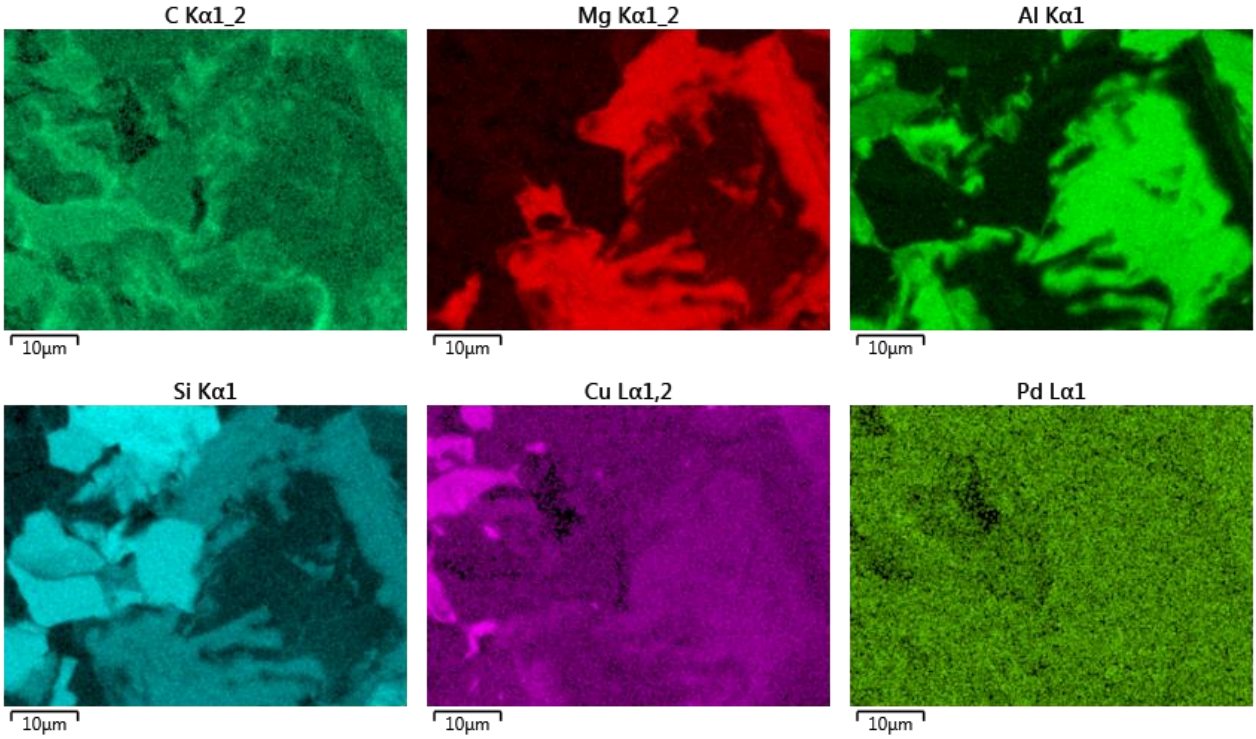
C Kα1_2
Mg Kα1_2
Al Kα1
10μm
10μm
10μm
Si Kα1
Cu Lα1,2
Pd Lα1
10μm
10μm
10μm

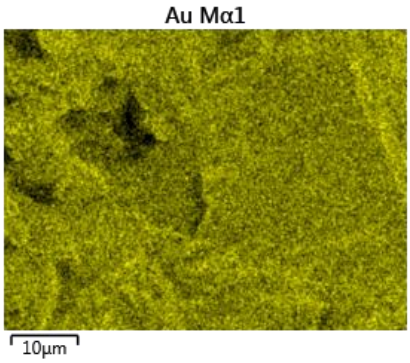
Au Mα1
10μm

Electron Image 5

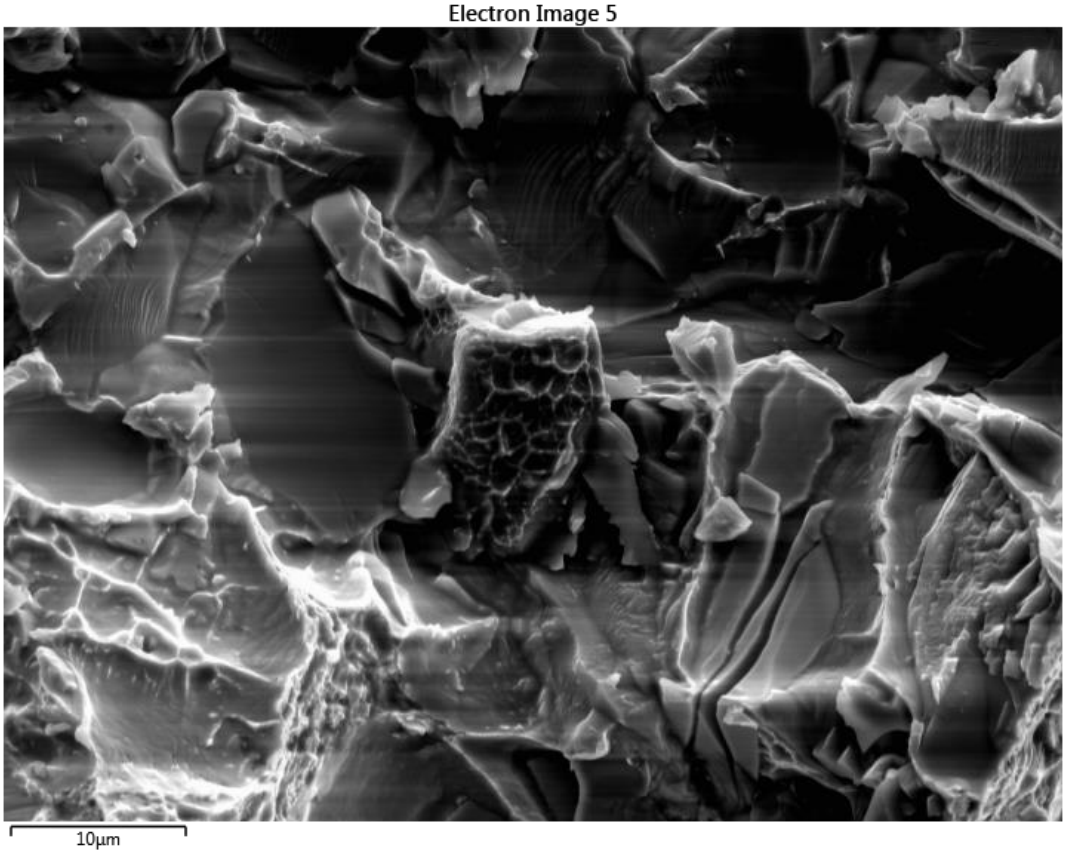

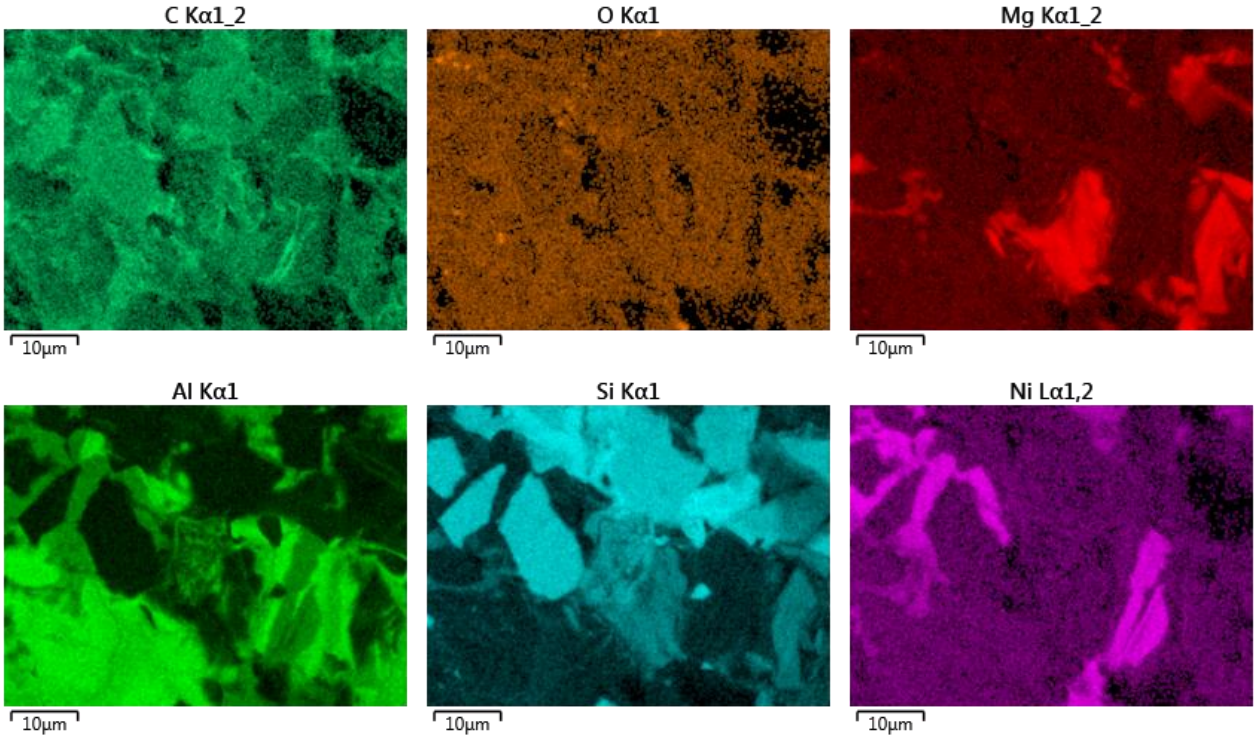
C Kα1_2
O Kα1
Mg Kα1_2
10μm
10μm
10μm
Al Kα1
Si Kα1
Ni Lα1,2
10μm
10μm
10μm

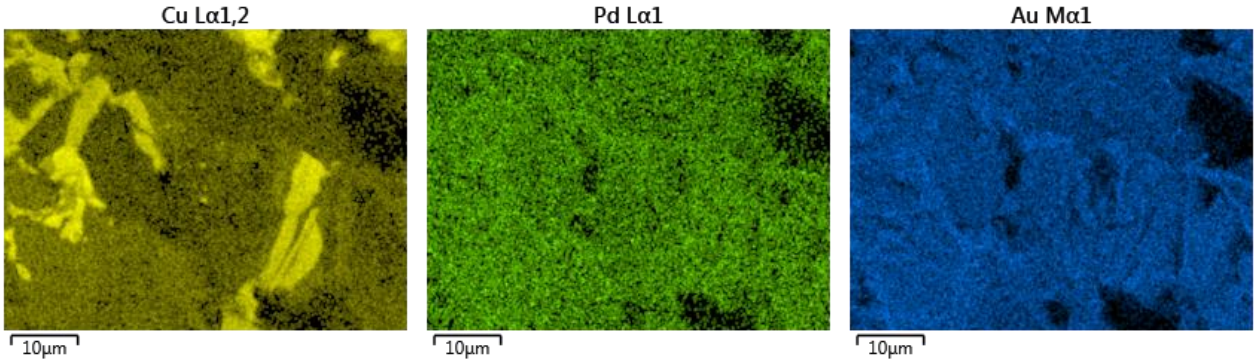
Cu Lα1,2
10μm
Pd Lα1
10μm
Au Mα1
10μm

Electron Image 6

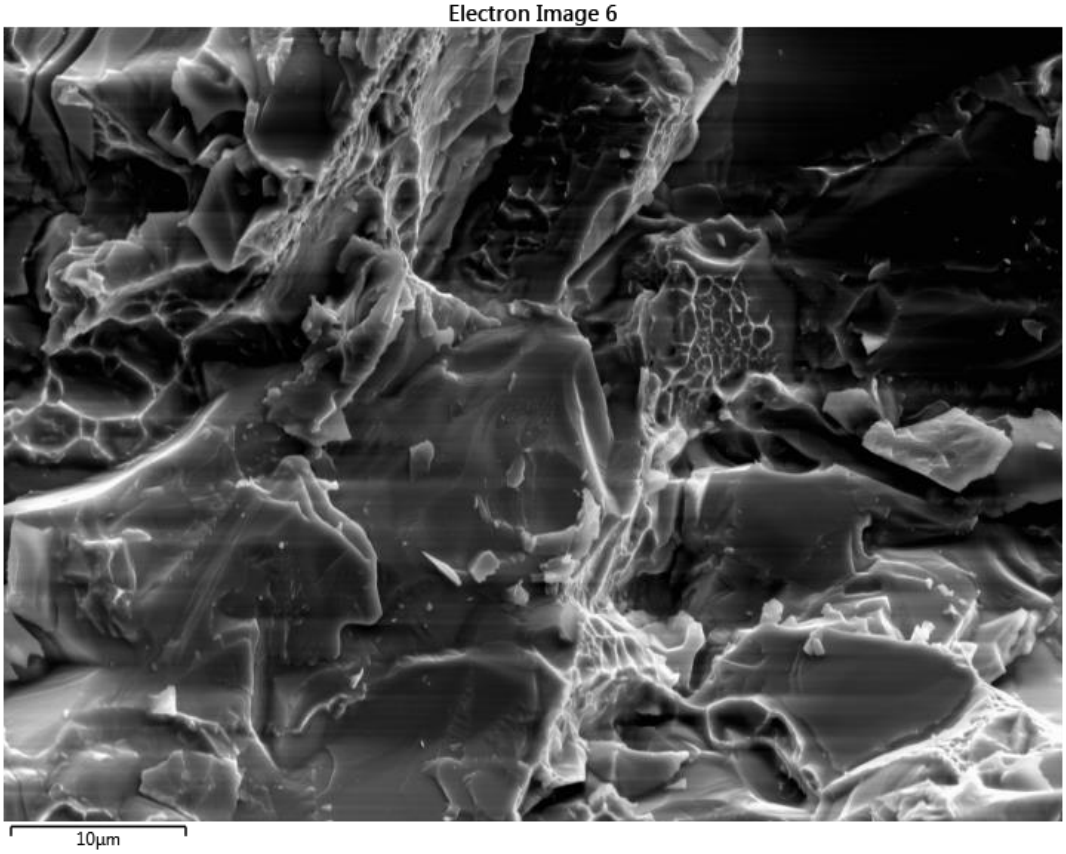

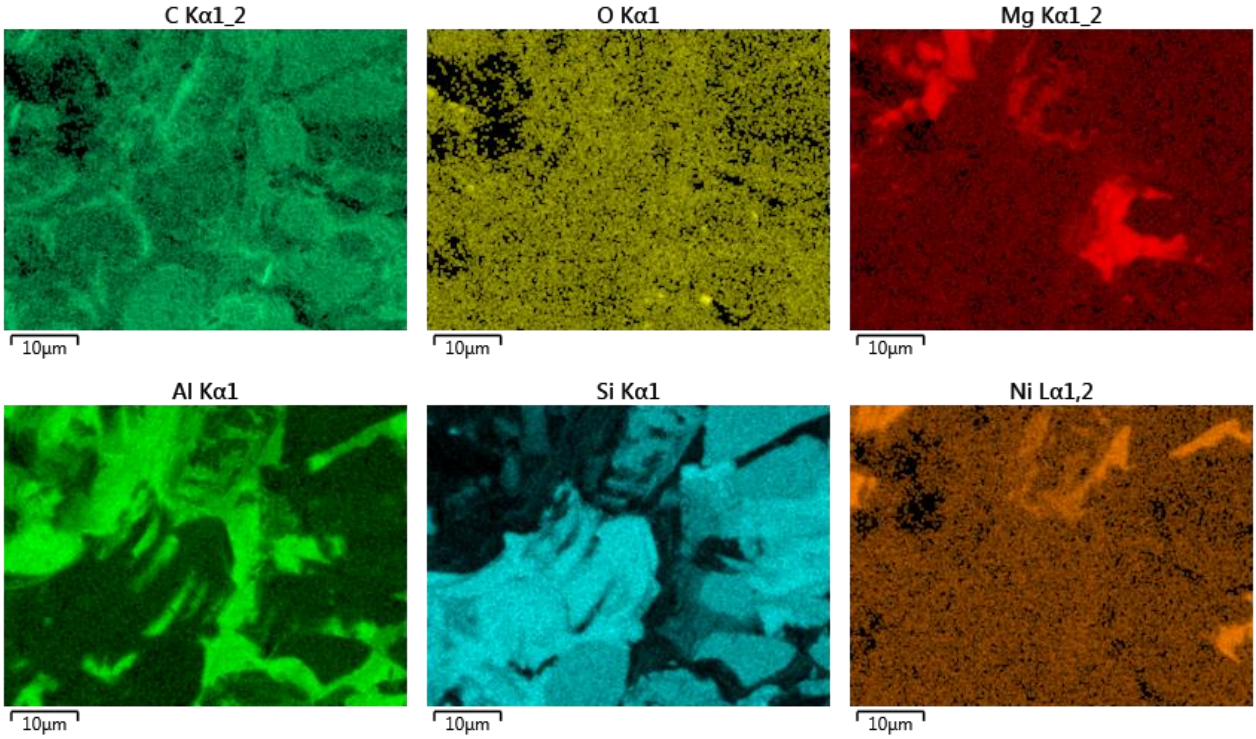
C Kα1_2
O Kα1
Mg Kα1_2
10μm
10μm
10μm
Al Kα1
Si Kα1
Ni Lα1,2
10μm
10μm
10μm

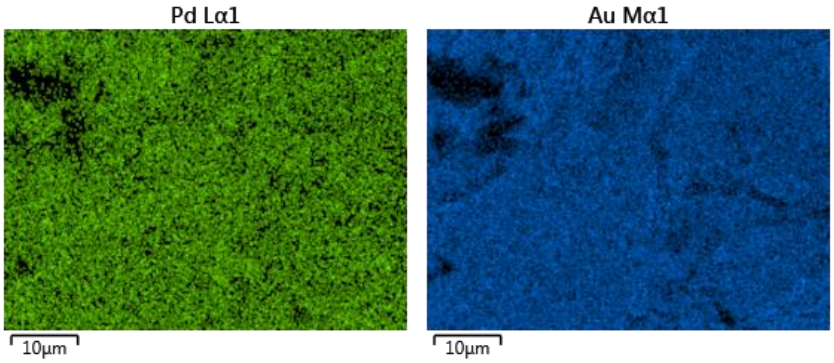
Pd Lα1
10μm
Au Mα1
10μm

Electron Image 8

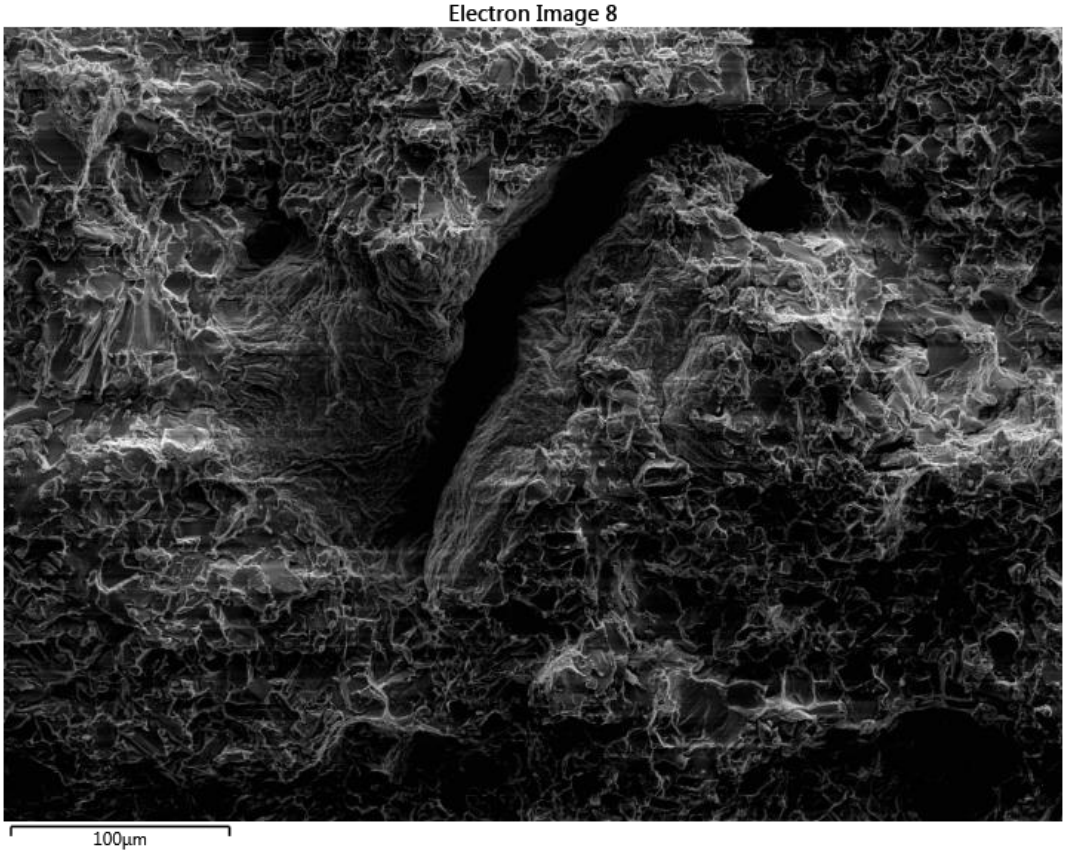

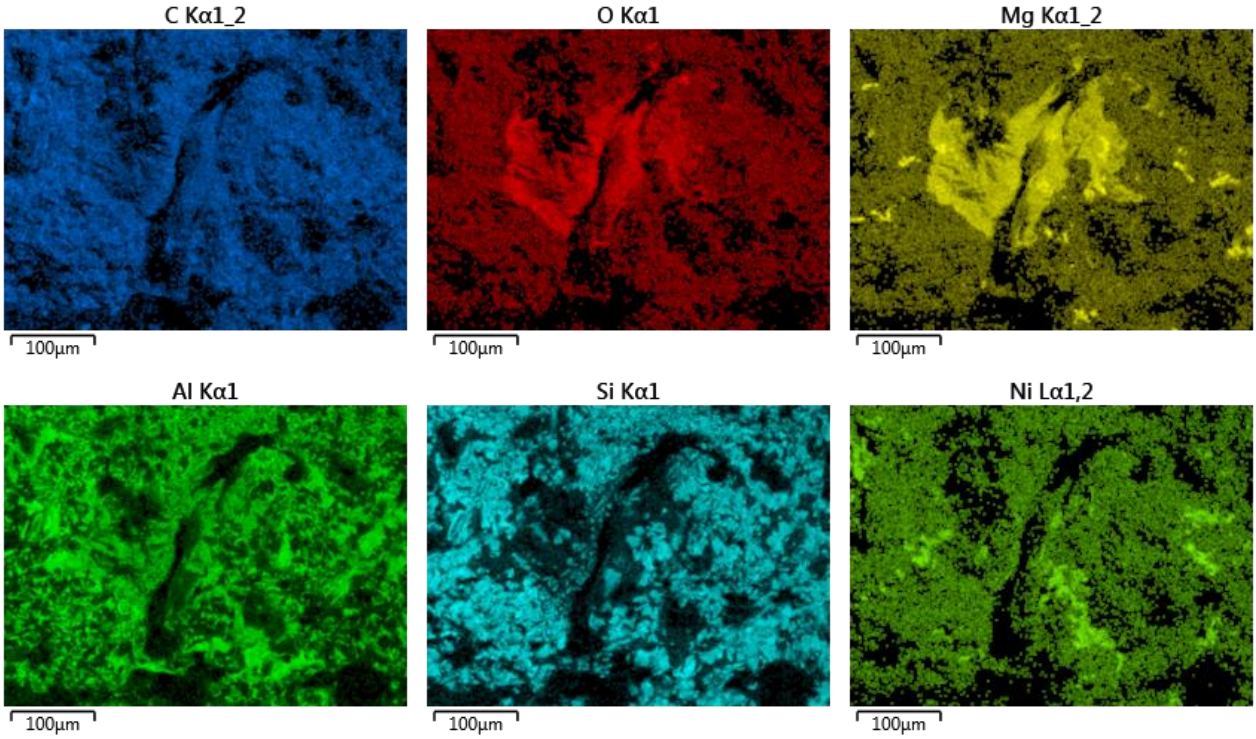
C Kα1_2
O Kα1
Mg Kα1_2
100µm
100µm
100µm
Al Kα1
Si Kα1
Ni Lα1,2
100µm
100µm
100µm

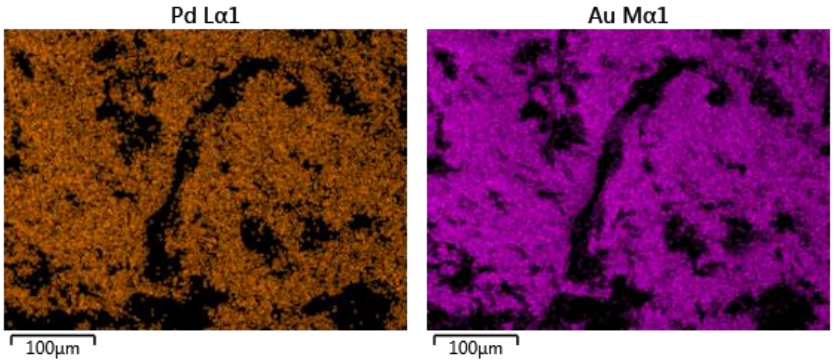
Pd Lα1
100μm
Au Mα1
100μm

Electron Image 9

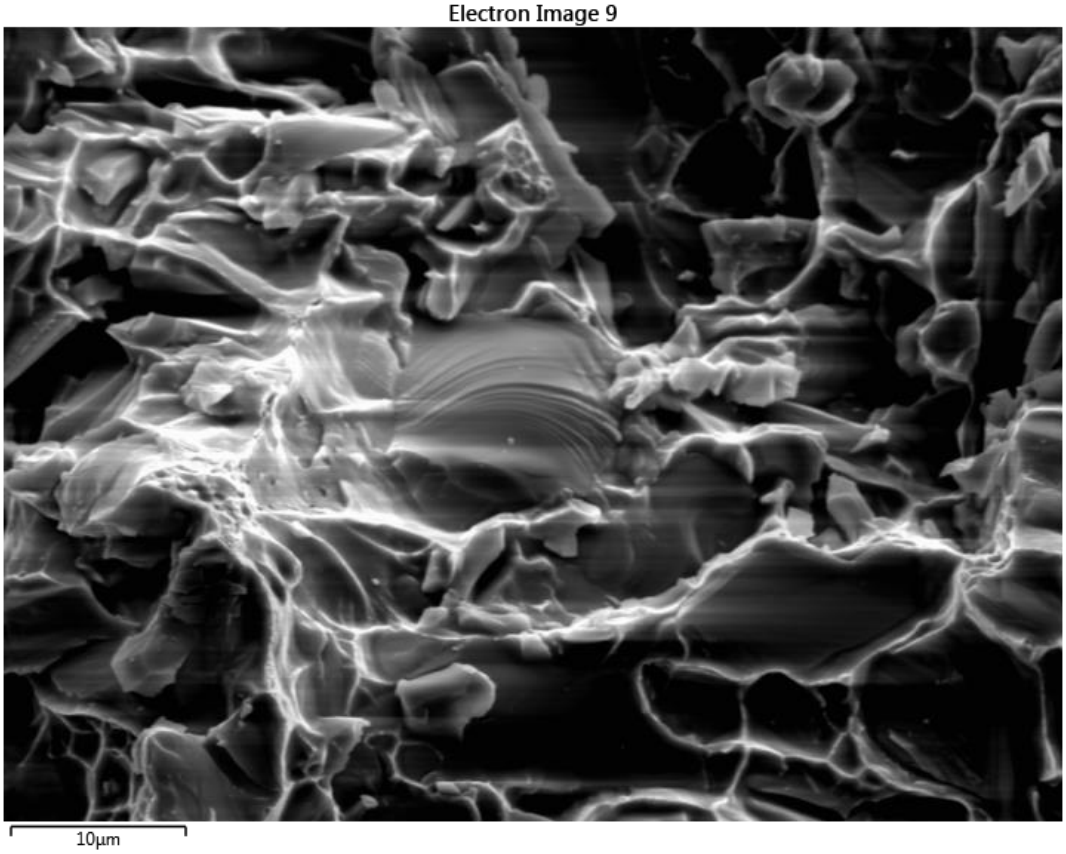

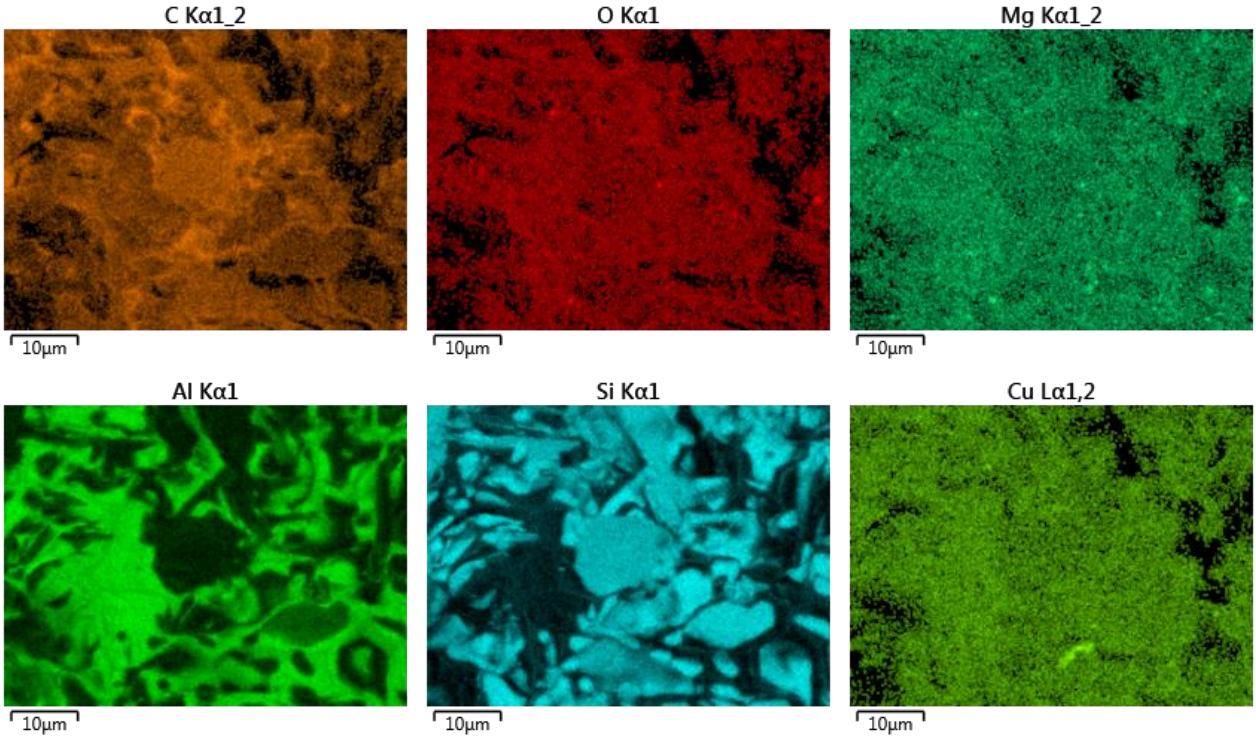
C Kα1_2
O Kα1
Mg Kα1_2
10µm
10µm
10µm
Al Kα1
Si Kα1
Cu Lα1,2
10µm
10µm
10µm

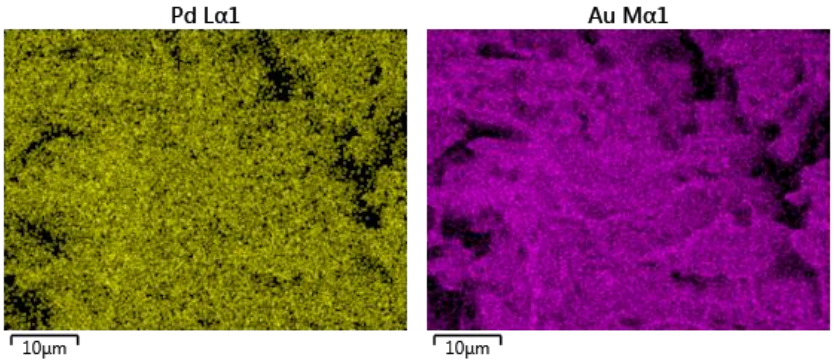
Pd Lα1
10μm
Au Mα1
10μm

F.6.2 NA-6

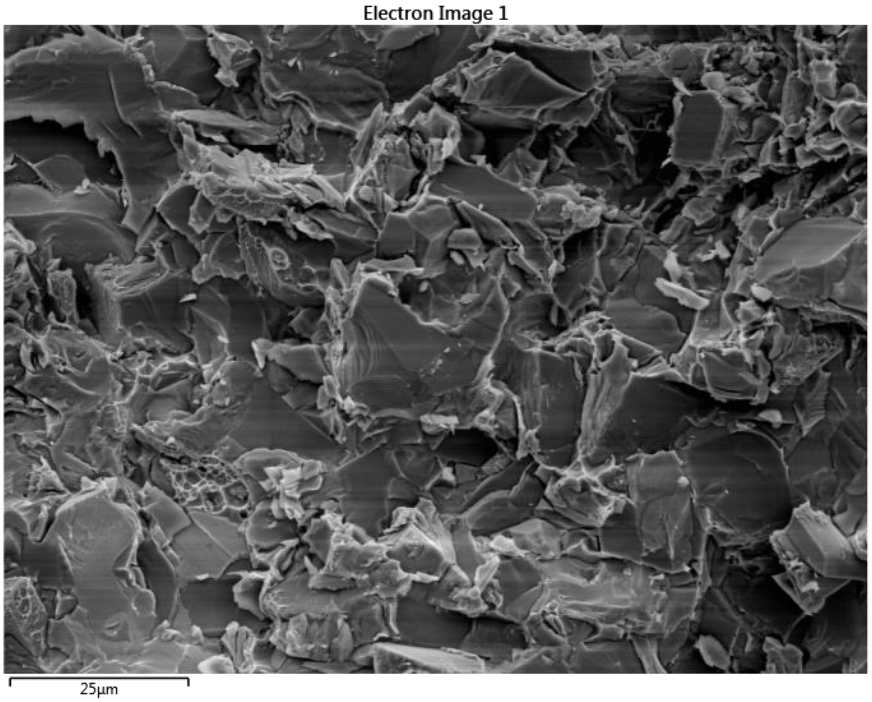

EDS Layered Image 1

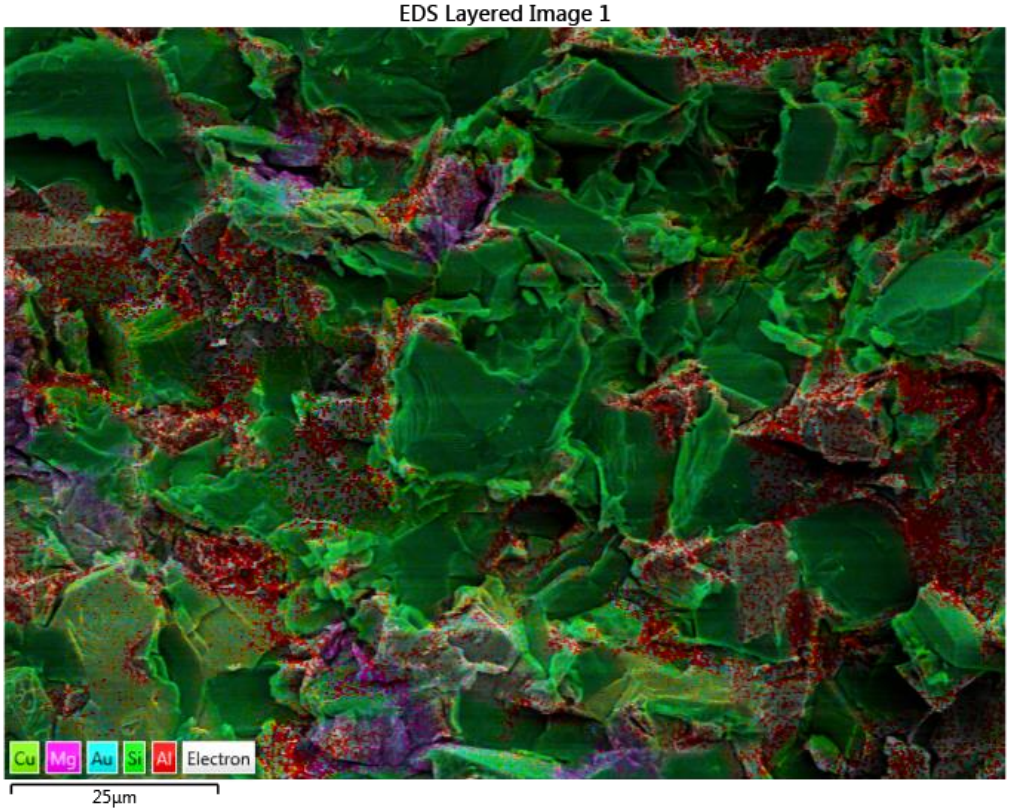

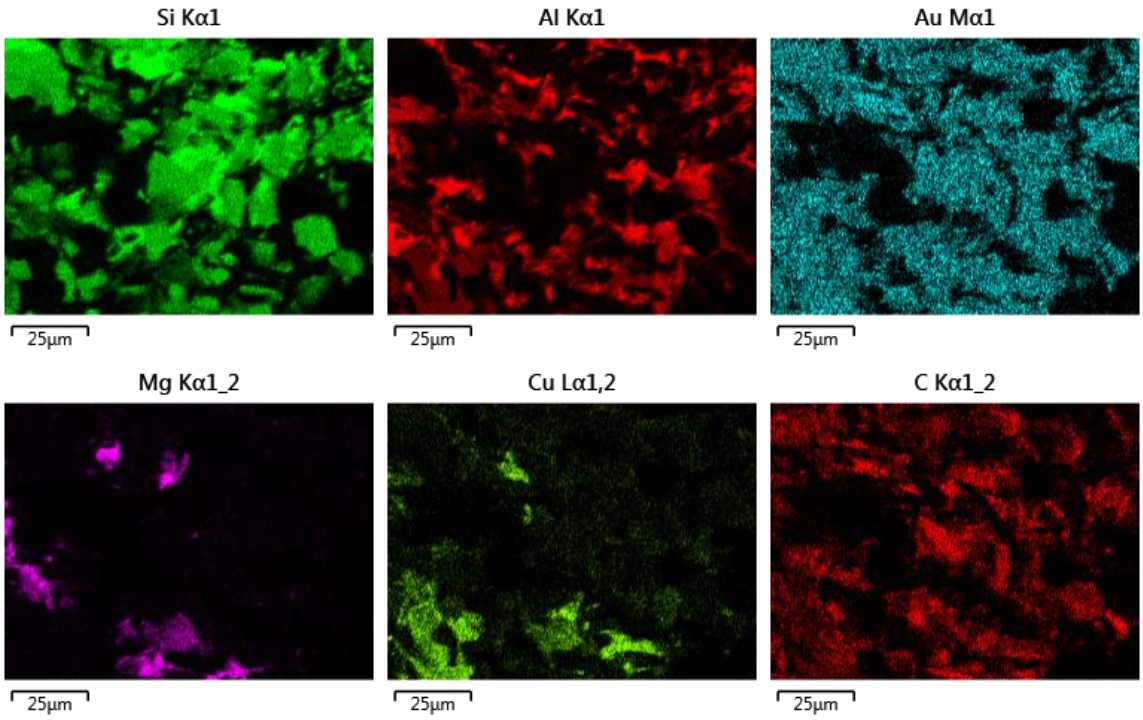
Si Kα1
Al Kα1
Au Mα1
25µm
25µm
25µm
Mg Kα1_2
Cu Lα1,2
C Kα1_2
25µm
25µm
25µm

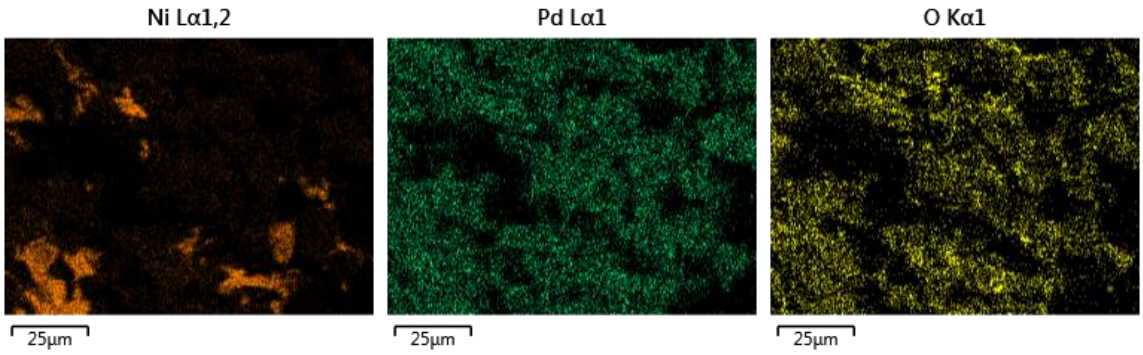
Ni Lα1,2
Pd Lα1
O Kα1
25µm
25µm
25µm

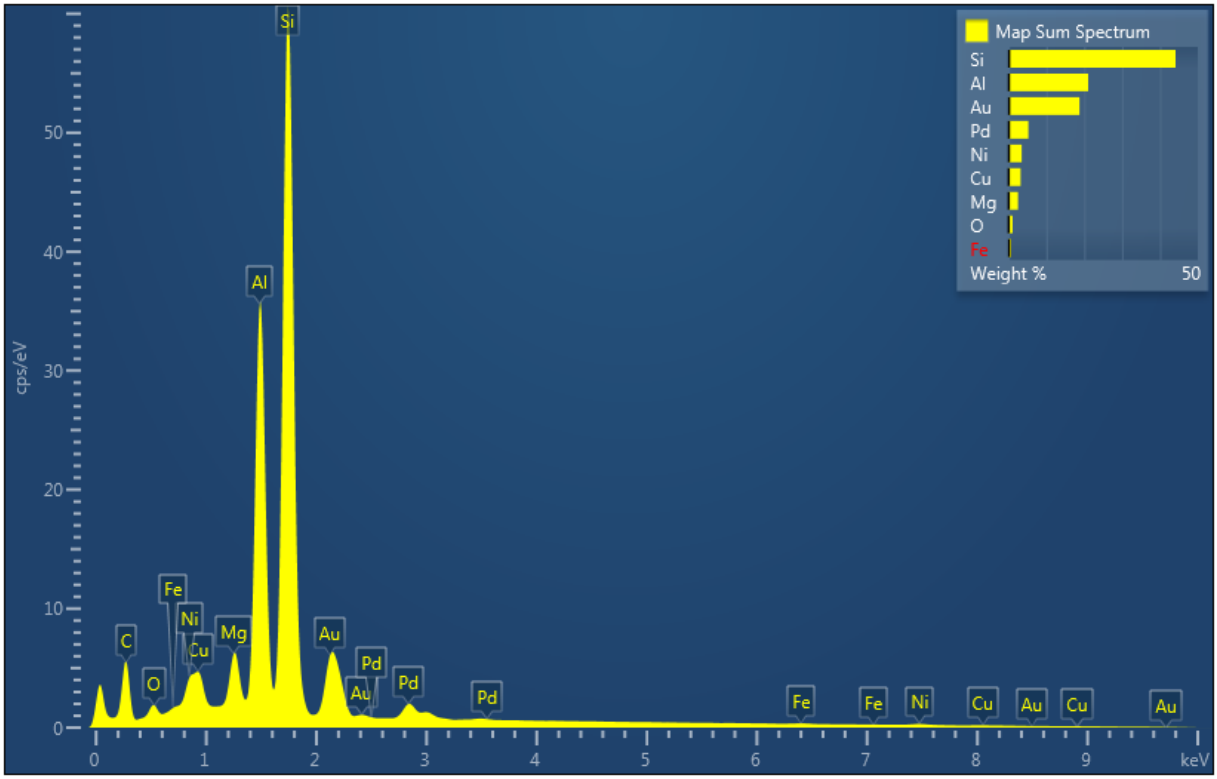
Map Sum Spectrum
Si
Al
Au
Pd
Ni
Cu
Mg
O
Fe
Weight %
50
cps/eV
0
10
20
30
40
50
0
1
2
3
4
5
6
7
8
9
keV
Si
Al
Fe
Ni
Cu
Mg
C
O
Au
Pd
Au
Pd
Pd
Fe
Fe
Ni
Cu
Au
Cu
Au

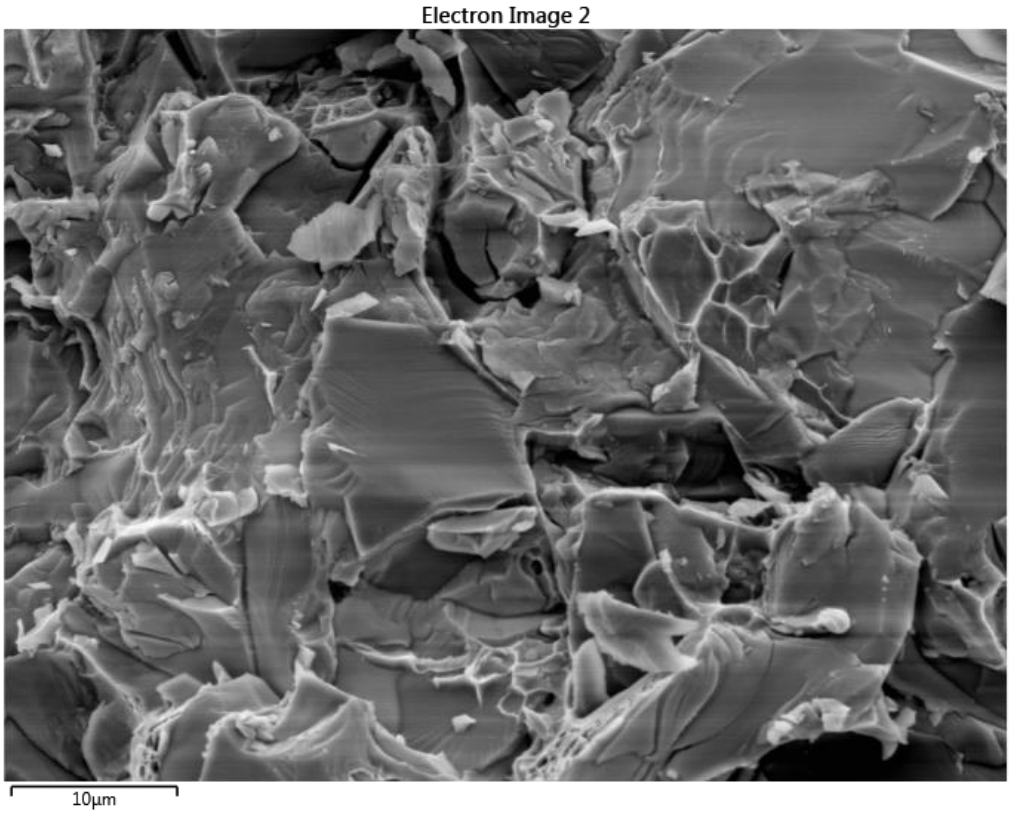
Electron Image 2
10µm

EDS Layered Image 2

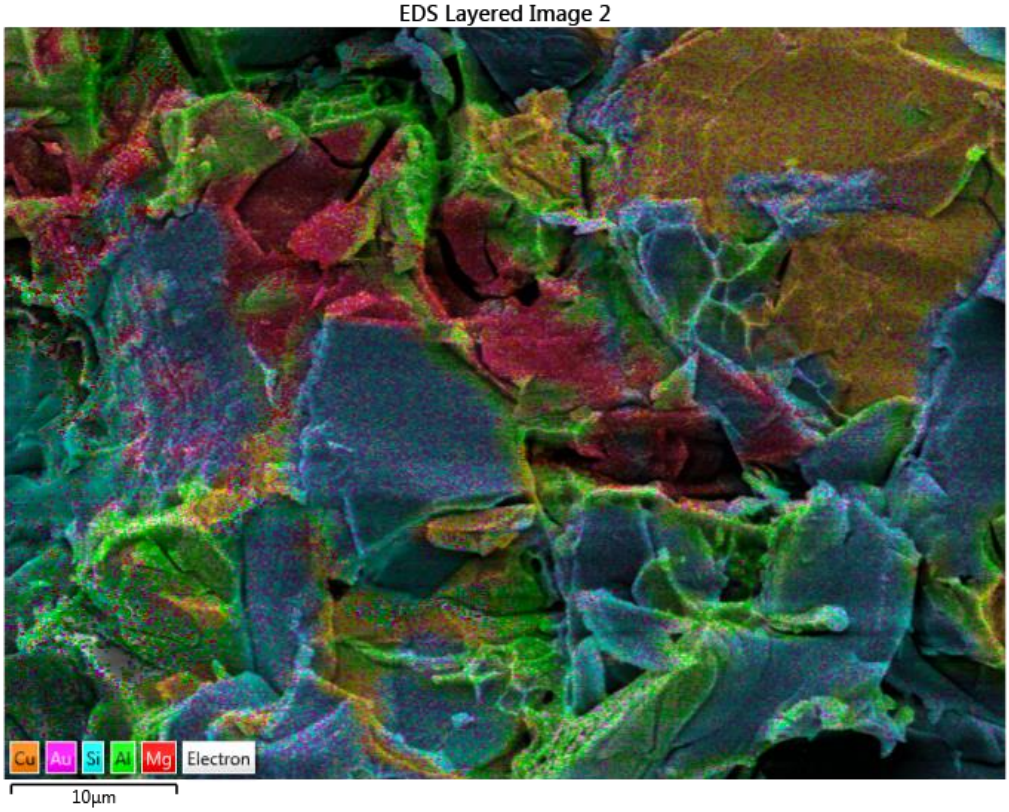

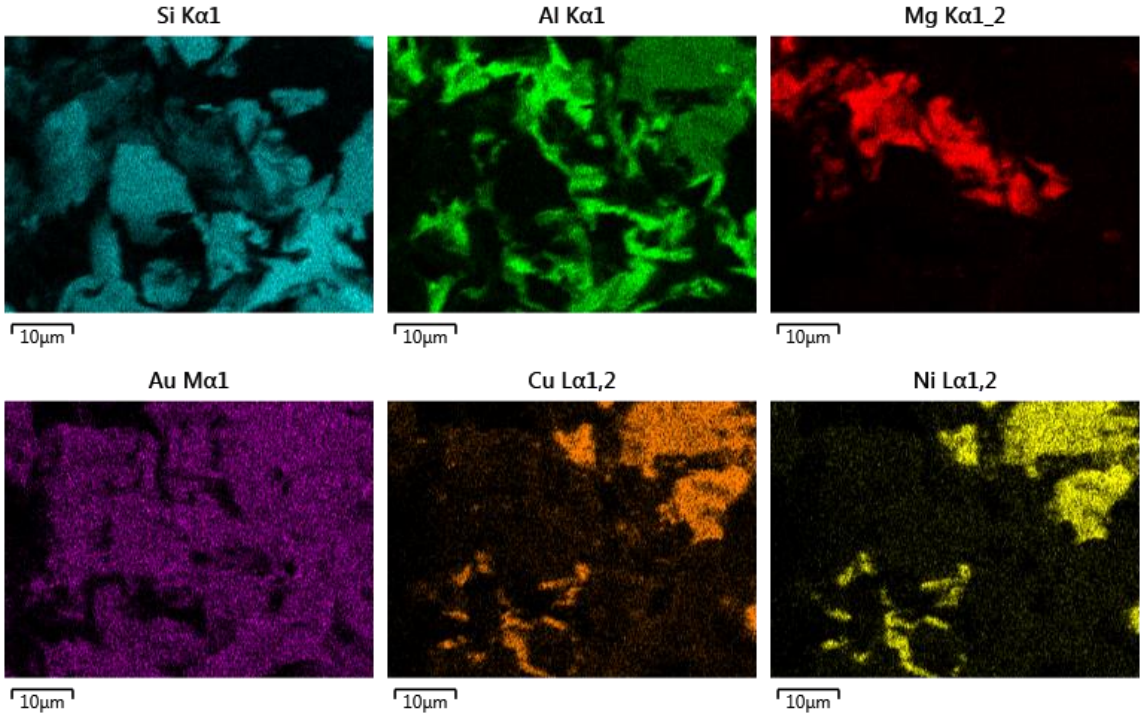
Si Kα1
Al Kα1
Mg Kα1_2
10µm
10µm
10µm
Au Mα1
Cu Lα1,2
Ni Lα1,2
10µm
10µm
10µm

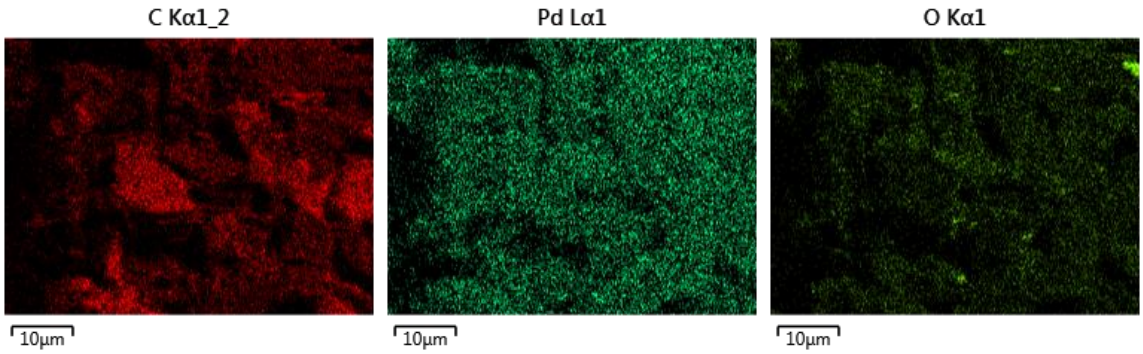
C Kα1_2
Pd Lα1
O Kα1
10μm
10μm
10μm

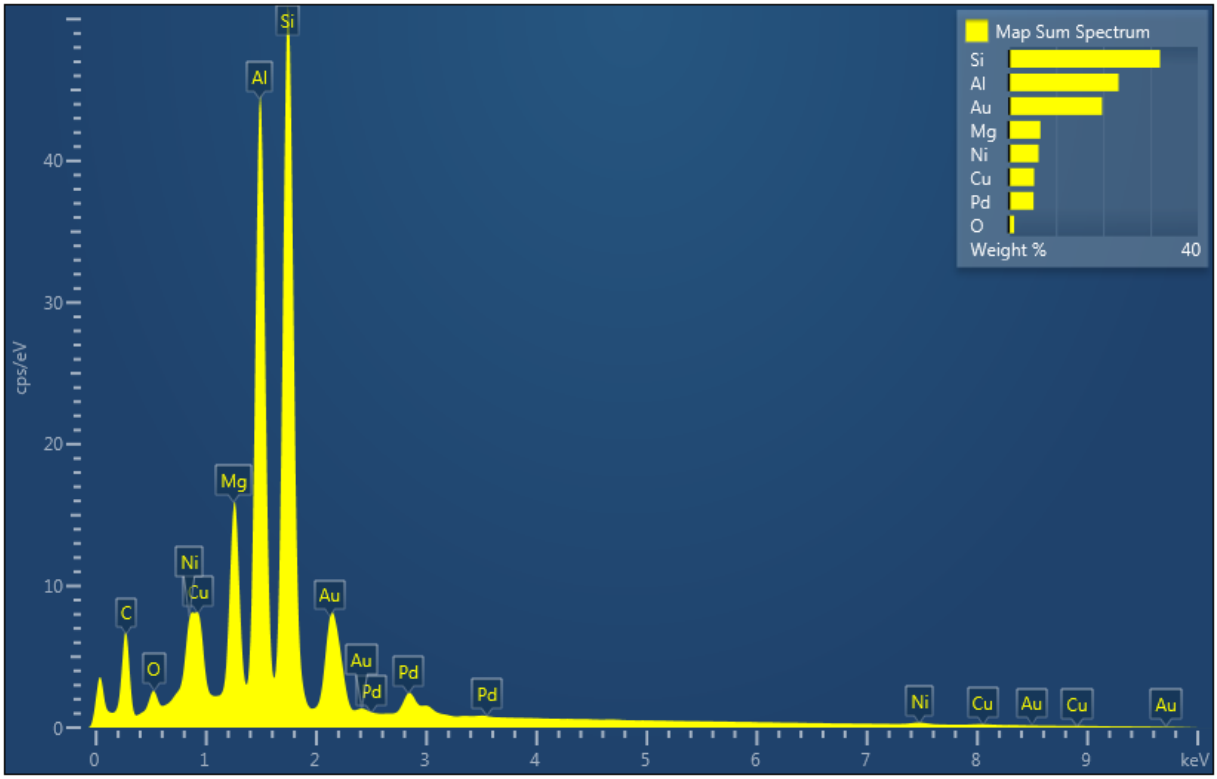
Map Sum Spectrum
Si
Al
Au
Mg
Ni
Cu
Pd
O
Weight %
40
cps/eV
0
10
20
30
40
0
1
2
3
4
5
6
7
8
9
keV
Si
Al
Mg
Ni
Cu
C
O
Au
Au
Pd
Pd
Pd
Ni
Cu
Au
Cu
Au

Electron Image 3

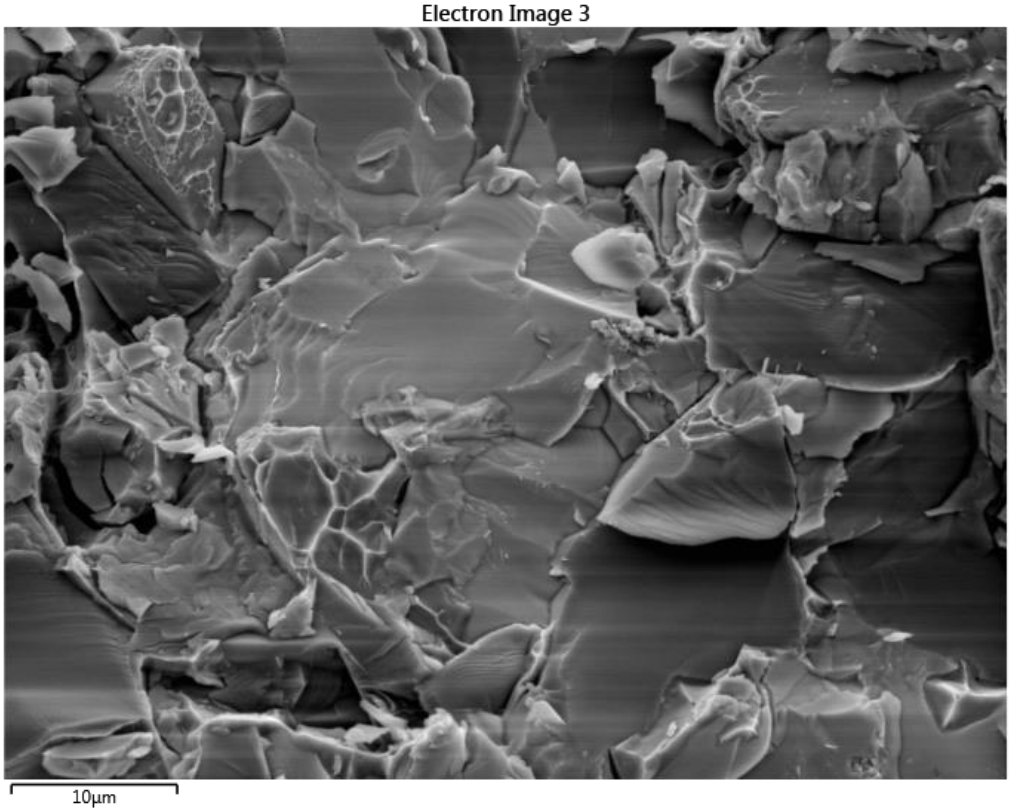

EDS Layered Image 3

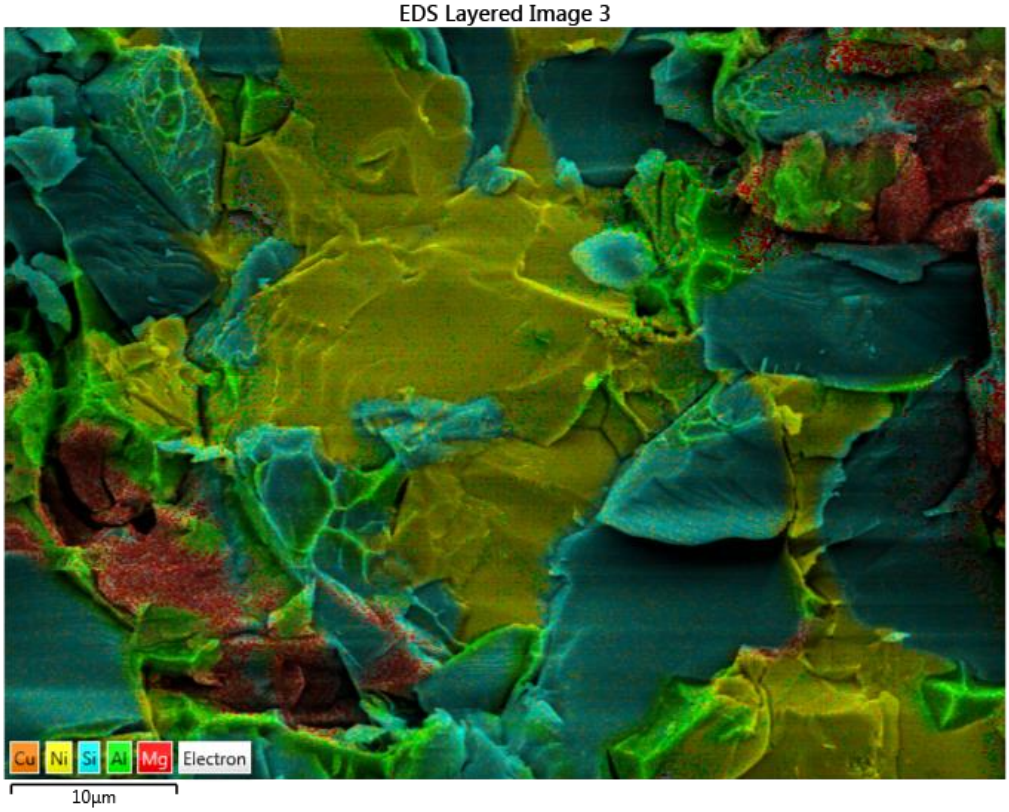

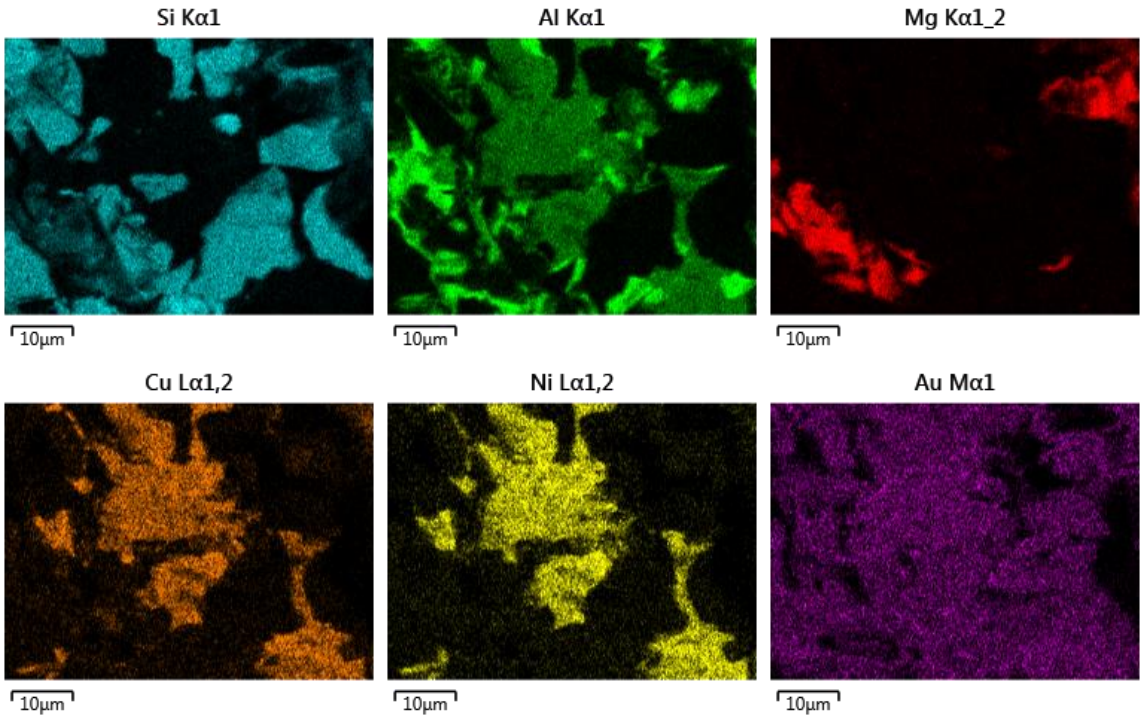
Si Kα1
Al Kα1
Mg Kα1_2
10µm
10µm
10µm
Cu Lα1,2
Ni Lα1,2
Au Mα1
10µm
10µm
10µm

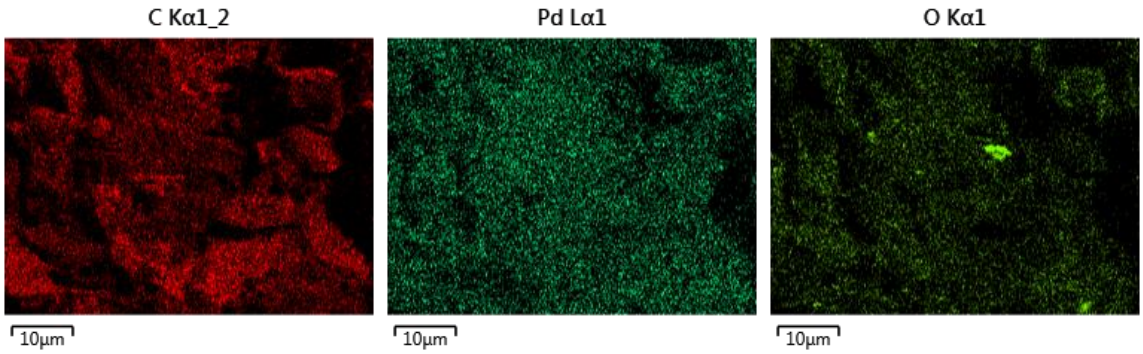
C Kα1_2
Pd Lα1
O Kα1
10μm
10μm
10μm

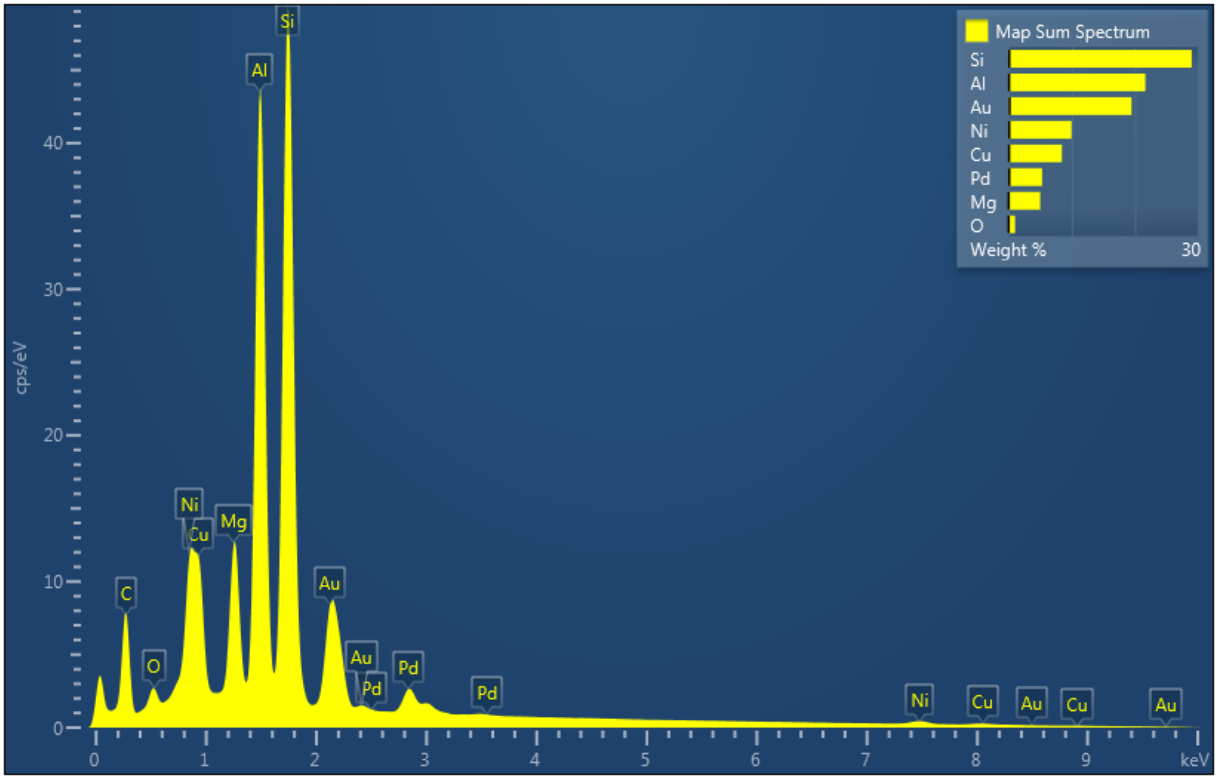
Map Sum Spectrum
Si
Al
Au
Ni
Cu
Pd
Mg
O
Weight %
30
cps/eV
0
10
20
30
40
C
O
Ni
Cu
Mg
Al
Si
Au
Au
Pd
Pd
Ni
Cu
Au
Cu
Au
0
1
2
3
4
5
6
7
8
9
keV

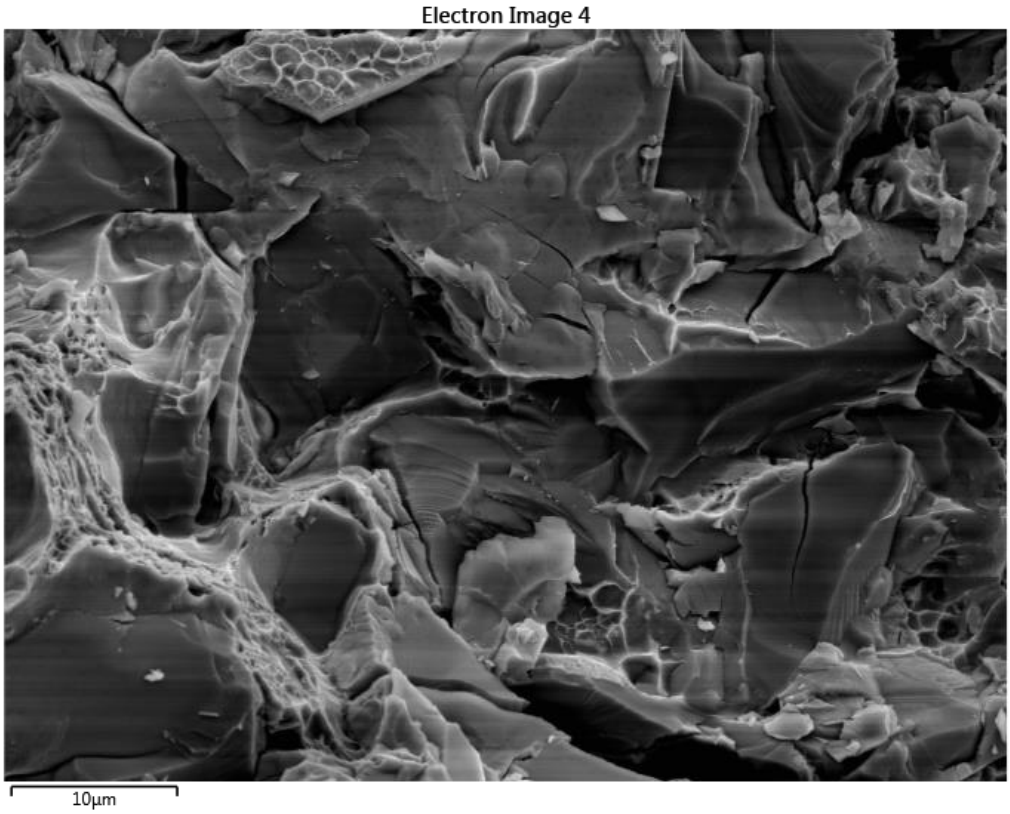
Electron Image 4
10µm

EDS Layered Image 4

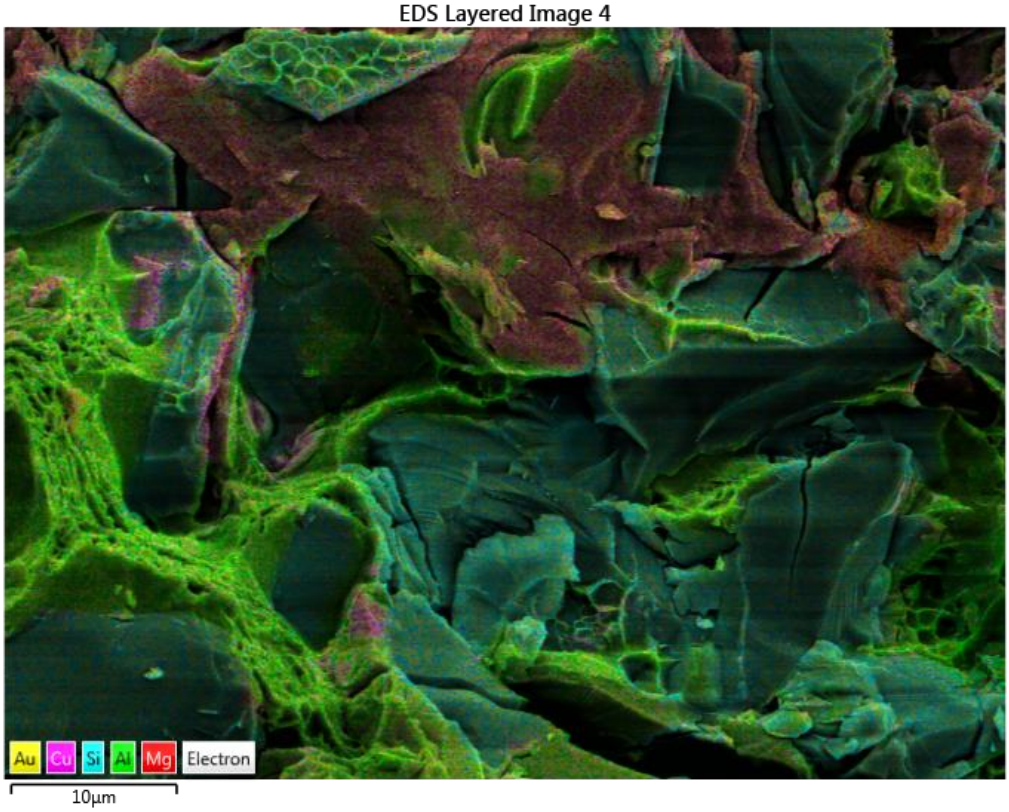

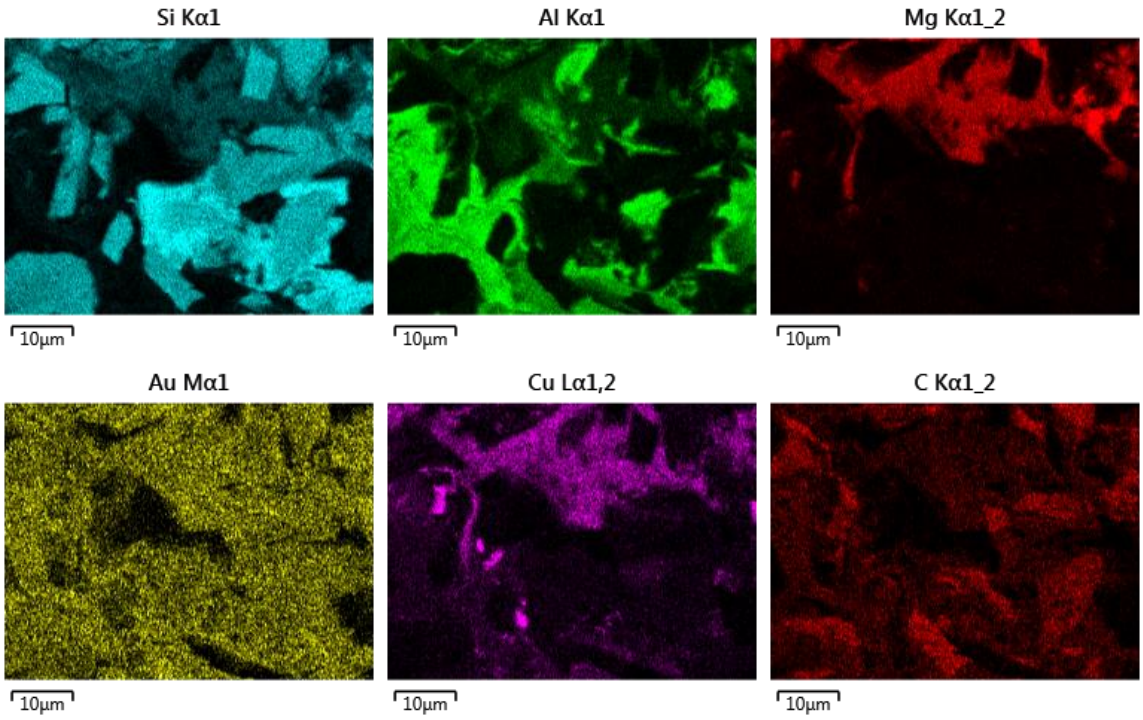
Si Kα1
Al Kα1
Mg Kα1_2
10μm
10μm
10μm
Au Mα1
Cu Lα1,2
C Kα1_2
10μm
10μm
10μm

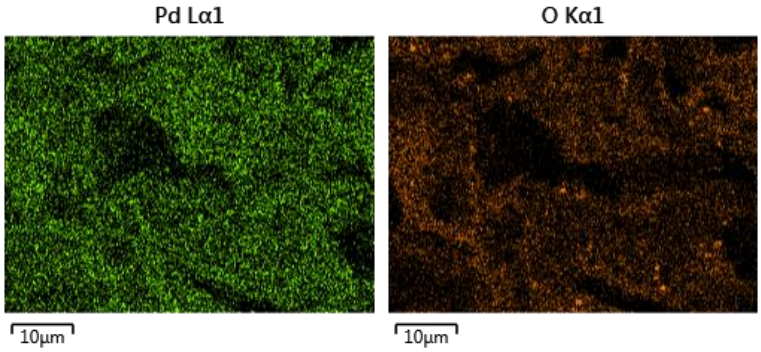
Pd Lα1
O Kα1
10μm
10μm

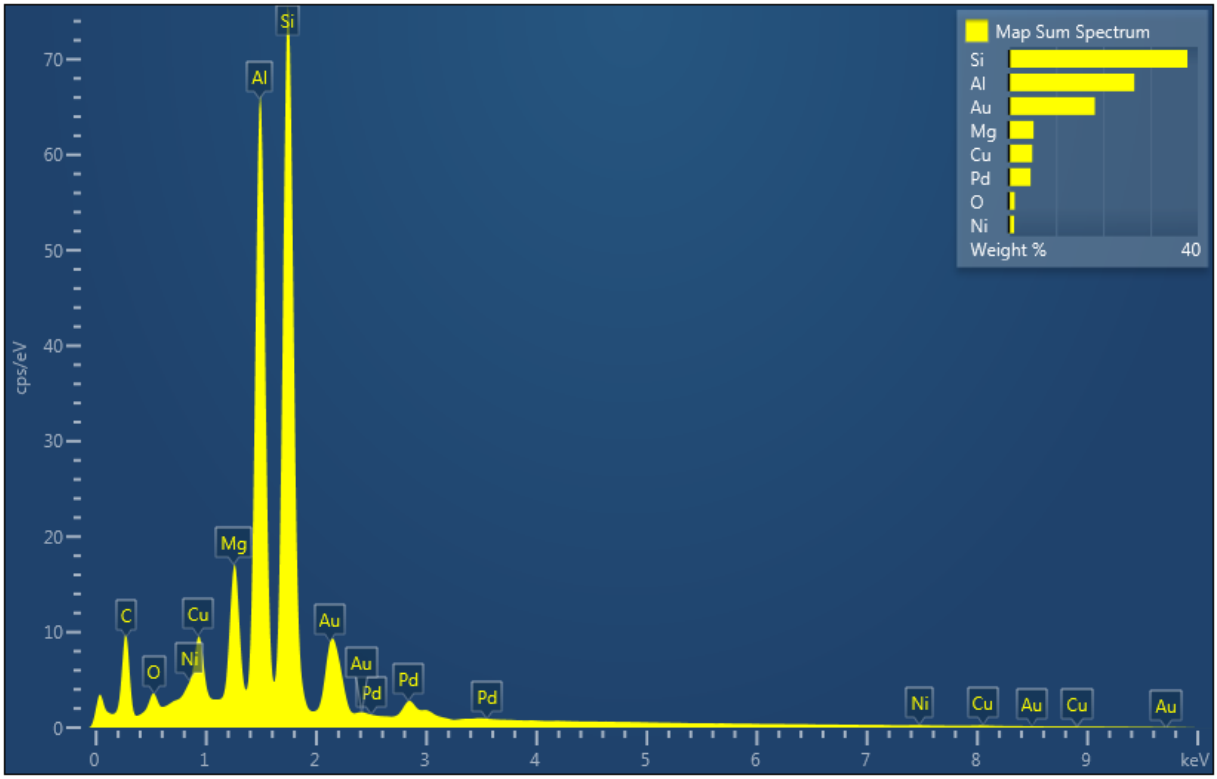
Map Sum Spectrum
Si
Al
Au
Mg
Cu
Pd
O
Ni
Weight %
40
cps/eV
70
60
50
40
30
20
10
0
C
O
Ni
Cu
Mg
Al
Si
Au
Au
Pd
Pd
Pd
Ni
Cu
Au
Cu
Au
0
1
2
3
4
5
6
7
8
9
keV

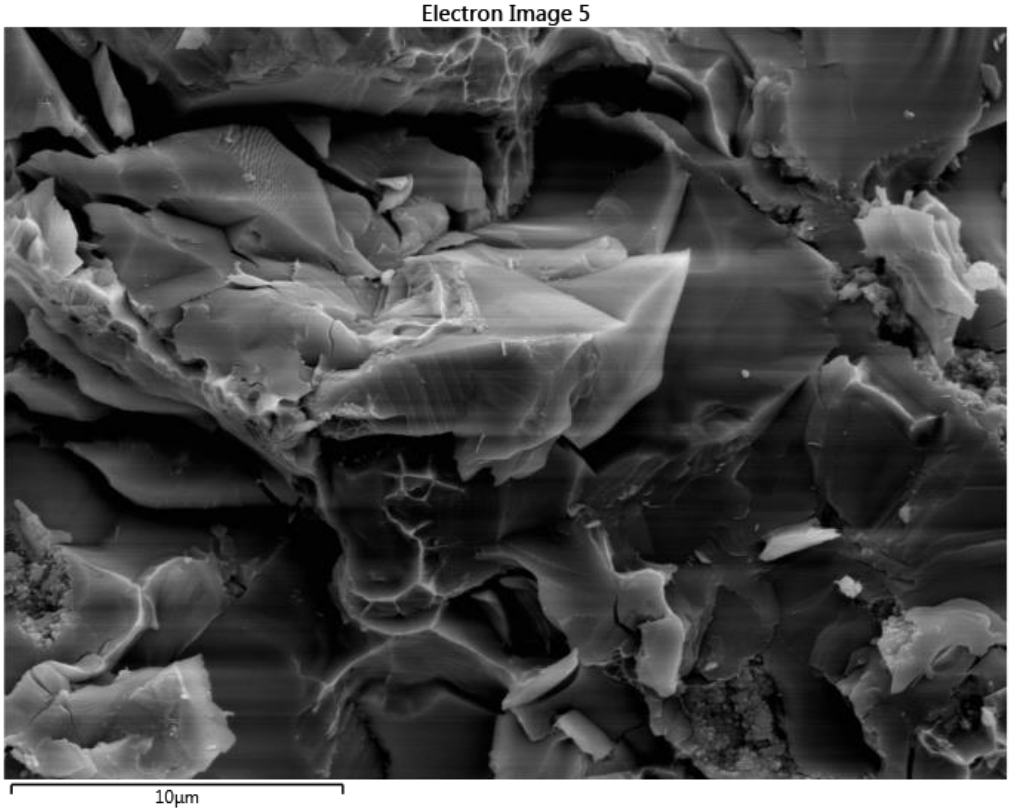
Electron Image 5
10µm

EDS Layered Image 5

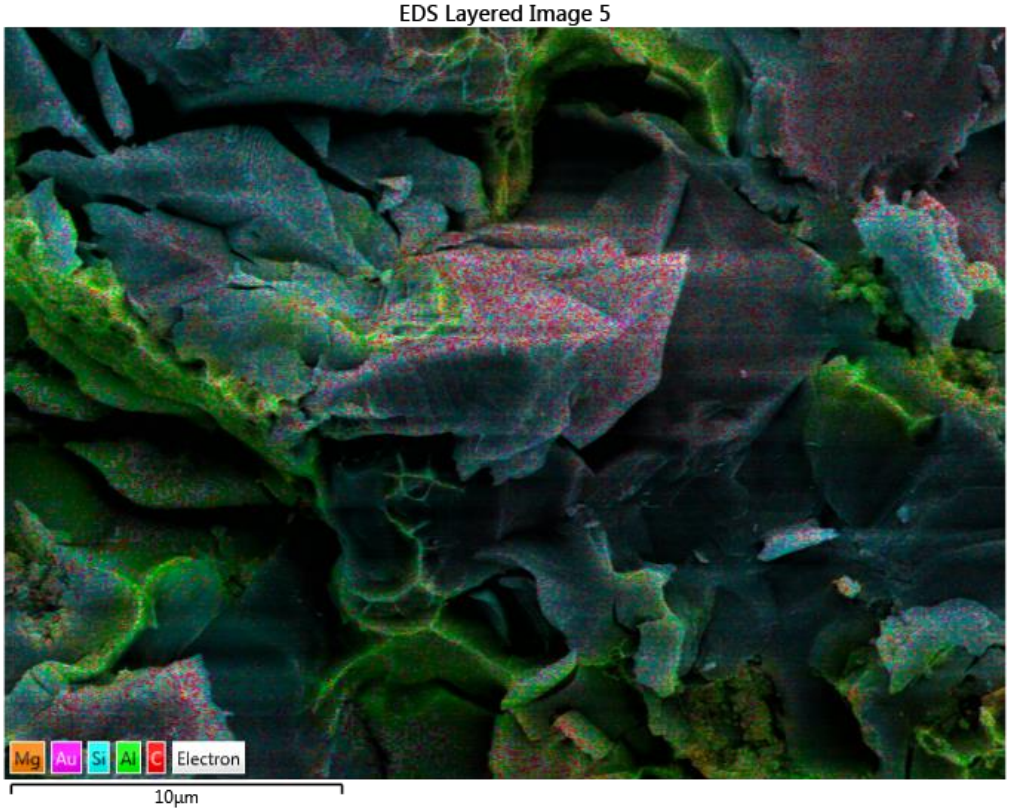

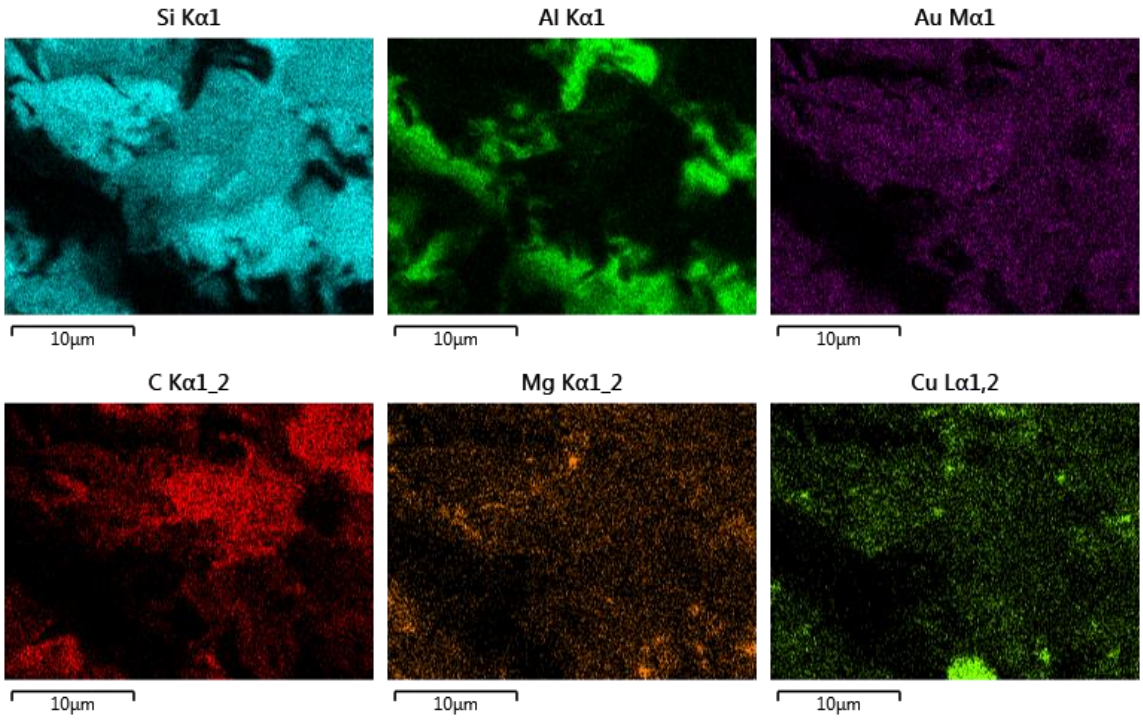
Si Kα1
Al Kα1
Au Mα1
10µm
10µm
10µm
C Kα1_2
Mg Kα1_2
Cu Lα1,2
10µm
10µm
10µm

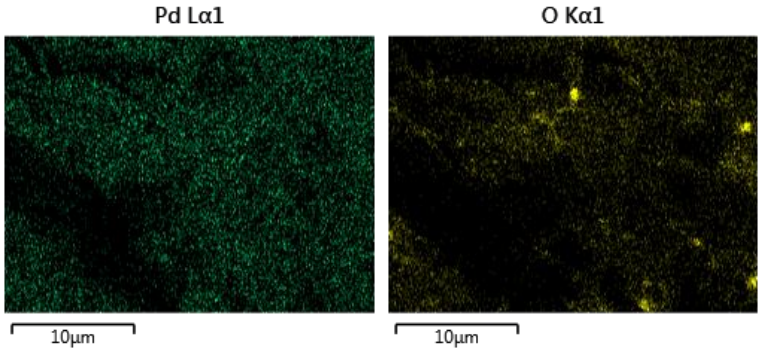
Pd Lα1
O Kα1
10μm
10μm

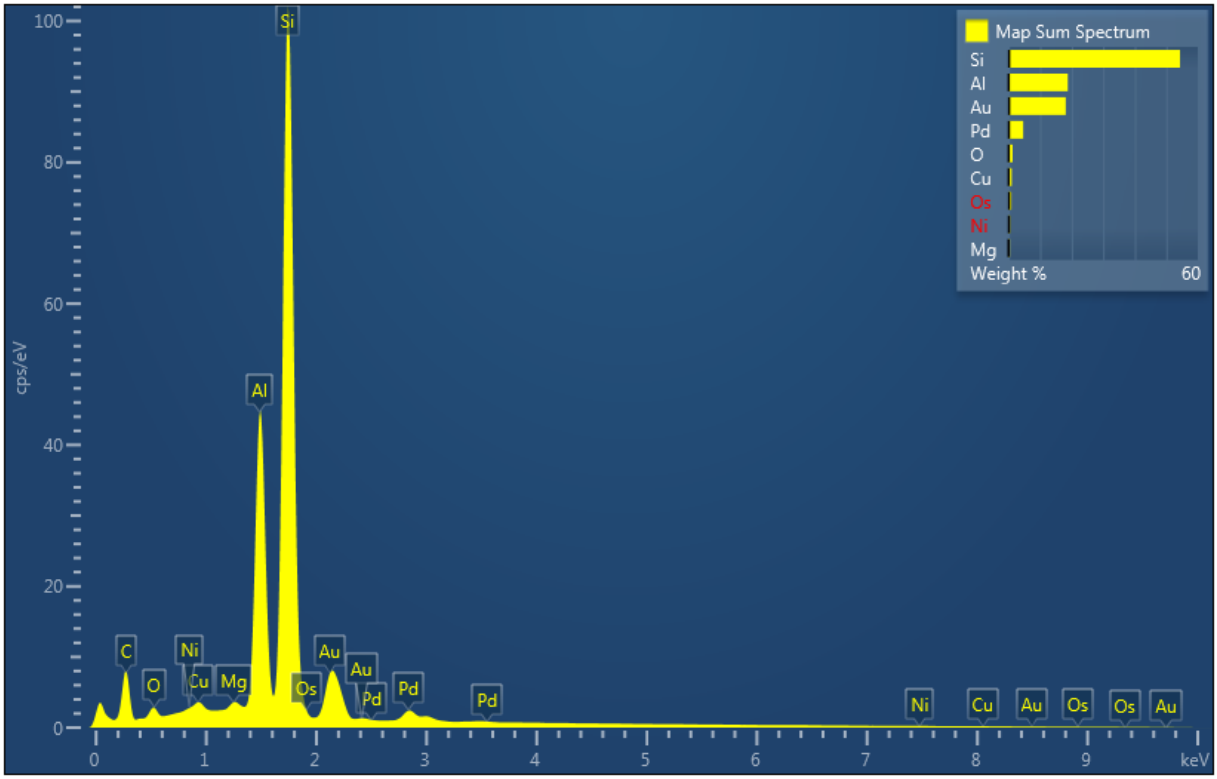
Map Sum Spectrum
Si
Al
Au
Pd
O
Cu
Os
Ni
Mg
Weight %
60
cps/eV
100
80
60
40
20
0
C
O
Ni
Cu
Mg
Al
Si
Os
Au
Au
Pd
Pd
Pd
Ni
Cu
Au
Os
Os
Au
0
1
2
3
4
5
6
7
8
9
keV

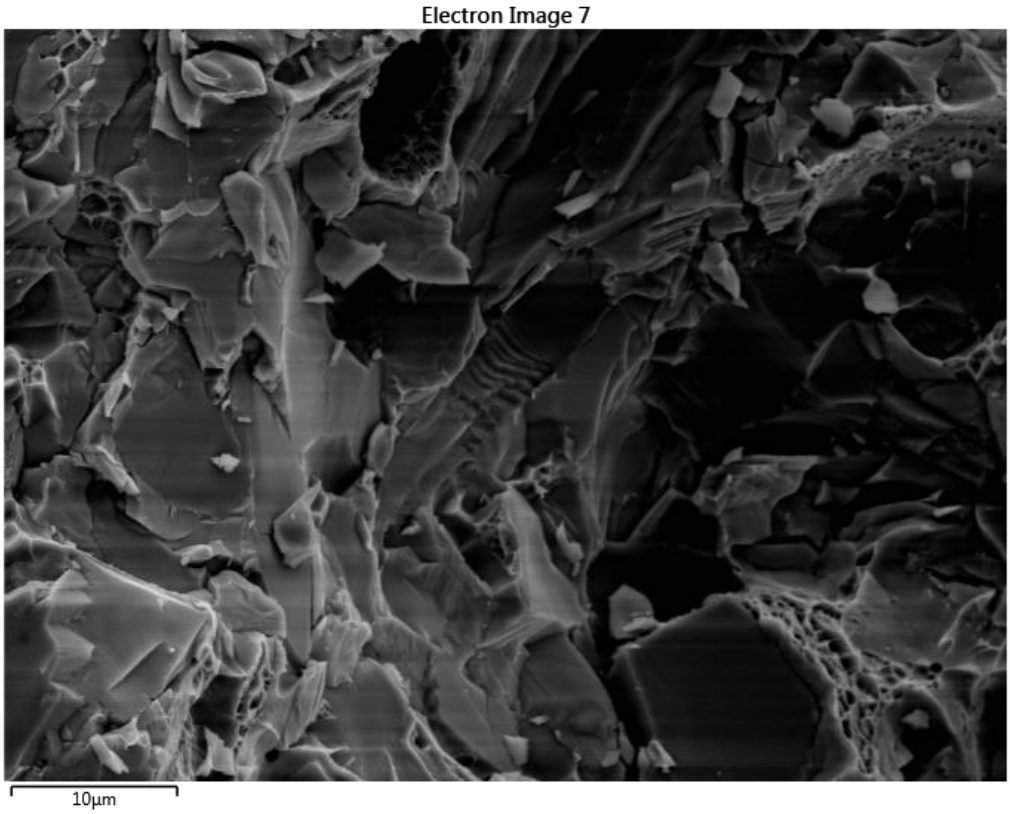
Electron Image 7
10µm

EDS Layered Image 7

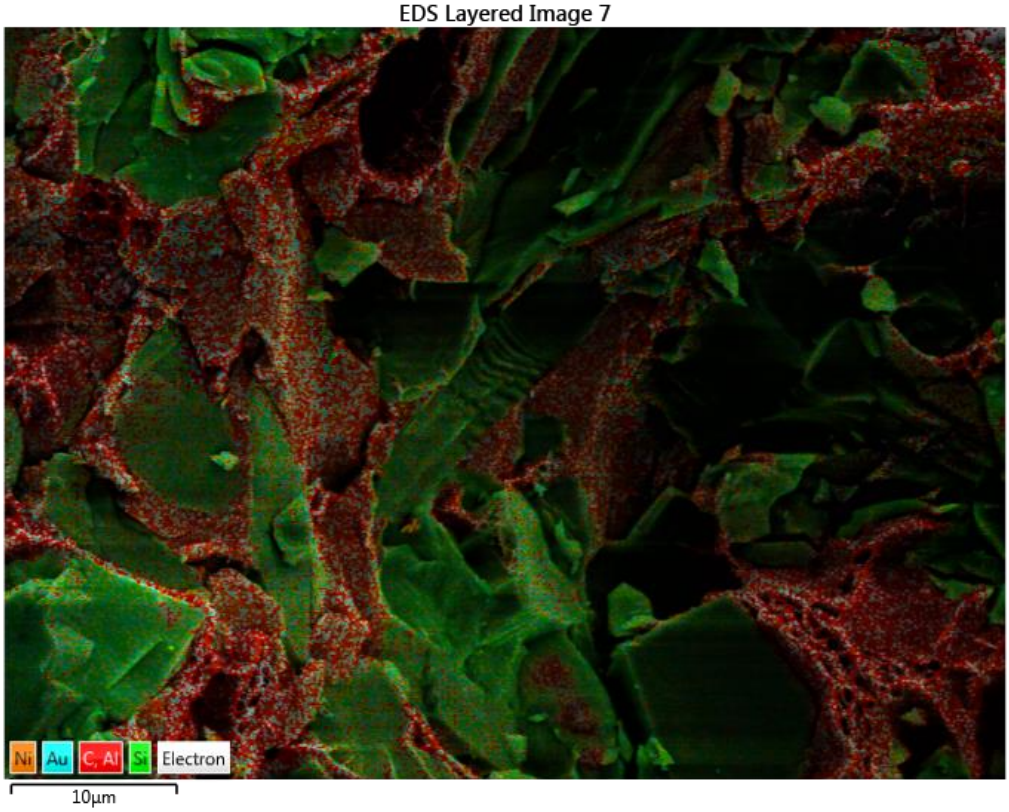

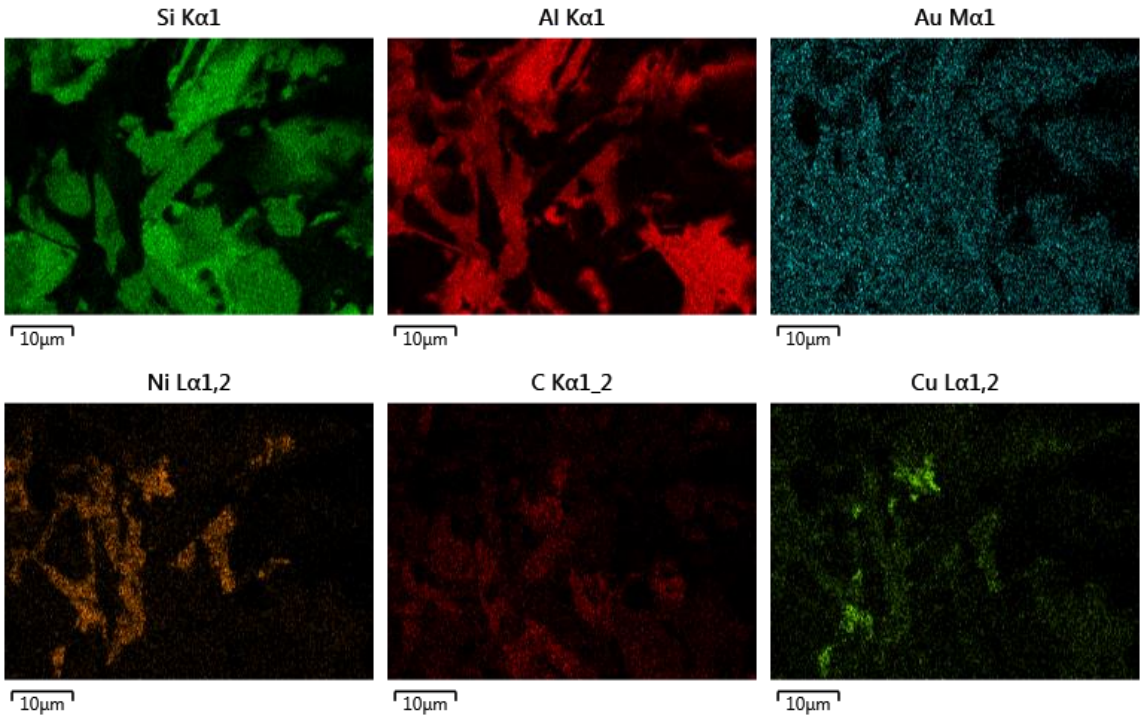
Si Kα1
Al Kα1
Au Mα1
10μm
10μm
10μm
Ni Lα1,2
C Kα1_2
Cu Lα1,2
10μm
10μm
10μm

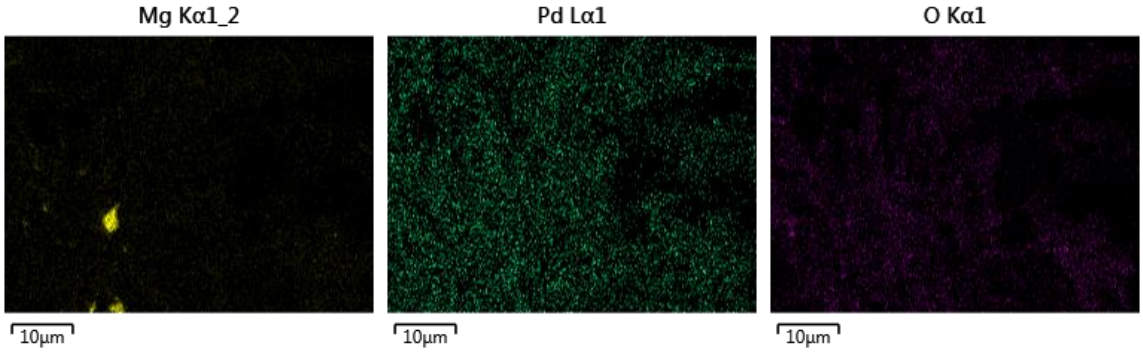
Mg Kα1_2
Pd Lα1
O Kα1
10µm
10µm
10µm

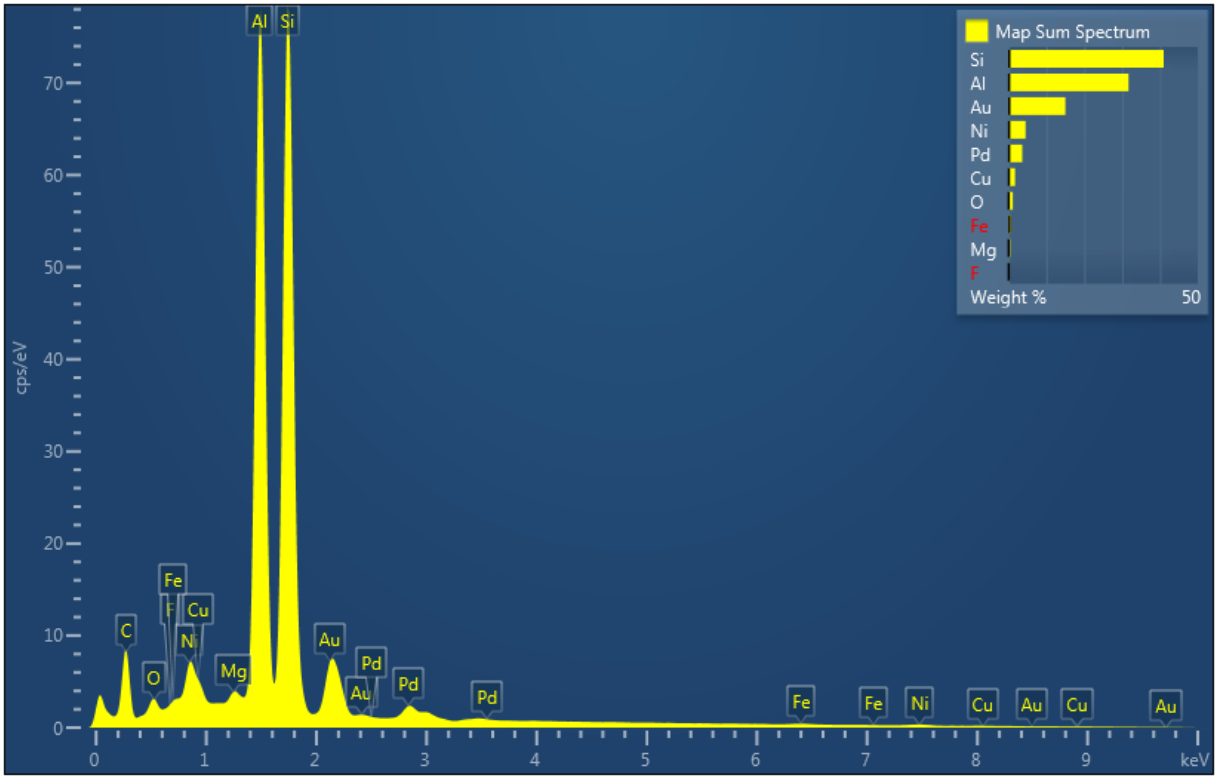
Map Sum Spectrum
Si
Al
Au
Ni
Pd
Cu
O
Fe
Mg
F
Weight %
50
cps/eV
0
10
20
30
40
50
60
70
0
1
2
3
4
5
6
7
8
9
keV
C
O
Fe
F
Cu
Ni
Mg
Al
Si
Au
Au
Pd
Pd
Pd
Fe
Fe
Ni
Cu
Au
Cu
Au

Electron Image 8

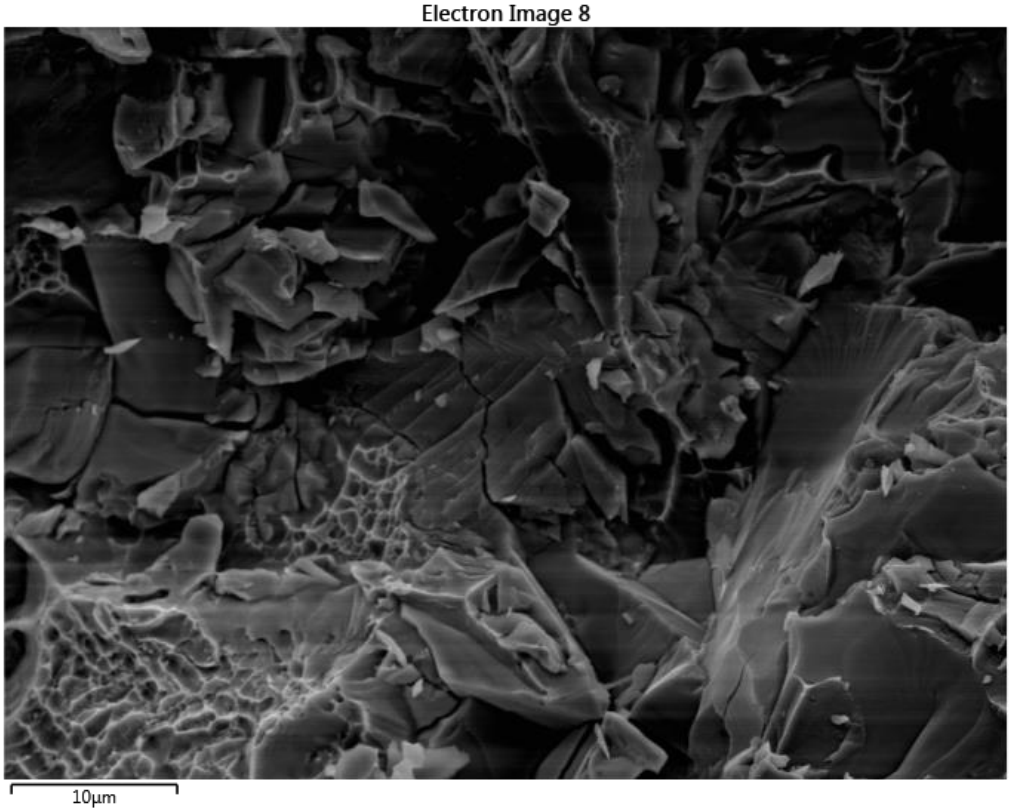

EDS Layered Image 8

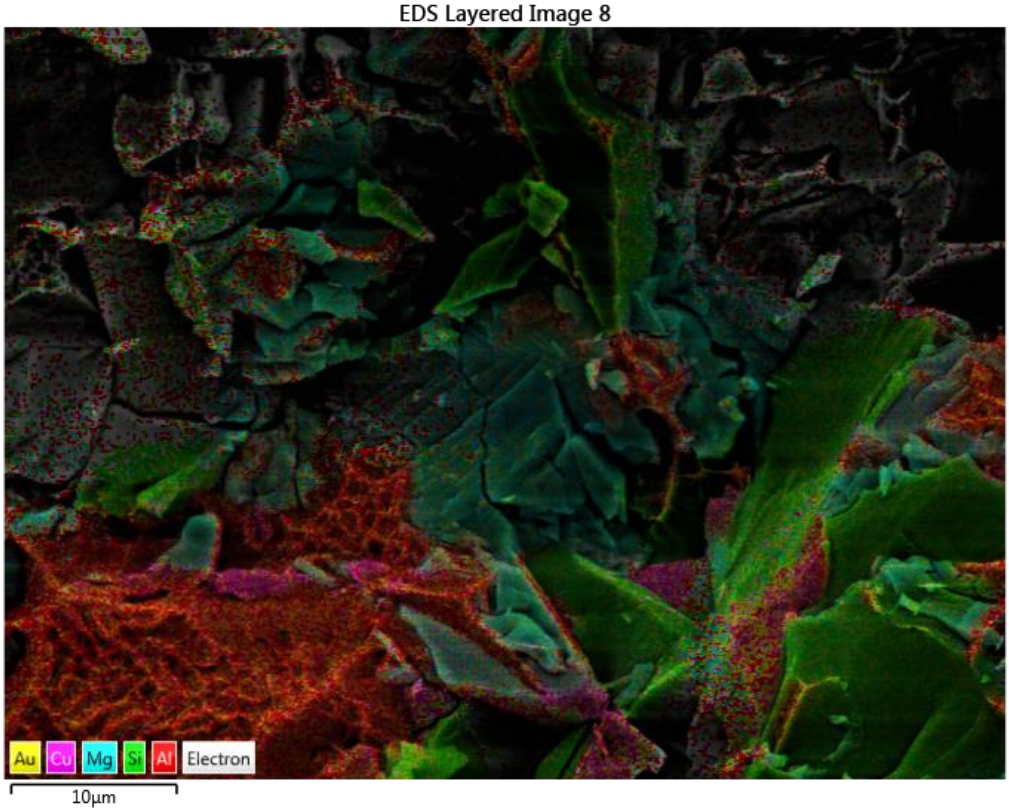

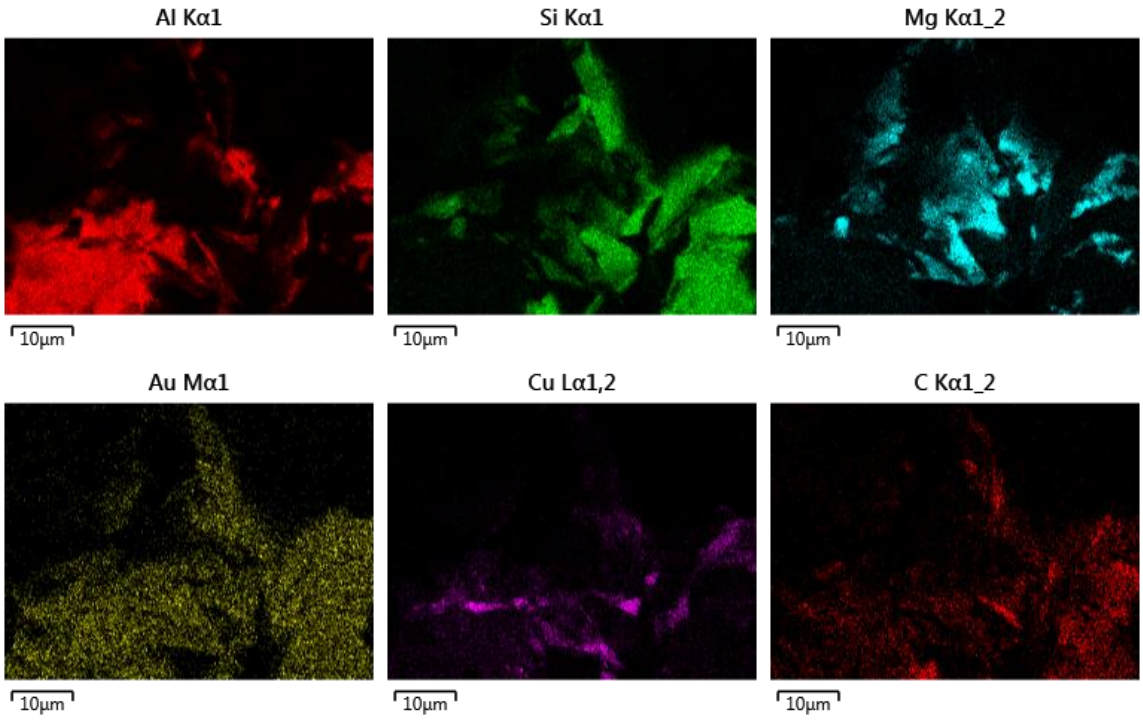
Al Kα1
Si Kα1
Mg Kα1_2
10μm
10μm
10μm
Au Mα1
Cu Lα1,2
C Kα1_2
10μm
10μm
10μm

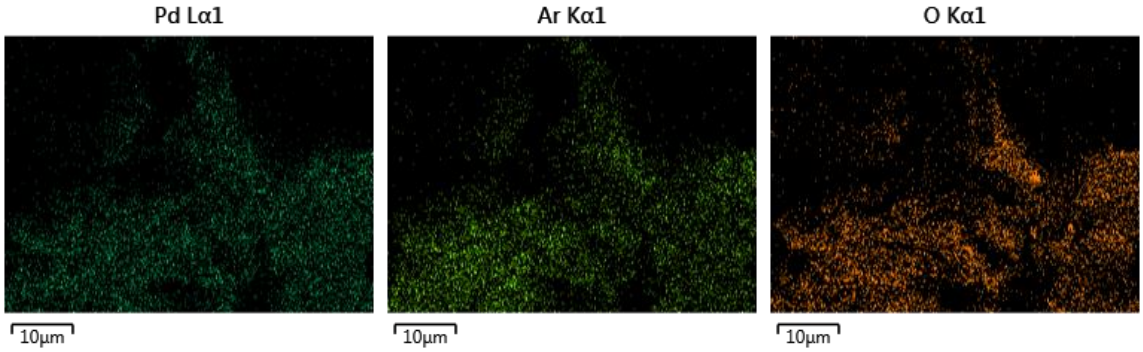
Pd Lα1
Ar Kα1
O Kα1
10μm
10μm
10μm

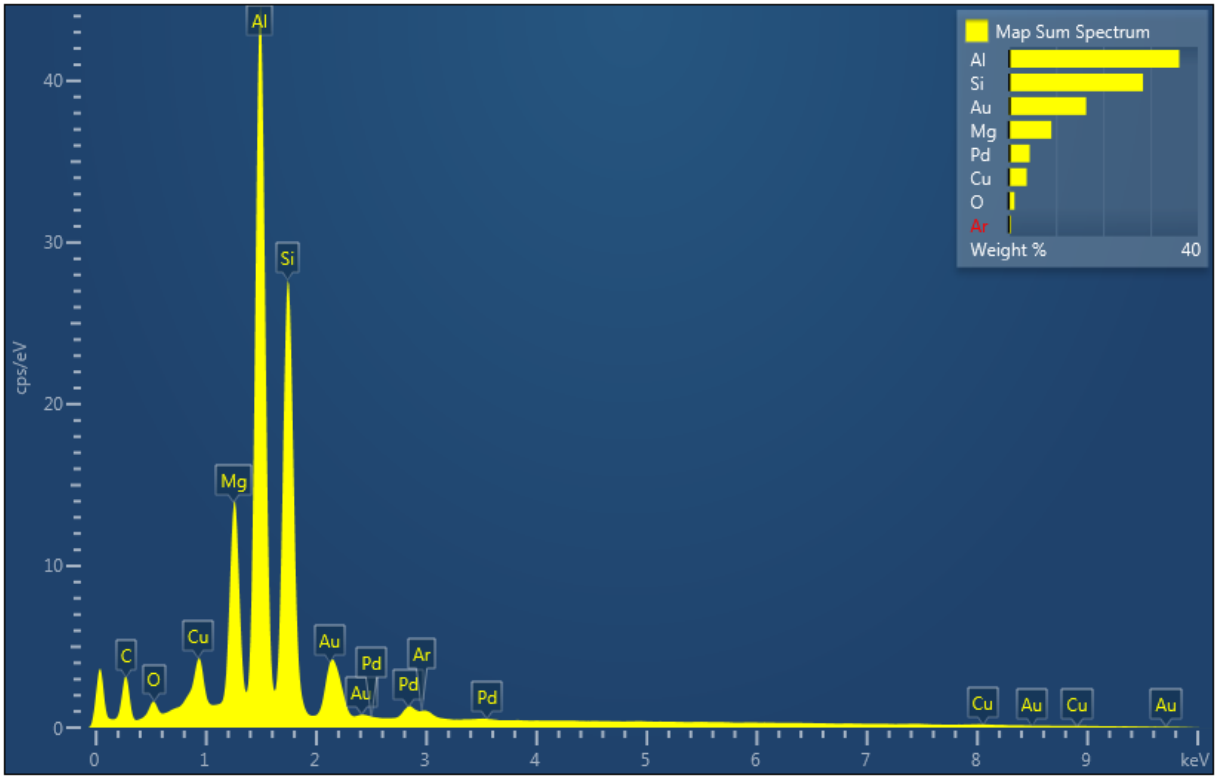
Map Sum Spectrum
Al
Si
Au
Mg
Pd
Cu
O
Ar
Weight %
40
cps/eV
0
10
20
30
40
0
1
2
3
4
5
6
7
8
9
keV
Al
Si
Mg
Cu
C
O
Au
Pd
Ar
Pd
Au
Pd
Cu
Au
Cu
Au

F.6.3 NA-9

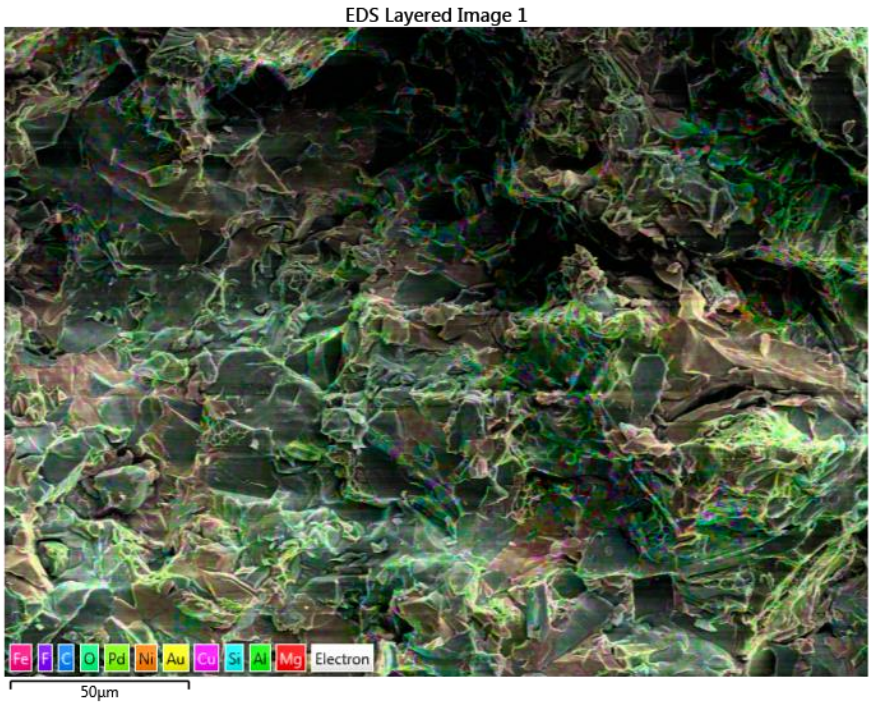

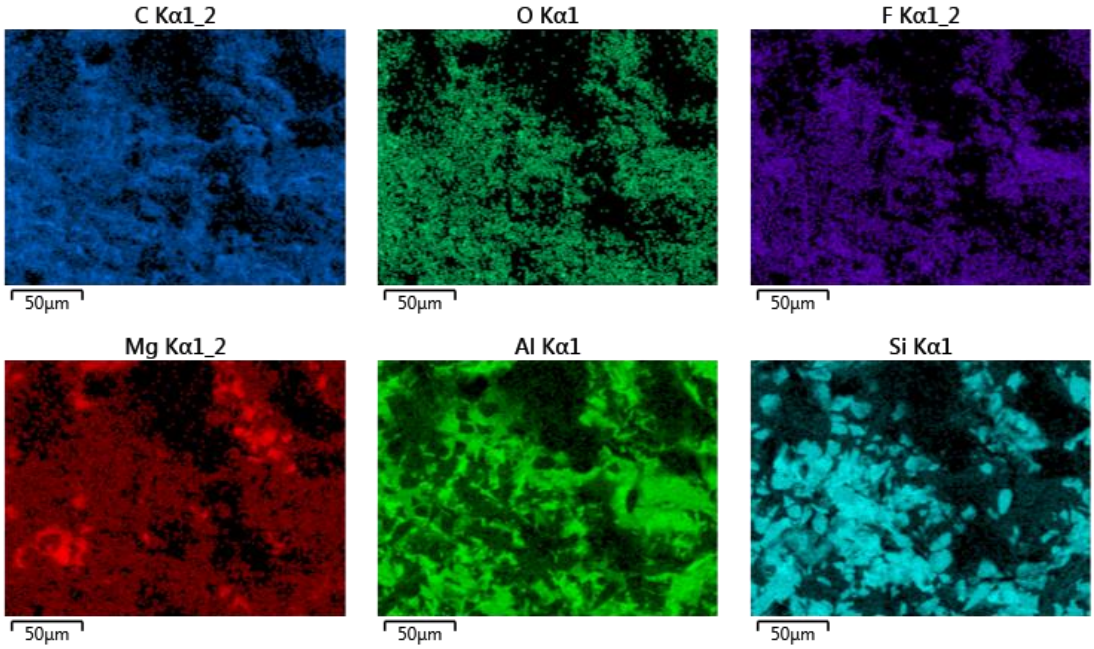
C Kα1_2
O Kα1
F Kα1_2
50μm
50μm
50μm
Mg Kα1_2
Al Kα1
Si Kα1
50μm
50μm
50μm

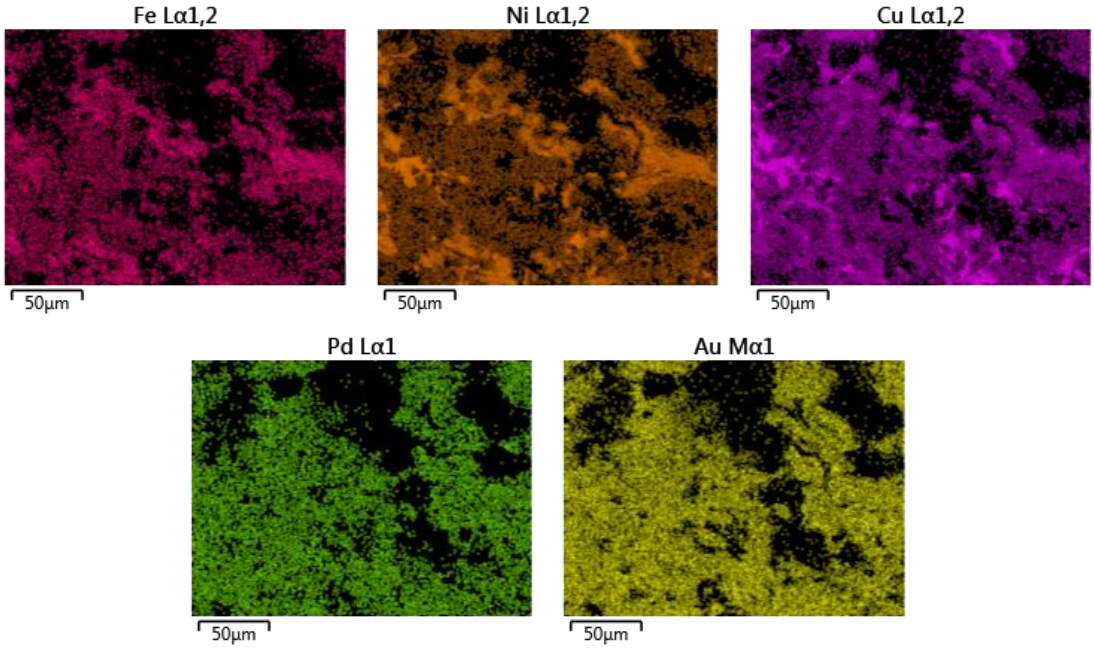
Fe Lα1,2
50µm
Ni Lα1,2
50µm
Cu Lα1,2
50µm
Pd Lα1
50µm
Au Mα1
50µm

EDS Layered Image 2

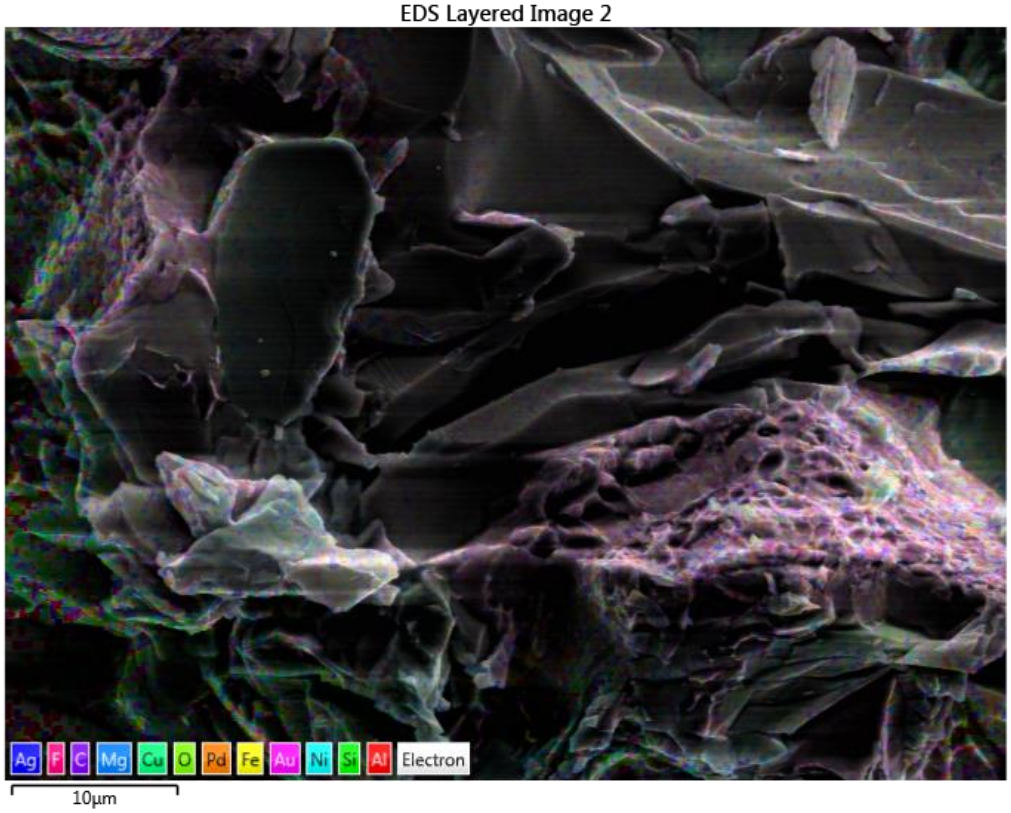

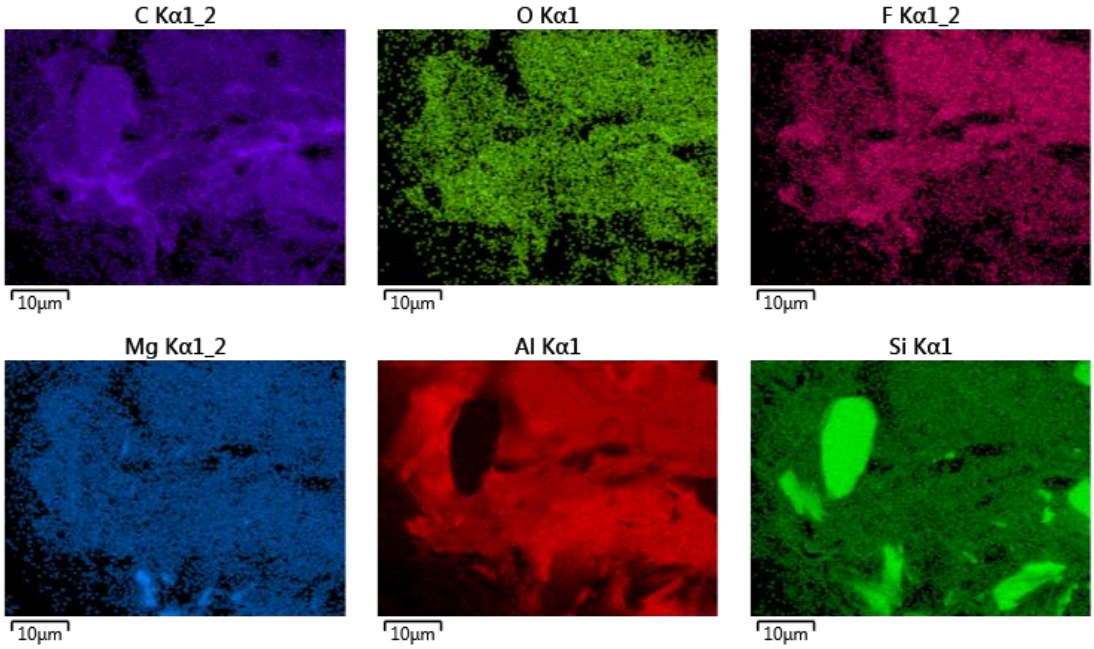
C Kα1_2
O Kα1
F Kα1_2
10μm
10μm
10μm
Mg Kα1_2
Al Kα1
Si Kα1
10μm
10μm
10μm

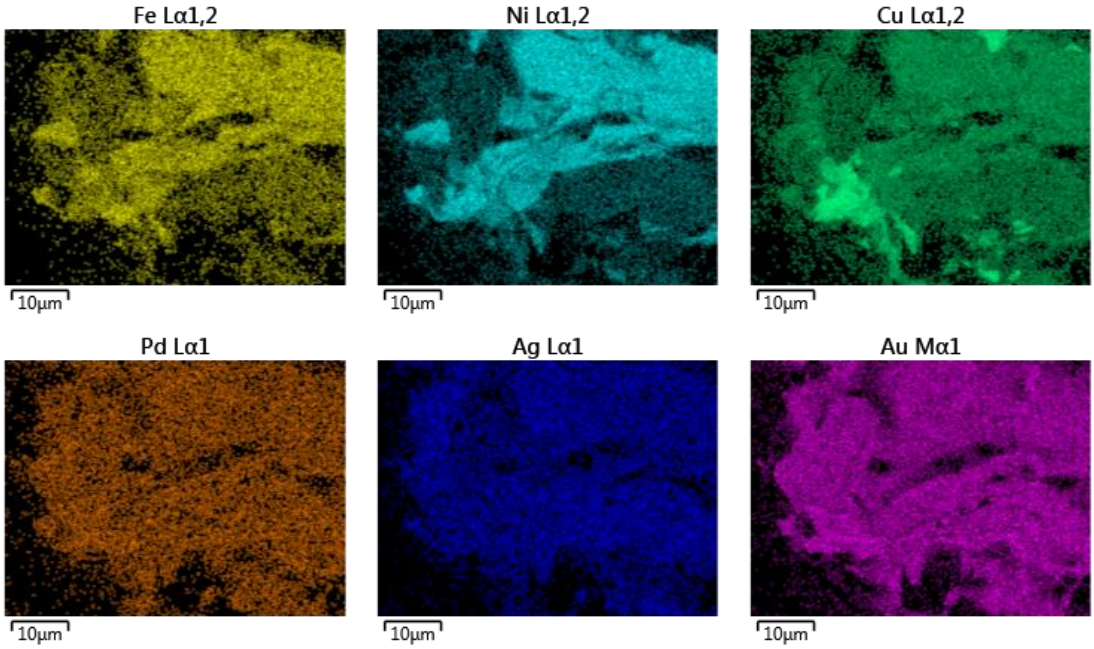
Fe Lα1,2
Ni Lα1,2
Cu Lα1,2
10µm
10µm
10µm
Pd Lα1
Ag Lα1
Au Mα1
10µm
10µm
10µm

EDS Layered Image 3

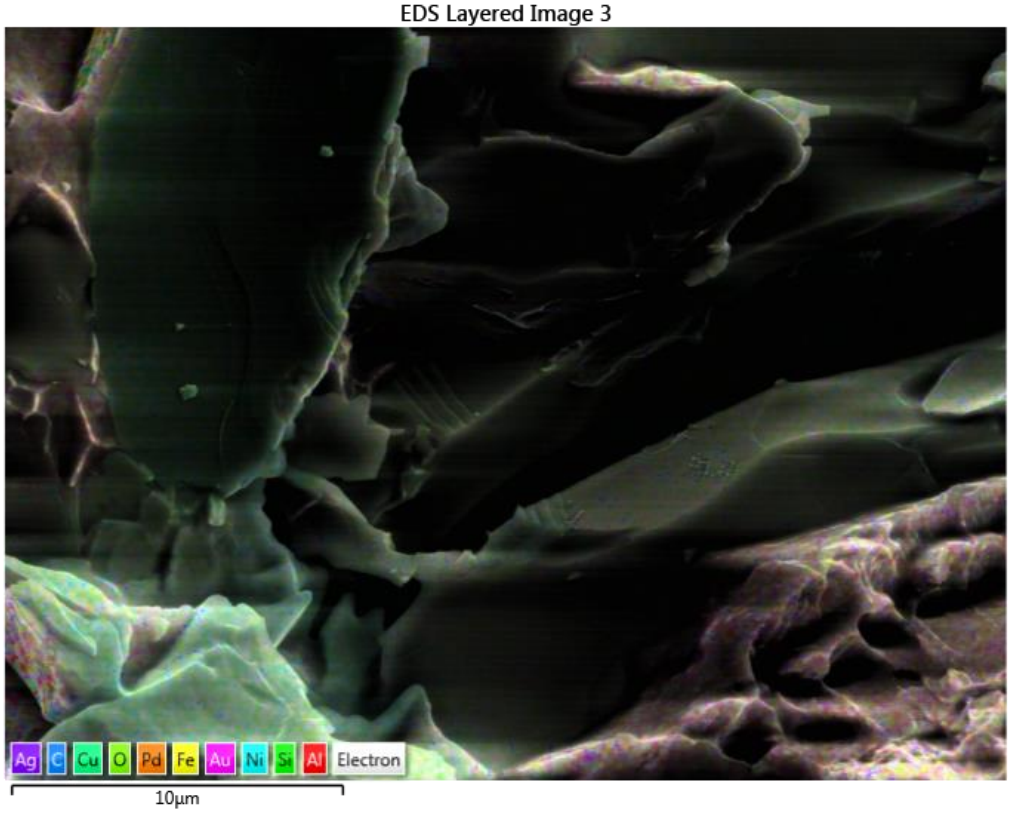

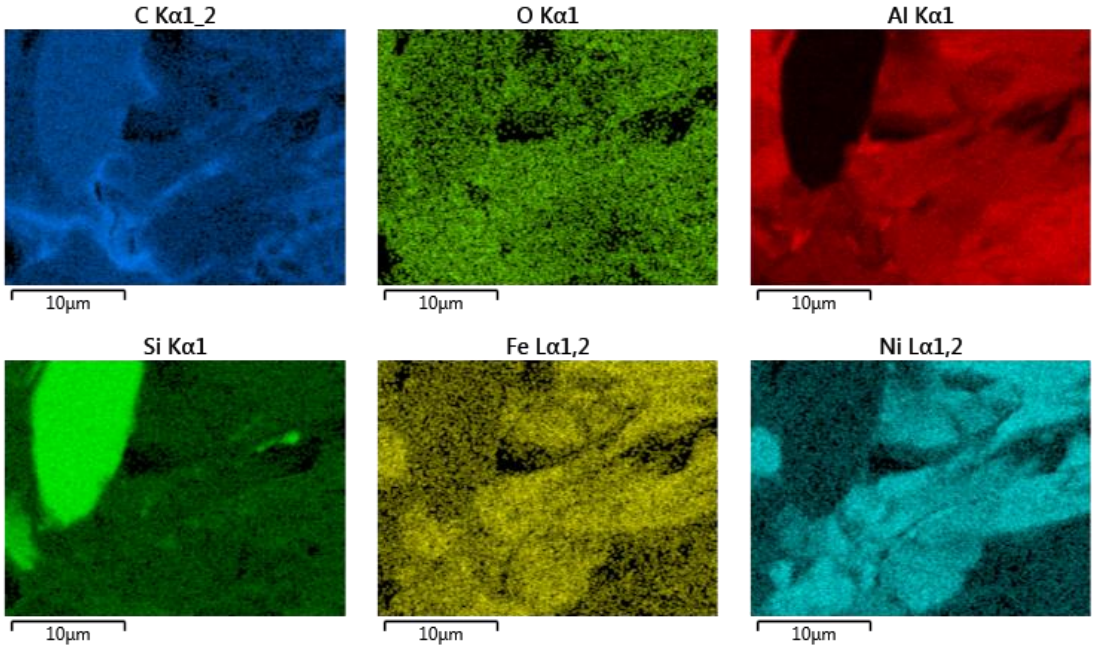
C Kα1_2
O Kα1
Al Kα1
10µm
10µm
10µm
Si Kα1
Fe Lα1,2
Ni Lα1,2
10µm
10µm
10µm

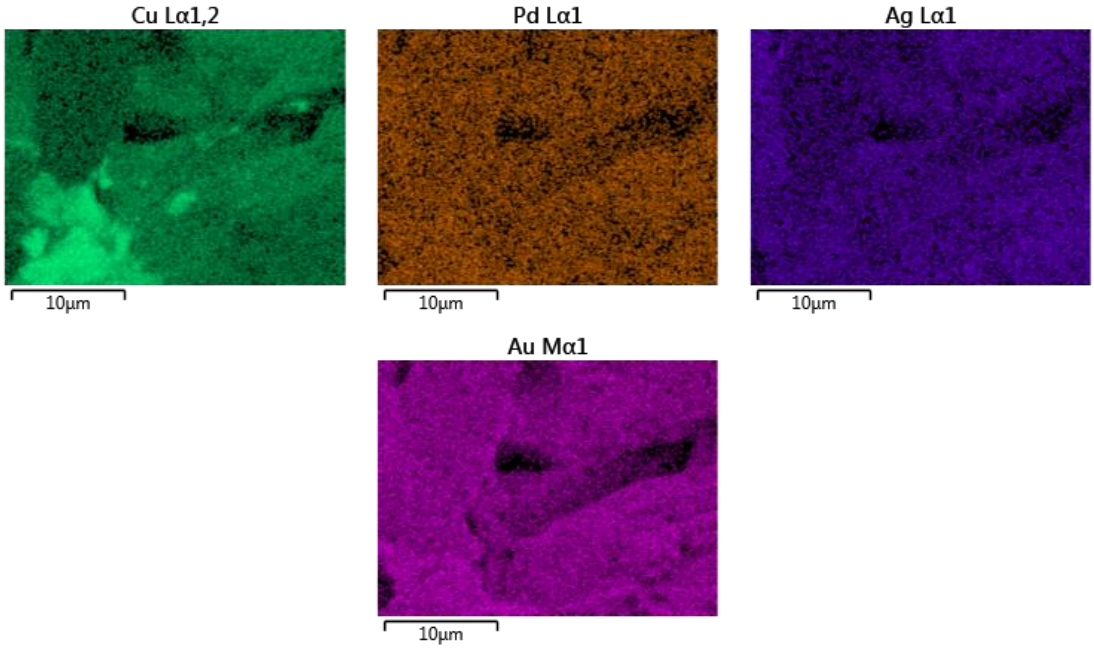
Cu Lα1,2
10μm
Pd Lα1
10μm
Ag Lα1
10μm
Au Mα1
10μm

EDS Layered Image 4

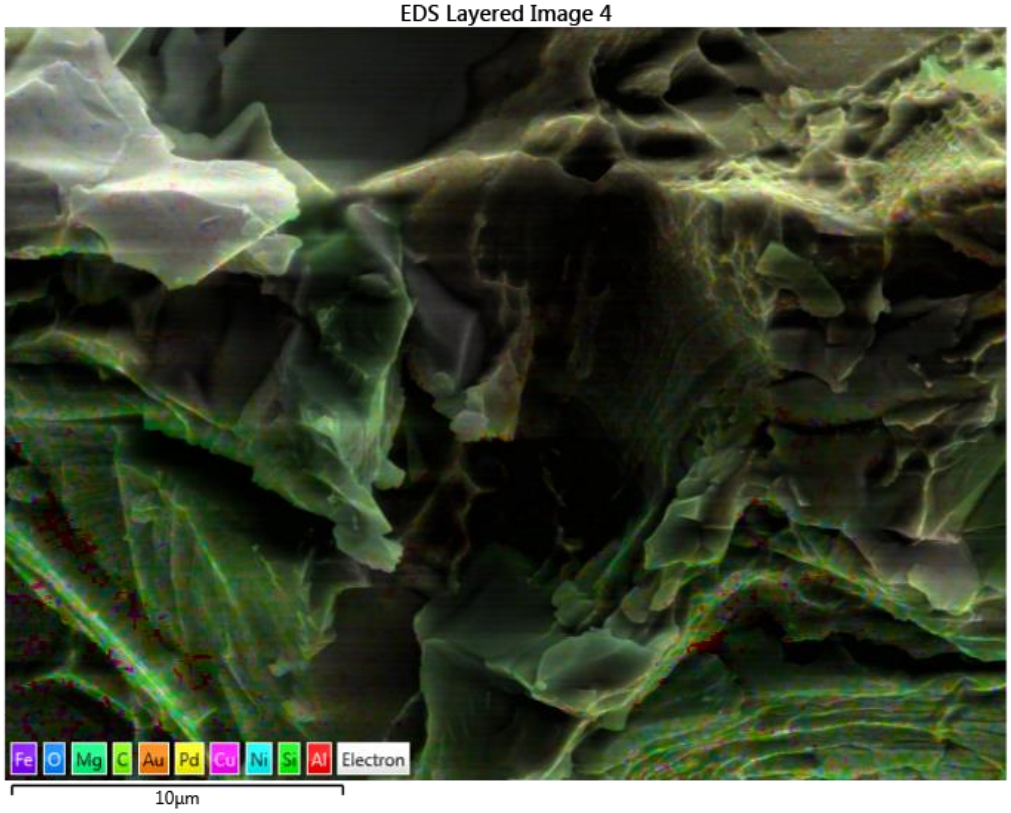

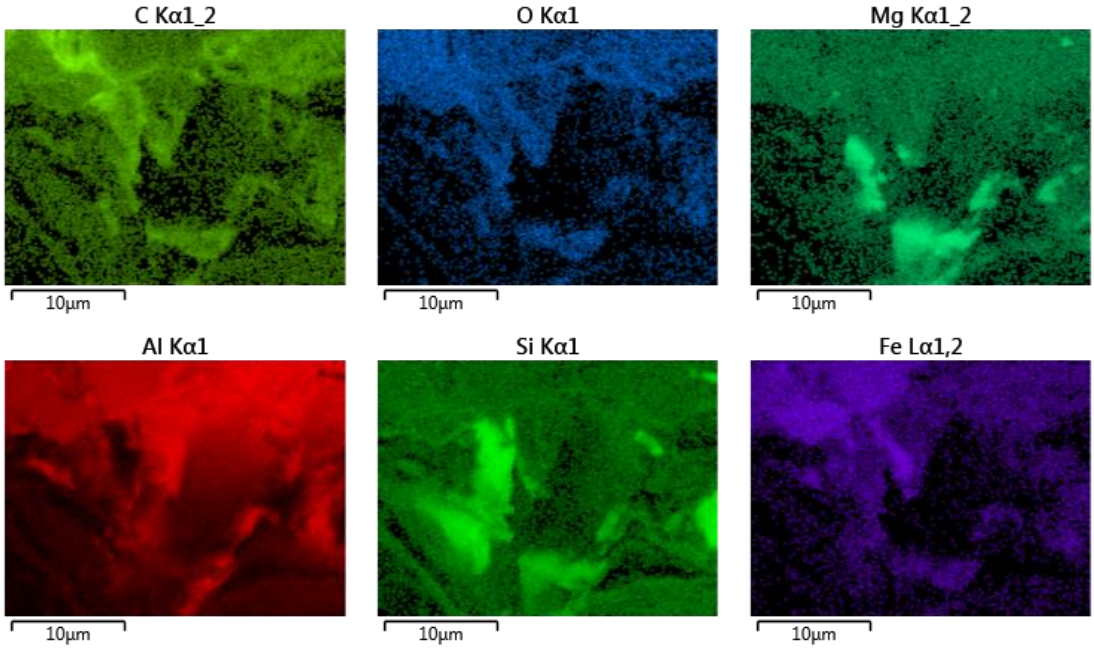
C Kα1_2
O Kα1
Mg Kα1_2
10μm
10μm
10μm
Al Kα1
Si Kα1
Fe Lα1,2
10μm
10μm
10μm

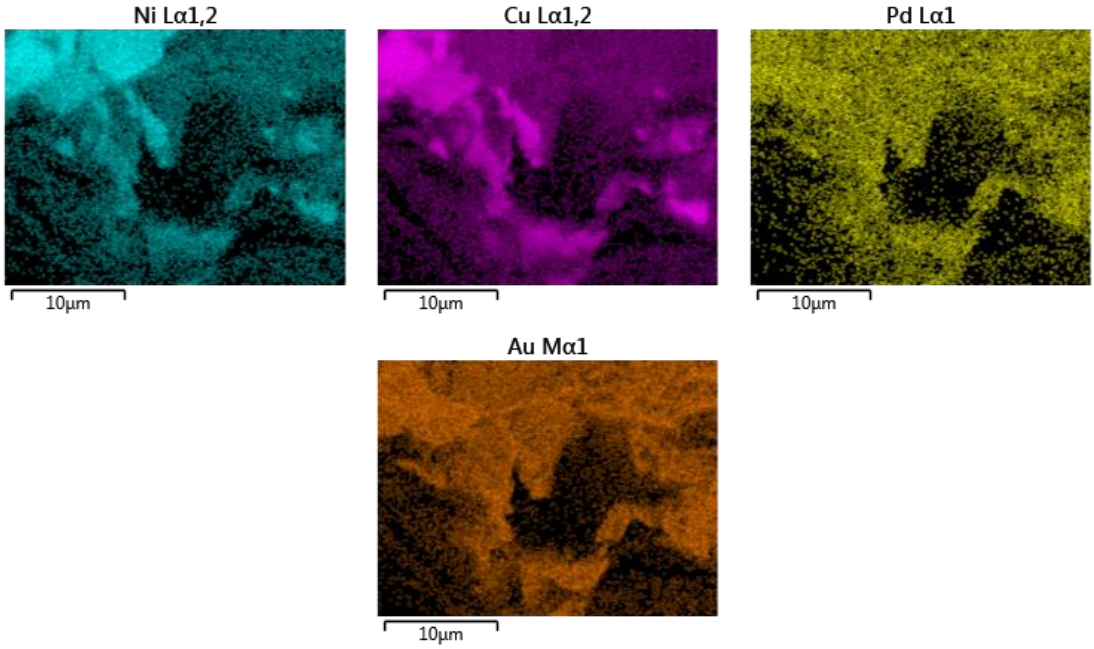
Ni Lα1,2
10μm
Cu Lα1,2
10μm
Pd Lα1
10μm
Au Mα1
10μm

EDS Layered Image 5

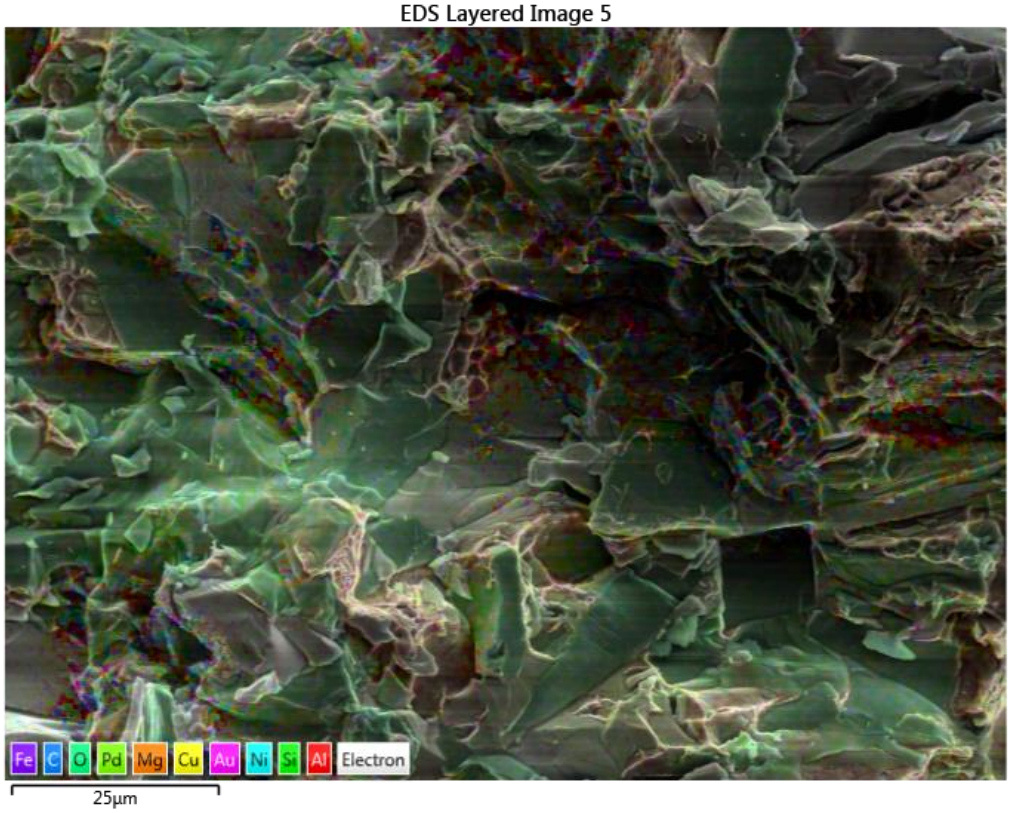

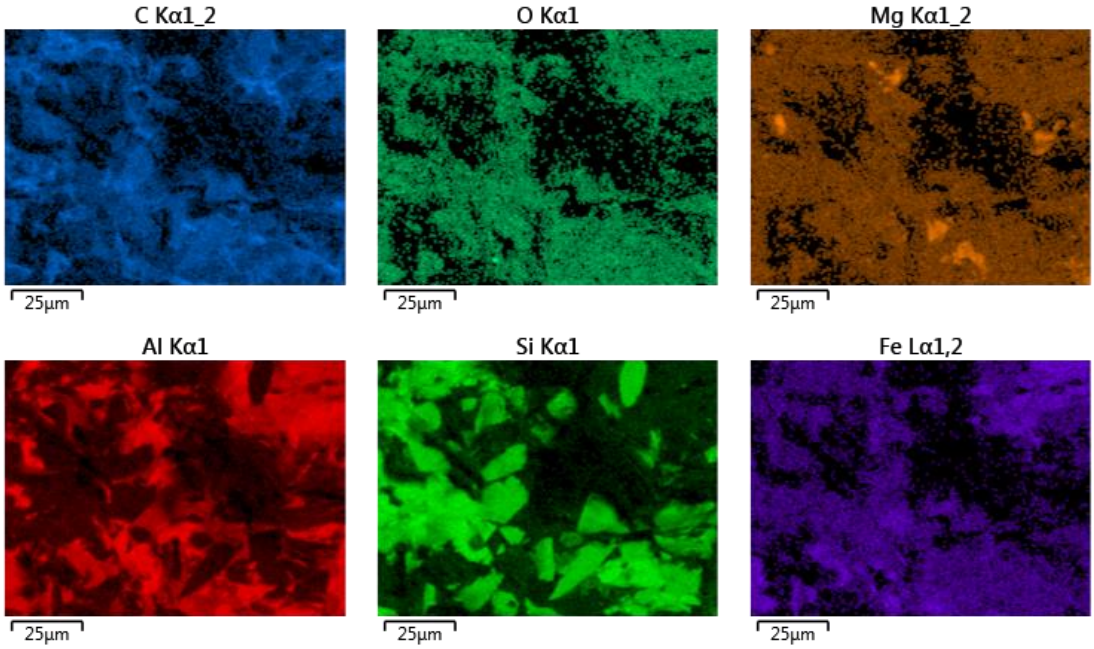
C Kα1_2
O Kα1
Mg Kα1_2
25µm
25µm
25µm
Al Kα1
Si Kα1
Fe Lα1,2
25µm
25µm
25µm

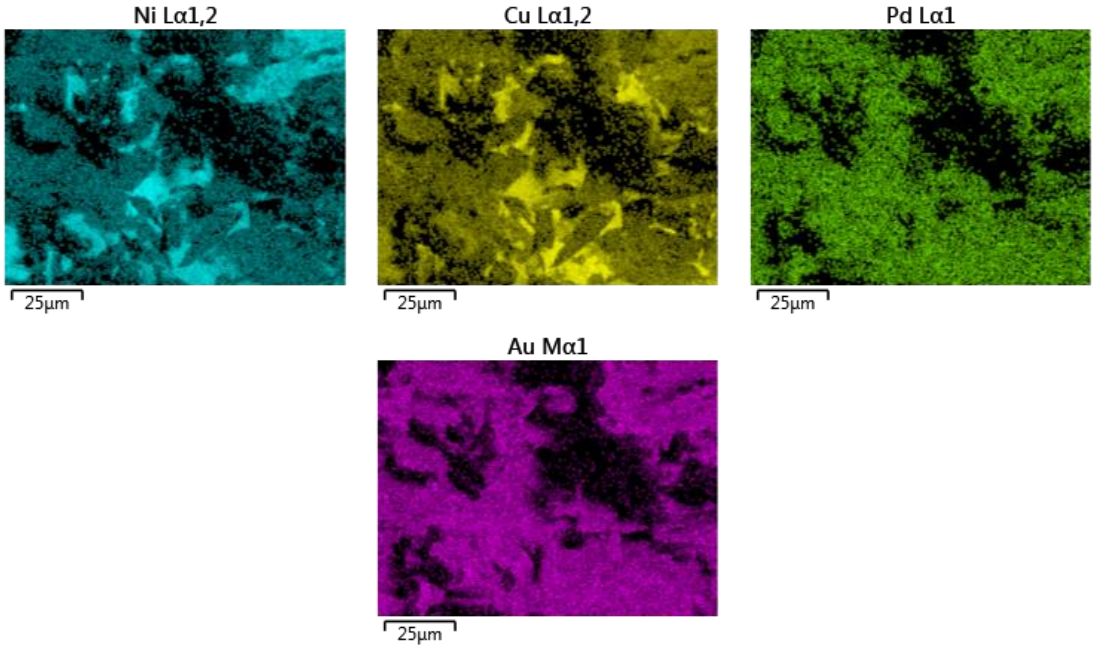
Ni Lα1,2
25μm
Cu Lα1,2
25μm
Pd Lα1
25μm
Au Mα1
25μm

F.6.4 NA-24

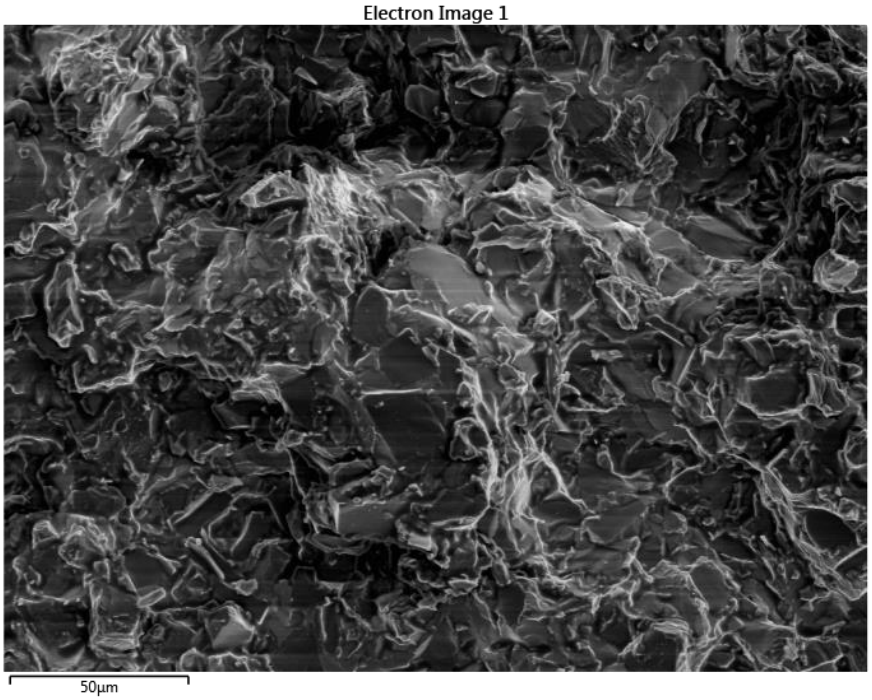

EDS Layered Image 1

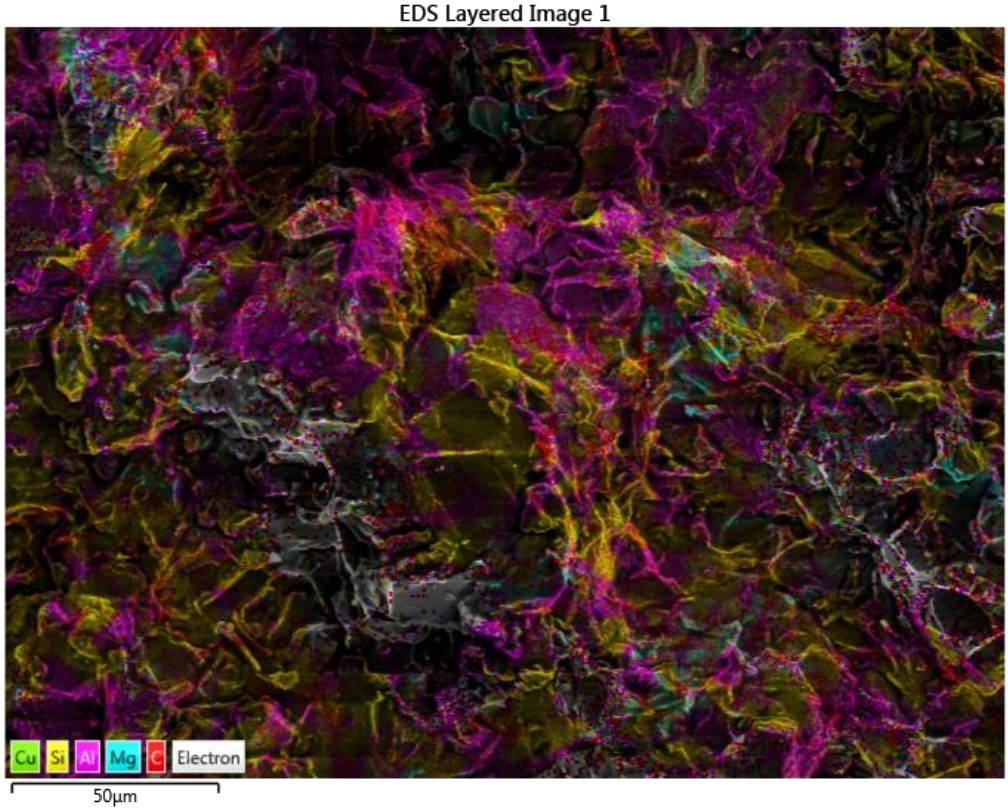

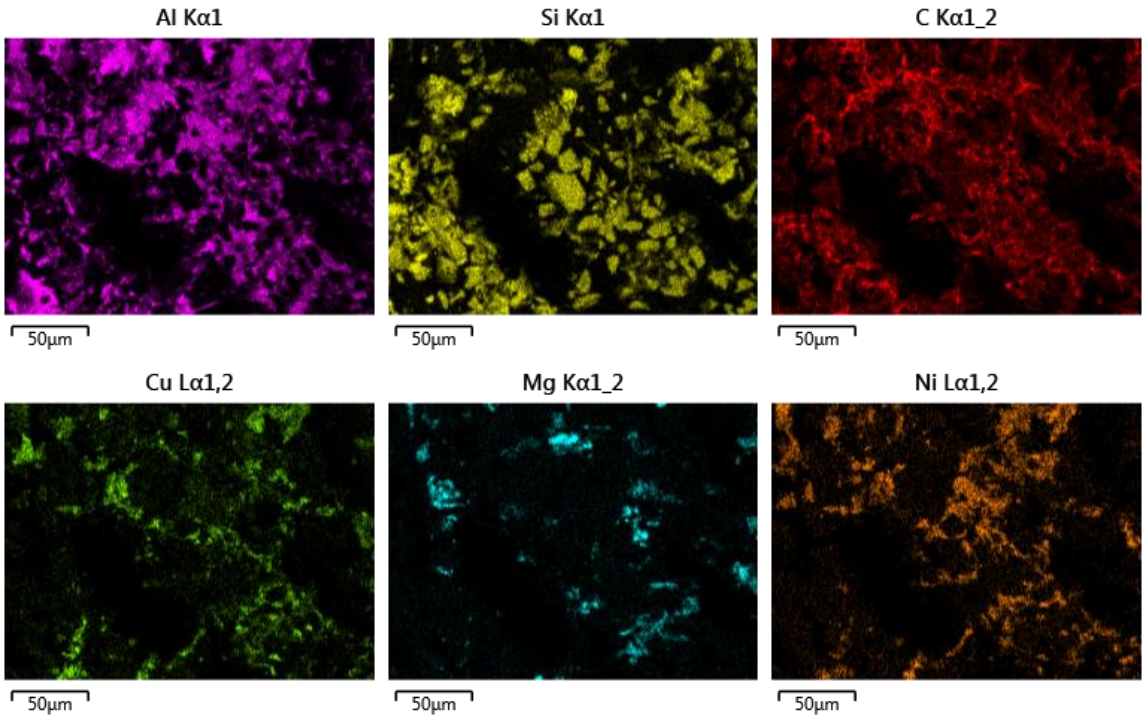
Al Kα1
Si Kα1
C Kα1_2
50µm
50µm
50µm
Cu Lα1,2
Mg Kα1_2
Ni Lα1,2
50µm
50µm
50µm

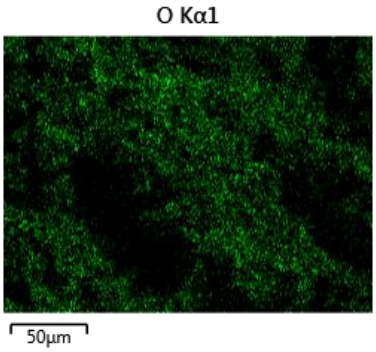
O Kα1
50µm

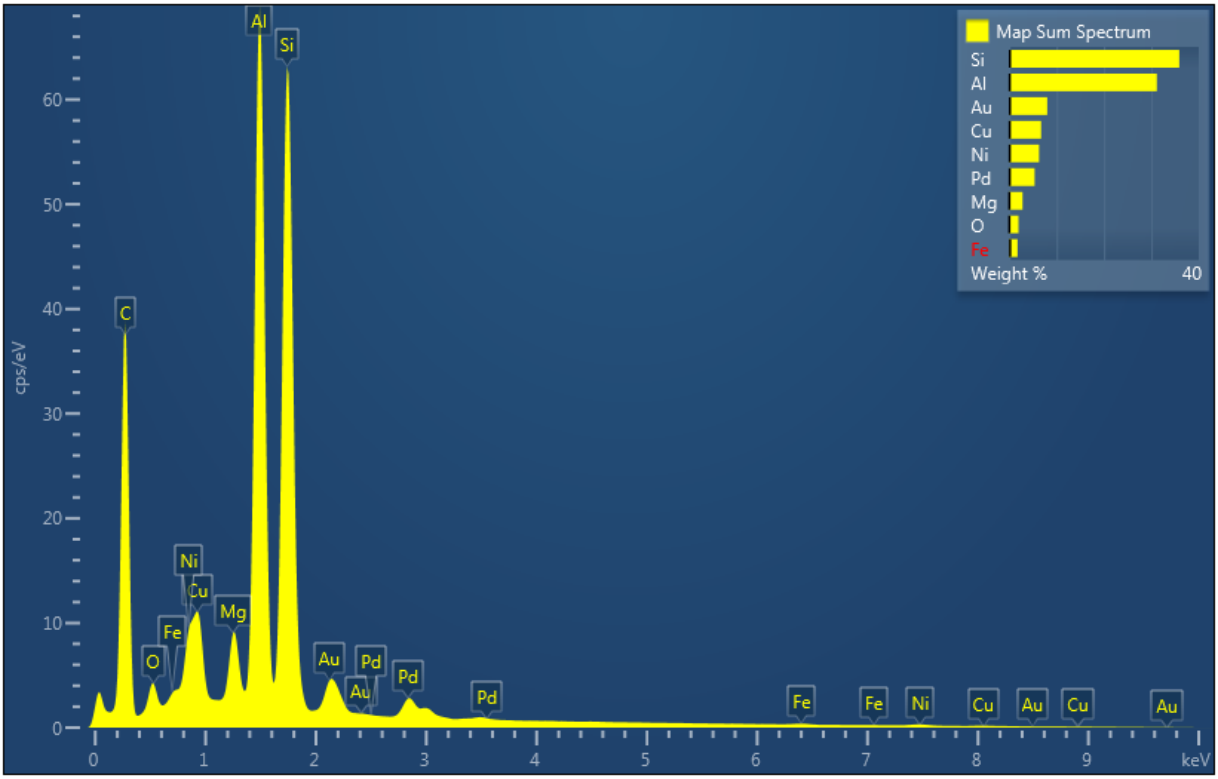
Map Sum Spectrum
Si
Al
Au
Cu
Ni
Pd
Mg
O
Fe
Weight %
40
cps/eV
0
10
20
30
40
50
60
C
O
Fe
Ni
Cu
Mg
Al
Si
Au
Au
Pd
Pd
Pd
Fe
Fe
Ni
Cu
Au
Cu
Au
0
1
2
3
4
5
6
7
8
9
keV

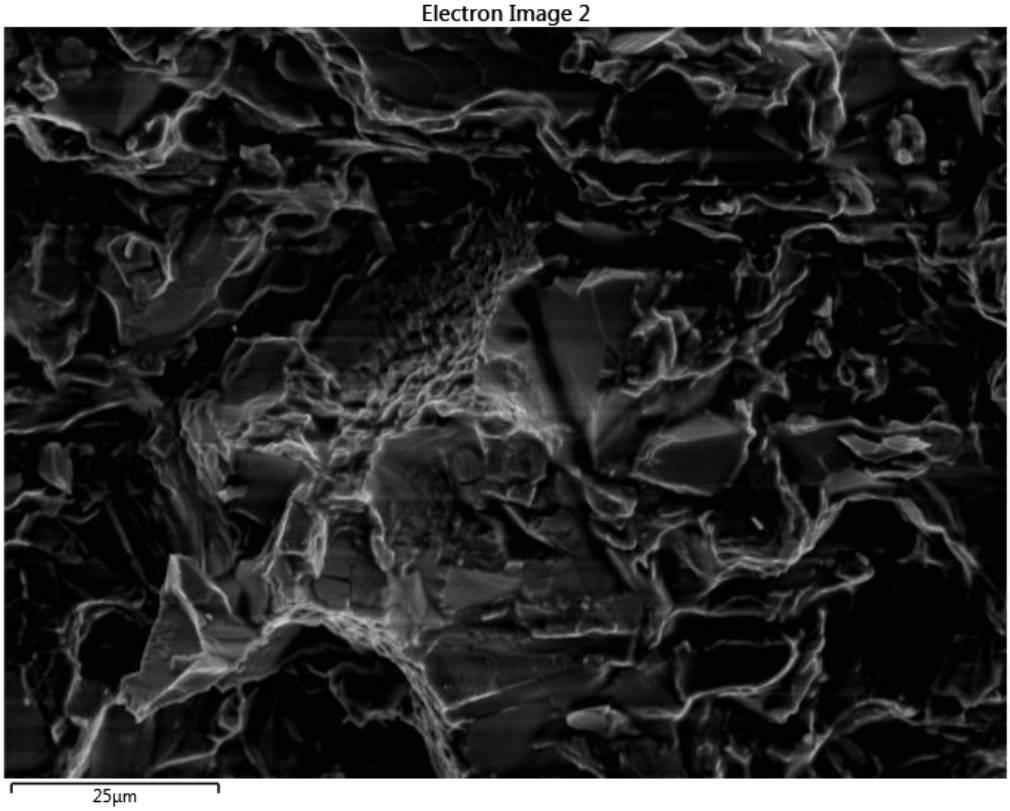
Electron Image 2
25µm

EDS Layered Image 2

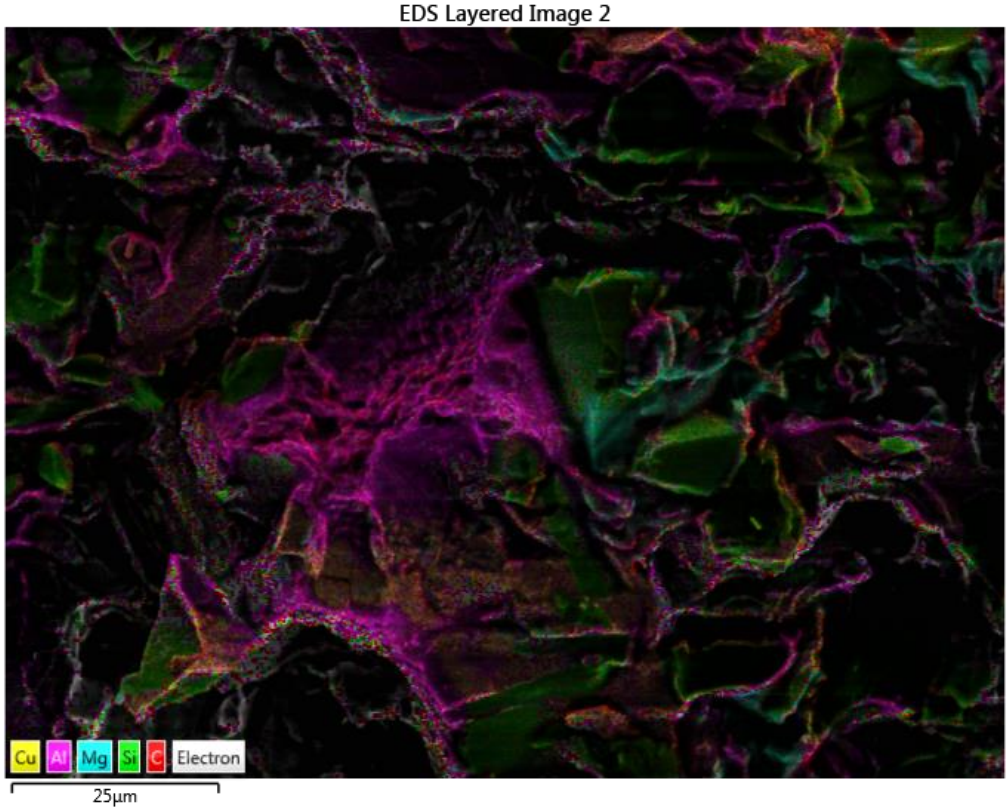

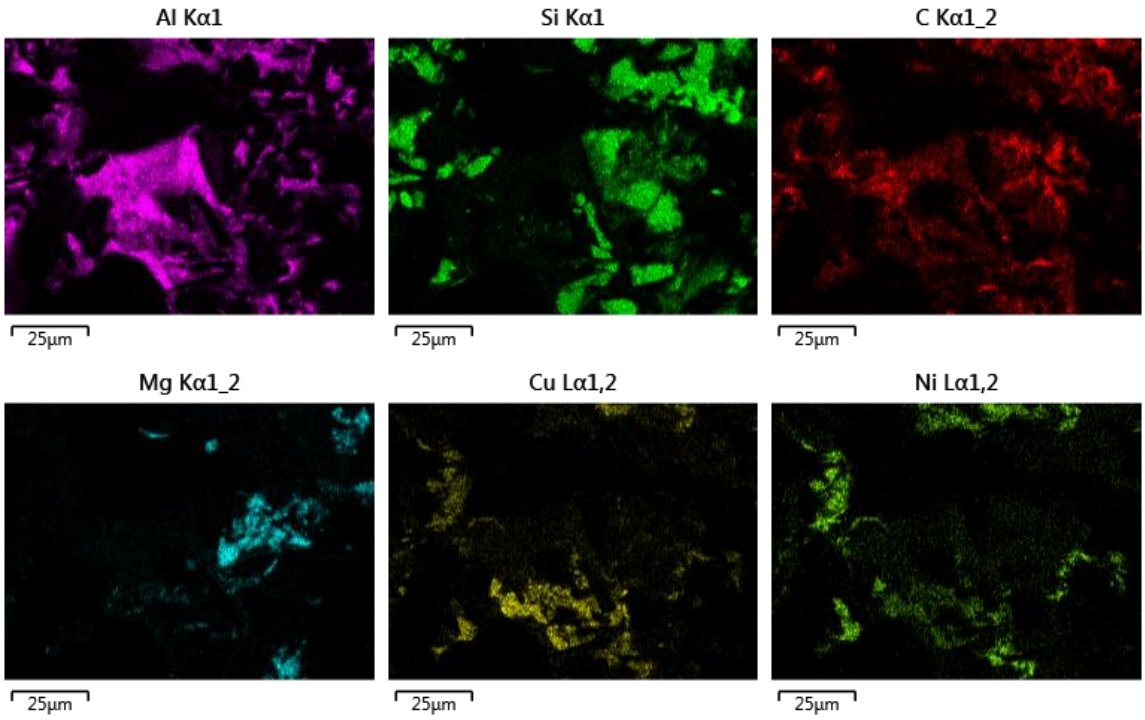
Al Kα1
Si Kα1
C Kα1_2
25µm
25µm
25µm
Mg Kα1_2
Cu Lα1,2
Ni Lα1,2
25µm
25µm
25µm

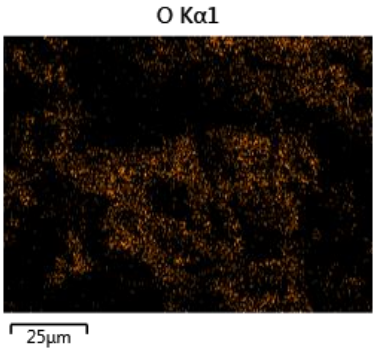
O Kα1
25µm

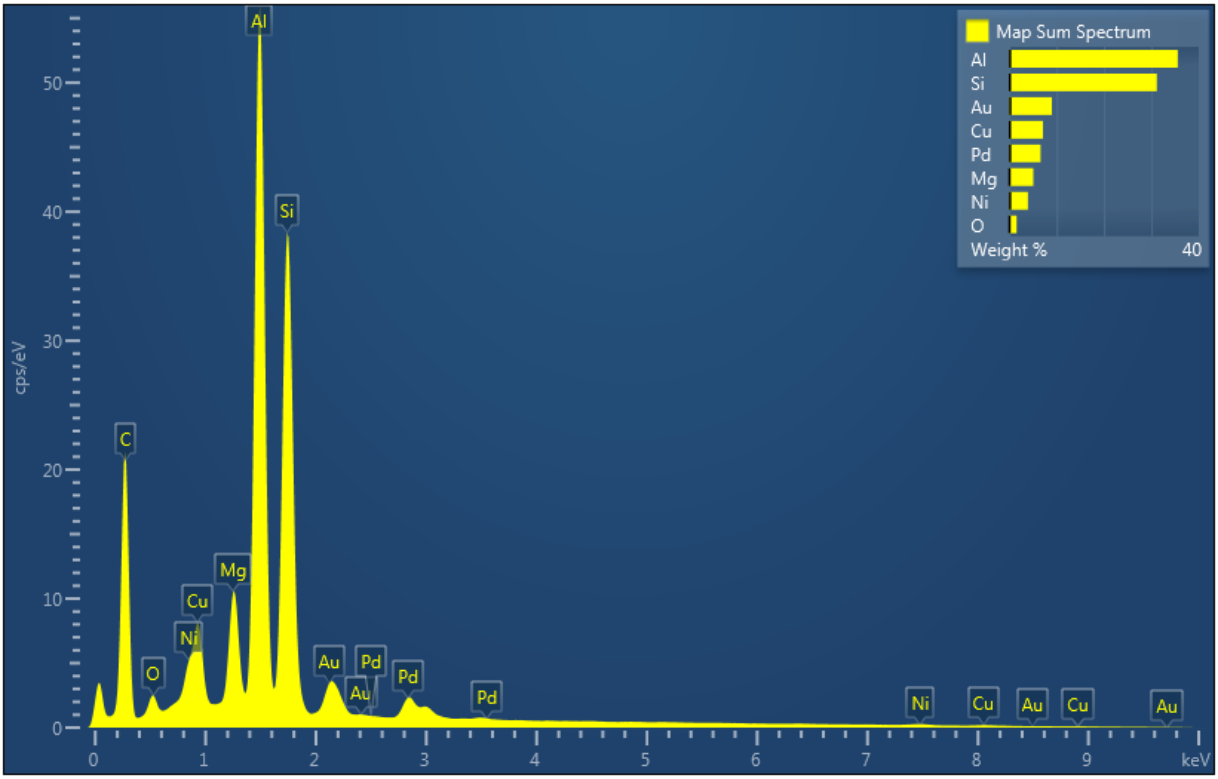
Map Sum Spectrum
Al
Si
Au
Cu
Pd
Mg
Ni
O
Weight %
40
cps/eV
0
10
20
30
40
50
C
O
Ni
Cu
Mg
Al
Si
Au
Au
Pd
Pd
Pd
Ni
Cu
Au
Cu
Au
0
1
2
3
4
5
6
7
8
9
keV

Electron Image 3

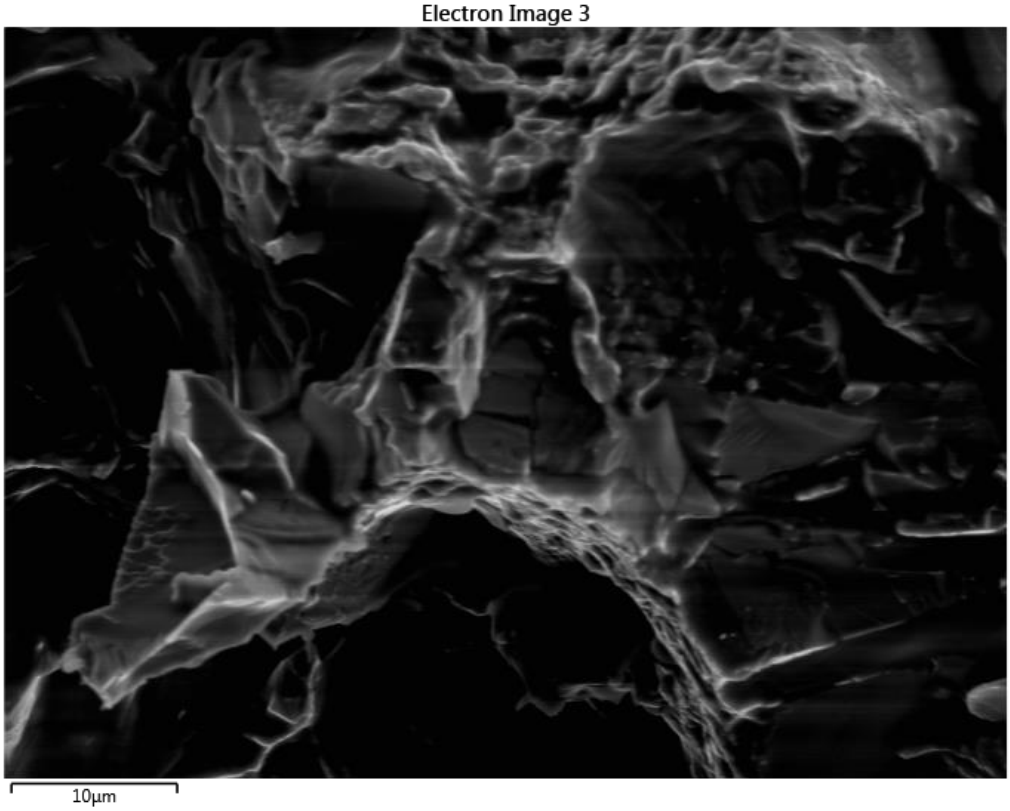

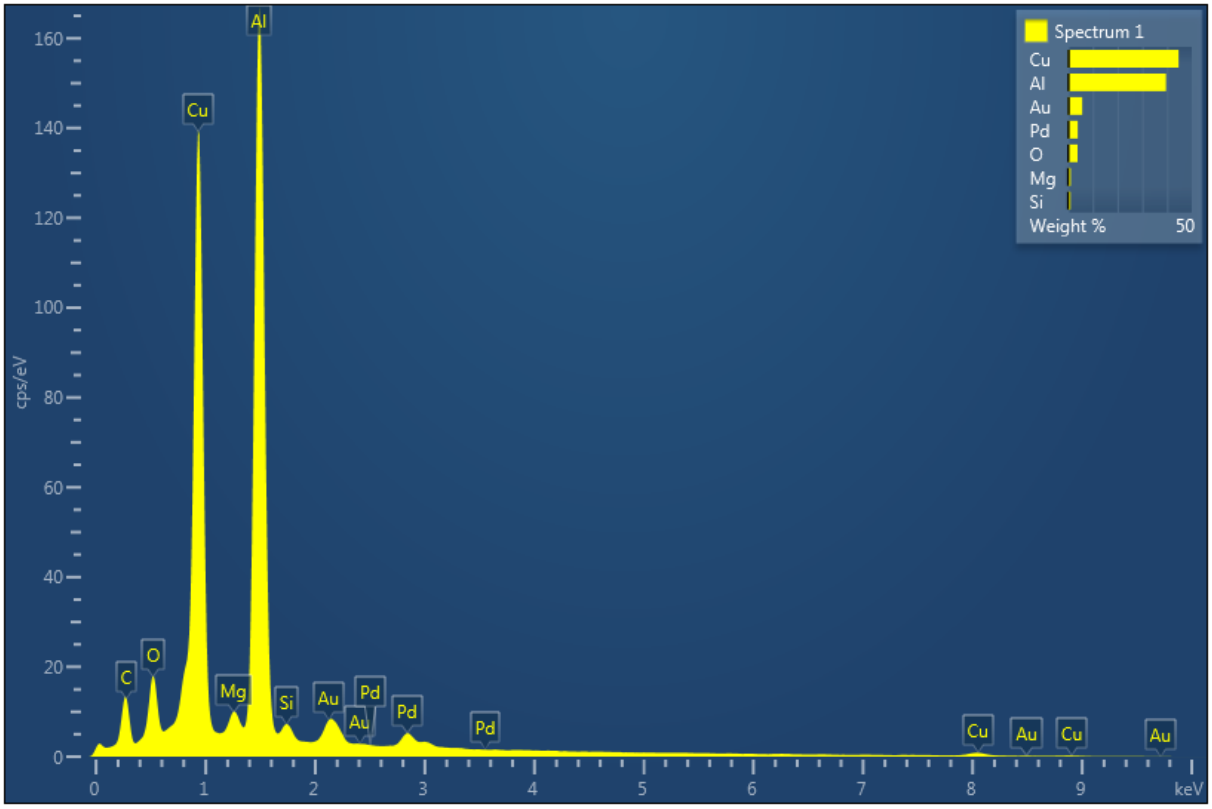
Spectrum 1
Cu
Al
Au
Pd
O
Mg
Si
Weight %
50
cps/eV
160
140
120
100
80
60
40
20
0
0
1
2
3
4
5
6
7
8
9
keV
C
O
Cu
Mg
Al
Si
Au
Au
Pd
Pd
Pd
Cu
Au
Cu
Au

Element	Line Type	Apparent Concentration	k Ratio	Wt%	Wt% Sigma	Standard Label	Factory Standard	Standard Calibration Date
O	K series	2.28	0.00766	3.87	0.11	SiO2	Yes	
Mg	K series	0.41	0.00272	1.13	0.07	MgO	Yes	
Al	K series	14.95	0.10741	39.55	0.26	Al2O3	Yes	
Si	K series	0.35	0.00274	1.04	0.07	SiO2	Yes	
Cu	L series	13.34	0.13335	44.67	0.29	Cu	Yes	
Pd	L series	1.05	0.01053	3.97	0.25	Pd	Yes	
Au	M series	1.30	0.01297	5.77	0.32	Au	Yes	
Total:				100.00				

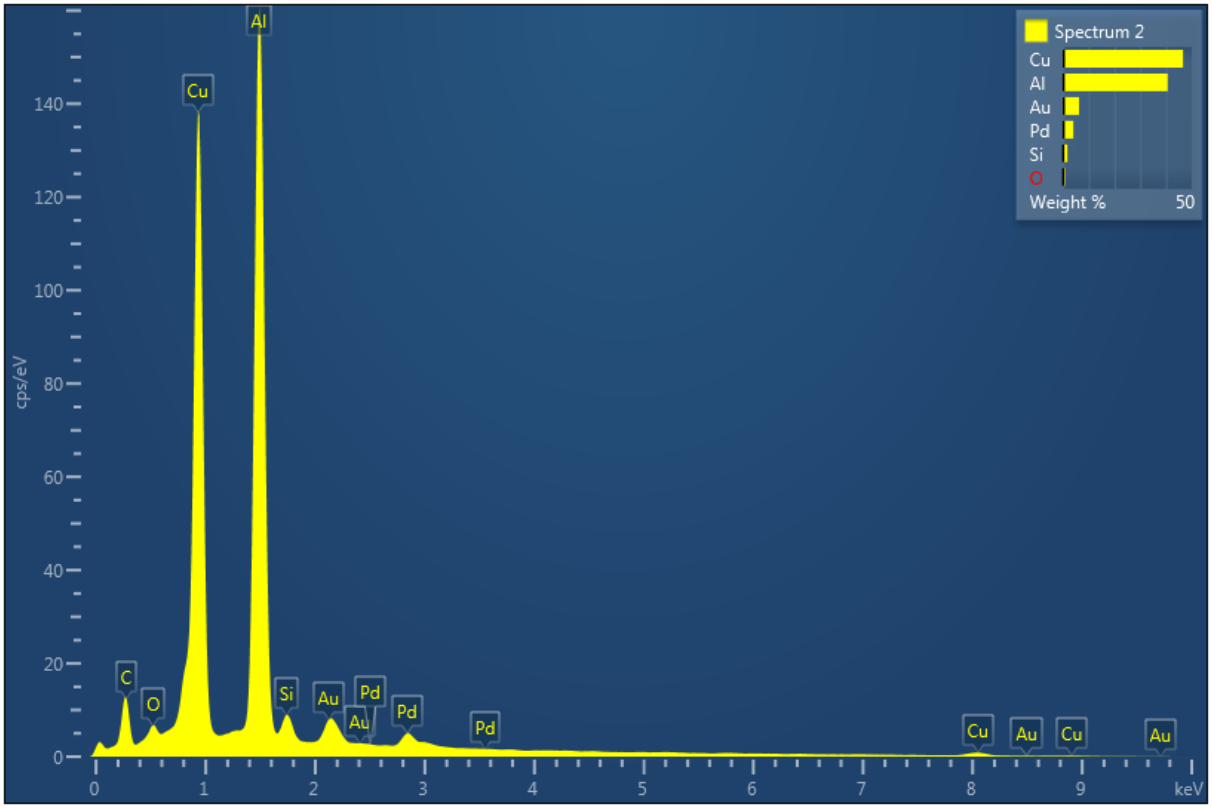
Spectrum 2
Cu
Al
Au
Pd
Si
O
Weight %
50
cps/eV
keV
C
O
Cu
Al
Si
Au
Au
Pd
Pd
Pd
Cu
Au
Cu
Au

Element	Line Type	Apparent Concentration	k Ratio	Wt%	Wt% Sigma	Standard Label	Factory Standard	Standard Calibration Date
O	K series	0.44	0.00150	0.82	0.09	SiO2	Yes	
Al	K series	14.36	0.10314	40.65	0.26	Al2O3	Yes	
Si	K series	0.53	0.00422	1.72	0.08	SiO2	Yes	
Cu	L series	13.21	0.13210	46.63	0.29	Cu	Yes	
Pd	L series	0.98	0.00981	3.97	0.26	Pd	Yes	
Au	M series	1.30	0.01298	6.21	0.33	Au	Yes	
Total:				100.00				

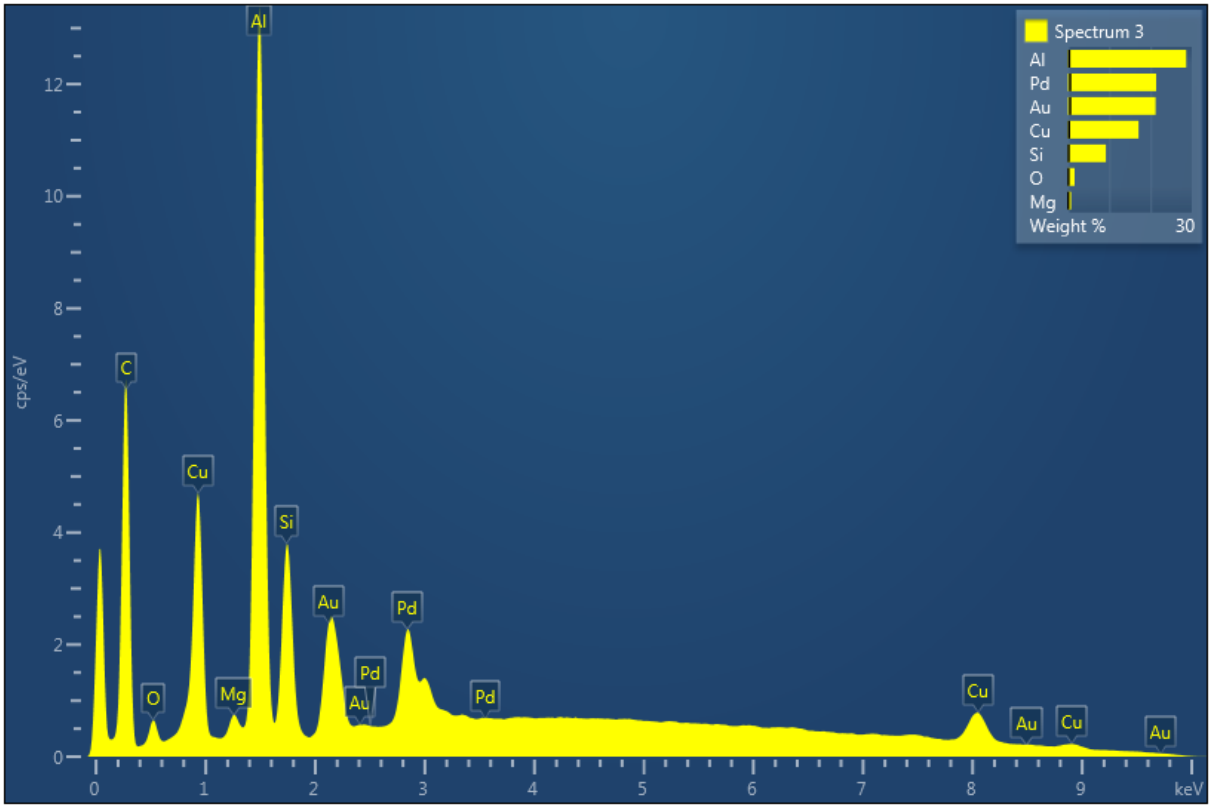
Spectrum 3
Al
Pd
Au
Cu
Si
O
Mg
Weight %
30
cps/eV
keV
C
O
Mg
Al
Si
Cu
Au
Pd
Pd
Au
Pd
Cu
Au
Cu
Au

Element	Line Type	Apparent Concentration	k Ratio	Wt%	Wt% Sigma	Standard Label	Factory Standard	Standard Calibration Date
O	K series	0.07	0.00024	1.64	0.12	SiO2	Yes	
Mg	K series	0.03	0.00021	0.78	0.07	MgO	Yes	
Al	K series	1.19	0.00856	28.66	0.32	Al2O3	Yes	
Si	K series	0.34	0.00273	9.21	0.16	SiO2	Yes	
Cu	L series	0.42	0.00415	17.09	0.28	Cu	Yes	
Pd	L series	0.56	0.00556	21.37	0.53	Pd	Yes	
Au	M series	0.50	0.00496	21.25	0.51	Au	Yes	
Total:				100.00				

F.6.5 NA-21

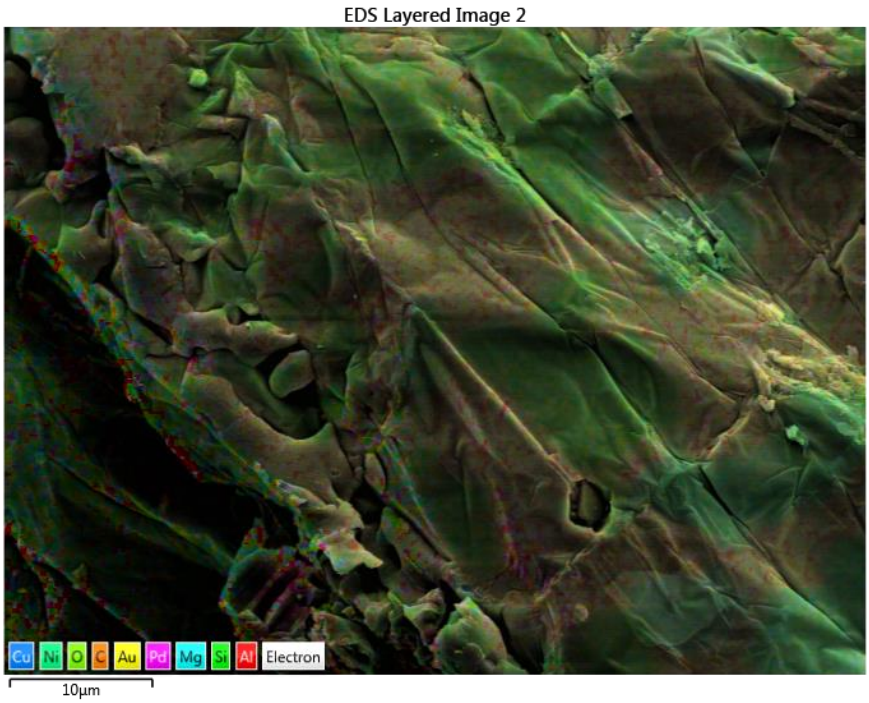

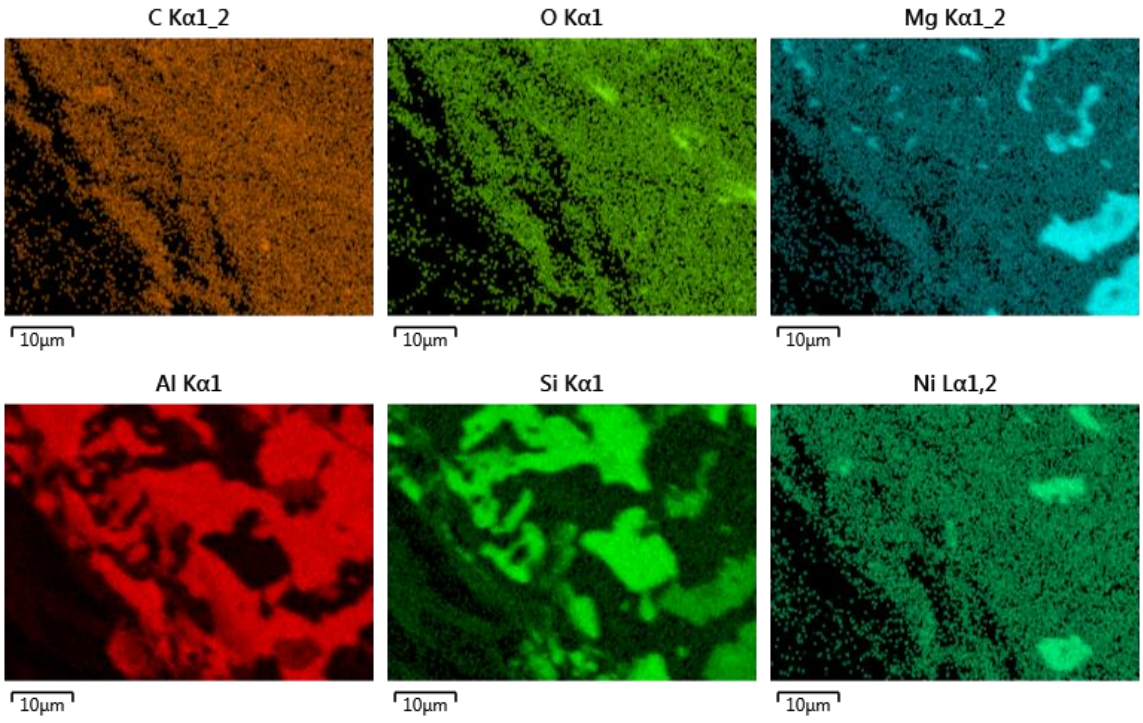
C Kα1_2
O Kα1
Mg Kα1_2
10µm
10µm
10µm
Al Kα1
Si Kα1
Ni Lα1,2
10µm
10µm
10µm

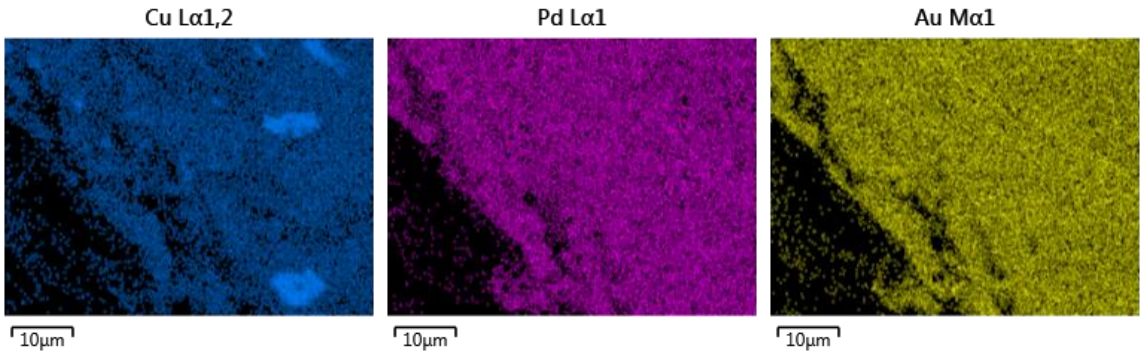
Cu Lα1,2
Pd Lα1
Au Mα1
10μm
10μm
10μm

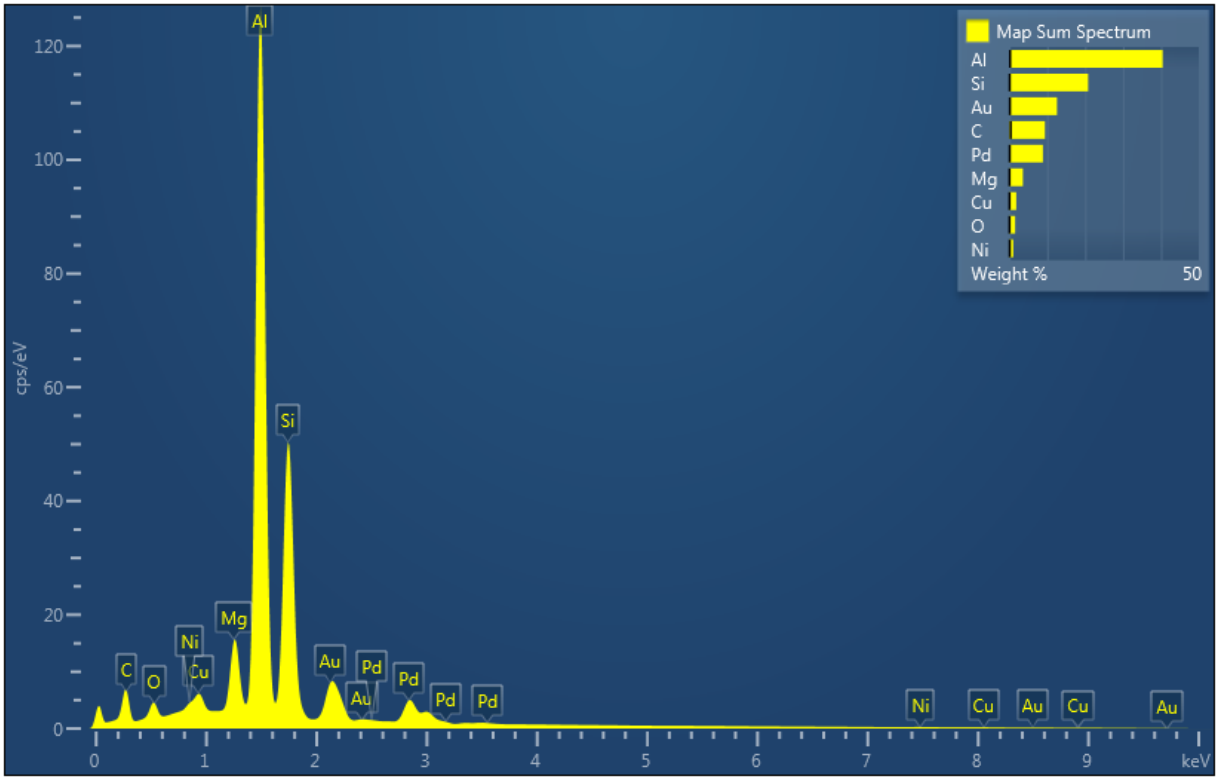
Map Sum Spectrum
Al
Si
Au
C
Pd
Mg
Cu
O
Ni
Weight %
50
cps/eV
120
100
80
60
40
20
0
0
1
2
3
4
5
6
7
8
9
keV
Al
Si
C
O
Ni
Cu
Mg
Au
Pd
Pd
Pd
Au
Pd
Ni
Cu
Au
Cu
Au

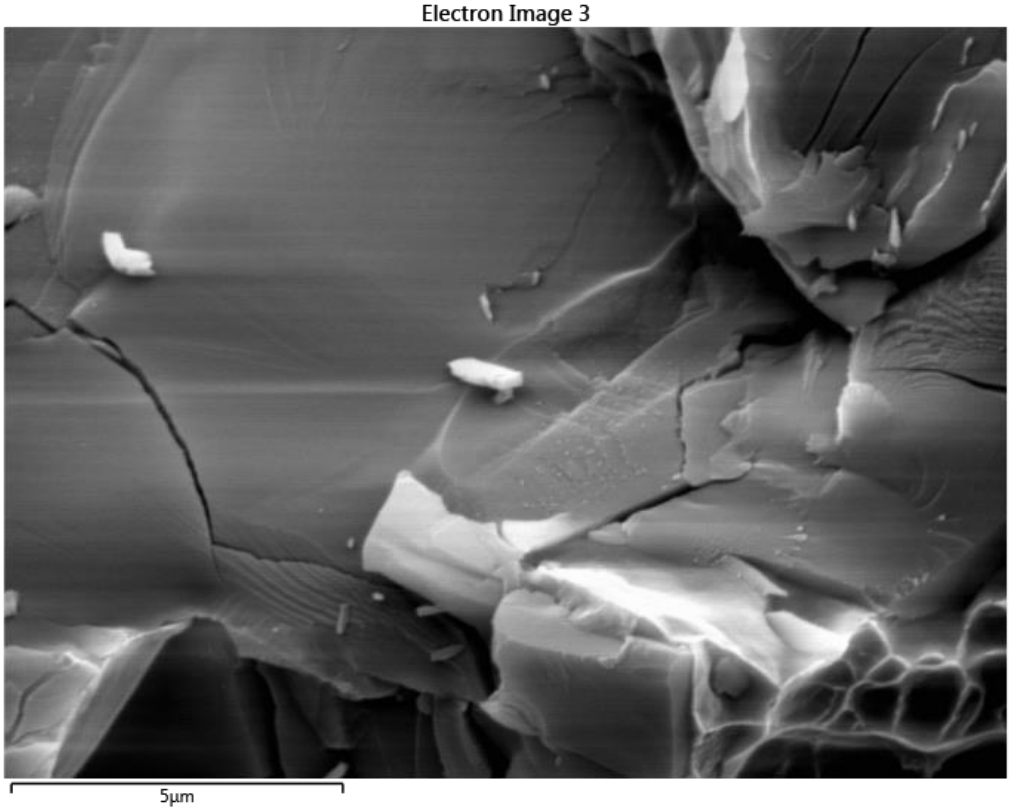
Electron Image 3
5µm

EDS Layered Image 4

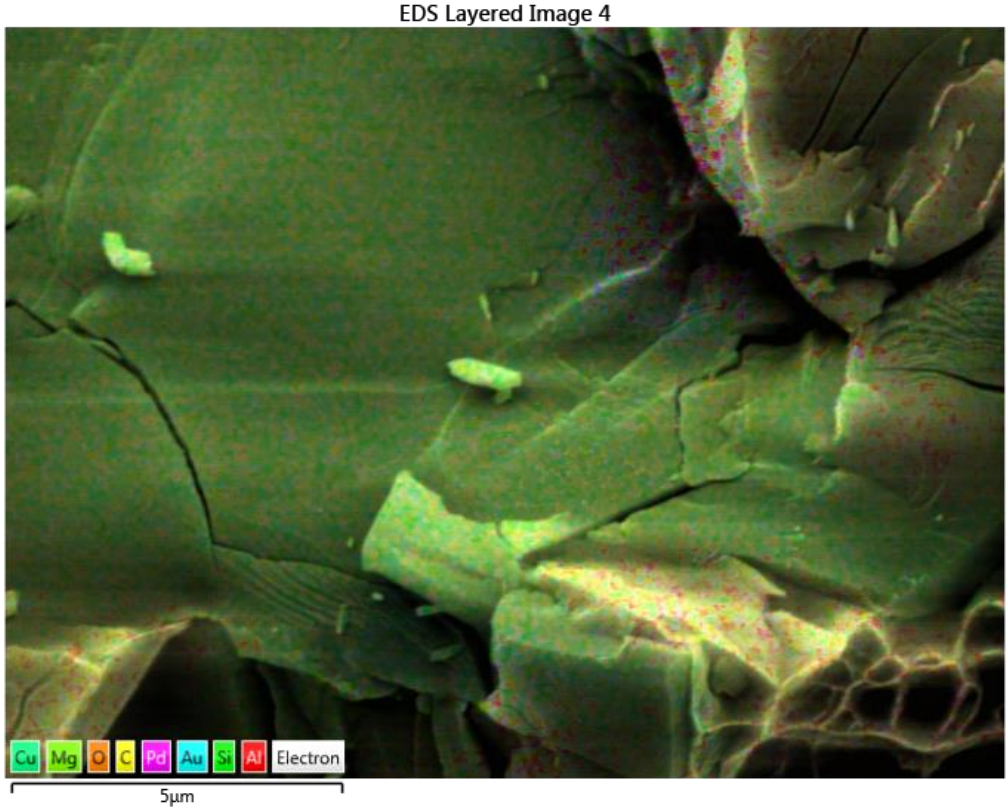

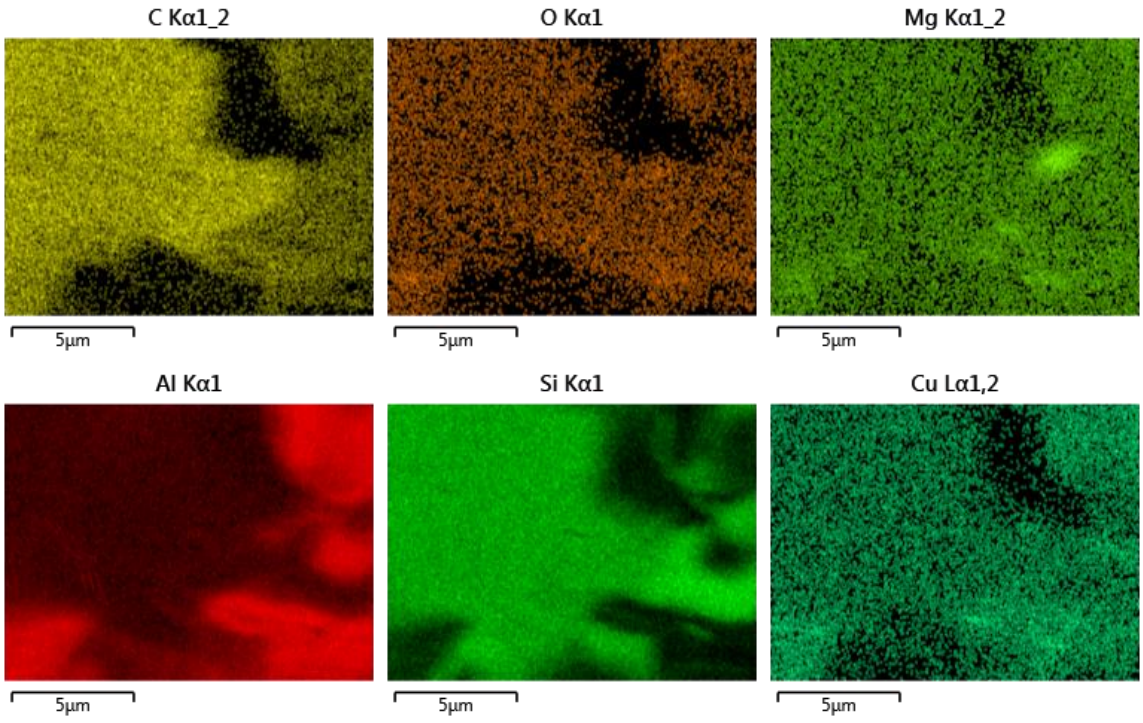
C Kα1_2
O Kα1
Mg Kα1_2
5μm
5μm
5μm
Al Kα1
Si Kα1
Cu Lα1,2
5μm
5μm
5μm

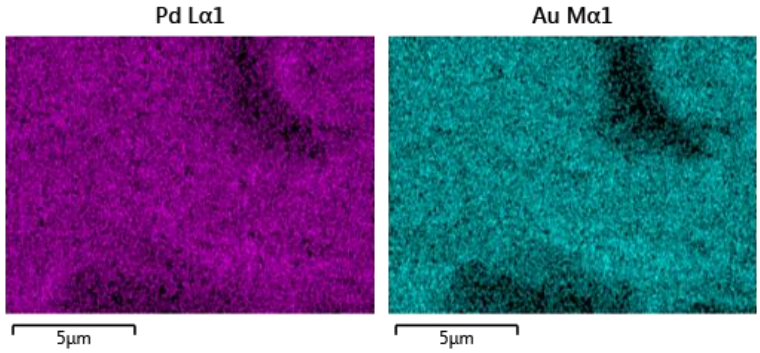
Pd Lα1
Au Mα1
5µm
5µm

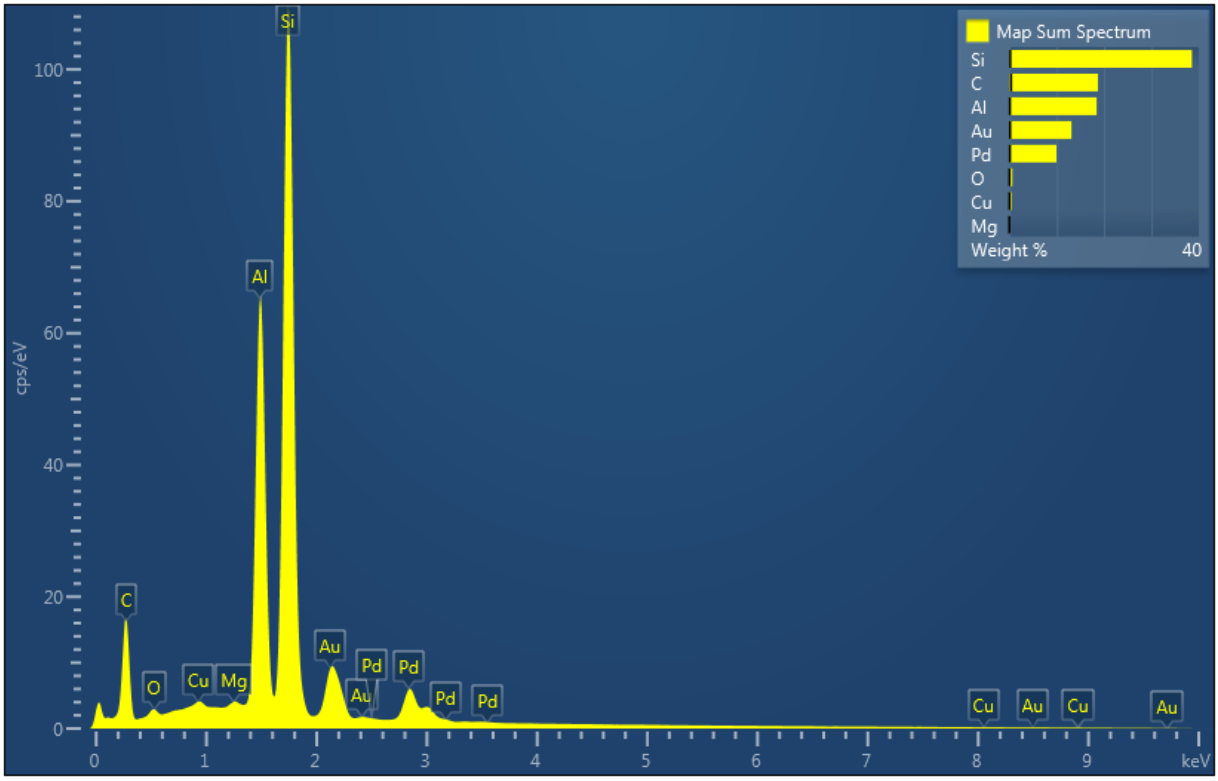
Map Sum Spectrum
Si
C
Al
Au
Pd
O
Cu
Mg
Weight %
40
cps/eV
100
80
60
40
20
0
Si
Al
C
O
Cu
Mg
Au
Pd
Pd
Au
Pd
Pd
Cu
Au
Cu
Au
0
1
2
3
4
5
6
7
8
9
keV

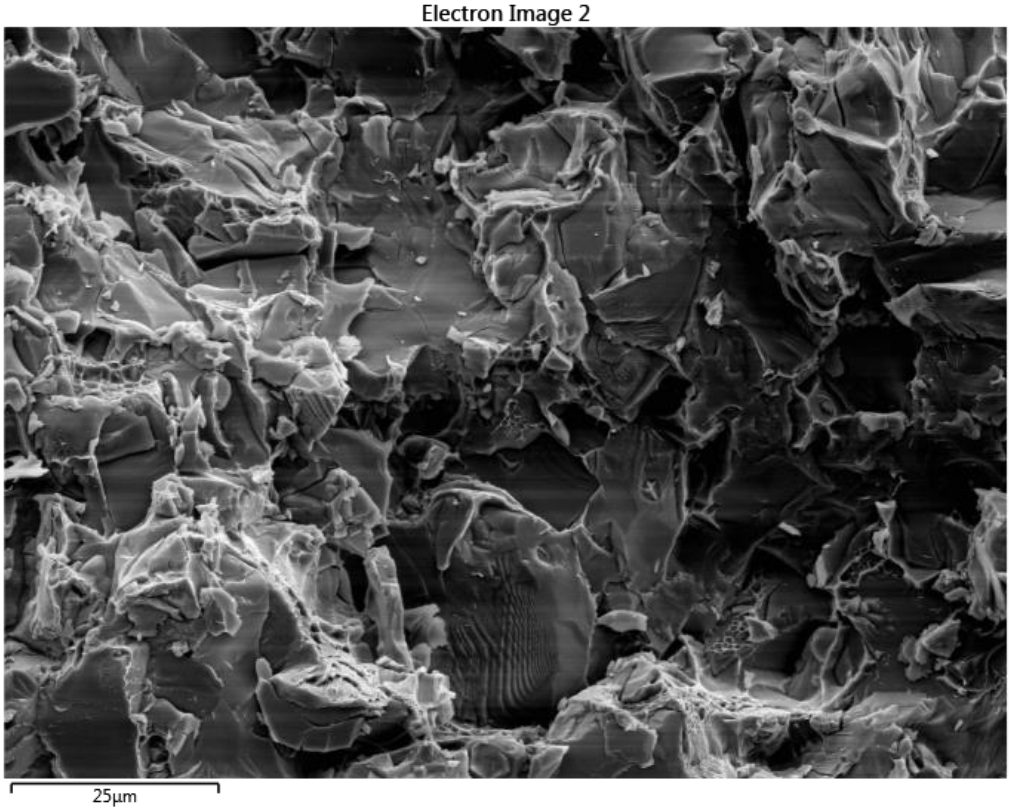
Electron Image 2
25µm

EDS Layered Image 3

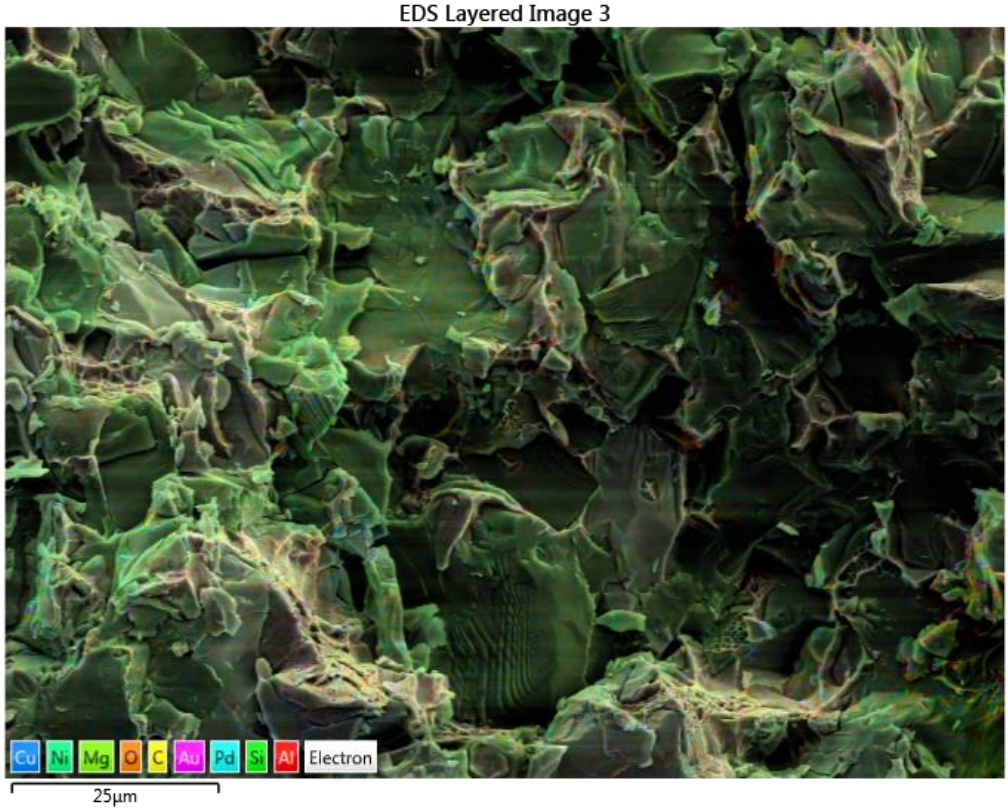

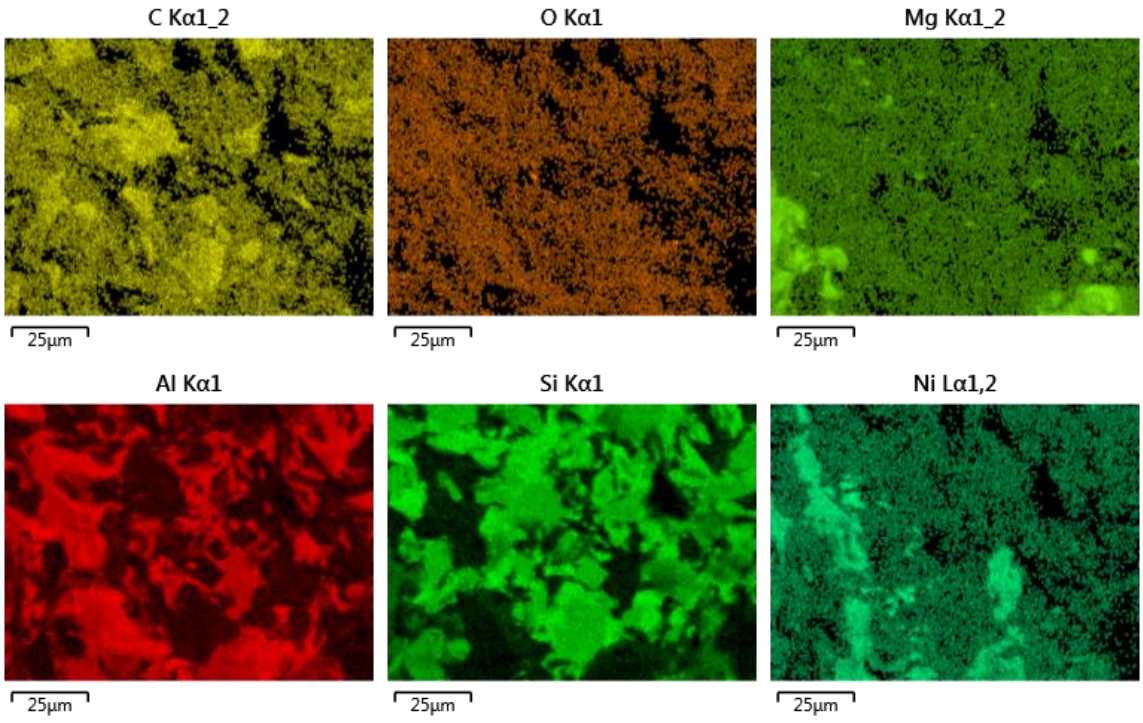
C Kα1_2
O Kα1
Mg Kα1_2
25µm
25µm
25µm
Al Kα1
Si Kα1
Ni Lα1,2
25µm
25µm
25µm

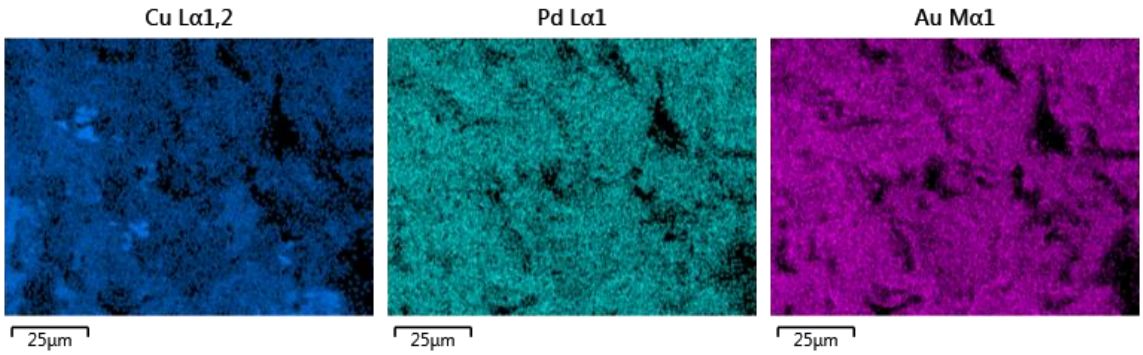
Cu Lα1,2
Pd Lα1
Au Mα1
25µm
25µm
25µm

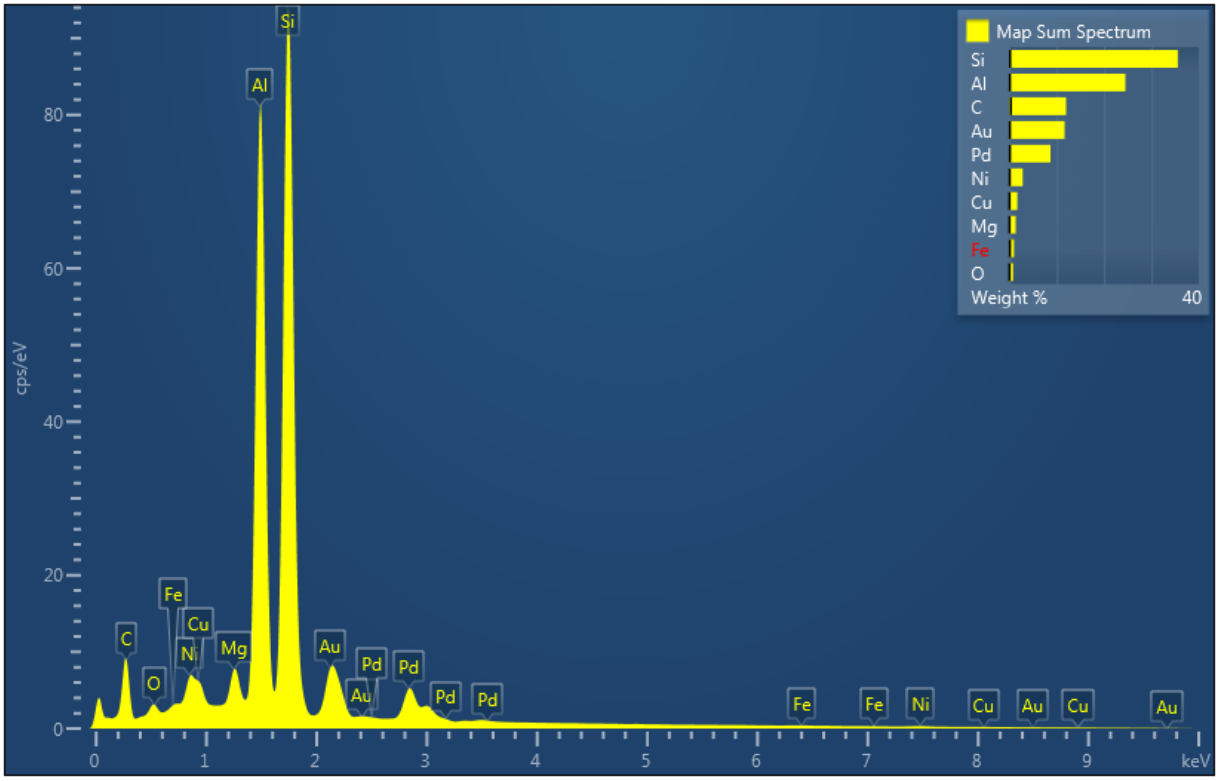
Map Sum Spectrum
Si
Al
C
Au
Pd
Ni
Cu
Mg
Fe
O
Weight %
40
cps/eV
0
20
40
60
80
0
1
2
3
4
5
6
7
8
9
keV
Si
Al
Fe
Cu
Ni
Mg
C
O
Au
Pd
Pd
Pd
Au
Pd
Fe
Fe
Ni
Cu
Au
Cu
Au

Electron Image 4

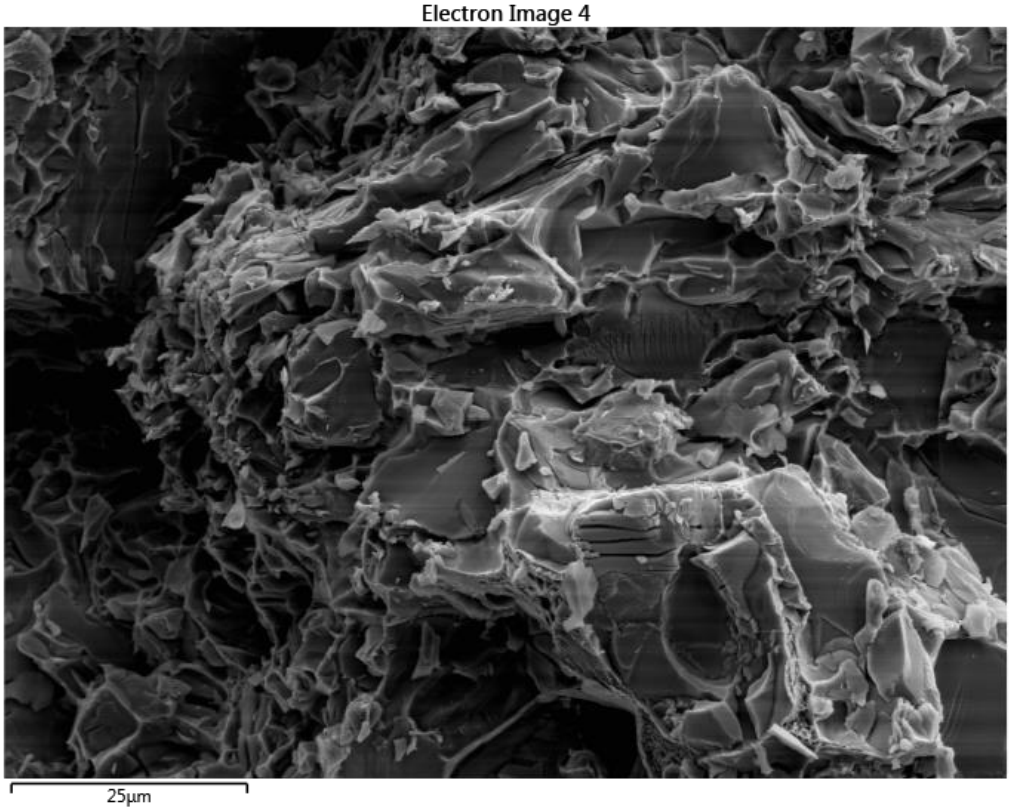

EDS Layered Image 5

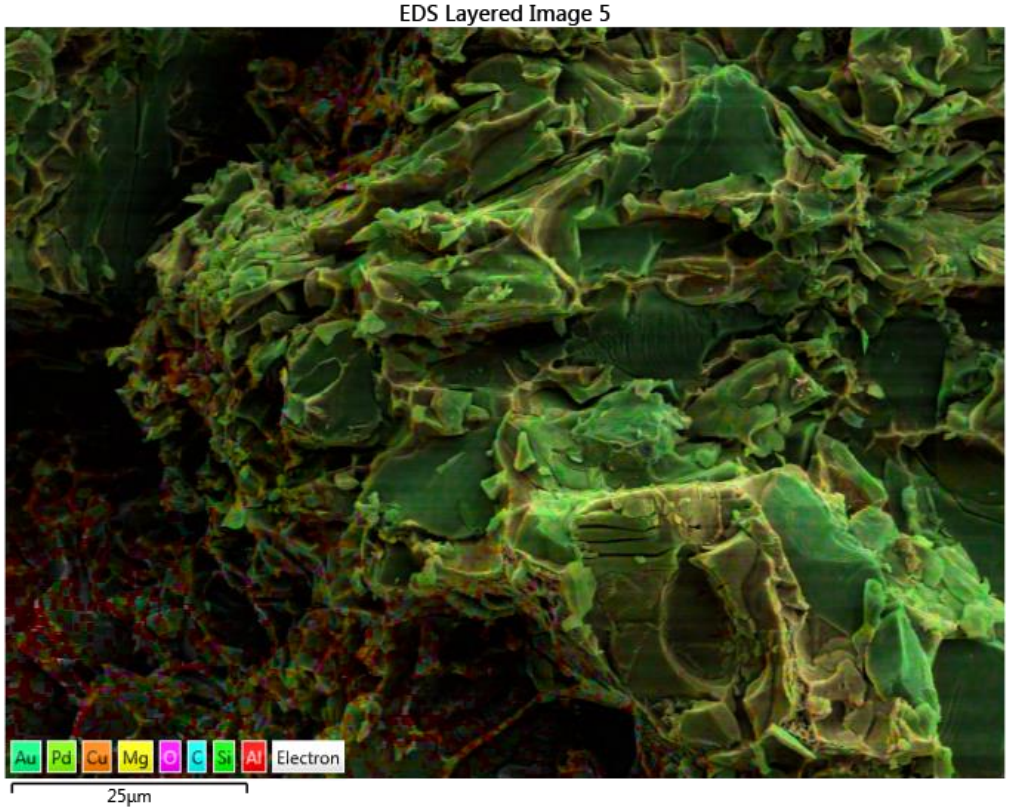

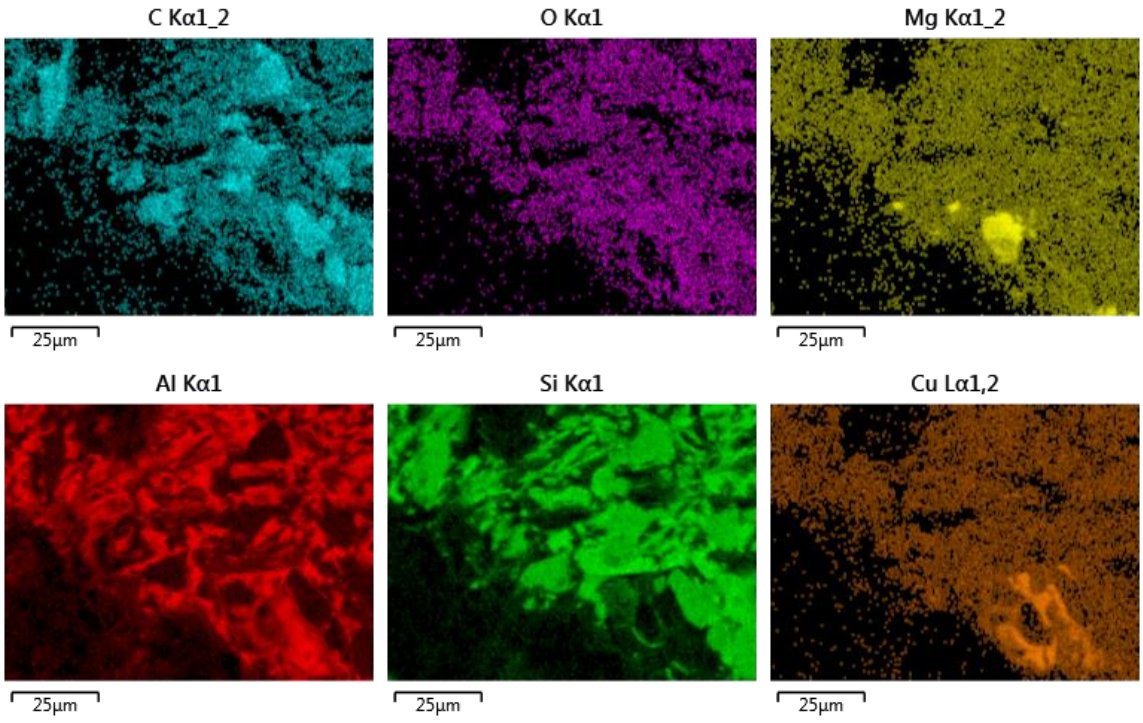
C Kα1_2
O Kα1
Mg Kα1_2
25µm
25µm
25µm
Al Kα1
Si Kα1
Cu Lα1,2
25µm
25µm
25µm

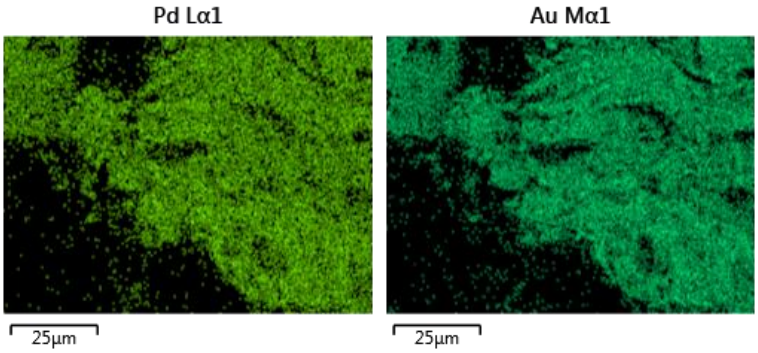
Pd Lα1
Au Mα1
25µm
25µm

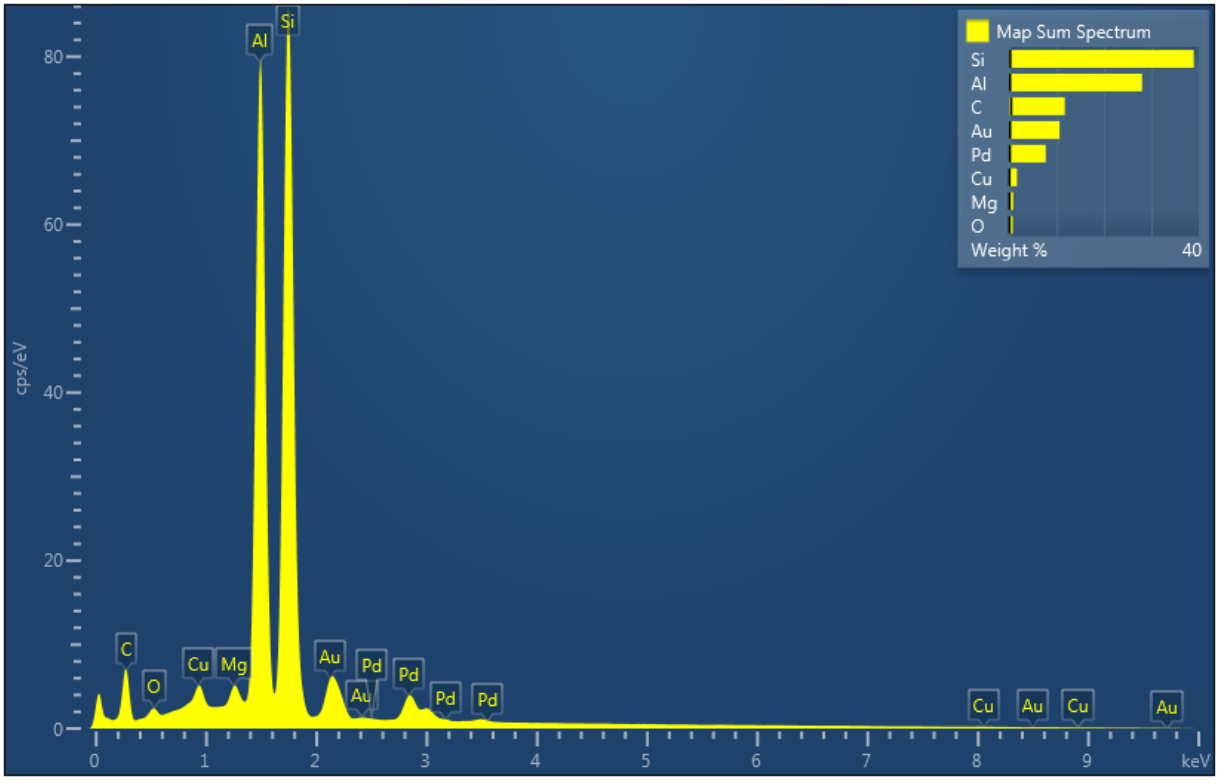
Map Sum Spectrum
Si
Al
C
Au
Pd
Cu
Mg
O
Weight %
40
cps/eV
0
20
40
60
80
0
1
2
3
4
5
6
7
8
9
keV
Al
Si
C
O
Cu
Mg
Au
Au
Pd
Pd
Pd
Pd
Cu
Au
Cu
Au

Electron Image 5

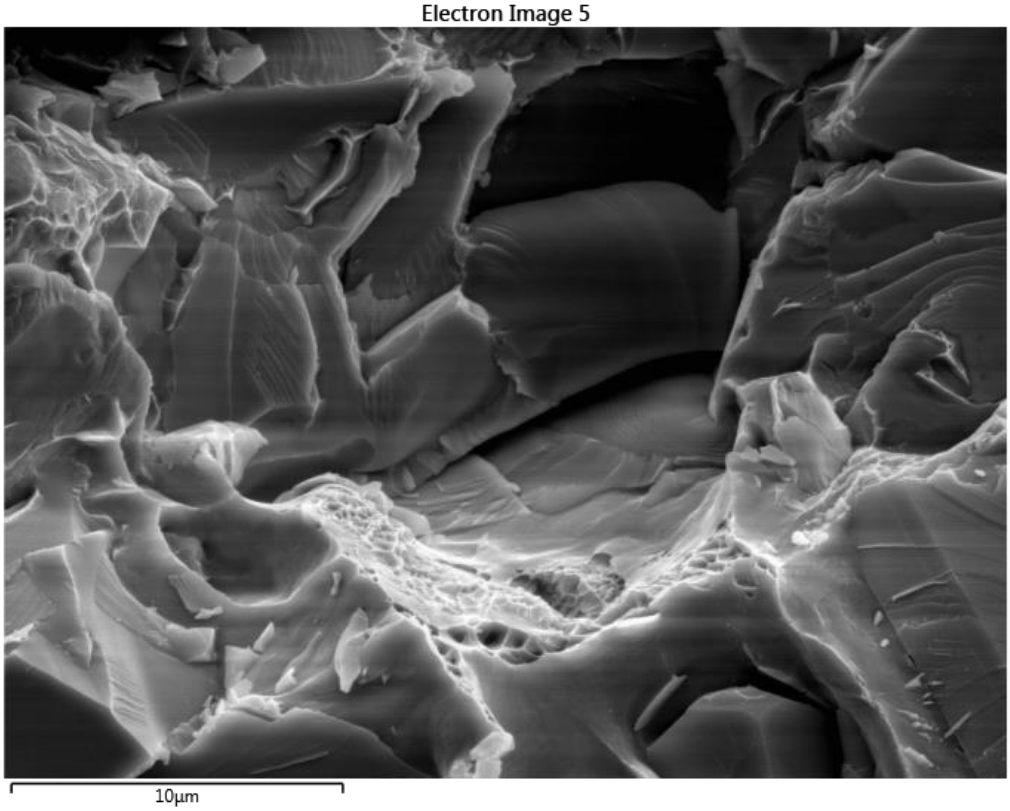

EDS Layered Image 6

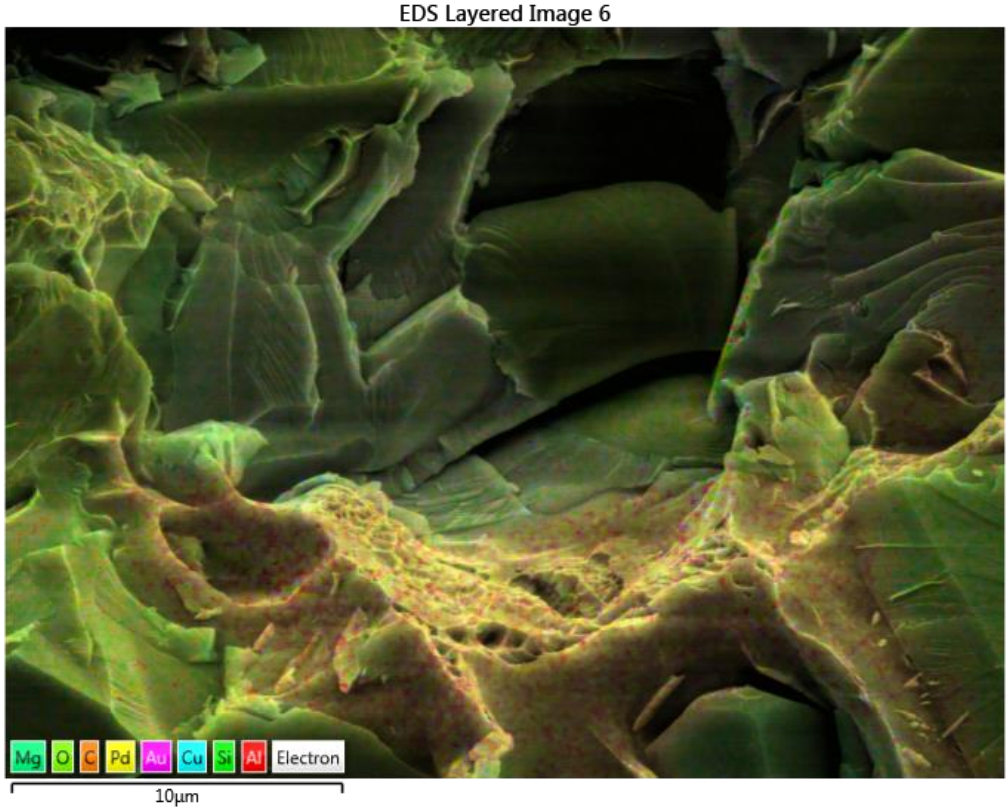

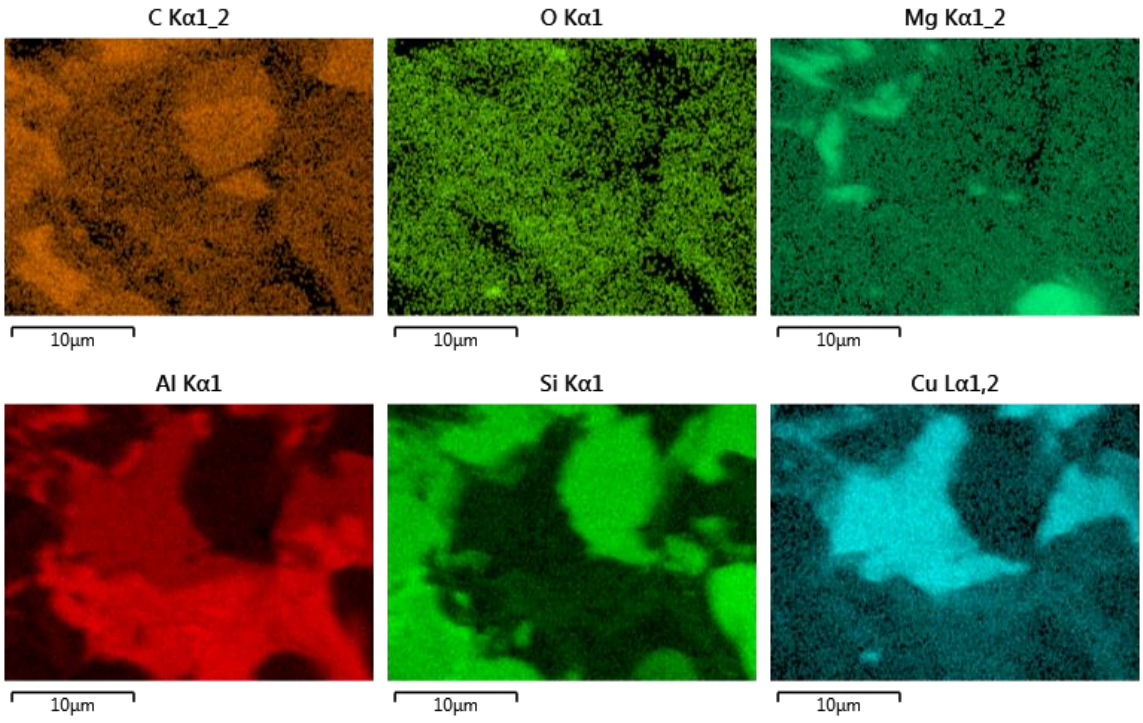
C Kα1_2
O Kα1
Mg Kα1_2
10μm
10μm
10μm
Al Kα1
Si Kα1
Cu Lα1,2
10μm
10μm
10μm

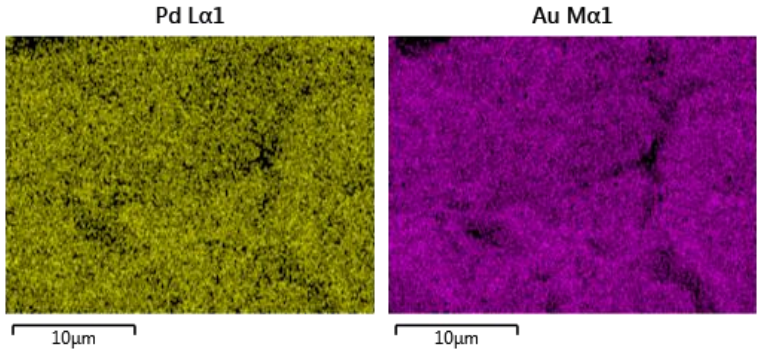
Pd Lα1
Au Mα1
10μm
10μm

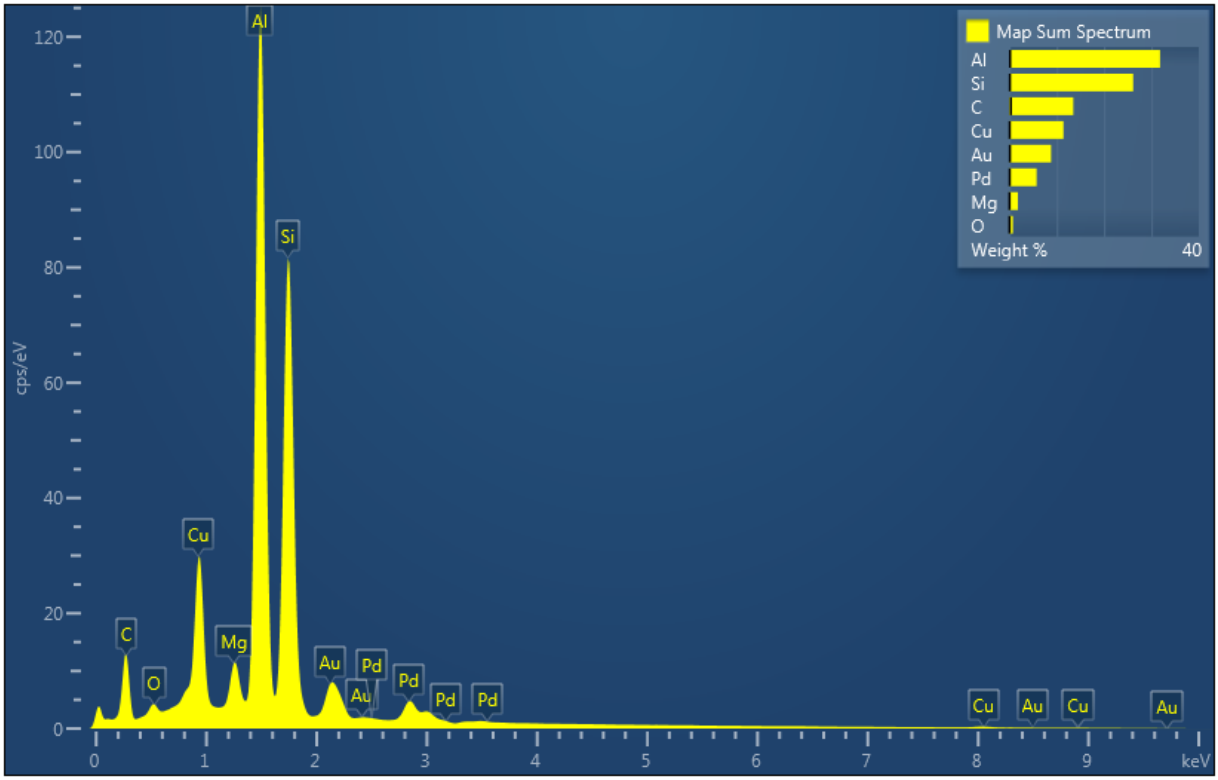
Map Sum Spectrum
Al
Si
C
Cu
Au
Pd
Mg
O
Weight %
40
cps/eV
120
100
80
60
40
20
0
Al
Si
C
O
Cu
Mg
Au
Au
Pd
Pd
Pd
Pd
Cu
Au
Cu
Au
0
1
2
3
4
5
6
7
8
9
keV

Electron Image 6

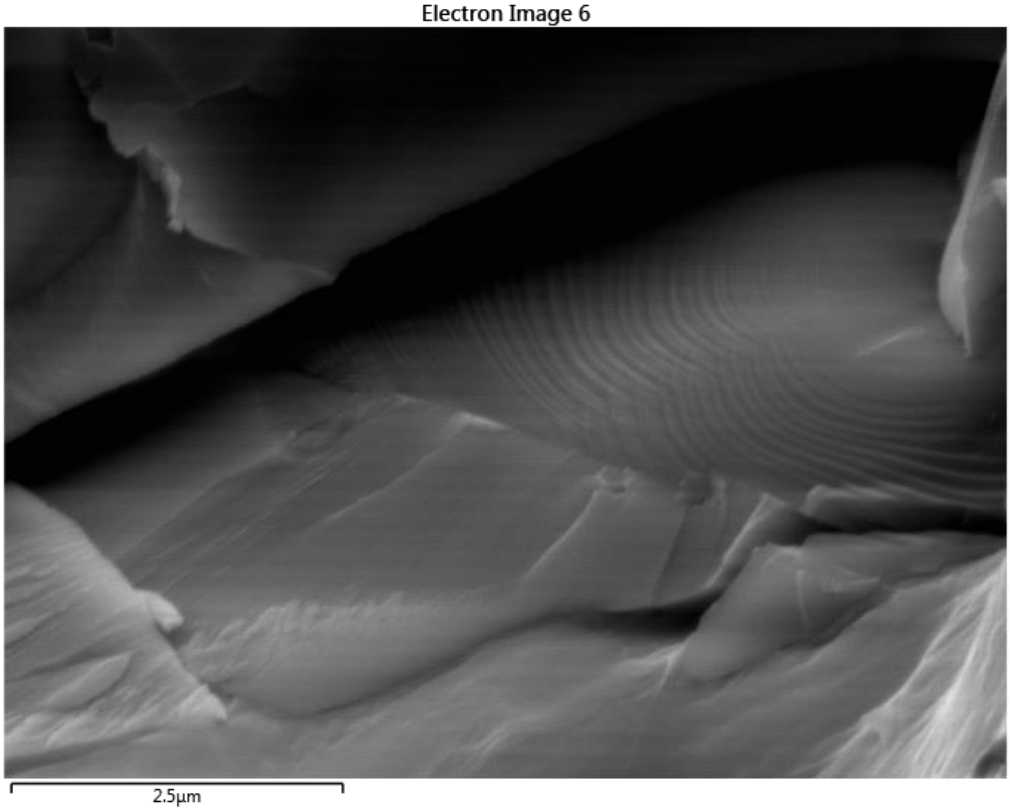

EDS Layered Image 7



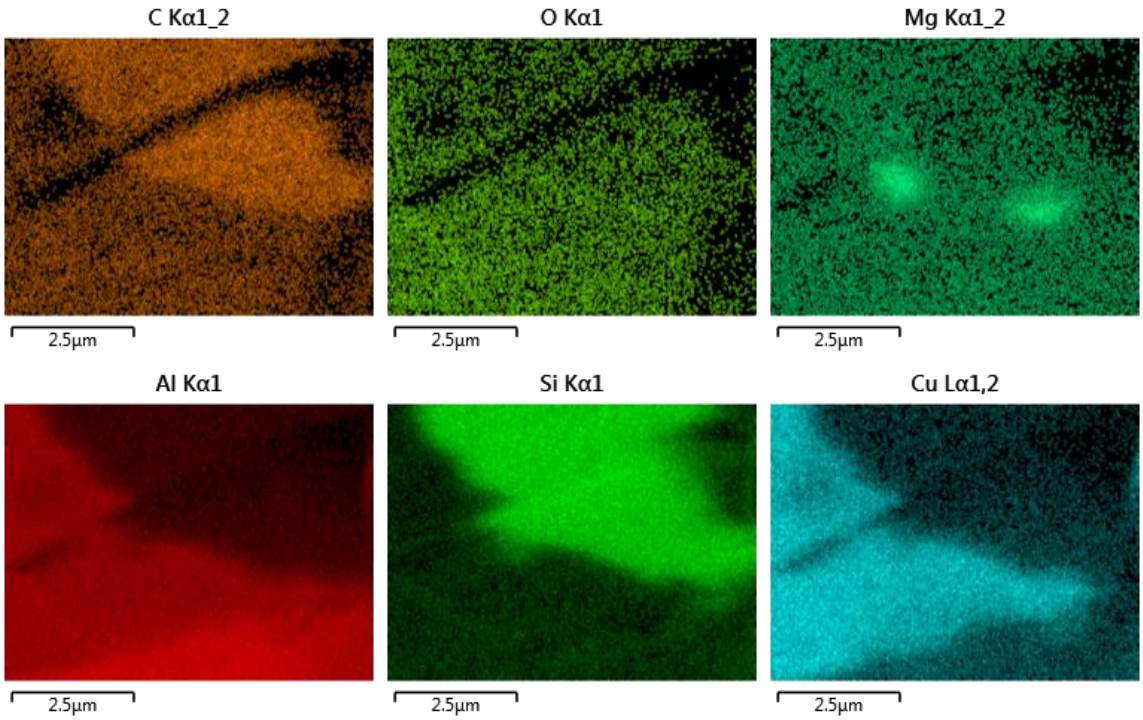
C Kα1_2
O Kα1
Mg Kα1_2
2.5µm
2.5µm
2.5µm
Al Kα1
Si Kα1
Cu Lα1,2
2.5µm
2.5µm
2.5µm

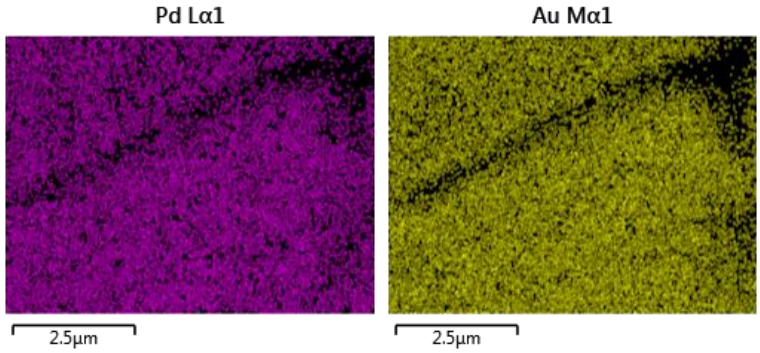
Pd Lα1
Au Mα1
2.5µm
2.5µm

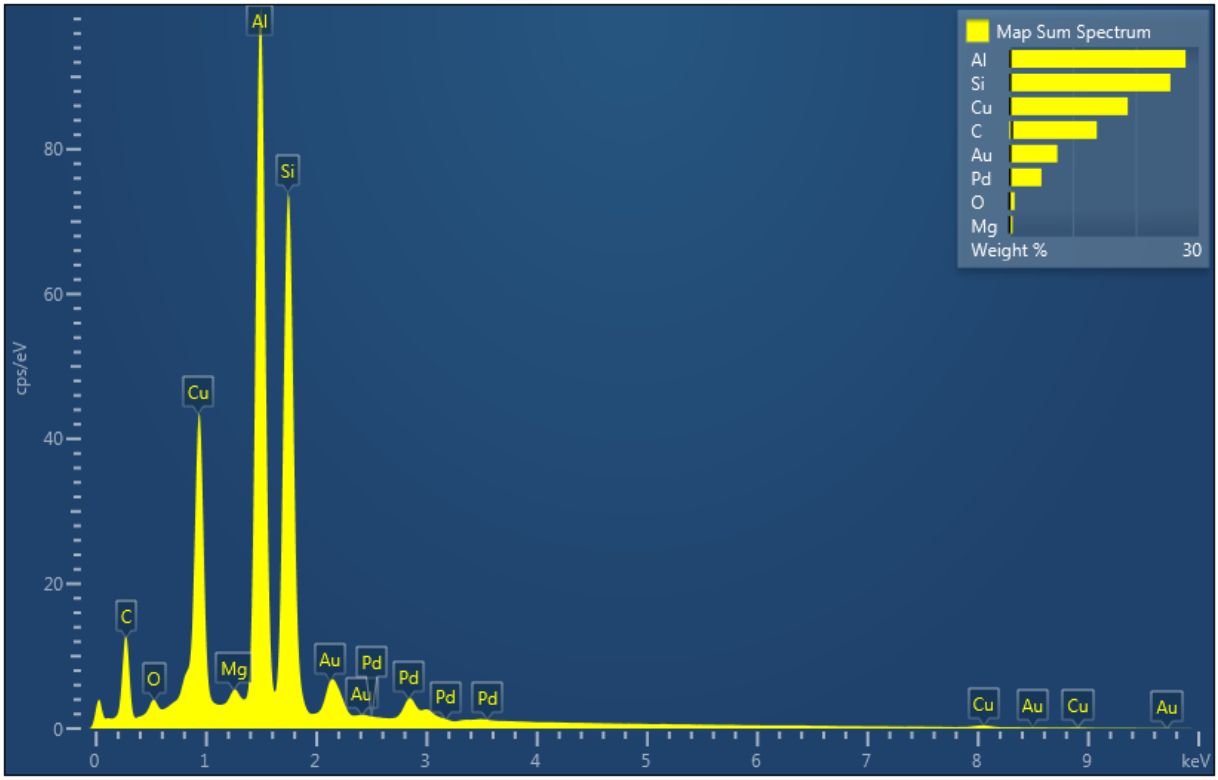
Map Sum Spectrum
Al
Si
Cu
C
Au
Pd
O
Mg
Weight %
30
cps/eV
0
20
40
60
80
C
O
Cu
Mg
Al
Si
Au
Au
Pd
Pd
Pd
Pd
Cu
Au
Cu
Au
0
1
2
3
4
5
6
7
8
9
keV

Electron Image 7

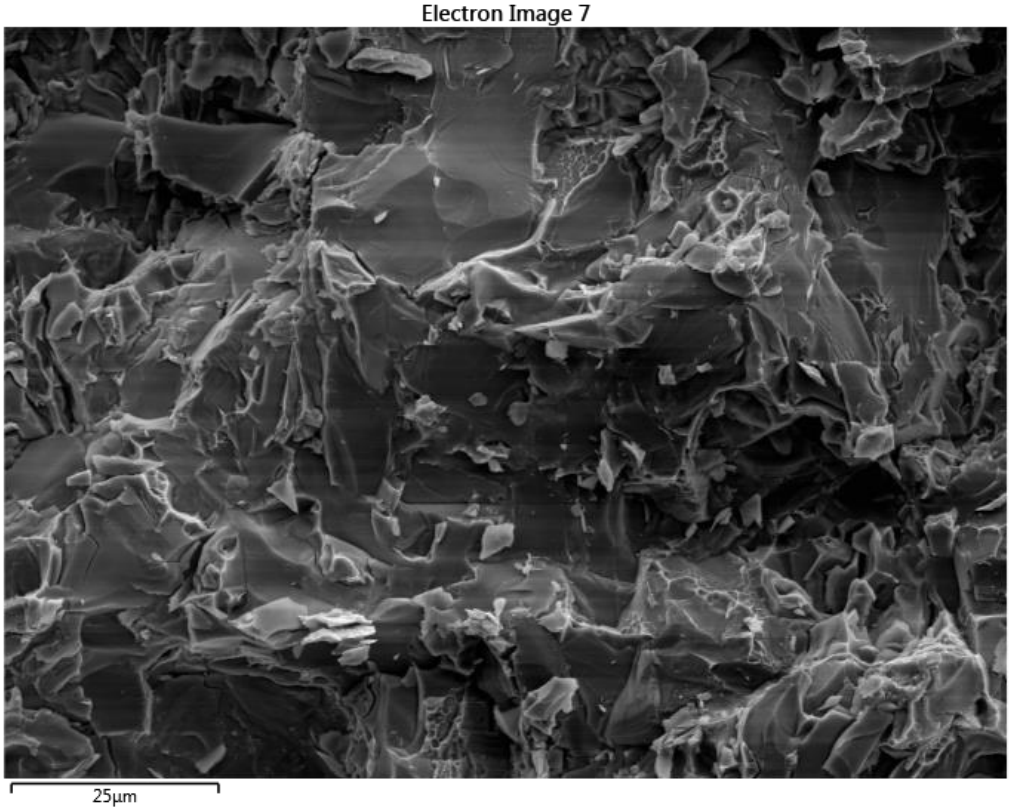

EDS Layered Image 8

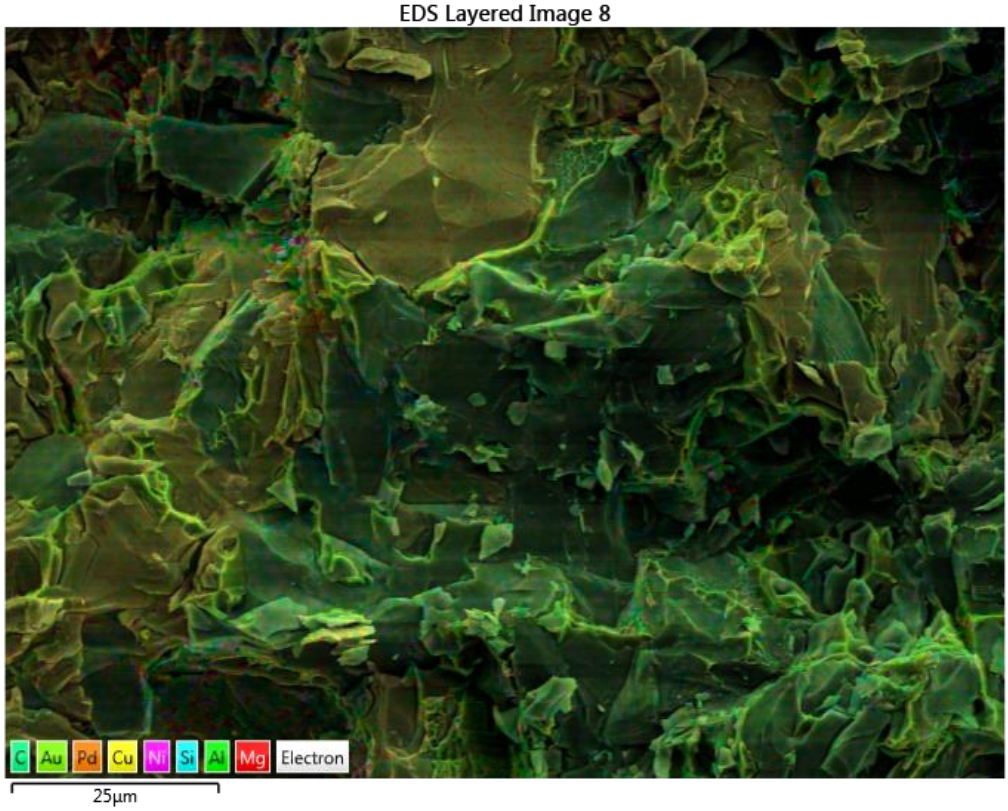

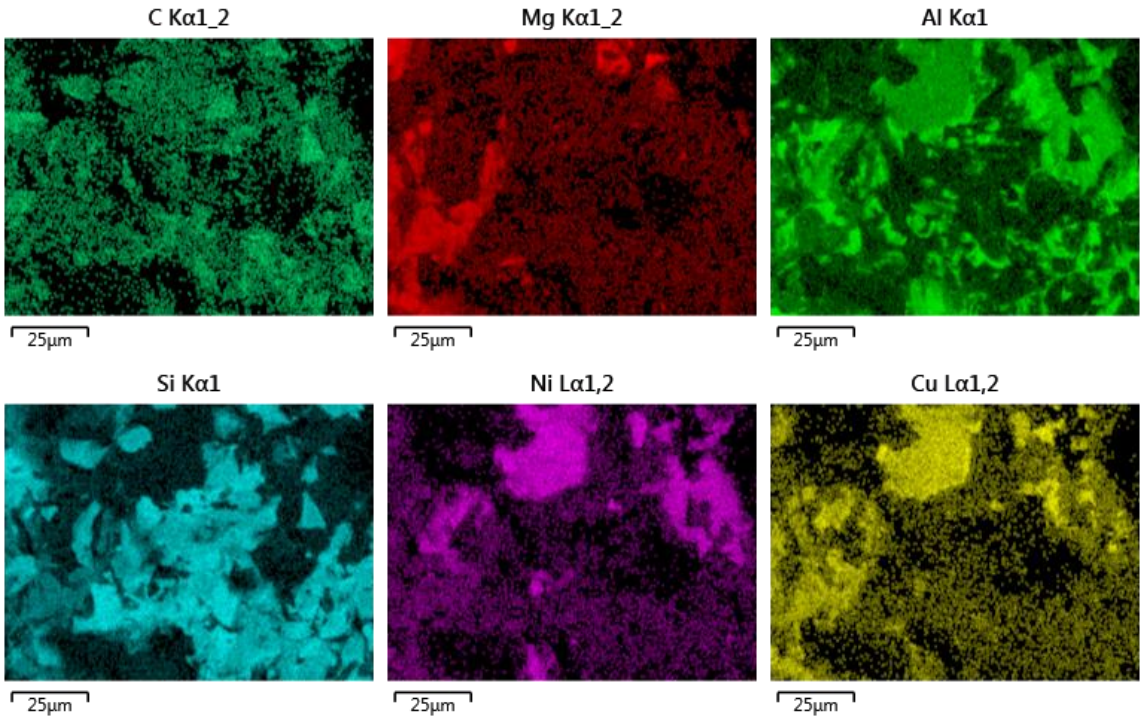
C Kα1_2
Mg Kα1_2
Al Kα1
25µm
25µm
25µm
Si Kα1
Ni Lα1,2
Cu Lα1,2
25µm
25µm
25µm

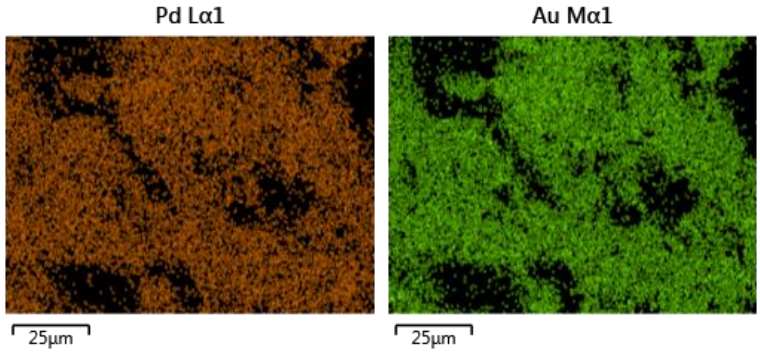
Pd Lα1
Au Mα1
25μm
25μm

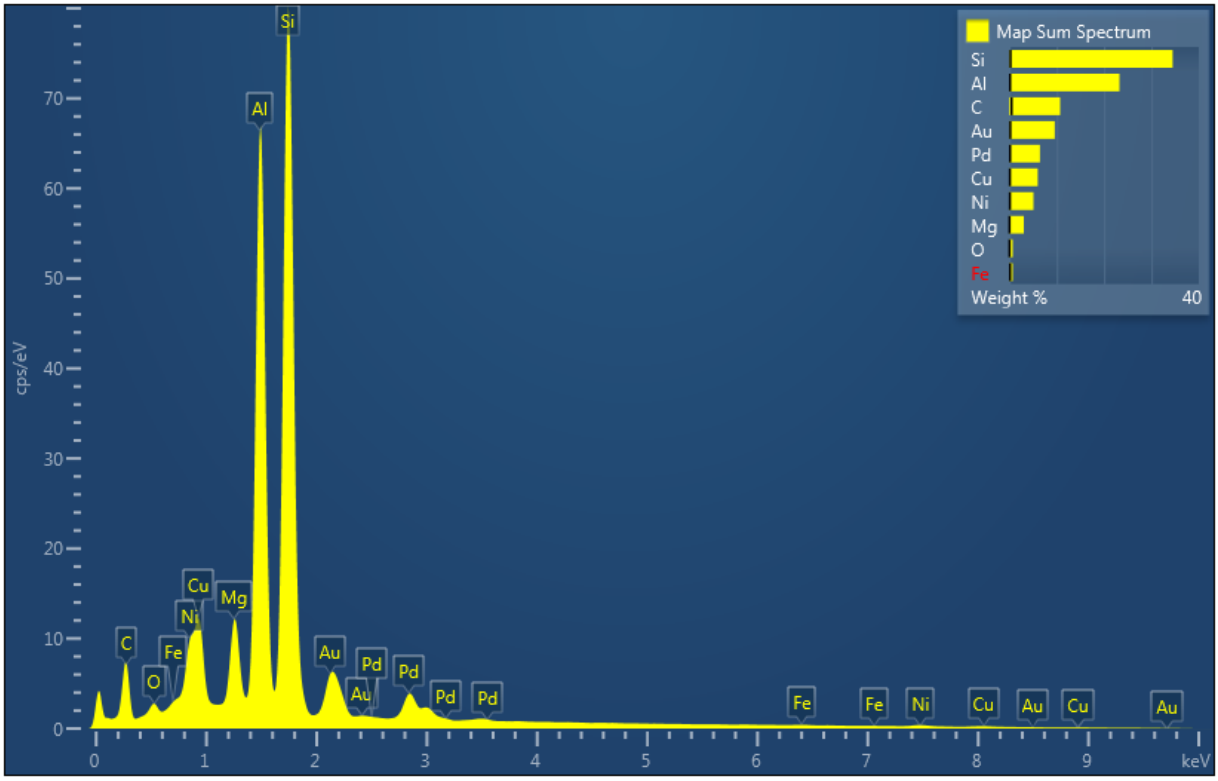
Map Sum Spectrum
Si
Al
C
Au
Pd
Cu
Ni
Mg
O
Fe
Weight %
40
cps/eV
keV
0
10
20
30
40
50
60
70
0
1
2
3
4
5
6
7
8
9
Si
Al
C
O
Fe
Ni
Mg
Cu
Au
Pd
Fe
Fe
Ni
Cu
Au
Cu
Au

Appendix G

AZ91/SiC_P COMPOSITE FATIGUE

G.1 Surface Profiles

G.1.1 Feed: 0.1 mm/rev, Spindle speed: 1000 RPM

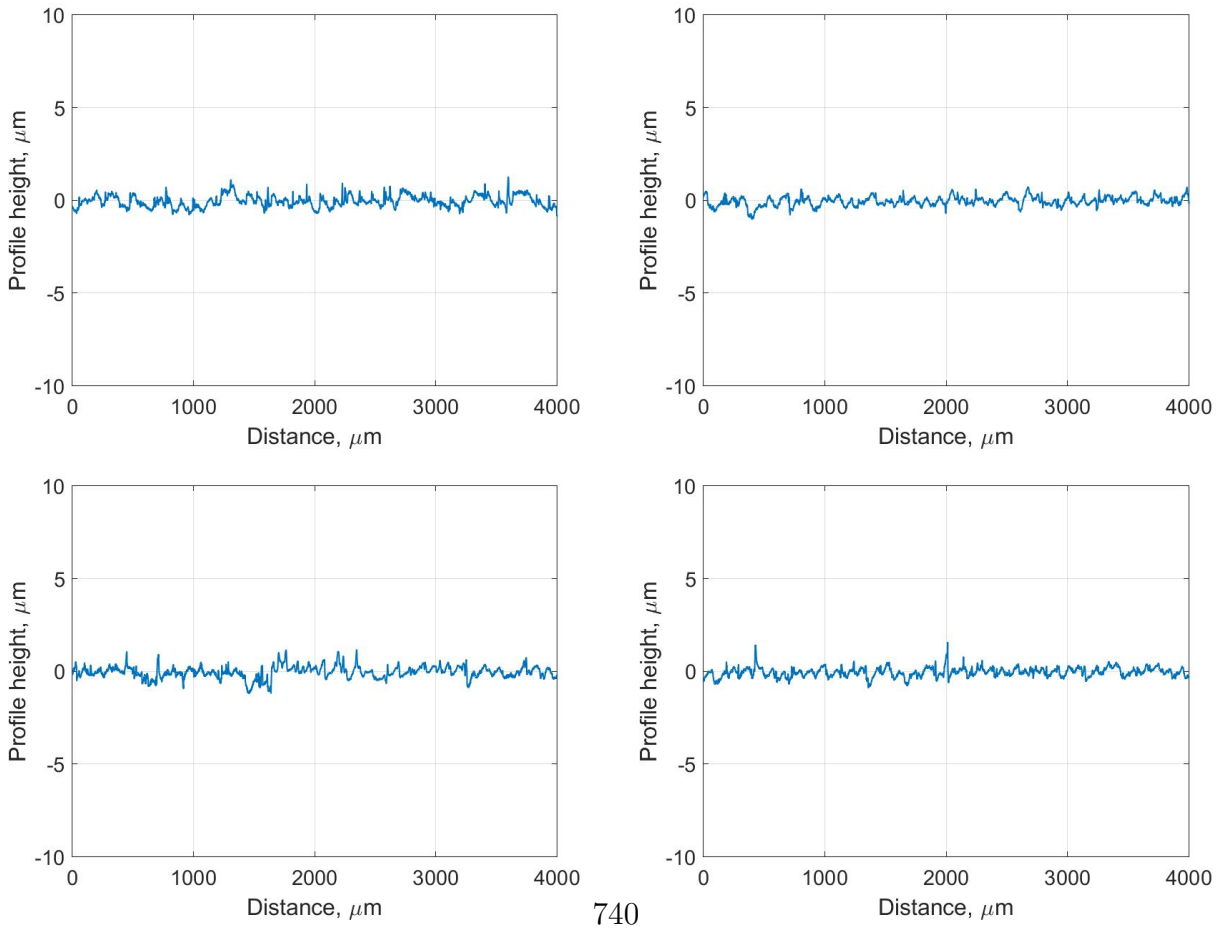

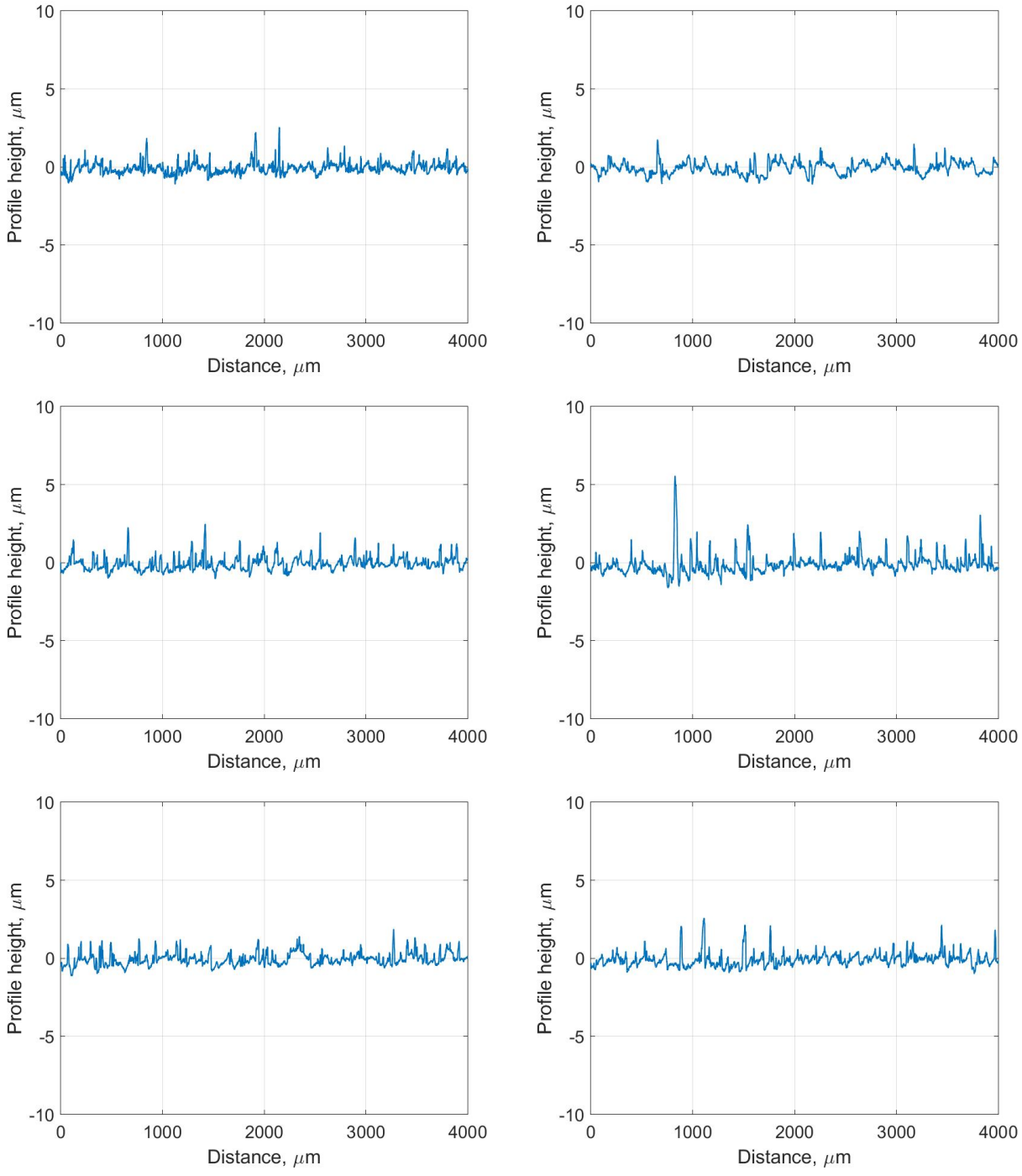
Profile height, μm
Distance, μm
10
5
0
-5
-10
0
1000
2000
3000
4000

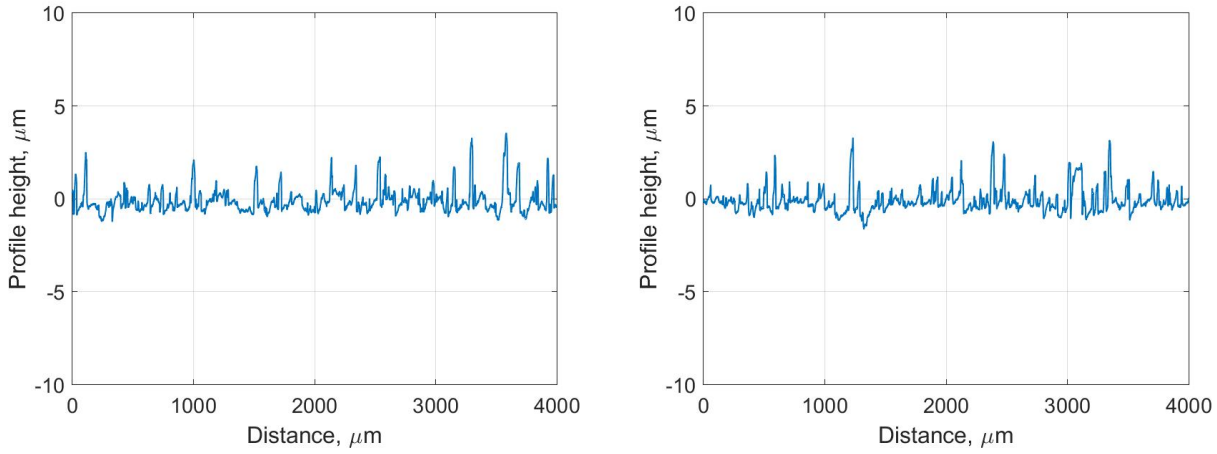

G.1.2 Feed: 0.1 mm/rev, Spindle speed: 3000 RPM

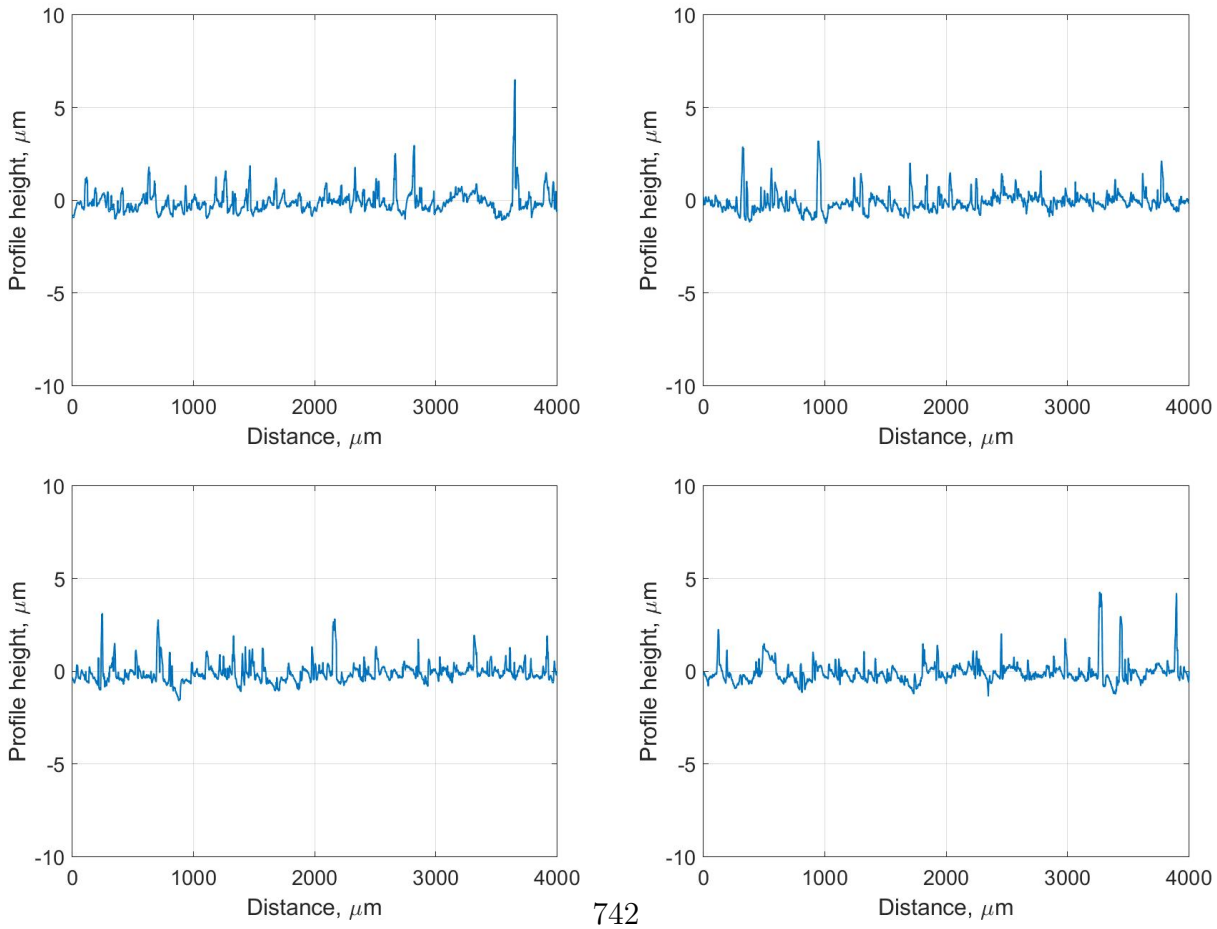

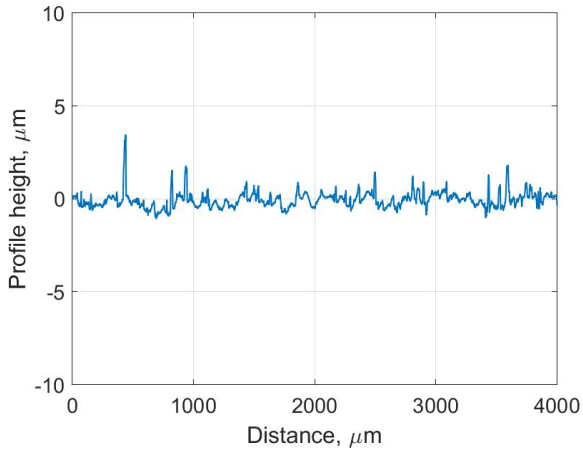
Profile height, μm
Distance, μm
10
5
0
-5
-10
0
1000
2000
3000
4000

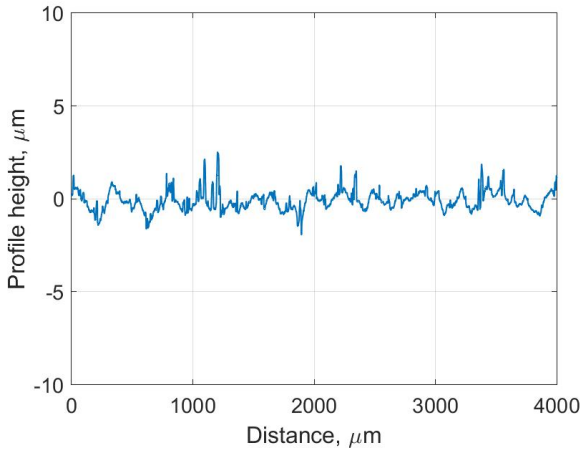
Profile height, μm
Distance, μm
10
5
0
-5
-10
0
1000
2000
3000
4000

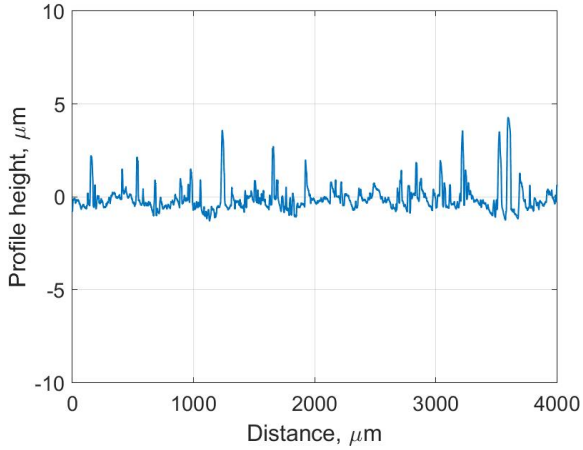
Profile height, μm
Distance, μm
10
5
0
-5
-10
0
1000
2000
3000
4000

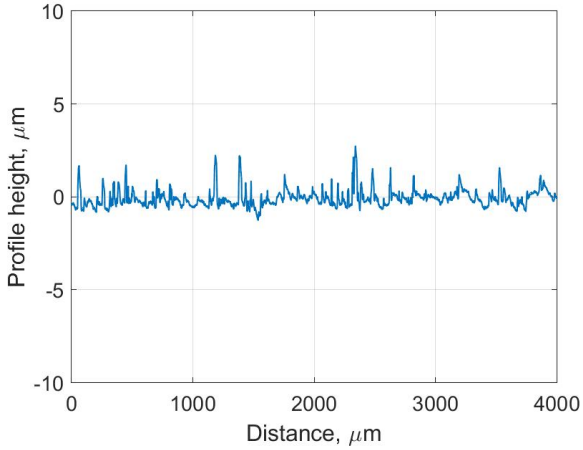
Profile height, μm
Distance, μm
10
5
0
-5
-10
0
1000
2000
3000
4000

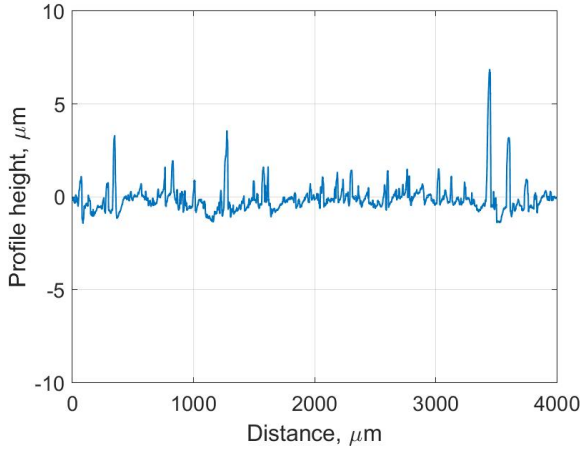
Profile height, μm
Distance, μm
10
5
0
-5
-10
0
1000
2000
3000
4000

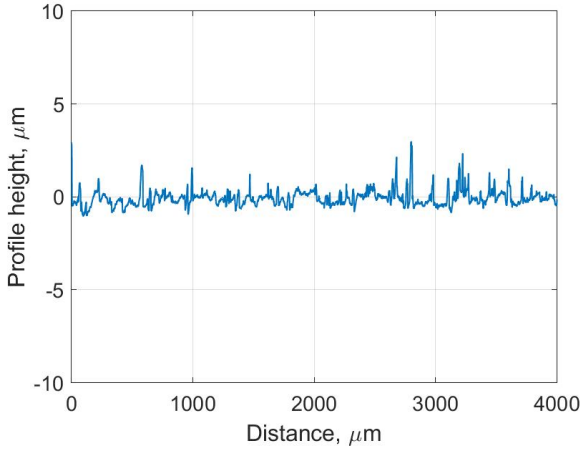
Profile height, μm
Distance, μm
10
5
0
-5
-10
0
1000
2000
3000
4000

G.1.3 Feed: 0.3 mm/rev, Spindle speed: 1000 RPM

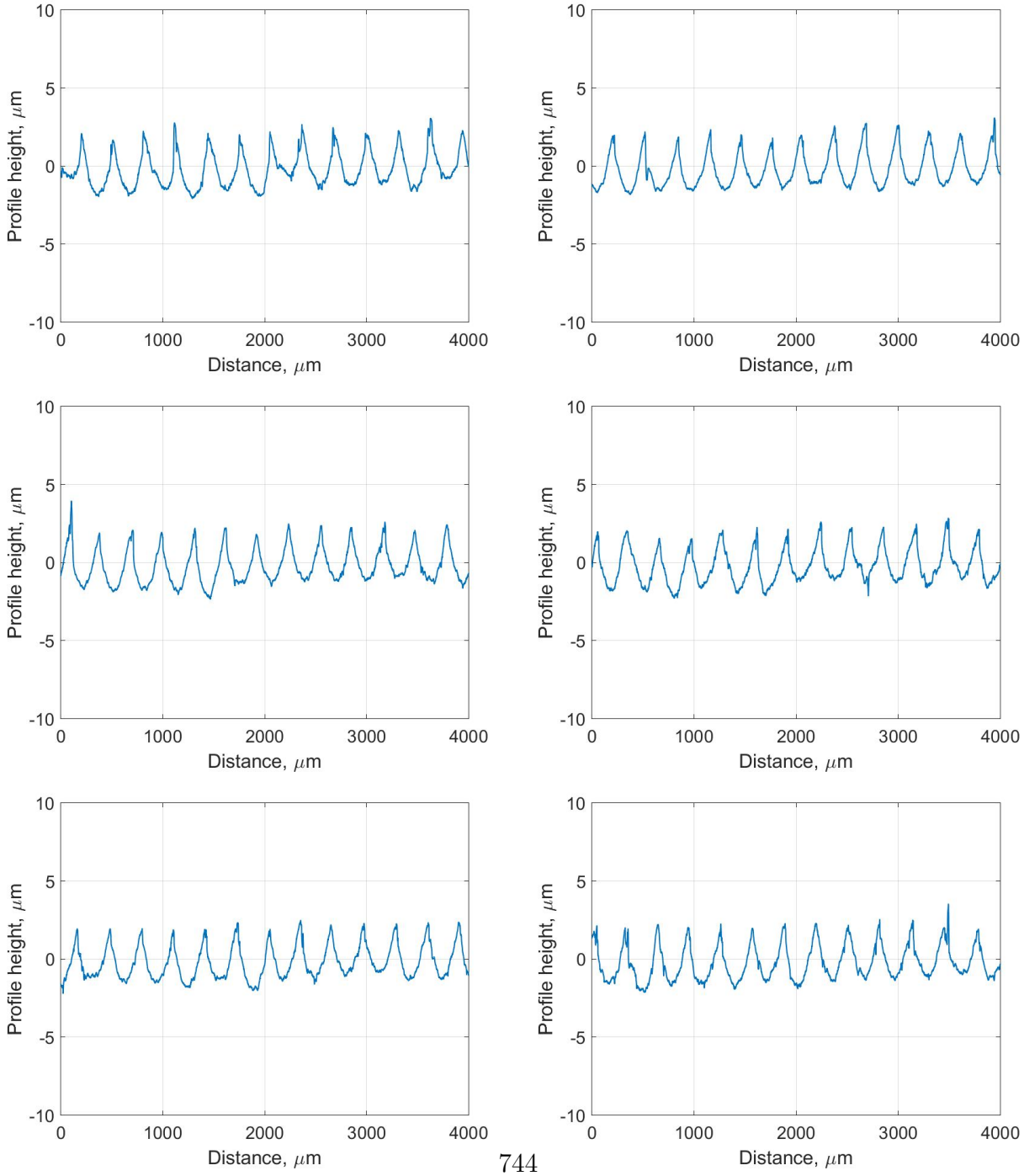

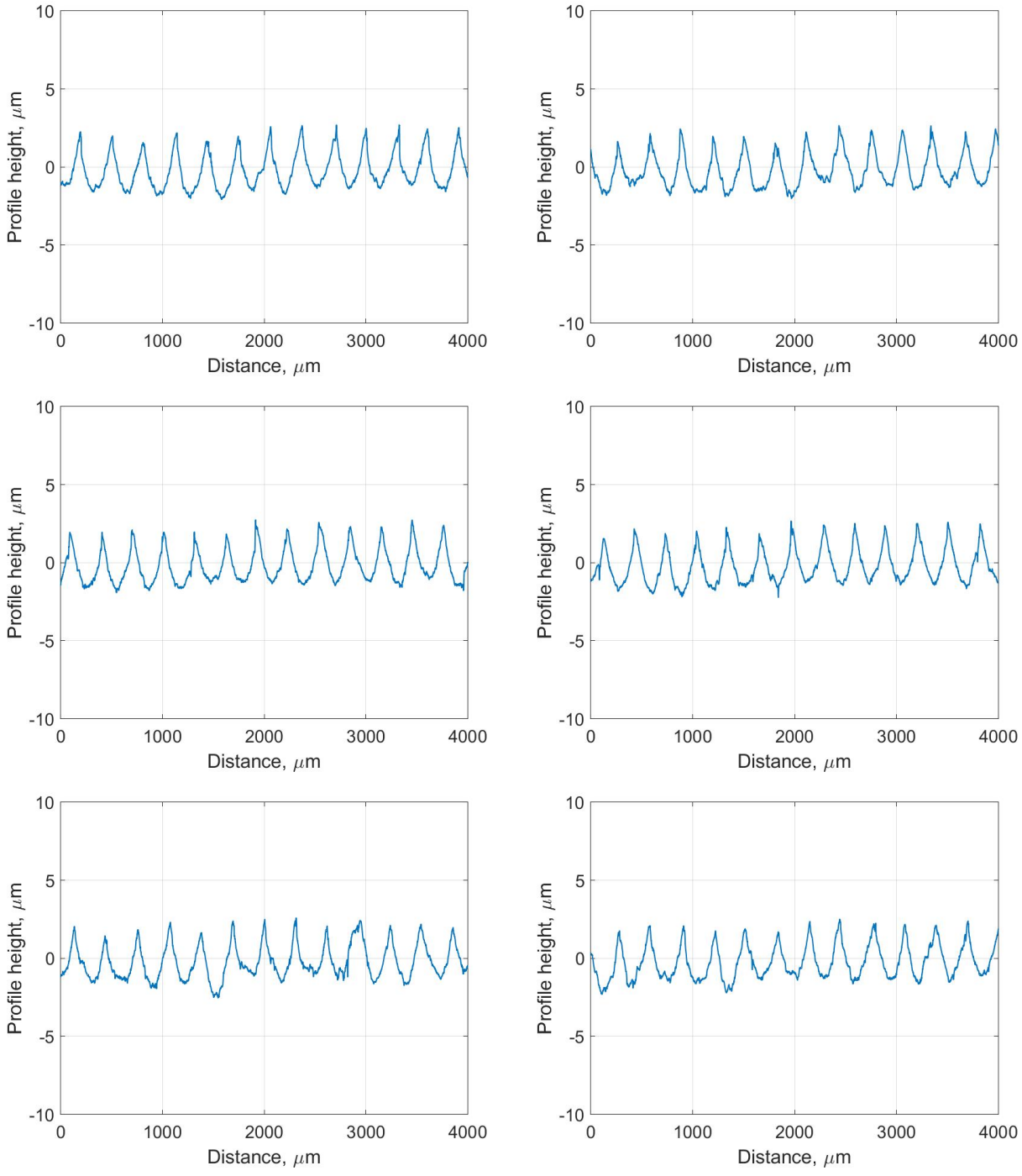
Profile height, μm
Distance, μm
10
5
0
-5
-10
0
1000
2000
3000
4000

G.1.4 Feed: 0.3 mm/rev, Spindle speed: 3000 RPM

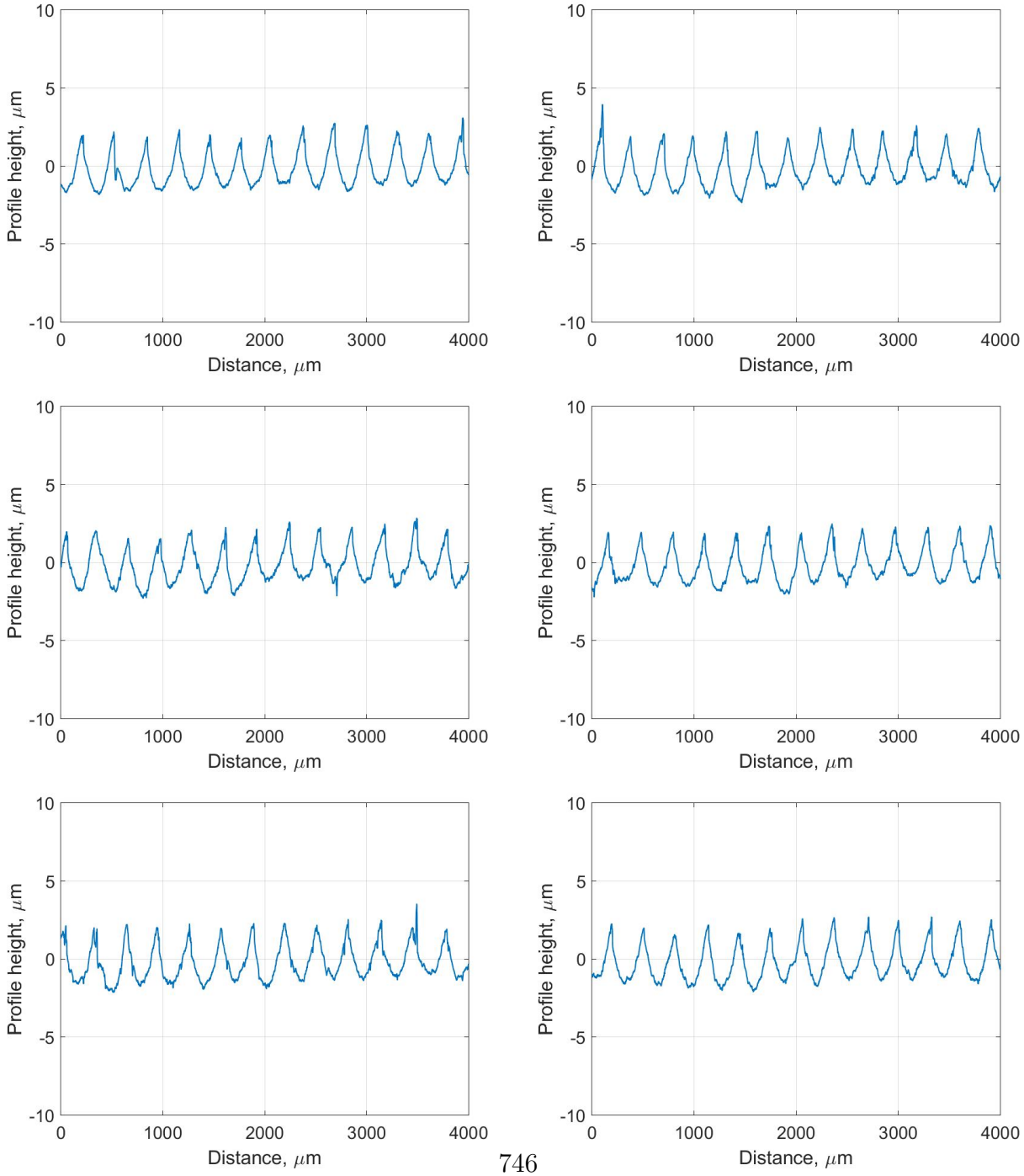

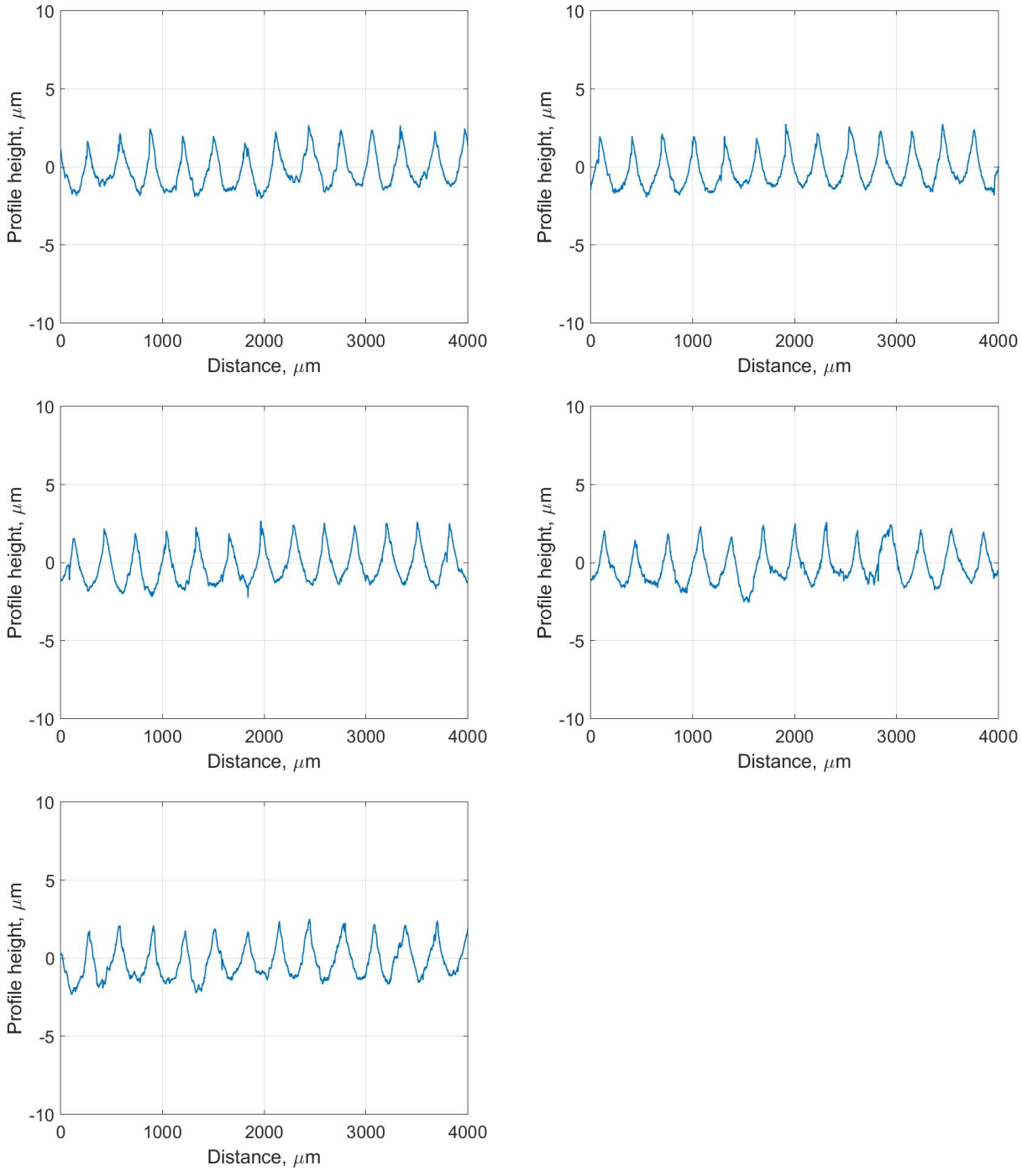

G.2 Fatigue Performance

Sample No	$\frac{S}{S_{ut}}$	Load amplitude, N	Load mean, N	Area, m^2	Speed, RPM	Feed, mm/rev	number of cycles, N
NA-1	0.6	1480.93	1810.0	0.000015	1000	0.1	4545
NA-2	0.6	1487.30	1817.8	1.530E-05	1000	0.1	8497
NA-3	0.8	1729.32	2113.7	0.000013	1000	0.1	2043
NA-4	0.4	928.64	1135.0	0.000014	1000	0.1	5538943
NA-5	0.8	1606.8	1963.9	1.234E-05	1000	0.1	2736
NA-6	0.25	621.87	760.06	1.55E-05	1000	0.1	5698289
NA-7	0.6	1380.8	1687.7	1.42E-05	1000	0.1	30677
NA-8	0.8	1510.4	1846.0	1.55E-05	3000	0.1	1526
NA-9	0.6	1510.4	1846.0	1.554E-05	3000	0.1	5891
NA-10	0.8	2074.2	2535.1	0.000016	3000	0.1	2296
NA-11	0.6	1886.97	2306.3	0.000014	3000	0.1	10385

NA-12	0.4	972.1037	1188.1	1.50E-05	3000	0.1	5938898
NA-13	0.25	607.5	742.5	0.000015	3000	0.1	5798845
NA-14	0.8	1944	2376	0.000015	1000	0.3	152
NA-15	0.6	1424.962	1741.62	1.461E-05	1000	0.3	1473
NA-16	0.25	508.2345	621.17	0.0000125	1000	0.3	5956654
NA-17	0.4	825.552	1009.0	0.000012	1000	0.3	5723257
NA-18	0.6	1368.391	1672.5	1.407E-05	1000	0.3	2984
NA-19	0.8	1937.261	2367.7	0.000015	1000	0.3	72
NA-20	0.6	1784.281	2180.7	1.377E-05	3000	0.3	8083
NA-21	0.6	1333.72	1630.1	1.37E-05	3000	0.3	6442
NA-22	0.8	1812.145	2214.84	1.39E-05	3000	0.3	760
NA-23	0.8	1291.905	1578.9	1.33E-05	3000	0.3	1507
NA-24	0.4	990.1764	1210.2	1.53E-05	3000	0.3	5725627
NA-25	0.25	576.8982	705.09	1.44E-05	3000	0.3	5931327

G.3 SEM micrographs of the machined surface

G.3.1 Peripherally milled, Feed: 0.1 mm/rev, Spindle speed: 1000 RPM

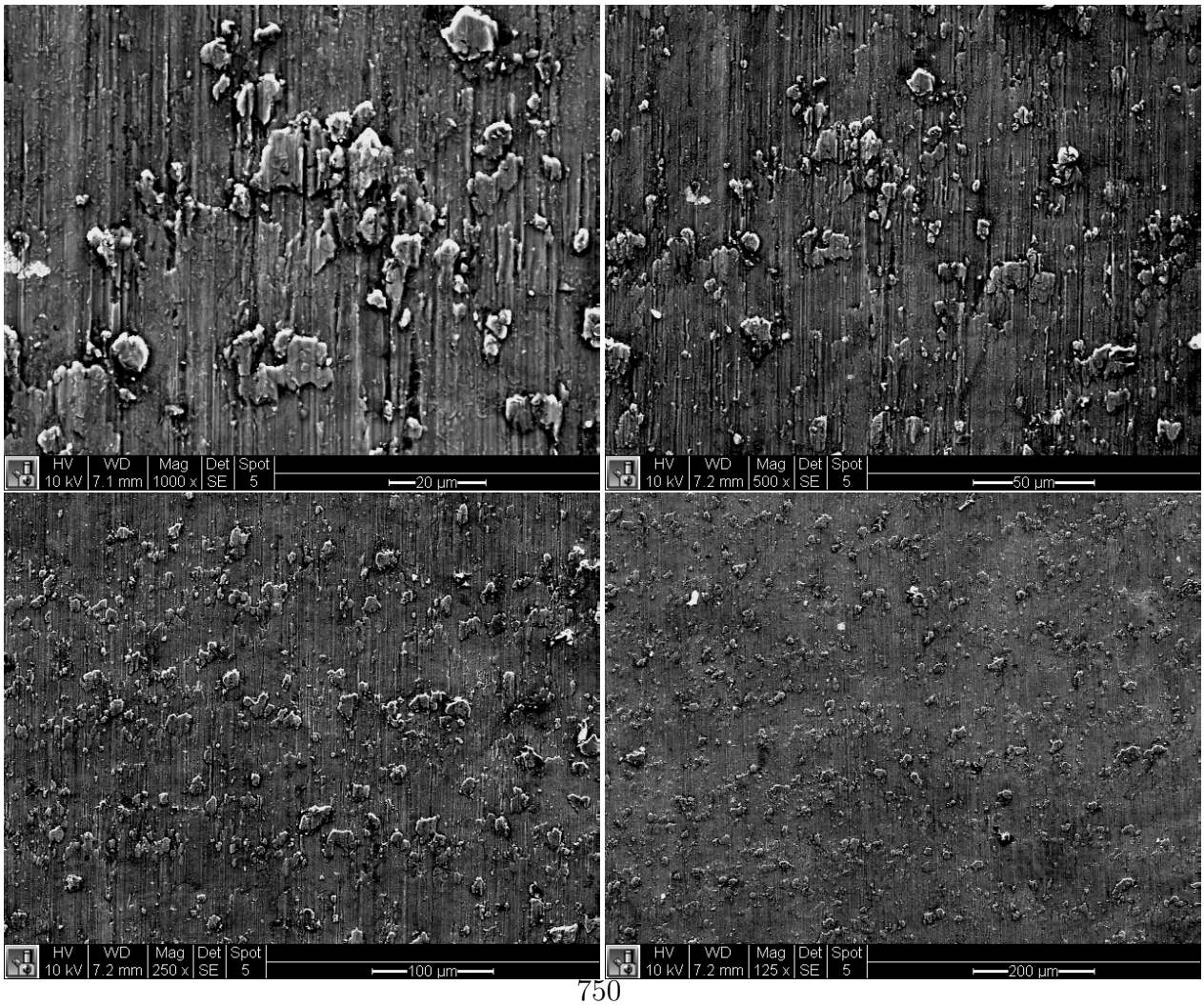

G.3.2 Peripherally milled, Feed: 0.1 mm/rev, Spindle speed: 3000 RPM

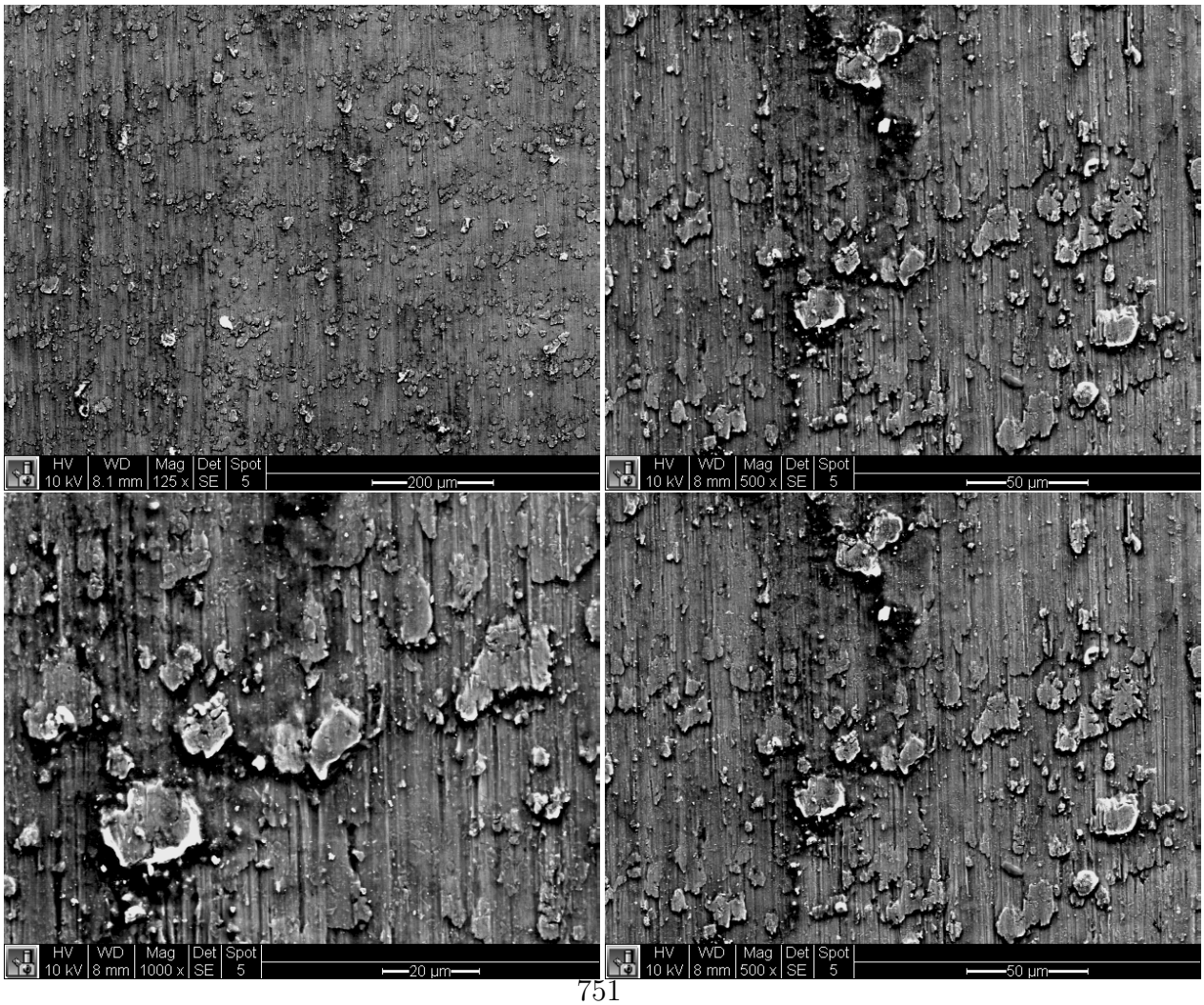

G.3.3 Peripherally milled, Feed: 0.3 mm/rev, Spindle speed: 1000 RPM

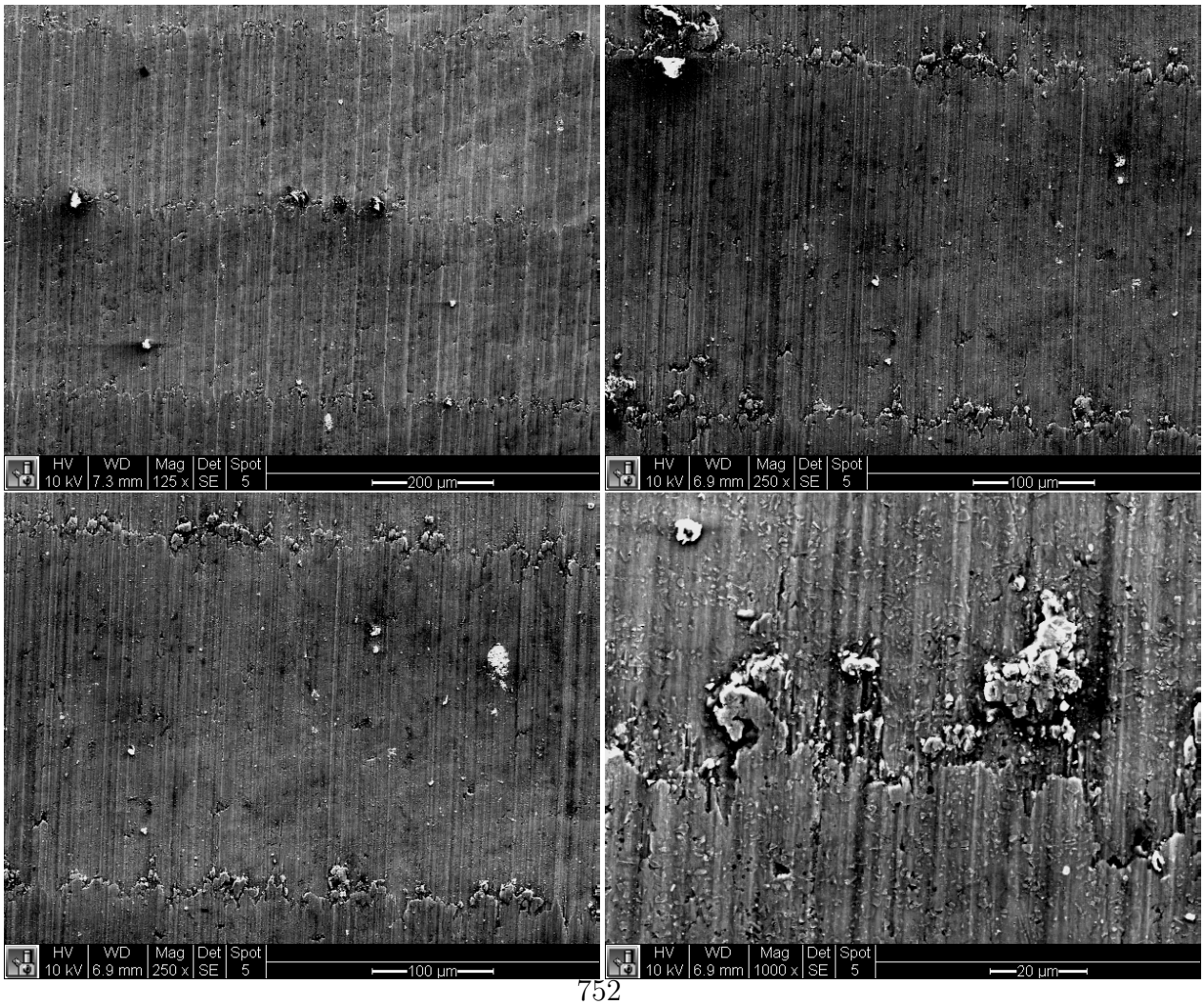

G.3.4 Peripherally milled, Feed: 0.3 mm/rev, Spindle speed: 1000 RPM

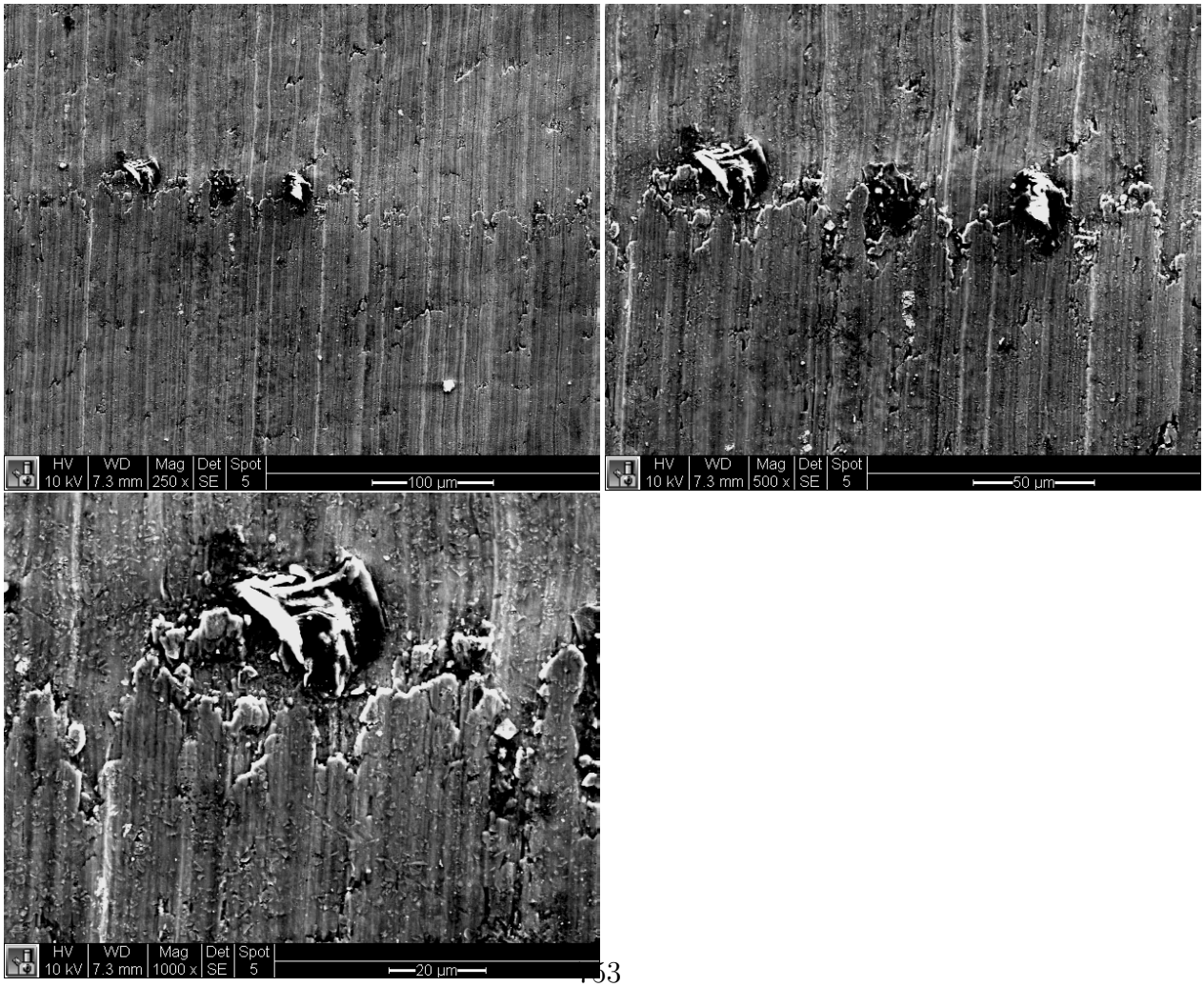

G.3.5 Face milled surface,Feed: 0.3 mm/rev, Spindle speed: 3000 RPM

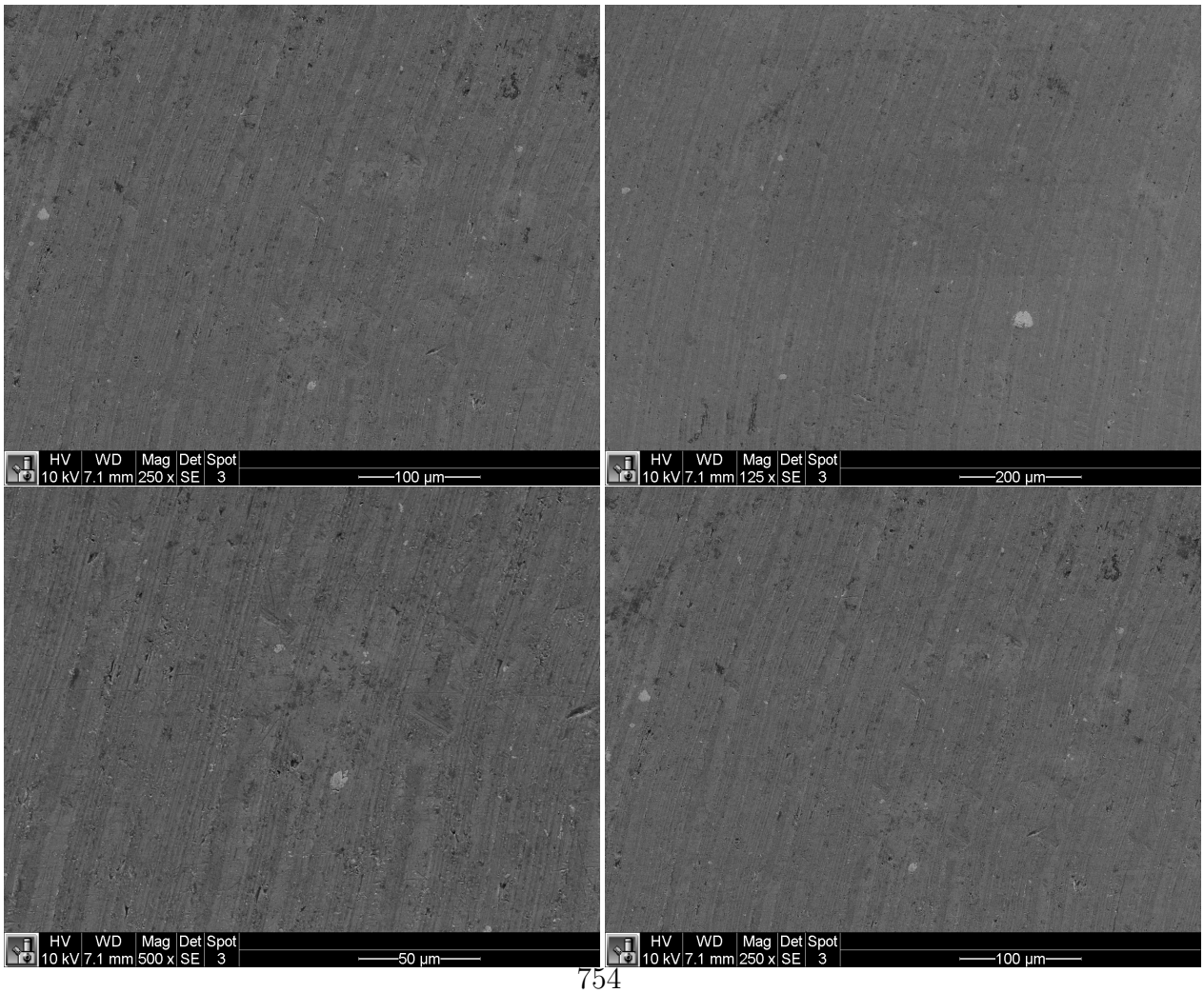

G.4 Fractography

G.4.1 $0.6S/S_{ut}$*, 0.1 mm/rev, 1000 RPM*

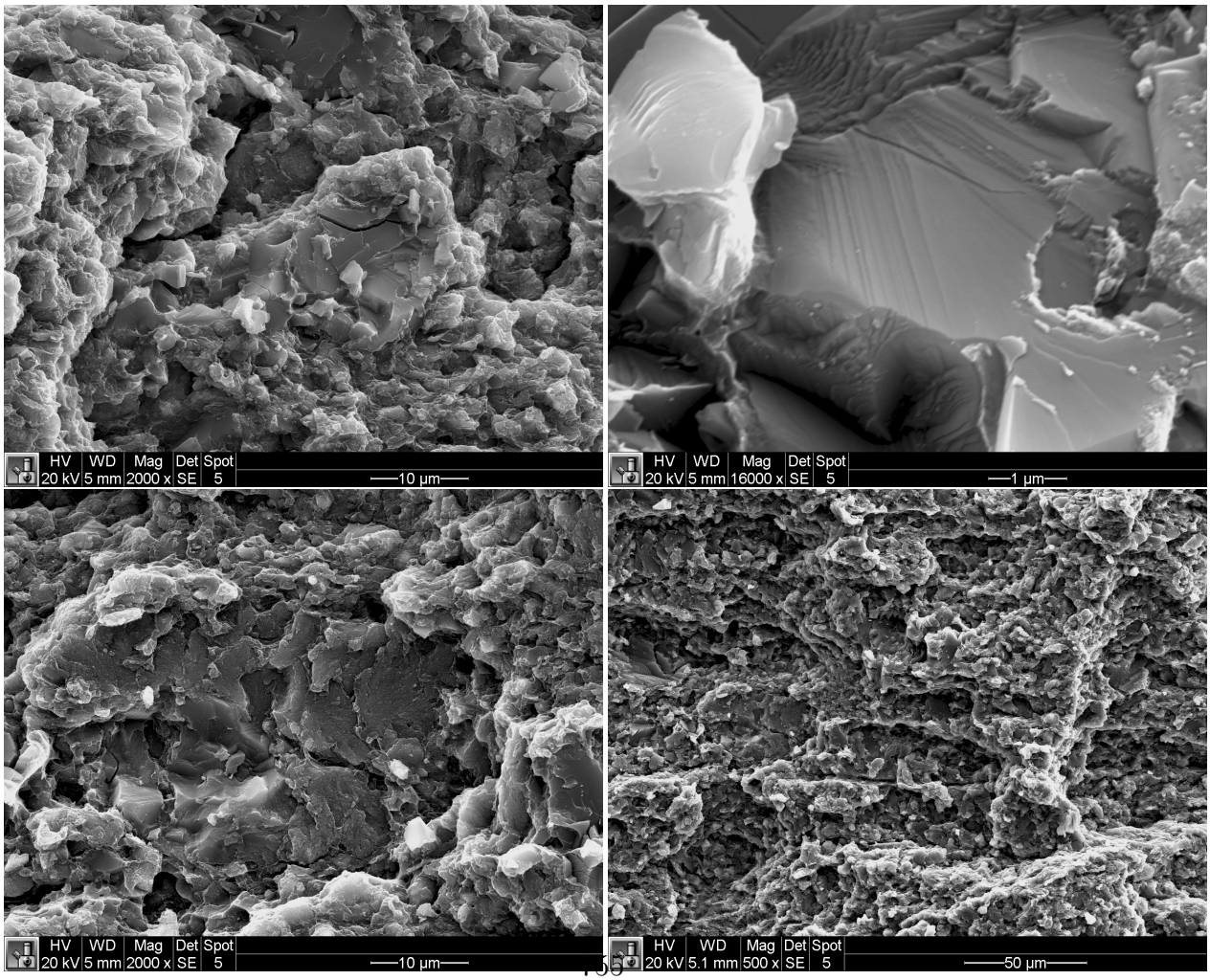

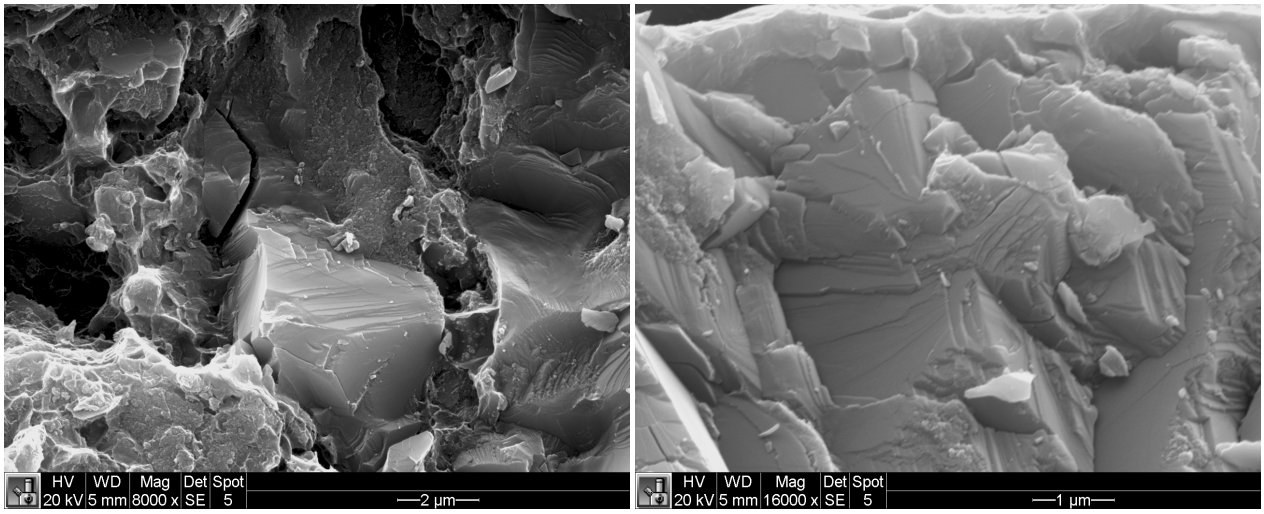
HV
20 kV
WD
5 mm
Mag
8000 x
Det
SE
Spot
5
2 µm
HV
20 kV
WD
5 mm
Mag
16000 x
Det
SE
Spot
5
1 µm

G.4.2 $0.6S/S_{ut}$*, 0.3 mm/rev, 3000 RPM*

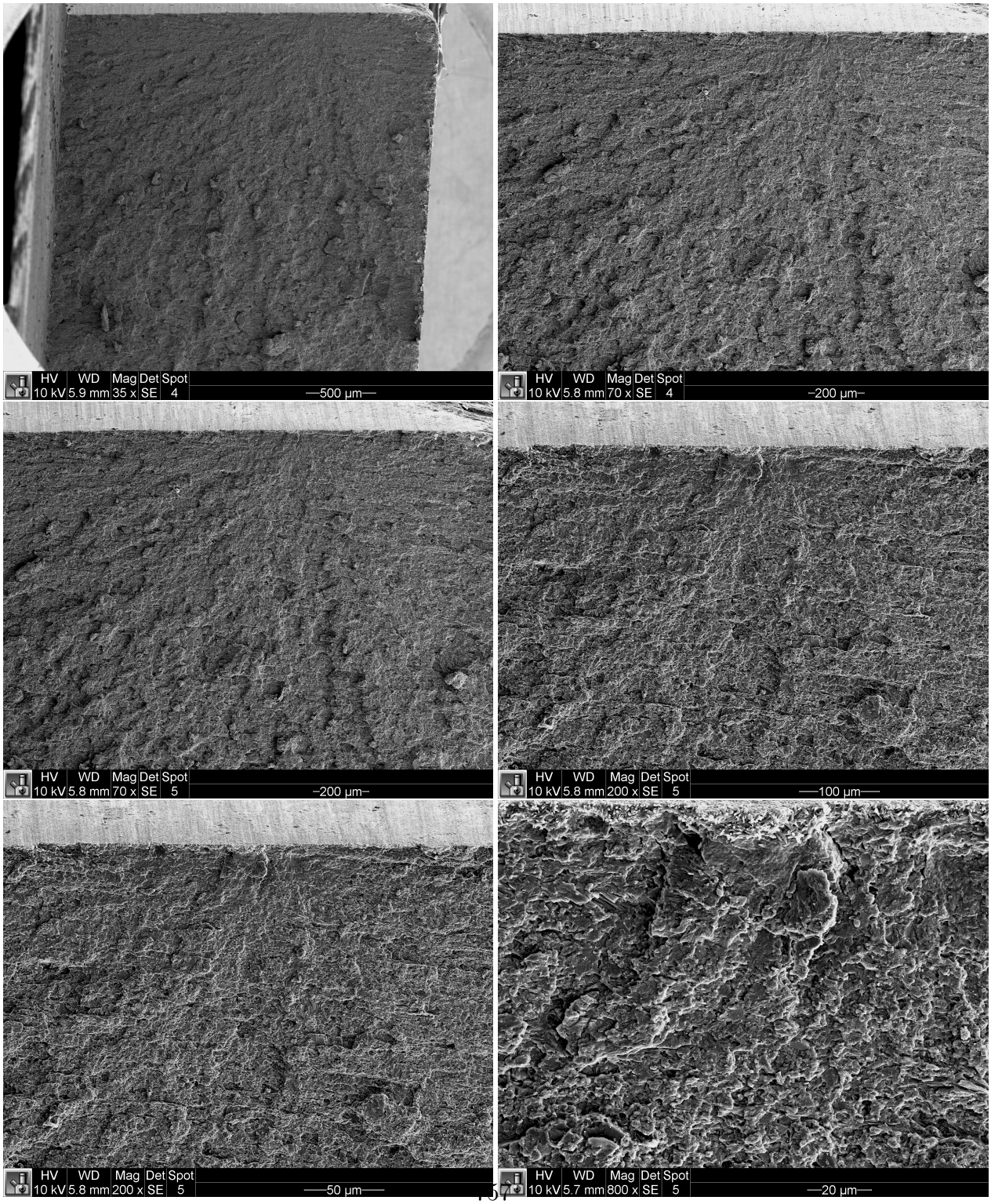

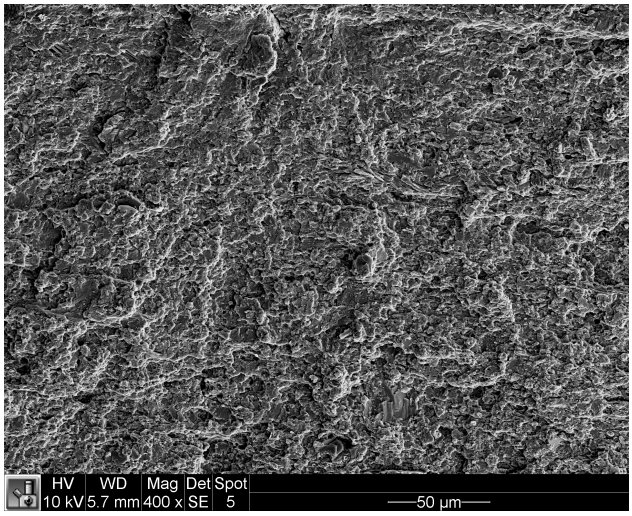
HV
10 kV
WD
5.7 mm
Mag
400 x
Det
SE
Spot
5
50 µm

G.4.3 Fracture mechanism, $0.8S/S_{ut}$, 0.3 mm/rev, 3000 RPM

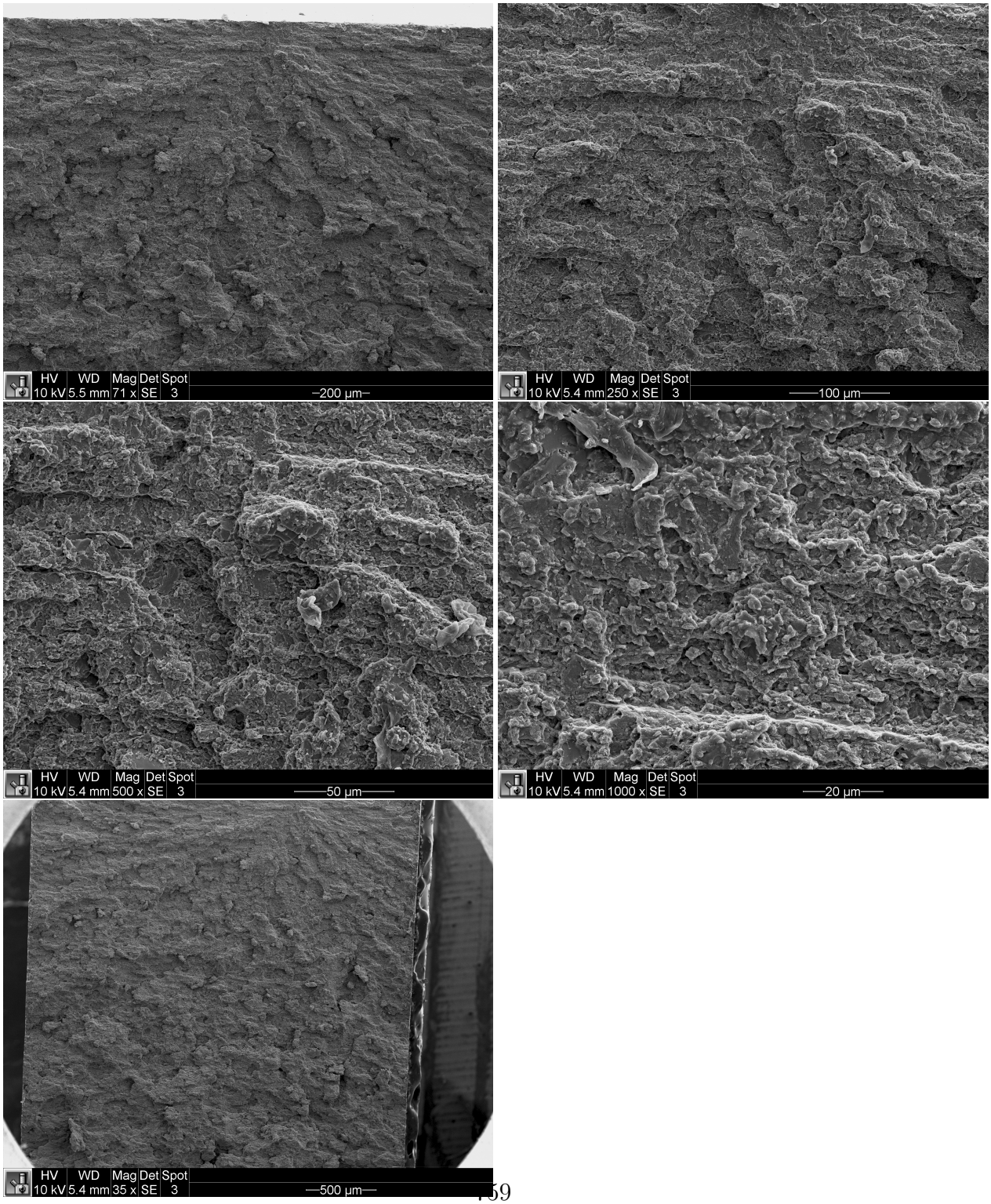

G.5 Fractured specimen, some used for further analysis

G.5.1 NA-1



G.5.2 NA-2



G.5.3 NA-4



G.5.4 NA-5

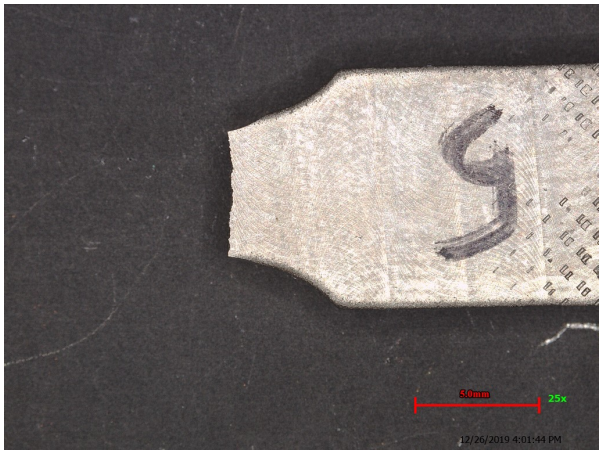

G.5.5 NA-7

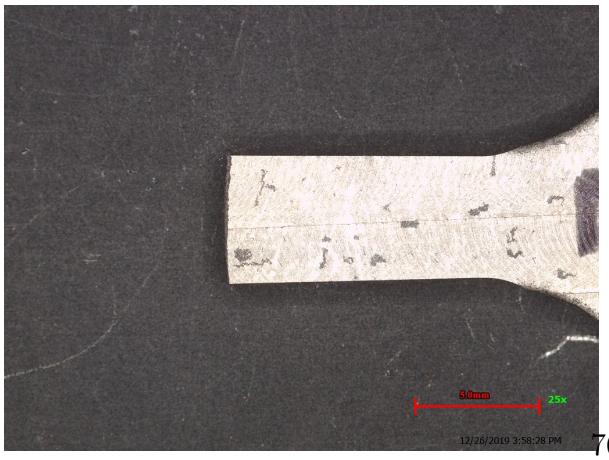

G.5.6 NA-10

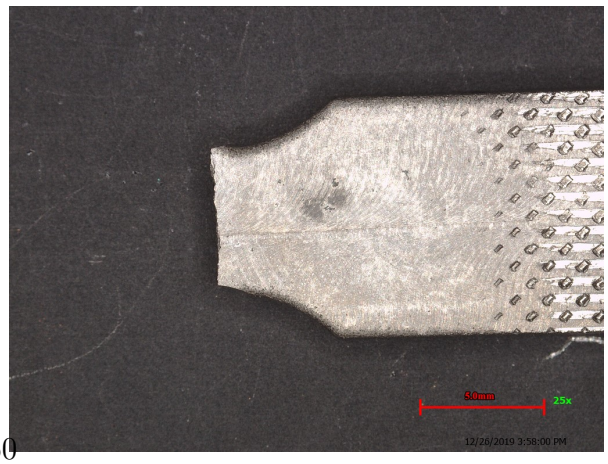

G.5.7 NA-11



G.5.8 NA-13

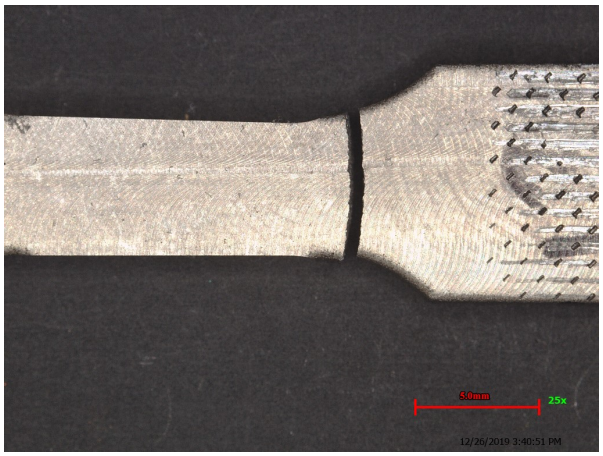

G.5.9 NA-19



G.5.10 NA-18

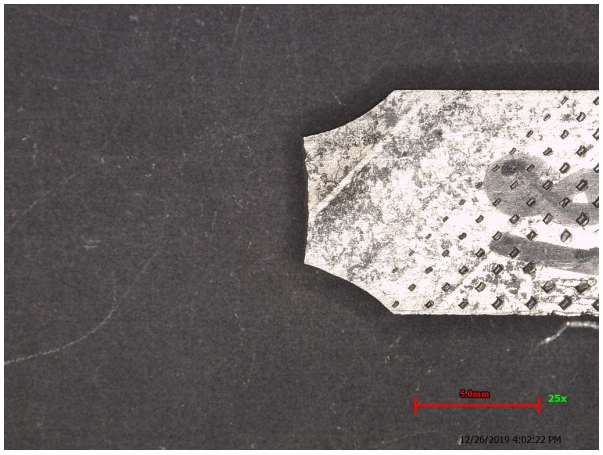

G.5.11 NA-20

G.6 Fractography, EDS results

G.6.1 NA-3

G.6.2 NA-6

G.6.3 NA-1



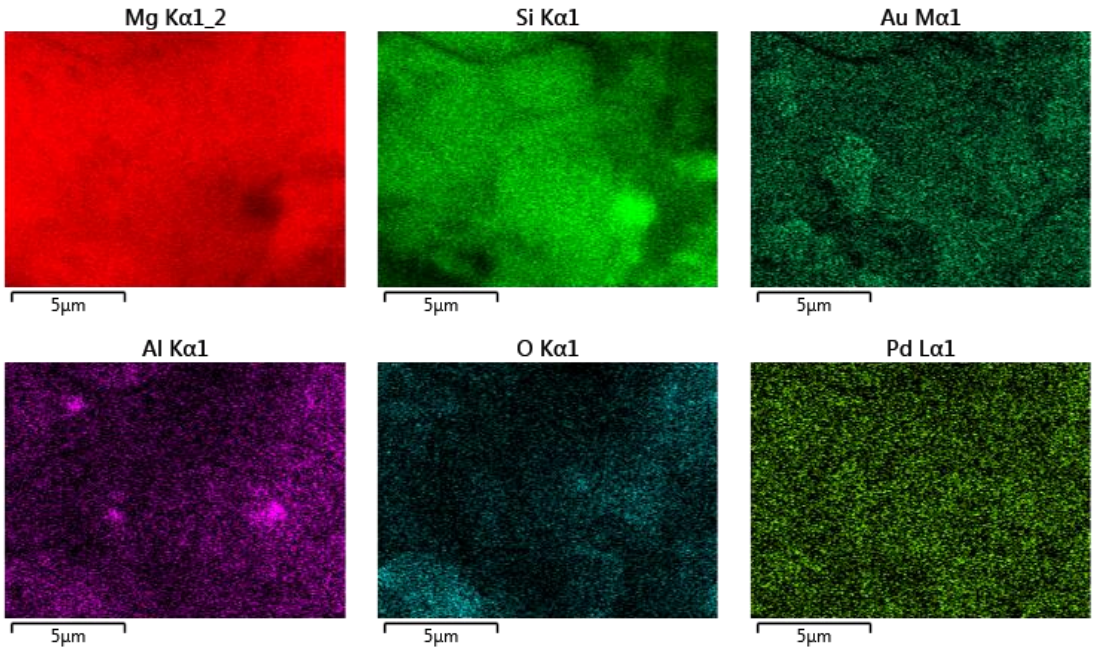
Mg Kα1_2
5µm
Si Kα1
5µm
Au Mα1
5µm
Al Kα1
5µm
O Kα1
5µm
Pd Lα1
5µm

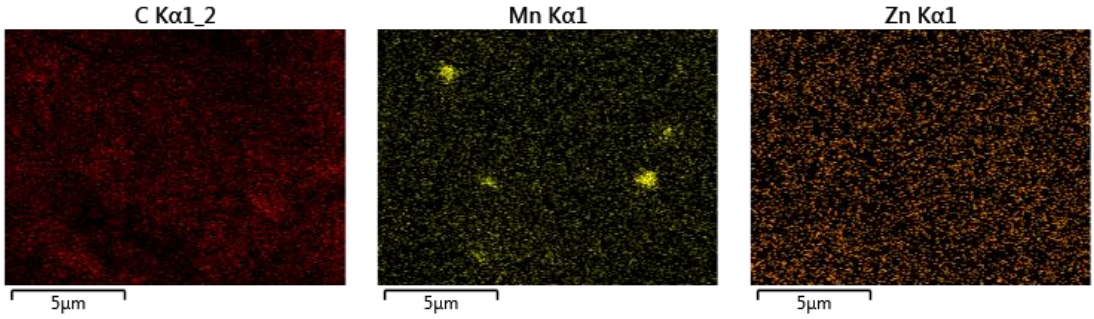
C Kα1_2
5µm
Mn Kα1
5µm
Zn Kα1
5µm

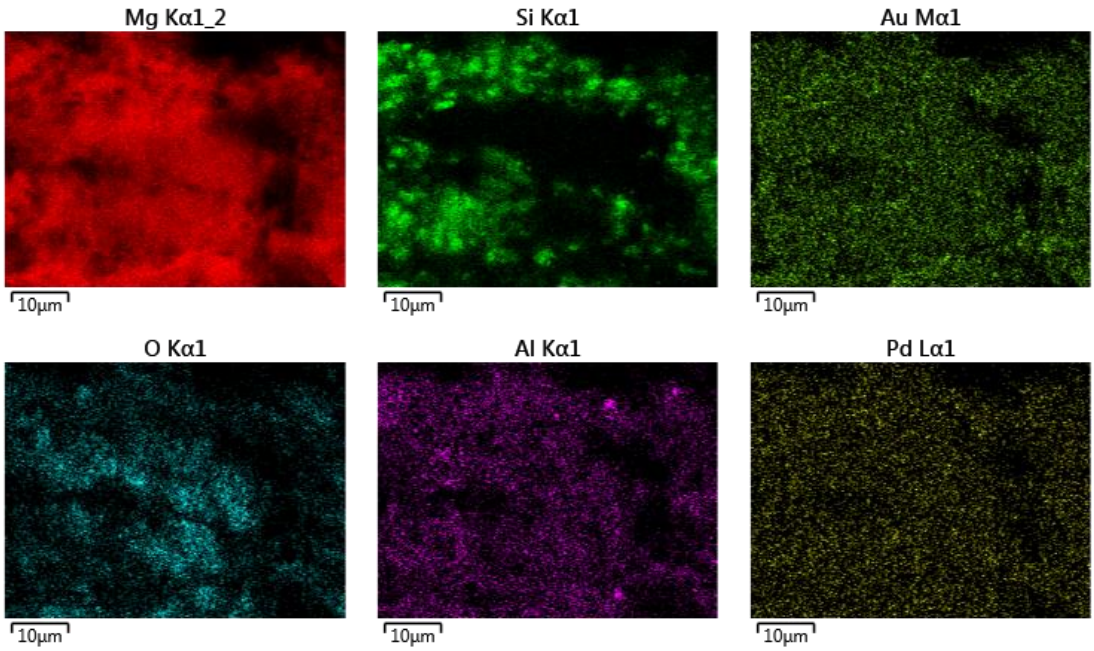
Mg Kα1_2
Si Kα1
Au Mα1
O Kα1
Al Kα1
Pd Lα1
10µm

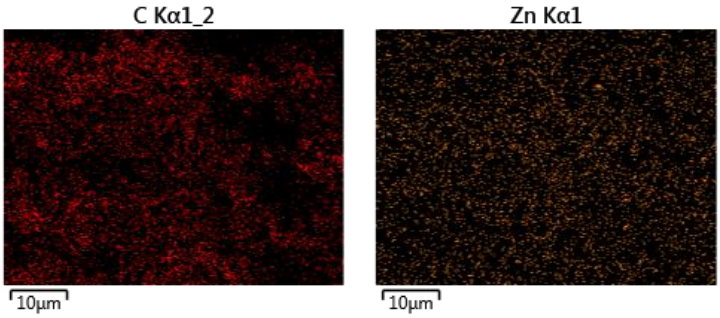
C Kα1_2
10μm
Zn Kα1
10μm

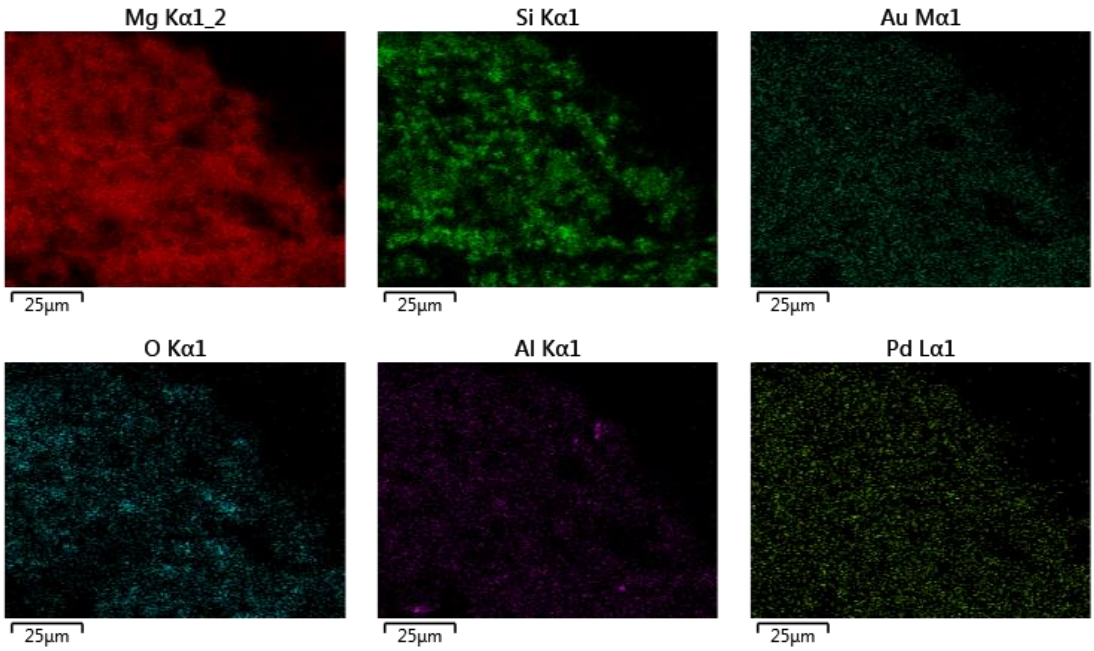
Mg Kα1_2
25µm
Si Kα1
25µm
Au Mα1
25µm
O Kα1
25µm
Al Kα1
25µm
Pd Lα1
25µm

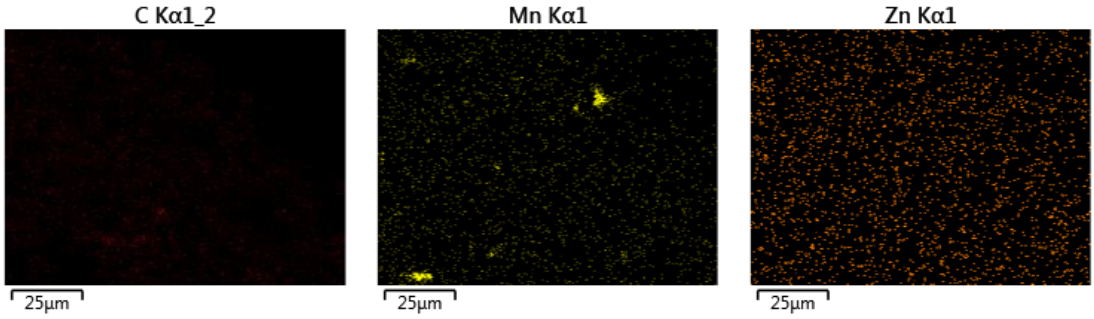
C Kα1_2
Mn Kα1
Zn Kα1
25µm
25µm
25µm

G.6.4 NA-21

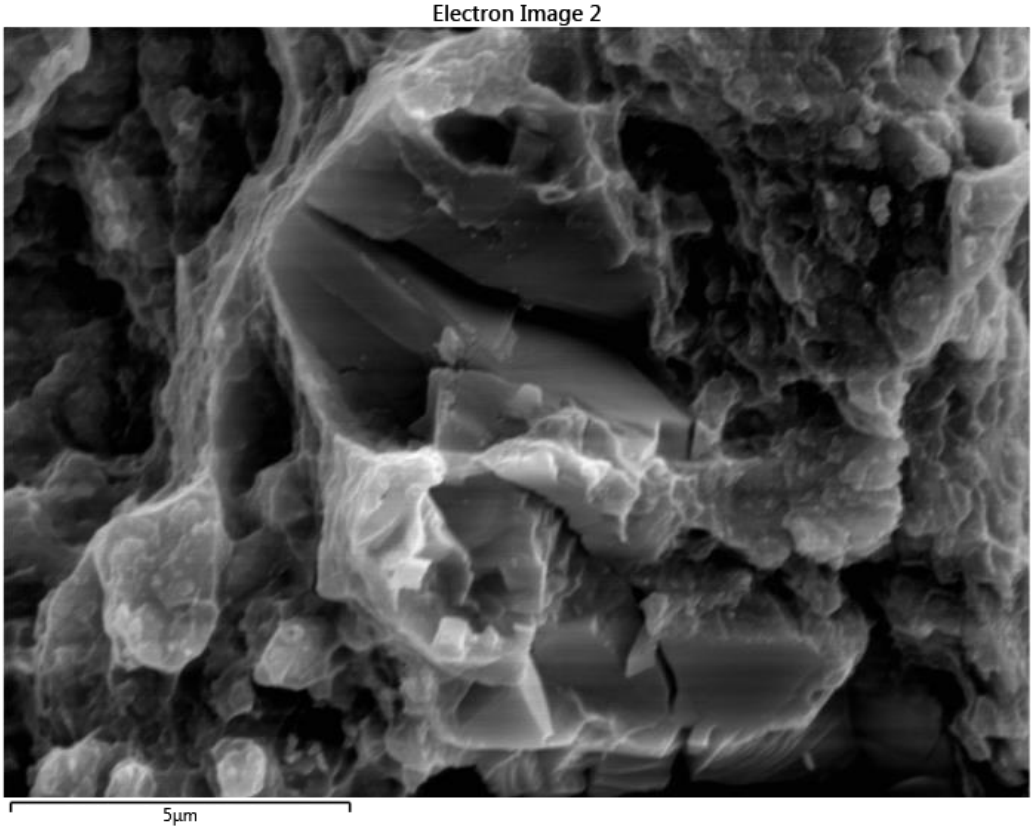
Electron Image 2
5µm

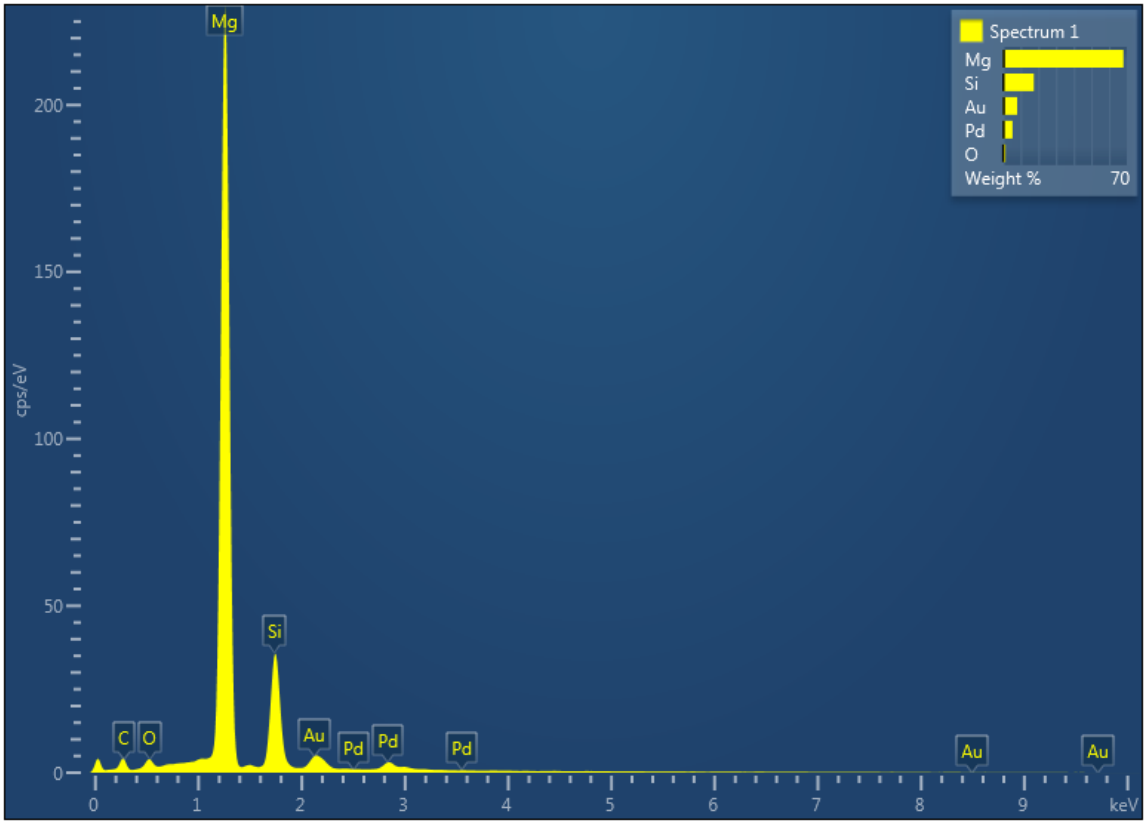
Spectrum 1
Mg
Si
Au
Pd
O
Weight %
70
cps/eV
200
150
100
50
0
Mg
Si
C
O
Au
Pd
Pd
Pd
Au
Au
0
1
2
3
4
5
6
7
8
9
keV

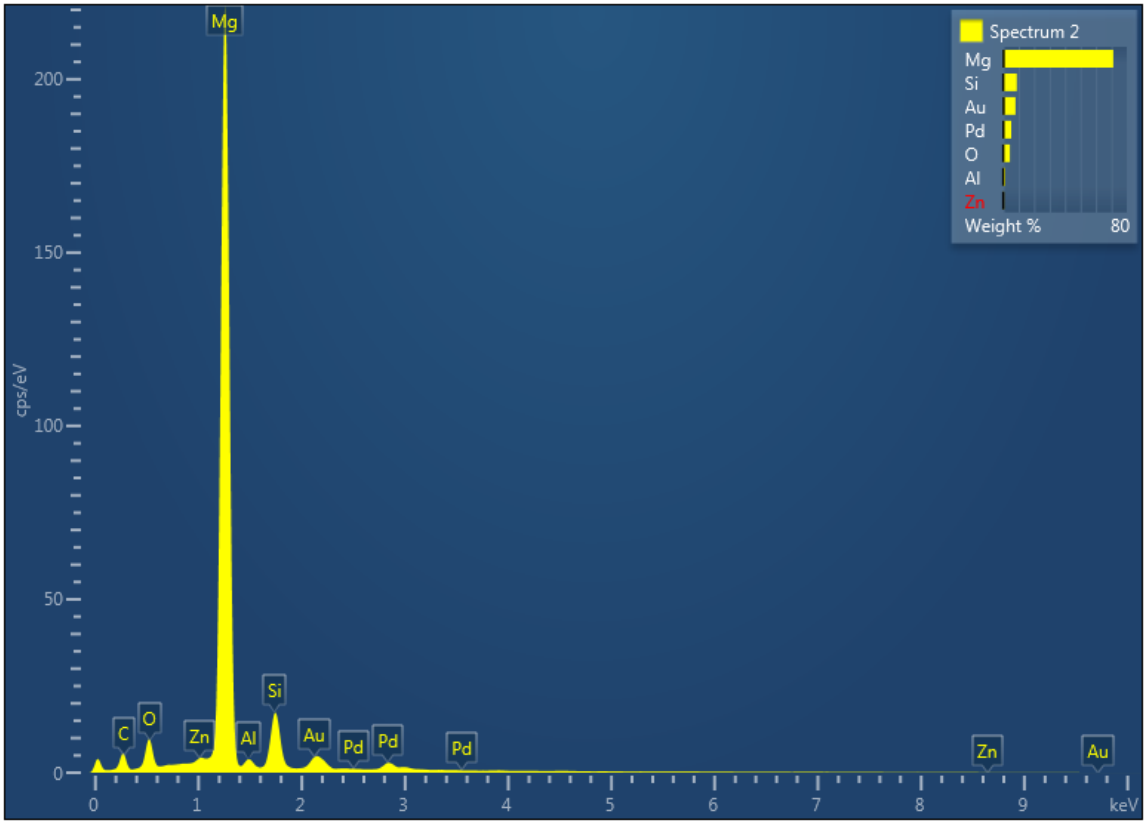
Spectrum 2
Mg
Si
Au
Pd
O
Al
Zn
Weight %
80
cps/eV
200
150
100
50
0
Mg
C
O
Zn
Al
Si
Au
Pd
Pd
Pd
Zn
Au
0
1
2
3
4
5
6
7
8
9
keV

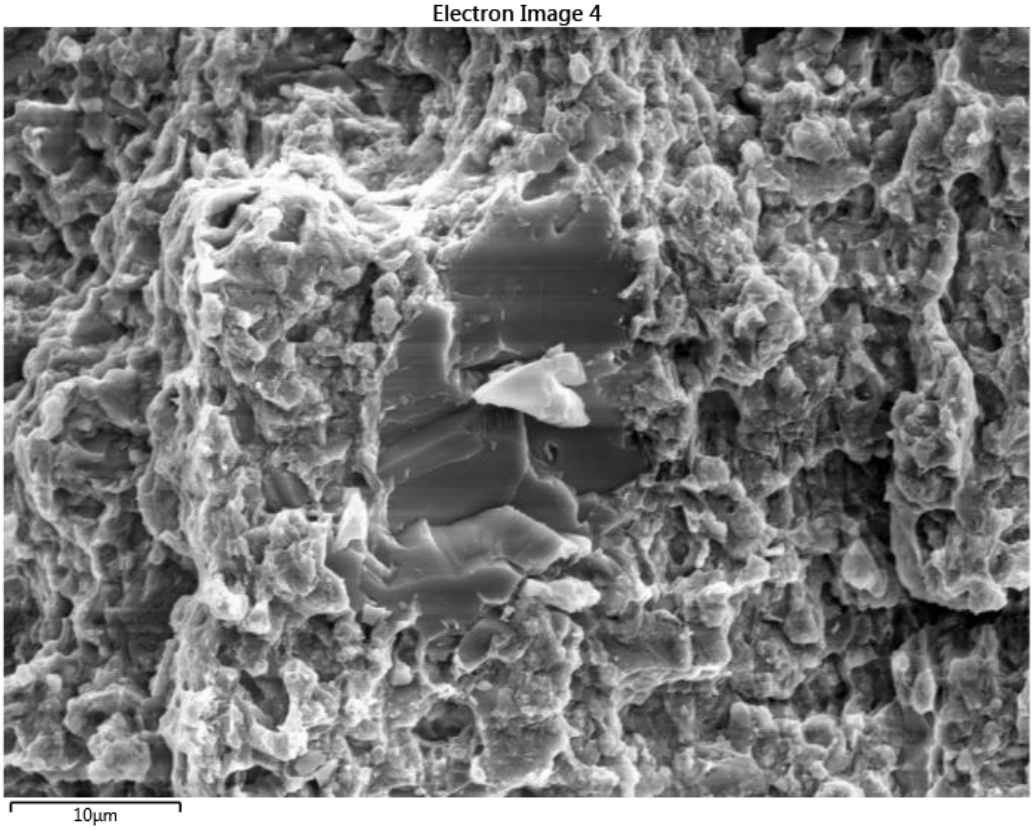
Electron Image 4
10µm

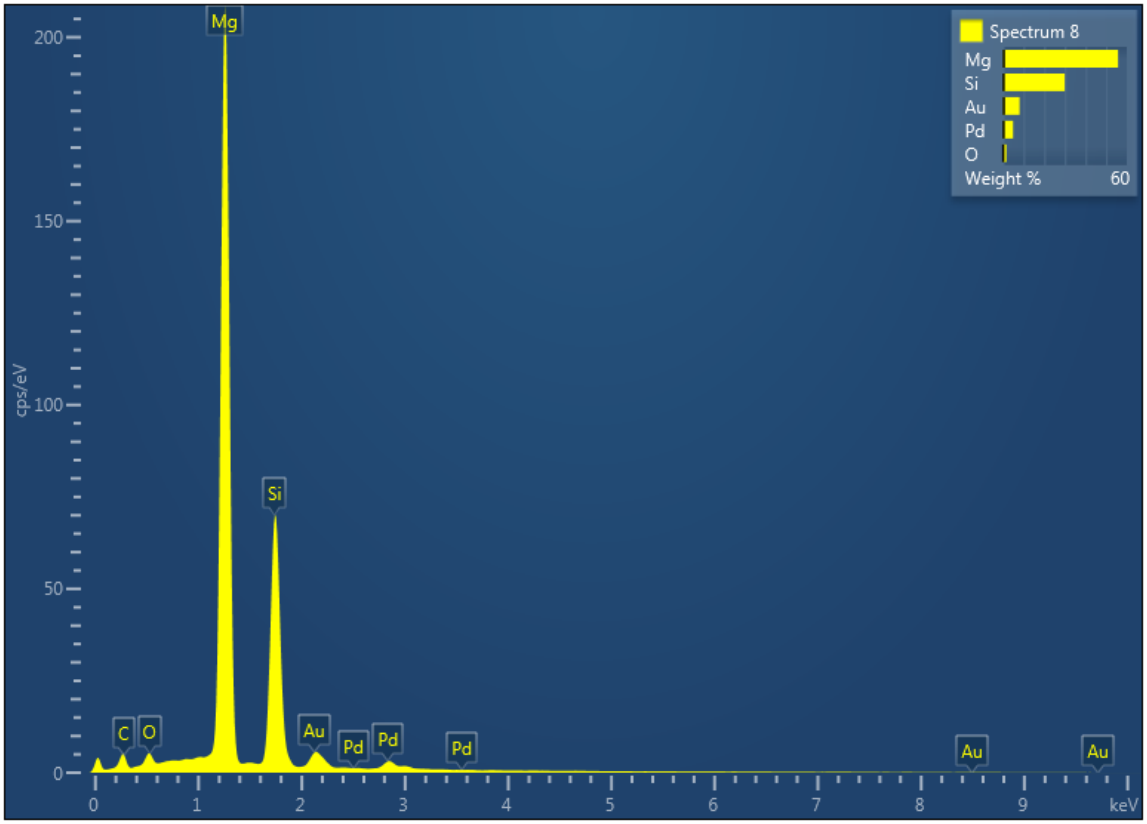
Spectrum 8
Mg
Si
Au
Pd
O
Weight %
60
cps/eV
200
150
100
50
0
Mg
Si
C
O
Au
Pd
Pd
Pd
Au
Au
0
1
2
3
4
5
6
7
8
9
keV

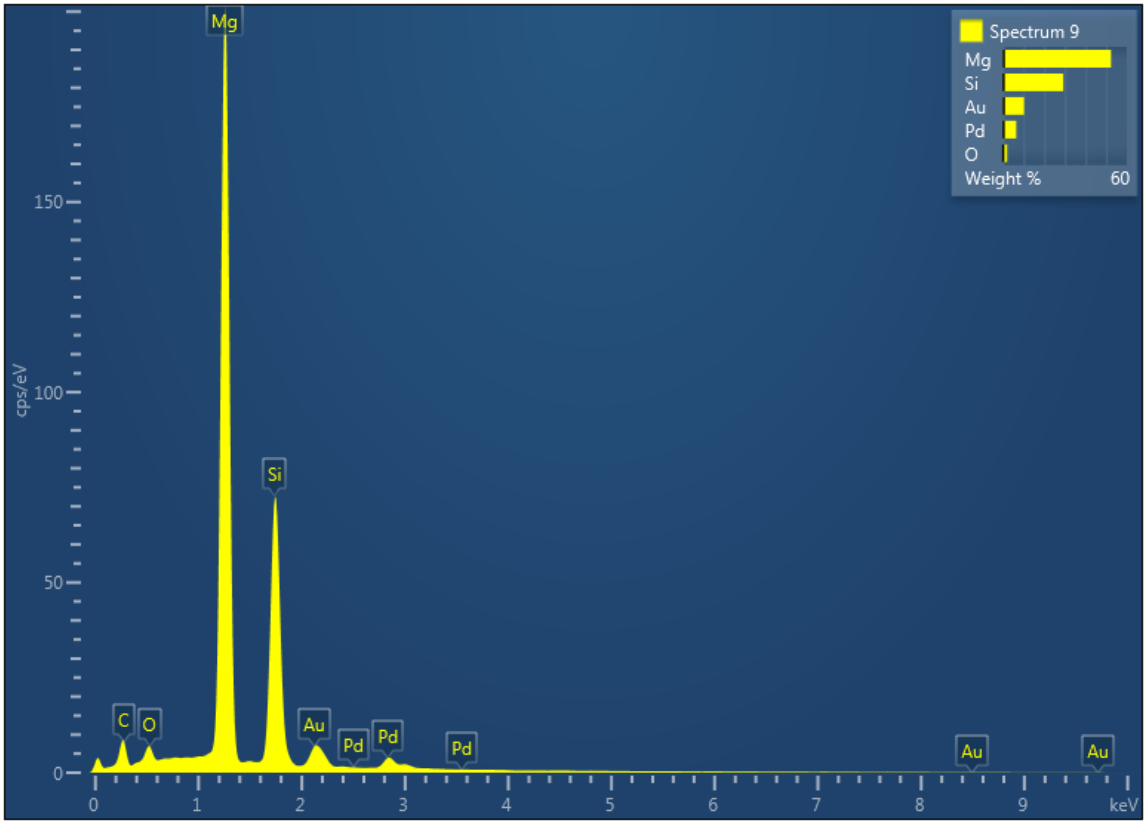
Spectrum 9
Mg
Si
Au
Pd
O
Weight %
60
cps/eV
150
100
50
0
Mg
Si
C
O
Au
Pd
Pd
Pd
Au
Au
0
1
2
3
4
5
6
7
8
9
keV

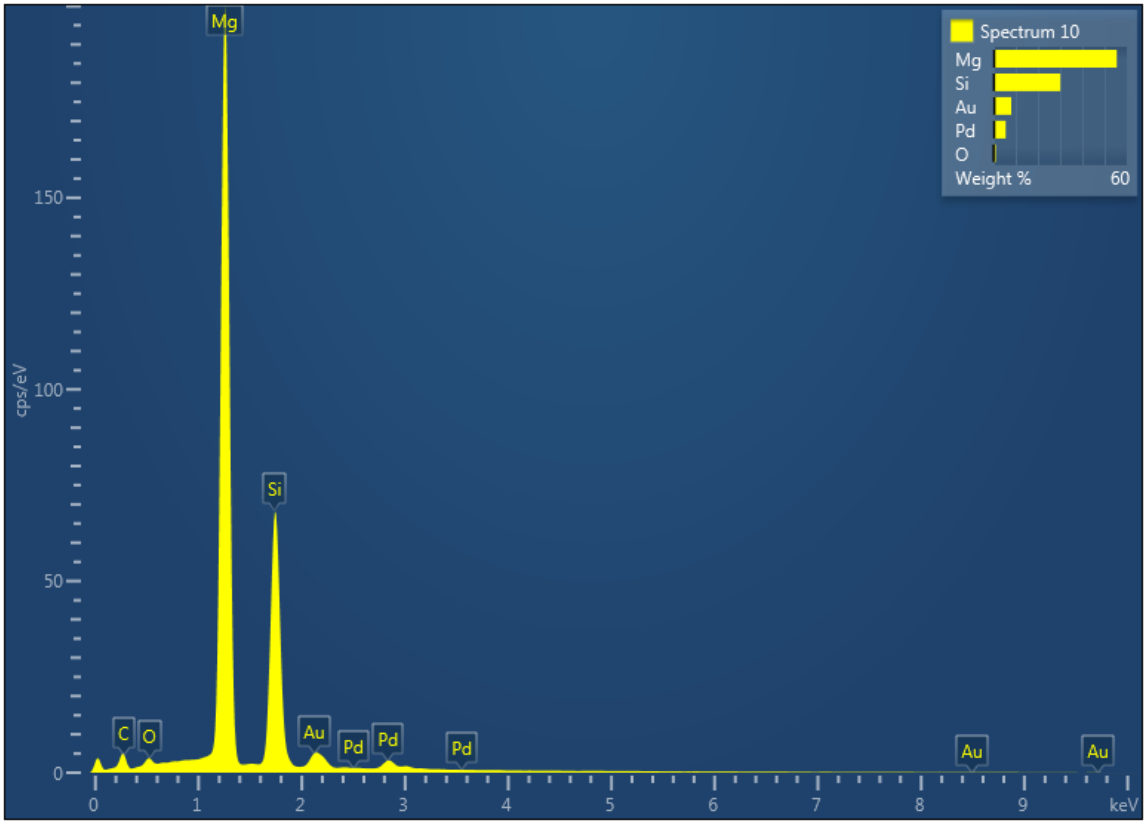
Spectrum 10
Mg
Si
Au
Pd
O
Weight %
60
cps/eV
150
100
50
0
Mg
Si
C
O
Au
Pd
Pd
Pd
Au
Au
0
1
2
3
4
5
6
7
8
9
keV

Electron Image 5

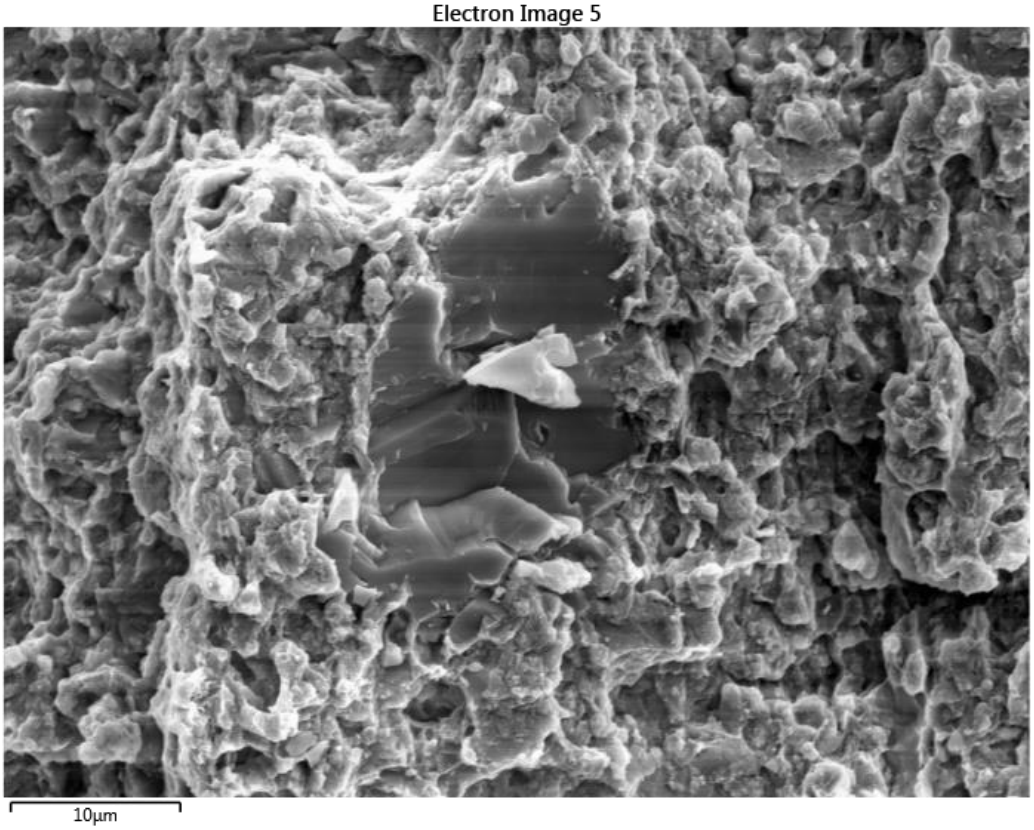

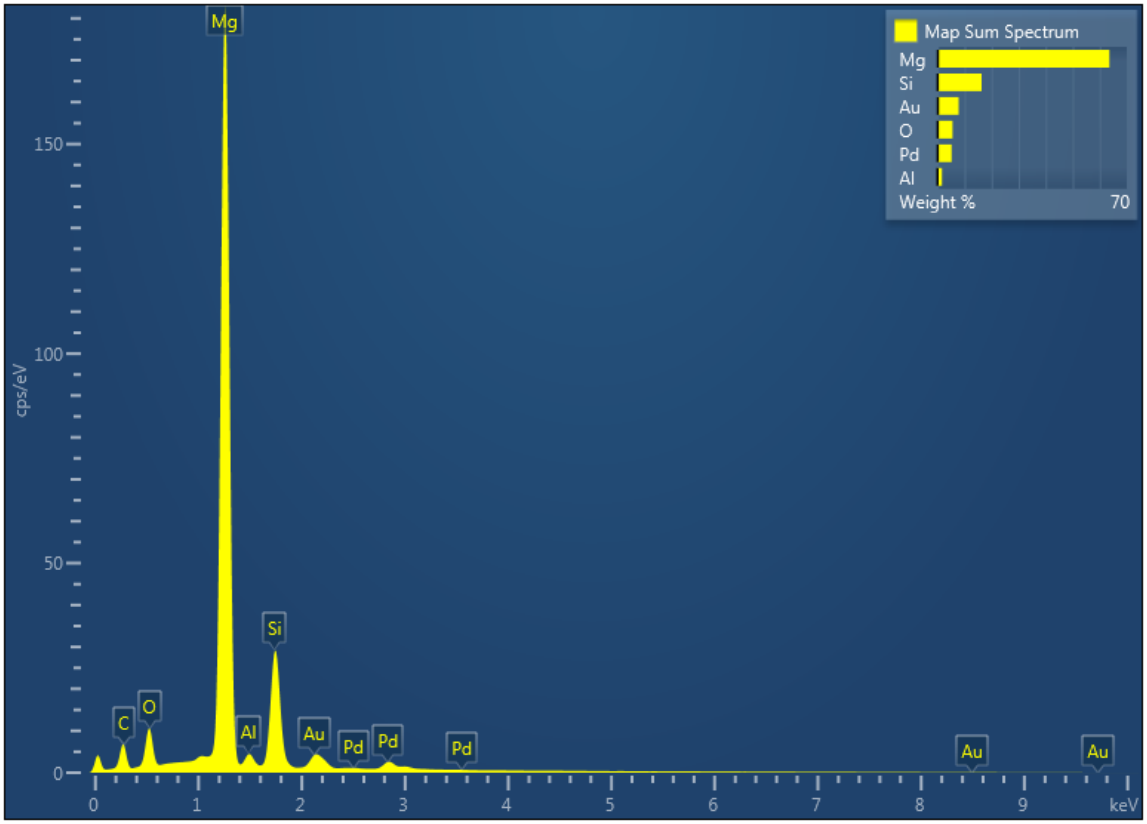
Map Sum Spectrum
Mg
Si
Au
O
Pd
Al
Weight %
70
cps/eV
150
100
50
0
C
O
Mg
Al
Si
Au
Pd
Pd
Pd
Au
Au
0
1
2
3
4
5
6
7
8
9
keV

G.6.5 NA-2

EDS Layered Image 1

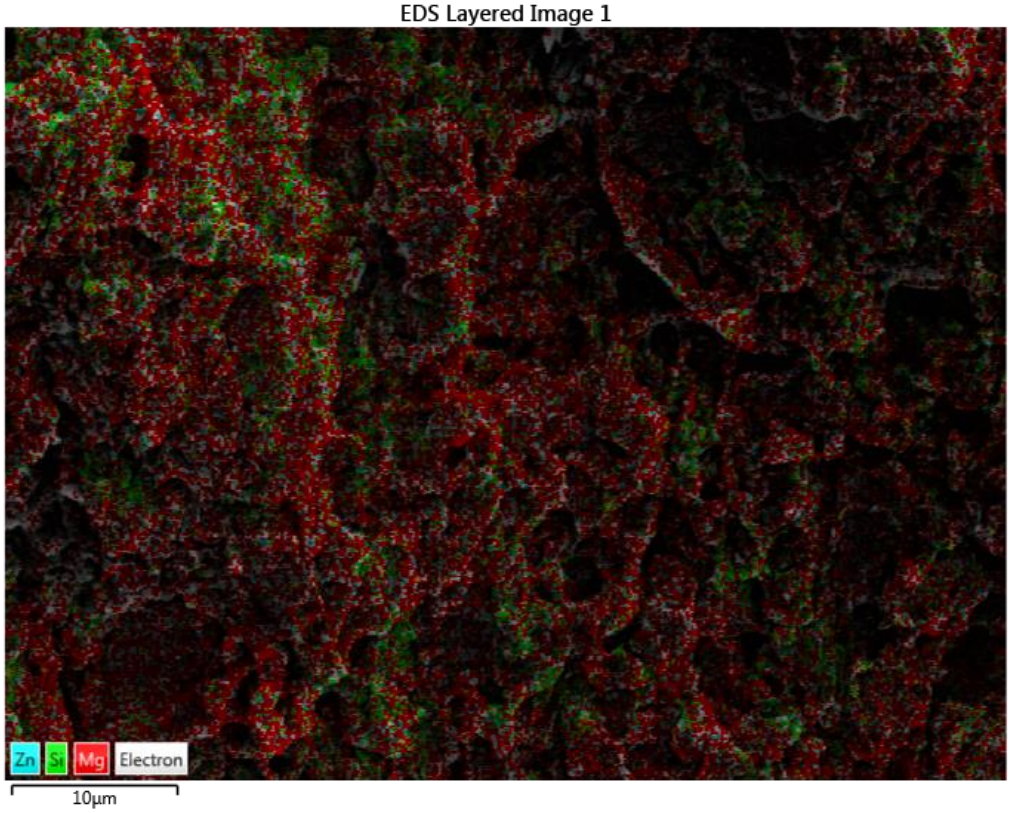

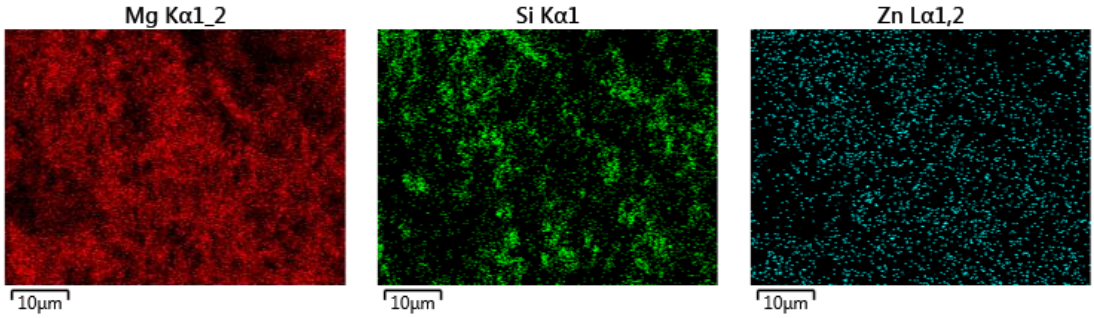
Mg Kα1_2
Si Kα1
Zn Lα1,2
10µm
10µm
10µm

EDS Layered Image 2

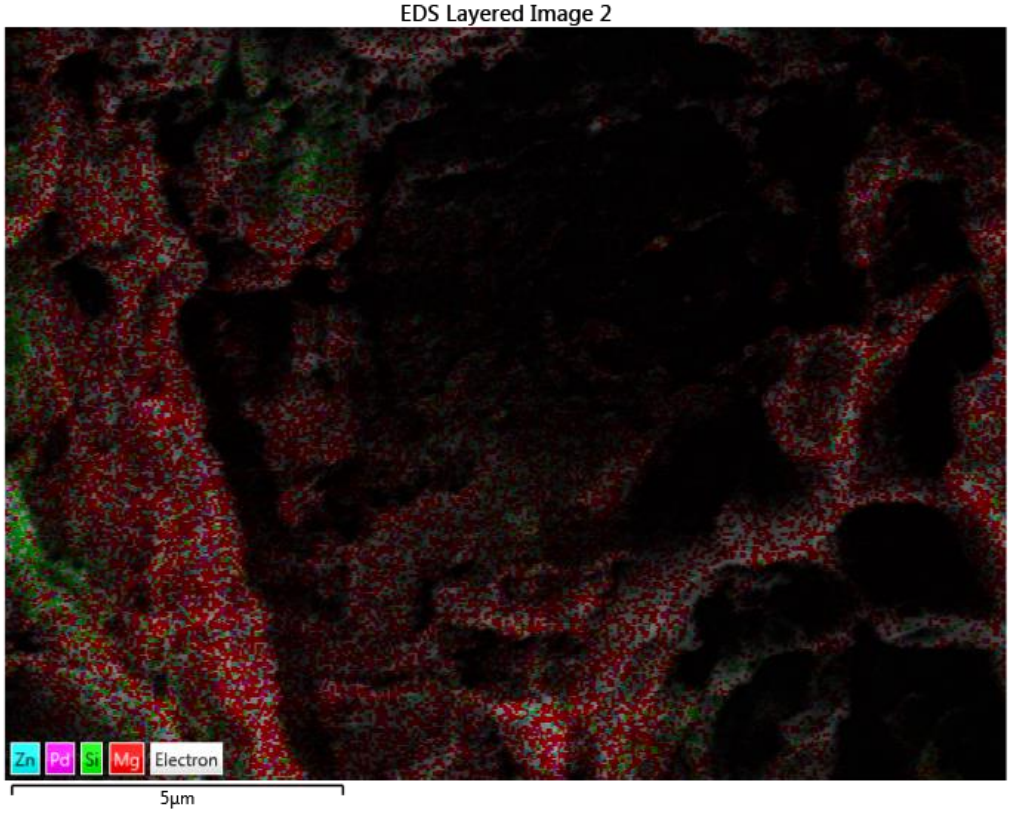

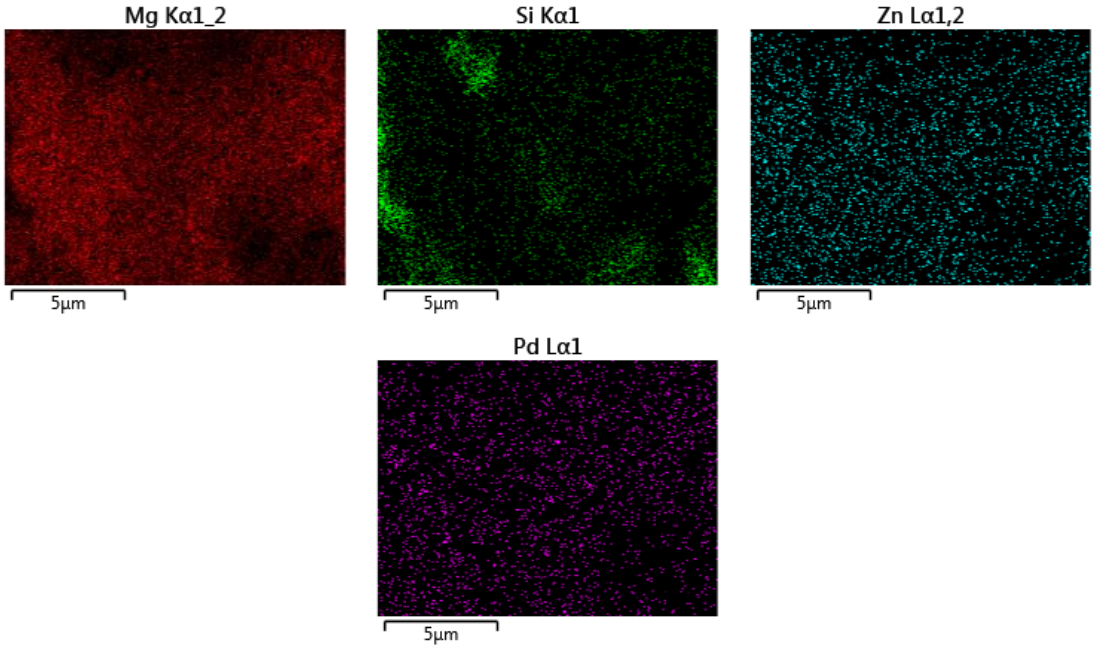
Mg Kα1_2
5µm
Si Kα1
5µm
Zn Lα1,2
5µm
Pd Lα1
5µm

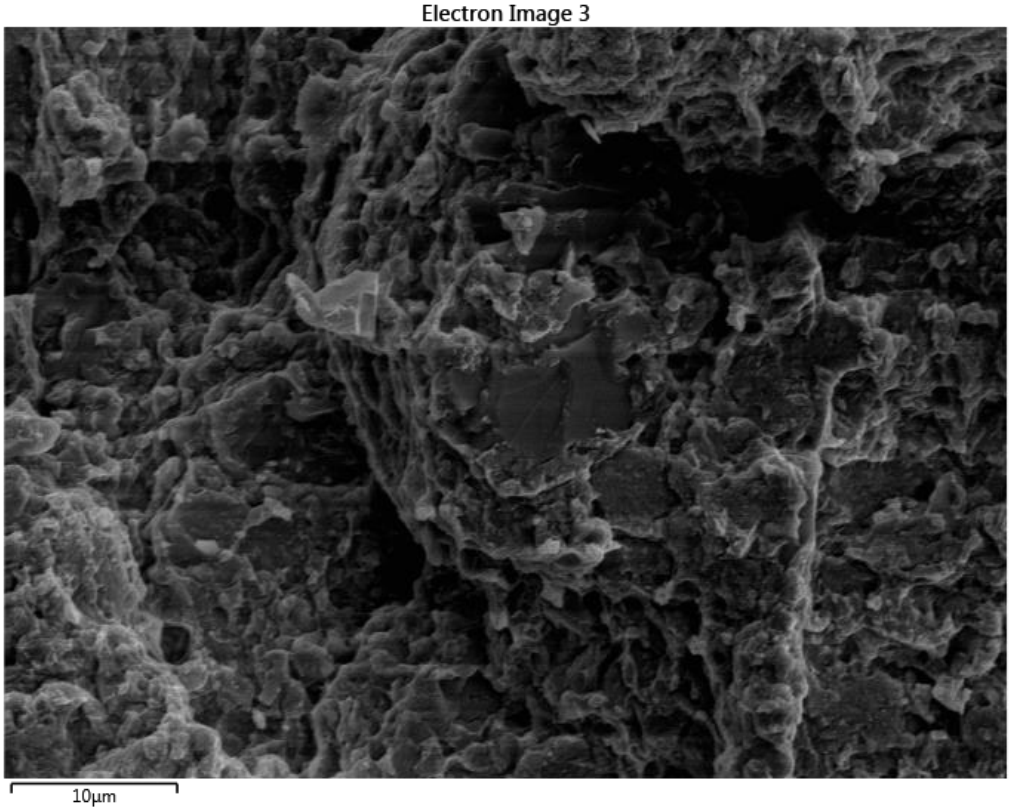
Electron Image 3
10µm

EDS Layered Image 3

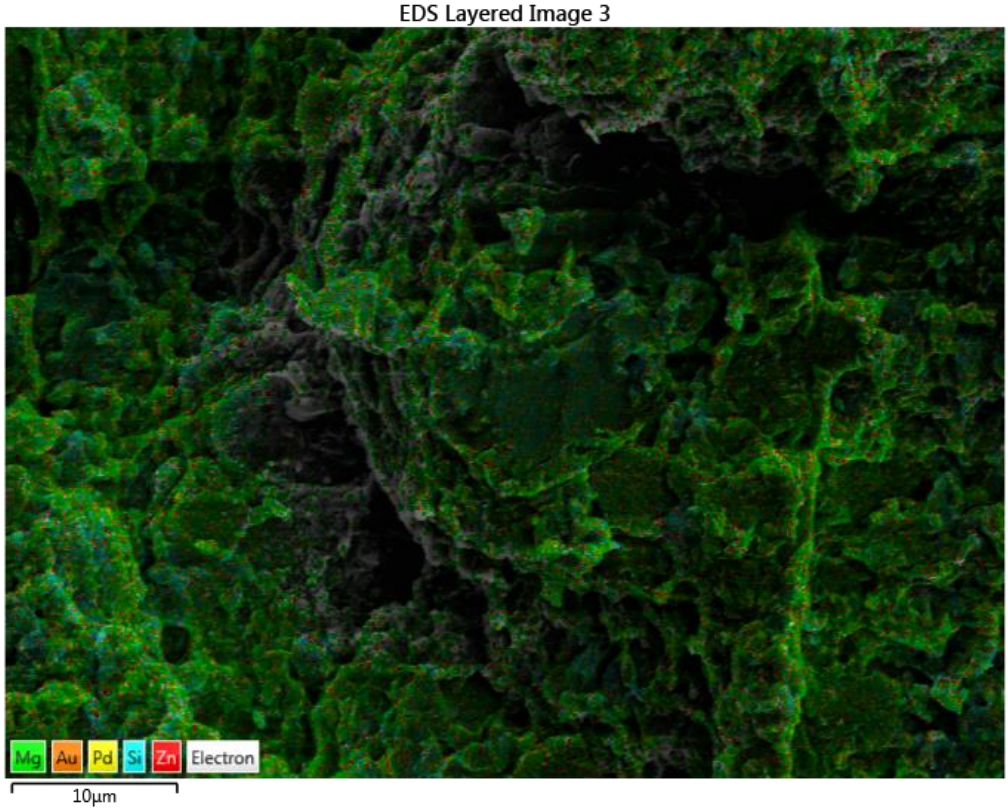

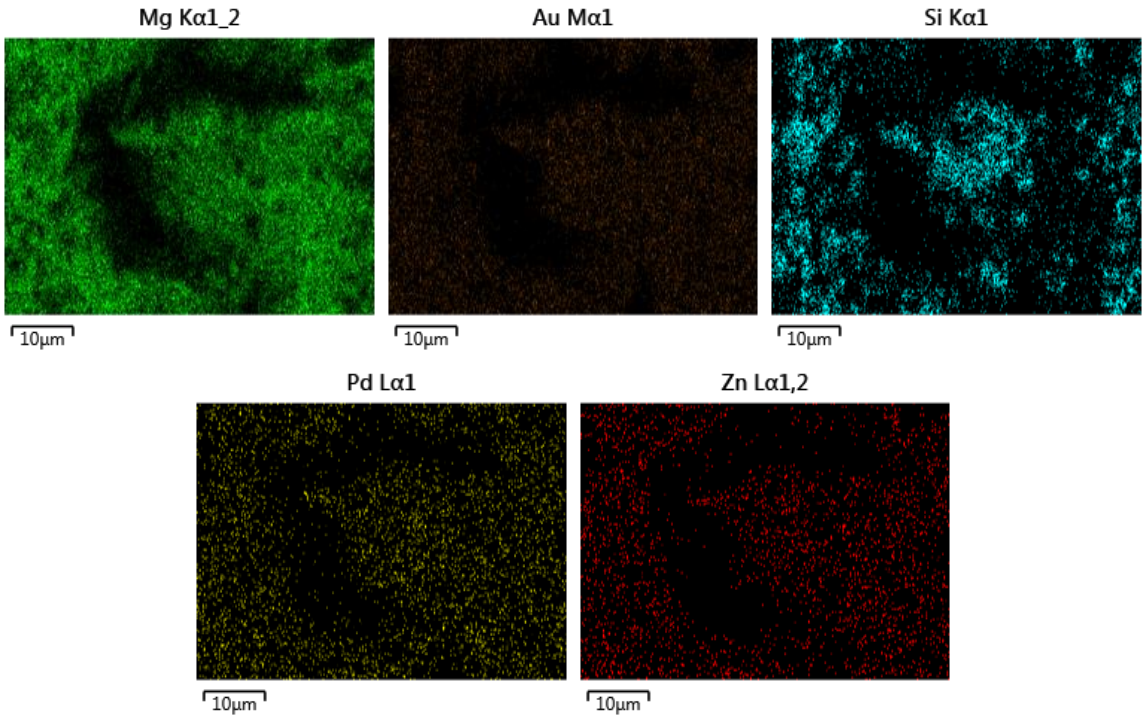
Mg Kα1_2
10µm
Au Mα1
10µm
Si Kα1
10µm
Pd Lα1
10µm
Zn Lα1,2
10µm

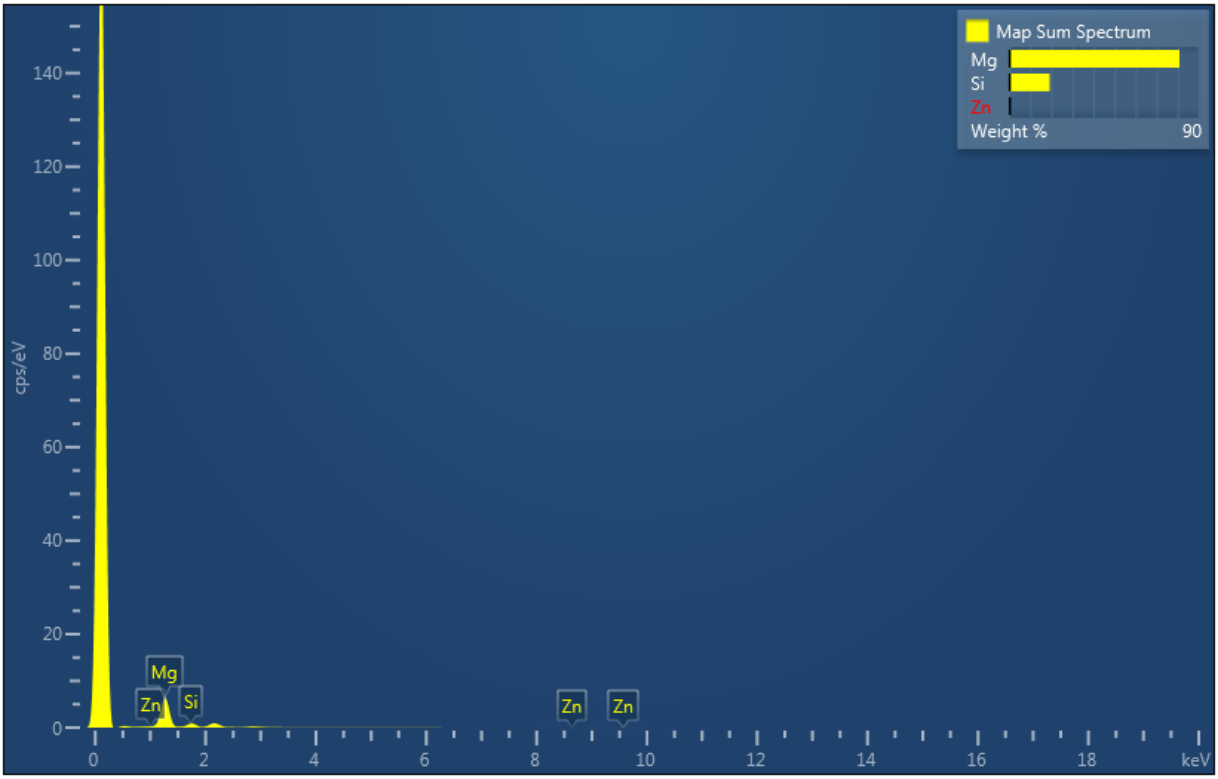
Map Sum Spectrum
Mg
Si
Zn
Weight %
90
cps/eV
140
120
100
80
60
40
20
0
Mg
Zn
Si
Zn
Zn
0
2
4
6
8
10
12
14
16
18
keV

G.6.6 NA-7

EDS Layered Image 1

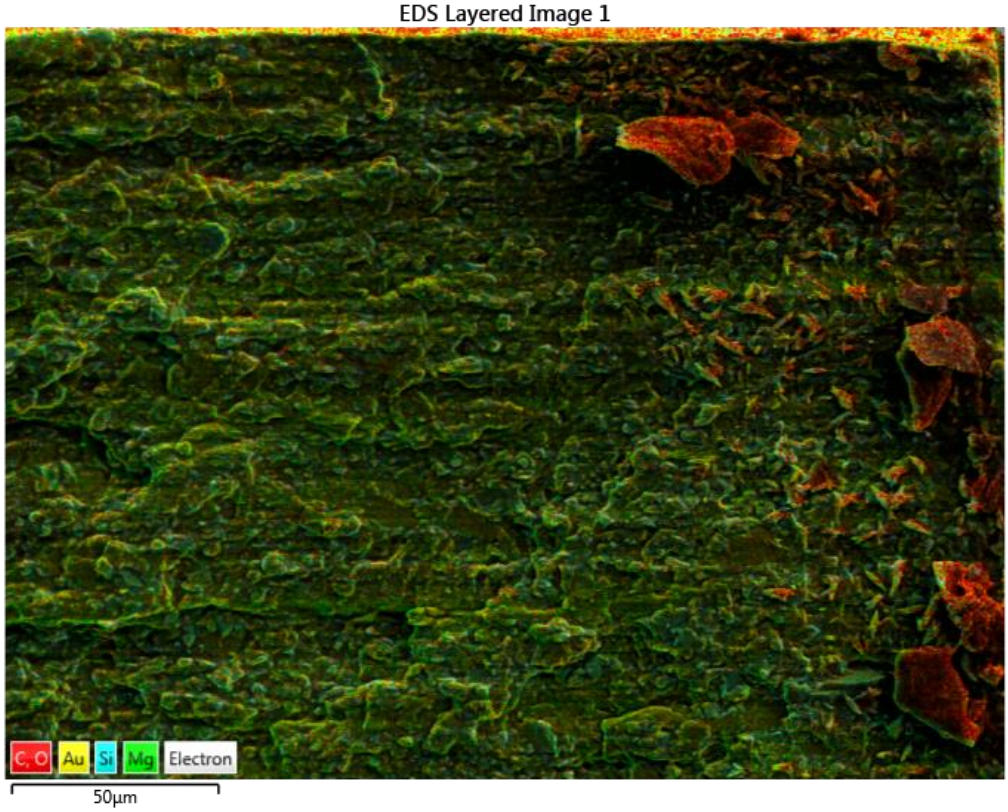

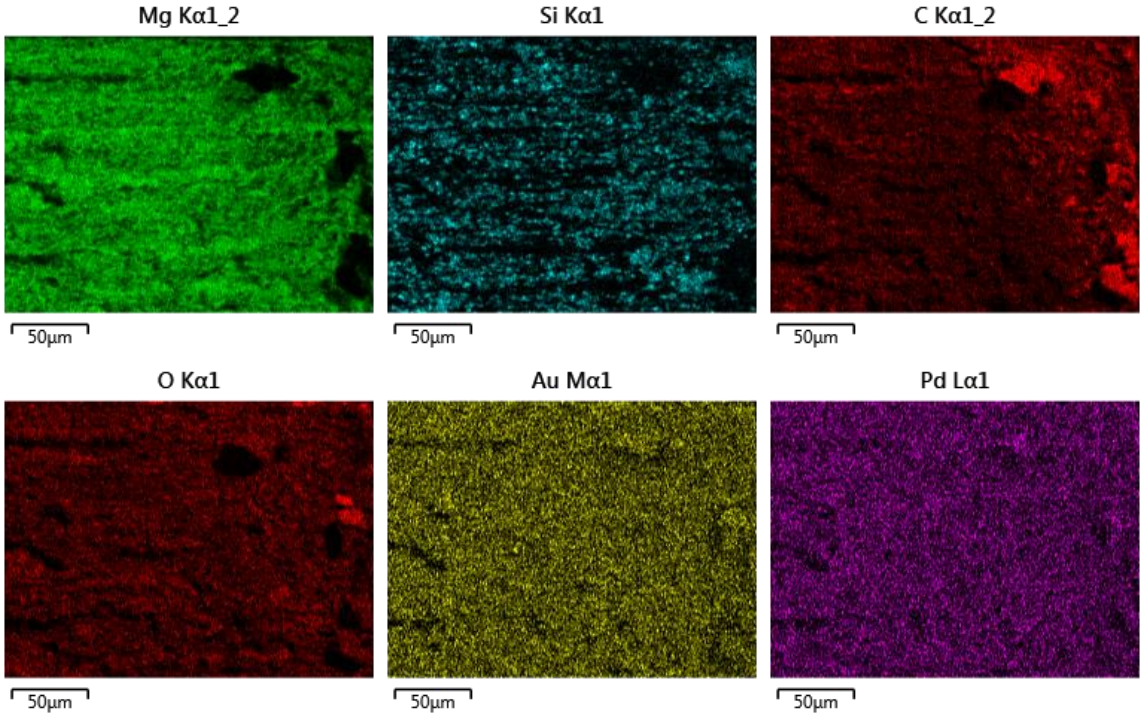
Mg Kα1_2
Si Kα1
C Kα1_2
50µm
50µm
50µm
O Kα1
Au Mα1
Pd Lα1
50µm
50µm
50µm

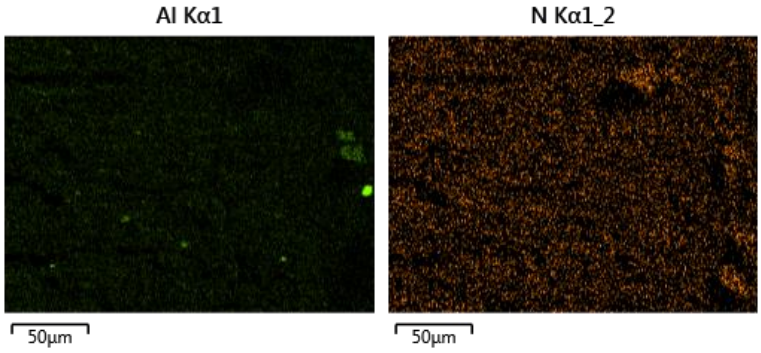
Al Kα1
N Kα1_2
50μm
50μm

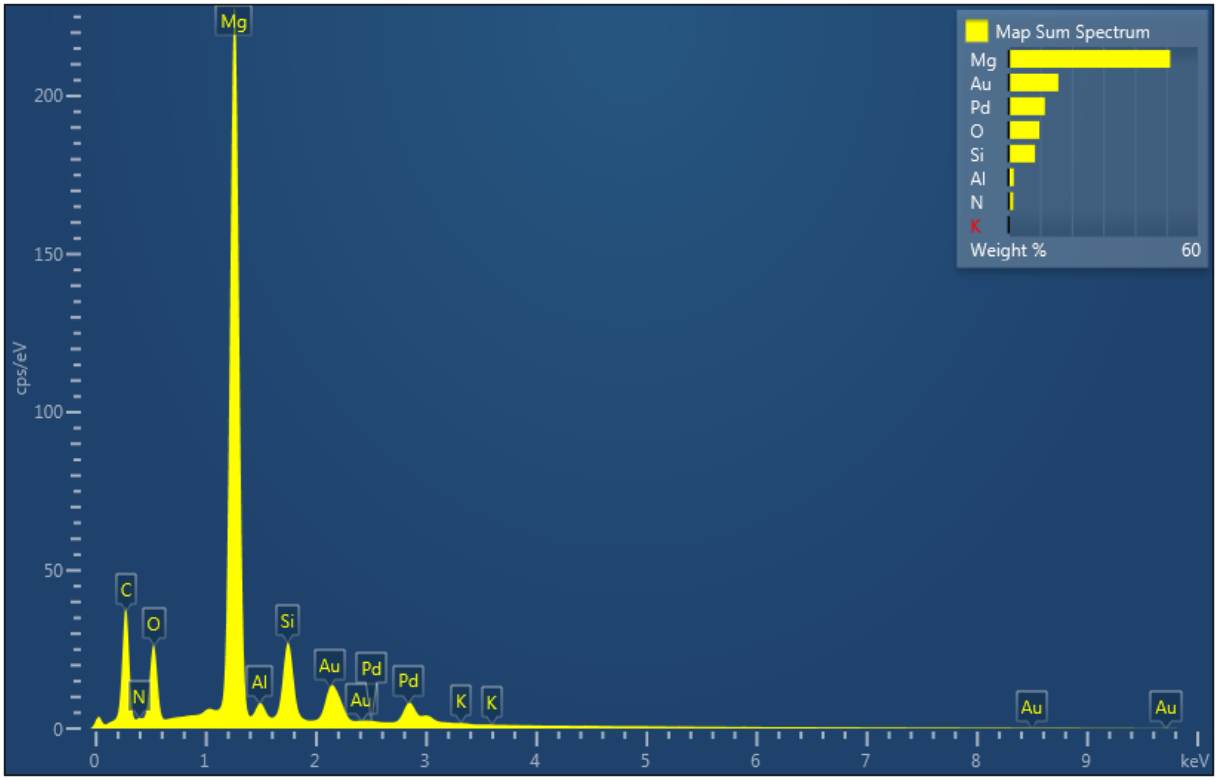
Map Sum Spectrum
Mg
Au
Pd
O
Si
Al
N
K
Weight %
60
cps/eV
200
150
100
50
0
0
1
2
3
4
5
6
7
8
9
keV
Mg
C
O
N
Al
Si
Au
Pd
Au
Pd
K
K
Au
Au